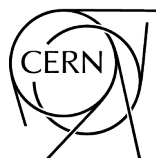


# Physics at the FCC-hh, a 100 TeV $pp$ collider

Editor: M. L. Mangano



CERN Yellow Reports: Monographs

Published by CERN, CH-1211 Geneva 23, Switzerland

ISBN 978-92-9083-453-3 (paperback)

ISBN 978-92-9083-454-0 (PDF)

ISSN 2519-8068 (Print)

ISSN 2519-8076 (Online)

DOI <https://doi.org/10.23731/CYRM-2017-003>

Accepted for publication by the CERN Report Editorial Board (CREB) on 19 June 2017

Available online at <https://e-publishing.cern.ch/> and <https://cds.cern.ch/>

Copyright © CERN, 2017, unless otherwise specified

© Creative Commons Attribution 4.0

Knowledge transfer is an integral part of CERN's mission.

CERN publishes this volume Open Access under the Creative Commons Attribution 4.0 license (<http://creativecommons.org/licenses/by/4.0/>) in order to permit its wide dissemination and use.

The submission of a contribution to a CERN Yellow Reports series shall be deemed to constitute the contributor's agreement to this copyright and license statement. Contributors are requested to obtain any clearances that may be necessary for this purpose.

This volume is indexed in: CERN Document Server (CDS), INSPIRE.

This volume should be cited as:

Physics at the FCC-hh, a 100 TeV *pp* collider, edited by M. L. Mangano, CERN Yellow Reports: Monographs, Vol.3/2017, CERN-2017-003-M (CERN, Geneva, 2017). <https://doi.org/10.23731/CYRM-2017-003>

A contribution in this volume should be cited as:

[Author name(s)], in Physics at the FCC-hh, a 100 TeV *pp* collider, edited by M. L. Mangano, CERN Yellow Reports: Monographs, Vol.3/2017, CERN-2017-003-M (CERN, Geneva, 2017), pp. [first page] – [lastpage], <https://doi.org/10.23731/CYRM-2017-003>. [first page]

# Foreword

A 100 TeV  $pp$  collider is under consideration, by the high-energy physics community [1, 2], as an important step for the future development of our field, following the completion of the LHC and High-luminosity LHC physics programmes. In particular, CERN is considering 100 TeV  $pp$  collisions as the key target of a Future Circular Collider facility [1], built around a  $\sim 100$  km tunnel and designed to deliver  $pp$ ,  $e^+e^-$  and  $ep$  collisions, in addition to a programme with heavy ion beams and with the injector complex. CERN is coordinating an international study tasked with the completion, by the end of 2018, of a Conceptual Design Report (CDR) for this facility.

This document presents the first results of the assessment of the physics potential of the hadronic part of this research programme (FCC-hh). The general considerations on the strengths and reach of very high energy hadron colliders were introduced long ago in the classic pre-SSC EHLQ review [3]. The main physics motivations for a 100 TeV  $pp$  collider, in the light of the status of high energy physics after the first years of LHC data, were recently discussed in [4]. Here, we take a more systematic look, collecting the results of many studies that have been carried out since the launch of the FCC initiative in 2014. The five Chapters of this Report address (i) the general features of Standard Model processes and observables at 100 TeV, (ii) the potential for precision and discovery physics in the electroweak symmetry breaking sector, (iii) the targets and prospects of the searches for physics Beyond the Standard Model, (iv) the goals of a heavy ion programme with collisions of Pb ions, and (v) a first overview of the potential of the collider injector complex. A first attempt at defining the luminosity goals of the 100 TeV collider was presented recently in [5]. The resulting targets, in the range of 20-30  $\text{ab}^{-1}$ , are consistent with the preliminary luminosity estimates provided by the accelerator studies [1], and will be used throughout this report.

The studies presented here are mostly of phenomenological nature. The purpose is to illustrate the immense physics potential of the FCC-hh, in the light of the key questions that may be left still open after the completion of the LHC programme and of the other ongoing and forthcoming experimental efforts in high-energy physics worldwide. Work is now underway to define reference detector designs, and to evaluate them in detail simulating in a more realistic way some of the outstanding physics benchmarks that have emerged from this report. This work, and new ideas that are now emerging in the literature on a daily basis, will converge in the CDR, for a more complete and robust overall assessment of the preliminary projections discussed here.

Studies on the physics programme of the  $e^+e^-$  collider (FCC-ee) and of the  $ep$  collider (FCC-eh) are proceeding in parallel, and preliminary results are documented in [6] (for FCC-ee) and in [7] (for the LHeC precursor of FCC-eh). A global assessment of the overall complementarity and synergy of these three components of the FCC programme will be documented in the CDR.

I warmly thank all editors and authors of the five Chapters of this volume, for the dedication and enthusiasm that have driven their work over the two years of preparation of this Yellow Report.

M. L. Mangano

## References

- [1] M. Benedikt, FCC study overview and status, talk at the FCC week 2016, Rome, 11-15 April 2016. <http://indico.cern.ch/event/438866/contributions/1085016/>

- [2] CEPC project website. <http://cepc.ihep.ac.cn>
- [3] E. Eichten, I. Hinchliffe, K. D. Lane, and C. Quigg, Super Collider Physics, *Rev. Mod. Phys.* 56 (1984) 579–707. [Addendum: *Rev. Mod. Phys.* 58,1065(1986)].
- [4] N. Arkani-Hamed, T. Han, M. Mangano, and L.-T. Wang, Physics Opportunities of a 100 TeV Proton-Proton Collider, arXiv:1511.06495 [hep-ph].
- [5] I. Hinchliffe, A. Kotwal, M. L. Mangano, C. Quigg, and L.-T. Wang, Luminosity goals for a 100-TeV pp collider, *Int. J. Mod. Phys. A* 30 (2015) no. 23, 1544002, arXiv:1504.06108 [hep-ph].
- [6] TLEP Design Study Working Group Collaboration, M. Bicer et al., First Look at the Physics Case of TLEP, *JHEP* 01 (2014) 164, arXiv:1308.6176 [hep-ex].
- [7] LHeC Study Group Collaboration, J. L. Abelleira Fernandez et al., A Large Hadron Electron Collider at CERN: Report on the Physics and Design Concepts for Machine and Detector, *J. Phys. G* 39 (2012) 075001, arXiv:1206.2913 [physics.acc-ph].

# Contents

<b>Foreword</b>	<b>iii</b>
<b>Chapter 1: Standard Model Processes</b>	<b>1</b>
1 Introduction	3
2 Parton distribution functions	4
2.1 Introduction	4
2.2 PDFs and their kinematical coverage at 100 TeV	5
2.3 PDF luminosities at 100 TeV	11
2.4 The top quark as a massless parton	14
2.5 Photon- and lepton-initiated processes at 100 TeV	17
2.6 Electroweak gauge bosons as massless partons	24
2.7 High-energy resummation of PDF evolution	27
3 Global event properties	31
3.1 Minimum bias collisions	32
3.2 Underlying event in high- $p_T$ triggered events	39
4 Inclusive vector boson production	44
4.1 Inclusive $W/Z$ rates and distributions	44
4.2 $W/Z$ boson production at small $q_T$	46
4.3 DY production at large $p_T$ and at large mass	48
4.4 Production of gauge bosons at the highest energies	49
5 $V$ +jets	53
5.1 Setup	53
5.2 Inclusive cross sections	55
5.3 Cross-section ratios	60
5.4 Scaling behaviour: jet multiplicities or transverse momenta	66
5.5 Perturbative stability	66
6 Vector boson and heavy flavours	70
6.1 Overview	70
6.2 Fully differential $Wb\bar{b} + X$ production	71
7 Gauge boson pair production	81
7.1 ZZ production	81
7.2 WW production	83
7.3 $\gamma\gamma$ production	87
7.4 Anomalous couplings from $WW$ and $W\gamma$ production	91
7.5 $VV$ +jet production	94
8 Electroweak production of gauge bosons in VBF and VBS processes	100
8.1 Input parameters and setup	100
8.2 $W^+W^+jj$	101
8.3 $W^+Zjj$	104
8.4 $ZZjj$	104
8.5 $W^+W^-jj$	106

8.6	Single gauge-boson production via VBF . . . . .	107
8.7	Benchmark cross sections . . . . .	108
9	Jets . . . . .	111
9.1	Inclusive jet and dijet production . . . . .	111
9.2	Spectroscopy with high-mass dijets . . . . .	112
9.3	SM physics of boosted objects . . . . .	115
9.4	Boosted boson tagging . . . . .	126
9.5	Jet fragmentation at large $p_T$ . . . . .	130
10	Multijets . . . . .	137
10.1	Computational setup . . . . .	137
10.2	Leading order inclusive cross sections and distributions . . . . .	138
10.3	NLO cross sections and K-factors . . . . .	141
10.4	Scaling behaviour in multi-jet production . . . . .	146
11	Heavy flavour production . . . . .	152
11.1	Inclusive bottom production . . . . .	154
11.2	Inclusive top pair production . . . . .	155
11.3	Bottom and top production at large $Q^2$ . . . . .	157
11.4	Single top production . . . . .	160
12	Associated production of top quarks and gauge bosons . . . . .	163
12.1	$t\bar{t}V$ production . . . . .	163
12.2	Photon emission off the top quark decay products . . . . .	176
13	Top properties . . . . .	178
14	Production of multiple heavy objects . . . . .	182
14.1	Production of multiple gauge bosons . . . . .	183
14.2	Multi-top and top-vector-boson associated production . . . . .	185
14.3	Multi Higgs boson production by gluon fusion and VBF . . . . .	186
14.4	Multi Higgs boson production in association with top quarks or gauge bosons . . . . .	189
15	Loop-induced processes . . . . .	190
15.1	Cross-sections at 100 TeV . . . . .	190
16	Electroweak corrections . . . . .	193
16.1	Tools . . . . .	194
16.2	Drell-Yan . . . . .	195
16.3	Gauge boson pairs and Higgsstrahlung . . . . .	197
16.4	V+jets . . . . .	202
16.5	Di-jets . . . . .	209
16.6	$t\bar{t}$ , $t\bar{t}$ +jets and $t\bar{t}H$ . . . . .	212
16.7	Real radiation . . . . .	214
17	Sources of missing transverse energy . . . . .	220
	References . . . . .	221
<b>Chapter 2: Higgs and EW Symmetry Breaking Studies</b>		<b>255</b>
1	Introduction . . . . .	257
2	SM Higgs production . . . . .	259

2.1	Inclusive $gg \rightarrow H$ production . . . . .	259
2.2	Higgs plus jet and Higgs $p_T$ spectrum in $gg \rightarrow H$ . . . . .	266
2.3	Higgs plus jets production in $gg \rightarrow H$ . . . . .	271
2.4	Associated $VH$ production . . . . .	281
2.5	VBF Higgs production . . . . .	284
2.6	Associated $t\bar{t}H$ production . . . . .	295
2.7	Rare production modes . . . . .	301
3	Prospects for measurements of SM Higgs properties . . . . .	303
3.1	Higgs acceptance . . . . .	304
3.2	Small-BR $H$ final states at intermediate $p_T$ . . . . .	307
3.3	Associated $VH$ production . . . . .	310
3.4	Measurement of top Yukawa coupling from the $t\bar{t}H/t\bar{t}Z$ ratio . . . . .	313
3.5	Combined determination of $y_t$ and $\Gamma(H)$ from $t\bar{t}H$ vs $t\bar{t}t\bar{t}$ production . . . . .	315
3.6	Rare SM Exclusive Higgs decays . . . . .	319
4	Multi-Higgs production . . . . .	325
4.1	Parametrizing the Higgs interactions . . . . .	325
4.2	Double Higgs production from gluon fusion . . . . .	330
4.3	Triple Higgs production and the quartic Higgs self-coupling . . . . .	349
5	BSM aspects of Higgs physics and EWSB . . . . .	358
5.1	Introduction . . . . .	358
5.2	Overview . . . . .	358
5.3	Electroweak Phase Transition and Baryogenesis . . . . .	365
5.4	Dark Matter . . . . .	374
5.5	The Origins of Neutrino Mass and Left-right symmetric model . . . . .	377
5.6	Naturalness . . . . .	388
5.7	BSM Higgs Sectors . . . . .	398
	References . . . . .	412
<b>Chapter 3: Beyond the Standard Model Phenomena</b>		<b>441</b>
1	Introduction . . . . .	443
2	Supersymmetry . . . . .	446
2.1	Introduction . . . . .	446
2.2	Cross Sections for Production of SUSY Particles . . . . .	455
2.3	Stop Squarks . . . . .	458
2.4	Gluinos . . . . .	464
2.5	Squarks . . . . .	471
2.6	Electroweakinos . . . . .	473
2.7	Long-lived Charged Particles . . . . .	477
2.8	Indirect Probes . . . . .	480
2.9	Model-Specific Interpretations . . . . .	482
2.10	Supersymmetry Post-Discovery at 100 TeV . . . . .	486
2.11	Summary of Phenomenological Studies . . . . .	494
3	Dark Matter . . . . .	497

3.1	Introduction . . . . .	497
3.2	Experimental searches for DM . . . . .	499
3.3	WIMP Dark Matter, Standard Model Mediators . . . . .	504
3.4	WIMP Dark Matter, BSM Mediators (Simplified Models) . . . . .	517
3.5	WIMP, Non-Minimal Models . . . . .	533
3.6	Beyond WIMP DM . . . . .	535
3.7	DM Summary . . . . .	541
4	Other BSM Signatures . . . . .	544
4.1	New Bosonic Resonances . . . . .	548
4.2	New Fermionic Resonances . . . . .	578
4.3	Non-Resonant Signatures . . . . .	588
	References . . . . .	595
<b>Chapter 4: Heavy Ions at the Future Circular Collider</b>		<b>635</b>
1	Executive summary . . . . .	637
2	Heavy-ion performance of FCC-hh . . . . .	640
3	QGP studies: bulk properties and soft observables . . . . .	642
3.1	Global characteristics of Pb–Pb collisions . . . . .	642
3.2	Collective phenomena from heavy-ion to pp collisions . . . . .	644
3.3	Effect of the charm quark on the QGP equation of state . . . . .	647
3.4	Hadrochemistry . . . . .	647
4	QGP studies: hard probes . . . . .	649
4.1	Jet quenching . . . . .	649
4.2	Open and closed charm and bottom production . . . . .	654
5	Small- $x$ and nPDF studies . . . . .	659
5.1	Small- $x$ and nPDF studies in hadronic p–A and A–A collisions . . . . .	659
5.2	Exclusive photoproduction of heavy quarkonia . . . . .	669
6	Contributions to other sectors of high-energy physics . . . . .	671
6.1	Photon–photon collisions . . . . .	671
6.2	Fixed-target collisions using the FCC proton and lead beams . . . . .	674
	References . . . . .	679
<b>Chapter 5: Physics Opportunities with the FCC-hh Injectors</b>		<b>693</b>
1	Introduction . . . . .	694
2	CERN hadron injector complex for FCC . . . . .	695
2.1	FCC-hh proton pre-injector chain . . . . .	695
2.2	FCC High Energy Booster options . . . . .	695
3	Possibilities for a high-luminosity collider experiment in the HEB . . . . .	697
3.1	Physics opportunities with a very high luminosity pp collider . . . . .	697
3.2	Possible high luminosity insertion design in the different HEB lattices . . . . .	698
4	Performance reach of Fixed Target beams extracted from the FCC injectors . . . . .	699
4.1	Extraction types and limitations for Fixed Target beams . . . . .	699
4.2	Future opportunities using fixed-target beams at FCC-hh pre-injectors . . . . .	700

5 Polarized protons . . . . . 701  
5.1 EDM storage rings . . . . . 701  
5.2 Polarized beams for FCC in light of RHIC experience . . . . . 702  
6 Summary . . . . . 702  
References . . . . . 704



## Chapter 1: Standard Model Processes

*M.L. Mangano*<sup>1</sup>, *G. Zanderighi*<sup>1</sup> (conveners), *J.A. Aguilar Saavedra*<sup>2</sup>, *S. Alekhin*<sup>3,4</sup>, *S. Badger*<sup>5</sup>, *C.W. Bauer*<sup>6</sup>, *T. Becher*<sup>7</sup>, *V. Bertone*<sup>8</sup>, *M. Bonvini*<sup>8</sup>, *S. Boselli*<sup>9</sup>, *E. Bothmann*<sup>10</sup>, *R. Boughezal*<sup>11</sup>, *M. Cacciari*<sup>12,13</sup>, *C.M. Carloni Calame*<sup>14</sup>, *F. Caola*<sup>1</sup>, *J. M. Campbell*<sup>15</sup>, *S. Carrazza*<sup>1</sup>, *M. Chiesa*<sup>14</sup>, *L. Cieri*<sup>16</sup>, *F. Cimaglia*<sup>17</sup>, *F. Febres Cordero*<sup>18</sup>, *P. Ferrarese*<sup>10</sup>, *D. D'Enterria*<sup>19</sup>, *G. Ferrera*<sup>17</sup>, *X. Garcia i Tormo*<sup>7</sup>, *M. V. Garzelli*<sup>3</sup>, *E. Germann*<sup>20</sup>, *V. Hirschi*<sup>21</sup>, *T. Han*<sup>22</sup>, *H. Ita*<sup>18</sup>, *B. Jäger*<sup>23</sup>, *S. Kallweit*<sup>24</sup>, *A. Karlberg*<sup>8</sup>, *S. Kuttimalai*<sup>25</sup>, *F. Krauss*<sup>25</sup>, *A. J. Larkoski*<sup>26</sup>, *J. Lindert*<sup>16</sup>, *G. Luisoni*<sup>1</sup>, *P. Maierhöfer*<sup>27</sup>, *O. Mattelaer*<sup>25</sup>, *H. Martinez*<sup>9</sup>, *S. Moch*<sup>3</sup>, *G. Montagna*<sup>9</sup>, *M. Moretti*<sup>28</sup>, *P. Nason*<sup>29</sup>, *O. Nicrosini*<sup>14</sup>, *C. Oleari*<sup>29</sup>, *D. Pagani*<sup>30</sup>, *A. Papaefstathiou*<sup>1</sup>, *F. Petriello*<sup>31</sup>, *F. Piccinini*<sup>14</sup>, *M. Pierini*<sup>19</sup>, *T. Pierog*<sup>32</sup>, *S. Pozzorini*<sup>16</sup>, *E. Re*<sup>33</sup>, *T. Robens*<sup>34</sup>, *J. Rojo*<sup>8</sup>, *R. Ruiz*<sup>25</sup>, *K. Sakurai*<sup>25</sup>, *G. P. Salam*<sup>1</sup>, *L. Salfelder*<sup>23</sup>, *M. Schönherr*<sup>28</sup>, *M. Schulze*<sup>1</sup>, *S. Schumann*<sup>10</sup>, *M. Selvaggi*<sup>30</sup>, *A. Shivaji*<sup>14</sup>, *A. Siodmok*<sup>1,35</sup>, *P. Skands*<sup>20</sup>, *P. Torrielli*<sup>36</sup>, *F. Tramontano*<sup>37</sup>, *I. Tsinikos*<sup>30</sup>, *B. Tweedie*<sup>22</sup>, *A. Vicini*<sup>17</sup>, *S. Westhoff*<sup>38</sup>, *M. Zaro*<sup>13</sup>, *D. Zeppenfeld*<sup>32</sup>

<sup>1</sup> CERN, TH Department, CH-1211 Geneva, Switzerland

<sup>2</sup> Departamento de Física Teórica y del Cosmos, Universidad de Granada, E-18071 Granada, Spain

<sup>3</sup> II. Institute for Theoretical Physics, University of Hamburg, Germany

<sup>4</sup> Institute for High Energy Physics, 142281 Protvino, Moscow region, Russia

<sup>5</sup> Higgs Centre for Theoretical Physics, School of Physics and Astronomy, The University of Edinburgh, Edinburgh EH9 3JZ, Scotland, UK

<sup>6</sup> Ernest Orlando Lawrence Berkeley National Laboratory (LBNL), Physics Division and University of California, Berkeley, CA 94720, USA

<sup>7</sup> Albert Einstein Center for Fundamental Physics, Institut für Theoretische Physik, Universität Bern, Sidlerstrasse 5, CH-3012 Bern, Switzerland

<sup>8</sup> Rudolf Peierls Centre for Theoretical Physics, University of Oxford, 1 Keble Road, Oxford OX1 3NP, UK

<sup>9</sup> Dipartimento di Fisica, Università di Pavia and INFN Sezione di Pavia, via A. Bassi 6, I-27100 Pavia, Italy

<sup>10</sup> II. Physikalisches Institut, Georg-August-Universität Göttingen, 37077 Göttingen, Germany

<sup>11</sup> Argonne National Laboratory, High Energy Physics Division, Bldg 362, 9700 South Cass Avenue, Argonne, IL 60439, USA

<sup>12</sup> Université Paris Diderot, F-75013 Paris, France

<sup>13</sup> Sorbonne Universités, UPMC Univ. Paris 06, UMR 7589, LPTHE, F-75005, Paris, France; CNRS, UMR 7589, LPTHE, F-75005, Paris, France

<sup>14</sup> INFN Sezione di Pavia, via A. Bassi 6, I-27100 Pavia, Italy

<sup>15</sup> Theory Group, Fermilab, PO Box 500, Batavia, IL, USA

<sup>16</sup> Universität Zürich, Physik-Institut, Winterthurerstrasse 190, CH-8057 Zürich, Switzerland

<sup>17</sup> Dipartimento di Fisica, Università degli Studi di Milano and INFN, Sezione di Milano, Via Celoria 16, I-20133 Milano, Italy

<sup>18</sup> Fakultät für Mathematik und Physik, Physikalisches Institut, Hermann-Herder-Strasse 3, 79104 Freiburg, Germany

<sup>19</sup> CERN, EP Department, CH-1211 Geneva, Switzerland

<sup>20</sup> School of Physics and Astronomy, Monash University, VIC-3800, Australia

<sup>21</sup> SLAC, National Accelerator Laboratory, 2575 Sand Hill Road, Menlo Park, CA 94025-7090, USA

<sup>22</sup> Department of Physics and Astronomy, Univ. of Pittsburgh, Pittsburgh, PA 15260, USA

<sup>23</sup> Institute for Theoretical Physics, University of Tübingen, Auf der Morgenstelle 14, 72076 Tübingen, Germany

<sup>24</sup> Institut für Physik & PRISMA Cluster of Excellence, Johannes Gutenberg Universität, 55099 Mainz, Germany

<sup>25</sup> Institute for Particle Physics Phenomenology, Durham University, Durham DH1 3LE, UK

<sup>26</sup> Center for the Fundamental Laws of Nature, Harvard University, Cambridge, MA 02138 USA

<sup>27</sup> Physikalisches Institut, Albert-Ludwigs-Universität Freiburg, 79104 Freiburg, Germany

<sup>28</sup> Dipartimento di Fisica e Scienze della Terra, Università di Ferrara and INFN, Sezione di Ferrara, v. Saragat 1, I-44100 Ferrara, Italy

<sup>29</sup> Università di Milano-Bicocca and INFN, Sezione di Milano-Bicocca, Piazza della Scienza 3, 20126 Milano, Italy

<sup>30</sup> Center for Cosmology, Particle Physics and Phenomenology (CP3), Université Catholique de Louvain, Chemin du Cyclotron 2, B-1348 Louvain-la-Neuve, Belgium

<sup>31</sup> Northwestern University, Department of Physics and Astronomy, 2145 Sheridan Road, Evanston, Illinois 60208-3112, USA

<sup>32</sup> Institute for Theoretical Physics, Karlsruhe Institute of Technology, 76128 Karlsruhe, Germany

<sup>33</sup> LAPTH, Univ. de Savoie, CNRS, B.P.110, Annecy-le-Vieux F-74941, France

<sup>34</sup> IKTP, TU Dresden, Zellescher Weg 19, 01069 Dresden, Germany

<sup>35</sup> Institute of Nuclear Physics, Polish Academy of Sciences, ul. Radzikowskiego 152, 31-342 Krakow, Poland

<sup>36</sup> Dipartimento di Fisica, Università di Torino, and INFN, Sezione di Torino, Via P. Giuria 1, I-10125, Turin, Italy

<sup>37</sup> Università di Napoli “Federico II” and INFN, Sezione di Napoli, 80126 Napoli, Italy

<sup>38</sup> Institut für Theoretische Physik, Universität Heidelberg, 69120 Heidelberg, Germany

### **Abstract**

This Chapter documents the production rates and typical distributions for a number of benchmark Standard Model processes, and discusses new dynamical phenomena arising at the highest energies available at this collider. We discuss the intrinsic physics interest in the measurement of these Standard Model processes, as well as their role as backgrounds for New Physics searches.

## 1 Introduction

Standard Model particles play multiple roles in the 100 TeV collider environment. In the context of BSM phenomena, and for most scenarios, new BSM particles eventually decay to the lighter SM states, which therefore provide the signatures for their production. BSM interactions, furthermore, can influence the production properties of SM particles, and the observation of SM final states can probe the existence of an underlying BSM dynamics. SM processes therefore provide both signatures and potential backgrounds for any exploration of BSM phenomena. SM backgrounds have an impact on BSM studies in different ways: on one side they dilute, and can hide, potential BSM signals; on the other, SM processes influence the trigger strategies, since they determine the irreducible contributions to trigger rates and may affect the ability to record data samples of interest to the BSM searches.

The observation of SM processes has also an interest per se. The huge rates available at 100 TeV allow, in principle, to push to new limits the exploration of rare phenomena (e.g. rare decays of top quarks or Higgs bosons), the precision in the determination of SM parameters, and the test of possible deviations from SM dynamics. The extremely high energy kinematical configurations probe the shortest distances, and provide an independent sensitivity to such deviations.

Finally, SM processes provide a necessary reference to benchmark the performance of the detectors, whether in the context of SM measurements, or in the context of background mitigation for the BSM searches.

In this Chapter we review the key properties of SM processes at 100 TeV, having in mind the above considerations. This will serve as a reference for future studies, and to stimulate new ideas on how to best exploit the immense potential of this collider. We shall focus on the production of key SM objects, such as jets, heavy quarks, gauge bosons. The SM Higgs boson will be discussed in the Higgs Chapter of this report [1]. We shall not address issues like the current or expected precision relative to given processes. On one side, and with some well understood exceptions notwithstanding, leading-order calculations are typically sufficient to give a reliable estimate of the production rates, and assess possible implications for trigger rates, background contributions, and detector specifications. On the other, any statement about the precision of theoretical calculations made today will be totally obsolete by the time this collider will operate, and assumptions about the accuracy reach cannot but be overly conservative.

## 2 Parton distribution functions<sup>1</sup>

### 2.1 Introduction

The accurate determination of the parton distribution functions (PDFs) of the proton is an essential ingredient of the LHC physics program [2–6], and will be even more so at any future higher-energy hadron collider. In particular, a new hadron collider with a center-of-mass energy of  $\sqrt{s} = 100$  TeV will probe PDFs in several currently unexplored kinematical regions, such as the ultra low- $x$  region,  $x \lesssim 10^{-5}$ , or the region of very large momentum transfers,  $Q^2 \geq (10 \text{ TeV})^2$ . In addition, concerning the phenomenological implications of PDFs, the situation is much more complex (and interesting) than simply assuming that the FCC can be treated as a rescaled version of the LHC. Indeed, understanding PDFs at 100 TeV involves addressing a number of qualitatively new phenomena that have received limited attention up to now.

It is extremely difficult to forecast what the status of our knowledge about the proton structure will be in 20 or 25 years from now. Progress in PDF determinations [7–13] will strongly depend, on the one hand, on the full exploitation of the information on PDF-sensitive measurements contained by LHC Run I and Run II data [4], as well as by the corresponding HL-LHC measurements, and on the other hand, on the progress in higher-order calculational techniques allowing to include many LHC differential distributions in the PDF analysis at NNLO (and beyond), see [14–16] for some recent examples.

Moreover, progress in global PDF analysis can also be driven by methodological improvements, for instance in more efficient methods to parametrize PDFs, or better techniques to estimate experimental, model, and theoretical PDF uncertainties. Another important factor to take into account is the fact that our understanding of the proton structure would be substantially improved in the case a new electron-nucleon collider would be operative before the start-up of the FCC operations, such as the Large Hadron Electron Collider (LHeC) at CERN [17] or the Electron Ion Collider (EIC) in the U.S.A. [18]. In addition, in the long term, progress in non-perturbative lattice calculations might also shed further light on the proton structure and provide a useful complement to global PDF fits.

For these reasons, in this section we will concentrate on qualitative aspects of PDFs that are important for a exploratory evaluation of the physics potential of the FCC, which is the main goal of this report. In particular we will focus on:

- What are the most relevant generic differences for PDFs when moving from the LHC energies,  $\sqrt{s} = 14$  TeV, to the FCC energies,  $\sqrt{s} = 100$  TeV. This includes the kinematical coverage in the  $(x, Q^2)$  plane of a 100 TeV collider, the ratios of PDF luminosities and their uncertainties between  $\sqrt{s} = 100$  TeV and  $\sqrt{s} = 14$  TeV, and the assessment of how available PDF sets extrapolate into the new kinematical regions covered by the FCC.
- Qualitatively new phenomena about PDFs and DGLAP evolution that, while not essential for the exploitation of the LHC data, might become relevant at the extreme energies at which the FCC would operate. These include QED and weak effects in the PDF evolution, high-energy resummation effects, and the possibility of treating the top quark as a massless parton. In addition, we also study the role of photon-initiated contributions for electroweak processes at 100 TeV.

The outline of this section is the following. In Section 2.2 we quantify the coverage of PDFs at the FCC in the  $(x, Q^2)$  plane, and study the behavior of PDFs in the extreme large- $x$ , large- $Q^2$  and small- $x$  regions accessible at the FCC. In Section 2.3 we present a comparison of PDF luminosities at 100 TeV for the most updated global PDF sets, and compute various ratios of parton luminosities between 100 TeV and 14 TeV. In Section 2.4 we study the validity of the massless approximation for the top quark at a 100 TeV collider. In Section 2.5 we quantify the role of photon and lepton-initiated contributions at 100 TeV, relevant when electroweak corrections are accounted for. In Section 2.6 we explore the possibility of

---

<sup>1</sup>Editor: J. Rojo

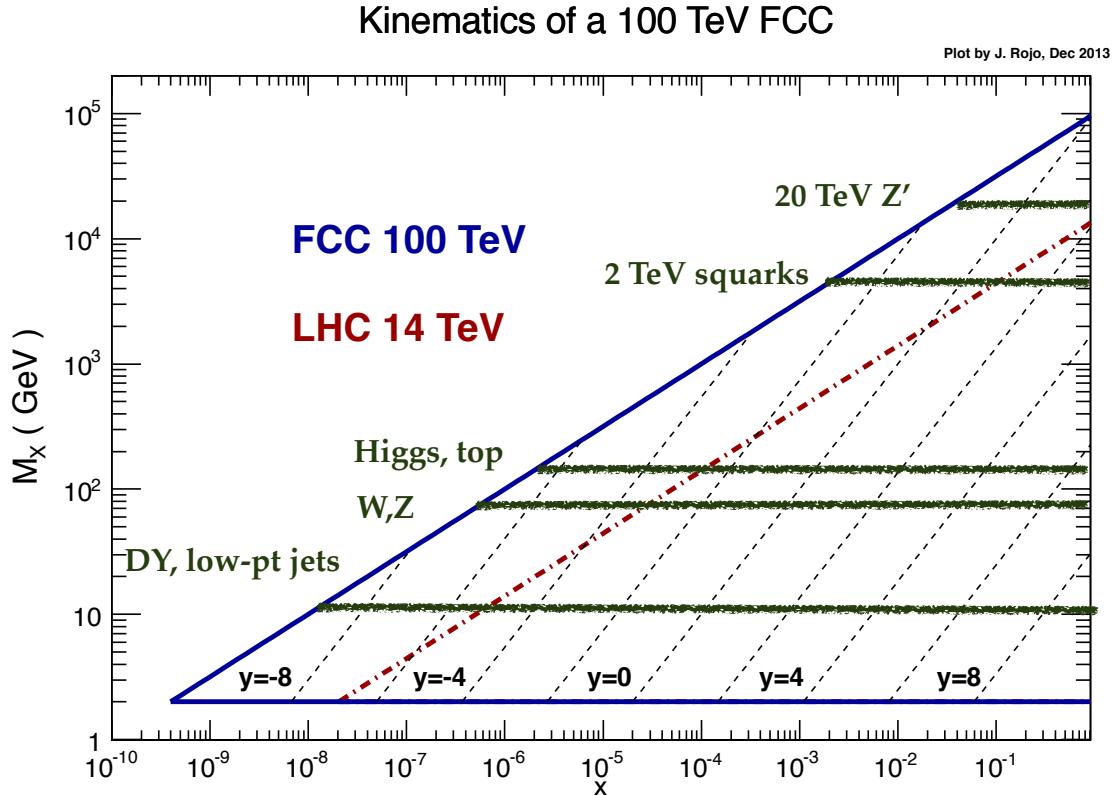


Fig. 1: Kinematical coverage in the  $(x, M_X)$  plane of a  $\sqrt{s} = 100$  TeV hadron collider (solid blue line), compared with the corresponding coverage of the LHC at  $\sqrt{s} = 14$  TeV (dot-dashed red line). The dotted lines indicate regions of constant rapidity  $y$  at the FCC. We also indicate the relevant  $M_X$  regions for phenomenologically important processes, from low masses (Drell-Yan, low  $p_T$  jets), electroweak scale processes (Higgs,  $W$ ,  $Z$ , top), and possible new high-mass particles (squarks,  $Z'$ ).

treating electroweak gauge bosons as massless and their inclusion into the DGLAP evolution equations. Finally in Section 2.7 we discuss the possible relevance of high-energy (small- $x$ ) resummation effects for a 100 TeV collider.

## 2.2 PDFs and their kinematical coverage at 100 TeV

We begin by quantifying the kinematical coverage in the  $(x, M_X)$  plane that PDFs probe in a 100 TeV hadron collider, with  $M_X$  being the invariant mass of the produced final states. In Fig. 1 we represent the kinematical coverage in the  $(x, M_X)$  plane of a  $\sqrt{s} = 100$  TeV hadron collider compared with the corresponding coverage of the LHC at  $\sqrt{s} = 14$  TeV. The dotted lines indicate regions of constant rapidity  $y$  at the FCC. In this plot, we also indicate the relevant  $M_X$  regions for phenomenologically important processes, from low masses (such as Drell-Yan or low  $p_T$  jets), electroweak scale processes (such as Higgs,  $W$ ,  $Z$ , or top production), and possible new high-mass particles (such as a 2 TeV squark or a 20 TeV  $Z'$ ).

In the low-mass region, for  $M_X \leq 10$  GeV, PDFs would be probed down to  $x \simeq 5 \cdot 10^{-5}$  in the central region,  $y \simeq 0$ , and down to  $x \simeq 5 \cdot 10^{-7}$  at forward rapidities,  $y \simeq 5$ . At even forward rapidities, for example those that can be probed by using dedicated detectors down the beam pipe, PDFs could be probed down to  $x \simeq 10^{-8}$ . While these extreme regions of very low  $x$  are not relevant for neither electroweak scale physics nor for high-mass New Physics searches, they are crucial for the tuning of soft and semi-hard physics in Monte Carlo event generators [19] and therefore it is important to ensure that the PDFs exhibit a sensible behaviour in this region. Moreover, forward instrumentation would also be

relevant for the measurement of the total  $pp$  cross-section at 100 TeV as well as to provide input for the modelling of ultra-high energy cosmic ray collisions [20]. The prospects for soft physics at the FCC is studied in detail in Section 3 of this report.

Concerning the production of electroweak particles such as weak gauge bosons, the Higgs boson and top quarks, PDFs are probed down to  $x \simeq 5 \cdot 10^{-4}$  in the central region,  $y \simeq 0$ , and down to  $x \simeq 2 \cdot 10^{-6}$  at forward rapidities,  $y \simeq 5$ . This indicates that a good coverage of the forward region is also instrumental for electroweak scale physics, whose production is much less central than at the LHC. In the case of Higgs production, if the Higgs can be reconstructed up to rapidities of  $y \simeq 4$ , then this process would probe PDFs down to  $x \simeq 10^{-5}$ . Therefore, at a 100 TeV hadron collider a good knowledge of small- $x$  PDFs becomes crucial not only for soft and semi-hard physics, or for low scale processes such as low-mass Drell-Yan or charm production, but also for electroweak scale processes.

In the high-invariant mass region,  $M_X \geq 5$  TeV, only medium and large- $x$  PDFs would be probed, and these are currently known with reasonable accuracy, except for very high  $M_X$  values. For instance, for the pair-production of 2 TeV squarks, only the knowledge of PDFs for  $x \gtrsim 10^{-3}$  is required. The production of multi-TeV heavy particles is of course very central, requiring instrumentation only down to  $|y| \simeq 3$  at most. For the heavier particles that can be probed at the FCC, such as a 20 or 30 TeV  $Z'$ , PDFs have large uncertainties since the very large- $x$  region is being probed, and this region is affected by the lack of direct constraints, as we discuss below.

In Table 1 we summarize the kinematical coverage in the  $(x, M_X)$  plane for various phenomenologically important processes at the FCC, both for central, intermediate and forward rapidities. For each value of the invariant mass  $M_X$  and the absolute rapidity  $|y|$ , the smallest value of Bjorken- $x$  required corresponds to  $x_{\min} = (M_X/\sqrt{s}) \exp(-|y|)$ . This table conveys a similar message to that of Fig. 1: at a 100 TeV hadron collider, accurate knowledge of PDFs is required in a very wide kinematical region, ranging from ultra low- $x$  to very large- $x$ , and from momentum transfers close to  $\Lambda_{\text{QCD}}$  up to the highest values where the FCC has sensitivity for new heavy particles,  $M_X \simeq 50$  TeV. That is, a huge range spanning 8 orders of magnitude in  $x$  and 10 in  $Q^2$ .

Process	$M_X$	$x_{\min}$		
		$y = 0$	$ y  = 2$	$ y  = 4$
Soft QCD				
Charm pair production	1 (10) GeV	$10^{-5}$ ( $10^{-4}$ )	$1.4 \cdot 10^{-6}$ ( $1.4 \cdot 10^{-5}$ )	$1.8 \cdot 10^{-7}$ ( $1.8 \cdot 10^{-6}$ )
Low-mass Drell-Yan				
$W$ and $Z$ production				
Top pair production	80 (400) GeV	$8 \cdot 10^{-4}$ ( $4 \cdot 10^{-3}$ )	$1.1 \cdot 10^{-4}$ ( $5.4 \cdot 10^{-4}$ )	$1.5 \cdot 10^{-5}$ ( $7.3 \cdot 10^{-5}$ )
Inclusive Higgs				
Heavy New Physics	5 (25) TeV	0.05 (0.25)	0.007 (-)	–

Table 1: Kinematical coverage in the  $(x, M_X)$  plane for representative processes at a 100 TeV hadron collider. For each type of process (low mass, electroweak scale processes, and heavy new physics) we indicate the relevant range for the final-state invariant mass  $M_X$  and the approximate minimum value of  $x$  probed in the PDFs,  $x_{\min} = (M_X/\sqrt{s}) \exp(-|y|)$ , for central ( $y = 0$ ), intermediate ( $|y| = 2$ ) and forward ( $|y| = 4$ ) rapidities.

Given this, it is important to verify that available PDF sets have a sensible behaviour in all the relevant kinematical regions, specially in the extrapolation regions at very small- $x$  and very large  $Q^2$  which are not relevant for most LHC applications. The goal here is not to understand similarities or differences between PDF sets, but to ensure that PDF sets that will be used for FCC simulations have a physical behaviour in the entire range of  $x$  and  $Q$  required.

In the following, PDFs are accessed through the LHAPDF6 interface [21], version 6.1.5, with the most updated grid data files. It should be emphasized the importance of using this specific version, since previous versions had different options for the default PDF extrapolations. In addition, both the interpolation accuracy and the treatment of the extrapolation regions, as well as the overall computa-

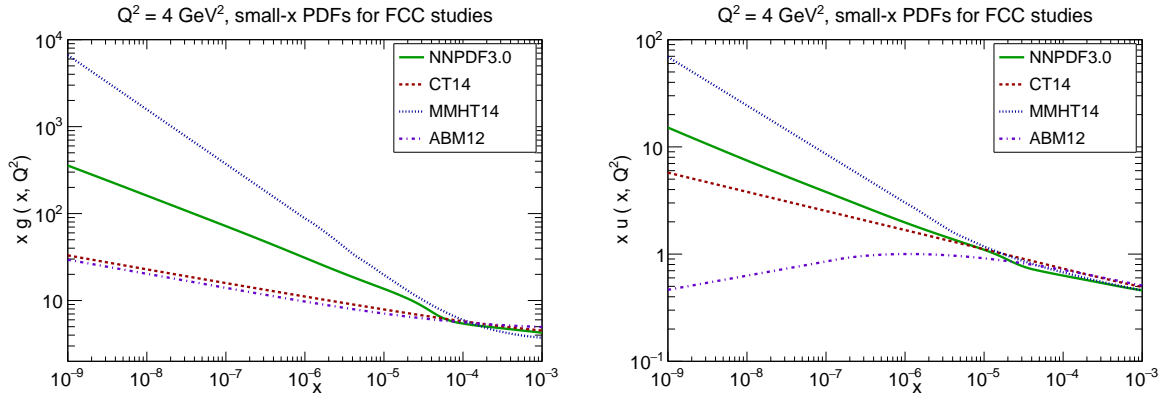


Fig. 2: Central values of the gluon (left) and the up quark PDFs (right) at NLO, comparing the ABM12, CT14 and MMHT14 and NNPDF3.0 sets for  $Q^2 = 4 \text{ GeV}^2$ . All PDF sets shown are NLO except for ABM12 where the NNLO set is used. In this small- $x$  region, PDF uncertainties (not shown here) can be large, see Fig. 3.

tional performance, have been substantially improved in LHAPDF6 as compared to its Fortran counterpart LHAPDF5, and therefore the use of the latter for FCC studies should be discouraged.<sup>2</sup>

We begin by discussing the PDF behavior in the small- $x$  extrapolation region. As shown in Fig. 1, for low scales and forward rapidities, as those required for the description of soft QCD physics and for Monte Carlo tuning, knowledge of PDFs would be required down to  $x \gtrsim 10^{-9}$ . In Fig. 2 we show the central values of the gluon (upper) and the up quark PDFs (lower plots), comparing ABM12, CT14, MMHT14 and NNPDF3.0 for  $Q^2 = 4 \text{ GeV}^2$ . All PDF sets shown are NLO except for ABM12 where the NNLO set is used. The comparison is performed down to  $x = 10^{-9}$ , to ensure that the entire region relevant for FCC studies is covered. In all cases we observe a sensible extrapolation into the very small- $x$  region. Here we use the default extrapolating settings of LHAPDF6.1.5, and we verified that the behaviour was instead unphysical if older versions were used, where PDFs were frozen for some  $x \leq x_{\min}$  threshold.

While in Fig. 2 we only show the central values of the three PDF sets, in the small- $x$  region these are affected by substantial uncertainties [22] due to the lack of direct experimental constraints, for instance, the HERA structure functions data stops at  $x_{\min} \simeq 5 \cdot 10^{-5}$ , see for instance the measurement of the longitudinal structure function  $F_L(x, Q^2)$  [11, 23]. To illustrate this point, in Fig. 3 we show the relative 68% CL PDF uncertainties at  $Q^2 = 100 \text{ GeV}^2$  in the small- $x$  region for the ABM12, CT14, MMHT14 and NNPDF3.0 NNLO sets. Depending on the model chosen to parametrize PDF uncertainties towards the region without experimental constraints, we observe a rapid increase in PDF uncertainties for some sets (CT14, MMHT, NNPDF3.0), where for  $x < 10^{-5}$  uncertainties are already larger than 50%, while other sets (ABM12, but also CJ15, JR14 not shown here) display small PDF uncertainties down to  $x = 10^{-7}$ .

Recently, a number LHC measurements to constrain PDFs at small- $x$  has been proposed. The use of charmed meson forward production from LHCb has been recently shown [22, 24, 25] to provide useful constraints on the small- $x$  gluon PDF.<sup>3</sup> Another possibility is the use of forward quarkonium production, such as  $J/\Psi$ , which has a similar sensitivity in  $x$  [26]. Taking this into account, one expects that before the FCC start-up our knowledge of the small- $x$  PDFs would be substantially improved. The corresponding measurements at the FCC have the potential to extend the constrains on the small- $x$  PDF by almost two orders of magnitude, though here the instrumentation of the forward region will be crucial. Measurements of very-small- $x$  PDFs are also of direct importance for particle astrophysics, such as the

<sup>2</sup>In LHAPDF5 the default extrapolation was simply to freeze the PDF below some value of  $x_{\min}$ , which could be as high as  $10^{-5}$  for some widely used PDF sets, which can potentially lead to incorrect results if used for FCC studies.

<sup>3</sup>The PDF dependence of heavy quark production at a 100 TeV collider is discussed in more detail in Sect. 11 of this report.

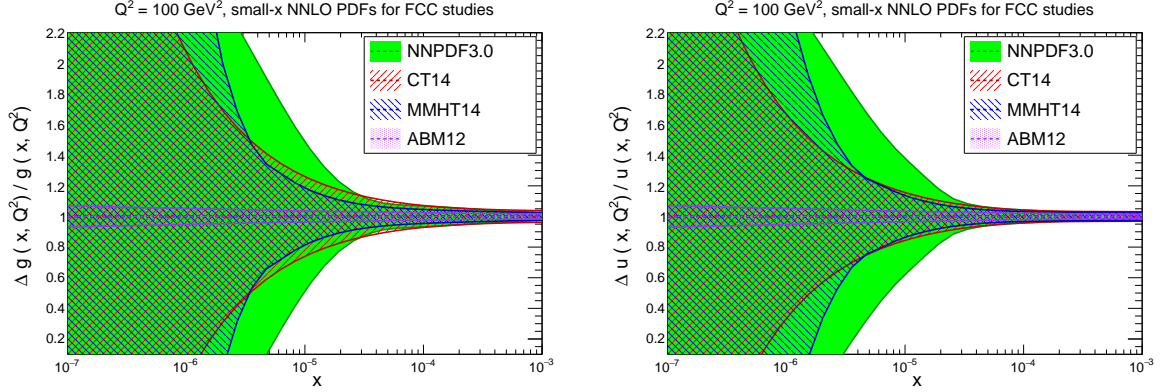


Fig. 3: The relative 68% CL PDF uncertainties at  $Q^2 = 100 \text{ GeV}^2$  in the small- $x$  region computed with the ABM12, CT14, MMHT14 and NNPDF3.0 NNLO sets. With the exception of ABM12, one finds a rapid increase in PDF uncertainties as we move towards the small- $x$  region  $x \lesssim 5 \cdot 10^{-5}$ , where current experimental information is limited.

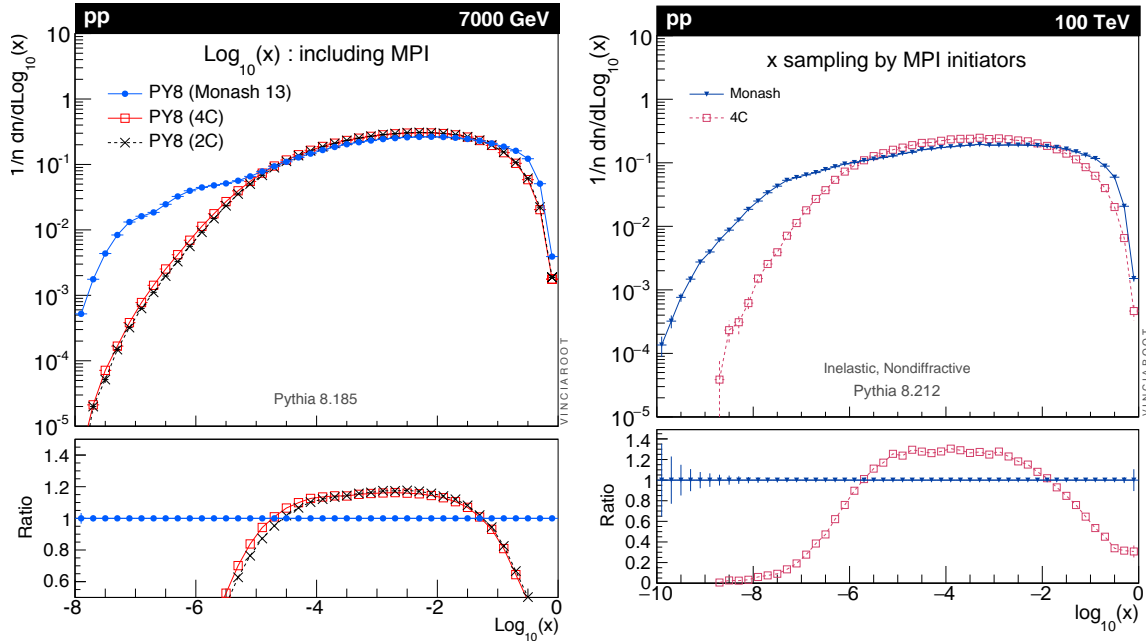


Fig. 4: Sampling of the values of Bjorken- $x$  probed in Multiple Parton Interactions (MPI) at the LHC 7 TeV (left) and at the FCC 100 TeV (right plot) in Pythia8 with the Monash 2013 tune, compared to older tunes, 4C and 2C (at 100 TeV we show only the comparison with the 4C tune). The lower panel shows the ratio between the Monash 2013 tune and the older Pythia8 tunes.

ultra-high-energy neutrino cross-sections [27] and the prompt lepton fluxes [28–30] that are required for the interpretation of the IceCube astrophysical neutrinos [31].

Another strategy to quantify the relevant range of Bjorken- $x$  for which PDFs are required in the modeling of soft and semi-hard physics at the FCC is by sampling of the values of  $x$  of the PDFs required in the calculation of Multiple Parton Interactions (MPI) for different values of the collider center-of-mass energy  $\sqrt{s}$ . In Fig. 4 we compare the MPI sampling of  $x$  between the LHC 7 TeV and the FCC 100 TeV using Pythia8.2 [32]. The results of the most update tune, Monash 2013 [19] are compared with the older tunes 2C and 4C [33]. From this comparison we observe that, with the Monash 2013 tune, at LHC7, PDFs with  $x \gtrsim 10^{-6}$  lead to a sizable contribution,  $\gtrsim 5\%$ , to the MPI distribution. With the same settings, the FCC100 samples values of  $x$  down to  $x \gtrsim 10^{-8}$ , a region far from any direct experimental

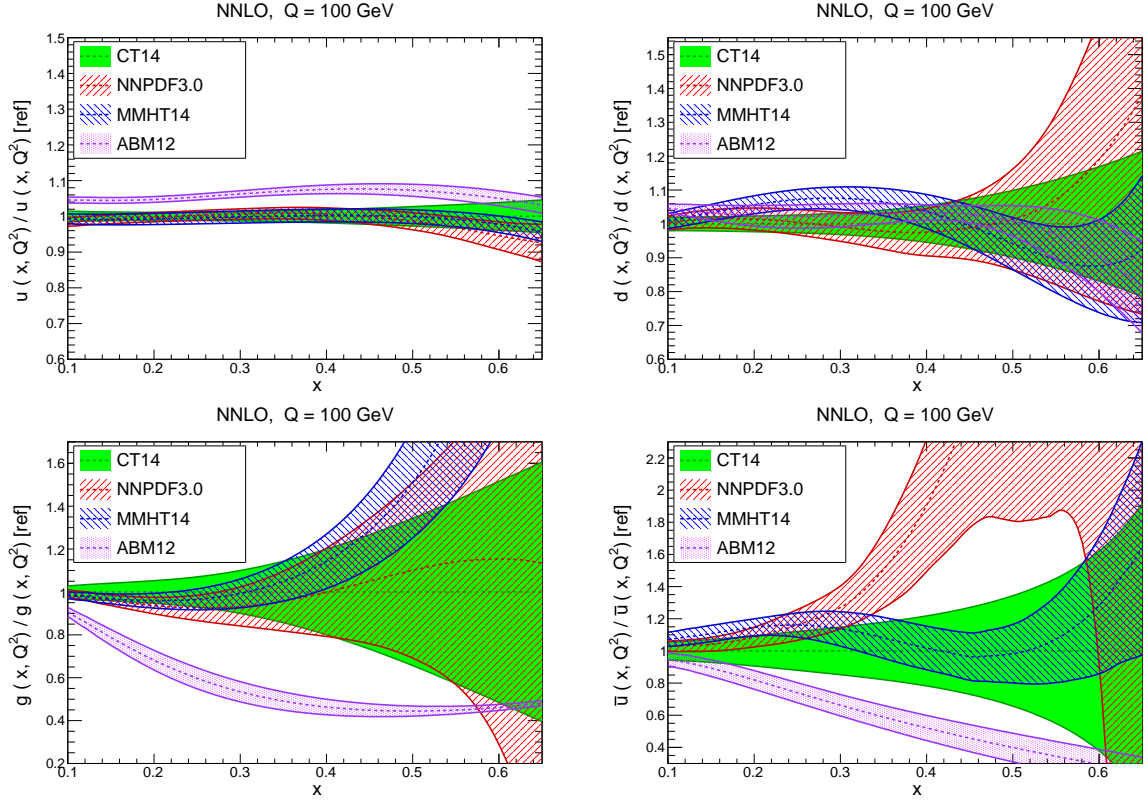


Fig. 5: The large- $x$  behaviour of the up, down, anti-up quark and gluon PDFs evaluated at  $Q = 100$  GeV. We compare the results of ABM12, CT14, MMHT14 and NNPDF3.0 NNLO, with the corresponding 68% CL PDF uncertainty in each case. The comparison is presented normalising to the central value of CT14.

constraint. This illustrates the relevance of ultra-low  $x$  PDFs for the modelling of soft QCD at a 100 TeV collider.

Now we turn to discuss the region of large values of Bjorken- $x$ . This region is also affected by substantial PDF uncertainties due to the limited direct experimental constraints. To estimate the coverage in the large- $x$  region, it is useful to use the result that for the production of a final state with invariant mass  $M_X$  and rapidity  $y$  at a hadron collider with center-of-mass energy  $\sqrt{s}$ , the LO values of the PDF momentum fractions  $x_1$  and  $x_2$  are  $x_{1,2} = (M_X/\sqrt{s}) \exp(\pm y)$ . Therefore, for a centrally produced final-state ( $y = 0$ ) of invariant mass  $M_X \simeq 7$  TeV (50 TeV) at  $\sqrt{s} = 14$  TeV (100 TeV) we will have  $\langle x_{1,2} \rangle \simeq 0.5$ , while already for slightly non-central production,  $y \simeq 0.5$ , PDFs are being probed up to  $x_1 \simeq 0.8$  for both colliders.

In Fig. 5 we illustrate the large- $x$  behaviour of the up, down, anti-up quark and gluon PDFs, evaluated at  $Q = 100$  GeV. We compare the results of the ABM12, CT14, NNPDF3.0 and MMHT14 NNLO PDF sets, with the corresponding 68% CL PDF uncertainty in each case, normalising to the central value of CT14.<sup>4</sup> As discussed above, the central production of a heavy system with  $M_X = 10$  (30 or 50) TeV would probe the large- $x$  PDFs for  $x \gtrsim 0.1$  (0.3 or 0.5) at a 100 TeV collider. As we can see, while for valence quarks (up and down) PDF uncertainties in the region relevant for heavy particle production at the FCC are moderate, for the gluon and anti-quarks PDF uncertainties are large, thus degrading the accuracy of any theory prediction that requires knowledge of PDFs in this region. In addition, there is a significant spread between the central values of the four sets.

As in the case of small- $x$ , new measurements from the LHC and other experiments should allow to

<sup>4</sup>In these plots, the ABM12 curves have been obtained using the internal interpolation routine provided by the authors, since the LHAPDF6 results were found to exhibit poor numerical stability at large  $x$ .

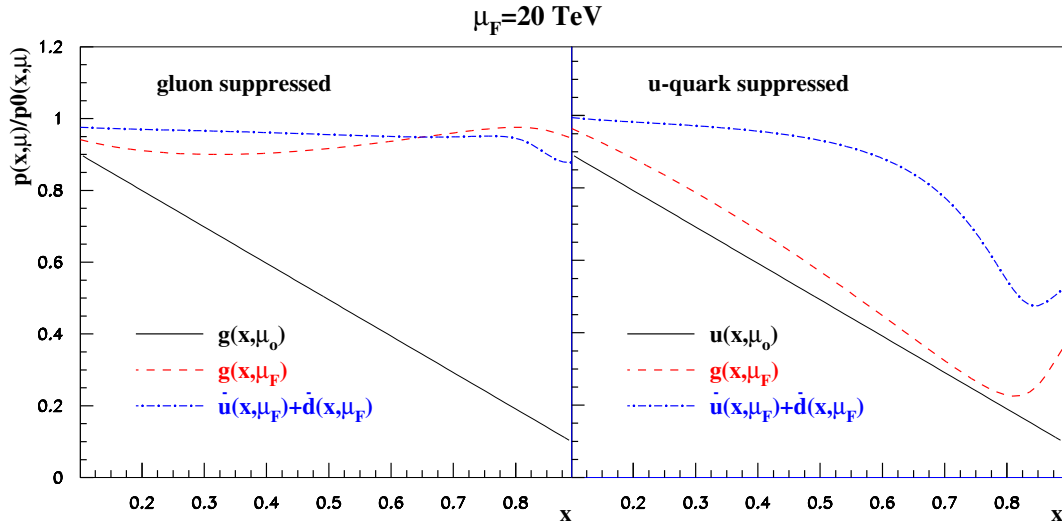


Fig. 6: The ratio of parton distributions,  $p(x, \mu)$  with respect to the initial parametrization  $p(x, \mu_0)$  for the gluon and sea distributions at large  $x$ . The solid line denotes the initial PDF  $p(x, \mu_0)$  suppressed by a factor of  $(1-x)$  for the gluon (left panel) and up quarks (right panel) and the dotted and dashed-dotted lines the respective results of the evolution up to  $\mu = 20$  TeV.

substantially reduce these PDF uncertainties before the start of FCC operations. For instance, the large- $x$  gluon can be constrained with data on inclusive and differential top quark pair production [34,35]. Moreover, since at large- $x$  and large- $Q$  the gluon and sea quark distributions receive large contributions from radiation off valence quarks, measurements aiming to constrain these will also lead to improved gluons and sea quarks in the kinematic region relevant for the FCC. This effect is illustrated in Fig. 6, where we show the ratio of parton distributions,  $p(x, \mu)$  with respect to the initial parametrization  $p(x, \mu_0)$  for the gluon and sea distributions at large  $x$ . The solid line denotes the initial PDF  $p(x, \mu_0)$  suppressed by a factor of  $(1-x)$  for the gluon (left panel) and up quarks (right panel) and the dotted and dashed-dotted lines the respective results of the evolution up to  $\mu = 20$  TeV. One should also note that, as in the case of small- $x$ , the behaviour of PDFs in the large- $x$  extrapolation region is sensitive to the underlying assumptions concerning the PDF parametrization [36].

PDFs at large- $x$  are also affected by a number of theoretical uncertainties, from potential higher twists, enhanced higher-order threshold logarithmic corrections, or nuclear effects from the inclusion in the PDF fit of deuteron and heavy nuclear data. A version of NNPDF3.0 including large- $x$  threshold resummation was presented in [37], and then used [38] to produce threshold-improved NLO+NLL predictions for high-mass squark and gluino production cross-sections at the LHC. This study showed that threshold logarithms in PDF fits are much smaller than PDF uncertainties, provided NNLO calculations are used. Therefore, PDFs with threshold resummation do not appear to be required for FCC studies, since NNLO and N3LO calculations will be the standard by then. Likewise, other theory uncertainties like higher twists and nuclear effects are subleading as compared to PDF uncertainties (see the discussion in [5, 39] and references therein), and moreover by the time the FCC starts operation, reliable collider-only PDF sets, free of these ambiguities, will be available.

The other kinematic region for which knowledge of PDFs will be required in a previously unexplored region is that of very large momentum transfers, for values of  $Q$  between 5 TeV and 50 TeV. This region is relevant for the production of possible massive BSM particles. As opposed to the small- and large- $x$  regions, the extrapolation into very high  $Q^2$  values is determined purely by perturbative DGLAP evolution, and therefore the only requirement is that that available PDF tabulations of current sets extend up to 100 TeV. We have verified that this is the case for the modern PDF sets discussed in this chapter. However, the argument above however holds only for QCD evolution. It should be taken into account

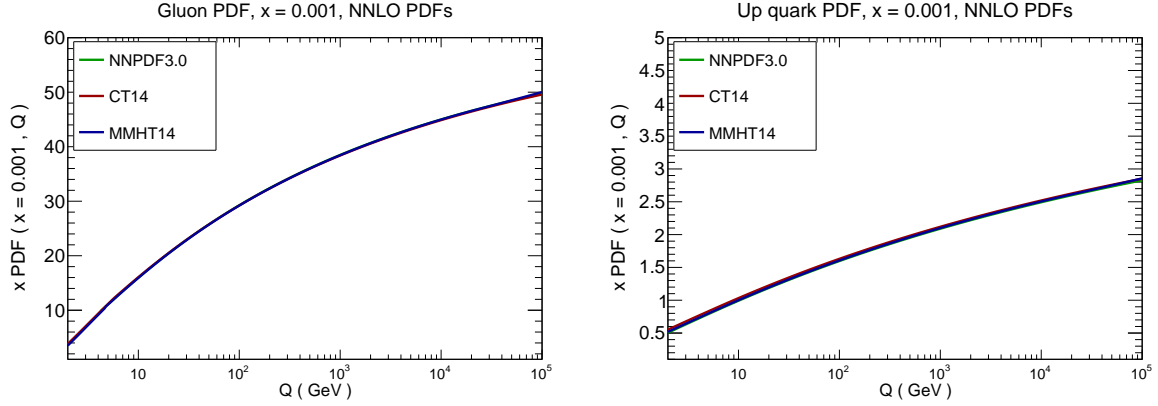


Fig. 7: The effects of DGLAP evolution on the central value of the up quark (left) and gluon PDFs (right plot) at  $x = 0.001$  when evolved from  $Q = 2$  GeV up to  $Q = 100$  TeV. We show the results from the NNPDF3.0, CT14 and MMHT14 NNLO sets, the three exhibiting a very similar behaviour. PDF uncertainties are not included in this comparison.

that differences in the upwards evolution in  $Q^2$  can arise if the evolution equations are modified, for instance in the case of electroweak corrections to DGLAP evolution, Section 2.6, or in the presence of high-energy resummation effects, Section 2.7.

In Fig. 7 we compare, for  $x = 0.001$ , the evolution of the central values of the gluon and up quark PDFs for the NNPDF3.0, CT14 and MMHT14 NNLO sets, from a very low scale,  $Q = 2$  GeV, up to the highest possible scales that the FCC can reach,  $Q = 100$  TeV. It can be verified, by comparing with public PDF evolution packages such as HOPPET [40] or APFEL [41], that the tabulated extrapolation up to very high  $Q^2$  of modern PDF sets is consistent with DGLAP evolution as expected.<sup>5</sup> We conclude that, provided modern PDF sets are used, the extrapolation of the DGLAP evolution in  $Q^2$  to the region relevant at the FCC is reliable.

### 2.3 PDF luminosities at 100 TeV

Parton luminosities are useful to estimate the PDF dependence of hadron collider cross-sections, by taking into account the most relevant initial-state production channels. While several definitions of the PDF luminosity can be adopted, in the following we will use the luminosities as a function of the invariant mass of the produced final state,  $M_X$ , defined as

$$\mathcal{L}_{ij}(M_X, \sqrt{s}) \equiv \frac{1}{s} \int_{\tau}^1 \frac{dx}{x} f_i(x, M_X) f_j(\tau/x, M_X), \quad (1)$$

where  $i$  and  $j$  are PDF flavour indices,  $\tau = M_X^2/s$ , and  $\sqrt{s}$  is the collider center-of-mass energy. Another useful way of representing PDF luminosities is as two-dimensional functions of rapidity  $y$  and invariant mass  $M_X$  of the final state,

$$\tilde{\mathcal{L}}_{ij}(M_X, y, \sqrt{s}) = \frac{1}{s} f_i\left(\frac{M_X e^y}{\sqrt{s}}, M_X\right) f_j\left(\frac{M_X e^{-y}}{\sqrt{s}}, M_X\right), \quad (2)$$

which leads to Eq. (1) upon integration over the kinematically allowed range for the rapidity  $y$ , that is,

$$\mathcal{L}_{ij}(M_X, \sqrt{s}) = \int_{-\ln \sqrt{s}/M_X}^{\ln \sqrt{s}/M_X} dy \tilde{\mathcal{L}}_{ij}(M_X, y, \sqrt{s}). \quad (3)$$

<sup>5</sup>Again, this is not necessarily true for older PDF sets. In some cases the coverage in  $Q^2$  was restricted to 10 TeV, and from there upwards an unphysical (non-DGLAP) extrapolation was used. As in the case of large and small- $x$ , use of these older sets can lead to incorrect results in the context of FCC simulations.

Typically PDF luminosities are presented summing over quark flavor indices, and here we adopt the following convention:

$$\begin{aligned}
 \mathcal{L}_{qg}(M_X) &= \sum_{i=-5}^5 (\mathcal{L}_{i0}(M_X) + \mathcal{L}_{0i}(M_X)), \quad i \neq 0, \\
 \mathcal{L}_{qq}(M_X) &= \sum_{i=-5}^5 \sum_{j=-5}^5 \mathcal{L}_{ij}(M_X), \quad i \neq 0, \quad j \neq 0, \\
 \mathcal{L}_{q\bar{q}}(M_X) &= \sum_{i=-5}^5 \mathcal{L}_{i,-i}(M_X), \quad i \neq 0,
 \end{aligned} \tag{4}$$

for the luminosities integrated in rapidity Eq. (1), and similar definitions for the double differential luminosities Eq. (2). Eq. (4) can be trivially generalized to the case in which the top quark is treated as a massless parton.

In Fig. 8 we show the rapidity-integrated PDF luminosities Eq. (1), as a function of the invariant mass of the system  $M_X$ , for the PDF4LHC15\_nn1o\_mc PDF set [5, 42], with PDF uncertainties computed at 68% confidence levels.

We show the gluon-gluon, quark-gluon, quark-quark and quark-antiquark luminosities, normalized to the corresponding central value, for the case of a  $\sqrt{s} = 100$  TeV collider. Similar comparisons in the case of the LHC 14 TeV can be found in [5]. We find PDF uncertainties are at the 5% level for  $200 \text{ GeV} \lesssim M_X \lesssim 5 \text{ TeV}$  for all four PDF luminosities. They become more important at larger values of  $M_X$ , relevant for heavy particle searches, and for smaller values of  $x$ , relevant for electroweak physics and semi-hard QCD. For instance, at  $M_X \simeq 20$  TeV the gluon-gluon PDF luminosity has an associated uncertainty of around 20%. For the production of electroweak scale particles PDF uncertainties are increased when going from the LHC to the FCC, due to the smaller values of  $x$  probed in the latter case. For  $M_X \simeq 100$  GeV, relevant for inclusive Higgs and weak gauge boson production, PDF uncertainties are around the 10% level. It can also be instructive to plot the absolute PDF luminosities in each channel together with the corresponding PDF uncertainties, this is done in Sect. 2.5 later in this chapter.

We now turn to discuss the double-differential PDF luminosities, Eq. (2), evaluated for a center of mass energy  $\sqrt{s} = 100$  TeV. In Fig. 9 shows the PDF uncertainties, evaluated as 68% CL, on the luminosities as a function of  $M_X$  and of the rapidity  $y$ . As above, the PDF4LHC15\_nn1o\_mc PDF set is used as input. Fig. 9 represents the contours of constant PDF uncertainties in the different flavour combinations. One sees that for all flavour combinations, the uncertainties are smallest, of the order of 1–2%, for pair invariant masses of the order of a TeV. They also all have a characteristic dip at rapidities of about  $|y| = 1-2$ . One may speculate that this is a consequence of an anti-correlation between moderately large and small- $x$  parton distributions caused by momentum conservation. For partonic-pair masses at the electroweak scale and in the region above a few TeV, uncertainties grow larger. In all cases PDF uncertainties grow large near the kinematic boundaries, since these are sensitive to PDFs at small and large- $x$  that currently are constrained by few experimental measurements.

Next we compute the ratio of the rapidity-integrated PDF luminosities between 100 TeV and 14 TeV, for different initial-state partonic channels, defined as:

$$R_{ij}(M_X, \sqrt{s_1}, \sqrt{s_2}) \equiv \frac{\mathcal{L}_{ij}(M_X, \sqrt{s_1})}{\mathcal{L}_{ij}(M_X, \sqrt{s_2})}, \tag{5}$$

with  $\sqrt{s_1} = 100$  TeV and  $\sqrt{s_2} = 14$  TeV. Such ratios provide a convenient rule of thumb to rescale production cross-sections between 14 and 100 TeV, for processes dominated by a single initial-state luminosity. Eq. (5) can thus be used to estimate ratios of cross-sections between the different center-of-mass energies. These cross-section ratios, in addition to providing stringent SM tests and potential

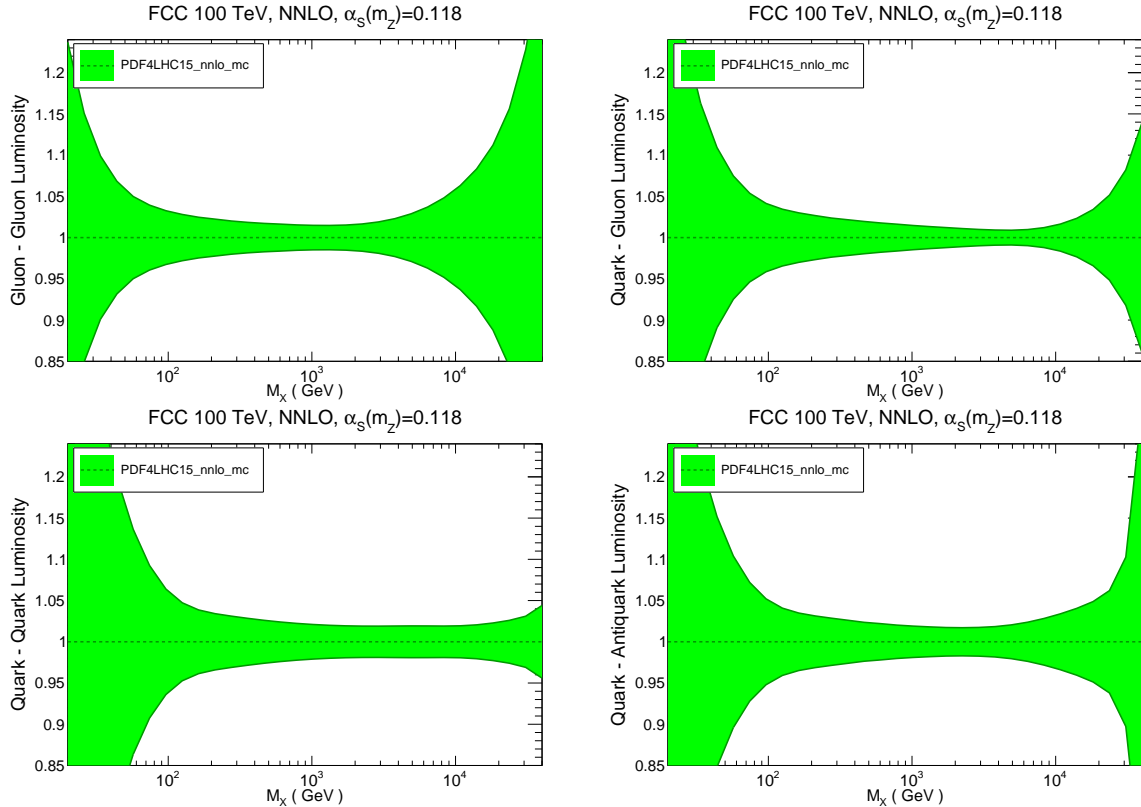


Fig. 8: The relative uncertainties in the rapidity-integrated PDF luminosity at the FCC with  $\sqrt{s} = 100$  TeV computed with the PDF4LHC15\_nnlo\_mc set, as a function of the final state invariant mass  $M_X$ . From left to right and from top to bottom we show the gluon-gluon, quark-gluon, quark-quark and quark-antiquark luminosities.

PDF-constraining information, could also be used as an alternative method to search for new physics at the FCC [43].

In Fig. 10 we show the ratio of PDF luminosities, Eq. (5), between the FCC  $\sqrt{s_1} = 100$  TeV and the LHC  $\sqrt{s_2} = 14$  TeV, for the four different initial-state channels. These ratios have been computed with both the NNPDF3.0 and the PDF4LHC15\_nnlo\_mc NNLO sets, to illustrate that the generically  $R_{ij}(M_X, \sqrt{s_1}, \sqrt{s_2})$  depends only very mildly of the specific input PDF set used. In Fig. 10 we also include the 68% CL PDF uncertainties in the luminosity ratio, accounting for the correlations between the results at the two values of the center-of-mass energy. The ratio is computed between  $M_X = 10$  GeV and  $M_X = 6$  TeV, the highest invariant masses that the LHC can reach. From this comparison, we observe that for low invariant masses,  $M_x \lesssim 100$  GeV, the increase in parton luminosities when going from the LHC to the FCC is moderate, a factor 10 at most. In this region the luminosity ratio is affected by large PDF uncertainties, arising from the production of a small  $M_X$  final state at the FCC, which probes small- $x$  PDF.

On the other hand, the luminosity ratio increases rapidly as we move away from the electroweak scale, since the increase in energy of the FCC dramatically dominates over the large- $x$  fall-off of the PDFs at the LHC. For invariant masses around  $M_X \simeq 1$  TeV, for instance, the  $gg$ ,  $qg$ ,  $q\bar{q}$  and  $qq$  luminosity ratios are  $\simeq 100$ , 50, 20 and 10, respectively. Gluon-initiated processes are those that benefit more from the increase in center-of-mass energy due to the rapid rise of the gluon PDF at medium- and small- $x$  from DGLAP evolution. For the highest invariant masses that can be probed at the LHC,  $M_X \simeq 7$  TeV, the values of the ratios (in the same order) are  $10^5$ ,  $10^4$ ,  $5 \cdot 10^3$  and 200. The hierarchy  $R_{gg} > R_{qg} > R_{q\bar{q}} > R_{qq}$  is maintained for all invariant masses above  $M_X \geq 200$  GeV.

The results in Fig. 10 can be used to compare with the various ratios of cross-sections between

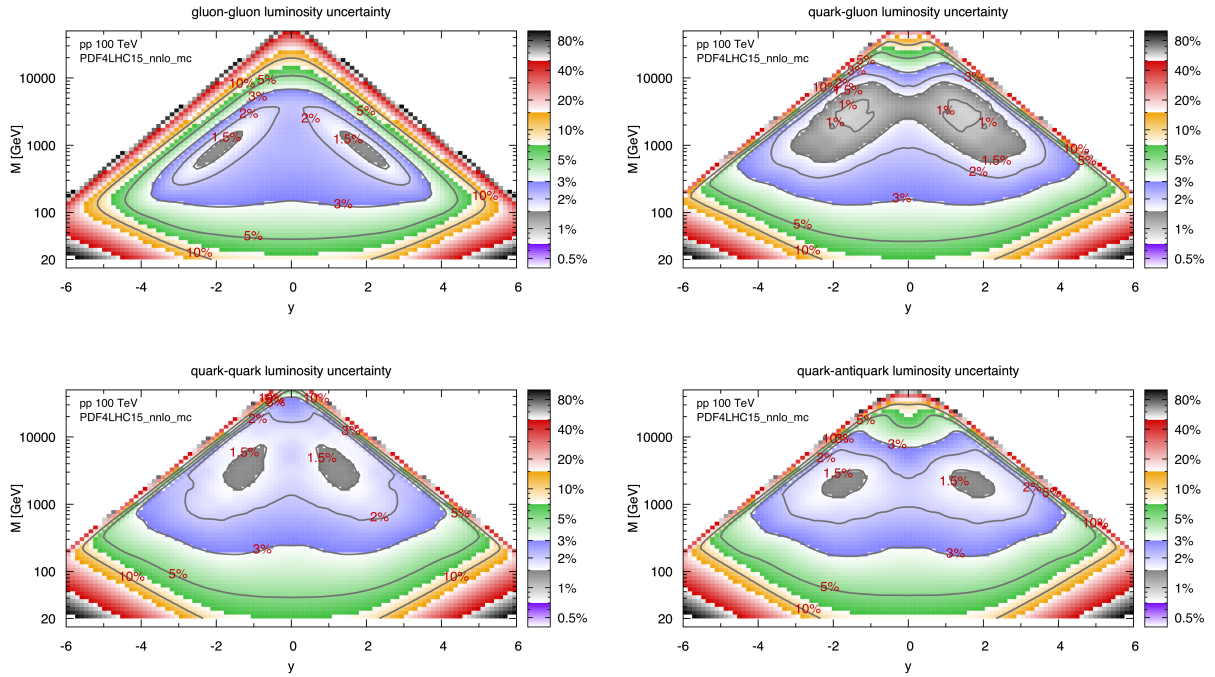


Fig. 9: The contours of constant PDF uncertainty for the double-differential PDF luminosities Eq. (2) evaluated for a center of mass energy  $\sqrt{s} = 100$  TeV, with PDF4LHC15\_nnlo\_mc PDF set used as input.

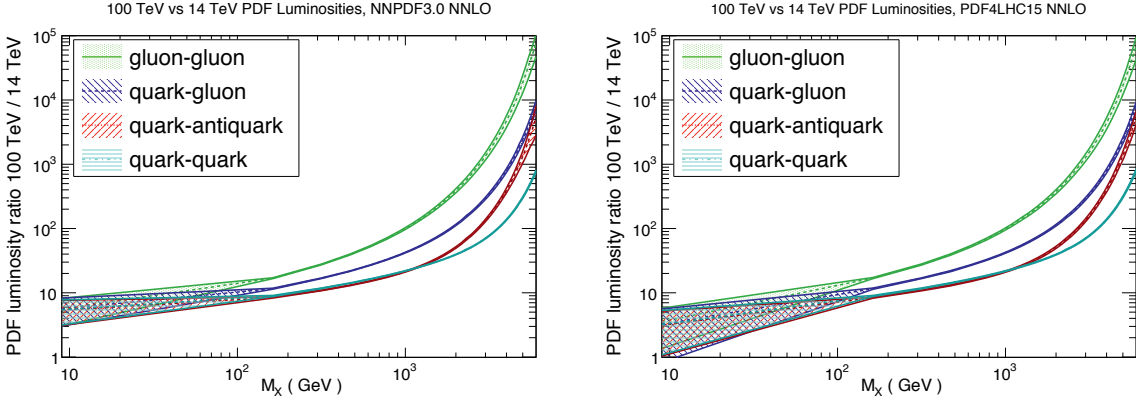


Fig. 10: The ratio of PDF luminosities, Eq. (5), between the FCC  $\sqrt{s_1} = 100$  TeV and the LHC  $\sqrt{s_2} = 14$  TeV center-of-mass energies, for different initial-state channels, together with the corresponding 68% CL PDF uncertainties. These ratios have been computed with the NNPDF3.0 (left plot) and PDF4LHC15 (right plot) NNLO PDFs.

100 TeV and 14 TeV collected elsewhere in this report. In order to facilitate the comparison with ratios of cross-sections between different center-of-mass energies presented elsewhere in this report, in Table 2 we provide the corresponding numerical values of the PDF luminosity ratios show in Fig. 10 for the case of the PDF4LHC15\_nnlo\_mc PDF set.

## 2.4 The top quark as a massless parton

At a 100 TeV hadron collider, particles with masses around the electroweak scale appear as comparably light as the bottom quark at the Tevatron collision energy of  $\sqrt{s} \sim 2$  TeV. When a very heavy scale is involved in the process, the gluon splitting into a top-antitop pair may present a large logarithmic

$M_X$ (GeV)	$\mathcal{L}_{gg}^{(100)}/\mathcal{L}_{gg}^{(14)}$	$\mathcal{L}_{qg}^{(100)}/\mathcal{L}_{qg}^{(14)}$	$\mathcal{L}_{q\bar{q}}^{(100)}/\mathcal{L}_{q\bar{q}}^{(14)}$	$\mathcal{L}_{qq}^{(100)}/\mathcal{L}_{qq}^{(14)}$
50	$8.8 \pm 0.3$	$6.9 \pm 0.3$	$5.7 \pm 0.4$	$5.9 \pm 0.4$
58	$9.5 \pm 0.3$	$7.4 \pm 0.3$	$5.9 \pm 0.4$	$6.3 \pm 0.4$
68	$10.3 \pm 0.3$	$7.9 \pm 0.3$	$6.3 \pm 0.3$	$6.6 \pm 0.3$
80	$11.2 \pm 0.3$	$8.5 \pm 0.3$	$6.6 \pm 0.3$	$7.0 \pm 0.3$
94	$12.2 \pm 0.3$	$9.1 \pm 0.2$	$7.0 \pm 0.2$	$7.3 \pm 0.2$
111	$13.4 \pm 0.3$	$9.7 \pm 0.2$	$7.4 \pm 0.2$	$7.8 \pm 0.2$
130	$14.7 \pm 0.3$	$10.5 \pm 0.2$	$7.8 \pm 0.2$	$8.2 \pm 0.2$
152	$16.2 \pm 0.4$	$11.3 \pm 0.2$	$8.2 \pm 0.2$	$8.7 \pm 0.2$
178	$18.0 \pm 0.4$	$12.2 \pm 0.2$	$8.7 \pm 0.2$	$9.2 \pm 0.2$
209	$20.0 \pm 0.4$	$13.3 \pm 0.2$	$9.2 \pm 0.2$	$9.8 \pm 0.2$
245	$22.5 \pm 0.4$	$14.5 \pm 0.2$	$9.8 \pm 0.2$	$10.5 \pm 0.2$
287	$25.4 \pm 0.5$	$15.8 \pm 0.2$	$10.5 \pm 0.2$	$11.3 \pm 0.2$
336	$28.9 \pm 0.6$	$17.4 \pm 0.2$	$11.1 \pm 0.2$	$11.9 \pm 0.3$
394	$33.2 \pm 0.8$	$19.3 \pm 0.3$	$12.0 \pm 0.2$	$13.0 \pm 0.2$
462	$38.6 \pm 0.9$	$21.5 \pm 0.3$	$13.0 \pm 0.2$	$14.0 \pm 0.2$
541	$45.1 \pm 1.2$	$24.2 \pm 0.3$	$14.1 \pm 0.2$	$15.2 \pm 0.2$
634	$54.0 \pm 1.6$	$27.4 \pm 0.4$	$15.4 \pm 0.3$	$16.5 \pm 0.2$
744	$65.3 \pm 2.2$	$31.4 \pm 0.5$	$17.0 \pm 0.3$	$18.1 \pm 0.2$
872	$80.8 \pm 2.8$	$36.4 \pm 0.6$	$19.0 \pm 0.4$	$19.9 \pm 0.3$
1022	$101 \pm 4$	$42.9 \pm 0.7$	$21.6 \pm 0.5$	$22.0 \pm 0.3$
1198	$131 \pm 6$	$51.6 \pm 1.0$	$25.1 \pm 0.6$	$24.7 \pm 0.3$
1403	$173 \pm 9$	$63.5 \pm 1.4$	$29.9 \pm 0.8$	$27.9 \pm 0.4$
1646	$238 \pm 14$	$80.3 \pm 1.8$	$37.0 \pm 1.1$	$32.5 \pm 0.7$
1928	$341 \pm 25$	$105 \pm 3$	$47.6 \pm 1.8$	$37.7 \pm 0.6$
2260	$517 \pm 45$	$143 \pm 5$	$65.0 \pm 2.9$	$45.4 \pm 0.7$
2649	$837 \pm 90$	$207 \pm 9$	$94.7 \pm 4.9$	$56.7 \pm 1.0$
3105	$1454 \pm 200$	$322 \pm 15$	$151 \pm 9$	$74.8 \pm 1.4$
3639	$2815 \pm 512$	$546 \pm 33$	$269 \pm 18$	$106 \pm 2$
4265	$6233 \pm 1395$	$1047 \pm 84$	$549 \pm 50$	$168 \pm 5$
5000	$16646 \pm 4557$	$2356 \pm 249$	$1366 \pm 207$	$308 \pm 10$

Table 2: Numerical values of the ratios of PDF luminosities, Eq. (5), between  $\sqrt{s_1} = 100$  TeV and  $\sqrt{s_2} = 14$  TeV computed with the PDF4LHC14\_nnlo\_mc set. The graphical representation of these ratios is presented in Fig. 10 (right).

enhancement. For  $Q \sim 10$  TeV, for instance,  $\alpha_s(Q) \log(Q^2/m_t^2) \sim 0.6$ , which makes a perturbative expansion of the hard process questionable. Therefore, one might wonder if the concept of top quark PDF is relevant at the FCC, just as charm and bottom PDFs are commonly used in LHC calculations. The question is then what is more suitable and advantageous, from a calculational point of view, to use at the FCC: a fixed-flavor number (FFN) scheme, where the top is a massive quark, or a variable-flavor number (VFN) scheme, where the top is a massless parton? The discussion is thus completely analogous to the case of bottom quarks at the LHC [44].

As with the charm and bottom quarks, introducing a PDF for the top quark inside the proton allows us to resum potentially large collinear logarithms of the form  $\alpha_s^n(Q) \log^n(Q^2/m_t^2)$  to all orders in perturbation theory. The generalization of the DGLAP evolution equations to include a top PDF up to NNLO is straightforward, and indeed most modern PDF sets provide variants where the maximum number of light quarks in the PDF evolution is set to  $n_f = 6$ . Indeed, the majority PDF fits are performed in a VFN scheme with a maximum of  $n_f = 5$  light partons, since in the fitted hard cross-sections top is always treated as a massive quark, and the resulting PDFs at  $\mu_F = m_t$  can then be used as boundary condition to construct the  $n_f = 6$  PDFs including a top quark.

In Fig. 11 we show the top quark PDF, evaluated at  $Q = 10$  TeV, compared with the other light

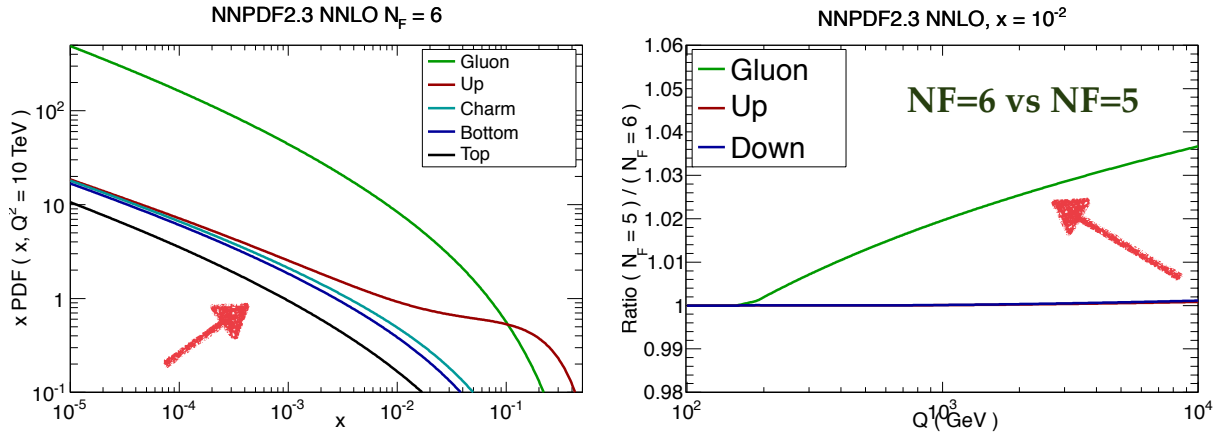


Fig. 11: Left plot: the top quark PDF compared with the other light partons, in the NNPDF2.3NNLO  $n_f = 6$  PDF set evaluated at  $Q = 10$  TeV. Right plot: Ratio between the gluon PDF in the  $n_f = 5$  and  $n_f = 6$  factorization schemes, as a function of the factorization scale  $Q$ .

partons, in the case of the NNPDF2.3NNLO  $n_f = 6$  PDF set [45]. We observe that the top quark PDF can be of a similar size as the light quark PDFs, in particular at medium and small- $x$ , the region where the effects of DGLAP evolution are dominant. We also see that the charm and bottom PDFs are essentially indistinguishable from the light quark PDFs for  $x \lesssim 10^{-3}$ . In Fig. 11 we also show the ratio between the gluon PDF between the  $n_f = 5$  and  $n_f = 6$  schemes, as a function of the factorization scale  $Q$ . We observe that the differences between the two schemes can be up to several percent for  $Q \geq 1$  TeV, a region well covered by the FCC kinematics. Therefore, the use of the  $n_f = 6$  scheme would also have implications for precision calculations involving gluons and light quarks, and not only those with initial state top quarks.

So while technically generating a top quark PDF is straightforward, it still needs to be determined if it provides any calculational advantage over using the standard FFN scheme approach, where the top quark is always treated as massive, even for the extreme energies of a 100 TeV collider. This issue has been recently studied in [46, 47], both reaching similar conclusions: a purely massless treatment of top quarks is unreliable even at the FCC, but the concept of a top quark PDFs is certainly relevant in the context of matched calculations. To illustrate this point, in the left plot of Fig. 12, taken from [46], we show a comparison of calculations in the 5-flavor, massless 6-flavor, and ACOT matched [48, 49] schemes for the inclusive production of a hypothetical heavy scalar, labeled  $H^0$ , at a 100 TeV proton-proton collider. This calculation uses as input the NNPDF2.3NNLO  $n_f = 6$  set [45]. The ACOT scheme shows the desired behavior of interpolating between the region near the top threshold and the very high energy limit (where collinear logarithms in the top quark mass become large). It should be stressed that the simplest LO  $n_f = 6$  calculation is unreliable even for masses as large as 10 TeV, indicating that the minimum scale above which a parton interpretation for the top quark becomes justified is much larger than the top mass itself.

The fact that the massless approximation for top production works rather worse than for charm and bottom quarks can be traced back, at least partially, to the fact that the resummed collinear logarithms are substantially smaller as compared to the other heavy quarks. This is illustrated by the right plot in Fig. 12, taken from [47], which compares the size of the collinear logarithm  $\alpha_s(\mu) \ln \mu^2/m_q^2$  as a function of the ratio  $\mu/m_q$  for the three heavy quarks: charm, bottom and top. Even for very large ratios  $\mu/m_q \sim 100$ , the need for resummation of collinear logarithms in the top quark mass is not evident, since  $\alpha_s(\mu) \ln \mu^2/m_q^2$ , while being large, is perturbative in the relevant kinematical range. This is opposed to charm, and to a lesser extent bottom, whose corresponding logarithms eventually become

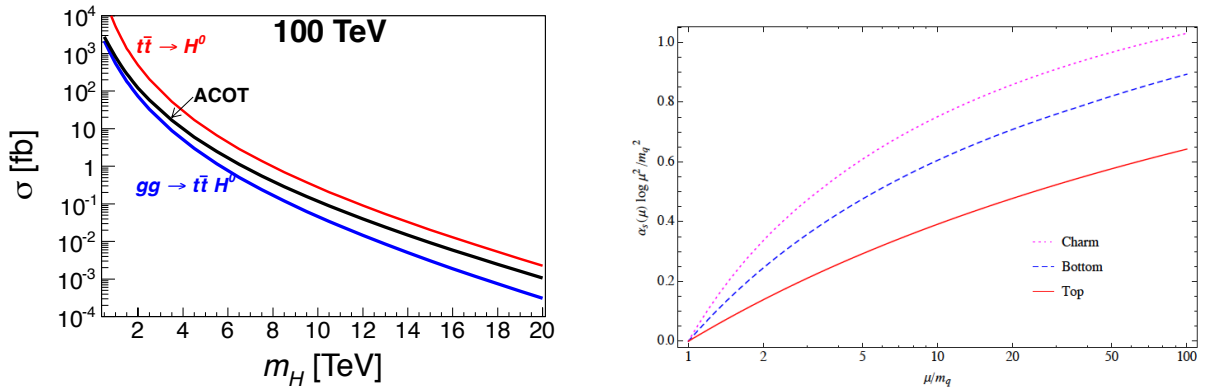


Fig. 12: Left plot: Inclusive cross section for  $H$  production with Yukawa coupling  $y = 1$  at 100 TeV versus its mass  $m_H$ , in the 5-flavor scheme (bottom blue), the 6-flavor scheme (upper red), and the ACOT scheme (middle black), from [46]. Right plot: the size of the collinear logarithm  $\alpha_s(\mu) \ln \mu^2/m_q^2$  as a function of  $\mu/m_q$  for charm, bottom and top, from [47].

non-perturbative and require collinear resummation. One reason that partially explains this difference is the fact that  $\alpha_s(m_t) \ll \alpha_s(m_c)$ , which allows a much larger lever arm in  $Q$  before resummation is required.

So in conclusion, current studies indicate, while the purely massless approximation for top quarks is unreliable even at the extreme FCC energies, the concept of top quark PDF is certainly useful in order to construct matched calculations. This way, one can supplement and improve massive fixed-order calculations with all-order resummations of collinear logarithms in matched schemes such as ACOT [48, 49] or FONLL [50, 51]. For example, as shown in the heavy quark chapter of this report, Section 11, it is possible to generalize the FONLL calculation for the  $p_T^h$  distribution in for heavy flavor differential distributions [50] to the case of top quark production at the FCC. The matched calculation is found to provide a more precise estimate in the region of transverse momenta up to 10 TeV. Eventually, this matching can be performed up to NNLO order, using the corresponding calculations for jet production [14] and for top quark production [15].

## 2.5 Photon- and lepton-initiated processes at 100 TeV

A 100 TeV Future Circular Collider is bound to probe the interactions of elementary particles at extreme energies with high accuracy. In order to correctly identify possible BSM effects, the theoretical predictions for the SM processes have to match the precision of the corresponding experimental measurements. In other words, the impact of higher-order corrections on phenomenological predictions has to be under control. To this purpose, the computation of NLO QCD corrections is necessary, but often not sufficient. In fact, at fixed order the inclusion of the NNLO QCD corrections in QCD as well as of the EW corrections is in general desirable and in particular cases even essential. The implications of higher-order EW corrections to matrix elements for FCC processes is discussed elsewhere in this report.

In order to formally achieve the desired level of accuracy, not only the matrix elements of the hard processes, but also the parton distribution functions (PDFs) of the proton, have to be known at the same level of precision. While most PDF groups provide since some time PDF sets accurate up to NNLO in QCD [7–11], for EW corrections the situation is less satisfactory. Indeed, EW corrections require the calculation of photon-induced processes, and thus PDFs both with QED effects in the evolution and with a determination of the photon PDF  $\gamma(x, Q)$  are necessary for consistent calculations. In this respect, a number of PDF sets with a photon PDF and QED effects are available in LHAPDF: MRST2004QED [52], NNPDF2.3QED [53] and the recent CT14QED [54]. In addition, PDF evolu-

tion with QED effects has been implemented in the APFEL PDF evolution program [41, 55] at LL, and inclusion of NLL QED splitting functions [56] is underway.

The determination of the photon PDF obtained by the three groups differ in a number of important aspects. First, different data sets are used in the fits. Second, the form of the photon distribution at the initial scale  $Q_0$  is different. Finally, the DGLAP evolution from  $Q_0$  to the final scale  $Q$  is not the same in all cases. As far as the functional form of the PDF at the initial scale  $\gamma(x, Q_0)$  is concerned, NNPDF2.3QED only assumes that the photon PDF is positive-definite. In a first step, PDF replicas for all partons are fitted to deep-inelastic structure functions, which only provide very loose constraints on the photon PDF. In a second step, the photon PDF is constrained from LHC Drell-Yan data. This constraint enters at LO, however, because the photon-initiated component of Drell-Yan production is small, even the relatively precise LHC data constrain the photon PDF only weakly. In particular, since no data is available at large  $x$  and no functional form is assumed, in this region PDF uncertainties on  $\gamma(x, Q)$  turn out to be quite large.<sup>6</sup>

In contrast to the NNPDF2.3QED determination, the CT14QED and MRST2004QED sets are based on the assumption that the functional form of the photon PDF at the initial scale can be determined by the valence-quark distributions. In essence, they are given by a convolution of valence-quark distributions with the  $P_{\gamma q}$  splitting functions, with a normalization for the up- and down-type distributions that differ in the two approaches. Determining the photon PDF reduces then to fixing one or two parameters in the CT14QED and MRST2004QED approaches, respectively. For the CT14QED, set the constraints are obtained by fitting ZEUS data for the production of isolated photons in DIS, while for MRST2004QED an assumption is made for the normalization coefficients and no data are used to constraint the photon PDF.

Recently the CT collaboration also released a photon PDF that includes the elastic component of the photon PDF (CT14QEDinc) obtained in the so-called photon equivalent approximation, which involves an integration over the proton electromagnetic form factors. In fact, the photon PDF, unlike the quark and gluon PDFs, has a large elastic component in which the proton remains intact (see [58–60] and references therein). This component has not been discussed in the NNPDF2.3QED and MRST2004QED fits, but is included in the photon PDF determination of [59]. Another important difference is connected to the DGLAP evolution: in the evolution of the CT14QED and MRST2004QED the scale is evolved simultaneously for the QCD and for the QED evolution, while in the NNPDF2.3QED approach the two scales run independently. Very recently, in Ref. [61], the NNPDF3.0QED set has been derived, which combines the NNPDF3.0 quark and gluon PDFs with the NNPDF2.3 photon PDF using the same solution of the DGLAP equations as CT14QED and MRST2004QED.

All these differences result in predictions for the photon PDF from different sets that are not always compatible. In particular, as compared to NNPDF2.3QED, the CT14QED and MRST2004QED photon distribution functions are softer at large  $x$ , and exhibit smaller PDF uncertainties due to their more restrictive parametrizations. It will be important to understand and resolve the sources of these differences between QED PDF sets. In the following we will present results based on the NNPDF2.3QED set, with the caveat that conclusions could be rather different if other QED sets were used as input to the calculations.

At very high energies, even PDFs for electroweak massive gauge bosons might be required, and this possibility is discussed in Section 2.6 below. On top of the photon-induced processes, higher-order EW corrections also induce lepton-initiated channels whose computation formally requires the knowledge of the leptonic content of the proton [62]. To determine the lepton PDFs, the first step is to include them in the DGLAP evolution equations with QED corrections [62], which mixes the evolution of the lepton and photon PDFs with that of quarks and gluons. Next one needs to adopt suitable boundary conditions *i.e.*, the initial scale lepton PDFs. Since a determination of lepton PDFs from data is hardly

<sup>6</sup>High-statistics Drell-Yan measurements at the LHC such as the recent ATLAS 8 TeV high-mass analysis [57] should provide additional information in this region.

achievable because of their smallness, here we assume that the light lepton PDFs, *i.e.*, electrons and muons, are purely generated by photon splitting at the respective mass scales.

Under this assumption, one can approximate their distributions at the initial scale  $Q_0 \simeq 1$  GeV as:

$$\ell^\pm(x, Q_0) = \frac{\alpha(Q_0)}{4\pi} \ln\left(\frac{Q_0^2}{m_\ell^2}\right) \int_x^1 \frac{dy}{y} P_{\ell\gamma}^{(0)}\left(\frac{x}{y}\right) \gamma(y, Q_0), \quad l^\pm = e^\pm, \mu^\pm, \quad (6)$$

with  $\alpha$  the QED running coupling constant. The  $\tau^\pm$  lepton PDFs are then dynamically generated from threshold using the standard variable-flavour-number scheme [48, 51, 63]. Here we will use the `apfel_nn23qedn1o0118_lept` set of PDFs [62] generated starting from the NNPDF2.3QED NLO set using the Ansatz in Eq. (6) for the light lepton PDFs.

Before studying the size of photon- and lepton-initiated processes at a 100 TeV collider, it is useful to study the behaviour of the parton luminosities of the different initial states, by including also photon and leptons initiated processes. Parton luminosities can either be defined as a function of  $M_X$ , the invariant mass of the final state, as done in Eqns. (1)–(4), or in terms of  $y$ , the rapidity of the final state, integrating over the invariant mass,

$$\Psi_{ij}(y) \equiv 2e^{-2y} \int_{\sqrt{\tau_{\text{cut}}e^y}}^{e^{-y}} dx x f_i(x, \sqrt{s}xe^{-y}) f_j(xe^{-2y}, \sqrt{s}xe^{-y}), \quad (7)$$

with  $\tau_{\text{cut}} \equiv M_{X,\text{cut}}^2/s$ . In Eq. (7) the lower bound of the integral, proportional to  $\sqrt{\tau_{\text{cut}}}$ , implies that  $M_X \geq M_{X,\text{cut}}$ .

In Fig. 13 we compare the size and the shape of the different parton luminosities for an hadron collider with a center of mass energy  $\sqrt{S} = 100$  TeV, both as a function of the invariant mass  $M_X$  (left plot) and of the final-state system rapidity  $y$  (right plot). For the rapidity-dependent luminosities, we impose a cut of  $M_{X,\text{cut}} = 10$  GeV. In Fig. 13 we also plot the corresponding 68% confidence level PDF uncertainties for each luminosity type, separating the luminosities involving photon or lepton PDFs (central panel) and those involving only quarks or gluons (lower panel). The central value of the luminosities is assigned to be the midpoint of the 68% confidence level interval, and thus by construction PDF uncertainties will not exceed 100%, as can be seen in the central panel of Fig. 13 (left).

The relative size of the plotted luminosities follows the expected pattern. In general, the photon PDF suppresses the luminosity by a factor of  $\alpha \simeq 10^{-2}$  with respect to the (anti)quark PDFs and, analogously, the lepton PDFs suppress the luminosity by an additional factor of  $\alpha$  with respect to the photon PDF. This can be easily seen in Fig. 13, *e.g.* by comparing  $\Phi_{\gamma\ell}(\Psi_{\gamma\ell})$  with  $\Phi_{\gamma\gamma}(\Psi_{\gamma\gamma})$  and  $\Phi_{\ell+\ell^-}(\Psi_{\ell+\ell^-})$ , the three lowest curves. However, from Fig. 13 we also notice that this hierarchy is not satisfied at large invariant masses. In this kinematic region, large  $M_X$ , one is probing PDFs at rather large values of  $x$ , and here the pure-QCD luminosity combinations,  $\Phi_{q\bar{q}}$ ,  $\Phi_{gq}$  and  $\Phi_{gg}$ , become closer to the luminosities involving photons and leptons, with important phenomenological implications: as opposed to the naive expectation, photon- and lepton-initiated contributions can become as large as the standard quark-initiated contributions. However, it is important to keep in mind that the uncertainty in the NNPDF2.3QED luminosity determinations involving photons (shown in the middle panel of Fig. 13) is very large, and that the NNPDF2.3QED results are not compatible with other determinations that instead predict a lower photon PDF effects at large  $M_X$ . In the NNPDF approach, it can be shown that this effect is partially caused by the relative behaviour of the strong coupling  $\alpha_s$  with respect to the QED coupling  $\alpha$  as functions of the scale  $M_X$ , together with the fact that PDF uncertainties for the photon (and thus for the lepton) PDFs at large- $x$  are huge,  $\geq 50\%$  for  $M_X \geq 10$  TeV, see the central panel of Fig. 13 (left).

From Fig. 13 we also see that, contrary to the  $\Phi_{ij}(M_X)$  luminosities, the rapidity-dependent luminosities  $\Psi_{ij}(y)$  maintain the same hierarchy all over the range in  $y$ . The reason for this is that the value of the final state system rapidity  $y$  is not directly related to the value of  $M_X$ , which also in this case is used as factorisation scale. Thus, the previous argument justifying the suppression of the QCD luminosities

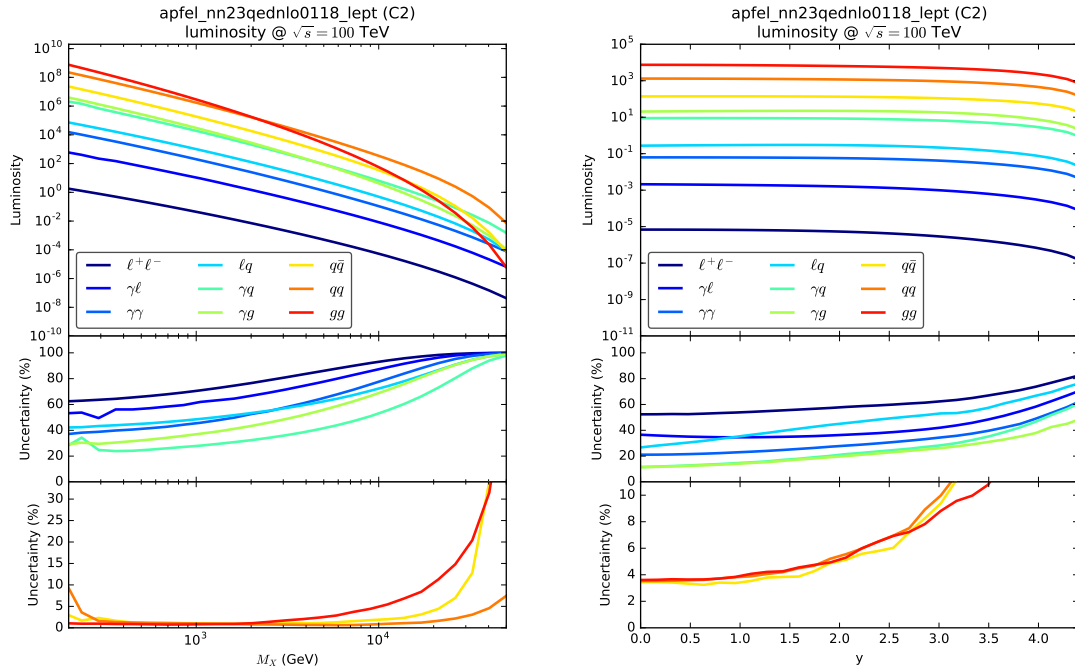


Fig. 13: PDF luminosities for the quark-quark ( $qq$ ), quark-antiquark ( $q\bar{q}$ ) and gluon-gluon ( $gg$ ) initial states compared with the different photon- and lepton-initiated channels, as a function of the invariant mass  $M_X$  of the final-state system (left) and of its rapidity  $y$  (right). The central and lower panels show the corresponding 68% confidence level PDF uncertainties in the various cases. Note that in the right plot the rapidity  $y$  is that of the final-state system, not the rapidity of the final-state particles. In the rapidity-dependent luminosity, the minimum value of the final-state invariant mass is set to  $M_{X,\text{cut}} = 10$  GeV.

with respect to the QED ones does not apply for the case of  $\Psi_{ij}$ . Note that for the rapidity-dependent luminosity in Fig. 13, the rapidity  $y$  is that of the final-state system (say a  $Z'$  boson in inclusive  $Z'$  production), not the rapidity of the final-state particles (in this case the leptons from the  $Z'$  decay).

Following this discussion of the PDF luminosities including photon- and lepton-initiated channels, now we present predictions for electroweak production processes at a 100 TeV hadron collider. We concentrate on the differential distributions as a function of the final state invariant mass  $M_X$ , allowing a direct mapping with the corresponding PDF luminosities collected in Fig. 13. Our results have been obtained with MADGRAPH5\_AMC@NLO [64] using the `apfel_nn23qednlo0118_lept` PDF set. The relevant SM input parameters have been set to the following values:

$$\begin{aligned}
 \alpha_s(m_Z) &= 0.118, & G_F &= 1.16639 \times 10^{-5}, \\
 m_Z &= 91.1876 \text{ GeV}, & m_W &= 80.385 \text{ GeV}, \\
 m_H &= 125 \text{ GeV}, & \Gamma_Z &= 2.4952 \text{ GeV}, & \Gamma_W &= 2.085 \text{ GeV}.
 \end{aligned} \tag{8}$$

The masses of all quarks (except the top quark) and leptons are neglected. We set the renormalisation and factorisation scales to  $\mu_F = \mu_R = H_T/2$ , where  $H_T$  is the scalar sum of the transverse masses of the final-state particles. We restrict ourselves to LO results at the parton level, since NLO corrections and parton shower effects would not modify qualitatively the results. We separately identify the contributions from initial states with only (anti)quarks and gluons, initial states with at least one photon and no leptons, and initial states with at least one lepton.

In this report, we aim only to disentangle the contributions of the photon and lepton-initiated

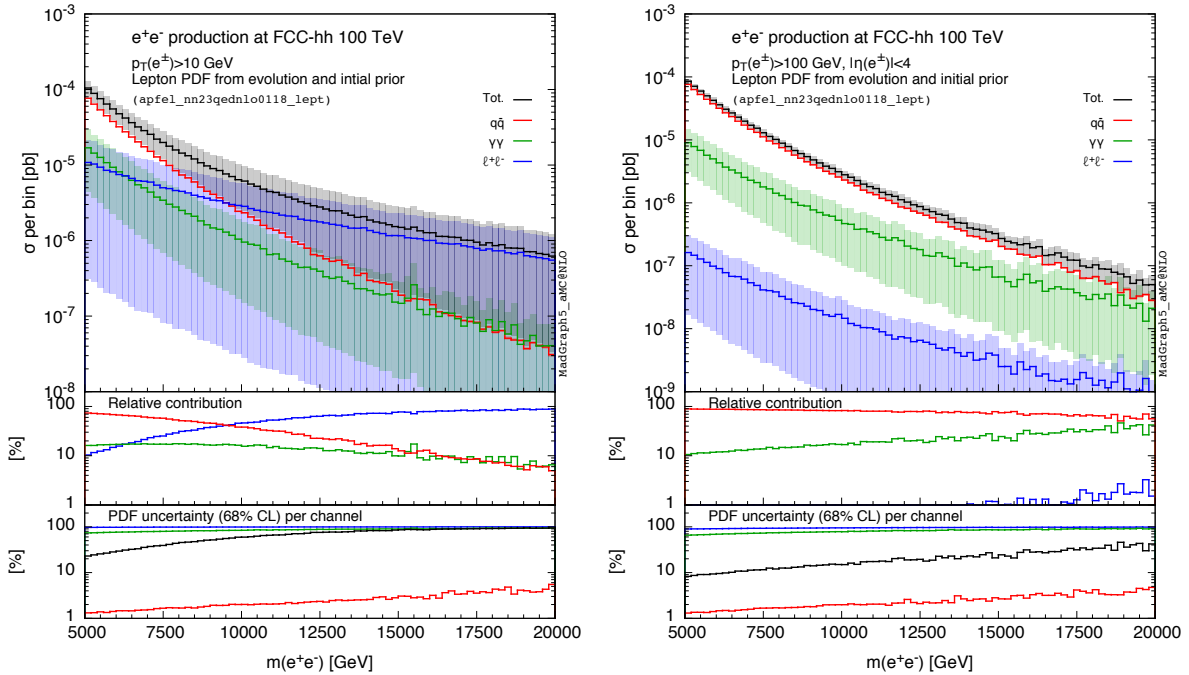


Fig. 14: Upper panel: the invariant mass distribution in  $e^+e^-$  production at a 100 TeV hadron collider. In the left plot, the transverse momentum of the leptons must satisfy a  $p_T^{e^\pm} \geq 10$  GeV cut, while in the right plot the  $p_T$  selection requirement is  $p_T^{e^\pm} \geq 100$  GeV and in addition there is a rapidity acceptance requirement of  $|\eta_{e^\pm}| \leq 4$ . The center panels shows the relative contribution of each initial state, while the lower panel shows the corresponding PDF uncertainty in each case.

channels compared to the quark and gluon initiated channels for 100 TeV processes. A more refined phenomenological study of these processes would require to include the NLO EW corrections, which in general cannot be neglected. The interplay between photon-initiated processes and NLO EW corrections have been studied, among others, in [65] for neutral current Drell-Yan and [66] for  $WW$  production, as well as in [67] for squark-antisquark production.

We start by considering the case of the production of an electron-positron pair at  $\sqrt{s} = 100$  TeV. At leading order we have the usual quark-antiquark annihilation diagram (neutral current Drell-Yan), and in the presence of EW corrections we also need to account for the photon-photon electron-positron initial states. Similarly, also  $\mu^+\mu^-$  and  $\tau^+\tau^-$  initial states can contribute to the corresponding final states. Each initial state leads to a different contribution to the  $M_X$  invariant mass distributions:  $q\bar{q}$  has a  $s$ -channel diagram,  $\gamma\gamma$  has  $t$ - and  $u$ -channel diagrams, while the  $e^+e^-$  initial state has  $s$ - and  $t$ -channel diagrams. These three partonic processes yield LO cross sections of  $\mathcal{O}(\alpha^2)$ , thus they all contribute to the same order in the perturbative expansion.

In Fig. 14 we show the invariant mass distribution of the lepton pair in neutral Drell-Yan production at a 100 TeV hadron collider for  $m_{e^+e^-} \geq 5$  TeV. We also investigate how the results are modified in the presence of realistic acceptance cuts. In the left plot of Fig. 14, the transverse momentum of the leptons must satisfy a  $p_T^{e^\pm} \geq 10$  GeV cut, while in the right plot the  $p_T$  selection requirement is  $p_T^{e^\pm} \geq 100$  GeV and in addition there is a rapidity acceptance requirement of  $|\eta_{e^\pm}| \leq 4$ . The center panels shows the relative contribution of each initial state, while the lower panel shows the corresponding PDF uncertainty in each case.

We see that in the case of loose (and unrealistic) acceptance cuts, left plot of Fig. 14, the contribution of the  $l^+l^-$  channel is not negligible and is even dominant for  $m_{e^+e^-} \geq 5$  TeV. This behaviour is

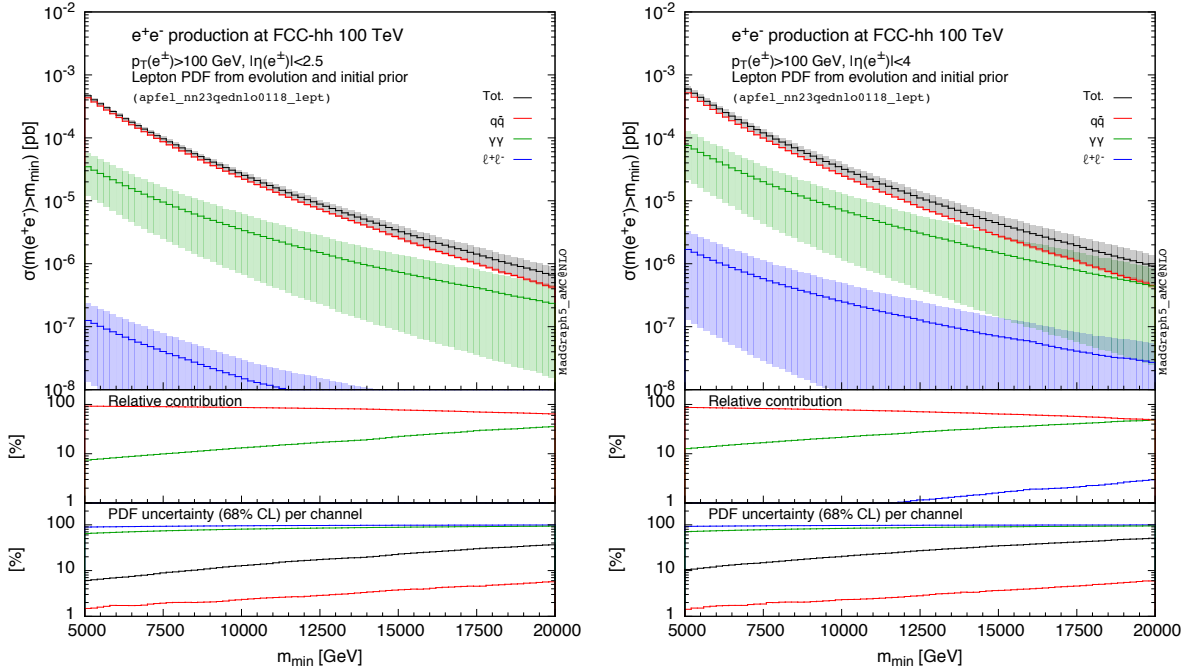


Fig. 15: Same as Fig. 14, now we showing the total integrated cross-section above a minimum value of the invariant mass of the dilepton pair  $m_{\min}$ . The leptons are required to have a transverse momentum  $p_T^{e^\pm} \geq 100$  GeV and to lie in the rapidity range  $|\eta^{e^\pm}| \leq 2.5$  (4.0) in the left (right) plot.

due to the fact that the partonic cross-section for the  $e^+e^- \rightarrow e^+e^-$  process with massless electrons has a collinear divergence for electrons collinear to the beam pipe. However, once a reasonable acceptance cuts in the lepton transverse momentum  $p_T^{e^\pm} \geq 100$  GeV and in their rapidity  $|\eta^{e^\pm}| \leq 4$ , the contribution of the  $\ell^+\ell^-$  initial state is strongly suppressed (right plot).

Note also that, even for realistic acceptance cuts, the photon-photon initiated contribution is  $\geq 10\%$  for all the range in invariant mass, although with very large associated uncertainties, and thus is mandatory to include it in any precision calculation. Part of this effect is the consequence of the relative behaviour of the  $M_X$ -differential luminosities shown in the left panel of Fig. 13 where the  $\Phi_{\gamma\gamma}$  luminosity is relatively less suppressed as compared to  $\Phi_{q\bar{q}}$  at large invariant masses. Moreover, the  $q\bar{q}$ -channel receives an additional kinematic suppression due to  $s$ -channel diagrams that are instead absent in the  $\gamma\gamma$ -channel. We also note that the  $\gamma\gamma$  contribution is affected by very large PDF uncertainties, but these will have been greatly reduced before the start of the operations of the FCC thanks to the full exploitation of the constrains from the LHC data [4].

In Fig. 15 we show the total integrated cross-section for the production of a dilepton pair at  $\sqrt{s} = 100$  TeV with invariant mass above a given threshold  $m_{\min}$ . The final-state leptons are required to have a transverse momentum  $p_T^{e^\pm} \geq 100$  GeV and to lie in the rapidity range  $|\eta^{e^\pm}| \leq 2.5$  (4.0) in the left (right) plot. Given the integrated luminosities expected at the FCC, we see that one can expect sizable rates of dilepton events with invariant masses above 20 TeV. As in Fig. 14, the contribution of the lepton PDFs is negligible once the calculation is restricted to the experimentally accessible region. At the highest possible invariant masses, the contribution from the  $\gamma\gamma$  initial state could be as large as that from the  $q\bar{q}$  initial state, although current uncertainties on the photon PDF are still too large to draw any definitive conclusion.

Next we turn to the production of electroweak gauge boson pairs at 100 TeV, in particular, we consider at  $W^+W^-$  production with undecayed  $W$  bosons. A more detailed study of di-boson production

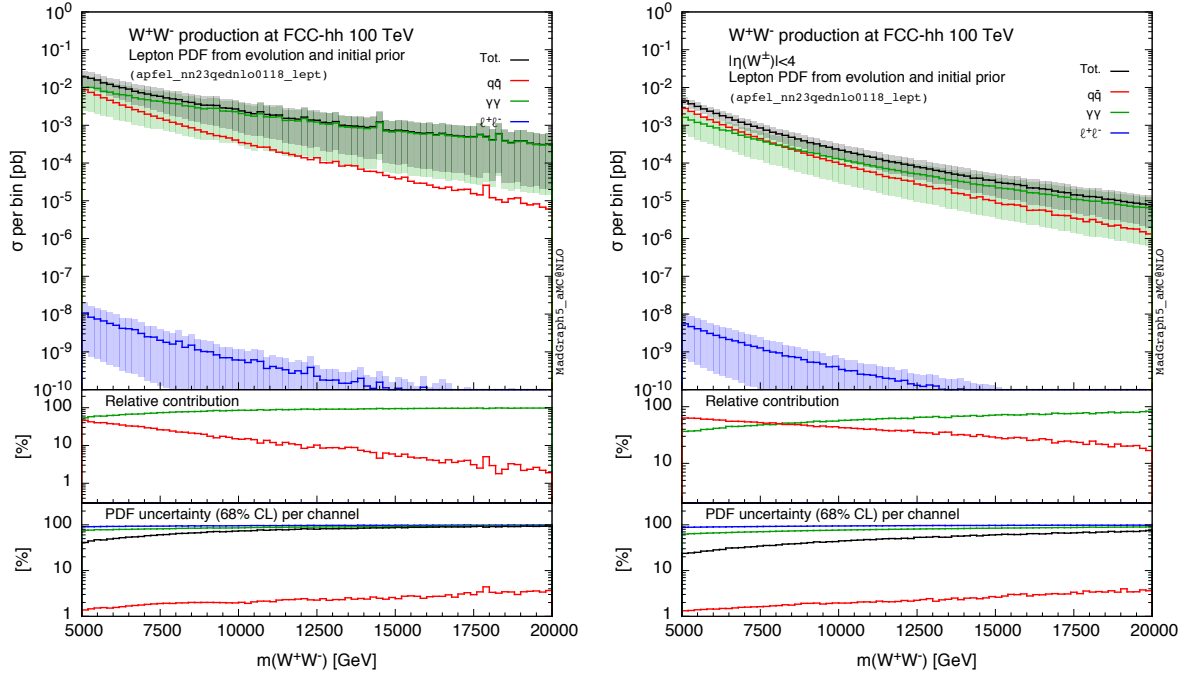


Fig. 16: Same as Fig. 14 for the production of  $W^+W^-$  pairs at a 100 TeV hadron collider. In the left plot we have not imposed any acceptance cut, while in the right plot the rapidity of the electroweak gauge bosons is required to satisfy  $|\eta_{W^\pm}| \leq 4$ .

at 100 TeV can be found in Section 7 of this report. In the calculation, we keep the  $W$  boson stable so that we can estimate the effects due only to the  $\ell^+\ell^-$  luminosity, as opposed to also the matrix-element enhancements. In Fig. 16 we show the differential distributions for the invariant mass of the di-boson pair  $m_{W^+W^-}$  using the same format as for di-lepton production in Fig. 14. In the left plot we have not imposed any acceptance cut, while in the right plot the rapidity of the electroweak gauge bosons is required to satisfy  $|\eta_{W^\pm}| \leq 4$ .

First of all, we observe that also for  $W^+W^-$  production the contribution from the lepton PDFs can be safely neglected, as was the case in di-lepton production. On the other hand, the photon-initiated contribution dominates over the quark-antiquark annihilation for  $m_{W^+W^-} \geq 7.5$  TeV in the case of realistic selection cuts. One should however take into account that this  $\gamma\gamma$  contribution is affected by very substantial PDF uncertainties for all the relevant range of  $m_{W^+W^-}$  values.

As in the case of di-lepton production, the increase of the relative importance of the  $\gamma\gamma$  channel for large  $m_{W^+W^-}$  is consistent with the behaviour of the  $\Phi_{\gamma\gamma}$  and  $\Phi_{q\bar{q}}$  luminosities shown in Fig. 13. Again, no suppression from  $s$ -channel diagrams is present in  $\gamma\gamma \rightarrow W^+W^-$  production, leading to a further relative enhancement with respect to the  $q\bar{q}$  channel at high  $m_{W^+W^-}$ . On the other hand, in the  $\gamma\gamma$ -channel the  $W$  bosons are produced more peripherally than in the  $q\bar{q}$ -channel. Therefore, the cut in pseudorapidity reduces the relative impact of the  $\gamma\gamma$  channel, but it does not modify the qualitative conclusions.

In Fig. 17 we show a similar comparison as that in Fig. 16, but now plotting the total integrated cross-section above a minimum value of the invariant mass of the  $W^+W^-$  pair  $m_{\min}$ , rather than the cross-section per bin. The rapidity of the  $W$  bosons is restricted to lie in the  $|\eta^{W^\pm}| \leq 2.5$  (4.0) region in the left (right) plot. Therefore, the rates for di-boson production will be substantial even for invariant masses as large as  $m_{\min} \simeq 20$  TeV, specially if also hadronic decay channels can be reconstructed.

To summarize, in this contribution we have explored the impact of photon- and lepton-initiated

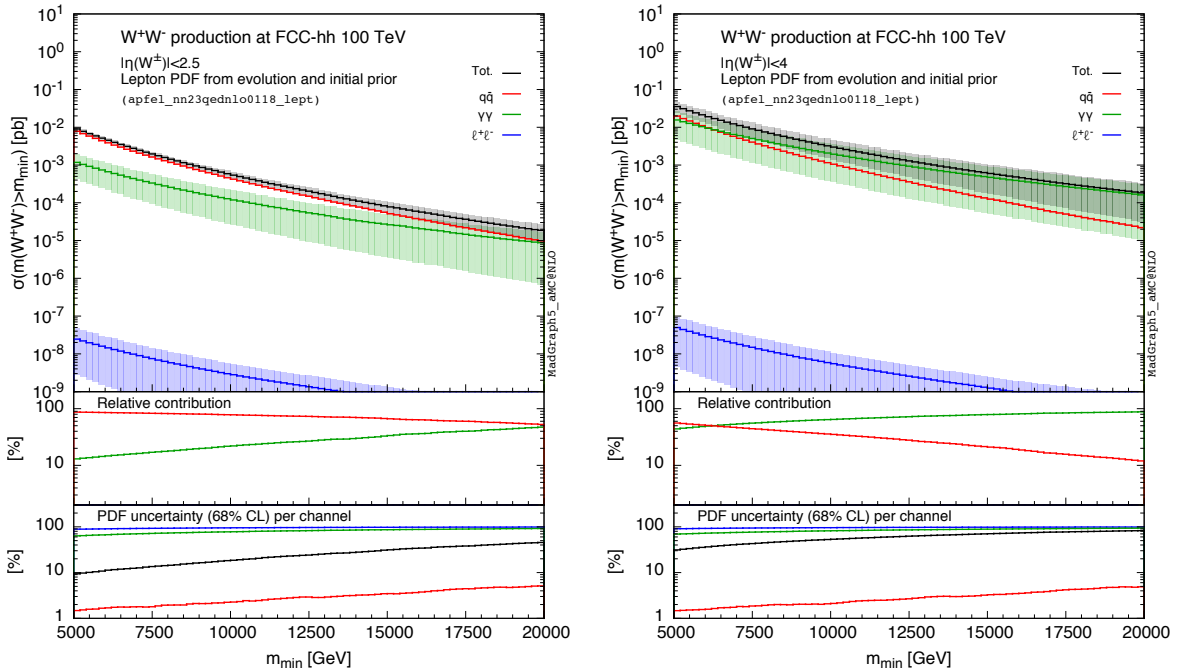


Fig. 17: Same as Fig. 16, now showing the total integrated cross-section above a minimum value of the invariant mass of the  $W^+W^-$  pair  $m_{\min}$ . The rapidity of the  $W$  bosons is restricted to lie in the  $|\eta^{W^\pm}| \leq 2.5$  (4.0) region in the left (right) plot.

contributions to electroweak processes at a 100 TeV hadron collider. We find that both for Drell-Yan and for  $WW$  production, the contribution from the  $\gamma\gamma$  initial state is comparable to that from  $q\bar{q}$  annihilation within the large uncertainties of the former. While the photon-initiated contribution currently is affected by large PDF uncertainties, this should not be a major issue at the FCC since these uncertainties can be substantially reduced using the information from available and future LHC measurements. We also find that, provided realistic acceptance cuts are imposed, the contribution from lepton-initiated processes is as expected completely negligible.

## 2.6 Electroweak gauge bosons as massless partons

For processes that involve energies much greater than the electroweak scale, it might be more adequate to treat massive electroweak gauge bosons as massless partons, in a way similar to what can be done with heavy quarks; see Sect. 2.4. The justification to consider EW bosons as initial-state partons at very high energies is discussed in more detail in Sect. 4.4, where relevant technical issues are addressed. In this section, we present instead some preliminary results for the effects of including weak gauge bosons as massless partons into the DGLAP evolution equations for parton distributions.

Electroweak evolution equations are substantially more involved than their QED and QCD counterparts; see [68] and references therein. However, one can obtain a first approximation of their effects by studying the fixed-order splitting rates of quarks into  $W$  and  $Z$  bosons. This approach, which generalizes the usual Weizsäcker-Williams calculation for collinear photon radiation off a relativistic charge, is known as the effective  $W$  approximation [69, 70]. Note that this approximation formally breaks down when the interference between transverse and longitudinal polarizations is important [69]. Sub-dominant contributions to this approximation include power corrections of  $\mathcal{O}(M_{W/Z}^2/Q^2)$  [71] as well as higher-order perturbative QCD [71, 72] and EW corrections [71].

One major novelty is the appearance of longitudinal polarization modes. For radiation of a  $W$

boson off an unpolarized light quark  $q$  in the initial state, carrying an energy fraction  $z \equiv E_W/E_q$ , in the limit where  $E_W \gg m_W$  the leading-order transverse and longitudinal  $W$  content of the proton [69] is then given by:

$$f_{W_T \in q}(z, Q^2) = \frac{C_V^2 + C_A^2}{8\pi^2} \left( \frac{1 + (1-z)^2}{z} \right) \log \left( \frac{Q^2}{M_W^2} \right), \quad (9)$$

$$f_{W_0 \in q}(z) = \frac{C_V^2 + C_A^2 (1-z)}{4\pi^2} \frac{1}{z}, \quad C_V = -C_A = \frac{g}{2\sqrt{2}}.$$

Up to the different gauge couplings  $C_V$  and  $C_A$ , the expressions for the  $Z$  boson radiation off quarks are identical [69, 70]. It should be mentioned though that in some cases, interference with photon emissions might become sizable, requiring a coherent mixed-state treatment [68].

The scale  $Q$  appearing in Eq. (9) in the logarithm for transverse emission is a maximum (space-like) virtuality cutoff or transverse momentum cutoff, typically set by the scale of the hard process in which the  $W$  is participating. For  $Q \gg M_W$ , the logarithm asymptotically diverges, necessitating collinear resummation, in close analogy with massless gauge theories. Numerically, the impact of this resummation at FCC energies has not yet been assessed. In this respect, the interplay with QCD evolution might be particularly important, as the quark PDFs that source the heavy vector PDFs does evolve appreciably between  $O(100 \text{ GeV})$  and  $O(10 \text{ TeV})$ . The integrated longitudinal structure function in Eq. (9), by contrast, does not contain a logarithm. This is because longitudinal emission off of massless fermions is only possible at transverse momentum scales of order  $M_W$ , and does not receive further contributions as we integrate out to higher momentum scales. This behavior is a manifestation of the Goldstone Boson equivalence theorem [73, 74]: when the transverse momentum becomes much larger than the weak scale, longitudinal gauge bosons act like Goldstone bosons, and thus decouple from light fermions.

Fixed-order (unresummed) weak boson PDFs for the proton can be obtained by a convolution of the above distributions with the standard quark PDFs,

$$f_{W \in P}(\xi, Q_W^2, Q_q^2) = \sum_q \int_{\xi}^1 \frac{dz}{z} f_{W \in q}(z, Q_W^2) f_{q \in P} \left( \frac{\xi}{z}, Q_q^2 \right). \quad (10)$$

Note that in performing this procedure, the energy fractions of the electroweak gauge bosons are implicitly bounded from below by  $M_W/E_q$ , else the effective  $W$  approximation is not valid. In Eq. (10) we have also allowed for independent factorization scales for the quarks and for the vector boson. Due to the strong-ordering effect, we must have  $Q_W \geq Q_q$ .

For transverse vector bosons,  $Q_W$  should be evaluated near the hard process scale. To the extent that the fixed-order approach is adequate, also choosing  $Q_q$  near the hard process scale is naively appropriate. However, since quarks of a given virtuality can only source vectors at *larger* virtualities, there is intrinsically some error implicit in this choice. Similarly, a choice  $Q_q \sim M_W$  would miss potentially  $O(10\% - 100\%)$  corrections from QCD evolution. The best scale choice of  $Q_q$  for a fixed-order treatment of the electroweak PDFs likely lies somewhere in between. For longitudinal vectors there is less ambiguity. Since they are only resolved out of the quarks at  $Q \sim M_W$ , quark PDFs evaluated near  $M_W$  are likely adequate. As explained above, the longitudinal structure functions  $f_{W_0 \in q}$  do not contain explicit scale dependence. In the following we will for simplicity set  $Q_q = Q_W$  for transverse bosons, and  $Q_q = M_W$  for longitudinal.

At a hadron collider, we define partonic luminosities by the general formula

$$\frac{d\mathcal{L}_{ij}}{d\tau}(Q_i^2, Q_j^2) = \frac{1}{(\delta_{ij} + 1)} \int_{\tau}^1 \frac{d\xi}{\xi} \left[ f_{i \in P}(\xi, Q_i^2) f_{j \in P} \left( \frac{\tau}{\xi}, Q_j^2 \right) + f_{i \in P} \left( \frac{\tau}{\xi}, Q_i^2 \right) f_{j \in P}(\xi, Q_j^2) \right], \quad (11)$$

where  $\tau \equiv s/S$  is the ratio between the partonic  $\sqrt{s}$  and hadronic  $\sqrt{S}$  center-of-mass energies squared. Luminosities involving massive vector bosons can be derived by plugging Eq. (10) into Eq. (11). Leaving

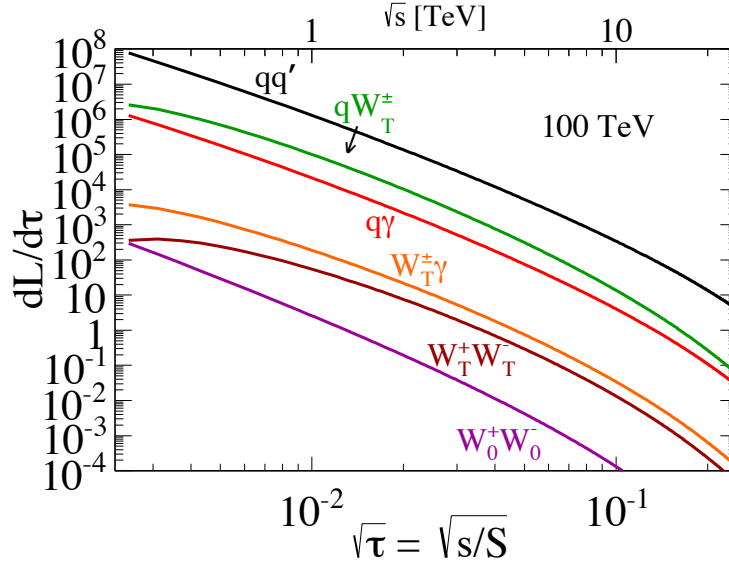


Fig. 18: Partonic luminosities,  $dL/d\tau$  Eq. 11, for a hadronic center-of-mass energy of  $\sqrt{S} = 100$  TeV, as a function of  $\sqrt{\tau} = \sqrt{s/S}$ , the ratio of the partonic  $\sqrt{s}$  and hadronic  $\sqrt{S}$  center-of-mass energies. We compare the standard  $qq'$  luminosity with the luminosities involving photons and electroweak gauge bosons.

for simplicity the factorization scales implicit, one finds the following result for the  $qW$  luminosity

$$\frac{d\mathcal{L}_{qW}}{d\tau} = \int_{\tau}^1 \frac{d\xi}{\xi} \int_{\tau/\xi}^1 \frac{dz}{z} \sum_{q'} \left[ f_{q \in P}(\xi) f_{W \in q'}(z) f_{q' \in P} \left( \frac{\tau}{\xi z} \right) + f_{q \in P} \left( \frac{\tau}{\xi z} \right) f_{W \in q'}(z) f_{q' \in P}(\xi) \right] \quad (12)$$

while for the different  $WW$  processes the corresponding luminosities are instead

$$\frac{d\mathcal{L}_{WW'}}{d\tau} = \frac{1}{(\delta_{WW'} + 1)} \int_{\tau}^1 \frac{d\xi}{\xi} \int_{\tau/\xi}^1 \frac{dz_1}{z_1} \int_{\tau/\xi/z_1}^1 \frac{dz_2}{z_2} \sum_{q,q'} \left[ f_{W \in q}(z_2) f_{W' \in q'}(z_1) f_{q \in P}(\xi) f_{q' \in P} \left( \frac{\tau}{\xi z_1 z_2} \right) + f_{W \in q}(z_2) f_{W' \in q'}(z_1) f_{q \in P} \left( \frac{\tau}{\xi z_1 z_2} \right) f_{q' \in P}(\xi) \right]. \quad (13)$$

In Fig. 18, we represent the parton luminosities Eq. (11) for various initial states at a 100 TeV hadron-hadron collider. We include as well the photon PDF, derived analogously to the transverse  $W$  PDF, using an effective virtuality cutoff at  $\Lambda_{\gamma} = \sqrt{1.5 \text{ GeV}^2} \approx 1.22 \text{ GeV}$ , and again ignoring possible coherence effects with  $Z$  emission within the region  $Q \gtrsim M_Z$ . Note that below the cut-off  $\Lambda_{\gamma}$ , the PDF should be matched with the non-perturbative intrinsic photon PDF [53, 75, 76], see Sect. 2.5 for a discussion of recent determination non-perturbative photon PDF. For most of the luminosities, a common factorization scale of  $Q^2 = s/4$  is used, with  $\sqrt{s}$  the partonic CoM energy. For the longitudinal  $W$ , we choose to use instead  $Q^2 = M_W^2$ . In Fig. 19 we also show the ratio the various partonic luminosities shown in Fig. 18 between center-of-mass energies of 100 TeV and 14 TeV. Note also that the photon-initiated luminosities can be substantially enhanced once the non-perturbative photon PDF  $\gamma(x, Q_0^2)$  is taken into account.

One immediate observation from comparing the  $W_T \gamma$  and  $W_T W_T$  luminosities is their similarity. That transverse weak bosons begin to appear on the same footing as photons is a manifestation of the restoration of EW symmetry. The longitudinal bosons are sourced from the quarks as described above without a logarithmic enhancement, and hence with individual splitting rates that are  $\log(s/4m_W^2) \sim$

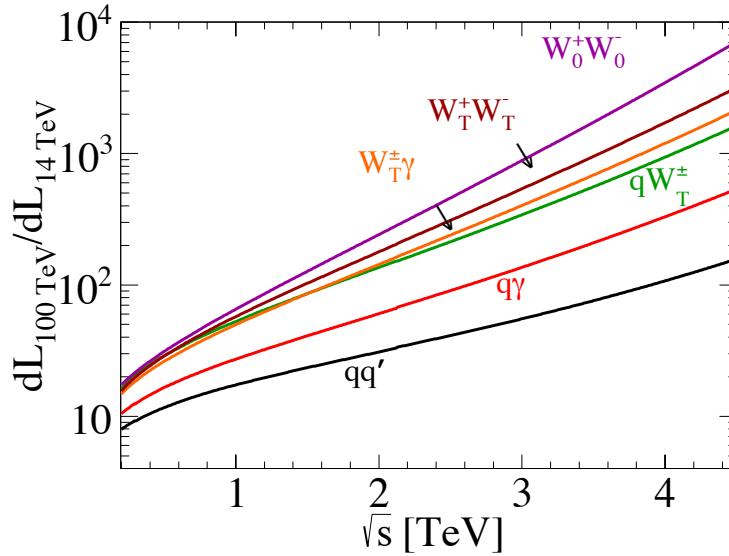


Fig. 19: Ratio of the various partonic luminosities shown in Fig. 18 between center-of-mass energies of 100 TeV and 14 TeV.

$\mathcal{O}(3 - 10)$  times smaller than their transverse counterparts at multi-TeV energies. This leads to  $\mathcal{O}(10 - 100)$  times smaller luminosities.

For the vector-boson-fusion (VBF) process initiated by the longitudinal bosons, the electroweak PDF approach effectively integrates out the usual forward tagging jets, treating them as part of the “beam”. This of course becomes progressively more justifiable at higher partonic CM energies, as the tagging jets with  $p_T \sim M_W$  will appear at extremely high rapidities, and may anyway become a less distinctive feature to discriminate against backgrounds in the presence of copious QCD initial-state radiation at similar values of the transverse momentum. From a practical perspective, the ability to treat VBF as a  $2 \rightarrow 2$  process rather than  $2 \rightarrow 4$  would significantly reduce the computational burden for event simulation. The tagging jets can then be resolved using the usual initial-state radiation machinery, appropriately adapted for this unique electroweak splitting process. In particular, merging with a matrix element description for higher  $p_T$  may remain important for obtaining a detailed understanding of central jet vetoes. Nonetheless, this might still be simplified to a  $2 \rightarrow 3$  scattering question by exploiting the electroweak PDFs.

Similar considerations apply to other processes involving longitudinal weak bosons in the initial state, such as the production of heavy top- or bottom-partners through  $W_0 b$  or  $Z_0 b$  fusion. The electroweak PDF approach may also be useful for new physics processes involving initial-state transverse bosons, such as resonant production of a heavy graviton or enhanced continuum scattering from higher-dimensional operators. In particular, due to the large  $SU(2)_L$  non-abelian self-coupling, collinear-enhanced secondary radiation of weak bosons from the initial state may become relevant at the level of 10’s of percent. Subtly, emissions of this type will affect not only the energy spectrum of the initial weak bosons, but also their isospin composition. These effects can only be efficiently captured in the fully interleaved QCD+EW DGLAP evolution.

## 2.7 High-energy resummation of PDF evolution

When Bjorken- $x$  is small enough, logarithms of the form  $\ln^k 1/x$  in the DGLAP splitting functions and in partonic matrix elements become numerically large, and might hamper the standard perturbative expansion. In principle these logarithms should thus be resummed to all orders in the strong coupling  $\alpha_S(Q^2)$  for those processes that probe the small- $x$  region. On the other hand, so far there is no conclusive evidence for the onset of high-energy resummation in HERA or LHC data, though the recently reported

instability of QCD fits to the legacy HERA combination in the small- $x$  and  $Q^2$  region is certainly tantalizing [11, 77, 78]. As summarized in Fig. 1, the FCC will probe small values of  $x$  for many relevant processes, and thus it is important to assess the importance of such logarithms and of their resummation in the context of FCC phenomenology. It is the purpose of this section to provide a qualitative estimate of the size and impact of high-energy resummation for a 100 TeV hadron collider.

These small- $x$  logarithms arise from radiation of highly energetic gluons, and appear as single logarithms of the form  $\alpha_S^n \ln^k x$  with  $k \leq n$  to all orders  $n$  in  $\alpha_S$ . In the  $\overline{\text{MS}}$  scheme, or a variant of this scheme often considered in small- $x$  resummation called  $Q_0\overline{\text{MS}}$ , both the PDF evolution (in the singlet sector) and the partonic coefficient functions are affected by small- $x$  logarithmic enhancement. Therefore, to properly account for small- $x$  resummation effects, refitting PDFs with resummed splitting functions and coefficient functions is mandatory. This is very important, because for many processes most of the resummation effect is expected to come from the resummation in PDF evolution, which is always leading in the singlet sector, while resummation of coefficient functions starts at NLLx for processes which are quark initiated at tree level.

Small- $x$  resummation is based on the fundamental  $k_t$  factorization theorem [79–83], valid in the high-energy limit  $s \gg Q^2$ . It generalises the standard collinear factorization to the case of off-shell initial-state partons, and reduces to it in the on-shell limit. Resummation of small- $x$  logarithms in the evolution of parton distribution can be achieved using the duality between the complementary BFKL and DGLAP evolutions, which describe the evolution of the PDFs in  $x$  and  $Q^2$  respectively, both derivable from the high-energy factorization. This duality can be exploited to resum to all orders in  $\alpha_S$  singular small- $x$  contributions to the DGLAP gluon anomalous dimensions up to NLLx [84]. Obtaining perturbatively stable and reliable resummed anomalous dimensions requires the addition of some extra ingredients, namely the resummation of anti-collinear contributions [85, 86] and resummation of sub-leading running coupling contributions [87–89]. Finally, resummation of quark anomalous dimensions and coefficient functions can be performed (to the lowest non-trivial logarithmic order) from high-energy factorization [83, 90].

Despite the fact that the formalism for consistently resumming DGLAP anomalous dimensions as well as the coefficient functions for the main processes entering a PDF fit has been available for quite some time, no global PDF analysis has been performed including the effects of small- $x$  resummation.<sup>7</sup> Therefore, unfortunately no consistent application of NLLx small- $x$  resummation to hadron collider phenomenology has been performed.<sup>8</sup> Part of the reason for this resides in the complexity of the small- $x$  resummation formalism which makes a reliable numerical implementation challenging.

Ongoing work [92] aims at providing resummed anomalous dimensions and coefficient functions through a fast C++ code named HELL (standing for High Energy Large Logarithms). This code has been interfaced to the APFEL [41] PDF evolution package, which is then able to perform DGLAP evolution with LLx and NLLx small- $x$  resummation matched to the fixed order LO and NLO. Ongoing developments aim at including also the small- $x$  resummation of deep-inelastic coefficient functions in HELL and thus also in APFEL. Once the implementation has been finalized, it will be possible to perform for the first time fully consistent PDF fits with small- $x$  resummation; preliminary results obtained in the context of the NNPDF methodology [93] are reported below.

It is possible to estimate the effect of small- $x$  resummation at a 100 TeV collider as follows. We show in Fig. 20 how the gluon (left plot) and the quark singlet (right plot) PDFs are modified when performing fixed NLO DGLAP evolution as compared to resummed NLO+NLLx evolution. The initial condition for the evolution is the NNPDF30\_nlo\_as\_0118 set at  $Q_0 = 2$  GeV, which is evolved upwards in  $Q^2$  using APFEL+HELL up to a typical electroweak scale  $Q = 100$  GeV. Recall from Fig. 1 that at the FCC, for  $Q = 100$  GeV, the kinematic region down to  $x \simeq 10^{-5}$  will be probed (assuming a rapidity coverage of  $|y| \lesssim 4$ ).

<sup>7</sup>See also Ref. [91] for a study of the impact of small- $x$  resummation in the MRST fits.

<sup>8</sup>On the other hand, NNPDF fits with large- $x$  threshold resummation have recently become available [37].

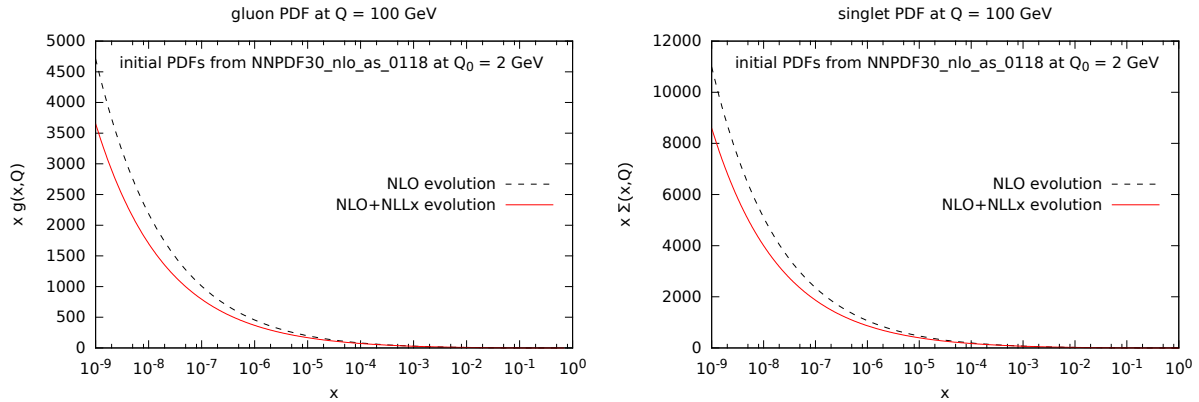


Fig. 20: Gluon (left) and the total quark singlet (right) PDFs obtained evolving the NNPDF30\_nlo\_as\_0118 PDFs from an initial scale  $Q_0 = 2$  GeV up to the EW scale  $Q = 100$  GeV with fixed NLO (black dashed) and resummed NLO+NLLx (red solid) DGLAP evolution.

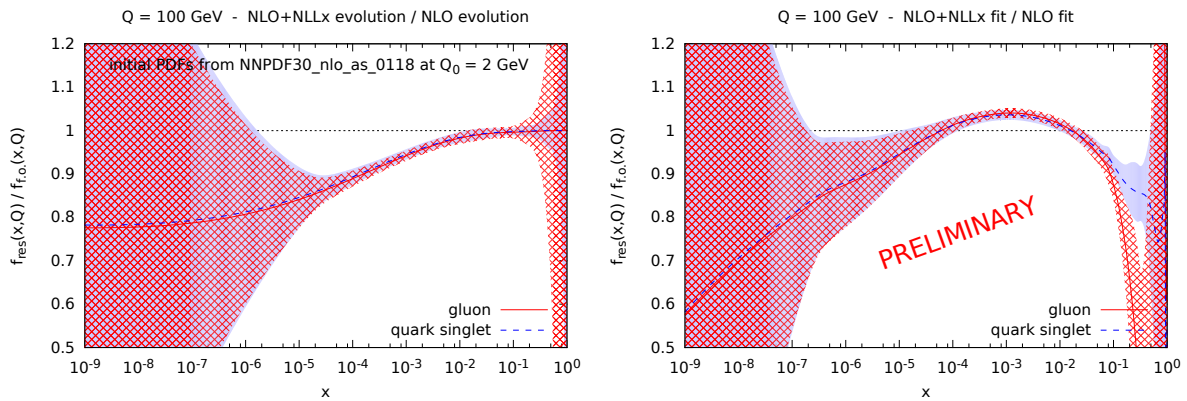


Fig. 21: Left plot: ratio of the gluon (solid red) and quark singlet (dashed blue) PDFs evolved with resummed NLO+NLLx evolution to the same input PDF evolved with fixed-order NLO evolution at  $Q = 100$  GeV. In this case the input PDF set at  $Q_0 = 2$  GeV is NNPDF3.0 NLO. We also show the 68% CL PDF uncertainty band for the numerator of this ratio. Right plot: same comparison, now using as input a preliminary DIS-only NNPDF fit performed using the resummed NLO+NLLx splitting functions in the DGLAP evolution, resulting in different input PDFs at the initial parametrization scale  $Q_0$ .

In Fig. 21 (left) we show the corresponding ratio of the gluon and quark singlet PDFs evolved with resummed NLO+NLLx evolution to the same PDF evolved with fixed-order NLO evolution at  $Q = 100$  GeV. In this comparison, we also include the 68% CL uncertainties, to compare them with the shift induced by the small- $x$  resummation effects. We observe a sizable effect of reducing the gluon and quark singlet PDFs, by approximately  $-20\%$  for  $x \lesssim 10^{-6}$ , but also by as much as  $-5\%$  at intermediate values of  $x \simeq 10^{-3}$ .

However, we note that in general refitting the PDFs with resummed evolution and coefficient functions will modify also the PDFs at the input parametrization scale, partially compensating some of the observed differences. Therefore, the actual effects of small- $x$  resummation will be different as compared to what Fig. 21 indicates; in fact, fitted resummed PDFs could even be larger than their fixed-order counterparts for some values of  $x$ . To illustrate this point, in Fig. 21 (right) we show a similar comparison as in Fig. 21 (left), but now using as input boundary condition for the evolution a preliminary NNPDF DIS-only small- $x$  resummed fit. In this preliminary small- $x$  fit, DGLAP evolution has been performed with NLO+NLLx DGLAP splitting functions rather than the standard NLO ones used in

fixed-order fits (but coefficients functions are still fixed-order NLO). As compared to using NLO PDFs as input, we observe that, when using a (partially) consistent resummed PDF set as input, the suppression at small- $x$  appears to be reduced, and a moderate enhancement of the PDFs at intermediate  $x$  is found, followed by a further suppression at large- $x$ . While all these results are very preliminary, Figs. 20–21 strongly suggest that the small- $x$  resummation effects will be relevant for precision physics at a 100 TeV collider.

It is also useful to estimate the potential impact of small- $x$  resummation effects for physical observables at the FCC. To do so, we consider the effect of resummed PDFs on a process which is directly sensitive to the medium and small- $x$  gluons, namely Higgs production in gluon fusion. We define

$$R_h \equiv \frac{\sigma_{\text{NLO}}(\text{NLO+NLL}_x \text{ PDFs})}{\sigma_{\text{NLO}}(\text{NLO PDFs})} \quad (14)$$

to be the ratio of the NLO cross section obtained with resummed NLO+NLL $_x$  PDFs to the NLO cross section obtained with NLO PDFs. In absence of fully consistent fitted resummed PDFs, we use the same approximate strategy used above of evolving with resummed NLO+NLL $_x$  anomalous dimensions the NLO PDFs from  $Q_0 = 2$  GeV up to the Higgs mass ( $m_h = 125$  GeV).

We find that  $R_h \simeq 0.96$  for the LHC at 13 TeV while  $R_h \simeq 0.89$  for the FCC at 100 TeV. Consistently with Fig. 21, the cross section is reduced by a sizable amount,  $-4\%$  at LHC and  $-11\%$  at FCC, where the larger effect at the FCC arises because the gluons fusing into the Higgs are on average at smaller  $x$ . Using refitted resummed PDFs will of course modify these estimates, most likely reducing the effect of the resummation, or even giving an enhancement of the cross section. Indeed, if one repeats the exercise using the preliminary fitted PDFs, the effect turns out to be an enhancement of  $+0.5\%$  at LHC and of  $+7\%$  at FCC. None of these estimates is fully reliable, however they clearly show that small- $x$  resummation will have a sizable impact at FCC. Note that for the specific case of Higgs pair production in gluon fusion, one should also consistently resum the small- $x$  logarithms in the partonic cross section: the effect of this resummation has not been studied yet, but the small- $x$  contributions are known to be non-negligible for high collider energies [94], and will be another fundamental ingredient for precision phenomenology at FCC.

### 3 Global event properties<sup>9</sup>

Unlike hard SM and BSM probes, which target small fractions of the total  $pp$  cross section, the aim with minimum-bias (MB) physics studies is to examine highly inclusive event samples, subject only to detector-acceptance limits and minimal trigger conditions (hence the name “minimum bias”<sup>10</sup>). The absence of any explicit requirement of hard activity implies that the particle production in such events is dominated by soft and semihard QCD processes. On the soft side, given the extended composite nature of hadrons, even at asymptotically large energies, a non-negligible fraction of inelastic p-p interactions involve “peripheral” scatterings with small transverse momentum transfer, described in terms of a Pomeron ( $\mathbb{P}$ ) contribution, identified perturbatively with a colour-singlet multi-gluon exchange, responsible for diffractive dissociation. Elastic and diffractive scatterings account for a noticeable fraction, about a third, of the total p-p cross section at high energies. In the semihard domain, at increasingly larger c.m. energies the inelastic cross section receives major contributions from the region of low parton fractional momenta ( $x = p_{\text{parton}}/p_{\text{hadron}}$ ), where the gluon distribution rises very fast. As a matter of fact, at  $\sqrt{s} = 100$  TeV the partonic cross section saturates the total inelastic cross section (i.e.  $\sigma_{\text{pQCD}} \approx \sigma_{\text{inel}} \approx 100$  mb) at momenta much larger than  $\Lambda_{\text{QCD}}$ ,  $p_{\text{T}} \approx 10$  GeV/c (see e.g. [95]). Such a “divergent” behaviour (taking place *well* above the infrared regime around  $\Lambda_{\text{QCD}} \approx 0.2$  GeV) is solved by reinterpreting this observation as a consequence of the increasing number of multiparton interactions (MPI) occurring in a single p-p collision. The energy evolution of such MPI and low- $x$  effects is implemented phenomenologically in all MCs through a transverse momentum cutoff  $p_{\perp 0}$  of a few GeV that tames the fastly-rising  $1/p_{\text{T}}^4$  minijet cross section (e.g., in PYTHIA the cutoff is introduced through a multiplicative  $1/(p_{\text{T}}^2 + p_{\perp 0}^2)^2$  factor). This  $p_{\perp 0}$  regulator is commonly defined so as to run with c.m. energy following a slow power-law (or logarithmic) dependence, closely mimicking the “saturation scale”  $Q_{\text{sat}}$  that controls the onset of non-linear (gluon fusion) effects saturating the growth of the PDFs as  $x \rightarrow 0$  [96]. Last but not least, all MC generators, both based on pQCD or Reggeon Field Theory (RFT) alike, use parton-to-hadron fragmentation approaches fitted to the experimental data – such as the Lund string [97], area law [98] or cluster hadronisation [99] models – to hadronise the coloured degrees of freedom once their virtuality evolves below  $\mathcal{O}(1 \text{ GeV})$ .

Closely connected to multiparton interactions is the “underlying event” (UE) activity denoting the global enhancement of softer particle production that accompanies the hardest partonic interactions in the event, contributing a “pedestal” term to jet energies and reducing particle isolation. Finally, for high-luminosity colliders, the additional “pileup” events that are recorded in the same bunch crossing as a primary triggered event are essentially unbiased<sup>11</sup>, hence the determination of pileup characteristics also falls under the minimum-bias physics program.

Notwithstanding the challenges posed by understanding and modelling semihard and non-perturbative dynamics, very large minimum-bias event samples can typically be accumulated in a matter of days, allowing for excellent high-statistics studies of a large range of physical observables which in turn furnish important constraints on phenomenological QCD models, hypotheses, and fits. The questions asked are often rather simple, such as: *what does the average collision look like?* and *how sizable are the event-to-event fluctuations?* Indeed, the charged-particle multiplicity distribution is typically the first physics measurement that a new collider experiment publishes. But importantly, the tails of distributions are also coming under increasing scrutiny, in particular towards large multiplicities and by using rare particles (such as ones containing multiple strange quarks, or  $c$  and  $b$  quarks) as tracers of the underlying physics mechanisms. The term “minimum bias” is perhaps then slightly misleading. Nonetheless,

<sup>9</sup>Editors: D. d’Enterria, P. Skands

<sup>10</sup>A “minimum-bias” trigger typically relies on hits in a set of forward detectors to ensure that at least a minimal amount of observable activity was produced. If hits are required on both sides of the event, the term “non-single-diffractive” (NSD) is also sometimes used. Triggers with zero bias are also possible, typically provided by a simple synchronisation with the bunch-crossing clock — hence a zero-bias sample can include some empty events where nothing actually happened.

<sup>11</sup>Note however, that a trigger event accompanied by an upwards fluctuation in pileup activity, is more likely to pass a given jet  $p_{\perp}$  trigger threshold than the same event accompanied by a low pileup level, hence the bias is not completely zero.

since these studies still do not rely on any conventional “hard trigger”, we retain the term MB as a catch-all phrase, including also diffractive and elastic scattering as well as more exclusive (biased) subsets of the MB data sample.

### 3.1 Minimum bias collisions

The general-purpose Monte Carlo (MC) models used in high-energy collider physics, such as PYTHIA 6 [100], PYTHIA 8 [32], HERWIG ++ [101], and SHERPA [102], are fully based on a pQCD framework which then incorporates soft diffractive scatterings in a more or less ad hoc manner. In contrast, MC models commonly used in cosmic-ray physics [20] such as EPOS [103–105], QGSJET 01 [106, 107], QGSJET-II [108–111] and SIBYLL [112], as well as PHOJET [113–115] and DPMJET [116, 117] mostly used for collider environments, are based on simple quantum field-theory principles –such as unitarity and analyticity of scattering amplitudes as implemented in the RFT model [118]. The latter MCs start off from a construction of the hadron-hadron elastic scattering amplitude to determine the total, elastic and inelastic (including diffractive) cross sections, extended to include hard processes via “cut (hard) Pomerons” (also known as “parton ladder”) diagrams. In this section, we compare the basic properties of the MB observables characterising the final states produced in proton-proton collisions at  $\sqrt{s} = 100$  TeV, predicted by pQCD- and RFT-based hadronic interaction models [119].

The basic ingredients of the PYTHIA 6 and 8 event generators are leading-order (LO) pQCD  $2 \rightarrow 2$  matrix elements, complemented with initial- and final-state parton radiation (ISR and FSR), folded with PDFs (interfaced here via the LHAPDF v6.1.6 package [120]), and the Lund string model [97] for parton hadronisation. The decomposition of the inelastic cross section into non-diffractive and diffractive components is based on a Regge model [121]. For the minimum-bias studies we use the PYTHIA event generator in two flavours: the Fortran version 6.428 [100], as well as the C++ version PYTHIA 8.170 [122]. We consider two different “tunes” of the parameters governing the non-perturbative and semi-hard dynamics (ISR and FSR showering, MPI, beam-remnants, final-state colour-reconnection (CR), and hadronisation). For PYTHIA 6.4 we use the Perugia 2011 tune (MSTP(5)=350) [33], while for PYTHIA 8 we use the Monash 2013 (Tune: ee=7; Tune: pp=14) [19]. Both sets of parameters (Table 3) have been obtained from recent (2011 and 2013 respectively) analysis of MB, underlying-event (UE), and/or Drell-Yan data in p-p collisions at  $\sqrt{s} = 7$  TeV.

Version	Tuning	Diffraction	Semihard dynamics		Initial state		Final state	
			$p_{\perp 0}(7 \text{ TeV})$	power $b$	PDF	p-p overlap	CR	hadr
6.428	Perugia 2011	Regge [121]	2.93 GeV	0.265	CTEQ5L	$\exp(-r^{1.7})$	moderate	Lund model
8.170	Monash 2013	Improved [123]	2.28 GeV	0.215	NNPDF2.3 LO	$\exp(-r^{1.85})$	moderate	Lund model

Table 3: Comparison of the various ingredients controlling the non-perturbative and semihard (MPI, saturation) dynamics in the two PYTHIA MCs used in this work. See text for details.

For the initial state, PYTHIA 6 (Perugia 2011) uses the CTEQ5L parton densities [124] and PYTHIA 8 (Monash) the more recent NNPDF2.3 LO set [53]. For the description of the transverse parton density, both models use a proton-proton overlap function proportional to  $\exp(-r^n)$ , with slightly different exponents ( $n = 1.7$  and  $1.85$  respectively). The Perugia-2011 choice results in a slightly broader p-p overlap function which thereby enhances the fluctuations in the number of MPI relative to the Monash-2013 choice. The perturbative MPI cross sections are suppressed below a regularisation scale,  $p_{\perp 0}$ , whose evolution with c.m. energy is driven by a power law,

$$p_{\perp 0}^2(s) = p_{\perp 0}^2(s_0) \cdot (s/s_0)^b, \quad (15)$$

with the parameters quoted in Table 3 (with  $\sqrt{s_0} = 7$  TeV). Given that the generation of additional parton-parton interactions in the UE is suppressed below  $p_{\perp 0}$ , a *higher* scaling power  $b$  implies a *slower* increase of the overall hadronic activity. Thus, the Monash tune results in a slower evolution of  $p_{\perp 0}$ ,

yielding larger MPI activity at 100 TeV compared to the Perugia tune. The treatment of diffraction has improved in PYTHIA 8 compared to 6, by viewing a diffractive system as a Pomeron-proton collision which can include hard scatterings subject to all the same ISR/FSR and MPI dynamics as for a “normal” parton-parton process [123, 125]. For the final-state, the two tunes have strong final-state colour reconnections (implemented through different models [32, 126, 127]), which act to *reduce* the number of final-state particles (for a given  $p_{\perp 0}$  value), or, equivalently, lower the  $p_{\perp 0}$  value that is required to reach a given average final-state multiplicity. The Lund hadronisation parameters for light- and heavy-quarks have been updated in PYTHIA 8 compared to PYTHIA 6 by refitting updated sets of LEP and SLD data [19].

The RFT-based models used in this work differ in various approximations for the collision configurations (e.g. the distributions for the number of cut Pomerons, and for the energy-momentum partition among them), the treatment of diffractive and semihard dynamics, the details of particle production from string fragmentation, and the incorporation or not of other final-state effects (Table 4). Whereas the RFT approach is applied using only Pomerons and Reggeons in the case of QGSJET-II and PHOJET, EPOS extends it to include partonic constituents [128]. In the latter case, this is done with an exact implementation of energy sharing between the different constituents of a hadron at the amplitude level. The evolution of the parton ladders from the projectile and the target side towards the center (small  $x$ ) is governed by the DGLAP equations [129–131]. For the minijet production cutoff, PHOJET uses dependence of the form  $p_{\perp 0}(s) \sim p_{\perp 0} + C \cdot \log(\sqrt{s})$ , whereas EPOS and QGSJET-II use a fixed value of  $p_{\perp 0}$ . The latter resums low- $x$  effects dynamically through enhanced diagrams corresponding to multi-Pomeron interactions [108, 132, 133]. In that framework, high mass diffraction and parton screening and saturation are related to each other, being governed by the chosen multi-Pomeron vertices, leading to impact-parameter and density-dependent saturation at low momenta [134]. LHC data were used to tune the latest QGSJET-II-04 release [111] shown here. EPOS on the other hand, uses the wealth of RHIC proton-proton and nucleus-nucleus data to parametrise the low- $x$  behaviour of the parton densities in a more phenomenological way [103] (correcting the  $\mathbb{P}$  amplitude used for both cross-section and particle production). The EPOS MC is run with the LHC tune [105] which includes collective final-state string interactions which result in an extra radial flow of the final hadrons produced in more central pp collisions. Among all the MC models presented here, PHOJET is the only one which does not take into account any retuning using LHC data (its last parameter update dates from year 2000).

Model (version)	Diffraction	Semihard dynamics		Final state
		$p_{\perp 0}$	evolution	
EPOS-LHC [105]	effective diffractive $\mathbb{P}$	2.0 GeV	power-law corr. of $\mathbb{P}$	area law hadronisation + collective flow
QGSJET-II-04 [108–110]	G.-W. [135] + $\mathbb{P}$ cut-enhanced	1.6 GeV	enhanced $\mathbb{P}$ -graphs	simplified string hadronisation
PHOJET 1.12 [113, 114]	G.-W. [135]	2.5 GeV	$p_{\perp 0}(s) \propto \log(\sqrt{s})$	hadronisation via PYTHIA 6.115

Table 4: Comparison of the main ingredients controlling the non-perturbative and semi-hard dynamics present in the RFT-based event generators used in this work.

The results are presented, in the case of PYTHIA 6 and 8, for primary charged particles, defined as all charged particles produced in the collision including the products of strong and electromagnetic decays but excluding products of weak decays, obtained by decaying all unstable particles<sup>12</sup> for which  $c\tau < 10$  mm. For the RFT MCs, unless stated otherwise, the results correspond to the primary charged hadrons (with the same  $c\tau$  requirement) but without charged leptons which, nonetheless, represent a very small correction (amounting to about 1.5% of the total charged yield, mostly from the Dalitz  $\pi^0$  decay). Unless explicitly stated, no requirement on the minimum  $p_T$  of the particles is applied in any of the results presented.

<sup>12</sup>PYTHIA 6.4: MSTJ(22)=2,PARJ(71)=10. PYTHIA 8: ParticleDecays:limitTau0 = on, ParticleDecays:tau0Max = 10.

### 3.1.1 Inelastic pp cross section

The most inclusive quantity measurable in p-p collisions is the total hadronic cross section  $\sigma_{\text{tot}}$  and its separation into elastic and inelastic (and, in particular, diffractive) components. In both PYTHIA 6 and 8, the total hadronic cross section is calculated using the Donnachie-Landshoff parametrisation [136], including Pomeron and Reggeon terms, whereas the elastic and diffractive cross sections are calculated using the Schuler-Sjöstrand model [121]. The predictions for the inelastic cross sections in p-p at  $\sqrt{s} = 100$  TeV, obtained simply from  $\sigma_{\text{tot}} - \sigma_{\text{el}}$ , yield basically the same value,  $\sigma_{\text{inel}} \approx 107$  mb, for both PYTHIA 6 and 8. The RFT-based MCs, based on  $\mathbb{P}$  amplitudes, predict slightly lower values  $\sigma_{\text{inel}} = 105.4, 104.8, 103.1$  mb for EPOS-LHC, QGSJET-II and PHOJET respectively. The  $\sqrt{s}$  dependence of the inelastic cross section predicted by all models is shown in Fig. 22 together with the available data from p- $\bar{p}$  (UA5 [137], E710 [138] and CDF [139]) and p-p (ALICE [140], ATLAS [141, 142], CMS [143, 144], TOTEM [145]) colliders, as well as the AUGER result at  $\sqrt{s} = 57$  TeV derived from cosmic-ray data<sup>13</sup> [146]. Interestingly, all model curves cross at about  $\sqrt{s} \approx 60$  TeV, and predict about the same inelastic cross section at the nominal FCC-pp c.m. energy of 100 TeV. A simple average among

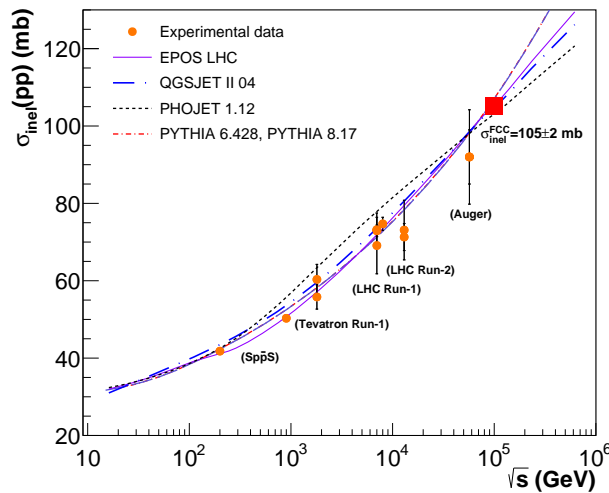


Fig. 22: Inelastic p-p cross section  $\sigma_{\text{inel}}$  as a function of c.m. energy in the range  $\sqrt{s} \approx 10$  GeV–500 TeV. Experimental data points at various collider and cosmic-ray energies [137–146] are compared to the predictions of EPOS-LHC, QGSJET-II-04, PHOJET 1.12, and PYTHIA (both 6.428 and 8.17 predict the same dependence). The red box indicates the average prediction of all models at 100 TeV.

all predictions yields  $\sigma_{\text{inel}}(100 \text{ TeV}) = 105.1 \pm 2.0$  mb, whereas larger differences in the energy evolution of  $\sigma_{\text{inel}}$  appear above the  $\sqrt{s} \approx 300$  TeV, i.e. around and above the maximum energy observed so far in high-energy cosmic rays impinging the Earth atmosphere [20]. The expected increase in the inelastic p-p cross section at FCC(100 TeV) is about 45% compared to the LHC results at 13 TeV ( $\sigma_{\text{inel}} = 73.1 \pm 7.7$  mb [142] from ATLAS, and preliminarily  $71.3 \pm 3.5$  mb [144] from CMS).

### 3.1.2 Particle and energy pseudorapidity densities

Figure 23 shows the distribution of charged particles produced per unit of pseudorapidity, as a function of pseudorapidity ( $dN_{\text{ch}}/d\eta$ ) in p-p collisions at 100 TeV, as predicted by the different models. About 10 charged particles are produced at midrapidity at FCC-pp. The left plot shows the so-called “non single-diffractive” (NSD) distribution, mimicking the typical experimental requirement of a two-arm trigger<sup>14</sup> with particles in opposite hemispheres to eliminate backgrounds from beam-gas collisions and

<sup>13</sup>Note: AUGER measures p-Air cross sections and extrapolates to p-p via a Glauber model.

<sup>14</sup>In PYTHIA 6 and 8 this is achieved by directly switching off single-diffractive contributions via: MSUB(92)=MSUB(93)=0, and SoftQCD:singleDiffraction=off.

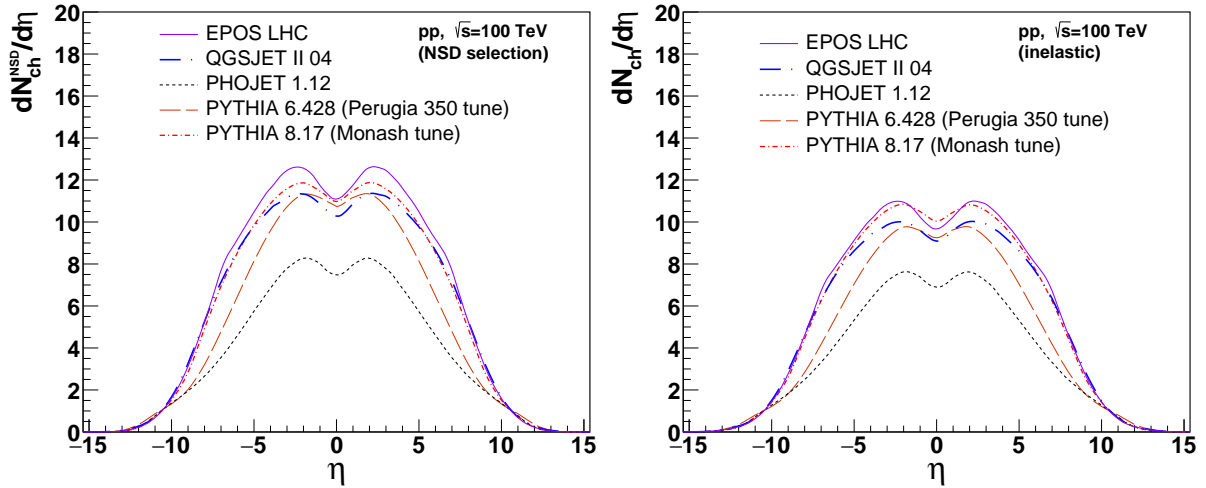


Fig. 23: Distributions of the pseudorapidity density of charged particles in non single-diffractive (left) and inelastic (right) p-p collisions at  $\sqrt{s} = 100$  TeV, predicted by different hadronic MC generators.

cosmic-rays. Such NSD topology reduces significantly the detection rate of (single) diffractive collisions characterised by the survival of one of the colliding protons and particle production in just one hemisphere. The right plot shows the inclusive inelastic distribution which, including lower-multiplicity diffractive interactions, has a smaller average number of particles produced. At midrapidity ( $\eta = 0$ ), all models (except PHOJET) predict very similar number of hadrons produced. Taking a (non-weighted) average of all the predictions (except PHOJET which is systematically lower by  $\sim 40\%$ ), we obtain:  $dN_{ch}^{NSD}/d\eta|_{\eta=0} = 10.8 \pm 0.3$  and  $dN_{ch}/d\eta|_{\eta=0} = 9.6 \pm 0.2$ . However, at forward rapidities (equivalent to small  $x \approx p_T/\sqrt{s} \cdot e^{-\eta}$ ) PYTHIA 6 and PHOJET predict noticeably “thinner” distributions than the rest, due to lower underlying gluon densities at scales around  $p_{\perp 0}$ , than those from the NNPDF 2.3 LO set used in PYTHIA 8 [19]. A significant fraction of the particles produced issue from the fragmentation of partons from semihard MPI, the hardest partonic collision in the MB event producing only a small fraction of them. The fact that PHOJET misses about  $\sim 40\%$  of the particles yields is indicative of missing multiparton contributions in this Monte Carlo generator.

The energy dependence of the charged hadron pseudorapidity density at  $\eta = 0$  predicted by the different models in the range  $\sqrt{s} = 10$  GeV–700 TeV is presented in Fig. 24 compared to the existing NSD (left panel) and inelastic (right panel) data measured at Sp $\bar{p}$ S (UA1 [147], and UA5 [148]), Tevatron (CDF [149, 150]) and LHC (ALICE [151, 152], ATLAS [153] and CMS [154]) colliders. As aforementioned, the NSD selection has central densities which are about 15% larger than those obtained with the less-biased INEL trigger, which has less particles produced on average as it includes (most of) diffractive production. All models (except PHOJET, whose results are not actually trustable beyond  $\sqrt{s} = 75$  TeV) more or less reproduce the available experimental data up to LHC, and show a very similar trend with  $\sqrt{s}$  up to FCC energies. Beyond 100 TeV, however, EPOS-LHC tends to produce higher yields than the rest of MCs.

The FCC experiments aim at fully tracking coverage in the central  $|\eta| < 5$  region. The total number of charged particles expected in the tracker system is obtained by integrating the  $dN_{ch}/d\eta$  distributions over that interval, which yields an average of  $N_{ch}(\Delta\eta=10) \approx 100$ . For the expected FCC pileups, in the range  $\mathcal{O}(200 - 1000)$ , this value implies that the trackers would sustain on average a total number of 20–100 thousand tracks per bunch crossing. Such a value is of the same order of magnitude as a *single* central Pb-Pb collision at LHC energies [156], and thus perfectly manageable for the high-granularity FCC tracker designs. Further integrating the  $dN_{ch}/d\eta$  distributions over all pseudorapidities, one obtains the total number of charged particles produced in an average p-p collision at 100 TeV. The EPOS, PYTHIA 8 and QGSJET-II models predict the largest total charged multiplicities,  $N_{ch}(N_{ch}^{NSD}) = 161$  (184),

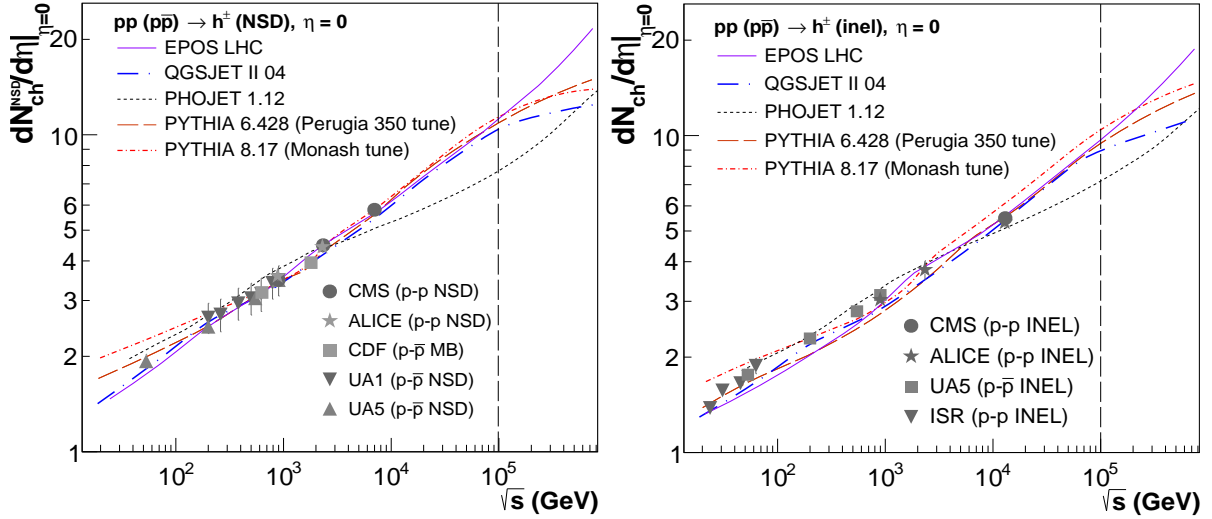


Fig. 24: Evolution of the charged particle pseudorapidity density at midrapidity,  $dN_{\text{ch}}/d\eta|_{\eta=0}$ , as a function of collision energy,  $\sqrt{s}$ , for non-single diffractive (left) and inelastic (right) p-p collisions. The data points show existing collider data [147, 148, 153–155]. The vertical line indicates the FCC energy at 100 TeV.

160 (170), 152 (172) respectively; followed by PYTHIA 6,  $N_{\text{ch}} (N_{\text{ch}}^{\text{NSD}}) = 131 (150)$ ; and PHOJET,  $N_{\text{ch}} (N_{\text{ch}}^{\text{NSD}}) = 103 (111)$ .

The plots in Fig. 25 show the energy density as a function of pseudorapidity. The left plot shows the distribution for total energy, and the right one for the energy carried by charged particles above a minimum  $p_{\text{T}} = 100 \text{ MeV}/c$ . PHOJET predicts the lowest energy produced at all rapidities (consistent with the lower particle yields produced by the model) whereas PYTHIA 8 predicts the highest. At  $\eta = 0$ ,

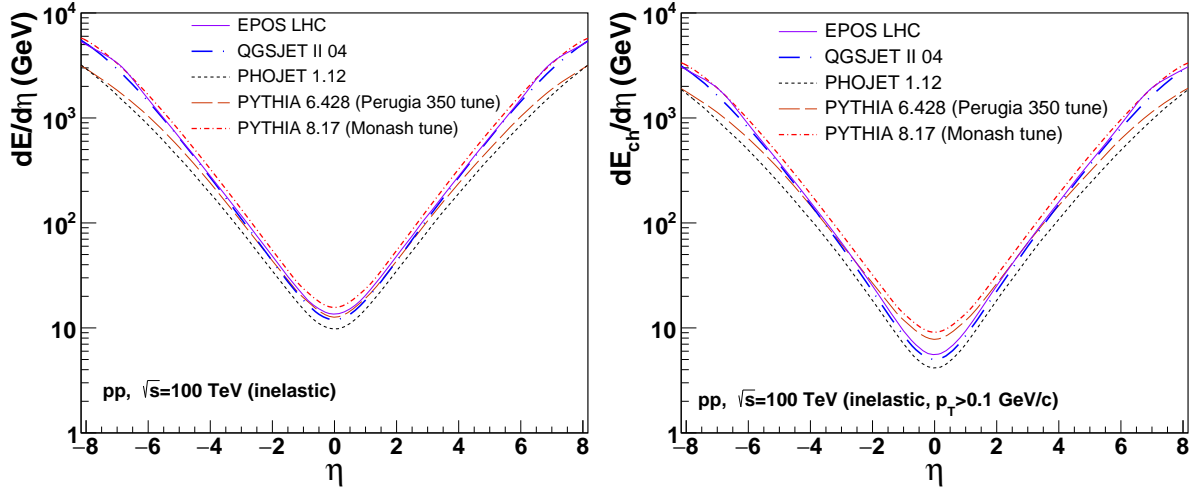


Fig. 25: Distribution of the energy pseudorapidity density of all particles (left) and of charged particles with  $p_{\text{T}} > 0.1 \text{ GeV}/c$  (right) in inelastic p-p collisions at  $\sqrt{s} = 100 \text{ TeV}$ , predicted by the different MCs considered in this work.

the total energy produced per unit rapidity is  $dE/d\eta = 9.9, 12.2, 12.6, 13.7$  and  $15.6 \text{ GeV}$  for PHOJET, QGSJET-II, PYTHIA 6, EPOS-LHC and PYTHIA 8 respectively. The same values at the forward edges of typical detector coverages ( $|\eta| = 5$ ) are  $dE/d\eta \approx 410, 525, 670, 700$  and  $760 \text{ GeV}$  for PHOJET, PYTHIA 6, QGSJET-II, EPOS-LHC and PYTHIA 8 respectively. The trend for PYTHIA 6 is to predict a

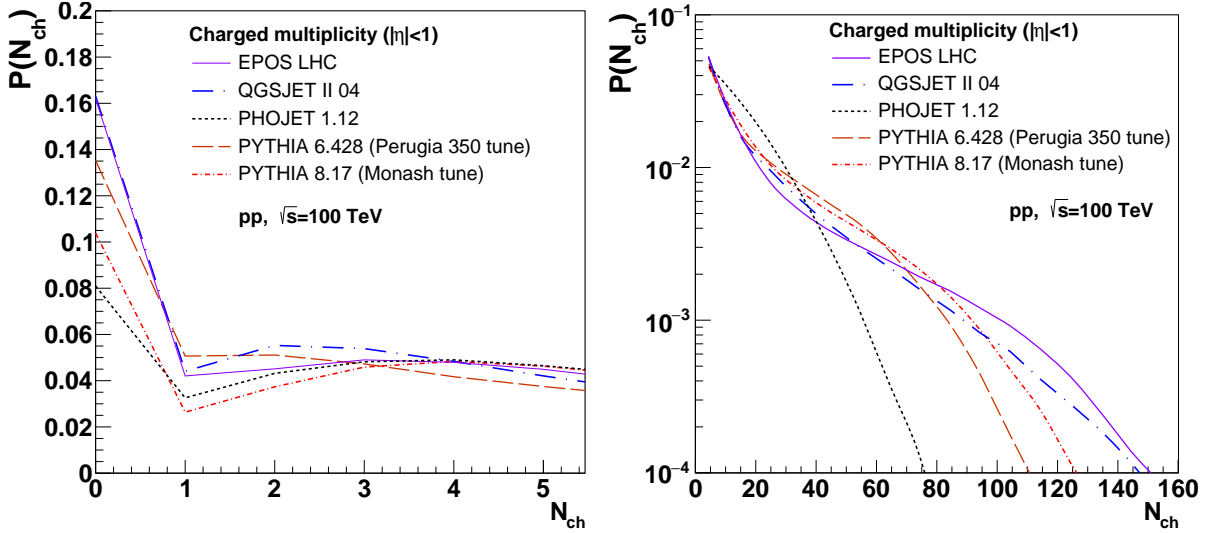


Fig. 26: Per-event charged particle probability (within  $|\eta| < 1$ ) in inelastic p-p collisions at  $\sqrt{s} = 100$  TeV: full distribution (right), zoom at low multiplicities  $P(N_{\text{ch}}) < 5$  (left).

smaller relative increase of energy density as a function of rapidity compared to the rest of models due, again, to a more relatively depleted underlying gluon density at the increasingly lower  $x$  values probed at forward  $\eta$ .

### 3.1.3 Multiplicity distribution

The multiplicity distribution  $P(N_{\text{ch}})$ , i.e. the probability to produce  $N_{\text{ch}}$  charged particles in a p-p event, provides important differential constraints on the internal details of the hadronic interaction models. Figure 26 shows the distribution for charged particles produced at central rapidities ( $|\eta| < 1$ ) in inelastic p-p collisions at the FCC. The tail of the  $P(N_{\text{ch}})$  distribution (left) gives information on the relative contribution of multiparton scatterings (multi-Pomeron exchanges), whereas the low multiplicity part (right) is mostly sensitive to the contributions from diffraction (single Pomeron exchanges). The different MCs predict quite different distribution in both ends of the spectrum. The RFT-based models EPOS-LHC and QGSJET-II both predict higher yields at very low ( $N_{\text{ch}} < 3$ ) and very high ( $N_{\text{ch}} > 100$ ) particle multiplicities, whereas PYTHIA 6 and 8 feature higher yields in the intermediate region  $N_{\text{ch}} \approx 30$ –80, and PHOJET has a very similar  $P(N_{\text{ch}})$  distribution to PYTHIA but clearly produces much fewer particles at intermediate and high multiplicities, compared to the rest of models (which is, again, indicative of missing MPI contributions in this MC).

### 3.1.4 Transverse momentum distribution

Figure 27 (left) shows the  $p_{\text{T}}$ -differential distributions of charged particles at midrapidity ( $|\eta| < 2.5$ ) in NSD p-p collisions at FCC(100 TeV) predicted by all models except PHOJET. All spectra have been absolutely normalised at their value at  $p_{\text{T}} \approx 0.5$  GeV to be able to easily compare their shapes. Both PYTHIA 6 and 8 feature the largest yields at the high- $p_{\text{T}}$  end of the distributions (not shown here), QGSJET-II features the “softest” spectrum, whereas EPOS shows higher yields in the region  $p_{\text{T}} \approx 1$ –5 GeV/c, due to collective partonic flow boosting the semihard region of the spectra, but then progressively falls below the pure-pQCD PYTHIA MC generators. The PHOJET spectrum has a more convex shape, being comparatively depleted at intermediate  $p_{\text{T}} \approx 1$ –3 GeV/c but rising at its tail. Studying the  $\sqrt{s}$ -evolution of the average  $p_{\text{T}}$  of the spectra provides useful (integrated) information. At high energies, the peak of the perturbative cross section comes from interactions between partons whose transverse momentum is around the saturation scale,  $\langle p_{\text{T}} \rangle \approx Q_{\text{sat}}$ , producing (mini)jets of a few GeV which fragment

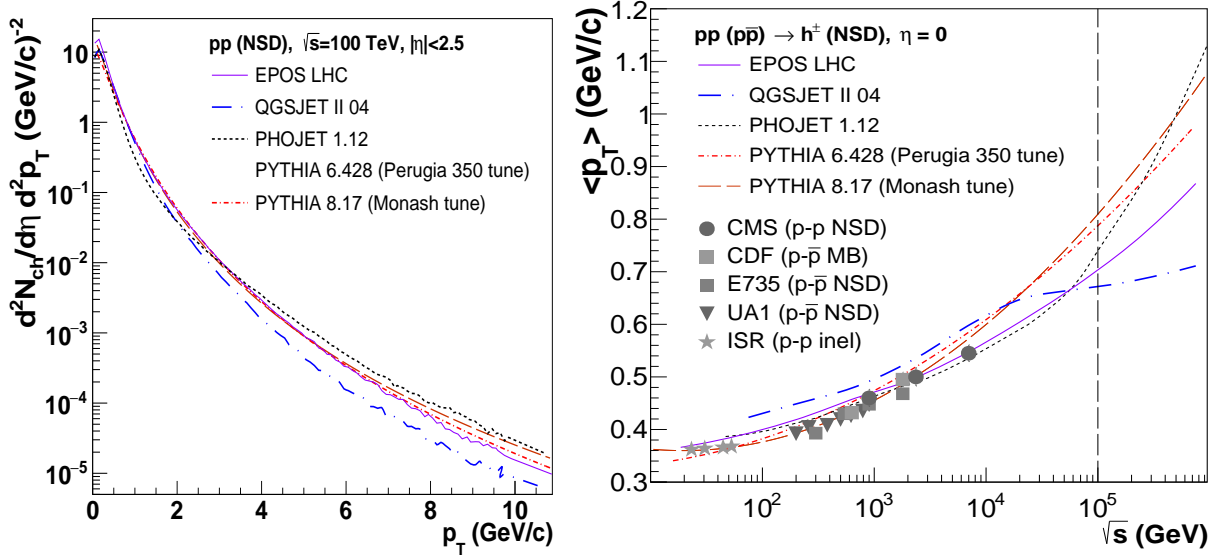


Fig. 27: Left: Transverse momentum spectrum in p-p collisions at  $\sqrt{s} = 100$  TeV predicted by the different MCs considered in this work (absolutely normalised at a common value at  $p_T \approx 0.5$  GeV/c). Right: Evolution of  $\langle p_T \rangle$  at midrapidity as a function of c.m. energy  $\sqrt{s}$ . Data points show existing collider results [147, 150, 154, 157, 157, 158], and the vertical line indicates the FCC(100 TeV) energy.

into hadrons. As explained in the introduction, PYTHIA and PHOJET MCs have an energy-dependent  $p_T$  cutoff that mimics the power-law evolution of  $Q_{sat}$ , while EPOS and QGSJET-II have a fixed  $p_T$  cutoff and the low- $x$  saturation dynamics is implemented through corrections to the multi-Pomeron dynamics. The different behaviors are seen in the  $\sqrt{s}$ -evolution of the average  $p_T$  shown in Fig. 27 (right). All MCs, except QGSJET-II, predict a (slow) powerlaw-like increase of  $\langle p_T \rangle$  with energy. Both PYTHIA 6 and 8—whose dynamics is fully dominated by (mini)jet production—predict a higher  $\langle p_T \rangle$  than the rest of models, yielding  $\langle p_T \rangle \approx 0.82$  GeV/c at FCC(100 TeV) to be compared with 0.71 and 0.67 GeV/c from EPOS-LHC and QGSJET-II respectively. Above  $\sqrt{s} \approx 20$  TeV, QGSJET-II predicts a flattening of  $\langle p_T \rangle$  whereas the EPOS-LHC evolution continues to rise due to the final-state collective flow which increases the  $\langle p_T \rangle$  with increasing multiplicity.

### 3.1.5 Minimum bias summary

In summary, the global properties of the final states produced in hadronic interactions of protons at center-of-mass energies of the Future Hadron Collider, have been studied with various Monte Carlo event generators used in collider physics (PYTHIA 6, PYTHIA 8, and PHOJET) and in ultrahigh-energy cosmic-rays studies (EPOS, and QGSJET-II). Despite their different underlying modeling of hadronic interactions, their predictions for proton-proton (p-p) collisions at  $\sqrt{s} = 100$  TeV are quite similar (excluding PHOJET, whose parameters have not been improved with the available collider data in the last 15 years). Table 5 lists the predictions of these basic kinematical observables for all MCs considered. The averages of all MC predictions (except PHOJET) for the different observables are: (i) p-p inelastic cross sections  $\sigma_{inel} = 105 \pm 2$  mb (to be compared with  $\sigma_{inel} \approx 72$  mb at the LHC(13 TeV), i.e., a  $\sim 45\%$  increase), (ii) total charged multiplicity  $N_{ch}$  ( $N_{ch}^{NSD}$ ) =  $150$  ( $170$ )  $\pm 20$ , (iii) charged particle pseudorapidity density at midrapidity  $dN_{ch}/d\eta|_{\eta=0} = 9.6 \pm 0.2$  (to be compared with the LHC(13 TeV) result of  $dN_{ch}/d\eta|_{\eta=0} = 5.4 \pm 0.2$ , i.e., an increase of  $\sim 80\%$ ), and  $dN_{ch}^{NSD}/d\eta|_{\eta=0} = 10.8 \pm 0.3$  for the NSD selection, (iv) energy density at midrapidity  $dE/d\eta|_{\eta=0} = 13.6 \pm 1.5$  GeV, and energy density at the edge of the central region  $dE/d\eta|_{\eta=5} = 670 \pm 70$  GeV, and (v) average transverse momenta at midrapidities  $\langle p_T \rangle = 0.76 \pm 0.07$  GeV/c (to be compared with  $= 0.55 \pm 0.16$  at the LHC(8 TeV), i.e., a  $\sim 40\%$  increase). The per-event multiplicity probabilities  $P(N_{ch})$ , have been also compared: EPOS-LHC

	PYTHIA 6	PYTHIA 8	EPOS-LHC	QGSJET-II	PHOJET	Average*
$\sigma_{\text{inel}}$ (mb)	106.9	107.1	105.4	104.8	103.1	$105.1 \pm 2.0$
$N_{\text{ch}}(N_{\text{ch}}^{\text{NSD}})$	131 (150)	160 (170)	161 (184)	152 (172)	101 (121)	$150 (170) \pm 20$
$dN_{\text{ch}}/d\eta _{\eta=0}$	$9.20 \pm 0.01$	$10.10 \pm 0.06$	$9.70 \pm 0.16$	$9.10 \pm 0.15$	$6.90 \pm 0.13$	$9.6 \pm 0.2$
$dN_{\text{ch}}^{\text{NSD}}/d\eta _{\eta=0}$	$10.70 \pm 0.06$	$10.90 \pm 0.06$	$11.10 \pm 0.18$	$10.30 \pm 0.17$	$7.50 \pm 0.15$	$10.8 \pm 0.3$
$dE/d\eta _{\eta=0}$ (GeV)	$12.65 \pm 0.07$	$15.65 \pm 0.02$	$13.70 \pm 0.02$	$12.2 \pm 0.02$	$9.9 \pm 0.01$	$13.6 \pm 1.5$
$dE/d\eta _{\eta=5}$ (GeV)	$525 \pm 4$	$760 \pm 1$	$700 \pm 1$	$670 \pm 1$	$410 \pm 1$	$670 \pm 70$
$P(N_{\text{ch}} < 5)$	0.28	0.22	0.35	0.36	0.25	–
$P(N_{\text{ch}} > 100)$	$3.3 \cdot 10^{-3}$	0.011	0.025	0.018	$10^{-5}$	–
$\langle p_T \rangle$ (GeV/c)	$0.80 \pm 0.02$	$0.84 \pm 0.02$	$0.71 \pm 0.02$	$0.67 \pm 0.02$	$0.73 \pm 0.02$	$0.76 \pm 0.07$

Table 5: Comparison of the basic properties of particle production in p-p collisions at  $\sqrt{s} = 100$  TeV, predicted by PYTHIA 6 and 8, EPOS-LHC, QGSJET-II, and PHOJET: Inelastic cross section  $\sigma_{\text{inel}}$ ; total charged multiplicities ( $N_{\text{ch}}$ ), and pseudorapidity charged particle densities at midrapidity ( $dN_{\text{ch}}/d\eta|_{\eta=0}$ ) for inelastic and NSD selections; energy densities at midrapidity ( $dE/d\eta|_{\eta=0}$ ), and at more forward rapidities ( $dE/d\eta|_{\eta=5}$ ); typical values of the charged multiplicity probabilities  $P(N_{\text{ch}})$  (over  $|\eta| < 1$ ) for low and high values of  $N_{\text{ch}}$ ; and mean charged particle transverse momentum  $\langle p_T \rangle$  over  $|\eta| < 2.5$ . The quoted uncertainties on the individual predictions are just the MC statistical ones. The last column indicates the average of all MCs (except PHOJET)\* for each observable, with uncertainties approximately covering the range of the predictions.

and QGSJET-II both predict higher yields at very low ( $N_{\text{ch}} < 3$ ) and very high ( $N_{\text{ch}} > 100$ ) particle multiplicities, whereas PYTHIA 6 and 8 feature higher yields in the intermediate region  $N_{\text{ch}} \approx 30$ –80. These results are useful to estimate the expected detector occupancies and energy deposits from pileup collisions at high luminosities of relevance for planned FCC detector designs.

### 3.2 Underlying event in high- $p_T$ triggered events

The fact that hard jets (or more generally, high- $p_{\perp}$  triggered events of any kind) are accompanied by a global “pedestal” of additional particle production, called the “underlying event” (UE), has been known since the days of UA1 [159]. It originates from the same additional parton-parton interactions (or cut Pomerons, depending on the language) as those that drive the tail towards large multiplicities in MB events. However, the imposition of a hard trigger biases the event selection towards events with many MPI (each of which has a chance to be the trigger reaction). Average particle multiplicities and  $E_T$  sums in the UE are therefore typically several times larger than in MB events at the same c.m. energy.

The average properties of the UE have been well established by measurements at RHIC, the Tevatron, and LHC, and are generally well reproduced by MC models that include hard (perturbative) QCD interactions and MPI. We here consider extrapolations to 100 TeV of several recent UE tunes of HERWIG 7 [101, 160] (version 3.0) and PYTHIA 8 [32] (version 8.215), which incorporate slightly different MPI models, described below. To facilitate comparisons between the MB and UE results presented in this study, we choose one of the PYTHIA 8 tunes to be the same (Monash 2013) as in the plots in the previous subsection.

The amount of transverse energy associated with the UE is relevant to a broad range of studies, since it enters as an additive term in jet energy calibrations. Independently of the details of jet algorithms and calibration techniques, the average  $E_T$  density (per unit  $\Delta\eta \times \Delta\phi$ ) furnishes a salient basic characterisation of the UE level, and we take this as our main observable for this study. The relative improvement obtainable from calibration techniques that take the in-situ (per-event) UE level into account can be estimated from the event-by-event fluctuations, which are sizable (larger than a naive Poissonian  $\sqrt{\langle E_T \rangle}$ ) at the LHC [161]. Thus we also include the standard deviation of the  $E_T$  density. To put these results in a tracking context, we also include results for the charged-track densities and the average track

$p_{\perp}$ . We do not attempt to include an estimate of the inhomogeneities in the UE distribution within each event.

We consider a fictitious detector spanning  $|\eta| < 6$  (which can roughly be considered the “central” rapidity plateau at 100 TeV energies, spanning the seagull-shaped peak of the  $dN_{\text{ch}}/d\eta$  distribution, cf. the preceding subsection) and use the conventional “Transverse Region” to define the UE phase space, covering the azimuth range  $60^{\circ} < |\Delta\phi| < 120^{\circ}$  with respect to the highest- $p_{\perp}$  track in the event. Within the transverse region, we include all stable charged final-state particles,  $\leq$ , subject to two different  $p_{\perp}$  cuts, at 100 and 500 MeV respectively. These cuts are carried over from the ATLAS study this analysis is modelled on [161]. The lower one includes the peak of soft particle production with transverse momenta  $p_{\perp} \sim \Lambda_{\text{QCD}}$  while the higher one focuses on the tail with  $p_{\perp} > \Lambda_{\text{QCD}}$ .

These observables are intended to give a first idea of what the UE may look like at 100 TeV, for detector-design and physics-analysis / jet-calibration estimation purposes. They do not address the more detailed physics studies of the UE *dynamics* that could be possible at 100 TeV. It is nonetheless worth emphasising that an increasing number of such studies are now being undertaken at the LHC, driven by tantalising hints of non-trivial global hadronisation effects in p-p collisions which go beyond the ability of most current models to describe. Among the most intriguing observations are the appearance in high-multiplicity p-p collisions of qualitative features that are traditionally associated with collective / flow-like effects and/or with an increased energy scale for particle production. Examples are the CMS “ridge” effect [162], the by now well-established gradual increase of  $\langle p_{\perp} \rangle$  with multiplicity, and the seemingly increased rates of strangeness and baryon production, relative to models that correctly describe equivalent observables in  $e^{+}e^{-}$  environments (see, e.g., the plots available on `mcp1ots.cern.ch` [163]). We expect that an analogous fruitful programme of new measurements exploring the UE dynamics in further detail can be carried out at 100 TeV. From the point of view of detector design, we note that hadron-flavour dependence (and hence particle identification capability) has emerged as a powerful tool [164–173] to disentangle the trends along axes of mass, strangeness, spin, and baryon number.

### 3.2.1 MC Models

The current MPI model in HERWIG 7 includes hard [174] (similar to the JIMMY [175] package) and soft components [176] of multiple partonic interactions as well as improved colour reconnection models [177]. The main parameters of the model are  $p_{\perp}^{\text{min}}$  which sets a transition scale between the hard and soft (non-perturbative) components,  $\mu$  which can be interpreted as the inverse radius of the proton (governing the difference in matter overlap between central and peripheral p-p collisions), and  $p_{\text{reco}}$  which parametrises the probability of colour reconnection. The value of  $p_{\perp}^{\text{min}}$  is allowed to vary with c.m. energy according to the same power law as in PYTHIA, eq. (15), and, in fact, it is  $p_{\perp,0}^{\text{min}}$  and  $b$  that are fit to data, with  $E_0 = 7$  TeV. (Note that  $p_{\perp}^{\text{min}}$  is the only parameter in HERWIG 7 which varies explicitly with the energy, similarly to the case in PYTHIA.) The detailed description of how the MPI parameters were fitted to the experimental data can be found in [178]. The most recent and default tune of HERWIG 7.0 (H7-UE-MMHT) gives a good description of the underlying event data from Tevatron’s lowest energy point [179],  $\sqrt{s} = 300$  GeV to the LHC’s [161] highest  $\sqrt{s} = 13$  TeV (although the LHC’s highest energy UE data [180] was not used for the tune). Therefore, we use H7-UE-MMHT as “the best” prediction of HERWIG 7 for 100 TeV UE analysis. For comparison we also show results of an older HERWIG ++ tune UE-EE-4.

In PYTHIA 8, there is no sharp distinction between soft and hard MPI [181]; instead there is a single eikonalised  $p_{\perp}$ -ordered framework, with interleaved evolution [182] of parton showers and MPI. The baseline implementation in PYTHIA 8 is described in [183]. Similarly to HERWIG, the main model parameters are: 1) an IR regularisation scale for the QCD  $2 \rightarrow 2$  cross section,  $p_{\perp,0}$ ; 2) a parameter governing the assumed transverse shape of the proton mass distribution, and 3) a parameter controlling the strength of final-state colour reconnections. In the original PYTHIA modeling [181], the energy dependence of the total cross section was taken as the guideline for the energy evolution of the  $p_{\perp,0}$

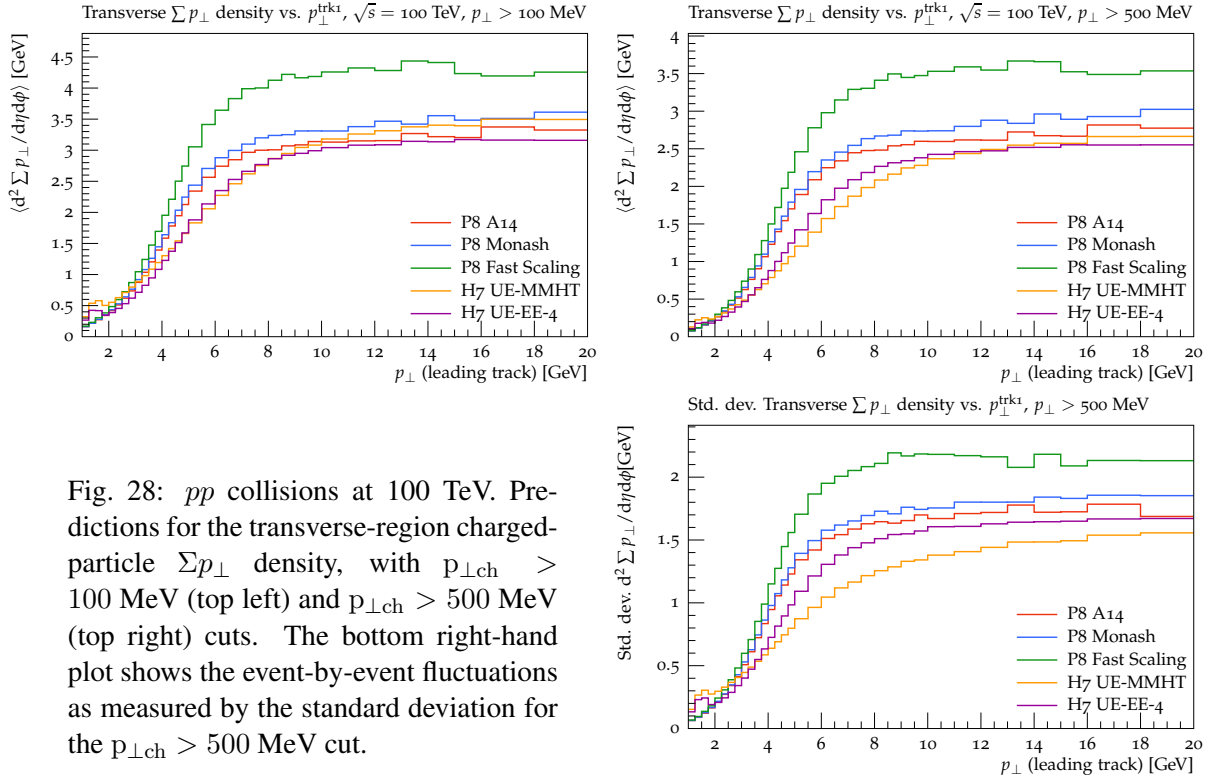


Fig. 28:  $pp$  collisions at 100 TeV. Predictions for the transverse-region charged-particle  $\Sigma p_{\perp}$  density, with  $p_{\perp\text{ch}} > 100$  MeV (top left) and  $p_{\perp\text{ch}} > 500$  MeV (top right) cuts. The bottom right-hand plot shows the event-by-event fluctuations as measured by the standard deviation for the  $p_{\perp\text{ch}} > 500$  MeV cut.

parameter, with a power  $b = 0.16$  in Eq. 15 motivated by a cross section scaling like  $s^{0.08}$ . This  $p_{\perp 0}$  scaling was ruled out by Tevatron measurements [184] as producing a too fast growth of the UE with c.m. energy, though it was occasionally retained for variations. Modern tunes have  $b$  values in the range  $0.21 - 0.26$ . The Monash 2013 tune [19] uses a relatively low value,  $b = 0.215$  (see table 3), and this was left unchanged in the ATLAS A14 tune [185]. Preliminary comparisons at 13 TeV [180] indicate continued good agreement, though a slightly higher scaling power around  $b = 0.23$  (resulting in a slower  $\sqrt{s}$  scaling of UE and MB quantities) may be preferred. In this study, we include the baseline Monash 2013 and A14 tunes, as well as a “Fast Scaling” variant of the Monash tune that uses the old  $b = 0.16$  scaling power, for a conservative upper-limit estimate of the extrapolated activity.

### 3.2.2 Results: UE Extrapolations to 100 TeV

In Fig. 28, we show the HERWIG and PYTHIA extrapolations to 100 TeV for the summed charged-particle  $p_{\perp}$  density in the transverse region, as defined above, focusing on the region  $p_{\perp\text{lead}} < 20$  GeV in which the transition to the UE plateau occurs. The top left- and right-hand plots show the two different charged-particle  $p_{\perp}$  cuts, while the bottom right-hand one shows the standard-deviation fluctuations for the  $p_{\perp\text{ch}} > 500$  MeV cut. Given the order-of-magnitude extrapolation in c.m. energy, there is a remarkable level of agreement between the central models (i.e., excluding the extreme Fast Scaling one), with the charged-particle UE plateau characterised by

$$\left\langle \sum p_{\perp\text{ch}} \right\rangle_{p_{\perp\text{ch}} > 100 \text{ MeV}} \text{ (per unit } \Delta\eta\Delta\phi) = 3.3 \pm 0.5 \text{ GeV}, \quad (16)$$

$$\left\langle \sum p_{\perp\text{ch}} \right\rangle_{p_{\perp\text{ch}} > 500 \text{ MeV}} \text{ (per unit } \Delta\eta\Delta\phi) = 2.7 \pm 0.4 \text{ GeV}, \quad (17)$$

within slightly inflated 15% uncertainties, and the Fast Scaling variant defining conservative upper-limit densities of 4.4 and 3.6 GeV, respectively. Note that the total summed  $p_{\perp}$  in the transverse region rises slowly with jet  $p_{\perp}$ , and that including both charged and neutral particles would result in numbers approximately a factor 1.6 higher.

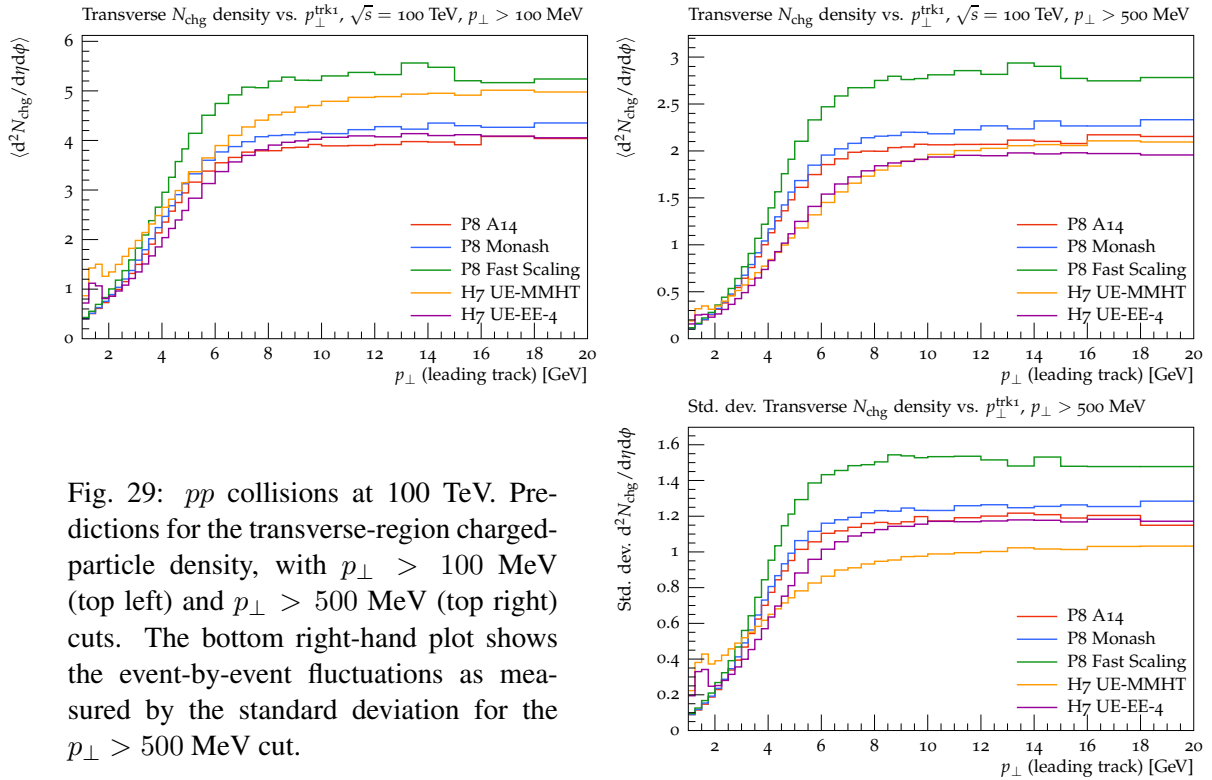


Fig. 29:  $pp$  collisions at 100 TeV. Predictions for the transverse-region charged-particle density, with  $p_{\perp} > 100$  MeV (top left) and  $p_{\perp} > 500$  MeV (top right) cuts. The bottom right-hand plot shows the event-by-event fluctuations as measured by the standard deviation for the  $p_{\perp} > 500$  MeV cut.

We emphasise that there is some arbitrariness whether to use the lower or higher cut to estimate UE contributions to jets. For the charged component, particles with  $p_{\perp} < 500$  MeV typically do not make it to the calorimeter and hence do not contribute to calorimetric energy measurements. On the other hand, low- $p_{\perp}$  neutral particles (including photons) may or may not be absorbed in the inner detector. A phenomenology calculation could therefore well use the lower cut (assuming experimental results will be corrected for loss effects) while a calorimeter study could use some combination of the two.

For comparison, the Snowmass study in [186], which considered extrapolations to 100 TeV using the latest set of ‘‘Perugia 2012’’ tunes [33] of the PYTHIA 6 event generator [100] (version 6.428), found, for a reference sample of 100-GeV dijets, in the region  $|\eta| < 2.5$ , a neutral+charged  $p_{\perp}$  density in the transverse region of  $4.4 \pm 0.45$  GeV. Translated to the phase-space region studied here, this prediction is somewhat lower than the ones above, consistent with the Perugia 2012 tune’s higher  $p_{\perp 0}$  scaling power  $b = 0.24$ .

Finally, we note that the small bumps on the HERWIG 7 curves at very low  $p_{\text{lead}}$  are due to the colour structure of soft MPI and will be addressed in the next release.

The charged-particle densities shown in Fig. 29 exhibit a larger spread between the models. In particular for the soft end of the spectrum, highlighted by the top left-hand plot, the H7 UE-MMHT model predicts the same density as the Fast Scaling PYTHIA tune, 30% above the level of the other models. In the right-hand plot, however, with the  $p_{\perp}$  cut of 500 MeV, the H7 UE-MMHT level drops down to that of the other central tunes, while the Fast Scaling PYTHIA tune remains above. Interestingly, the H7 UE-EE-4 level is lower, but its fluctuations higher, than those of H7 UE-MMHT. We note that the former has a smaller inverse proton size,  $\mu^2 = 1.11$  compared to UE-MMHT  $\mu^2 = 2.30$ .

The final plot in Fig. 30 displays a remarkable agreement on the average  $p_{\perp}$  of charged particles. Despite the underlying model differences, and the significant uncertainties surrounding aspects such as colour reconnections, the predictions are virtually indistinguishable, the only exception being the H7 UE-MMHT model in the turn-on region below  $p_{\perp \text{lead}} = 10$  GeV.

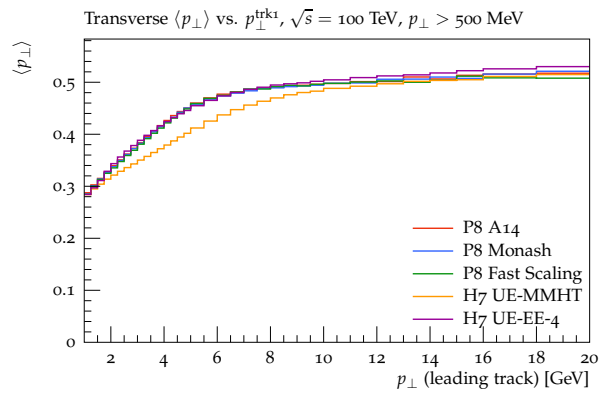


Fig. 30:  $pp$  collisions at 100 TeV. Predictions for the transverse-region average  $p_{\perp}$  of charged particles for the  $p_{\perp} > 500$  MeV cut.

## 4 Inclusive vector boson production

The production of  $W$  and  $Z$  bosons is a valuable probe of both EW and QCD dynamics. The total production rate of  $W^\pm$  ( $Z^0$ ) bosons at 100 TeV is about 1.3 (0.4)  $\mu\text{b}$ . This corresponds to samples of  $O(10^{11})$  leptonic ( $e, \mu$ ) decays per  $\text{ab}^{-1}$ . The production properties are known today up to next-to-next-to-leading order (NNLO) in QCD, leading to a precision of the order of the percent. A detailed discussion of the implications of this precision, and of the possible measurements possible with  $W$  and  $Z$  final states at 100 TeV, is outside the scope of this review, also because the LHC has only started exploiting the full potential of what can be done with them (for a recent review, see Ref. [187]). We shall therefore focus here on documenting some basic rates and distributions, to show the extreme kinematical configurations that may be accessed at 100 TeV, and to highlight some of the novel features of EW interactions that will emerge at these energies.

### 4.1 Inclusive $W/Z$ rates and distributions

First of all, we compute the PDF uncertainties in the inclusive cross-sections (and their ratios) for electroweak gauge boson production at both 14 TeV and 100 TeV. We use the NNLO inclusive calculation of Ref. [188] as implemented in the VRAP code. We compare the results from four modern PDF sets: ABM12 [10], CT14 [8], MMHT14 [9] and NNPDF3.0 [7]. These four NNLO sets have  $\alpha_s(M_Z) = 0.118$ , except ABM12 for which the native value is  $\alpha_s(M_Z) = 0.1132$ . The PDF sets are accessed via the LHAPDF6 interface.

In Table 6 we show the total NNLO inclusive cross-sections (including the leptonic branching fractions) and the corresponding percentage PDF uncertainties for weak gauge boson production at the LHC 14 TeV. We also indicate the shift in the central cross-section of the different PDFs as compared to a reference cross-section, which here is taken to be that of NNPDF3.0 NNLO. The corresponding results at 100 TeV are shown in Table 7. We observe a substantial increase on the PDF systematics when going from 14 TeV to 100 TeV, specially for NNPDF3.0 but also for CT14 and MMHT14.

	14 TeV							
	NNPDF3.0		CT14		MMHT14		ABM12	
	$\sigma(\text{nb}) \pm \delta_{\text{pdf}}$	$\sigma/\sigma_{\text{ref}}$						
$W^+$	$12.2 \pm 2.3\%$	1	$12.4 \pm 2.4\%$	1.01	$12.5 \pm 1.5\%$	1.02	$12.7 \pm 1.2\%$	1.04
$W^-$	$9.1 \pm 2.4\%$	1	$9.2 \pm 2.3\%$	1.02	$9.3 \pm 1.5\%$	1.03	$9.3 \pm 1.2\%$	1.03
$Z$	$2.0 \pm 2.2\%$	1	$2.1 \pm 2.2\%$	1.01	$2.1 \pm 1.6\%$	1.02	$2.1 \pm 1.2\%$	1.00
$W^+/W^-$	$1.4 \pm 0.8\%$	1	$1.3 \pm 2.4\%$	1.00	$1.3 \pm 1.5\%$	1.00	$1.4 \pm 1.2\%$	1.01
$W/Z$	$10.5 \pm 0.4\%$	1	$10.5 \pm 1.4\%$	1.00	$10.5 \pm 0.9\%$	1.00	$10.5 \pm 0.7\%$	1.00

Table 6: The PDF uncertainties for the NNLO inclusive cross-sections for weak gauge boson production at the LHC 14 TeV. We also indicate the shift in the central cross-section of the different PDFs as compared to a reference cross-section, which here is taken to be that of NNPDF3.0. The calculation has been performed with the VRAP code. The leptonic branching fractions have been included in the calculation.

	100 TeV							
	NNPDF3.0		ABM12		CT14		MMHT14	
	$\sigma(\text{nb}) \pm \delta_{\text{pdf}}$	$\sigma/\sigma_{\text{ref}}$						
$W^+$	$77.0 \pm 13.1\%$	1	$74.9 \pm 7.2\%$	0.97	$71.8 \pm 4.8\%$	0.93	$74.1 \pm 2.0\%$	0.96
$W^-$	$63.4 \pm 8.5\%$	1	$62.9 \pm 5.9\%$	0.99	$61.3 \pm 3.6\%$	0.97	$62.2 \pm 2.0\%$	0.98
$Z$	$14.1 \pm 7.9\%$	1	$13.9 \pm 5.7\%$	0.99	$13.7 \pm 3.7\%$	0.97	$13.9 \pm 2.0\%$	0.98
$W^+/W^-$	$1.2 \pm 4.3\%$	1	$1.2 \pm 7.1\%$	0.98	$1.2 \pm 4.8\%$	0.97	$1.2 \pm 2.0\%$	0.98
$W/Z$	$9.9 \pm 2.9\%$	1	$9.9 \pm 3.9\%$	1.00	$9.7 \pm 2.6\%$	0.98	$9.8 \pm 1.1\%$	0.99

Table 7: Same as Table 6 now for  $\sqrt{s} = 100$  TeV.

To investigate the impact of realistic acceptance cuts, we have used MCFM v7.0.1 to compute the NLO cross-sections (using NNLO PDFs) including the decays of the gauge bosons. We have considered three different cases for the final-state cuts:

- No cuts
- *LHC* cuts:  $p_T^l \geq 20$  GeV,  $|\eta_l| \leq 2.5$
- *FCC* cuts:  $p_T^l \geq 20$  GeV,  $|\eta_l| \leq 5$

In addition, jets are reconstructed with the anti- $k_t$  algorithm with  $R = 0.4$ , but no cuts are imposed on the kinematics of this jet. The results are summarized in Table 8, where we show the production cross-sections and the corresponding percentage PDF uncertainties for weak gauge bosons at 14 TeV and 100 TeV with different kinematical cuts on the final state particles. The calculation has been performed at NLO with MCFM v7.0.1, using the NNPDF3.0 NNLO PDF set. We observe that PDF uncertainties are reduced if the rapidity of the final-state leptons is restricted to the central region, indicating that the increase of PDF errors from 14 to 100 TeV arises from the forward region, sensitive to the poorly-known small- $x$  PDFs.

NNPDF3.0 NNLO					
$\sigma(pp \rightarrow V \rightarrow l_1 l_2)$ [nb] ( $\pm \delta_{\text{pdf}} \sigma$ )	14 TeV		100 TeV		
	No cuts	<i>LHC</i> cuts	No cuts	<i>LHC</i> cuts	<i>FCC</i> cuts
$W^+$	12.2 (2.2%)	6.5 (2.2%)	77.3 (13.1%)	28.3 (3.3%)	54.3 (6.5%)
$W^-$	9.2 (2.3%)	4.9 (2.3%)	64.3 (8.9%)	27.2 (3.3%)	45.5 (4.0%)
$Z$	2.1 (2.1%)	1.5 (2.1%)	14.5 (7.7%)	8.3 (3.3%)	12.8 (5.0%)

Table 8: The production cross-sections for weak gauge bosons at 14 TeV and 100 TeV, including the leptonic decays, with different kinematical cuts on the final state particles, see text for more details. We provide both the total cross-section and the corresponding percentage PDF uncertainty. The calculation has been performed at NLO with MCFM v7.0.1, using the NNPDF3.0 NNLO PDF set.

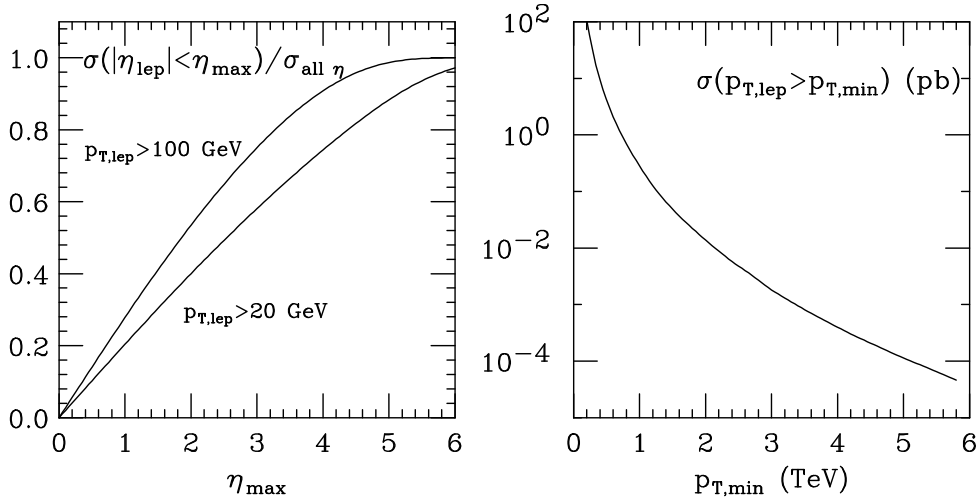


Fig. 31: Left: rapidity acceptance for leptons from inclusive  $W$  production and decay, for  $p_T$  thresholds of 20 and 100 GeV. Right: inclusive lepton  $p_T$  spectrum.

At 100 TeV, gauge bosons will have a rather broad rapidity distribution and, as shown in the left plot of Fig. 31, more than 50% of the leptons with  $p_T > 20$  GeV will be produced at  $|\eta| > 2.5$  (w.r.t.  $\sim 30\%$  at 14 TeV). Even leptons with  $p_T > 100$  GeV will have a large forward rate, with about 40% of them at  $|\eta| > 2.5$  ( $\sim 10\%$  at 14 TeV). Their  $p_T$  spectrum will also extend to large values, as shown in

the right plot of Fig. 31. The largest fraction of these high- $p_T$  leptons will arise from  $W$ 's produced at large  $p_T$ , in association with jets.

We focus now on the charged lepton rapidity distributions. In  $pp$  collisions rapidity distributions are forward-backward symmetric and only the positive (or negative) the rapidity range needs to be shown. The  $W^+$  bosons are produced at larger rapidities and with a larger production rate than the  $W^-$  bosons. This is because the production of  $W^+$  ( $W^-$ ) bosons is mainly controlled by  $u\bar{d}$  ( $\bar{u}d$ ) quarks collisions. The rapidity asymmetry is the result of  $u(x)/d(x)$  becoming larger at larger  $x$ . The total rate difference is due to the  $u$  quark density being larger than that of the  $d$  density (the antiquark  $\bar{u}$  and  $\bar{d}$  densities are relatively similar, especially at small values of parton momentum fractions). Due to parity violation in the  $W$  boson production and decay, the charged (anti)lepton tends to be produced in the direction of the initial-state (anti)quark. Therefore  $\ell^-$  prefers the direction of the  $d$ -type quark, and  $\ell^+$  the direction of the  $\bar{d}$ -type antiquark. The rapidity distribution of charged leptons is therefore the result of opposite physical effects: the parton densities of the colliding hadrons favour forward production of  $W^+$  over  $W^-$  bosons, but their decays favour forward emission of  $\ell^-$  over  $\ell^+$  leptons. This leads to a peculiar structure of the leptonic charge asymmetry, which changes sign at some  $p_T$ -dependent value of rapidity.

In Fig. 32 we show the normalized rapidity distribution of the  $W^\pm$  and  $Z$  bosons in NLO QCD computed with the DYNNLO parton level Monte Carlo [189] by using NNPDF3.0 [7] parton densities at NLO with  $\alpha_S(M_Z^2) = 0.118$ . The leptonic charge asymmetry is shown in Fig. 33, for various lepton  $p_T$  thresholds. Notice that, while at LHC energies the asymmetry changes sign at  $\eta \sim 2.5$  for  $p_T \gtrsim 20$  GeV, here the zero is shifted to much higher  $\eta$  values, as a result of the much wider boson rapidity spectrum. The asymmetry is also very small in the central  $\eta$  region, since at 100 TeV, for the values of  $x$  relevant to central  $W$  production, the valence component of quark densities is suppressed with respect to the sea, and thus  $u(x) \sim d(x)$ .

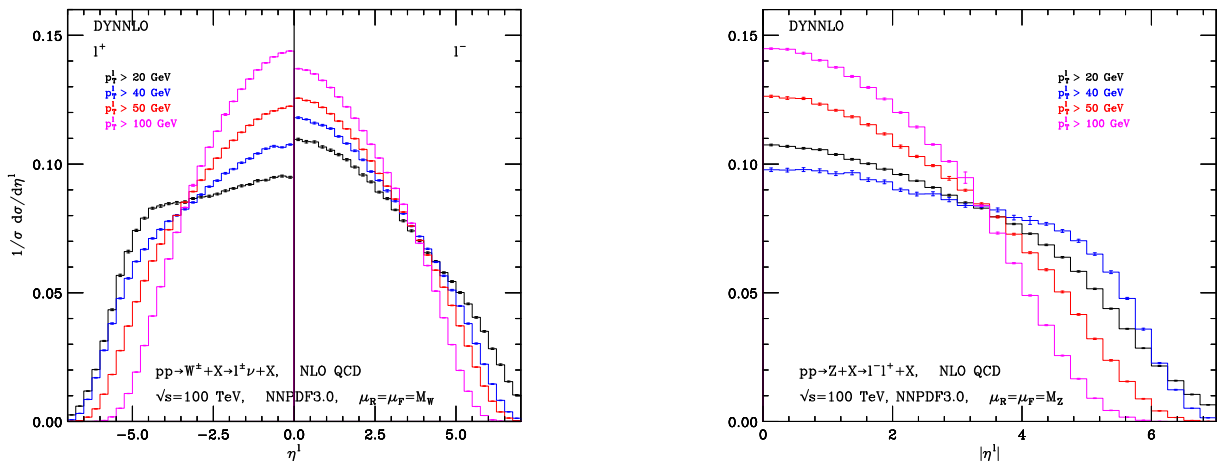


Fig. 32: Normalized rapidity distribution of the charged leptons from  $W^\pm$  (left panel) and  $Z$  (right panel) boson decays, at  $\sqrt{s} = 100$  TeV. The charged leptons are required to have a minimum  $p_T$  of 20, 40, 50 and 100 GeV. The error bars reported in the histograms refer to an estimate of the numerical error in the Monte Carlo integration carried out by the DYNNLO code.

## 4.2 $W/Z$ boson production at small $q_T$

An observable particularly relevant in  $W/Z$  boson production is the transverse-momentum ( $q_T$ ) distribution of the vector boson. In the large  $q_T$  region ( $q_T \gtrsim M_V$ ) QCD corrections are known in analytic form up to  $\mathcal{O}(\alpha_S^2)$  [190–192] and fully exclusive computations of  $W/Z$  bosons in association with a jet are available up to  $\mathcal{O}(\alpha_S^3)$  [193, 194].

However the bulk of the  $W/Z$  bosons are produced at small  $q_T$  ( $q_T \ll M_V$ ) where

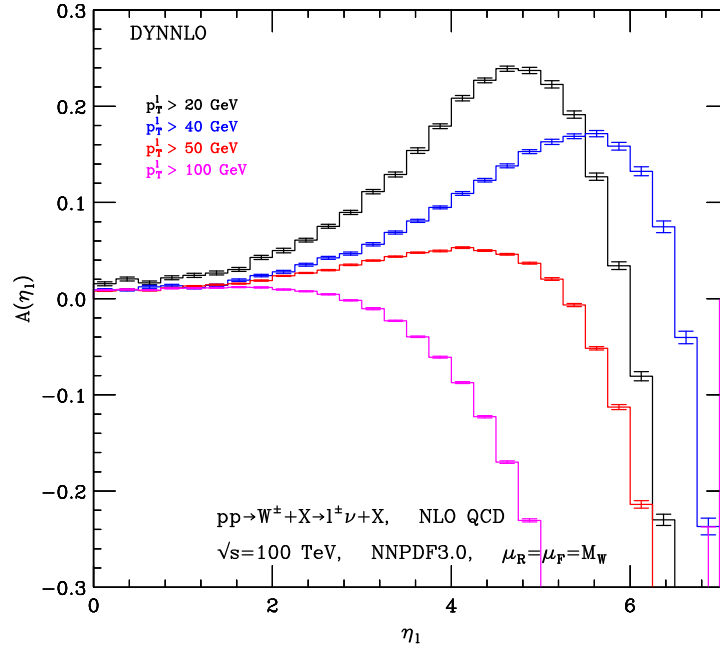


Fig. 33: Leptonic charge asymmetry, for different lepton  $p_T$  thresholds.

the reliability of fixed-order calculations is spoiled by large logarithmic corrections of the form  $\alpha_S^n (M_V^2/q_T^2) \ln^m(M_V^2/q_T^2)$  (with  $0 \leq m \leq 2n - 1$ ) due to soft and/or collinear parton emissions. At a centre-of-mass energy of 100 TeV about half of  $W/Z$  bosons are produced in the region where  $q_T \lesssim 15$  GeV. In order to restore the reliability of perturbation theory in the small- $q_T$  region, these logarithmically-enhanced terms have to be systematically resummed to all perturbative orders. The resummed and fixed-order predictions can be consistently matched at intermediate values of  $q_T$  to obtain a uniform theoretical accuracy in a wide range of transverse momenta.

We consider the processes  $pp \rightarrow W^\pm \rightarrow l\nu_l$  and  $pp \rightarrow Z \rightarrow l^+l^-$  at  $\sqrt{s} = 100$  TeV centre-of-mass energy and we compute the transverse-momentum distribution by using the resummation formalism proposed in Refs. [195–197]. The numerical results are obtained by using the code DYqT, which is based on the results presented in Refs. [198, 199]. An analogous but more general computation [200], which includes the full dependence on the final-state lepton(s) kinematics, is encoded in the numerical program DYRes. We provide predictions at NNLL+NNLO (NLL+NLO) accuracy by using NNPDF3.0 [7] parton densities at NNLO (NLO) with  $\alpha_S(M_Z^2) = 0.118$  and  $\alpha_S$  evaluated at 3-loop (2-loop) order. As for the EW couplings, we use the values quoted in the PDG 2014 [201] within the so called  $G_\mu$  scheme, where the input parameters are  $G_F, M_Z, M_W$ .

The NLL+NLO and NNLL+NNLO results for the  $q_T$  spectrum of on-shell  $W$  and  $Z$  bosons produced at  $\sqrt{s} = 100$  TeV are presented in Fig. 34. The bands provide an estimate of the perturbative uncertainties due to missing higher-order contributions. The bands are obtained through independent variations of factorization ( $\mu_F$ ), renormalization ( $\mu_R$ ) and resummation ( $Q$ ) scales in the range  $M_V/4 \leq \{\mu_F, \mu_R, Q\} \leq 2M_V$  with the constraints  $0.5 \leq \mu_F/\mu_R \leq 2$  and  $0.5 \leq Q/\mu_R \leq 2$ . The lower panels present the ratio of the scale-dependent NNLL+NNLO and NLL+NLO results with respect to the NNLL+NNLO result at the central value  $\mu_F = \mu_R = Q = M_V/2$  of the scales.

The region of small and intermediate values of  $q_T$  is shown in the main panels of Fig. 34. The shape of the  $W$  and  $Z$   $q_T$  spectra is qualitatively similar, with the  $Z$  spectrum slightly harder than the  $W$  spectrum. Both the  $W/Z$  NNLL+NNLO  $q_T$  spectra are harder than the corresponding spectra at NLL+NLO accuracy with a sensible reduction of the scale-variation band going from the NLL+NLO to the NNLL+NNLO band. The NLL+NLO and NNLL+NNLO bands overlap at small transverse momenta

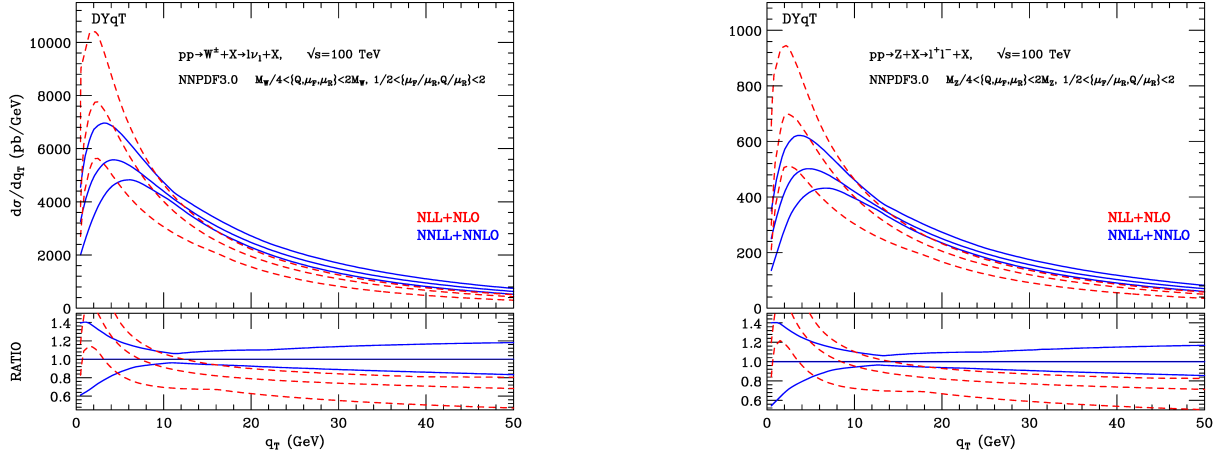


Fig. 34: The  $q_T$  spectrum of  $W^\pm$  (left panel) and  $Z$  (right panel) bosons in  $pp$  collisions at  $\sqrt{s} = 100$  TeV. The bands are obtained by performing  $\{\mu_F, \mu_R, Q\}$  variations (as described in the text) around the central value  $M_W/2$ . The lower panel presents the ratio of the NLL+NLO and NNLL+NNLO bands with respect to the NNLL+NNLO result at the central value of the scales.

and remain very close by increasing  $q_T$ . The NNLL+NNLO uncertainty is about  $\pm 20\%$  at the peak, it decreases to about  $\pm 6\%$  at  $q_T \simeq 10 - 15$  GeV and increases to about  $\pm 15\%$  at  $q_T \sim 50$  GeV.

### 4.3 DY production at large $p_T$ and at large mass

The left plot in Fig. 35 shows the integrated  $p_T$  spectrum of  $W$  bosons, from a LO calculation. With luminosities in excess of  $1 \text{ ab}^{-1}$ , data will extend beyond 15 TeV. The immense kinematical reach of DY distributions at 100 TeV is also displayed by the right plot in the same Figure, which shows the integrated dilepton invariant mass distribution, for one lepton family, with  $|\eta_\ell| < 2.5$ . The DY statistics, with the anticipated  $O(20) \text{ ab}^{-1}$ , will extend out to  $M_{\ell\ell} \sim 20$  TeV.

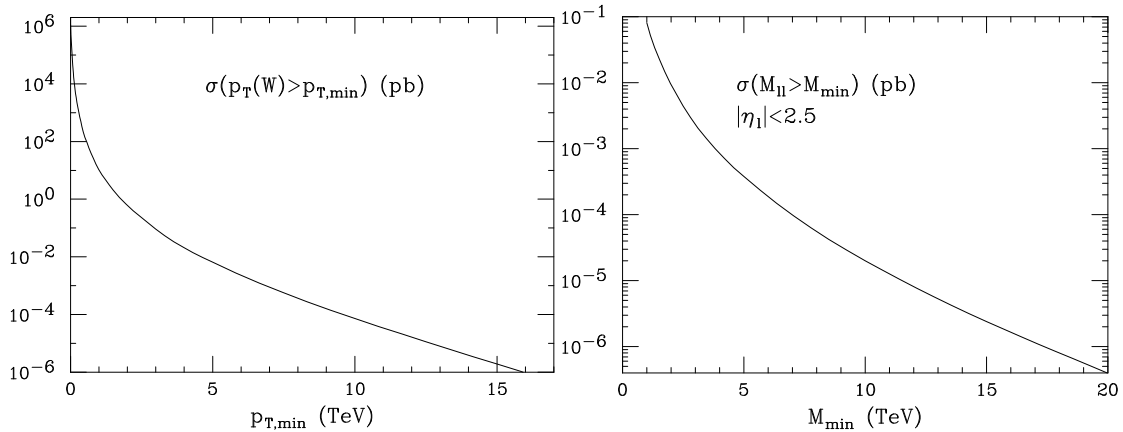


Fig. 35: Left: inclusive  $p_T$  spectrum of  $W$  bosons. Right: Integrated dilepton invariant mass distribution, for one lepton family, with  $|\eta_\ell| < 2.5$ .

NNLO results have recently become available for the  $W/Z$ +jet transverse momentum distributions [193, 194, 202]. For a gauge boson produced at large  $p_T$ , there is always at least one jet recoiling against it, and therefore one can assume that this calculation provides NNLO accuracy for the  $W/Z$  inclusive  $p_T$  spectrum. The  $p_T(W)$  differential distribution at 100 TeV is shown in the left plot of Fig. 36, which shows also the comparison with the NLO result. The calculation [193] was performed

using anti- $k_t$  jets [203] at  $R=0.4$ ,  $|\eta_J| < 5$ ,  $\mu^2 = M_W^2 + \sum_j p_{T,j}^2$  and CT14 NNLO PDFs. A minimum threshold  $p_T > 1$  TeV was applied to the leading jet: this biases the  $W$   $p_T$  spectrum in the region below  $O(1.5)$  TeV, but has no impact above that. On the right of Fig. 36 we show the integrated spectrum of the leading jet in  $W$ +jet events. We notice the huge increase from LO to NLO, due to the appearance at  $O(\alpha_s^2)$  of processes where two jets recoil against each other, the  $W$  being radiated from the initial state or from one of them (this will be discussed more extensively in the section subsection). The LO jet spectrum matches well the result of the  $W$  spectrum in the left plot, corresponding to the LO configurations where the  $W$  recoils against a jet. We point out that the NNLO/NLO  $K$  factors are very close to one, suggesting that after inclusion of the new NLO topologies one has reached a rather stable perturbative expansion. We also recall that this calculation only includes the QCD effects. For  $p_T$  beyond the TeV scale, the effects of virtual EW corrections are known to lead to important corrections [204], as will be discussed in Section 16.

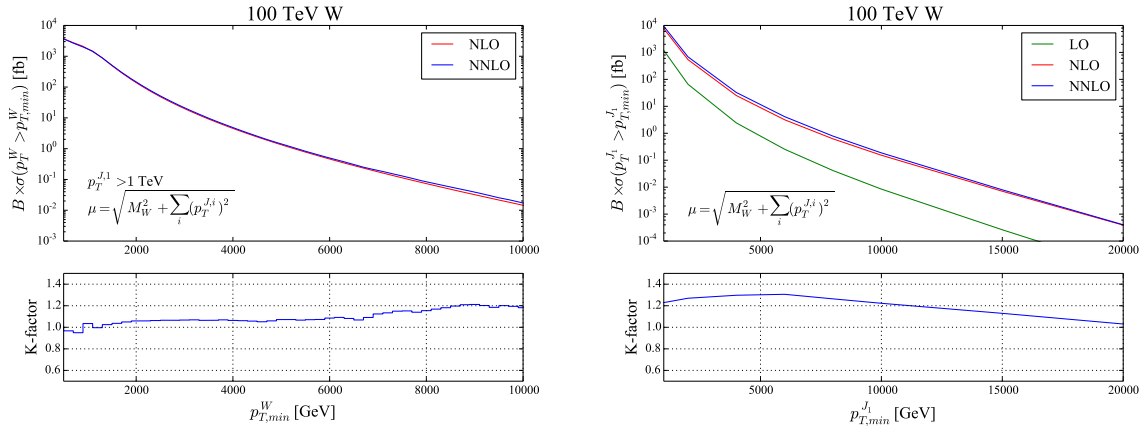
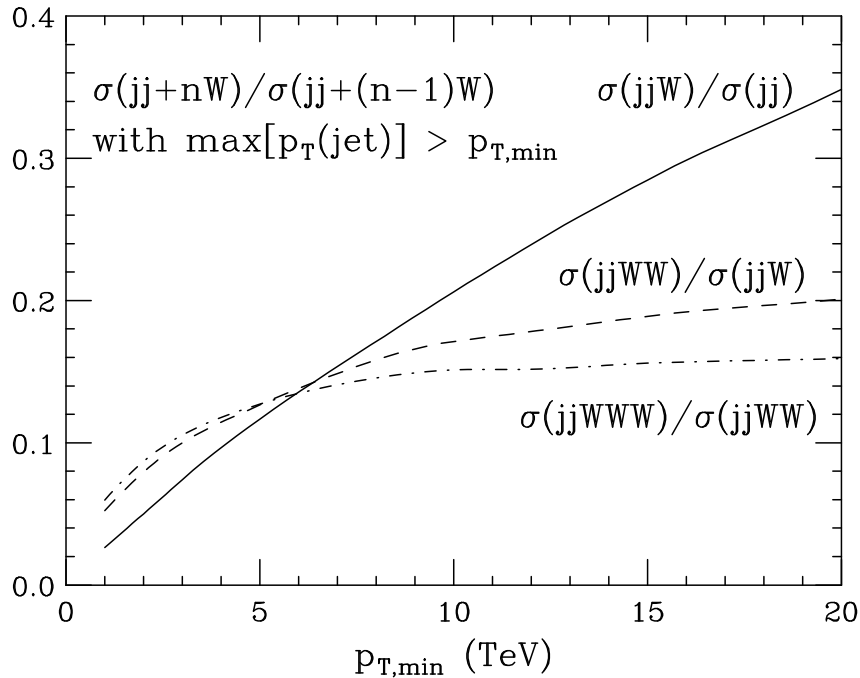
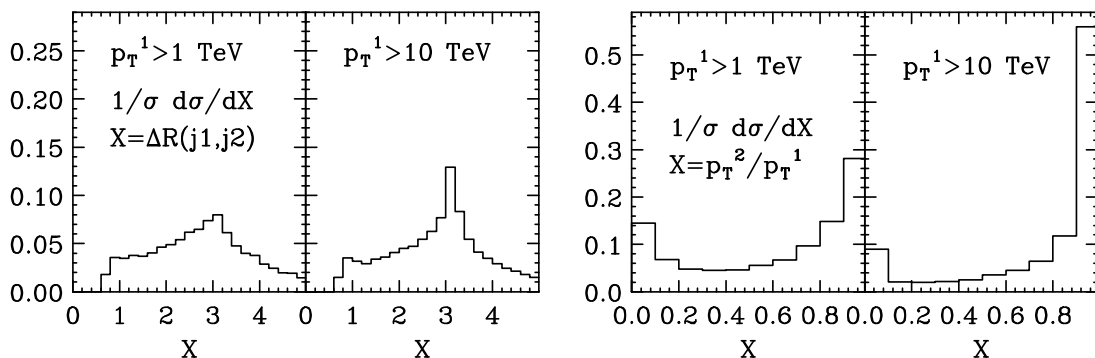


Fig. 36:  $BR(W \rightarrow e\nu) \times \sigma(p_T^X > p_{T,min}^X)$  at NNLO and NLO, with  $X = W$  (left) and  $X = j_1$  (right) is the leading jet in  $W + jet$  inclusive events. The lowest  $p_{T,min}^{j_1}$  entry in the right plot corresponds to  $p_{T,min}^{j_1} = 1$  TeV. Lower insets: the NNLO/NLO  $K$  factors.

#### 4.4 Production of gauge bosons at the highest energies

For processes involving gauge bosons and jets at such large energies, a very interesting new phenomenon emerges, namely the growth of the gauge boson emission probability from high- $p_T$  jets. If we ask what is the most likely mechanism to produce gauge bosons in final states with at least one multi-TeV jet, it turns out that this is not the LO QCD process where the gauge boson simply recoils against the jet, but the higher-order process where it is a second jet that absorbs the leading jet recoil, and the gauge boson is radiated off some of the quarks [205]. In other words, the parton-level scattering  $qq \rightarrow qqV$  dominates over  $qq \rightarrow qV$  (for simplicity, we do not show explicitly the possibly different quark flavour types involved in the processes). The emission probability of gauge bosons in this case is enhanced by large logarithms of  $p_{T,jet}/m_V$ , and can reach values in the range of 10% and more, as shown in Fig. 37. This gives the emission probability for one or more  $W$  bosons in events in which there is at least one jet above a given  $p_T$  threshold. The kinematical properties of these events are illustrated for various distributions in Figs. 38 (at LO) and 39 (at (N)NLO). To highlight the kinematical evolution with jet  $p_T$  we show results for final states with a jet above 1 TeV, and above 10 TeV. In the case of largest  $p_T$ , we see the dominance of events in which the two jets balance each other in transverse momentum, while the  $W$  carries a very small fraction of the leading jet momentum. One third of the  $W$ 's are emitted within  $\Delta R < 1$  from the subleading jet, with a large tail of emission at larger angles, due in part to  $W$  radiation from the initial state.


 Fig. 37: Emission probability for additional  $W$  bosons in dijet events at large  $p_T$ .

 Fig. 38: Kinematical correlations, at LO, in high- $p_T$  jet events with  $W$  radiation, for values of the leading jet  $p_T > 1$  and 10 TeV.

The process considered above is just one manifestation of the general fact that, in hard electroweak interactions at multi-TeV energies, the soft/collinear structure of almost *any* multi-TeV process can become significantly altered, as the logarithmic enhancements familiar from QED and QCD will become active for electroweak emissions (see, e.g., [206–210]). Obtaining correct descriptions of the complete event structure when  $\sqrt{\hat{S}} \gg m_W$  can be then greatly facilitated by incorporating factorization and resummation, such as that provided by parton showering and parton distribution functions. In effect, we will begin to see weak bosons (including the Higgs boson) behaving as nearly-massless partons, in stark contrast to the conventional perspective in which they are viewed as “heavy” particles. Jets, whether initiated by QCD processes, electroweak process, or new physics processes, will be found to contain electroweak splittings with probabilities at the  $O(10\%)$  level. Similarly, weak bosons can usefully be thought of as collinear components of the protons, at the same level as gluons and photons.

To develop some intuition of the collinear splitting behavior of electroweak “partons,” it is useful to first consider a conceptual limit with an unbroken  $SU(2) \times U(1)$  gauge symmetry with massless gauge bosons and fermions, supplemented by a massless scalar doublet field  $\phi$  without a VEV (the would-be

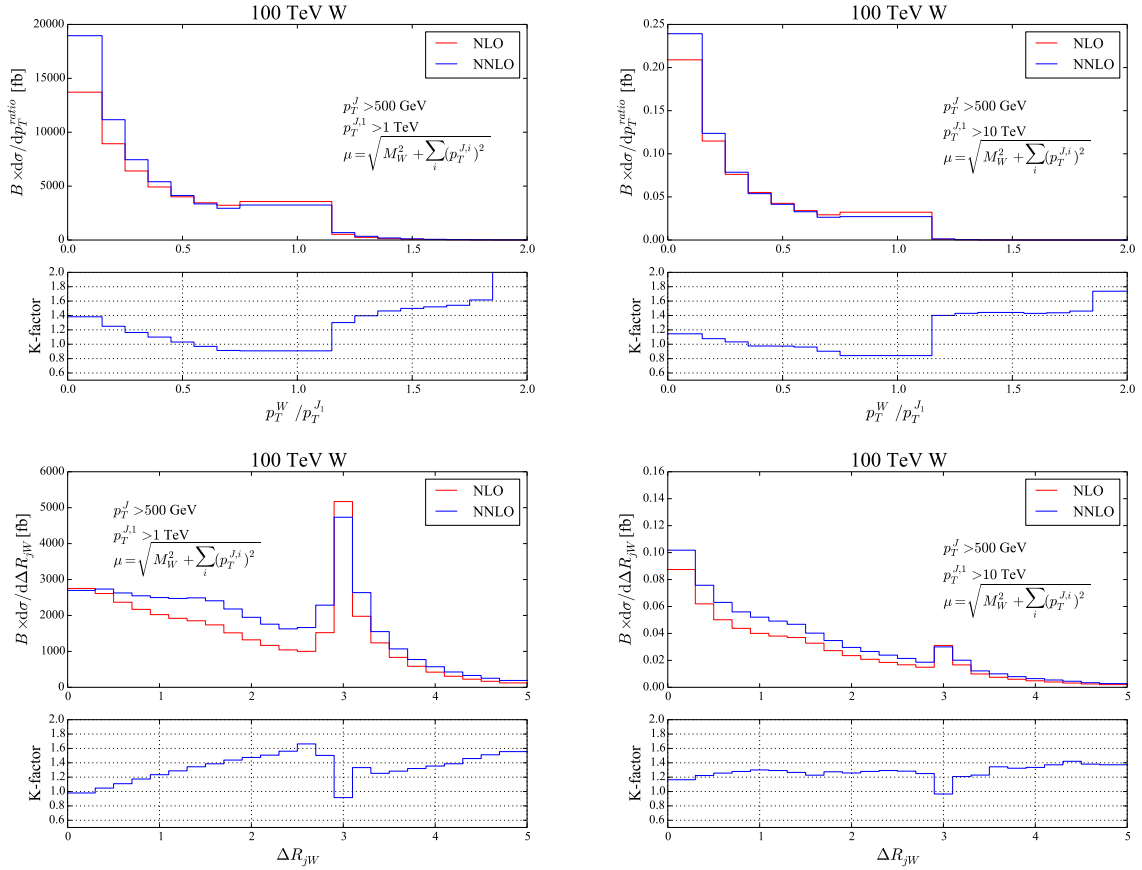


Fig. 39: Kinematical correlations at (N)NLO in  $W$ +jet(s) events, for values of the leading jet  $p_T > 1$  and 10 TeV.

Higgs doublet). In this limit, many processes are direct analogs of those in QED and QCD. Fermions with appropriate quantum numbers may emit (transverse)  $SU(2)$  and  $U(1)$  gauge bosons with both soft and collinear enhancements. The  $SU(2)$  bosons couple to one another via their non-abelian gauge interactions, and undergo soft/collinear splittings of the schematic form  $W \rightarrow WW$ , similar to  $g \rightarrow gg$ . All of the electroweak gauge bosons may also undergo collinear-enhanced splittings into fermion pairs, similar to  $g \rightarrow q\bar{q}$  or  $\gamma \rightarrow f\bar{f}$ . Beyond these, the major novelty is the introduction of the scalar degrees of freedom. First, the scalars may themselves radiate  $SU(2)$  and  $U(1)$  gauge bosons, with soft/collinear limits identical to their counterparts with fermionic sources. Second, the electroweak gauge bosons can split into a pair of scalars, again in close analog with splittings to fermion pairs. Third, fermions with appreciable Yukawa couplings to the scalar doublet can emit a scalar and undergo a chirality flip. Finally, the scalars can split into collinear fermion pairs.

In the realistic case of spontaneously-broken symmetry, several important changes take place. Primarily, all of the soft and collinear divergences associated with the above splittings become physically regulated, effectively shutting off at  $p_T \lesssim m_W$  (or  $m_h, m_t$  where appropriate). Roughly speaking,  $m_W$  plays a role similar to  $\Lambda_{\text{QCD}}$  in the QCD parton shower, albeit with far less ambiguity of the detailed IR structure since this regulation occurs at weak coupling. Another major difference is the mixing of the scalar doublet's Goldstone degrees of freedom into the  $W$  and  $Z$  gauge bosons, allowing for the appearance of longitudinal modes. In many cases, the longitudinal gauge bosons behave identically to the original scalars, as dictated by the Goldstone equivalence theorem [73, 74]. For example the splitting  $W_T^+ \rightarrow W_L^+ Z_L$  is, up to finite mass effects, an exact analog of  $W_T^+ \rightarrow \phi^+ \text{Im}(\phi^0)$  in the unbroken theory. Similarly for longitudinal gauge boson emissions from heavy fermions, such as the equivalence

Process	$\mathcal{P}(p_T)$	$\mathcal{P}(1 \text{ TeV})$	$\mathcal{P}(10 \text{ TeV})$
$f \rightarrow V_T f$	$(3 \times 10^{-3}) \left[ \log \frac{p_T}{m_{EW}} \right]^2$	1.7%	7%
$f \rightarrow V_L f$	$(2 \times 10^{-3}) \log \frac{p_T}{m_{EW}}$	0.5%	1%
$V_T \rightarrow V_T V_T$	$(0.01) \left[ \log \frac{p_T}{m_{EW}} \right]^2$	6%	22%
$V_T \rightarrow V_L V_T$	$(0.01) \log \frac{p_T}{m_{EW}}$	2%	5%
$V_T \rightarrow f \bar{f}$	$(0.02) \log \frac{p_T}{m_{EW}}$	5%	10%
$V_T \rightarrow V_L h$	$(4 \times 10^{-4}) \log \frac{p_T}{m_{EW}}$	0.1%	0.2%
$V_L \rightarrow V_T h$	$(2 \times 10^{-3}) \left[ \log \frac{p_T}{m_{EW}} \right]^2$	1%	4%

Table 9: An illustrative set of approximate total electroweak splitting rates in final-state showers [211].

between  $t_L \rightarrow Z_L t_R$  and  $t_L \rightarrow \text{Im}(\phi^0) t_R$ .

But important exceptional cases now also occur for emissions near  $p_T \sim m_W$ . Most well known, even a massless fermion exhibits a kind of soft/collinear-enhanced emission of  $W_L$  and  $Z_L$  [69, 70]. These emissions have no Goldstone equivalent analog, and are highly power-suppressed for  $p_T \gtrsim m_W$ . But the overall population of emissions at the boundary between “broken” and “unbroken” behavior nonetheless grows logarithmically with the fermion energy. This is formally sub-dominant to the double-logarithmic growth of transverse emissions, but remains numerically important at multi-TeV energy scales. Emissions from massless quarks also cause the energetic initial-state protons to act as sources of longitudinal boson beams, allowing for studies of the high-energy interactions of the effective Goldstone bosons through weak boson scattering (discussed further below). Similar types of emissions occur in the splittings of transverse bosons, such as  $W_T^+ \rightarrow Z_L W_T^+ / Z_T W_L^+$ .

Table 9 provides a few estimates for total splitting rates of individual final-state particles, including approximate numerical values for particles produced at  $p_T = 1 \text{ TeV}$  and  $10 \text{ TeV}$ . The  $SU(2)$  self-interactions amongst transverse gauge bosons tend to give the largest rates, quickly exceeding 10% as the energy is raised above 1 TeV (these rates are slightly lower than those extracted from Fig. 37, since there an important contribution to  $W$  emission came from initial state radiation). This has significant impact on processes with prompt transverse boson production such as  $W/Z/\gamma$ +jets, and especially on multiboson production including transverse boson scattering. Generally, it is important to appreciate that *any* particle in an event, whether initial-state or final-state, or even itself produced inside of a parton shower, can act as a potential electroweak radiator. Consequently, the total rate for finding one or more electroweak splittings within a given event must be compounded, and can sometimes add up to  $O(1)$ .

## 5 $V$ +jets<sup>15</sup>

In this section we study the associated production of a weak vector boson and jets at a proton-proton collider with  $\sqrt{s} = 100$  TeV and an expected accumulated total integrated luminosity of several  $ab^{-1}$ . Such a collider will allow to explore extreme kinematical configurations for processes like  $V$ +many jets ( $V = W^\pm, Z$ ), giving yet newer ways to test the Standard Model of particle physics at scales significantly above the TeV scale. Even more, many new physics scenarios predict enhancements in the production of vector bosons and jets, and so a clear understanding of SM model predictions is important.

We present here general properties of total and differential cross sections in order to obtain a first characterisation of the collision environment. Two broad classes of kinematical cuts are explored, called ‘democratic’ and ‘hierarchical’ below. The ‘democratic’ cuts are characterized by imposing a single minimum jet  $p_T$  cut on all jets, while ‘hierarchical’ cuts impose a very large  $p_T$  cut on the hardest jet in the event and keep a softer cut for all other jets. These choices are known to affect the perturbative behaviour of QCD, and we explore it now in this new high-energy environment. In particular we will be interested in regions of phase space where the various cuts imply large scale ratios and thereby induce correspondingly large logarithms.

Because uncertainties largely cancel in ratios of observables, we devote our attention to scaling properties of jet ratios – for example the behaviour of cross sections in dependence on jet multiplicities, and ratios between different types of vector bosons. We also explore a number of differential cross sections, such as integrated  $p_T$  spectra. Finally, we record parton-distribution function uncertainties on the processes’ inclusive cross sections.

The predictions are obtained employing a number of current methods. These include primarily as fixed-order predictions at leading order (LO) and next-to-leading order (NLO) in QCD, but for some sensitive observables we also establish the impact of parton-shower effects.

### 5.1 Setup

In our discussion of  $V$ +jets results we consider only vector bosons decaying to leptons of the first generation. Thus the final-state signatures include electrons, electron neutrinos and jets. For  $Z$ -bosons the decay products are explicitly specified being either pairs of electrons or neutrinos, mimicking the missing signature, while  $W$  bosons decay to  $e\nu_e$  pairs. We consider in detail five distinct phase-space regions for these processes, which are defined by ‘basic’, ‘low-democratic’, ‘high-democratic’, ‘low-hierarchical’ and ‘high-hierarchical’ sets of cuts, given in eqs. (18) and in Table 10. The ‘basic’ cuts treat all jets on equal terms with a minimum jet transverse momentum  $p_T^{\min}$  that it is varied between 50 GeV and 1000 GeV. The labels ‘low’/‘high’ refer to the low and high transverse momentum ( $p_T$ ) cuts on all final state objects, whereas the labels ‘democratic’/‘hierarchical’ refer to a uniform  $p_T$  cut on all jets or requiring a distinguished jet with high  $p_T$ . For simplicity identical  $p_T$  cuts are applied to charged leptons and missing neutrinos, which are measured as missing energy. We denote the transverse energy of the jets by  $p_T^{\text{jet}}$  and  $p_T^{\text{lead-jet}}$  for the jet with the largest transverse momentum  $p_T$ . The transverse momentum cut of the charged leptons and single neutrinos (missing energy) will be uniformly denoted by  $p_T^{\text{lepton}} := p_T^e = p_T^\nu$ . In general, jets are reconstructed with the anti- $k_T$  algorithm with a radius parameter of  $R = 0.4$ , using the FASTJET package [203, 212].

The following cuts on jet- and lepton-pseudo rapidities  $\eta^{\text{jet},e}$  and on  $Z$  mass ( $M_{ee}$ ) and  $W$  transverse mass ( $M_T^W$ ) are common to all five kinematical regions:

$$\begin{aligned}
 \text{rapidity cuts:} & \quad |\eta^{\text{jet}}| < 5, \quad |\eta^e| < 4 \\
 \text{W-bosons:} & \quad M_T^W > 40 \text{ GeV} \\
 \text{Z-bosons:} & \quad Z \rightarrow e^+e^- : \quad 66 \text{ GeV} < M_{ee} < 116 \text{ GeV}, \\
 & \quad Z \rightarrow \nu_e\bar{\nu}_e : \quad E_{T,\text{miss}} > 100 \text{ GeV},
 \end{aligned} \tag{18}$$

<sup>15</sup>Editors: F. Febres Cordero and F. Krauss

Phase-space cuts for $pp \rightarrow Z/W + jets + X$				
basic	low-democratic	high-democratic	low-hierarchical	high-hierarchical
$p_T^{\text{jet}} > p_T^{\text{min}}$	$p_T^{\text{jet}} > 50 \text{ GeV}$	$p_T^{\text{jet}} > 500 \text{ GeV}$	$p_T^{\text{jet}} > 50 \text{ GeV}$	$p_T^{\text{jet}} > 500 \text{ GeV}$
—	$p_T^{\text{lead-jet}} > 10^2 \text{ GeV}$	$p_T^{\text{lead-jet}} > 10^3 \text{ GeV}$	$p_T^{\text{lead-jet}} > 2 \cdot 10^3 \text{ GeV}$	$p_T^{\text{lead-jet}} > 10^4 \text{ GeV}$
$p_T^{\text{lepton}} > 30 \text{ GeV}$	$p_T^{\text{lepton}} > 30 \text{ GeV}$	$p_T^{\text{lepton}} > 50 \text{ GeV}$	$p_T^{\text{lepton}} > 30 \text{ GeV}$	$p_T^{\text{lepton}} > 50 \text{ GeV}$

Table 10: The five phase-space regions considered. For the ‘basic’ set of cuts  $p_T^{\text{min}}$  will be varied from 50 GeV to 1 TeV.

where the missing transverse energy  $E_{\text{miss}}$  is given by the sum of all transverse (anti-)neutrino momenta  $E_{T,\text{miss}} = |\vec{p}_T^{\nu} + \vec{p}_T^{\bar{\nu}}|$ .

### 5.1.1 Computational setup

For the fixed-order results at leading order (LO), the SHERPA framework [102, 213] has been used, in particular the COMIX matrix-element generator [214]. For calculations at next-to-leading order (NLO) accuracy in the strong-coupling expansion, the combination of the BLACKHAT [215] and SHERPA packages are used. The virtual matrix elements are provided by the BLACKHAT library. For  $V+4$ -jet production we have employed a leading-color approximation of the one-loop matrix elements<sup>16</sup>. The remaining Born-level, real radiation corrections as well as integration framework is provided by SHERPA. Infrared subtraction is consistently treated by the Catani-Seymour method [222], automated in SHERPA [223]. For parton-level results including parton-shower effects the multi-jet merging technology of [224, 225] is used, with the parton shower built on Catani-Seymour subtraction kernels as proposed in Ref. [226] and implemented in Ref. [227]. Higher-order accuracy is included based on the MC@NLO method [228] in the version implemented in SHERPA [229, 230] and the multi-jet merging at NLO described in Refs. [231, 232] are employed. The zero-jet inclusive cross section is obtained in NLO accuracy with the higher-jet multiplicities being leading order in strong-coupling expansion. All calculations employ the CT14nlo parton-distribution functions (PDF) for NLO results, and CT14llo for the reference LO results. The PDFs are accessed through the LHAPDF interface [21]. The PDFs also provides the strong coupling  $\alpha_S(\mu)$  throughout.

In the fixed-order calculations, the renormalisation scale ( $\mu_R$ ) and the factorisation scale ( $\mu_F$ ) are chosen identical and defined through,

$$\mu_R = \mu_F = \bar{H}_T := E_T^V + \frac{1}{N_J} \sum_{j=1}^{N_J} p_{T,j}^{\text{jet}}, \quad (19)$$

where,  $E_T^V = \sqrt{m_V^2 + p_{T,V}^2}$  and  $N_J$  is the overall number of jets in the process. Transverse momenta of the jets are denoted by  $p_{T,j}^{\text{jet}}$ . For the fixed order LO and NLO QCD results we employ the total partonic transverse energy,

$$\mu_R = \mu_F = \hat{H}'_T := E_T^V + \sum_{i=1}^{N_P} p_{T,i}^{\text{parton}}, \quad (20)$$

where  $N_P$  denotes the total number of final-state partons. The parton momenta are denoted by  $p_{T,i}^{\text{parton}}$ . We set the renormalization and factorization scales equal and vary them according to  $\mu = \mu_R = \mu_F = c_s \hat{H}'_T$ , with  $c_s \in \{1/2, 1/\sqrt{2}, 1, \sqrt{2}, 2\}$ , to obtain the conventional estimate of the size due to the truncation of the perturbative series.

<sup>16</sup> For details of the calculation, the reader is referred to the corresponding articles for the cases of  $W$ +jets [216–219] and  $Z$ +jets [220, 221].

Standard Model input parameters are defined through the  $G_\mu$  scheme with

$$\begin{aligned}
 m_Z &= 91.188 \text{ GeV}, & \Gamma_Z &= 2.49 \text{ GeV}, \\
 m_W &= 80.419 \text{ GeV}, & \Gamma_W &= 2.06 \text{ GeV}, \\
 m_H &= 125 \text{ GeV}, & \Gamma_H &= 0.00407 \text{ GeV}, \\
 m_t &= 175 \text{ GeV}, & \Gamma_t &= 1.5 \text{ GeV}, \\
 G_\mu &= 1.16639 \times 10^{-5} \text{ GeV}^{-2}, & \sin^2 \theta_W &= 1 - \tilde{m}_W^2 / \tilde{m}_Z^2,
 \end{aligned} \tag{21}$$

where  $\tilde{m}_V^2 = m_V^2 + i\Gamma_V m_V$ . Unstable particles are consistently treated through the complex mass scheme [233] in all but the NLO calculations, in which the decay products are distributed according to a Breit–Wigner distribution and real values for all coupling constants are maintained.

## 5.2 Inclusive cross sections

### 5.2.1 Leading-order cross sections

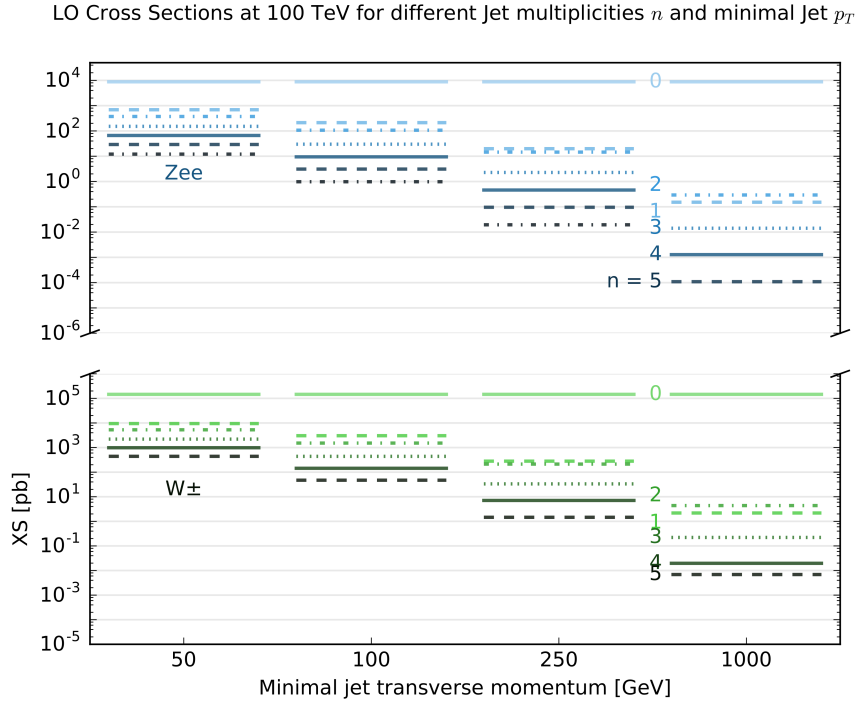


Fig. 40: The leading-order cross sections against  $p_T^{\min}$  given by 50 GeV, 100 GeV, 250 GeV and 1000 GeV for the associated production of jets and a  $Z$  or  $W$  boson decaying into leptons.

In Tables 11 and 12 leading-order cross sections for the production of a weak vector boson  $V$  ( $V = W^\pm$  or  $Z$ ), which decays into a massless lepton pair, in conjunction with up to six jets are shown, employing the ‘basic’ type of kinematical cuts. The production cross sections are displayed with four distinct values of  $p_T^{\min}$  varied over the values 50 GeV, 100 GeV, 250 GeV and 1000 GeV. As a function of  $p_T^{\min}$  total cross sections are reduced by up to four orders of magnitude, but they still reach a few attobarns for the highest multiplicities. The cross sections range over about 9 orders of magnitude from a few to a few dozen nanobarns for inclusive production to a few attobarns when the vector bosons are accompanied by six TeV jets. Even for relatively soft jets with a minimal transverse momentum of 50 GeV, the cross sections for  $V+6$  jets are still of the order of tens of picobarns. Irrespective of potentially large higher-order corrections, these first few numbers already indicate that a future  $\sqrt{s} = 100$  TeV collider will

provide a very busy environment. An obvious result of this is that very large QCD backgrounds, even at high scales, will render this a challenging environment for searches that involve signatures with many jets. These findings are condensed in Figure 40, which exhibits the cross section  $W^\pm$  and  $Z$  production in association with jets, using ‘democratic’ cuts, and in Figure 41, displaying the cumulative cross sections, including parton shower effects in a simulation invoking also parton showering effects, based on multi-jet merging technology. In Fig. 42 the  $p_\perp$  distribution of the few first jets – if existent – and the  $W$  boson is shown, based on the same simulation. Focusing on the regime of transverse momenta, this figure suggests that for leading jets with transverse momenta above around a TeV the recoil is mainly provided by a second jet rather than by the  $W$  boson. Such kinematical situations are therefore probably better identified as a (real) weak correction to QCD dijet production rather than the real QCD correction to  $Vj$ -associated production.

$n/p_T^{\min}$	$pp \rightarrow W^+ + n\text{-jet}+X$				$pp \rightarrow W^- + n\text{-jet}+X$			
	50 GeV	100 GeV	250 GeV	1000 GeV	50 GeV	100 GeV	250 GeV	1000 GeV
0	40.51(5) nb				34.29(4) nb			
1	2617(5) pb	847(1) pb	80.3(1) pb	673(1) fb	2202(4) pb	699(1) pb	62.5(1) pb	443(1) fb
2	1482(8) pb	427(2) pb	60.9(2) pb	1368(6) fb	1199(6) pb	339(1) pb	45.8(1) pb	886(3) fb
3	626(3) pb	125(1) pb	9.94(9) pb	71.2(6) fb	461(4) pb	94.6(9) pb	6.75(6) pb	39.9(3) fb
4	286(1) pb	42.6(2) pb	2166(9) fb	6.65(2) fb	208(1) pb	29.8(1) pb	1390(6) fb	3.51(1) fb
5	128(1) pb	14.1(1) pb	461(3) fb	592(3) ab	89.9(7) pb	9.09(7) pb	276(1) fb	289(1) ab
6	54.9(5) pb	4.67(4) pb	100.3(9) fb	53.3(4) ab	37.2(3) pb	2.94(2) pb	57.4(5) fb	24.8(1) ab

Table 11: Leading-order cross sections for the production of a leptonically decaying  $W^+$  or  $W^-$  in association with  $n$  jets. ‘Basic’ cuts have been employed, with transverse momentum cuts ranging from  $p_T^{\min} = 50$  GeV to  $p_T^{\min} = 1$  TeV.

$n/p_T^{\min}$	$pp \rightarrow Z(\rightarrow e\bar{e}) + n\text{-jet}+X$				$pp \rightarrow Z(\rightarrow \nu\bar{\nu}) + n\text{-jet}+X$			
	50 GeV	100 GeV	250 GeV	1000 GeV	50 GeV	100 GeV	250 GeV	1000 GeV
0	8921(8) pb				17619(18) pb			
1	696(2) pb	213.8(4) pb	20.04(4) pb	151.7(3) fb	1372(3) pb	421.8(9) pb	39.56(8) pb	300.3(2) fb
2	378(2) pb	106.7(5) pb	14.57(6) pb	293(2) fb	745(4) pb	212(1) pb	28.9(2) pb	58.6(2) fb
3	151(2) pb	29.0(3) pb	2.24(2) pb	14.2(2) fb	293(3) pb	58.5(6) pb	4.37(4) pb	28.1(2) fb
4	66.8(3) pb	9.54(4) pb	463(2) fb	1280(5) ab	132.1(6) pb	18.7(1) pb	905(4) fb	250.3(2) fb
5	28.4(3) pb	3.11(3) pb	95.3(6) fb	109.0(7) ab	56.4(5) pb	6.07(6) pb	186(2) fb	213.3(2) fb
6	12.1(2) pb	0.98(1) pb	19.4(2) fb	< 1 fb	24.4(3) pb	1.95(2) pb	40.2(4) fb	< 1 fb

Table 12: Leading-order cross sections for the production of a  $Z$  boson decaying either into a lepton or neutrino pair in association with  $n$  jets. ‘Basic’ cuts have been employed with transverse momentum cut ranging from  $p_T^{\min} = 50$  GeV to  $p_T^{\min} = 1$  TeV.

### 5.2.2 Next-to-leading order QCD corrections

In Tables 13-15 we give LO and NLO total inclusive cross sections for vector boson production in association with 1 to 5 jets. We show sensitivity to renormalization and factorization scales as superscripts and subscripts, respectively. In parenthesis we quote the associated statistical integration error for each total cross section. The cross sections at 100 TeV range over several orders of magnitude, reaching cross

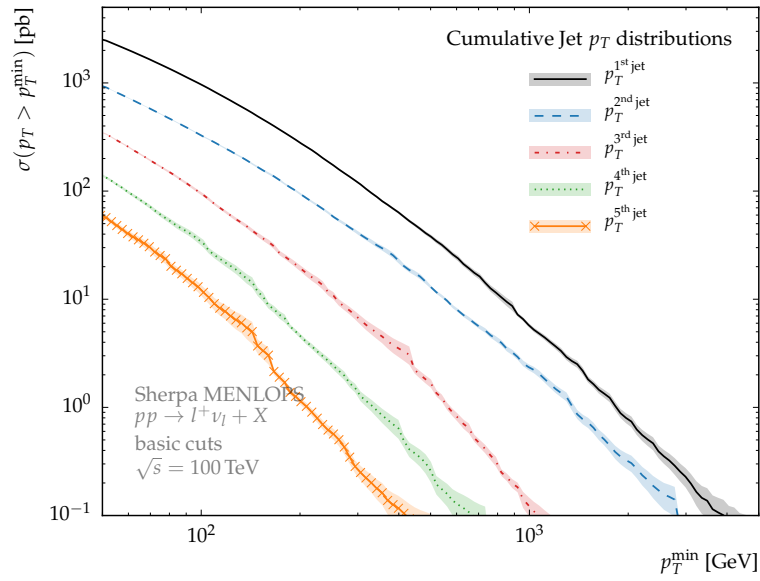


Fig. 41: The total cross sections for the production of  $W^+ + n$ -jets ( $n = 1, \dots, 5$ ) as a function of the  $p_T^{\text{min}}$ , with the ‘basic’ set of cuts.

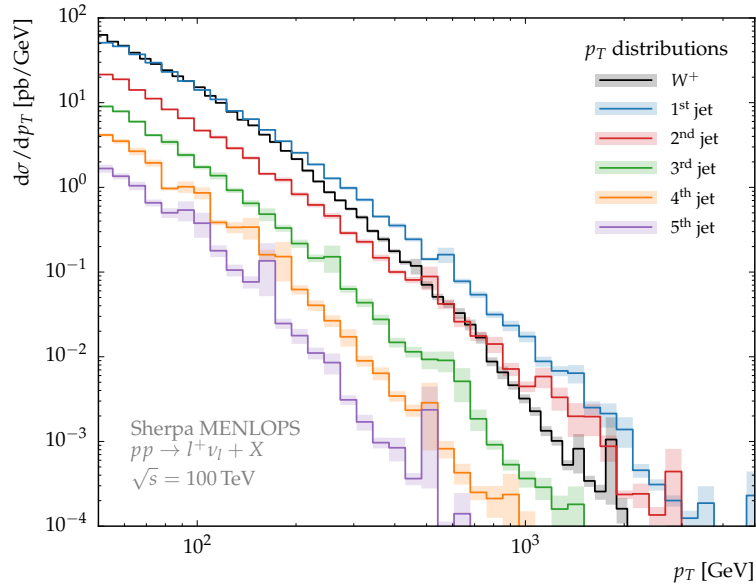


Fig. 42: Jet- $p_T$  distributions in an inclusive sample of  $W^+$  production. Also shown is the  $p_T^{W^+}$  distribution.

sections of only few attobarns in the case of high-hierarchical cuts. The theoretical control over the cross section predictions is estimated with a number of indicators: the scale variation dependence, jet ratios and PDF-uncertainties. In what follows, we discuss the scale variation dependence, but postpone the discussion of jet ratios and PDF uncertainties to Sections 5.3 and 5.5.

Perturbative calculations depend on the unphysical renormalization and factorization scales due to the truncation of the perturbative series for the scattering processes. As commonly done, we estimate the size truncated higher-order terms by varying the renormalization and factorization scales.

In Tables 13-15 the upper and lower scale variation is given super/sub scripts. Renormalization and factorization are set to equal values and varied simultaneously (see Section 5.1.1). We observe the expected increase in scale dependence with growing jet multiplicities due to the higher powers in the strong coupling  $\alpha_S(\mu)$ . The linear growth of the scale dependence at LO is significantly reduced at NLO. The systematic of the scale variation dependence is comparable for the different types of vector bosons. To summarize the results in the tables: the scale variation dependence reduces at 100 TeV from between 20% to 50% at LO to about 10% at NLO for all non-hierarchical cuts. The case of hierarchical cuts is perturbatively unstable, as can be seen from cross sections increasing with jet multiplicity at LO, from the large difference of LO and NLO cross sections, and also from the scale dependence at NLO which is not as much reduced as in the non-hierarchical cases. Such behavior, however, is not unexpected, as LO hard matrix element will over estimate rates of soft radiation, which are common in the hierarchical environment. Nevertheless NLO results give a better description, which can be compared to the jet-ratio results from the shower predictions results presented in Section 5.3.

$pp \rightarrow W^- + n\text{-jet} + X$				
	low-democratic (100 TeV)[pb]		high-democratic (100 TeV)[fb]	
$n$	LO	NLO	LO	NLO
1	481.2(4) $^{+0.0}_{-2.5}$	811(4) $^{+38}_{-31}$	258.9(4) $^{+25.7}_{-22.5}$	1139(30) $^{+160}_{-131}$
2	526.2(7) $^{+68.6}_{-59.0}$	524(10) $^{+2}_{-7}$	749(2) $^{+146}_{-116}$	885(10) $^{+34}_{-50}$
3	253.5(7) $^{+68.0}_{-50.8}$	212(7) $^{+1}_{-15}$	151.0(6) $^{+46.2}_{-33.5}$	164(4) $^{+4}_{-11}$
4	101.1(7) $^{+41.0}_{-27.5}$	92(5) $^{+2}_{-9}$	21.3(1) $^{+8.8}_{-5.9}$	21.2(9) $^{+1.7}_{-2.8}$
5	36.4(5) $^{+19.7}_{-12.1}$	—	2.81(4) $^{+1.48}_{-0.92}$	—
	low-hierarchical (100 TeV)[pb]		high-hierarchical (100 TeV)[fb]	
1	0.01394(1) $^{+0.00174}_{-0.00148}$	0.1003(3) $^{+0.0173}_{-0.0139}$	0.001330(1) $^{+0.000266}_{-0.000210}$	0.01730(6) $^{+0.00393}_{-0.00304}$
2	0.1117(2) $^{+0.0236}_{-0.0185}$	0.127(1) $^{+0.004}_{-0.007}$	0.01880(2) $^{+0.00484}_{-0.00365}$	0.0230(2) $^{+0.0017}_{-0.0020}$
3	0.212(1) $^{+0.065}_{-0.047}$	0.103(8) $^{+0.013}_{-0.037}$	0.01363(3) $^{+0.00471}_{-0.00333}$	0.0143(2) $^{+0.0006}_{-0.0012}$
4	0.240(2) $^{+0.099}_{-0.066}$	0.08(2) $^{+0.02}_{-0.06}$	0.00559(2) $^{+0.00245}_{-0.00162}$	0.0056(2) $^{+0.0004}_{-0.0007}$
5	0.204(3) $^{+0.106}_{-0.066}$	—	0.00165(2) $^{+0.00089}_{-0.00055}$	—

Table 13: Fixed order  $W^- + n\text{-jet} + X$  cross sections. The setup is specified by the low/high/democratic/hierarchical phase-space regions described in Section 5.1.1. Scale dependence variation is given in lower and upper limits and the statistical integration errors is given by the number in parenthesis next to the central value.

To illustrate the stability of the NLO QCD results, in Figs. 43 and 44 we show a full set of scale dependence plots for all kinematical regimes in  $Z + n\text{-jet}$  production. It is clear that the dynamical scale choice  $\mu = \hat{H}'_T$  represents a natural scale for all the cuts considered, and even does a good job over phase space. In Fig. 45 we actually show differential cross sections for the  $p_T$  of the  $n$ -th jet in inclusive  $W^-$  production. In the bottom panel we show differential LO/NLO ratios together with scale bands. Except for the well known giant K-factor in the 1 jet bin, all perturbative corrections appear as mild for configuration with jets with  $p_T$  of up to 10 TeV. Notice that in the highest bins, cross sections per bin are

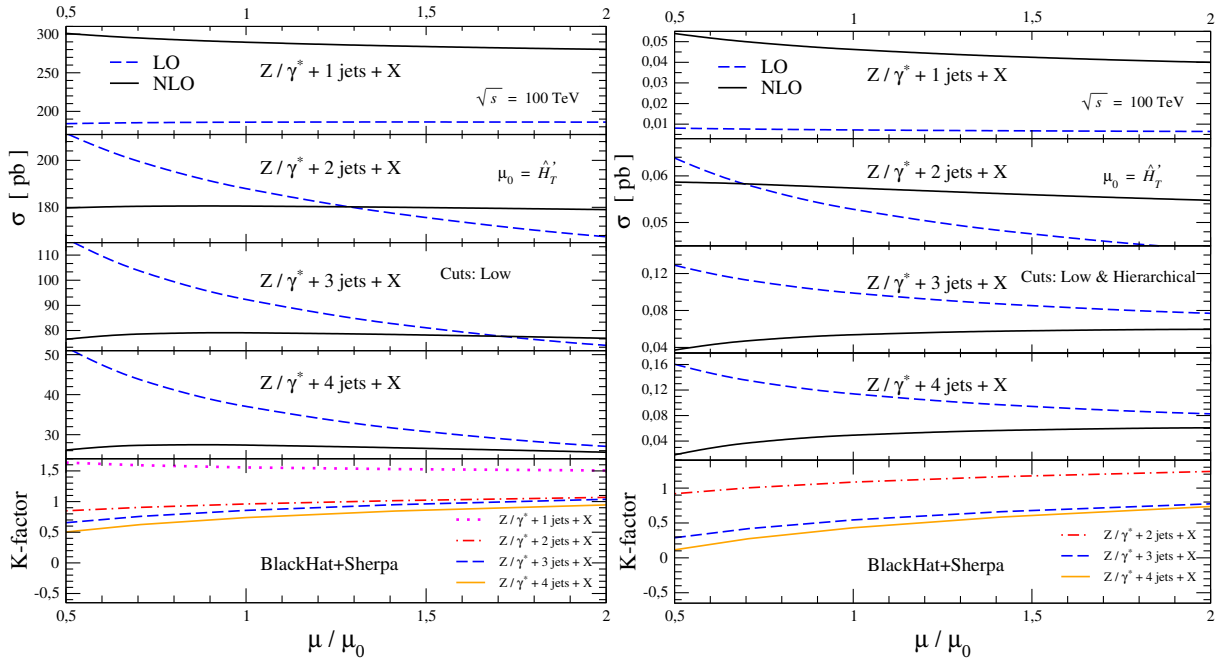


Fig. 43: Scale sensitivity for total cross sections with ‘low’ cuts in  $Z(\rightarrow ee)+n$ -jet production at LO and NLO. K-factors are shown in the bottom panels. On the left we show cases with ‘low-democratic’ cuts and on the right with ‘low-hierarchical’.

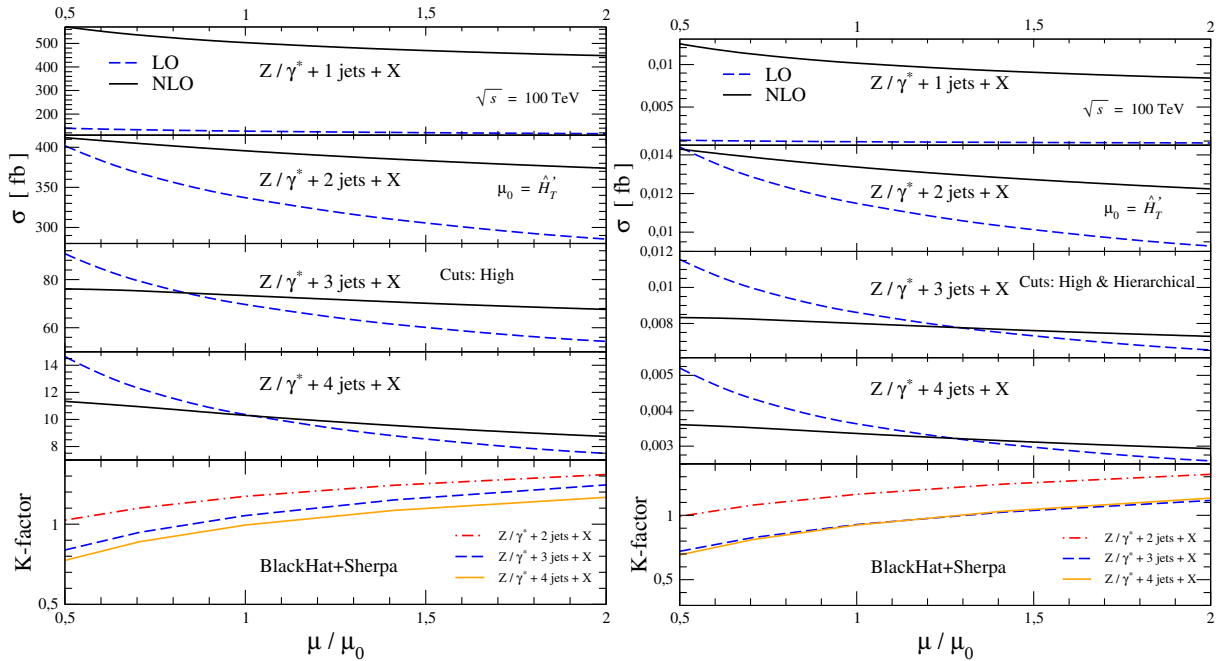


Fig. 44: Scale sensitivity for total cross sections with High cuts in  $Z$ +jets production at LO and NLO. K-factors are shown in the bottom panels. On the left we show cases with ‘high-democratic’ cuts and on the right with high-hierarchical.

$pp \rightarrow W^+ + n\text{-jet} + X$				
	low-democratic (100 TeV)[pb]		high-democratic (100 TeV)[fb]	
$n$	LO	NLO	LO	NLO
1	$563.1(5)^{+0.0}_{-2.8}$	$926(7)^{+45}_{-36}$	$405.3(8)^{+39.8}_{-34.8}$	$1714(20)^{+238}_{-195}$
2	$622.5(9)^{+81.9}_{-70.2}$	$593(10)^{+4}_{-10}$	$1148(2)^{+223}_{-177}$	$1362(20)^{+58}_{-82}$
3	$314(1)^{+84}_{-63}$	$279(8)^{+0}_{-11}$	$247(2)^{+75}_{-55}$	$256(10)^{+7}_{-17}$
4	$127.2(9)^{+51.4}_{-34.5}$	$98(8)^{+0}_{-8}$	$37.3(3)^{+15.4}_{-10.3}$	$37(2)^{+2}_{-4}$
5	$49.3(7)^{+26.5}_{-16.3}$	—	$5.03(6)^{+2.62}_{-1.64}$	—
	low-hierarchical (100 TeV)[pb]		high-hierarchical (100 TeV)[fb]	
1	$0.02499(1)^{+0.00304}_{-0.00259}$	$0.1673(8)^{+0.0284}_{-0.0228}$	$0.004191(2)^{+0.000802}_{-0.000639}$	$0.0445(1)^{+0.0099}_{-0.0077}$
2	$0.1922(4)^{+0.0402}_{-0.0315}$	$0.208(3)^{+0.005}_{-0.010}$	$0.05128(6)^{+0.01295}_{-0.00982}$	$0.0584(3)^{+0.0040}_{-0.0048}$
3	$0.371(2)^{+0.113}_{-0.082}$	$0.19(1)^{+0.02}_{-0.06}$	$0.0393(1)^{+0.0134}_{-0.0095}$	$0.0354(7)^{+0.0012}_{-0.0030}$
4	$0.437(9)^{+0.178}_{-0.120}$	$0.13(2)^{+0.04}_{-0.12}$	$0.0168(1)^{+0.0072}_{-0.0048}$	$0.0144(5)^{+0.0010}_{-0.0018}$
5	$0.39(1)^{+0.20}_{-0.12}$	—	$0.0052(1)^{+0.0028}_{-0.0017}$	—

Table 14: Fixed order  $W^+ + n\text{-jet} + X$  cross sections. The setup is specified by the low/high/democratic/hierarchical phase-space regions described in Section 5.1.1. Scale dependence variation is given in lower and upper limits and the statistical integration errors is given by the number in parenthesis next to the central value.

at the order of few attobarns.

The NLO QCD predictions for the  $n^{\text{th}}$ -jet  $p_T$  shown in Fig. 45 allow to explore the accessibility of very hard jets at the  $\sqrt{s} = 100$  TeV machine. The threshold for producing a few events with a single hard jet (considering an integrated luminosity of several inverse attobarns) is around 20 TeV. Not surprisingly, all these events will be accompanied with a second hard jet, as we can see from inspecting the tail of the second jet  $p_T$ . On the other hand, few events will be recorded with three jets (and a weak vector boson) with more than 5 TeV of  $p_T$ , and for four jets the threshold is around 3 TeV.

An interesting picture emerges from the hadronic  $H_T$  distributions shown in Fig. 46. The very large NLO corrections in the  $W^- + 1\text{jet}$  process is understood by the release of a kinematical constraint that basically allows the vector boson to be soft in events with large  $H_T$ . But here we can also see that quantum corrections tend to increase the  $H_T$  distributions for samples with two or more jets. Extra jet radiation is favored in high  $H_T$  environments, again not surprisingly. This effect is such that for the larger multiplicities we see that the differential cross sections are quite similar for the  $n = 2, 3$  and 4 in the very high- $H_T$  tails. One should then expect a sizable set of events with very large numbers of jets. In Fig. 47 we show the di-jet mass distributions for the pairs  $(j_1, j_2)$  and  $(j_3, j_4)$  in  $W^- + 4\text{-jet}$  production. For both distributions corrections are generally mild, but shape changes are clear for  $M_{j_1 j_2}$ . The radiation steepens the slope of the  $M_{j_1 j_2}$  spectrum, but events with invariant masses larger than 30 TeV will be abundant. In Fig. 48 we present the  $R$  separation of the second and third-hardest jet in a high-hierarchical configuration. Those are the hardest jets below the very hard jet required. As can be seen these jets are produced in a collimated fashion, with the potential singularity cut by the jet algorithm (with  $R = 0.4$  for us). Extra radiation push the jets even more close, as can be inferred from the change in shape of the distribution.

### 5.3 Cross-section ratios

We present ratios of cross sections: Jet-production ratios,

$$R_n = \frac{\sigma^{V+n\text{-jet}}}{\sigma^{V+(n-1)\text{-jet}}} \quad (22)$$

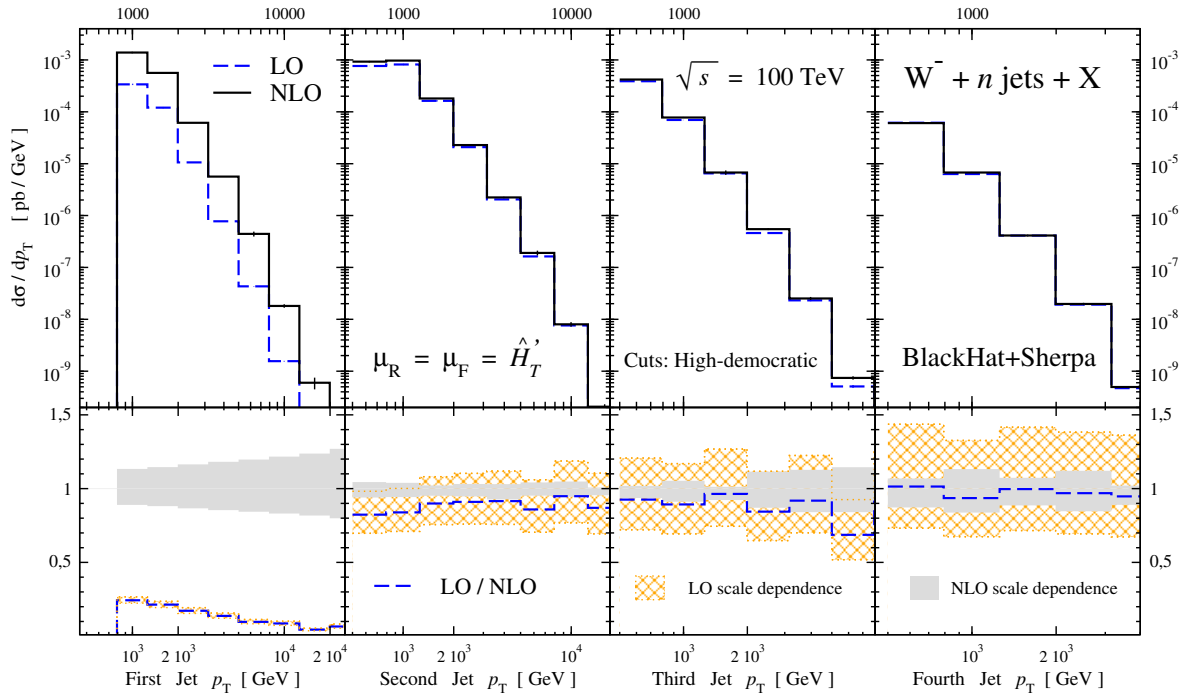


Fig. 45: Differential cross sections for inclusive  $W^-$  production in the  $n^{\text{th}}$ -jet  $p_T$ . Results are shown employing ‘high-democratic’ cuts. The bottom panels show LO/NLO ratios as well as scale sensitivity.

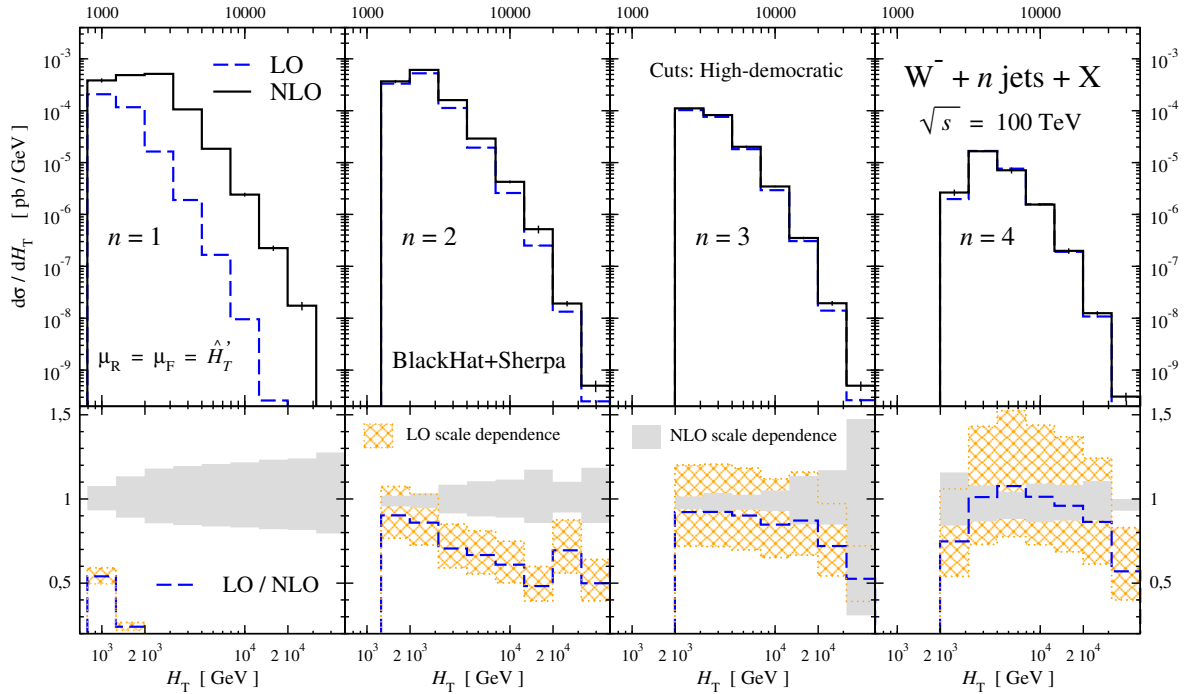


Fig. 46: Hadronic  $H_T$  distribution in samples of  $W^- + n$ -jets ( $n = 1, 2, 3, 4$ ). Results are shown employing ‘high-democratic’ cuts. The bottom panels show LO/NLO ratios as well as scale sensitivity.

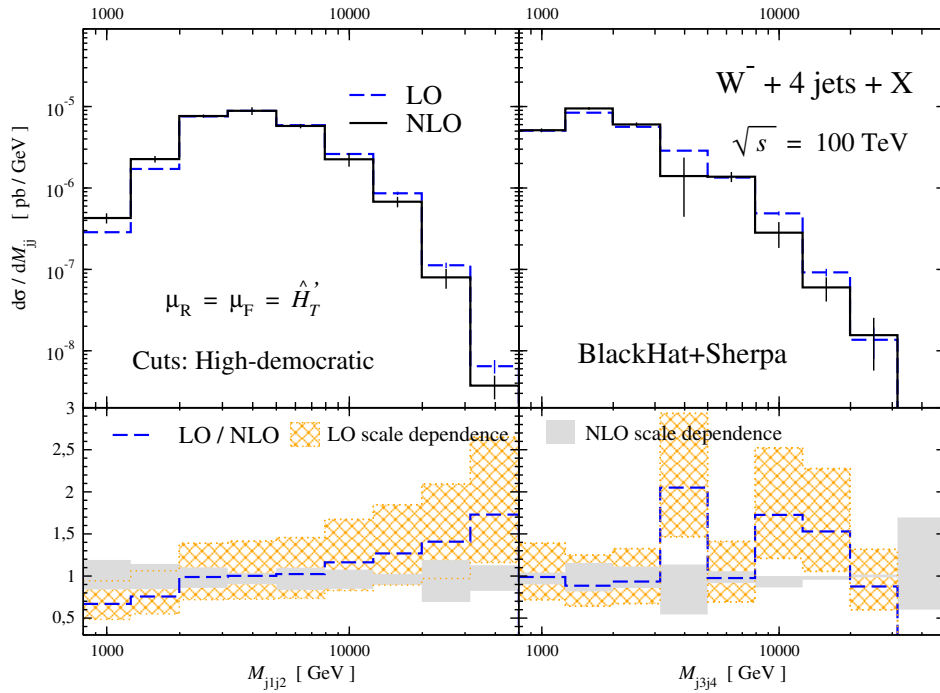


Fig. 47: Jet pair invariant masses  $M_{j_1j_2}$  and  $M_{j_3j_4}$  in  $W^- + 4$ -jet production. Results are shown employing ‘high-democratic’ cuts. The bottom panels show LO/NLO ratios as well as scale sensitivity.

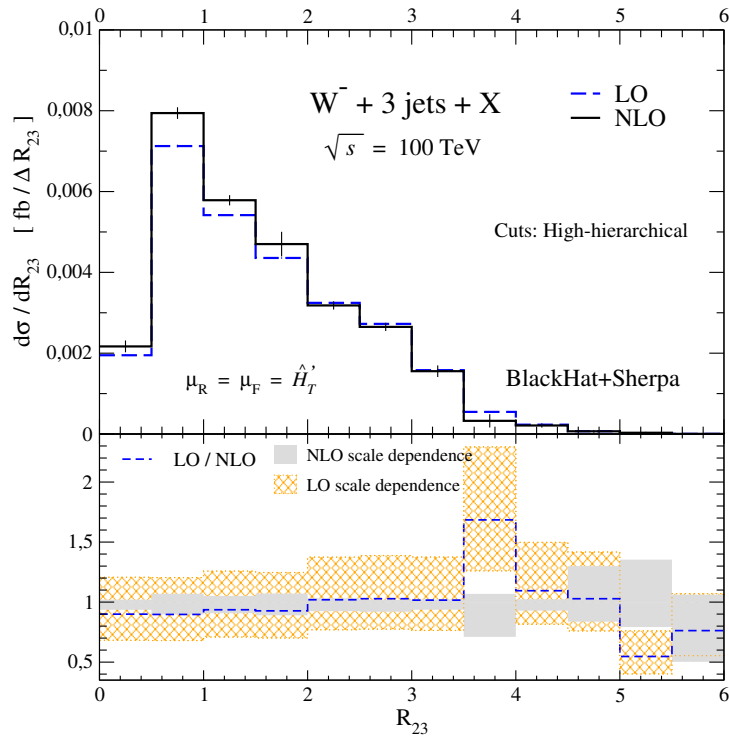


Fig. 48:  $\Delta R$  separation between the sub-leading jets in  $W^- + 3$ -jet production. Results are shown employing ‘high-hierarchical’ cuts. The bottom panel shows LO/NLO ratio as well as scale sensitivity.

$pp \rightarrow Z + n\text{-jet} + X$				
	low-democratic (100 TeV)[pb]		high-democratic (100 TeV)[fb]	
$n$	LO	NLO	LO	NLO
1	186.0(2) $^{+0.2}_{-2.0}$	290(1) $^{+11}_{-9}$	127.4(2) $^{+12.3}_{-10.8}$	504(2) $^{+67}_{-55}$
2	188.0(3) $^{+23.6}_{-20.5}$	181(3) $^{+0}_{-2}$	337.1(7) $^{+64.8}_{-51.6}$	396(6) $^{+16}_{-22}$
3	92.3(1) $^{+24.3}_{-18.2}$	79(2) $^{+0}_{-3}$	69.6(1) $^{+21.1}_{-15.3}$	73(1) $^{+3}_{-6}$
4	37.1(1) $^{+14.8}_{-10.0}$	27(1) $^{+0}_{-2}$	10.36(4) $^{+4.28}_{-2.87}$	10.3(4) $^{+1.0}_{-1.6}$
5	13.8(1) $^{+7.4}_{-4.5}$	—	1.38(1) $^{+0.72}_{-0.45}$	—
	low-hierarchical (100 TeV)[pb]		high-hierarchical (100 TeV)[fb]	
1	0.007193(3) $^{+0.000875}_{-0.000745}$	0.0462(1) $^{+0.0077}_{-0.0062}$	0.0009173(4) $^{+0.0001777}_{-0.0001412}$	0.01017(2) $^{+0.00227}_{-0.00176}$
2	0.05284(8) $^{+0.01101}_{-0.00864}$	0.0574(6) $^{+0.0013}_{-0.0026}$	0.01149(1) $^{+0.00292}_{-0.00221}$	0.01337(5) $^{+0.00093}_{-0.00113}$
3	0.0989(2) $^{+0.0302}_{-0.0219}$	0.054(3) $^{+0.006}_{-0.017}$	0.00861(1) $^{+0.00294}_{-0.00209}$	0.0080(2) $^{+0.0003}_{-0.0007}$
4	0.1140(3) $^{+0.0465}_{-0.0313}$	0.049(6) $^{+0.012}_{-0.031}$	0.003631(8) $^{+0.001576}_{-0.001046}$	0.00336(9) $^{+0.00025}_{-0.00043}$
5	0.096(1) $^{+0.050}_{-0.031}$	—	0.001095(9) $^{+0.000582}_{-0.000362}$	—

Table 15: Fixed order  $Z + n\text{-jet} + X$  cross sections for production. The setup is specified by the low/high/democratic/hierarchical phase-space regions described in Section 5.1.1. Scale dependence variation is given in lower and upper limits and the statistical integration errors is given by the number in parenthesis next to the central value.

are considered, giving the probability for the emission of an additional jet. The resulting ratios are displayed in Table 16. Theoretical uncertainties tend to be reduced in these ratios, as many common features (like PDF's, alphas, scale dependence) largely cancel in the ratios. This renders them particularly helpful for comparisons with experimental measurements. For the present study we are interested in the systematic behaviour of the ratios  $R_n$  for two reasons.

- On the one hand, the understanding of the systematics of the ratio as a function of jet-multiplicity ( $n$ ) allows to extrapolate from low to high jet multiplicities. This gives a handle to explore the collision environment. Higher jet multiplicities are required for a definitive statement. We refer to ‘staircase’-behaviour when a convergence of the jet ratios to a fixed value  $R_n \rightarrow R_s$  for increasing  $n$  is observed. ‘Poisson-scaling’, meaning that the emission of additional jets follows a Poisson distribution and thus a decreasing probability  $R_n \rightarrow \bar{n}/(n+1)$  for intermediate jet multiplicities  $n$  (with  $\bar{n}$  a constant). Based on the predictions in Table 16 we expect ‘staircase’ in the ‘democratic’ setup at 100 TeV. The asymptotic jet emission probability depends on the phase-space configuration. For the high-hierarchical setup the presented ratios suggest a Poisson scaling, which is expected for the statistical character of an additional soft-jet emission given the high- $p_T$  jet enforced by the cuts. For reasons explained in Section 5.5 the ratios  $R_2$  including the predictions for single-jet production require the addition of even higher QCD corrections [194, 202].
- On the other hand the ratios give a tool to probe the validity of the perturbative computations in the respective phase-space regions (see Section 5.5).

The picture just described can be explored much more deeply by the results from the shower calculation. Indeed, in Figs. 49-50 we show the scaling properties of the jet production ratios employing our MENLOPS results. With this we are able to look at production of up to 14 jets and we clearly see the staircase and Poissonian scaling. We have added fits to these scalings by fitting the ratios with  $n = 1, \dots, 4$ , and it appears that the extrapolations work remarkably well, making them a useful tool for further studies.

Ratios $R_n$ for $pp \rightarrow W^- + n\text{-jet} + X$ over $pp \rightarrow W^- + (n-1)\text{-jet} + X$				
	low-democratic (100 TeV)		high-democratic (100 TeV)	
$n$	LO	NLO	LO	NLO
2	1.094(2)	0.65(1)	2.894(8)	0.78(2)
3	0.481(1)	0.40(2)	0.201(1)	0.186(5)
4	0.398(3)	0.43(3)	0.141(1)	0.129(6)
5	0.361(5)	—	0.132(2)	—
	low-hierarchical (100 TeV)		high-hierarchical (100 TeV)	
2	8.01(2)	1.27(2)	14.13(2)	1.32(1)
3	1.90(1)	0.81(7)	0.725(2)	0.62(1)
4	1.13(1)	0.7(2)	0.410(2)	0.39(1)
5	0.85(2)	—	0.295(5)	—

Table 16: Jet-production ratios for the  $pp \rightarrow W^- + n\text{-jet} + X$  processes are given. The numbers are based on Table 13.

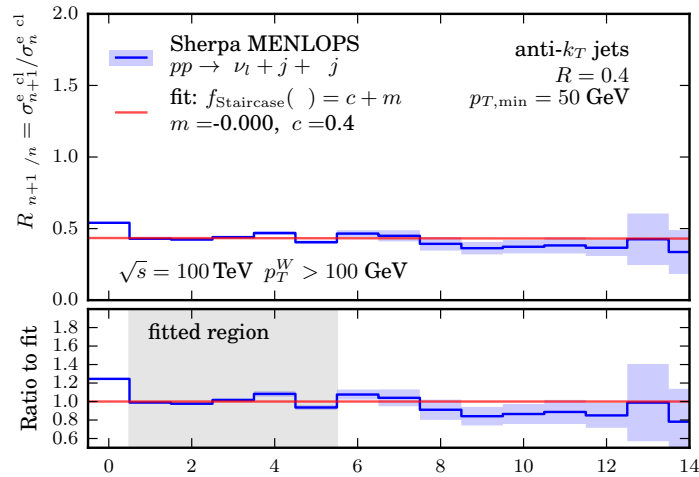


Fig. 49: Scaling properties of jet-production ratios for ‘low-democratic’ configurations. Corresponding fits are shown in solid (red) lines, as extracted from fitting the shaded regions.

Tables 17-18 display ratios of the inclusive cross section of different vector-boson types,

$$R_n^{V/V'} = \frac{\sigma^{V+n\text{-jet}}}{\sigma^{V'+n\text{-jet}}} . \quad (23)$$

The ratios point to the dominant productions channels and the respective parton luminosities in the respective phase-space regions. The monotonically decreasing ratios can be attributed to the increasing up-quark to down-quark ratio with increasing Bjorken- $x$  values [234]. Thus for increasing collision energies, lower  $x$ -values are probed leading to a reduction of the up-down ratio. This leads to a relative increase of the  $W^+$  production as compared to  $W^-$  and  $Z$ -production. In contrast, harder cuts enforce higher  $x$ -values, thus reducing  $W^+$  production compared to the other heavy vector bosons. Similarly,

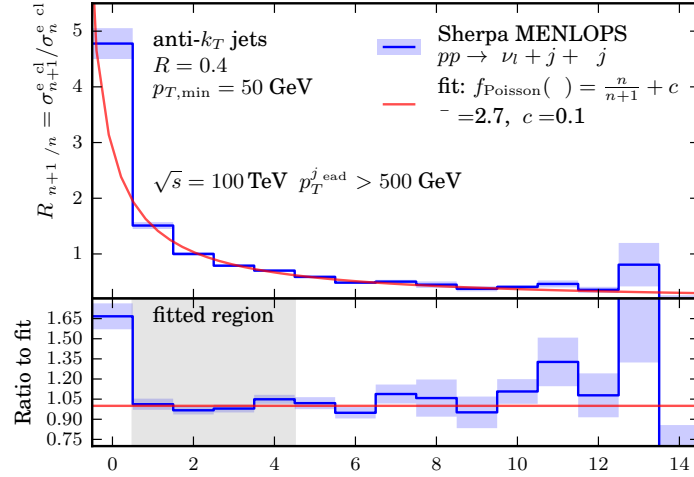


Fig. 50: Scaling properties of jet-production ratios for ‘low-hierarchical’ (right) configurations. Corresponding fits are shown in solid (red) lines, as extracted from fitting the shaded regions.

the production of additional final state jets requires higher partonic initial-state energies increasing the  $x$ -value and thus reducing the relative size of  $W^+$  production. These mechanisms explain the monotonicity systematic of the charge asymmetry ratios in Tables 17-18.

Ratios	$R_n^{W^-/W^+}$ for $pp \rightarrow W^- + n\text{-jet}+X$		over $pp \rightarrow W^+ + n\text{-jet}+X$	
	low-democratic (100 TeV)		high-democratic (100 TeV)	
$n$	LO	NLO	LO	NLO
1	0.8545(0.0010)	0.8765(0.0083)	0.6388(0.0016)	0.6647(0.0188)
2	0.8454(0.0017)	0.8836(0.0261)	0.6528(0.0019)	0.6501(0.0125)
3	0.8073(0.0035)	0.7575(0.0332)	0.6106(0.0055)	0.6416(0.0348)
4	0.7948(0.0082)	0.9385(0.0931)	0.5701(0.0052)	0.5689(0.0342)
5	0.7388(0.0145)	—	0.5574(0.0103)	—
	low-hierarchical (100 TeV)		high-hierarchical (100 TeV)	
1	0.5580(0.0005)	0.5993(0.0032)	0.3174(0.0002)	0.3887(0.0016)
2	0.5812(0.0015)	0.6118(0.0125)	0.3666(0.0005)	0.3937(0.0035)
3	0.5712(0.0042)	0.5365(0.0531)	0.3471(0.0012)	0.4033(0.0098)
4	0.5492(0.0117)	0.5990(0.2074)	0.3336(0.0024)	0.3877(0.0175)
5	0.5283(0.0170)	—	0.3160(0.0090)	—

Table 17: Ratios of the  $W^+ + n\text{-jet}$  production cross sections divided by the  $W^- + n\text{-jet}$  production cross section (Table 13 with respect to Table 14).

Ratios $R_n^{Z/W^+}$ for $pp \rightarrow Z + n\text{-jet} + X$ over $pp \rightarrow W^+ + n\text{-jet} + X$				
	low-democratic (100 TeV)		high-democratic (100 TeV)	
$n$	LO	NLO	LO	NLO
1	0.3303(0.0004)	0.3128(0.0028)	0.3143(0.0008)	0.2939(0.0043)
2	0.3020(0.0006)	0.3044(0.0084)	0.2938(0.0009)	0.2904(0.0062)
3	0.2941(0.0011)	0.2830(0.0107)	0.2816(0.0023)	0.2864(0.0151)
4	0.2913(0.0023)	0.2803(0.0274)	0.2779(0.0023)	0.2765(0.0162)
5	0.2790(0.0049)	—	0.2737(0.0041)	—
	low-hierarchical (100 TeV)		high-hierarchical (100 TeV)	
1	0.2879(0.0002)	0.2764(0.0014)	0.2189(0.0001)	0.2284(0.0007)
2	0.2749(0.0007)	0.2754(0.0055)	0.2241(0.0003)	0.2289(0.0015)
3	0.2663(0.0015)	0.2807(0.0224)	0.2193(0.0007)	0.2260(0.0079)
4	0.2611(0.0053)	0.3902(0.0881)	0.2167(0.0013)	0.2331(0.0103)
5	0.2498(0.0075)	—	0.2097(0.0054)	—

Table 18: Ratios of the  $Z + n\text{-jet}$  production cross sections divided by the  $W^+ + n\text{-jet}$  production cross section (Table 15 with respect to Table 14).

#### 5.4 Scaling behaviour: jet multiplicities or transverse momenta

In this section we consider cross sections as a function of input parameters or jet-multiplicities. Considering the behaviour of cross sections as a function of initial state energies or transverse momentum cuts allows one to understand the discovery potential as a function of collision parameters. For ‘basic’ sets of cuts, we display the dependence of the inclusive, fixed-order, NLO cross sections as a function of the jet transverse-momentum cuts in Figs. 51 and 52, for  $\sqrt{s} = 100$  and 14 TeV respectively. Comparing these two figures we see that for the largest multiplicity shown ( $n = 4$ ) a variation in  $p_T^{\min}$  from 50 GeV to 200 GeV reduces cross sections by one extra order of magnitude at  $\sqrt{s} = 14$  TeV. Larger decreases are of course expected for larger multiplicities, as the energy available for extra radiation is increased by more than a factor of 7.

A very important observation extracted from Figs. 51 and 52 is the stability of the quantum corrections, related in part to the dynamical scale choice  $\mu = \hat{H}_T^i$  that helps the LO predictions to remain close to the more scale-independent NLO predictions. This trend is associated with also the stability of total cross sections explored in all kinematical regimes in Tables 13-15.

#### 5.5 Perturbative stability

Finally in this section, we validate the reliability of the perturbative description of the scattering processes. We explore both the relative size of the quantum corrections ( $K$ -factors) and the uncertainties associated to PDF’s, as extracted from the error sets provided by CT14nlo.

For convenience in Table 19 we give explicit tables of the relative size of NLO corrections compared to the fixed order LO predictions. The  $K$ -factors, defined by  $K_V^n = \sigma_{\text{NLO}}^{\text{V}+n\text{-jet}} / \sigma_{\text{LO}}^{\text{V}+n\text{-jet}}$  are given in Table 19. For our scale choice (20) the corrections are modest for the ‘democratic’ jet cuts ranging from a  $K$ -factor 0.7 to 1.1 of associated production of 2 to 4 jets. The  $K$ -factors increase with jet multiplicity. The case of single jet production behaves in a different way reaching  $K$ -factors of 1.7. This increase is attributed to the known phenomenon that additional production channels open in the real radiation at NLO as well as the increasing phase space of hadrons recoiling against the heavy vector boson [205, 235], and

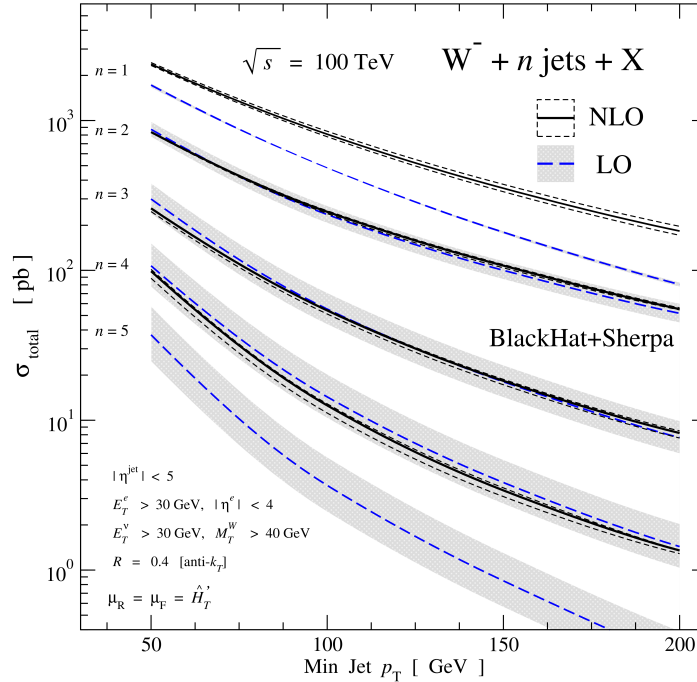


Fig. 51: Cross sections for  $W^- + n$ -jets production as a function of the  $p_T^{\min}$ , as part of the ‘basic’ set of cuts, with  $\sqrt{s} = 100$  TeV. Top lines are for  $n = 1$  and bottom for  $n = 5$ . Solid-black (dashed-blue) lines show corresponding NLO (LO) results, and we include also scale dependence bands with the small-dashed lines (shade).

it can be seen even more markedly on the first jet differential distribution in Fig. 45 (notice that NNLO QCD corrections stabilize the perturbative prediction [194, 202]). NLO corrections for  $\sqrt{s} = 14$  TeV and  $\sqrt{s} = 100$  TeV are comparable in size. For hierarchical phase space cuts K-factors increase to the ranges 1.2 - 0.8 for  $\sqrt{s} = 14$  TeV and spread out to 1.1 - 0.3 at  $\sqrt{s} = 100$  TeV for 2,3 and 4 associated jets. Single jet production receives large corrections by a factor of 3.5 at  $\sqrt{s} = 14$  TeV and up to factor of 7 at  $\sqrt{s} = 100$  TeV. Reliable predictions for the associated production of heavy vector bosons and a single jet require the inclusion of further corrections. The hierarchical cuts introduce an additional scale as compared to the ‘democratic’ setup. The NLO prediction gives a better description of the multi-scale processes as compared to the LO computation. The scale setting, providing a renormalization and factorization scales depending on the event kinematics, leads to a reliable predictions for inclusive cross sections at LO.

A further indicator for the validity of the perturbative predictions are the jet ratios (22). In the perturbative regime an additional hard emission is dressed with a factor of the strong coupling constant. The emission of additional jets should thus be suppressed and jet ratios are expected to be small, i.e. smaller than one. In Table 16 we give the jet ratios for the predictions Tables 13-15. For  $n > 2$  we observe ratios of the order one pointing to the consistency of the fixed-order predictions. Further discussions of the scaling of the inclusive cross sections can be found in Section 5.3. As a final probe of our current ability to make meaningful quantitative predictions for proton-proton collisions at a 100 TeV machine, we collect the variance of the cross sections induced by the PDF uncertainties. In table (20) we present the one-sigma relative uncertainties induced by the PDF’s for the NLO predictions of Tables 13-15.

We observe a comparable PDF uncertainties in  $\sqrt{s} = 14$  TeV and  $\sqrt{s} = 100$  TeV predictions from 1–2% for moderate cuts (‘low-democratic’). The uncertainties rise in more extreme regions of phases space; in the ‘high-democratic’ region 1 – 3% uncertainty intervals are observed, in low-hierarchical 2 – 3%

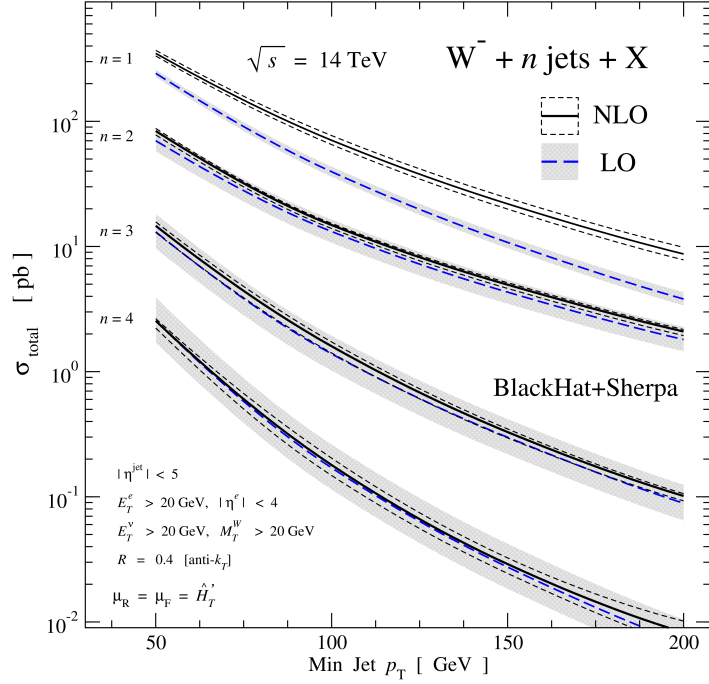


Fig. 52: Cross sections for  $W^- + n$ -jets production as a function of the  $p_T^{\text{min}}$ , with  $\sqrt{s} = 14 \text{ TeV}$ . The phase-space regions of the final-state objects is adjusted to the initial-state energies as indicated in the figure. Top lines are for  $n = 1$  and bottom lines for  $n = 4$ . Solid-black (dashed-blue) lines show corresponding NLO (LO) results, and we include also scale dependence bands with the small-dashed lines (shade).

and in the high-hierarchical uncertainty intervals up to 7% are observed for the highest jet multiplicities.  $W^+ + n$ -jet predictions are performing best as expected for the proton-proton initial state. We also notice slightly larger PDF errors for  $W^-$  cross sections as compared to  $W^+$ , pointing to larger contributions from better-constrained valence quarks in the latter. Of course, with the data collected finally at the LHC, better understanding shall follow, and these PDF uncertainties will then be further reduced.

K-factors for $pp \rightarrow W^- + n\text{-jet}+X$			
$n$	low-democratic (14 TeV)	low-democratic (100 TeV)	high-democratic (100 TeV)
1	1.78(1)	1.686(9)	4.4(1)
2	1.12(2)	1.00(2)	1.18(2)
3	1.01(2)	0.84(3)	1.09(3)
4	0.96(3)	0.91(5)	1.00(4)
	low-hierarchical (14 TeV)	low-hierarchical (100 TeV)	high-hierarchical (100 TeV)
1	3.49(1)	7.19(2)	13.01(4)
2	1.16(1)	1.14(1)	1.223(9)
3	0.90(2)	0.48(4)	1.05(1)
4	0.81(4)	0.32(9)	1.00(3)

Table 19: K-factors for  $W^- + n\text{-jet} + X$  predictions for Table 13. The size of the NLO corrections is representative for all types of heavy vector bosons discussed.

	$pp \rightarrow W^- + n\text{-jet}+X$			$pp \rightarrow W^+ + n\text{-jet}+X$			$pp \rightarrow Z + n\text{-jet}+X$		
	democratic								
	low		high	low		high	low		high
$n/\sqrt{s}$	14 TeV	100 TeV	100 TeV	14 TeV	100 TeV	100 TeV	14 TeV	100 TeV	100 TeV
1	1.42%	1.89%	1.42%	1.17%	1.76%	1.17%	1.19%	1.85%	1.36%
2	1.42%	1.60%	1.55%	1.13%	1.56%	1.19%	1.25%	1.52%	1.43%
3	1.65%	1.44%	2.08%	1.23%	1.48%	1.76%	1.48%	1.46%	2.03%
4	2.25%	1.45%	2.76%	1.59%	1.43%	2.02%	2.05%	1.49%	2.69%
	hierarchical								
1	2.88%	2.18%	5.43%	2.05%	1.62%	3.30%	2.51%	1.99%	3.80%
2	2.90%	2.14%	5.83%	2.09%	1.61%	3.11%	2.55%	2.01%	3.63%
3	3.14%	2.10%	5.83%	2.31%	1.57%	3.32%	2.88%	2.06%	4.14%
4	3.57%	3.03%	6.80%	2.61%	1.26%	4.01%	3.36%	2.30%	4.70%

Table 20: Percentage PDF errors for one-sigma error bands for NLO  $pp \rightarrow V + n\text{-jet}+X$  cross sections in Tables 13-15.

## 6 Vector boson and heavy flavours<sup>17</sup>

### 6.1 Overview

The production of a weak vector boson,  $V = W^\pm, Z$ , with a pair of heavy quarks is important for a number of reasons. These processes admit the study of mechanisms of heavy flavor production for events that can be more easily controlled experimentally, due to the presence of the weak boson, particularly if it decays leptonically. These channels therefore open the possibility of constraining, for instance, hypotheses of intrinsic heavy quark contributions to the proton distribution functions. For the case of bottom quarks the resulting final states provide important backgrounds for many studies that will be of high interest at a 100 TeV collider. For example,  $Vb\bar{b}$  production is an irreducible background to associated Higgs production with subsequent Higgs boson decay,  $H \rightarrow b\bar{b}$ , and the case  $V = W^\pm$  represents backgrounds to several top quark production processes.

Since the top quark is relatively short-lived and decays before hadronizing, these cases are qualitatively different from  $c$ - and  $b$ -quark production; the top production processes will therefore be considered instead in Section 12. For definiteness, here we focus on the case of bottom quarks. For the case of two identified, well-separated heavy quarks at transverse momenta of order 20 GeV or higher, there is essentially no difference between the rates for  $Wb\bar{b}$  and  $Wc\bar{c}$  production. The  $Zc\bar{c}$  production rate differs from that for  $Zb\bar{b}$  due to the change from a down-type to up-type coupling to quarks. Due to the dominance of the  $gg \rightarrow Zb\bar{b}$  channel at 100 TeV, the  $Zc\bar{c}$  rate is very well-approximated from a rescaling by the ratio,

$$\frac{V_c^2 + A_c^2}{V_b^2 + A_b^2} \approx 0.78, \quad (24)$$

where  $V_q$  and  $A_q$  are the vector and axial couplings of the  $Z$  boson to quarks.

The  $Vb\bar{b}$  rates for representative processes at a  $pp$  collider operating at 100 TeV are indicated in figure 53.<sup>18</sup> Decays of the vector bosons into the cleanest leptonic modes is assumed, accounting for a single family of leptons only, i.e.  $W \rightarrow e\nu$  and  $Z \rightarrow e^-e^+$ . No acceptance cuts are placed on the vector boson decay products while the bottom quarks are clustered into  $b$ -jets using the anti- $k_T$  jet algorithm with  $R = 0.4$ . Events are only accepted if they contain at least two  $b$ -jets, that are initially subject to only very loose cuts,

$$p_T^b, p_T^{\bar{b}} > 20 \text{ GeV}, \quad |y^b|, |y^{\bar{b}}| < 10. \quad (25)$$

The impact of stricter cuts on the transverse momentum and rapidity of the  $b$ -jets is also assessed. In Fig. 53 (left) the cross-section is shown as a function of the minimum transverse momentum of the  $b$ -jets. Over the range shown all of the cross-sections are of similar size. This is purely coincidental since the branching ratio for  $Z \rightarrow e^-e^+$  is much smaller than for  $W \rightarrow e\nu$ ; before the vector boson decay the  $Zb\bar{b}$  process is much larger since it proceeds through LO diagrams with two gluons in the initial state. The reduction of the cross-section due to more-realistic cuts on the  $b$ -jet rapidities can be gauged from Fig. 53 (right). This shows the acceptance, defined as  $\sigma(|y_b| < |y_b^{max}|) / \sigma(|y_b| < 10)$ , for a possible operating point represented by the cut  $p_T^b > 50$  GeV. The acceptance is rather similar for all  $Wb\bar{b}$  and  $Zb\bar{b}$  cases, although the somewhat broader  $b$ -jet rapidity distribution for the  $Zb\bar{b}$  process results in the smallest acceptance for a given rapidity. Efficient  $b$ -tagging to rapidities of around 3 would capture approximately 70% of the cross-section, while the 90% level is only attained at 4 units of rapidity. A summary of the cross-sections at a few representative working points is shown in Table 21.

Finally, Fig. 54 shows the shapes of the rapidity distributions of the charged leptons in each process. For the  $Zb\bar{b}$  process the dominance of the gluon pdf contributions leads to a rather central distribution, with most leptons produced in the region  $|y| \lesssim 3$ . For  $Wb\bar{b}$  production there is still a significant valence-quark contribution that leads to a wider central plateau, with a substantial number of events produced out to four units of rapidity.

<sup>17</sup>Editor: J. Campbell

<sup>18</sup>Cross-sections have been computed at NLO in MCFM [236–238], using default parameters and the NLO CT14 pdf set with the scale choice  $\mu_r = \mu_f = m_V$ .

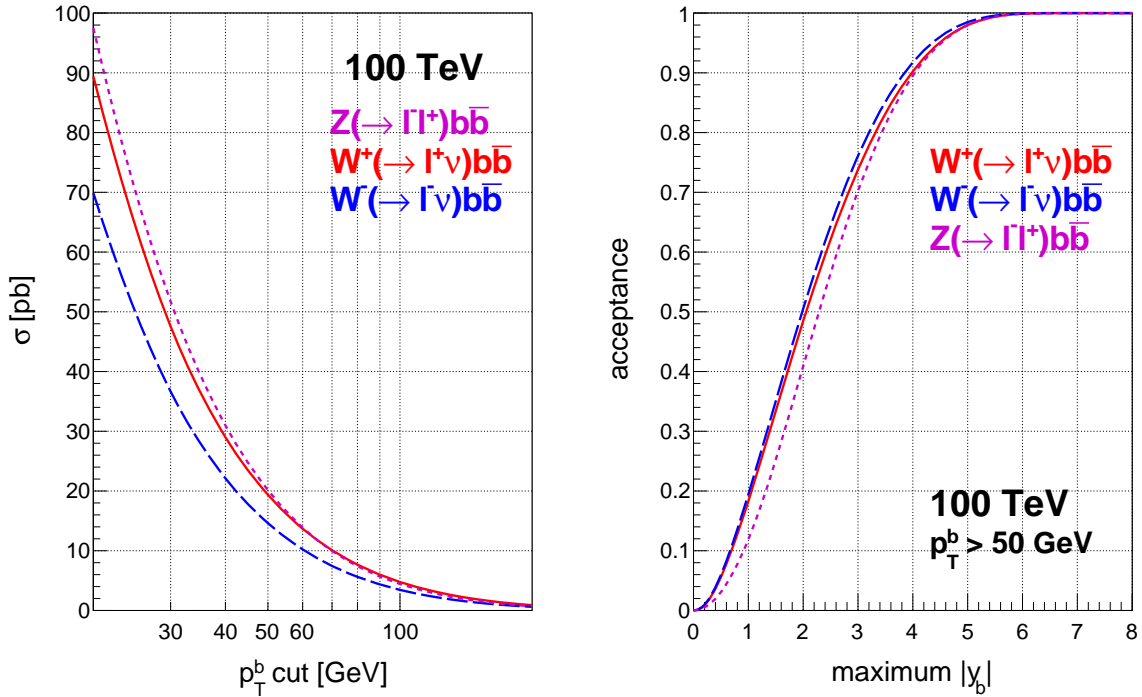


Fig. 53: Left: cross-sections for  $Vb\bar{b}$  processes as a function of the minimum  $b$ -jet transverse momentum. Right: the fraction of events accepted for a given maximum  $b$ -jet rapidity, for the case  $p_T^b > 50$  GeV.

Process	$p_T^b > 50$ GeV	$p_T^b > 50$ GeV, $ y_b  < 3$	$p_T^b > 100$ GeV
$W^+(\rightarrow \ell^+\nu)b\bar{b}$	19.4	14.3	4.76
$W^-(\rightarrow \ell^-\bar{\nu})b\bar{b}$	14.7	11.2	3.45
$Z(\rightarrow \ell^-\ell^+)b\bar{b}$	20.3	14.3	4.44

Table 21: Cross-sections (in pb) for  $Vb\bar{b}$  processes under various  $b$ -jet acceptance cuts.

## 6.2 Fully differential $Wb\bar{b} + X$ production

We now turn to a careful investigation of  $Wb\bar{b} + X$  production using a fully differential calculation of the process in which a  $W$  boson is produced in association with two  $b$  jets and a further light jet. Through the use of the MinLO prescription [239] this calculation can be used to describe not only the emission of additional light jets, but also inclusive  $Wb\bar{b}$  production. We will use this calculation to study these final states under three sets of selection cuts, that are appropriate for studies of  $Wb\bar{b} + X$  production itself, or as a background to  $HW$  or single-top searches, respectively.

### 6.2.1 Computational setup

The computation is performed using the `Wbb` and `Wbbj` generators available in the POWHEG BOX framework [240–242] and developed in [243]. The tree-level amplitudes, which include Born, real, spin- and colour-correlated Born amplitudes, were automatically generated using an interface [244] to MadGraph4 [245, 246], whereas the one-loop amplitudes were generated with GoSam [247, 248] via the BinOth-Les-Houches (BLHA) interface [249, 250], presented for the POWHEG BOX and GoSam in [251].

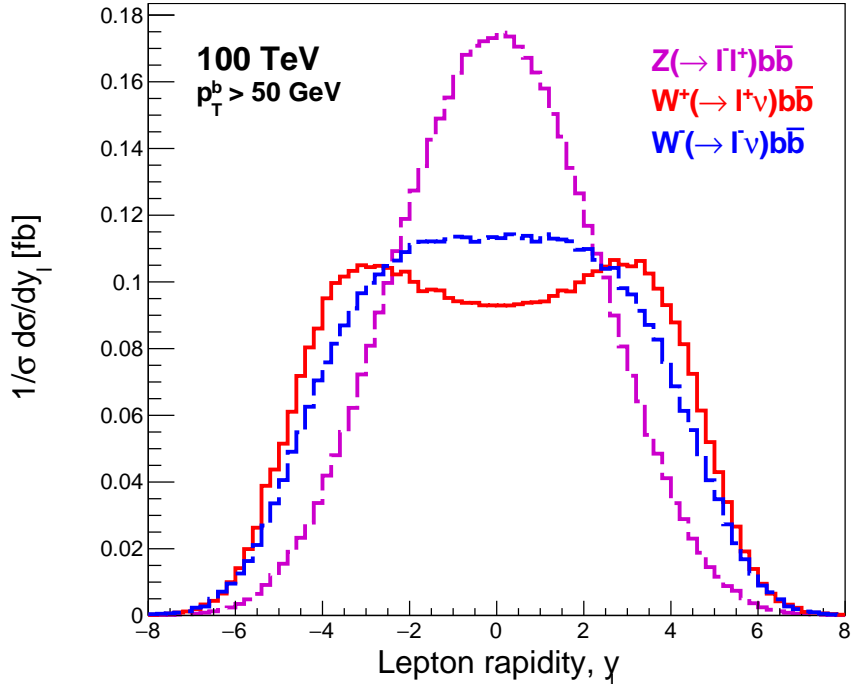


Fig. 54: The normalized rapidity distributions for the charged leptons produced in the  $Vb\bar{b}$  processes, for the  $b$ -jet transverse momentum cut  $p_T^b > 50$  GeV.

The version of GoSam [248] that was run is the 2.0: it uses QGRAF [252], FORM [253] and SPINNEY [254] for the generation of the Feynman diagrams. These diagrams are then computed at running time with Ninja [255, 256], which is a reduction program based on the Laurent expansion of the integrand [257], and using OneLoop [258] for the evaluation of the scalar one-loop integrals. For unstable phase-space points, the reduction automatically switches to GoLem95 [259], that allows to compute the same one-loop amplitude evaluating tensor integrals. The  $Wb\bar{b}$  and  $Wbbj$  generators include bottom-mass effects and spin correlations of the leptonic decay products of the  $W$  boson. Despite the fact that the computation is performed with massive quarks in the decoupling scheme [260], where  $\alpha_s$  is running with 4 light flavours, a switch to allow for a running with 5 light flavours and the usage of pdfs with 5 flavours, as proposed in [50], has been implemented. The details technical for the switch in the case at hand can be found in the Appendix of the Ref. [243].

All the results have been obtained setting the bottom mass to  $m_b = 4.75$  GeV and using the MMHT2014nlo68cl [9] pdf set. Jets have been clustered with the Fastjet package [212, 261], with radii which depend on the type of analysis performed. The renormalization and factorization scales have been set according the MinLO prescription [239], as described in Ref. [243]. The results presented in the following sections have been computed at fixed next-to-leading order level, plus MinLO. Parton-shower effects have not been taken into account. The errors in the plots and in the tables have a statistic origin and come from the numeric integration of the results. No scales or pdf variations have been studied in this contribution.

### 6.2.2 $Wb\bar{b}$ selection cuts

We begin by presenting results for the production of a  $W$  boson in association with two hard  $b$  jets in the final state. For this analysis we use the anti- $k_T$  jet algorithm [203] with jet radius set to  $R = 0.4$ . We require the presence of exactly two  $b$  jets with transverse momentum  $p_T^b > 50$  GeV and we apply three different cuts on the transverse momentum of additional light jets, i.e.  $p_T^j > 1, 100$  or 500 GeV. This

allows to investigate the fully inclusive  $Wb\bar{b}$  production, where the light jet can become unresolved, as well as final states where additional light jets are present. We stress that the former case can be explored only due to the use of the MiNLO prescriptions, where appropriate Sudakov form factors damp the soft and collinear regions associated with the extra light jet. We also show some comparisons with the NLO predictions obtained with the Wbb generator, in which the renormalization and factorization scales have been set to  $\mu = \sqrt{\hat{s}}/4$ , where  $\hat{s}$  is the square of the partonic center-of-mass energy, as suggested in Ref. [243]. For exclusive kinematic regions, where the jet is resolved and has high transverse momentum, the Wbb code describes the jet at LO, while the Wbbj one gives a description at NLO.

Results for the fiducial cross sections are reported in Table 22 for the Wbb generator, and in the top rows of Table 23, for the Wbbj one, where we also report the corresponding values computed at  $\sqrt{s} = 14$  TeV. The increase in the cross section from 14 to 100 TeV is much larger than the relative increase in the center-of-mass energy (roughly a factor of 7), and it becomes larger by sharpening the cuts on the transverse momenta of  $b$  and light jets. Furthermore, there is a 20% difference between the NLO  $Wb\bar{b}$  cross section and the one for  $Wb\bar{b} + 1$  jet with  $p_T^j > 1$  GeV. Instead, we note that the 100 TeV result for Wbbj for the most inclusive case ( $p_T^j > 1$  GeV) and two  $b$ -jets with  $p_T^b > 50$  GeV ( $34.0 \pm 0.6$ pb) agrees extremely well with the pure NLO prediction of 34.1pb computed at  $\mu = m_W$  that has been presented in Table 21.<sup>19</sup>

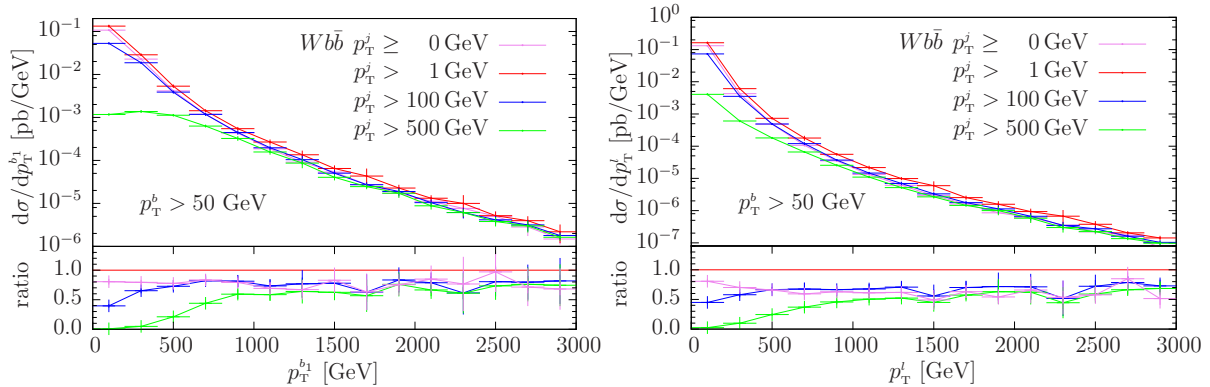


Fig. 55: Transverse-momentum distributions of the hardest  $b$  jet (left) and of the charged lepton (right) for  $Wb\bar{b}j$  production at  $\sqrt{s} = 100$  TeV. The results using the NLO Wbb code are shown too.

Figure 55 shows the transverse-momentum distribution of the hardest  $b$  jet and of the charged lepton, respectively. These observables can be described also by the Wbb generator, and we plot the corresponding curves for comparison. Figures 56 and 57 display, on the left panels, the transverse momentum and the rapidity distribution of the two- $b$  jet system, respectively. The right panels in the figures will be discussed in Section 6.2.3. In all these plots the different  $p_T$  cuts on the light jets induce differential ratios which vary only in the low transverse-momentum regions, while being almost constant elsewhere. For the transverse-momentum distributions the differences between  $p_T^j > 100$  GeV and  $p_T^j > 500$  GeV are restricted to the region below 1 TeV, where the bulk of the cross section sits. For harder transverse momenta the cut on the light jet loses its importance, leading to ratios of order one. The impact of the transverse-momentum cut on the light jet on the rapidity distributions of the two- $b$  jet system has instead larger effects, as can be seen in Fig. 57, with constant ratios in the considered rapidity range.

Figures 58 and 59 show the normalized distribution of the azimuthal angle  $\Delta\phi^{W,b\bar{b}}$  and the radial distance  $\Delta R^{W,b\bar{b}}$  between the  $W$  boson and the two- $b$  jet system respectively. In the most inclusive case ( $p_T^j > 1$  GeV), the  $W$  boson and the  $b\bar{b}$ -system are preferably produced back-to-back in azimuth and

<sup>19</sup>Apart from the difference in the method of calculation, there is also a small mismatch in the choice of PDFs.

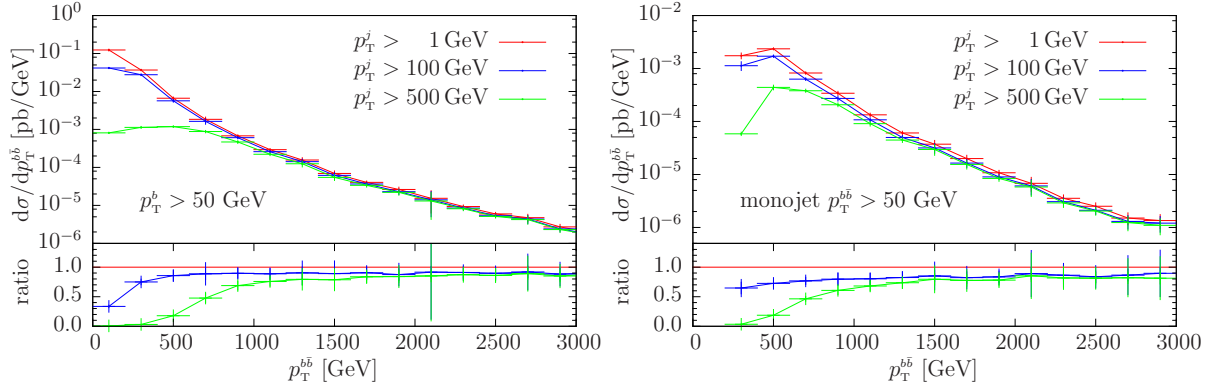


Fig. 56: Transverse-momentum distributions of the two- $b$  jet system (left) and of the  $b\bar{b}$ -monojet (right) for  $Wb\bar{b}j$  production at  $\sqrt{s} = 100$  TeV. Details of the jet algorithm employed in the two cases are reported in the text.

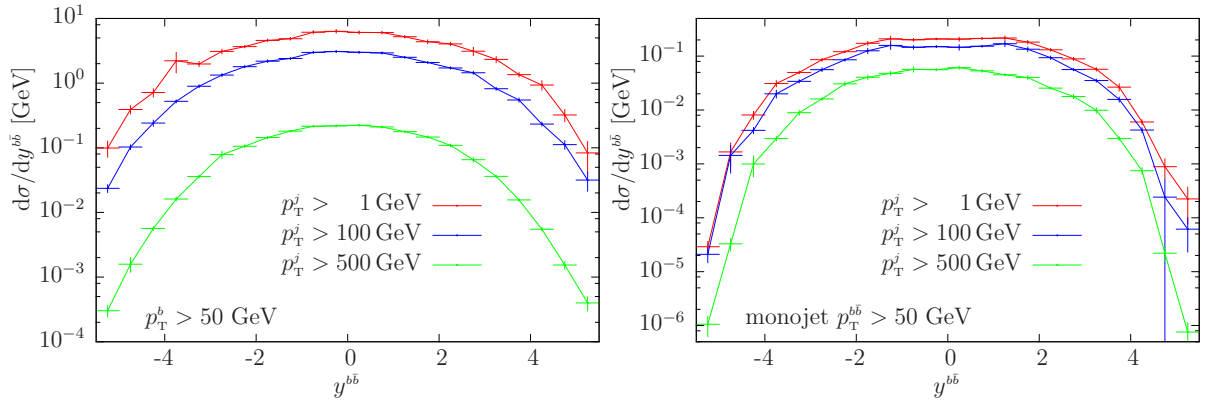


Fig. 57: Rapidity distributions of the two- $b$  jet system (left) and of the  $b\bar{b}$ -monojet (right) for  $Wb\bar{b}j$  production at  $\sqrt{s} = 100$  TeV. Details of the jet algorithm employed in the two cases are reported in the text.

tend to have a large radial distance. In addition, when extra hard jet radiation is required, the distributions become flatter as the hardness of the additional jet is increased.

Finally, in Fig. 60 the transverse momentum spectra of the  $W$  boson, the two- $b$  jet system and the extra light tagged jet are compared. A clear difference in the distribution of the vector boson with respect to the other twos can be seen, the former being much softer at high transverse momentum. In the high- $p_T$  tail, we note that the jet tends to be slightly harder than the two- $b$  jet system.

### 6.2.3 Higgsstrahlung selection cuts

In this section we investigate  $Wb\bar{b} + X$  production as irreducible background for the associated production of a Higgs boson and a  $W$ , where the Higgs boson decays into a  $b\bar{b}$  pair. It is well known that, for boosted-boson kinematics, the signal to background ratio for Higgs detection improves considerably [262]. In fact, in this case, there is a high probability that the two  $b$  quarks are clustered into a single fat jet. We study then the level of background to this associated Higgs production channel, by looking at events where the  $W$  boson is produced in association with a fat  $b$ -flavoured monojet, containing the  $b\bar{b}$  quark pair. These events are likely to become very frequent at center-of-mass energies of the order of hundreds of TeV. In this analysis, jets are reconstructed using the Cambridge/Aachen algorithm [263]

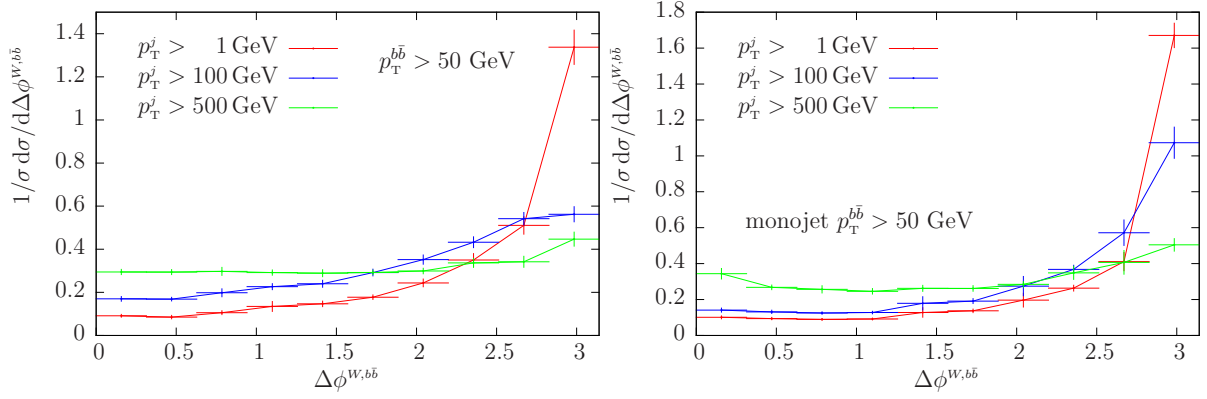


Fig. 58: Normalized differential cross-section distribution as a function of the azimuthal angle separation between the  $W$  boson and the two- $b$  jet system, on the left, and the  $b\bar{b}$ -monojet, on the right, respectively, at  $\sqrt{s} = 100$  TeV. Details of the jet algorithm employed in the two cases are reported in the text.

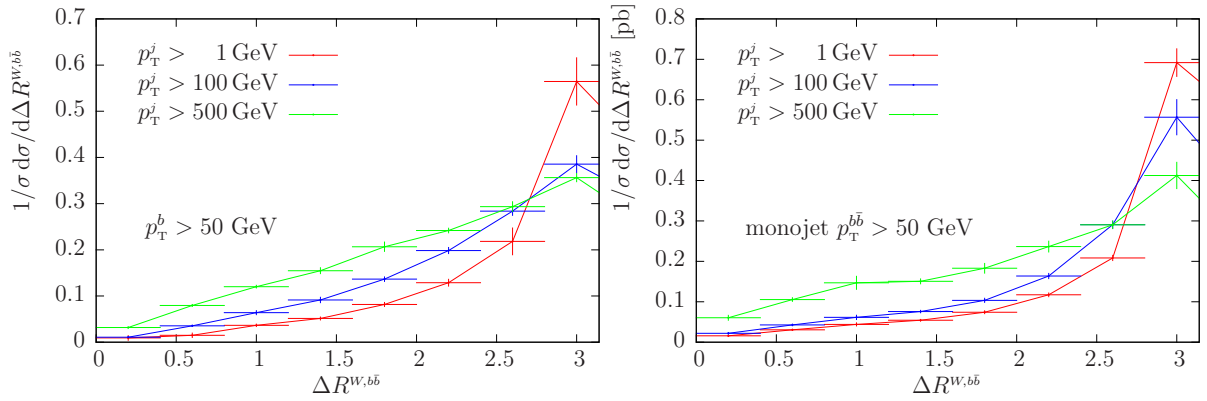


Fig. 59: Normalized differential cross-section distribution as a function of the radial distance between the  $W$  boson and the two- $b$  jet system, on the left, and the  $b\bar{b}$ -monojet, on the right, respectively, at  $\sqrt{s} = 100$  TeV. Details of the jet algorithm employed in the two cases are reported in the text.

with a jet radius  $R = 0.7$ . Furthermore we require the invariant mass of the monojet  $m^{b\bar{b}}$  to be between 100 and 150 GeV, and a minimum transverse momentum of  $p_T^{b\bar{b}} > 50$  GeV. As done in Section 6.2.2, we impose three different transverse-momentum cuts on the extra light jets, i.e.  $p_T^j > 1, 100$  or 500 GeV. The fiducial cross sections computed at 14 and 100 TeV are presented in the central rows of Table 23.

Coming to the differential distributions, in the right panels of the Figs. 56–60 we plot the same kinematic distributions as plotted in the left panels, this time considering the monojet instead of the two  $b$  jets. Due to the presence of the additional cut on the invariant mass of the  $b\bar{b}$  system, these distributions are two order of magnitude smaller than the corresponding ones in the left panels, but present similar shapes. The right panel of Fig. 59 shows the differential cross section as a function of the azimuthal angle  $\Delta\phi^{W,b\bar{b}}$ . This distribution is almost insensitive to a cut on the transverse momentum of the light jet of 100 GeV, while it shows larger deviations with respect to the most inclusive case, when the cut is increased to 500 GeV. In the latter case, the distribution becomes nearly flat over the whole kinematical range.

Dedicated analyses are needed to compare directly signal and background, in order to assess the effectiveness of these cuts.

As far as the differential cross section as a function of the radial distance  $\Delta R^{W,b\bar{b}}$  is concerned,

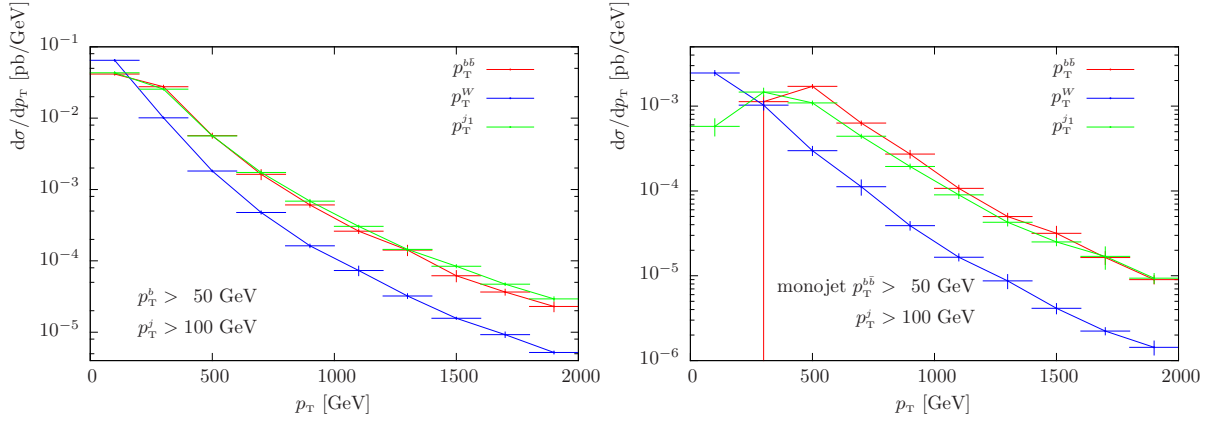


Fig. 60: Transverse-momentum distribution of the two- $b$  jet system, of the  $W$  boson and of the hardest light jet. Ratio plots are shown too. The differential cross section has a cut on the  $b$  jet, in the left panels, and on the monojet in the right ones.

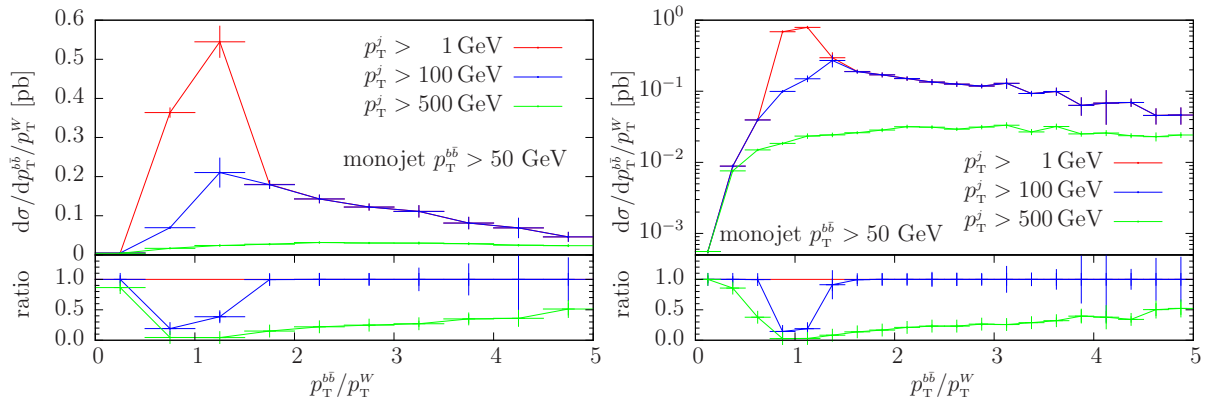


Fig. 61: Differential cross sections as a function of the ratio of the transverse momentum of the two- $b$  jet system over the  $W$  boson one.

Fig. 59 shows that only the events separated by a large  $\Delta R^{W,bb}$  are more affected by the harder cut on the additional jet transverse momentum.

The behavior of the ratios of the transverse momentum spectra of the  $W$  boson, of the two- $b$  jet system and of the extra light tagged jet, shown in the right panels of Fig. 60, for the monojet search, is similar to the ones in the left panels.

In the study of the monojet selection cuts, it is interesting to study the differential cross section as a function of the ratio  $p_T^{bb}/p_T^W$ , which is shown in Fig. 61. The two panels show the same distribution on a linear (left panel) and logarithmic scale (right panel). While for the most inclusive case, the bulk of the cross section is given by events where the ratio of the transverse momenta is close to one, as the cut on the extra jet gets harder, the distributions flatten, showing that events where the  $W$  boson is softer than the two- $b$  jet system clearly prevail.

In Fig. 62, on the left panel, the number of events as function of the minimal invariant mass of the  $Wb\bar{b}$  system is shown. The right panel of Fig. 62 shows instead the number of events as a function of the minimum transverse momentum of the monojet. In both cases, an integrated luminosity of  $\mathcal{L} = 20 \text{ ab}^{-1}$  is assumed. It is striking that, with the aforementioned cuts, the number of background events induced by  $Wb\bar{b} + X$  is around  $10^6$ , with a transverse-momentum cut on the monojet of the order of 1 TeV, even

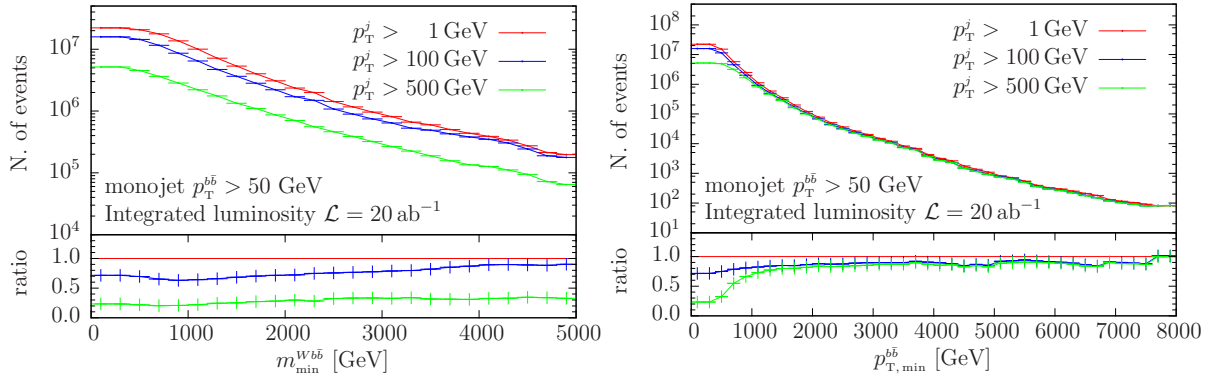


Fig. 62: Invariant-mass distribution of the  $b\bar{b}$  system (left) and number of events as a function of the minimum transverse momentum of the  $b\bar{b}$  system (right) in the monojet search at  $\sqrt{s} = 100$  TeV. The number of events is computed assuming an integrated luminosity of  $\mathcal{L} = 20 \text{ ab}^{-1}$ .

in the case where the light-jet transverse momentum is required to be above 500 GeV. This fact should be kept in mind in order to assess the experimental sensitivity, in searches of massive particles decaying into a pair of boosted bottom quarks, in association with a hard lepton and missing transverse energy.

#### 6.2.4 Single-top selection cuts

The last scenario we consider is single-top production. To estimate the size and shape of the background induced by  $Wb\bar{b} + X$  production on single-top searches, we require the presence of exactly two resolved jets in the final state, one of which must be a  $b$  jet, while the other has to be a light jet. We have recombined the partons using the anti- $k_T$  algorithm with  $R = 0.4$  and have not distinguished between jets containing only one  $b$  quark, one  $b$  anti-quark or a  $b\bar{b}$  pair, considering them on the same footing as a  $b$  jet. We have computed kinematic distributions applying the following cuts on the transverse momentum of the  $b$  jet and of the light jet

$$p_T^{j/b} > 50, 100 \text{ GeV}.$$

Furthermore, we have imposed a cut on the transverse momentum of the sum of the momenta of the  $W$  and of the  $b$  jet, to simulate the effect of a cut on a reconstructed top-quark momentum  $p^t$ , in single-top production

$$p_T^t > 0, 500, 1000 \text{ GeV}.$$

We refer to the reconstructed  $Wb$  system as “top” jet, in the following.

In the last rows of Table 23 we give the fiducial cross sections computed within the acceptance cuts reported above. We observe an inversion when comparing the effect of the transverse-momentum cut on the  $b$  jet for  $p_T^t > 0$  GeV and  $p_T^t > 500, 1000$  GeV. In the former case, the fiducial cross section decreases both at 14 and at 100 TeV, whereas in the latter two, the cross sections increase when applying harder cuts. This is due to the peculiarity of the adopted event selection: in fact, requiring only one resolved  $b$  jet induces automatically a veto on the second  $b$  jet present at LO. By hardening the cut on  $p_T^b$ , a wider kinematic region opens up for the additional unresolved  $b$  jet, leading to the observed increase. It would be interesting in the future to study the sensitivity of the single-top signal to this cut, and to compare it to the one we are studying here. The inversion is also clearly visible in the first bin in the left panel of Fig. 63, which shows the transverse-momentum distribution of the “top” jet for  $p_T^{j/b} > 50$  GeV and  $p_T^t > 100$  GeV. On the right panel of Fig. 63, we plot the transverse-momentum distributions of the light tagged jet for different cuts on the “top” jet transverse momentum. Finally, in Figs. 64–66 we plot the differential cross sections as a function of the rapidity of the light jet, of the rapidity of the “top” jet and of the cosine of the angle  $\theta^*$  between the charged lepton and the light jet in the “top” rest frame.

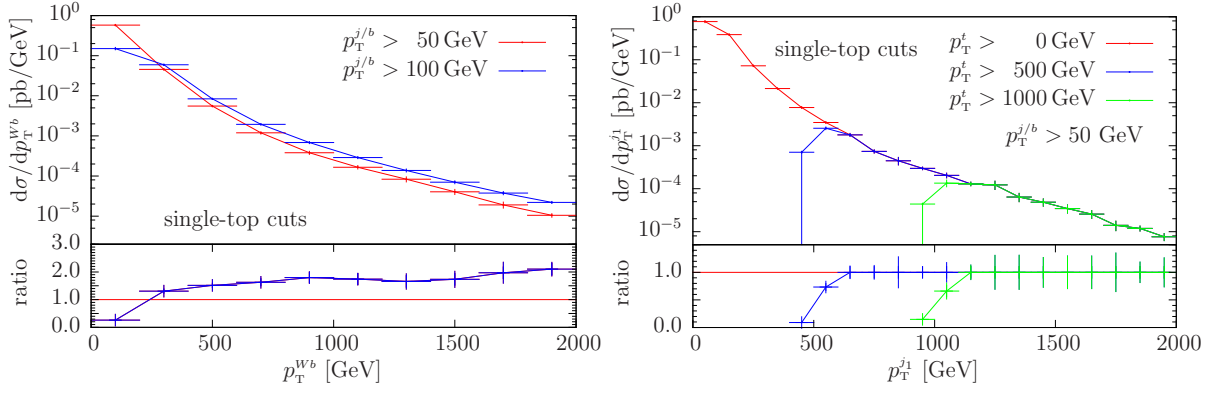


Fig. 63: Transverse-momentum distributions of the  $Wb$  system (left) and of the light jet (right) at  $\sqrt{s} = 100$  TeV.

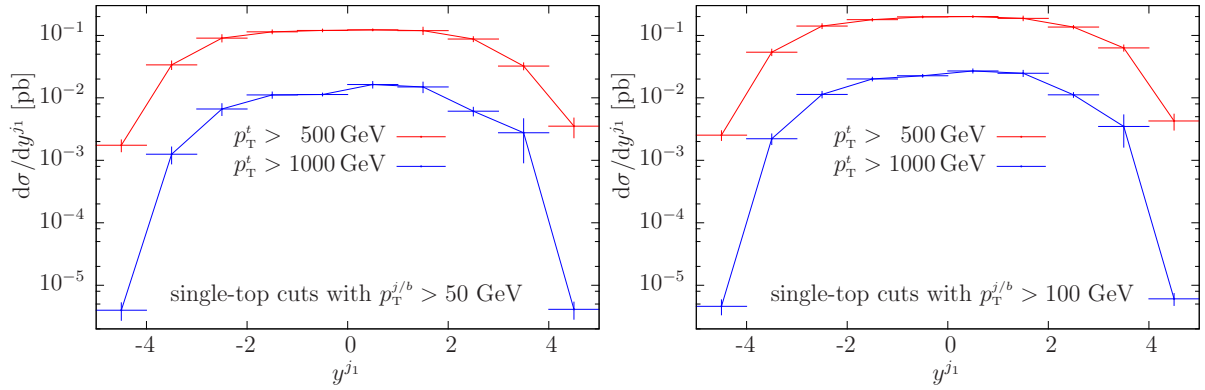


Fig. 64: Rapidity distribution of the light jet for two different transverse-momentum cuts on the reconstructed jets and on the “top”, i.e. the  $Wb$  system, at  $\sqrt{s} = 100$  TeV.

In the left panels of these figures we consider a cut on the  $b$  and light jet of  $p_T^{j/b} > 50$  GeV, while in the right panels, this cut has been set to  $p_T^{j/b} > 100$  GeV. While the shape of the curves in the two panels are very similar, increasing the cut on the “top” jet decreases the distributions by more than one order of magnitude.

$\sigma_{\text{NLO}}^{Wb\bar{b}}$ [pb] @ 14 TeV		$\sigma_{\text{NLO}}^{Wb\bar{b}}$ [pb] @ 100 TeV	
$Wb\bar{b}$ selection cuts			
$p_T^b > 0$ GeV	$p_T^b > 50$ GeV	$p_T^b > 0$ GeV	$p_T^b > 50$ GeV
$102.83 \pm 0.07$	$1.399 \pm 0.001$	$988 \pm 11$	$27.28 \pm 0.03$

Table 22:  $Wb\bar{b}$  fiducial cross sections in pb at NLO accuracy for the scenario considered in Section 6.2.2, for a proton-proton collider at 14 and 100 TeV, computed with the `Wbb` code.

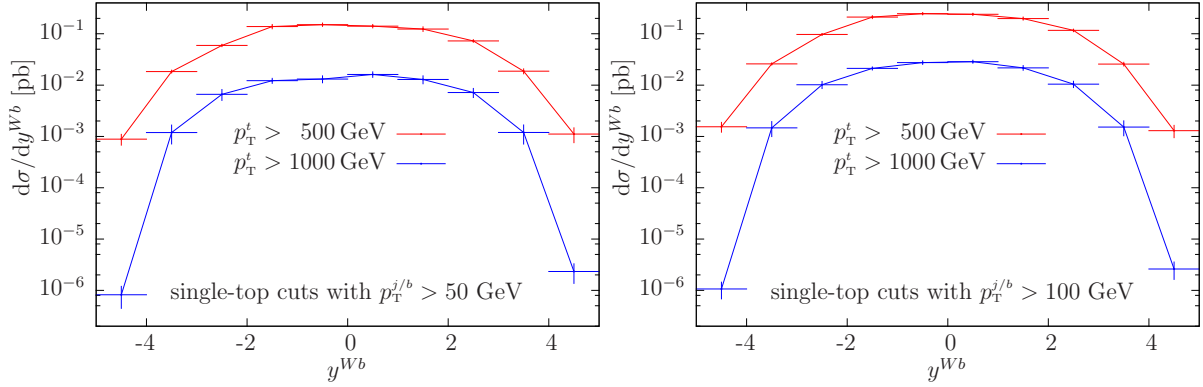


Fig. 65: Rapidity distribution of the “top” system for two different transverse-momentum cuts on the reconstructed jets, at  $\sqrt{s} = 100$  TeV.

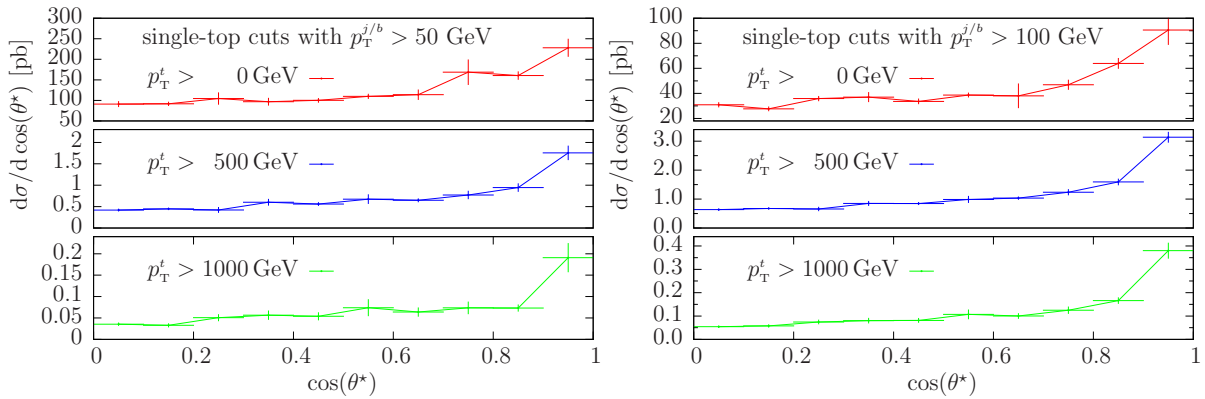


Fig. 66: Differential cross section as a function of the cosine of the angle  $\theta^*$  between the charged lepton and the light jet, in the “top” rest frame, at  $\sqrt{s} = 100$  TeV.

	$\sigma_{\text{NLO+MiNLO}}$ [pb] @ 14 TeV		$\sigma_{\text{NLO+MiNLO}}$ [pb] @ 100 TeV	
<i>Wb<math>\bar{b}</math></i> selection cuts				
	$p_{\text{T}}^b > 0$ GeV	$p_{\text{T}}^b > 50$ GeV	$p_{\text{T}}^b > 0$ GeV	$p_{\text{T}}^b > 50$ GeV
$p_{\text{T}}^j > 1$ GeV	$96.0 \pm 6.7$	$1.78 \pm 0.13$	$1179 \pm 46$	$34.0 \pm 0.6$
$p_{\text{T}}^j > 100$ GeV	$5.84 \pm 0.09$	$0.416 \pm 0.008$	$149 \pm 4.0$	$15.5 \pm 0.1$
$p_{\text{T}}^j > 500$ GeV	$0.0355 \pm 0.0003$	$0.00764 \pm 0.00004$	$3.80 \pm 0.17$	$1.00 \pm 0.01$
Higgsstrahlung selection cuts				
	$p_{\text{T}}^b > 50$ GeV		$p_{\text{T}}^b > 50$ GeV	
$p_{\text{T}}^j > 1$ GeV	$0.0215 \pm 0.0003$		$1.11 \pm 0.022$	
$p_{\text{T}}^j > 100$ GeV	$0.0122 \pm 0.0002$		$0.794 \pm 0.021$	
$p_{\text{T}}^j > 500$ GeV	$0.00237 \pm 0.00002$		$0.259 \pm 0.005$	
Single-top selection cuts				
	$p_{\text{T}}^{j/b} > 50$ GeV	$p_{\text{T}}^{j/b} > 100$ GeV	$p_{\text{T}}^{j/b} > 50$ GeV	$p_{\text{T}}^{j/b} > 100$ GeV
$p_{\text{T}}^t > 0$ GeV	$6.00 \pm 0.18$	$1.62 \pm 0.06$	$126 \pm 4$	$44.3 \pm 1.6$
$p_{\text{T}}^t > 500$ GeV	$0.009 \pm 0.001$	$0.12 \pm 0.001$	$0.72 \pm 0.02$	$1.16 \pm 0.03$
$p_{\text{T}}^t > 1000$ GeV	$0.0005 \pm 0.0001$	$0.0006 \pm 0.0001$	$0.070 \pm 0.004$	$0.123 \pm 0.005$

Table 23: *Wb $\bar{b}j$*  fiducial cross sections in pb at NLO+MiNLO accuracy for the different scenarios considered in Sections 6.2.2, 6.2.3 and 6.2.4 for a proton-proton collider at 14 and 100 TeV, computed with the *Wbbj* code.

## 7 Gauge boson pair production<sup>20</sup>

### 7.1 ZZ production

All numerical results in this section and the next have been produced with the MATRIX code<sup>21</sup>. For the SM parameters we use  $m_W = 80.399$  GeV,  $m_Z = 91.1876$  GeV,  $\Gamma_W = 2.1054$  GeV,  $\Gamma_Z = 2.4952$  GeV and  $G_F = 1.6639 \cdot 10^{-5}$  GeV<sup>-2</sup>.

We start by considering the rapidity acceptance of  $ZZ \rightarrow e^+e^-\mu^+\mu^-$  production. We apply basic  $ZZ$  selection cuts of  $66 \text{ GeV} < m_{\ell\ell} < 116 \text{ GeV}$  on the invariant mass of oppositely charged leptons of the same flavour and consider two different  $p_T$  thresholds of 20 and 100 GeV on the leptons. Renormalization and factorization scales are set to the sum of transverse energies of the two  $Z$  bosons,  $\mu_R = \mu_F = \mu = E_T^{Z,1} + E_T^{Z,2}$ , with  $E_T^Z = \sqrt{m_Z^2 + (p_T^Z)^2}$ , and we use LO, NLO and NNLO MMHT2012 sets [9] at the LO, NLO and NNLO respectively. Table 24 shows the fiducial cross section corresponding to this setup at LO, NLO and NLO+gg, in which the finite and gauge invariant gluon-fusion contribution is included. For comparison, Table 24 also provides the inclusive cross section without any transverse-momentum cut at 100 TeV, for which we also provide the NNLO cross section. It can be seen that at 100 TeV the gluon-fusion contribution provides roughly 70% of the full NNLO correction, consistent with Ref. [264].

$\sqrt{s}$ (TeV)	$\sigma_{\text{LO}}$ (fb)	$\sigma_{\text{NLO}}$ (fb)	$\sigma_{\text{NLO+gg}}$ (fb)	$\sigma_{\text{NNLO}}$ (fb)
14 ( $p_T^\ell > 20$ GeV)	15.51	21.63	23.71	
100 (incl.)	284.7	361	430	460
100 ( $p_T^\ell > 20$ GeV)	181.8	230.2	269.2	
100 ( $p_T^\ell > 100$ GeV)	0.4778	0.888	1.514	

Table 24: Fiducial cross section for  $ZZ$  production at the LHC at LO, NLO and NLO+gg. Leptonic branching ratios included.

Figure 67 shows the rapidity acceptance  $\sigma(|\eta^\ell| < \eta_{\text{cut}})/\sigma$  for the final-state leptons as a function of the maximum rapidity cut. For a cut on the minimal lepton transverse momentum of 20 GeV, a rapidity cut with  $\eta_{\text{cut}} \approx 3$  removes around 50% of the total cross section. If the lepton transverse momentum cut is increased to 100 GeV, the leptons are forced to be more transverse, and a rapidity cut of  $\eta_{\text{cut}} \approx 2$  retains 50% of the cross section.

For comparison, Fig. 68 shows the rapidity acceptance at a center of mass energy of 14 TeV and a minimum lepton transverse momentum of 20 GeV. Compared to the situation at 100 TeV, the events are more central and a rapidity cut of  $\eta_{\text{cut}} \approx 3$  retains more than 70% of the cross section.

Figure 69 shows the acceptance as a function of the minimal lepton transverse momentum. The cross section is rapidly falling when increasing the transverse momentum requirements on the leptons, and a cut of 100 GeV leads to a reduction of the cross section of more than a factor of 200 when compared to the original cut of 20 GeV.

New physics at very high energies can be described by an effective field theory at lower energies, where heavy particles running in loops might modify the couplings between SM particles. The effective operators are suppressed by the scale of new physics, and are therefore most pronounced in the high-energy tails of distributions. Figure 70 shows the 4 lepton cross section above a minimal cut on the

<sup>20</sup>Editor: D. Rathlev

<sup>21</sup>MATRIX is the abbreviation of ‘‘MUNICH Automates qT subtraction and Resummation to Integrate Cross Sections’’, by M. Grazzini, S. Kallweit, D. Rathlev, M. Wiesemann. In preparation.

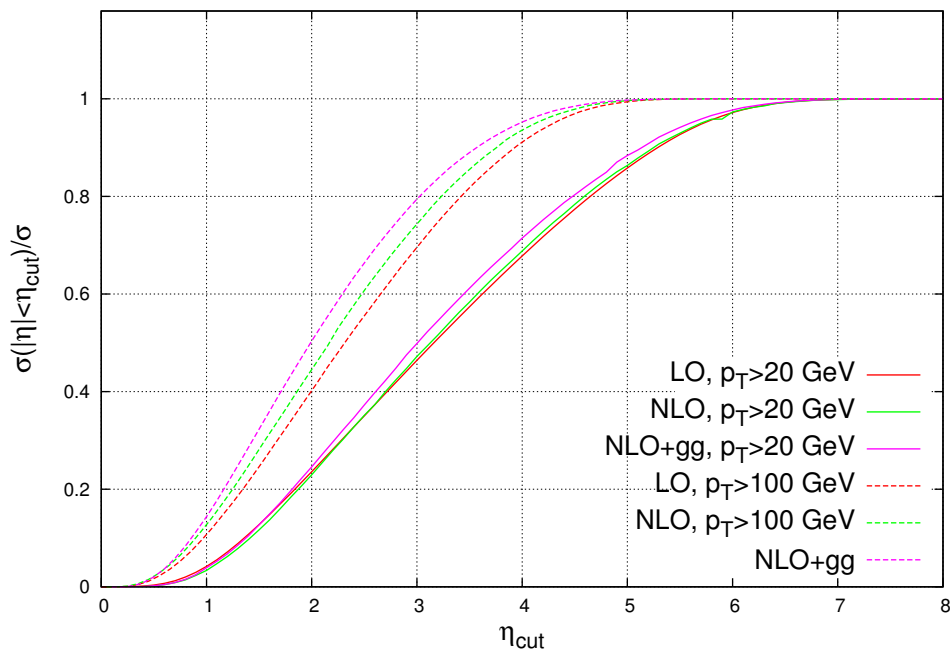


Fig. 67: Rapidity acceptance of 4 lepton production at 100 TeV as a function of the maximum lepton rapidity at LO (red), NLO (green) and NNLO (blue) with a  $p_T^\ell > 20$  GeV (solid) and a  $p_T^\ell > 100$  GeV cut (dashed).

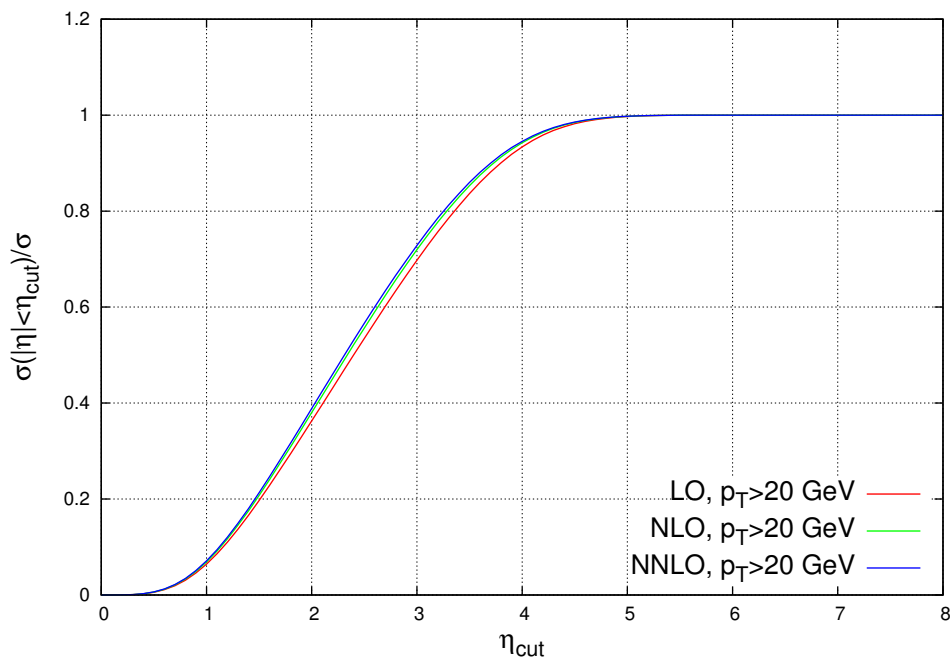


Fig. 68: Rapidity acceptance of 4 lepton production at 14 TeV as a function of the maximum lepton rapidity at LO, NLO and NNLO for  $p_T^\ell > 20$  GeV.

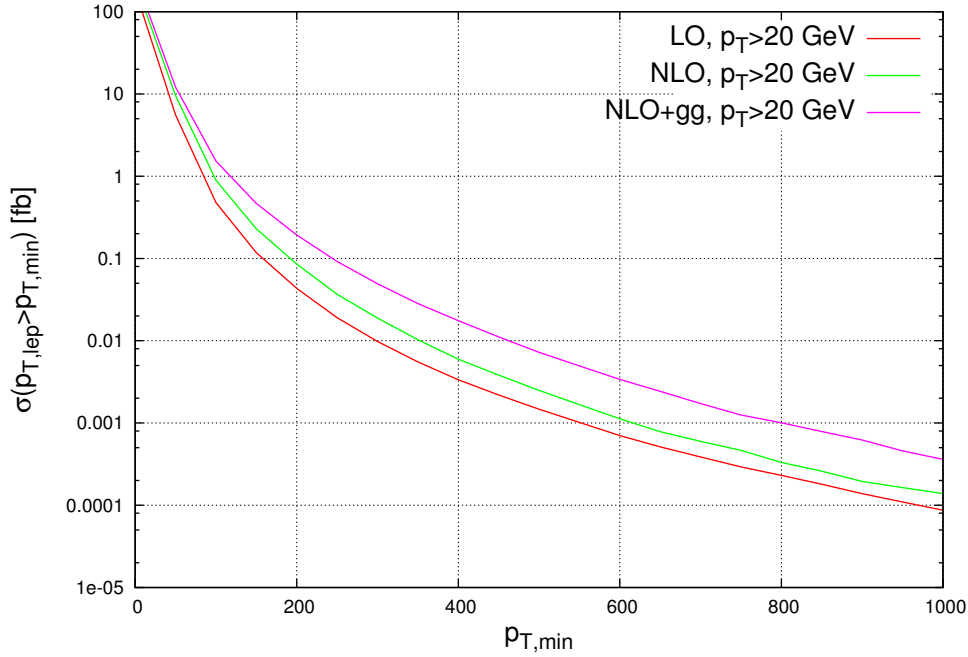


Fig. 69: 4 lepton production cross section at 100 TeV as a function of the minimum lepton transverse momentum at LO, NLO and NNLO.

invariant mass of the final-state system. Although it drops off rapidly, even at very high invariant masses of  $\sim 2$  TeV a cross section of around 1 fb remains.

## 7.2 WW production

### 7.2.1 Top-contamination issues

We now move to  $W^+W^-$  production. Compared to  $ZZ$  production,  $W^+W^-$  production comes with the additional complication that the inclusive cross section is not straight-forwardly defined in perturbation theory. The reason lies in the contamination by  $Wt$  and  $t\bar{t}$  production entering at NLO and NNLO, respectively, if the bottom-quark is considered massless [265]. Figure 71 shows diagrams contributing to the single-real correction to  $W^+W^-$  production. While the non-resonant diagrams (left) are part of the genuine QCD corrections, also resonant  $Wt$  diagrams appear in the same partonic channel. Resonant  $Wt$  production amounts to around 30% of the LO  $W^+W^-$  cross section. The problem is even more severe at NNLO, where diagrams as the one shown in Fig.72 start to contribute in the double-real emission correction. Besides QCD corrections to  $W^+W^-$  production (left), the same channel also contains diagrams from resonant  $t\bar{t}$  production, leading to an increase of the cross section of around 400%.

While the top-contamination only affects partonic channels involving b-quarks in the external states, these channels cannot straight-forwardly be neglected in the computation, as they are crucial to the cancellation of collinear divergences. However, they can be rendered IR finite by specifying a finite b-quark mass, i.e. by working in a 4-flavour scheme (4FS). In a 4FS, all partonic channels with external b-quarks and thus the top-contamination can be removed from the computation, resulting in a sensible definition of the  $W^+W^-$  cross section. This procedure leads to additional theoretical uncertainties on the level of 2% for LHC collider energies, which is well below the remaining scale dependence even at NNLO (see Ref. [265] for more details).

However, using a finite b-quark at a 100 TeV collider is much less justified, and one might worry about missing significant contributions from  $b\bar{b}$  initial states. To obtain a rough estimate of the size of these effects, one can compare the LO cross sections obtained in the 4FS and in the 5FS. We find that

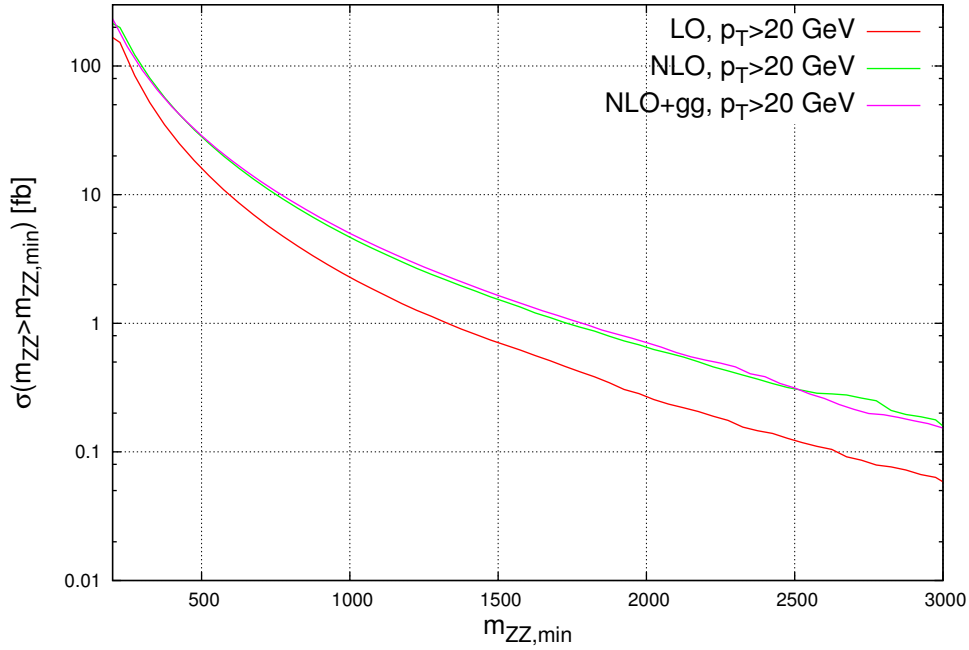


Fig. 70: 4 lepton production cross section at 100 TeV as a function of the minimum invariant mass of the final-state system at LO and NLO.

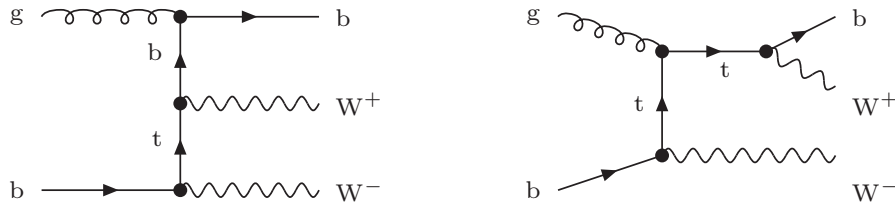
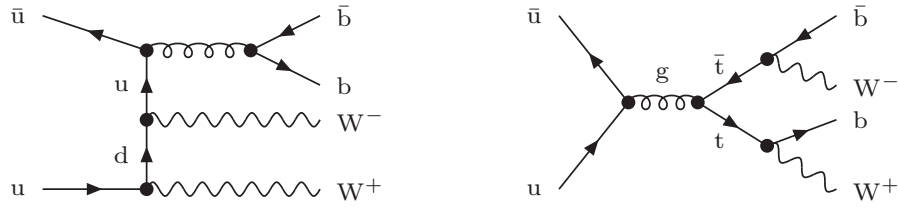


Fig. 71: Feynman diagrams contributing to the  $gb \rightarrow W^+W^-b$  subprocess.

with NNPDF3.0 sets, the difference is negligible at 14 TeV, and amounts to  $\sim -5\%$  at a 100 TeV proton-proton collider. We conclude that while the top-contamination problem cannot be considered solved at 100 TeV, a 4FS computation can be used to obtain a useful estimate of the cross sections for  $W^+W^-$  production at a future 100 TeV collider.

### 7.2.2 Predictions at 100 TeV

We apply a lower cut of 10 GeV on the invariant mass of the electron-muon pair and consider two different  $p_T$  thresholds of 20 and 100 GeV. In both setups we require a minimal missing transverse momentum equal to the lepton  $p_T$  threshold. Renormalization and factorization scales are set to the sum of transverse energies of the two  $W$  bosons,  $\mu = E_T^{W^+} + E_T^{W^-}$ , with  $E_T^{W^\pm} = \sqrt{m_W^2 + (p_T^{W^\pm})^2}$ . As the full NNLO calculation including the leptonic decay is not available yet, we limit the discussion to the NLO results. We do however include the gluon-fusion contribution. Table 25 shows the fiducial cross sections at 14 and 100 TeV. The scale uncertainties are on the level of  $\pm 15\%$  at LO and  $\pm 4\%$  at NLO. The PDF uncertainties are estimated to be  $\pm 7\%$  at LO and reduce to  $\pm 1\%$  at NLO. We note that there are huge NLO corrections when applying a strict transverse-momentum cut of 100 GeV. This is


 Fig. 72: Feynman diagrams contributing to the  $u\bar{u} \rightarrow W^+W^-b\bar{b}$  subprocess.

in contrast to the analogous results for  $ZZ$  production in Table 24. The difference is due to the fact that the missing transverse-momentum cut (instead of the cut on individual leptons as in the  $ZZ$  case) suppresses configurations with back-to-back neutrinos, and favors final states with a large total transverse momentum of the  $W^+W^-$  system. Non-vanishing  $W^+W^-$  transverse momenta only arise at the next-to-leading order.

$\sqrt{s}$ (TeV)	$\sigma_{\text{LO}}$ (fb)	$\sigma_{\text{NLO}}$ (fb)	$\sigma_{\text{NLO+gg}}$ (fb)	$\sigma_{\text{NNLO}}$ (fb)
14 ( $p_T^\ell > 20$ GeV)	509	759	805	
100 (incl.)	8162	12877	13992	15362
100 ( $p_T^\ell > 20$ GeV)	4685	8027	8738	
100 ( $p_T^\ell > 100$ GeV)	18.09	89.6	98.3	

 Table 25: Fiducial cross section for  $W^+W^-$  production at the LHC at LO, NLO and NLO+gg. Leptonic branching ratios included.

Figure 73 shows the rapidity acceptance  $\sigma(|\eta^\ell| < \eta_{\text{cut}})/\sigma$  for the final-state leptons as a function of the maximum rapidity cut. For a cut on the minimal lepton transverse momentum of 20 GeV, a rapidity cut with  $\eta_{\text{cut}} \approx 3$  removes around 45% of the total cross section. If the lepton transverse momentum cut is increased to 100 GeV, the leptons are forced to be more transverse, and a rapidity cut of  $\eta_{\text{cut}} \approx 2$  retains 50% of the cross section.

Figure 74 shows the cross section as a function of the minimal lepton transverse momentum. Transverse momentum cuts higher than  $\sim 150$  GeV cut away more than 99% of the fiducial cross section.

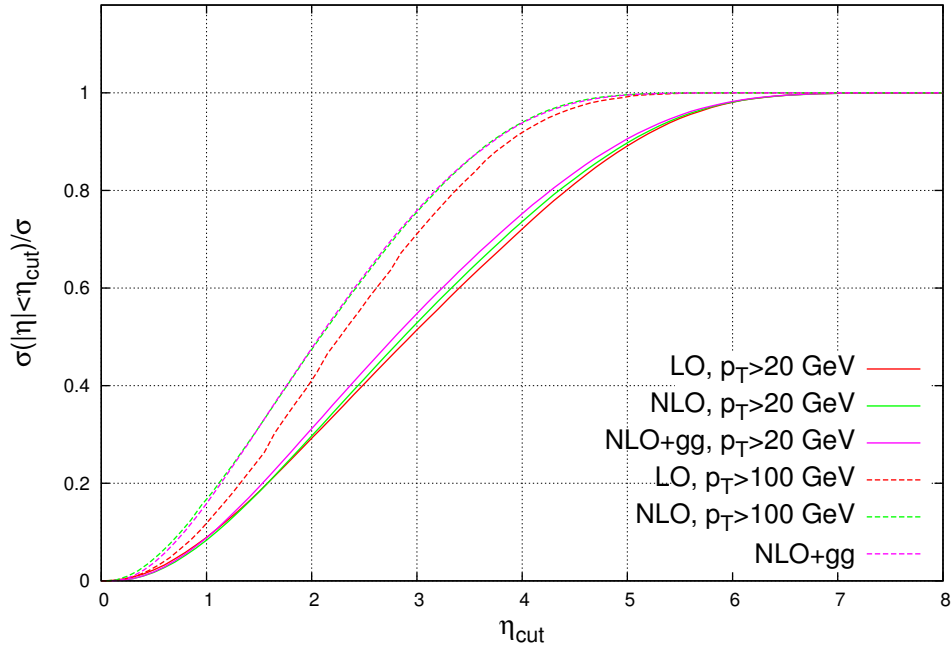


Fig. 73: Rapidity acceptance of  $W^+W^-$  production at 100 TeV as a function of the maximum lepton rapidity at LO (red) and NLO (green) with a  $p_T^\ell > 20$  GeV (solid) and a  $p_T^\ell > 100$  GeV cut (dashed).

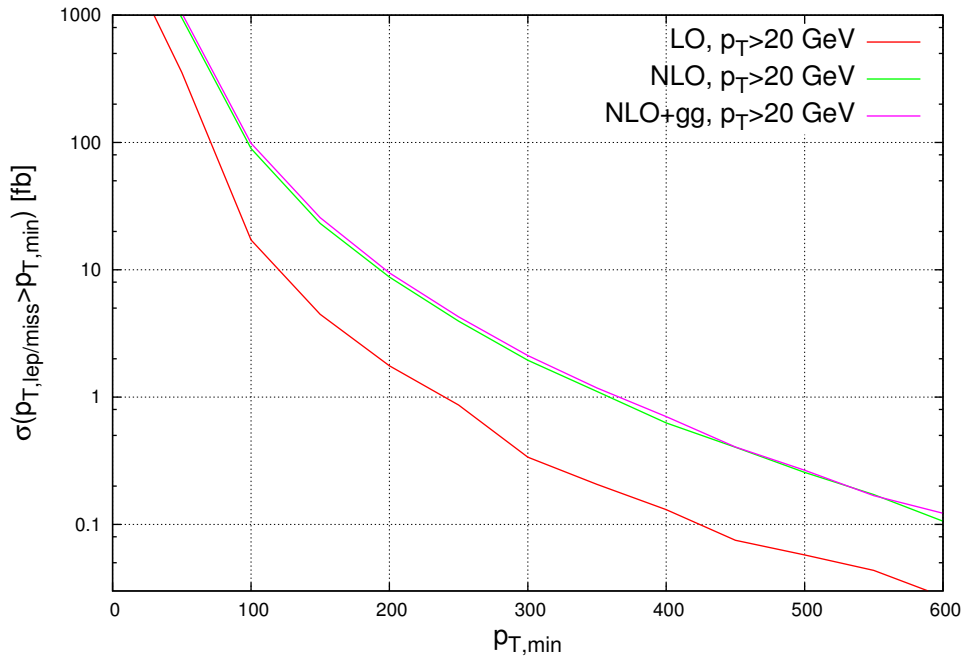


Fig. 74:  $W^+W^-$  cross section at 100 TeV as a function of the minimum lepton transverse momentum at LO and NLO.

### 7.3 $\gamma\gamma$ production

Diphoton production at hadronic colliders is a very relevant process, both from the point of view of testing the SM predictions [266–271] as for new physics searches. *Direct* or *prompt* photons provide an ideal test to QCD since they constitute a theoretically and experimentally clean final state: on the theory side, because they do not have QCD interactions with other final state particles; experimentally, because photon energies and momenta can be measured with high precision by modern detectors.

Besides purely QCD-related considerations, diphoton final states have played a crucial role in the recent discovery of the Higgs boson at the LHC [272, 273]. They are also important in many new physics scenarios [274, 275], in particular in the search for extra-dimensions [276] or supersymmetry [277]. And, recently [278, 279], an excess in the diphoton invariant mass spectrum was observed in searches for new physics in high mass diphoton events in  $pp$  collisions at 13 TeV.

We are interested in the process  $pp \rightarrow \gamma\gamma X$ . The lowest-order process ( $\mathcal{O}(\alpha_S^0)$ ) occurs via the quark annihilation subprocess  $q\bar{q} \rightarrow \gamma\gamma$ . The next-to-leading order (NLO) QCD corrections have been computed and implemented in the fully-differential Monte Carlo codes DIPHOX [280], 2gammaMC [281] and MCFM [237]. A calculation that includes the effects of transverse-momentum resummation is implemented in Resbos [282].

At next-to-next-to-leading order (NNLO), all the ( $\mathcal{O}(\alpha_S^2)$ ) contributions were put together in a complete and consistent calculation in the  $2\gamma$ NNLO code [283] for first time. The next-order gluonic corrections to the box contribution  $gg \rightarrow \gamma\gamma$  (which are part of the  $N^3$ LO QCD corrections to diphoton production) were also computed in ref. [281] and found to have a moderate quantitative effect.

The transverse momentum  $p_T$  spectrum of the diphoton pair has been calculated in fully-differential Monte Carlo codes at LO [237, 280–282] and at NLO [283–285]. Recently, first calculations for diphoton production in association with two [286–288] and three [288] jets at NLO became available. The transverse momentum resummation for diphoton production at NNLL + NNLO was recently presented in Ref. [289] and implemented in the  $2\gamma$ Res numerical code.

Besides direct photon production from the hard subprocess, photons can also be produced from the fragmentation of QCD partons. The computation of fragmentation subprocesses requires (the poorly known) non-perturbative information, in the form of parton fragmentation functions of the photon (the complete single- and double-fragmentation contributions are implemented in DIPHOX [280] for diphoton production at the first order in  $\alpha_S$ ). However, the effect of the fragmentation contributions is sizeably reduced by the photon isolation criteria that are necessarily applied in hadron collider experiments to suppress the very large irreducible background (*e.g.*, photons that are faked by jets or produced by hadron decays). Two such criteria are the so-called “standard” cone isolation and the “smooth” cone isolation proposed by Frixione [290]. The standard cone isolation is easily implemented in experiments, but it only suppresses a fraction of the fragmentation contribution. By contrast, the smooth cone isolation (formally) eliminates the entire fragmentation contribution. All the results presented in this section were obtained with the smooth isolation prescription, which, for the parameters used in the experimental analysis reproduces the standard result within a 1% accuracy [291] at NLO.

In this section we present some benchmark results on diphoton production at  $\sqrt{s} = 100$  TeV, of possible relevance to Higgs boson studies as well as to BSM searches. We compute the NLO and NNLO QCD radiative corrections at the fully-differential level. In all the NLO results presented in this section we consider also the box contribution at the lowest order in the strong coupling constant ( $\mathcal{O}(\alpha_S^2)$ ).

The acceptance criteria used in the numerical results presented in this section are the following:  $p_T^\gamma \geq 30$  GeV and the rapidity of both photons has to satisfy  $|y_\gamma| < 2.5$ . We use the MSTW2008 [292] sets of parton distributions, with densities and  $\alpha_S$  evaluated at each corresponding order (*i.e.*, we use  $(n+1)$ -loop  $\alpha_S$  at  $N^n$ LO, with  $n = 0, 1, 2$ ), and we consider  $N_f = 5$  massless quarks/antiquarks and gluons in the initial state. The default renormalization ( $\mu_R$ ) and factorization ( $\mu_F$ ) scales are set to the value  $\mu_R = \mu_F = \sqrt{M_{\gamma\gamma}^2 + p_{T\gamma\gamma}^2}$ . The QED coupling constant  $\alpha$  is fixed to  $\alpha = 1/137$ .

The smooth cone isolation prescription is as follows: we consider a cone of radius  $r = \sqrt{(\Delta\eta)^2 + (\Delta\phi)^2}$  around each photon and we require that the total amount of hadronic (partonic) transverse energy  $E_T$  inside the cone is smaller than  $E_{T\max}(r)$ ,

$$E_{T\max}(r) \equiv \epsilon_\gamma p_T^\gamma \left( \frac{1 - \cos r}{1 - \cos R} \right)^n, \quad (26)$$

where  $p_T^\gamma$  is the photon transverse momentum; the isolation criterion  $E_T < E_{T\max}(r)$  has to be fulfilled for all cones with  $r \leq R$ . The isolation parameters are set to the values  $\epsilon_\gamma = 0.05$ ,  $n = 1$  and  $R = 0.4$  in all the numerical results presented in this section. In Ref. [291] it was shown that implementing  $\epsilon_\gamma = 0.05$  the effects of the fragmentation contribution are under control, in the sense that the NLO cross section obtained with the smooth cone isolation criterion coincides with the corresponding NLO cross section obtained with the standard cone isolation criterion at the percent level.

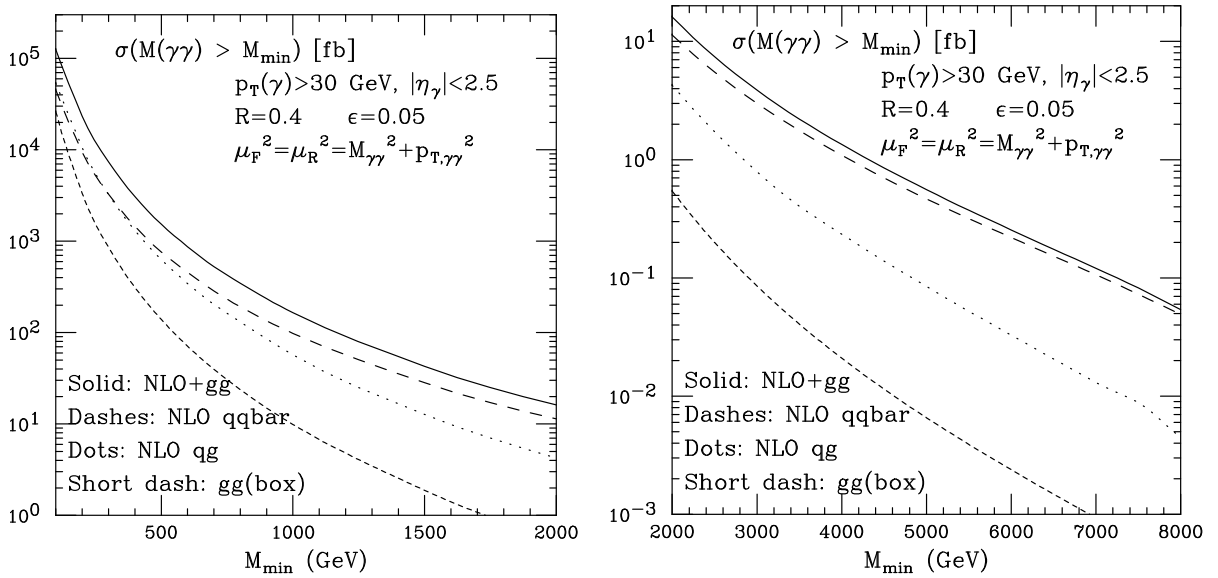


Fig. 75: Integrated diphoton invariant mass distribution, over different mass ranges. We display the full NLO cross-section, inclusive of the box contribution at the lowest order ( $\mathcal{O}(\alpha_S^2)$ ), with the different partonic channels present at this perturbative level.

In Fig. 75 we present our results for the integrated invariant mass distribution. While for low values of  $M_{\gamma\gamma}$  the box contribution (formally  $\mathcal{O}(\alpha_S^2)$ ) is of the same order of the LO  $q\bar{q}$  contribution ( $\mathcal{O}(\alpha_S^0)$ ), for large values of the invariant mass, the LO cross section is at least one order larger than the box contribution. Moreover, notice that for large values of the lower cut in the diphoton invariant mass ( $M_{\gamma\gamma}^{\min} > 400$  GeV), the contribution to the cross section due to partonic channels containing at least a gluon (in the initial state) is negligible with respect to the  $q\bar{q}$  channel. This is mostly due to the greater impact of the isolation cut, which affects directly processes like  $qg \rightarrow qg\gamma\gamma$ , where, to have a large  $M_{\gamma\gamma}$ , one of the two photons is preferentially radiated by the final state quark.

We note that the cross-section is of the order of a several tens of ab for  $M_{\gamma\gamma} \gtrsim 8$  TeV, meaning of order 1000 events for the expected integrated luminosity (20-30  $\text{ab}^{-1}$ ).

In Fig. 76 we show the integrated diphoton transverse momentum distribution requiring  $|M_H - M_{\gamma\gamma}| < 4$  GeV ( $M_H = 125$  GeV). The restriction of the diphoton invariant mass to this interval is kept in all plots of interest for Higgs physics. The notation NLO vs NNLO refers here to the order at which the inclusive  $\gamma\gamma + X$  process is evaluated, namely  $\mathcal{O}(\alpha_S)$  and  $\mathcal{O}(\alpha_S^2)$ , respectively. In this language, NLO is actually the first order at which the photon pair develops a transverse momentum, and NNLO is

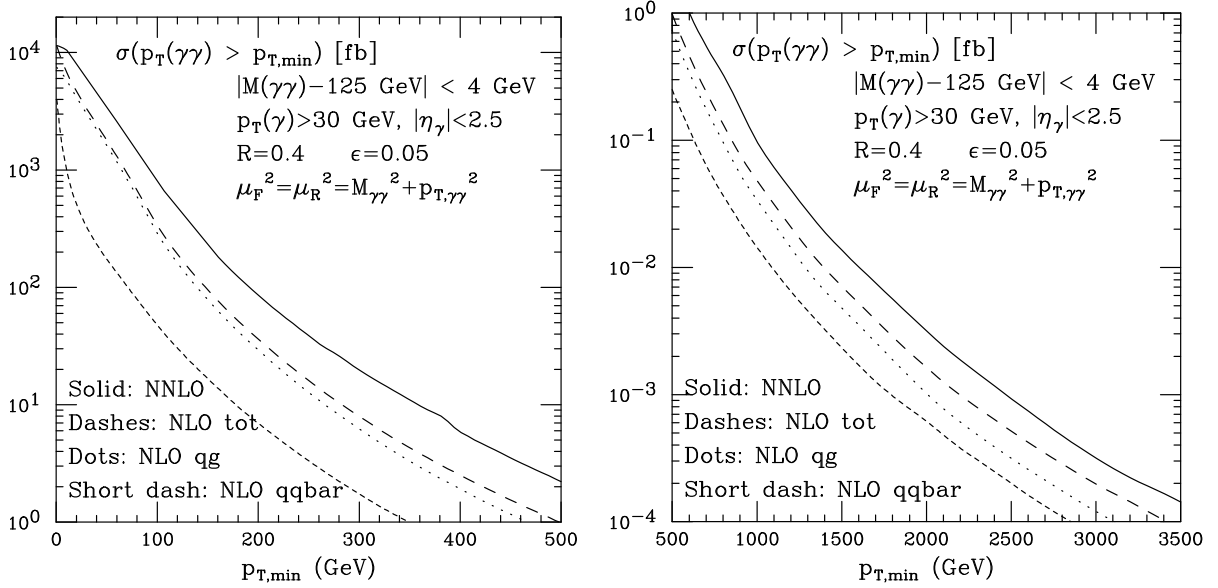


Fig. 76: Integrated diphoton transverse momentum distribution, subject to the constraint  $|M_H - M_{\gamma\gamma}| < 4$  GeV ( $M_H = 125$  GeV). We compare the NNLO and the NLO cross-sections, and the relative contributions of the  $qg$  and  $q\bar{q}$  processes at NLO.

the first genuine radiative correction to the  $p_T$  distribution. Notice that at  $O(\alpha_S^2)$  the  $gg$  box contribution does not generate a transverse momentum for the diphoton pair, this will only arise at  $O(\alpha_S^3)$ . The tree-level  $gg$  contributions of  $O(\alpha_S^2)$  are small and, while they are included in the NNLO, they are not shown separately in the plot.

In the left panel we compare the NNLO contribution with the NLO cross-section. We are not considering here transverse momentum resummation (as implemented in  $2\gamma\text{Res}$  or  $\text{Resbos}$ ), since the  $p_T$  range of interest in these plots is well above the values where Sudakov effects are relevant.

While for the integrated invariant mass distribution (Fig. 75) the  $q\bar{q}$  partonic channel dominates the cross section, in the diphoton integrated transverse momentum distribution the  $q\bar{q}$  and  $qg$  channels are at the same order over the whole transverse momentum range. It is easy to see that the invariant mass cut on the diphoton pair forces the two photons to be close to each other, and thus the  $qg$  initial state process does not need to be penalized by the isolation requirement which suppresses this channel in the large-mass spectrum.

In Fig. 77 we show the  $K$  factors for the diphoton mass and  $p_T$  spectra, calculated for Fig. 75 and Fig. 76.

We observe that the NLO contributions introduce very large corrections to the cross-section mainly for low and moderate values of the invariant mass distribution  $M_{\gamma\gamma}^{\min} < 1$  TeV. At high mass the  $K$  factors (NLO+box)/LO or (NLO)/LO tend to 1.4 (at  $\sqrt{s} = 14$  TeV,  $K=\text{NNLO}/\text{NLO} \simeq 1.2$  for  $M_{\gamma\gamma}^{\min} \simeq 3$  TeV). Likewise the  $K$  factor of the diphoton  $p_T$  spectrum tends to be larger than 2 up to  $p_T \sim 400$  GeV, and to diminish after that.

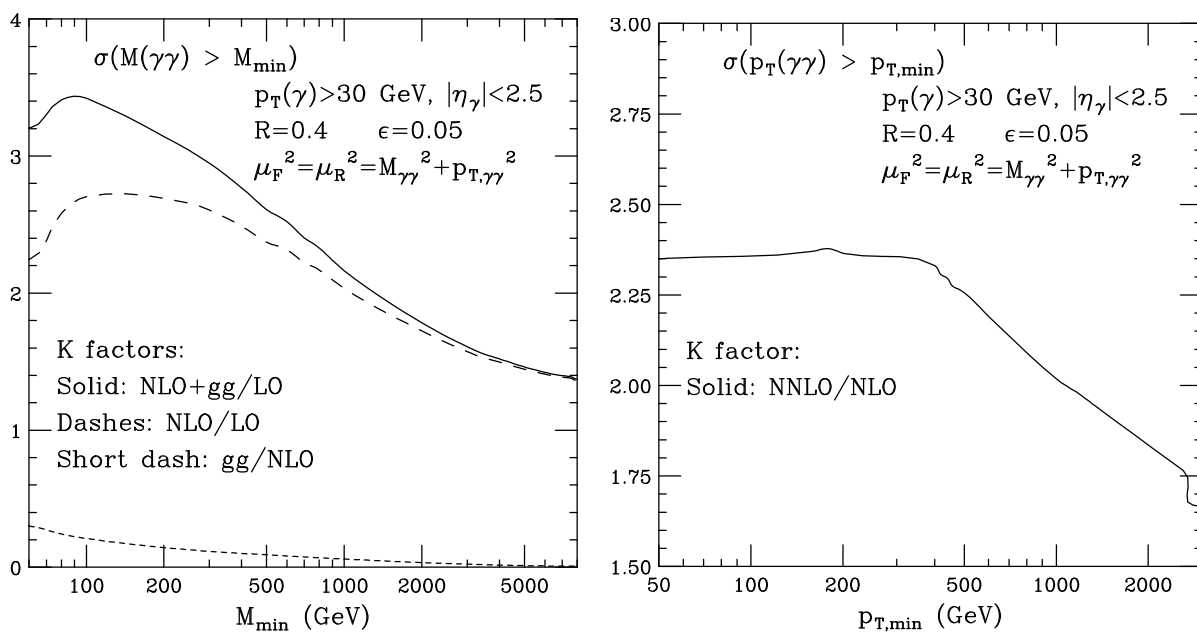


Fig. 77: Left panel: K factors for the diphoton invariant mass distribution from Fig. 75. Right panel: K factors for the diphoton  $p_T$  distribution from Fig. 76.

#### 7.4 Anomalous couplings from $WW$ and $W\gamma$ production

In this section we explore the potential of the FCC to constraint or measure anomalous triple-gauge couplings. As an example, we consider  $W^+W^-$  with  $W$  bosons decaying into electrons or muons and  $W^+\gamma$  production with  $W^+$  decaying into a positron and a neutrino.

We consider an extension of the SM Lagrangian which includes up to dimension six operators

$$\mathcal{L} = \mathcal{L}_{\text{SM}} + \sum_i \frac{c_i}{\Lambda^2} \mathcal{O}_i + \dots \quad (27)$$

In particular, we consider the effect of the following, CP-conserving, dimension six operators [293]

$$\begin{aligned} \mathcal{O}_{WWW} &= \text{Tr}[W_{\mu\nu} W^{\nu\rho} W_\rho^\mu], \\ \mathcal{O}_W &= (D_\mu \Phi)^\dagger W^{\mu\nu} (D_\nu \Phi), \\ \mathcal{O}_B &= (D_\mu \Phi)^\dagger B^{\mu\nu} (D_\nu \Phi), \end{aligned} \quad (28)$$

with  $\Phi$  being the Higgs doublet field and

$$\begin{aligned} D_\mu &= \partial_\mu + \frac{i}{2} g \tau^I W_\mu^I + \frac{i}{2} g' B_\mu, \\ W_{\mu\nu} &= \frac{i}{2} g \tau^I (\partial_\mu W_\nu^I - \partial_\nu W_\mu^I + g \epsilon_{IJK} W_\mu^J W_\nu^K), \\ B_{\mu\nu} &= \frac{i}{2} g' (\partial_\mu B_\nu - \partial_\nu B_\mu). \end{aligned} \quad (29)$$

We remark that since the higher dimensional operators can be seen as low energy remnants of some new heavy degrees of freedom integrated out at scale  $\Lambda$ , we are implicitly assuming the scale of new physics  $\Lambda$  to be larger than the energy range we are probing.

The effect of these operators can also be equivalently expressed in terms of anomalous couplings. The corresponding modification of the SM Lagrangian is written as

$$\begin{aligned} \mathcal{L}_{TGC} &= i g_{WWV} (g_1^V (W_{\mu\nu}^+ W^{-\nu} - W^{+\mu} W_{\mu\nu}^-) V_\nu + \kappa_V W_\mu^+ W_\nu^- V^{\mu\nu} + \\ &\quad \frac{\lambda_V}{m_W^2} W_\mu^{+\nu} W_\nu^{-\rho} V_\rho^\mu), \end{aligned} \quad (30)$$

where  $V = \gamma, Z$ ,  $W_{\mu\nu}^\pm = \partial_\mu W_\nu^\pm - \partial_\nu W_\mu^\pm$ ,  $V_{\mu\nu}^\pm = \partial_\mu V_\nu - \partial_\nu V_\mu$ ,  $g_{WW\gamma} = -e$  and  $g_{WWZ} = -e \cot \theta_w$ . At tree level the anomalous couplings can be related to the coefficients of the dimension six operators via the following relations

$$\begin{aligned} g_1^Z &= 1 + c_w \frac{m_Z^2}{2\Lambda^2}, \\ \kappa_\gamma &= 1 + (c_w + c_b) \frac{m_W^2}{2\Lambda^2}, \\ \kappa_Z &= 1 + (c_w - c_b \tan^2 \theta_W) \frac{m_W^2}{2\Lambda^2}, \\ \lambda_\gamma &= \lambda_Z = c_{\text{www}} \frac{3g^2 m_W^2}{2\Lambda^2}. \end{aligned} \quad (31)$$

For  $W^+W^-$ , we consider predictions at Les Houches event level obtained with the POWHEG  $WW$  code [294, 295]. In this way NLO corrections are included together with Sudakov effects associated with the hardest radiation, but the effects of the subsequent parton shower, hadronization, or underlying event corrections are not included. We remark that we do not include here loop-induced gluon-gluon channels. We consider the following minimal set of cuts on the charged leptons  $p_{t,l} > 20$  GeV,  $|\eta_l| < 2.5$ , and a cut of 20 GeV on the missing transverse momentum. Jets are reconstructed using the anti- $k_t$  algorithm [203]

with  $R = 0.6$ . Furthermore, in order to reduce the top background, we veto events where the invariant mass of any charged lepton combined with any jet is below 200 GeV. We have verified that, in the distributions that we have considered, lowering this cut does not lead to significant changes, and that the top contribution is negligible.

For  $W^+\gamma$ , when NLO QCD corrections are taken into account, real gluon induced diagrams arise. For these contributions we need a strategy for the treatment of photon fragmentation contribution, namely the infrared divergent configurations where the photon becomes soft or collinear to the emitting quark. Since in the POWHEG BOX approach [296] for the treatment of photon fragmentation contribution there are two underlying Born configurations at LHE level,  $W^+\gamma$  and  $W^+j$ , the analysis at event level would be highly inefficient because of the  $W^+j$  contribution which would largely dominate. Therefore we consider predictions at NLO accuracy with smooth isolation prescription [290] applied at generation stage. In our analysis following cuts are applied:  $p_T^l > 20$  GeV,  $|\eta_i| < 2.5$  with  $i = e^+, \gamma$  and  $\Delta R_{l\gamma} > 0.7$ . Moreover, in order to improve the efficiency, since we are interested in the  $p_{t,\gamma}$  distribution only, we have put a generation cut at 100 GeV, after checking that the effect of the cut is negligible in the high  $p_t$  region.

All the results have been obtained using NNPDF30\_nlo\_as\_0118 [7]. In order to understand the sensitivity to the different operators we turn on the coefficient of one operator at a time. We examined several observables and find that, as well-known, the sensitivity to dimension six operators appears in the region of large transverse momenta or invariant masses. As an example, we consider the invariant mass  $m_{ll}$  of the dilepton pair for  $W^+W^-$  and the photon's transverse momentum for  $W^+\gamma$ .

Our results, presented in Fig. 78 for  $W^+\gamma$  and in Figs. 79, 80 (left) for  $W^+W^-$  are shown in terms of integrated rates. In particular, in the upper panels, we show the number of events assuming  $10 \text{ ab}^{-1}$  of integrated luminosity for different values of the coefficients of the operators. In the lower panels we quantify the significance of the excess by showing the ratio of the number of events in excess of the SM prediction divided by the squared-root of the number of events predicted in the SM,  $(N_C - N_{SM})/\sqrt{N_{SM}}$ . Under the assumption that SM backgrounds can be measured and predicted precisely, the above quantity gives a rough indication of the significance that can be reached with an integrated luminosity of  $10 \text{ ab}^{-1}$ . The two horizontal lines in the lower panels indicate the  $3\sigma$  and  $5\sigma$  significance. For each operator, we show the distributions corresponding to three choices of the coefficients of the operators, that envelope the  $3\sigma$  and  $5\sigma$  lines. For  $W^+W^-$  the maximal sensitivity has a peak for given values of  $m_{ll}$ . This corresponds to a value where the departure from the SM predictions are big enough, but the statistics remains significant. This is not the case for  $W^+\gamma$  distributions when we consider the departures from the SM prediction due to  $\mathcal{O}_W + \mathcal{O}_B$ . In this case the positive effect due to the presence of the anomalous coupling  $\kappa_\gamma$  is not sufficient to compensate the drop in the number of events in the distributions' tails. Therefore the sensitivity does not peak in the region of large transverse momenta. We also remark that, in order to achieve a significance around  $5\sigma$  for the  $W^+\gamma$  process, we have taken values of  $c_w$  and  $c_b$  which are roughly two orders of magnitude higher with respect to the  $W^+W^-$  case. In other words, the  $W^+W^-$  process is more effective in constraining the coefficients  $c_w$  and/or  $c_b$  than the  $W^+\gamma$  process.

We see that, compared to current bounds from 8 TeV LHC [297, 298], bounds improve by more than two orders of magnitude.

For  $W^+W^-$  production, the right plot in Fig. 80 shows the value of the scale  $\Lambda$  such that we enter the strong coupling regime, according to the rules of dimensional analysis given in Ref. [299]. Looking for example at the  $c_{ww}/\Lambda^2 = 0.04 \text{ TeV}^{-2}$  case, we see that the non perturbative region is at scales of several tens of TeV, where our optimal region for the determination of the anomalous couplings is below 10 TeV. The situation is somewhat worse for the  $c_W/\Lambda^2 = 0.08$  and especially for the  $c_b/\Lambda^2 = 0.2$  cases, where the non-perturbative region is reached near 10 TeV, and the optimal scale for the determination of the anomalous couplings is near 8 TeV.

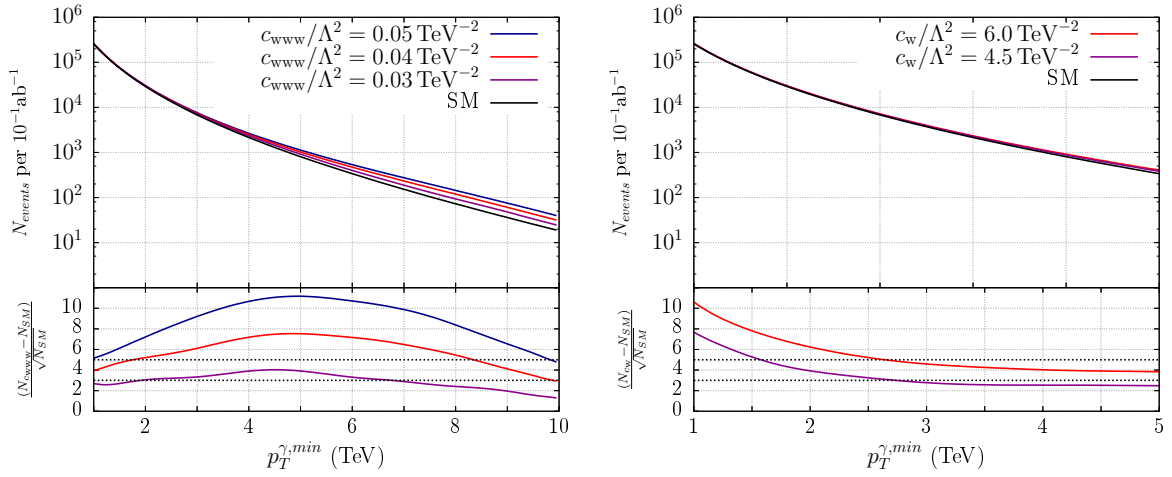


Fig. 78: Upper panels: number of events with  $p_{t,\gamma} > p_{t,\gamma}^{\text{min}}$  in the SM and for various values of  $c_{www}$  (left) and  $c_w$  (right) for an accumulated luminosity of  $10 \text{ ab}^{-1}$  (the effect of  $c_b$  is the same of  $c_w$ ). Lower panels: significance computed as  $(N_{c_i} - N_{SM})/\sqrt{N_{SM}}$ .

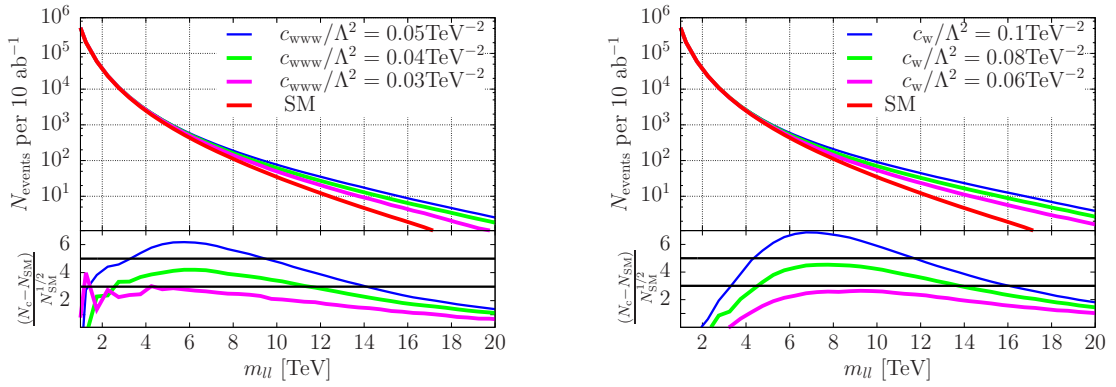


Fig. 79: Upper panels: number of events with  $m_{ll} > m_{ll}^{\text{min}}$  in the SM and for various values of  $c_{www}$  (left) and  $c_w$  (right) for an accumulated luminosity of  $10 \text{ ab}^{-1}$ . Lower panels: significance computed as  $(N_{c_i} - N_{SM})/\sqrt{N_{SM}}$ .

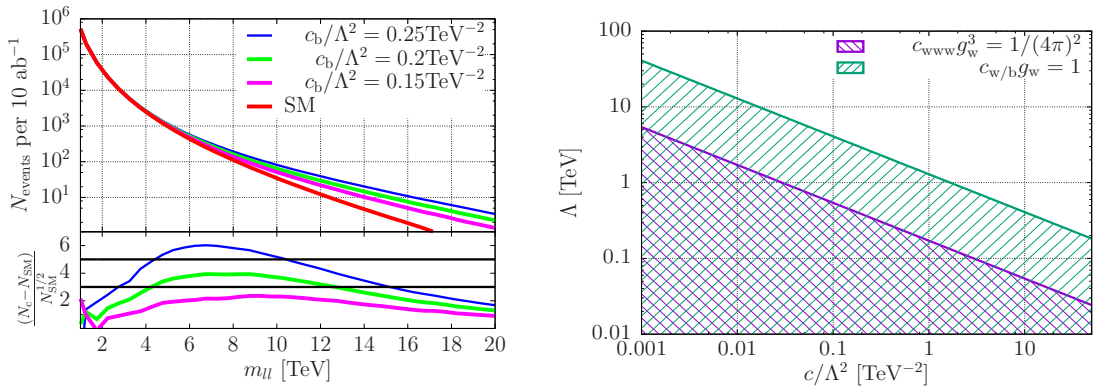


Fig. 80: Left: same as Fig. 79 for  $c_b$ . Right: the perturbative region (hatched regions) in the  $c/\Lambda^2 - \Lambda$  plane.

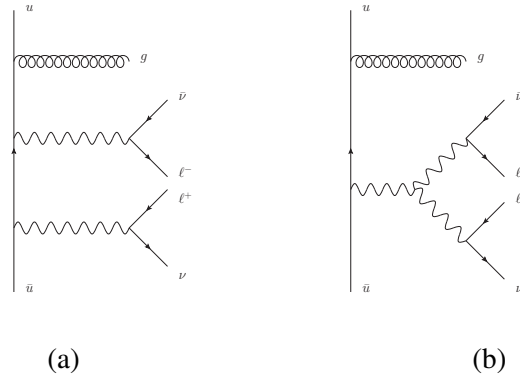


Fig. 81: Sample diagrams entering the calculation of the leading order amplitude for the  $WW$ +jet process, corresponding to (a)  $W$  emission from the quark line and (b) emission from an intermediate  $Z$  boson or photon.

## 7.5 $VV$ +jet production

### 7.5.1 Overview

We here consider the hadronic production of  $W$  pairs in association with a single jet at next-to-leading order (NLO) in QCD at a proton collider with a center-of-mass energy of 100 TeV. The  $W$  bosons decay leptonically, with all spin correlations included. At tree level this process corresponds to the partonic reaction,

$$\begin{aligned}
 q + \bar{q} &\rightarrow W^+ + W^- + g \\
 &\quad \left\{ \begin{array}{l} \rightarrow \mu^- + \nu_\mu \\ \rightarrow \nu_e + e^+ \end{array} \right. \quad (32)
 \end{aligned}$$

with all possible crossings of the partons between initial and final states. Tree level diagrams for this process are shown in Fig. 81.

At next-to-leading order we must include the emission of an additional parton, either as a virtual particle to form a loop amplitude, or as a real external particle. Sample diagrams for virtual NLO contributions are shown in Fig. 82; in addition, one-loop corrections to Fig. 81 (b) must be included. All results presented in the following have been obtained using the calculation of Ref. [300]<sup>22</sup>, where virtual corrections have been obtained using generalized unitarity methods [302–307]. The combination of the virtual contributions with born and real emission diagrams has implemented into MCFM [236, 238]. Note that we do not include the effects of any third-generation quarks, either as external particles or in internal loops.

### 7.5.2 Total cross sections

The results presented in this section have been obtained using the parameters shown in Table 26. In calculations of LO quantities we employ the CTEQ6L1 PDF set [308], while at NLO we use CT10 [309]. The renormalization and factorization scales are usually chosen to be the same,  $\mu_R = \mu_F = \mu$ , with our default scale choice  $\mu = \mu_0$  given by,

$$\mu_0 \equiv \frac{H_T}{2} = \frac{1}{2} \sum_i p_\perp^i. \quad (33)$$

<sup>22</sup>See also [301].

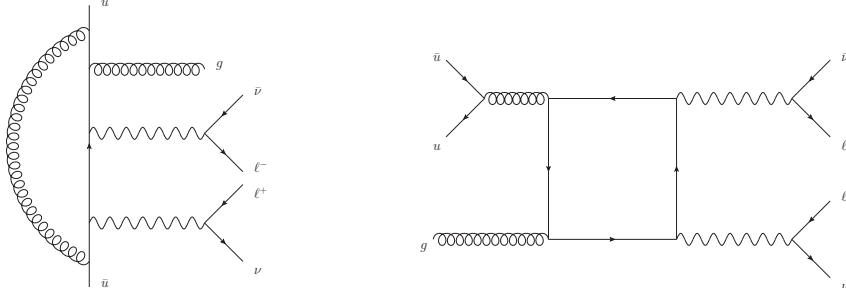


Fig. 82: Sample diagrams entering the calculation of the one-loop amplitude for the  $WW$ +jet process. The one-loop diagrams can be categorized according to whether a gluon dresses a leading-order amplitude (left), or whether the diagram includes a closed fermion loop (right).

$m_W$	80.385 GeV	$\Gamma_W$	2.085 GeV
$m_Z$	91.1876 GeV	$\Gamma_Z$	2.4952 GeV
$e^2$	0.095032	$g_W^2$	0.42635
$\sin^2 \theta_W$	0.22290	$G_F$	$0.116638 \times 10^{-4} \text{ GeV}^{-2}$

Table 26: The values of the mass, width and electroweak parameters used to produce the results in this subsection.

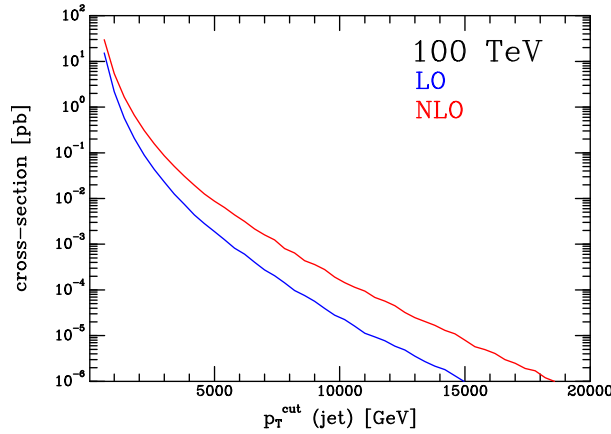


Fig. 83: Cross-sections at 100 TeV, as a function of the transverse momentum cut on the jet.

The sum over the index  $i$  runs over all final state leptons and partons. Jets are defined using the anti- $k_T$  algorithm with separation parameter  $R = 0.5$  and must satisfy,

$$p_{\perp}^{\text{jet}} > p_{\perp, \text{cut}}^{\text{jet}}, \quad |\eta^{\text{jet}}| < 4.5. \quad (34)$$

The cross-sections predicted at LO and NLO are shown in Fig. 83, as a function of  $p_{\perp, \text{cut}}^{\text{jet}}$  and for values as large as 20 TeV. The cross-sections at NLO are significantly larger than those at LO, by as much as an order of magnitude at 10 TeV and beyond.

As useful operating points, we use  $p_{\perp, \text{cut}}^{\text{jet}} = 25 \text{ GeV}$  and also choose to study the additional case  $p_{\perp, \text{cut}}^{\text{jet}} = 300 \text{ GeV}$ , which we will label 100 TeV\* in the following. The cross-sections for  $WW$ +jet production, together with the corresponding values for the 14 TeV LHC and under the basic jet cuts of

$\sqrt{s}$	$p_{\perp, \text{cut}}^{\text{jet}}$	$\sigma_{LO}$ [pb]	$\sigma_{NLO}$ [pb]
14 TeV	25 GeV	$39.5^{+11.7\%}_{-11.0\%}$	$48.6^{+3.8\%}_{-4.0\%}$
100 TeV	25 GeV	$648^{+22.3\%}_{-19.3\%}$	$740^{+4.5\%}_{-9.3\%}$
100 TeV	300 GeV	$30.3^{+11.22\%}_{-10.56\%}$	$53.7^{+8.0\%}_{-7.6\%}$

Table 27: Cross-sections for the process  $pp \rightarrow WW + \text{jet}$  at proton-proton colliders of various energies, together with estimates of the theoretical uncertainty from scale variation as described in the text. Monte Carlo uncertainties are at most a single unit in the last digit shown in the table.

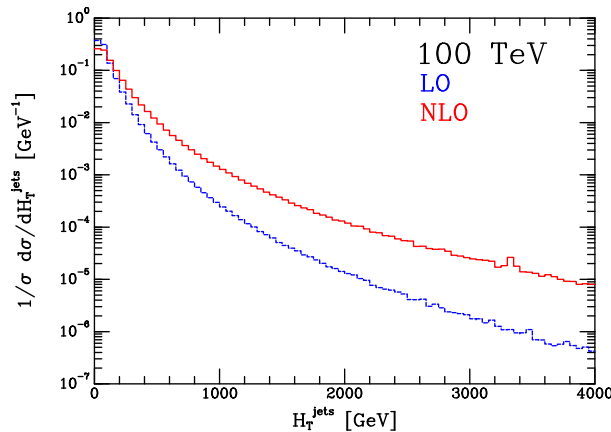


Fig. 84: The distribution of the observable  $H_T^{\text{jets}} = \sum_{\text{jets}} p_{\perp}^{\text{jet}}$  at LO and NLO.

Eq. (34), are collated in Table 27<sup>23</sup>. Note that the effect of the decays of the  $W$  bosons is not included. At the 100 TeV machine, the jet cut of 300 GeV has been chosen so that the cross section is similar in size to the 14 TeV cross section, as can be seen from Table 27. This cut provides a useful benchmark in a different kinematic regime that may be more appropriate at that collider energy.

An interesting feature of the higher order corrections to processes such as the one at hand is the existence of so-called ‘‘giant K-factors’’ [205, 310, 311]. An observable that exemplifies this effect is  $H_T^{\text{jets}}$ , which is defined to be the scalar sum of all jet transverse momenta in a given event. At NLO, real radiation contributions arise in which two hard partons are produced approximately back-to-back, with the  $W^+W^-$  system relatively soft. Such configurations are not captured at all by the LO calculations, in which the parton and  $W^+W^-$  system are necessarily balanced in the transverse plane. This results in the by now well-known feature of huge NLO corrections at large  $H_T^{\text{jets}}$ , as shown in Fig. 84.

We see that the NLO predictions are at least an order of magnitude larger than their LO counterparts in the tails of the distributions<sup>24</sup>. This onset occurs well before the interesting multi-TeV region.

Another interesting topic to investigate is the *total* number of events for selection cuts, i.e.

$$\sigma_{\text{tot}}(\text{cut}) = \int d\sigma \Theta(\text{cut}), \quad (35)$$

where the cuts for dimensionful quantities can reach  $\mathcal{O}(\text{TeV})$ . Figure 85 displays similar distributions

<sup>23</sup>Note that there is a minor typographical error in Ref. [300] in the relative uncertainty due to scale variations for the LO cross section at 100 TeV, which we have corrected here.

<sup>24</sup>This effect also appears at a 14 TeV LHC, cfr. e.g. [301].

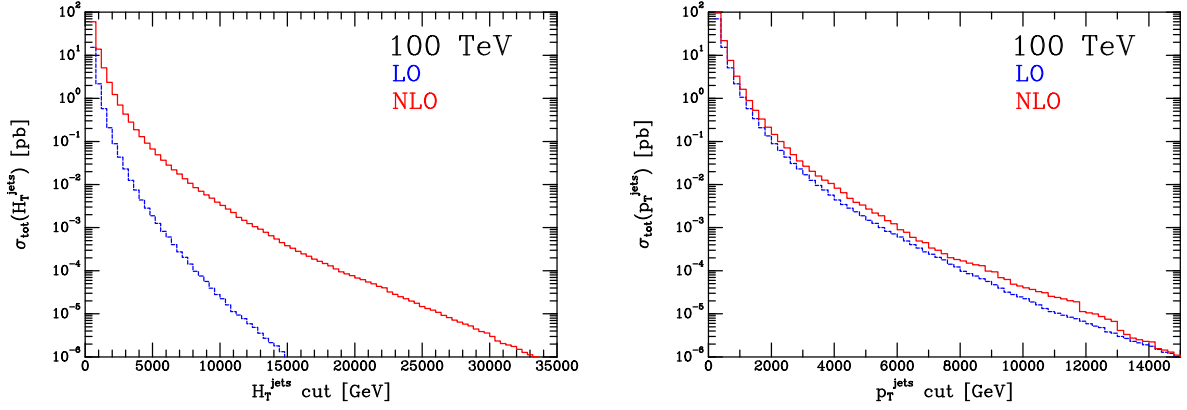


Fig. 85: Total integrated cross sections (cf. Eq. (35)) at LO and NLO, for the quantity  $H_T^{\text{jets}} = \sum_{\text{jets}} p_{\perp}^{\text{jet}}$  (left) and  $|p_T^{WW}| \equiv |p_T^{\text{jets}}|$ , the transverse momentum of the *complete* jet system (right), with  $p_{\perp}^{\text{cut}} = 25$  GeV in both cases.

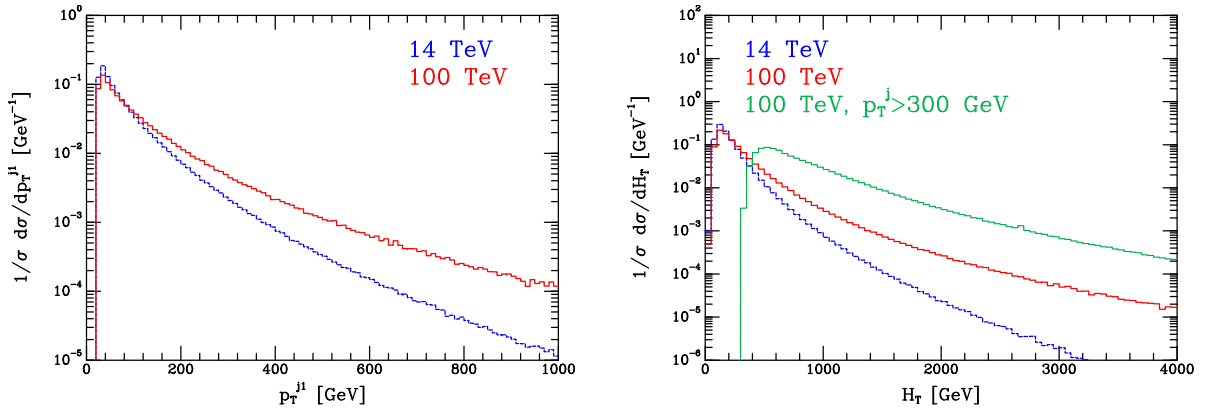


Fig. 86: NLO  $p_{\perp,j}$  (left) and  $H_T$  (right) distributions, normalized by the respective total cross sections, for 14 TeV (red), 100 TeV (blue), and 100 TeV\* (green)

for the quantities  $H_{T,\text{jets}}$  and  $p_T^{WW}$ .

### 7.5.3 Differential distributions

To illustrate some of the key differences between the predictions for  $WW$ +jet production at the two collider energies, we now examine NLO predictions for a number of kinematic distributions. For this study we consider leptonic decays of the  $W^+$  and  $W^-$  bosons, but do not apply any cuts on the decay products. We also show the respective distributions at the 14 TeV LHC for comparison. Fig. 86 shows two quantities that characterize the overall nature of this process, the transverse momentum of the leading jet and the scalar sum of all jet and lepton transverse momenta,  $H_T$ . All histograms have been normalized to the total NLO cross-sections given earlier, in order to better compare their shapes. At 100 TeV the leading jet is significantly harder than at 14 TeV. The  $H_T$  distribution is also harder at 100 TeV with, of course, a significant shift in the peak once the jet cut is raised.<sup>25</sup>

Turning to leptonic observables, Fig. 87 shows the transverse momentum and rapidity of the positron from the  $W^+$  decay. The transverse momentum spectrum of the positron falls much less steeply

<sup>25</sup>This observable is also frequently used as a cut variable in searches for physics beyond the SM, for example in Refs. [312, 313], where cuts are placed in the range  $\sim 0.6$ –2 TeV depending on the details of the search strategy.

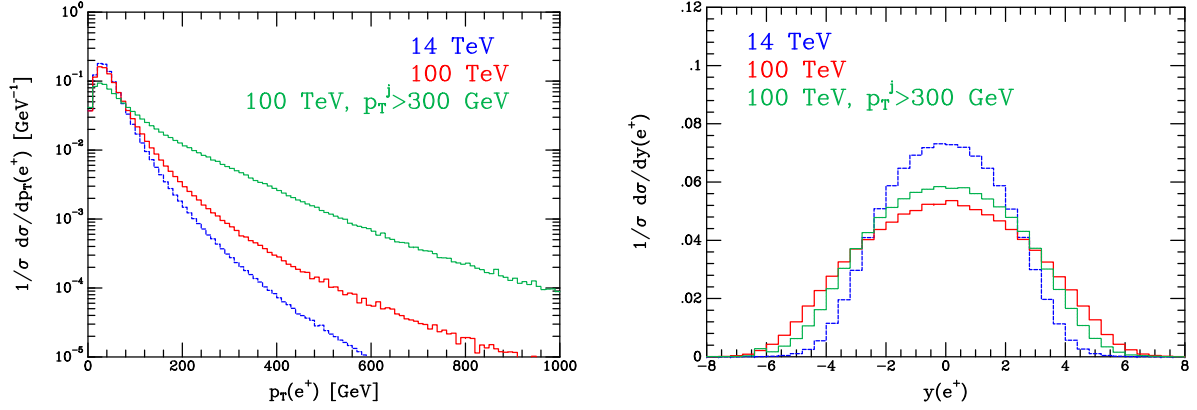


Fig. 87: NLO  $p_{\perp,\ell}$  (left) and  $\eta_\ell$  (right) distributions, normalized by the respective total cross sections, for 14 TeV(red), 100 TeV(blue), and 100 TeV\* (green)

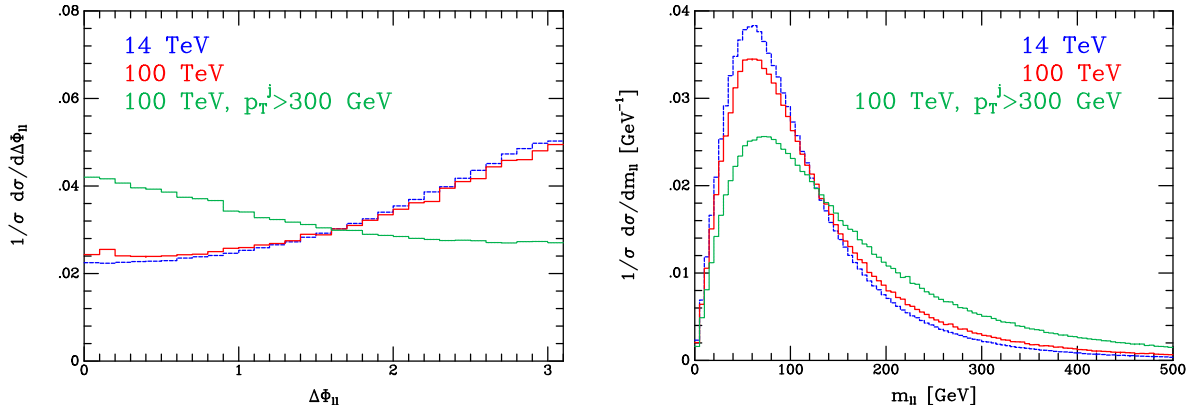


Fig. 88: NLO  $\Delta\Phi_{\ell\ell}$  (left) and  $m_{\ell\ell}$  (right) distributions, normalized by the respective total cross sections, for 14 TeV(red), 100 TeV(blue), and 100 TeV\* (green)

at 100 TeV, and even less so with a higher jet cut. The rapidity distribution of the positron is also changed non-trivially, with the broader peak at 100 TeV reflecting the fact that the process is probing a much smaller parton fraction. When the jet cut is raised to 300 GeV the required parton fraction is again larger so that the shape is a little closer to the one found at 14 TeV.<sup>26</sup> An observable that is particularly interesting for this process is the azimuthal angle between the electron and the positron, which can be used to isolate contributions to this final state from Higgs boson decays. As shown in Fig. 88, under the usual jet cuts at 14 TeV, this distribution is peaked towards  $\Delta\Phi_{\ell\ell} = \pi$ , a feature which persists at 100 TeV using the same jet cut. Once the jet cut is raised significantly, the recoil of the  $W^+W^-$  system results in the two leptons instead being preferentially produced closer together, i.e. in the region  $\Delta\Phi_{\ell\ell} \rightarrow 0$ . This is the same region of  $\Delta\Phi_{\ell\ell}$  that is favoured by events produced via the Higgs boson decay. Even if the jet threshold at a 100 TeV collider were not as high as 300 GeV, such a shift in this distribution could be an important consideration in optimizing Higgs-related analyses in the  $W^+W^-$  decay channel. Despite this shift to smaller  $\Delta\Phi_{\ell\ell}$ , the combination of this effect with the change in the  $p_{\perp,\ell}$  distribution shown earlier results in a relatively similar distribution for  $m_{\ell\ell}$ , albeit with a longer tail.

Finally, we show the distribution of the transverse momentum for the dilepton system  $p_{\perp}^{\ell\ell}$ , after cutting on the dilepton invariant mass. The corresponding cross section values are given in Table 28,

<sup>26</sup>Although not shown here, the jet rapidity exhibits a similar behaviour.

$m_{\ell\ell}^{\max}$	$\sigma_{LO}$ [pb]	$\sigma_{NLO}$ [pb]
125 GeV	4.76	5.34
50 GeV	1.48	1.64

Table 28: Cross-sections for the process  $pp \rightarrow WW+\text{jet}$  at a 100 TeV proton-proton collider, for two different cuts on the dilepton invariant mass. The listed values include leptonic branching ratios. Monte Carlo uncertainties are at most a single unit in the last digit shown in the table.

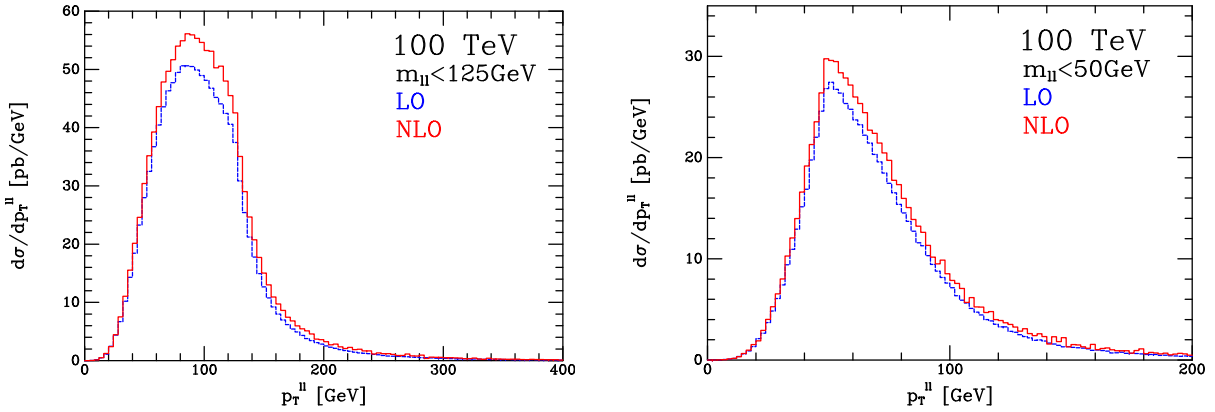


Fig. 89: Transverse momentum of the dilepton system at LO and NLO, for  $m_{\ell\ell} < 125$  GeV (left) and  $m_{\ell\ell} < 50$  GeV (right).

while distributions are shown in Fig. 89.

#### 7.5.4 Summary

Of course, at 100 TeV dimensional variables, such as  $p_{\perp}$  and  $m_{\ell\ell}$ , exhibit longer tails in the distributions than at 14 TeV. This simply reflects the increased center-of-mass energy of the system. However this increase of the center-of-mass energy also leads to broader rapidity distributions. Furthermore, applying a higher  $p_{\perp}$  cut significantly changes distributions for the dilepton azimuthal angle  $\Delta\Phi_{\ell\ell}$  as well as the total transverse momentum of the visible system  $H_T$ , which are frequently used for background suppression for Higgs measurements or BSM searches, respectively. In case such an increased cut is applied, this needs to be taken into account when devising the respective search strategies at a 100 TeV machine.

## 8 Electroweak production of gauge bosons in VBF and VBS processes<sup>27</sup>

Vector boson fusion (VBF) and vector boson scattering (VBS) processes provide particularly promising means for probing the mechanism of electroweak symmetry breaking. At hadron colliders, this class of reactions proceeds via the scattering of (anti-)quarks by the exchange of weak gauge bosons in the  $t$ -channel with subsequent emission of weak gauge bosons, i.e. the purely electroweak (EW) reactions  $pp \rightarrow Vjj$  and  $pp \rightarrow VVjj$ , respectively (with  $V$  denoting a  $W^\pm$  or a  $Z$  boson). In this report, we focus on leptonic decays of the weak bosons. The jets emerging from the quarks in VBF and VBS reactions are typically located in the forward and backward regions of the detector. Little QCD activity is encountered in the central region of rapidity. These characteristic features can be exploited for a powerful suppression of a priori large QCD backgrounds. In the following, we will consider EW  $W^+jj$ ,  $Zjj$ ,  $W^+W^+jj$ ,  $W^+Zjj$ ,  $W^+W^-jj$ , and  $ZZjj$  production at a 100 TeV proton-proton collider in the context of the Standard Model. We will devise selection cuts tailored for an optimization of the respective signal processes in the presence of the most abundant QCD backgrounds, in particular QCD-induced  $VVjj$  processes and, in the case of  $W^+W^-jj$  final states, backgrounds constituted by  $t\bar{t}$  production in association with up to two jets. For VBS reactions, we assume, for simplicity, that each gauge boson is decaying into a different type of lepton pair, and neglect interference effects that in principle could arise from final states involving same-type leptons. Off-shell and non-resonant contributions to the respective 2-lepton+2-jet or 4-lepton+2-jet final states are fully taken into account in all signal channels.

After a description of the general setup and input parameters of our study in Section 8.1, we will discuss various VBS-induced double and single gauge-boson production processes in Sections 8.2–8.5, and Section 8.6, respectively. In Section 8.7 benchmark cross sections for the various VBS signal processes are provided.

### 8.1 Input parameters and setup

Our numerical calculations are performed with the VBFNLO Monte Carlo package [314–322] for all  $Vjj$  and  $VVjj$  processes apart from the QCD-induced  $W^+W^-jj$  mode, and the Madgraph code package [323] for the remaining processes, including the top-induced backgrounds. In principle, the public POWHEG-BOX package [240–242] provides implementations for several VBS signal and background processes including NLO-QCD corrections matched with parton showers [324–333]. However, since the major goal of this study is to explore the capabilities of a future high-energy collider facility rather than to perform a precision analysis, we will refrain from using this tool here.

For the results presented in this section we use the SM masses and widths,

$$\begin{aligned}
 M_W &= 80.385 \text{ GeV}, & \Gamma_W &= 2.097547 \text{ GeV}, \\
 M_Z &= 91.1876 \text{ GeV}, & \Gamma_Z &= 2.508827 \text{ GeV}, \\
 M_H &= 125.09 \text{ GeV}, & \Gamma_H &= 0.004066 \text{ GeV}, \\
 m_{\text{top}} &= 172.5 \text{ GeV}, & \Gamma_{\text{top}} &= 1.340488 \text{ GeV}.
 \end{aligned}
 \tag{36}$$

The EW coupling constant is computed in the  $G_\mu$  scheme from the above input parameters and the Fermi constant  $G_\mu = 1.1663787 \times 10^{-5} \text{ GeV}^{-2}$ , via

$$\alpha_{G_\mu} = \frac{\sqrt{2} G_\mu M_W^2}{\pi} \left( 1 - \frac{M_W^2}{M_Z^2} \right).
 \tag{37}$$

External  $b$ - and  $t$ -quark contributions are disregarded throughout in all matrix elements. For the parton distribution functions (PDFs) of the proton, we use the MMHT2014lo/nlo68cl sets [9] at LO and NLO, respectively, and the corresponding values of  $\alpha_s$  as provided by the LHAPDF repository [21]. As

<sup>27</sup>Editor: B.Jäger

factorization scale,  $\mu_F$ , and renormalization scale,  $\mu_R$ , for the EW  $VVjj$  processes we use

$$\mu_F = \mu_R = Q_i, \quad (38)$$

where the  $Q_i$  denote the momentum transfer of the incoming to the outgoing quark on the upper and lower fermion lines, respectively. For the QCD induced  $VVjj$  processes, we use

$$\mu_F = \mu_R = \frac{1}{2}H_T, \quad (39)$$

with

$$H_T = \sum_i p_{T,i} + E_T(V_1) + E_T(V_2), \quad (40)$$

where the summation is running over all final-state partons in an event, and the transverse energy of each weak boson is determined by its transverse momentum,  $p_{T,V}$ , and mass,  $M_V$ , via

$$E_T(V) = \sqrt{p_{T,V}^2 + M_V^2}. \quad (41)$$

For our numerical analysis, we use a set of minimal selection cuts. For the reconstruction of jets, we use the anti- $k_T$  algorithm with  $R = 0.4$ , and demand a minimum transverse momentum,

$$p_{T,\text{jet}} \geq 50 \text{ GeV}. \quad (42)$$

The two hardest jets fulfilling the cut of Eq. (42) are called ‘‘tagging jets’’. These two jets are required to reside in opposite hemispheres of the detector,

$$y_{j_1} \times y_{j_2} < 0. \quad (43)$$

For charged leptons we impose cuts on transverse momenta, rapidities, and jet-lepton separations in the rapidity-azimuthal angle plane,

$$p_{T,\ell} \geq 20 \text{ GeV}, \quad |y_\ell| \leq 5, \quad \Delta R_{\text{jet},\ell} \geq 0.4. \quad (44)$$

A very powerful tool for the suppression of background processes is provided by requiring the charged leptons to be located in between the two tagging jets in rapidity,

$$y_{j,\text{min}}^{\text{tag}} < y_\ell < y_{j,\text{max}}^{\text{tag}}. \quad (45)$$

For the  $ZZjj$ ,  $W^\pm Zjj$ , and  $Zjj$  processes, to suppress contributions from photons of very small virtuality we furthermore require a minimal invariant mass for all pairs of oppositely charged leptons,

$$M_{\ell^+\ell^-} > 15 \text{ GeV}. \quad (46)$$

In addition to these minimal cuts, process-specific selection cuts are devised for each channel.

## 8.2 $W^+W^+jj$

For the  $W^+W^+jj$  channel, we consider the representative  $\nu_e e^+ \nu_\mu \mu^+ jj$  final state. We found that the EW signal in the presence of QCD-induced  $W^+W^+jj$  production can be improved by a set of selection cuts that are imposed in addition to the minimal cuts of Eqs. (42)–(45). Because of the absence of gluon-induced contributions in the QCD-induced production mode a very large signal-to-background ( $S/B$ ) ratio of 29.35 can be achieved by rather moderate customized cuts on the separation of the two tagging jets,

$$m_{jj} > 500 \text{ GeV}, \quad \Delta y_{jj} > 1.5. \quad (47)$$

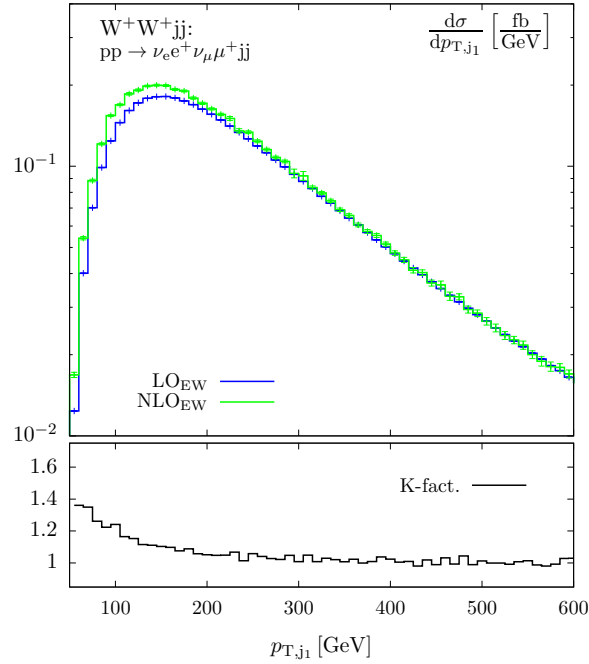


Fig. 90: Transverse-momentum distribution of the hardest jet in  $pp \rightarrow \nu_e e^+ \nu_\mu \mu^+ jj$  via VBS, within the selection cuts of Eqs. (42)–(45) and Eq. (47). The upper panel shows the LO (blue line) and the NLO-QCD results (green line) for the EW process, while the lower panel displays the K-factor that is defined as the ratio of the NLO to the LO result.

With this set of cuts, we obtain cross sections of  $\sigma^{\text{EW}} = 49.335(8)$  fb and  $\sigma^{\text{QCD}} = 1.681(2)$  fb for EW- and QCD-induced  $W^+W^+jj$  production, respectively, at LO. The NLO-QCD corrections to the EW signal process are small, resulting in a cross section of  $\sigma_{\text{NLO}}^{\text{EW}} = 52.56(2)$  fb. We note, however, that the NLO-QCD corrections are not flat, but affect bulk and tail of distributions in a non-trivial manner. To illustrate this effect, we depict the transverse momentum distribution of the hardest jet at LO and NLO QCD in Fig. 90. Despite the non-negligible impact of NLO-QCD corrections, in the following we restrict our analysis to LO, since at this time details of a possible experimental setup represent the dominant source of uncertainties.

Figure 91 shows the EW signal and the QCD background for the same distribution and, in addition, for the transverse mass distribution of the gauge-boson system. In order to spot new physics that mostly impacts the tails of invariant-mass and transverse-momentum distributions, searches typically focus on the kinematic region of large invariant masses of the gauge-boson system. In the presence of two neutrinos, this quantity is not fully reconstructible. In this case, the transverse mass of the  $W^+W^+$  system is considered instead, that is defined by

$$M_{T_{WW}} = \sqrt{(E_T^{\ell\ell} + E_T^{\text{miss}})^2 - (\vec{p}_T^{\ell\ell} + \vec{p}_T^{\text{miss}})^2}, \quad (48)$$

where

$$E_T^{\ell\ell} = \sqrt{(\vec{p}_T^{\ell\ell})^2 + M_{\ell\ell}^2}, \quad E_T^{\text{miss}} = |\vec{p}_T^{\text{miss}}|. \quad (49)$$

Here,  $\vec{p}_T^{\ell\ell}$  denotes the transverse momentum of the charged-lepton system, and  $\vec{p}_T^{\text{miss}}$  the total transverse momentum of the neutrino system.

The transverse-mass distribution depicted in Fig. 91 clearly exhibits that the EW signal is dominating over the entire kinematic range. Thus, even after the application of a severe cut on  $M_{T_{WW}}$  that

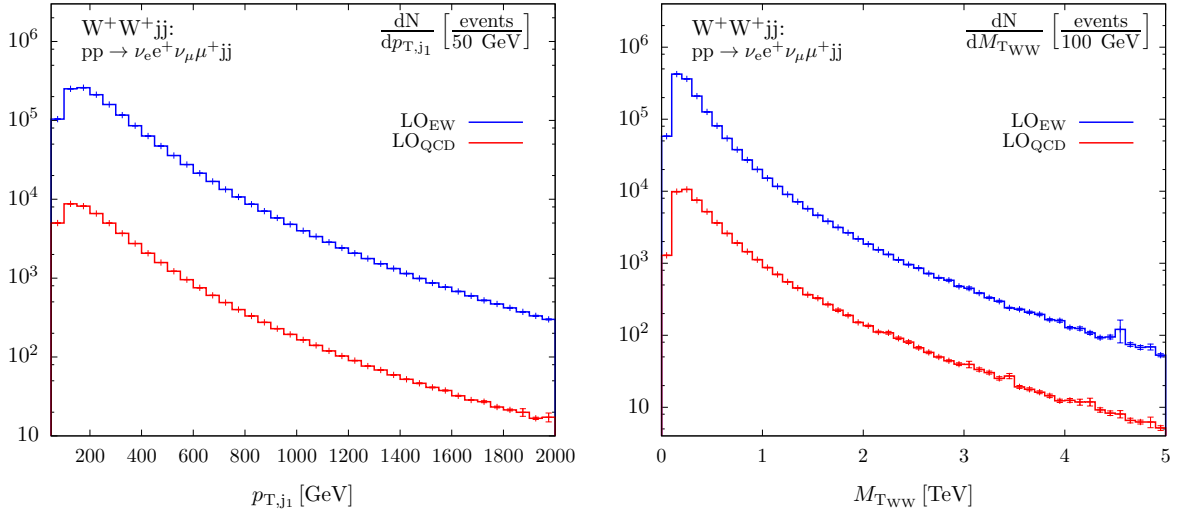


Fig. 91: Transverse-momentum distribution of the hardest jet (l.h.s.) and transverse-mass distribution of the gauge-boson system (r.h.s) for the EW-induced (blue line) and QCD-induced (red line) contributions to  $pp \rightarrow \nu_e e^+ \nu_\mu \mu^+ jj$ , within the selection cuts of Eqs. (42)–(45) and Eq. (47) for an integrated luminosity of  $30 \text{ ab}^{-1}$ .

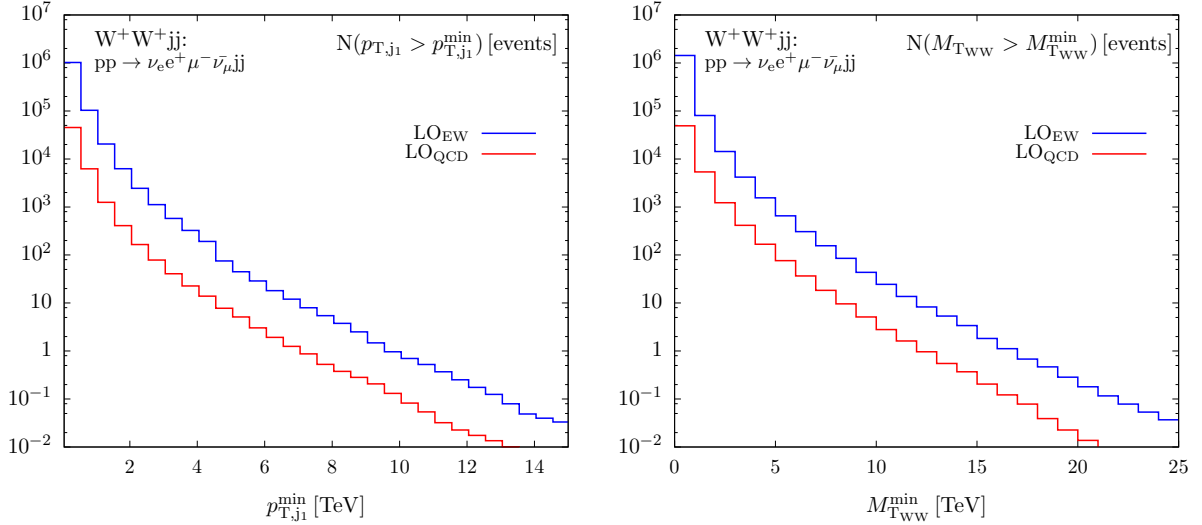


Fig. 92: Total number of events produced with  $p_{T,j_1} > p_{T,j_1}^{\min}$  (l.h.s.) and with  $M_{T,WW} > M_{T,WW}^{\min}$  (r.h.s.) for the EW-induced (blue line) and QCD-induced (red line) contributions to  $pp \rightarrow \nu_e e^+ \nu_\mu \mu^+ jj$ , within the selection cuts of Eqs. (42)–(45) and Eq. (47) for an integrated luminosity of  $30 \text{ ab}^{-1}$ .

might be necessary in new physics searches, the impact of the QCD-induced background on the VBS signal will remain small. In order to quantify the number of events per bin we are assuming an integrated luminosity of  $30 \text{ ab}^{-1}$ .

In Fig. 92 we show the number of events above a specific value of the tagging jets' transverse momentum and the gauge-boson system's transverse mass, respectively, assuming an integrated luminosity of  $30 \text{ ab}^{-1}$ .

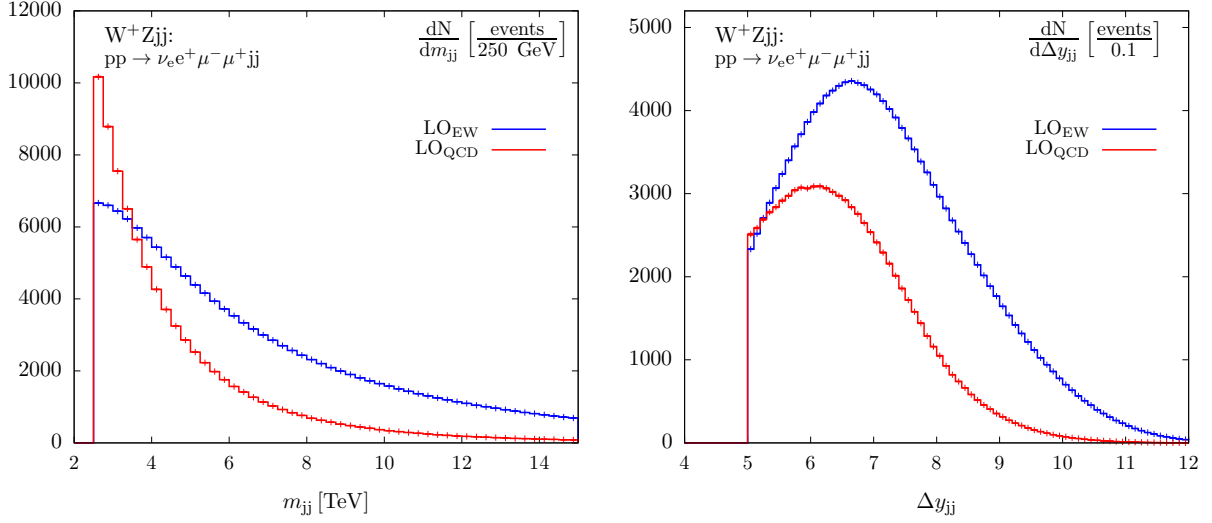


Fig. 93: Invariant-mass distribution (l.h.s.) and rapidity separation of the two tagging jets (r.h.s.) for the EW-induced (blue line) and QCD-induced (red line) contributions to  $pp \rightarrow \nu_e e^+ \mu^- \mu^+ jj$ , within the selection cuts of Eqs. (42)–(46) and Eq. (50) for an integrated luminosity of  $30 \text{ ab}^{-1}$ .

### 8.3 $W^+Zjj$

For the  $W^+Zjj$  channel, we consider the representative  $\nu_e e^+ \mu^- \mu^+ jj$  final state. An optimization of the  $S/B$  ratio in the  $W^+Zjj$  channel can be achieved when in addition to the cuts of Eqs. (42)–(46) the following process-specific cuts are imposed:

$$m_{jj} > 2500 \text{ GeV}, \quad \Delta y_{jj} > 5. \quad (50)$$

With the cuts of Eqs. (42)–(46) and Eq. (50), we obtain a cross section of  $\sigma^{\text{EW}} = 5.0547(7) \text{ fb}$  and  $\sigma^{\text{QCD}} = 2.801(1) \text{ fb}$  for EW- and QCD-induced  $W^+Zjj$  production, respectively, at LO, resulting in an  $S/B$  ratio of 1.80. For this setup, the invariant mass distribution and the rapidity separation of the two tagging jets are shown in Fig. 93. Obviously, in the QCD-induced production mode the two jets tend to be closer, which is essential for the design of cuts for the improvement of the  $S/B$  ratio.

In contrast to  $W^+W^+jj$  and  $W^+W^-jj$  final states where the invariant mass of the two-gauge-boson system cannot be determined in the fully leptonic decay modes, such a reconstruction is possible in the  $W^+Zjj$  channel using kinematical constraints to estimate the longitudinal component of the neutrino momentum. The distribution of the invariant mass computed from these reconstructed momenta is depicted in Fig. 94 together with the number of events above a specific value of  $M_{WZ}$ , assuming an integrated luminosity of  $30 \text{ ab}^{-1}$ .

### 8.4 $ZZjj$

The  $ZZjj$  channel is of particular phenomenological relevance, both, as VBS process that is sensitive, for instance, to new scalar resonances in the TeV regime, and as background to Higgs production via vector boson fusion in the  $H \rightarrow ZZ$  decay mode. Here, we focus on the fully leptonic final state where each  $Z$  boson decays into a lepton pair of different type, i.e. the process  $pp \rightarrow e^- e^+ \mu^- \mu^+ jj$ .

Proceeding in the same manner as for the  $W^+W^+jj$  and  $W^+Zjj$  processes, we devise a set of selection cuts enhancing the impact of the EW production mode with respect to QCD-induced  $ZZjj$  production. To this end, we impose the basic selection cuts of Eqs. (42)–(46), amended by the extra cuts of

$$m_{jj} > 2000 \text{ GeV}, \quad \Delta y_{jj} > 3. \quad (51)$$

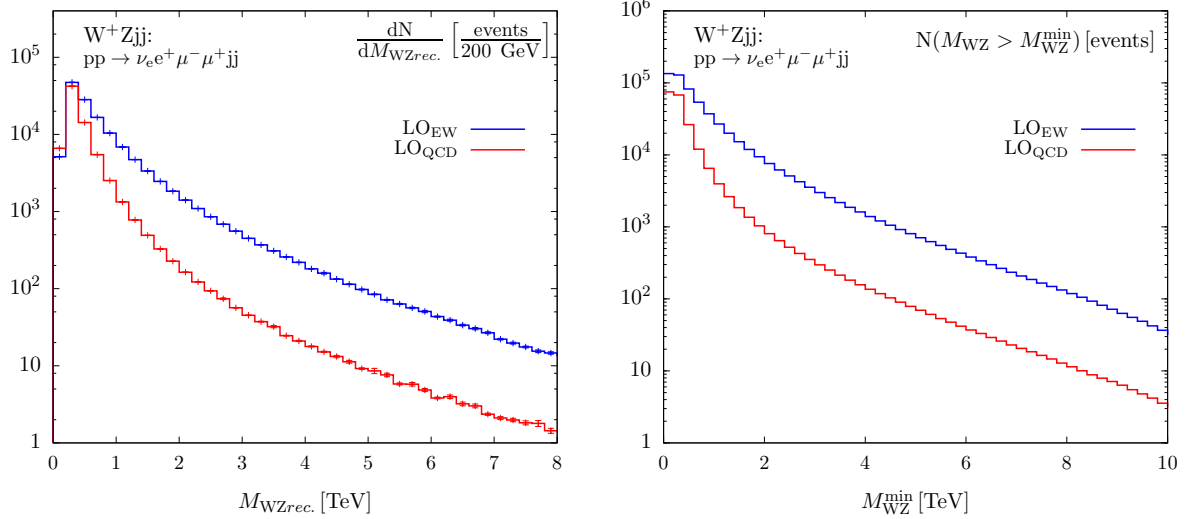


Fig. 94: Invariant-mass distribution of the  $WZ$  system reconstructed from the lepton momenta (l.h.s.) and total number of events produced with  $M_{WZ} > M_{WZ}^{\min}$  (r.h.s) for the EW-induced (blue line) and QCD-induced (red line) contributions to  $pp \rightarrow \nu_e e^+ \mu^- \mu^+ jj$ , within the selection cuts of Eqs. (42)–(46) and Eq. (50). An integrated luminosity of  $30 \text{ ab}^{-1}$  is assumed.

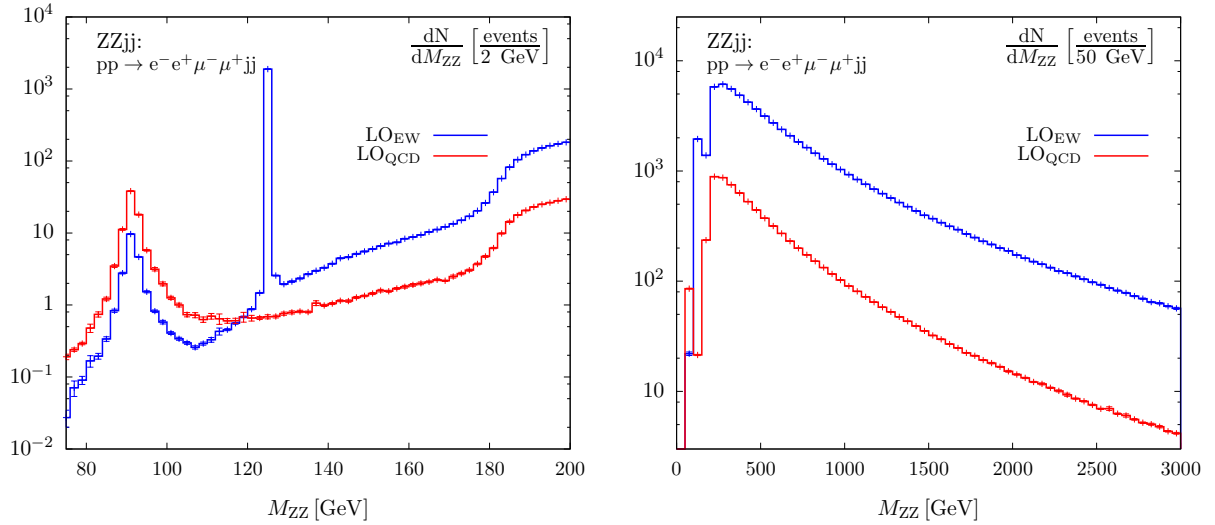


Fig. 95: Invariant-mass distribution of the four-lepton system for two different ranges of the EW-induced (blue line) and QCD-induced (red line) contributions to  $pp \rightarrow e^- e^+ \mu^- \mu^+ jj$ , within the selection cuts of Eqs. (42)–(46) and Eq. (51). An integrated luminosity of  $30 \text{ ab}^{-1}$  is assumed.

With these cuts, we find a LO cross section of  $\sigma^{\text{EW}} = 2.1506(7) \text{ fb}$  and  $\sigma^{\text{QCD}} = 0.2533(2) \text{ fb}$  for EW- and QCD-induced  $ZZjj$  production, respectively, resulting in an  $S/B$  ratio of 8.49.

The invariant mass of the  $ZZ$  system can be fully reconstructed from the momenta of the final-state charged leptons. Figure 95 shows the four-lepton invariant-mass distribution in two different ranges. At low values of  $M_{ZZ}$ , an interesting structure can be observed that is due to the  $Z$  peak around 91 GeV and, for the EW production mode, the Higgs resonance at 125 GeV. Both channels exhibit a broad continuum contribution above the  $Z$ -pair production threshold with the QCD contribution decreasing slightly faster than the EW contribution. In Fig. 96 we show the number of events above a specific value of the tagging

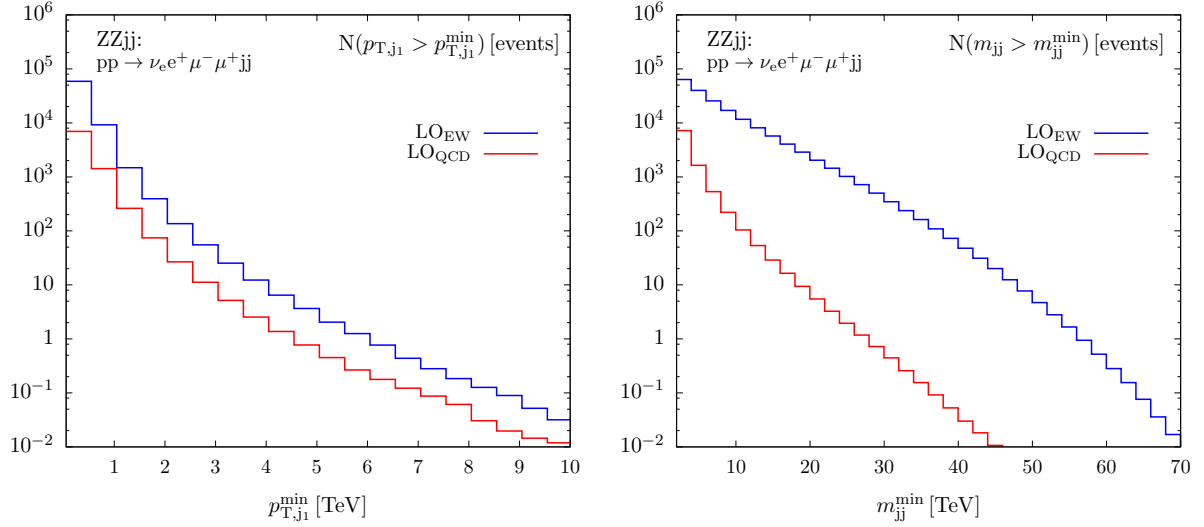


Fig. 96: Total number of events produced with  $p_{T,j_1} > p_{T,j_1}^{\min}$  (l.h.s.) and with  $m_{jj} > m_{jj}^{\min}$  (r.h.s.) for the EW-induced (blue line) and QCD-induced (red line) contributions to  $pp \rightarrow e^- e^+ \mu^- \mu^+ jj$ , within the selection cuts of Eqs. (42)–(46) and Eq. (51). An integrated luminosity of  $30 \text{ ab}^{-1}$  is assumed.

jets' transverse momenta and invariant mass, respectively, assuming an integrated luminosity of  $30 \text{ ab}^{-1}$ .

### 8.5 $W^+W^-jj$

The strategy applied to the  $W^+W^-jj$  channel differs from the respective analyses of other channels, as in this case the dominant source of background to the VBS signal is provided not by QCD-induced  $W^+W^-jj$  production, but by top-pair production in association with jets. In the  $t\bar{t}$  channel, when the dominant decay modes of the top quarks into  $W$  bosons and bottom quarks are considered, the bottom quarks can be misidentified as light-flavor tag jets. Even more problematic are modes where a  $t\bar{t}$  pair is produced in association with one or two jets that may mimic the tag jets of a VBS event. Because of the large event rates, despite the application of efficient  $b$ -veto techniques it is difficult to reduce the background associated with these various  $t\bar{t}$  processes below the level of the signal cross section with cut-based techniques. In order to find an optimal set of selection cuts for EW  $W^+W^-jj$  production, we therefore take  $t\bar{t}$ ,  $t\bar{t}+1$  jet,  $t\bar{t}+2$  jet, and QCD-induced  $W^+W^-jj$  production processes into account. We use MadGraph5 for the simulation of the top backgrounds that we generically refer to as  $t\bar{t}+\text{jets}$ . We focus on final states with different types of leptons,  $e^+ \nu_e \mu^- \bar{\nu}_\mu jj$ .

An optimal  $S/B$  ratio is obtained with the basic selection cuts of Eqs. (42)–(45) and additional cuts on the separation of the two tagging jets,

$$m_{jj} > 2000 \text{ GeV}, \quad \Delta y_{jj} > 5. \quad (52)$$

For the suppression of the  $t\bar{t}+\text{jets}$  backgrounds, we veto any events with an identified  $b$  quark, assuming the  $b$ -tagging efficiencies listed in Table 29. Events passing the  $b$ -veto are rejected, if they exhibit any jet in the rapidity interval between the two tagging jets,

$$y_{j,\min}^{\text{tag}} < y_j^{\text{veto}} < y_{j,\max}^{\text{tag}}. \quad (53)$$

Note that in our LO calculation the VBS signal and the QCD-induced  $W^+W^-jj$  background never exhibit more than two jets and thus always pass the cut of Eq. (53). With the full set of selection cuts and the  $b$ -veto procedure we apply, we find cross sections of  $\sigma^{\text{EW}} = 58.28(2) \text{ fb}$ ,  $\sigma^{\text{QCD}} = 17.1(1) \text{ fb}$ , and  $\sigma^{t\bar{t}+\text{jets}} = 5.2(4) \text{ fb}$ .

$p_{T_j}^{veto}$ [GeV]	$1.4 <  \eta_j^{veto} $	$ \eta_j^{veto}  < 1.4$
20 - 50	60%	70%
50 - 80	65%	75%
80 - 120	70%	80%
120 - 170	70%	80%
> 170	65%	75%

Table 29: Assumed  $b$ -tagging efficiencies as functions of the transverse momentum of the jet for different rapidity ranges (adapted from Ref. [334]).

### 8.6 Single gauge-boson production via VBF

The efficient suppression of QCD backgrounds is much more challenging for single gauge-boson production via VBF than in the case of gauge-boson pair production via VBS. A simple cut-based analysis is not capable of yielding  $S/B$  ratios much larger than one. More advanced techniques will be necessary for a clean isolation of the VBF signal in these cases. We nonetheless report our results for a simple cut-based study here to convey which orders of magnitude are to be expected for signal and background cross sections after VBF-specific selection cuts are imposed. We consider the representative  $e^-e^+jj$  and  $\nu_e e^+jj$  final states for the  $Zjj$  and  $W^+jj$  processes, respectively.

We impose the cuts of Eqs. (42)–(45). Furthermore, the tagging jets are required to exhibit a large invariant mass and be well-separated in rapidity,

$$m_{jj} > 2000 \text{ GeV}, \quad \Delta y_{jj} > 5. \quad (54)$$

For the  $Zjj$  production process, in addition the cut of Eq. (46) is applied to the decay leptons.

The cut on the lepton rapidity relative to the tagging jets, Eq. (45), is particularly important for the suppression of the QCD backgrounds that typically feature leptons not located in between the tagging jets. The impact of this cut is illustrated by Fig. 97, where for  $pp \rightarrow \nu_e e^+jj$  we show the distribution of the  $y_\ell^*$  variable, defined as

$$y_\ell^* = y_\ell - \frac{y_{j_1}^{tag} + y_{j_2}^{tag}}{2}, \quad (55)$$

without and with the cut of Eq. (45). The cut has an impact of about 40% on the QCD background, while it reduces the EW signal cross section only marginally.

With the above-listed cuts (including the requirement on the lepton rapidity), the cross sections given in Table 30 are obtained for the EW signal and the respective QCD background processes in the  $W^+jj$  and  $Zjj$  modes when decays of the gauge bosons into a specific lepton pair are considered.

The larger  $S/B$  ratios given in Table 31 can be obtained, if the more severe cuts

$$m_{jj} > 3000 \text{ GeV}, \quad \Delta y_{jj} > 6, \quad |y_\ell| \leq 1, \quad (56)$$

are imposed on the tagging jets and the charged leptons.

In Figs. 98 and 99, for the  $Zjj$  and  $W^+jj$  production modes we show the number of events above a specific value of the tagging jets' transverse momenta and invariant mass, respectively, assuming an integrated luminosity of  $30 \text{ ab}^{-1}$ .

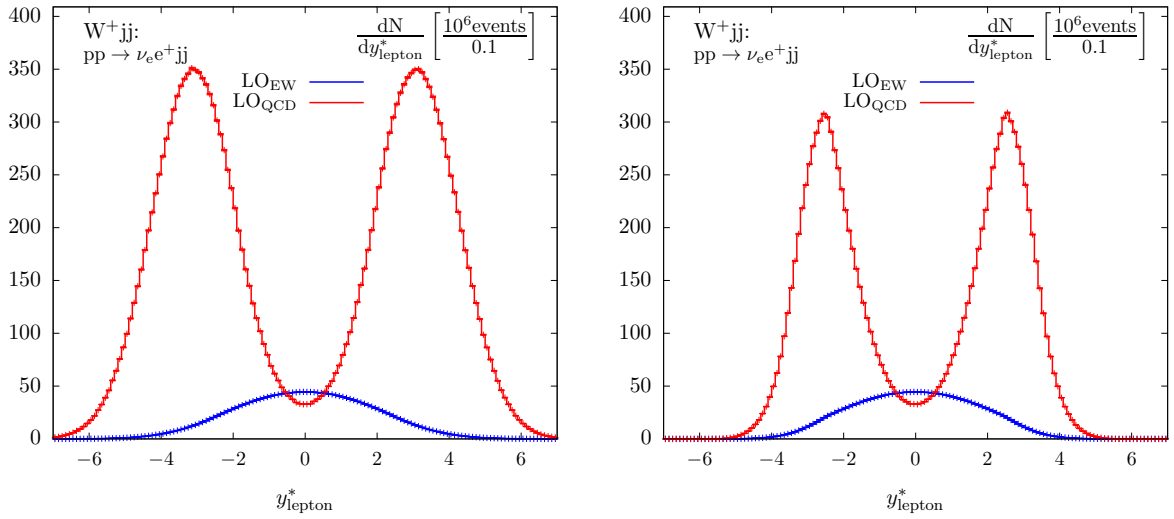


Fig. 97: Distribution of the  $y_{\ell}^*$  variable for the EW-induced (blue line) and QCD-induced (red line) contributions to  $pp \rightarrow \nu_e e^+ jj$ , within the selection cuts of Eqs. (42)–(44) and Eq.(54), without (l.h.s.) and with (r.h.s.) the lepton rapidity-gap cut of Eq. (45). An integrated luminosity of  $30 \text{ ab}^{-1}$  is assumed.

	EW production	QCD production	$S/B$
$\sigma^{\text{LO}}(W^+ jj)$	6980.1(8)	41324(10)	0.17
$\sigma^{\text{LO}}(Z jj)$	1079.5(3)	5164(1)	0.21

Table 30: Cross sections for the EW-induced  $Vjj$  production processes together with the irreducible QCD background and the signal-to-background ratio,  $S/B$ , within the default cuts for  $Vjj$  processes discussed in the text. Decays of the weak bosons into a specific leptonic final state are included as detailed in the text. All cross sections are given in [fb].

	EW production	QCD production	$S/B$
$\sigma^{\text{LO}}(W^+ jj)$	1488.1(4)	1227.8(8)	1.21
$\sigma^{\text{LO}}(Z jj)$	154.4(1)	138.0(1)	1.12

Table 31: Cross sections for the EW-induced  $Vjj$  production processes together with the irreducible QCD background and the signal-to-background ratio,  $S/B$ , within the default cuts for  $Vjj$  processes discussed in the text and the additional cuts of Eq. (56). Decays of the weak bosons into a specific leptonic final state are included as detailed in the text. All cross sections are given in [fb].

## 8.7 Benchmark cross sections

As we have shown above, dedicated sets of selection cuts are essential for obtaining optimal signal-to-background ratios in the environment of a high-energy hadron collider. Nonetheless, we here provide cross sections for the various VBS processes within simple cut scenarios to facilitate comparisons among the various channels.

In Table 32 we list numbers for an inclusive setup where we only impose the transverse-momentum cuts of Eq. (42) on the two tagging jets reconstructed via the anti- $k_T$  algorithm with  $R = 0.4$ . For

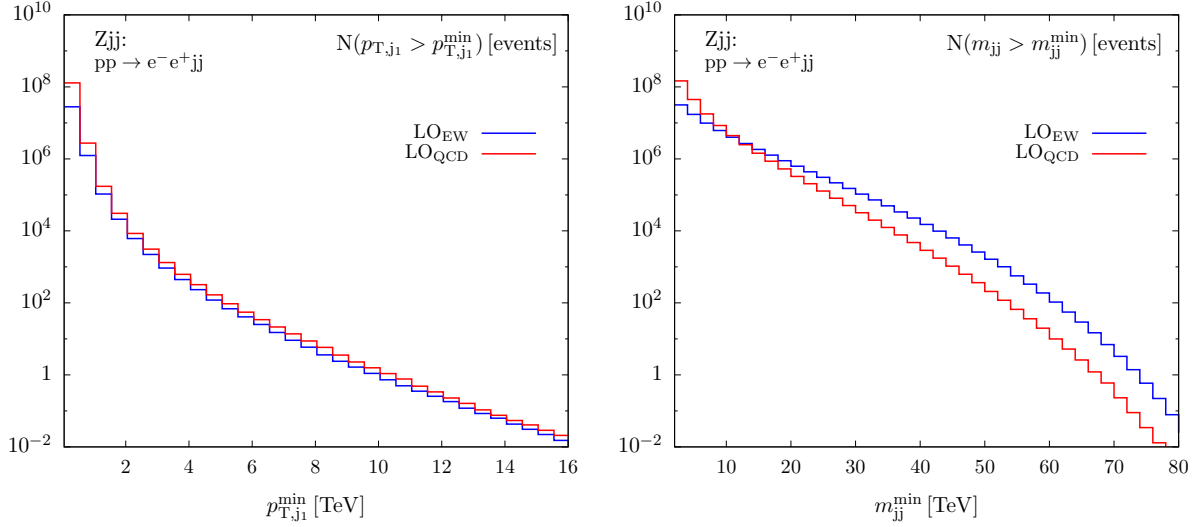


Fig. 98: Total number of events produced with  $p_{T,j_1} > p_{T,j_1}^{\min}$  (l.h.s.) and with  $m_{jj} > m_{jj}^{\min}$  (r.h.s.) for the EW-induced (blue line) and QCD-induced (red line) contributions to  $pp \rightarrow e^- e^+ jj$ , within the selection cuts of Eqs. (42)–(46), and Eq. (54). An integrated luminosity of  $30 \text{ ab}^{-1}$  is assumed.

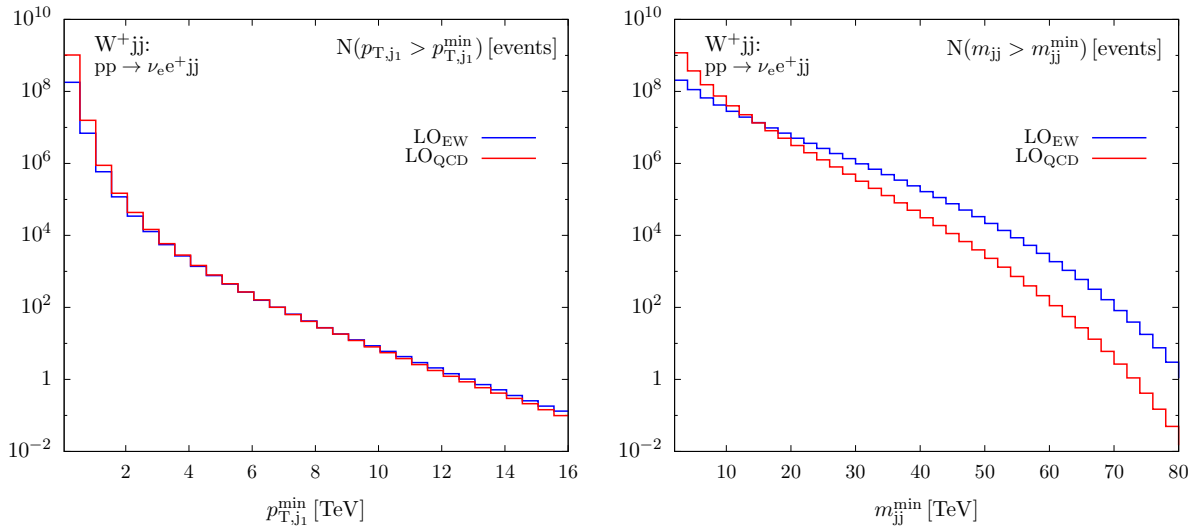


Fig. 99: Total number of events produced with  $p_{T,j_1} > p_{T,j_1}^{\min}$  (l.h.s.) and with  $m_{jj} > m_{jj}^{\min}$  (r.h.s.) for the EW-induced (blue line) and QCD-induced (red line) contributions to  $pp \rightarrow \nu_e e^+ jj$ , within the selection cuts of Eqs. (42)–(45), and Eq. (54). An integrated luminosity of  $30 \text{ ab}^{-1}$  is assumed.

processes with final-state  $Z$  bosons we additionally require

$$M_{\ell^+ \ell^-} > 66 \text{ GeV} \quad (57)$$

for all oppositely-signed lepton pairs to suppress contributions from photons splitting into lepton pairs.

In Tab. 33 we additionally impose VBS-specific cuts on the tagging jets,

$$y_{j1} \times y_{j2} < 0, \quad m_{jj} > 2000 \text{ GeV}, \quad \Delta y_{jj} > 5. \quad (58)$$

Cross sections with realistic cuts on the decay leptons as given in Eqs. (44)–(45) are listed in Tab. 34.

VBS channel	cross section [fb]
$W^+ jj$	41 200
$Z jj$	7 215
$W^+ W^- jj$	245.7
$W^+ W^+ jj$	104.8
$W^+ Z jj$	19.64
$ZZ jj$	5.372

Table 32: Cross sections for various VBS processes within the cuts of Eq. (42). For processes with  $Z$  bosons, additionally the cut of Eq. (57) is imposed. Decays of the weak bosons into a specific leptonic final state are included as detailed in the text. Statistical errors are at the permille level in each case.

VBS channel	cross section [fb]
$W^+ jj$	8 670
$Z jj$	1 461
$W^+ W^- jj$	93.27
$W^+ W^+ jj$	48.35
$W^+ Z jj$	8.312
$ZZ jj$	2.419

Table 33: Cross sections for various VBS processes within the cuts of Eqs. (42) and (58). For processes with  $Z$  bosons, additionally the cut of Eq. (57) is imposed. Decays of the weak bosons into a specific leptonic final state are included as detailed in the text. Statistical errors are at the permille level in each case.

VBS channel	cross section [fb]
$W^+ jj$	6 979
$Z jj$	1 050
$W^+ W^- jj$	58.30
$W^+ W^+ jj$	32.36
$W^+ Z jj$	4.875
$ZZ jj$	1.415

Table 34: Cross sections for various VBS processes within the cuts of Eqs. (42), (58), (44)–(45). For processes with  $Z$  bosons, additionally the cut of Eq. (57) is imposed. Decays of the weak bosons into a specific leptonic final state are included as detailed in the text. Statistical errors are at the permille level in each case.

## 9 Jets<sup>28</sup>

The production of jets is the process that by far dominates, at all distance scales, the final states emerging from hard collisions among the proton constituents.

### 9.1 Inclusive jet and dijet production

Figure 100 shows the integrated rates for the production of events with at least one jet of transverse momentum  $p_T$  larger than a given threshold. The distribution refers to jets with pseudorapidity  $\eta$  in the range  $|\eta| < 2.5$ . Figure 101 shows the probability that events with jets above certain  $p_T$  threshold be contained inside certain  $\eta$  ranges. Notice the huge  $\eta$  extension, even for jets with  $p_T$  in the TeV range. Assuming integrated luminosities in excess of  $1 \text{ ab}^{-1}$ , the reach in  $p_T$  extends well above 20 TeV. Fully containing and accurately measuring these jet energies sets important constraints on the design of calorimeters, e.g. requiring big depth and therefore large transverse size, with a big impact on the overall dimensions and weight of the detectors.

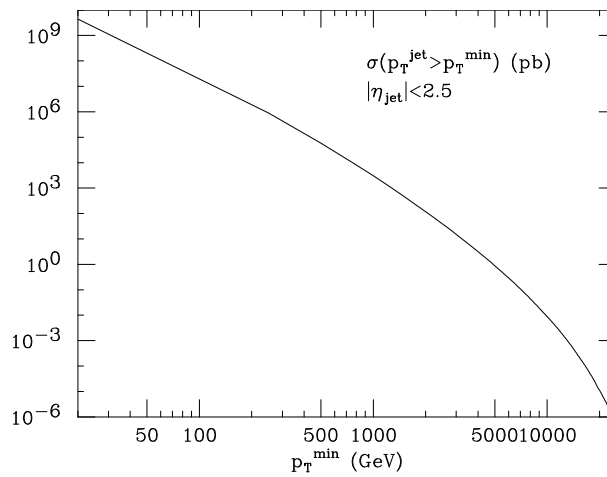


Fig. 100: Rates of events with one jet of  $|\eta| < 2.5$  and  $p_T > p_T^{\min}$ .

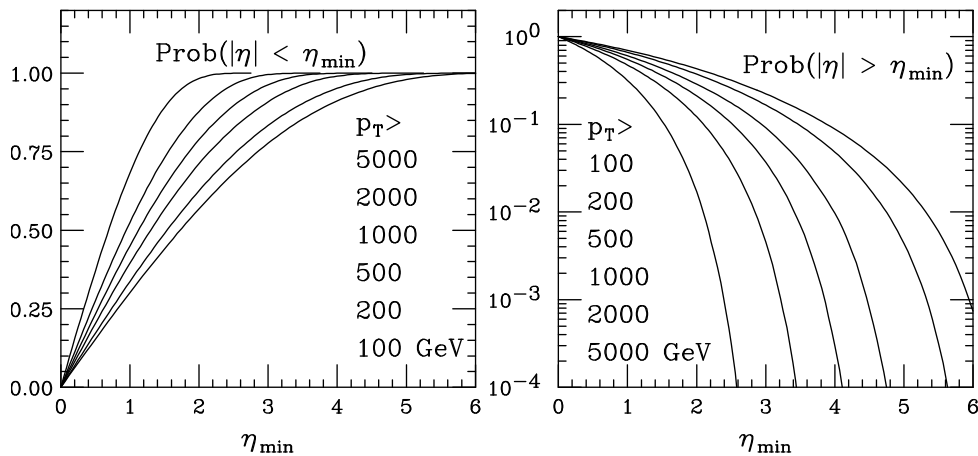


Fig. 101: Left: acceptance, for jets above various  $p_T$  thresholds, to be contained within  $|\eta_j| < \eta_{\min}$ . Right: probability to be outside the  $\eta_{\min}$  acceptance.

These choices become particularly relevant in the context of searches for high-mass resonances in dijet final states, where the separation from the continuum background of possibly narrow states requires

<sup>28</sup>Editors: A. Larkoski, M. Pierini, M. Selvaggi

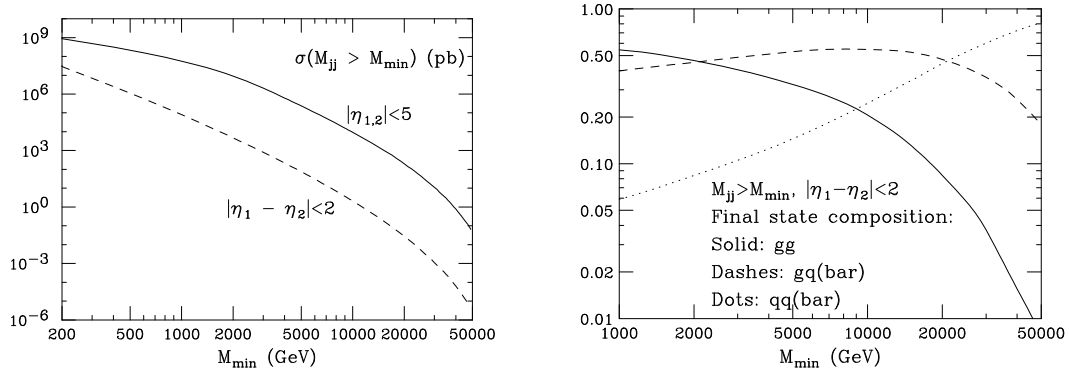


Fig. 102: Left: dijet mass spectra, for different  $\eta$  constraints. Right: partonic composition of dijet final states, as a function of the dijet mass.

good energy resolution. Figure 102 shows the rates for QCD production of final states with a dijet of invariant mass above a given threshold. We consider two cases: the dijet mass spectrum of all pairs with jets within  $|\eta| < 5$ , and the spectrum limited to jets produced at large angle in the dijet center of mass ( $|\eta_1 - \eta_2| < 2$ ), a configuration which is more typical of the production and decay of a possible resonance. Notice that, particularly at the largest masses, the former rates are several orders of magnitude larger than the latter ones. This is because one is dominated there by the low-angle scattering. But even for central production we have rates in excess of 1 event/ab<sup>-1</sup> for masses above 50 TeV. The relative partonic composition of central dijet events, as a function of the dijet mass, is shown in the right plot of Fig. 102. In the region  $2 \text{ TeV} \lesssim M_{jj} \lesssim 20 \text{ TeV}$  the final states are dominated by  $q\bar{q}$  pairs. Above 20 TeV, we find mostly  $q\bar{q}$  pairs (the  $q\bar{q}$  component is greatly suppressed throughout).

## 9.2 Spectroscopy with high-mass dijets

A central goal of the 100 TeV collider would be the discovery of new states with multi-TeV masses. If these states are able to be produced at a  $pp$  collider, then they must decay to light quarks and gluons. Additionally, these states may decay to electroweak-scale objects, especially if they are related to the (solution of the) hierarchy problem. The dominant decay modes of electroweak bosons and the top quark is to hadronic final states. Therefore, we should generically expect that final states with jets are among the most sensitive to new physics signals. In this section, we will study resonances that decay to pairs of QCD jets or electroweak objects and the sensitivity of jet algorithm parameters to reconstructing invariant mass spectra.

In this section, and the following sections, we simulate events as follows. Narrow color-singlet resonances with masses of 10, 20, 30, and 40 TeV that decay to pairs of top quarks,  $W$  bosons, light quarks, or gluons in  $pp$  collision events at 100 TeV are generated with MadGraph\_aMC@NLO v2.3.2.2 [64]. The top quark and  $W$  boson final states are decayed fully hadronically. The parton-level events are then showered with Pythia v8.2 [32] or Herwig++ v2.7.1 [101]. The resulting jets are clustered with the anti- $k_T$  algorithm [203] using FastJet v3.1.3 [212]. Only particles with pseudorapidity  $|\eta| < 2.5$  are included in the jet clustering and only jets with transverse momentum  $p_T$  larger than 20% of the mass of the mother resonance are included. This latter cut effectively imposes a cut on the pseudorapidity of the jets  $|\eta_J| \lesssim 1.5$ . For this analysis, we are most interested in the required performance and resolution of the detector to reconstruct the jets and the resonance, and so this cut will not directly affect that. It is to guarantee that the jets we are studying are indeed those that originated from the resonance decay.

In Figs. 103-106, we plot the invariant mass distribution of the two highest  $p_T$  jets from events with a 20 TeV resonance. We scan over the jets' radii ranging from  $R = 0.05$  to  $R = 0.5$ . Because the resonance is almost always produced at rest, the total invariant mass of these events will be about 20 TeV. As the radius of the jets increases, more radiation in the final state is captured in the jets. The long

tail of the mass distributions extending below 20 TeV indicates that there is some amount of radiation from the decay of the resonance that is not being captured in the two hardest jets. This tail decreases as the jet radius increases and is essentially absent for hadronically decaying  $W$  bosons, for the range of  $R$  considered.  $W$  bosons are color singlets, and so do not radiate at wide angles. Therefore, once the jet radius is large enough to capture the  $W$  decay products, then essentially all of the radiation in the final state is in the jets.

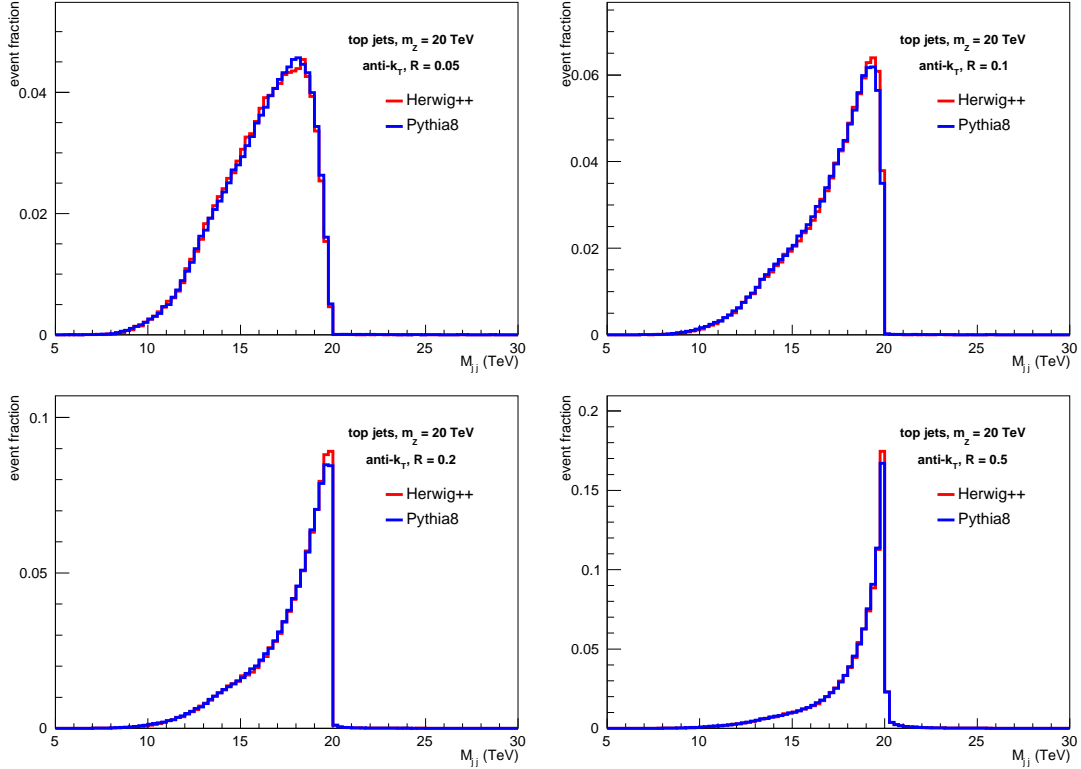


Fig. 103: Dijet invariant mass spectrum of boosted top quarks produced from the decay of a 20 TeV resonance with jet radii ranging from  $R = 0.05$  to  $R = 0.5$ .

For colored top quarks, light quarks, and gluons the tail is never completely removed, as long as there is radiation in the event not captured in the jet. There is always a non-zero probability that a colored parton will emit radiation outside of the jet and therefore will effectively lose energy. By increasing the jet radius, the tail of the resonance mass distribution extending to small masses can be reduced. In Fig. 107, we plot the dijet invariant mass for resonances decaying to gluons and light quark jets with jet radius  $R = 1.0$ . As compared to earlier plots, where the jet radius extended to only  $R = 0.5$ , the mass distribution is much more symmetric and the tail extending to small masses is nearly eliminated.

This effect on the  $p_T$  of the jet can be estimated in the small jet radius  $R$  limit. The average  $p_T$  loss  $\langle \delta p_T \rangle$  due to perturbative radiation is [335, 336]

$$\langle \delta p_T \rangle = \frac{\alpha_s}{\pi} L_i \log R + \mathcal{O}(\alpha_s). \quad (59)$$

$L_i$  is a constant that depends on the flavor of the jet:

$$L_q = \left( 2 \log 2 - \frac{3}{8} \right) C_F, \quad (60)$$

$$L_g = \left( 2 \log 2 - \frac{43}{96} \right) C_A + \frac{7}{48} n_f T_R. \quad (61)$$

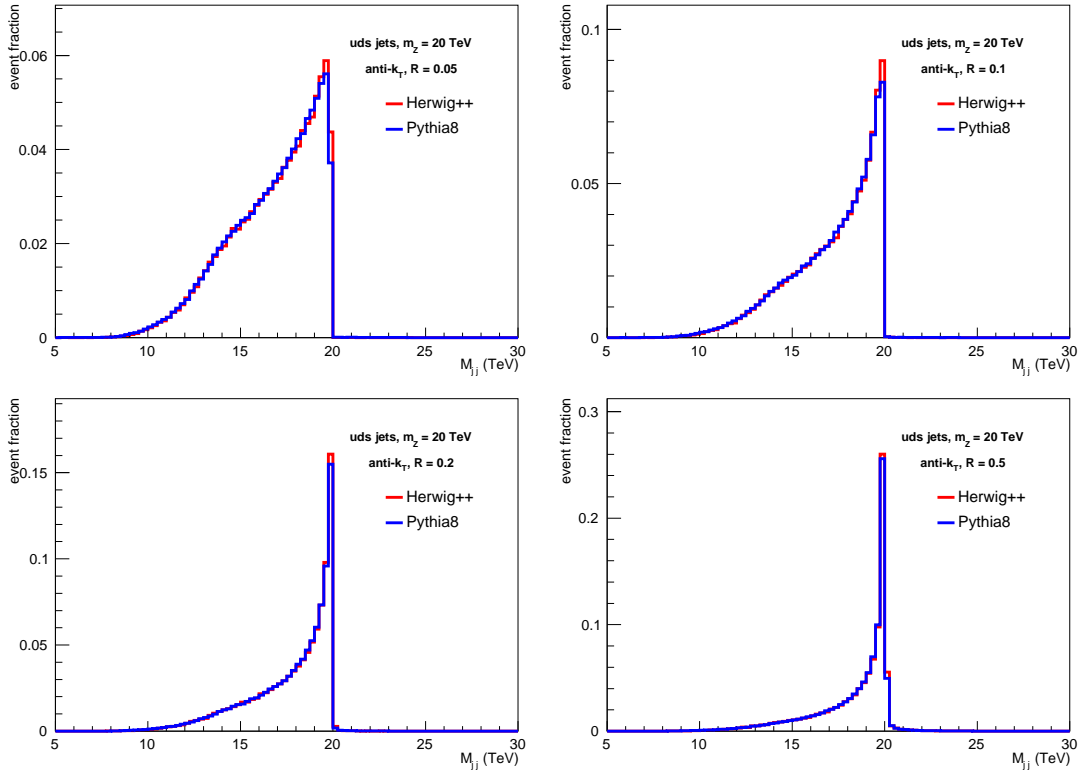


Fig. 104: Light QCD quark dijet invariant mass spectrum produced from the decay of a 20 TeV resonance with jet radii ranging from  $R = 0.05$  to  $R = 0.5$ .

For resonances that decay to two jets, this  $p_T$  loss can be translated into the average difference between the true resonance mass and the dijet invariant mass,  $\langle \delta m \rangle$ . To lowest order in the small jet radius limit, assuming that the resonance is produced at rest, this mass difference is approximately

$$\langle \delta m \rangle \simeq -m \frac{\alpha_s}{2\pi} L_i \log R + \mathcal{O}(\alpha_s), \quad (62)$$

where  $m$  is the mass of the resonance.

In Fig. 108, we plot the average difference between the dijet invariant mass and the true resonance mass  $\langle \delta m \rangle$  as a function of the jet radius  $R$ . On these plots, we have also included the analytic prediction of Eq. 62 for reference. Once the jet radius is large enough to capture all of the  $W$  decay products (above about  $R = 0.03$ ), the di- $W$  invariant mass is very close to the true resonance mass, as expected because it is a color-singlet. For light quark and gluon jets, the prediction in Eq. 62 agrees very well with the slope of the curve from the Monte Carlos. The offset differs, but is affected by  $R$ -independent  $\mathcal{O}(\alpha_s)$  corrections that we have not included. Like for  $W$ s, if the jet radius is too small, then all of the decay products of the top quark will not be captured in the jet. However, once the jet radius is above about  $R = 0.06$ , the top quark emits radiation outside of the jet in the same manner as a light quark.

As a quantitative measure of the optimal precision to which resonance masses can be reconstructed, in Fig. 109 we plot the fractional full-width half-maximum of the reconstructed 20 TeV resonance that decays to  $W$  bosons and gluons as a function of the jet radius. As illustrated in Fig. 106, the width of the resonance decaying to  $W$  bosons is exceptionally small, and appears to only be limited by the intrinsic width of the resonance. If the jet radius is too large, however, then more contamination radiation will be captured by the jet, smearing out the resonance peak. For resonances decaying to gluons, the opposite is true. If the jet radius is too narrow, then a significant amount of final state radiation will exit the jet, greatly reducing the resolution of the resonance peak. However, as the jet radius increases,

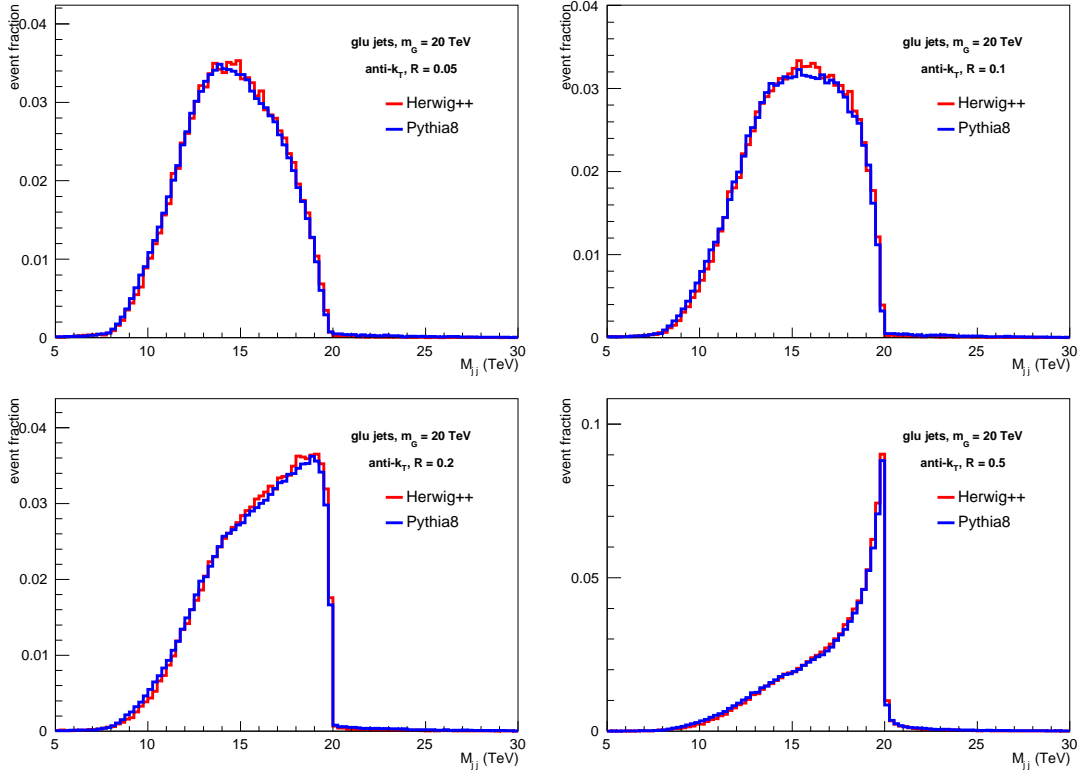


Fig. 105: Gluon dijet invariant mass spectrum produced from the decay of a 20 TeV resonance with jet radii ranging from  $R = 0.05$  to  $R = 0.5$ .

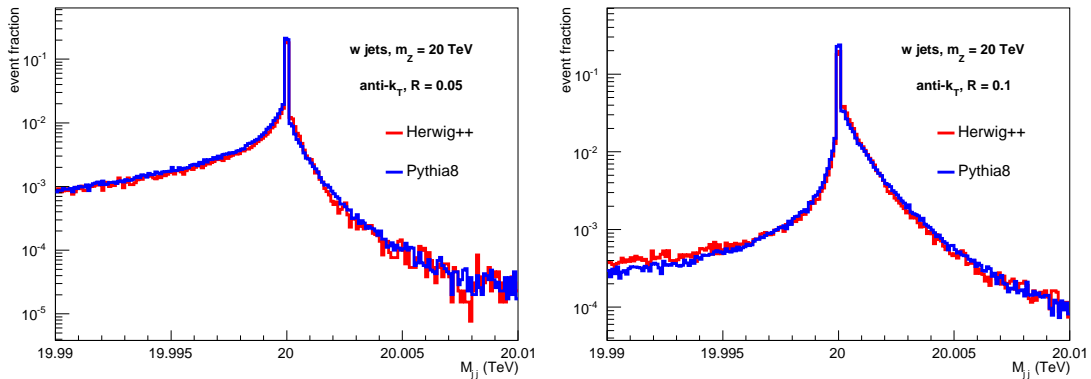


Fig. 106: Dijet invariant mass spectrum of boosted  $W$  bosons produced from the decay of a 20 TeV resonance with jet radii of  $R = 0.05$  and  $R = 0.1$ .

more of this radiation is captured in the jet, improving the resolution. Note, however, that even with the largest jet radius, the resolution of the resonance mass for gluons is at the percent level, as compared to less than a part per mille for  $W$ s.

### 9.3 SM physics of boosted objects

Given that jets or hadronically decaying electroweak objects may be the most powerful probe into new, high scale physics, it is necessary to efficiently identify their origin. For electroweak particles, the most sensitive single observable is the mass and jets with masses around 100 GeV are evidence of electroweak origin. Jets initiated by light QCD partons, on the other hand, have no intrinsic high-energy scale.

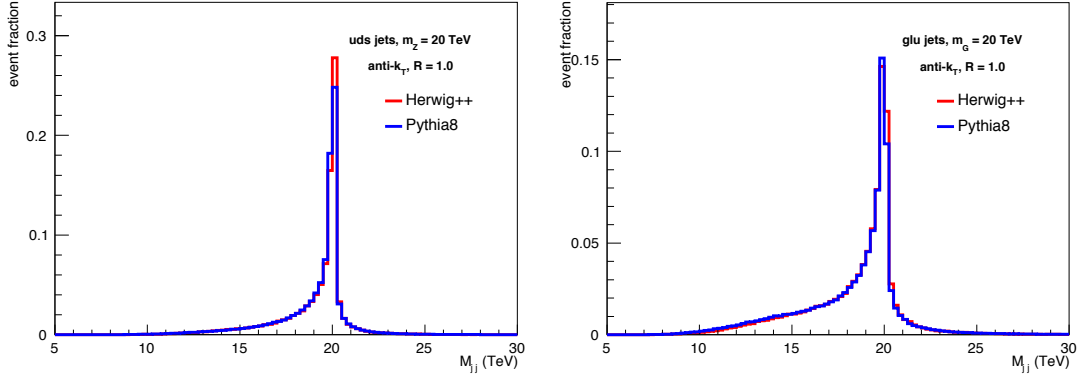


Fig. 107: Light quark dijet invariant mass spectrum (left) and gluon dijet invariant mass spectrum (right) produced from the decay of a 20 TeV resonance with jet radius of  $R = 1.0$ .

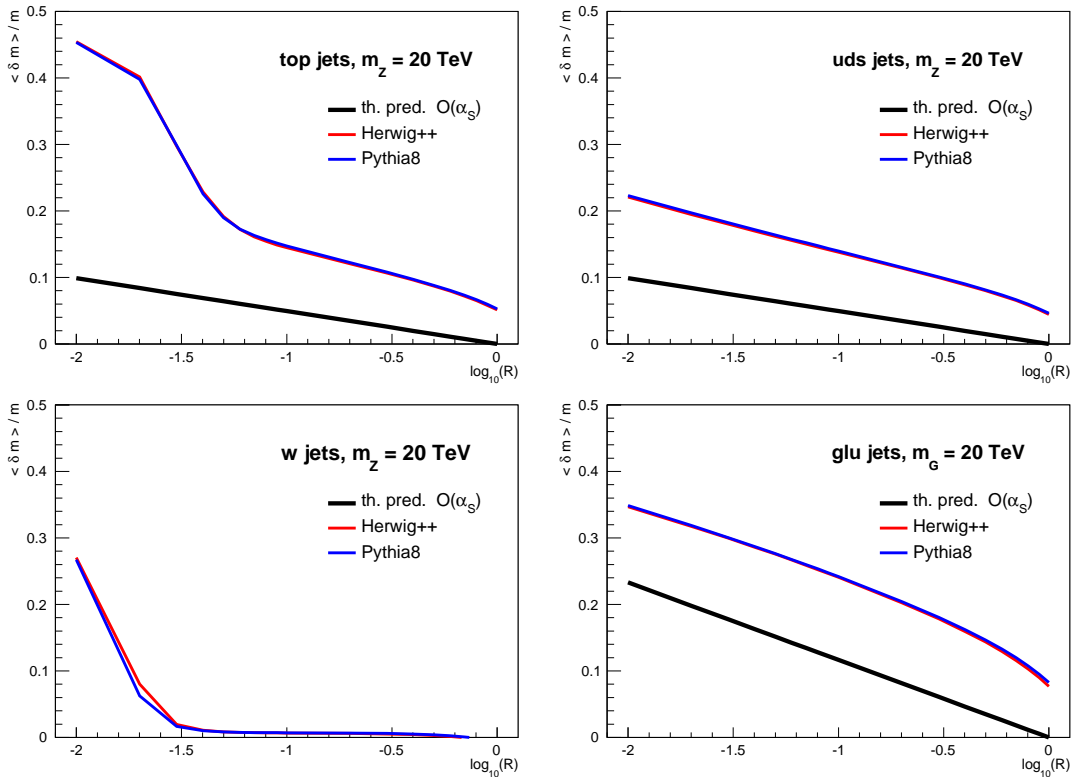


Fig. 108: Average fractional difference between dijet invariant mass from anti- $k_T$  jets with various radii and the true 20 TeV resonance that decays to tops, light QCD quarks,  $W$ s, and gluons. The prediction of Eq. 62 is shown for reference.

Depending on the cuts made on the jets as imposed by the jet algorithm, the mass spectra of QCD jets will be correspondingly sculpted and may peak in the electroweak mass window. More detailed analyses can be performed for identifying specific jets; see for example the studies in Refs. [337–339], dedicated to top quarks. We will review the conclusions of some of these top quark studies in Section 9.3.1.

Jet mass distributions are plotted in Figs. 110-113. Here, we plot the masses of the jets from the resonance decays studied in the previous section with the same cuts imposed. The mass of the resonance is fixed to 10 TeV, and the jet radius is varied from  $R = 0.05$  to  $R = 0.5$ . For quark and gluon jets, the mass distributions increase as the jet radius increases. For these jets, the peak of the mass distribution is

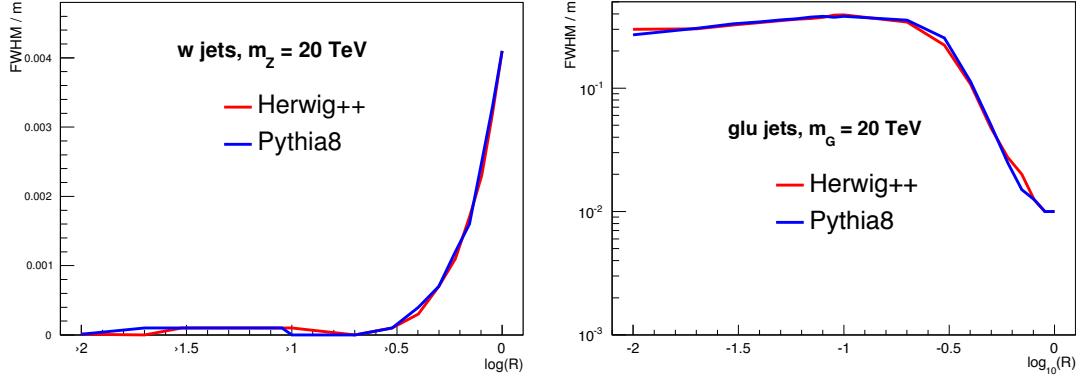


Fig. 109: Full-width half maximum of the 20 TeV resonance that decayed to boosted  $W$  bosons (left) and gluon jets (right).

located approximately at

$$m_{\text{peak}}^{\text{QCD}} \simeq \frac{\alpha_s}{\pi} C_i R p_T, \quad (63)$$

where  $C_i$  is the color of the jet and  $p_T$  is its transverse momentum. As illustrated in the plots, the peak of these QCD jets is in the electroweak mass range for  $R \gtrsim 0.2$ . Therefore, by decreasing the jet radius, we reduce the number of QCD jets that look like jets from hadronic decays of electroweak objects.

The mass of jets initiated by hadronic decays of top quarks or  $W$  bosons have very different dependence on jet radius. At the smallest jet radius studied,  $R = 0.05$ , there is a significant amount of radiation in the decays that are not captured in the jet. For  $W$  bosons, while there is a pronounced peak at the  $W$  mass, there is a tail at small masses indicating that a fraction of the jets do not contain both prongs of the  $W$  decay. For top quarks, there actually is no peak at the top mass whatsoever. Some jets do consist of the  $W$  from the decay, but the bulk is a smooth, falling distribution. As the radius is increased more of the decay products are included in the jets, and so for  $R \gtrsim 0.1$ , most of the top and  $W$  jets exhibit dominant peaks at their expected masses. As a rule of thumb, the critical jet radius necessary to capture all of the decay products for a resonance of mass  $m$  is approximately

$$R_{\text{crit}} \simeq \frac{2m}{p_T}. \quad (64)$$

When the jet radius is increased to  $R = 0.5$ , however, the mass distribution is significantly deformed. This is due to the inclusion of more contamination radiation in the jet, that is uncorrelated with the decay. This radiation may come from the initial state or underlying event and is approximately uniformly distributed over the area of the jet. Therefore, its contribution to the transverse momentum of the jet scales like the area of the jet,  $R^2$ , while its contribution to the mass of the jet scales like  $R^4$ . Roughly, in changing the jet radius from  $R = 0.2$  to  $R = 0.5$ , the effect of contamination radiation on the jet mass increased by a factor of almost 40. This illustrates that, to accurately reproduce the resonance peak, to reduce QCD backgrounds, and to eliminate contamination, a jet radius close to the critical radius  $R_{\text{crit}}$  in Eq. 64 should be used.

These observations are further illustrated in Figs. 114-117. Here, we have plotted the average energy fraction located within an angle  $\Delta R$  from the jet center. The jet radius is fixed to be  $R = 0.5$  and the mass of the resonance that decays to the jets ranges from 10 to 40 TeV. As expected from the approximate scale invariance of QCD, the average energy curves for quark and gluon jets is essentially independent of the  $p_T$  of the jet. The top mass jets exhibit small  $p_T$  dependence between the 10 and 20 TeV resonance mass samples, but are independent for the higher mass samples. For sufficiently high  $p_T$  jets, top quarks are just light quarks. For the boosted  $W$  bosons, on the other hand, almost all of the jet  $p_T$  is contained within the critical radius  $R_{\text{crit}}$ .  $W$  bosons are color singlets and so there is no scale

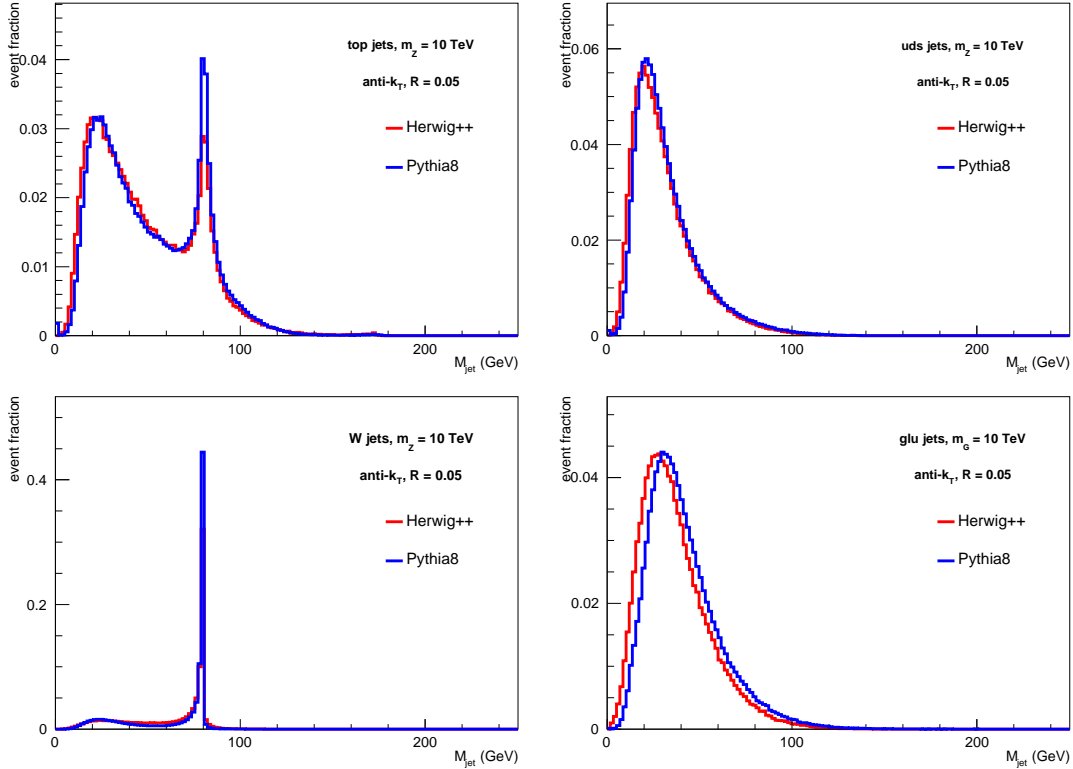


Fig. 110: Jet mass distribution of  $R = 0.05$  jets produced from 10 TeV resonance decays to tops, light QCD quarks,  $W$ s, and gluons.

above which their radiation pattern looks like light QCD jets. This suggests that isolation requirements, similar to that used for  $\tau$  identification at the LHC, could be used to purify a sample with boosted, hadronically-decaying  $W$  bosons.

### 9.3.1 Top Quark Tagging at FCC

Tagging hadronically-decaying boosted top quarks is a fundamental problem at the LHC and will be important at the FCC also. There has been significant effort devoted to the development of observables and algorithms for identification of top quarks at the LHC; see the reviews [340–344] and references therein. In this section, we will review recent studies of top quark identification at the FCC.

In the study of Ref. [339], top quarks produced at high boosts at the FCC were identified by measuring observables on jets that are sensitive to the three-prong structure of the hadronic top quark decay. Due to the extreme hierarchy between possible  $p_T$ s at the FCC and the top quark mass, there were several components of the tagging algorithm proposed by Ref. [339]. The tagging procedure used there was the following:

1. Jets are first clustered using the anti- $k_T$  algorithm with a fixed jet radius of  $R = 1.0$ . These  $R = 1.0$  jets are then reclustered with a radius  $R = 4m_{\text{top}}/p_T$ , where  $p_T$  is the transverse momentum of the original jet. Only the hardest jet found from this reclustering is kept. This procedure minimizes the effect of contamination radiation on the top quark mass measurement.
2. The invariant mass of the tracks  $m_{\text{tracks}}$  in the resulting jet is measured. To account for the bias of this mass measurement with respect to the total jet mass (at least on average), a rescaled track mass is defined as:

$$m_{\text{res}} = \frac{p_T}{p_{T,\text{tracks}}} m_{\text{tracks}},$$

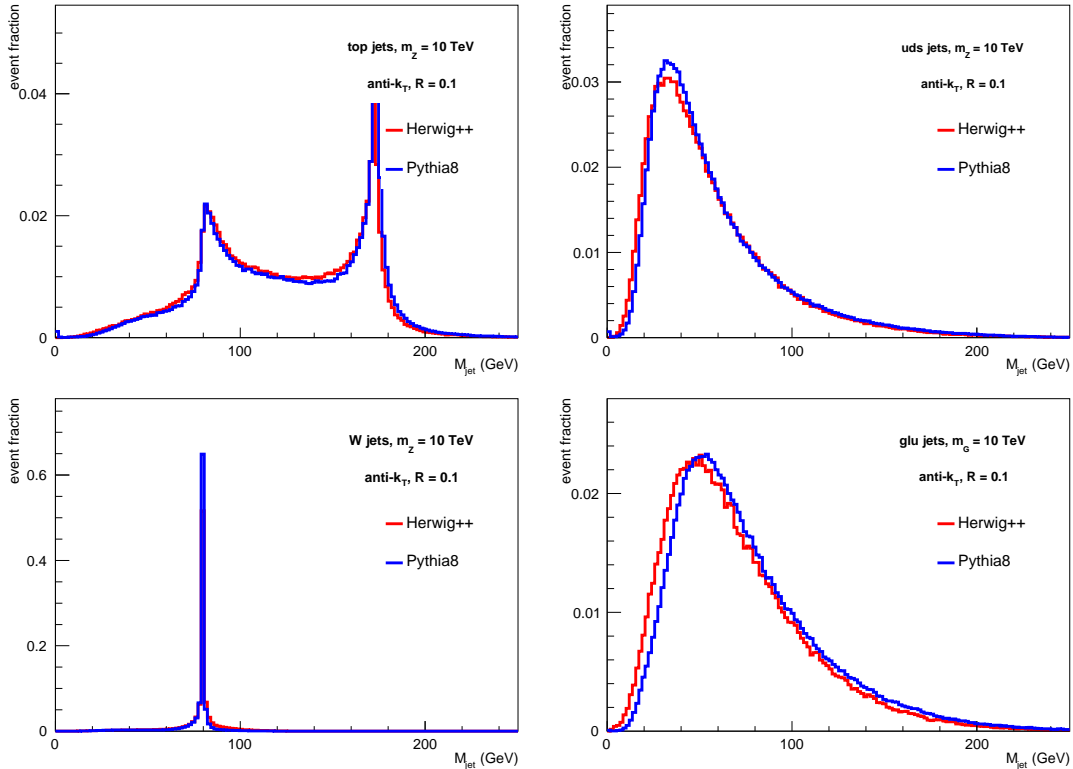


Fig. 111: Jet mass distribution of  $R = 0.1$  jets produced from 10 TeV resonance decays to tops, light QCD quarks,  $W$ s, and gluons.

where  $p_T$  is the total transverse momentum of the jet and  $p_T^{\text{tracks}}$  is just the transverse momentum in tracks. The rescaled jet mass was required to lie in the window  $m_{\text{res}} \in [120, 250]$  GeV around the top quark mass.

3. On these jets that passed the rescaled track mass cut, the substructure observables  $N$ -subjettiness [345, 346] and energy correlation functions [347] were measured exclusively on the tracks. Relevant for three-prong top quark jets, the  $N$ -subjettiness ratio  $\tau_3/\tau_2$  and the energy correlation function observable  $D_3$  [348] were used. Top quark signal jets take relatively small values for these observables while background jets initiated by light QCD partons have relatively large values, and so a cut can be applied to further discriminate boosted top quarks from background QCD jets.

Depending on acceptance or purity criteria, the precise cut on the observables  $\tau_3/\tau_2$  and  $D_3$  will change, so a useful way to illustrate the discrimination power of an observable is with a signal versus background efficiency curve, or ROC curve. To generate the results in this section only, we showered fixed-order events generated with MadGraph\_aMC@NLO v2.2.2 with Pythia v6.4. Complete details of event generation and the discrimination procedure are presented in Ref. [339].

To include at least a benchmark for detector effects, Ref. [339] used the fast detector simulator DELPHES [349], with a hypothetical future collider’s detector modeled off of the CMS detector [350]. The detector simulation parameters of the model CMS detector and FCC detector used in that study are summarized in Tables 35 and 36. Ref. [339] emphasized that the simulated detectors are both quite conservative and would require a full GEANT-based simulation [351] to truly accurately describe all features of the FCC detector.

A few of the detector parameters were customized for the extreme environment of the FCC, especially in the high density environment of the tracking system. The magnetic field strength  $B$ , the size of

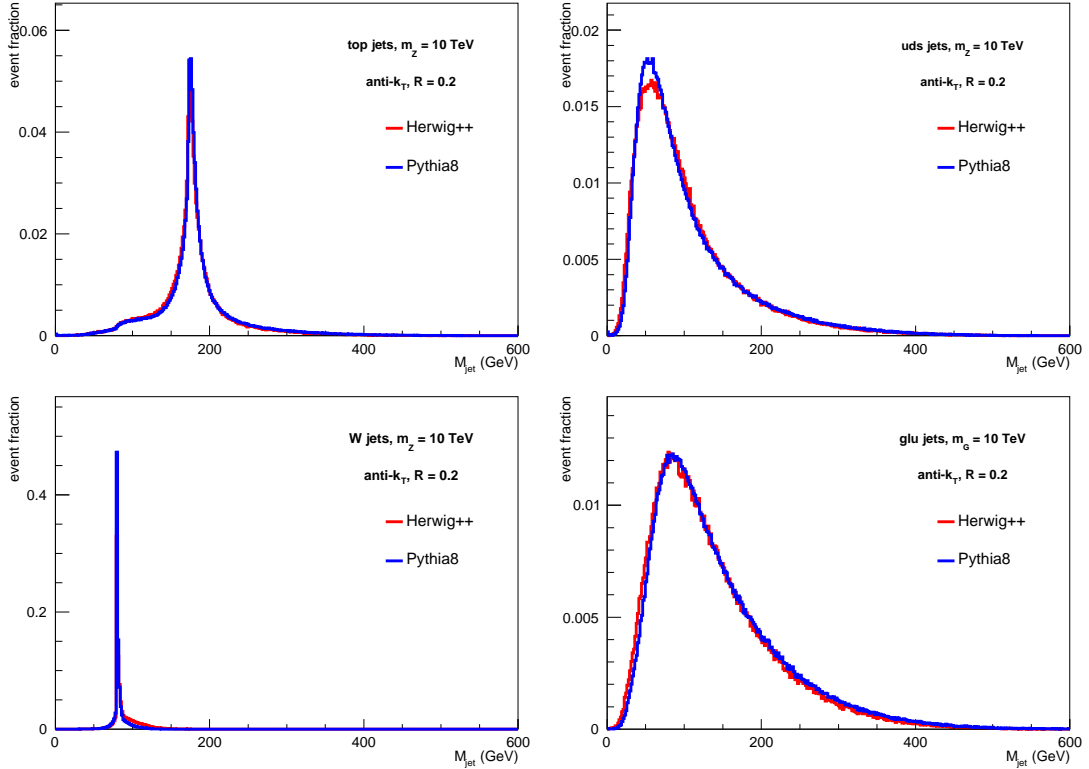


Fig. 112: Jet mass distribution of  $R = 0.2$  jets produced from 10 TeV resonance decays to tops, light QCD quarks,  $W$ s, and gluons.

	CMS	FCC
$B_z$ (T)	3.8	6.0
Length (m)	6	12
Radius (m)	1.3	2.6
$\epsilon_0$	0.90	0.95
$R^*$	0.002	0.001
$\sigma(p_T)/p_T$	$0.2 \cdot p_T$ (TeV/c)	$0.02 \cdot p_T$ (TeV/c)
$\sigma(\eta, \phi)$	0.002	0.001

Table 35: Tracking-related parameters for the CMS and FCC setup in Delphes.

the tracking radius  $L$  and the single hit spatial resolution  $\sigma_{r\phi}$  are the main parameters that constrain the resolution on the track transverse momentum:

$$\frac{\sigma(p_T)}{p_T} \approx \frac{\sigma_{r\phi}}{B \cdot L^2}. \quad (65)$$

The jet center has the highest density of charged particles, and so this should describe the dominant effect on the resolution. For tracks a distance  $R$  from the jet center, we define the track resolution efficiency

$$\epsilon(R) = \frac{2\epsilon_0}{\pi} \arctan\left(\frac{R}{R^*}\right). \quad (66)$$

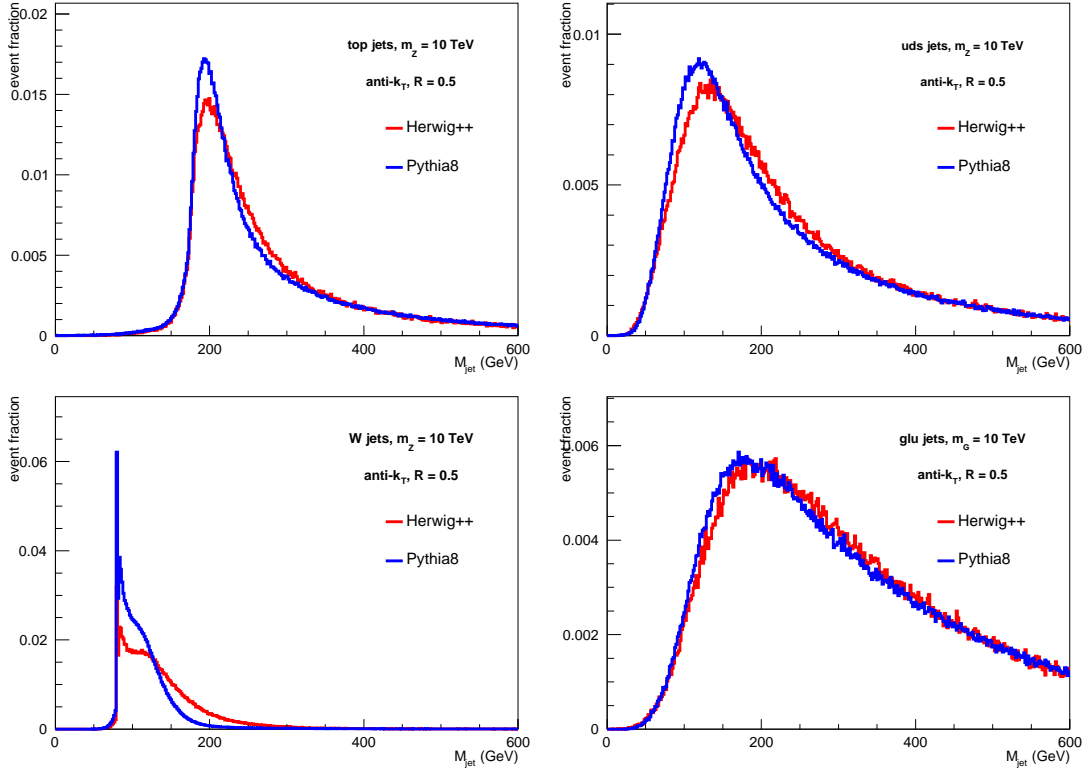


Fig. 113: Jet mass distribution of  $R = 0.5$  jets produced from 10 TeV resonance decays to tops, light QCD quarks,  $W$ s, and gluons.

	CMS	FCC
$\sigma(E)/E$ (ECAL)	$7\%/\sqrt{E} \oplus 0.7\%$	$3\%/\sqrt{E} \oplus 0.3\%$
$\sigma(E)/E$ (HCAL)	$150\%/\sqrt{E} \oplus 5\%$	$50\%/\sqrt{E} \oplus 1\%$
$\eta \times \phi$ cell size (ECAL)	$(0.02 \times 0.02)$	$(0.01 \times 0.01)$
$\eta \times \phi$ cell size (HCAL)	$(0.1 \times 0.1)$	$(0.05 \times 0.05)$

Table 36: Calorimeter parameters for the CMS and FCC setup in Delphes.

$R^*$  is a parameter that controls the angular resolution of the tracker, where we set  $R^* = 0.001$  for simulated FCC detector and  $R^* = 0.002$  for modeling the CMS detector.

Representative ROC curves are shown in Fig. 118 for discrimination of boosted top quarks from jets initiated by light QCD partons at the FCC for jets with  $p_T \in [15, 20]$  TeV. The quark and gluon jet backgrounds have been separated and the ROC curves for track- or calorimeter-based measurements are compared. The effect of the cut on the rescaled track jet mass is included in efficiencies. Table 37 lists background rejection rates in several jet  $p_T$  bins at fixed signal efficiencies of 20%, 40%, and 60%. The performance of the simulated CMS and FCC detectors are also compared.

Note from Table 37 that as the mass of the resonance increases (corresponding to increasing jet  $p_T$ ) the power to reject light QCD jets decreases, at fixed top quark efficiency. To have the same top quark efficiency at multiple jet  $p_T$ s requires changing observable cuts. As the jet  $p_T$  increases, one becomes more sensitive to the finite angular resolution of the detector, which will reduce the power to cleanly identify the three hard prongs of the boosted top quark. Therefore, as  $p_T$  increases, the observable cuts

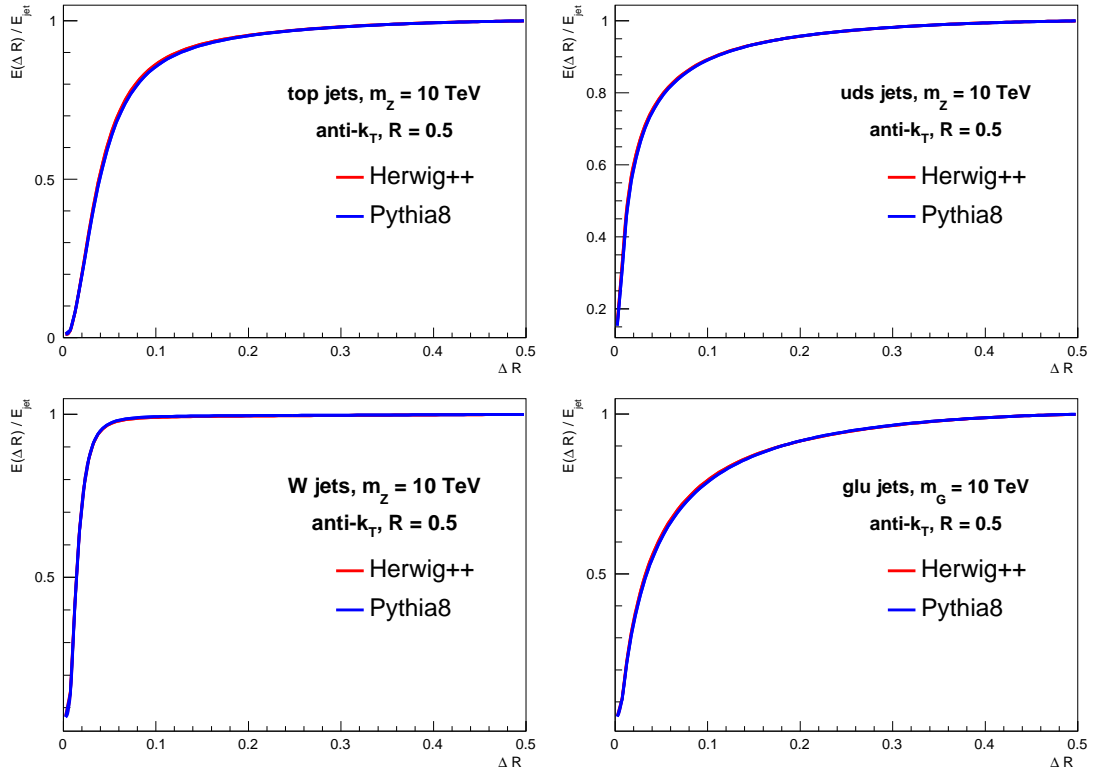


Fig. 114: Average energy fraction contained within and angular scale  $\Delta R$  of jets produced from 10 TeV resonance decays to tops, light QCD quarks,  $W$ s, and gluons.

must become looser, which in turn means that more background quark or gluon jets will also be included.

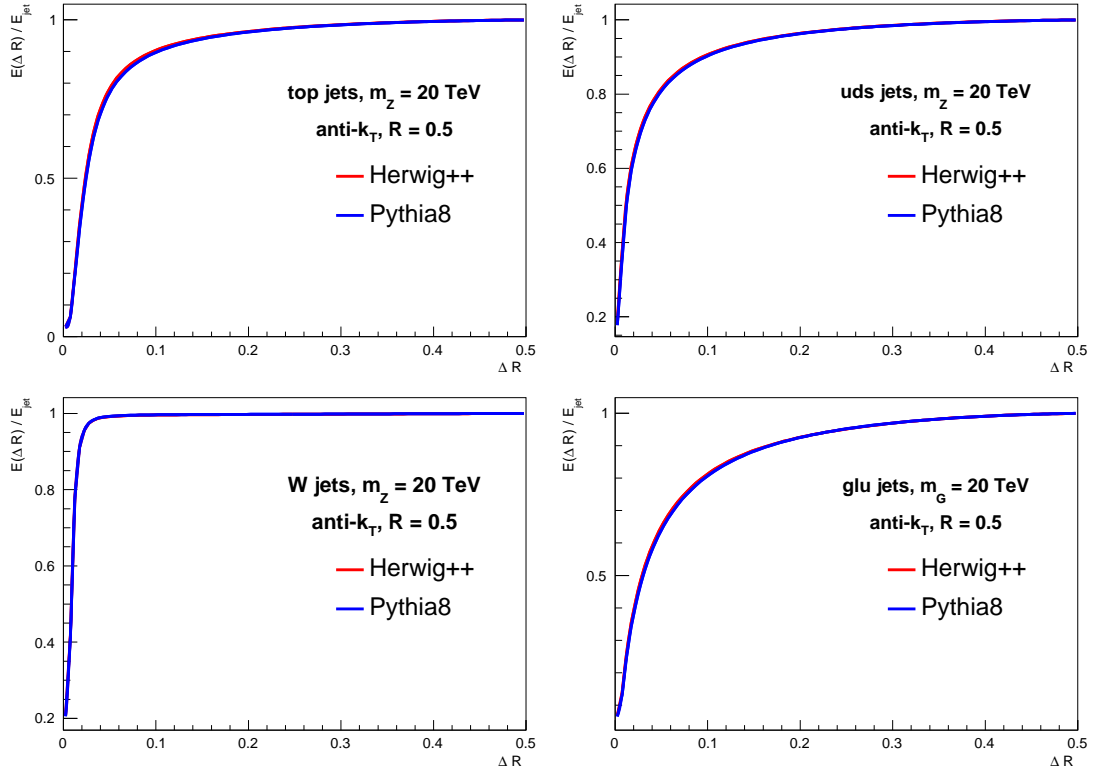


Fig. 115: Average energy fraction contained within and angular scale  $\Delta R$  of jets produced from 20 TeV resonance decays to tops, light QCD quarks,  $W$ s, and gluons.

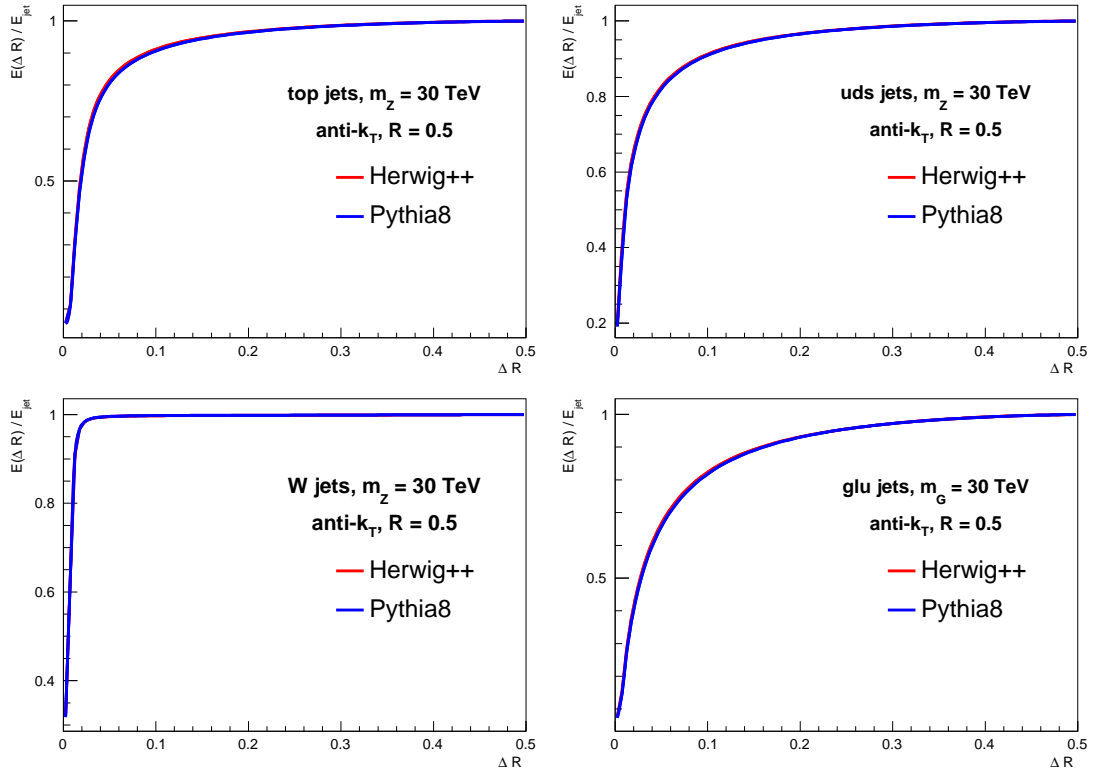


Fig. 116: Average energy fraction contained within and angular scale  $\Delta R$  of jets produced from 30 TeV resonance decays to tops, light QCD quarks,  $W$ s, and gluons.

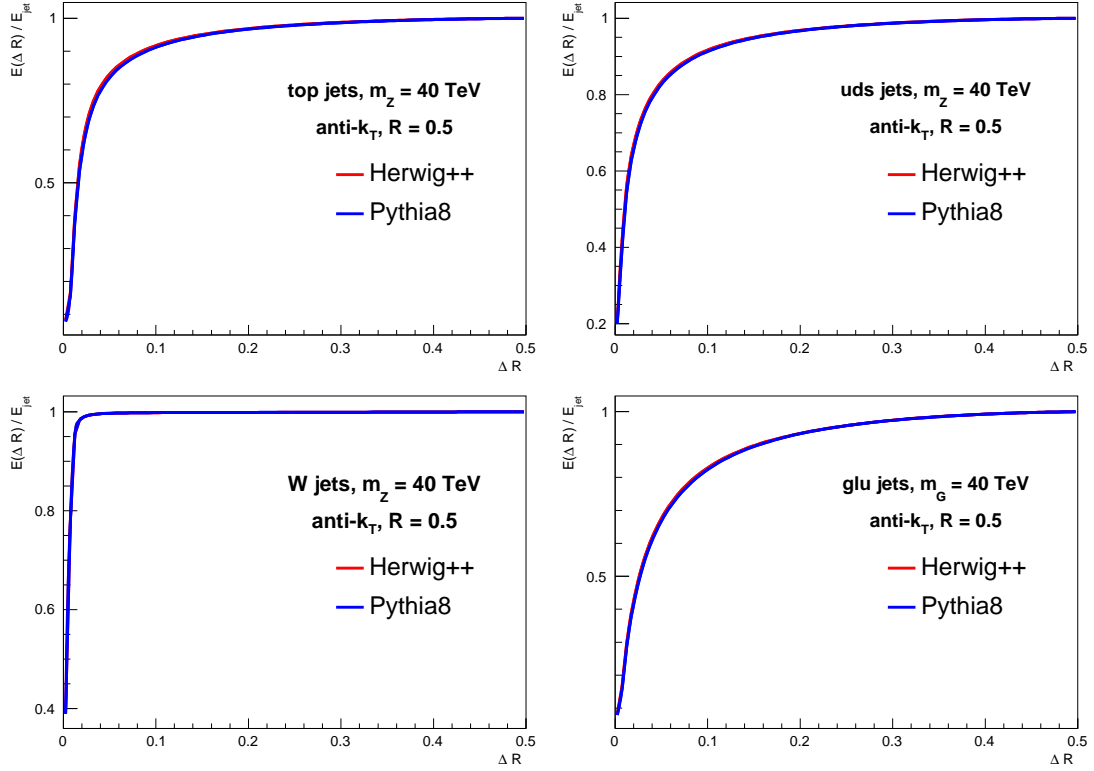


Fig. 117: Average energy fraction contained within and angular scale  $\Delta R$  of jets produced from 40 TeV resonance decays to tops, light QCD quarks,  $W$ s, and gluons.

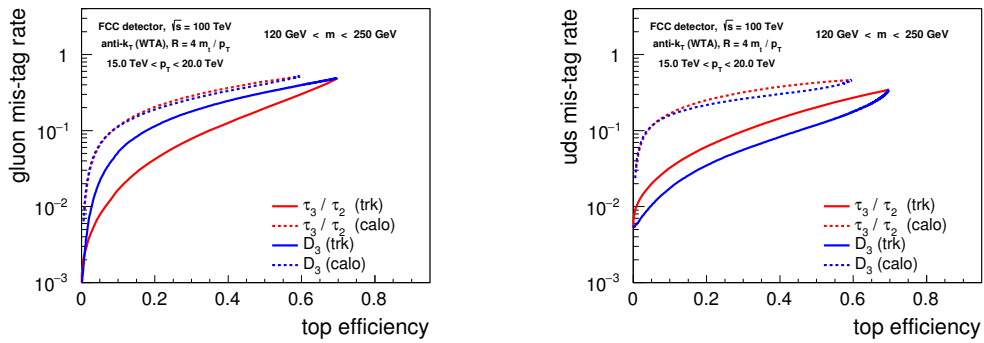


Fig. 118: Signal vs. background efficiency (ROC) curves for top quark identification from QCD background utilising  $\tau_{3,2}$  and  $D_3$  with the FCC detector for  $p_T \in [15, 20]$  TeV. (left) top quarks vs. gluon jets, (right) top quarks vs. light quark jets. The cut on the jet mass of  $m \in [120, 250]$  GeV is included in the efficiencies. Events were showered with Pythia v6.4.

		<b>20% Top Efficiency</b>				
	$p_T$ cut	[2.5, 5] TeV	[5, 7.5] TeV	[7.5, 10] TeV	[10, 15] TeV	[15, 20] TeV
gluons	CMS	2%	3%	4%	5%	6%
	FCC	1%	2%	2%	3%	4%
quarks	CMS	1%	2%	3%	5%	7%
	FCC	0.5%	1%	1.5%	2%	4%
		<b>40% Top Efficiency</b>				
	$p_T$ cut	[2.5, 5] TeV	[5, 7.5] TeV	[7.5, 10] TeV	[10, 15] TeV	[15, 20] TeV
gluons	CMS	7%	9%	10%	14%	17%
	FCC	5%	6%	7%	10%	12%
quarks	CMS	3%	5%	7%	11%	17%
	FCC	1.5%	2.5%	4%	5%	8%
		<b>60% Top Efficiency</b>				
	$p_T$ cut	[2.5, 5] TeV	[5, 7.5] TeV	[7.5, 10] TeV	[10, 15] TeV	[15, 20] TeV
gluons	CMS	18%	20%	24%	30%	38%
	FCC	13%	15%	20%	24%	25%
quarks	CMS	7%	10%	15%	22%	30%
	FCC	4%	6%	8%	11%	15%

Table 37: Table of background rejection rates at fixed signal efficiencies for jet  $p_T$ s ranging from 2.5 TeV to 20 TeV at the CMS or FCC detector. For gluon (quark) jet backgrounds, efficiencies are determined from cuts on  $\tau_{3,2}$  ( $D_3$ ) measured on tracks. The cut on the rescaled track-based jet mass of  $m_J \in [120, 250]$  GeV is included in the efficiencies. These results are from events showered with Pythia v6.4.

### 9.4 Boosted boson tagging

A boson of mass  $M$  decaying hadronically produces two quarks with angular separation  $\Delta R \approx 2M/p_T$ . At large momenta, the separation becomes smaller than the jet size. Such a boson would be seen in a detector as a single massive jet.

The identification of jets as hadronically decaying bosons opened new perspectives at the LHC. The development of an effective tagging algorithm for boosted vector bosons [352, 353] allowed to retain a good sensitivity to resonances decaying to two bosons and heavier than  $\approx 1$  TeV [354–360].

The reconstruction of heavy jets needs a new detector design. A good reconstruction of the boson mass requires both excellent energy and angular resolution, since the jet mass depends on both the momenta of the jet constituents and the angular separation among them. One can then study the jet mass as a benchmark for calorimeter granularity.

As a reference, we take the case of Randall Sundrum (RS) graviton  $G_{\text{RS}}$  decaying to two  $Z$  bosons and study the reconstructed mass resolution for different detector geometries. Signal events are generated with PYTHIA8 [32, 122] at a center-of-mass energy  $\sqrt{s} = 100$  TeV, for different values of the  $G_{\text{RS}}$  mass. The jets reconstructed in these events are compared to ordinary QCD jets, generated in  $G_{\text{RS}} \rightarrow q\bar{q}$  and  $G_{\text{RS}} \rightarrow gg$  decays. These samples have the same kinematic features (e.g.,  $p_T$  and  $\eta$  distributions) as the corresponding jets from  $Z$  bosons, as long as the  $p_T$  is much larger than the  $Z$  mass. Any difference observed in this study can then be interpreted as related to the nature of the jet ( $Z$  vs quarks and gluons).

Events are reconstructed with DELPHES3 [349, 361], using the default detector performances for the FCC detector, provided with the software distribution.

Three detector scenarios are defined: (i) the baseline detector geometry with calorimeter cells of size  $\phi \times \eta = 0.5^\circ \times 0.01$  for ECAL and  $2.5^\circ \times 0.05$  for HCAL. (ii) twice the cell size both for ECAL and HCAL, keeping the same ECAL/HCAL cell-size ratio. (iii) half the cell size for ECAL and HCAL, keeping the same ECAL/HCAL size ratio.

Jets are clustered using the FASTJET [212] implementation of the anti- $K_T$  algorithm [203] with jet-size parameter  $R = 0.25$ , giving as input to the jet algorithm the list of four-momenta for the particles reconstructed with the DELPHES implementation of the particle-flow algorithm. The performances of the tracking detector are fixed to the default parametrization. Any difference observed is then genuinely related to the change in the calorimeter geometry.

Figure 119 shows the jet mass distribution for different values of the  $G_{\text{RS}}$  mass, from 14 to 41 TeV. As a comparison, the corresponding distribution obtained clustering generated particles into jets (gen-jets) is shown, representing the ideal case of a perfect detector resolution. Table 38 summarises the resolution corresponding to each granularity scenario. The resolution is quantified with the  $\sigma$  parameter of a Gaussian fit to the distribution for mass values between 40 GeV and 140 GeV, scaled to the mean value of the Gaussian. Besides the worsening of the resolution with the coarser resolution, one should notice the increasing bias in the peak position and the larger non-Gaussian tails

$G_{\text{RS}}$ mass	gen-jets	baseline resolution	$\times 1/2$ granularity	$\times 2$ granularity
14 TeV	5%	16%	16%	28%
23 TeV	6%	22%	22%	29%
32 TeV	5%	24%	25%	33%
41 TeV	4%	28%	26%	36%

Table 38: Relative resolution of the jet mass peak for  $G_{\text{RS}} \rightarrow ZZ$  events produced in pp collisions at  $\sqrt{s} = 100$  TeV. The resolution is quantified as the ratio between the  $\sigma$  and  $m$  parameters of a Gaussian fit, in the jet mass range [40, 140] GeV.

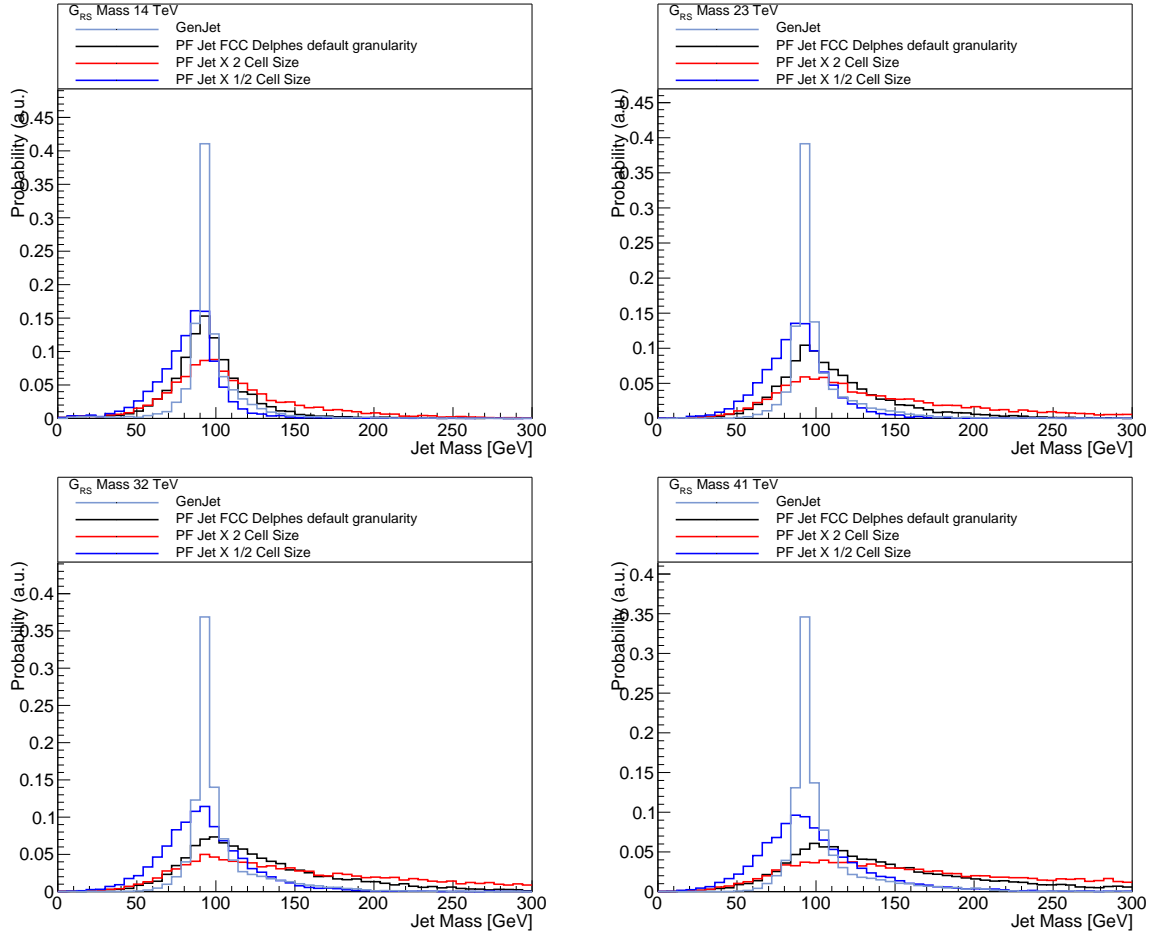


Fig. 119: Jet mass distribution for  $G_{RS}$  produced in pp collisions at  $\sqrt{s} = 100$  TeV and decaying to two  $Z$  bosons. The  $G_{RS}$  mass is fixed to 14 TeV (top left), 23 TeV (top right), 32 TeV (bottom left), and 41 TeV (bottom right). Different granularities are considered for the calorimeter cells. As a reference, the mass distribution for generator-level jets is also shown.

In Fig. 120, the mass distribution for the dijet system is shown for the same values of  $G_{RS}$  mass. The events are selected requiring  $80 < m_J \times m_Z / \text{mode}(m_J) < 100$  GeV for each jet. The dijet-mass reconstruction exhibits poor scale and resolution, induced by the small jet-size parameter  $R$ . In a realistic search, this effect could be cured using a wide cone for kinematic reconstruction and a narrow cone for jet tagging, similarly to what is currently done in some LHC search. In Fig. 120, the mass scale is partially compensated applying a  $m_Z / \text{mode}(m_J)$  rescale factor.

Besides the jet mass, the identification of boosted bosons usually exploits the so-called jet substructure, i.e. the study of the angular and momentum distribution of the jet constituents in a massive jet.

In the  $p_T$  range relevant for LHC searches, variables exploiting the jet substructure typically aim to identify jets whose constituents can be arranged into two subjets. At the FCC, the larger boost values accessible in 100 TeV collisions change substantially the experimental signature. The separation between the two subjets becomes very small for large  $G_{RS}$  mass values, as shown in Fig. 121.

Consequently, the boosted boson is better identified as a single narrow jet inside an otherwise empty jet, similarly to a  $\tau$  lepton. This is represented in Fig. 122, where the  $p_T$  flow of typical boosted bosons and ordinary QCD jets is shown for a small ( $m_{G_{RS}} = 5$  TeV) and a large ( $m_{G_{RS}} = 30$  TeV) value of  $m_{G_{RS}}$ . As a function of the  $\eta$  and  $\phi$  distance of each constituent from the jet centre, the constituent

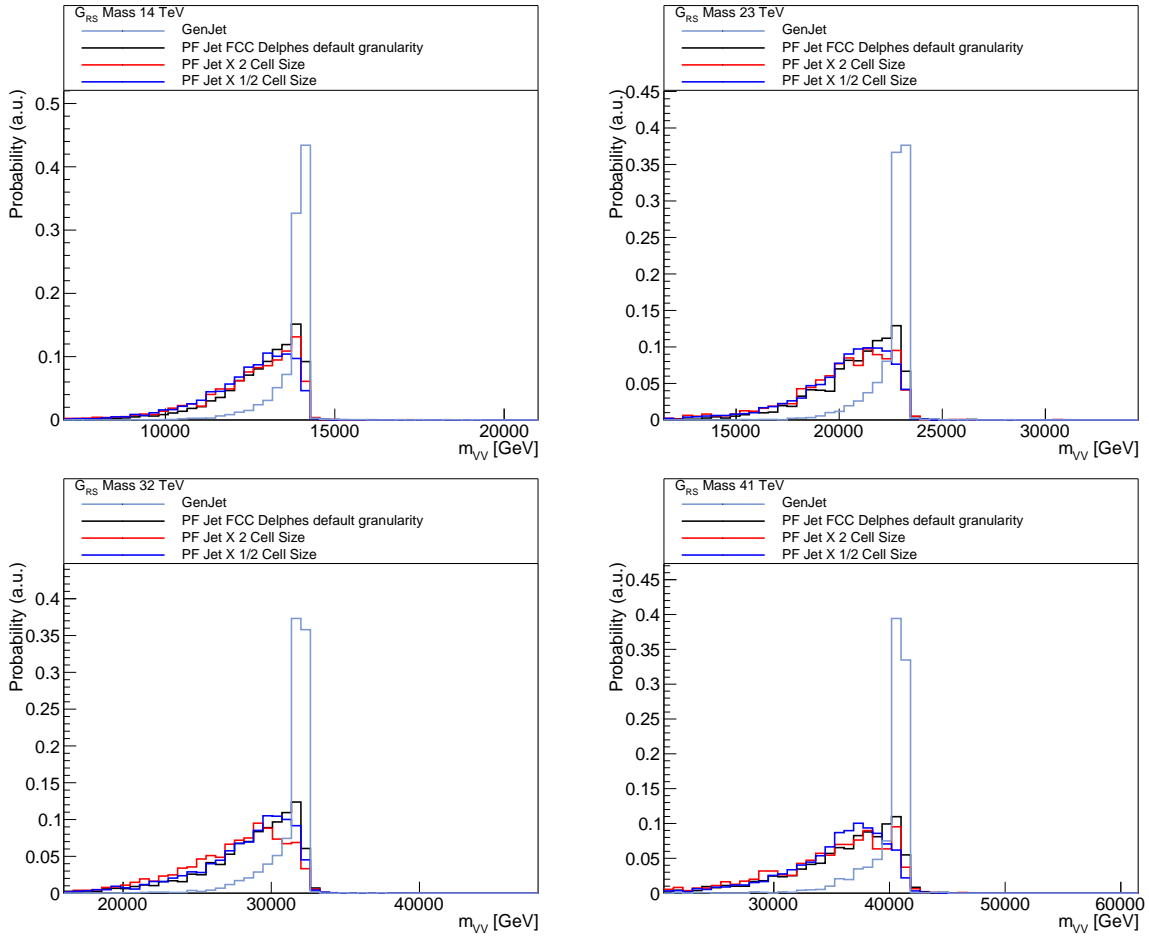


Fig. 120: Mass distribution for  $G_{RS}$  produced in pp collisions at  $\sqrt{s} = 100$  TeV and decaying to two  $Z$  bosons. The  $G_{RS}$  mass is fixed to 14 TeV (top left), 23 TeV (top right), 32 TeV (bottom left), and 41 TeV (bottom right). Different granularities are considered for the calorimeter cells. As a reference, the mass distribution for generator-level jets is also shown.

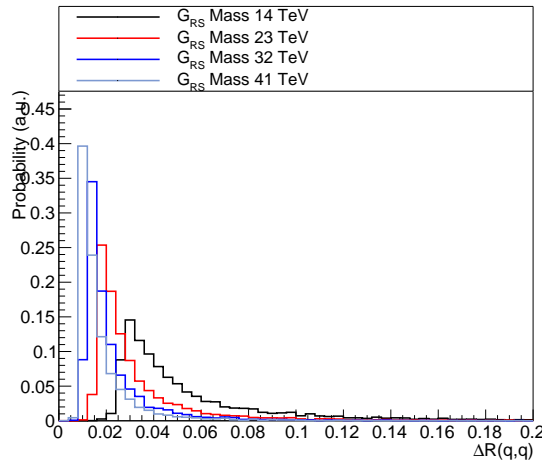


Fig. 121:  $\Delta R$  separation between the two quarks originating from the decay of a boosted  $Z$  bosons in  $G_{RS} \rightarrow ZZ$  events, for different values of the  $G_{RS}$  mass.

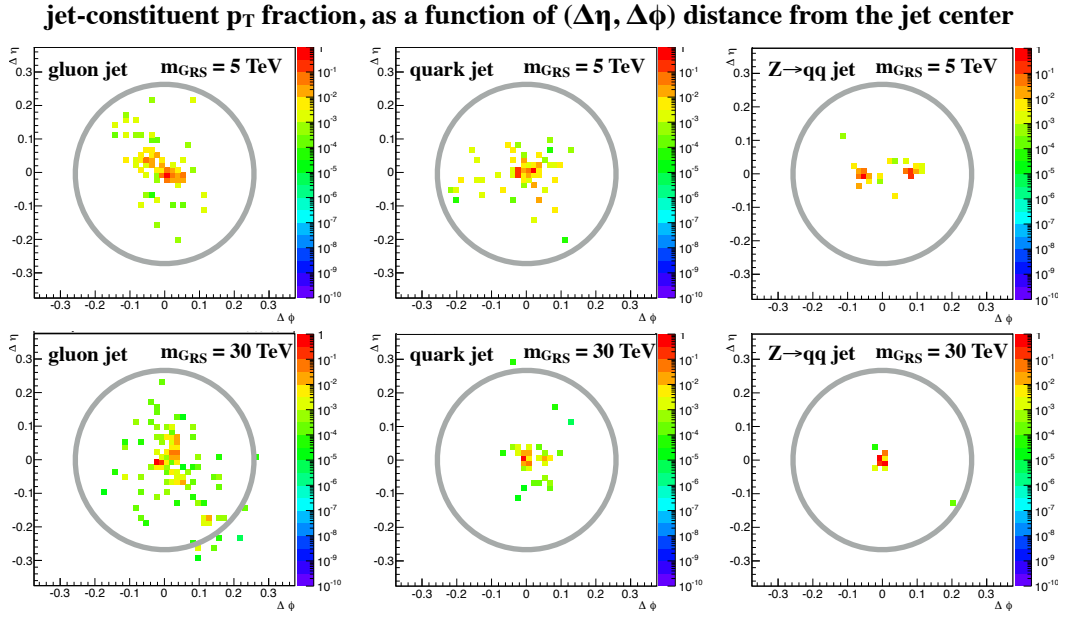


Fig. 122: Ratio between the  $p_T$  of jets constituents and jet  $p_T$  for jets originating from gluon (left), a quark (centre), and  $Z \rightarrow q\bar{q}$  (right), shown as a function of the  $\eta$  and  $\phi$  distance of each constituent from the jet centre. The top (bottom) plots refer to the highest- $p_T$  jet in a typical  $G_{RS}$  decay, for a mass value  $m_{G_{RS}} = 5$  TeV ( $m_{G_{RS}} = 30$  TeV). An angular matching to the generated  $Z$  boson is applied for  $Z \rightarrow q\bar{q}$ .

$p_T$  is shown, normalized to the jet  $p_T$ . For small  $m_{G_{RS}}$  two subjets in  $Z$  jets are visible inside the jet. For large  $m_{G_{RS}}$ , the two subjets merge into a single jet, while the rest of the jet is quite empty. For comparison, the corresponding distributions are shown for typical jets from gluons and quarks. No substantial change in the jet behavior is observed in this case.

In view of this difference, a change in strategy could improve the effectiveness of jet substructure as a tagging algorithm. As an example, we consider the five quantities:

$$Flow_{n,5} = \sum_p \frac{|p_T^p|}{|p_T^{jet}|} \quad (67)$$

where  $n = 1, \dots, 5$ ,  $p_T^{jet}$  and  $p_T^p$  are the jet and constituent transverse momenta, respectively. The sum in the equation extends over the jet constituents  $p$  such that

$$\frac{n-1}{5}R \leq \Delta R(p, jet) < \frac{n}{5}R, \quad (68)$$

where  $R$  is the jet size and  $\Delta R(p, jet) = \sqrt{(\Delta\eta)^2 + (\Delta\phi)^2}$  is the angular distance between a given jet constituent and the jet axis.

The five  $Flow_{n,5}$  quantities are used together with the jet mass as input features to train a boosted decision tree (BDT), using the TMVA package [362]. The BDT is trained using as a signal sample  $G_{RS} \rightarrow ZZ$  events with hadronically decaying  $Z$  bosons, while the background training sample is provided by jets from  $G_{RS} \rightarrow q\bar{q}$  events ( $q = u, d, c, s, b$ ). The training is repeated for several values of  $m_{G_{RS}}$ . For comparison, a BDT discriminant is trained with the same procedure, using as input features the jet mass and the subjettness ratio  $\tau_2/\tau_1$ . The subjettness variables [345] are here used as a reference

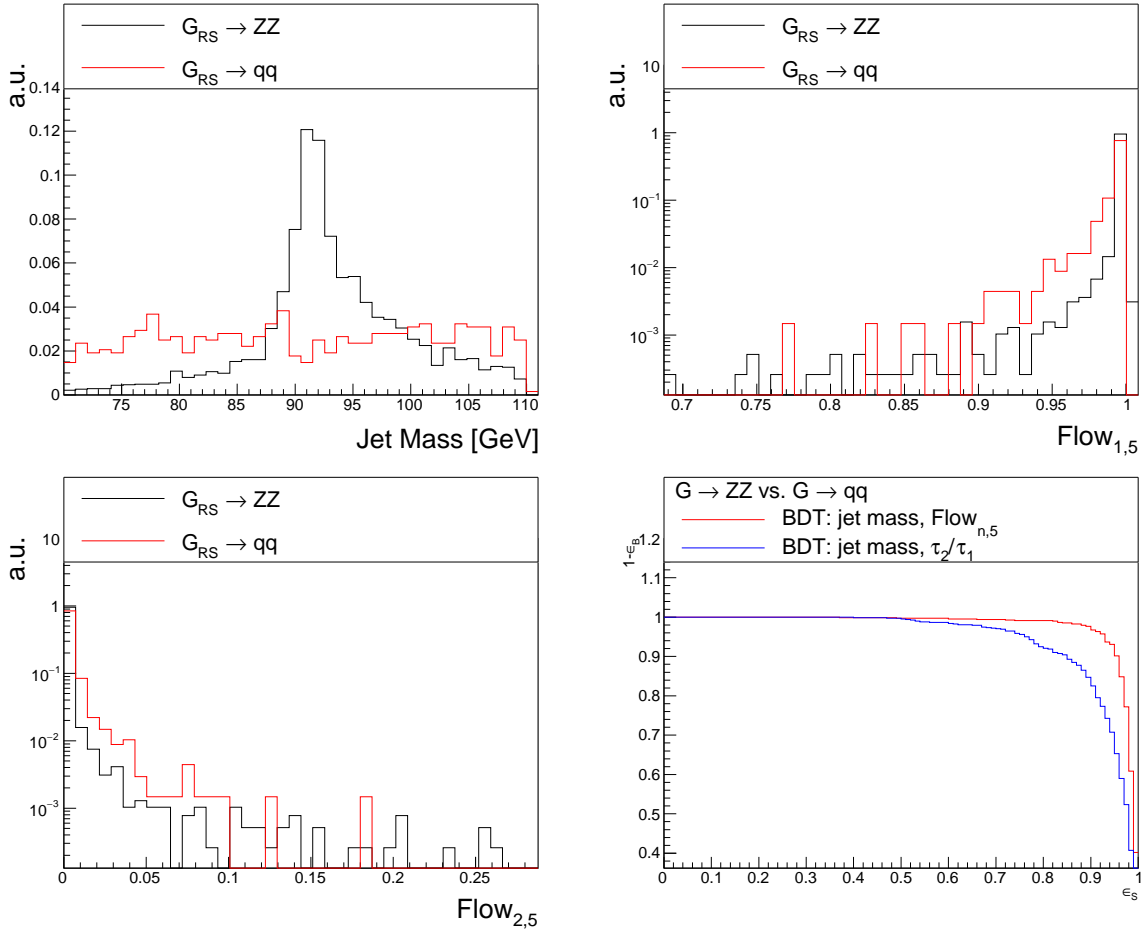


Fig. 123: Distribution of the Jet mass (top left),  $Flow_{1,5}$  (top right), and  $Flow_{2,5}$  (bottom left) for a signal hadronically decaying  $Z$  bosons in  $G_{RS} \rightarrow ZZ$  events and a background of jets in  $G_{RS} \rightarrow q\bar{q}$  events. The ROC curve for a BDT trained from the five  $Flow_{n,5}$  and the jet mass is shown in the bottom-right plot, compared to the corresponding ROC curve trained from the jet mass and the subjeettness ratio  $\tau_2/\tau_1$ . The  $G_{RS}$  mass is fixed to 32 TeV.

of the typical strategy followed for  $V$ -jet tagging at the LHC. The distribution of the jet mass,  $Flow_{1,5}$ ,  $Flow_{2,5}$ , and the ROC curves for the two BDTs are shown in Fig. 123.

The left plots in Fig. 124 show the tagging efficiency obtained as a function of the  $G_{RS}$  mass for the two discriminators when the false-positive rate (mistag) is fixed to 10%, training the algorithm against quark and gluon jets. The right plots in the same figure shows the mistag as a function of the  $G_{RS}$  mass, when the tagging efficiency is fixed to 80%. Similar results are obtained when  $G_{RS} \rightarrow gg$  events are used as background.

While this study highlights the importance of highly granular calorimeters in with largely boosted vector-boson tagging, the strategy discussed here is far from being an optimal exploitation of the information provided by a granular calorimeter. In this respect, progresses made on image recognition and deep learning could have a big impact on jet tagging in the future, as discussed in Ref. [363, 364].

## 9.5 Jet fragmentation at large $p_T$

The ability to tag a jet by measuring its mass or other properties requires excellent resolution of its constituent particles. For optimal energy and angular resolution, finely segmented calorimetry and precise tracking systems are required. The resolution of both will depend on the density of tracks and their

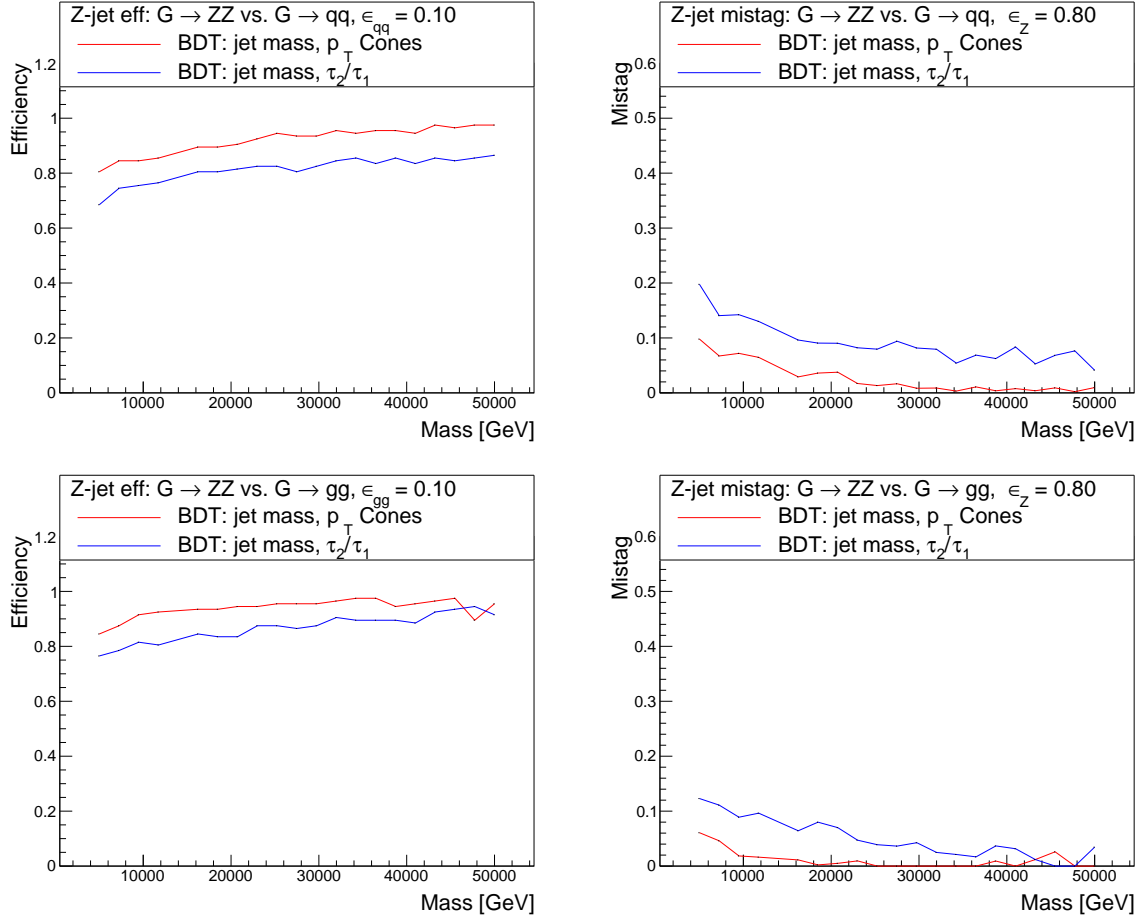


Fig. 124: Discrimination power of the V-tagging algorithms against quark (top) and gluon (bottom) jets: tagging efficiency as a function of the  $G_{RS}$  mass corresponding to a mistag rate of 10% (left) and mistag rate as a function of the  $G_{RS}$  mass for a tagging efficiency of 80% (right).

momentum. In a high-density environment, it will be challenging to identify individual tracks, thereby reducing mass resolution. At extremely high momenta, tracks will not bend substantially in the tracking magnetic field and their charge and momentum may not be able to be determined. Designing tracking systems that can resolve both of these issues will be required.

All plots in this section are generated using the same event and jet criteria as discussed in Section 9.2. In particular, we require that all particles used in identifying jets have pseudorapidity  $|\eta| < 2.5$ .

In Figs. 125-128, we plot the average (mean) number of tracks with  $p_T > p_T^{\min}$  in jets with radius  $R = 0.5$  from the resonance decays studied throughout this section. These plots demonstrate, for example, that a jet of any flavor from the decay of 10 TeV resonance will have at least one track with  $p_T \gtrsim 500$  GeV. For jets from the decays of 40 TeV resonances, every jet will have at least one track with  $p_T$  greater than about 2 TeV. For precision measurements, it may be necessary to consider rarer configurations; say, tracks that occur in 10% or even only 1% of jets. In this case, for jets from 10 TeV resonances, 1% of jets will have a track with  $p_T \gtrsim 2$  TeV, while for jets from 40 TeV resonances, this is increased to about 10 TeV.

While we have shown plots for jets with radius  $R = 0.5$ , except at low  $p_T$ , these plots are relatively insensitive to jet radius. Because these tracks carry such a large fraction of the total jet's transverse momentum, they must be located very near the center of the jet.

In addition to having a sufficiently high magnetic field to measure the momentum of high  $p_T$

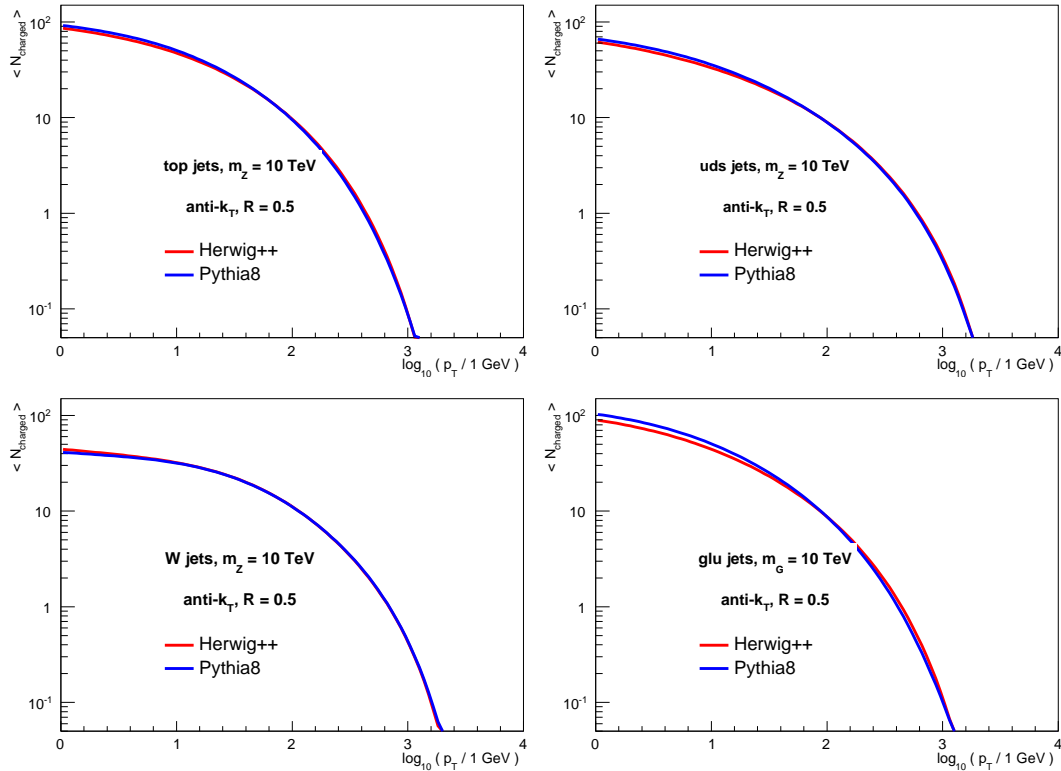


Fig. 125: Average number of charged tracks with  $p_T > p_T^{\min}$  in  $R = 0.5$  anti- $k_T$  jets produced from 10 TeV resonance decays to tops, light QCD quarks,  $W$ s, and gluons.

tracks, the tracking system must also be able to resolve particles in a high density environment. As a proxy for tracker densities, in Figs. 129-132, we plot the median angle  $\Delta \bar{R}$  between two tracks with  $p_T$  greater than a minimum value. The way that this median angle is defined is as follows. First, we take all tracks in a single jet with  $p_T$  greater than a minimum value and find the median distance between pairs of those tracks. Note that for a jet with two hard prongs (like a boosted  $W$ ), this median value will typically be either close to 0 or  $2m/p_T$ , depending on the precise distribution of tracks in the jet. We take the median rather than the mean pairwise track distance because the median is insensitive to outliers and corresponds to the angular scale at which half of the pairs have a larger angle and half a smaller angle. Then, the median pairwise angle of each jet is averaged over the ensemble.

These jets are produced from decays of resonances ranging from 10 to 40 TeV, and this median angle exhibits strong jet  $p_T$  and flavor dependence. The distribution of this median angle for quark and gluon flavor jets has no structure and the angle between tracks with the same  $p_T$  is approximately twice as large for gluons as compared to quarks. Because quark and gluon jets have no intrinsic high energy scale associate with them, the distributions with different jet  $p_T$ s are simply scaled by the ratio of their  $p_T$ s. In the high mass tail, the mass of the jet is determined by the relative angle of the hardest particles in the jet.

The median angle between high  $p_T$  tracks for top quark or  $W$  jets is very different. These jets do have an intrinsic scale, and so this median angle should manifest these scales. For a jet with two-prongs (like from a hadronically-decaying  $W$ ) with mass  $m$  and transverse momentum  $p_T$ , the characteristic angle between the hard prongs is  $\theta = 2m/p_T$ . Assuming that the prongs are very narrow and otherwise approximately identical, when averaged over the jet ensemble, the median pairwise angle will be roughly  $R^{\text{med}} \simeq m/p_T$ . For a jet with more hard prongs, like a top quark jet, the median angle will be closer to

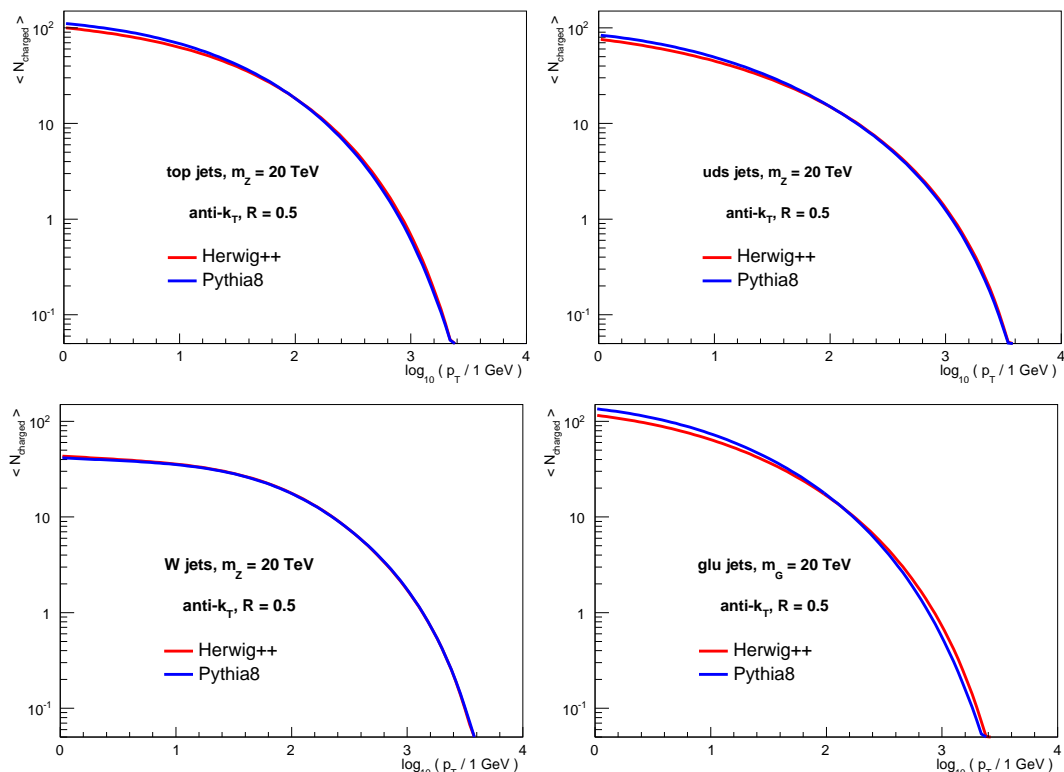


Fig. 126: Average number of charged tracks with  $p_T > p_T^{\min}$  in  $R = 0.5$  anti- $k_T$  jets produced from 20 TeV resonance decays to tops, light QCD quarks,  $W$ s, and gluons.

the characteristic jet angle. The characteristic angular scales in top quark jets and  $W$  jets are

$$R_t^{\text{med}} \simeq \frac{2m_t}{p_T}, \quad R_W^{\text{med}} \simeq \frac{m_W}{p_T}. \quad (69)$$

Especially at the highest resonance masses, features are present in the top and  $W$  distributions near these angles. Combining the information in Fig. 128 and Fig. 132, for instance, requires resolving angular scales of  $\Delta\tilde{R} \lesssim 10^{-3}$  to be able to reconstruct the substructure of boosted  $W$  bosons from 40 TeV resonances.

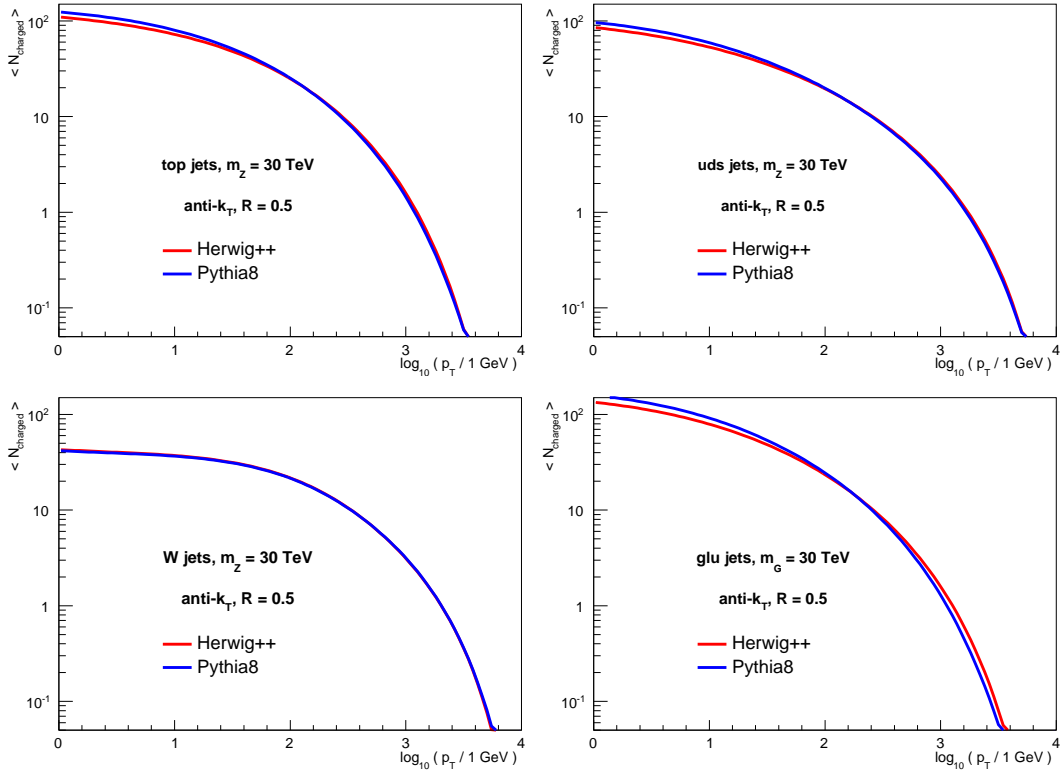


Fig. 127: Average number of charged tracks with  $p_T > p_T^{\min}$  in  $R = 0.5$  anti- $k_T$  jets produced from 30 TeV resonance decays to tops, light QCD quarks,  $W$ s, and gluons.

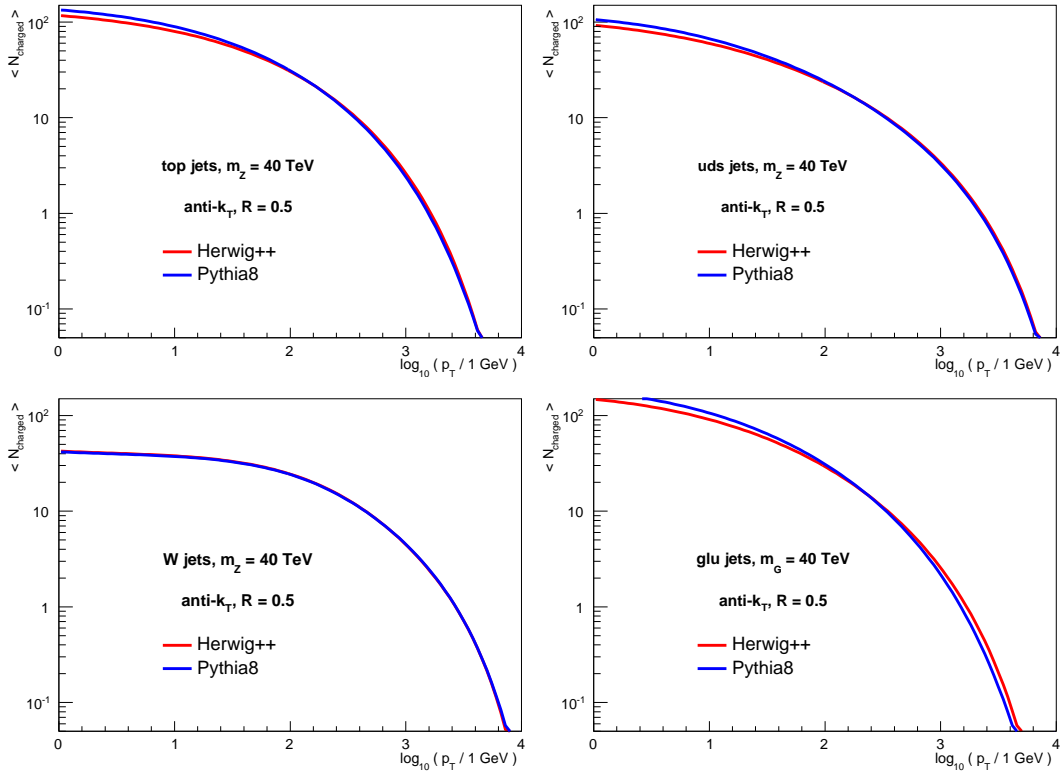


Fig. 128: Average number of charged tracks with  $p_T > p_T^{\min}$  in  $R = 0.5$  anti- $k_T$  jets produced from 40 TeV resonance decays to tops, light QCD quarks,  $W$ s, and gluons.

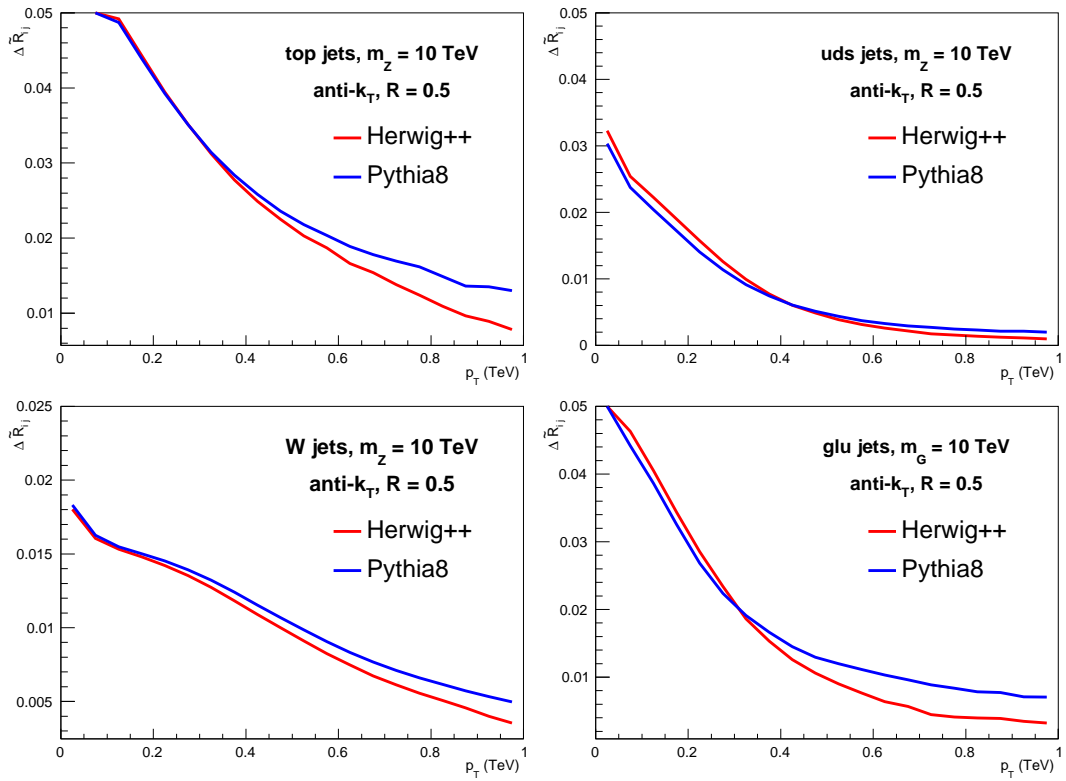


Fig. 129: Median angular separation  $\Delta\tilde{R}$  between charged tracks with  $p_T > p_T^{\min}$  in  $R = 0.5$  anti- $k_T$  jets produced from 10 TeV resonance decays to tops, light QCD quarks,  $W$ s, and gluons.

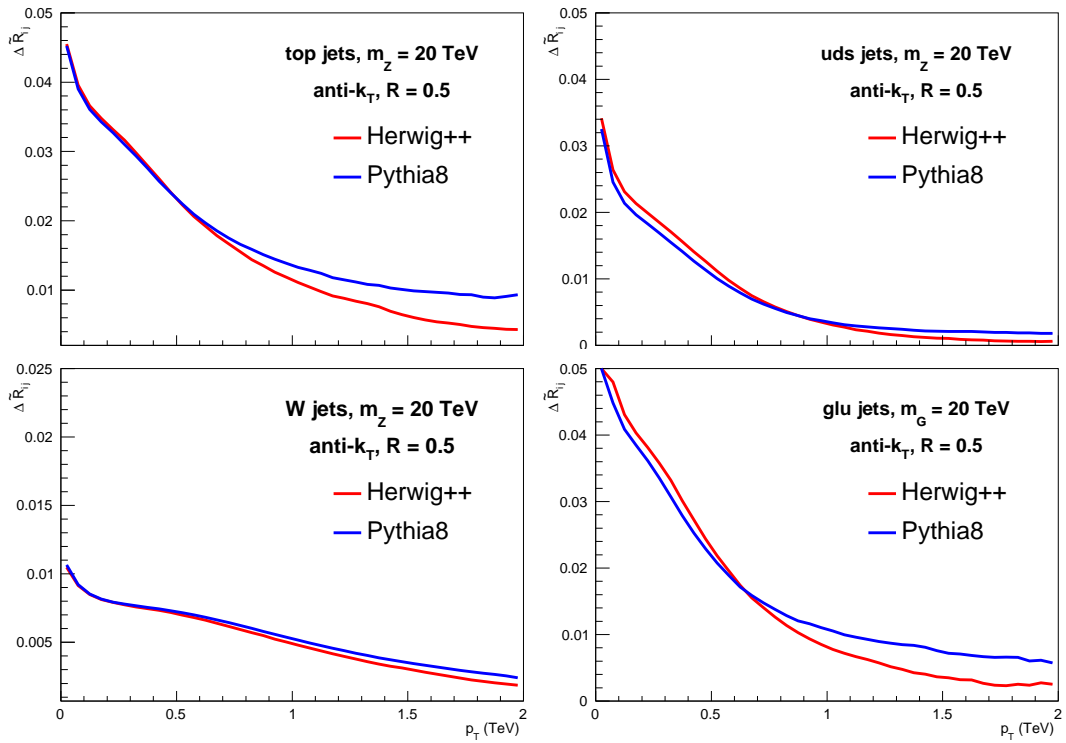


Fig. 130: Median angular separation  $\Delta\tilde{R}$  between charged tracks with  $p_T > p_T^{\min}$  in  $R = 0.5$  anti- $k_T$  jets produced from 20 TeV resonance decays to tops, light QCD quarks,  $W$ s, and gluons.

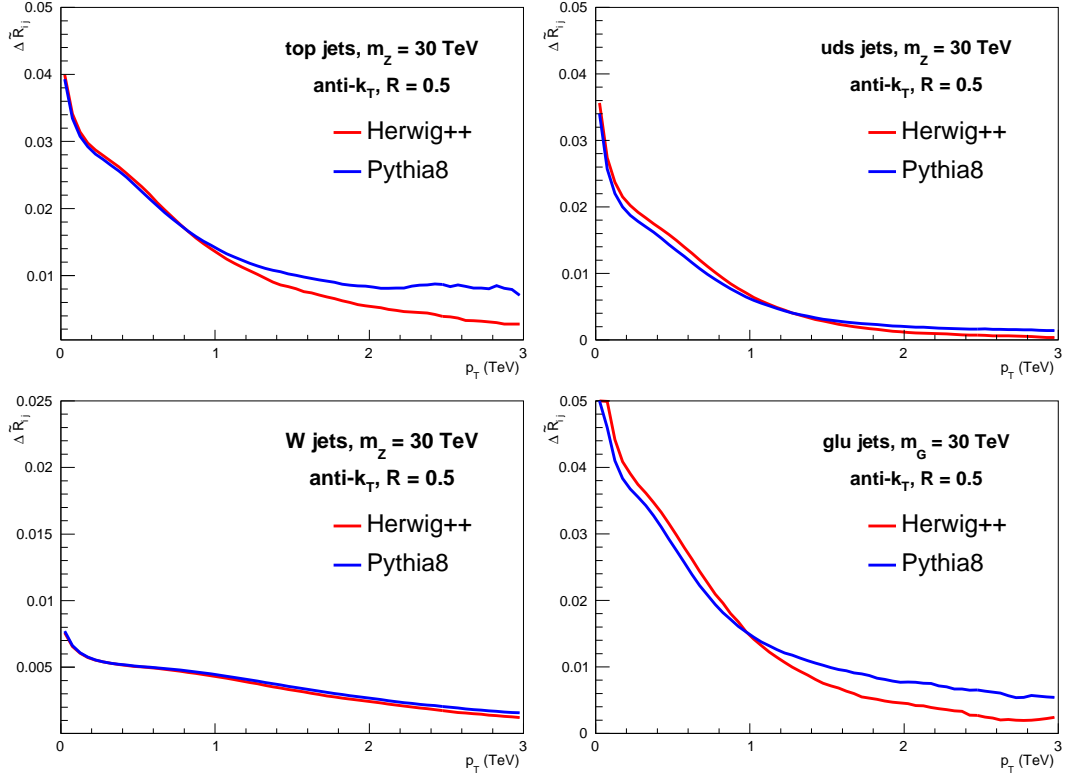


Fig. 131: Median angular separation  $\Delta \tilde{R}$  between charged tracks with  $p_T > p_T^{\min}$  in  $R = 0.5$  anti- $k_T$  jets produced from 30 TeV resonance decays to tops, light QCD quarks,  $W$ s, and gluons.

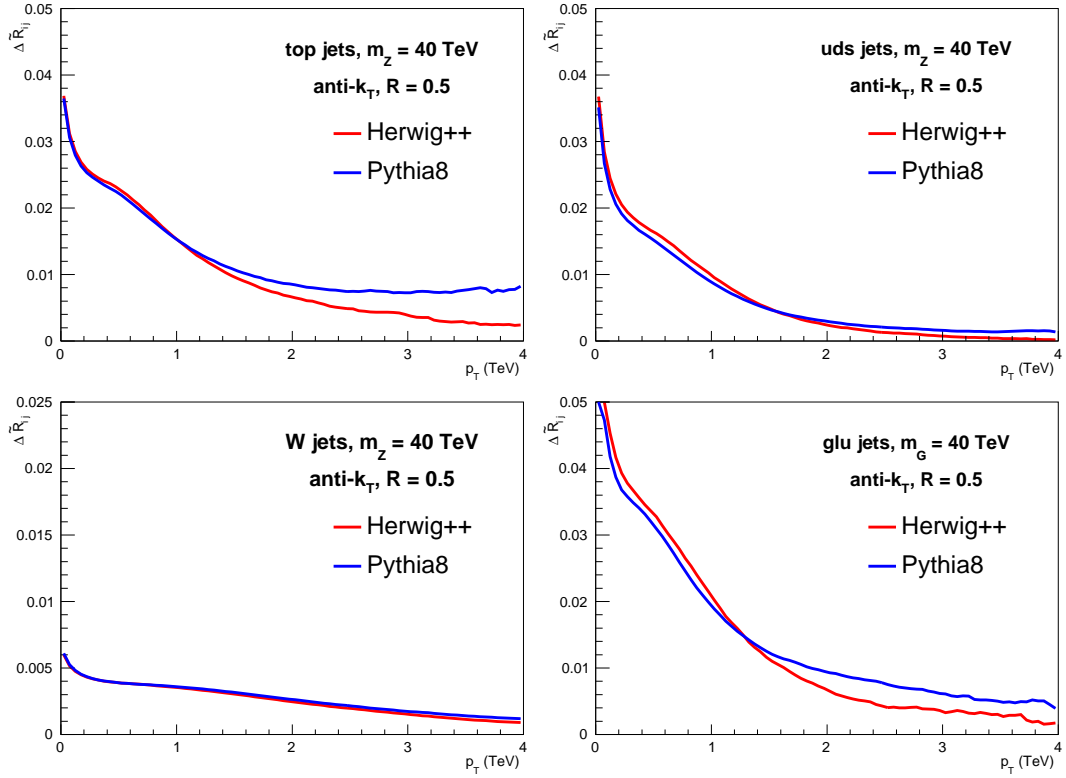


Fig. 132: Median angular separation  $\Delta \tilde{R}$  between charged tracks with  $p_T > p_T^{\min}$  in  $R = 0.5$  anti- $k_T$  jets produced from 40 TeV resonance decays to tops, light QCD quarks,  $W$ s, and gluons.

## 10 Multijets<sup>29</sup>

In this section we explore the total rates and distributions for final states with multiple jets and photons. An overall feature of the results presented here is the huge amount of multi-jet activity that could be measured within the first few days of running. This opens up many possibilities for searches of exotic physics beyond the Standard Model such as black holes or instantaneous decaying into jets. A large number of events containing systems with effective masses of 10 or even 20 TeV would be observed which will also explore a region where no prior experience of QCD exists.

A variety of different kinematic configurations are considered. These can be broadly classified into two categories: *democratic*, in which cuts on the transverse momenta of all jets are treated equally, and *hierarchical*, in which harder cuts on the leading jet are applied. The choices are known to affect the perturbative stability of the observables which we investigate in Section 10.3.

### 10.1 Computational setup

For the following studies, the SHERPA event generation framework [102, 213] has been used. Proton–proton collisions at centre-of-mass energies of 100 TeV are considered and, in relevant cases, compared to collisions at LHC scale energies of 14 TeV to highlight interesting features of energy scaling. Unless stated otherwise, jets are reconstructed with the anti- $k_{\perp}$  algorithm with a radius parameter of  $R = 0.4$ , using the FASTJET package [203, 212]. The Standard Model input parameters are defined through the  $G_{\mu}$  scheme. Unstable fermions and bosons are treated through the complex mass scheme [233]. All quarks apart from the top-quark are assumed to be massless. The effects of the top-quark are included in the running of  $\alpha_S$  for scales above the its mass. For matrix element generation and cross section calculations, the COMIX matrix element generator [214] is employed. For the proton PDFs the NNPDF3.0 NLO set [7] is used, which also provides the strong coupling  $\alpha_S$ . Renormalisation and factorisation scales are defined in a process-specific way, and are listed separately in the respective subsections. For most distributions the multijet merging technology of [224, 225, 365]<sup>30</sup> is employed, with the parton shower built on Catani-Seymour subtraction kernels as proposed in [226] and implemented in [227].

Next-to-leading order corrections are generated at fixed order using SHERPA together with the NJET one-loop matrix element provider [373]. Real radiation is provided via the Catani-Seymour subtraction method implemented in SHERPA [223] and the COMIX matrix element generator [214]. Root Ntuples are generated and analysed using the CT14nlo PDF set [8] which provides the strong coupling  $\alpha_S(m_Z) = 0.118$ .

#### 10.1.1 Kinematic cuts

Various cuts on the transverse momentum of the jets are considered and specified in the later discussions. For runs with LO+PS/MEPS@LO no additional kinematic requirements were taken for multi-jet production. For processes involving photons, the additional constraint that each photon should be at a radius of least  $\Delta R \geq 0.4$  from every jet was imposed.

At NLO a mild rapidity cut on all jets and photons  $|\eta_{j/\gamma}| < 8$  was taken in addition to these requirements. At NLO care must be taken to ensure photon final states are infrared safe. Accordingly, we used the standard Frixione smooth cone isolation [290] with parameters  $R = 0.4$ ,  $\varepsilon = 0.1$  and  $n = 1$ .

<sup>29</sup>Editors: S. Badger and F. Krauss

<sup>30</sup>It is worth noting that other merging techniques exist, like for instance [366–371], which however by far and large have been shown to yield comparable results at lower energies, see for example [372].

### 10.1.2 Scale choices

In this section, we use a dynamic choice in general for the factorisation and renormalisation scales,  $\mu_{F/R}$ , given by the sum of transverse momenta

$$\frac{1}{2}\hat{H}_T = \frac{1}{2} \left( \sum_i p_{T,i} \right). \quad (70)$$

For the fixed-order calculations in Section 10.3, the sum runs over final-state partons. This includes a single photon, if present. For processes with two photons in the final state, we use

$$\frac{1}{2}\hat{H}'_T = \frac{1}{2} \left( m_{T,\gamma\gamma} + \sum_{i \in \text{partons}} p_{T,i} \right), \quad (71)$$

with  $m_{T,\gamma\gamma}$  the transverse mass of the diphoton system. For the leading-order SHERPA setups considered in the following Section 10.2 the sum goes over anti- $k_T$  jets instead (and photons), and is averaged:

$$\bar{H}_T = \frac{1}{N_{\text{jet}} + N_\gamma} \sum_i p_{T,i}. \quad (72)$$

## 10.2 Leading order inclusive cross sections and distributions

We performed the calculations in this section with SHERPA at LO, unless stated otherwise. We begin with the inclusive multi-jet production rates for up to 8 eight final state jets in Table 39. The rates are calculated with varying a minimal  $p_T$  cut, ranging from 50 GeV to 1 TeV and two different values of the anti- $k_T$  radius parameter,  $R = 0.2$  and  $R = 0.4$ . Within the first days of running nanobarn cross-section events with 3 or 4 jets of 250 GeV could be observed and final states with up to eight 1 TeV jets will be observable with the order of a few thousand events with the planned integrated luminosity. We also show the scaling behaviour of the ratio  $\sigma(R = 0.4)/\sigma(R = 0.2)$  in Fig. 133b using various minimum  $p_T$  cuts. Assuming that jets are not overlapping, i.e. their distance  $\Delta R$  in  $\eta$ - $\phi$  being  $\Delta R > 2R$ , the total area  $a$  they cover is given by

$$a = N_J \pi R^2 \approx \begin{cases} 0.5 \cdot N_{\text{jet}} & \text{for } R = 0.4, \\ 0.13 \cdot N_{\text{jet}} & \text{for } R = 0.2. \end{cases} \quad (73)$$

For a detector with a coverage over 10 units in pseudo-rapidity, similar to ATLAS or CMS at the LHC, the total acceptance region is  $2\pi\Delta\eta \approx 63$ . In both cases of  $R = 0.4$  or  $R = 0.2$  the total coverage is much greater than the area of the jets and so the scaling behaviour is not driven by phase-space effects in acceptance but expected to be defined through QCD dynamics. The total inclusive cross sections are compared to the those at 14 TeV in Fig. 133a where one clearly sees the increasing multiplicity of events at the higher centre-of-mass energy.

In Table 40 we consider inclusive cross sections based on the corresponding leading order matrix elements for multijet events with a minimum  $p_T$  of 50 GeV and different values of minimum leading-jet transverse momentum. One sees again that extreme kinematic configurations are clearly accessible, opening up unexplored areas of QCD dynamics. However, one can observe that some of the leading order rate estimates do not decrease with increasing final state multiplicity. Having a much harder cut on the leading jet than on the subleading ones induces large scale hierarchies and thus necessitates to consider higher order (logarithmic) corrections, e.g. through a parton shower simulations, cf. Sections 10.3 and 10.4. Turning our attention to the  $p_T$  spectra, in Fig. 134 we show cumulative distributions for a democratic cut of 1 TeV on all jets for the first 6 jets ordered in  $p_T$ . This sample now has been generated using a MEPS@LO setup with matrix elements for up to two additional jets on top of the dijet

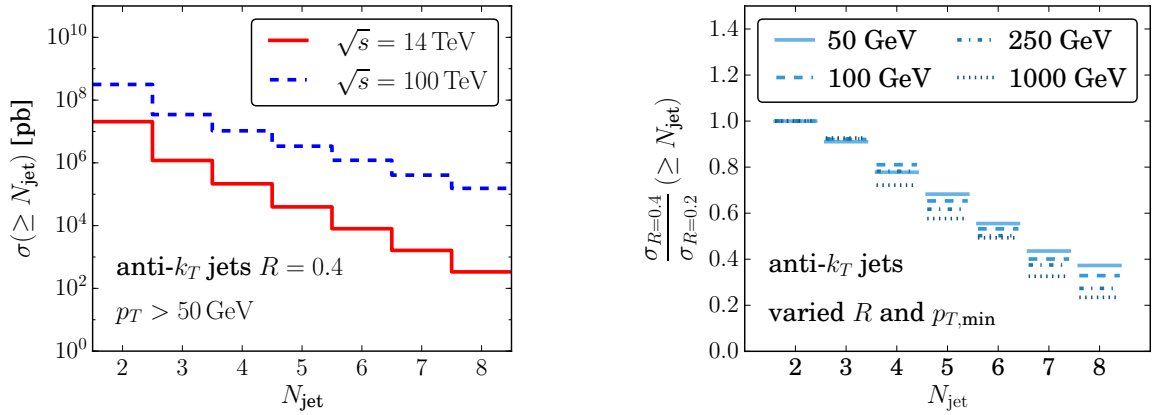
$j^n$ with $R = 0.2$				
$n / p_{T,j}$	50 GeV	100 GeV	250 GeV	1000 GeV
2	315(1) $\mu\text{b}$	29.9(1) $\mu\text{b}$	1045(4) nb	3483(10) pb
3	38.0(3) $\mu\text{b}$	2.51(2) $\mu\text{b}$	54.1(3) nb	72.0(4) pb
4	13.5(1) $\mu\text{b}$	665(7) nb	10.0(1) nb	6.83(7) pb
5	4.98(7) $\mu\text{b}$	199(2) nb	2.02(2) nb	621(4) fb
6	2.18(2) $\mu\text{b}$	65.8(7) nb	456(5) pb	57.8(4) fb
7	0.93(2) $\mu\text{b}$	23.5(3) nb	112(1) pb	7.21(6) fb
8	0.413(9) $\mu\text{b}$	8.1(2) nb	29.7(4) pb	0.832(8) fb
$j^n$ with $R = 0.4$				
$n / p_{T,j}$	50 GeV	100 GeV	250 GeV	1000 GeV
2	315(1) $\mu\text{b}$	29.9(1) $\mu\text{b}$	1045(4) nb	3483(10) pb
3	34.6(3) $\mu\text{b}$	2.31(1) $\mu\text{b}$	49.9(3) nb	66.7(3) pb
4	10.5(1) $\mu\text{b}$	539(5) nb	7.82(8) nb	4.93(4) pb
5	3.40(4) $\mu\text{b}$	130(1) nb	1.247(9) nb	358(2) fb
6	1.21(1) $\mu\text{b}$	35.0(3) nb	229(2) pb	28.5(1) fb
7	0.406(6) $\mu\text{b}$	9.42(9) nb	42.0(4) pb	2.35(2) fb
8	0.154(2) $\mu\text{b}$	2.66(4) nb	8.12(9) pb	0.195(1) fb

Table 39: Leading order cross sections for the production of anti- $k_T$  jets with varying minimal  $p_T$ , ranging from 50 GeV to 1 TeV and two different values of the jet algorithm radius parameter,  $R = 0.2$  and  $R = 0.4$ . For the calculation the scales  $\mu_{F,R} = \bar{H}_T$  have been used.

$j^n$ with $p_{T,j}^{\min} \geq 50$ GeV varying $p_{T,j}^{\text{lead}}$					
$n / p_{T,j}^{\text{lead}}$	500 GeV	1000 GeV	2000 GeV	5000 GeV	10000 GeV
2	67.4(2) nb	3.48(1) nb	139(1) pb	1.06(1) pb	11.3(1) fb
3	178(1) nb	11.0(1) nb	485(3) pb	3.91(2) pb	39.3(1) fb
4	214(2) nb	16.9(1) nb	864(8) pb	7.39(7) pb	74.6(6) fb
5	191(1) nb	18.7(1) nb	1093(7) pb	10.6(1) pb	102(1) fb
6	136(2) nb	16.3(2) nb	1133(1) pb	11.9(1) pb	113(1) fb

Table 40: Leading order cross sections for the production of anti- $k_T$  jets with minimal  $p_T$  of 50 GeV different values of leading-jet transverse momentum. For the calculation the scales  $\mu_{F,R} = \bar{H}_T$  have been used.

core process merged together and dressed with parton showers. Though the energy distribution for the highest multiplicity jets fall quickly many events where the 6th jet has still more than 400–500 GeV will



(a) Cross section comparison between collisions at  $\sqrt{s} = 14$  TeV and  $\sqrt{s} = 100$  TeV.

(b) Cross section ratios for different jet radii  $R = 0.4$  and  $R = 0.2$ . Four different  $p_{T,\min}$  cuts are employed.

Fig. 133: Inclusive multiplicity cross sections for anti- $k_T$  jet production at leading order for  $pp$  collisions. The scales are set to  $\mu_{F,R} = \bar{H}_T$ .

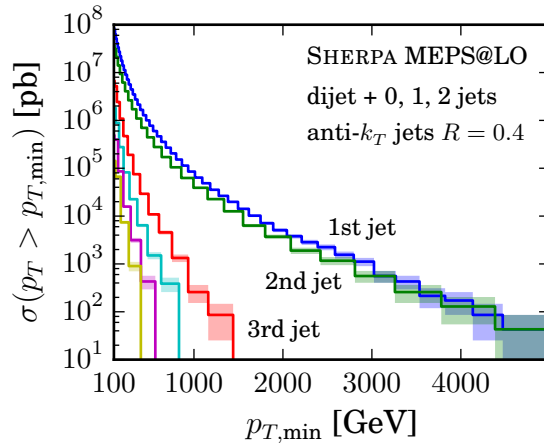


Fig. 134: Cumulative leading order  $p_T$  distributions for the first six highest  $p_T$  jets ordered in  $p_T$ . The labels for the 4th through 6th jet are omitted, but follow the natural order.

be observed. The leading jets are accessible at energies much greater than 3 TeV, which we will explore further in the next section.

### 10.2.1 Jet production in association with one or two photons

Multijet events in association with photons are important backgrounds to new physics searches. Ratios of  $Z/\gamma$  production can be used to estimate missing transverse energy from decays of the Z boson into neutrinos. Di-photon signals are particularly important when studying Higgs or potentially higher mass scalar resonances.

Table 41 shows leading order, i.e. pure tree-level, cross sections for the production of one or two photons in association with jets with varying minimal  $p_T$ , ranging from 50 GeV to 1 TeV and fixed  $R = 0.4$ . The transverse momentum of the photon(s) must satisfy  $p_{T,\gamma} \geq 50$  GeV, and the photon(s)

		$\gamma j^n$			
$n / p_{T,j}$	50 GeV	100 GeV	250 GeV	1000 GeV	
1	75.19(8) nb	9.38(2) nb	479.0(9) pb	3.045(6) pb	
2	27.3(1) nb	7.62(3) nb	932(4) pb	14.31(5) pb	
3	14.8(2) nb	2.37(3) nb	129(1) pb	573.(4) fb	
4	6.95(6) nb	757(6) pb	26.5(2) pb	52.1(5) fb	
5	3.20(3) nb	253(2) pb	5.61(4) pb	4.51(3) fb	
6	1.43(2) nb	82.7(8) pb	1.20(2) pb	0.404(3) fb	
7	0.603(7) nb	27.1(4) pb	0.262(3) pb	< 1 fb	
		$\gamma\gamma j^n$			
$n / p_{T,j}$	50 GeV	100 GeV	250 GeV	1000 GeV	
0	47.7(1) pb	47.7(1) pb	47.7(1) pb	47.7(1) pb	
1	29.74(7) pb	13.56(3) pb	2.007(5) pb	35.1(1) fb	
2	30.9(2) pb	12.02(7) pb	2.43(1) pb	84.3(4) fb	
3	21.0(8) pb	5.35(4) pb	532(4) fb	5.04(4) fb	
4	12.9(1) pb	2.25(1) pb	131.2(8) fb	519(2) ab	
5	7.02(6) pb	847(8) fb	30.6(3) fb	49.2(3) ab	

Table 41: Leading order cross sections for the production of anti- $k_T$  jets in association with one or two photons. Democratic cuts on all jet  $p_T$  are taken at 50, 100, 250 and 1000 GeV. The photon transverse momenta must be larger than  $p_{T,\gamma} > 50$  GeV and separated from all jets by at least  $\Delta R \geq 0.4$ .

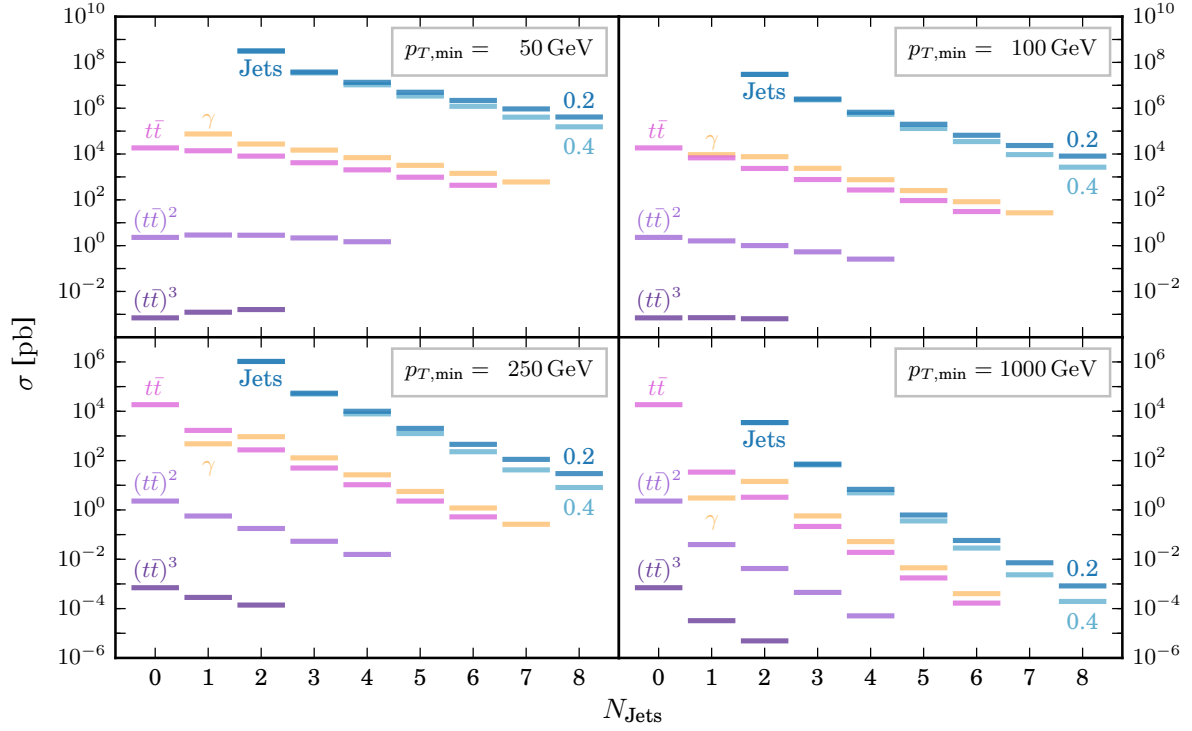
must be separated from jets or other photons by at least  $\Delta R \geq 0.4$ . Even though the additional powers of  $\alpha$  lower the production rates considerably diphoton production with up to 2 or 3 TeV jets could be observed with the full integrated luminosity.

To summarise the leading order results in this section we collect a number of multi-jet QCD processes in Fig. 135. For four different values of the minimum  $p_T$  we show pure jet productions with up to 8 jets and single photon with up to 7 jets. As a comparison we also show top pair production with up to 6 jets, two quark pairs with up to 4 jets and three top pairs with up to two jets. The fact that the latter processes are accessible with relatively high- $p_T$  jets impressively demonstrates the degree to which QCD can be studied in the 100 TeV environment, opening up huge amounts of phase-space for new physics searches.

### 10.3 NLO cross sections and K-factors

#### 10.3.1 Multijet production

To study the impact of NLO correction representative NLO/LO  $K$ -factors are presented with democratic cuts on all jets and hierarchical cuts on the leading jet. In Table 42 we show the LO and NLO cross-sections for up to four jets with democratic cuts on all jet transverse momenta of 50 or 500 GeV. Since the back-to-back configuration for di-jets cause the NLO phase-space to become singular the cross-section is


 Fig. 135: Inclusive cross section comparison between various QCD processes for different  $p_{T,\min}$ .

$n$	$p_T^{\min} > 50 \text{ GeV}$			$p_T^{\min} > 500 \text{ GeV}$		
	LO	NLO	K	LO	NLO	K
2	$289.0^{+8.7}_{-13.6} \mu\text{b}$	–	–	$66.0^{+12.2}_{-9.8} \text{nb}$	–	–
3	$28.5^{+7.1}_{-5.4} \mu\text{b}$	$15.1^{+3.1}_{-6.8} \mu\text{b}$	$0.5^{+0.26}_{-0.30}$	$1.7^{+0.6}_{-0.4} \text{nb}$	$1.4^{+0.0}_{-0.3} \text{nb}$	$0.8^{+0.27}_{-0.31}$
4	$6.9^{+2.9}_{-1.9} \mu\text{b}$	$2.2^{+1.3}_{-3.4} \mu\text{b}$	$0.3^{+0.40}_{-0.45}$	$153.2^{+68.3}_{-44.6} \text{pb}$	$132.8^{+0.0}_{-27.9} \text{pb}$	$0.9^{+0.34}_{-0.39}$

 Table 42: Inclusive cross-sections for multijet production at NLO and LO using democratic cuts of 50 and 500 GeV. Renormalisation and factorisation scales are chosen equal with a central values  $\mu_R = \mu_F = \hat{H}_T/2$  with theoretical uncertainty estimated through variations over the range  $[1/2, 2]$ . Cross-sections for massless  $2 \rightarrow 2$  scattering are not well defined at NLO so the results are omitted (see footnote on page 142).

not well defined and the numbers are not quoted<sup>31</sup>. In Fig. 136 we show distributions for the 1st and 2nd jets ordered in  $p_T$ . Variations in the unphysical factorisation and renormalisation scale choices at NLO leads to the expected reduction in theoretical uncertainty - in this case around 10% at NLO. The low

<sup>31</sup>This pathological behaviour of massless  $2 \rightarrow 2$  scattering processes is well known (see for example Eqs. (2.8) and (2.9) of Ref. [374]). In this case the unresolved contribution generates an additional singularity which is not cancelled by the virtual corrections in special back-to-back configurations. For reference, we quote the values missing from Table 42:

$$\begin{aligned} \sigma_{pp \rightarrow \geq 2j}^{\text{NLO}}(p_T^{\min} > 50 \text{ GeV}) &= -111.0^{+62.5}_{-66.0} \mu\text{b} \\ \sigma_{pp \rightarrow \geq 2j}^{\text{NLO}}(p_T^{\min} > 500 \text{ GeV}) &= 10.4^{+11.3}_{-18.4} \text{nb} \end{aligned}$$

$K$ -factors for three and four jet production with a  $p_T$  cut at 50 GeV suggest this cut is too soft for fixed order perturbation theory to work. With a the higher  $p_T$  cut of 500 GeV the  $K$ -factors are much more reasonable and the slight decrease is in agreement with previous computations at 7 and 8 TeV [375,376].

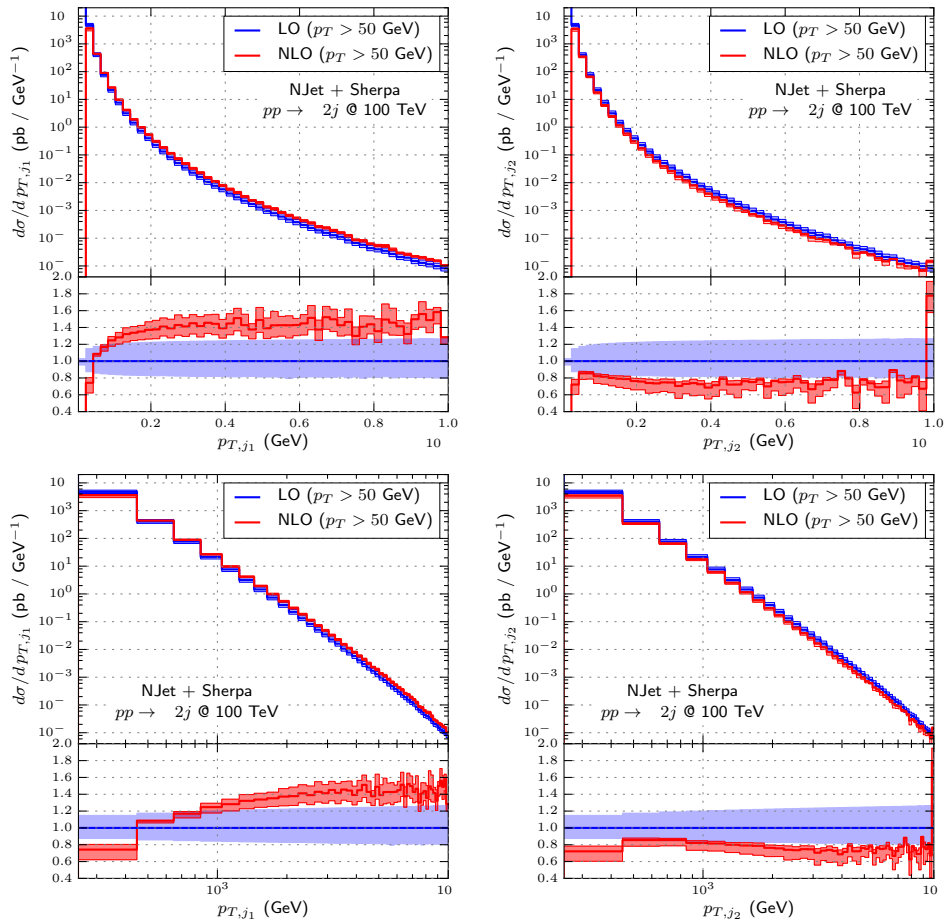


Fig. 136: 1st and 2nd leading jet  $p_T$  for  $pp \rightarrow \geq 2j$  at 100 TeV. LO and NLO scale variations in the range  $[1/2, 2]$  are shown around the central scale of  $\mu_R = \mu_F = \hat{H}_T/2$ . The top row shows a linear scale from 50 GeV to 10 TeV while the bottom row shows the same plot using a log scale over the range 250 GeV to 10 TeV in order to avoid the singularity which affects the first bin. All plots use events generated using a minimum  $p_T$  cut of 50 GeV.

In Fig. 137 we show distributions for the  $p_T$  ordered jets from 500 GeV to 10 TeV in  $pp \rightarrow 3j$  events while in Fig. 138 we show distributions for 4th leading jet from 500 GeV to 10 TeV in  $pp \rightarrow 4j$  events.

Figure 139 shows two plots of multi-jet cross ratios as a function of the leading jet  $p_T$ . Though scaling behaviour of multijet cross-sections will be covered in more detail in the Section 10.4, these observables at low multiplicity are highly sensitive to  $\alpha_s$  over a large range of energies and thus are interesting to look at differentially. The perturbative corrections to the  $R_{3j/2j}$  ratio are known to be more stable for the average of the leading and sub-leading jet  $\frac{1}{2}(p_{T,j_1} + p_{T,j_2})$  [205].

In Table 43 we look at representative NLO  $K$ -factors with additional cuts on the highest  $p_T$  jet, Even in this hierarchical configuration there appears to be problems with the scale choice at NLO. We examine this further in Fig. 140 looking the scale variation over a larger range of values than the traditional factor of 2 from the central value. This is done at 14 TeV for minimum  $p_T^{\min} = 30, 60, 100$  GeV

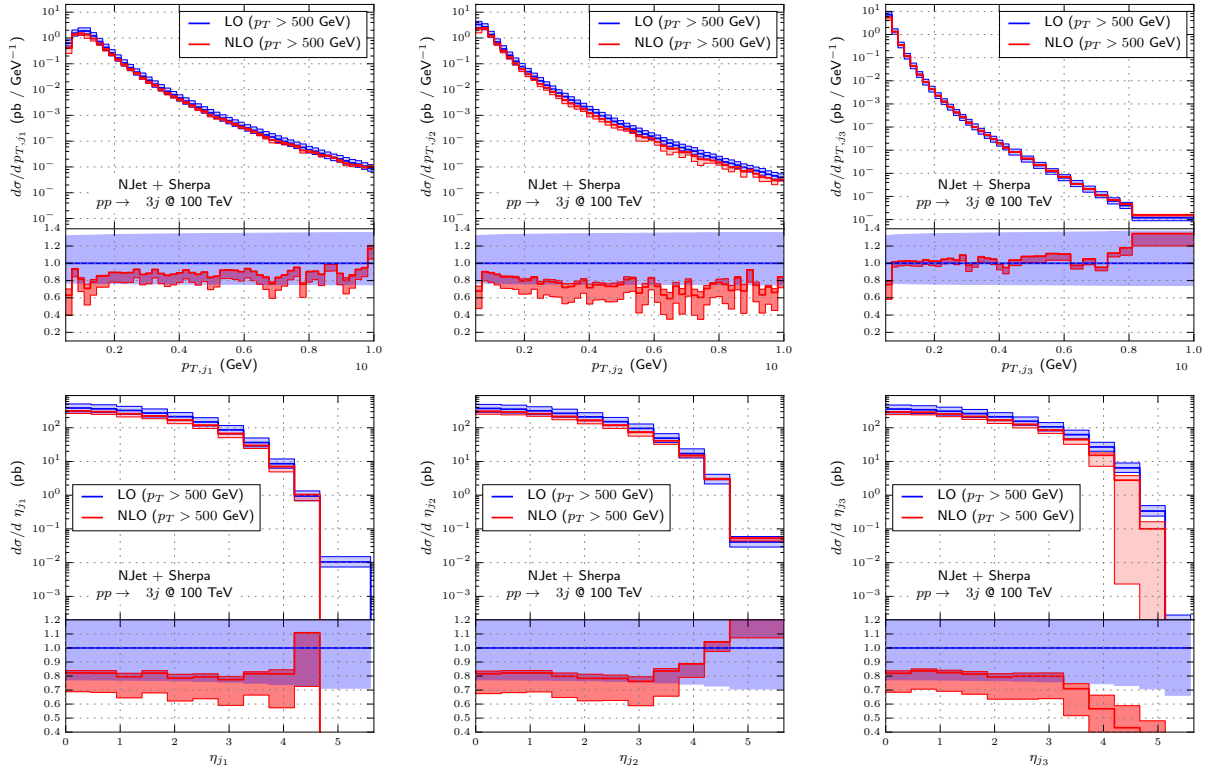


Fig. 137:  $p_T$  and rapidity distributions for the 1st, 2nd and 3rd leading jet ordered in  $p_T$  for  $pp \rightarrow \geq 3j$  at 100 TeV with a minimum  $p_T$  cut of 500 GeV. LO and NLO scale variations in the range  $[1/2, 2]$  are shown around the central scale of  $\mu_R = \mu_F = \hat{H}_T/2$ .

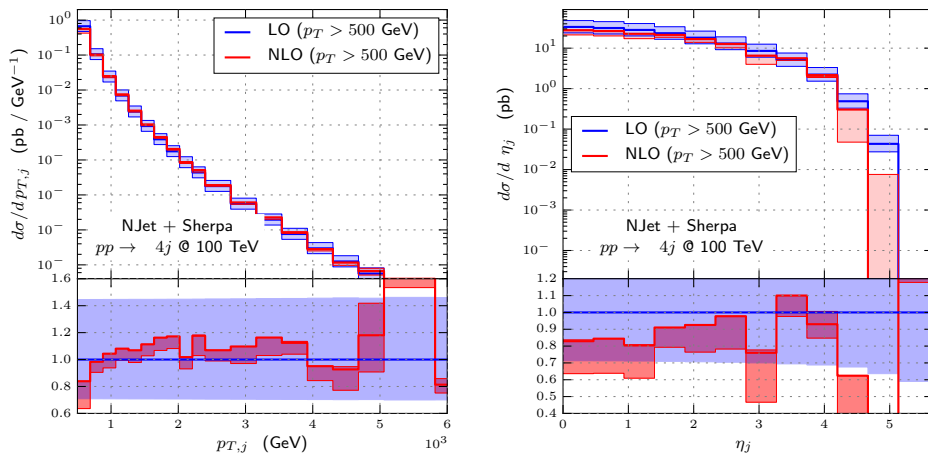


Fig. 138:  $p_T$  and rapidity distributions for the 4th jet ordered in  $p_T$  for  $pp \rightarrow \geq 4j$  at 100 TeV. LO and NLO scale variations in the range  $[1/2, 2]$  are shown around the central scale of  $\mu_R = \mu_F = \hat{H}_T/2$ .

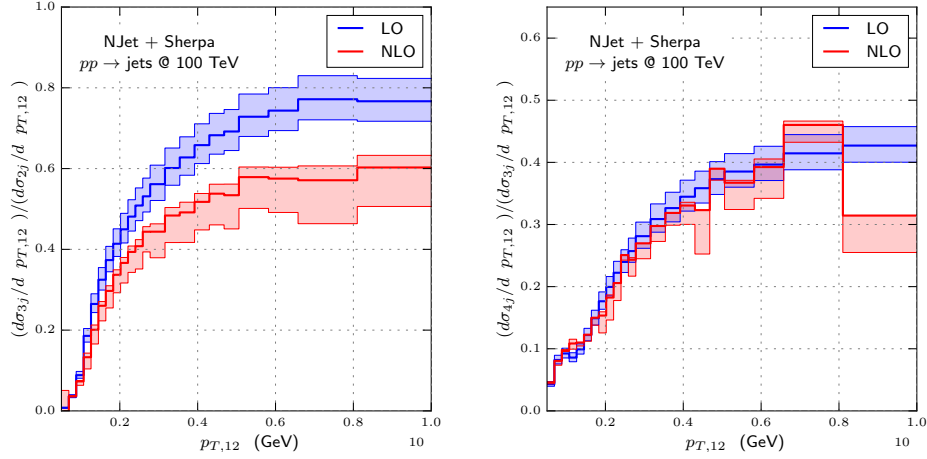


Fig. 139: The  $R_{3j/2j}$  and  $R_{4j/3j}$  ratios as a function of average transverse momentum of the two leading jets at 100 TeV.  $\langle p_{T,12} \rangle = \frac{1}{2} (p_{T,j_1} + p_{T,j_2})$

$n$	$p_{T,j_1} > 100 \text{ GeV } p_T^{\min} > 50 \text{ GeV}$			$p_{T,j_1} > 1000 \text{ GeV } p_T^{\min} > 500 \text{ GeV}$		
	LO	NLO	K	LO	NLO	K
2	$28.8^{+2.7}_{-2.6} \mu\text{b}$	$54.1^{+5.9}_{-4.7} \mu\text{b}$	$1.9^{+0.03}_{-0.00}$	$3.4^{+0.7}_{-0.6} \text{nb}$	$5.5^{+0.6}_{-0.5} \text{nb}$	$1.6^{+0.13}_{-0.14}$
3	$20.7^{+5.3}_{-4.0} \mu\text{b}$	$7.5^{+3.2}_{-6.4} \mu\text{b}$	$0.4^{+0.28}_{-0.32}$	$1.1^{+0.4}_{-0.3} \text{nb}$	$0.8^{+0.1}_{-0.2} \text{nb}$	$0.7^{+0.28}_{-0.32}$
4	$5.6^{+2.4}_{-1.6} \mu\text{b}$	$1.7^{+1.1}_{-2.8} \mu\text{b}$	$0.3^{+0.39}_{-0.45}$	$106.8^{+47.6}_{-31.1} \text{pb}$	$92.2^{+0.0}_{-20.0} \text{pb}$	$0.9^{+0.34}_{-0.40}$

Table 43: Inclusive cross-sections for multijet production at NLO and LO using democratic cuts of 50 and 500 GeV together with an additional restriction on the leading jet of 100 GeV or 1 TeV.

and at 100 TeV for  $p_T^{\min} = 50, 100, 250 \text{ GeV}$ . At NLO the cross section will have a maximum value with the choice of scale. For extremely low scales the cancellations between real and virtual contributions become unstable which is clearly seen at both 14 TeV and 100 TeV. For the cases of  $p_T > 30 \text{ GeV}$  at 14 TeV and  $p_T > 50 \text{ GeV}$  at 100 TeV this caused the cross section to become negative. The stable region of the cross-section occur near to the peak value, where it also happens that the LO cross section agrees with the NLO. The  $K$ -factors approach 1 for much higher values of the scale factor for low  $p_T$  cuts and the situation is exacerbated at 100 TeV.

We stress that having a  $K$ -factor of 1 is not the aim of this analysis but that even at NLO scale variations can be large. For the lower  $p_T$  cuts in multi-jets at 100 TeV it appears a central scale choice of  $\hat{H}_T$  rather than  $\hat{H}_T/2$  would give more realistic predictions.

Table 44 shows the dependence on the  $K$ -factor with respect to the anti- $k_T$  jet radius for  $pp \rightarrow 3j$  using a minimum  $p_T > 250 \text{ GeV}$ . Overall the dependence on the jet radius is relatively mild. As expected even with a relatively high  $p_T$  cut perturbative stability is compromised for  $R \lesssim 0.3$ .

### 10.3.2 Photon and diphoton production in association with jets

Representative NLO  $K$ -factors for photon plus jets final states are presented in Table 45 for two sets of minimum  $p_T^{\min}$ , 50 and 500 GeV, applied to all photons and jets, respectively. The appearance of additional production channels from LO at NLO gives rise to large  $K$ -factors in the low multiplicity cases. For the high energy cuts perturbative stability seems to be improved in all cases. We note that

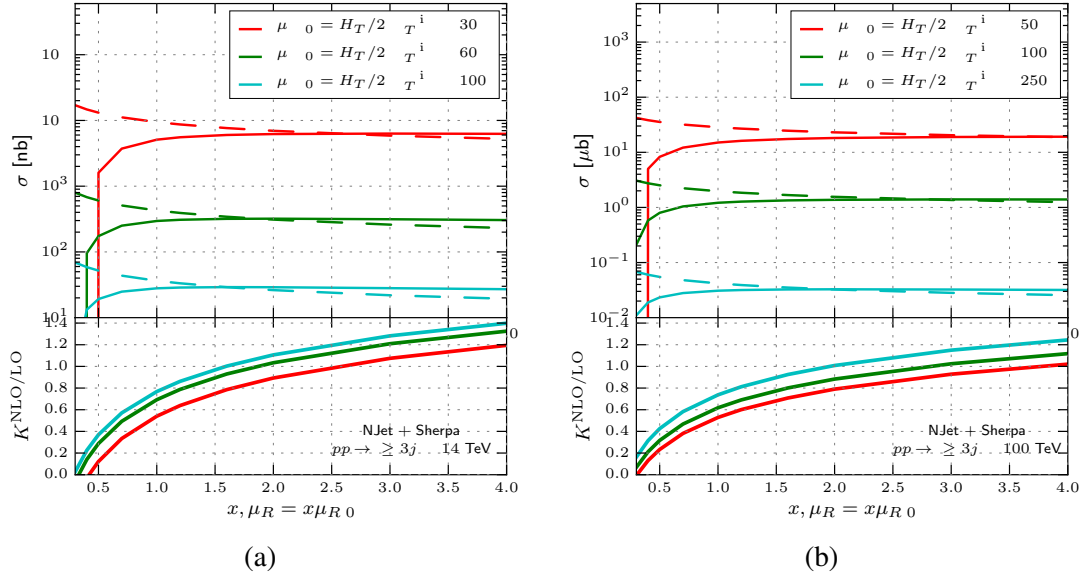


Fig. 140: Total cross sections for  $pp \rightarrow \geq 3j$  as a function of the scale choice for 3 different sets of minimum  $p_T$  at both 100 and 14 TeV. In the upper plot solid lines show NLO predictions while dashed lines show LO predictions. The lower plots show the NLO/LO  $K$ -factors.

	$j^3$ $p_T > 250$ GeV		
$R$	LO	NLO	K
0.2	$45.6^{+14.1}_{-10.2}$ nb	$22.4^{+5.2}_{-12.9}$ nb	$0.5^{+0.29}_{-0.33}$
0.3	$43.4^{+13.5}_{-9.7}$ nb	$27.6^{+3.2}_{-9.7}$ nb	$0.6^{+0.28}_{-0.32}$
0.4	$41.8^{+13.0}_{-9.4}$ nb	$30.8^{+1.9}_{-7.5}$ nb	$0.7^{+0.27}_{-0.31}$
0.5	$40.5^{+12.6}_{-9.1}$ nb	$33.5^{+0.8}_{-5.8}$ nb	$0.8^{+0.26}_{-0.31}$
0.6	$39.3^{+12.3}_{-8.8}$ nb	$35.6^{+0.0}_{-4.3}$ nb	$0.9^{+0.26}_{-0.30}$
0.7	$38.2^{+11.9}_{-8.6}$ nb	$36.8^{+0.0}_{-3.2}$ nb	$1.0^{+0.25}_{-0.29}$

Table 44: Inclusive three jet cross-section as a function of jet radius at NLO and LO using democratic cuts on all jets of 250 GeV. Renormalisation and factorisation scales are chosen equal with a central values  $\mu_R = \mu_F = \hat{H}_T/2$  with theoretical uncertainty estimated through variations over the range  $[1/2, 2]$ .

similar effects are seen in W and Z plus jet studies in Section 5.

Using the same set of cuts for di-photon production with up to two additional jets shows a similar pattern. In this case the  $K$ -factors are very high as the number of additional channels is more extreme than for the single photon case. Again the low  $p_T$  cut of 50 GeV appears to be disfavoured.

#### 10.4 Scaling behaviour in multi-jet production

When considering hadron collisions at highest energies QCD jet production processes are omnipresent. Even processes with very large multiplicity of (associated) jets exhibit sizable rates. Accurate predictions for such final states pose a severe challenge for Monte-Carlo event generators and one might have to resort to approximate methods. One such approach is based on the scaling behaviour of QCD jet rates with respect to jet multiplicity that this section shall be focused on.

$\gamma + j^n$						
$n$	$p_T^{\min} > 50 \text{ GeV}$			$p_T^{\min} > 500 \text{ GeV}$		
	LO	NLO	K	LO	NLO	K
1	$71.6^{+6.5}_{-8.2} \text{ nb}$	$115.5^{+5.0}_{-3.1} \text{ nb}$	$1.6^{+0.29}_{-0.17}$	$39.4^{+2.3}_{-2.2} \text{ pb}$	$46.9^{+1.4}_{-1.2} \text{ pb}$	$1.2^{+0.04}_{-0.03}$
2	$24.6^{+2.4}_{-2.2} \text{ nb}$	$32.7^{+1.7}_{-1.5} \text{ nb}$	$1.3^{+0.07}_{-0.06}$	$3.9^{+0.8}_{-0.6} \text{ pb}$	$4.8^{+0.2}_{-0.3} \text{ pb}$	$1.2^{+0.15}_{-0.16}$
3	$11.2^{+2.9}_{-2.2} \text{ nb}$	$10.1^{+0.0}_{-0.9} \text{ nb}$	$0.9^{+0.22}_{-0.25}$	$654.1^{+206.0}_{-147.9} \text{ fb}$	$671.1^{+0.0}_{-32.1} \text{ fb}$	$1.0^{+0.24}_{-0.28}$

Table 45: Inclusive cross-sections photon plus multijet production as a function of jet multiplicity at NLO and LO using democratic cuts on all jets of 50 and 500 GeV. Renormalisation and factorisation scales are chosen equal with a central values  $\mu_R = \mu_F = \hat{H}_T/2$  where the photon  $p_T$  is included. The theoretical uncertainty estimated through variations over the range  $[1/2, 2]$ .

$\gamma\gamma + j^n$						
$n$	$p_T^{\min} > 50 \text{ GeV}$			$p_T^{\min} > 500 \text{ GeV}$		
	LO	NLO	K	LO	NLO	K
0	$45.7^{+8.6}_{-8.5} \text{ pb}$	$100.1^{+3.8}_{-5.2} \text{ pb}$	$2.2^{+0.36}_{-0.28}$	$49.0^{+1.4}_{-1.7} \text{ fb}$	$68.7^{+1.4}_{-1.1} \text{ fb}$	$1.4^{+0.08}_{-0.06}$
1	$27.3^{+0.3}_{-0.6} \text{ pb}$	$61.7^{+3.7}_{-3.1} \text{ pb}$	$2.3^{+0.19}_{-0.13}$	$7.3^{+0.7}_{-0.6} \text{ fb}$	$12.5^{+1.0}_{-0.9} \text{ fb}$	$1.7^{+0.04}_{-0.04}$
2	$24.4^{+3.1}_{-2.7} \text{ pb}$	$31.6^{+1.3}_{-1.4} \text{ pb}$	$1.3^{+0.10}_{-0.10}$	$2.5^{+0.5}_{-0.4} \text{ fb}$	$3.2^{+0.1}_{-0.2} \text{ fb}$	$1.3^{+0.15}_{-0.17}$

Table 46: Inclusive cross-sections diphoton plus multijet production as a function of jet radius at NLO and LO using democratic cuts on all jets of 50 and 500 GeV. Renormalisation and factorisation scales are chosen equal with a central values  $\mu_R = \mu_F = \hat{H}'_T/2$  with theoretical uncertainty estimated through variations over the range  $[1/2, 2]$ .

In Fig. 141 anti- $k_T$  jet rates at NLO QCD differential in jet transverse momentum and additionally binned in jet rapidity  $y$  are presented. Results have been obtained with BLACKHAT+SHERPA [215], renormalisation and factorisation scale have been set to  $\mu_R = \mu_F = \frac{1}{2}H_T$ . Comparing rates for 14 and 100 TeV centre-of-mass energy an increase of about one order of magnitude for central jets with low and moderate  $p_T$  is observed. Considering larger  $p_T$  values the differences get more extreme, at  $p_T = 3.5 \text{ TeV}$  the FCC rates are more than three orders of magnitude larger than at the LHC. In fact, the FCC provides substantial jet rates even for very large rapidities: 200 GeV jets with  $5 < |y| < 6$  come with rates about two orders of magnitude larger than those for 200 GeV jets in the  $4 < |y| < 5$  bin at the LHC. From these rate estimates it can be concluded that one can expect at least ten times more jets at the FCC compared to the LHC, and this factor gets larger when looking into high  $p_T$  and/or high  $|y|$  regions or demanding large jet multiplicities. Accordingly, the rapidity coverage of general-purpose detectors at the FCC should increase with respect to ATLAS or CMS.

The QCD jet production rates to be anticipated at the FCC demand suitable theoretical methods even for very large jet multiplicities. While a fixed-order prediction for a given jet process is suitable to describe the corresponding jet multiplicity bin, matrix-element parton-shower merging techniques provide inclusive predictions, differential in the jet multiplicity, with high jet multiplicities being modelled through the parton shower. Alternatively, there has recently been progress in making (semi-)analytical predictions for jet rates at hadron colliders that account for small jet radii and high jet counts [377–379].

With the advent of such methods, the morphology of the entirety of the jet-multiplicity distribution can be studied. Guided by phenomenological evidence, supported by both fixed-order calculations and parton-shower simulations, certain jet-multiplicity scaling patterns can be identified [380] that find their

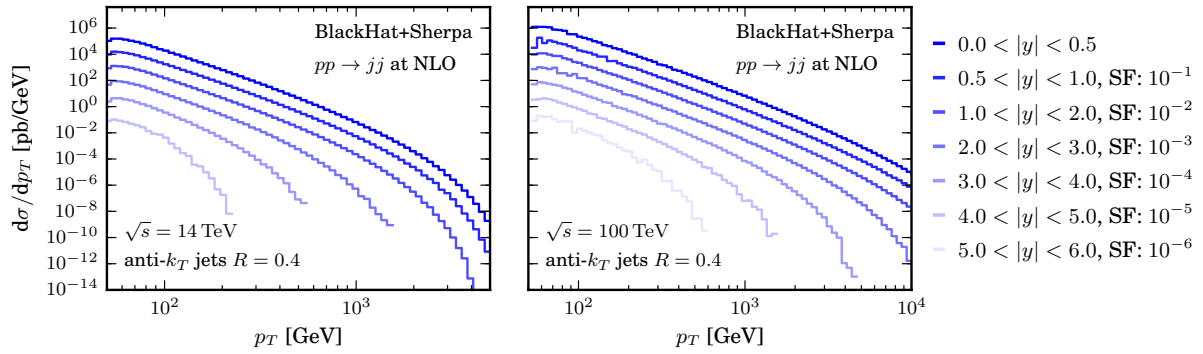


Fig. 141: NLO QCD inclusive jet cross sections for LHC (left) and FCC (right) collision energies, differential in  $p_T$  for different bins in jet rapidity  $y$ . Note that for illustrative purpose results have been multiplied by variable scaling factors (SF), as indicated in the legend.

analogue in the analytical jet-rate predictions [377, 378].

As already visible in Fig. 133a, jet rates differential in the number of jets exhibit a high degree of regularity. To study this feature one considers the ratio  $R_{(n+1)/n}$  of the exclusive  $n + 1$  over the  $n$ -jet cross section, i.e.

$$R_{(n+1)/n} \equiv \frac{\sigma_{n+1}^{\text{excl}}}{\sigma_n^{\text{excl}}}. \quad (74)$$

The approximately equal step size (on a logarithmic scale) between the subsequent exclusive jet rates observed in Fig. 133a translates into a flat plateau for  $R_{(n+1)/n}$ , i.e.  $R_{(n+1)/n} \sim \text{constant}$ , translating into a simple exponential form of the jet-rate distribution. This shape of the jet rates is called a Staircase Pattern. Another regularity in jet rates found is named Poisson Pattern. Jet cross sections following a simple Poisson statistics result in  $R_{(n+1)/n} \sim \bar{n}/(n + 1)$ , with the average number of jets given by  $\bar{n}$ .

Both these patterns have been observed in LHC data [381–384] and in Monte-Carlo studies [385–387]. They can be understood as the limiting cases for the jet-emission probability: for  $\alpha_S/\pi \log^2 Q/Q_0 \ll 1$  a Staircase Pattern is expected while for  $\alpha_S/\pi \log^2 Q/Q_0 \gg 1$  a Poisson Scaling is observed [377, 380, 388]. Here  $Q$  denotes the hard process scale and  $Q_0$  is of the order of the jet resolution scale, i.e.  $Q_0 \sim p_{T,\text{min}}$ . The derivation is based on the language of generating functionals for the jet rates. The two distinct regimes correspond to additional parton emissions being distributed either equally among all other partons or stemming predominantly from a single hard parton line. The latter follows a simple Sudakov decay-like model which results in a Poisson distribution, as it is the case for photon emissions from a hard electron line [389]. The case of democratic emissions (mainly gluons from gluons) on the other hand is exclusive to field theories with a non-abelian group structure as QCD.

In realistic measurements jet patterns will be overlaid and cut off by other effects, such as phase-space constraints. When the available energy for further jet emission is being depleted or jets already radiated cover a good fraction of the available solid angle [388], then higher multiplicities will quickly tend to zero. On the other hand, the first few emissions carry away sizable parts of the total energy available, such that the increase in the partonic momentum fractions at which any participating PDFs are evaluated is comparably large. This leads to somewhat steeper decrease of jet rates for the first few emissions and is known as the PDF suppression effect [380].

In view of the enormous phase space available for producing additional jets at the FCC collider, studies of the jet multiplicity distribution based on scaling patterns provide a handle to estimate and probe the tails of the distribution, where otherwise one has to largely rely on parton-shower simulations alone. Based on these predictions background subtractions for New Physics signatures resulting from decays of new heavy coloured particles yielding a distinct imprint on the multiplicity distribution might become feasible [385, 390].

Of course jet patterns will be overlaid and cut off by other effects, such as phase space effects: if the available energy is being depleted or the existing jets already cover the available solid angle [388], then higher multiplicities will quickly tend to zero.

To study in how far simple jet scaling patterns describe the jet multiplicity distributions at FCC energies fits of  $R_{(n+1)/n}$  in Monte-Carlo predictions are considered. For that purpose SHERPA Monte-Carlo samples for pure jet production are explored, triggering scaling patterns using either democratic or hierarchical, i.e. staggered, jet cuts. As mentioned before, here *democratic* reflects the fact that all jet  $p_{T,\min}$  are of the same order, i.e. uniform, whereas *hierarchical* refers to the scenario where the cut on the leading jet,  $p_{T,\min}^{\text{leading}}$ , is significantly increased.

label	$p_{T,\min}^{\text{leading}}$ [GeV]	$p_{T,\min}$ [GeV]	fit function	fit region	fit parameters
S1 (democratic)	100	50	$f_{\text{Staircase}}$	$3 \leq n \leq 5$	$c = 0.342, m = 0.006$
S2 (democratic)	200	100	$f_{\text{Staircase}}$	$3 \leq n \leq 5$	$c = 0.274, m = 0.003$
P1 (hierarchical)	500	50	$f_{\text{Poisson}}$	$1 \leq n \leq 5$	$\bar{n} = 2.21, c = 0.16$
P2 (hierarchical)	2000	50	$f_{\text{Poisson}}$	$1 \leq n \leq 5$	$\bar{n} = 2.64, c = 0.25$

Table 47: The jet-cut scenarios considered for pure jet production at FCC energies. Furthermore, the fit hypothesis used, cf. Eqs. (75) and (76), and the corresponding parameters are listed.

The cut scenarios considered for pure jet production are listed in Table 47. In all case the  $2 \rightarrow 2$  core process has been considered at MC@NLO accuracy, furthermore LO matrix elements for final-state multiplicities up to six partons are included, all consistently merged with the parton shower. In Fig. 142 the resulting  $R_{(n+1)/n}$  distributions are presented for the four considered selections. Note, the index  $n$  counts the number of jets radiated off the hard two-to-two core, i.e.  $n = 1$  corresponds to the production of three final-state jets.

As discussed in [386], jets assigned to the core process behave differently from jets emitted thereof, which is why they have to be dismissed from pattern fits through the data. Furthermore, PDF effects leave a non-universal imprint on the first few bins. Therefore, for the Staircase-like patterns found for the democratic cut scenarios, cf. the two upper panels of Fig. 142, the fits are based on the values from  $R_{4/3}$  through  $R_{6/5}$ . For the hierarchical cut scenarios PDF suppression effect are less prominent, due to hard cut on the leading jet that induces a much higher scale  $Q$  for the core process. Accordingly, the fits for the Poisson-like patterns, cf. the two lower panels in Fig. 142, are based on  $R_{2/1}$  up to  $R_{6/5}$ . To quantify the quality of the fits, term linear in  $n$  for the Staircase pattern and a constant term for the Poisson pattern have been added to the ideal scaling hypotheses. The resulting fit functions for the two scenarios read

$$f_{\text{Staircase}}(n) = c + m n, \quad (75)$$

$$f_{\text{Poisson}}(n) = \frac{\bar{n}}{n+1} + c. \quad (76)$$

All resulting fit parameters are listed in Table 47. For all cut scenarios the fit function and its extrapolation to higher jet bins describe the simulated data very well. For the two democratic scenarios, the constant  $c$  decreases from 0.35 to 0.29 when we increase the jet cuts, reflecting the fact that the *costs* for adding an additional jet gets higher.

Poisson patterns are obtained when hierarchical cuts are applied. Although the constant offset  $c$  increases from 0.16 to 0.25 when enlarging the gap between the leading jet cut and the overall jet cut  $p_{T,\min}$  one can see by eye that the fit quality is better for the larger cut gap, i.e. 2000 GeV vs. 50 GeV. For the smaller cut gap, i.e. 500 GeV vs. 50 GeV the fit increasingly underestimates  $R_{(n+1)/n}$  for growing  $n$ , which might indicate a faster transition to a more Staircase-like behaviour. As expected the average jet

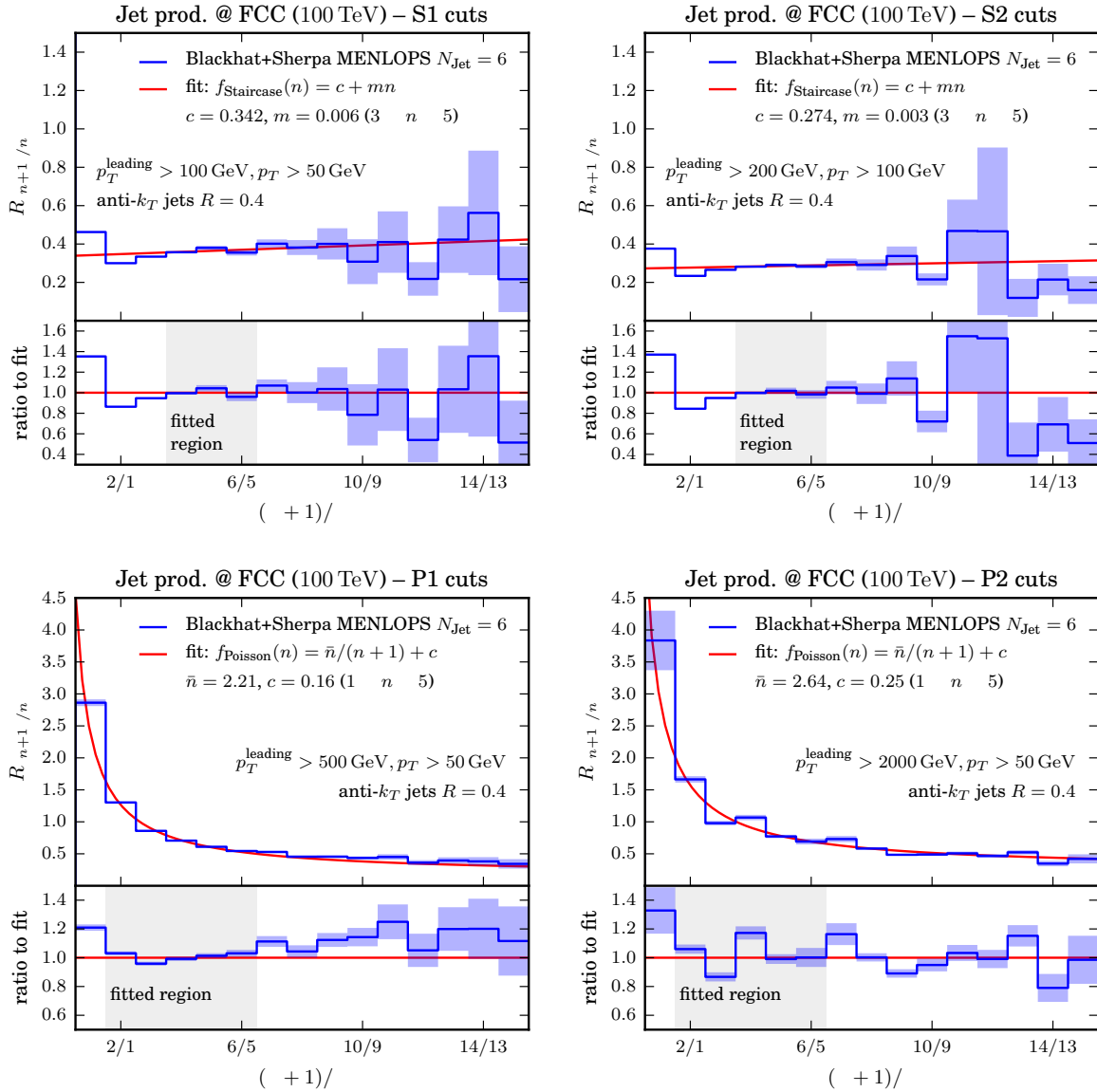


Fig. 142: The exclusive jet multiplicity ratio  $R_{(n+1)/n}$  in pure jet production at the FCC. Results are presented for the four cut scenarios described in Table 47 with fits for the Staircase and Poisson patterns, cf. Eqs. (75), (76).

multiplicity  $\bar{n}$  found from the fit increases with a larger leading jet cut (from 2.2 to 2.6). In particular the S2 and P2 cut scenarios are very well modelled by the simple scaling pattern hypotheses and allow for reliable extrapolations where explicit calculations based on fixed order or even parton shower simulations become computationally infeasible.

Both patterns can also be observed in  $W$  production in association with additional jets, as have been discussed Section 5.3.

To further illustrate the universality of jet scaling patterns, Fig. 143 compiles the exclusive jet multiplicity ratios for a variety of processes, including pure jets,  $\gamma$ +jets,  $t\bar{t}$ +jets and  $W/Z$ +jets. The predictions are based on dedicated  $n$ -jet tree-level matrix element calculations, without invoking parton showers. Democratic jet selection cuts are applied, i.e. requiring  $p_{T,j} > 50$  GeV in all processes. In addition, the photon production processes are regulated by the selection criteria  $p_{T,\gamma} > 50$  GeV and

$R_{j,\gamma} > 0.4$ , with  $R_{j,\gamma}$  the  $\eta - \phi$  distance between all jets and the photon.

There are a few remarkable aspects to note here. Apparently, for the pure jets and  $W$ +jets processes these LO rate estimates nicely reproduce the staircase scaling parameters found in the matrix-element plus parton-shower samples for the analogous jet-selection cuts, cf. Fig. 142 (upper left panel). This is supported by the fact that for exact Staircase scaling the cross section ratios for subsequent jet multiplicities are identical for exclusive and inclusive cross sections [380], i.e. in this limit

$$\frac{\sigma_{n+1}^{\text{excl}}}{\sigma_n^{\text{excl}}} = \frac{\sigma_{n+1}^{\text{incl}}}{\sigma_n^{\text{incl}}} = R = \text{const.} \quad (77)$$

Also note that the ratios of the three vector-boson production processes,  $W/Z/\gamma$ +jets, are basically the same, illustrating the fact that the actual gauge-boson mass does not yield a big imprint on the jet-production probabilities. The production of a pair of top-quarks, however, induces a large upper scale for subsequent jet emission. Correspondingly, the jet rates for the first few emissions are sizable, resulting in ratios  $R_{(n+1)/n} > 0.5$ , indicating that a pure leading-order approximation is inappropriate.

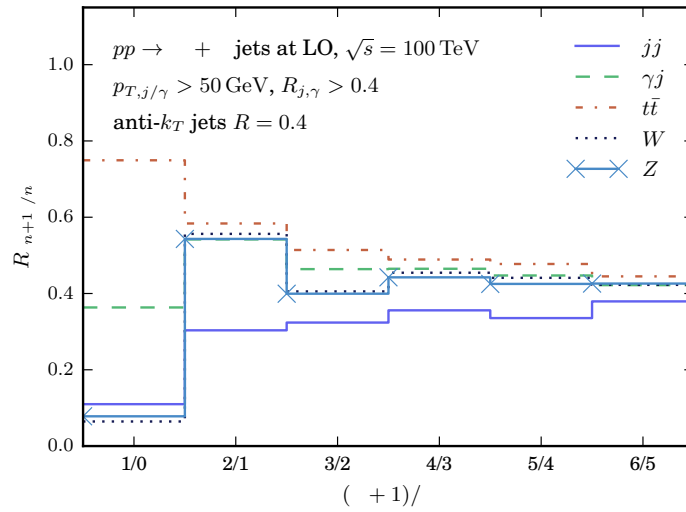


Fig. 143: The jet multiplicity ratio  $R_{(n+1)/n}$  for several processes calculated at LO for each final-state multiplicity. Note, the index  $n$  counts jets associated to the core process listed in the legend.

In conclusion to this section, it can be noted that it is possible to fit jet multiplicities  $n$  up to values of  $n = 15$  or even higher using results for much lower  $n$ . The underlying fits are based on the theoretical hypothesis of simple scaling pattern, namely Staircase and Poisson scaling. These extrapolations allow trustworthy predictions to be made for very high jet-multiplicity bins that will be populated by a variety of production processes at FCC energies. The methods discussed enable the use of techniques that discriminate New Physics signals and QCD backgrounds based on the shape of the jet multiplicity distribution.

## 11 Heavy flavour production<sup>32</sup>

Heavy quarks will be copiously produced at a 100 TeV collider. Charm and bottom quarks, in particular, have a probability of several percent to be produced in a  $pp$  collisions at 100 TeV. Considering the large number of concurrent  $pp$  interactions in individual bunch crossings, each bunch crossing will give rise to possibly several charm or bottom quark pairs. The value of the total production rates is however poorly known due to both perturbative (missing higher orders) and parametric uncertainties. Perturbative uncertainties (which, especially for the total cross sections of charm and bottom, can be quite significant) are usually estimated by varying the factorisation and renormalisation scales in the calculation. These uncertainties may be somewhat reduced by expressing the calculation in terms of the heavy quark  $\overline{\text{MS}}$  mass instead of the pole one [391], but they remain quite large in absolute terms, as shown for example in the case of the total  $\sigma(b\bar{b})$  in Fig. 144. The results here were obtained with the ABM11 PDFs [392]. The scale uncertainties corresponding to the vertical bars in Fig. 144, for the LO, NLO and NNLO calculations, are  $\sigma(b\bar{b})^{\text{LO}} = 1.20^{+0.56}_{-0.33}$  mb,  $\sigma(b\bar{b})^{\text{NLO}} = 2.45^{+0.85}_{-0.56}$  mb, and  $\sigma(b\bar{b})^{\text{NNLO}} = 3.09^{+0.42}_{-0.48}$  mb.

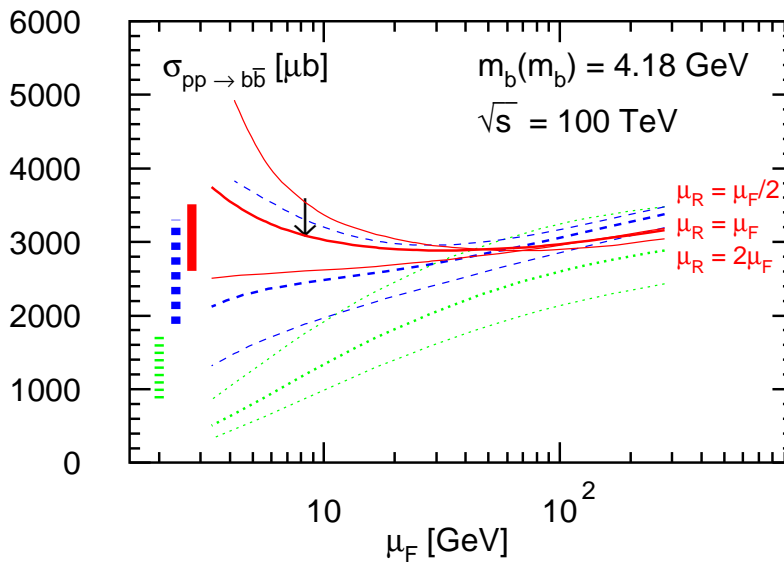


Fig. 144: Sensitivity of the total cross section for  $pp \rightarrow b\bar{b}$  to the factorization scale  $\mu_F$  at LO (green, dotted), NLO (blue, dashed), NNLO (red, solid) QCD accuracy, with  $m_b(m_b) = 4.18$  GeV in the  $\overline{\text{MS}}$  mass scheme. The central line at each order denotes the choice  $\mu_R = \mu_F$ , the upper and the lower line the choices  $\mu_R = \mu_F/2$  and  $\mu_R = 2\mu_F$  (as indicated explicitly for the NNLO results). The vertical bars give the size of the independent variation of  $\mu_R$  and  $\mu_F$  in the standard range  $\mu_0/2 \leq \mu_R, \mu_F \leq 2\mu_0$ , respectively, for  $\mu_0 = m_b(m_b)$  and with the restriction that  $1/2 \leq \mu_R/\mu_F \leq 2$ . The arrow indicates the scale  $\mu_R = \mu_F = 2\mu_0$ .

Parametric uncertainties are related to the value of the heavy quark mass (for charm and bottom) and of the parton distribution functions in the very small- $x$  region that will be probed at 100 TeV. Part of these uncertainties, including the scale uncertainties, can be reduced when considering ratios of cross sections at different energies, or shapes of  $y_Q$  distributions, due to intrinsic correlations. This was exploited for example in analyzing LHC data at various beam energies, in Refs. [24, 25, 28].

On the other hand, and as will be shown in the next sub-section, the range of  $x$  values relevant to inclusive production of charm and bottom quarks at 100 TeV will extend well below the  $10^{-5}$  level. In this region, one can question the reliability of the fixed-order perturbative calculations, in view of the presence of large small- $x$  logarithms that may need to be resummed [80, 393, 394]. On the PDF

<sup>32</sup>Editor: M.Cacciari

side, it is also necessary to rely on assumptions for the PDF functional behaviour at small  $x$  (in presence of potential saturation effects) and on the very reliability of the standard factorization framework (see Section 2 for a more detailed discussion).

To highlight the possible problems, we show in Table 48 the predictions for charm and bottom total cross sections obtained with several sets of PDFs. In the case of the bottom, the spread of central values is not larger than that due to the scale uncertainties, although the estimates of PDF uncertainties vary wildly among the different PDF sets. In the case of the charm, the situation is more dramatic, particularly if one considers the potentially most accurate estimates, namely those using NNLO matrix elements and NNLO PDFs. In this case, the results can be negative, or have a positive/negative uncertainty spread that largely exceeds the central values, leading to unphysical results, which are either negative, or which exceed the total  $pp$  cross sections. We notice that, in most of the pathological cases, the problems are enhanced by the use of NNLO PDFs, while using NLO PDFs with either the NLO or NNLO matrix elements gives typically sensible results (although with some residual exceptions). The only PDF sets that give rather stable results, regardless of the NLO or NNLO scenario, are the ABM sets and the JR14 set. The very small systematics obtained with these sets (less than 2% for JR and less than 10% with ABM), however, are likely to be over optimistic, considering the lack of data in these regions of  $x$  and  $Q^2$  and considering the potential uncertainties mentioned above (gluon saturation effects, resummation, etc).

PDF sets	$\sigma(c\bar{c})^{\text{NLO}}$ [mb]	$\sigma(c\bar{c})^{\text{NNLO}}$ [mb]	$\sigma(b\bar{b})^{\text{NLO}}$ [mb]	$\sigma(b\bar{b})^{\text{NNLO}}$ [mb]
ABM11 [392]	$29.5 \pm 2.7$	$36.6 \pm 2.6$ ( $54.9 \pm 3.8$ )	$3.57 \pm 0.13$	$3.06 \pm 0.11$ ( $4.52 \pm 0.18$ )
ABM12 [10] <sup>33</sup>	$17.3 \pm 2.0$	$33.2 \pm 2.6$	$2.36 \pm 0.10$	$2.97 \pm 0.12$
CJ15 [12] <sup>34</sup>	$18.4^{+5.3}_{-2.5}$	— ( $40.3^{+10.3}_{-4.6}$ )	$2.67^{+0.55}_{-0.26}$	— ( $3.42^{+0.69}_{-0.31}$ )
CT14 [8] <sup>35</sup>	$24.7^{+1315.5}_{-3.1}$	$31.8^{+624.3}_{-3.0}$ ( $47.9^{+1981.2}_{-5.2}$ )	$3.06^{+5.35}_{-0.25}$	$3.12^{+3.39}_{-0.21}$ ( $3.91^{+6.91}_{-0.30}$ )
HERAPDF2.0 [11] <sup>36</sup>	$19.0^{+3.8}_{-4.4}$	$3.2^{+10.1}_{-18.2}$ ( $41.5^{+5.2}_{-5.9}$ )	$3.14^{+0.10}_{-0.13}$	$2.70^{+0.21}_{-0.22}$ ( $4.01^{+0.13}_{-0.16}$ )
JR14 (dyn) [13]	$33.6 \pm 0.5$	$32.7 \pm 0.5$ ( $58.1 \pm 1.0$ )	$3.17 \pm 0.04$	$3.08 \pm 0.04$ ( $3.98 \pm 0.06$ )
MMHT14 [9] <sup>37</sup>	$140.0^{+187.0}_{-104.2}$	— ( $213.9^{+271.9}_{-149.4}$ )	$4.11^{+1.39}_{-0.90}$	$2.37^{+0.98}_{-0.90}$ ( $5.28^{+1.77}_{-1.14}$ )
NNPDF3.0 [7]	$40.5 \pm 62.2$	$190.3 \pm 547.7$ ( $67.9 \pm 84.3$ )	$2.99 \pm 0.99$	$4.46 \pm 4.87$ ( $3.82 \pm 1.23$ )

Table 48: The inclusive cross sections for charm- and bottom-quark pair production at NNLO in QCD at  $\sqrt{s} = 100$  TeV for  $\overline{\text{MS}}$  masses  $m_c(m_c) = 1.275$  GeV and  $m_b(m_b) = 4.18$  GeV at the nominal scales  $\mu_r = \mu_f = 2m_q(m_q)$  for  $q = c, b$  with the PDF (and, if available, also  $\alpha_s$ ) uncertainties. The numbers in parenthesis for the cross sections  $\sigma(q\bar{q})^{\text{NNLO}}$  have been obtained with NLO PDF sets.

The bottom line is that, while currently the extrapolation of charm cross sections to 100 TeV is not robust theoretically, charm production provides a rich terrain to improve our knowledge of PDFs and

small- $x$  dynamics.

The uncertainties are reduced if one considers central production or large  $p_T$ , which strongly bound the relevant  $x$  range. Table 49 shows the rates for central production,  $|y| < 2.5$ , and various transverse momentum cuts for charm, bottom and top quarks. The ratios with respect to the production at the LHC (13 TeV) are also given. As expected, large  $p_T$  production in particular gets a large boost from 13 to 100 TeV, being larger by a factor of 30-40 or so than at the LHC for a  $p_T$  cut of 100 GeV. If the  $p_T$  cut is pushed to 1 TeV, central heavy quark production at the 100 TeV is about a factor of one thousand larger than at the LHC. Top production is special in that, as expected, going from the LHC to 100 TeV the rate increases considerably also at moderate transverse momentum ( $p_T \sim 0$ ), by a factor of 40 or so, whereas charm and bottom production only increase by a factor of 3-5.

		$p_T > 0$	$p_T > 5 \text{ GeV}$	$p_T > 100 \text{ GeV}$	$p_T > 1000 \text{ GeV}$
Charm	$\sigma( y  < 2.5) [\mu\text{b}]$	$7.8 \times 10^3$	$1.7 \times 10^3$	0.52	$0.62 \times 10^{-4}$
	100 TeV/13 TeV	3.1	4.6	27	890
Bottom	$\sigma( y  < 2.5) [\mu\text{b}]$	$1.0 \times 10^3$	$0.56 \times 10^3$	0.46	$0.63 \times 10^{-4}$
	100 TeV/13 TeV	4.2	5	27	1020
Top	$\sigma( y  < 2.5) [\text{nb}]$	24.8	24.8	15.6	$2.6 \times 10^{-2}$
	100 TeV/13 TeV	37	37	42	920

Table 49: Central ( $|y| < 2.5$ ) heavy quark production at FCC 100 TeV, calculated to next-to-leading order [395] with the NNPDF30 [7] PDF set. Masses have been set to 1.5 GeV for charm, 4.75 GeV for bottom and 173 GeV for top.

In the rest of this Section we will consider in more detail production rates and kinematical distributions for bottom and top quark in proton-proton collisions at a centre of mass energy of 100 TeV.

### 11.1 Inclusive bottom production

Inclusive production of  $b$  hadrons in hadronic collisions offers unlimited opportunities for flavour studies in the  $b$  sector, as shown very well by the Tevatron and LHC experiments.

The long-term interest in these studies will depend on what future LHCb and Belle2 data will tell us, and on the flavour implications of possible LHC discoveries in the high- $Q^2$  region. But it is likely that heavy flavour studies will remain a pillar of the physics programme at 100 TeV. The flavour-physics aspects of the 100 TeV collider will be discussed in a future document.

The total  $b\bar{b}$  production cross section at 100 TeV is about 3mb, an increase by a factor of  $\sim 5$  relative to the LHC, and it is more than a 1% fraction of the total  $pp$  cross section. As discussed above, a large fraction of the total rate comes from gluons at very small  $x$  values, where the knowledge of PDFs is today rather poor. The upper plot of Fig. 145 shows that, for a detector like LHCb, covering the rapidity region  $2.5 < y < 5$ , about 50% of the  $b$  events produced at 100 TeV would originate from gluons with momentum  $x < 10^{-5}$ . This domain, at these rather large values of  $Q^2$ , is almost unexplored, although the first constraints [24, 25, 28] are emerging from forward charm and bottom production at the LHC [396, 397] (see also Section 2 for a discussion of small- $x$  issues at 100 TeV).

In Fig. 146 we show the rapidity distributions for  $b$  quarks produced above some thresholds of  $p_T$  and, for  $b$  quarks produced in the region  $2.5 < |y| < 5$ , the integrated spectrum in longitudinal momentum  $p_z$ , comparing results at 14 and 100 TeV. We note that, while the total production rate grows only by a factor of  $\sim 5$  from 14 to 100 TeV, the rate increase can be much larger once kinematic cuts are imposed on the final state. For example, at 100 TeV  $b$  quarks are produced in the forward region  $2.5 < |y| < 5$  with  $p_z > 1 \text{ TeV}$  at the astounding rate of  $10\mu\text{b}$ , 100 times more than at the LHC.

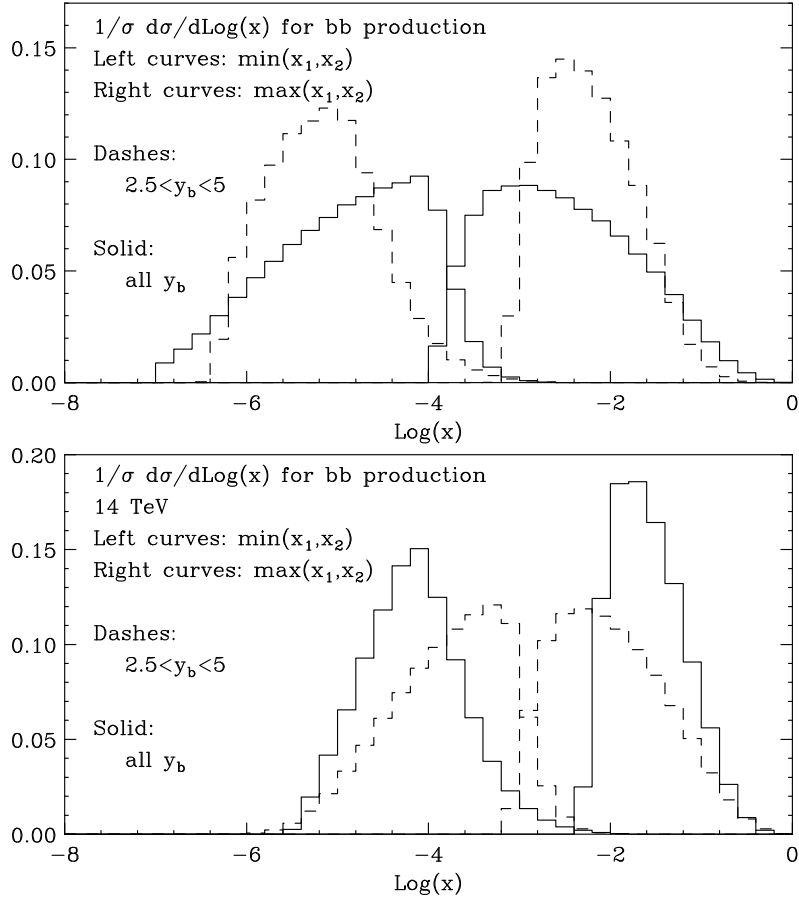


Fig. 145: Top (bottom) panel: distribution, at 100 (14) TeV, of the smaller and larger values of the initial partons momentum fractions in inclusive  $b\bar{b}$  events (solid) and in events with at least one  $b$  in the rapidity range  $2.5 < |y| < 5$  (dashes).

To what extent this opens opportunities for new interesting measurements, to be exploited by the future generation of detectors, remains to be studied.

## 11.2 Inclusive top pair production

Table 50 shows the NNLO cross section [398, 399] for inclusive  $t\bar{t}$  production at 100 TeV. For reference, the LO and NLO results obtained with the appropriate PDF sets of the NNPDF3.0 group are 24.3 nb and 31.9 nb, respectively. This means  $K$  factors of 1.3 (NLO/LO) and 1.1 (NNLO/NLO), indicating an excellent convergence and consistency of the perturbative expansion. Together with the small size of PDF uncertainties, this suggests that the predictions for top production at 100 TeV are already today rather robust. The  $\sim 30$  nb inclusive rate is more than 30 times larger than at 14 TeV. For the planned total integrated luminosity of  $O(20)\text{ab}^{-1}$  [400], two experiments would produce of the order of  $10^{12}$  (anti)top quarks. The possible applications emerging from this huge statistics have yet to be explored in detail. It would be interesting to consider the potential of experiments capable of recording all these events (only a small fraction of top quarks produced at the LHC survives for the analyses). Triggering on one of the tops, would allow for unbiased studies of the properties of the other top and of its decay products: studies of inclusive  $W$  decays [401] (which are impossible using the  $W$ 's produced via the Drell-Yan process), of charm and  $\tau$  leptons produced from those  $W$  decays, of flavour-tagged  $b$ 's from the top decay itself [402].

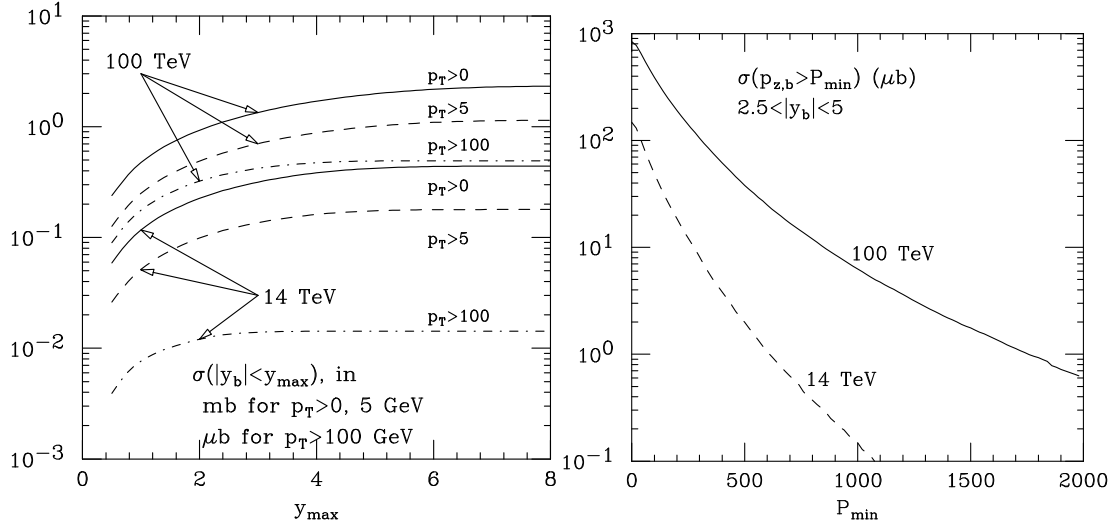


Fig. 146: Left: production rates for  $b$  quarks as a function of detection acceptance in  $y$ , for various  $p_T$  thresholds (rates in  $\mu\text{b}$  for  $p_T > 100 \text{ GeV}$ , in  $\text{mb}$  otherwise). Right: forward  $b$  production rates, as a function of the  $b$  longitudinal momentum.

PDF	$\sigma(\text{nb})$	$\delta_{\text{scale}}(\text{nb})$	(%)	$\delta_{\text{PDF}}(\text{nb})$	(%)
CT14	34.692	+1.000	(+2.9%)	+0.660	(+1.9%)
		-1.649	(-4.7%)	-0.650	(-1.9%)
NNPDF3.0	34.810	+1.002	(+2.9%)	+1.092	(+3.1%)
		-1.653	(-4.7%)	-1.311	(-3.8%)
PDF4LHC15	34.733	+1.001	(+2.9%)	$\pm 0.590$	( $\pm 1.7\%$ )
		-1.650	(-4.7%)		

Table 50: Total  $t\bar{t}$  production cross sections, at NNLO, for various PDF choices.  $m_{\text{top}} = 173.3 \text{ GeV}$ . The scale uncertainty is derived from the 7 scale choices of  $\mu_{R,F} = km_{\text{top}}$ , with  $k = 0.5, 1, 2$  and  $1/2 < \mu_R/\mu_F < 2$ . The PDF4LHC15 [5] recommendation combines the systematics from the following NLO PDF sets: NNPDF3.0 [7], MMHT2014 [9] and CT14 [8].

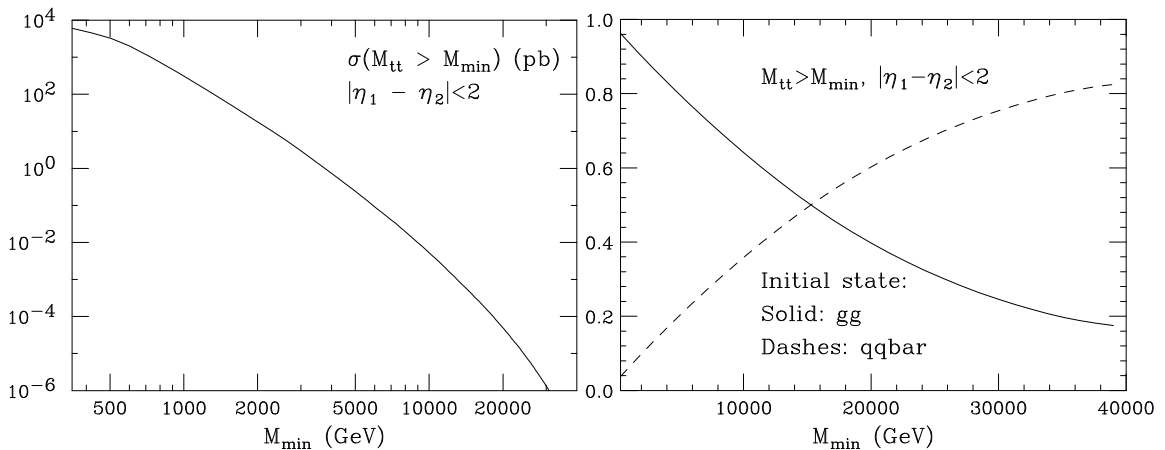


Fig. 147: Left: integrated invariant mass distribution for production of central  $t\bar{t}$  quark pairs. Right: initial state composition as a function of the  $t\bar{t}$  invariant mass.

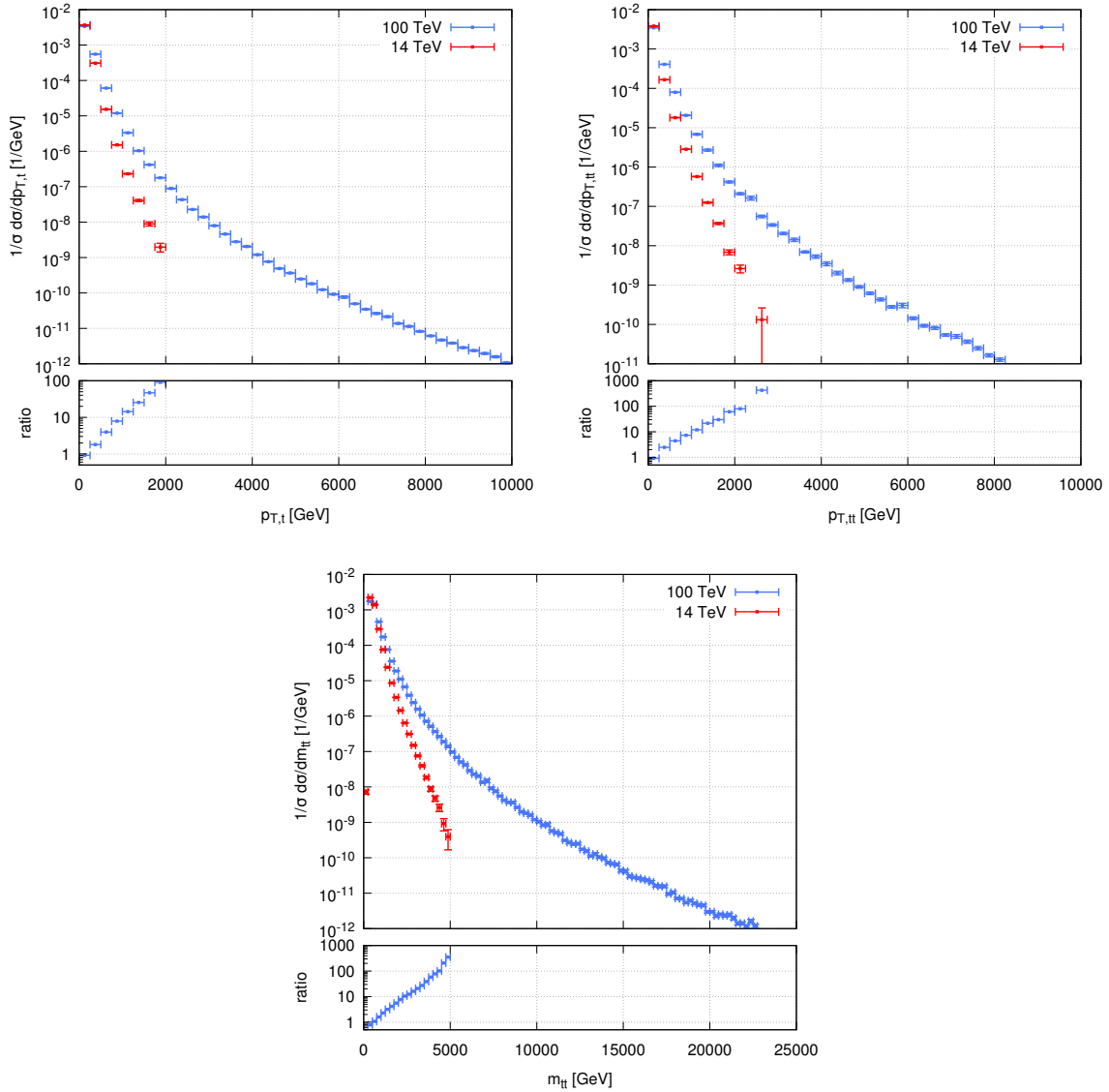


Fig. 148: Normalised distributions for, from left to right, top quark transverse momentum, transverse momentum of the  $t\bar{t}$  pair and its invariant mass, as evaluated by a NLO+PS calculation performed with the POWHEG-BOX implementation of heavy quark hadroproduction.

### 11.3 Bottom and top production at large $Q^2$

Production of bottom and top quarks at large  $Q^2$  is characterized by two regimes. On one side we have final states where the heavy quark and antiquark ( $Q$  and  $\bar{Q}$ ) give rise to separate jets, with a very large dijet invariant mass  $M_{Q\bar{Q}}$ . These are the configurations of relevance when, for example, we search for the  $Q\bar{Q}$  decay of massive resonances. In the case of top quarks, the left-hand side of Fig. 147 shows the production rate for central  $t\bar{t}$  pairs above a given invariant mass threshold. At 100 TeV there will be events well above  $M_{t\bar{t}} > 30$  TeV. The right plot in Fig. 147 furthermore shows that, due to the absence at LO of contributions from  $qq$  or  $qg$  initial states,  $gg$  initial states remain dominant up to very large mass,  $M_{t\bar{t}} \sim 15$  TeV. Well above  $M_{Q\bar{Q}} \sim \text{TeV}$ , the results for  $b\bar{b}$  pair production are similar to those of the top.

This first high- $Q^2$  regime can be further investigated by looking at other differential distributions for the top quark beyond the invariant mass. In the following we show results obtained using POWHEG-BOX implementation of the NLO calculation for heavy quark hadroproduction [241, 242, 332], matched

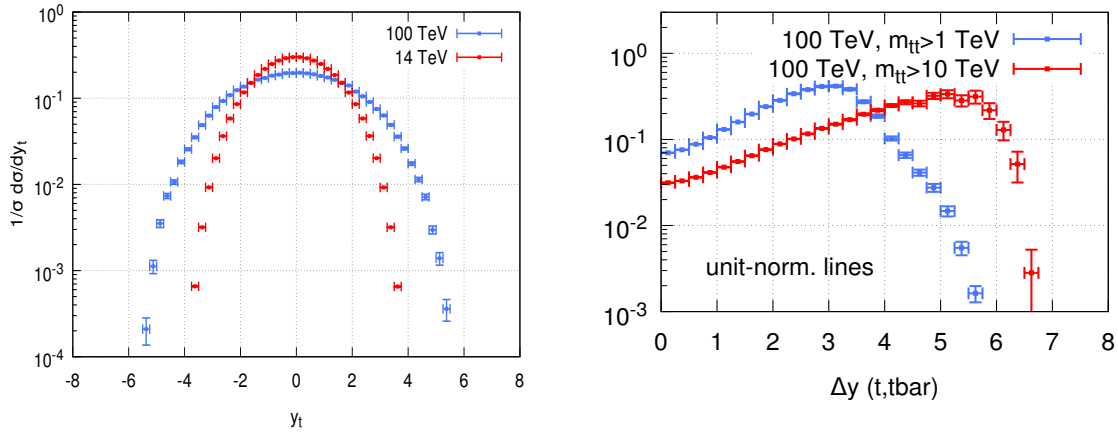


Fig. 149: Left plot: normalised rapidity distribution of top quarks at FCC100 and LHC14. Right plot: distribution of the rapidity difference  $\Delta y$  between the top and the anti-top at the FCC100, for two different invariant mass cuts.

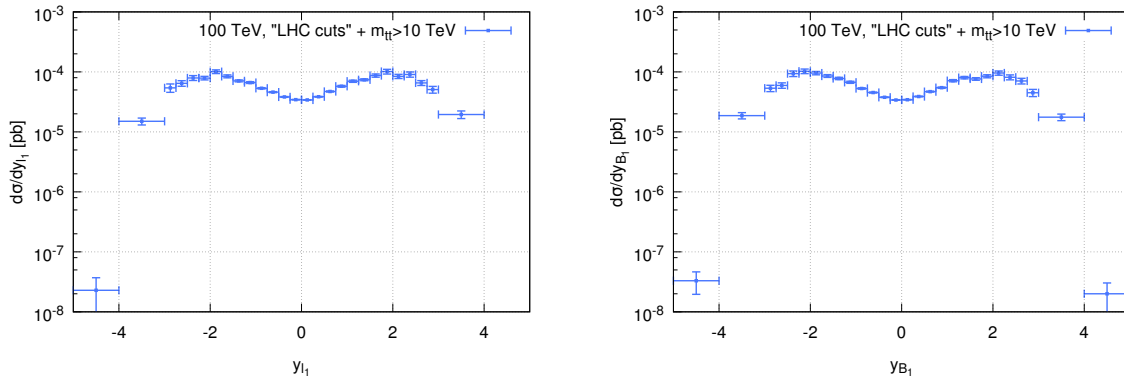


Fig. 150: Rapidity distributions of leptons (left plot) and  $B$  hadrons (right plot) from top decays. LHC-like cuts for transverse momenta and missing energies ( $p_{T,\ell} > 20$  GeV,  $p_{T,B} > 20$  GeV,  $E_{T,miss} > 20$  GeV) are used, but rapidity cuts were removed. An additional cut on the invariant mass of the  $t\bar{t}$  pair,  $m_{t\bar{t}} > 10$  TeV, is also included.

to the parton shower of PYTHIA 6 [100] (without MPI).<sup>38</sup> NNPDF30 PDFs are used throughout, and the factorisation/renormalisation scales are set equal to the top transverse mass. We first show, in Fig. 148, the distributions for the top transverse momentum, the transverse momentum of the  $t\bar{t}$  pair, and its invariant mass, both at 14 and at 100 TeV. In all three cases, as expected, the normalised distributions at FCC100 are much harder than at LHC14: they are larger by a factor of about 10 at a scale of 1 TeV, and of about 100 at 2 TeV.

Another characteristic of top distributions at high- $Q^2$  that one can study is the rapidity dependence. The plots in Fig. 149 show that at 100 TeV (and especially so at high invariant masses) top quarks tend to be produced at larger rapidity than at 14 TeV, and with a larger rapidity gap. This suggests that the top quarks at 100 TeV will be a copious source of large-rapidity lepton. Fig. 150 shows that this is indeed the case: one can see that rapidity distributions for the  $B$  hadrons and for the leptons produced by top decays are distributed quite uniformly in rapidity until at least  $y \simeq 3$ , and only fall off quite steeply beyond  $y \simeq 4$ .

<sup>38</sup>In order to improve the generation at high- $p_T$  a POWHEG “Born suppression factor”  $F(p_T) = [(p_T^2 + m^2)/(p_T^2 + m^2 + B^2)]^3$  with  $B = 10$  TeV has been used.  $m$  is the top quark mass.

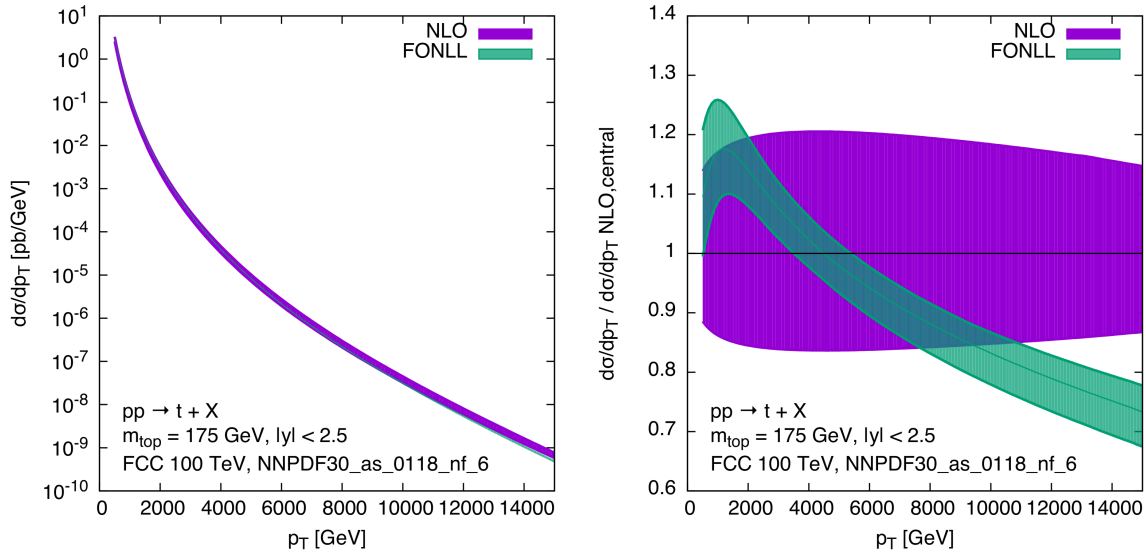


Fig. 151: Left plot: Transverse momentum distribution of top quarks in  $t\bar{t}$  hadroproduction, calculated to NLO and also with the FONLL approach. Uncertainties are estimated by varying the renormalisation and factorisation scales within a factor of two around the top transverse mass, with the constraint  $1/2 < \mu_R/\mu_F < 2$ . Right plot: ratios to the NLO central prediction.

As a consequence of these wide rapidity distributions, “LHC-like” lepton cuts, where the leptons are only measured in a central acceptance region  $|y_\ell| < 2.5$ , may turn out not to be ideal at 100 TeV. Moving this cut to at least  $y_\ell = 3\text{--}3.5$  would reduce the cross-section loss by a non-negligible amount.

Since the top quark transverse momentum distribution is expected to remain measurable at the FCC100 up to several TeV, it is worth studying how the cross section at such large transverse momenta (much larger than the top mass) is affected by multiple quasi-collinear emissions of gluons off the top quarks. Techniques exist to resum these emissions to all orders with next-to-leading logarithmic accuracy [403, 404], leading to a more reliable theoretical prediction. We show in Fig. 151 predictions obtained using the FONLL approach [50], compared to the next-to-leading order results. While the FONLL and the NLO predictions are largely compatible within their respective uncertainties (estimated varying the renormalisation and factorisation scales), as expected the FONLL distribution is softer, and has a smaller perturbative uncertainty.

The second regime of high- $Q^2$  production occurs when we request only one jet to be tagged as containing a heavy quark. This could be of interest, for example, in the context of high- $p_T$  studies of single top production. In this regime, configurations in which the heavy quark pair arises from the splitting of a large- $p_T$  gluon are enhanced. The final state will then contain a jet formed by the heavy-quark pair, recoiling against a gluon jet. An example of the role of these processes is shown in Fig. 152, where we compare the  $p_T$  spectrum of  $b$  jets in events where the  $b\bar{b}$  pair is produced back to back (as in the first case we discussed above), and the spectrum of jets containing the  $b$  pair (here jets are defined by a cone size  $R = 0.4$ ). The latter is larger by approximately one order of magnitude at the highest  $p_T$  values, leading to rates in excess of 1 event/ab $^{-1}$  for  $p_T > 15$  TeV. Similar considerations apply to the case of top quark production in this multi-TeV regime, as shown in the right plot of Fig. 152. In this case the rate for  $t\bar{t}$  jets is only slightly larger than that for single-top jets, due to the much larger mass of the top quark, which leads to a smaller probability of  $g \rightarrow t\bar{t}$  splitting.

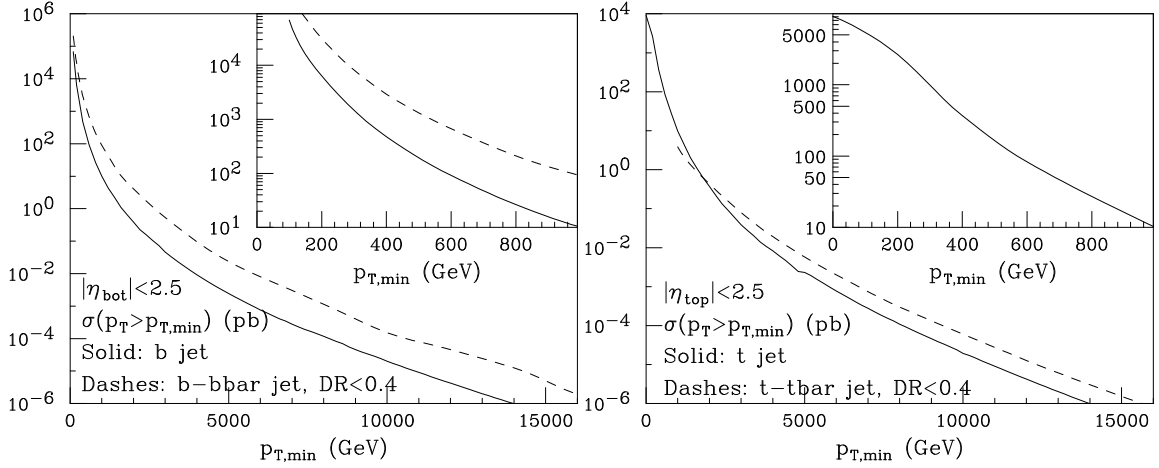


Fig. 152: Left: production rates for  $b$  jets (solid), and for jets containing a  $b\bar{b}$  pair within  $\Delta R < 0.4$  (dashes). Right: same, for top-quark jets (top treated as stable).

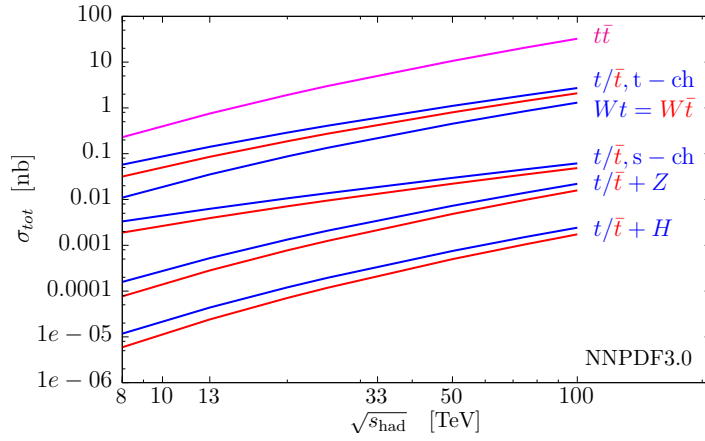


Fig. 153: Cross sections for top processes as a function of proton-proton collider energy. See text for details.

### 11.4 Single top production

Like  $t\bar{t}$  pairs, production of single top at 100 TeV is also increased by large factors with respect to LHC. However, since single top production is dominated by quark initiated  $t$ -channel production, the total  $t + \bar{t}$  production cross section grows by about a factor 25 with respect to the LHC13, compared to the growth of about 40 for the  $t\bar{t}$  cross-section (and of about 15 for its other major background,  $W$ +jets).

Figure 153 shows the total production cross section for various channels as a function of the centre of mass energy.  $t\bar{t}$  and single top results are computed at NLO QCD, while associated  $tZ$  and  $tH$  production are computed at LO QCD<sup>39</sup>. For (N)LO predictions (N)LO evolution of  $\alpha_s$  and parton distributions were employed. For all the results in this section we used the NNP3.0 parton set [7]. Apart from associated  $Wt$  production, all results here are fully inclusive and are computed with  $\mu_r = \mu_f = m_t = 172.5$  GeV. For  $Wt$  production, a  $b$ -jet veto of  $p_{b,t} = 80$  GeV is applied on additional  $b$ -jet radiation coming from  $gg \rightarrow Wtb$  diagrams to separate this process from the  $t\bar{t}$  background, see [406] for details. As suggested in [406], we used in this case a lower scale,  $\mu = p_{b,t,\text{veto}} = 80$  GeV. Results for 13 TeV and 100 TeV are also summarized in Table 51<sup>40</sup>.

<sup>39</sup>Predictions are obtained using HatHor [405] and MCFM [236–238].

<sup>40</sup>For the numbers in the table we computed  $t$ -channel production to NNLO QCD [407]. The difference with respect of NLO is however irrelevant for the considerations here.

	$pp, 13 \text{ TeV}$	$pp, 100 \text{ TeV}$
$\sigma_{\text{NNLO}}^{t, t\text{-channel}}$ [nb]	0.14	2.6
$\sigma_{\text{NNLO}}^{\bar{t}, t\text{-channel}}$ [nb]	0.08	2.0
$\sigma_{\text{NLO}}^{Wt} = \sigma_{\text{NLO}}^{W\bar{t}}$ [nb]	0.035	1.3
$\sigma_{\text{NLO}}^{t, s\text{-channel}}$ [pb]	6.3	61.5
$\sigma_{\text{NLO}}^{\bar{t}, s\text{-channel}}$ [pb]	3.9	48.6
$\sigma_{\text{LO}}^{tZ}$ [pb]	0.5	22.1
$\sigma_{\text{LO}}^{\bar{t}Z}$ [pb]	0.3	15.8
$\sigma_{\text{LO}}^{tH}$ [pb]	0.01	2.4
$\sigma_{\text{LO}}^{\bar{t}H}$ [pb]	0.006	1.7

Table 51: Single top cross sections in  $pp$  collisions at 13 TeV and 100 TeV. All values are for fully inclusive cross sections, with the exception of the  $Wt$  processes, see text for details.

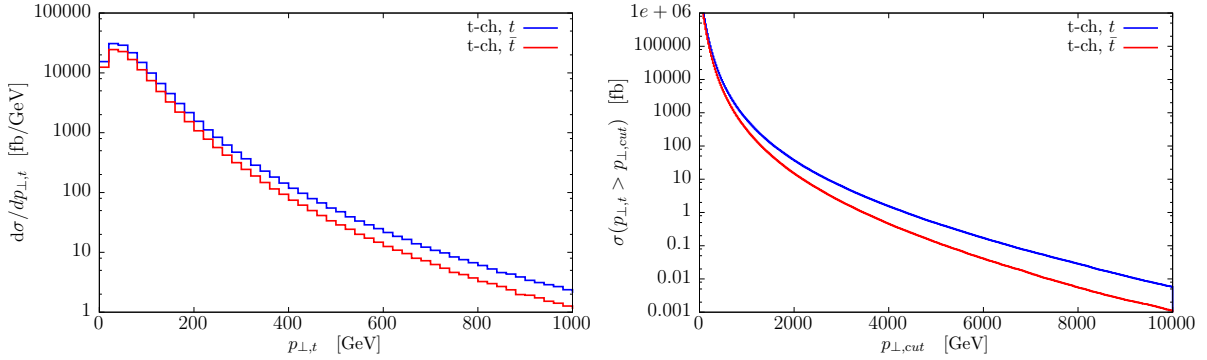


Fig. 154: Left: LO  $t$ -channel single top transverse momentum distribution. Right: LO cross section for  $t$ -channel production as a function of a cut on the top transverse momentum. See text for details.

	$p_T^{\text{min}} = 0$	$p_T^{\text{min}} = 1 \text{ TeV}$	$p_T^{\text{min}} = 5 \text{ TeV}$
$\sigma_{\text{NLO}}^{t, t\text{-channel}}(p_T > p_T^{\text{min}})$	2.7 nb	1.0 pb	0.5 fb
$\sigma_{\text{NLO}}^{\bar{t}, t\text{-channel}}(p_T > p_T^{\text{min}})$	2.0 nb	0.57 pb	0.2 fb

Table 52: NLO cross section for  $t$ -channel single top production as a function of a cut on the top transverse momentum. See text for details.

At 100 TeV,  $t$ -channel single top is about a factor of 20 larger than at 13 TeV, while  $s$ -channel production is about a factor of 10 larger. Associated production (with Higgs,  $Z$  or  $W$ ) tends to increase more, about a factor of 35 or so. A consequence of these different behaviours as a function of the centre of mass energy is that at 100 TeV the  $s$ -channel process becomes even less relevant, decreasing from 3% at LHC energy to 1% of the total single top cross section. This makes the (in principle unphysical) distinction between  $s$ - and  $t$ - channels non problematic at the FCC. On the other hand, the increased relative importance of  $Wt$  associated production (from 20% to 35% of the total cross-section) calls for a proper treatment of this process. This can be achieved by considering the physical  $WWb\bar{b}$  final state.

We also note that associated  $Zt$  and  $Ht$  production rates are sizable at FCC100. The first process is an important background to FCNC top decays. The second provides information on unitarity in the Higgs/top sector. For example, modification of the top Yukawa coupling can lead to unitarity violations in the few TeV regime, which can be exposed using  $Ht$  production. For more details on these processes

and their potential, we refer the reader to [408–410].

A study of differential cross sections in  $t$ -channel single top production is shown in Fig. 154 and in Table 52, where cross section values for  $t$  and  $\bar{t}$  integrated over a given minimum transverse momentum are given. Even above  $p_T = 5$  TeV the integrated cross section remains in the femtobarn range.

## 12 Associated production of top quarks and gauge bosons<sup>41</sup>

At 100 TeV, heavy particles and high-multiplicity final states are abundantly produced, giving the opportunity to scrutinise the dynamics and the strength of the interactions among the heaviest known particles: the gauge and Higgs bosons, and the top quark. The large rates, and the very high energies at which these particles can be produced, open new opportunities to test with greater precision and at smaller distances the couplings of the top quark with the  $W$ ,  $Z$  and Higgs bosons.

Final states involving the heaviest states of the SM are also an important ingredient of physics at 100 TeV, since they naturally lead to high-multiplicity final states (with or without missing transverse momentum). These signatures are typical in BSM scenarios featuring new heavy states decaying via long chains involving, e.g., dark matter candidates. Thus, whether as signal or as background processes, predictions for this class of SM processes need to be known with the best possible precision, to maximise the sensitivity to deviations from the SM.

Table 53 shows the NLO cross sections for the inclusive production of two top quark pairs, and for production in association with one and two gauge bosons. Comparing the rates for associated production,

	$t\bar{t}t\bar{t}$	$t\bar{t}W^\pm$	$t\bar{t}Z^0$	$t\bar{t}WW$	$t\bar{t}W^\pm Z$	$t\bar{t}ZZ$
$\sigma(\text{pb})$	4.93	20.5	64.2	1.34	0.21	0.20

Table 53: NLO cross sections for associated production of (multiple) top quark pairs and gauge bosons [411, 412].

in Table 53, with those in Table 58 for multiple gauge boson production, and considering that each top quark gives rise to a  $W$  through its decay, we remark that top quark processes at 100 TeV will provide the dominant source of final states with multiple  $W$  bosons, and thus with multiple leptons. This will have important implications for the search of new physics signals characterized by the presence of many gauge bosons or leptons from the decay of the new heavy particles.

Notice also that  $t\bar{t}Z^0$  production is more abundant than  $t\bar{t}W^\pm$ , contrary to the usual rule that  $W$  bosons are produced more frequently than  $Z^0$ 's in hadronic collisions. This is because the  $t\bar{t}Z^0$  process is driven by the  $gg$  initial state, which for these values of  $\hat{s}/S$  has a much larger luminosity than the  $q\bar{q}'$  initial state that produces  $t\bar{t}W$ . This also implies that studies of top production via initial state light quarks (e.g. in the context of  $t$  vs  $\bar{t}$  production asymmetries) will benefit from a higher purity of the  $q\bar{q}$  initial state w.r.t.  $gg$  if one requires the presence of a  $W$  boson (see e.g. Ref. [413]).

In this section we discuss in some detail the associated production of a top-quark pair with one boson ( $t\bar{t}V$ ), covering a broad range of kinematical regions. Associated production with a Higgs boson is discussed in more detail in the Higgs volume of this report. We review the impact of NLO QCD corrections, and the residual theoretical uncertainties due to missing higher orders, by considering the dependence of key observables on different definitions of central renormalisation and factorisation scales and on their variations. These results for 100 TeV mimic the detailed study presented for 13 TeV in Ref. [412]. We refer to this paper for more details.

### 12.1 $t\bar{t}V$ production

The NLO QCD corrections were calculated for  $t\bar{t}H$  in [414–417], for  $t\bar{t}\gamma$  in [418, 419], for  $t\bar{t}Z$  in [419–423], for  $t\bar{t}W^\pm$  in [413, 419, 423, 424] and for  $t\bar{t}t\bar{t}$  in [64, 425]. NLO electroweak and QCD corrections have also already been calculated for  $t\bar{t}H$  in [426–428] and for  $t\bar{t}W^\pm$  and  $t\bar{t}Z$  in [428]. Moreover, in the case of the  $t\bar{t}H$  process, NLO QCD corrections have been matched to parton showers [429, 430] and calculated for off-shell top (anti)quarks with leptonic decays in [431].

<sup>41</sup>Editors: D. Pagani, I. Tsinikos

The results presented here have been obtained in the MADGRAPH5\_AMC@NLO framework [64]. We start by defining the approach used to determine the theoretical systematic uncertainty, obtained from the variation of renormalisation and factorisation scales. Given the broad kinematical range accessible at 100 TeV, in addition to using a fixed scale we consider dynamical scales that depend on the transverse masses ( $m_{T,i}$ ) of the final-state particles. Following Ref. [412], we consider the arithmetic mean of the  $m_{T,i}$  of the final-state particles ( $\mu_a$ ) and the geometric mean ( $\mu_g$ ), which are defined by:

$$\mu_a = \frac{H_T}{N} := \frac{1}{N} \sum_{i=1, N(+1)} m_{T,i}, \quad (78)$$

$$\mu_g := \left( \prod_{i=1, N} m_{T,i} \right)^{1/N}. \quad (79)$$

Here,  $N$  is the number of final-state particles at LO and with  $N(+1)$  in Eq. (78) we understand that, for the real-emission events contributing at NLO, the transverse mass of the emitted parton is included.<sup>42</sup>

All the NLO and LO results have been produced with the MSTW2008 (68% c.l.) PDFs [292] respectively at NLO or LO accuracy, in the five-flavour-scheme (5FS) and with the associated values of  $\alpha_s$ . We use  $m_t = 173$  GeV,  $m_H = 125$  GeV and the CKM matrix is considered as diagonal. NLO computations assume the top quark and the vector bosons to be stable. If not stated otherwise photons are required to have a transverse momentum larger than 50 GeV ( $p_T(\gamma) > 50$  GeV) and Frixiene isolation [290] is imposed for jets and additional photons, with the technical cut  $R_0 = 0.4$ . The fine structure constant  $\alpha$  is set equal to its corresponding value in the  $G_\mu$ -scheme for all the processes.

As first step, we show for all the  $t\bar{t}V$  processes the dependence of the NLO total cross sections on the variation of the renormalisation and factorisation scales  $\mu_r$  and  $\mu_f$ . This dependence is shown in Fig. 155 by keeping  $\mu = \mu_r = \mu_f$  and varying it by a factor eight around the central value  $\mu = \mu_g$  (solid lines),  $\mu = \mu_a$  (dashed lines) and  $\mu = m_t$  (dotted lines). The scales  $\mu_a$  and  $\mu_g$  are respectively defined in eqs. (78) and (79).

As  $\mu_a$  is typically larger than  $\mu_g$  and  $m_t$ , the bulk of the cross sections originates from phase-space regions where  $\alpha_s(\mu_a) < \alpha_s(\mu_g), \alpha_s(m_t)$ . Consequently, such choice gives systematically smaller cross sections. On the other hand, the dynamical-scale choice  $\mu_g$  leads to results very close in shape and normalisation to a fixed scale of order  $m_t$ . Note that the scale dependence is monotone over this broad range for all scale choices. This is due to the  $gq$  initial states, which give a very large contribution and appear only at NLO. Consequently, no renormalisation and stabilisation of the  $\mu_r$  is present for the numerically dominant contribution.

As done in [412], in the following we use  $\mu_g$  as the reference scale, and vary  $\mu_f$  and  $\mu_r$  independently by a factor of two around the central value  $\mu_g$ ,  $\mu_g/2 < \mu_f, \mu_r < 2\mu_g$ , in order to estimate the uncertainty due to missing higher orders. This can be seen as a more conservative choice than  $\mu_a$  as central scale; as can be seen in Fig. 155, the scale dependence in the range  $\mu_a/2 < \mu_f, \mu_r < 2\mu_a$  is smaller than in the  $\mu_g/2 < \mu_f, \mu_r < 2\mu_g$  range.

Table 54 lists LO and NLO cross sections, with PDF and scale uncertainties, and  $K$ -factors for the central values. As expected, the scale dependence is strongly reduced from LO to NLO predictions.  $K$ -factors are very similar and close to 1, with the exception of  $t\bar{t}W^\pm$  production. For this process, which at LO includes only  $q\bar{q}$  initial states, the opening of  $gq$  channels in the initial state has a huge effect. Similar effects may be expected at NNLO, i.e., the first perturbative order including the  $gg$  initial state. However, as suggested by the detailed analysis presented in this section for the case of the  $p_T(t\bar{t})$  distributions, NNLO corrections should not have such a large impact. For the  $t\bar{t}\gamma$  process we also find

<sup>42</sup>This is not possible for  $\mu_g$ ; soft real emissions would lead to  $\mu_g \sim 0$ . Conversely,  $\mu_a$  can also be defined excluding partons from the real emission and, in the region where  $m_{T,i}$ 's are of the same order, is numerically equivalent to  $\mu_g$ . We remind that in MADGRAPH5\_AMC@NLO the renormalisation and factorisation scales are by default set equal to  $H_T/2$ .

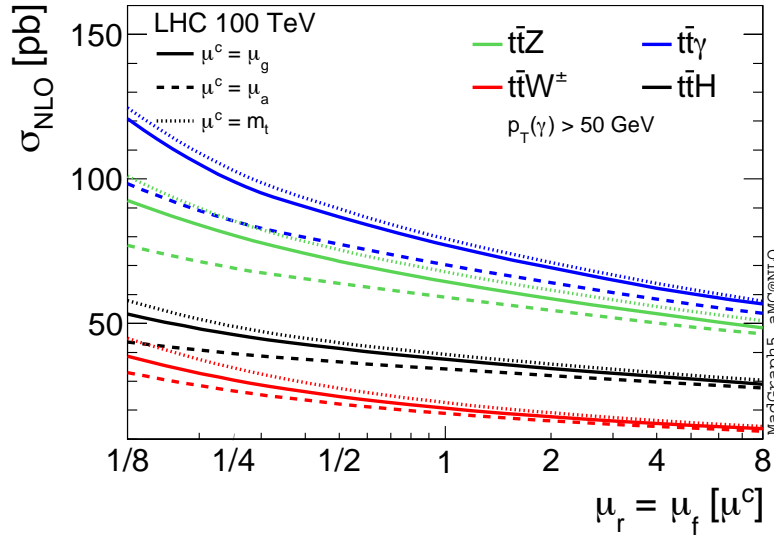


Fig. 155: Comparison of the NLO scale dependence in the interval  $\mu^c/8 < \mu < 8\mu^c$  for the three different choices of the central value  $\mu^c$ :  $\mu_g$ ,  $\mu_a$ ,  $m_t$ .

100 TeV $\sigma$ [pb]	$t\bar{t}H$	$t\bar{t}Z$	$t\bar{t}W^\pm$	$t\bar{t}\gamma$
NLO	$37.56^{+9.9\% +1.0\%}_{-9.8\% -1.3\%}$	$64.07^{+10.8\% +0.9\%}_{-10.9\% -1.2\%}$	$20.65^{+21.5\% +1.1\%}_{-18.0\% -0.8\%}$	$76.68^{+13.3\% +0.9\%}_{-12.6\% -1.2\%}$
LO	$34.26^{+25.6\% +0.9\%}_{-19.6\% -1.6\%}$	$54.57^{+25.3\% +0.9\%}_{-19.3\% -1.7\%}$	$9.39^{+34.1\% +0.9\%}_{-25.1\% -1.4\%}$	$61.51^{+26.8\% +0.9\%}_{-20.3\% -1.7\%}$
$K$ -factor	1.10	1.17	2.20	1.25

Table 54: NLO and LO cross sections for  $t\bar{t}V$  processes and  $t\bar{t}H$  production for  $\mu = \mu_g$ . The first uncertainty is given by the scale variation within  $\mu_g/2 < \mu_f, \mu_r < 2\mu_g$ , the second one by PDFs (MSTW2008). The relative statistical integration error is equal or smaller than one permille.

that in general the dependence of the cross-section scale variation is not strongly affected by the minimum  $p_T$  of the photon.

We now show the impact of NLO QCD corrections on important distributions and we discuss their dependence on the scale variation and on the definition of the scales. For all the processes that we analysed the distribution of the invariant mass of the top-quark pair and the  $p_T$  and the rapidity of the (anti)top quark, of the top-quark pair and of the vector or scalar boson. Here, we show only representative results; all the distributions considered and additional ones can be produced via the public code MADGRAPH5\_AMC@NLO.

For each figure, we display together the same type of distributions for the four different processes considered:  $t\bar{t}\gamma$ ,  $t\bar{t}H$ ,  $t\bar{t}W^\pm$  and  $t\bar{t}Z$ . Most of the plots, for each individual process, will be displayed in the format described in the following.

In each plot, the main panel shows the distribution at LO (blue) and NLO QCD (red) accuracy, with  $\mu = \mu_f = \mu_r$  equal to the reference scale  $\mu_g$ . In the first inset we display the scale and PDF uncertainties normalised to the blue curve, i.e., the LO with  $\mu = \mu_g$ . The light-grey band indicates the scale variation at LO for the standard range  $\mu_g/2 < \mu_f, \mu_r < 2\mu_g$ , while the dark-grey band shows the PDF uncertainty. The black dashed line is the central value of the light-grey band, thus it is by definition equal to one. The solid black line is the NLO QCD differential  $K$ -factor for the scale  $\mu = \mu_g$ , the red

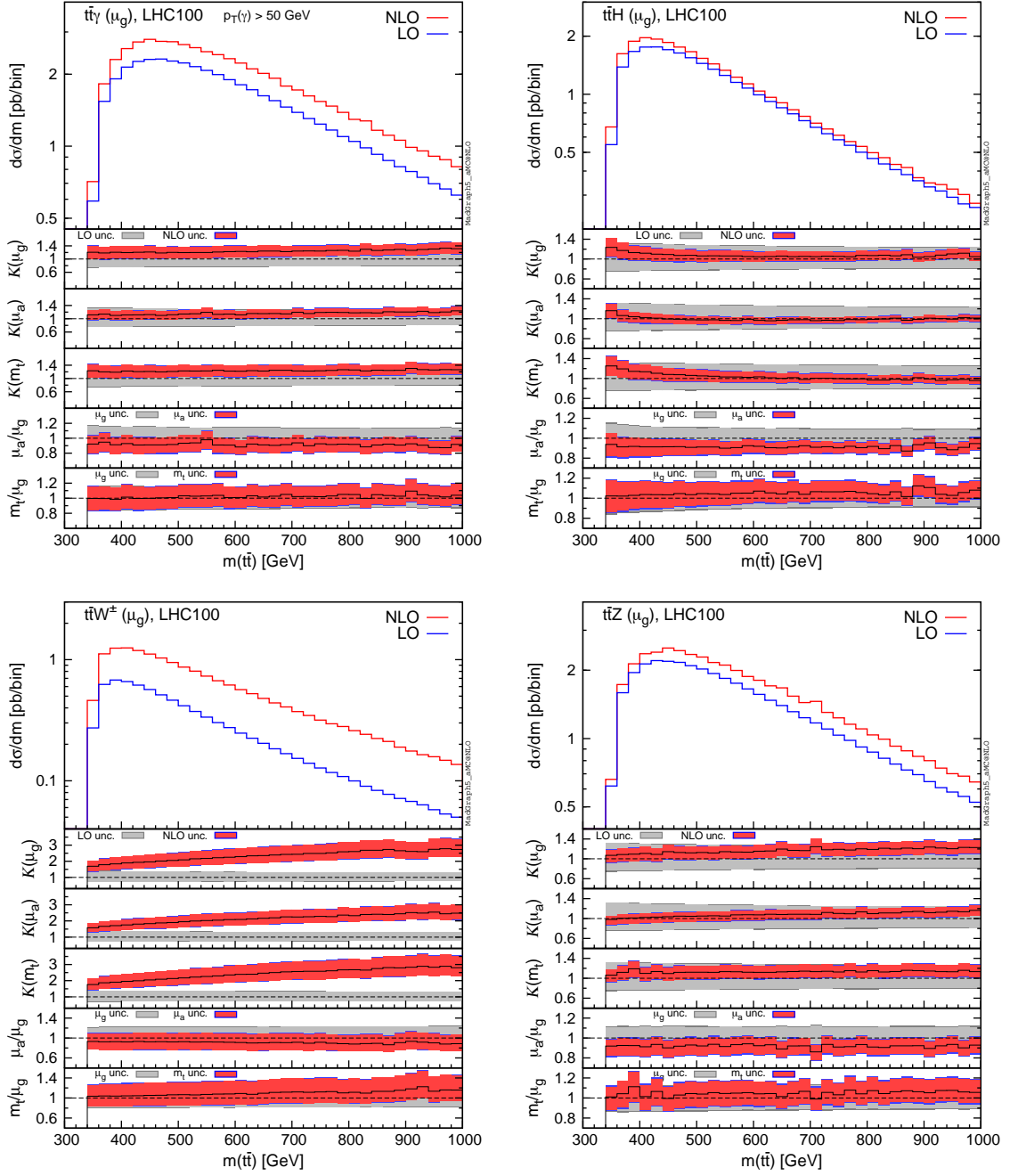


Fig. 156: Differential distributions for the invariant mass of top-quark pair,  $m(tt)$  at 100 TeV. The format of the plots is described in detail in the text.

band around it indicates the scale variation in the standard range  $\mu_g/2 < \mu_f, \mu_r < 2\mu_g$ . The additional blue borders show the PDF uncertainty. We stress that in the plots, as in the tables, scale uncertainties are always obtained by the independent variation of the factorisation and renormalisation scales, via the reweighting technique that has been introduced in [432]. The second and third insets show the same content of the first inset, but with different scale choices. In the second panel both LO and NLO have been evaluated with  $\mu = \mu_a$ , while in the third panel with  $\mu = m_t$ .

The fourth and the fifth panels show a comparison of NLO QCD predictions using the scale  $\mu_g$  and, respectively,  $\mu_a$  and  $m_t$ . All curves are normalised to the red curve in the main panel, i.e., the

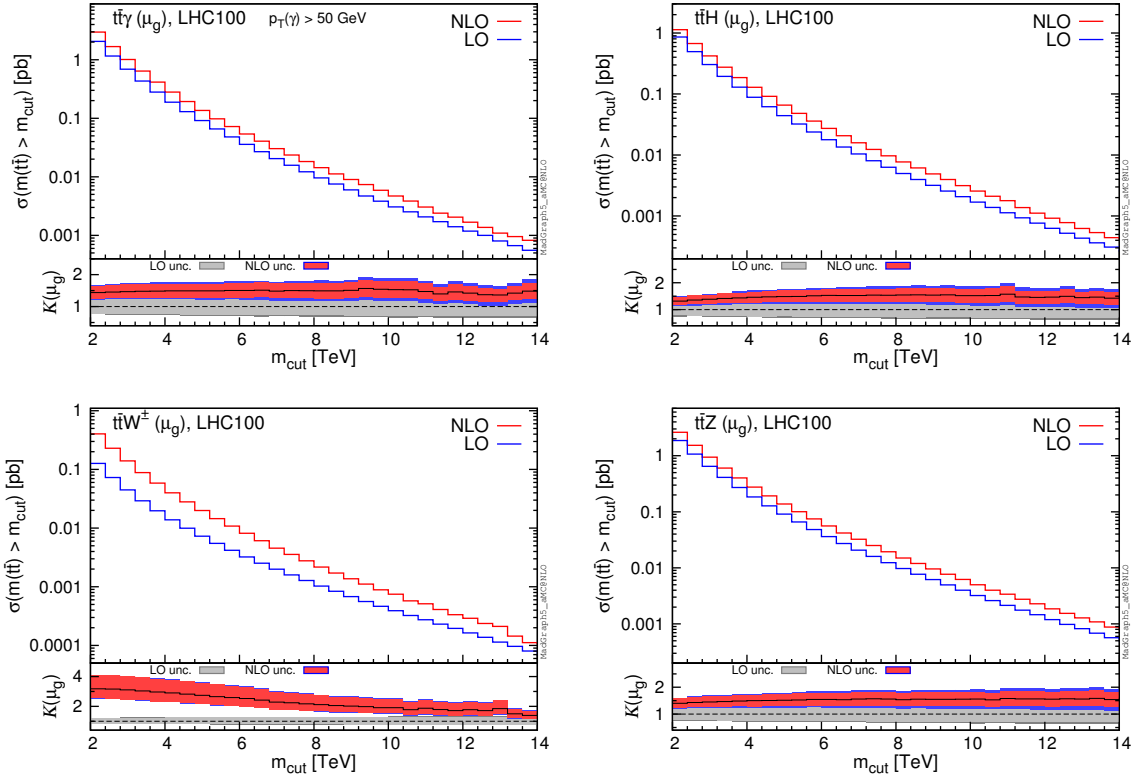


Fig. 157: Cumulative distributions for the invariant mass of top-quark pair,  $m(t\bar{t})$  at 100 TeV. The format of the plots is described in detail in the text.

NLO with  $\mu = \mu_g$ . The light-grey band now indicates the scale variation dependence of NLO QCD with  $\mu = \mu_g$ . Again the dashed black line, the central value, is by definition equal to one and the dark-grey borders include the PDF uncertainties. The black solid line in the fourth panel is the ratio of the NLO QCD predictions at the scales  $\mu_a$  and  $\mu_g$ . The red band shows the scale dependence of NLO QCD predictions at the scale  $\mu_a$ , normalised to the central value of NLO QCD at the scale  $\mu_g$ . Blue bands indicate the PDF uncertainties. The fifth panel is completely analogous to the fourth one, but it compares NLO QCD predictions with  $\mu_g$  and  $m_t$  as central scales.

We start with Fig. 156, which shows the distribution for the invariant mass of the top-quark pair ( $m(t\bar{t})$ ) for the four production processes. From this distribution it is possible to note some features that are typical for most of the distributions. As can be seen in the fourth insets, the use of  $\mu = \mu_a$  leads to NLO values compatible with, but also systematically smaller than, those obtained with  $\mu = \mu_g$ . Conversely, the use of  $\mu = m_t$  leads to scale uncertainties bands that overlap with those obtained with  $\mu = \mu_g$ . By comparing the first three insets for the four different processes, it can be noted that the reduction of the scale dependence from LO to NLO results is stronger in  $t\bar{t}H$  production than for the  $t\bar{t}V$  processes. As said, all these features are not peculiar for the  $m(t\bar{t})$  distribution, and they are consistent with the total cross section analysis presented before, see Fig. 155 and Table 54. From Fig. 156 one can also see that the two dynamical scales  $\mu_g$  and  $\mu_a$  yield slightly flatter  $K$ -factors than those obtained with the fixed scale  $m_t$ , supporting a posteriori such a reference scale.

However, at 100 TeV the  $K$ -factor for the ( $m(t\bar{t})$ ) distribution in  $t\bar{t}W^\pm$  production is not flat, independently of the scale definition employed, as can be seen in Fig. 156. This effect is induced by the  $qg(\bar{q}g)$  initial states, which have at 100 TeV a relative large PDF luminosity also for high values of  $m(t\bar{t})$  and especially  $t$ -channel-like diagrams for the top-quark pair, at variance with LO  $q\bar{q}'$  production.

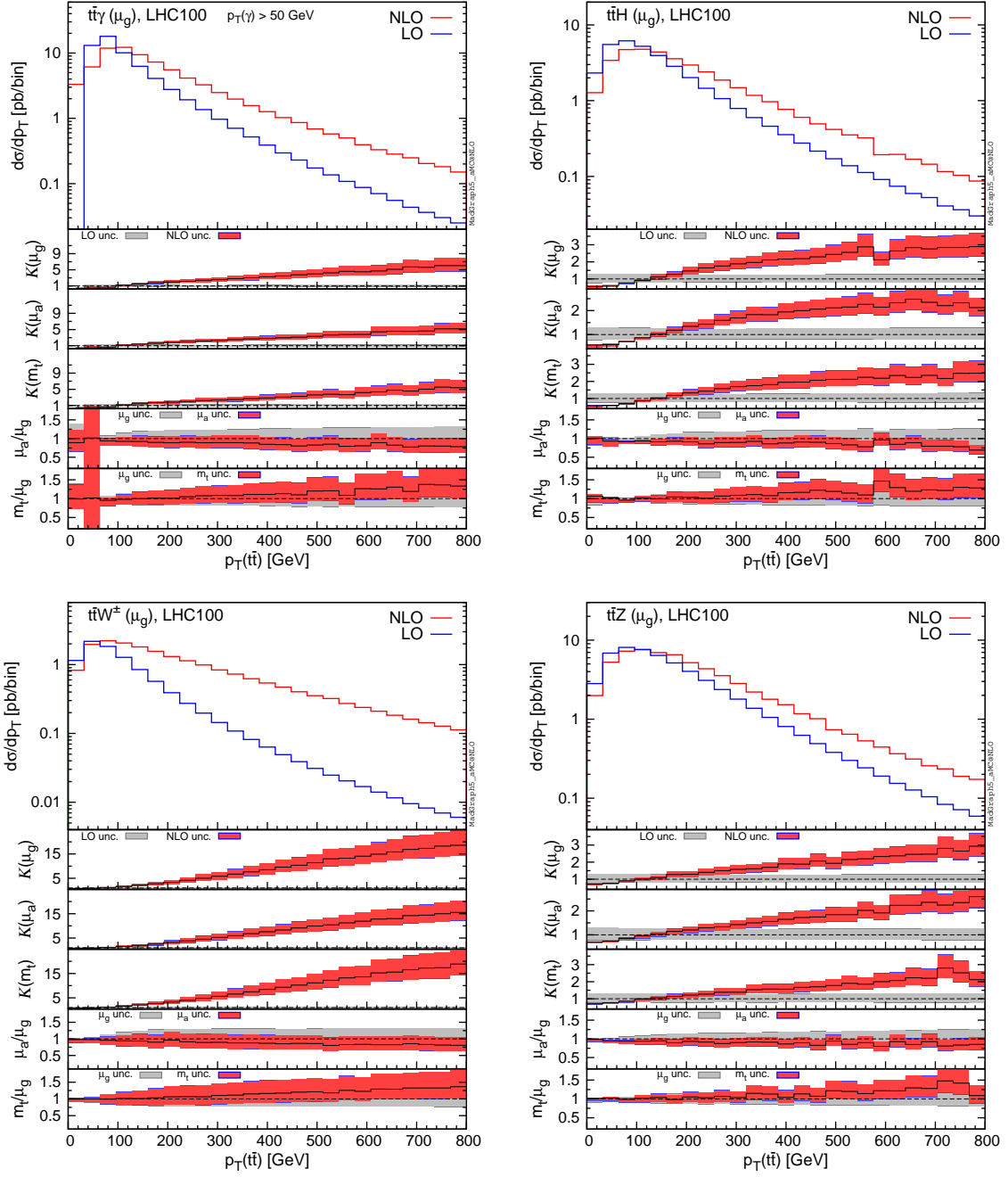


Fig. 158: Differential distributions for the  $p_T$  of top-quark pair,  $p_T(tt)$  at 100 TeV. The format of the plots is described in detail in the text.

In Fig. 157 we display for the same observable cumulative plots, i.e., we plot the dependence of the total cross sections on the cut  $m(tt) > m_{\text{cut}}$  by varying  $m_{\text{cut}}$ . We can notice that at very high values of  $m_{\text{cut}}$  the luminosities of the  $q\bar{q}(\bar{q}q)$  initial states are not the dominant ones, for example the  $K$ -factor of  $t\bar{t}W^\pm$  decreases accordingly. For cumulative distributions we show in the plots only results obtained by using  $\mu_g$  as central scale.

For particular observables and processes, like the  $p_T$  of the top-quark pair ( $p_T(tt)$ ) in  $t\bar{t}W^\pm$  and  $t\bar{t}\gamma$  production, the  $K$  factors show a strong kinematic dependence. This is shown in Figs. 158 and 159. The origin of these effects is well understood [66, 310, 311]. Top-quark pairs with a large  $p_T$  originate at

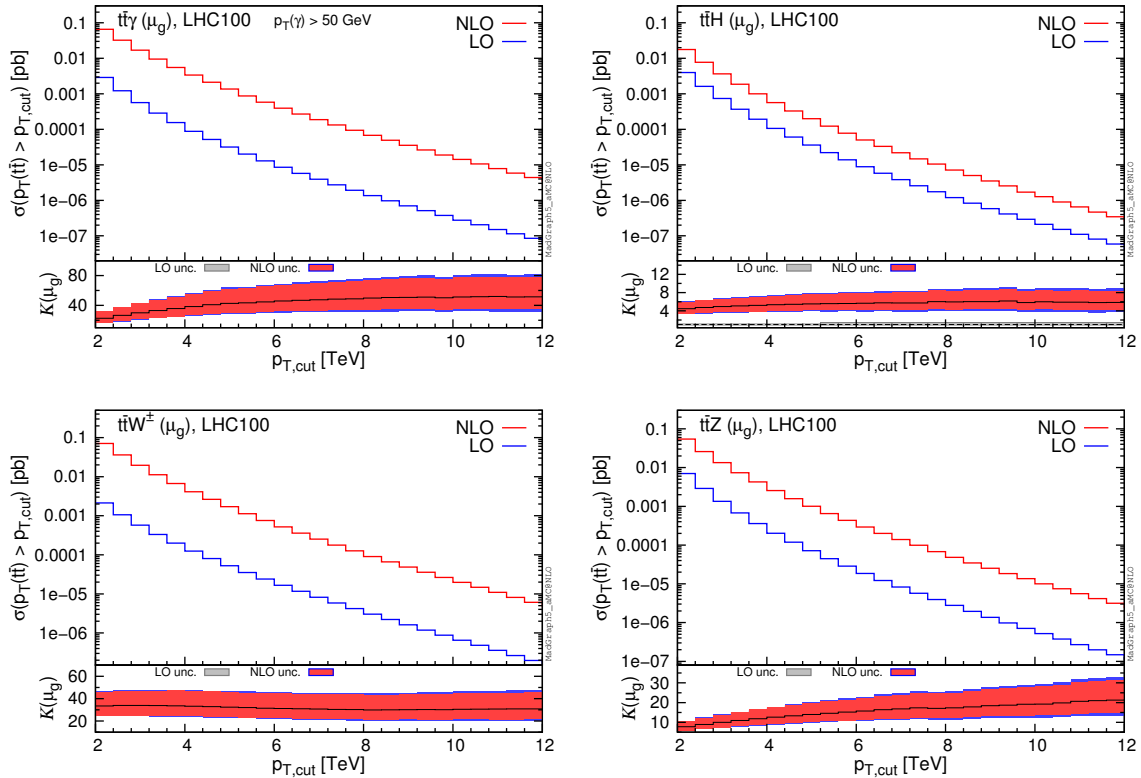


Fig. 159: Cumulative distributions for the  $p_T$  of top-quark pair,  $p_T(t\bar{t})$  at 100 TeV. The format of the plots is described in detail in the text.

LO from the recoil against a hard vector or a hard scalar boson. Conversely, at NLO, in this kinematical configuration the largest contribution emerges from the recoil of the top-quark pair against a hard jet and a soft scalar or vector boson. In particular, the cross section for a top-quark pair with a large  $p_T$  receives large corrections from the  $qg$  initial state, which appears for the first time only at NLO.

In the case of  $t\bar{t}W^\pm$  production, for instance, the emission of a  $W$  collinear to the final-state quark in  $qg \rightarrow t\bar{t}W^\pm q'$  can be approximated as the  $qg \rightarrow t\bar{t}q$  process times the  $q \rightarrow q'W^\pm$  splitting. For the  $W$  momentum, the splitting involves a soft and collinear singularity that is regulated by the  $W$  mass. Thus, once the  $W$  momentum is integrated, the  $qg \rightarrow t\bar{t}W^\pm q'$  process yields a contribution to the  $p_T(t\bar{t})$  distributions that is proportional to  $\alpha_s \log^2 [p_T(t\bar{t})/m_W]$ , leading to large corrections. The same argument clearly applies also to  $t\bar{t}Z$  for the  $q \rightarrow qZ$  splitting in  $qg \rightarrow t\bar{t}Zq$ . However, in the case of  $t\bar{t}W^\pm$ , this effect is further enhanced also by a different reason. Unlike the other production processes,  $t\bar{t}W^\pm$  production does not originate at LO from the gluon–gluon initial state, which has the largest partonic luminosity. Consequently, the relative corrections induced by the quark–gluon initial states have a larger impact.

The argument above clarifies the origin of the enhancement at high  $p_T$  of the  $t\bar{t}$  pairs, yet it raises the question of the reliability of NLO predictions for  $t\bar{t}V$  in this region of the phase space. In particular, the giant  $K$ -factors and the large scale dependence call for better predictions. One could argue that only a complete NNLO calculation for  $t\bar{t}V$  would settle this issue. However, since the dominant kinematic configurations involve a hard jet, it is possible to start from the  $t\bar{t}Vj$  final state and reduce the problem to the analysis of NLO corrections to  $t\bar{t}Vj$ , which can be automatically obtained with MADGRAPH5\_AMC@NLO. We have therefore computed results for different minimum  $p_T$  for the additional jet both at NLO and LO accuracy. In Fig. 160, we summarise the most important features of the  $t\bar{t}W^\pm(j)$  cross section as a function of the  $p_T(t\bar{t})$  as obtained from different calculations. Similar results,

even though less extreme, hold for  $t\bar{t}Z$  and  $t\bar{t}H$  final states and therefore we do not show them for sake of brevity. In Fig. 160, the solid blue and red curves correspond to the predictions of  $p_T(t\bar{t})$  as obtained from  $t\bar{t}W^\pm$  calculation at LO and NLO accuracy, respectively. The dashed light blue, purple and light-grey curves are obtained by calculating  $t\bar{t}W^\pm j$  at LO (with NLO PDFs and  $\alpha_s$  and same scale choice in order to consistently compare them with NLO  $t\bar{t}W^\pm$  results) with a minimum  $p_T$  cut for the jets of 50, 100, and 150 GeV, respectively. The three curves, while having a different threshold behaviour, they all tend smoothly to the  $t\bar{t}W^\pm$  prediction at NLO at high  $p_T(t\bar{t})$ , clearly illustrating that the dominant contributions come from kinematic configurations with a hard jet. Finally, the dashed green line is the  $p_T(t\bar{t})$  as obtained from  $t\bar{t}W^\pm j$  at NLO in QCD with the minimum  $p_T$  cut of the jet of 100 GeV. This prediction for  $p_T(t\bar{t})$  at high  $p_T$  is stable and reliable, and in particular it does not feature any large  $K$ -factor, as can be seen in the lower inset, which displays the differential  $K$ -factor for  $t\bar{t}W^\pm j$  production with the  $p_T$  cut of the jet of 100 GeV. For large  $p_T(t\bar{t})$ , NLO corrections to  $t\bar{t}W^\pm j$  reduce the scale dependence of the LO predictions, but do not increase their central value. Consequently, since we do not expect large effects from NNLO corrections in  $t\bar{t}W^\pm$  production at large  $p_T(t\bar{t})$ , a simulation of NLO  $t\bar{t}W^\pm j$  merged sample à la FxFx [433] should be sufficient in order to provide reliable predictions over the entire phase space.

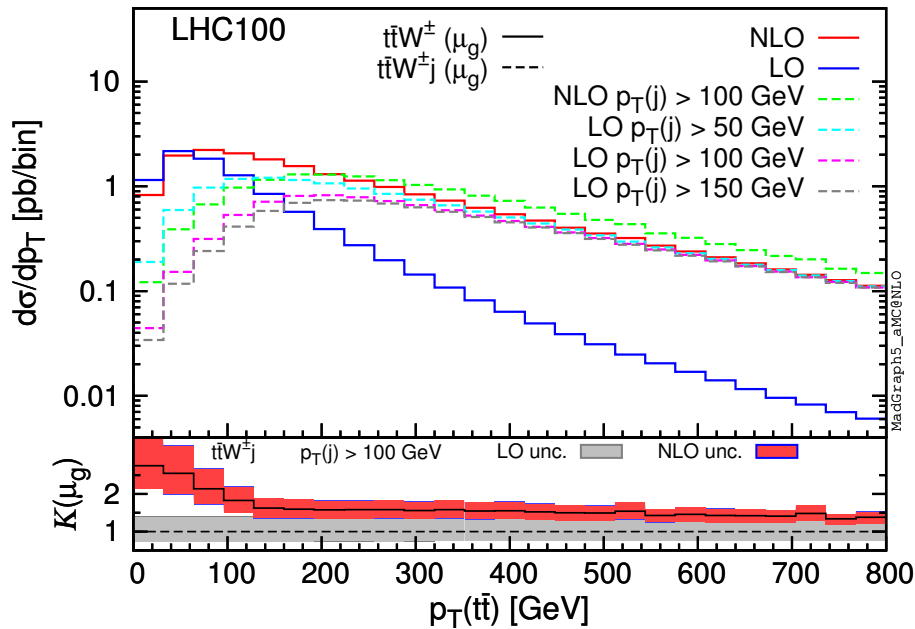


Fig. 160: Comparison at 100 TeV between differential distribution of the  $t\bar{t}$  transverse momentum in  $t\bar{t}W^\pm$  from calculations performed at different orders in QCD. The blue and red solid histograms are obtained from the  $t\bar{t}W^\pm$  calculation at LO and NLO, respectively. The dashed histograms are obtained from the  $t\bar{t}W^\pm j$  calculation at LO (light blue, purple, and light grey) and at NLO (green), for different minimum cuts (50, 100, 150 GeV) on the jet  $p_T$ . The lower inset shows the differential  $K$ -factor as well as the residual uncertainties given by the  $t\bar{t}W^\pm j$  calculation.

For completeness, we provide in Table 55 the total cross sections at LO and NLO accuracy for  $t\bar{t}W^\pm j$ ,  $t\bar{t}Zj$  and  $t\bar{t}Hj$  production, with a cut  $p_T(j) > 100$  GeV. At variance with what has been done in Fig. 160 LO cross sections are calculated with LO PDFs and the corresponding  $\alpha_s$ .

In Fig. 161 we show additional proofs for the argument discussed so far. We plot relevant distributions for the  $t\bar{t}W^\pm j$  production. One can see that the  $W$  and the jet tends to be collinear, especially for large  $p_T(t\bar{t})$ , and that the  $W$  is typically soft.

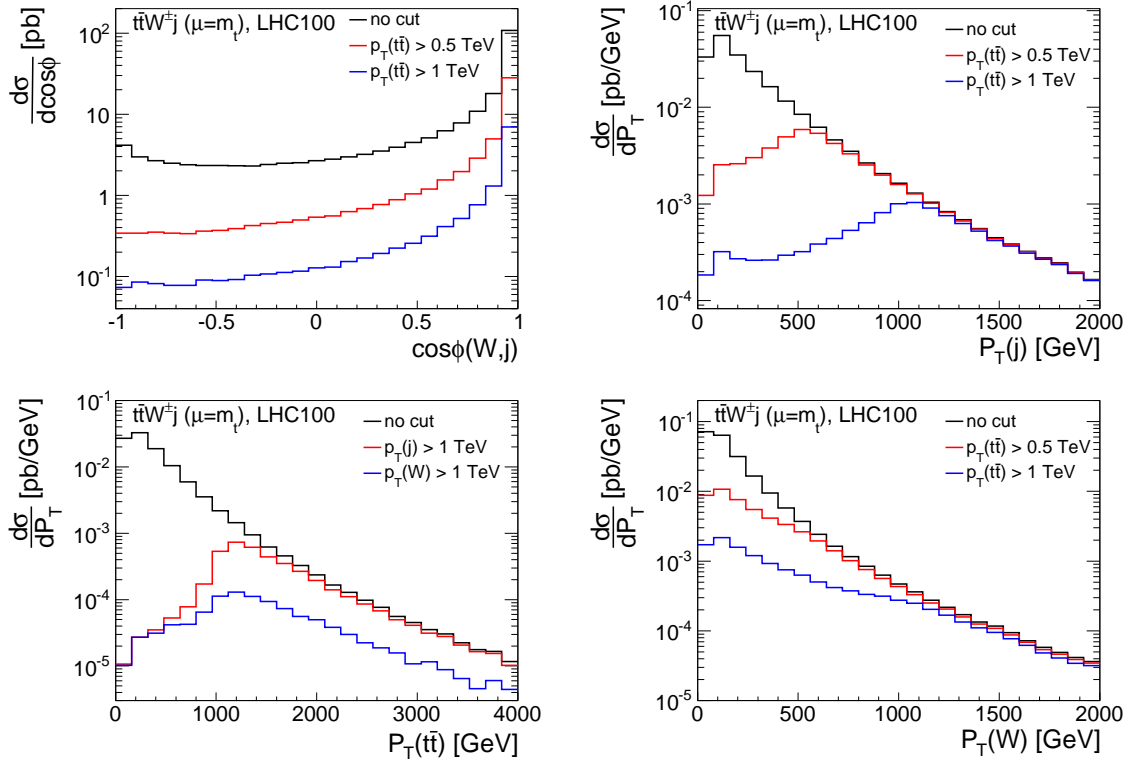


Fig. 161: Relevant distributions for  $t\bar{t}W^\pm j$  production, where the fixed scale  $\mu = m_t$  has been used. Black lines are without cuts, red and blue lines are with cuts.

100 TeV $\sigma$ [pb]	$t\bar{t}Hj$	$t\bar{t}Zj$	$t\bar{t}W^\pm j$
NLO	$19.42^{+0.7\%}_{-4.9\%} +1.0\%$	$32.38^{+2.4\%}_{-7.4\%} +0.9\%$	$17.16^{+14.9\%}_{-13.7\%} +0.7\%$
LO	$27.02^{+39.3\%}_{-26.4\%} +1.1\%$	$39.81^{+39.8\%}_{-26.7\%} +1.1\%$	$15.67^{+37.7\%}_{-25.5\%} +0.5\%$
<i>K</i> -factor	0.72	0.81	1.10

Table 55: Cross sections with  $p_T(j) > 100$  GeV. The renormalisation and factorisation scales are set equal to  $\mu_g$  for the  $t\bar{t}V$ . The (N)LO cross sections are calculated with (N)LO PDFs, the relative statistical integration error is equal or smaller than one permille.

The mechanism discussed in detail in previous paragraphs is also the source of the giant  $K$ -factors for large  $p_T(t\bar{t})$  in  $t\bar{t}\gamma$  production, see Fig. 158. This process can originate from the  $gg$  initial state at LO. However, the emission of a photon involves soft and collinear singularities that are not regulated by physical masses. When the photon is collinear to the final-state quark, the  $qg \rightarrow t\bar{t}\gamma q$  process can be approximated as the  $qg \rightarrow t\bar{t}q$  process times a  $q \rightarrow q\gamma$  splitting. In this case, soft and collinear divergences are regulated by both the cut on the  $p_T$  of the photon ( $p_T^{\text{cut}}$ ) and the Frixione-isolation parameter  $R_0$ . We have checked that, increasing the values of  $p_T^{\text{cut}}$  and/or  $R_0$ , the size of the  $K$ -factors is reduced. It is interesting to note that also corrections in the tail are much larger for  $\mu = \mu_g$  than  $\mu = \mu_a$ . This is due to the fact that the softest photons, which give the largest contributions, sizeably reduce the value of the scale  $\mu_g$ , whereas  $\mu_a$  is by construction larger than  $2p_T(t\bar{t})$ . This also suggests that  $\mu_g$  might be an appropriate scale choice for this process only when the minimum  $p_T$  cut and the isolation parameters on the photon are harder.

In Figs. 162 and 163 we respectively show the  $p_T$  distributions for the top quark and the vector or

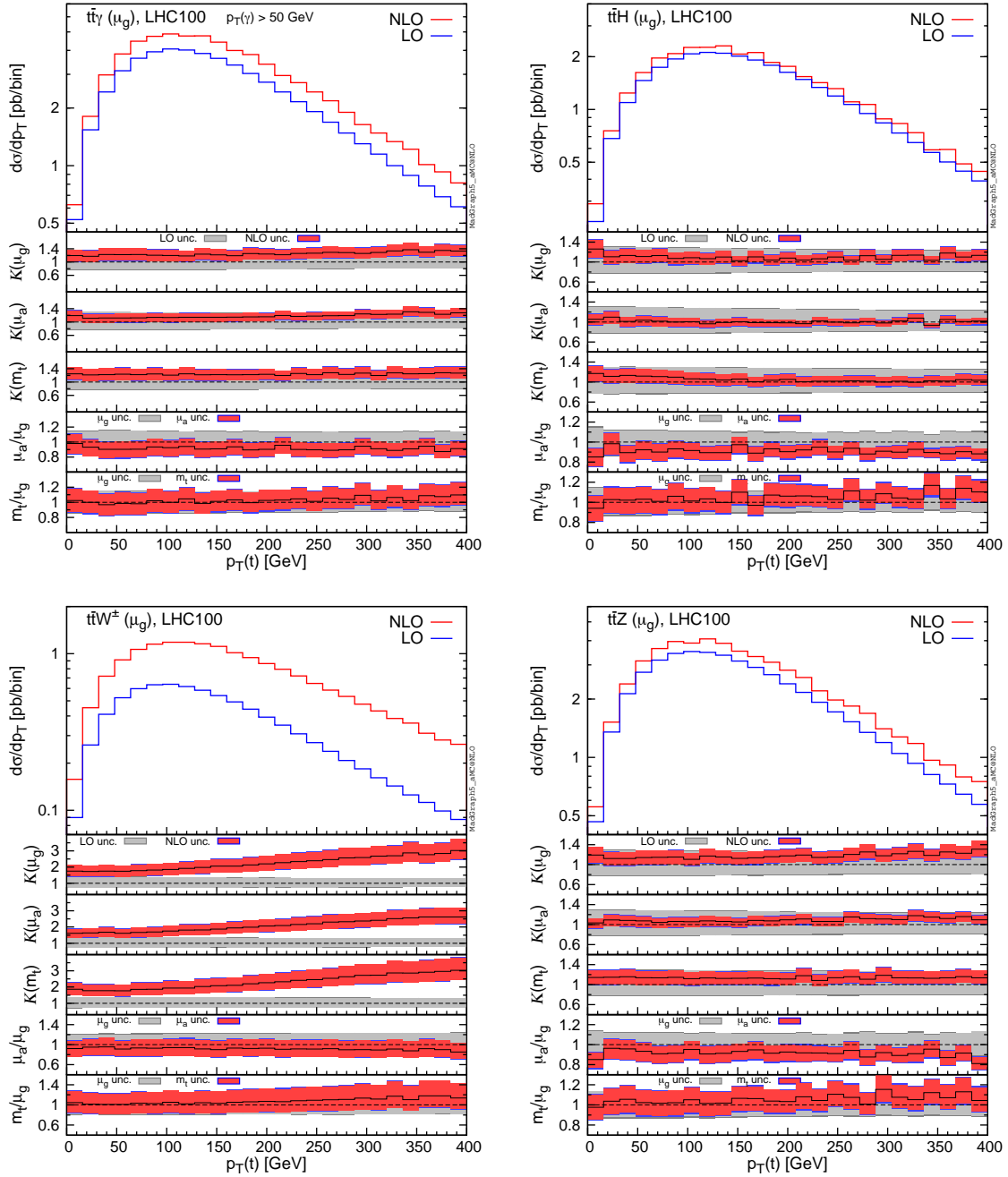


Fig. 162: Differential distributions for the  $p_T$  of top-quark,  $p_T(t)$  at 100 TeV. The format of the plots is described in detail in the text.

scalar boson,  $p_T(t)$  and  $p_T(V)$ . For these two observables, we find the general features that have already been addressed for the  $m(tt)$  distributions in Fig. 156. We display in Fig. 164 cumulative distributions for  $p_T(V)$ .

In Fig. 165 we display the distributions for the rapidity of the vector or scalar boson,  $y(V)$ . For the four processes considered here, the vector or scalar boson is radiated in different ways at LO. In  $t\bar{t}H$  production, the Higgs boson is not radiated from the initial state. In  $t\bar{t}Z$  and  $t\bar{t}\gamma$  production, in the quark–antiquark channels the vector boson can be emitted from the initial and final states, but in the gluon–gluon channel it can be radiated only from the final state. In  $t\bar{t}W^\pm$  production, the  $W$  is

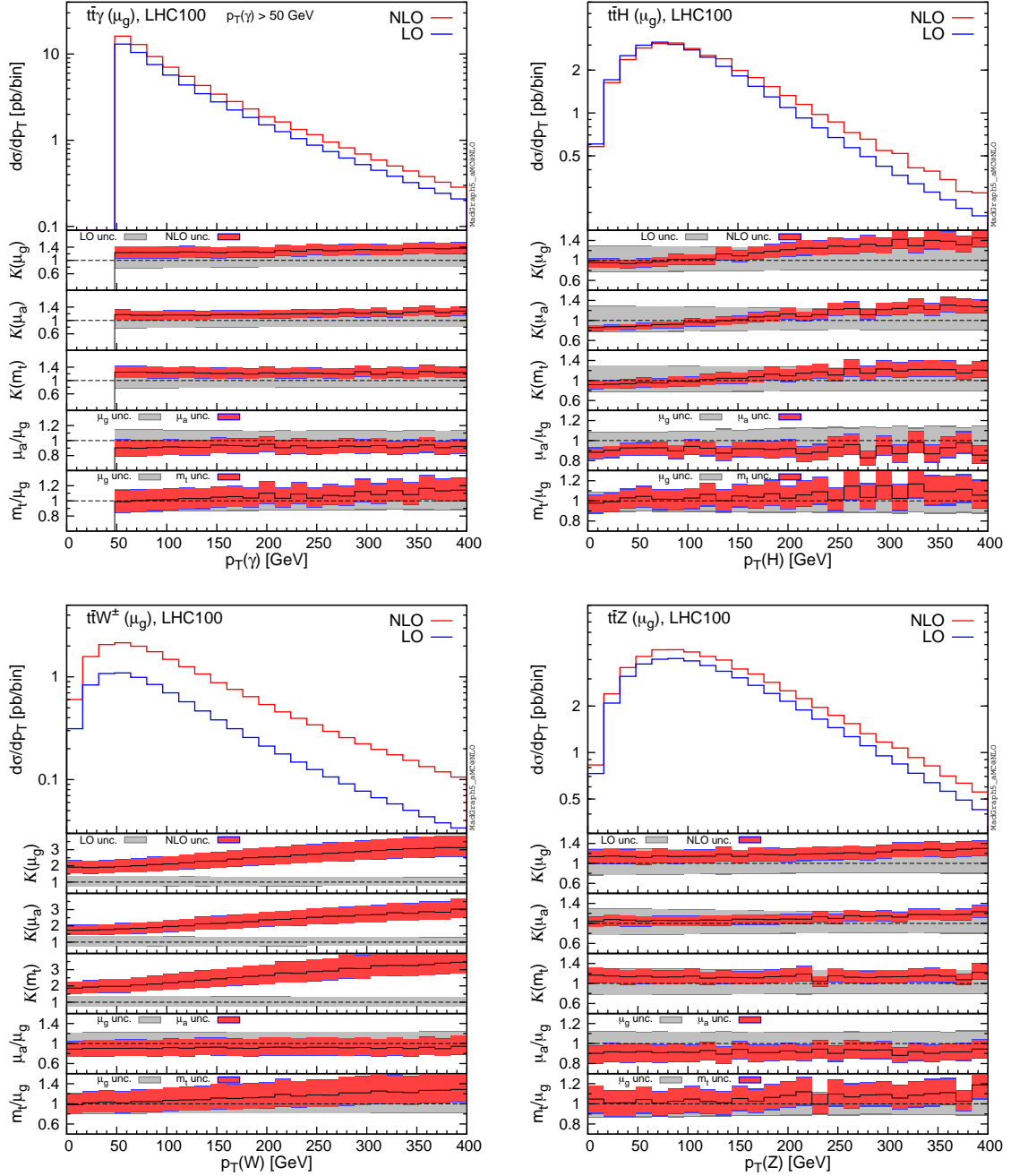


Fig. 163: Differential distributions for the  $p_T$  of the vector or scalar boson,  $p_T(V)$  at 100 TeV. The format of the plots is described in detail in the text.

always emitted from the initial-state quarks. The initial-state radiation of a vector boson is enhanced in the forward and backward directions, i.e., when it is collinear to the beam-pipe axis. Consequently, the vector boson is more peripherally distributed in  $t\bar{t}W^\pm$  production, which involves only initial state radiation, with respect to  $t\bar{t}\gamma$  and especially  $t\bar{t}Z$  production. In  $t\bar{t}H$  production, large values of  $|y(V)|$  are not related to any matrix-element enhancement and indeed the  $y(V)$  distribution is much more central than in  $t\bar{t}V$  processes. With NLO QCD corrections, in  $t\bar{t}W^\pm$  production the vector boson is even more peripherally distributed. On the contrary, NLO QCD corrections make the distribution of the rapidity of the Higgs boson even more central. In Fig. 165 one can also notice how the reduction of the scale

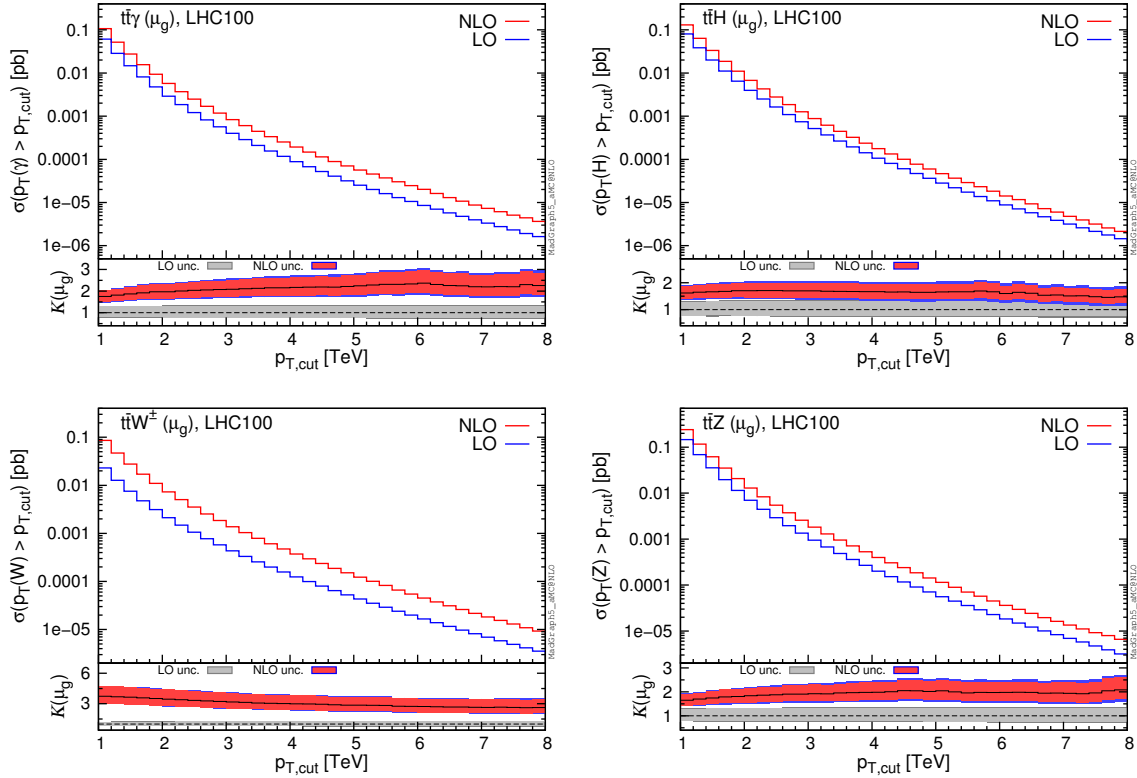


Fig. 164: Cumulative distributions for the  $p_T$  of the vector or scalar boson,  $p_T(V)$  at 100 TeV. The format of the plots is described in detail in the text.

dependence from LO to NLO results is much higher in  $t\bar{t}H$  production than in  $t\bar{t}V$  type processes. Furthermore, for this observable,  $K$ -factors are in general not flat also with the use of dynamical scales in the case of  $t\bar{t}W^\pm$  and  $t\bar{t}H$ . From a phenomenological point of view, this is particularly important for  $t\bar{t}W^\pm$ , since the cross section originating from the peripheral region is not suppressed.

In Fig. 166 we show distributions for the rapidities of the top quark and antiquark,  $y(t)$  and  $y(\bar{t})$ . In this case we use a different format for the plots. In the main panel, as in the previous plots, we show LO results in blue and NLO results in red. Solid lines correspond to  $y(t)$ , while dashed lines refer to  $y(\bar{t})$ . In the first and second insets we plot the ratio of the  $y(t)$  and  $y(\bar{t})$  distributions at NLO and LO accuracy, respectively. These ratios are in principle useful to identify which distribution is more central(peripheral) and if there is a central asymmetry for the top-quark pair.

In the case of  $t\bar{t}$  production the charge asymmetry  $A_c$ , which in proton–proton collisions corresponds to a central asymmetry defined as

$$A_c = \frac{\sigma(|y_t| > |y_{\bar{t}}|) - \sigma(|y_t| < |y_{\bar{t}}|)}{\sigma(|y_t| > |y_{\bar{t}}|) + \sigma(|y_t| < |y_{\bar{t}}|)}, \quad (80)$$

or to a forward-backward asymmetry in proton–antiproton collisions, originates from QCD and EW corrections. At NLO, the asymmetry receives contributions from the interference of initial- and final-state radiation of neutral vector bosons (gluon in QCD corrections, and photons or  $Z$  bosons in EW corrections) [434–439]. Thus, the real-radiation contributions involve, at LO, the processes  $pp \rightarrow t\bar{t}Z$  and  $pp \rightarrow t\bar{t}\gamma$ , which are analysed here both at LO and at NLO accuracy. The  $t\bar{t}\gamma$  production yields an asymmetry already at LO, and this feature has been studied in [440]. The  $t\bar{t}Z$  production central asymmetry is also expected to be non vanishing at LO. The asymmetry is instead analytically zero at LO for  $t\bar{t}W^\pm$  ( $t\bar{t}H$ ) production, where the interference of initial- and final-state  $W$ (Higgs) bosons is not

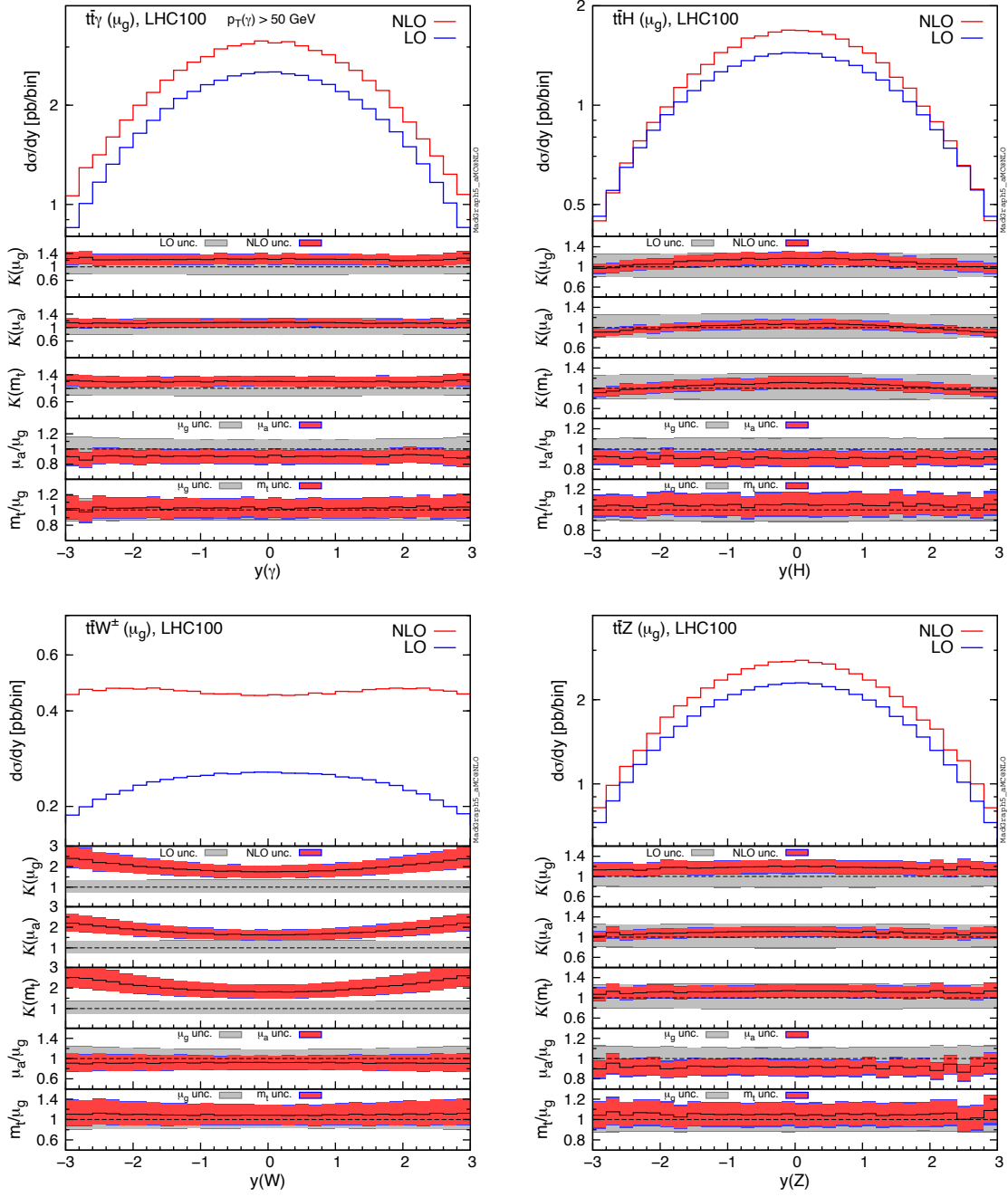


Fig. 165: Differential distributions for the rapidity of the vector or scalar boson,  $y(V)$  at 100 TeV. The format of the plots is described in detail in the text.

possible.<sup>43</sup>

Conversely, at NLO all the  $t\bar{t}V$  processes and the  $t\bar{t}H$  production have an asymmetry. However, both at LO and NLO asymmetric effects on  $y(t)$  and  $y(\bar{t})$  distributions are small at 100 TeV and difficult to be seen in Fig. 166. These effects can be better quantified by looking directly to the asymmetry  $A_c$  defined in Eq. (80). NLO and LO results for  $A_c$  are listed in Table 56, which clearly demonstrates, once again, that NLO QCD effects cannot be neglected in the predictions of the asymmetries. For  $t\bar{t}W^\pm$  and

<sup>43</sup>In principle, when the couplings of light-flavour quarks are considered as non-vanishing, the initial-state radiation of a Higgs boson is possible and also a very small asymmetry is generated. However, this possibility is ignored here.

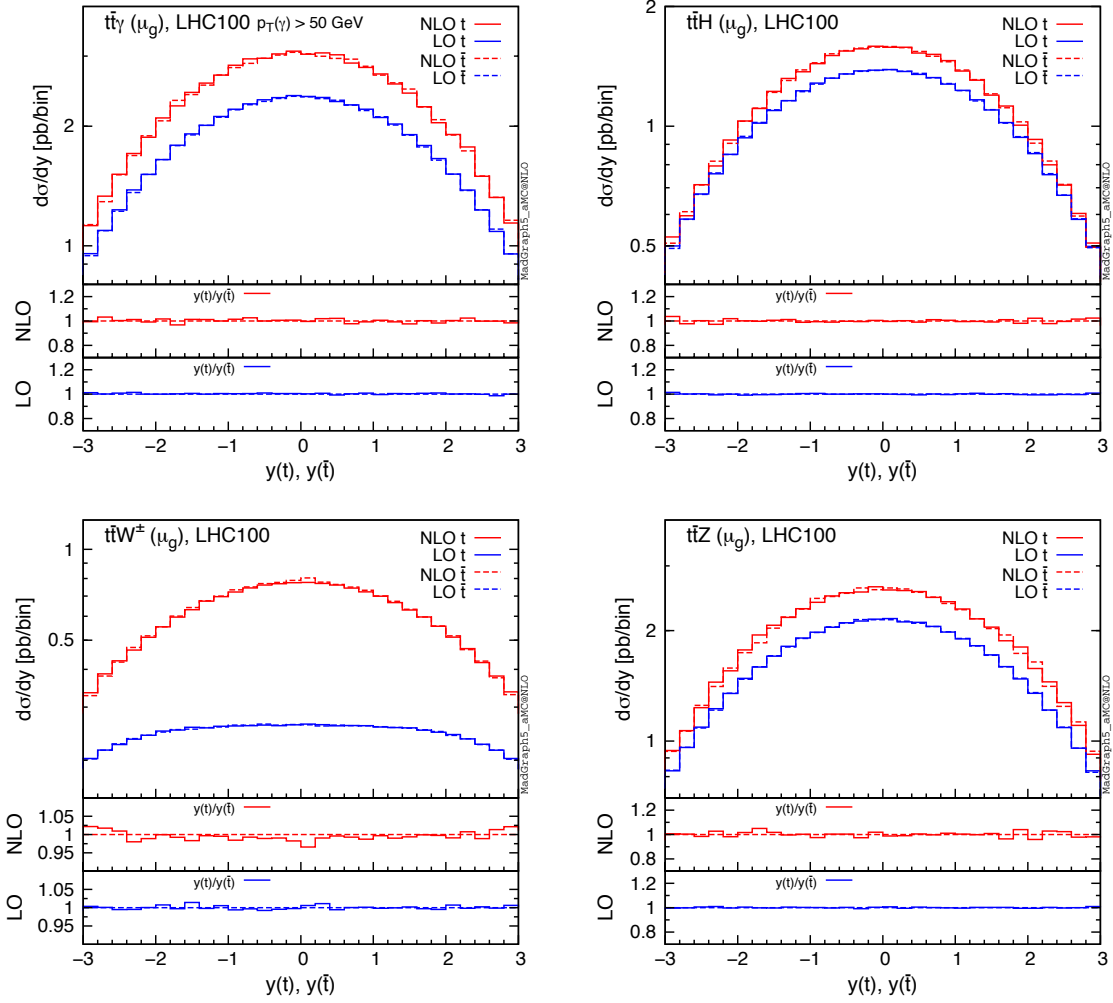


Fig. 166: Differential distributions for the rapidity of the top quark and antiquark,  $y(t)$  and  $y(\bar{t})$  at 100 TeV.

$t\bar{t}H$  production, an asymmetry is actually generated only at NLO. The case of  $t\bar{t}W^\pm$  production has been studied in detail in [413], also for 100 TeV collisions. Furthermore, NLO QCD corrections largely increase the asymmetry in  $t\bar{t}Z$  production, and decrease it by  $\sim 40\%$  in  $t\bar{t}\gamma$  production.

## 12.2 Photon emission off the top quark decay products

It is interesting to note that in  $t\bar{t} + \gamma$  final states the photon is not only radiated in the production stage (*i.e.* before the top quarks go on-shell), it is also emitted off the top quark decay products (after one of the top quarks has gone on-shell). The branching  $t \rightarrow bW + \gamma$  has a kinematically large phase space with allowed photon energies  $p_{\perp, \text{cut}}^\gamma \leq E_\gamma \leq m_t - M_W \approx 92$  GeV in the top quark rest frame. The small masses of the  $b$ -quark and  $W$  decay products lead to additional collinear enhancements. As a result, radiative top quark decays yield a large contribution to  $W^+W^-b\bar{b} + \gamma$  final states (with intermediate on-shell  $t\bar{t}$  pairs). In Fig. 167 we show their relative contribution to the total cross section and compare them to photons radiated in the production process. In this study, we assume photons with  $p_\perp^\gamma \geq 20$  GeV and require a separation of  $\Delta R = 0.2$  between photons and leptons or jets. At moderate photon transverse momenta (20-60 GeV), the contribution from radiative top quark decays dominates the total cross section with more than 70%. Beyond  $p_\perp^\gamma \approx 100$  GeV the contribution from the  $t\bar{t} + \gamma$  process with subsequent top quark decays takes over, but radiative top quark decays still matter at the 10% level up to transverse

100 TeV $A_c$ [%]	$t\bar{t}W^\pm$	$t\bar{t}\gamma$
LO	-	$(-0.70 \pm 0.05)^{+0.04}_{-0.04} \ ^{+0.03}_{-0.02}$
NLO	$(1.3 \pm 0.1)^{+0.23}_{-0.16} \ ^{+0.05}_{-0.03}$	$(-0.45 \pm 0.04)^{+0.05}_{-0.04} \ ^{+0.01}_{-0.02}$
100 TeV $A_c$ [%]	$t\bar{t}H$	$t\bar{t}Z$
LO	-	$(0.03 \pm 0.05)^{+0.001}_{-0.004} \ ^{+0.003}_{-0.01}$
NLO	$(0.17 \pm 0.01)^{+0.06}_{-0.04} \ ^{+0.01}_{-0.01}$	$(0.22 \pm 0.04)^{+0.06}_{-0.04} \ ^{+0.01}_{-0.01}$

Table 56: NLO and LO central asymmetries for  $t\bar{t}V$ -type processes and  $t\bar{t}H$  production at 100 TeV for  $\mu = \mu_g$ . The first uncertainty is due to the limited integration statistics. The second and third uncertainties reflect the scale variation within  $\mu_g/2 < \mu_f, \mu_r < 2\mu_g$ , and the PDFs. These were obtained by reweighting the distributions, during integration, on an event-by-event basis.

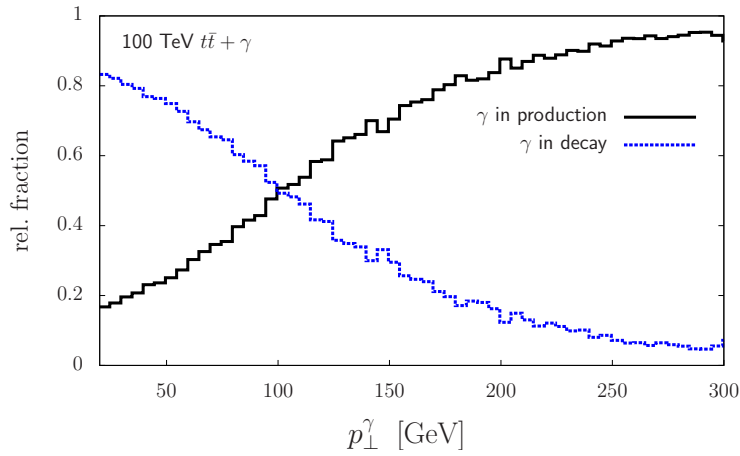


Fig. 167: Relative contribution of photons from the top quark production (black) and decay (blue) stage in  $W^+W^-b\bar{b} + \gamma$  final states at 100 TeV. Photons are required to have  $p_\perp \geq 20$  GeV and be separated from jets and leptons by  $\Delta R_{\gamma\ell} = \Delta R_{\gamma j} = 0.2$ .

photon momenta of 300 GeV. Dedicated selection cuts to remove the radiative top quark decay process have been presented in Refs. [440, 441]. However, at NLO QCD the fraction of  $t \rightarrow bW + \gamma$  events that still pass these cuts can be as large as 10% [418], the same order of magnitude as the NLO corrections themselves.

Because of these features specific to top quark pair production in association with a photon, certain care has to be taken when describing a realistic final state of  $W^+W^-b\bar{b} + \gamma$ . Recent experimental analyses at the LHC [442, 443] apply typical selection cuts on leptons, jets, missing energy and the photon, but do not explicitly suppress radiative top quark decays. Hence, neglecting this contribution in the theoretical description can lead to an underestimation of the event rate by a factor of up to 3.

### 13 Top properties<sup>44</sup>

In the SM, the top quark is possibly the particle whose production and decay properties are simpler. It lacks the rich phenomenology of hadronic spectroscopy characteristic of all other quarks; its decay is dominated by the  $Wb$  final state, with a tiny contamination of  $Ws$  and  $Wd$ , and all other SM-allowed decays (FCNC,  $t \rightarrow WZb$ , etc) being so small as to be beyond the experimental reach. On the other hand, its large mass implies a particular sensitivity to the mechanism of electroweak symmetry breaking. Thus, precision studies of the top-Higgs couplings, as well as the couplings of the top to the electroweak gauge bosons, are of great importance in understanding electroweak symmetry breaking and possibly challenging its SM realization. Furthermore, new physics unrelated to the mechanism of electroweak symmetry breaking might be revealed through modifications of SM interactions rather than through a direct discovery of new particles. For a general introduction to the study of top quark properties in hadronic collisions, we refer to the old report on SM physics at the LHC, Ref. [444].

We avoid here a discussion of the determination of the top mass at 100 TeV: any progress relative to what will be known at the end of the LHC will depend on theoretical progress that is hard to anticipate now, and on a very precise definition of the future experimental environment and detector performance. We focus in this section on the prospects to measure precisely the top couplings to EW bosons and to gluons, and to constrain possible deviations from the SM expectations.

The anomalous chromomagnetic and chromoelectric dipole moments  $d_V$  and  $d_A$  in

$$\mathcal{L} = \mathcal{L}_{\text{QCD}} + \frac{g_s}{m_t} \bar{t} \sigma^{\mu\nu} (d_V + i d_A \gamma_5) \frac{\lambda_a}{2} t G_{\mu\nu}^a \quad (81)$$

modify the couplings of top quarks to gluons and hence they affect any observable involving final state tops. Since top quark pairs are copiously produced in hadronic  $pp$  collisions, and since the production and decay dynamics of this process are very well understood,  $pp \rightarrow t\bar{t}$  is ideally suited to an investigation of the top-gluon interactions. In particular, the chromodipole moments are expected to have an important impact on the high energy behavior of this process. Numerous studies have investigated these effects in the LHC environment and a large number of sensitive observables have been described [445–453]. High energy production rates will be even more accessible at the 100 TeV FCC. A cross section analysis suggests that using  $m_{t\bar{t}} \gtrsim 10$  TeV at the FCC offers the best balance between the sensitivity of the high energy behavior and the statistics in this regime [338]. This leads to an improvement of the chromodipole moment constraints by an order of magnitude, as compared with a similar analysis for the high energy LHC run, see Fig. 168.

The abundant production of top quark pairs at the FCC will also improve the limits on top rare decays, for example those mediated by top flavour-changing neutral couplings to the gauge bosons,

$$\begin{aligned} \mathcal{L} = & \frac{g}{2c_W} \bar{q} \left[ \gamma^\mu (X_{qt}^L P_L + X_{qt}^R P_R) + \frac{i\sigma^{\mu\nu} q_\nu}{M_Z} (\kappa_{qt}^L P_L + \kappa_{qt}^R P_R) \right] t Z_\mu \\ & + e \bar{q} \frac{i\sigma^{\mu\nu} q_\nu}{m_t} (\lambda_{qt}^L P_L + \lambda_{qt}^R P_R) t A_\mu + \text{h.c.}, \end{aligned} \quad (82)$$

with  $q = u, c$ . There are not yet dedicated studies of the FCC sensitivity to such processes. Performing a naive rescaling of the LHC expectations for  $\sqrt{s} = 14$  TeV and  $100 \text{ fb}^{-1}$  [454, 455] and assuming a luminosity of  $10 \text{ ab}^{-1}$  for the FCC, one would expect an improvement of almost two orders of magnitude, reaching a sensitivity of  $\text{Br}(t \rightarrow qZ, q\gamma) \simeq 10^{-7}$ . However, at such a level of precision the systematic uncertainties in the background predictions will likely be dominant, and a more reliable estimation of the sensitivity requires a detailed analysis.

Let us now turn to the discussion of final states with top quarks in association with electroweak bosons. These processes yield direct sensitivity to the top quark electroweak couplings and are copiously

<sup>44</sup>Editors: M Schulze, J.A. Aguilar Saavedra

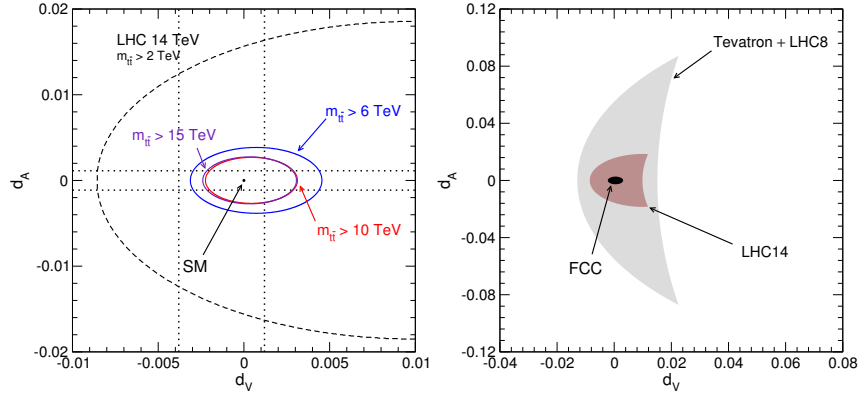


Fig. 168: (Left) Sensitivity of the  $\sqrt{s} = 14$  TeV LHC, and the  $\sqrt{s} = 100$  TeV FCC to the chromomagnetic and chromoelectric dipole moments  $d_V$  and  $d_A$  from  $t\bar{t}$  production. Three different definitions for the boosted regime at the FCC are shown. (Right) A comparison of constraints on  $d_V$  and  $d_A$  from past, present, and future hadron colliders. For more details, see Ref. [338]

produced in 100 TeV collisions. We postpone to the Higgs volume of this Report the more detailed discussion of top production with a Higgs boson and the determination of the top Yukawa coupling. Studies of the couplings of the top quark to the electroweak gauge bosons are complementary to studies of the top-Higgs interactions. The couplings of the neutral gauge bosons  $Z$  and  $\gamma$  to the top quark are fixed by the SM quantum numbers and gauge symmetries. Weak and electromagnetic dipole moments of the top quark arise effectively through loop corrections but are very small [456–458] in the SM. Possible anomalous contributions from physics beyond the SM can modify any of these couplings and are best studied in associated production with a top pair or single top. The sensitivity of  $t\bar{t}Z$  and  $t\bar{t}\gamma$  at the LHC to the top-electroweak couplings was first explored at LO in Ref. [459, 460], and more recently  $t\bar{t}Z$  studies at NLO QCD have been presented in Refs. [461–463], and for  $t\bar{t}\gamma$  with photon from the production process in Ref. [463]. The transverse momentum of the vector boson, and, in the case of  $t\bar{t}Z$  production, the azimuthal angle between the leptons arising from the decay of the  $Z$  boson, are particularly sensitive to the top-electroweak couplings. These couplings may also be probed through the charge asymmetry in  $t\bar{t}\gamma$  production, which appears at LO due to the  $q\bar{q}$  initial state [440]. Similar to  $t\bar{t}H$  production, the cross section for  $t\bar{t}Z$  production increases by a factor of about 50 at the FCC as compared to the  $\sqrt{s} = 13$  TeV LHC. Using the coupling parametrization

$$\mathcal{L}_{t\bar{t}Z} = e\bar{\psi}_t \left[ \gamma^\mu (C_{1,V} + \gamma_5 C_{1,A}) + \frac{i\sigma^{\mu\nu} q_\nu}{M_Z} (C_{2,V} + i\gamma_5 C_{2,A}) \right] \psi_t Z_\mu, \quad (83)$$

possible constraints on the couplings  $C_{1/2,V/A}$  at the  $\sqrt{s} = 13$  TeV LHC with  $3 \text{ ab}^{-1}$  of data has been presented in Refs. [461, 462] and are shown in Fig. 169 and Table 57 together with constraints achievable at the 100 TeV FCC with  $10 \text{ ab}^{-1}$ . These analyses take account of the theoretical uncertainty, currently at 15% but projected to decrease to 5% by the time the FCC is operational. Driven by the larger statistics and reduction of the theoretical uncertainties, the sensitivity of the FCC to the top- $Z$  couplings is anticipated to exceed that of the LHC by factors of 3-10. Moreover, the construction of cross section ratios to cancel various uncertainties has been proposed in Ref. [464] and can further boost sensitivity by factors of 2-4.

The process  $t\bar{t} + W$  is peculiar in this context as it does not yield an enhanced sensitivity to the  $Wtb$  coupling. The reason is the simple fact that the  $W$  boson can only be radiated off the  $q\bar{q}$  initial state. This also prohibits a  $gg$ -initiated process and, therefore, the production cross section is small with 587 fb at the 13 TeV LHC and 19 pb at the FCC [413], before branching of the top quarks and the  $W$  boson. Nevertheless, the authors of Ref. [413] pointed out that these particular features allow for the study of

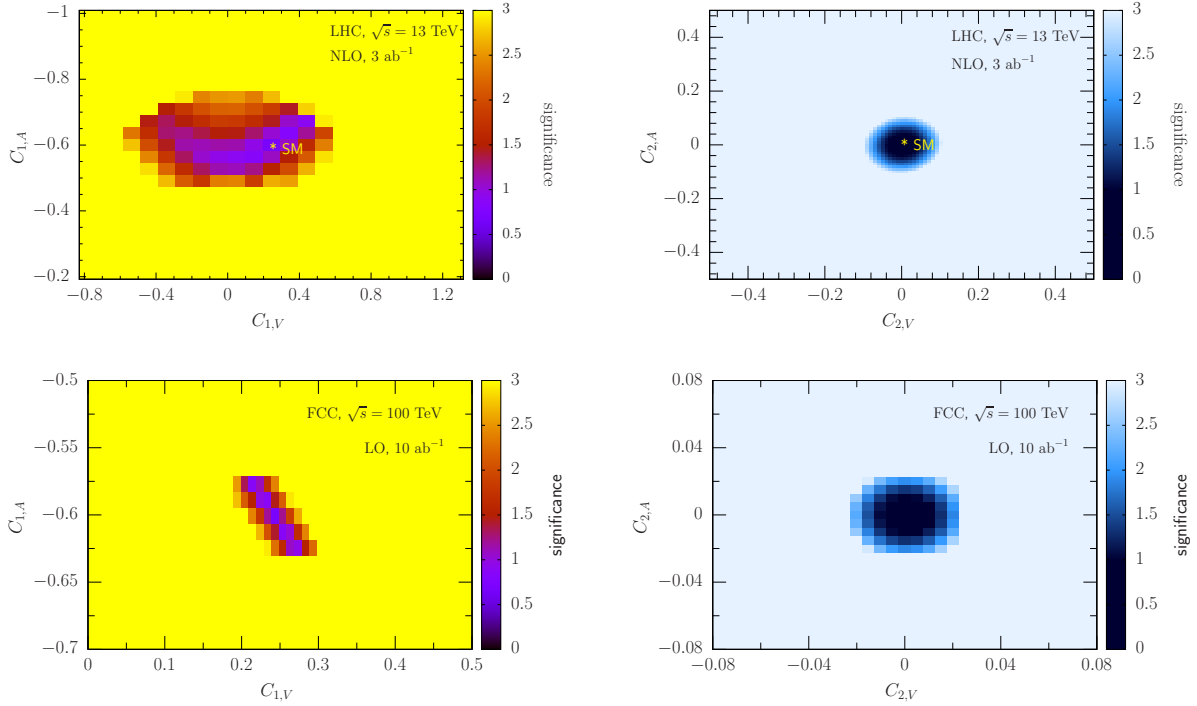


Fig. 169: Comparison of potential constraints on couplings  $C_{1/2,V/A}$  achievable at the LHC and FCC. For further details, see Refs. [461, 462].

a charge asymmetry as the top quarks largely inherit the polarization of the initial state. At a 100 TeV collider, a SM asymmetry of about +2% is expected and can be used to discriminate against new physics scenarios of axigluons [465, 466] which induce asymmetries of  $\mathcal{O}(10\%)$  for axigluon masses in the few TeV range [413]. It was shown in Ref. [440] that similar axigluon models can also be probed through asymmetries in  $t\bar{t} + \gamma$  production. (See Ref. [467] for a review.)

	$C_{1,V}$	$C_{1,A}$	$C_{2,V}$	$C_{2,A}$
SM value	0.24	-0.60	$< 0.001$	$\ll 0.001$
13 TeV, $3 \text{ ab}^{-1}$	$[-0.4, +0.5]$	$[-0.5, -0.7]$	$[-0.08, +0.08]$	$[-0.08, +0.08]$
100 TeV, $10 \text{ ab}^{-1}$	$[+0.2, +0.28]$	$[-0.63, -0.57]$	$[-0.02, +0.02]$	$[-0.02, +0.02]$

Table 57: Possible constraints on anomalous vector and axial couplings ( $C_{1,V/A}$ ) and weak dipole moment couplings ( $C_{2,V/A}$ ) in  $pp \rightarrow t\bar{t} + Z$  production at the LHC and FCC. The bounds correspond to the 95% C.L. exclusion for one coupling when all others are marginalized over. For further details, see Ref. [462].

As yet, no studies of the sensitivity of the single top +  $Z/\gamma$  processes to the flavor-conserving top couplings exist, despite the fact that associated production with a single top is known to have a comparable rate to production with a top pair [410]. Single top production plus a  $Z$  boson or a photon can also be mediated by top flavour-changing neutral couplings [468], in the processes  $gq \rightarrow Zt/\gamma t$ , with  $q = u, c$ . At the LHC, the potential of these processes to probe  $u - t$  couplings is similar to  $t\bar{t}$  production followed by a flavour-changing decay  $t \rightarrow uZ/u\gamma$  [455] but the sensitivity to  $c - t$  couplings is much worse, due to the lower parton luminosity for charm quarks. At the FCC, the  $gu \rightarrow Zt/\gamma t$  cross sections increase by a factor of 15 with respect to the LHC, and by a factor of 50 (40) for  $gc \rightarrow Zt(\gamma t)$ . (We assume here that  $Ztu$  and  $Ztc$  couplings have tensor structure.) The larger enhancement

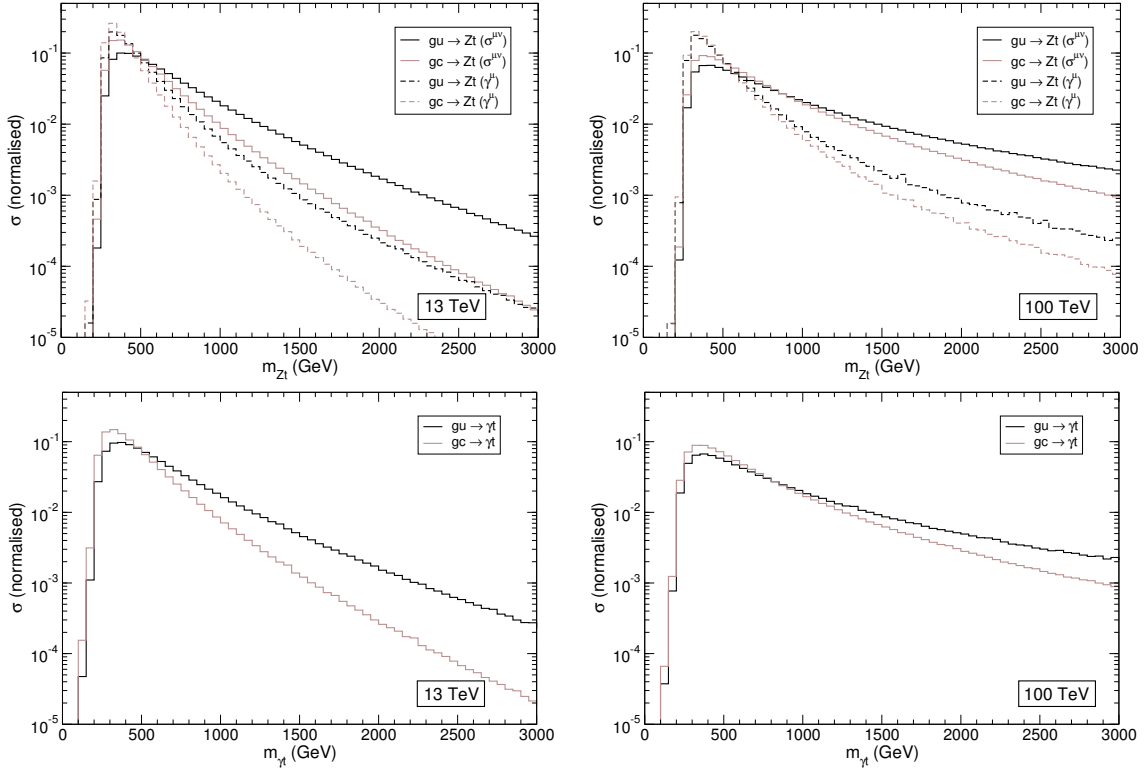


Fig. 170: Normalised invariant mass distributions for  $Zt$  and  $\gamma t$  production mediated by top flavour-changing couplings to the  $Z$  boson, at the LHC (left) and FCC (right). The pseudo-rapidities of the top quark and the  $Z/\gamma$  boson are required to be in the range  $|\eta| \leq 2.5$ .

for charm-initiated processes leads to a comparable sensitivity to  $u - t$  and  $c - t$  couplings. But, more interestingly, the production cross section for highly-energetic  $Zt/\gamma t$  pairs does not decrease as fast as for the SM backgrounds, due to the momentum dependence of the  $\sigma^{\mu\nu}$  vertex, as it is shown in Fig. 170. (The differential distributions for SM backgrounds are expected to be similar to the ones for  $gu \rightarrow Zt$  mediated by  $\gamma^\mu$  couplings, shown in Fig. 170.) With the large cross sections and luminosities expected for the FCC, it will be possible to explore the highly-boosted  $Zt/\gamma t$  regime, where SM backgrounds are small. It is then expected that the sensitivity to top flavour-changing neutral couplings will be excellent, though a quantitative statement and a comparison with  $t\bar{t}$  decays requires a detailed analysis.

## 14 Production of multiple heavy objects<sup>45</sup>

Standard Model processes featuring many heavy particles in the final state are challenging at colliders. On one side, the presence of many particles is indicative of the dynamic complexity of these processes, that entail several powers of the strong and/or of the electroweak coupling constant; on the other hand, the production of such heavy states requires considerable energy owing to the high mass thresholds. These effects are responsible for their small rates, which, together with the experiential difficulty in reconstructing such complicated topologies, makes their measurement a formidable task.

Nevertheless, from this very complexity stem the main reasons of interest in these processes. Their dynamic and kinematic structure is so rich that the measurement of one of them may probe several properties of the underlying theory at the same time; these reactions are typically sensitive to couplings of different nature which make them ideal tools for understanding in detail the interplay among different particle sectors. Moreover, their complex kinematics may lend them unique features, which allow cleaner signal extraction through the definition of elaborated event-selection strategies. Finally, they very often appear as important backgrounds to many BSM signals, for example those featuring heavy intermediate new-physics states with long decay chains to SM light particles.

While some of these reactions are out of reach at present colliders, a substantial increase in centre-of-mass energy and in luminosity may render them accessible at future accelerators, with a consequent step up in the level of detail to which fundamental interactions can be probed. A future 100 TeV hadronic collider may thus unleash the potential of some of these channels to measure SM parameters with unprecedented accuracy, to possibly discover new physics through rare production mechanisms, and to constrain BSM parameter spaces in new, more and more elaborated manners.

In the following, some of the processes that today are considered as ‘rare’ are presented, categorised according to their matter content, together with some physics opportunities they may give once their yield will be statistically significant at a 100-TeV collider. The rates shown in the tables and figures of this section are at the NLO in QCD, and have been obtained in [411] with the automatic code MadGraph5\_aMC@NLO [64]. The setup employed is summarised below.

- Non-zero particle masses are  $m_t = 173$  GeV,  $m_H = 125$  GeV,  $m_Z = 91.188$  GeV,  $m_W = 80.419$  GeV. The bottom-quark mass is set to  $m_b = 4.7$  GeV in the four-flavour-scheme (4FS) simulations, and to  $m_b = 0$  in the five-flavour-scheme (5FS) ones. The CKM matrix is  $V_{\text{CKM}} = 1$ , and the fine-structure constant is  $\alpha = 1/132.507$ .
- Renormalisation and factorisation scales are chosen as  $\mu_R = \mu_F = \frac{1}{2} \sum_k m_T^{(k)}$ ,  $m_T^{(k)}$  being the transverse mass of the  $k$ -th final-state particle. Independent variation of  $\mu_R$  and  $\mu_F$  in the range  $[1/2, 2]$  is obtained in an exact way without rerunning the code, through the reweighting technique described in [432]. The uncertainty associated with this variation is shown as a dark band in the plots of the section.
- As PDFs, the MSTW 2008 NLO (68% c.l.) sets [292] are used, relevant to four or five active flavours, depending on the flavour scheme employed in the simulation. PDF uncertainties are estimated according to the asymmetric-hessian prescription provided by the PDF set, and obtained automatically as in explained in [432]. They are shown as a light band in the plots of the section. The value and the running of the strong coupling constant  $\alpha_s$  are as well set according to the PDF set.
- Whenever relevant, photons are isolated by means of the Frixione smooth-cone criterion [290], with parameters  $R_0 = 0.4$ ,  $p_T(\gamma) > 20$  GeV,  $\epsilon_\gamma = n = 1$ .

---

<sup>45</sup>Editor: P. Torrielli

### 14.1 Production of multiple gauge bosons

Production processes featuring many gauge bosons in the final state are important for diverse reasons. On one hand they are backgrounds in many searches for BSM signals, characterised by multi-lepton signatures, with or without missing transverse energy (like for example SUSY [469] and extra dimensions [470]), or in searches for SM signals like  $VH$ , see for example [471]. On the other hand, and even more importantly, viewed themselves as signals they provide key tests of the SM, in that they are particularly sensitive to the gauge structure of its interactions.

In the SM, the couplings for triple and quadruple gauge-boson vertices are fixed as a consequence of its non-abelian gauge symmetry. Possible new physics in the gauge sector can be parametrised in a model-independent way through a set of higher-dimension operators involving gauge vectors, see for example [472–474]

$$\mathcal{L} = \mathcal{L}_{\text{SM}} + \sum_i \frac{c_i}{\Lambda^2} \mathcal{O}_{3V,i} + \sum_j \frac{f_j}{\Lambda^4} \mathcal{O}_{4V,j} + \dots, \quad (84)$$

giving rise to anomalous triple gauge couplings, (a)TGC's, anomalous quartic gauge couplings, (a)QGC's, and so on. The presence of anomalous couplings results in modified rates and spectra for multi-boson production processes, which are thus an ideal ground to set constraints on the gauge interactions of BSM models and on the scale  $\Lambda$  of possible new physics.

Process	$\sigma_{\text{NLO}}(8 \text{ TeV})$ [fb]	$\sigma_{\text{NLO}}(100 \text{ TeV})$ [fb]	$\rho$
$pp \rightarrow W^+W^-W^\pm$ (4FS)	$8.73 \cdot 10^1$ <sup>+6%</sup> <sub>-4%</sub> <sup>+2%</sup> <sub>-2%</sub>	$4.25 \cdot 10^3$ <sup>+9%</sup> <sub>-9%</sub> <sup>+1%</sup> <sub>-1%</sub>	49
$pp \rightarrow W^+W^-Z$ (4FS)	$6.41 \cdot 10^1$ <sup>+7%</sup> <sub>-5%</sub> <sup>+2%</sup> <sub>-2%</sub>	$4.01 \cdot 10^3$ <sup>+9%</sup> <sub>-9%</sub> <sup>+1%</sup> <sub>-1%</sub>	63
$pp \rightarrow W^\pm ZZ$	$2.16 \cdot 10^1$ <sup>+7%</sup> <sub>-6%</sub> <sup>+2%</sup> <sub>-2%</sub>	$1.36 \cdot 10^3$ <sup>+10%</sup> <sub>-10%</sub> <sup>+1%</sup> <sub>-1%</sub>	63
$pp \rightarrow ZZZ$	$5.97 \cdot 10^0$ <sup>+3%</sup> <sub>-3%</sub> <sup>+2%</sup> <sub>-2%</sub>	$2.55 \cdot 10^2$ <sup>+5%</sup> <sub>-7%</sub> <sup>+2%</sup> <sub>-1%</sub>	43
$pp \rightarrow W^+W^-W^\pm Z$ (4FS)	$3.48 \cdot 10^{-1}$ <sup>+8%</sup> <sub>-7%</sub> <sup>+2%</sup> <sub>-2%</sub>	$5.95 \cdot 10^1$ <sup>+7%</sup> <sub>-7%</sub> <sup>+1%</sup> <sub>-1%</sub>	171
$pp \rightarrow W^+W^-W^+W^-$ (4FS)	$3.01 \cdot 10^{-1}$ <sup>+7%</sup> <sub>-6%</sub> <sup>+2%</sup> <sub>-2%</sub>	$4.11 \cdot 10^1$ <sup>+7%</sup> <sub>-6%</sub> <sup>+1%</sup> <sub>-1%</sub>	137
$pp \rightarrow W^+W^-ZZ$ (4FS)	$2.01 \cdot 10^{-1}$ <sup>+7%</sup> <sub>-6%</sub> <sup>+2%</sup> <sub>-2%</sub>	$3.34 \cdot 10^1$ <sup>+6%</sup> <sub>-6%</sub> <sup>+1%</sup> <sub>-1%</sub>	166
$pp \rightarrow W^\pm ZZZ$	$3.40 \cdot 10^{-2}$ <sup>+10%</sup> <sub>-8%</sub> <sup>+2%</sup> <sub>-2%</sub>	$7.06 \cdot 10^0$ <sup>+8%</sup> <sub>-7%</sub> <sup>+1%</sup> <sub>-1%</sub>	208
$pp \rightarrow ZZZZ$	$8.72 \cdot 10^{-3}$ <sup>+4%</sup> <sub>-4%</sub> <sup>+3%</sup> <sub>-2%</sub>	$8.05 \cdot 10^{-1}$ <sup>+4%</sup> <sub>-4%</sub> <sup>+2%</sup> <sub>-1%</sub>	92
$pp \rightarrow ZZZZZ$	$1.07 \cdot 10^{-5}$ <sup>+5%</sup> <sub>-4%</sub> <sup>+3%</sup> <sub>-2%</sub>	$2.04 \cdot 10^{-3}$ <sup>+3%</sup> <sub>-3%</sub> <sup>+2%</sup> <sub>-1%</sub>	191

Table 58: Production of multiple vector bosons at NLO in QCD at 8 and 100 TeV from Ref. [411]. The rightmost column reports the ratio  $\rho$  of 100-TeV to 8-TeV cross sections. Theoretical uncertainties are due to scale and PDF variations, respectively.

In the first two sections of Table 58 and in Fig. 171 [411], sample cross sections are reported for the production of up to four undecayed electroweak vector bosons. Three-boson final states are abundantly produced at 100 TeV, and final states with four bosons are in principle observable even upon including branching ratios for the best leptonic decays of each boson.

The addition of a gauge boson brings production rates down typically by a factor of the order of, or slightly larger than  $\alpha$ , compatibly with the perturbative counting [475], and with the fact that an extra massive particle in the final state constrains the scattering to a region of larger Bjorken- $x$ , suppressing the cross section. The rate increase  $\rho$  from 8 to 100 TeV ranges from few tens to few hundreds, with

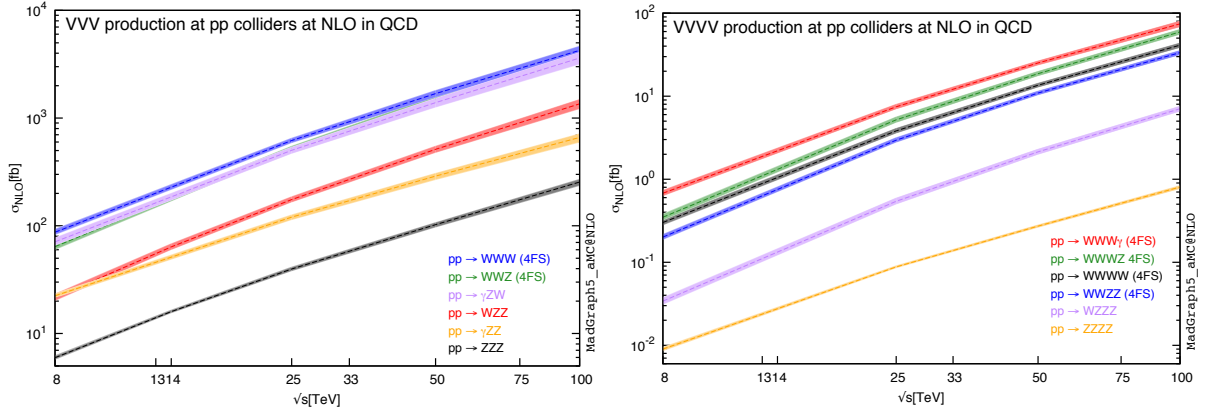


Fig. 171: NLO total cross section for production of three (left panel) and four (right panel) electroweak bosons, as a function of the hadronic-collider centre-of-mass energy.

larger values for larger multiplicities. It is relatively mild, owing to the fact that all of these channels proceed through  $q\bar{q}$  scattering. Theoretical uncertainties on the total cross sections, stemming from renormalisation/factorisation-scale variations and from PDFs, range between 5% and 10%.

Three-boson production is crucial to probe aQGC's. Although these couplings involve complicated topologies, featuring more bosons in the final state with respect to aTGC's, the information they carry is not a mere replica of the one contained in the latter. In some cases [473, 476], the exchange of heavy bosons can contribute at tree level to four-boson couplings while giving only a suppressed one-loop contribution to triple-boson vertices. In such scenarios, only QCG's would significantly deviate from the SM expectation, and could result mandatory to probe new physics. Moreover, in case aTCG's are observed at a 100-TeV machine, the measurement of aQGC's will acquire an even more relevant role, as capable of providing complementary insight about the strength, structure, and scale of new-physics forces.

A particularly interesting channel in this respect is  $W^\pm W^\pm W^\mp$ , which has the largest cross section among the triple-boson reactions, as displayed in Table 58 and Fig. 171. At 100 TeV the sensitivity to the dimension-8 operator  $f_{T0}/\Lambda^4 \text{Tr}[\hat{W}_{\mu\nu}\hat{W}^{\mu\nu}]\text{Tr}[\hat{W}_{\alpha\beta}\hat{W}^{\alpha\beta}]$  increases by a factor of 300 with respect to LHC-8, and of 25 with respect to LHC-14, assuming a common luminosity of  $3000 \text{ fb}^{-1}$  [477, 478]. The enhancement in sensitivity at 100 TeV is affected by the application of a unitarity-violation bound [477], which indicates that this channel is sensitive to the direct production of the heavy states integrated out in the effective field theory. This is expected to hold generically for three-boson production induced by dimension-8 operators, where the growth of the rate with energy is more rapid than with dimension-6 operators.

Four-boson production can in principle constrain yet higher-order (quintic, in this case) anomalous couplings, on top of carrying further complementary information on aTCG's and aQGC's. Production rates at 100 TeV range from few units to few tens of femtobarns. The sensitivity of the various channels has to be carefully assessed after inclusion of branching ratios for the bosons. In this respect, reactions with one or more photons in the final state could be useful if they have sufficient rate after selection cuts, as they are less affected by BR's.

Five-boson final states, of which an example is reported in the third section of Table 58, will be inaccessible at 100 TeV under the assumption of SM couplings, even with  $\mathcal{O}(10) \text{ ab}^{-1}$  luminosity, as they feature sub-femtobarn cross section.

## 14.2 Multi-top and top-vector-boson associated production

Processes with many top pairs, and associated top-pair vector-boson productions offer another remarkable set of tests of the structure of SM interactions, and of the mechanism of electroweak-symmetry breaking. The top quark plays a special role in this programme, as its large mass and its quantum numbers allow it to couple significantly with all of the bosons in the theory, hence to connect the interactions of different sectors. The accurate measurement and understanding of its properties is moreover believed to be an important mean to indirectly probe possible BSM physics, in case new states elude direct detection [338], owing to the closeness of its mass to the electroweak scale.

The cross sections for the production of two top-antitop pairs at 100 TeV is detailed in the first section of Table 59. Its very sizable growth  $\rho$  with the collider energy is due to the fact that this reaction predominantly proceeds through  $gg$  scattering [412], with a gluon PDF growing much faster than the quark ones at small  $x$ . Theoretical uncertainties are quite large, of the order of  $\pm 25\%$  at 100 TeV, mainly due to the presence of four powers of  $\alpha_s$  at the LO. The PDF uncertainty is reduced at 100 TeV, again due to the gluon PDF being probed at much smaller  $x$  than at 8 TeV. The study of this final state is interesting at hadron colliders as a probe of the nature of EWSB, see e.g. [479], and of many BSM models with modified symmetry-breaking sectors [480].

The final state with three top-antitop pairs has a cross section of the order of 1 fb at 100 TeV [481], hence, taking branching ratios into account, it cannot be seen directly with the luminosities usually assumed. The absence of the observation of this signal, which is also enhanced in many BSM scenarios with top partners, see e.g. [482], can be used to constrain the parameter space of these models, as nowadays is done with two top-antitop pairs at the LHC [483].

The second part of Table 59 reports cross sections for  $t\bar{t}V$  production, with  $V = W^\pm, Z$ . Viewed as signals, these channels are interesting in their own right as excellent tests for the SM, probing top couplings to the gauge sector, and thus giving direct insights on the mechanism of symmetry breaking. On the other hand, they are prominent backgrounds for many BSM signals, on top of playing an important role in  $t\bar{t}H$  searches [412] in case of multi-lepton signatures.

The rates for these processes make them well visible at 100 TeV. A comparison between these cross sections and those in Table 58 for multiple gauge-boson production shows [475] that top-quark processes at 100 TeV will provide the dominant source of multi- $W$  and thus multi-lepton final states, since each top gives rise to a  $W$  through its decay. This will have important implications for the search of new-physics signals characterised by the presence of many gauge bosons or leptons from the decay of the new heavy particles.

The larger growth  $\rho$  for the neutral channel  $t\bar{t}Z$  with respect to  $t\bar{t}W^\pm$  is again driven by the fact that the former proceeds through  $gg$  as opposed to  $q\bar{q}$  (see [412] for details). The absence of the  $gg$  contribution, although disadvantageous in terms of total number of expected events, makes  $t\bar{t}W^\pm$  particularly interesting as a handle to constrain new physics through asymmetry and polarisation effects [413]: charge asymmetry between  $t$  and  $\bar{t}$  is significantly enhanced in  $t\bar{t}W^\pm$  with respect to inclusive  $t\bar{t}$  production, and the final-state products display very asymmetric rapidity distributions, induced by the  $W$  acting as a polariser of the initial state. In this respect, a 100 TeV energy will be highly beneficial, allowing to reach few-percent statistical precision for these asymmetries (down to 3% for a luminosity of  $3000 \text{ fb}^{-1}$ , compared to 14% at the LHC-14 [413]), that could thus become precision measurements of the properties of QCD and powerful discriminators of BSM models.

The  $t\bar{t}Z$  channel is also interesting for various reasons. The weak electric and magnetic dipole moments of  $tZ$  interactions are an excellent probe of new physics given their small SM values [462]. For this purpose, the large rate at 100 TeV will improve the constraints on these moments by a factor of 3 to 10 compared to the LHC, at  $3000 \text{ fb}^{-1}$ . Moreover the  $t\bar{t}Z$  channel can be exploited to measure the top Yukawa coupling  $y_t$  down to 1% accuracy at 100 TeV, through the ratio  $\sigma(t\bar{t}H)/\sigma(t\bar{t}Z)$  [484].

The third part of Table 59 details the rates for  $t\bar{t}VV$  production at NLO in QCD [411, 412, 428].

The rate growth with collider energy follows the expected pattern, with the neutral channels,  $gg$ -dominated, displaying larger  $\rho$  with respect to  $t\bar{t}W^\pm Z$ . Theoretical uncertainties for these channels (as well as for  $t\bar{t}V$ ) are under better control with respect to  $t\bar{t}t\bar{t}$ , due to the presence of only two powers of the strong coupling at the LO. These processes, elusive at the LHC, will be accessible at 100 TeV, having cross sections in the  $10^2$  to  $10^3$  fb range. Exploiting asymmetry and polarisation effects to probe new physics is possible for this category as well [412], but the potential of this kind of observables for a 100-TeV collider still needs to be studied in detail.

Process	$\sigma_{\text{NLO}}(8 \text{ TeV})$ [fb]	$\sigma_{\text{NLO}}(100 \text{ TeV})$ [fb]	$\rho$
$pp \rightarrow t\bar{t}t\bar{t}$	$1.71 \cdot 10^0$ +25% +8% -26% -8%	$4.93 \cdot 10^3$ +25% +2% -21% -2%	2883
$pp \rightarrow t\bar{t}Z$	$1.99 \cdot 10^2$ +10% +3% -12% -3%	$5.63 \cdot 10^4$ +9% +1% -10% -1%	282
$pp \rightarrow t\bar{t}W^\pm$	$2.05 \cdot 10^2$ +9% +2% -10% -2%	$1.68 \cdot 10^4$ +18% +1% -16% -1%	82
$pp \rightarrow t\bar{t}W^+W^-$ (4FS)	$2.27 \cdot 10^0$ +11% +3% -13% -3%	$1.10 \cdot 10^3$ +9% +1% -9% -1%	486
$pp \rightarrow t\bar{t}W^\pm Z$	$9.71 \cdot 10^{-1}$ +10% +3% -11% -2%	$1.68 \cdot 10^2$ +16% +1% -13% -1%	173
$pp \rightarrow t\bar{t}ZZ$	$4.47 \cdot 10^{-1}$ +8% +3% -10% -2%	$1.58 \cdot 10^2$ +15% +1% -12% -1%	353

Table 59: Production of two top-antitop pairs, and of a top-antitop pair in association with up to two electroweak vector bosons at 8 and 100 TeV [411, 412]. The rightmost column reports the ratio  $\rho$  of the 100-TeV to the 8-TeV cross sections. Theoretical uncertainties are due to scale and PDF variations, respectively. Production of  $t\bar{t}t\bar{t}$  is with the setup of Ref. [412].

### 14.3 Multi Higgs boson production by gluon fusion and VBF

Processes featuring many Higgs bosons in the final state are of the utmost importance at colliders, as they offer direct information about Higgs self-interactions, which at present have not been observed at the LHC. These processes offer a unique handle on the nature of the Higgs potential, with crucial implications not only for SM and BSM phenomenology, but also for more fundamental questions like the origin of electroweak-symmetry breaking and the stability of the vacuum [485].

In the SM the Higgs potential is

$$V(H) = \frac{1}{2}m_H^2 H^2 + \lambda_{3H} v H^3 + \frac{1}{4}\lambda_{4H} H^4,$$

with triple and quadruple Higgs couplings equal to each other and predicted in terms of the Higgs mass and VEV,  $\lambda_{3H} = \lambda_{4H} \equiv \lambda_{\text{SM}} = m_H^2/2v^2$ ; measurement of multi-Higgs final states is thus the most direct way to confirm or disprove this prediction, and for example to provide information about the possible existence of a richer scalar sector, featuring additional scalar fields.

The dominant production mechanisms of a Higgs pair in the SM are displayed in Table 60 and in Fig. 173 [486], where the total rate at the NLO in QCD is shown as a function of the hadron-collider energy. The dominant channel is gluon fusion, as it is for single Higgs, followed by VBF, with a cross section smaller by more than an order of magnitude.

The cross section for gluon fusion is in excess of 1.5 pb at 100 TeV, see for example [487–489]. This rate is expected to provide a clear signal in the  $HH \rightarrow (b\bar{b})(\gamma\gamma)$  channel and to allow determination of  $\lambda_{3H}$  with an accuracy of 30–40% with a luminosity of  $3 \text{ ab}^{-1}$ , and of 5–10% with a luminosity of  $30 \text{ ab}^{-1}$  [490–492]. A rare decay channel which is potentially interesting is  $HH \rightarrow (b\bar{b})(ZZ) \rightarrow (b\bar{b})(4l)$ , with a few expected signal events against  $\mathcal{O}(10)$  background events at  $3 \text{ ab}^{-1}$  [493].

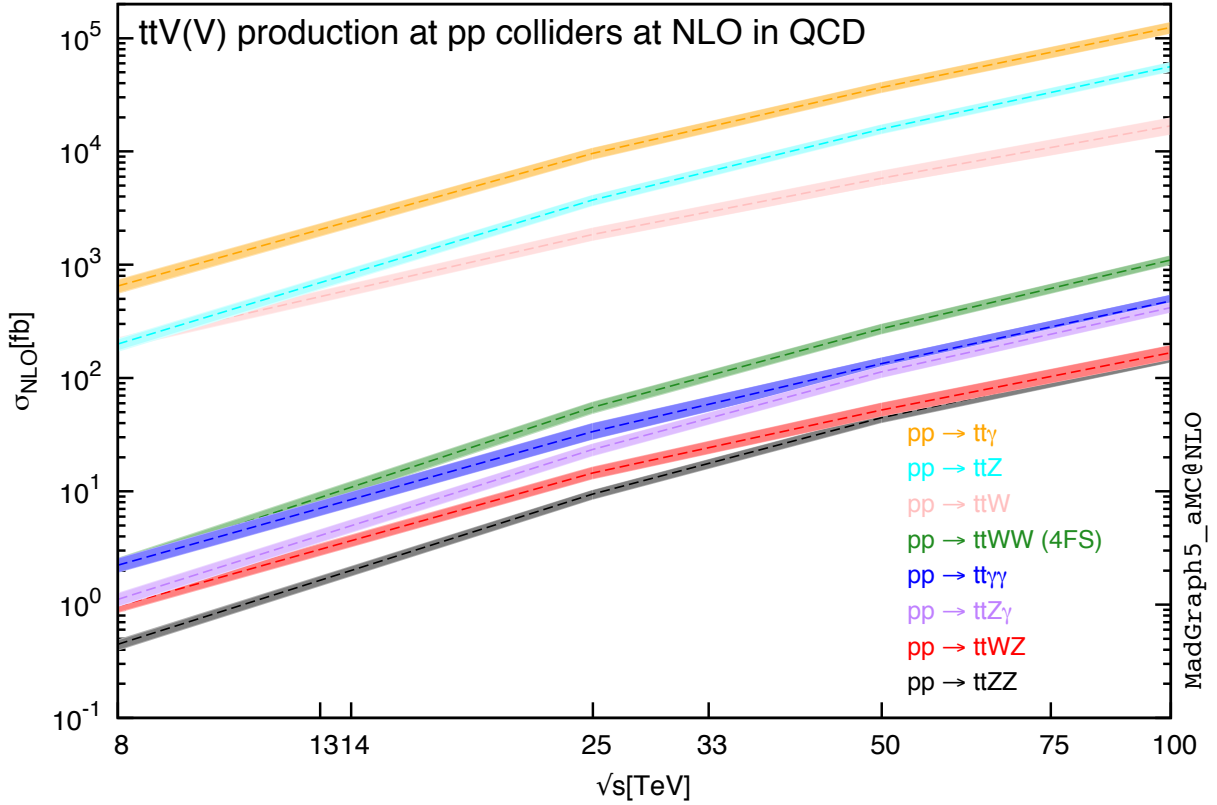


Fig. 172: NLO total cross section for production of a top-antitop pair in association with up to two electroweak bosons [411].

Process	$\sigma_{\text{NLO}}(100 \text{ TeV})$ [fb]
$pp \rightarrow HH$	$1.23 \cdot 10^3$ $^{+14\%}_{-14\%}$ $^{+1\%}_{-2\%}$
$pp \rightarrow t\bar{t}HH$	$8.62 \cdot 10^1$ $^{+7\%}_{-7\%}$ $^{+1\%}_{-1\%}$
$pp \rightarrow jjHH$ (VBF)	$8.09 \cdot 10^1$ $^{+1\%}_{-1\%}$ $^{+2\%}_{-2\%}$
$pp \rightarrow W^\pm HH$	$8.09 \cdot 10^0$ $^{+2\%}_{-3\%}$ $^{+2\%}_{-1\%}$
$pp \rightarrow ZHH$	$5.46 \cdot 10^0$ $^{+2\%}_{-4\%}$ $^{+2\%}_{-1\%}$
$pp \rightarrow tjHH$	$4.58 \cdot 10^0$ $^{+8\%}_{-8\%}$ $^{+0\%}_{-1\%}$

Table 60: NLO total cross section for the dominant production channels of a Higgs pair at 100 TeV [486].

Given the similarity of single- and double-Higgs production mechanisms, the cross-section ratio  $\sigma(gg \rightarrow HH)/\sigma(gg \rightarrow H)$  has been advocated [494] as a good observable to constrain  $\lambda_{3H}$  at the LHC, being more theoretically stable than the cross section itself. The similarity of these two processes renders double-Higgs production also a good tool to lift the degeneracy in the parameter space of Higgs anomalous couplings that currently affects the precise measurement of  $gg \rightarrow H$  [491, 495]. The considerations at the basis of these statements are expected to be largely independent of collider energy, making  $gg \rightarrow HH$  a golden channel for precision Higgs physics at 100 TeV.

Vector-boson fusion is the second production mechanism for Higgs pairs, as well as for single

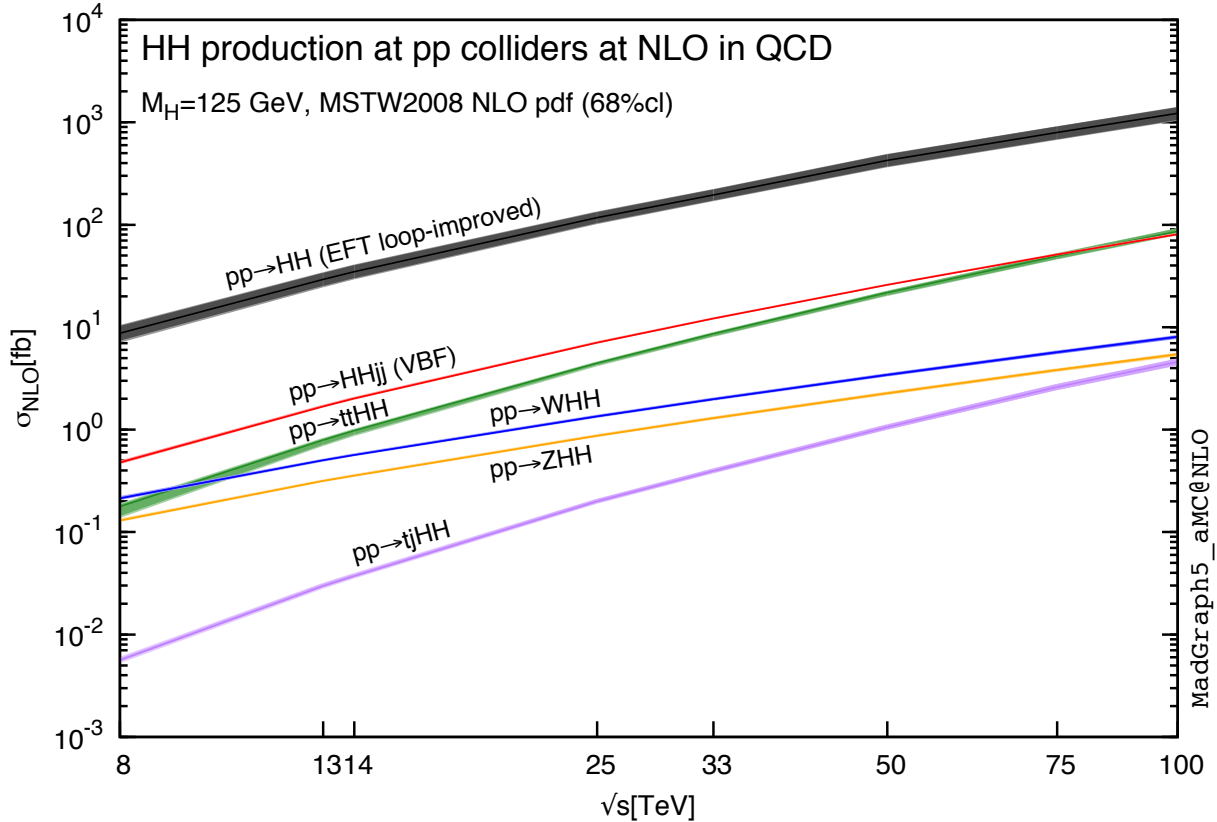


Fig. 173: NLO total cross section for the dominant production channels of a Higgs pair [486].

Higgs. The relevance of this channel is twofold: on one side, it provides an independent way to constrain  $\lambda_{3H}$ ; on the other hand, it is the main channel that is sensitive to the Higgs-gauge couplings  $W^+W^-HH$  and  $ZZHH$ . The cross section for this process, computed up to NNLO in QCD, is 80 fb at 100 TeV [496]. Despite the smaller cross section (by a factor of roughly 20) with respect to gluon fusion, VBF has a clear experimental signature, with the Higgs pair produced at central rapidity and two hard jets in the forward/backward region, hence it makes background reduction feasible. Moreover, its sensitivity to  $\lambda_{3H}$  is quite high, so that a deviation of this coupling from its SM value can significantly enhance the VBF cross section (see for example Fig. 5 of [496]).

The cross sections for triple-Higgs production processes are obviously much smaller than those for double-Higgs production, both due to the presence of an extra weak coupling, and to the fact that an extra massive particle implies larger  $x$ . The gluon-fusion channel is again the dominant one, but compatibly with what just outlined, its cross section at 100 TeV is of the order of 5 fb [487], i.e. more than 300 times smaller than double-Higgs production, which makes it a challenging process. This channel is in principle sensitive to both triple and quadruple Higgs self interactions, but the contribution from the triangle diagrams, the ones featuring  $\lambda_{4H}$ , is particularly small [487]: the production rate indeed depends very mildly on the quartic coupling, with a variation of only  $\pm 10\%$  upon varying the quartic in the range  $[0, m_H^2/v^2]$ , and assuming  $\lambda_{3H} = \lambda_{\text{SM}}$  [497]. The extraction of  $\lambda_{4H}$  from triple-Higgs production is thus unlikely at 100 TeV. The  $HHH \rightarrow (b\bar{b})(b\bar{b})(\gamma\gamma)$  decay channel could in principle be exploited to constrain a dimension-6 operator  $c_6\lambda_{\text{SM}}H^6/\Lambda^2$ , but it turns out to be effective only in a possible high-luminosity phase (of the order of  $30 \text{ ab}^{-1}$ ) of the 100-TeV collider [497].

#### 14.4 Multi Higgs boson production in association with top quarks or gauge bosons

Associated production of a Higgs pair with a top-antitop pair or with a vector boson are the main subdominant double-Higgs production channels. Inspection of Fig. 173 [486] shows that while at the LHC the cross sections for these three channels are of the same order (within a factor of two), at 100 TeV  $t\bar{t}HH$  production grows roughly ten times more than  $VHH$ , since it proceeds through  $gg$ . This fact causes its cross section to be very close to (or even slightly larger than) that for VBF, roughly 85 fb. Detailed analyses [498, 499] show that this channel can provide significant statistical power to increase the sensitivity to  $\lambda_{3H}$ , and that the presence of the top pair is crucial for a substantial reduction of the backgrounds with respect to gluon fusion.

$VHH$  processes are also relevant for the determination of  $\lambda_{3H}$ . Studies of these channels show a good sensitivity to  $\lambda_{3H}$  already at the HL-LHC [500], and the cross-section increase, which is modest with respect to  $t\bar{t}HH$  but still of a factor of roughly 40 from 8 to 100 TeV, should further extend their potential, especially in a high-luminosity phase.

Production of a  $tjHH$  final state, namely a single top in association with a Higgs pair, is also potentially interesting at 100 TeV, and completes the programme for the determination of the trilinear. While at 8 TeV its cross section is below  $10^{-2}$  fb, which makes it phenomenologically irrelevant for the present, at 100 TeV its rate grows by roughly a factor of  $10^3$  and becomes comparable to that for  $VHH$ , see Fig. 173. This process is of interest because it has the largest sensitivity to  $\lambda_{3H}$  among the double-Higgs channels, see Fig. 3 of [486], and it may become clearly visible at 100 TeV in case the trilinear significantly deviates from the SM expectation. In addition to that, it is sensitive to couplings to both vector bosons and top quarks, and to their relative phases [486].

## 15 Loop-induced processes<sup>46</sup>

Loop-induced processes are defined as processes that do not receive any contribution from tree-level Feynman-diagrams. Such processes are especially relevant in the case of the SM Higgs boson, which does not couple directly to massless partons and is therefore produced predominantly via gluon fusion, through a loop of heavy quarks. In the case of single Higgs production, the effective theory obtained by integrating out the top quark running in the loop provides a good approximation and the corresponding cross-section for  $gg \rightarrow H$  has been computed up to  $N^3\text{LO}$  in [501]. Corrections due to finite bottom and top quark mass effects have been computed at lower orders in [502, 503] and give rise to the largest theoretical error at  $N^3\text{LO}$  (see the Higgs Chapter of this Report for a more detailed discussion).

Because of its relevance for the measurement of the trilinear Higgs self-interaction, the case of Higgs pair production has also been extensively studied and the  $NN\text{LO}$  inclusive cross-section in the heavy top-quark limit was presented in [488], later supplemented by the resummation of the next-to-next-to-leading logarithms in the threshold expansion  $\frac{m_{HH}^2}{\hat{s}} \rightarrow 1$ , where  $m_{HH}$  the invariant mass of the Higgs pair and  $\hat{s}$  the partonic center-of-mass energy. Corrections from top-quark mass effects are expected to be large in Higgs pair production, but their exact analytic expressions are still unknown at NLO accuracy. However, the impact of these corrections on the inclusive cross-section has recently been computed in [504], using `SECDDEC` [505] for evaluating the analytically unknown two-loop master integrals. Also, partial results including the exact top quark mass dependence everywhere except in the double virtual contribution are presented in [486], while the work of [506, 507] presents the complete top-quark mass effects in an expansion up to terms of  $\mathcal{O}(\frac{1}{m_t^8})$ .

For many final states, the gluon-initiated loop-induced process  $gg \rightarrow \{X\}$  is actually a NNLO correction to the corresponding process  $pp \rightarrow \{X\}$  with initial state quarks. However, because of the large gluon luminosity, the  $gg$  contribution is often non-negligible. For example, as reported in [264], it amounts to  $\sim 60\%$  of the total NNLO correction to  $pp \rightarrow ZZ$ . Furthermore, the difference in the quark and gluon PDFs and in the production topologies often cause the kinematic dependence of the gluon-fusion contribution to be very different from the corresponding tree-level one, so that a global rescaling of the LO distributions is not applicable. This fact is illustrated in Fig. 174, showing the differential distribution of the transverse momenta of bosons in the processes  $pp \rightarrow W^+W^-$ ,  $pp \rightarrow ZZ$  and  $pp \rightarrow ZH$ . The difference in shape is particularly manifest for the  $pp \rightarrow ZH$  process because the tree-level contribution, in this case, is exclusively an  $s$ -channel process.

With the extensive availability of one-loop matrix elements providers [247, 419, 508–510], the computation of the loop-induced matrix-element is now straightforward. However, the automation of the tools to compute inclusive cross-sections and generate events is only done in a fully automatic (and public) way in the `MADGRAPH5_AMC@NLO` Monte-Carlo framework, for arbitrary loop-induced processes at LO [511]. Except when otherwise stated, all results of this section are obtained using this framework.

### 15.1 Cross-sections at 100 TeV

In this section, we present the cross sections for various loop-induced SM processes involving associated production of Higgs and gauge bosons. The calculations are performed in the four-flavour scheme with the SM parameters described in the Table 61. Whenever relevant, photons are isolated by means of the Frixiere smooth-cone criterion [290], with parameters  $R_0 = 0.4$ ,  $p_T(\gamma) > 20$  GeV,  $\epsilon_\gamma = n = 1$ . In the case of the pair production of heavy boson, a technical cut of 1 GeV on the transverse momenta of the final state bosons is applied in order to avoid the integrable singularity at  $p_t^V \rightarrow 0$ .

The evolution of the cross-sections with the collider energy is shown in Fig. 175 for the production of multiple Higgs (left) [512] and various di-boson production processes (right). In order to be able to easily compare the cross-sections, they are all computed at exact LO, even for the ones of lower multi-

<sup>46</sup>Editors: V. Hirschi, O. Mattelaer

# CHAPTER 1: STANDARD MODEL PROCESSES

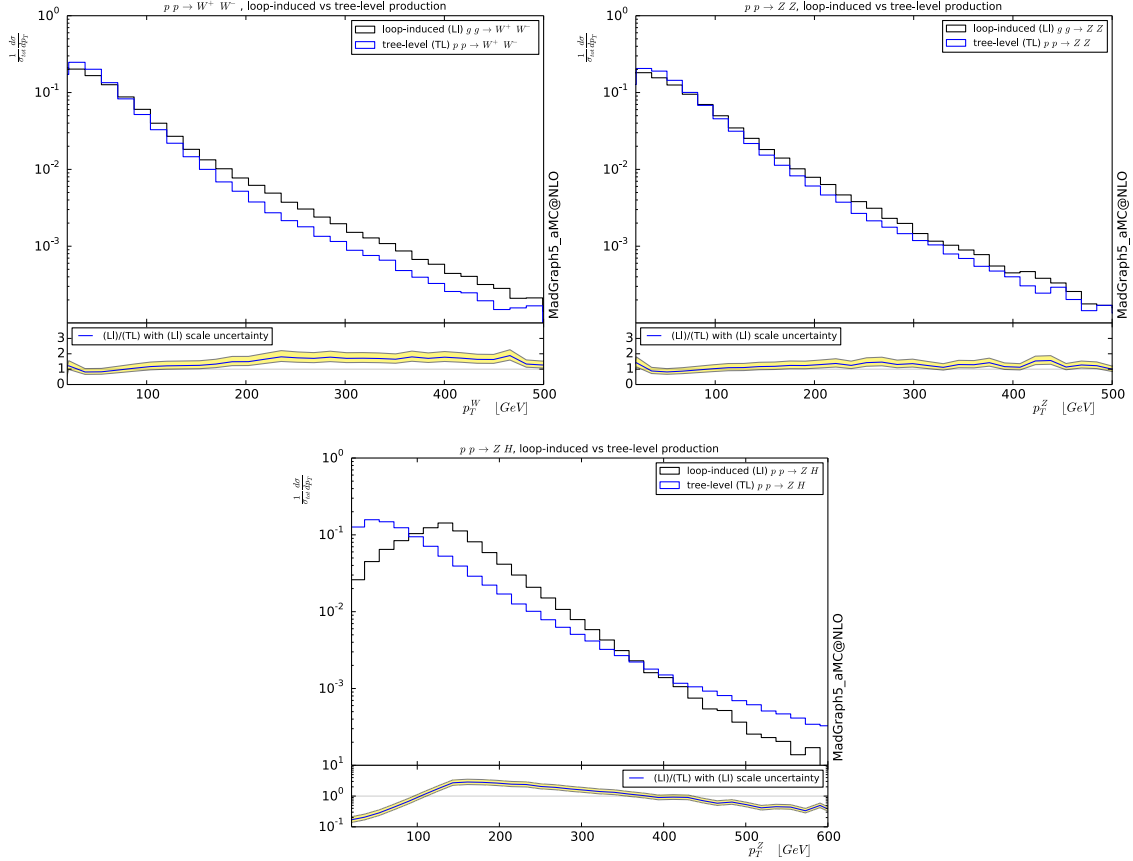


Fig. 174: Comparison of the transverse momentum of bosons produced in pair at tree-level and via gluon-fusion.

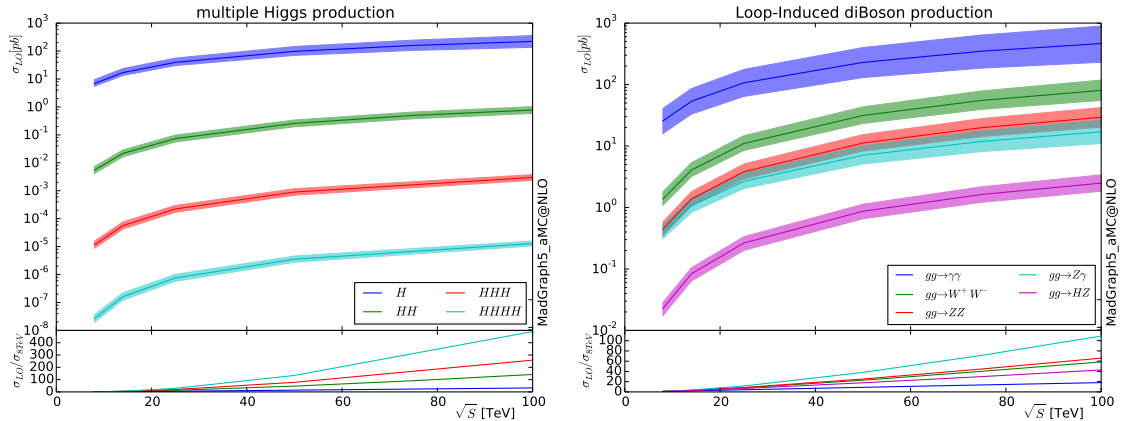


Fig. 175: Increase of the LO cross section with the collider energy, for various loop-induced processes with initial-state gluons.

licity which are available in the literature at higher QCD orders; all those cross-sections are expected to have a large NLO QCD K-factor of around two. As expected, the cross-section increases with the energy of the collider, and it does so at about the same rate for all Higgs multiplicities. As a rule of thumb (rather accurate at higher energies), producing an additional Higgs in the final state costs three orders of magnitude in the production cross-section. Increasing the energy is therefore required in order to be able

Parameter	value	Parameter	value
$\alpha_S(m_Z^2)$	0.13355	$n_f$	4
$\mu_R = \mu_F$	$\hat{\mu} = \frac{H_T}{2}$	$m_b = y_b$	4.7
$m_t = y_t$	173.0	$\Gamma_t$	0
$G_F$	1.16639e-05	$\alpha^{-1}$	132.507
$m_Z$	91.188	$\Gamma_Z$	2.4414
$m_W$	$\frac{M_Z}{\sqrt{2}} \sqrt{1 + \sqrt{1 - \frac{4\pi}{\sqrt{2}} \frac{\alpha}{G_F M_Z^2}}}$	$\Gamma_W$	2.0476
$m_H$	125.0	$\Gamma_H$	0.00638
$V_{ij}^{CKM}$	$\delta_{ij}$	$m_{e^\pm} = m_{\mu^\pm}$	0.0
$m_{\tau^\pm} = y_{\tau^\pm}$	1.777	$\Gamma_{\tau^\pm}$	0.0

Table 61: SM parameters used for obtaining the results presented in table 62. Dimensionful parameters are given in powers of GeV.

to observe multiple Higgs production processes. The case of double vector boson production processes is different because the opening of the phase-space at larger energy is less relevant and the corresponding factor  $\rho = \frac{\sigma_{100\text{TeV}}}{\sigma_{8\text{TeV}}}$  is therefore smaller. The shape of the cross-section increase with the collider energy is quite different for the processes  $gg \rightarrow \gamma\gamma$  and  $gg \rightarrow Z\gamma$  because they do not receive contributions from three-point loop diagrams.

A collection of results for the 100 TeV energy is given in Table 62.

Loop Induced Process	$\sigma_{\text{LO}}(100 \text{ TeV})$ [fb]	Loop Induced Process	$\sigma_{\text{LO}}(100 \text{ TeV})$ [fb]
$gg \rightarrow H$	$2.21 \cdot 10^{+5}$ $\begin{smallmatrix} +58\% & +1\% \\ -39\% & -1\% \end{smallmatrix}$	$gg \rightarrow HZ$	$2.50 \cdot 10^{+3}$ $\begin{smallmatrix} +35\% & +1\% \\ -26\% & -1\% \end{smallmatrix}$
$gg \rightarrow Hj$	$2.77 \cdot 10^{+5}$ $\begin{smallmatrix} +67\% & +24\% \\ -39\% & +22\% \end{smallmatrix}$	$gg \rightarrow Hjj$	$2.02 \cdot 10^{+5}$ $\begin{smallmatrix} +66\% & +0\% \\ -38\% & -1\% \end{smallmatrix}$
$gg \rightarrow HW^+W^-$	16.8 $\begin{smallmatrix} +31\% & +8\% \\ -23\% & +6\% \end{smallmatrix}$	$gg \rightarrow HZZ$	7.29 $\begin{smallmatrix} +28\% & +0\% \\ -22\% & -1\% \end{smallmatrix}$
$gg \rightarrow HZ\gamma$	0.279 $\begin{smallmatrix} +33\% & +0\% \\ -25\% & -1\% \end{smallmatrix}$	$gg \rightarrow H\gamma\gamma$	0.374 $\begin{smallmatrix} +33\% & +10\% \\ -25\% & +9\% \end{smallmatrix}$
$gg \rightarrow HH$	$7.74 \cdot 10^{+2}$ $\begin{smallmatrix} +32\% & +0\% \\ -24\% & -1\% \end{smallmatrix}$	$gg \rightarrow HHZ$	3.35 $\begin{smallmatrix} +29\% & +0\% \\ -22\% & -1\% \end{smallmatrix}$
$gg \rightarrow HHH$	2.99 $\begin{smallmatrix} +29\% & +5\% \\ -22\% & +4\% \end{smallmatrix}$	$gg \rightarrow HHHH$	$1.30 \cdot 10^{-2}$ $\begin{smallmatrix} +23\% & +1\% \\ -18\% & -1\% \end{smallmatrix}$
$gg \rightarrow W^+W^-$	$8.06 \cdot 10^{+4}$ $\begin{smallmatrix} +48\% & +31\% \\ -33\% & +29\% \end{smallmatrix}$	$gg \rightarrow ZZ$	$2.92 \cdot 10^{+4}$ $\begin{smallmatrix} +42\% & +1\% \\ -30\% & -1\% \end{smallmatrix}$
$gg \rightarrow Z\gamma$	$1.70 \cdot 10^{+4}$ $\begin{smallmatrix} +52\% & +1\% \\ -35\% & -1\% \end{smallmatrix}$	$gg \rightarrow \gamma\gamma$	$4.59 \cdot 10^{+5}$ $\begin{smallmatrix} +89\% & +3\% \\ -50\% & -3\% \end{smallmatrix}$
$gg \rightarrow W^+W^-Z$	$4.71 \cdot 10^{+2}$ $\begin{smallmatrix} -100\% & +0\% \\ -100\% & +0\% \end{smallmatrix}$	$gg \rightarrow ZZZ$	4.00 $\begin{smallmatrix} +30\% & +0\% \\ -23\% & -1\% \end{smallmatrix}$
$gg \rightarrow \gamma ZZ$	0.13 $\begin{smallmatrix} +34\% & +1\% \\ -25\% & -1\% \end{smallmatrix}$	$gg \rightarrow Z\gamma\gamma$	3.42 $\begin{smallmatrix} +44\% & +1\% \\ -31\% & -1\% \end{smallmatrix}$

Table 62: Cross sections for loop-induced associated production of gauge and Higgs bosons, at 100 TeV. Theoretical uncertainties describe scale and PDF variations, respectively. The numerical integration error is always smaller than theoretical uncertainties, and is not shown. Jets are within  $|\eta| < 5$  and have  $p_T > 20$  GeV. For  $pp \rightarrow HVjj$ , furthermore,  $m(jj) > 100$  GeV.

## 16 Electroweak corrections<sup>47</sup>

The electroweak coupling constant  $\alpha$  is more than a factor of 10 smaller than the QCD coupling constant  $\alpha_s$ , and therefore perturbative corrections from QCD are typically much larger than those from electroweak effects. From the size of the coupling constants, one can expect that NLO electroweak corrections are roughly comparable to NNLO QCD corrections. For colliders at relatively low energies (such that the partonic center of mass energy does not exceed the electroweak scale significantly), this scaling in general holds, but of course depends on the process under consideration.

At partonic energies which far exceed the electroweak scale, however, electroweak corrections receive a logarithmic enhancement. For each power in the electroweak coupling constant, one finds two powers of the logarithm

$$L_V(s) = \ln \frac{m_V^2}{s}, \quad (85)$$

where  $\sqrt{s}$  is the partonic center of mass of the hard collision. This implies that each order in perturbation theory gives a factor

$$\frac{\alpha}{4\pi} L_V^2(s). \quad (86)$$

For a concrete example, consider the Drell-Yan process  $pp \rightarrow \ell^+ \ell^-$ , where  $\ell$  denotes either an electron or a muon. At fixed order, the electroweak corrections due to the exchanges of  $W$  and  $Z$  bosons are given by

$$\frac{\sigma^{\text{NLO}}(s)}{\sigma^{\text{LO}}(s)} = 1 - \frac{\alpha}{4\pi} [1.56 L_W^2(s) + 1.78 L_Z^2(s) + \dots] \quad (87)$$

where we have only kept the terms enhanced by two powers of  $L_V(s)$ . For  $\sqrt{s} \gtrsim 1$  TeV electroweak corrections are at the 10% level and above, and for  $\sqrt{s} \gtrsim 10$  TeV the corrections become larger than the Born results, such that fixed order electroweak perturbation theory is expected to break down completely.

Note that the virtual corrections in the above results are infrared (IR) finite by themselves. This is contrary to virtual corrections involving massless gauge bosons, which are IR divergent, and only yield finite answers when they are combined with the soft and collinear radiation of real massless gauge bosons. The reason is that the soft and collinear divergences that are present for massless gauge theories are regulated by the masses of the vector bosons, such that both the virtual and the real radiation are separately finite, albeit with logarithmic sensitivity to the gauge boson masses. This makes of course physical sense; the real radiation of massive gauge bosons (even those with infinitely soft or collinear momentum) can always be observed experimentally, such that both the virtual and real contributions lead to experimentally observable cross sections and therefore they have to be finite by themselves. The logarithmic sensitivity on the gauge boson masses is a consequence of the fact that in the massless limit we have to recover the usual result where both virtual and real corrections are separately divergent.

From the above argument it of course follows that not only the virtual corrections are logarithmically sensitive to the masses of the gauge bosons, but the real corrections have to be as well. This logarithmic sensitivity should cancel for completely inclusive quantities. To see this, let us consider the process

$$\sigma_{q_1 q_2} \equiv \sum_{l_1, l_2} \sigma_{q_1 q_2 \rightarrow l_1 l_2} + \sum_{l_1, l_2, V} \sigma_{q_1 q_2 \rightarrow l_1 l_2 V}. \quad (88)$$

To double logarithmic accuracy for the NLO correction  $\delta\sigma_{q_1 q_2}$  one finds

$$\delta\sigma_{u\bar{u}}(s) = \delta\sigma_{d\bar{d}}(s) = -\delta\sigma_{u\bar{d}}(s) = -\delta\sigma_{d\bar{u}}(s). \quad (89)$$

<sup>47</sup>Editor: F. Piccinini

Thus, if we sum over the flavors of the initial state on top of the flavor of the final state (thus calculating a completely inclusive quantity), all double logarithms cancel

$$\delta\sigma \equiv \sum_{q_1, q_2} \delta\sigma_{q_1 q_2} = 0 + \mathcal{O}\left(\frac{\alpha}{4\pi}\right). \quad (90)$$

The result of Eq. (90) is of course the result of the KLN theorem, which states that all IR sensitivity will cancel in completely inclusive observables. However, the sum over initial states as performed in Eq. (90) is of course not possible for a hadron collider, since each cross-section is weighted by their parton luminosities which are not equal to one another. This gives the important result that at a hadron collider the logarithmic sensitivity on the gauge boson masses do not cancel, even for completely inclusive observables. This can be understood easily by noting that the protons in the initial state are not singlets under the SU(2) gauge group, such that the initial state breaks the inclusivity of the observable.

The fixed order results can be calculated using standard techniques for NLO calculations, however the presence of several mass scales means that the required calculations are typically more difficult than the corresponding calculation for massless gauge theories such as QCD. Much effort has been put into understanding the electroweak logarithms arising from virtual corrections [513–537] and the structure of the logarithmic terms at one and two loops was derived for a general process in Refs. [525, 529] and [530–532, 536], respectively. The issue of real weak boson emission has been addressed in Refs. [68, 207, 522, 523, 527, 528, 538–544] and, on a more phenomenological ground, in Refs. [207, 209, 426, 428, 545–548]. Since as discussed the logarithmic terms dominate over the terms not logarithmically enhanced, this general result provides a good approximation to the exact NLO corrections at sufficiently high partonic center of mass energies. This approximation is often called the Sudakov log approximation.

The resummation of the logarithmic terms that arise in the virtual exchanges of  $W$  and  $Z$  has been the subject of a considerable amount of work over the past decade [515, 520–522, 525, 529, 530, 533, 535, 549–558]. In [533, 535] a completely general method to resum these logarithms for an arbitrary process was developed, using soft-collinear effective theory [559–562]. The resummation of the real radiation has so far not received much attention yet, even though the large logarithms originating from the real radiation are by the KLN theorem as large as those resulting from virtual exchanges. In a recent paper [544], it was shown how to resum the double logarithmic corrections from the real radiation of  $W$  and  $Z$  bosons.

From the above discussion it is clear that a real paradigm shift is happening with regards to electroweak corrections when partonic center of mass energies exceed a few TeV, which can easily happen at a future 100 TeV machine. Thus, at such a machine, electroweak corrections are *much more* important than at current colliders. While at past and current colliders electroweak corrections were usually computed to obtain high precision for a few observables, electroweak corrections at a 100 TeV collider are required even to get rough estimates of the expected cross-sections at the highest available phase space corners. Furthermore, at high enough center of mass energies, not only are the electroweak corrections required at fixed order accuracy, but the leading logarithms need to be resummed.

In this section we give a brief account of the available tools and algorithms for the calculation of electroweak corrections at hadronic colliders and discuss the phenomenological impact of electroweak corrections (at  $\sqrt{s} = 100$  TeV) to the following benchmark Standard Model processes: Drell-Yan, weak boson pairs ( $WW$ ,  $WZ$ ,  $WH$  and  $ZH$ ),  $V$ + jets, dijet production,  $t\bar{t}$ ,  $t\bar{t}H$  and  $t\bar{t}$ + jets. A last section will be devoted to the issue of the inclusion of real radiation.

## 16.1 Tools

In the past exact NLO corrections have been calculated and implemented in simulation tools for a limited class of hadronic collision processes. In particular for charged and neutral Drell-Yan, the most important processes for the precision physics program of Tevatron and LHC, a number of dedicated codes have

been developed, such as HORACE [563, 564], RADY [565–567], SANC [568, 569], WGRAD [570], WINHAC [571, 572] and ZGRAD [573]. In particular SANC also includes NLO QCD corrections, while HORACE includes the effect of all order photon radiation properly matched to the  $\mathcal{O}(\alpha)$  corrections. NLO EW corrections are added to the  $\mathcal{O}(\alpha_S^2)$  ones in the FEWZ code [574], while factorized NLO EW and NLO QCD corrections to the single  $W$  and  $Z$  production matched with QED and QCD parton shower have been implemented in the POWHEG-BOX Monte Carlo event generator [575–577].

The large center of mass energy and the high luminosity of LHC run II and beyond will require the inclusion of at least  $\mathcal{O}(\alpha)$  corrections in theoretical predictions for several processes, as documented, for example, in the Les Houches wish-list in Tables 1-3 of Ref. [578].

Besides Drell Yan processes, full one loop electroweak (EW) corrections have been calculated also for  $V + 1$  jet ( $V = Z, W, \gamma$ ) [579–582], dilepton+jets [204, 583, 584], single top [585–587],  $t\bar{t}$  [588–594], dijet [206, 208, 595],  $Z/W + H$  [596, 597] (including the  $Z/W$  decay products),  $H$  production in vector boson fusion [598, 599],  $VV'$  (with on-shell vector bosons or in pole approximation) [66, 600–604],  $WW + 1$  jet [605],  $WZZ$  [606],  $WWZ$  [607],  $W\gamma$  production [608],  $Z\gamma$  production [609]  $t\bar{t}+H$  [426, 427]. All these calculations have been carried out on a process-by-process basis. In the QCD sector, during last ten years we have witnessed the so called “NLO revolution”: several groups succeeded in building new codes able to calculate NLO QCD corrections in a completely automatic way, such as BLACKHAT [215], GoSAM [247, 248], HELAC-NLO [610], MADLOOP [419]/ MADGRAPH/MADGRAPH5\_AMC@NLO [64, 323], NJET [373], OPENLOOPS [510] and RECOLA [611]. In various cases the automation of hadron collider simulations is realised in combination with the Sherpa Monte Carlo [102]. These developments towards the automatic computation of NLO QCD corrections allowed recent progress in the calculation of NLO EW corrections, despite the difficulties of virtual EW corrections, mainly due to the presence of several mass scales and of unstable particles in the loops, as well as of the chiral structure of electroweak interactions. For a recent review on these items see Ref. [612]. With these automatic algorithms, exact  $\mathcal{O}(\alpha)$  corrections to  $Z(\rightarrow \bar{l}l) + 2$  jets [613],  $W + n$  jets ( $n \leq 3$ ) [614],  $W + n/Z + n$  jets ( $n \leq 2$  including off-shell vector boson decays and matching with Parton Shower) [615],  $t\bar{t} + H/Z/W$  [426, 428] and  $\mu^+\mu^-e^+e^-$  [616] have been computed for the first time.

As far as only the Sudakov regime is concerned, the universality of the infrared limit of weak corrections can be exploited to develop general algorithms for the calculation of the EW corrections in the logarithmic approximation [515, 525, 529, 535]. Following this approach, the Sudakov corrections to diboson [600, 617–619], vector boson plus one [620] or several jets [547],  $t\bar{t}$ +jets [558],  $H$  [621, 622] and  $H$ +jet [619] production have been computed pointing out further the phenomenological impact of the EW corrections at high energies. Order  $\alpha$  corrections to dijet, Drell-Yan and  $t\bar{t}$  production have been recently included in the MCFM Monte Carlo program [623]: both the Sudakov approximation and the full one loop corrections have been implemented in order to provide a tool for the fast evaluation of the approximated  $\mathcal{O}(\alpha)$  corrections that also allows to assess the validity of the approximated results [624]. Following the work presented in Ref. [547], the algorithm for double and single logs has been implemented in the ALPGEN [625] LO matrix element event generator, for the processes  $V +$  multijets, QCD multijet and heavy flavour plus jets.

## 16.2 Drell-Yan

We consider the processes  $pp \rightarrow W^{+,*} \rightarrow \mu^+\nu_\mu + (X)$  and  $pp \rightarrow \gamma^*/Z^* \rightarrow \mu^+\mu^- + (X)$ , at the c.m. energy  $\sqrt{s} = 100$  TeV and using the NNPDF 2.3QED PDF set [53] with factorization/renormalization scale  $\mu = M(\bar{\ell}\ell^{(\prime)}\gamma)$ . We applied the following acceptance cuts:

$$p_{\perp}^{\mu}, p_{\perp}^{\nu} \geq 25 \text{ GeV}, \quad |\eta_{\mu}| \leq 2.5. \quad (91)$$

Muons are considered “bare” (*i.e.* without photon recombination). In order to focus on the high energy dynamics, we further impose the additional cut on the transverse mass  $M_T \geq 5$  TeV, where  $M_T$  is

defined as  $M_T = \sqrt{2p_\perp^\ell p_\perp^{\nu} (1 - \cos \phi)}$  (with  $\phi$  the angle between lepton and neutrino in the transverse plane), for the charged Drell-Yan process and  $M(\ell^+ \ell^-) \geq 5$  TeV for the neutral current process.

The results, with NLO accuracy in the electroweak coupling, have been obtained with the code HORACE [563, 564] using the  $G_\mu$  scheme and the following input parameters

$$\begin{array}{lll}
 G_\mu = 1.1663787 \cdot 10^{-5} \text{ GeV}^{-2} & M_W = 80.385 \text{ GeV} & M_Z = 91.1876 \text{ GeV} \\
 \Gamma_W = 2.4952 \text{ GeV} & \sin^2 \theta_W = 1 - M_W^2/M_Z^2 & M_{\text{Higgs}} = 125 \text{ GeV} \\
 m_e = 510.998928 \text{ KeV} & m_\mu = 105.6583715 \text{ MeV} & m_\tau = 1.77682 \text{ GeV} \\
 m_u = 69.83 \text{ MeV} & m_c = 1.2 \text{ GeV} & m_t = 173 \text{ GeV} \\
 m_d = 69.83 \text{ MeV} & m_s = 150 \text{ MeV} & m_b = 4.6 \text{ GeV} \\
 V_{ud} = 0.975 & V_{us} = 0.222 & V_{ub} = 0 \\
 V_{cd} = 0.222 & V_{cs} = 0.975 & V_{cb} = 0 \\
 V_{td} = 0 & V_{ts} = 0 & V_{tb} = 1
 \end{array}$$

For the coupling of external photons to charged particles needed for the evaluation of photonic corrections we use  $\alpha = \alpha(0) = 1/137.03599911$  and  $\alpha_s(\mu)$  from the PDF set.

In Fig. 176 we present the integrated transverse mass  $M_T$  and charged lepton transverse momentum  $p_\perp^\ell$  (integrated) distributions in the window [5–25] TeV. The effects of the NLO EW corrections with respect to the LO predictions are huge and negative, exceeding 60% in absolute value for  $M_\perp^\ell \geq 10$  TeV (red line in the lower left panel). The shaded bands around the lines give the estimate of the PDF uncertainty according to the NNPDF prescription, which is contained within 10% level. In the same window of [5–25] TeV the corrections to  $p_\perp^\ell$  are even larger, because a given bin of the  $p_\perp^\ell$  distribution corresponds roughly to a bin twice larger in the transverse mass distribution.

A general issue regarding EW corrections is the relevance of the inverse bremsstrahlung (also called “gamma”-induced) processes which are a contribution to the real radiation. In fact the elementary scattering process is  $\gamma q \rightarrow \mu^+ \nu_\mu q'$ , whose amplitude can be obtained by crossing symmetry from the standard real radiation amplitude  $qq' \rightarrow \mu^+ \nu_\mu \gamma$ . These contributions have been discussed in the literature [564, 567, 626, 627], with particular reference to LHC. An essential ingredient is the photon PDF, which is discussed in Section 2. At present it is affected by very large uncertainties, which blow up at large energy scales. However, in the future, these uncertainties will be constrained by LHC data. For the transverse mass, Fig. 176, left panel, blue line, the central value of the inverse bremsstrahlung contribution is positive, at the % level up to 10 TeV and increases up to values of around 10% at 25 TeV. These effects should be considered with caution because of the above mentioned large uncertainties. In fact for  $p_\perp^\ell$  not only the uncertainty but also the central value blows up. For comparison, we have included also the effect of higher order photonic corrections (violet line)<sup>48</sup>, which are positive and become of the order of 10% at scales of the order of 20 TeV. In Fig. 177, left panel, we show the effects of the same higher order contributions discussed above for the integrated lepton pseudorapidity distribution, where no particular shape is present except for the overall normalization effects.

In Fig. 177, right panel, and Figs. 178 and 179 we plot the predictions for the neutral Drell Yan process  $pp \rightarrow \gamma^*/Z^* \rightarrow \mu^+ \mu^- + (X)$ . In particular, Fig. 177, right panel, displays the invariant mass  $M_{\mu^+ \mu^-}$  integrated distribution, while Fig. 178 contains the leading (left panel) and softest (right panel) lepton transverse momentum integrated distribution. For the invariant mass the NLO EW corrections are slightly smaller than for the charged Drell Yan case: they reach the size of 60% at scales above 20 TeV. The corrections are of the same order for the leading lepton transverse momentum, while they are larger for the softest one, as can be expected with phase space arguments.

For the neutral current Drell Yan process there is a contribution from  $\gamma$ -induced processes already

<sup>48</sup>In HORACE the higher order effects are included by means of a proper matching between fixed order calculation and all orders Parton Shower. Other approaches can be adopted for the simulation of higher order photonic corrections, such as, for instance, the YFS formalism used in Refs. [628–631].

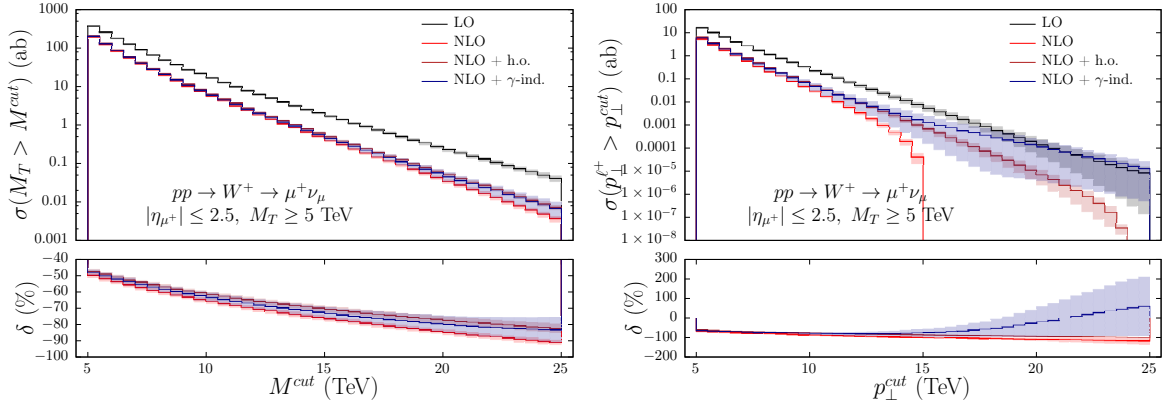


Fig. 176: Left: the distribution of the transverse mass for  $W^+$  production. Right: the distribution of the charged lepton transverse momentum. The black lines represent the LO predictions, the red lines give the NLO EW predictions, the violet lines include also higher order photonic corrections and the blue lines include the contribution of the  $\gamma$ -induced processes, in addition to the NLO EW corrections. The lower panels contain the relative deviations of the various levels of approximation with respect to the tree-level predictions.

at tree level, i.e. from  $\gamma\gamma \rightarrow \mu^+\mu^-$ . For the considered observables, we plot separately the LO prediction including/excluding (green/black lines) the tree-level  $\gamma\gamma \rightarrow \mu^+\mu^-$  contribution and the NLO prediction with and without (blue and red lines, respectively)  $\gamma$ -induced contributions. The blue lines include both the tree-level and the radiative  $\gamma$ -induced processes. As can be seen in Figs. 177, 178, 179 the largest effects come from the tree-level  $\gamma\gamma \rightarrow \mu^+\mu^-$  process, ranging from few % at  $M_{\ell^+\ell^-} = 5$  TeV to a factor of two at  $M_{\ell^+\ell^-} = 20$  TeV. The effects of the radiative  $\gamma$ -induced processes can be inferred by looking at the difference between the blue and red lines of the lower panels. They are positive and moderate in size, reaching about 50% at scales above 20 TeV. However, given the very large uncertainties of photon PDF's, all the predictions involving  $\gamma$ -induced processes should be taken with caution.

In summary, the effects of the EW NLO corrections on Drell-Yan processes at a future hadron collider at 100 TeV are very large, spoiling the stability of fixed order perturbative calculations and calling for resummed approaches, in order to obtain reliable predictions. The inverse bremsstrahlung processes could have a relevant impact, even if at present it is difficult to put on a quantitative ground. To this aim, reliable photon PDF's would be necessary, which will be available after the scheduled LHC runs.

### 16.3 Gauge boson pairs and Higgsstrahlung

In the present section we focus on the EW and QCD corrections to the diboson production at the FCC at 100 TeV. In particular, we discuss the impact of NLO QCD and EW corrections to the processes  $VV'$  (i.e.  $W^+W^-$ ,  $ZW^\pm$  and  $ZZ$ ) and  $HV$  ( $V = W^\pm, Z$ ) computed by means of the automated tool MADGRAPH5\_AMC@NLO [64] and a currently private extension that allows to calculate NLO QCD and EW corrections [426, 428]. We work in the  $G_\mu$  scheme with:

$$G_\mu = 1.16639 \cdot 10^{-5} \text{ GeV}^{-2}, \quad M_W = 80.385 \text{ GeV}, \quad M_Z = 91.188 \text{ GeV}, \quad (92)$$

the top quark and Higgs boson masses being set to 173.3 GeV and 125 GeV, respectively. We use the NNPDF 2.3QED PDF set [53] with the following factorization and renormalization scales:

$$\mu_F = \mu_R = \mu = \frac{H_T}{2}, \quad H_T = \sum_i \sqrt{m_i^2 + p_{T,i}^2}, \quad (93)$$

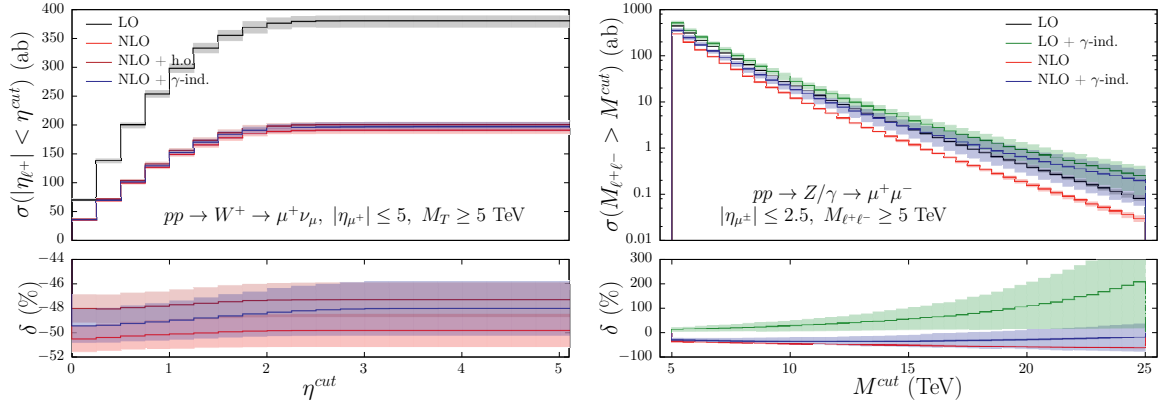


Fig. 177: Left: the distribution of the lepton pseudorapidity for  $W^+$  production. The meaning of the lines is the same as for Fig. 176. Right: the distribution of the invariant mass for  $\ell^+\ell^-$  production. In the right panel the black line represents the LO predictions while the green line includes the LO  $\mathcal{O}(\alpha^3)\gamma$ -induced process. The red line shows the EW NLO predictions while the blue line includes the NLO  $\mathcal{O}(\alpha^3)\gamma$ -induced processes (both tree-level and radiative diagrams). In the lower panel the green line is the relative deviation of the LO prediction including the tree-level  $\gamma\gamma \rightarrow \mu^+\mu^-$  process with respect to the pure LO. The red line gives the size of the EW NLO corrections excluding  $\gamma$ -induced processes; the blue line quantifies the deviation of the complete EW NLO corrections (including all  $\gamma$ -induced processes) with respect to the the LO order predictions which include the tree-level  $\gamma\gamma \rightarrow \mu^+\mu^-$  process.

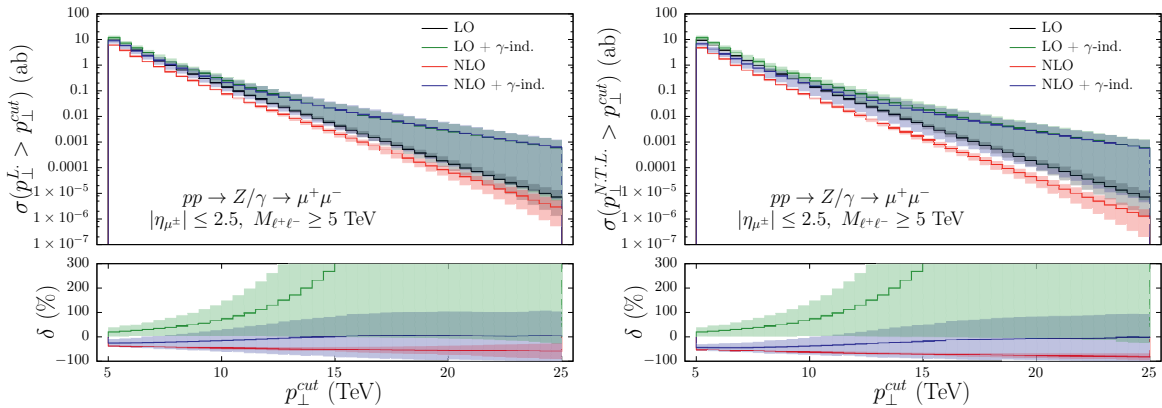


Fig. 178: The distribution of the leading (left) and softest (right) lepton pt for  $\ell^+\ell^-$  production. The meaning of the lines is the same as in Fig. 177, right panel.

where the index  $i$  runs over all the final state particles. Scale uncertainties are estimated by varying independently the scales  $\mu_F$  and  $\mu_R$  in the range  $[\mu/2, 2\mu]$ . Massive external particles are treated as stable and no cuts are applied at the analysis level.

One loop EW corrections to  $VV'$  production at hadron colliders have been computed in the Sudakov approximation in Refs. [617–619], while the full  $\mathcal{O}(\alpha)$  results can be found in Refs. [66, 603] for on-shell  $V$  and  $V'$  and in Refs. [602, 604, 616] including vector boson decays. Here, we show predictions at NLO QCD and EW accuracy, taking into account the contribution from initial-state photons and evaluating the corresponding PDF uncertainties, which are expected to be large.

In Fig. 180 we show predictions at NLO QCD and NLO EW accuracy for cumulative distributions in  $ZW^-$  production (results for  $ZW^+$  are qualitatively identical). In the upper row we show the

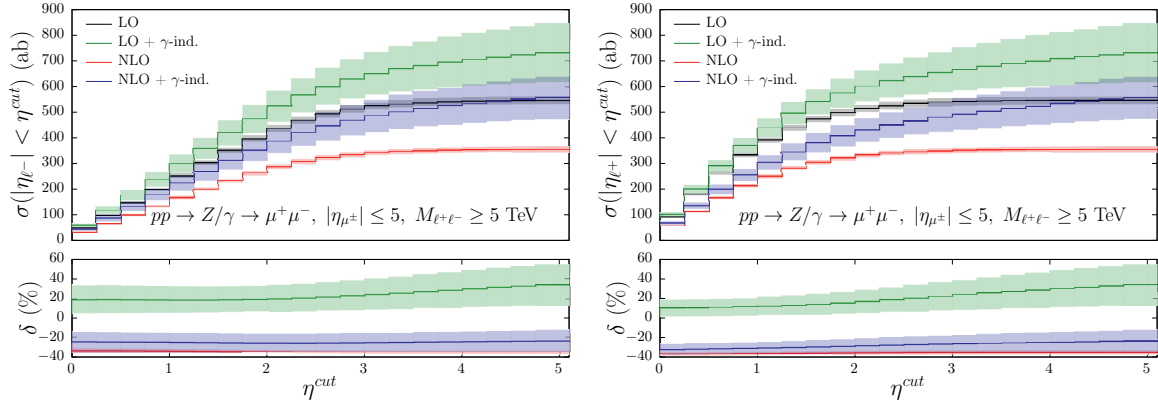


Fig. 179: The distribution of  $\mu^-$  (left) and  $\mu^+$  (right) pseudorapidity for  $\ell^+\ell^-$  production. The meaning of the lines is the same as in Fig. 177, right panel.

dependence of the cross section on a cut on the  $Z$  transverse momentum ( $p_T(Z)$ ). In the lower row we show the dependence on a cut on the  $ZW^-$  invariant mass ( $m(ZW^-)$ ). The plots on the left do not include any contribution from the photon in the initial state, *i.e.*, the photon PDF has been artificially set to zero. On the contrary, the plots on the right do include these contributions. The left plots allow to better identify the negative contributions due to the Sudakov logarithms and disentangle them from those related to photon-initiated processes (quark radiation from  $\gamma q$  initial-states). Instead, the plots on the right include this kind of processes and thus the comparison with those on the right is useful for estimate the photon-induced contributions, which typically have huge PDF uncertainties and are very large with opposite sign w.r.t the Sudakov logarithms. It is important to note that the plots on the right strongly depend on the PDF set used and their large uncertainty are due to the currently poor determinations of the photon PDF.

In each plot we display in the main panel LO (black), LO + NLO QCD (blue) and LO + NLO QCD + NLO EW (red) distributions. In the first inset we show the (LO + NLO QCD)/LO ratio with scale uncertainties (blue band), *i.e.* the QCD  $K$ -factor, and the (LO + NLO QCD + NLO EW)/LO ratio (red line). In the second inset we show only the (LO + NLO EW)/LO ratio without NLO QCD contributions, but including the PDF uncertainties for the numerator in order to enlighten the qualitative difference for the EW corrections in the cases with (right) and without (left) photons in the initial state. As can be seen in the left plots, the effect of Sudakov logarithms is very large; for  $p_T(Z) > 5$  TeV the NLO EW corrections are  $\sim -80\%$  of the LO, while for  $m(ZW^-) > 8$  TeV they are  $\sim -20\%$ . The origin of the huge  $K$ -factor in the QCD corrections has already been studied in the literature [310, 311]. At LO a hard  $Z$  has to recoil against a hard  $W^-$ , while at NLO QCD the dominant kinematic configuration is given by a hard  $Z$  recoiling against a hard jet and a soft  $W$ . In the case of quark radiation, this kinematical configurations involve corrections  $\sim \alpha_s \log^2(p_T(Z)/m_W)$  that are further enhanced by the large gluon PDF luminosity at the 100 TeV collider.<sup>49</sup> A similar dynamic is present also in the photon-initiated corrections (left plots), where a correction  $\sim \alpha \log^2(p_T(Z)/m_W)$  is present for the same reason [66]. However, on top of that, the photon in the initial state can also directly couple to the  $W$  boson originating new  $t$ -channel configurations, which on the contrary are not present in NLO QCD. This effect compensates the suppression due to the  $\alpha$  coupling and explains also why photon-induced contributions, at variance to NLO QCD corrections, are large and strongly depend also on the  $m(ZW^-)$  cut; if no rapidity cuts are applied  $t$ -channel configurations are much less suppressed at high invariant masses w.r.t  $s$ -channel ones. These photon-induced contributions strongly depend on the PDF set employed

<sup>49</sup>Similar arguments are present for the  $p_T(t\bar{t})$  in NLO QCD corrections in  $t\bar{t}V$  production and are discussed in some details in Section 12.1 of this report.

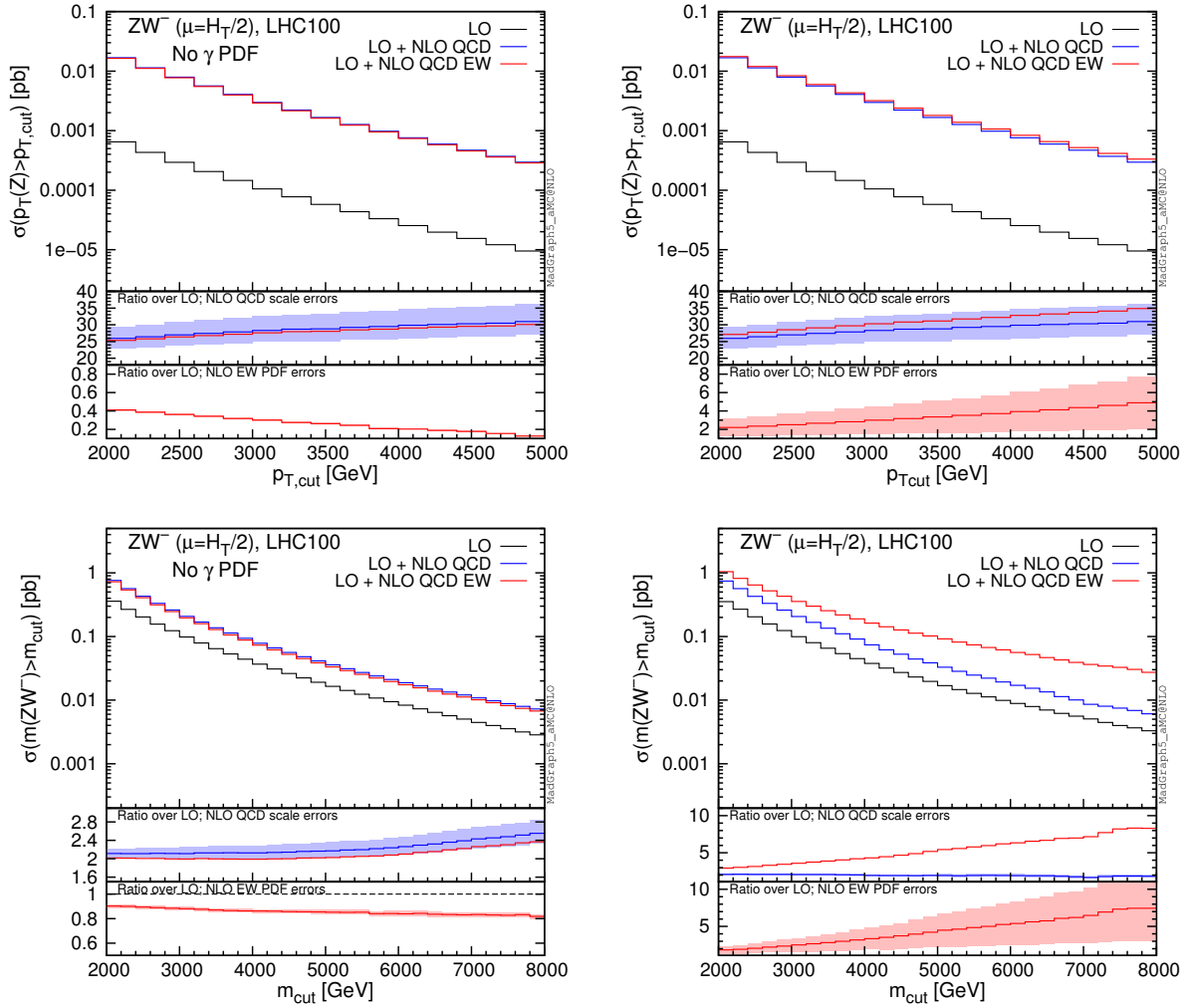


Fig. 180: Cumulative distributions for  $ZW^-$  production at NLO QCD and NLO EW accuracy. The upper plots show the dependence of the total cross sections on a cut on the  $p_T(Z)$ , the lower ones on a cut on the  $m(ZW^-)$ . The plots on the left do not include contribution from photons in the initial state; they are included in the right plots. See text for further details.

and, in the case of the NNPDF 2.3QED used here, they have large uncertainties. Moreover it is clear that a possible jet-veto, as in LHC analyses, would not only decrease the NLO QCD  $K$ -factor and its dependence on  $p_T(Z)$ , but it would also strongly suppress the large photon-initiated contribution.

In Fig. 181 we show similar cumulative distributions for  $W^+W^-$  production. In this case we show only results with the photon PDF set equal to zero. However,  $W^+W^-$  production receives contribution from initial-state photons already at LO via the  $\gamma\gamma$  initial states and their impact on  $m(W^+W^-)$  distributions is discussed in Section 2.5 and shown in Fig. 17. As can be seen in Fig. 181 NLO QCD corrections shows the typical behaviour of  $VV'$  production, with a large dependence on the  $p_T$  of the vector boson. The NLO EW corrections involve very large Sudakov logarithms that are  $\sim -120\%$  of the LO at  $p_T(W^+) > 5$  TeV and thus they have to be resummed.

In the case of  $ZZ$  production, which we do not show here, NLO QCD and NLO EW corrections are qualitatively similar to the  $ZW^\pm$  and  $W^+W^-$  production. However, since the photon cannot directly couple to the  $Z$  boson, no new  $t$ -channel is created for  $\gamma q$  initial state and, as consequence, their contribution is relatively much smaller w.r.t the case of  $ZW^\pm$  and  $W^+W^-$  production.

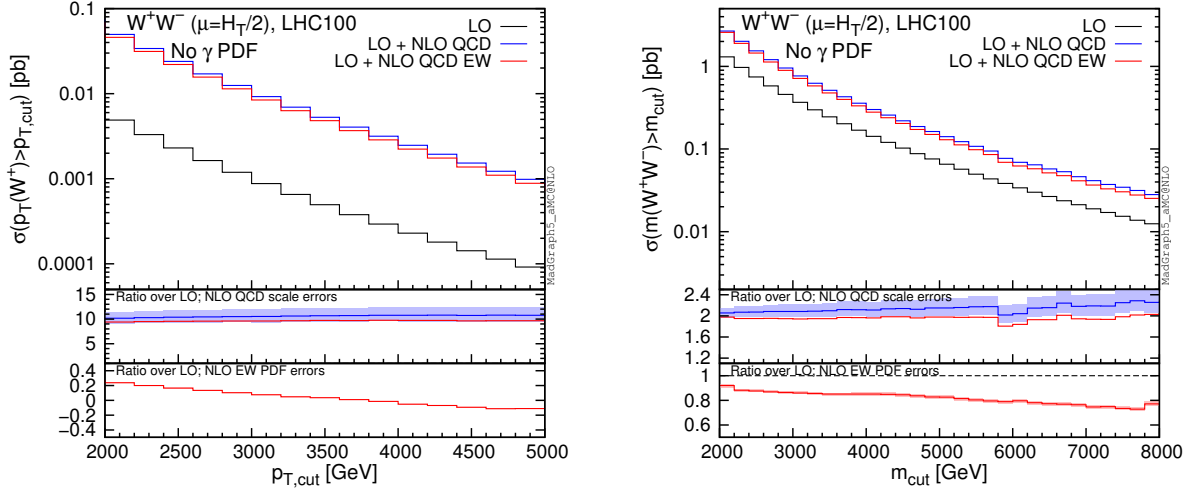


Fig. 181: Cumulative distributions for  $W^+W^-$  production at NLO QCD and NLO EW accuracy. Both plots do not include contribution from photons in the initial state. The left plot shows the dependence of the total cross sections on a cut on the  $p_T(W^+)$ , the right one on a cut on the  $m(W^+W^-)$ . See text for further details.

We now turn to the case of  $HV$  production. One loop EW corrections to  $HV$  production have been computed in Ref. [597] for on-shell  $V$  and in Ref. [596] including the off-shell decay of the vector boson. Here, we show predictions at NLO QCD and EW accuracy, taking into account the contribution of initial-state photons and evaluating their large PDF uncertainties.

Figure 182 is analogous to Fig. 180 and displays the corresponding quantities for  $HW^-$  production (the  $HW^+$  case is qualitatively identical). In the second insets the purple line, which is not present only in the bottom-right plot, is the ratio  $(\text{NLO EW} + \text{HBR})/\text{LO}$  where with HBR (Heavy-Boson-Radiation) we denote the emission of an extra Heavy-Boson. From the comparison with the red lines in the same insets we can notice a partial cancellation of the effects due to the Sudakov logarithms, which also in this case are very large:  $\sim -100\%$  of the LO for  $p_T(H) > 6$  TeV and  $\sim -80\%$  for  $m(HW^-) > 10$  TeV.

At variance with the  $ZW^-$  case, neither NLO QCD and photon-initiated contributions in NLO EW corrections contain terms proportional to  $\log^2(p_T(H)/m_W)$ .<sup>50</sup> However, initial-state photons can couple directly to the  $W$  and open  $t$ -channel configuration for the  $HW^-$  pair. Since at LO no  $t$ -channel diagrams are present at all, the LO contribution is much more suppressed at high  $m(HW^-)$  w.r.t. the NLO EW, to the point that NLO EW corrections are  $\sim 400$  times larger than the LO for  $m(HW^-) > 10$  TeV. It is worth to notice that this estimate strongly depends on the PDF set used and on possible additional cuts. For instance, we explicitly verified that by simply requiring  $|\eta(H)|, |\eta(W^-)| < 4$  the NLO EW  $K$ -factor for  $m(HW^-) > 10$  TeV is reduced from  $\sim 400$  to  $\sim 10$ . A possible additional jet-veto would further suppress the photon-induced contribution.

The case of  $HZ$  production is similar to  $HW^-$  production, but photons cannot couple directly to the  $Z$  and consequently, without new  $t$ -channel production channels, no large enhancement from photon induced processes is present for large invariant masses.

<sup>50</sup>The reason is that  $Hj$  production is not possible at the tree-level. Thus, in the real quark radiation, the limit of a  $W$  collinear to a final-state jet cannot be decomposed into  $Hj$  production times an integrated  $q \rightarrow q'W$  splitting that leads to a  $\log^2(p_T(H)/m_W)$  enhancement.

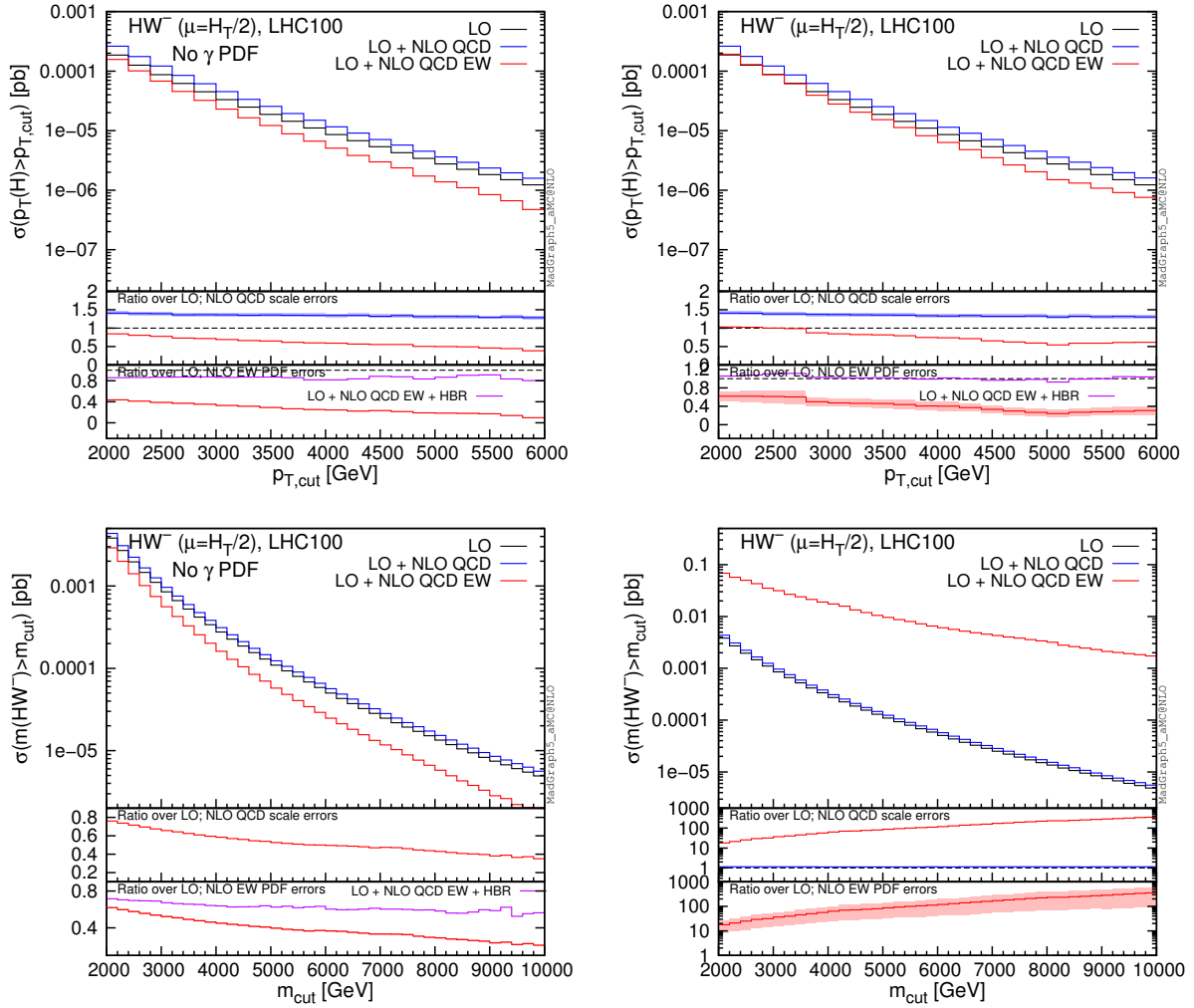


Fig. 182: Cumulative distributions for  $HW^-$  production at NLO QCD and NLO EW accuracy. The upper plots show the dependence of the total cross sections on a cut on the  $p_T(H)$ , the lower ones on a cut on the  $m(HW^-)$ . The plots on the left do not include contribution from photons in the initial state; they are included in the right plots. See text for further details.

## 16.4 $V + \text{jets}$

The production of a vector boson  $V$  ( $V = Z, W, \gamma$ ) in association with jets is a process of great interest at hadron colliders and precise theoretical predictions for  $V + \text{multijets}$  are mandatory. In the literature, the one loop weak corrections to  $V + 1 \text{ jet}$  ( $V = Z, \gamma$ ) have been computed in Refs [579–581], while the full NLO EW corrections have been computed for the processes  $W + 1 \text{ jet}$  [582], monojet [584] and dilepton+jets production [204, 583]. Besides the exact calculations, the  $\mathcal{O}(\alpha)$  corrections to  $V + 1 \text{ jet}$  in the Sudakov approximation have been computed in Refs. [580, 632, 633] by means of the algorithm of Refs. [525, 529] and in Ref. [620] in the SCET framework [535], while in Refs. [547, 634, 635] the phenomenological impact of the  $\mathcal{O}(\alpha)$  corrections to  $Z + 2/3 \text{ jets}$  in the Sudakov limit has been investigated in the context of the direct searches for New Physics at the LHC and at higher energy future colliders. More recently, the exact NLO EW and QCD corrections to the processes  $Z(\rightarrow l^+l^-) + 2 \text{ jets}$  [613] and  $W + n \text{ jets}$  ( $n = 1, 2, 3$ ) [614] have been computed by means of the automated tools RECOLA [611] and MUNICH/SHERPA+OPENLOOPS [510], respectively. The full  $\mathcal{O}(\alpha)$  to  $W^+ + 2 \text{ jets}$  have also been computed in Ref. [612] in the GOSAM+MADDIPOLE framework. In Ref. [615] the NLO

QCD and EW corrections to  $Z/W + 0, 1, 2$  jets including the effect of off-shell vector boson decays and multijet merging have been computed.

In this section we study the phenomenological impact of the  $\mathcal{O}(\alpha)$  corrections on some distributions of interest for the production of a vector boson in association with up to three jets. We work in the  $G_\mu$  scheme with input parameters:

$$G_\mu = 1.16637 \cdot 10^{-5} \text{ GeV}^{-2}, \quad M_W = 80.385 \text{ GeV}, \quad M_Z = 91.1876 \text{ GeV}. \quad (94)$$

We use the PDF set NNPDF2.3QED with factorization and renormalization scale set to:

$$\mu = \frac{H'_T}{2}, \quad H'_T = \sum_{j=1}^{N_{\text{jets}}} p_{T,j} + p_{T,\gamma} + \sqrt{M_V^2 + p_{T,V}^2}, \quad (95)$$

where  $p_{T,\gamma}$  stands for the transverse momentum of the photon in the real radiation contribution (for the exact  $\mathcal{O}(\alpha)$  predictions). In order to evaluate the NLO EW corrections we set the remaining as follows:

$$M_H = 126 \text{ GeV}, \quad M_{\text{top}} = 173.2 \text{ GeV}, \quad (96)$$

while all the light fermions are massless. We consider the following set of cuts:

$$p_{T,j} \geq 300 \text{ GeV}, \quad |\eta_j| \leq 4.5, \quad (97)$$

where the jets are selected according to the anti- $k_T$  algorithm [203] with  $R$  separation 0.4 for the exact  $\mathcal{O}(\alpha)$  predictions, while for the calculation in the Sudakov approximation we simply require  $\Delta R_{\text{min}}(jj) \geq 0.4$ , as the number of partons is fixed and no real corrections are included. The results for  $\gamma + 1, 2, 3$  jets have been obtained by imposing the additional cuts on the photon:

$$p_{T,\gamma} \geq 300 \text{ GeV}, \quad |\eta_\gamma| \leq 4.5, \quad \Delta R(j - \gamma) > 0.4. \quad (98)$$

No cuts are applied on the massive vector bosons that are treated as stable particles.

We collect in Figs. 183-185 the theoretical predictions for the production of a  $W^+$  boson in association with one and two jets at the FCC at 100 TeV both at LO accuracy and including the effect of the full one NLO EW and QCD corrections computed by means of the program OPENLOOPS [636] interfaced with SHERPA [102, 223] and MUNICH [637]. In particular, we focus on the following distributions:  $W$  boson  $p_T$ , leading jet  $p_T$  and the total transverse activity defined as  $H_T = \sum_{\text{jets}} p_{T,j} + p_{T,V}$ . NLO results are obtained by combining QCD and EW results according to the additive prescription:

$$\sigma_{\text{QCD+EW}}^{\text{NLO}} = \sigma^{\text{LO}} + \delta\sigma_{\text{QCD}} + \delta\sigma_{\text{EW}}, \quad (99)$$

as well as in the factorized prescription:

$$\sigma_{\text{QCD} \times \text{EW}}^{\text{NLO}} = \sigma_{\text{QCD}}^{\text{NLO}} \left( 1 + \frac{\sigma_{\text{EW}}^{\text{NLO}}}{\sigma_{\text{LO}}^{\text{NLO}}} \right) = \sigma_{\text{EW}}^{\text{NLO}} \left( 1 + \frac{\sigma_{\text{QCD}}^{\text{NLO}}}{\sigma_{\text{LO}}^{\text{NLO}}} \right), \quad (100)$$

taking the difference of the two results as an estimate of the uncertainty related to the missing higher order terms. The corrections are shown normalized to the QCD NLO results: this corresponds to the usual definition of  $\delta_{\text{EW}}$  for the factorized corrections.

In Figs. 183-185 we consider only the leading  $\mathcal{O}(\alpha_S \alpha)$  and  $\mathcal{O}(\alpha_S^2 \alpha)$  terms contributing to  $W + 1$  jet and  $W + 2$  jets, respectively, while the NLO QCD and the NLO EW corrections to the process of  $\mathcal{O}(\alpha_S^m \alpha^n)$  are defined as the sum of the one loop virtual and real contribution of  $\mathcal{O}(\alpha_S^{m+1} \alpha^n)$  and  $\mathcal{O}(\alpha_S^m \alpha^{n+1})$ , respectively. In particular, in the case of  $W + 1$  jets, this implies that the real corrections receive contributions from the interference of amplitudes of  $\mathcal{O}(\alpha^{3/2})$  with ones of  $\mathcal{O}(\alpha_S \alpha^{1/2})$ : at this

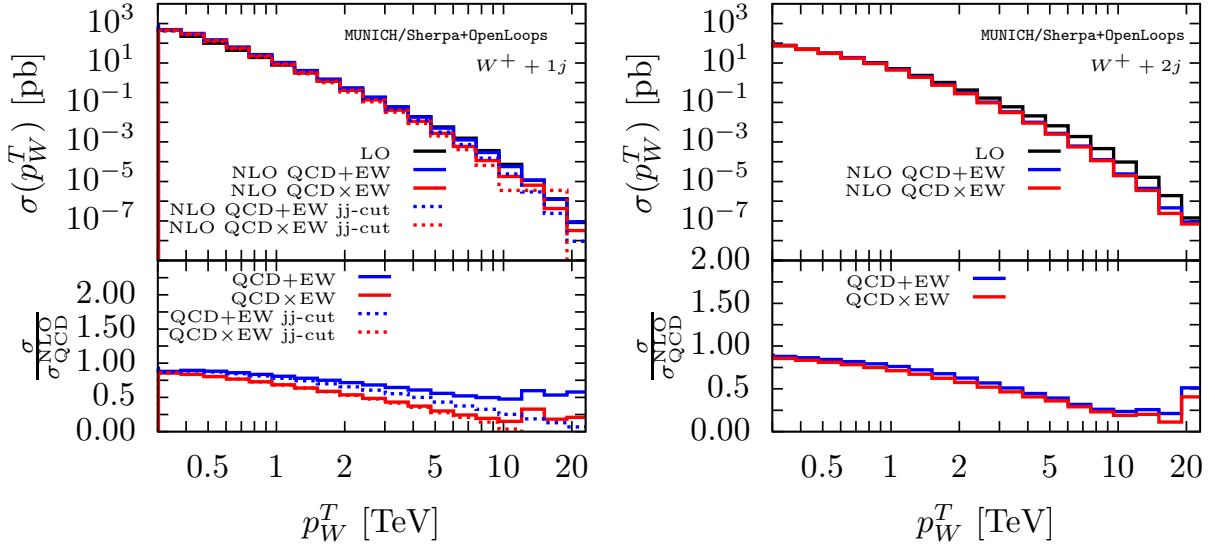


Fig. 183: Integrated  $p_T W$  distribution for  $W^+ + 1$  jet (left panel) and  $W^+ + 2$  jet (right panel) at the FCC at 100 TeV. LO predictions (solid black lines) correspond to the leading  $\mathcal{O}(\alpha_S\alpha)$  and  $\mathcal{O}(\alpha_S^2\alpha)$  tree level contributions to  $W^+ + 1$  jet and  $W^+ + 2$  jets, respectively. The predictions including the full NLO EW and QCD corrections (MUNICH/SHERPA+OPENLOOPS) according to the additive and to the multiplicative prescriptions correspond to the solid red and blue lines, respectively. The results for  $W^+ + 1$  jet after imposing the veto on the dijet-like configuration correspond to dashed lines in the left plot. Lower panels: effect of the full NLO EW and QCD corrections in both the additive and the multiplicative prescriptions normalized to the full one loop QCD corrections.

order these mixed interference terms are finite because of color flow, but in general do not vanish in the presence of identical quarks.

As can be seen from Figs. 183-185, the one loop corrections to  $W + 2$  jets are negative and large, reaching the order of  $-50\%$  in the tails of the distributions under consideration. The same behaviour can be observed in the NLO corrections to  $W + 1$  jet for the  $p_T W$  distribution, where the corrections are however larger than in the case of  $W + 2$  jets and can become of order  $-100\%$  for  $p_T W \simeq 20$  TeV. The picture is different if we consider the NLO predictions for the leading  $p_{Tj}$  and the  $H_T$  distributions for  $W + 1$  jets: in fact, the corrections become positive for  $p_{Tj} \simeq 5$  TeV and  $H_T \simeq 9$  TeV, respectively. The increase in the cross section results from a new kinematical configuration which is available for  $W + 2$  jets and has no LO counterpart: namely, the one where the leading jet  $p_T$  is balanced by a second hard jet and the vector bosons tend to be soft. This part of the cross section can be separated by applying a veto on the events with an angular separation between the two jets larger than  $3\pi/4$  (jj-cut in the plots). Once the veto on the dijet-like configurations is imposed on the corrections to  $W + 1$  jet, the effects on the leading jet  $p_T$  and on the  $H_T$  distributions become similar to the ones on the  $p_T W$  distribution.

In Refs. [525, 529] a process independent algorithm for the computation of NLO EW corrections in the Sudakov approximation has been developed. According to the algorithm, the  $\mathcal{O}(\alpha)$  corrections to a generic process involving  $N$  external particles of flavour  $i_1, \dots, i_N$  in the high energy limit factorize as follows:

$$\delta\mathcal{M}_{i_1 \dots i_n}^{NLL} \Big|_{\text{Sudakov}} = \sum_{k=1}^N \sum_{l>k} \delta_{kl}^{DL} \mathcal{M}_{i_1 \dots j_k \dots j_l \dots i_n}^{LO} + \sum_{k=1}^N \delta_k^{SL} \mathcal{M}_{i_1 \dots j_k \dots i_n}^{LO} + \delta^{PR} \mathcal{M}_{i_1 \dots i_n}^{NLL}. \quad (101)$$

In Eq. (101), the radiator functions  $\delta_{kl}^{DL}$  and  $\delta_k^{SL}$  contain the Sudakov double and single logarithmic contributions, respectively. They depend only on the flavour and on the kinematics of the external parti-

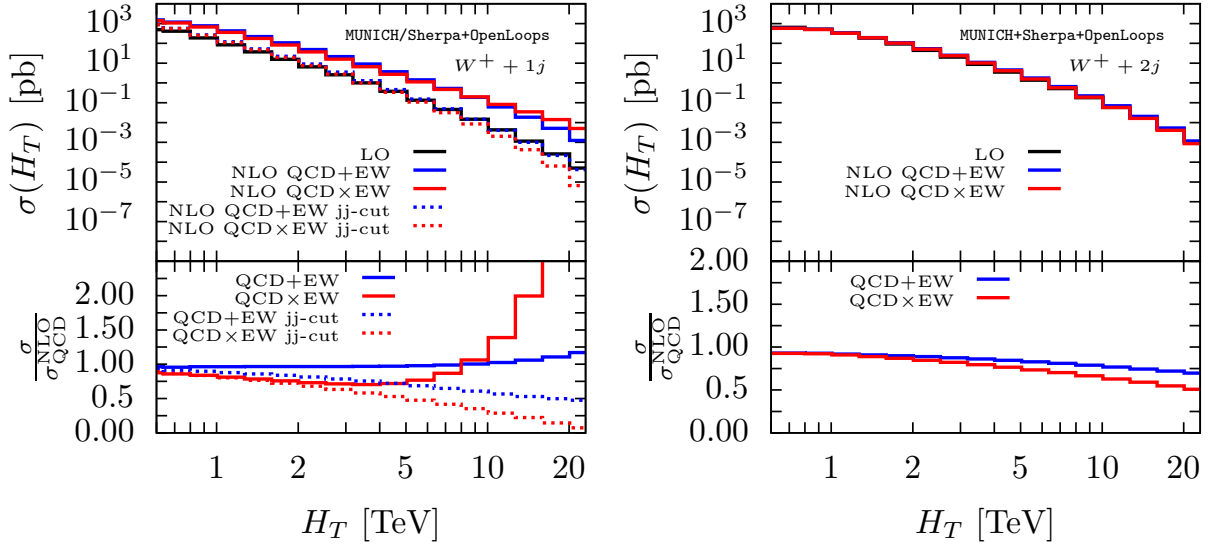


Fig. 184: Integrated  $H_T$  distribution for  $W + 1$  jet (left panel) and  $W + 2$  jet (right panel) at the FCC at 100 TeV. Same notations and conventions as in Fig. [183].

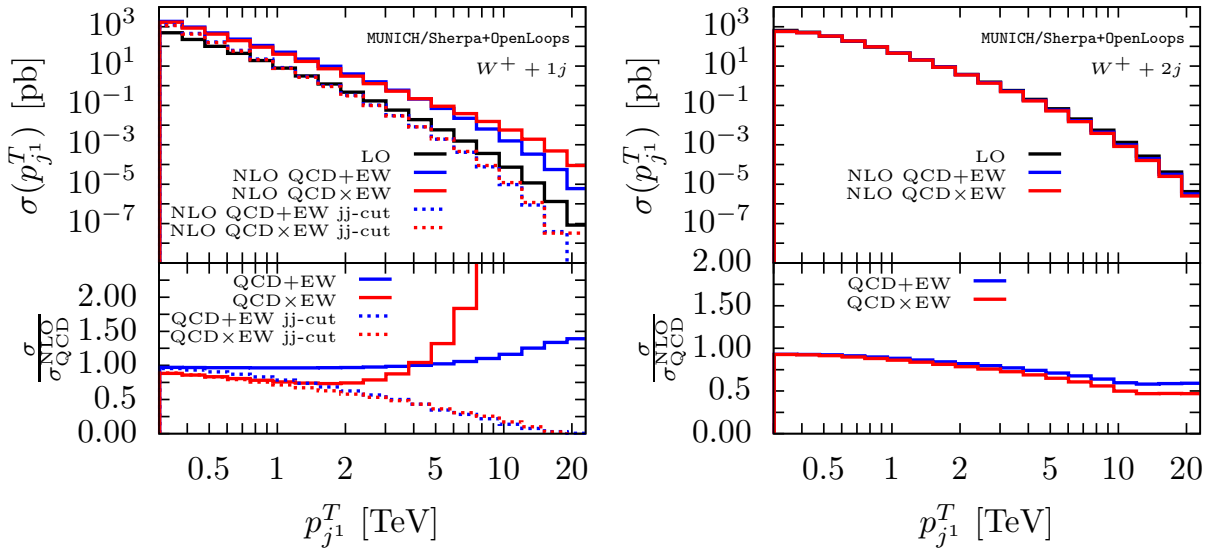


Fig. 185: Integrated  $p_{Tj}$  distribution for the leading jet for the processes  $W + 1$  jet (left panel) and  $W + 2$  jet (right panel) at the FCC at 100 TeV. Same notations and conventions as in Fig. [183].

cles. These terms multiply leading order matrix elements that are obtained from the one of the process  $i_1, \dots, i_N$  under  $SU(2)$  transformations of pair or single external legs,  $j_k$  being in Eq. (101) the  $SU(2)$  transformed of the particle  $i_k$ . The last term in Eq. (101) comes from parameter renormalization:

$$\delta^{PR} \mathcal{M}_{i_1 \dots i_n}^{NLL} = \delta e \frac{\delta \mathcal{M}_{i_1 \dots i_n}^{LO}}{\delta e} + \delta c_W \frac{\delta \mathcal{M}_{i_1 \dots i_n}^{LO}}{\delta c_W} + \delta h_t \frac{\delta \mathcal{M}_{i_1 \dots i_n}^{LO}}{\delta h_t} + \delta h_H \frac{\delta \mathcal{M}_{i_1 \dots i_n}^{LO}}{\delta h_H}, \quad (102)$$

where  $h_t = m_t/M_W$ ,  $h_H = M_H^2/M_W^2$  and  $c_W = M_W/M_Z$ . In Ref. [547], the algorithm of Refs. [525, 529] has been implemented in the ALPGEN [625] event generator: the analytic expressions of the process-independent radiator functions have been coded and all the required leading order matrix elements are computed numerically by means of the ALPHA algorithm [638]. According to

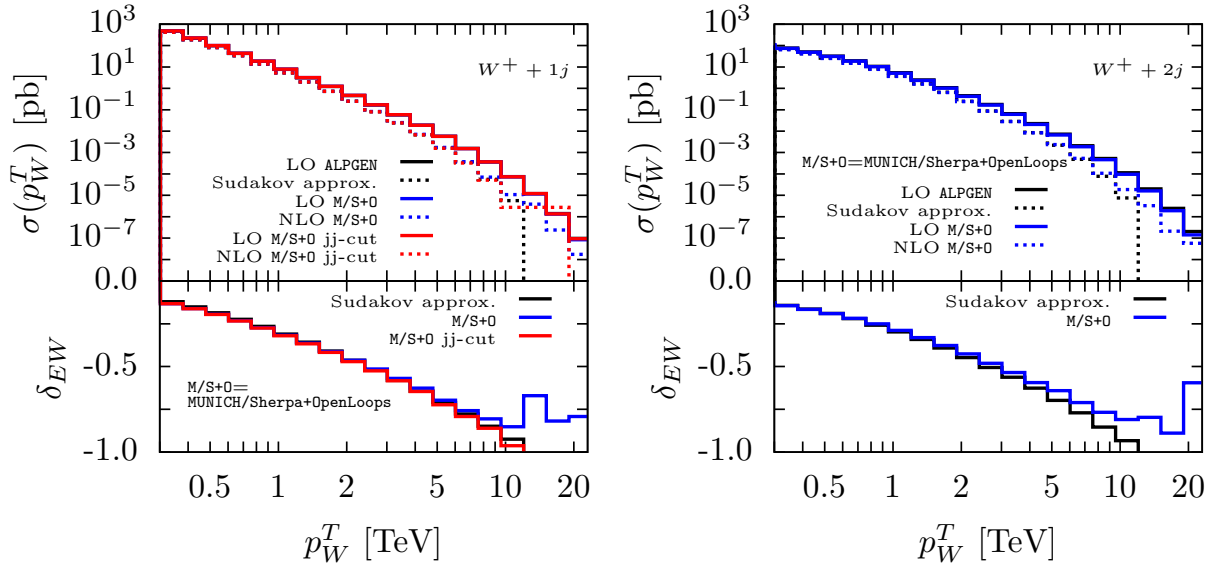


Fig. 186: Integrated  $p_{T W}$  distribution for  $W + 1$  jet (left panel) and  $W + 2$  jet (right panel) at the FCC at 100 TeV. Comparison between the the exact  $\mathcal{O}(\alpha)$  predictions (MUNICH/SHERPA+OPENLOOPS) and the ones computed in the Sudakov approximation (ALPGEN). For  $W + 1$  jets, the MUNICH/SHERPA+OPENLOOPS predictions are shown both with and without the veto on the dijet-like configurations.

Refs. [525, 529] the purely weak part of the corrections can be isolated by setting to  $M_W$  the value of the photon mass in the virtual corrections. In the following we consider only this part of the correction neglecting the QED part: this in particular means that no real radiation contribution is included in the approximated results. The results for the weak corrections in the Sudakov limit computed by means of the modified version of ALPGEN described above are compared to the exact  $\mathcal{O}(\alpha)$  predictions by MUNICH/SHERPA+OPENLOOPS in Figs. 186-187: as can be seen, the approximated results are in good agreement with the exact ones for  $W + 2$  jets and  $W + 1$  jet once the veto on the dijet-like configurations is imposed. The differences between the predictions by ALPGEN and the ones by MUNICH/SHERPA+OPENLOOPS for  $W + 1$  jet when the veto is not imposed come from the fact that the approximated results do not include real corrections and in particular no mixed interference terms: these terms could however be included as separate tree level-like contributions regardless of the Sudakov approximation. We point out, however, that in order to obtain more reliable predictions, especially at high jet  $p_T$ , it is important to include EW $\times$ QCD interference effects (which are neglected throughout in this section) and to merge NLO QCD+EW predictions with different jet multiplicities [615].

The Sudakov approximation and the exact  $\mathcal{O}(\alpha)$  calculation basically agree for  $W +$  jets. Having assessed the validity of the logarithmic approximation, in Figs. 188-190 we show the predictions for the NLO EW corrections in the Sudakov limit to the production of a vector boson  $V$  ( $Z$ ,  $W^+$ ,  $\gamma$ ) in association with 1, 2 and 3 jets. Looking at the  $p_{T V}$  distributions, we can notice that the corrections in the high energy limit are negative, large and independent of the jet multiplicity. Conversely, if we consider the  $p_{T j}$  and  $H_T$  distributions for  $Z/W + n$  jets, the corrections for  $n = 2$  and  $n = 3$  are similar, while the ones for  $n = 1$  turn out to be larger. This is a consequence of the event selection in eq. (97) where no cuts are imposed on the massive vector bosons: as a result, while for  $Z/W + 1$  jet the high  $p_{T j}$  or  $H_T$  region corresponds to the kinematical configurations where the vector boson is hard, this is no longer the case for high jet multiplicities. On the contrary, when the same cuts are imposed on both the vector boson and on the jets, as in the case of  $\gamma +$  jets production, the EW corrections are in general weakly dependent on the jet multiplicity for all the observables under consideration. At the FCC

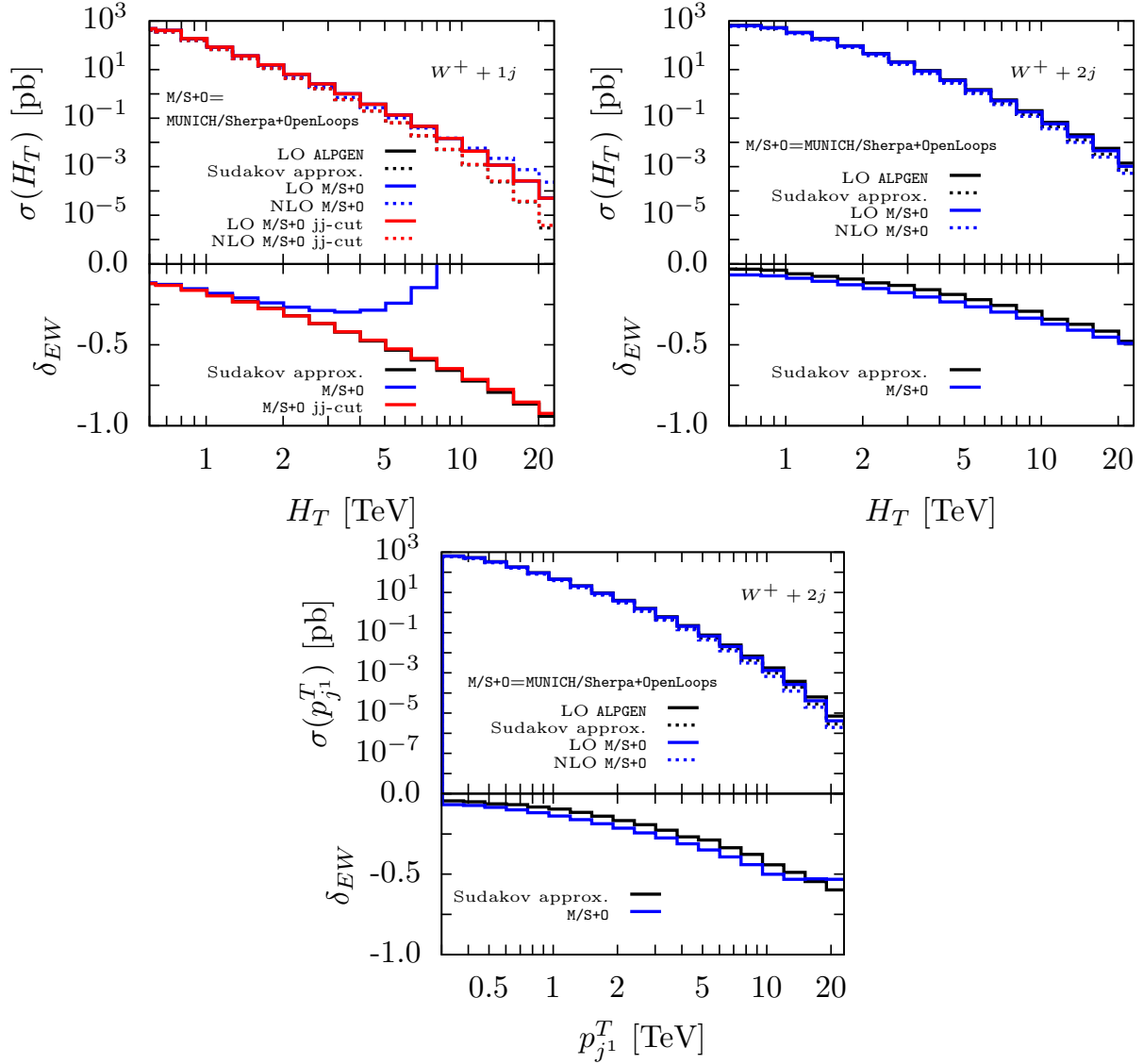


Fig. 187: Integrated  $H_T$  distribution for  $W + 1$  jet (left panel) and  $W + 2$  jet (right panel) at the FCC at 100 TeV. Comparison between the the exact  $\mathcal{O}(\alpha)$  predictions ( MUNICH/SHERPA+OPENLOOPS) and the ones computed in the Sudakov approximation (ALPGEN). For  $W + 1$  jets, the MUNICH/SHERPA+OPENLOOPS predictions are shown both with and without the veto on the dijet-like configurations. Lower plot: Comparison between the the exact  $\mathcal{O}(\alpha)$  predictions ( MUNICH/SHERPA+OPENLOOPS) and the ones computed in the Sudakov approximation (ALPGEN) for the leading jet  $p_T$  distribution.

the size of the NLO EW corrections to  $V +$  multijet production turns out to be large, reaching the order of  $-100\%$  for  $p_{TV}$  around 10 TeV (with the exception of  $p_{TV}$  which receives smaller corrections): this is an indication that the NLO approximation is not reliable anymore in these regions of phase space and higher order effects should be included in theoretical predictions. The EW corrections to the vector boson  $p_T$  distribution are shown in Fig. 191, once the leading logarithmic terms have been resummed in the framework of SCET [535, 620]: the resummed corrections are smaller than the ones computed at fixed order, even though they remain large, becoming of the order of  $-50\%$  for  $p_{TV} \simeq 20$  TeV.

We conclude this section studying the impact of the NLO EW corrections on the ratio of differen-

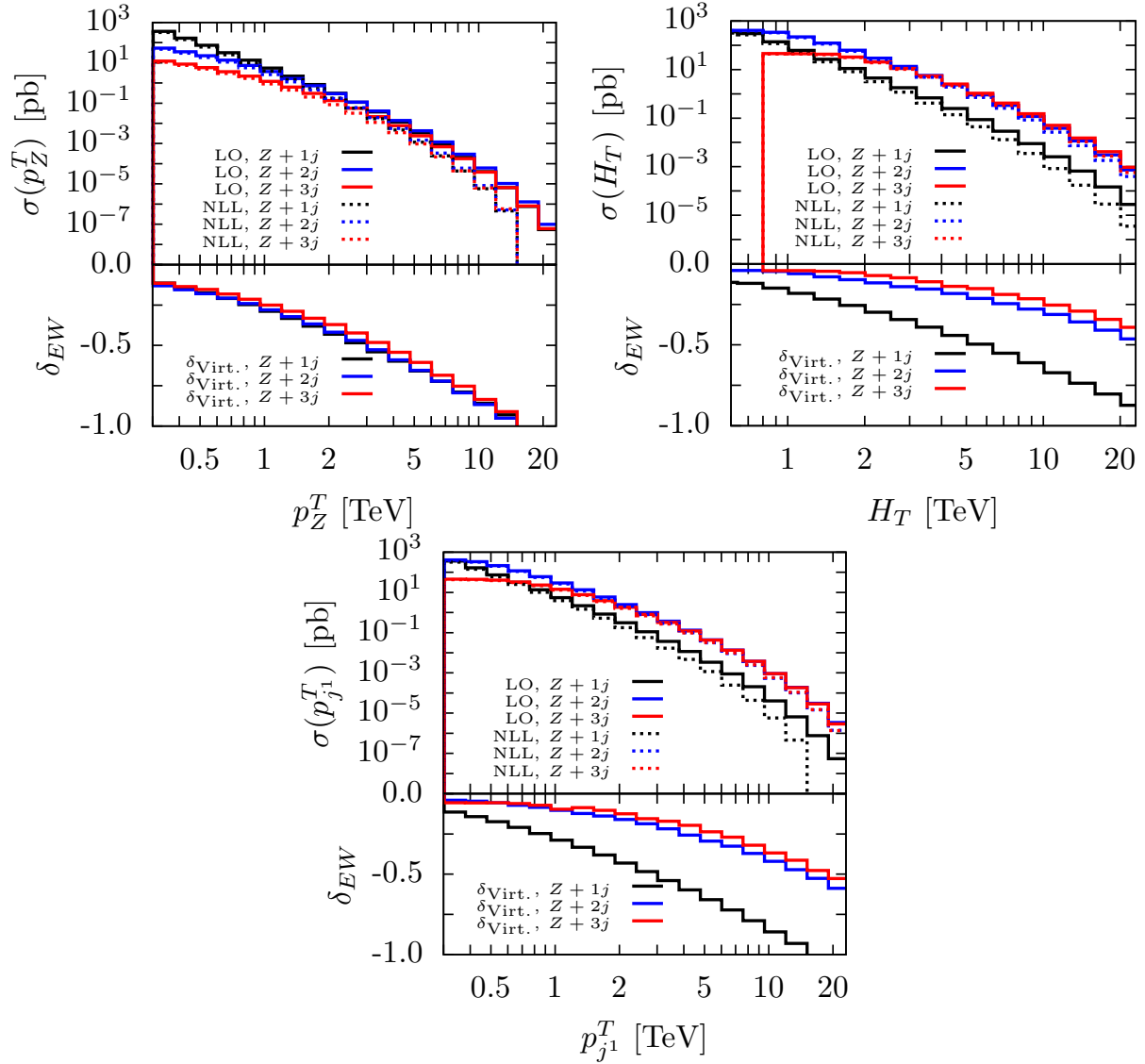


Fig. 188: Upper panels: integrated  $p_Z^T$  (upper left plot),  $H_T$  (upper right plot) and leading jet  $p_T$  (lower plot) distributions for the processes  $Z + 1, 2$  and  $3$  jets at LO and approximated NLO accuracy (solid and dashed lines, respectively) at the FCC at 100 TeV. Lower panels: relative corrections  $\delta_{EW}$ .

tial distributions for  $Z$ ,  $W$  and  $\gamma$  plus jets. More precisely, in Fig. 192 we consider the ratios:

$$R_\gamma^Z = \frac{d\sigma^Z}{dp_Z^T} / \frac{d\sigma^\gamma}{dp_\gamma^T} \quad \text{and} \quad R_Z^W = \frac{d\sigma^{W+}}{dp_W^T} / \frac{d\sigma^Z}{dp_Z^T}. \quad (103)$$

for the three different jet multiplicities. In Figs. 188-190 it is shown how the EW corrections for  $Z +$  multijets and  $W +$  multijets are similar, while the ones for  $\gamma +$  multijets are smaller. As a result, the  $R_Z^W$  ratio is basically unaffected by the EW corrections, while this is not the case for the  $R_\gamma^Z$  ratio, where the Sudakov corrections change significantly the shape of the  $R_\gamma^Z$  distribution. It is worth mentioning that a reliable prediction for  $R_\gamma^Z$  should also include NLO QCD corrections, as for small transverse momenta mass effects are not negligible.

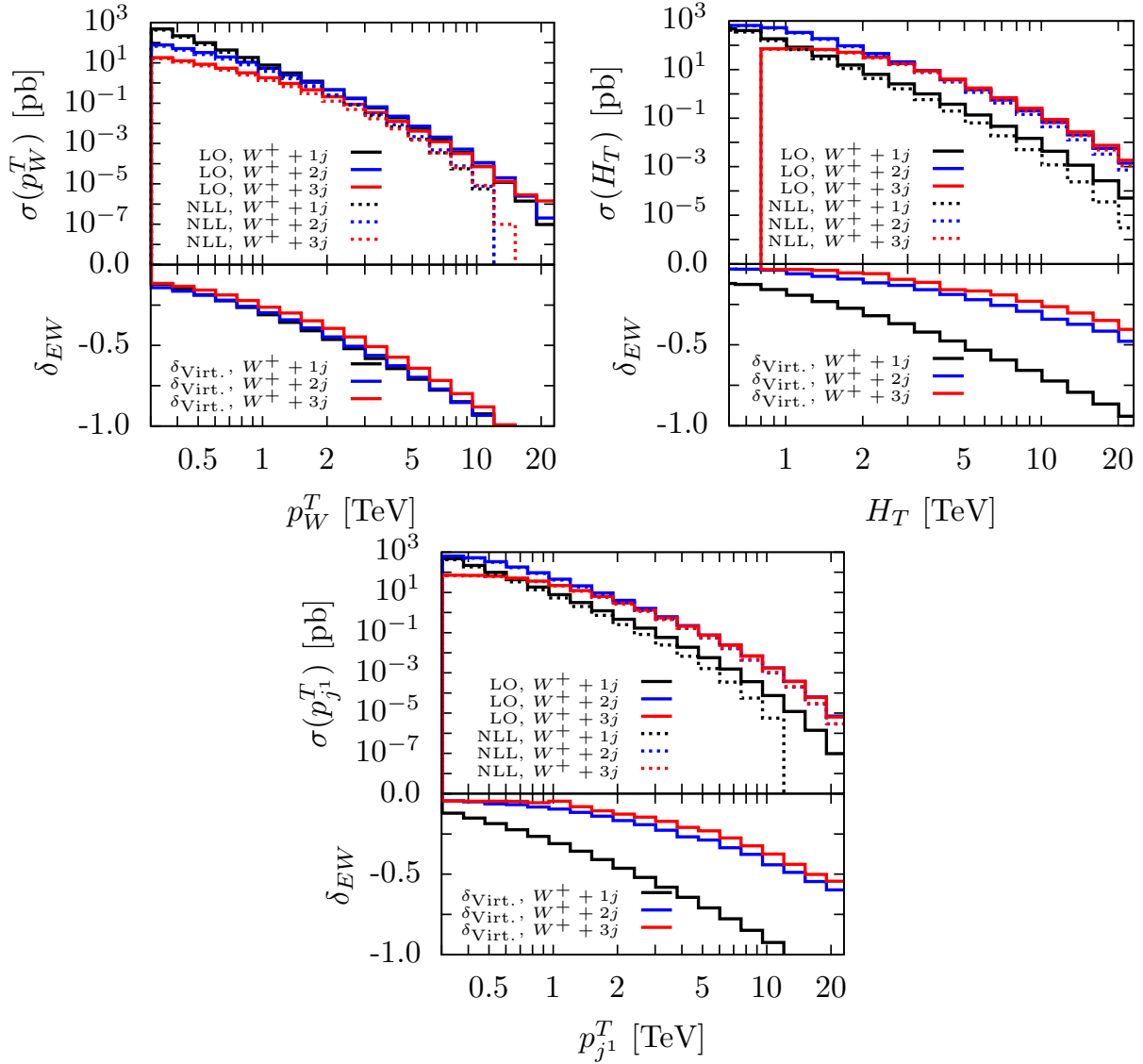


Fig. 189: Upper panels: integrated  $p_W^T$  (upper left plot),  $H_T$  (upper right plot) and leading jet  $p_T$  (lower plot) distributions for the processes  $W^+ + 1, 2$  and  $3$  jets at LO and approximated NLO accuracy (solid and dashed lines, respectively) at the FCC at 100 TeV. Lower panels: relative corrections  $\delta_{EW}$ .

### 16.5 Di-jets

The electroweak contributions to di-jet production can be safely classified according to the coupling constant power of  $\mathcal{O}(\alpha_s^2\alpha)$ . While the tree-level processes involving two or more gluons are of  $\mathcal{O}(\alpha_s^2)$ , the processes with four quarks can proceed through the exchange of electroweak gauge bosons. This implies that there are two classes of contributions at  $\mathcal{O}(\alpha_s^2\alpha)$ : the one-loop virtual EW NLO corrections on QCD tree-level processes of  $\mathcal{O}(\alpha_s^2)$  (involving tree-level diagrams with two as well as four quark legs) and the QCD NLO corrections to the interferences between  $\mathcal{O}(\alpha_s)$  tree-level diagrams with  $\mathcal{O}(\alpha)$  tree-level diagrams (the colour structure allows a non-zero contribution from this interference only between u- and t-channel diagrams). The former can be calculated in a gauge invariant way separating the genuine weak corrections (which involve  $W$  and  $Z$  exchanges in the loops and are the interesting contributions at high energies) from the photonic corrections. The complete calculation of the  $\mathcal{O}(\alpha_s^2\alpha)$  contributions, neglecting photonic corrections, have been presented in Ref. [208]. Previous results have been presented

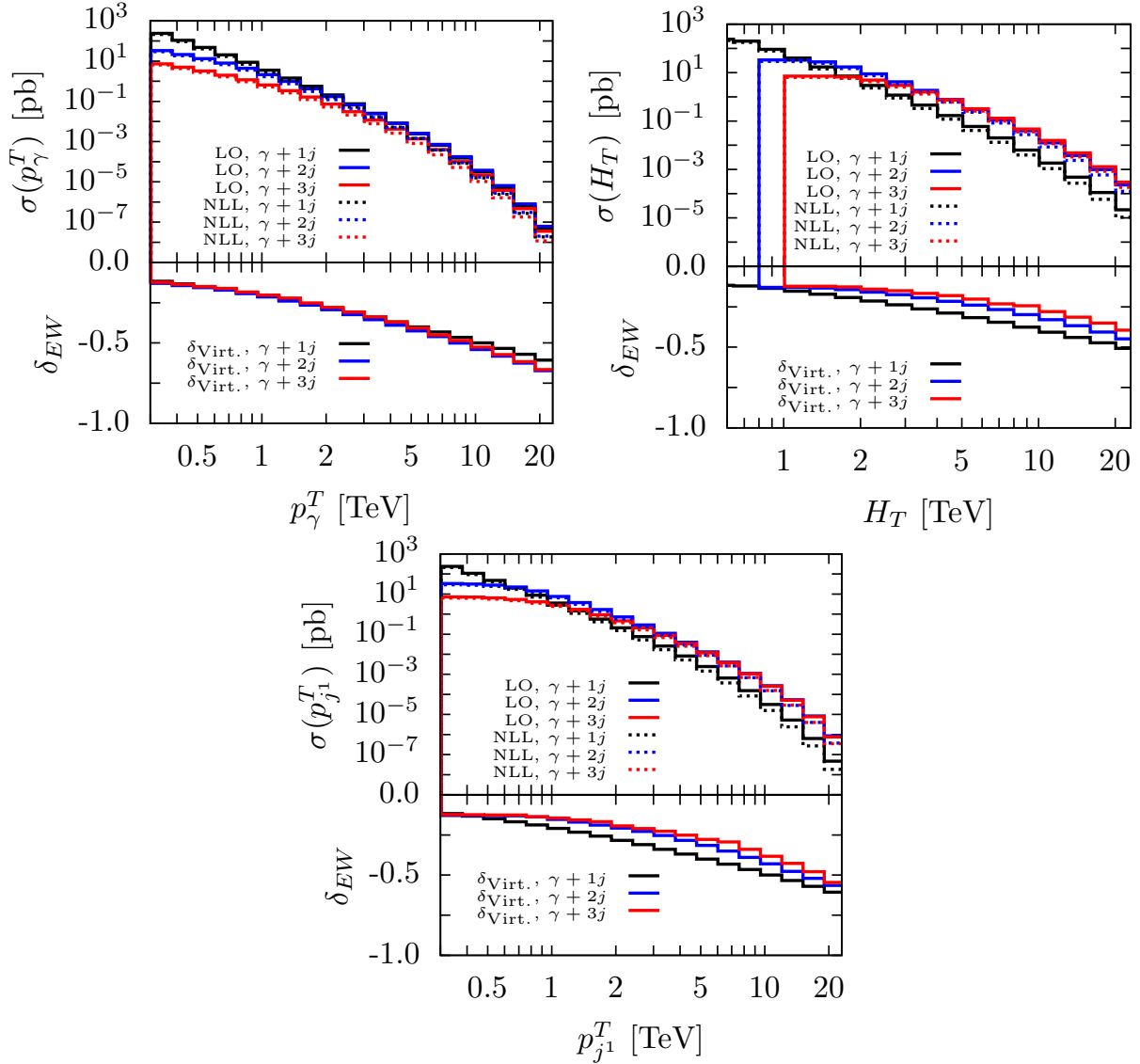


Fig. 190: Upper panels: integrated  $p_\gamma^T$  (upper left plot),  $H_T$  (upper right plot) and leading jet  $p_T$  (lower plot) distributions for the processes  $\gamma + 1, 2$  and  $3$  jets at LO and approximated NLO accuracy (solid and dashed lines, respectively) at the FCC at 100 TeV. Lower panels: relative corrections  $\delta_{EW}$ .

in Refs. [206, 595, 639, 640]. The investigation of the phenomenological impact of  $\mathcal{O}(\alpha_s^2\alpha)$  terms at the LHC and higher energy future colliders have been presented in Refs. [208, 634, 635, 641], for jet-jet invariant mass and jet transverse momentum distributions.

The  $\mathcal{O}(\alpha_s^2\alpha)$  interference terms are positive and tend to partially cancel the negative effect of the virtual corrections to the  $\mathcal{O}(\alpha_s^2)$  LO contribution. However, as can be seen from Figs. [1-3] of Ref. [634], the relevance of the tree-level interferences tends to decrease with the increase of the collider energy, being of the order of 1% for jet transverse momenta of 3 TeV. At variance with the interference terms, the virtual corrections to the  $\mathcal{O}(\alpha_s^2)$  LO contributions, instead, are negative and grow up in size at the level of 10%. It is worth remarking that the corrections on the di-jet invariant mass are smaller with respect to the jet transverse momenta, due to the fact that the requirement of large jet transverse momenta guarantees that all invariants are much larger than the weak vector boson masses (*i.e.* Sudakov logs are dominating), while the high invariant mass region is dominated by the forward region, where

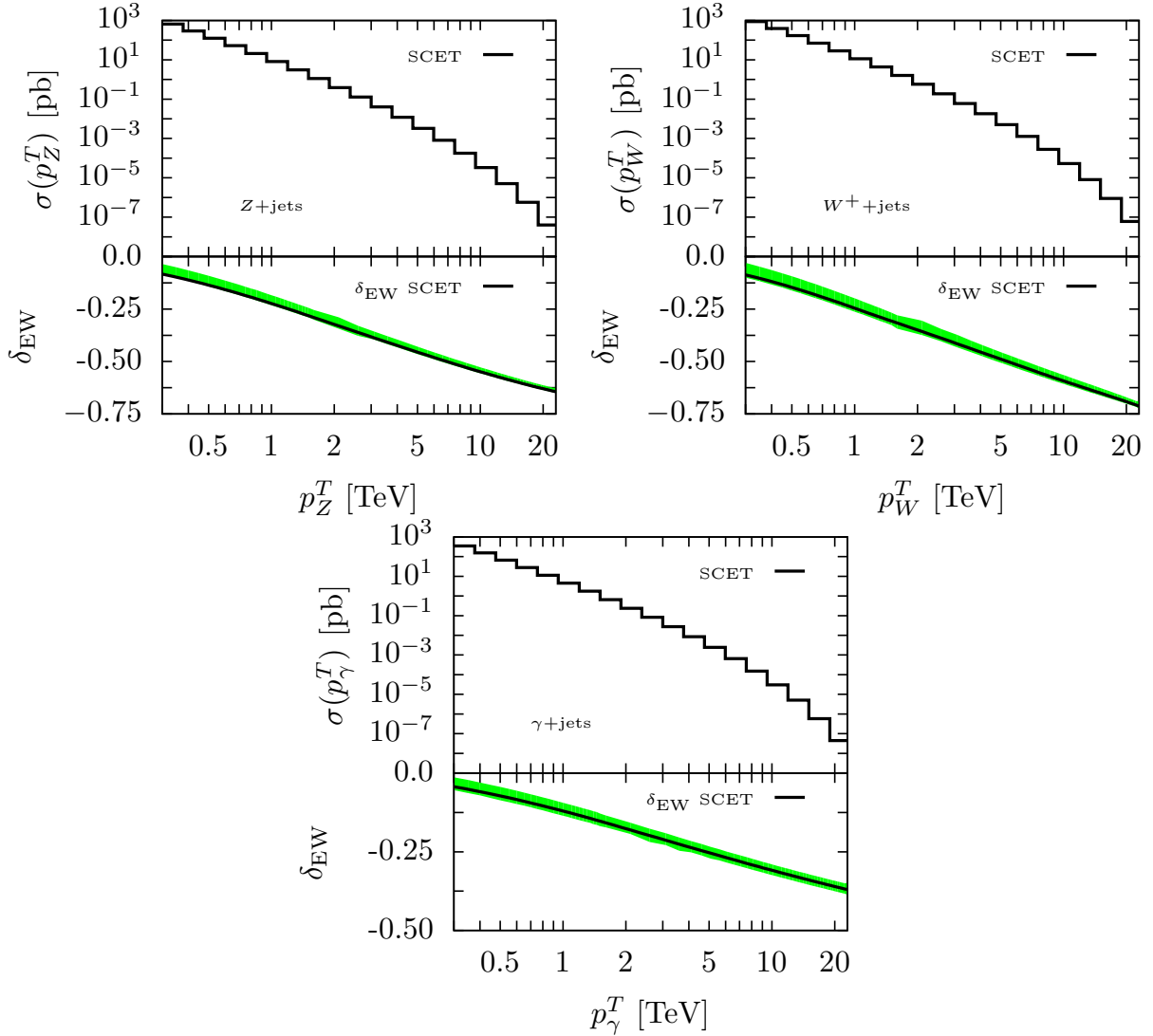


Fig. 191: Predictions within the SCET framework of resummed leading EW corrections to the integrated inclusive  $Z$  boson  $p_T$  (upper left plot),  $W$  boson  $p_T$  (upper right plot) and  $p_T^\gamma$  (lower plot) at the FCC at 100 TeV. The lower panels display the relative corrections  $\delta_{EW}$ . The bands have been obtained by varying the EW matching scale.

the  $t$  and  $u$  invariants remain small. This feature is not present for event selections with tight cuts on the jet transverse momenta. In this subsection we present results for di-jet invariant mass ( $m_{jj}$ ) and leading  $p_T$  jet distributions ( $p_T^{j1}$ ), integrated from the lower edge to the kinematical limit, as obtained with the modified version of ALPGEN v2.14 to include NLO EW corrections to pure QCD LO contributions with logarithmic accuracy [547], up to single logs. While the approximation is not expected to be fully reliable for the di-jet invariant mass distribution, as discussed above, it should give reliable predictions for  $p_T^{j1}$ , where the condition for the validity of the Sudakov approximation is fully satisfied. The numerical results have been obtained at parton level, with the following set of cuts:

$$p_T^j \geq 25 \text{ GeV}, \quad |\eta_j| \leq 2.5 \quad \Delta R_{jj} \geq 0.6. \quad (104)$$

The running parameters have been kept the default ones of ALPGEN v2.14, in particular the renormalization and factorization scales are  $\mu_F = \mu_R = \sqrt{(p_T^{j1})^2 + (p_T^{j2})^2}$ . As can be seen, the estimated

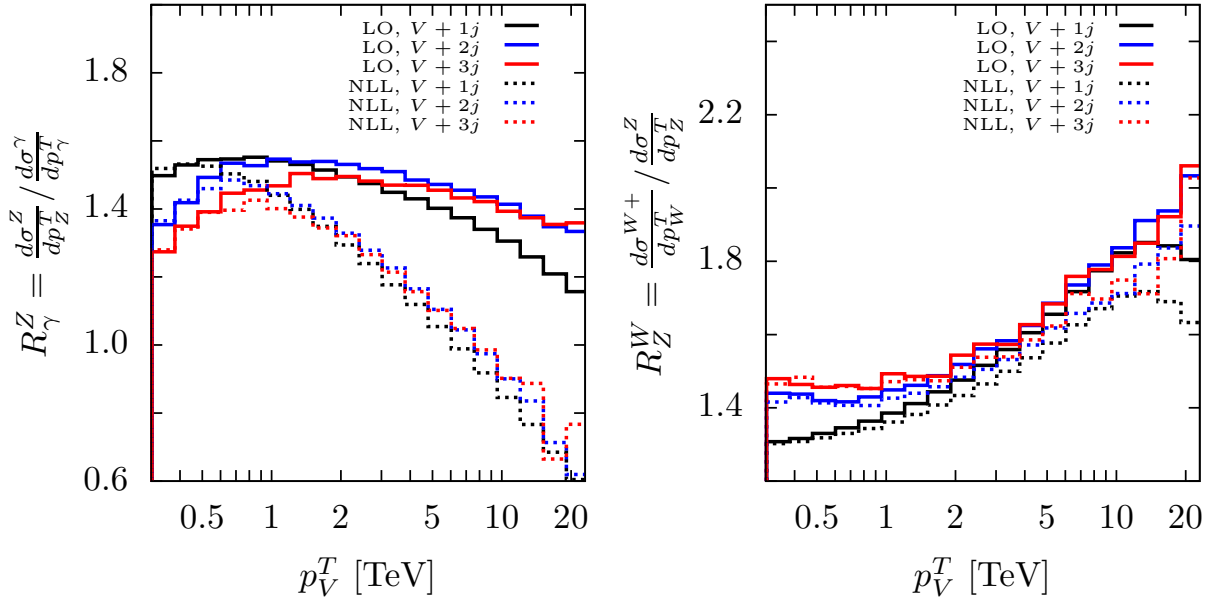


Fig. 192: Differential distributions of the ratios  $R_\gamma^Z$  (left plot) and  $R_Z^W$  (right plot) for  $V + 1, 2$  and  $3$  jets at the FCC at  $100$  TeV. Solid lines and dotted lines correspond to the LO and the approximated NLO predictions, respectively. The results for the  $R_\gamma^Z$  ratio have been obtained imposing the same cuts of Eq. (98) on both the photon and the  $Z$  boson.

corrections are moderate (at the level of about 10%), even at the multi-TeV scales accessible at the  $\sqrt{s} = 100$  TeV collider.

### 16.6 $t\bar{t}, t\bar{t} + \text{jets}$ and $t\bar{t}H$

In this subsection we present exact NLO results for the EW corrections to  $t\bar{t}$  pair production and NLO Weak corrections to  $t\bar{t}H$  production. Also, approximate results, using the logarithmic approximation, for  $t\bar{t} + n$  jets, with  $n = 0, 1, 2, 3$  are given. As for the case of dijet production, we have both  $\mathcal{O}(\alpha_s^2)$  as well as  $\mathcal{O}(\alpha_s\alpha)$  tree-level diagrams. The EW corrections (or some subset of them) have been calculated in the literature [588–594] and have been included recently in the Monte Carlo code [623].

The numerical results for  $t\bar{t}$  production at  $100$  TeV have been obtained by means of the automatic code MADGRAPH5\_AMC@NLO [64] and a currently private extension that allows to calculate NLO QCD and EW corrections [426,428]. In Fig. 194 we present the integrated distributions of the  $t\bar{t}$  invariant mass in the range [8-30] TeV (left panel) and of the top quark transverse momentum in the range [4-17] TeV (right panel). The format of the plots is the same of those in Fig. 180, which is described in the text. As can be seen in the lower panels, the effect of NLO EW radiative corrections is negative and moderate for the  $t\bar{t}$  invariant mass, ranging from  $\sim -10\%$  for  $M(t\bar{t}) > 10$  TeV to  $\sim -20\%$  for  $M(t\bar{t}) > 30$  TeV. QCD corrections are also presented and display a positive effect of the order of 60%, almost flat over the entire invariant mass range. The uncertainty estimate given by the scale variation is at the 10% level, dominating with respect to the PDF uncertainty.

A more pronounced effects of the EW corrections is present on the transverse momentum distribution, where it ranges from  $-30\%$  for  $p_T^{\min} = 4$  TeV to  $-50\%$  for  $p_T^{\min} = 17$  TeV. In the same interval the QCD corrections range from a factor of almost 2.5 over the LO predictions to about  $+50\%$ , giving rise to large cancellation between the two kinds of corrections in the very large tail of the distribution.

In these plots we did not include the effect from photon-initiated processes. However, at  $\mathcal{O}(\alpha_s\alpha)$  also the contribution from the  $\gamma g$  initial state is present [593]. We explicitly verified that, with

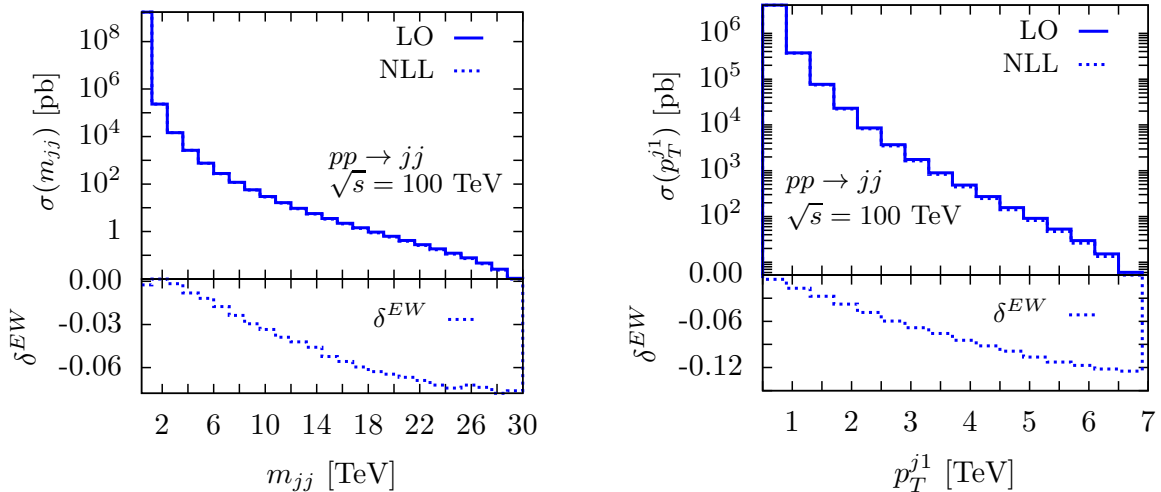


Fig. 193: Integrated invariant mass distribution (left panel) and Integrated leading jet  $p_T$  distribution for the process  $pp \rightarrow jj$  at  $\sqrt{s} = 100$  TeV. The lower panels give the relative effects of the EW corrections (calculated with leading logarithmic accuracy, as described in the text) with respect to the LO order predictions.

NNPDF2.3QED, this contribution would compensate the NLO EW corrections for  $M(t\bar{t}) > 20$  TeV and would relatively grow for even larger  $M(t\bar{t})$  values. However, the  $\gamma g$  initial-state has huge PDF uncertainties in this region ( $\sim 100\%$ ) and the growth is totally given by the PDF luminosity and not by matrix-element enhancements. In the case of cumulative top quark transverse momentum we observe a milder effect from the  $\gamma g$  initial state; it compensates the NLO EW corrections only at the end of the explored range. Additional plots, including effects due the photon PDF, can be found in ref. [642], where a detailed discussion on the compensation of EW Sudakov logarithms and photon-induced contributions is presented.

For the signature  $t\bar{t} + n$  jets (with  $n$  up to 3), the results have been obtained with the upgraded version of ALPGEN mentioned in Subsection 16.1 and briefly described in Subsection 16.4. Since the logarithmic approximation has been shown to largely overestimate the EW corrections for the  $t\bar{t}$  invariant mass [624], when no cut on the transverse momentum of the top quarks is imposed, we present only results for the inclusive transverse momentum of the top quarks (Fig. 195, left panel) and for the transverse momentum of the  $t\bar{t}$  pair (Fig. 195, right panel), in the range [0-6] TeV. The numerical results, obtained with ALPGEN, are based on the default parameters of the version v2.14 of the code, with a minimum transverse momentum threshold of 50 GeV both for top quarks and light partons. In addition, for the light partons a cut of 5 units in the maximum pseudorapidity is required, and a separation in  $\Delta R$  of 0.7. The factorization/renormalization scale is taken as  $\mu_F = \mu_R = \sqrt{E_{1T}^2 + E_{2T}^2 + \sum_i p_{iT}^2}$ , where  $E_{iT}^2$  is the transverse energy of the  $i$ -th top quark. By comparison of the black dotted line of the left-lower panel of Fig. 195 with the red line of the right-lower panel of Fig. 194, we can see a nice agreement between the logarithmic approximation and the exact NLO calculation for  $n_{jets} = 0$ . The effect of the EW corrections for higher parton multiplicities are slightly smaller. For the  $t\bar{t}$  pair transverse momentum the effect of the corrections is almost the same for all the studied multiplicities.

As a last comment, we observe that the EW corrections to  $t\bar{t}$  and  $t\bar{t} +$  jets are moderate even if larger than the ones for dijet production. This can be qualitatively understood because of the presence of processes involving only gluons and due to the average over flavours in dijet production with respect to  $t\bar{t}$ .

We also show NLO Weak differential corrections for the production of a top-quark pair in asso-

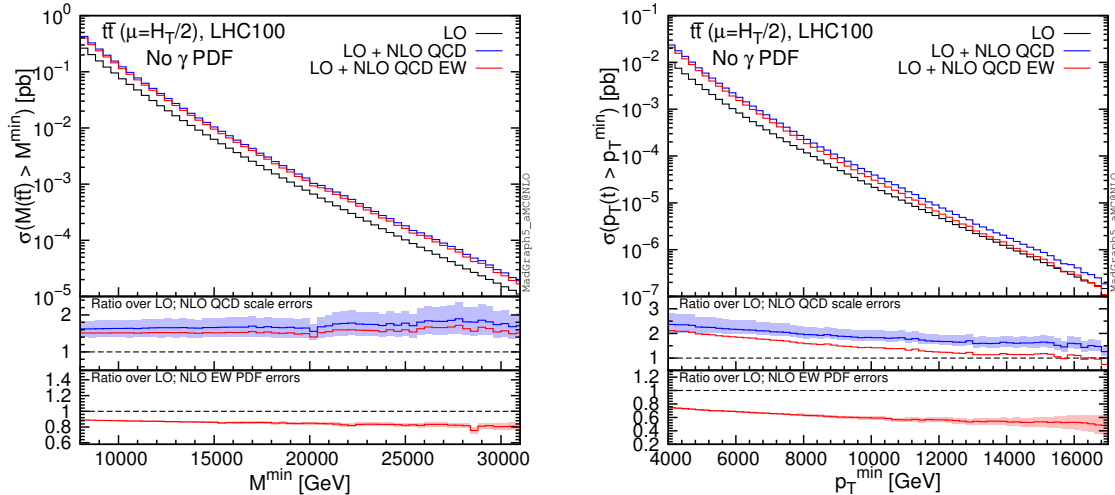


Fig. 194: Left: the cumulative distribution of the  $t\bar{t}$  invariant mass. Right: the cumulative distribution of the  $p_T(t)$ . as obtained with MADGRAPH5\_AMC@NLO. The blue lines display the effects of NLO QCD corrections, while the red lines correspond to the predictions with NLO EW corrections on top of NLO QCD accurate distributions. In the lower panels, which display the relative effects of the NLO QCD and EW corrections, also the effects of scale variations and PDF uncertainties are considered.

ciation with the Higgs boson ( $t\bar{t}H$ ). For this process, NLO Weak and QED corrections are separately gauge invariant and the former, which contain all the Sudakov logarithms, have been calculated in [426], from where plots in Fig. 196 have been directly taken. Results for NLO EW (Weak+QED) corrections at 100 TeV for  $t\bar{t}H$ ,  $t\bar{t}Z$  and  $t\bar{t}W^\pm$  total cross sections can be found in [428]. In the main panel of plots in Fig. 196 we show the NLO Weak contributions from each partonic subprocess and their sum (in black) and also the contribution from Heavy-Boson-Radiation (HBR), *i.e.*,  $t\bar{t}HV$  with  $V = H, W^\pm, Z$ . In the lower inset we display the ratios of the quantities in the main panel with the LO prediction, using the corresponding colors. The left and right plots show the  $p_T(H)$  and the  $m(t\bar{t}H)$  distributions, respectively. Weak corrections reach  $\sim -10\%$  level in the range explored and are almost completely given by the  $gg$  initial state, which is dominant due to the larger value of the gluon PDF. It is worth to note also that HBR contributions lead to a partial cancellation of the Sudakov logarithms from NLO Weak corrections.

### 16.7 Real radiation

As discussed in Section 16, the electroweak corrections grow with the center of mass energy  $Q = \sqrt{s}$  of the partonic collision, due to the appearance of two powers of  $L_V$  for each order in perturbation theory. Thus, as the center of mass energy grows, the convergence of electroweak perturbative theory gets worse, until it breaks down completely for

$$\alpha_{\text{ew}} L_V^2 \sim 1. \quad (105)$$

As one can see from the results in this chapter, perturbative electroweak corrections at the 100 TeV FCC become very large at high center of mass energies. A consistent resummation of these Sudakov logarithms improves the convergences of perturbation theory significantly, and becomes crucially important for measurements at the highest energies available.

As already mentioned in the introduction, Sudakov logarithms in exclusive cross-sections (without extra radiation of additional electroweak gauge bosons) have been resummed for many processes. A general formalism based on soft-collinear effective theory [559–562] was developed to perform this resummation at NLL (and in principle to higher accuracy as well). However, for the energies that can be

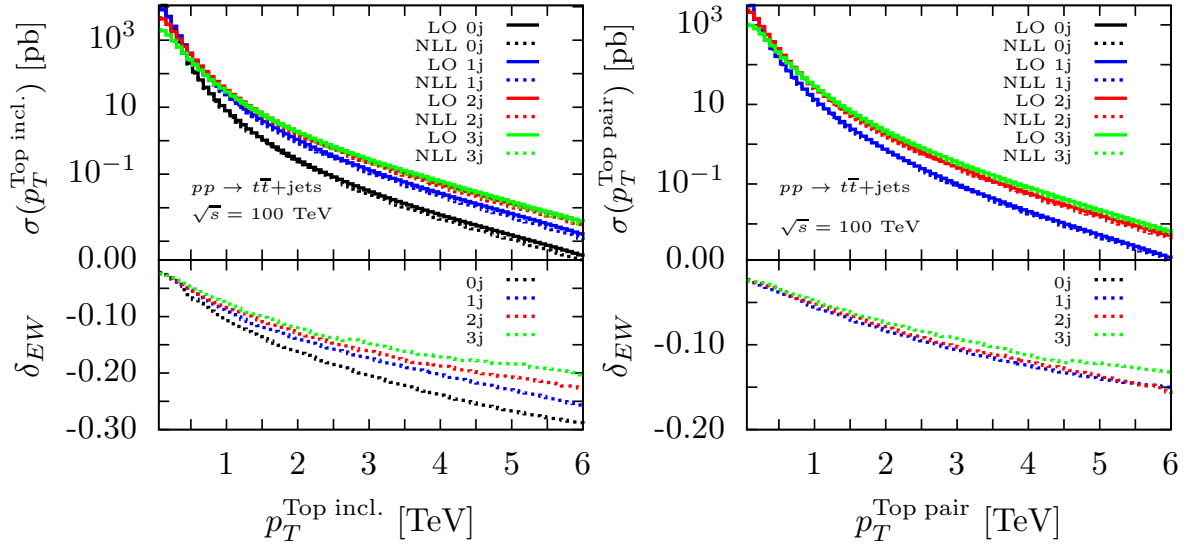


Fig. 195: Left: the distribution of the inclusive top quark transverse momentum for the final states  $t\bar{t} + n$  jets, with  $n = 0, 1, 2, 3$ . Right: the distribution of the  $t\bar{t}$  pair transverse momentum for the final states  $t\bar{t} + n$  jets, with  $n = 0, 1, 2, 3$ . The lower panels give the relative effects of the EW corrections (calculated with leading logarithmic accuracy, as described in the text) with respect to the LO order predictions.

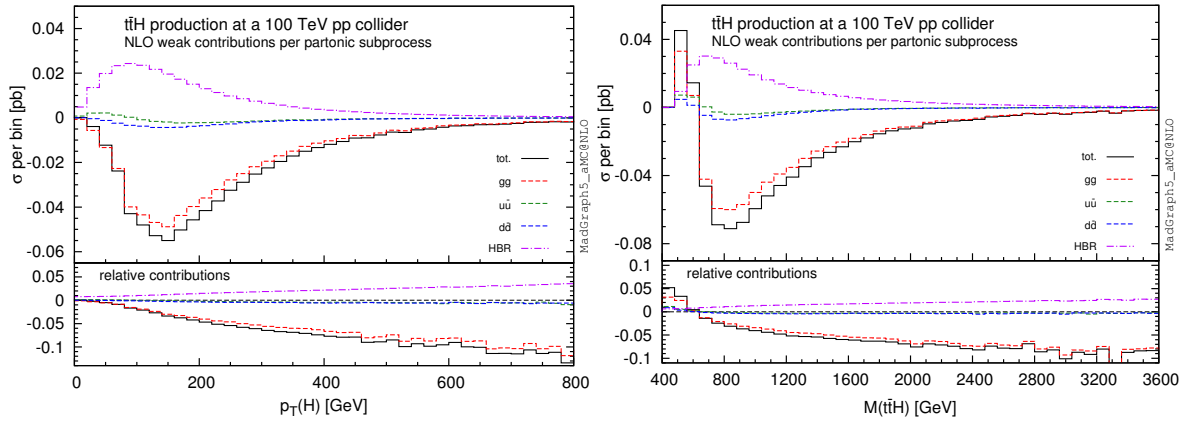


Fig. 196: NLO Weak corrections for the distribution of the  $p_T(H)$  (left) and of the  $m(t\bar{t}H)$  (right). Plots are taken from [426] and explained in the text.

reached at the FCC, it is only the leading logarithms that need to be resummed; the subleading logarithms can still be treated in fixed order perturbation theory until the partonic center of mass energy becomes large enough such that  $\alpha_{\text{ew}} L_V \sim 1$ .

To LL accuracy, the resummation of the double logarithms can be obtained using the coherent branching formalism [101, 643, 644] that underlies parton shower algorithms, used extensively to describe the emissions of extra particles in the strong interaction. In this approach [515, 544] one uses the fact that, to LL accuracy, the cross-sections factorize into products of emission probabilities. These emission probabilities are given by the Altarelli-Parisi splitting functions, supplemented by a so-called no-branching probability, given by an integral over the Altarelli-Parisi splitting functions.

This approach reproduces the known resummation of the exclusive results, but can also be used to

obtain resummed results for the real radiation of  $W$  and  $Z$  bosons. In the remainder of this section, we will provide the results for the production of lepton pairs at the FCC, but the method can be applied to any other process as well. The results given below are taken from [544], where details on their derivation can be found.

The partonic cross-sections for the exclusive cross section  $q_1 \bar{q}_2 \rightarrow \ell_1 \ell_2$  at partonic center of mass energy  $s = Q^2 = x_a x_b S$ , where  $\ell_i$  denotes either a charged lepton or a neutrino, are given by

$$\hat{\sigma}_{q_1^H q_2^H \rightarrow \ell_1^H \ell_2^H}^{\text{LL}}(s) = \hat{\sigma}_{q_1^H q_2^H \rightarrow \ell_1^H \ell_2^H}^B \Delta_{q_1^H q_2^H \ell_1^H \ell_2^H}(m_V^2, s; s) \Delta_{q_1^H q_2^H \ell_1^H \ell_2^H}^{\text{em}}(\Lambda^2, m_V^2; s). \quad (106)$$

where the superscript  $H$  denotes the helicity of the fermions. The Born cross-sections are given by

$$\begin{aligned} \hat{\sigma}_{q^{Hq} q^{Hq} \rightarrow \ell^{H\ell} \ell^{H\ell}}^B &= \frac{\pi}{8 N_C s} \frac{8 \left( \alpha_2 T_{q^{Hq}}^3 T_{\ell^{H\ell}}^3 + \alpha_1 Y_{q^{Hq}} Y_{\ell^{H\ell}} \right)^2}{3} \\ \hat{\sigma}_{q_1^L q_2^L \rightarrow \ell_1^L \ell_2^L}^B &= \frac{\pi}{8 N_C s} \frac{2\alpha_2^2}{3}, \end{aligned} \quad (107)$$

where  $T_{fH}^3$  denotes the weak isospin of the fermion  $f = q/\ell$  with helicity  $H$ ,  $Y_{fH}$  its weak hypercharge with normalization  $Y_i = Q_i - T_i^3$ , and  $\alpha_2$  and  $\alpha_1$  are the couplings of the SU(2) and U(1)<sub>Y</sub> gauge group, respectively.

The Sudakov factor  $\Delta_{q_1^H q_2^H \ell_1^H \ell_2^H}(m_V^2, s; s)$  describes the evolution from  $s$  to  $m_V^2$  and factors into two pieces, one for the SU(2) and one for the U(1) symmetry

$$\Delta_{q_1^H q_2^H \ell_1^H \ell_2^H}(m_V^2, s; s) = \Delta_{q_1^H q_2^H \ell_1^H \ell_2^H}^{\text{SU}(2)}(m_V^2, s; s) \Delta_{q_1^H q_2^H \ell_1^H \ell_2^H}^{\text{U}(1)}(m_V^2, s; s). \quad (108)$$

The SU(2) and U(1) contributions are given by

$$\begin{aligned} \Delta_{q_1^H q_2^H \ell_1^H \ell_2^H}^{\text{SU}(2)}(m_V^2, s; s) &= \exp \left[ -\frac{A_{q_1^H q_2^H \ell_1^H \ell_2^H}^{\text{SU}(2)}}{2} \ln^2 \frac{m_V^2}{s} \right] \\ \Delta_{q_1^H q_2^H \ell_1^H \ell_2^H}^{\text{U}(1)}(m_V^2, s; s) &= \exp \left[ -\frac{A_{q_1^H q_2^H \ell_1^H \ell_2^H}^{\text{U}(1)}}{2} \ln^2 \frac{m_V^2}{s} \right], \end{aligned} \quad (109)$$

with

$$A_{q_1^H q_2^H \ell_1^H \ell_2^H}^{\text{SU}(2)} = \frac{\alpha_2}{2\pi} \sum_i T_i^2, \quad A_{q_1^H q_2^H \ell_1^H \ell_2^H}^{\text{U}(1)} = \frac{\alpha_1}{2\pi} \sum_i Y_i^2, \quad (110)$$

and the sum is running over all fermions  $i \in \{q_1^H, q_2^H, \ell_1^H, \ell_2^H\}$ . For scales below  $m_V$  only photons can be exchanged, and the resulting Sudakov factor

$$\Delta_{q_1^H q_2^H \ell_1^H \ell_2^H}^{\text{em}}(\Lambda^2, m_V^2; s) = \exp \left[ -\frac{\alpha(Q) Q_{\text{tot}}^2}{4\pi} \left( \ln^2 \frac{\Lambda^2}{s} - \ln^2 \frac{m_V^2}{s} \right) \right], \quad (111)$$

only depends on the electromagnetic charges of the fermions

$$Q_{\text{tot}}^2 = \sum_i Q_i^2. \quad (112)$$

This agrees with the results of [515], and summing over all possible helicity structures, one reproduce the resummed results of [533–535].

Using the same coherent branching formalism, one can calculate the partonic real radiation cross section  $q_i q_j \rightarrow \ell \ell V$ , where, as before,  $\ell$  denotes either a charged lepton or a neutrino,  $V$  denotes either

a  $Z$  or a  $W$  boson. Following the results of [544] one obtains for the exclusive emission of a  $W^\pm$  boson (exclusive here means that emissions of additional gauge bosons are vetoed)

$$\begin{aligned}
 & \hat{\sigma}_{q_1^H q_2^H \rightarrow \ell_1^H \ell_2^H + W^\pm}^{\text{LL}} \\
 &= \left[ \Delta_{q_1^H q_2^H \ell_1^H \ell_2^H}(m_V^2, s; s) \Delta_{q_1^H q_2^H \ell_1^H \ell_2^H W^\pm}^{\text{em}}(\Lambda^2, m_V^2; s) \int_{m_V^2}^s \frac{dk_T^2}{k_T^2} \ln \frac{s}{k_T^2} \Delta_V(m_V^2, k_T^2; k_T^2) \right] \\
 & \quad \times \left( \hat{\sigma}_{q_1^H q_2^H \rightarrow \ell_1^H \ell_2^H}^B A_{q_1^H}^{W^\pm} + \hat{\sigma}_{q_1^H q_2^H \rightarrow \ell_1^H \ell_2^H}^B A_{q_2^H}^{W^\pm} + \hat{\sigma}_{q_1^H q_2^H \rightarrow \ell_1^H \ell_2^H}^B A_{\ell_1^H}^{W^\pm} + \hat{\sigma}_{q_1^H q_2^H \rightarrow \ell_1^H \ell_2^H}^B A_{\ell_2^H}^{W^\pm} \right) \\
 &= \left[ \Delta_{q_1^H q_2^H \ell_1^H \ell_2^H}(m_V^2, s; s) \Delta_{q_1^H q_2^H \ell_1^H \ell_2^H W^\pm}^{\text{em}}(\Lambda^2, m_V^2; s) I_1(m_V^2, s) \right] \\
 & \quad \times \left( \hat{\sigma}_{q_1^H q_2^H \rightarrow \ell_1^H \ell_2^H}^B A_{q_1^H}^{W^\pm} + \hat{\sigma}_{q_1^H q_2^H \rightarrow \ell_1^H \ell_2^H}^B A_{q_2^H}^{W^\pm} + \hat{\sigma}_{q_1^H q_2^H \rightarrow \ell_1^H \ell_2^H}^B A_{\ell_1^H}^{W^\pm} + \hat{\sigma}_{q_1^H q_2^H \rightarrow \ell_1^H \ell_2^H}^B A_{\ell_2^H}^{W^\pm} \right), \tag{113}
 \end{aligned}$$

where  $f'$  is the fermion  $f$  becomes after having radiated a  $W^\pm$  that is  $u' = d$ ,  $d' = u$ ,  $l' = \nu$  and  $\nu' = l$  and for any flavor set which allows a  $W^\pm$  emission there is one of the Born cross sections which is zero because its electromagnetic charge is not conserved. The Sudakov factor

$$\Delta_V(m_V^2, k_T^2; k_T^2) = \exp \left[ -\frac{\alpha_2 C_A}{4\pi} \ln^2 \frac{m_V^2}{k_T^2} \right] \tag{114}$$

is written in term of the Casimir  $C_A = 2$  for the SU(2) gauge group and describes the no-branching probability of the extra  $W$  boson radiated. We have also defined  $\Lambda$  to be the scale below which a photon becomes unresolved, as well as

$$A_{fL}^{W^\pm} = \frac{\alpha_2(Q)}{4\pi}, \quad A_{fR}^{W^\pm} = 0. \tag{115}$$

The integral over  $k_T^2$  has been performed using the general result

$$\begin{aligned}
 I_\beta(m_V^2, s) &\equiv \int_{m_V^2}^s \frac{dk_T^2}{k_T^2} \ln \frac{s}{k_T^2} [\Delta_V(m_V^2, k_T^2; k_T^2)]^\beta \\
 &= \frac{2\pi}{\alpha_2 \beta C_A} \left[ \frac{\sqrt{\alpha_2 \beta C_A}}{2} \ln \frac{m_V^2}{s} \text{Erf} \left( \sqrt{\frac{\alpha_2 \beta C_A}{4\pi}} \ln \frac{m_V^2}{s} \right) + \Delta_V^\beta(m_V^2, s; s) - 1 \right]. \tag{116}
 \end{aligned}$$

For the emissions of a  $Z$  bosons and photon, one needs to take into account the mixing between the third component of SU(2) gauge symmetry and the U(1) gauge symmetry. After a few lines of algebra (see [544]) one finds for the emission of a  $Z$  boson

$$\begin{aligned}
 \hat{\sigma}_{q_1^H q_2^H \rightarrow \ell_1^H \ell_2^H + Z}^{\text{LL}} &= \hat{\sigma}_{q_1^H q_2^H \rightarrow \ell_1^H \ell_2^H}^B \Delta_{q_1^H q_2^H \ell_1^H \ell_2^H}(m_V^2, s; s) \Delta_{q_1^H q_2^H \ell_1^H \ell_2^H}^{\text{em}}(\Lambda^2, m_V^2; s) \\
 & \quad \times \int_{m_V^2}^s \frac{dk_T^2}{k_T^2} \ln \frac{s}{k_T^2} \left( s_W^2 A_{q_1^H q_2^H \ell_1^H \ell_2^H}^{\text{U}(1)} - A_{q_1^H q_2^H \ell_1^H \ell_2^H}^{\text{mixing}} \sqrt{\Delta_W(m_V^2, k_T^2; k_T^2)} \right. \\
 & \quad \left. + c_W^2 A_{q_1^H q_2^H \ell_1^H \ell_2^H}^{\text{SU}(2)} \Delta_W(m_V^2, k_T^2; k_T^2) \right) \\
 &= \hat{\sigma}_{q_1^H q_2^H \rightarrow \ell_1^H \ell_2^H}^B \Delta_{q_1^H q_2^H \ell_1^H \ell_2^H}(m_V^2, s; s) \Delta_{q_1^H q_2^H \ell_1^H \ell_2^H}^{\text{em}}(\Lambda^2, m_V^2; s) \\
 & \quad \left( s_W^2 A_{q_1^H q_2^H \ell_1^H \ell_2^H}^{\text{U}(1)} \frac{1}{2} \ln^2 \frac{m_V^2}{s} - A_{q_1^H q_2^H \ell_1^H \ell_2^H}^{\text{mixing}} I_{\frac{1}{2}}(m_V^2, s) \right. \\
 & \quad \left. + c_W^2 A_{q_1^H q_2^H \ell_1^H \ell_2^H}^{\text{SU}(2)} I_1(m_V^2, s) \right). \tag{117}
 \end{aligned}$$

The factors  $A^{\text{SU}(2)}$  and  $A^{\text{U}(1)}$  are given in Eq. (110), and the term arising from the mixing of the  $W^3$  and  $B$  is given by

$$A_{q_1^H q_2^H \ell_1^H \ell_2^H}^{\text{mixing}} = \frac{\alpha_{\text{em}}}{\pi} \sum_i T_i^3 Y_i. \quad (118)$$

The emission of a photon is obtained in a similar manner, but one has to include the extra emissions that can happen for scales  $\Lambda < \mu < m_V$ . This gives

$$\begin{aligned} \hat{\sigma}_{q_1^H q_2^H \rightarrow \ell_1^H \ell_2^H + \gamma}^{\text{LL}} &= \hat{\sigma}_{q_1^H q_2^H \rightarrow \ell_1^H \ell_2^H}^B \Delta_{q_1^H q_2^H \ell_1^H \ell_2^H}(m_V^2, s; s) \\ &\times \left[ \Delta_{q_1^H q_2^H \ell_1^H \ell_2^H}^{\text{em}}(\Lambda^2, m_V^2; s) \left( c_W^2 A_{q_1^H q_2^H \ell_1^H \ell_2^H}^{\text{U}(1)} \frac{1}{2} \log^2\left(\frac{m_V^2}{s}\right) \right. \right. \\ &\quad \left. \left. + A_{q_1^H q_2^H \ell_1^H \ell_2^H}^{\text{mixing}} I_{\frac{1}{2}}(m_V^2, s) + s_W^2 A_{q_1^H q_2^H \ell_1^H \ell_2^H}^{\text{SU}(2)} I_1(m_V^2, s) \right) + \right. \\ &\quad \left. \int_{\Lambda^2}^{m_V^2} dk_T^2 \frac{d}{dk_T^2} \left[ \Delta_{q_1^H q_2^H \ell_1^H \ell_2^H}^{\text{em}}(k_T^2, m_V^2; s) \right] \Delta_{q_1^H q_2^H \ell_1^H \ell_2^H}^{\text{em}}(\Lambda^2, k_T^2; s) \right] \\ &= \hat{\sigma}_{q_1^H q_2^H \rightarrow \ell_1^H \ell_2^H}^B \Delta_{q_1^H q_2^H \ell_1^H \ell_2^H}(m_V^2, s; s) \Delta_{q_1^H q_2^H \ell_1^H \ell_2^H}^{\text{em}}(\Lambda^2, m_V^2; s) \\ &\times \left[ c_W^2 A_{q_1^H q_2^H \ell_1^H \ell_2^H}^{\text{U}(1)} \frac{1}{2} \log^2\left(\frac{m_V^2}{s}\right) + A_{q_1^H q_2^H \ell_1^H \ell_2^H}^{\text{mixing}} I_{\frac{1}{2}}(m_V^2, s) + \right. \\ &\quad \left. s_W^2 A_{q_1^H q_2^H \ell_1^H \ell_2^H}^{\text{SU}(2)} I_1(m_V^2, s) + \frac{\alpha Q_{\text{tot}}^2}{4\pi} \left( \ln^2 \frac{\Lambda^2}{s} - \ln^2 \frac{m_V^2}{s} \right) \right]. \quad (119) \end{aligned}$$

In Fig. 197 we show the resulting cross-sections as function of the center of mass energy of the system [ $s = (p_{\ell_1} + p_{\ell_2} + p_V)^2$ ]. In the top plot we show the size of the perturbative corrections relative to the Born cross-section, where the virtual corrections are in black, while the real radiation of a  $Z$ ,  $\gamma$ ,  $W^+$  and  $W^-$  are shown in green, orange, red and blue, respectively. The fixed order results (only including the double logarithmic term) are shown by the dashed lines, while the resummed results by the solid lines. One can clearly see that the size of the perturbative corrections grows as the center of mass energy is raised, and that the resummation decreases the overall size. To illustrate the importance of resummation, we show in the lower plot the difference between the fixed order and resummed result, normalized to the resummed. One can clearly see that the effect of resummation is very important for large center of mass energies, and that the resummation of the real corrections is even more important than the resummation of the virtual corrections.

The results of this section have shown that resummation of electroweak Sudakov logarithms becomes crucial for center of mass energies in the multi-TeV range, which are easily reached at the FCC. This is true not only for exclusive cross-sections where extra radiation is vetoed, but also for the radiation of additional massive gauge bosons. Including these effects in theoretical calculations will be crucial, not only for precision studies.

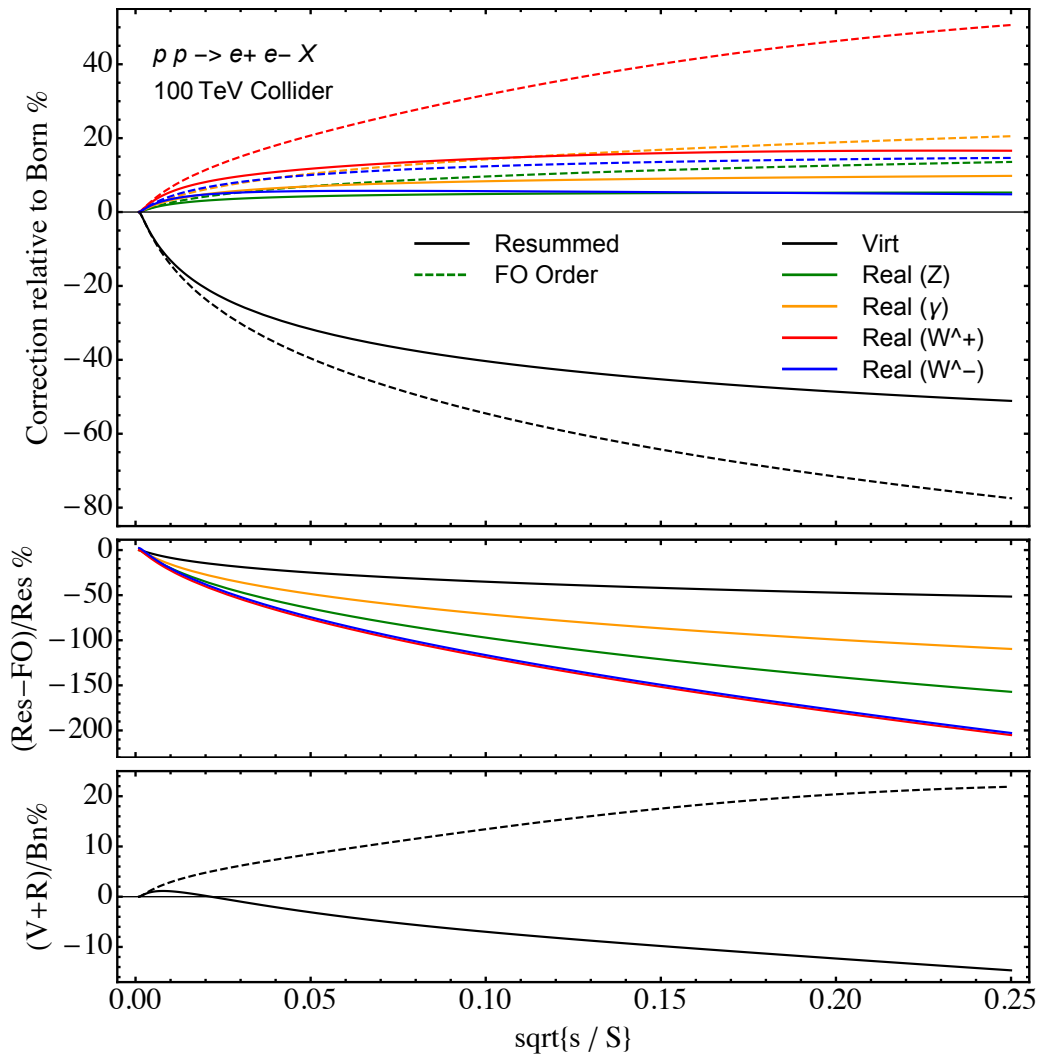


Fig. 197: The cross-section for  $pp \rightarrow e^+e^- + X$ . Virtual corrections are shown in black, while real corrections are shown in green, orange, red and blue for  $Z$ ,  $\gamma$ ,  $W^+$  and  $W^-$  emissions, . Resummed corrections are shown in solid lines, while fixed order results are dashed.

## 17 Sources of missing transverse energy

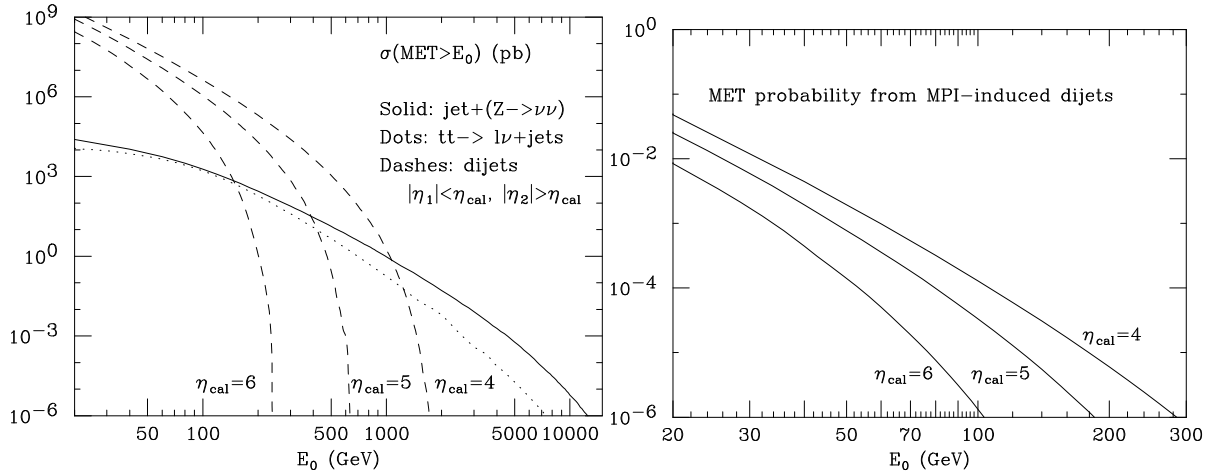


Fig. 198: Left: Missing transverse energy rates, from  $\text{jet}+(Z \rightarrow \nu\bar{\nu})$  events and from dijets, with a jet escaping undetected at large rapidity. Right: Missing transverse energy probability induced by multiparton interactions, for different values of the jet rapidity acceptance.

Missing transverse energy ( $\cancel{E}_T$ ) is an important signature for many BSM processes. At 100 TeV, SM sources of  $\cancel{E}_T$  can contribute with very large rates of irreducible backgrounds. We consider here, for illustration, the effect of three of the leading sources of irreducible  $\cancel{E}_T$ : the associated production of jets and a  $Z^0$  boson decaying to neutrinos, the semileptonic decay of top quarks, and the production of jets outside the calorimeter acceptance. The latter channel is important, since the high energy available in the CM allows for the production of large  $p_T$  jets at very forward rapidities. This is shown in Fig. 198, where the dashed lines correspond to the rate of dijet events in which one jet is within the calorimeter acceptance (defined by the  $\eta_{cal}$  label), and the other is outside. With the standard LHC calorimeter coverage,  $\eta_{cal} = 5$ , dijets would give a  $\cancel{E}_T$  signal larger than  $Z$ +jets for  $\cancel{E}_T$  up to  $\sim 400$  GeV. This is reduced to  $\sim 150$  GeV with a calorimeter extending out to  $\eta_{cal} = 6$ .

It must be noticed that the limited calorimeter acceptance can induce a  $\cancel{E}_T$  signal in any hard process, due to the finite probability of the coincidence of a multiparton interaction. Multiparton interactions are hard scatterings taking place among the partons not engaged in the primary hard process, and cannot be separated experimentally since the resulting particles emerge from exactly the same vertex as the primary scattering. The probability that a multiparton interaction leads to a secondary hard process  $X$  in addition to the primary one is parametrized as  $\sigma(X)/\sigma_0$ , where  $\sigma_0$  is a process-independent parameter. The right plot of Fig. 198 shows the probability of multiparton interactions leading to dijet final states, with one jet inside the calorimeter and the other outside. For this example we chose  $\sigma_0 = 30$  mb, a number consistent with the direct experimental determinations from Tevatron and LHC data.  $\cancel{E}_T$  signals in the range of 30-70 GeV are induced with probability of about  $10^{-3}$  if  $\eta_{cal}$  is in the range 4 to 6, stressing once again the need to instrument the detectors with a calorimetric coverage more extended than at the LHC.

**Acknowledgements**

C.W. B. is supported by the Office of High Energy Physics of the U.S. Department of Energy under contract DE-AC02-05CH11231. The work of M.B., V.B. and J.R. is supported by an European Research Council Starting Grant “*PDF4BSM*”. J.R. is also supported by STFC Rutherford Fellowship and Grant ST/K005227/1 and ST/M003787/1. The work of D.P. and M.L.M. is supported by the European Research Council advanced grant 291377 “*LHCtheory*”: *Theoretical predictions and analyses of LHC physics: advancing the precision frontier*. The work of S. W. has been partially supported by the U.S. National Science Foundation under Grant PHY-1212635. The research of WA, WB, and GZ is supported by the ERC consolidator grant 614577 “HICCUP – High Impact Cross Section Calculations for Ultimate Precision” The work of M. Z. is supported by the European Union’s Horizon 2020 research and innovation programme under the Marie Skłodowska-Curie grant agreement N. 660171. M. C. and M. Z. are supported in part by the ILP LABEX (ANR-10-LABX-63), in turn supported by French state funds managed by the ANR within the “Investissements d’Avenir” programme under reference ANR-11-IDEX-0004-02. H.I.’s work is supported by a Marie Skłodowska-Curie Action Career-Integration Grant PCIG12-GA-2012-334228 of the European Union. The work of F.F.C. is supported by the Alexander von Humboldt Foundation, in the framework of the Sofja Kovalevskaja Award 2014, endowed by the German Federal Ministry of Education and Research. The work of F.Piccinini has been partially supported by CERN TH-Unit. F.Petriello is supported by the U.S. DOE grants DE-FG02-91ER40684 and DE-AC02-06CH11357. R.B. is supported by the DOE contract DE-AC02-06CH11357 The work of R.B. and F.Petriello used resources of the Argonne Leadership Computing Facility, which is a DOE Office of Science User Facility supported under Contract DE-AC02-06CH11357. P. S. is the recipient of an Australian Research Council Future Fellowship, FT130100744. This work was also supported in part by the ARC Centre of Excellence for Particle Physics at the Terascale. The work of M.S. is supported by the National Fund for Scientific Research (F.R.S.-FNRS Belgium), by the IISN “MadGraph” convention 4.4511.10, by the IISN “Fundamental interactions” convention 4.4517.08, and in part by the Belgian Federal Science Policy Office through the Interuniversity Attraction Pole P7/37. This research used computing resources from the Rechenzentrum Garching.

**References**

- [1] R. Contino et al., *Physics at a 100 TeV pp collider: Higgs and EW symmetry breaking studies*, [arXiv:1606.09408 \[hep-ph\]](#).
- [2] S. Forte and G. Watt, *Progress in the Determination of the Partonic Structure of the Proton*, *Ann.Rev.Nucl.Part.Sci.* **63** (2013) 291–328, [arXiv:1301.6754 \[hep-ph\]](#).
- [3] R. D. Ball, S. Carrazza, L. Del Debbio, S. Forte, J. Gao, et al., *Parton Distribution Benchmarking with LHC Data*, *JHEP* **1304** (2013) 125, [arXiv:1211.5142 \[hep-ph\]](#).
- [4] J. Rojo et al., *The PDF4LHC report on PDFs and LHC data: Results from Run I and preparation for Run II*, *J. Phys.* **G42** (2015) 103103, [arXiv:1507.00556 \[hep-ph\]](#).
- [5] J. Butterworth et al., *PDF4LHC recommendations for LHC Run II*, *J. Phys.* **G43** (2016) 023001, [arXiv:1510.03865 \[hep-ph\]](#).
- [6] A. Accardi et al., *Recommendations for PDF usage in LHC predictions*, [arXiv:1603.08906 \[hep-ph\]](#).
- [7] NNPDF Collaboration, R. D. Ball et al., *Parton distributions for the LHC Run II*, *JHEP* **04** (2015) 040, [arXiv:1410.8849 \[hep-ph\]](#).
- [8] S. Dulat, T.-J. Hou, J. Gao, M. Guzzi, J. Huston, P. Nadolsky, J. Pumplin, C. Schmidt, D. Stump, and C. P. Yuan, *New parton distribution functions from a global analysis of quantum chromodynamics*, *Phys. Rev.* **D93** (2016) no. 3, 033006, [arXiv:1506.07443 \[hep-ph\]](#).
- [9] L. A. Harland-Lang, A. D. Martin, P. Motylinski, and R. S. Thorne, *Parton distributions in the*

- LHC era: MMHT 2014 PDFs*, *Eur. Phys. J.* **C75** (2015) no. 5, 204, [arXiv:1412.3989](#) [[hep-ph](#)].
- [10] S. Alekhin, J. Bluemlein, and S. Moch, *The ABM parton distributions tuned to LHC data*, *Phys. Rev.* **D89** (2014) no. 5, 054028, [arXiv:1310.3059](#) [[hep-ph](#)].
- [11] ZEUS, H1 Collaboration, H. Abramowicz et al., *Combination of measurements of inclusive deep inelastic  $e^\pm p$  scattering cross sections and QCD analysis of HERA data*, *Eur. Phys. J.* **C75** (2015) no. 12, 580, [arXiv:1506.06042](#) [[hep-ex](#)].
- [12] A. Accardi, L. T. Brady, W. Melnitchouk, J. F. Owens, and N. Sato, *Constraints on large- $x$  parton distributions from new weak boson production and deep-inelastic scattering data*, [arXiv:1602.03154](#) [[hep-ph](#)].
- [13] P. Jimenez-Delgado and E. Reya, *Delineating parton distributions and the strong coupling*, *Phys. Rev.* **D89** (2014) no. 7, 074049, [arXiv:1403.1852](#) [[hep-ph](#)].
- [14] J. Currie, A. Gehrmann-De Ridder, E. W. N. Glover, and J. Pires, *NNLO QCD corrections to jet production at hadron colliders from gluon scattering*, *JHEP* **01** (2014) 110, [arXiv:1310.3993](#) [[hep-ph](#)].
- [15] M. Czakon, D. Heymes, and A. Mitov, *High-precision differential predictions for top-quark pairs at the LHC*, [arXiv:1511.00549](#) [[hep-ph](#)].
- [16] R. Boughezal, F. Caola, K. Melnikov, F. Petriello, and M. Schulze, *Higgs boson production in association with a jet at next-to-next-to-leading order*, *Phys. Rev. Lett.* **115** (2015) no. 8, 082003, [arXiv:1504.07922](#) [[hep-ph](#)].
- [17] LHeC Study Group Collaboration, J. L. Abelleira Fernandez et al., *A Large Hadron Electron Collider at CERN: Report on the Physics and Design Concepts for Machine and Detector*, *J. Phys.* **G39** (2012) 075001, [arXiv:1206.2913](#) [[physics.acc-ph](#)].
- [18] D. Boer, M. Diehl, R. Milner, R. Venugopalan, W. Vogelsang, et al., *Gluons and the quark sea at high energies: Distributions, polarization, tomography*, [arXiv:1108.1713](#) [[nucl-th](#)].
- [19] P. Skands, S. Carrazza, and J. Rojo, *Tuning PYTHIA 8.1: the Monash 2013 Tune*, *Eur. Phys. J.* **C74** (2014) no. 8, 3024, [arXiv:1404.5630](#) [[hep-ph](#)].
- [20] D. d’Enterria, R. Engel, T. Pierog, S. Ostapchenko, and K. Werner, *Constraints from the first LHC data on hadronic event generators for ultra-high energy cosmic-ray physics*, *Astropart. Phys.* **35** (2011) 98–113, [arXiv:1101.5596](#) [[astro-ph.HE](#)].
- [21] A. Buckley, J. Ferrando, S. Lloyd, K. Nordström, B. Page, M. Rufenacht, M. Schönherr, and G. Watt, *LHAPDF6: parton density access in the LHC precision era*, *Eur. Phys. J.* **C75** (2015) 132, [arXiv:1412.7420](#) [[hep-ph](#)].
- [22] R. Gauld, J. Rojo, L. Rottoli, and J. Talbert, *Charm production in the forward region: constraints on the small- $x$  gluon and backgrounds for neutrino astronomy*, *JHEP* **11** (2015) 009, [arXiv:1506.08025](#) [[hep-ph](#)].
- [23] H1 Collaboration, F. D. Aaron et al., *Measurement of the Inclusive  $e^\pm p$  Scattering Cross Section at High Inelasticity  $y$  and of the Structure Function  $F_L$* , *Eur. Phys. J.* **C71** (2011) 1579, [arXiv:1012.4355](#) [[hep-ex](#)].
- [24] M. Cacciari, M. L. Mangano, and P. Nason, *Gluon PDF constraints from the ratio of forward heavy quark production at the LHC at  $\sqrt{S} = 7$  and 13 TeV*, [arXiv:1507.06197](#) [[hep-ph](#)].
- [25] PROSA Collaboration, O. Zenaiev et al., *Impact of heavy-flavour production cross sections measured by the LHCb experiment on parton distribution functions at low  $x$* , *Eur. Phys. J.* **C75** (2015) no. 8, 396, [arXiv:1503.04581](#) [[hep-ph](#)].
- [26] S. P. Jones, A. D. Martin, M. G. Ryskin, and T. Teubner, *Exclusive  $J/\psi$  and  $\Upsilon$  photoproduction and the low  $x$  gluon*, [arXiv:1507.06942](#) [[hep-ph](#)].
- [27] A. Cooper-Sarkar, P. Mertsch, and S. Sarkar, *The high energy neutrino cross-section in the*

- Standard Model and its uncertainty*, **JHEP** **08** (2011) 042, [arXiv:1106.3723 \[hep-ph\]](#).
- [28] R. Gauld, J. Rojo, L. Rottoli, S. Sarkar, and J. Talbert, *The prompt atmospheric neutrino flux in the light of LHCb*, **JHEP** **02** (2016) 130, [arXiv:1511.06346 \[hep-ph\]](#).
- [29] A. Bhattacharya, R. Enberg, M. H. Reno, I. Sarcevic, and A. Stasto, *Perturbative charm production and the prompt atmospheric neutrino flux in light of RHIC and LHC*, **JHEP** **06** (2015) 110, [arXiv:1502.01076 \[hep-ph\]](#).
- [30] M. V. Garzelli, S. Moch, and G. Sigl, *Lepton fluxes from atmospheric charm revisited*, **JHEP** **10** (2015) 115, [arXiv:1507.01570 \[hep-ph\]](#).
- [31] IceCube Collaboration, M. G. Aartsen et al., *Observation of High-Energy Astrophysical Neutrinos in Three Years of IceCube Data*, **Phys. Rev. Lett.** **113** (2014) 101101, [arXiv:1405.5303 \[astro-ph.HE\]](#).
- [32] T. Sjöstrand, S. Ask, J. R. Christiansen, R. Corke, N. Desai, P. Ilten, S. Mrenna, S. Prestel, C. O. Rasmussen, and P. Z. Skands, *An Introduction to PYTHIA 8.2*, **Comput. Phys. Commun.** **191** (2015) 159–177, [arXiv:1410.3012 \[hep-ph\]](#).
- [33] P. Z. Skands, *Tuning Monte Carlo Generators: The Perugia Tunes*, **Phys. Rev.** **D82** (2010) 074018, [arXiv:1005.3457 \[hep-ph\]](#).
- [34] M. Czakon, M. L. Mangano, A. Mitov, and J. Rojo, *Constraints on the gluon PDF from top quark pair production at hadron colliders*, **JHEP** **07** (2013) 167, [arXiv:1303.7215 \[hep-ph\]](#).
- [35] M. Guzzi, K. Lipka, and S.-O. Moch, *Top-quark pair production at hadron colliders: differential cross section and phenomenological applications with DiffTop*, **JHEP** **01** (2015) 082, [arXiv:1406.0386 \[hep-ph\]](#).
- [36] R. D. Ball, E. R. Nocera, and J. Rojo, *The asymptotic behaviour of parton distributions at small and large  $x$* , [arXiv:1604.00024 \[hep-ph\]](#).
- [37] M. Bonvini, S. Marzani, J. Rojo, L. Rottoli, M. Ubiali, R. D. Ball, V. Bertone, S. Carrazza, and N. P. Hartland, *Parton distributions with threshold resummation*, **JHEP** **09** (2015) 191, [arXiv:1507.01006 \[hep-ph\]](#).
- [38] W. Beenakker, C. Borschensky, M. Kramer, A. Kulesza, E. Laenen, S. Marzani, and J. Rojo, *NLO+NLL squark and gluino production cross-sections with threshold-improved parton distributions*, **Eur. Phys. J.** **C76** (2016) no. 2, 53, [arXiv:1510.00375 \[hep-ph\]](#).
- [39] NNPDF Collaboration, R. D. Ball, V. Bertone, L. Del Debbio, S. Forte, A. Guffanti, J. Rojo, and M. Ubiali, *Theoretical issues in PDF determination and associated uncertainties*, **Phys. Lett.** **B723** (2013) 330–339, [arXiv:1303.1189 \[hep-ph\]](#).
- [40] G. P. Salam and J. Rojo, *A Higher Order Perturbative Parton Evolution Toolkit (HOPPET)*, **Comput. Phys. Commun.** **180** (2009) 120–156, [arXiv:0804.3755 \[hep-ph\]](#).
- [41] V. Bertone, S. Carrazza, and J. Rojo, *APFEL: A PDF Evolution Library with QED corrections*, **Comput. Phys. Commun.** **185** (2014) 1647–1668, [arXiv:1310.1394 \[hep-ph\]](#).
- [42] S. Carrazza, J. I. Latorre, J. Rojo, and G. Watt, *A compression algorithm for the combination of PDF sets*, **Eur. Phys. J.** **C75** (2015) 474, [arXiv:1504.06469 \[hep-ph\]](#).
- [43] M. L. Mangano and J. Rojo, *Cross Section Ratios between different CM energies at the LHC: opportunities for precision measurements and BSM sensitivity*, **JHEP** **08** (2012) 010, [arXiv:1206.3557 \[hep-ph\]](#).
- [44] F. Maltoni, G. Ridolfi, and M. Ubiali,  *$b$ -initiated processes at the LHC: a reappraisal*, **JHEP** **07** (2012) 022, [arXiv:1203.6393 \[hep-ph\]](#). [Erratum: JHEP04,095(2013)].
- [45] R. D. Ball et al., *Parton distributions with LHC data*, **Nucl. Phys.** **B867** (2013) 244–289, [arXiv:1207.1303 \[hep-ph\]](#).
- [46] T. Han, J. Sayre, and S. Westhoff, *Top-Quark Initiated Processes at High-Energy Hadron Colliders*, **JHEP** **04** (2015) 145, [arXiv:1411.2588 \[hep-ph\]](#).

- [47] S. Dawson, A. Ismail, and I. Low, *A Redux on "When is the Top Quark a Parton?"*, *Phys.Rev.* **D90** (2014) no. 1, 014005, [arXiv:1405.6211 \[hep-ph\]](#).
- [48] M. A. G. Aivazis, J. C. Collins, F. I. Olness, and W.-K. Tung, *Leptoproduction of heavy quarks. 2. A Unified QCD formulation of charged and neutral current processes from fixed target to collider energies*, *Phys. Rev.* **D50** (1994) 3102–3118, [arXiv:hep-ph/9312319 \[hep-ph\]](#).
- [49] J. C. Collins, *Hard scattering factorization with heavy quarks: A General treatment*, *Phys. Rev.* **D58** (1998) 094002, [arXiv:hep-ph/9806259 \[hep-ph\]](#).
- [50] M. Cacciari, M. Greco, and P. Nason, *The  $P(T)$  spectrum in heavy flavor hadroproduction*, *JHEP* **05** (1998) 007, [arXiv:hep-ph/9803400 \[hep-ph\]](#).
- [51] S. Forte, E. Laenen, P. Nason, and J. Rojo, *Heavy quarks in deep-inelastic scattering*, *Nucl. Phys.* **B834** (2010) 116–162, [arXiv:1001.2312 \[hep-ph\]](#).
- [52] A. D. Martin, R. G. Roberts, W. J. Stirling, and R. S. Thorne, *Parton distributions incorporating QED contributions*, *Eur. Phys. J.* **C39** (2005) 155–161, [arXiv:hep-ph/0411040 \[hep-ph\]](#).
- [53] NNPDF Collaboration, R. D. Ball, V. Bertone, S. Carrazza, L. Del Debbio, S. Forte, A. Guffanti, N. P. Hartland, and J. Rojo, *Parton distributions with QED corrections*, *Nucl. Phys.* **B877** (2013) 290–320, [arXiv:1308.0598 \[hep-ph\]](#).
- [54] C. Schmidt, J. Pumplin, D. Stump, and C. P. Yuan, *CT14QED PDFs from Isolated Photon Production in Deep Inelastic Scattering*, [arXiv:1509.02905 \[hep-ph\]](#).
- [55] S. Carrazza, A. Ferrara, D. Palazzo, and J. Rojo, *APFEL Web: a web-based application for the graphical visualization of parton distribution functions*, *J. Phys.* **G42** (2015) no. 5, 057001, [arXiv:1410.5456 \[hep-ph\]](#).
- [56] D. de Florian, G. F. R. Sborlini, and G. Rodrigo, *QED corrections to the Altarelli-Parisi splitting functions*, [arXiv:1512.00612 \[hep-ph\]](#).
- [57] ATLAS Collaboration, G. Aad et al., *Measurement of the double-differential high-mass Drell-Yan cross section in pp collisions at  $\sqrt{s} = 8$  TeV with the ATLAS detector*, [arXiv:1606.01736 \[hep-ex\]](#).
- [58] A. D. Martin and M. G. Ryskin, *The photon PDF of the proton*, *Eur. Phys. J.* **C74** (2014) 3040, [arXiv:1406.2118 \[hep-ph\]](#).
- [59] L. A. Harland-Lang, V. A. Khoze, and M. G. Ryskin, *The photon PDF in events with rapidity gaps*, *Eur. Phys. J.* **C76** (2016) no. 5, 255, [arXiv:1601.03772 \[hep-ph\]](#).
- [60] L. A. Harland-Lang, M. G. Ryskin, and V. A. Khoze, *Sudakov effects in photon-initiated processes*, [arXiv:1605.04935 \[hep-ph\]](#).
- [61] V. Bertone and S. Carrazza, *Combining NNPDF3.0 and NNPDF2.3QED through the APFEL evolution code*, [arXiv:1606.07130 \[hep-ph\]](#).
- [62] V. Bertone, S. Carrazza, D. Pagani, and M. Zaro, *On the Impact of Lepton PDFs*, [arXiv:1508.07002 \[hep-ph\]](#).
- [63] R. S. Thorne and R. G. Roberts, *An Ordered analysis of heavy flavor production in deep inelastic scattering*, *Phys. Rev.* **D57** (1998) 6871–6898, [arXiv:hep-ph/9709442 \[hep-ph\]](#).
- [64] J. Alwall, R. Frederix, S. Frixione, V. Hirschi, F. Maltoni, et al., *The automated computation of tree-level and next-to-leading order differential cross sections, and their matching to parton shower simulations*, *JHEP* **1407** (2014) 079, [arXiv:1405.0301 \[hep-ph\]](#).
- [65] R. Boughezal, Y. Li, and F. Petriello, *Disentangling radiative corrections using the high-mass Drell-Yan process at the LHC*, *Phys. Rev.* **D89** (2014) no. 3, 034030, [arXiv:1312.3972 \[hep-ph\]](#).
- [66] J. Baglio, L. D. Ninh, and M. M. Weber, *Massive gauge boson pair production at the LHC: a next-to-leading order story*, *Phys. Rev.* **D88** (2013) 113005, [arXiv:1307.4331](#).
- [67] W. Hollik, J. M. Lindert, E. Mirabella, and D. Pagani, *Electroweak corrections to*

- squark-antisquark production at the LHC*, *JHEP* **08** (2015) 099, [arXiv:1506.01052 \[hep-ph\]](#).
- [68] P. Ciafaloni and D. Comelli, *Electroweak evolution equations*, *JHEP* **11** (2005) 022, [arXiv:hep-ph/0505047 \[hep-ph\]](#).
- [69] S. Dawson, *The Effective W Approximation*, *Nucl. Phys.* **B249** (1985) 42–60.
- [70] G. L. Kane, W. W. Repko, and W. B. Rolnick, *The Effective  $W^{+-}$ , Z0 Approximation for High-Energy Collisions*, *Phys. Lett.* **B148** (1984) 367–372.
- [71] Z. Kunszt and D. E. Soper, *On the Validity of the Effective W Approximation*, *Nucl. Phys.* **B296** (1988) 253.
- [72] S. Dawson, *Radiative Corrections to the Effective W Approximation*, *Phys. Lett.* **B217** (1989) 347.
- [73] B. W. Lee, C. Quigg, and H. B. Thacker, *Weak Interactions at Very High-Energies: The Role of the Higgs Boson Mass*, *Phys. Rev.* **D16** (1977) 1519.
- [74] M. S. Chanowitz and M. K. Gaillard, *The TeV Physics of Strongly Interacting W's and Z's*, *Nucl. Phys.* **B261** (1985) 379.
- [75] M. Drees, R. M. Godbole, M. Nowakowski, and S. D. Rindani, *gamma gamma processes at high-energy p p colliders*, *Phys. Rev.* **D50** (1994) 2335–2338, [arXiv:hep-ph/9403368 \[hep-ph\]](#).
- [76] D. Alva, T. Han, and R. Ruiz, *Heavy Majorana neutrinos from  $W\gamma$  fusion at hadron colliders*, *JHEP* **02** (2015) 072, [arXiv:1411.7305 \[hep-ph\]](#).
- [77] F. Caola, S. Forte, and J. Rojo, *HERA data and DGLAP evolution: Theory and phenomenology*, *Nucl. Phys.* **A854** (2011) 32–44, [arXiv:1007.5405 \[hep-ph\]](#).
- [78] F. Caola, S. Forte, and J. Rojo, *Deviations from NLO QCD evolution in inclusive HERA data*, *Phys. Lett.* **B686** (2010) 127–135, [arXiv:0910.3143 \[hep-ph\]](#).
- [79] S. Catani, M. Ciafaloni, and F. Hautmann, *Gluon contributions to small-x heavy flavor production*, *Phys. Lett.* **B242** (1990) 97.
- [80] S. Catani, M. Ciafaloni, and F. Hautmann, *High-energy factorization and small x heavy flavor production*, *Nucl. Phys.* **B366** (1991) 135–188.
- [81] S. Catani, M. Ciafaloni, and F. Hautmann, *High-energy factorization in QCD and minimal subtraction scheme*, *Phys. Lett.* **B307** (1993) 147–153.
- [82] S. Catani and F. Hautmann, *Quark anomalous dimensions at small x*, *Phys. Lett.* **B315** (1993) 157–163.
- [83] S. Catani and F. Hautmann, *High-energy factorization and small x deep inelastic scattering beyond leading order*, *Nucl. Phys.* **B427** (1994) 475–524, [arXiv:hep-ph/9405388 \[hep-ph\]](#).
- [84] G. Altarelli, R. D. Ball, and S. Forte, *Resummation of singlet parton evolution at small x*, *Nucl. Phys.* **B575** (2000) 313–329, [arXiv:hep-ph/9911273 \[hep-ph\]](#).
- [85] G. P. Salam, *A Resummation of large subleading corrections at small x*, *JHEP* **07** (1998) 019, [arXiv:hep-ph/9806482 \[hep-ph\]](#).
- [86] G. Altarelli, R. D. Ball, and S. Forte, *Perturbatively stable resummed small x evolution kernels*, *Nucl. Phys.* **B742** (2006) 1–40, [arXiv:hep-ph/0512237 \[hep-ph\]](#).
- [87] G. Camici and M. Ciafaloni, *k factorization and small x anomalous dimensions*, *Nucl. Phys.* **B496** (1997) 305–336, [arXiv:hep-ph/9701303 \[hep-ph\]](#). [Erratum: *Nucl. Phys.* **B607**, 431(2001)].
- [88] G. Altarelli, R. D. Ball, and S. Forte, *Factorization and resummation of small x scaling violations with running coupling*, *Nucl. Phys.* **B621** (2002) 359–387, [arXiv:hep-ph/0109178 \[hep-ph\]](#).
- [89] R. D. Ball, *Resummation of Hadroproduction Cross-sections at High Energy*, *Nucl. Phys.* **B796** (2008) 137–183, [arXiv:0708.1277 \[hep-ph\]](#).
- [90] G. Altarelli, R. D. Ball, and S. Forte, *Small x Resummation with Quarks: Deep-Inelastic*

- Scattering*, *Nucl. Phys.* **B799** (2008) 199–240, [arXiv:0802.0032 \[hep-ph\]](#).
- [91] C. D. White and R. S. Thorne, *A Global Fit to Scattering Data with NLL BFKL Resummations*, *Phys. Rev.* **D75** (2007) 034005, [arXiv:hep-ph/0611204 \[hep-ph\]](#).
- [92] M. Bonvini, S. Marzani, and T. Peraro, *Small- $x$  resummation from HELL*, [arXiv:1607.02153 \[hep-ph\]](#).
- [93] NNPDF Collaboration, R. D. Ball et al., *in preparation*, .
- [94] R. D. Ball, M. Bonvini, S. Forte, S. Marzani, and G. Ridolfi, *Higgs production in gluon fusion beyond NNLO*, *Nucl. Phys.* **B874** (2013) 746–772, [arXiv:1303.3590 \[hep-ph\]](#).
- [95] P. Skands, *Modelling hadronic interactions in HEP MC generators*, *EPJ Web Conf.* **99** (2015) 09001, [arXiv:1412.3525 \[hep-ph\]](#).
- [96] L. V. Gribov, E. M. Levin, and M. G. Ryskin, *Semihard Processes in QCD*, *Phys. Rept.* **100** (1983) 1–150.
- [97] B. Andersson, G. Gustafson, G. Ingelman, and T. Sjostrand, *Parton Fragmentation and String Dynamics*, *Phys. Rept.* **97** (1983) 31–145.
- [98] X. Artru and G. Mennessier, *String model and multiproduction*, *Nucl. Phys.* **B70** (1974) 93–115.
- [99] G. Marchesini, B. R. Webber, G. Abbiendi, I. G. Knowles, M. H. Seymour, and L. Stanco, *HERWIG: A Monte Carlo event generator for simulating hadron emission reactions with interfering gluons. Version 5.1 - April 1991*, *Comput. Phys. Commun.* **67** (1992) 465–508.
- [100] T. Sjöstrand, S. Mrenna, and P. Z. Skands, *PYTHIA 6.4 Physics and Manual*, *JHEP* **05** (2006) 026, [arXiv:hep-ph/0603175 \[hep-ph\]](#).
- [101] M. Bahr et al., *Herwig++ Physics and Manual*, *Eur. Phys. J.* **C58** (2008) 639–707, [arXiv:0803.0883 \[hep-ph\]](#).
- [102] T. Gleisberg, S. Hoeche, F. Krauss, M. Schonherr, S. Schumann, F. Siegert, and J. Winter, *Event generation with SHERPA 1.1*, *JHEP* **02** (2009) 007, [arXiv:0811.4622 \[hep-ph\]](#).
- [103] K. Werner, F.-M. Liu, and T. Pierog, *Parton ladder splitting and the rapidity dependence of transverse momentum spectra in deuteron-gold collisions at RHIC*, *Phys. Rev.* **C74** (2006) 044902, [arXiv:hep-ph/0506232 \[hep-ph\]](#).
- [104] T. Pierog and K. Werner, *EPOS Model and Ultra High Energy Cosmic Rays*, *Nucl. Phys. Proc. Suppl.* **196** (2009) 102–105, [arXiv:0905.1198 \[hep-ph\]](#).
- [105] T. Pierog, I. Karpenko, J. M. Katzy, E. Yatsenko, and K. Werner, *EPOS LHC: Test of collective hadronization with data measured at the CERN Large Hadron Collider*, *Phys. Rev.* **C92** (2015) no. 3, 034906, [arXiv:1306.0121 \[hep-ph\]](#).
- [106] N. N. Kalmykov, S. S. Ostapchenko, and A. I. Pavlov, *Quark-Gluon String Model and EAS Simulation Problems at Ultra-High Energies*, *Nucl. Phys. Proc. Suppl.* **52** (1997) 17–28.
- [107] N. N. Kalmykov and S. S. Ostapchenko, *The Nucleus-nucleus interaction, nuclear fragmentation, and fluctuations of extensive air showers*, *Phys. Atom. Nucl.* **56** (1993) 346–353. [*Yad. Fiz.* 56N3,105(1993)].
- [108] S. Ostapchenko, *Non-linear screening effects in high energy hadronic interactions*, *Phys. Rev.* **D74** (2006) 014026, [arXiv:hep-ph/0505259 \[hep-ph\]](#).
- [109] S. Ostapchenko, *QGSJET-II: Towards reliable description of very high energy hadronic interactions*, *Nucl. Phys. Proc. Suppl.* **151** (2006) 143–146, [arXiv:hep-ph/0412332 \[hep-ph\]](#).
- [110] S. Ostapchenko, *Status of QGSJET*, *AIP Conf. Proc.* **928** (2007) 118–125, [arXiv:0706.3784 \[hep-ph\]](#).
- [111] S. Ostapchenko, *Monte Carlo treatment of hadronic interactions in enhanced Pomeron scheme: I. QGSJET-II model*, *Phys. Rev.* **D83** (2011) 014018, [arXiv:1010.1869 \[hep-ph\]](#).
- [112] E.-J. Ahn, R. Engel, T. K. Gaisser, P. Lipari, and T. Stanev, *Cosmic ray interaction event*

- generator SIBYLL 2.1*, *Phys. Rev.* **D80** (2009) 094003, [arXiv:0906.4113 \[hep-ph\]](#).
- [113] R. Engel, *Photoproduction within the two component dual parton model. 1. Amplitudes and cross-sections*, *Z. Phys.* **C66** (1995) 203–214.
- [114] R. Engel and J. Ranft, *Hadronic photon-photon interactions at high-energies*, *Phys. Rev.* **D54** (1996) 4244–4262, [arXiv:hep-ph/9509373 \[hep-ph\]](#).
- [115] R. Engel, J. Ranft, and S. Roesler, *Hard diffraction in hadron hadron interactions and in photoproduction*, *Phys. Rev.* **D52** (1995) 1459–1468, [arXiv:hep-ph/9502319 \[hep-ph\]](#).
- [116] J. Ranft, *The Dual parton model at cosmic ray energies*, *Phys. Rev.* **D51** (1995) 64–84.
- [117] S. Roesler, R. Engel, and J. Ranft, *The Monte Carlo event generator DPMJET-III*, in *Advanced Monte Carlo for radiation physics, particle transport simulation and applications. Proceedings, Conference, MC2000, Lisbon, Portugal, October 23-26, 2000*, pp. 1033–1038. 2000. [arXiv:hep-ph/0012252 \[hep-ph\]](#).
- [118] V. N. Gribov, *A Reggeon Diagram Technique*, *Sov. Phys. JETP* **26** (1968) 414–422. [*Zh. Eksp. Teor. Fiz.*53,654(1967)].
- [119] D. d’Enterria and T. Pierog, *Global properties of proton-proton collisions at  $\sqrt{s} = 100$  TeV*, [arXiv:1604.08536 \[hep-ph\]](#).
- [120] D. Bourilkov, R. C. Group, and M. R. Whalley, *LHAPDF: PDF use from the Tevatron to the LHC*, in *TeV4LHC Workshop - 4th meeting Batavia, Illinois, October 20-22, 2005*. 2006. [arXiv:hep-ph/0605240 \[hep-ph\]](#).
- [121] G. A. Schuler and T. Sjöstrand, *Hadronic diffractive cross-sections and the rise of the total cross-section*, *Phys. Rev.* **D49** (1994) 2257–2267.
- [122] T. Sjöstrand, S. Mrenna, and P. Z. Skands, *A Brief Introduction to PYTHIA 8.1*, *Comput.Phys.Commun.* **178** (2008) 852–867, [arXiv:0710.3820 \[hep-ph\]](#).
- [123] S. Navin, *Diffraction in Pythia*, [arXiv:1005.3894 \[hep-ph\]](#).
- [124] CTEQ Collaboration, H. L. Lai, J. Huston, S. Kuhlmann, J. Morfin, F. I. Olness, J. F. Owens, J. Pumplin, and W. K. Tung, *Global QCD analysis of parton structure of the nucleon: CTEQ5 parton distributions*, *Eur. Phys. J.* **C12** (2000) 375–392, [arXiv:hep-ph/9903282 \[hep-ph\]](#).
- [125] C. O. Rasmussen, *Hard Diffraction in Pythia 8*, in *45th International Symposium on Multiparticle Dynamics (ISMD 2015) Kreuth, Germany, October 4-9, 2015*. 2015. [arXiv:1512.05872 \[hep-ph\]](#). <https://inspirehep.net/record/1410600/files/arXiv:1512.05872.pdf>.
- [126] M. Sandhoff and P. Z. Skands, *Colour annealing - a toy model of colour reconnections*, in *Physics at TeV colliders. Proceedings, Workshop, Les Houches, France, May 2-20, 2005*. 2005. [http://lss.fnal.gov/cgi-bin/find\\_paper.pl?conf-05-518-t](http://lss.fnal.gov/cgi-bin/find_paper.pl?conf-05-518-t).
- [127] P. Z. Skands and D. Wicke, *Non-perturbative QCD effects and the top mass at the Tevatron*, *Eur. Phys. J.* **C52** (2007) 133–140, [arXiv:hep-ph/0703081 \[HEP-PH\]](#).
- [128] H. J. Drescher, M. Hladik, S. Ostapchenko, T. Pierog, and K. Werner, *Parton based Gribov-Regge theory*, *Phys. Rept.* **350** (2001) 93–289, [arXiv:hep-ph/0007198 \[hep-ph\]](#).
- [129] V. N. Gribov and L. N. Lipatov, *Deep inelastic  $e p$  scattering in perturbation theory*, *Sov. J. Nucl. Phys.* **15** (1972) 438–450. [*Yad. Fiz.*15,781(1972)].
- [130] G. Altarelli and G. Parisi, *Asymptotic Freedom in Parton Language*, *Nucl. Phys.* **B126** (1977) 298.
- [131] Y. L. Dokshitzer, *Calculation of the Structure Functions for Deep Inelastic Scattering and  $e+e-$  Annihilation by Perturbation Theory in Quantum Chromodynamics.*, *Sov. Phys. JETP* **46** (1977) 641–653. [*Zh. Eksp. Teor. Fiz.*73,1216(1977)].
- [132] S. Ostapchenko, *On the re-summation of enhanced Pomeron diagrams*, *Phys. Lett.* **B636** (2006) 40–45, [arXiv:hep-ph/0602139 \[hep-ph\]](#).

- [133] S. Ostapchenko, *Enhanced Pomeron diagrams: Re-summation of unitarity cuts*, *Phys. Rev.* **D77** (2008) 034009, [arXiv:hep-ph/0612175](#) [hep-ph].
- [134] S. Ostapchenko, *Non-linear effects in high energy hadronic interactions*, in *INFN Eloisatron Project 44th Workshop on QCD at Cosmic Energies: The Highest Energy Cosmic Rays and QCD Erice, Italy, August 29-September 5, 2004*. 2005. [arXiv:hep-ph/0501093](#) [hep-ph].
- [135] M. L. Good and W. D. Walker, *Diffraction dissociation of beam particles*, *Phys. Rev.* **120** (1960) 1857–1860.
- [136] A. Donnachie and P. V. Landshoff, *Total cross-sections*, *Phys. Lett.* **B296** (1992) 227–232, [arXiv:hep-ph/9209205](#) [hep-ph].
- [137] UA5 Collaboration, G. J. Alner et al., *Antiproton-proton cross sections at 200 and 900 GeV c.m. energy*, *Z. Phys.* **C32** (1986) 153–161.
- [138] E710 Collaboration, N. A. Amos et al., *Measurement of  $\rho$ , the ratio of the real to imaginary part of the  $\bar{p}p$  forward elastic scattering amplitude, at  $\sqrt{s} = 1.8$ -TeV*, *Phys. Rev. Lett.* **68** (1992) 2433–2436.
- [139] CDF Collaboration, F. Abe et al., *Measurement of the  $\bar{p}p$  total cross-section at  $\sqrt{s} = 546$  GeV and 1800-GeV*, *Phys. Rev.* **D50** (1994) 5550–5561.
- [140] ALICE Collaboration, B. Abelev et al., *Measurement of inelastic, single- and double-diffraction cross sections in proton–proton collisions at the LHC with ALICE*, *Eur. Phys. J.* **C73** (2013) no. 6, 2456, [arXiv:1208.4968](#) [hep-ex].
- [141] ATLAS Collaboration, G. Aad et al., *Measurement of the Inelastic Proton-Proton Cross-Section at  $\sqrt{s} = 7$  TeV with the ATLAS Detector*, *Nature Commun.* **2** (2011) 463, [arXiv:1104.0326](#) [hep-ex].
- [142] *Measurement of the Inelastic Proton-Proton Cross Section at  $\sqrt{s} = 13$  TeV with the ATLAS Detector at the LHC*, ATLAS-CONF-2015-038, CERN, Geneva, Aug, 2015. <https://cds.cern.ch/record/2045064>.
- [143] CMS Collaboration, S. Chatrchyan et al., *Measurement of the inelastic proton-proton cross section at  $\sqrt{s} = 7$  TeV*, *Phys. Lett.* **B722** (2013) 5–27, [arXiv:1210.6718](#) [hep-ex].
- [144] CMS Collaboration, *Measurement of the inelastic proton-proton cross section at  $\sqrt{s} = 13$  TeV*, CMS-PAS-FSQ-15-005, CERN, Geneva, 2016. <https://cds.cern.ch/record/2145896>.
- [145] G. Antchev et al., *First measurement of the total proton-proton cross section at the LHC energy of  $\sqrt{s} = 7$  TeV*, *Europhys. Lett.* **96** (2011) 21002, [arXiv:1110.1395](#) [hep-ex].
- [146] Pierre Auger Collaboration, P. Abreu et al., *Measurement of the proton-air cross-section at  $\sqrt{s} = 57$  TeV with the Pierre Auger Observatory*, *Phys. Rev. Lett.* **109** (2012) 062002, [arXiv:1208.1520](#) [hep-ex].
- [147] UA1 Collaboration, C. Albajar et al., *A Study of the General Characteristics of  $p\bar{p}$  Collisions at  $\sqrt{s} = 0.2$ -TeV to 0.9-TeV*, *Nucl. Phys.* **B335** (1990) 261–287.
- [148] UA5 Collaboration, G. J. Alner et al., *Scaling of Pseudorapidity Distributions at c.m. Energies Up to 0.9-TeV*, *Z. Phys.* **C33** (1986) 1–6.
- [149] CDF Collaboration, F. Abe et al., *Pseudorapidity distributions of charged particles produced in  $\bar{p}p$  interactions at  $\sqrt{s} = 630$  GeV and 1800 GeV*, *Phys. Rev.* **D41** (1990) 2330. [,119(1989)].
- [150] CDF Collaboration, F. Abe et al., *Transverse Momentum Distributions of Charged Particles Produced in  $\bar{p}p$  Interactions at  $\sqrt{s} = 630$  GeV and 1800 GeV*, *Phys. Rev. Lett.* **61** (1988) 1819.
- [151] ALICE Collaboration, K. Aamodt et al., *Charged-particle multiplicity measurement in proton-proton collisions at  $\sqrt{s} = 0.9$  and 2.36 TeV with ALICE at LHC*, *Eur. Phys. J.* **C68** (2010) 89–108, [arXiv:1004.3034](#) [hep-ex].
- [152] ALICE Collaboration, K. Aamodt et al., *Charged-particle multiplicity measurement in proton-proton collisions at  $\sqrt{s} = 7$  TeV with ALICE at LHC*, *Eur. Phys. J.* **C68** (2010) 345–354,

- [arXiv:1004.3514](#) [[hep-ex](#)].
- [153] ATLAS Collaboration, G. Aad et al., *Charged-particle multiplicities in pp interactions measured with the ATLAS detector at the LHC*, *New J. Phys.* **13** (2011) 053033, [arXiv:1012.5104](#) [[hep-ex](#)].
- [154] CMS Collaboration, V. Khachatryan et al., *Transverse momentum and pseudorapidity distributions of charged hadrons in pp collisions at  $\sqrt{s} = 0.9$  and 2.36 TeV*, *JHEP* **02** (2010) 041, [arXiv:1002.0621](#) [[hep-ex](#)].
- [155] CMS Collaboration, V. Khachatryan et al., *Pseudorapidity distribution of charged hadrons in proton-proton collisions at  $\sqrt{s} = 13$  TeV*, *Phys. Lett.* **B751** (2015) 143–163, [arXiv:1507.05915](#) [[hep-ex](#)].
- [156] ALICE Collaboration, J. Adam et al., *Centrality dependence of the charged-particle multiplicity density at mid-rapidity in Pb-Pb collisions at  $\sqrt{s_{NN}} = 5.02$  TeV*, [arXiv:1512.06104](#) [[nucl-ex](#)].
- [157] A. M. Rossi, G. Vannini, A. Bussiere, E. Albini, D. D’Alessandro, and G. Giacommelli, *Experimental Study of the Energy Dependence in Proton Proton Inclusive Reactions*, *Nucl. Phys.* **B84** (1975) 269–305.
- [158] T. Alexopoulos et al., *Multiplicity Dependence of the Transverse Momentum Spectrum for Centrally Produced Hadrons in Anti-proton - Proton Collisions at  $\sqrt{s} = 1.8$ -tev*, *Phys. Rev. Lett.* **60** (1988) 1622.
- [159] UA1 Collaboration, G. Arnison et al., *Hadronic Jet Production at the CERN Proton - anti-Proton Collider*, *Phys. Lett.* **B132** (1983) 214.
- [160] J. Bellm et al., *Herwig 7.0 / Herwig++ 3.0 Release Note*, [arXiv:1512.01178](#) [[hep-ph](#)].
- [161] ATLAS Collaboration, G. Aad et al., *Measurement of underlying event characteristics using charged particles in pp collisions at  $\sqrt{s} = 900$ GeV and 7 TeV with the ATLAS detector*, *Phys. Rev.* **D83** (2011) 112001, [arXiv:1012.0791](#) [[hep-ex](#)].
- [162] CMS Collaboration, V. Khachatryan et al., *Observation of Long-Range Near-Side Angular Correlations in Proton-Proton Collisions at the LHC*, *JHEP* **09** (2010) 091, [arXiv:1009.4122](#) [[hep-ex](#)].
- [163] A. Karneyeu, L. Mijovic, S. Prestel, and P. Z. Skands, *MCPLOTS: a particle physics resource based on volunteer computing*, *Eur. Phys. J.* **C74** (2014) 2714, [arXiv:1306.3436](#) [[hep-ph](#)].
- [164] CDF Collaboration, F. Abe et al.,  *$K_s^0$  production in  $\bar{p}p$  interactions at  $\sqrt{s} = 630$  GeV and 1800 GeV*, *Phys. Rev.* **D40** (1989) 3791–3794.
- [165] CDF Collaboration, D. Acosta et al.,  *$K_S^0$  and  $\Lambda^0$  production studies in  $p\bar{p}$  collisions at  $\sqrt{s} = 1800$ -GeV and 630-GeV*, *Phys. Rev.* **D72** (2005) 052001, [arXiv:hep-ex/0504048](#) [[hep-ex](#)].
- [166] STAR Collaboration, B. I. Abelev et al., *Strange particle production in p+p collisions at  $s^{*(1/2)} = 200$ -GeV*, *Phys. Rev.* **C75** (2007) 064901, [arXiv:nucl-ex/0607033](#) [[nucl-ex](#)].
- [167] ALICE Collaboration, K. Aamodt et al., *Strange particle production in proton-proton collisions at  $\sqrt{s} = 0.9$  TeV with ALICE at the LHC*, *Eur. Phys. J.* **C71** (2011) 1594, [arXiv:1012.3257](#) [[hep-ex](#)].
- [168] S. P. Baranov, A. M. Snigirev, and N. P. Zotov, *Double heavy meson production through double parton scattering in hadronic collisions*, *Phys. Lett.* **B705** (2011) 116–119, [arXiv:1105.6276](#) [[hep-ph](#)].
- [169] ALICE Collaboration, B. Abelev et al., *Multi-strange baryon production in pp collisions at  $\sqrt{s} = 7$  TeV with ALICE*, *Phys. Lett.* **B712** (2012) 309–318, [arXiv:1204.0282](#) [[nucl-ex](#)].
- [170] LHCb Collaboration, R. Aaij et al., *Measurement of prompt hadron production ratios in pp collisions at  $\sqrt{s} = 0.9$  and 7 TeV*, *Eur. Phys. J.* **C72** (2012) 2168, [arXiv:1206.5160](#) [[hep-ex](#)].
- [171] CMS Collaboration, S. Chatrchyan et al., *Measurement of neutral strange particle production in*

- the underlying event in proton-proton collisions at  $\sqrt{s} = 7$  TeV*, *Phys. Rev.* **D88** (2013) 052001, [arXiv:1305.6016 \[hep-ex\]](#).
- [172] C. Bierlich and J. R. Christiansen, *Effects of color reconnection on hadron flavor observables*, *Phys. Rev.* **D92** (2015) no. 9, 094010, [arXiv:1507.02091 \[hep-ph\]](#).
- [173] T. Martin, P. Skands, and S. Farrington, *Probing Collective Effects in Hadronisation with the Extremes of the Underlying Event*, [arXiv:1603.05298 \[hep-ph\]](#).
- [174] M. Bähr, S. Gieseke, and M. H. Seymour, *Simulation of multiple partonic interactions in Herwig++*, *JHEP* **07** (2008) 076, [arXiv:0803.3633 \[hep-ph\]](#).
- [175] J. M. Butterworth, J. R. Forshaw, and M. H. Seymour, *Multiparton interactions in photoproduction at HERA*, *Z. Phys.* **C72** (1996) 637–646, [arXiv:hep-ph/9601371 \[hep-ph\]](#).
- [176] M. Bahr, J. M. Butterworth, S. Gieseke, and M. H. Seymour, *Soft interactions in Herwig++*, in *Proceedings, 1st International Workshop on Multiple Partonic Interactions at the LHC (MPI08)*, pp. 239–248. 2009. [arXiv:0905.4671 \[hep-ph\]](#).  
<https://inspirehep.net/record/821555/files/arXiv:0905.4671.pdf>.
- [177] S. Gieseke, C. Rohr, and A. Siodmok, *Colour reconnections in Herwig++*, *Eur. Phys. J.* **C72** (2012) 2225, [arXiv:1206.0041 \[hep-ph\]](#).
- [178] M. H. Seymour and A. Siodmok, *Constraining MPI models using  $\sigma_{eff}$  and recent Tevatron and LHC Underlying Event data*, *JHEP* **10** (2013) 113, [arXiv:1307.5015 \[hep-ph\]](#).
- [179] CDF Collaboration, T. A. Aaltonen et al., *Study of the energy dependence of the underlying event in proton-antiproton collisions*, *Phys. Rev.* **D92** (2015) no. 9, 092009, [arXiv:1508.05340 \[hep-ex\]](#).
- [180] ATLAS Collaboration, *Detector level leading track underlying event distributions at 13 TeV measured in ATLAS*, ATL-PHYS-PUB-2015-019.
- [181] T. Sjöstrand and M. van Zijl, *A Multiple Interaction Model for the Event Structure in Hadron Collisions*, *Phys. Rev.* **D36** (1987) 2019.
- [182] T. Sjöstrand and P. Z. Skands, *Transverse-momentum-ordered showers and interleaved multiple interactions*, *Eur. Phys. J.* **C39** (2005) 129–154, [arXiv:hep-ph/0408302 \[hep-ph\]](#).
- [183] R. Corke and T. Sjöstrand, *Interleaved Parton Showers and Tuning Prospects*, *JHEP* **03** (2011) 032, [arXiv:1011.1759 \[hep-ph\]](#).
- [184] CDF Collaboration, D. Acosta et al., *The underlying event in hard interactions at the Tevatron  $\bar{p}p$  collider*, *Phys. Rev.* **D70** (2004) 072002, [arXiv:hep-ex/0404004 \[hep-ex\]](#).
- [185] *ATLAS Run 1 Pythia8 tunes*, ATL-PHYS-PUB-2014-021, CERN, Geneva, Nov, 2014.  
<http://cds.cern.ch/record/1966419>.
- [186] P. Z. Skands, *Soft-QCD and UE spectra in pp collisions at very high CM energies (a Snowmass white paper)*, [arXiv:1308.2813 \[hep-ph\]](#).
- [187] M. L. Mangano, *Production of electroweak bosons at hadron colliders: theoretical aspects*, [arXiv:1512.00220 \[hep-ph\]](#).
- [188] C. Anastasiou, L. J. Dixon, K. Melnikov, and F. Petriello, *High precision QCD at hadron colliders: Electroweak gauge boson rapidity distributions at NNLO*, *Phys. Rev.* **D69** (2004) 094008, [arXiv:hep-ph/0312266](#).
- [189] S. Catani, L. Cieri, G. Ferrera, D. de Florian, and M. Grazzini, *Vector boson production at hadron colliders: a fully exclusive QCD calculation at NNLO*, *Phys. Rev. Lett.* **103** (2009) 082001, [arXiv:0903.2120 \[hep-ph\]](#).
- [190] R. K. Ellis, G. Martinelli, and R. Petronzio, *Lepton Pair Production at Large Transverse Momentum in Second Order QCD*, *Nucl. Phys.* **B211** (1983) 106.
- [191] P. B. Arnold and M. H. Reno, *The Complete Computation of High  $p(t)$  W and Z Production in 2nd Order QCD*, *Nucl. Phys.* **B319** (1989) 37. [Erratum: *Nucl. Phys.*B330,284(1990)].

- [192] R. J. Gonsalves, J. Pawłowski, and C.-F. Wai, *QCD Radiative Corrections to Electroweak Boson Production at Large Transverse Momentum in Hadron Collisions*, *Phys. Rev.* **D40** (1989) 2245.
- [193] R. Boughezal, C. Focke, X. Liu, and F. Petriello, *W-boson production in association with a jet at next-to-next-to-leading order in perturbative QCD*, *Phys. Rev. Lett.* **115** (2015) no. 6, 062002, [arXiv:1504.02131 \[hep-ph\]](#).
- [194] A. Gehrmann-De Ridder, T. Gehrmann, E. W. N. Glover, A. Huss, and T. A. Morgan, *Precise QCD predictions for the production of a Z boson in association with a hadronic jet*, [arXiv:1507.02850 \[hep-ph\]](#).
- [195] S. Catani, D. de Florian, and M. Grazzini, *Universality of nonleading logarithmic contributions in transverse momentum distributions*, *Nucl. Phys.* **B596** (2001) 299–312, [arXiv:hep-ph/0008184 \[hep-ph\]](#).
- [196] G. Bozzi, S. Catani, D. de Florian, and M. Grazzini, *Transverse-momentum resummation and the spectrum of the Higgs boson at the LHC*, *Nucl. Phys.* **B737** (2006) 73–120, [arXiv:hep-ph/0508068 \[hep-ph\]](#).
- [197] G. Bozzi, S. Catani, D. de Florian, and M. Grazzini, *Higgs boson production at the LHC: Transverse-momentum resummation and rapidity dependence*, *Nucl. Phys.* **B791** (2008) 1–19, [arXiv:0705.3887 \[hep-ph\]](#).
- [198] G. Bozzi, S. Catani, G. Ferrera, D. de Florian, and M. Grazzini, *Transverse-momentum resummation: A Perturbative study of Z production at the Tevatron*, *Nucl. Phys.* **B815** (2009) 174–197, [arXiv:0812.2862 \[hep-ph\]](#).
- [199] G. Bozzi, S. Catani, G. Ferrera, D. de Florian, and M. Grazzini, *Production of Drell-Yan lepton pairs in hadron collisions: Transverse-momentum resummation at next-to-next-to-leading logarithmic accuracy*, *Phys. Lett.* **B696** (2011) 207–213, [arXiv:1007.2351 \[hep-ph\]](#).
- [200] S. Catani, D. de Florian, G. Ferrera, and M. Grazzini, *Vector boson production at hadron colliders: transverse-momentum resummation and leptonic decay*, *JHEP* **12** (2015) 047, [arXiv:1507.06937 \[hep-ph\]](#).
- [201] Particle Data Group Collaboration, K. A. Olive et al., *Review of Particle Physics*, *Chin. Phys.* **C38** (2014) 090001.
- [202] R. Boughezal, J. M. Campbell, R. K. Ellis, C. Focke, W. T. Giele, X. Liu, and F. Petriello, *Z-boson production in association with a jet at next-to-next-to-leading order in perturbative QCD*, [arXiv:1512.01291 \[hep-ph\]](#).
- [203] M. Cacciari, G. P. Salam, and G. Soyez, *The Anti-k(t) jet clustering algorithm*, *JHEP* **04** (2008) 063, [arXiv:0802.1189 \[hep-ph\]](#).
- [204] A. Denner, S. Dittmaier, T. Kasprzik, and A. Muck, *Electroweak corrections to dilepton + jet production at hadron colliders*, *JHEP* **06** (2011) 069, [arXiv:1103.0914 \[hep-ph\]](#).
- [205] M. Rubin, G. P. Salam, and S. Sapeta, *Giant QCD K-factors beyond NLO*, *JHEP* **09** (2010) 084, [arXiv:1006.2144 \[hep-ph\]](#).
- [206] S. Moretti, M. R. Nolten, and D. A. Ross, *Weak corrections to four-parton processes*, *Nucl. Phys.* **B759** (2006) 50–82, [arXiv:hep-ph/0606201 \[hep-ph\]](#).
- [207] G. Bell, J. H. Kuhn, and J. Rittinger, *Electroweak Sudakov Logarithms and Real Gauge-Boson Radiation in the TeV Region*, *Eur. Phys. J.* **C70** (2010) 659–671, [arXiv:1004.4117 \[hep-ph\]](#).
- [208] S. Dittmaier, A. Huss, and C. Speckner, *Weak radiative corrections to dijet production at hadron colliders*, *JHEP* **11** (2012) 095, [arXiv:1210.0438 \[hep-ph\]](#).
- [209] J. R. Christiansen and T. Sjöstrand, *Weak Gauge Boson Radiation in Parton Showers*, *JHEP* **04** (2014) 115, [arXiv:1401.5238 \[hep-ph\]](#).
- [210] A. Hook and A. Katz, *Unbroken SU(2) at a 100 TeV collider*, *JHEP* **09** (2014) 175, [arXiv:1407.2607 \[hep-ph\]](#).

- [211] J. Chen, T. Han, R. Ruiz, and B. Tweedie. In preparation.
- [212] M. Cacciari, G. P. Salam, and G. Soyez, *FastJet User Manual*, *Eur. Phys. J.* **C72** (2012) 1896, [arXiv:1111.6097 \[hep-ph\]](#).
- [213] T. Gleisberg, S. Hoeche, F. Krauss, A. Schalicke, S. Schumann, and J.-C. Winter, *SHERPA 1. alpha: A Proof of concept version*, *JHEP* **02** (2004) 056, [arXiv:hep-ph/0311263 \[hep-ph\]](#).
- [214] T. Gleisberg and S. Hoeche, *Comix, a new matrix element generator*, *JHEP* **0812** (2008) 039, [arXiv:0808.3674 \[hep-ph\]](#).
- [215] C. F. Berger, Z. Bern, L. J. Dixon, F. Febres Cordero, D. Forde, H. Ita, D. A. Kosower, and D. Maitre, *An Automated Implementation of On-Shell Methods for One-Loop Amplitudes*, *Phys. Rev.* **D78** (2008) 036003, [arXiv:0803.4180 \[hep-ph\]](#).
- [216] C. F. Berger, Z. Bern, L. J. Dixon, F. Febres Cordero, D. Forde, T. Gleisberg, H. Ita, D. A. Kosower, and D. Maitre, *Precise Predictions for  $W + 3$  Jet Production at Hadron Colliders*, *Phys. Rev. Lett.* **102** (2009) 222001, [arXiv:0902.2760 \[hep-ph\]](#).
- [217] C. F. Berger, Z. Bern, L. J. Dixon, F. Febres Cordero, D. Forde, T. Gleisberg, H. Ita, D. A. Kosower, and D. Maitre, *Next-to-Leading Order QCD Predictions for  $W+3$ -Jet Distributions at Hadron Colliders*, *Phys. Rev.* **D80** (2009) 074036, [arXiv:0907.1984 \[hep-ph\]](#).
- [218] C. F. Berger, Z. Bern, L. J. Dixon, F. Febres Cordero, D. Forde, T. Gleisberg, H. Ita, D. A. Kosower, and D. Maitre, *Precise Predictions for  $W + 4$  Jet Production at the Large Hadron Collider*, *Phys. Rev. Lett.* **106** (2011) 092001, [arXiv:1009.2338 \[hep-ph\]](#).
- [219] Z. Bern, L. J. Dixon, F. Febres Cordero, S. Höche, H. Ita, D. A. Kosower, D. Maitre, and K. J. Ozeren, *Next-to-Leading Order  $W + 5$ -Jet Production at the LHC*, *Phys. Rev.* **D88** (2013) no. 1, 014025, [arXiv:1304.1253 \[hep-ph\]](#).
- [220] H. Ita, Z. Bern, L. J. Dixon, F. Febres Cordero, D. A. Kosower, and D. Maitre, *Precise Predictions for  $Z + 4$  Jets at Hadron Colliders*, *Phys. Rev.* **D85** (2012) 031501, [arXiv:1108.2229 \[hep-ph\]](#).
- [221] C. F. Berger, Z. Bern, L. J. Dixon, F. Febres Cordero, D. Forde, T. Gleisberg, H. Ita, D. A. Kosower, and D. Maitre, *Next-to-Leading Order QCD Predictions for  $Z, \gamma^* + 3$ -Jet Distributions at the Tevatron*, *Phys. Rev.* **D82** (2010) 074002, [arXiv:1004.1659 \[hep-ph\]](#).
- [222] S. Catani and M. H. Seymour, *The Dipole formalism for the calculation of QCD jet cross-sections at next-to-leading order*, *Phys. Lett.* **B378** (1996) 287–301, [arXiv:hep-ph/9602277 \[hep-ph\]](#).
- [223] T. Gleisberg and F. Krauss, *Automating dipole subtraction for QCD NLO calculations*, *Eur.Phys.J.* **C53** (2008) 501–523, [arXiv:0709.2881 \[hep-ph\]](#).
- [224] S. Catani, F. Krauss, R. Kuhn, and B. Webber, *QCD matrix elements + parton showers*, *JHEP* **0111** (2001) 063, [arXiv:hep-ph/0109231 \[hep-ph\]](#).
- [225] S. Hoeche, F. Krauss, S. Schumann, and F. Siegert, *QCD matrix elements and truncated showers*, *JHEP* **0905** (2009) 053, [arXiv:0903.1219 \[hep-ph\]](#).
- [226] Z. Nagy and D. E. Soper, *Matching parton showers to NLO computations*, *JHEP* **0510** (2005) 024, [arXiv:hep-ph/0503053 \[hep-ph\]](#).
- [227] S. Schumann and F. Krauss, *A Parton shower algorithm based on Catani-Seymour dipole factorisation*, *JHEP* **03** (2008) 038, [arXiv:0709.1027 \[hep-ph\]](#).
- [228] S. Frixione and B. R. Webber, *Matching NLO QCD computations and parton shower simulations*, *JHEP* **0206** (2002) 029, [arXiv:hep-ph/0204244 \[hep-ph\]](#).
- [229] S. Hoeche, F. Krauss, M. Schonherr, and F. Siegert, *NLO matrix elements and truncated showers*, *JHEP* **1108** (2011) 123, [arXiv:1009.1127 \[hep-ph\]](#).
- [230] S. Hoeche, F. Krauss, M. Schonherr, and F. Siegert, *A critical appraisal of NLO+PS matching methods*, *JHEP* **1209** (2012) 049, [arXiv:1111.1220 \[hep-ph\]](#).

- [231] T. Gehrmann, S. Hoche, F. Krauss, M. Schonherr, and F. Siegert, *NLO QCD matrix elements + parton showers in  $e^+e^- \rightarrow$  hadrons*, **JHEP** **01** (2013) 144, [arXiv:1207.5031 \[hep-ph\]](#).
- [232] S. Hoeche, F. Krauss, M. Schonherr, and F. Siegert, *QCD matrix elements + parton showers: The NLO case*, **JHEP** **1304** (2013) 027, [arXiv:1207.5030 \[hep-ph\]](#).
- [233] A. Denner, S. Dittmaier, M. Roth, and D. Wackerroth,  *$O(\alpha)$  corrections to  $e^+e^- \rightarrow WW \rightarrow$  four fermions (+ gamma): First numerical results from RACOON WW*, **Phys. Lett.** **B475** (2000) 127–134, [arXiv:hep-ph/9912261 \[hep-ph\]](#).
- [234] C.-H. Kom and W. J. Stirling, *Charge asymmetry in  $W$  + jets production at the LHC*, **Eur. Phys. J.** **C69** (2010) 67–73, [arXiv:1004.3404 \[hep-ph\]](#).
- [235] S. Catani and B. R. Webber, *Infrared safe but infinite: Soft gluon divergences inside the physical region*, **JHEP** **10** (1997) 005, [arXiv:hep-ph/9710333 \[hep-ph\]](#).
- [236] J. M. Campbell and R. K. Ellis, *An Update on vector boson pair production at hadron colliders*, **Phys.Rev.** **D60** (1999) 113006, [arXiv:hep-ph/9905386 \[hep-ph\]](#).
- [237] J. M. Campbell, R. K. Ellis, and C. Williams, *Vector boson pair production at the LHC*, **JHEP** **1107** (2011) 018, [arXiv:1105.0020 \[hep-ph\]](#).
- [238] J. M. Campbell, R. K. Ellis, and W. T. Giele, *A Multi-Threaded Version of MCFM*, **Eur.Phys.J.** **C75** (2015) no. 6, 246, [arXiv:1503.06182 \[physics.comp-ph\]](#).
- [239] K. Hamilton, P. Nason, and G. Zanderighi, *MINLO: Multi-Scale Improved NLO*, **JHEP** **10** (2012) 155, [arXiv:1206.3572 \[hep-ph\]](#).
- [240] P. Nason, *A New method for combining NLO QCD with shower Monte Carlo algorithms*, **JHEP** **0411** (2004) 040, [arXiv:hep-ph/0409146 \[hep-ph\]](#).
- [241] S. Frixione, P. Nason, and C. Oleari, *Matching NLO QCD computations with Parton Shower simulations: the POWHEG method*, **JHEP** **11** (2007) 070, [arXiv:0709.2092 \[hep-ph\]](#).
- [242] S. Alioli, P. Nason, C. Oleari, and E. Re, *A general framework for implementing NLO calculations in shower Monte Carlo programs: the POWHEG BOX*, **JHEP** **1006** (2010) 043, [arXiv:1002.2581 \[hep-ph\]](#).
- [243] G. Luisoni, C. Oleari, and F. Tramontano,  *$Wb\bar{b}j$  production at NLO with POWHEG+MiNLO*, **JHEP** **04** (2015) 161, [arXiv:1502.01213 \[hep-ph\]](#).
- [244] J. M. Campbell, R. K. Ellis, R. Frederix, P. Nason, C. Oleari, et al., *NLO Higgs Boson Production Plus One and Two Jets Using the POWHEG BOX, MadGraph4 and MCFM*, **JHEP** **1207** (2012) 092, [arXiv:1202.5475 \[hep-ph\]](#).
- [245] T. Stelzer and W. F. Long, *Automatic generation of tree level helicity amplitudes*, **Comput. Phys. Commun.** **81** (1994) 357–371, [arXiv:hep-ph/9401258 \[hep-ph\]](#).
- [246] J. Alwall, P. Demin, S. de Visscher, R. Frederix, M. Herquet, et al., *MadGraph/MadEvent v4: The New Web Generation*, **JHEP** **0709** (2007) 028, [arXiv:0706.2334 \[hep-ph\]](#).
- [247] G. Cullen et al., *Automated One-Loop Calculations with GoSam*, [arXiv:1111.2034 \[hep-ph\]](#).
- [248] G. Cullen et al., *GOSAM-2.0: a tool for automated one-loop calculations within the Standard Model and beyond*, **Eur. Phys. J.** **C74** (2014) no. 8, 3001, [arXiv:1404.7096 \[hep-ph\]](#).
- [249] T. Binoth, F. Boudjema, G. Dissertori, A. Lazopoulos, A. Denner, et al., *A Proposal for a standard interface between Monte Carlo tools and one-loop programs*, **Comput.Phys.Commun.** **181** (2010) 1612–1622, [arXiv:1001.1307 \[hep-ph\]](#).
- [250] S. Alioli et al., *Update of the Binoth Les Houches Accord for a standard interface between Monte Carlo tools and one-loop programs*, **Comput. Phys. Commun.** **185** (2014) 560–571, [arXiv:1308.3462 \[hep-ph\]](#).
- [251] G. Luisoni, P. Nason, C. Oleari, and F. Tramontano,  *$HW^\pm/HZ + 0$  and 1 jet at NLO with the POWHEG BOX interfaced to GoSam and their merging within MiNLO*, **JHEP** **1310** (2013) 083, [arXiv:1306.2542 \[hep-ph\]](#).

- [252] P. Nogueira, *Automatic Feynman graph generation*, *J. Comput. Phys.* **105** (1993) 279–289.
- [253] J. Kuipers, T. Ueda, J. A. M. Vermaseren, and J. Vollinga, *FORM version 4.0*, *Comput. Phys. Commun.* **184** (2013) 1453–1467, [arXiv:1203.6543 \[cs.SC\]](#).
- [254] G. Cullen, M. Koch-Janusz, and T. Reiter, *Spinney: A Form Library for Helicity Spinors*, *Comput. Phys. Commun.* **182** (2011) 2368–2387, [arXiv:1008.0803 \[hep-ph\]](#).
- [255] H. van Deurzen, G. Luisoni, P. Mastrolia, E. Mirabella, G. Ossola, and T. Peraro, *Multi-leg One-loop Massive Amplitudes from Integrand Reduction via Laurent Expansion*, *JHEP* **03** (2014) 115, [arXiv:1312.6678 \[hep-ph\]](#).
- [256] T. Peraro, *Ninja: Automated Integrand Reduction via Laurent Expansion for One-Loop Amplitudes*, *Comput. Phys. Commun.* **185** (2014) 2771–2797, [arXiv:1403.1229 \[hep-ph\]](#).
- [257] P. Mastrolia, E. Mirabella, and T. Peraro, *Integrand reduction of one-loop scattering amplitudes through Laurent series expansion*, *JHEP* **06** (2012) 095, [arXiv:1203.0291 \[hep-ph\]](#). [Erratum: JHEP11,128(2012)].
- [258] A. van Hameren, *OneLOop: For the evaluation of one-loop scalar functions*, *Comput.Phys.Commun.* **182** (2011) 2427–2438, [arXiv:1007.4716 \[hep-ph\]](#).
- [259] G. Cullen, J. P. Guillet, G. Heinrich, T. Kleinschmidt, E. Pilon, T. Reiter, and M. Rodgers, *Golem95C: A library for one-loop integrals with complex masses*, *Comput. Phys. Commun.* **182** (2011) 2276–2284, [arXiv:1101.5595 \[hep-ph\]](#).
- [260] J. C. Collins, F. Wilczek, and A. Zee, *Low-Energy Manifestations of Heavy Particles: Application to the Neutral Current*, *Phys. Rev.* **D18** (1978) 242.
- [261] M. Cacciari and G. P. Salam, *Dispelling the  $N^3$  myth for the  $k_t$  jet-finder*, *Phys. Lett.* **B641** (2006) 57–61, [arXiv:hep-ph/0512210 \[hep-ph\]](#).
- [262] J. M. Butterworth, A. R. Davison, M. Rubin, and G. P. Salam, *Jet substructure as a new Higgs search channel at the LHC*, *Phys.Rev.Lett.* **100** (2008) 242001, [arXiv:0802.2470 \[hep-ph\]](#).
- [263] Y. L. Dokshitzer, G. D. Leder, S. Moretti, and B. R. Webber, *Better jet clustering algorithms*, *JHEP* **08** (1997) 001, [arXiv:hep-ph/9707323 \[hep-ph\]](#).
- [264] F. Cascioli, T. Gehrmann, M. Grazzini, S. Kallweit, P. Maierhöfer, A. von Manteuffel, S. Pozzorini, D. Rathlev, L. Tancredi, and E. Weihs, *ZZ production at hadron colliders in NNLO QCD*, *Phys. Lett.* **B735** (2014) 311–313, [arXiv:1405.2219 \[hep-ph\]](#).
- [265] T. Gehrmann, M. Grazzini, S. Kallweit, P. Maierhöfer, A. von Manteuffel, S. Pozzorini, D. Rathlev, and L. Tancredi,  *$W^+W^-$  Production at Hadron Colliders in Next to Next to Leading Order QCD*, *Phys. Rev. Lett.* **113** (2014) no. 21, 212001, [arXiv:1408.5243 \[hep-ph\]](#).
- [266] CMS Collaboration, S. Chatrchyan et al., *Measurement of the Production Cross Section for Pairs of Isolated Photons in  $pp$  collisions at  $\sqrt{s} = 7$  TeV*, *JHEP* **01** (2012) 133, [arXiv:1110.6461 \[hep-ex\]](#).
- [267] CDF Collaboration, T. Aaltonen et al., *Measurement of the Cross Section for Prompt Isolated Diphoton Production in  $p\bar{p}$  Collisions at  $\sqrt{s} = 1.96$  TeV*, *Phys. Rev.* **D84** (2011) 052006, [arXiv:1106.5131 \[hep-ex\]](#).
- [268] CMS Collaboration, S. Chatrchyan et al., *Measurement of differential cross sections for the production of a pair of isolated photons in  $pp$  collisions at  $\sqrt{s} = 7$  TeV*, *Eur. Phys. J.* **C74** (2014) no. 11, 3129, [arXiv:1405.7225 \[hep-ex\]](#).
- [269] D0 Collaboration, V. M. Abazov et al., *Measurement of the differential cross sections for isolated direct photon pair production in  $p\bar{p}$  collisions at  $\sqrt{s} = 1.96$  TeV*, *Phys. Lett.* **B725** (2013) 6–14, [arXiv:1301.4536 \[hep-ex\]](#).
- [270] ATLAS Collaboration, G. Aad et al., *Measurement of the isolated di-photon cross-section in  $pp$  collisions at  $\sqrt{s} = 7$  TeV with the ATLAS detector*, *Phys. Rev.* **D85** (2012) 012003, [arXiv:1107.0581 \[hep-ex\]](#).

- [271] ATLAS Collaboration, G. Aad et al., *Measurement of isolated-photon pair production in pp collisions at  $\sqrt{s} = 7$  TeV with the ATLAS detector*, *JHEP* **01** (2013) 086, [arXiv:1211.1913 \[hep-ex\]](#).
- [272] CMS Collaboration, S. Chatrchyan et al., *Observation of a new boson at a mass of 125 GeV with the CMS experiment at the LHC*, *Phys. Lett.* **B716** (2012) 30–61, [arXiv:1207.7235 \[hep-ex\]](#).
- [273] ATLAS Collaboration, G. Aad et al., *Observation of a new particle in the search for the Standard Model Higgs boson with the ATLAS detector at the LHC*, *Phys. Lett.* **B716** (2012) 1–29, [arXiv:1207.7214 \[hep-ex\]](#).
- [274] ATLAS Collaboration, G. Aad et al., *Search for diphoton events with large missing transverse momentum in 7 TeV proton-proton collision data with the ATLAS detector*, *Phys. Lett.* **B718** (2012) 411–430, [arXiv:1209.0753 \[hep-ex\]](#).
- [275] CMS Collaboration, S. Chatrchyan et al., *Search for new physics in events with photons, jets, and missing transverse energy in pp collisions at  $\sqrt{s} = 7$  TeV*, *JHEP* **03** (2013) 111, [arXiv:1211.4784 \[hep-ex\]](#).
- [276] ATLAS Collaboration, G. Aad et al., *Search for Extra Dimensions in diphoton events using proton-proton collisions recorded at  $\sqrt{s} = 7$  TeV with the ATLAS detector at the LHC*, *New J. Phys.* **15** (2013) 043007, [arXiv:1210.8389 \[hep-ex\]](#).
- [277] CMS Collaboration, S. Chatrchyan et al., *Search for supersymmetry in events with photons and low missing transverse energy in pp collisions at  $\sqrt{s} = 7$  TeV*, *Phys. Lett.* **B719** (2013) 42–61, [arXiv:1210.2052 \[hep-ex\]](#).
- [278] CMS Collaboration, *Search for new physics in high mass diphoton events in proton-proton collisions at  $\sqrt{s} = 13$  TeV*, CMS-PAS-EXO-15-004, CERN, Geneva, 2015. <http://cds.cern.ch/record/2114808>.
- [279] *Search for resonances decaying to photon pairs in  $3.2 \text{ fb}^{-1}$  of pp collisions at  $\sqrt{s} = 13$  TeV with the ATLAS detector*, ATLAS-CONF-2015-081, CERN, Geneva, Dec, 2015. <https://cds.cern.ch/record/2114853>.
- [280] T. Binoth, J. P. Guillet, E. Pilon, and M. Werlen, *A Full next-to-leading order study of direct photon pair production in hadronic collisions*, *Eur. Phys. J.* **C16** (2000) 311–330, [arXiv:hep-ph/9911340 \[hep-ph\]](#).
- [281] Z. Bern, L. J. Dixon, and C. Schmidt, *Isolating a light Higgs boson from the diphoton background at the CERN LHC*, *Phys. Rev.* **D66** (2002) 074018, [arXiv:hep-ph/0206194 \[hep-ph\]](#).
- [282] C. Balazs, E. L. Berger, P. M. Nadolsky, and C. P. Yuan, *Calculation of prompt diphoton production cross-sections at Tevatron and LHC energies*, *Phys. Rev.* **D76** (2007) 013009, [arXiv:0704.0001 \[hep-ph\]](#).
- [283] S. Catani, L. Cieri, D. de Florian, G. Ferrera, and M. Grazzini, *Diphoton production at hadron colliders: a fully-differential QCD calculation at NNLO*, *Phys. Rev. Lett.* **108** (2012) 072001, [arXiv:1110.2375 \[hep-ph\]](#).
- [284] V. Del Duca, F. Maltoni, Z. Nagy, and Z. Trocsanyi, *QCD radiative corrections to prompt diphoton production in association with a jet at hadron colliders*, *JHEP* **0304** (2003) 059, [arXiv:hep-ph/0303012 \[hep-ph\]](#).
- [285] T. Gehrmann, N. Greiner, and G. Heinrich, *Photon isolation effects at NLO in  $\gamma\gamma + \text{jet}$  final states in hadronic collisions*, *JHEP* **06** (2013) 058, [arXiv:1303.0824 \[hep-ph\]](#). [Erratum: *JHEP*06,076(2014)].
- [286] Z. Bern, L. Dixon, F. Febres Cordero, S. Hoeche, H. Ita, et al., *Next-to-Leading Order Gamma Gamma + 2-Jet Production at the LHC*, [arXiv:1402.4127 \[hep-ph\]](#).
- [287] T. Gehrmann, N. Greiner, and G. Heinrich, *Precise QCD predictions for the production of a photon pair in association with two jets*, *Phys.Rev.Lett.* **111** (2013) 222002, [arXiv:1308.3660](#)

- [hep-ph].
- [288] S. Badger, A. Guffanti, and V. Yundin, *Next-to-leading order QCD corrections to di-photon production in association with up to three jets at the Large Hadron Collider*, [arXiv:1312.5927](#) [hep-ph].
- [289] L. Cieri, F. Coradeschi, and D. de Florian, *Diphoton production at hadron colliders: transverse-momentum resummation at next-to-next-to-leading logarithmic accuracy*, *JHEP* **06** (2015) 185, [arXiv:1505.03162](#) [hep-ph].
- [290] S. Frixione, *Isolated photons in perturbative QCD*, *Phys. Lett.* **B429** (1998) 369–374, [arXiv:hep-ph/9801442](#) [hep-ph].
- [291] J. R. Andersen et al., *Les Houches 2013: Physics at TeV Colliders: Standard Model Working Group Report*, [arXiv:1405.1067](#) [hep-ph].
- [292] A. D. Martin, W. J. Stirling, R. S. Thorne, and G. Watt, *Parton distributions for the LHC*, *Eur. Phys. J.* **C63** (2009) 189–285, [arXiv:0901.0002](#) [hep-ph].
- [293] D. Zeppenfeld and S. Willenbrock, *Probing the Three Vector - Boson Vertex at Hadron Colliders*, *Phys. Rev.* **D37** (1988) 1775.
- [294] T. Melia, P. Nason, R. Rontsch, and G. Zanderighi, *W+W-, WZ and ZZ production in the POWHEG BOX*, *JHEP* **1111** (2011) 078, [arXiv:1107.5051](#) [hep-ph].
- [295] P. Nason and G. Zanderighi, *W+W-, WZ and ZZ production in the POWHEG BOX V2*, [arXiv:1311.1365](#) [hep-ph].
- [296] L. Barze, M. Chiesa, G. Montagna, P. Nason, O. Nicrosini, F. Piccinini, and V. Prospero, *W $\gamma$  production in hadronic collisions using the POWHEG+MiNLO method*, *JHEP* **12** (2014) 039, [arXiv:1408.5766](#) [hep-ph].
- [297] CMS Collaboration, V. Khachatryan et al., *Measurement of the W<sup>+</sup>W<sup>-</sup> cross section in pp collisions at  $\sqrt{s} = 8$  TeV and limits on anomalous gauge couplings*, [arXiv:1507.03268](#) [hep-ex].
- [298] ATLAS Collaboration, G. Aad et al., *Measurement of the WW + WZ cross section and limits on anomalous triple gauge couplings using final states with one lepton, missing transverse momentum, and two jets with the ATLAS detector at  $\sqrt{s} = 7$  TeV*, *JHEP* **01** (2015) 049, [arXiv:1410.7238](#) [hep-ex].
- [299] B. M. Gavela, E. E. Jenkins, A. V. Manohar, and L. Merlo, *Analysis of General Power Counting Rules in Effective Field Theory*, [arXiv:1601.07551](#) [hep-ph].
- [300] J. M. Campbell, D. J. Miller, and T. Robens, *Next-to-Leading Order Predictions for WW+Jet Production*, *Phys. Rev.* **D92** (2015) no. 1, 014033, [arXiv:1506.04801](#) [hep-ph].
- [301] J. Campbell, D. Miller, and T. Robens, *W<sup>+</sup>W<sup>-</sup> + Jet: Compact Analytic Results*, in *Proceedings, 12th International Symposium on Radiative Corrections (Radcor 2015) and LoopFest XIV (Radiative Corrections for the LHC and Future Colliders)*. 2016. [arXiv:1601.03563](#) [hep-ph]. <http://inspirehep.net/record/1415284/files/arXiv:1601.03563.pdf>.
- [302] R. Britto, F. Cachazo, and B. Feng, *Generalized unitarity and one-loop amplitudes in N=4 super-Yang-Mills*, *Nucl.Phys.* **B725** (2005) 275–305, [arXiv:hep-th/0412103](#) [hep-th].
- [303] R. Britto, E. Buchbinder, F. Cachazo, and B. Feng, *One-loop amplitudes of gluons in SQCD*, *Phys.Rev.* **D72** (2005) 065012, [arXiv:hep-ph/0503132](#) [hep-ph].
- [304] R. Britto, B. Feng, and P. Mastrolia, *The Cut-constructible part of QCD amplitudes*, *Phys.Rev.* **D73** (2006) 105004, [arXiv:hep-ph/0602178](#) [hep-ph].
- [305] D. Forde, *Direct extraction of one-loop integral coefficients*, *Phys.Rev.* **D75** (2007) 125019, [arXiv:0704.1835](#) [hep-ph].
- [306] P. Mastrolia, *Double-Cut of Scattering Amplitudes and Stokes' Theorem*, *Phys.Lett.* **B678** (2009) 246–249, [arXiv:0905.2909](#) [hep-ph].

- [307] S. Badger, *Direct Extraction Of One Loop Rational Terms*, **JHEP** **0901** (2009) 049, [arXiv:0806.4600 \[hep-ph\]](#).
- [308] J. Pumplin, D. Stump, J. Huston, H. Lai, P. M. Nadolsky, et al., *New generation of parton distributions with uncertainties from global QCD analysis*, **JHEP** **0207** (2002) 012, [arXiv:hep-ph/0201195 \[hep-ph\]](#).
- [309] H.-L. Lai, M. Guzzi, J. Huston, Z. Li, P. M. Nadolsky, et al., *New parton distributions for collider physics*, **Phys.Rev.** **D82** (2010) 074024, [arXiv:1007.2241 \[hep-ph\]](#).
- [310] S. Frixione, P. Nason, and G. Ridolfi, *Strong corrections to  $WZ$  production at hadron colliders*, **Nucl.Phys.** **B383** (1992) 3–44.
- [311] S. Frixione, *A Next-to-leading order calculation of the cross-section for the production of  $W^+W^-$  pairs in hadronic collisions*, **Nucl.Phys.** **B410** (1993) 280–324.
- [312] ATLAS Collaboration, G. Aad et al., *Search for microscopic black holes and string balls in final states with leptons and jets with the ATLAS detector at  $\sqrt{s} = 8$  TeV*, **JHEP** **08** (2014) 103, [arXiv:1405.4254 \[hep-ex\]](#).
- [313] ATLAS Collaboration, G. Aad et al., *Search for supersymmetry in events containing a same-flavour opposite-sign dilepton pair, jets, and large missing transverse momentum in  $\sqrt{s} = 8$  TeV  $pp$  collisions with the ATLAS detector*, **Eur. Phys. J.** **C75** (2015) no. 7, 318, [arXiv:1503.03290 \[hep-ex\]](#).
- [314] K. Arnold, M. Bahr, G. Bozzi, F. Campanario, C. Englert, et al., *VBFNLO: A Parton level Monte Carlo for processes with electroweak bosons*, **Comput.Phys.Commun.** **180** (2009) 1661–1670, [arXiv:0811.4559 \[hep-ph\]](#).
- [315] C. Oleari and D. Zeppenfeld, *QCD corrections to electroweak  $\nu(l)jj$  and  $l+l-jj$  production*, **Phys. Rev.** **D69** (2004) 093004, [arXiv:hep-ph/0310156 \[hep-ph\]](#).
- [316] B. Jager, C. Oleari, and D. Zeppenfeld, *Next-to-leading order QCD corrections to  $W^+W^-$  production via vector-boson fusion*, **JHEP** **07** (2006) 015, [arXiv:hep-ph/0603177 \[hep-ph\]](#).
- [317] B. Jager, C. Oleari, and D. Zeppenfeld, *Next-to-leading order QCD corrections to  $Z$  boson pair production via vector-boson fusion*, **Phys. Rev.** **D73** (2006) 113006, [arXiv:hep-ph/0604200 \[hep-ph\]](#).
- [318] G. Bozzi, B. Jager, C. Oleari, and D. Zeppenfeld, *Next-to-leading order QCD corrections to  $W^+Z$  and  $W^-Z$  production via vector-boson fusion*, **Phys. Rev.** **D75** (2007) 073004, [arXiv:hep-ph/0701105 \[hep-ph\]](#).
- [319] B. Jager, C. Oleari, and D. Zeppenfeld, *Next-to-leading order QCD corrections to  $W^+W^+jj$  and  $W^-W^-jj$  production via weak-boson fusion*, **Phys. Rev.** **D80** (2009) 034022, [arXiv:0907.0580 \[hep-ph\]](#).
- [320] F. Campanario, M. Kerner, L. D. Ninh, and D. Zeppenfeld,  *$WZ$  Production in Association with Two Jets at Next-to-Leading Order in QCD*, **Phys. Rev. Lett.** **111** (2013) 052003, [arXiv:1305.1623 \[hep-ph\]](#).
- [321] F. Campanario, M. Kerner, L. D. Ninh, and D. Zeppenfeld, *Next-to-leading order QCD corrections to  $W^+W^+$  and  $W^-W^-$  production in association with two jets*, [arXiv:1311.6738 \[hep-ph\]](#).
- [322] F. Campanario, M. Kerner, L. D. Ninh, and D. Zeppenfeld, *Next-to-leading order QCD corrections to  $ZZ$  production in association with two jets*, **JHEP** **07** (2014) 148, [arXiv:1405.3972 \[hep-ph\]](#).
- [323] J. Alwall, M. Herquet, F. Maltoni, O. Mattelaer, and T. Stelzer, *MadGraph 5 : Going Beyond*, **JHEP** **06** (2011) 128, [arXiv:1106.0522 \[hep-ph\]](#).
- [324] B. Jager and G. Zanderighi, *NLO corrections to electroweak and QCD production of  $W^+W^+$  plus two jets in the POWHEGBOX*, **JHEP** **11** (2011) 055, [arXiv:1108.0864 \[hep-ph\]](#).

- [325] B. Jager, S. Schneider, and G. Zanderighi, *Next-to-leading order QCD corrections to electroweak  $Zjj$  production in the POWHEG BOX*, *JHEP* **1209** (2012) 083, [arXiv:1207.2626 \[hep-ph\]](#).
- [326] F. Schissler and D. Zeppenfeld, *Parton Shower Effects on W and Z Production via Vector Boson Fusion at NLO QCD*, *JHEP* **1304** (2013) 057, [arXiv:1302.2884](#).
- [327] B. Jager and G. Zanderighi, *Electroweak  $W+W$ -jj production at NLO in QCD matched with parton shower in the POWHEG-BOX*, *JHEP* **1304** (2013) 024, [arXiv:1301.1695 \[hep-ph\]](#).
- [328] B. Jager, A. Karlberg, and G. Zanderighi, *Electroweak  $ZZjj$  production in the Standard Model and beyond in the POWHEG-BOX V2*, [arXiv:1312.3252 \[hep-ph\]](#).
- [329] T. Melia, P. Nason, R. Rontsch, and G. Zanderighi,  *$W^+W^+$  plus dijet production in the POWHEGBOX*, *Eur. Phys. J.* **C71** (2011) 1670, [arXiv:1102.4846 \[hep-ph\]](#).
- [330] E. Re, *NLO corrections merged with parton showers for  $Z+2$  jets production using the POWHEG method*, *JHEP* **1210** (2012) 031, [arXiv:1204.5433 \[hep-ph\]](#).
- [331] J. M. Campbell, R. K. Ellis, P. Nason, and G. Zanderighi, *W and Z bosons in association with two jets using the POWHEG method*, *JHEP* **1308** (2013) 005, [arXiv:1303.5447 \[hep-ph\]](#).
- [332] S. Frixione, P. Nason, and G. Ridolfi, *A Positive-weight next-to-leading-order Monte Carlo for heavy flavour hadroproduction*, *JHEP* **0709** (2007) 126, [arXiv:0707.3088 \[hep-ph\]](#).
- [333] S. Alioli, S.-O. Moch, and P. Uwer, *Hadronic top-quark pair-production with one jet and parton showering*, *JHEP* **1201** (2012) 137, [arXiv:1110.5251 \[hep-ph\]](#).
- [334] C. Englert, B. Jager, M. Worek, and D. Zeppenfeld, *Observing Strongly Interacting Vector Boson Systems at the CERN Large Hadron Collider*, *Phys. Rev.* **D80** (2009) 035027, [arXiv:0810.4861 \[hep-ph\]](#).
- [335] M. Dasgupta, L. Magnea, and G. P. Salam, *Non-perturbative QCD effects in jets at hadron colliders*, *JHEP* **02** (2008) 055, [arXiv:0712.3014 \[hep-ph\]](#).
- [336] G. P. Salam, *Towards Jetography*, *Eur. Phys. J.* **C67** (2010) 637–686, [arXiv:0906.1833 \[hep-ph\]](#).
- [337] B. Auerbach, S. Chekanov, J. Love, J. Proudfoot, and A. V. Kotwal, *Sensitivity to new high-mass states decaying to  $t\bar{t}$  at a 100 TeV collider*, *Phys. Rev.* **D91** (2015) no. 3, 034014, [arXiv:1412.5951 \[hep-ph\]](#).
- [338] J. A. Aguilar-Saavedra, B. Fuks, and M. L. Mangano, *Pinning down top dipole moments with ultra-boosted tops*, *Phys. Rev.* **D91** (2015) 094021, [arXiv:1412.6654 \[hep-ph\]](#).
- [339] A. J. Larkoski, F. Maltoni, and M. Selvaggi, *Tracking down hyper-boosted top quarks*, *JHEP* **06** (2015) 032, [arXiv:1503.03347 \[hep-ph\]](#).
- [340] A. Abdesselam et al., *Boosted objects: A Probe of beyond the Standard Model physics*, *Eur. Phys. J.* **C71** (2011) 1661, [arXiv:1012.5412 \[hep-ph\]](#).
- [341] T. Plehn and M. Spannowsky, *Top Tagging*, *J. Phys.* **G39** (2012) 083001, [arXiv:1112.4441 \[hep-ph\]](#).
- [342] A. Altheimer et al., *Jet Substructure at the Tevatron and LHC: New results, new tools, new benchmarks*, *J. Phys.* **G39** (2012) 063001, [arXiv:1201.0008 \[hep-ph\]](#).
- [343] A. Altheimer et al., *Boosted objects and jet substructure at the LHC. Report of BOOST2012, held at IFIC Valencia, 23rd-27th of July 2012*, *Eur. Phys. J.* **C74** (2014) no. 3, 2792, [arXiv:1311.2708 \[hep-ex\]](#).
- [344] D. Adams et al., *Towards an Understanding of the Correlations in Jet Substructure*, *Eur. Phys. J.* **C75** (2015) no. 9, 409, [arXiv:1504.00679 \[hep-ph\]](#).
- [345] J. Thaler and K. Van Tilburg, *Identifying Boosted Objects with  $N$ -subjettiness*, *JHEP* **03** (2011) 015, [arXiv:1011.2268 \[hep-ph\]](#).
- [346] J. Thaler and K. Van Tilburg, *Maximizing Boosted Top Identification by Minimizing  $N$ -subjettiness*, *JHEP* **02** (2012) 093, [arXiv:1108.2701 \[hep-ph\]](#).

- [347] A. J. Larkoski, G. P. Salam, and J. Thaler, *Energy Correlation Functions for Jet Substructure*, [JHEP \*\*06\*\* \(2013\) 108](#), [arXiv:1305.0007 \[hep-ph\]](#).
- [348] A. J. Larkoski, I. Moutl, and D. Neill, *Building a Better Boosted Top Tagger*, [Phys. Rev. \*\*D91\*\* \(2015\) no. 3, 034035](#), [arXiv:1411.0665 \[hep-ph\]](#).
- [349] DELPHES 3 Collaboration, J. de Favereau, C. Delaere, P. Demin, A. Giammanco, V. Lemaitre, A. Mertens, and M. Selvaggi, *DELPHES 3, A modular framework for fast simulation of a generic collider experiment*, [JHEP \*\*02\*\* \(2014\) 057](#), [arXiv:1307.6346 \[hep-ex\]](#).
- [350] CMS Collaboration, G. L. Bayatian et al., *CMS physics: Technical design report*, CERN-LHCC-2006-001, CMS-TDR-008-1, 2006.
- [351] GEANT4 Collaboration, S. Agostinelli et al., *GEANT4: A Simulation toolkit*, [Nucl. Instrum. Meth. \*\*A506\*\* \(2003\) 250–303](#).
- [352] ATLAS Collaboration, G. Aad et al., *Performance of jet substructure techniques for large- $R$  jets in proton-proton collisions at  $\sqrt{s} = 7$  TeV using the ATLAS detector*, [JHEP \*\*09\*\* \(2013\) 076](#), [arXiv:1306.4945 \[hep-ex\]](#).
- [353] CMS Collaboration, V. Khachatryan et al., *Identification techniques for highly boosted  $W$  bosons that decay into hadrons*, [JHEP \*\*12\*\* \(2014\) 017](#), [arXiv:1410.4227 \[hep-ex\]](#).
- [354] ATLAS Collaboration, G. Aad et al., *Search for high-mass diboson resonances with boson-tagged jets in proton-proton collisions at  $\sqrt{s} = 8$  TeV with the ATLAS detector*, [JHEP \*\*12\*\* \(2015\) 055](#), [arXiv:1506.00962 \[hep-ex\]](#).
- [355] ATLAS Collaboration, G. Aad et al., *Search for resonant diboson production in the  $\ell q \bar{q}$  final state in  $pp$  collisions at  $\sqrt{s} = 8$  TeV with the ATLAS detector*, [Eur. Phys. J. \*\*C75\*\* \(2015\) 69](#), [arXiv:1409.6190 \[hep-ex\]](#).
- [356] ATLAS Collaboration, G. Aad et al., *Search for production of  $WW/WZ$  resonances decaying to a lepton, neutrino and jets in  $pp$  collisions at  $\sqrt{s} = 8$  TeV with the ATLAS detector*, [Eur. Phys. J. \*\*C75\*\* \(2015\) no. 5, 209](#), [arXiv:1503.04677 \[hep-ex\]](#). [Erratum: [Eur. Phys. J. \*\*C75\*\*,370\(2015\)](#)].
- [357] CMS Collaboration, V. Khachatryan et al., *Search for A Massive Resonance Decaying into a Higgs Boson and a  $W$  or  $Z$  Boson in Hadronic Final States in Proton-Proton Collisions at  $\sqrt{s} = 8$  TeV*, [arXiv:1506.01443 \[hep-ex\]](#).
- [358] CMS Collaboration, V. Khachatryan et al., *Search for Narrow High-Mass Resonances in proton-proton Collisions at  $\sqrt{s} = 8$  TeV Decaying to a  $Z$  and a Higgs Boson*, [Phys. Lett. \*\*B748\*\* \(2015\) 255–277](#), [arXiv:1502.04994 \[hep-ex\]](#).
- [359] CMS Collaboration, V. Khachatryan et al., *Search for massive resonances in dijet systems containing jets tagged as  $W$  or  $Z$  boson decays in  $pp$  collisions at  $\sqrt{s} = 8$  TeV*, [JHEP \*\*08\*\* \(2014\) 173](#), [arXiv:1405.1994 \[hep-ex\]](#).
- [360] CMS Collaboration, V. Khachatryan et al., *Search for massive resonances decaying into pairs of boosted bosons in semi-leptonic final states at  $\sqrt{s} = 8$  TeV*, [JHEP \*\*08\*\* \(2014\) 174](#), [arXiv:1405.3447 \[hep-ex\]](#).
- [361] S. Oryn, X. Rouby, and V. Lemaitre, *DELPHES, a framework for fast simulation of a generic collider experiment*, [arXiv:0903.2225 \[hep-ph\]](#).
- [362] A. Hocker et al., *TMVA - Toolkit for Multivariate Data Analysis*, PoS [ACAT \(2007\) 040](#), [arXiv:physics/0703039 \[PHYSICS\]](#).
- [363] L. G. Almeida, M. Backovic, M. Cliche, S. J. Lee, and M. Perelstein, *Playing Tag with ANN: Boosted Top Identification with Pattern Recognition*, [JHEP \*\*07\*\* \(2015\) 086](#), [arXiv:1501.05968 \[hep-ph\]](#).
- [364] L. de Oliveira, M. Kagan, L. Mackey, B. Nachman, and A. Schwartzman, *Jet-Images – Deep Learning Edition*, [arXiv:1511.05190 \[hep-ph\]](#).
- [365] F. Krauss, *Matrix elements and parton showers in hadronic interactions*, [JHEP \*\*0208\*\* \(2002\) 015](#),

- [arXiv:hep-ph/0205283](#) [hep-ph].
- [366] L. Lonnblad, *Correcting the color dipole cascade model with fixed order matrix elements*, *JHEP* **0205** (2002) 046, [arXiv:hep-ph/0112284](#) [hep-ph].
- [367] L. Lonnblad and S. Prestel, *Matching Tree-Level Matrix Elements with Interleaved Showers*, *JHEP* **1203** (2012) 019, [arXiv:1109.4829](#) [hep-ph].
- [368] L. Lonnblad and S. Prestel, *Unitarising Matrix Element + Parton Shower merging*, *JHEP* **1302** (2013) 094, [arXiv:1211.4827](#) [hep-ph].
- [369] M. L. Mangano, M. Moretti, and R. Pittau, *Multijet matrix elements and shower evolution in hadronic collisions:  $Wb\bar{b} + n$  jets as a case study*, *Nucl. Phys.* **B632** (2002) 343–362, [arXiv:hep-ph/0108069](#) [hep-ph].
- [370] M. L. Mangano, M. Moretti, F. Piccinini, and M. Treccani, *Matching matrix elements and shower evolution for top-quark production in hadronic collisions*, *JHEP* **0701** (2007) 013, [arXiv:hep-ph/0611129](#) [hep-ph].
- [371] K. Hamilton, P. Richardson, and J. Tully, *A Modified CKKW matrix element merging approach to angular-ordered parton showers*, *JHEP* **0911** (2009) 038, [arXiv:0905.3072](#) [hep-ph].
- [372] J. Alwall, S. Hoche, F. Krauss, N. Lavesson, L. Lonnblad, et al., *Comparative study of various algorithms for the merging of parton showers and matrix elements in hadronic collisions*, *Eur.Phys.J.* **C53** (2008) 473–500, [arXiv:0706.2569](#) [hep-ph].
- [373] S. Badger, B. Biedermann, P. Uwer, and V. Yundin, *Numerical evaluation of virtual corrections to multi-jet production in massless QCD*, *Comput.Phys.Commun.* **184** (2013) 1981–1998, [arXiv:1209.0100](#) [hep-ph].
- [374] S. Frixione and G. Ridolfi, *Jet photoproduction at HERA*, *Nucl. Phys.* **B507** (1997) 315–333, [arXiv:hep-ph/9707345](#) [hep-ph].
- [375] Z. Bern, G. Diana, L. Dixon, F. Febres Cordero, S. Hoeche, et al., *Four-Jet Production at the Large Hadron Collider at Next-to-Leading Order in QCD*, *Phys.Rev.Lett.* **109** (2012) 042001, [arXiv:1112.3940](#) [hep-ph].
- [376] S. Badger, B. Biedermann, P. Uwer, and V. Yundin, *NLO QCD corrections to multi-jet production at the LHC with a centre-of-mass energy of  $\sqrt{s} = 8$  TeV*, *Phys.Lett.* **B718** (2013) 965–978, [arXiv:1209.0098](#) [hep-ph].
- [377] E. Gerwick, S. Schumann, B. Gripaios, and B. Webber, *QCD Jet Rates with the Inclusive Generalized  $kt$  Algorithms*, *JHEP* **04** (2013) 089, [arXiv:1212.5235](#) [hep-ph].
- [378] E. Gerwick, *Recursive prescription for logarithmic jet rate coefficients*, *Phys. Rev.* **D88** (2013) no. 9, 094009, [arXiv:1305.6319](#) [hep-ph].
- [379] M. Dasgupta, F. Dreyer, G. P. Salam, and G. Soyez, *Small-radius jets to all orders in QCD*, *JHEP* **04** (2015) 039, [arXiv:1411.5182](#) [hep-ph].
- [380] E. Gerwick, T. Plehn, S. Schumann, and P. Schichtel, *Scaling Patterns for QCD Jets*, *JHEP* **10** (2012) 162, [arXiv:1208.3676](#) [hep-ph].
- [381] ATLAS Collaboration, G. Aad et al., *Measurement of multi-jet cross sections in proton-proton collisions at a 7 TeV center-of-mass energy*, *Eur.Phys.J.* **C71** (2011) 1763, [arXiv:1107.2092](#) [hep-ex].
- [382] ATLAS Collaboration, G. Aad et al., *Measurement of the production cross section of jets in association with a Z boson in pp collisions at  $\sqrt{s} = 7$  TeV with the ATLAS detector*, *JHEP* **07** (2013) 032, [arXiv:1304.7098](#) [hep-ex].
- [383] ATLAS Collaboration, G. Aad et al., *Measurements of the W production cross sections in association with jets with the ATLAS detector*, *Eur. Phys. J.* **C75** (2015) no. 2, 82, [arXiv:1409.8639](#) [hep-ex].
- [384] CMS Collaboration, V. Khachatryan et al., *Differential cross section measurements for the*

- production of a W boson in association with jets in proton-proton collisions at  $\sqrt{s} = 7$  TeV*, *Phys. Lett.* **B741** (2015) 12–37, [arXiv:1406.7533 \[hep-ex\]](#).
- [385] C. Englert, T. Plehn, P. Schichtel, and S. Schumann, *Jets plus Missing Energy with an Autofocus*, *Phys. Rev.* **D83** (2011) 095009, [arXiv:1102.4615 \[hep-ph\]](#).
- [386] C. Englert, T. Plehn, P. Schichtel, and S. Schumann, *Establishing Jet Scaling Patterns with a Photon*, *JHEP* **02** (2012) 030, [arXiv:1108.5473 \[hep-ph\]](#).
- [387] Z. Bern, L. Dixon, F. Febres Cordero, S. Höche, H. Ita, D. Kosower, and D. Maitre, *Extrapolating W-Associated Jet-Production Ratios at the LHC*, *Phys. Rev.* **D92** (2015) no. 1, 014008, [arXiv:1412.4775 \[hep-ph\]](#).
- [388] E. Gerwick and P. Schichtel, *Jet properties at high-multiplicity*, [arXiv:1412.1806 \[hep-ph\]](#).
- [389] M. E. Peskin and D. V. Schroeder, *An Introduction to quantum field theory*, .
- [390] S. El Hedri, A. Hook, M. Jankowiak, and J. G. Wacker, *Learning How to Count: A High Multiplicity Search for the LHC*, *JHEP* **08** (2013) 136, [arXiv:1302.1870](#).
- [391] S. Alekhin, A. Djouadi, and S. Moch, *The top quark and Higgs boson masses and the stability of the electroweak vacuum*, *Phys. Lett.* **B716** (2012) 214–219, [arXiv:1207.0980 \[hep-ph\]](#).
- [392] S. Alekhin, J. Bluemlein, and S. Moch, *Parton Distribution Functions and Benchmark Cross Sections at NNLO*, *Phys. Rev.* **D86** (2012) 054009, [arXiv:1202.2281 \[hep-ph\]](#).
- [393] J. C. Collins and R. K. Ellis, *Heavy quark production in very high-energy hadron collisions*, *Nucl. Phys.* **B360** (1991) 3–30.
- [394] R. D. Ball and R. K. Ellis, *Heavy quark production at high-energy*, *JHEP* **05** (2001) 053, [arXiv:hep-ph/0101199 \[hep-ph\]](#).
- [395] P. Nason, S. Dawson, and R. K. Ellis, *The Total Cross-Section for the Production of Heavy Quarks in Hadronic Collisions*, *Nucl.Phys.* **B303** (1988) 607.
- [396] LHCb Collaboration, R. Aaij et al., *Measurements of prompt charm production cross-sections in pp collisions at  $\sqrt{s} = 13$  TeV*, [arXiv:1510.01707 \[hep-ex\]](#).
- [397] LHCb Collaboration, R. Aaij et al., *Measurement of forward  $J/\psi$  production cross-sections in pp collisions at  $\sqrt{s} = 13$  TeV*, *JHEP* **10** (2015) 172, [arXiv:1509.00771 \[hep-ex\]](#).
- [398] M. Czakon, P. Fiedler, and A. Mitov, *Total Top-Quark Pair-Production Cross Section at Hadron Colliders Through  $O(\frac{4}{3})$* , *Phys. Rev. Lett.* **110** (2013) 252004, [arXiv:1303.6254 \[hep-ph\]](#).
- [399] M. Czakon and A. Mitov, *Top++: A Program for the Calculation of the Top-Pair Cross-Section at Hadron Colliders*, *Comput. Phys. Commun.* **185** (2014) 2930, [arXiv:1112.5675 \[hep-ph\]](#).
- [400] I. Hinchliffe, A. Kotwal, M. L. Mangano, C. Quigg, and L.-T. Wang, *Luminosity goals for a 100-TeV pp collider*, *Int. J. Mod. Phys.* **A30** (2015) no. 23, 1544002, [arXiv:1504.06108 \[hep-ph\]](#).
- [401] M. Mangano and T. Melia, *Rare exclusive hadronic W decays in a  $t\bar{t}$  environment*, *Eur. Phys. J.* **C75** (2015) no. 6, 258, [arXiv:1410.7475 \[hep-ph\]](#).
- [402] O. Gedalia, G. Isidori, F. Maltoni, G. Perez, M. Selvaggi, et al., *Top B Physics at the LHC*, *Phys.Rev.Lett.* **110** (2013) no. 23, 232002, [arXiv:1212.4611 \[hep-ph\]](#).
- [403] B. Mele and P. Nason, *The Fragmentation function for heavy quarks in QCD*, *Nucl. Phys.* **B361** (1991) 626–644.
- [404] M. Cacciari and M. Greco, *Large  $p_T$  hadroproduction of heavy quarks*, *Nucl. Phys.* **B421** (1994) 530–544, [arXiv:hep-ph/9311260 \[hep-ph\]](#).
- [405] P. Kant, O. M. Kind, T. Kintscher, T. Lohse, T. Martini, S. MÃulbitz, P. Rieck, and P. Uwer, *HatHor for single top-quark production: Updated predictions and uncertainty estimates for single top-quark production in hadronic collisions*, *Comput. Phys. Commun.* **191** (2015) 74–89, [arXiv:1406.4403 \[hep-ph\]](#).
- [406] J. M. Campbell and F. Tramontano, *Next-to-leading order corrections to  $Wt$  production and*

- decay*, *Nucl.Phys.* **B726** (2005) 109–130, [arXiv:hep-ph/0506289](#) [hep-ph].
- [407] M. Brucherseifer, F. Caola, and K. Melnikov, *On the NNLO QCD corrections to single-top production at the LHC*, *Phys. Lett.* **B736** (2014) 58–63, [arXiv:1404.7116](#) [hep-ph].
- [408] F. Maltoni, K. Paul, T. Stelzer, and S. Willenbrock, *Associated production of Higgs and single top at hadron colliders*, *Phys. Rev.* **D64** (2001) 094023, [arXiv:hep-ph/0106293](#) [hep-ph].
- [409] M. Farina, C. Grojean, F. Maltoni, E. Salvioni, and A. Thamm, *Lifting degeneracies in Higgs couplings using single top production in association with a Higgs boson*, *JHEP* **05** (2013) 022, [arXiv:1211.3736](#) [hep-ph].
- [410] J. Campbell, R. K. Ellis, and R. Rontsch, *Single top production in association with a Z boson at the LHC*, *Phys.Rev.* **D87** (2013) 114006, [arXiv:1302.3856](#) [hep-ph].
- [411] P. Torrielli, *Rare Standard Model processes for present and future hadronic colliders*, [arXiv:1407.1623](#) [hep-ph].
- [412] F. Maltoni, D. Pagani, and I. Tsirikos, *Associated production of a top-quark pair with vector bosons at NLO in QCD: impact on  $t\bar{t}H$  searches at the LHC*, [arXiv:1507.05640](#) [hep-ph].
- [413] F. Maltoni, M. L. Mangano, I. Tsirikos, and M. Zaro, *Top-quark charge asymmetry and polarization in  $t\bar{t}W^\pm$  production at the LHC*, *Phys. Lett.* **B736** (2014) 252–260, [arXiv:1406.3262](#) [hep-ph].
- [414] W. Beenakker, S. Dittmaier, M. Kramer, B. Plumper, M. Spira, et al., *Higgs radiation off top quarks at the Tevatron and the LHC*, *Phys.Rev.Lett.* **87** (2001) 201805, [arXiv:hep-ph/0107081](#) [hep-ph].
- [415] W. Beenakker, S. Dittmaier, M. Kramer, B. Plumper, M. Spira, et al., *NLO QCD corrections to  $t$  anti- $t$   $H$  production in hadron collisions*, *Nucl.Phys.* **B653** (2003) 151–203, [arXiv:hep-ph/0211352](#) [hep-ph].
- [416] S. Dawson, L. Orr, L. Reina, and D. Wackerroth, *Associated top quark Higgs boson production at the LHC*, *Phys.Rev.* **D67** (2003) 071503, [arXiv:hep-ph/0211438](#) [hep-ph].
- [417] S. Dawson, C. Jackson, L. Orr, L. Reina, and D. Wackerroth, *Associated Higgs production with top quarks at the large hadron collider: NLO QCD corrections*, *Phys.Rev.* **D68** (2003) 034022, [arXiv:hep-ph/0305087](#) [hep-ph].
- [418] K. Melnikov, M. Schulze, and A. Scharf, *QCD corrections to top quark pair production in association with a photon at hadron colliders*, *Phys.Rev.* **D83** (2011) 074013, [arXiv:1102.1967](#) [hep-ph].
- [419] V. Hirschi, R. Frederix, S. Frixione, M. V. Garzelli, F. Maltoni, et al., *Automation of one-loop QCD corrections*, *JHEP* **1105** (2011) 044, [arXiv:1103.0621](#) [hep-ph].
- [420] A. Lazopoulos, T. McElmurry, K. Melnikov, and F. Petriello, *Next-to-leading order QCD corrections to  $t\bar{t}Z$  production at the LHC*, *Phys.Lett.* **B666** (2008) 62–65, [arXiv:0804.2220](#) [hep-ph].
- [421] M. Garzelli, A. Kardos, C. Papadopoulos, and Z. Trocsanyi,  *$Z0$  - boson production in association with a top anti-top pair at NLO accuracy with parton shower effects*, *Phys.Rev.* **D85** (2012) 074022, [arXiv:1111.1444](#) [hep-ph].
- [422] A. Kardos, Z. Trocsanyi, and C. Papadopoulos, *Top quark pair production in association with a Z-boson at NLO accuracy*, *Phys.Rev.* **D85** (2012) 054015, [arXiv:1111.0610](#) [hep-ph].
- [423] M. Garzelli, A. Kardos, C. Papadopoulos, and Z. Trocsanyi,  *$t\bar{t}W^{+-}$  and  $t\bar{t}Z$  Hadroproduction at NLO accuracy in QCD with Parton Shower and Hadronization effects*, *JHEP* **1211** (2012) 056, [arXiv:1208.2665](#) [hep-ph].
- [424] J. M. Campbell and R. K. Ellis,  *$t\bar{t}W^{+-}$  production and decay at NLO*, *JHEP* **1207** (2012) 052, [arXiv:1204.5678](#) [hep-ph].
- [425] G. Bevilacqua and M. Worek, *Constraining BSM Physics at the LHC: Four top final states with*

- NLO accuracy in perturbative QCD*, *JHEP* **1207** (2012) 111, [arXiv:1206.3064 \[hep-ph\]](#).
- [426] S. Frixione, V. Hirschi, D. Pagani, H. Shao, and M. Zaro, *Weak corrections to Higgs hadroproduction in association with a top-quark pair*, *JHEP* **1409** (2014) 065, [arXiv:1407.0823 \[hep-ph\]](#).
- [427] Y. Zhang, W.-G. Ma, R.-Y. Zhang, C. Chen, and L. Guo, *QCD NLO and EW NLO corrections to  $t\bar{t}H$  production with top quark decays at hadron collider*, *Phys. Lett.* **B738** (2014) 1–5, [arXiv:1407.1110 \[hep-ph\]](#).
- [428] S. Frixione, V. Hirschi, D. Pagani, H. S. Shao, and M. Zaro, *Electroweak and QCD corrections to top-pair hadroproduction in association with heavy bosons*, *JHEP* **06** (2015) 184, [arXiv:1504.03446 \[hep-ph\]](#).
- [429] R. Frederix, S. Frixione, V. Hirschi, F. Maltoni, R. Pittau, and P. Torielli, *Scalar and pseudoscalar Higgs production in association with a top-antitop pair*, *Phys.Lett.* **B701** (2011) 427–433, [arXiv:1104.5613 \[hep-ph\]](#).
- [430] M. Garzelli, A. Kardos, C. Papadopoulos, and Z. Trocsanyi, *Standard Model Higgs boson production in association with a top anti-top pair at NLO with parton showering*, *Europhys.Lett.* **96** (2011) 11001, [arXiv:1108.0387 \[hep-ph\]](#).
- [431] A. Denner and R. Feger, *NLO QCD corrections to off-shell top-antitop production with leptonic decays in association with a Higgs boson at the LHC*, [arXiv:1506.07448 \[hep-ph\]](#).
- [432] R. Frederix, S. Frixione, V. Hirschi, F. Maltoni, R. Pittau, and P. Torrielli, *Four-lepton production at hadron colliders: aMC@NLO predictions with theoretical uncertainties*, *JHEP* **02** (2012) 099, [arXiv:1110.4738 \[hep-ph\]](#).
- [433] R. Frederix and S. Frixione, *Merging meets matching in MC@NLO*, *JHEP* **1212** (2012) 061, [arXiv:1209.6215 \[hep-ph\]](#).
- [434] J. H. Kuhn and G. Rodrigo, *Charge asymmetry in hadroproduction of heavy quarks*, *Phys.Rev.Lett.* **81** (1998) 49–52, [arXiv:hep-ph/9802268 \[hep-ph\]](#).
- [435] J. H. Kuhn and G. Rodrigo, *Charge asymmetry of heavy quarks at hadron colliders*, *Phys.Rev.* **D59** (1999) 054017, [arXiv:hep-ph/9807420 \[hep-ph\]](#).
- [436] W. Bernreuther and Z.-G. Si, *Distributions and correlations for top quark pair production and decay at the Tevatron and LHC.*, *Nucl.Phys.* **B837** (2010) 90–121, [arXiv:1003.3926 \[hep-ph\]](#).
- [437] W. Hollik and D. Pagani, *The electroweak contribution to the top quark forward-backward asymmetry at the Tevatron*, *Phys.Rev.* **D84** (2011) 093003, [arXiv:1107.2606 \[hep-ph\]](#).
- [438] J. H. Kuhn and G. Rodrigo, *Charge asymmetries of top quarks at hadron colliders revisited*, *JHEP* **1201** (2012) 063, [arXiv:1109.6830 \[hep-ph\]](#).
- [439] W. Bernreuther and Z.-G. Si, *Top quark and leptonic charge asymmetries for the Tevatron and LHC*, *Phys.Rev.* **D86** (2012) 034026, [arXiv:1205.6580 \[hep-ph\]](#).
- [440] J. Aguilar-Saavedra, E. Alvarez, A. Juste, and F. Rubbo, *Shedding light on the  $t\bar{t}$  asymmetry: the photon handle*, *JHEP* **1404** (2014) 188, [arXiv:1402.3598 \[hep-ph\]](#).
- [441] U. Baur, M. Buice, and L. H. Orr, *Direct measurement of the top quark charge at hadron colliders*, *Phys. Rev.* **D64** (2001) 094019, [arXiv:hep-ph/0106341 \[hep-ph\]](#).
- [442] ATLAS Collaboration, G. Aad et al., *Observation of top-quark pair production in association with a photon and measurement of the  $t\bar{t}\gamma$  production cross section in pp collisions at  $\sqrt{s} = 7$  TeV using the ATLAS detector*, *Phys. Rev.* **D91** (2015) no. 7, 072007, [arXiv:1502.00586 \[hep-ex\]](#).
- [443] CMS Collaboration, *Measurement of the inclusive top-quark pair + photon production cross section in the muon + jets channel in pp collisions at 8 TeV*, CMS-PAS-TOP-13-011, 2014.
- [444] M. Beneke et al., *Top quark physics*, in *1999 CERN Workshop on standard model physics (and*

- more) at the LHC, CERN, Geneva, Switzerland, 25-26 May: *Proceedings*. 2000.  
[arXiv:hep-ph/0003033](https://arxiv.org/abs/hep-ph/0003033) [hep-ph].  
<http://weblib.cern.ch/abstract?CERN-TH-2000-100>.
- [445] R. Martinez and J. A. Rodriguez, *The Anomalous chromomagnetic dipole moment of the top quark in the standard model and beyond*, *Phys. Rev.* **D65** (2002) 057301, [arXiv:hep-ph/0109109](https://arxiv.org/abs/hep-ph/0109109) [hep-ph].
- [446] D. Atwood, A. Kagan, and T. G. Rizzo, *Constraining anomalous top quark couplings at the Tevatron*, *Phys. Rev.* **D52** (1995) 6264–6270, [arXiv:hep-ph/9407408](https://arxiv.org/abs/hep-ph/9407408) [hep-ph].
- [447] R. Martinez, M. A. Perez, and N. Poveda, *Chromomagnetic Dipole Moment of the Top Quark Revisited*, *Eur. Phys. J.* **C53** (2008) 221–230, [arXiv:hep-ph/0701098](https://arxiv.org/abs/hep-ph/0701098) [hep-ph].
- [448] Z. Hioki and K. Ohkuma, *Search for anomalous top-gluon couplings at LHC revisited*, *Eur. Phys. J.* **C65** (2010) 127–135, [arXiv:0910.3049](https://arxiv.org/abs/0910.3049) [hep-ph].
- [449] Z. Hioki and K. Ohkuma, *Addendum to: Search for anomalous top-gluon couplings at LHC revisited*, *Eur. Phys. J.* **C71** (2011) 1535, [arXiv:1011.2655](https://arxiv.org/abs/1011.2655) [hep-ph].
- [450] Z. Hioki and K. Ohkuma, *Latest constraint on nonstandard top-gluon couplings at hadron colliders and its future prospect*, *Phys. Rev.* **D88** (2013) 017503, [arXiv:1306.5387](https://arxiv.org/abs/1306.5387) [hep-ph].
- [451] J. F. Kamenik, M. Papucci, and A. Weiler, *Constraining the dipole moments of the top quark*, *Phys. Rev.* **D85** (2012) 071501, [arXiv:1107.3143](https://arxiv.org/abs/1107.3143) [hep-ph]. [Erratum: *Phys. Rev.* **D88**, no.3, 039903(2013)].
- [452] W. Bernreuther and Z.-G. Si, *Top quark spin correlations and polarization at the LHC: standard model predictions and effects of anomalous top chromo moments*, *Phys. Lett.* **B725** (2013) 115–122, [arXiv:1305.2066](https://arxiv.org/abs/1305.2066) [hep-ph]. [Erratum: *Phys. Lett.* **B744**, 413(2015)].
- [453] D. Buarque Franzosi and C. Zhang, *Probing the top-quark chromomagnetic dipole moment at next-to-leading order in QCD*, *Phys. Rev.* **D91** (2015) no. 11, 114010, [arXiv:1503.08841](https://arxiv.org/abs/1503.08841) [hep-ph].
- [454] T. Han, R. D. Peccei, and X. Zhang, *Top quark decay via flavor changing neutral currents at hadron colliders*, *Nucl. Phys.* **B454** (1995) 527–540, [arXiv:hep-ph/9506461](https://arxiv.org/abs/hep-ph/9506461) [hep-ph].
- [455] J. A. Aguilar-Saavedra, *Top flavor-changing neutral interactions: Theoretical expectations and experimental detection*, *Acta Phys. Polon.* **B35** (2004) 2695–2710, [arXiv:hep-ph/0409342](https://arxiv.org/abs/hep-ph/0409342) [hep-ph].
- [456] J. Bernabeu, D. Comelli, L. Lavoura, and J. P. Silva, *Weak magnetic dipole moments in two Higgs doublet models*, *Phys.Rev.* **D53** (1996) 5222–5232, [arXiv:hep-ph/9509416](https://arxiv.org/abs/hep-ph/9509416) [hep-ph].
- [457] A. Czarnecki and B. Krause, *On the dipole moments of fermions at two loops*, *Acta Phys.Polon.* **B28** (1997) 829–834, [arXiv:hep-ph/9611299](https://arxiv.org/abs/hep-ph/9611299) [hep-ph].
- [458] W. Hollik, J. I. Illana, S. Rigolin, C. Schappacher, and D. Stockinger, *Top dipole form-factors and loop induced CP violation in supersymmetry*, *Nucl.Phys.* **B551** (1999) 3–40, [arXiv:hep-ph/9812298](https://arxiv.org/abs/hep-ph/9812298) [hep-ph].
- [459] U. Baur, A. Juste, L. H. Orr, and D. Rainwater, *Probing electroweak top quark couplings at hadron colliders*, *Phys. Rev.* **D71** (2005) 054013, [arXiv:hep-ph/0412021](https://arxiv.org/abs/hep-ph/0412021) [hep-ph].
- [460] U. Baur, A. Juste, D. Rainwater, and L. H. Orr, *Improved measurement of  $t\bar{t}Z$  couplings at the CERN LHC*, *Phys. Rev.* **D73** (2006) 034016, [arXiv:hep-ph/0512262](https://arxiv.org/abs/hep-ph/0512262) [hep-ph].
- [461] R. Rontsch and M. Schulze, *Constraining couplings of top quarks to the Z boson in  $t\bar{t} + Z$  production at the LHC*, *JHEP* **07** (2014) 091, [arXiv:1404.1005](https://arxiv.org/abs/1404.1005) [hep-ph]. [Erratum: *JHEP* **09**, 132(2015)].
- [462] R. Rontsch and M. Schulze, *Probing top-Z dipole moments at the LHC and ILC*, *JHEP* **08** (2015) 044, [arXiv:1501.05939](https://arxiv.org/abs/1501.05939) [hep-ph].
- [463] O. B. Bylund, F. Maltoni, I. Tsinikos, E. Vryonidou, and C. Zhang, *Probing top quark neutral*

- couplings in the Standard Model Effective Field Theory at NLO QCD*, [arXiv:1601.08193 \[hep-ph\]](#).
- [464] M. Schulze and Y. Soreq, *Pinning down electroweak dipole operators of the top quark*, [arXiv:1603.08911 \[hep-ph\]](#).
- [465] P. Ferrario and G. Rodrigo, *Constraining heavy colored resonances from top-antitop quark events*, *Phys. Rev.* **D80** (2009) 051701, [arXiv:0906.5541 \[hep-ph\]](#).
- [466] P. H. Frampton, J. Shu, and K. Wang, *Axigluon as Possible Explanation for  $p$  anti- $p \rightarrow t$  anti- $t$  Forward-Backward Asymmetry*, *Phys. Lett.* **B683** (2010) 294–297, [arXiv:0911.2955 \[hep-ph\]](#).
- [467] J. A. Aguilar-Saavedra, D. Amidei, A. Juste, and M. Perez-Victoria, *Asymmetries in top quark pair production at hadron colliders*, *Rev. Mod. Phys.* **87** (2015) 421–455, [arXiv:1406.1798 \[hep-ph\]](#).
- [468] F. del Aguila and J. A. Aguilar-Saavedra, *Multilepton production via top flavor changing neutral couplings at the CERN LHC*, *Nucl. Phys.* **B576** (2000) 56–84, [arXiv:hep-ph/9909222 \[hep-ph\]](#).
- [469] H. Baer, C.-h. Chen, F. Paige, and X. Tata, *Signals for minimal supergravity at the CERN large hadron collider. 2: Multi - lepton channels*, *Phys. Rev.* **D53** (1996) 6241–6264, [arXiv:hep-ph/9512383 \[hep-ph\]](#).
- [470] H.-C. Cheng, K. T. Matchev, and M. Schmaltz, *Bosonic supersymmetry? Getting fooled at the CERN LHC*, *Phys. Rev.* **D66** (2002) 056006, [arXiv:hep-ph/0205314 \[hep-ph\]](#).
- [471] S. Hoeche, F. Krauss, S. Pozzorini, M. Schoenherr, J. M. Thompson, and K. C. Zapp, *Triple vector boson production through Higgs-Strahlung with NLO multijet merging*, *Phys. Rev.* **D89** (2014) no. 9, 093015, [arXiv:1403.7516 \[hep-ph\]](#).
- [472] G. Belanger and F. Boudjema, *Probing quartic couplings of weak bosons through three vectors production at a 500-GeV NLC*, *Phys. Lett.* **B288** (1992) 201–209.
- [473] O. J. P. Eboli, M. C. Gonzalez-Garcia, and S. M. Lietti, *Bosonic quartic couplings at CERN LHC*, *Phys. Rev.* **D69** (2004) 095005, [arXiv:hep-ph/0310141 \[hep-ph\]](#).
- [474] O. J. P. Eboli, M. C. Gonzalez-Garcia, and J. K. Mizukoshi,  *$pp \rightarrow jj e^+ \mu^+ \nu \nu$  and  $jj e^+ \mu^+ \nu \nu$  at  $O(\alpha(\text{em})^6)$  and  $O(\alpha(\text{em})^4 \alpha(s)^2)$  for the study of the quartic electroweak gauge boson vertex at CERN LHC*, *Phys. Rev.* **D74** (2006) 073005, [arXiv:hep-ph/0606118 \[hep-ph\]](#).
- [475] N. Arkani-Hamed, T. Han, M. Mangano, and L.-T. Wang, *Physics Opportunities of a 100 TeV Proton-Proton Collider*, [arXiv:1511.06495 \[hep-ph\]](#).
- [476] K. Ye, D. Yang, and Q. Li, *CERN LHC sensitivity on measuring  $W^\pm Z\gamma$  production and anomalous  $WWZ\gamma$  coupling*, *Phys. Rev.* **D88** (2013) 015023, [arXiv:1305.5979 \[hep-ph\]](#).
- [477] C. Degrande et al., *Studies of Vector Boson Scattering And Triboson Production with DELPHES Parametrized Fast Simulation for Snowmass 2013*, in *Community Summer Study 2013: Snowmass on the Mississippi (CSS2013) Minneapolis, MN, USA, July 29-August 6, 2013*. 2013. [arXiv:1309.7452 \[physics.comp-ph\]](#).  
<http://inspirehep.net/record/1256110/files/arXiv:1309.7452.pdf>.
- [478] Y. Wen, H. Qu, D. Yang, Q.-s. Yan, Q. Li, and Y. Mao, *Probing triple-W production and anomalous  $WWWW$  coupling at the CERN LHC and future  $\mathcal{O}(100)$  TeV proton-proton collider*, *JHEP* **03** (2015) 025, [arXiv:1407.4922 \[hep-ph\]](#).
- [479] M. Spira and J. D. Wells, *Higgs bosons strongly coupled to the top quark*, *Nucl. Phys.* **B523** (1998) 3–16, [arXiv:hep-ph/9711410 \[hep-ph\]](#).
- [480] G. Cacciapaglia, R. Chierici, A. Deandrea, L. Panizzi, S. Perries, and S. Tosi, *Four tops on the real projective plane at LHC*, *JHEP* **10** (2011) 042, [arXiv:1107.4616 \[hep-ph\]](#).

- [481] A. Deandrea and N. Deutschmann, *Multi-tops at the LHC*, *JHEP* **08** (2014) 134, [arXiv:1405.6119 \[hep-ph\]](#).
- [482] G. Cacciapaglia, A. Deandrea, D. Harada, and Y. Okada, *Bounds and Decays of New Heavy Vector-like Top Partners*, *JHEP* **11** (2010) 159, [arXiv:1007.2933 \[hep-ph\]](#).
- [483] CMS Collaboration, C. Collaboration, *Search for standard model four top quark production at 8 TeV in the lepton + jets channel*, CMS-PAS-TOP-13-012, 2013.
- [484] M. Mangano, T. Plehn, P. Reimitz, T. Schell, and H.-S. Shao, *Measuring the Top Yukawa Coupling at 100 TeV*, [arXiv:1507.08169 \[hep-ph\]](#).
- [485] G. Degrandi, S. Di Vita, J. Elias-Miro, J. R. Espinosa, G. F. Giudice, G. Isidori, and A. Strumia, *Higgs mass and vacuum stability in the Standard Model at NNLO*, *JHEP* **08** (2012) 098, [arXiv:1205.6497 \[hep-ph\]](#).
- [486] R. Frederix, S. Frixione, V. Hirschi, F. Maltoni, O. Mattelaer, P. Torrielli, E. Vryonidou, and M. Zaro, *Higgs pair production at the LHC with NLO and parton-shower effects*, *Phys. Lett.* **B732** (2014) 142–149, [arXiv:1401.7340 \[hep-ph\]](#).
- [487] F. Maltoni, E. Vryonidou, and M. Zaro, *Top-quark mass effects in double and triple Higgs production in gluon-gluon fusion at NLO*, *JHEP* **11** (2014) 079, [arXiv:1408.6542 \[hep-ph\]](#).
- [488] D. de Florian and J. Mazzitelli, *Higgs Boson Pair Production at Next-to-Next-to-Leading Order in QCD*, *Phys. Rev. Lett.* **111** (2013) 201801, [arXiv:1309.6594 \[hep-ph\]](#).
- [489] J. Grigo, K. Melnikov, and M. Steinhauser, *Virtual corrections to Higgs boson pair production in the large top quark mass limit*, *Nucl. Phys.* **B888** (2014) 17–29, [arXiv:1408.2422 \[hep-ph\]](#).
- [490] A. J. Barr, M. J. Dolan, C. Englert, D. E. F. de Lima, and M. Spannowsky, *Higgs Self-Coupling Measurements at a 100 TeV Hadron Collider*, [arXiv:1412.7154 \[hep-ph\]](#).
- [491] A. Azatov, R. Contino, G. Panico, and M. Son, *Effective field theory analysis of double Higgs production via gluon fusion*, [arXiv:1502.00539 \[hep-ph\]](#).
- [492] H.-J. He, J. Ren, and W. Yao, *Probing New Physics of Cubic Higgs Interaction via Higgs Pair Production at Hadron Colliders*, [arXiv:1506.03302 \[hep-ph\]](#).
- [493] A. Papaefstathiou, *Discovering Higgs boson pair production through rare final states at a 100 TeV collider*, *Phys. Rev.* **D91** (2015) no. 11, 113016, [arXiv:1504.04621 \[hep-ph\]](#).
- [494] F. Goertz, A. Papaefstathiou, L. L. Yang, and J. Zurita, *Higgs Boson self-coupling measurements using ratios of cross sections*, *JHEP* **06** (2013) 016, [arXiv:1301.3492 \[hep-ph\]](#).
- [495] Q.-H. Cao, B. Yan, D.-M. Zhang, and H. Zhang, *Resolving the Degeneracy in Single Higgs Production with Higgs Pair Production*, *Phys. Lett.* **B752** (2016) 285–290, [arXiv:1508.06512 \[hep-ph\]](#).
- [496] L.-S. Ling, R.-Y. Zhang, W.-G. Ma, L. Guo, W.-H. Li, and X.-Z. Li, *NNLO QCD corrections to Higgs pair production via vector boson fusion at hadron colliders*, *Phys. Rev.* **D89** (2014) no. 7, 073001, [arXiv:1401.7754 \[hep-ph\]](#).
- [497] A. Papaefstathiou and K. Sakurai, *Triple Higgs boson production at a 100 TeV proton-proton collider*, [arXiv:1508.06524 \[hep-ph\]](#).
- [498] C. Englert, F. Krauss, M. Spannowsky, and J. Thompson, *Di-Higgs phenomenology in  $t\bar{t}hh$ : The forgotten channel*, *Phys. Lett.* **B743** (2015) 93–97, [arXiv:1409.8074 \[hep-ph\]](#).
- [499] T. Liu and H. Zhang, *Measuring Di-Higgs Physics via the  $t\bar{t}hh \rightarrow t\bar{t}b\bar{b}b\bar{b}$  Channel*, [arXiv:1410.1855 \[hep-ph\]](#).
- [500] Q.-H. Cao, Y. Liu, and B. Yan, *Measuring Trilinear Higgs Coupling in  $WHH$  and  $ZHH$  Productions at the HL-LHC*, [arXiv:1511.03311 \[hep-ph\]](#).
- [501] C. Anastasiou, C. Duhr, F. Dulat, F. Herzog, and B. Mistlberger, *Higgs Boson Gluon-Fusion Production in QCD at Three Loops*, *Phys. Rev. Lett.* **114** (2015) 212001, [arXiv:1503.06056 \[hep-ph\]](#).

- [502] R. Mueller and D. G. Oetzuerk, *On the computation of finite bottom-quark mass effects in Higgs boson production*, [arXiv:1512.08570 \[hep-ph\]](#).
- [503] A. Banfi, P. F. Monni, and G. Zanderighi, *Quark masses in Higgs production with a jet veto*, *JHEP* **01** (2014) 097, [arXiv:1308.4634 \[hep-ph\]](#).
- [504] S. Borowka, N. Greiner, G. Heinrich, S. P. Jones, M. Kerner, J. Schlenk, U. Schubert, and T. Zirke, *Higgs boson pair production in gluon fusion at NLO with full top-quark mass dependence*, [arXiv:1604.06447 \[hep-ph\]](#).
- [505] S. Borowka, G. Heinrich, S. P. Jones, M. Kerner, J. Schlenk, and T. Zirke, *SecDec-3.0: numerical evaluation of multi-scale integrals beyond one loop*, *Comput. Phys. Commun.* **196** (2015) 470–491, [arXiv:1502.06595 \[hep-ph\]](#).
- [506] J. Grigo, J. Hoff, K. Melnikov, and M. Steinhauser, *On the Higgs boson pair production at the LHC*, *Nucl. Phys.* **B875** (2013) 1–17, [arXiv:1305.7340 \[hep-ph\]](#).
- [507] J. Grigo, J. Hoff, and M. Steinhauser, *Higgs boson pair production: top quark mass effects at NLO and NNLO*, *Nucl. Phys.* **B900** (2015) 412–430, [arXiv:1508.00909 \[hep-ph\]](#).
- [508] T. Hahn, *Generating Feynman diagrams and amplitudes with FeynArts 3*, *Comput.Phys.Comm.* **140** (2001) 418–431, [arXiv:hep-ph/0012260 \[hep-ph\]](#).
- [509] T. Hahn and M. Perez-Victoria, *Automatized one loop calculations in four-dimensions and D-dimensions*, *Comput.Phys.Comm.* **118** (1999) 153–165, [arXiv:hep-ph/9807565 \[hep-ph\]](#).
- [510] F. Cascioli, P. Maierhöfer, and S. Pozzorini, *Scattering Amplitudes with Open Loops*, *Phys.Rev.Lett.* **108** (2012) 111601, [arXiv:1111.5206 \[hep-ph\]](#).
- [511] V. Hirschi and O. Mattelaer, *Automated event generation for loop-induced processes*, *JHEP* **10** (2015) 146, [arXiv:1507.00020 \[hep-ph\]](#).
- [512] C. Degrande, V. V. Khoze, and O. Mattelaer, *Multi-Higgs production in gluon fusion at 100 TeV*, [arXiv:1605.06372 \[hep-ph\]](#).
- [513] M. Beccaria, G. Montagna, F. Piccinini, F. M. Renard, and C. Verzegnassi, *Rising bosonic electroweak virtual effects at high-energy  $e^+ e^-$  colliders*, *Phys. Rev.* **D58** (1998) 093014, [arXiv:hep-ph/9805250 \[hep-ph\]](#).
- [514] P. Ciafaloni and D. Comelli, *Sudakov enhancement of electroweak corrections*, *Phys. Lett.* **B446** (1999) 278–284, [arXiv:hep-ph/9809321 \[hep-ph\]](#).
- [515] V. S. Fadin, L. N. Lipatov, A. D. Martin, and M. Melles, *Resummation of double logarithms in electroweak high-energy processes*, *Phys. Rev.* **D61** (2000) 094002, [arXiv:hep-ph/9910338 \[hep-ph\]](#).
- [516] M. Melles, *Subleading Sudakov logarithms in electroweak high-energy processes to all orders*, *Phys. Rev.* **D63** (2001) 034003, [arXiv:hep-ph/0004056 \[hep-ph\]](#).
- [517] M. Melles, *Mass gap effects and higher order electroweak Sudakov logarithms*, *Phys. Lett.* **B495** (2000) 81–86, [arXiv:hep-ph/0006077 \[hep-ph\]](#).
- [518] M. Melles, *Resummation of Yukawa enhanced and subleading Sudakov logarithms in longitudinal gauge boson and Higgs production*, *Phys. Rev.* **D64** (2001) 014011, [arXiv:hep-ph/0012157 \[hep-ph\]](#).
- [519] M. Melles, *Electroweak renormalization group corrections in high-energy processes*, *Phys. Rev.* **D64** (2001) 054003, [arXiv:hep-ph/0102097 \[hep-ph\]](#).
- [520] M. Melles, *Electroweak radiative corrections in high-energy processes*, *Phys. Rept.* **375** (2003) 219–326, [arXiv:hep-ph/0104232 \[hep-ph\]](#).
- [521] P. Ciafaloni and D. Comelli, *Electroweak Sudakov form-factors and nonfactorizable soft QED effects at NLC energies*, *Phys. Lett.* **B476** (2000) 49–57, [arXiv:hep-ph/9910278 \[hep-ph\]](#).
- [522] M. Ciafaloni, P. Ciafaloni, and D. Comelli, *Bloch-Nordsieck violating electroweak corrections to*

- inclusive TeV scale hard processes*, *Phys. Rev. Lett.* **84** (2000) 4810–4813, [arXiv:hep-ph/0001142](#) [hep-ph].
- [523] M. Ciafaloni, P. Ciafaloni, and D. Comelli, *Electroweak Bloch-Nordsieck violation at the TeV scale: 'Strong' weak interactions?*, *Nucl. Phys.* **B589** (2000) 359–380, [arXiv:hep-ph/0004071](#) [hep-ph].
- [524] M. Ciafaloni, P. Ciafaloni, and D. Comelli, *Electroweak double logarithms in inclusive observables for a generic initial state*, *Phys. Lett.* **B501** (2001) 216–222, [arXiv:hep-ph/0007096](#) [hep-ph].
- [525] A. Denner and S. Pozzorini, *One loop leading logarithms in electroweak radiative corrections. 1. Results*, *Eur. Phys. J.* **C18** (2001) 461–480, [arXiv:hep-ph/0010201](#) [hep-ph].
- [526] M. Melles, *Resummation of angular dependent corrections in spontaneously broken gauge theories*, *Eur. Phys. J.* **C24** (2002) 193–204, [arXiv:hep-ph/0108221](#) [hep-ph].
- [527] M. Ciafaloni, P. Ciafaloni, and D. Comelli, *Bloch-Nordsieck violation in spontaneously broken Abelian theories*, *Phys. Rev. Lett.* **87** (2001) 211802, [arXiv:hep-ph/0103315](#) [hep-ph].
- [528] M. Ciafaloni, P. Ciafaloni, and D. Comelli, *Enhanced electroweak corrections to inclusive boson fusion processes at the TeV scale*, *Nucl. Phys.* **B613** (2001) 382–406, [arXiv:hep-ph/0103316](#) [hep-ph].
- [529] A. Denner and S. Pozzorini, *One loop leading logarithms in electroweak radiative corrections. 2. Factorization of collinear singularities*, *Eur. Phys. J.* **C21** (2001) 63–79, [arXiv:hep-ph/0104127](#) [hep-ph].
- [530] A. Denner, M. Melles, and S. Pozzorini, *Two loop electroweak angular dependent logarithms at high-energies*, *Nucl. Phys.* **B662** (2003) 299–333, [arXiv:hep-ph/0301241](#) [hep-ph].
- [531] A. Denner and S. Pozzorini, *An Algorithm for the high-energy expansion of multi-loop diagrams to next-to-leading logarithmic accuracy*, *Nucl. Phys.* **B717** (2005) 48–85, [arXiv:hep-ph/0408068](#) [hep-ph].
- [532] A. Denner, B. Jantzen, and S. Pozzorini, *Two-loop electroweak next-to-leading logarithmic corrections to massless fermionic processes*, *Nucl. Phys.* **B761** (2007) 1–62, [arXiv:hep-ph/0608326](#) [hep-ph].
- [533] J.-y. Chiu, F. Golf, R. Kelley, and A. V. Manohar, *Electroweak Sudakov corrections using effective field theory*, *Phys. Rev. Lett.* **100** (2008) 021802, [arXiv:0709.2377](#) [hep-ph].
- [534] J.-y. Chiu, F. Golf, R. Kelley, and A. V. Manohar, *Electroweak Corrections in High Energy Processes using Effective Field Theory*, *Phys. Rev.* **D77** (2008) 053004, [arXiv:0712.0396](#) [hep-ph].
- [535] J.-y. Chiu, R. Kelley, and A. V. Manohar, *Electroweak Corrections using Effective Field Theory: Applications to the LHC*, *Phys. Rev.* **D78** (2008) 073006, [arXiv:0806.1240](#) [hep-ph].
- [536] A. Denner, B. Jantzen, and S. Pozzorini, *Two-loop electroweak next-to-leading logarithms for processes involving heavy quarks*, *JHEP* **11** (2008) 062, [arXiv:0809.0800](#) [hep-ph].
- [537] J.-y. Chiu, A. Fuhrer, R. Kelley, and A. V. Manohar, *Factorization Structure of Gauge Theory Amplitudes and Application to Hard Scattering Processes at the LHC*, *Phys. Rev.* **D80** (2009) 094013, [arXiv:0909.0012](#) [hep-ph].
- [538] M. Ciafaloni, P. Ciafaloni, and D. Comelli, *Towards collinear evolution equations in electroweak theory*, *Phys. Rev. Lett.* **88** (2002) 102001, [arXiv:hep-ph/0111109](#) [hep-ph].
- [539] P. Ciafaloni, D. Comelli, and A. Vergine, *Sudakov electroweak effects in transversely polarized beams*, *JHEP* **07** (2004) 039, [arXiv:hep-ph/0311260](#) [hep-ph].
- [540] P. Ciafaloni and D. Comelli, *The Importance of weak bosons emission at LHC*, *JHEP* **09** (2006) 055, [arXiv:hep-ph/0604070](#) [hep-ph].
- [541] M. Ciafaloni, P. Ciafaloni, and D. Comelli, *Electroweak double-logs at small x*, *JHEP* **05** (2008)

- 039, [arXiv:0802.0168 \[hep-ph\]](#).
- [542] P. Ciafaloni, D. Comelli, A. Riotto, F. Sala, A. Strumia, and A. Urbano, *Weak Corrections are Relevant for Dark Matter Indirect Detection*, *JCAP* **1103** (2011) 019, [arXiv:1009.0224 \[hep-ph\]](#).
- [543] W. J. Stirling and E. Vryonidou, *Electroweak corrections and Bloch-Nordsieck violations in 2-to-2 processes at the LHC*, *JHEP* **04** (2013) 155, [arXiv:1212.6537](#).
- [544] C. W. Bauer and N. Ferland, *Resummation of electroweak Sudakov logarithms for real radiation*, [arXiv:1601.07190 \[hep-ph\]](#).
- [545] U. Baur, *Weak Boson Emission in Hadron Collider Processes*, *Phys. Rev.* **D75** (2007) 013005, [arXiv:hep-ph/0611241 \[hep-ph\]](#).
- [546] Z. Bern, G. Diana, L. J. Dixon, F. Febres Cordero, S. Höche, H. Ita, D. A. Kosower, D. Maitre, and K. J. Ozeren, *Missing Energy and Jets for Supersymmetry Searches*, *Phys. Rev.* **D87** (2013) no. 3, 034026, [arXiv:1206.6064 \[hep-ph\]](#).
- [547] M. Chiesa, G. Montagna, L. Barzè, M. Moretti, O. Nicrosini, F. Piccinini, and F. Tramontano, *Electroweak Sudakov Corrections to New Physics Searches at the LHC*, *Phys. Rev. Lett.* **111** (2013) no. 12, 121801, [arXiv:1305.6837 \[hep-ph\]](#).
- [548] F. Krauss, P. Petrov, M. Schoenherr, and M. Spannowsky, *Measuring collinear  $W$  emissions inside jets*, *Phys. Rev.* **D89** (2014) no. 11, 114006, [arXiv:1403.4788 \[hep-ph\]](#).
- [549] J. H. Kuhn, A. A. Penin, and V. A. Smirnov, *Summing up subleading Sudakov logarithms*, *Eur. Phys. J.* **C17** (2000) 97–105, [arXiv:hep-ph/9912503 \[hep-ph\]](#).
- [550] M. Beccaria, F. M. Renard, and C. Verzegnassi, *Top quark production at future lepton colliders in the asymptotic regime*, *Phys. Rev.* **D63** (2001) 053013, [arXiv:hep-ph/0010205 \[hep-ph\]](#).
- [551] M. Hori, H. Kawamura, and J. Kodaira, *Electroweak Sudakov at two loop level*, *Phys. Lett.* **B491** (2000) 275–279, [arXiv:hep-ph/0007329 \[hep-ph\]](#).
- [552] W. Beenakker and A. Werthenbach, *Electroweak two loop Sudakov logarithms for on-shell fermions and bosons*, *Nucl. Phys.* **B630** (2002) 3–54, [arXiv:hep-ph/0112030 \[hep-ph\]](#).
- [553] S. Pozzorini, *Next to leading mass singularities in two loop electroweak singlet form-factors*, *Nucl. Phys.* **B692** (2004) 135–174, [arXiv:hep-ph/0401087 \[hep-ph\]](#).
- [554] B. Feucht, J. H. Kuhn, A. A. Penin, and V. A. Smirnov, *Two loop Sudakov form-factor in a theory with mass gap*, *Phys. Rev. Lett.* **93** (2004) 101802, [arXiv:hep-ph/0404082 \[hep-ph\]](#).
- [555] B. Jantzen, J. H. Kuhn, A. A. Penin, and V. A. Smirnov, *Two-loop electroweak logarithms*, *Phys. Rev.* **D72** (2005) 051301, [arXiv:hep-ph/0504111 \[hep-ph\]](#). [Erratum: *Phys. Rev.* **D74**, 019901(2006)].
- [556] B. Jantzen, J. H. Kuhn, A. A. Penin, and V. A. Smirnov, *Two-loop electroweak logarithms in four-fermion processes at high energy*, *Nucl. Phys.* **B731** (2005) 188–212, [arXiv:hep-ph/0509157 \[hep-ph\]](#). [Erratum: *Nucl. Phys.* **B752**, 327(2006)].
- [557] B. Jantzen and V. A. Smirnov, *The Two-loop vector form-factor in the Sudakov limit*, *Eur. Phys. J.* **C47** (2006) 671–695, [arXiv:hep-ph/0603133 \[hep-ph\]](#).
- [558] A. V. Manohar and M. Trott, *Electroweak Sudakov Corrections and the Top Quark Forward-Backward Asymmetry*, *Phys. Lett.* **B711** (2012) 313–316, [arXiv:1201.3926 \[hep-ph\]](#).
- [559] C. W. Bauer, S. Fleming, and M. E. Luke, *Summing Sudakov logarithms in  $B \rightarrow X(s \text{ gamma})$  in effective field theory*, *Phys. Rev.* **D63** (2000) 014006, [arXiv:hep-ph/0005275 \[hep-ph\]](#).
- [560] C. W. Bauer, S. Fleming, D. Pirjol, and I. W. Stewart, *An Effective field theory for collinear and soft gluons: Heavy to light decays*, *Phys. Rev.* **D63** (2001) 114020, [arXiv:hep-ph/0011336 \[hep-ph\]](#).
- [561] C. W. Bauer and I. W. Stewart, *Invariant operators in collinear effective theory*, *Phys. Lett.* **B516**

- (2001) 134–142, [arXiv:hep-ph/0107001](#) [[hep-ph](#)].
- [562] C. W. Bauer, D. Pirjol, and I. W. Stewart, *Soft collinear factorization in effective field theory*, *Phys. Rev.* **D65** (2002) 054022, [arXiv:hep-ph/0109045](#) [[hep-ph](#)].
- [563] C. Carloni Calame, G. Montagna, O. Nicrosini, and A. Vicini, *Precision electroweak calculation of the charged current Drell-Yan process*, *JHEP* **0612** (2006) 016, [arXiv:hep-ph/0609170](#) [[hep-ph](#)].
- [564] C. Carloni Calame, G. Montagna, O. Nicrosini, and A. Vicini, *Precision electroweak calculation of the production of a high transverse-momentum lepton pair at hadron colliders*, *JHEP* **0710** (2007) 109, [arXiv:0710.1722](#) [[hep-ph](#)].
- [565] S. Dittmaier and M. Kramer, *Electroweak radiative corrections to  $W$  boson production at hadron colliders*, *Phys.Rev.* **D65** (2002) 073007, [arXiv:hep-ph/0109062](#) [[hep-ph](#)].
- [566] S. Brensing, S. Dittmaier, M. Kramer, and A. Muck, *Radiative corrections to  $W^-$  boson hadroproduction: Higher-order electroweak and supersymmetric effects*, *Phys.Rev.* **D77** (2008) 073006, [arXiv:0710.3309](#) [[hep-ph](#)].
- [567] S. Dittmaier and M. Huber, *Radiative corrections to the neutral-current Drell-Yan process in the Standard Model and its minimal supersymmetric extension*, *JHEP* **1001** (2010) 060, [arXiv:0911.2329](#) [[hep-ph](#)].
- [568] A. Arbuzov, D. Bardin, S. Bondarenko, P. Christova, L. Kalinovskaya, et al., *One-loop corrections to the Drell-Yan process in SANC. I. The Charged current case*, *Eur.Phys.J.* **C46** (2006) 407–412, [arXiv:hep-ph/0506110](#) [[hep-ph](#)].
- [569] A. Arbuzov, D. Bardin, S. Bondarenko, P. Christova, L. Kalinovskaya, et al., *One-loop corrections to the Drell-Yan process in SANC. (II). The Neutral current case*, *Eur.Phys.J.* **C54** (2008) 451–460, [arXiv:0711.0625](#) [[hep-ph](#)].
- [570] U. Baur and D. Wackerroth, *Electroweak radiative corrections to  $p\bar{p} \rightarrow W^\pm \rightarrow \ell^\pm \nu$  beyond the pole approximation*, *Phys.Rev.* **D70** (2004) 073015, [arXiv:hep-ph/0405191](#) [[hep-ph](#)].
- [571] W. Placzek and S. Jadach, *Multiphoton radiation in leptonic  $W$  boson decays*, *Eur.Phys.J.* **C29** (2003) 325–339, [arXiv:hep-ph/0302065](#) [[hep-ph](#)].
- [572] D. Bardin, S. Bondarenko, S. Jadach, L. Kalinovskaya, and W. Placzek, *Implementation of SANC EW corrections in WINHAC Monte Carlo generator*, *Acta Phys.Polon.* **B40** (2009) 75–92, [arXiv:0806.3822](#) [[hep-ph](#)].
- [573] U. Baur, O. Brein, W. Hollik, C. Schappacher, and D. Wackerroth, *Electroweak radiative corrections to neutral current Drell-Yan processes at hadron colliders*, *Phys.Rev.* **D65** (2002) 033007, [arXiv:hep-ph/0108274](#) [[hep-ph](#)].
- [574] Y. Li and F. Petriello, *Combining QCD and electroweak corrections to dilepton production in FEWZ*, *Phys.Rev.* **D86** (2012) 094034, [arXiv:1208.5967](#) [[hep-ph](#)].
- [575] L. Barze, G. Montagna, P. Nason, O. Nicrosini, and F. Piccinini, *Implementation of electroweak corrections in the POWHEG BOX: single  $W$  production*, *JHEP* **1204** (2012) 037, [arXiv:1202.0465](#) [[hep-ph](#)].
- [576] C. Bernaciak and D. Wackerroth, *Combining NLO QCD and Electroweak Radiative Corrections to  $W$  boson Production at Hadron Colliders in the POWHEG Framework*, *Phys. Rev.* **D85** (2012) 093003, [arXiv:1201.4804](#) [[hep-ph](#)].
- [577] L. Barze, G. Montagna, P. Nason, O. Nicrosini, F. Piccinini, et al., *Neutral current Drell-Yan with combined QCD and electroweak corrections in the POWHEG BOX*, *Eur.Phys.J.* **C73** (2013) no. 6, 2474, [arXiv:1302.4606](#) [[hep-ph](#)].
- [578] J. Butterworth, G. Dissertori, S. Dittmaier, D. de Florian, N. Glover, et al., *Les Houches 2013: Physics at TeV Colliders: Standard Model Working Group Report*, [arXiv:1405.1067](#) [[hep-ph](#)].

- [579] E. Maina, S. Moretti, and D. A. Ross, *One loop weak corrections to gamma / Z hadroproduction at finite transverse momentum*, *Phys.Lett.* **B593** (2004) 143–150, [arXiv:hep-ph/0403050 \[hep-ph\]](#).
- [580] J. H. Kuhn, A. Kulesza, S. Pozzorini, and M. Schulze, *Electroweak corrections to hadronic photon production at large transverse momenta*, *JHEP* **0603** (2006) 059, [arXiv:hep-ph/0508253 \[hep-ph\]](#).
- [581] J. H. Kuhn, A. Kulesza, S. Pozzorini, and M. Schulze, *One-loop weak corrections to hadronic production of Z bosons at large transverse momenta*, *Nucl.Phys.* **B727** (2005) 368–394, [arXiv:hep-ph/0507178 \[hep-ph\]](#).
- [582] J. H. Kuhn, A. Kulesza, S. Pozzorini, and M. Schulze, *Electroweak corrections to hadronic production of W bosons at large transverse momenta*, *Nucl.Phys.* **B797** (2008) 27–77, [arXiv:0708.0476 \[hep-ph\]](#).
- [583] A. Denner, S. Dittmaier, T. Kasprzik, and A. Muck, *Electroweak corrections to W + jet hadroproduction including leptonic W-boson decays*, *JHEP* **0908** (2009) 075, [arXiv:0906.1656 \[hep-ph\]](#).
- [584] A. Denner, S. Dittmaier, T. Kasprzik, and A. Mück, *Electroweak corrections to monojet production at the LHC*, *Eur.Phys.J.* **C73** (2013) no. 2, 2297, [arXiv:1211.5078 \[hep-ph\]](#).
- [585] M. Beccaria, G. Macorini, F. Renard, and C. Verzegnassi, *Single top production in the t-channel at LHC: A Realistic test of electroweak models*, *Phys.Rev.* **D74** (2006) 013008, [arXiv:hep-ph/0605108 \[hep-ph\]](#).
- [586] M. Beccaria, C. Carloni Calame, G. Macorini, E. Mirabella, F. Piccinini, et al., *A Complete one-loop calculation of electroweak supersymmetric effects in t-channel single top production at CERN LHC*, *Phys.Rev.* **D77** (2008) 113018, [arXiv:0802.1994 \[hep-ph\]](#).
- [587] D. Bardin, S. Bondarenko, L. Kalinovskaya, V. Kolesnikov, and W. von Schlippe, *Electroweak Radiative Corrections to Single-top Production*, *Eur.Phys.J.* **C71** (2011) 1533, [arXiv:1008.1859 \[hep-ph\]](#).
- [588] W. Beenakker, A. Denner, W. Hollik, R. Mertig, T. Sack, et al., *Electroweak one loop contributions to top pair production in hadron colliders*, *Nucl.Phys.* **B411** (1994) 343–380.
- [589] J. H. Kuhn, A. Scharf, and P. Uwer, *Electroweak corrections to top-quark pair production in quark-antiquark annihilation*, *Eur.Phys.J.* **C45** (2006) 139–150, [arXiv:hep-ph/0508092 \[hep-ph\]](#).
- [590] S. Moretti, M. Nolten, and D. Ross, *Weak corrections to gluon-induced top-antitop hadro-production*, *Phys.Lett.* **B639** (2006) 513–519, [arXiv:hep-ph/0603083 \[hep-ph\]](#).
- [591] W. Bernreuther, M. Fuecker, and Z.-G. Si, *Weak interaction corrections to hadronic top quark pair production*, *Phys.Rev.* **D74** (2006) 113005, [arXiv:hep-ph/0610334 \[hep-ph\]](#).
- [592] J. H. Kuhn, A. Scharf, and P. Uwer, *Electroweak effects in top-quark pair production at hadron colliders*, *Eur.Phys.J.* **C51** (2007) 37–53, [arXiv:hep-ph/0610335 \[hep-ph\]](#).
- [593] W. Hollik and M. Kollar, *NLO QED contributions to top-pair production at hadron collider*, *Phys.Rev.* **D77** (2008) 014008, [arXiv:0708.1697 \[hep-ph\]](#).
- [594] W. Bernreuther, M. Fucker, and Z.-G. Si, *Weak interaction corrections to hadronic top quark pair production: Contributions from quark-gluon and b anti-b induced reactions*, *Phys.Rev.* **D78** (2008) 017503, [arXiv:0804.1237 \[hep-ph\]](#).
- [595] S. Moretti, M. Nolten, and D. Ross, *Weak corrections and high E(T) jets at Tevatron*, *Phys.Rev.* **D74** (2006) 097301, [arXiv:hep-ph/0503152 \[hep-ph\]](#).
- [596] A. Denner, S. Dittmaier, S. Kallweit, and A. Muck, *Electroweak corrections to Higgs-strahlung off W/Z bosons at the Tevatron and the LHC with HAWK*, *JHEP* **1203** (2012) 075, [arXiv:1112.5142 \[hep-ph\]](#).

- [597] M. Ciccolini, S. Dittmaier, and M. Kramer, *Electroweak radiative corrections to associated  $WH$  and  $ZH$  production at hadron colliders*, *Phys.Rev.* **D68** (2003) 073003, [arXiv:hep-ph/0306234 \[hep-ph\]](#).
- [598] M. Ciccolini, A. Denner, and S. Dittmaier, *Electroweak and QCD corrections to Higgs production via vector-boson fusion at the LHC*, *Phys.Rev.* **D77** (2008) 013002, [arXiv:0710.4749 \[hep-ph\]](#).
- [599] M. Ciccolini, A. Denner, and S. Dittmaier, *Strong and electroweak corrections to the production of Higgs + 2jets via weak interactions at the LHC*, *Phys.Rev.Lett.* **99** (2007) 161803, [arXiv:0707.0381 \[hep-ph\]](#).
- [600] E. Accomando, A. Denner, and C. Meier, *Electroweak corrections to  $W\gamma$  and  $Z\gamma$  production at the LHC*, *Eur.Phys.J.* **C47** (2006) 125–146, [arXiv:hep-ph/0509234 \[hep-ph\]](#).
- [601] A. Bierweiler, T. Kasprzik, H. Kuhn, and S. Uccirati, *Electroweak corrections to  $W$ -boson pair production at the LHC*, [arXiv:1208.3147 \[hep-ph\]](#).
- [602] M. Billoni, S. Dittmaier, B. Jager, and C. Speckner, *Next-to-leading order electroweak corrections to  $pp \rightarrow W+W^- \rightarrow 4$  leptons at the LHC in double-pole approximation*, *JHEP* **1312** (2013) 043, [arXiv:1310.1564 \[hep-ph\]](#).
- [603] A. Bierweiler, T. Kasprzik, and J. H. Kuhn, *Vector-boson pair production at the LHC to  $\mathcal{O}(\alpha^3)$  accuracy*, *JHEP* **1312** (2013) 071, [arXiv:1305.5402 \[hep-ph\]](#).
- [604] S. Gieseke, T. Kasprzik, and J. H. Kuhn, *Vector-boson pair production and electroweak corrections in HERWIG++*, *Eur.Phys.J.* **C74** (2014) no. 8, 2988, [arXiv:1401.3964 \[hep-ph\]](#).
- [605] L. Wei-Hua, Z. Ren-You, M. Wen-Gan, G. Lei, L. Xiao-Zhou, and Z. Yu, *NLO QCD and EW corrections to  $WW$  + jet production with leptonic  $W$ -boson decays at LHC*, [arXiv:1507.07332 \[hep-ph\]](#).
- [606] D. T. Nhung, L. D. Ninh, and M. M. Weber, *NLO corrections to  $WWZ$  production at the LHC*, *JHEP* **1312** (2013) 096, [arXiv:1307.7403 \[hep-ph\]](#).
- [607] S. Yong-Bai, Z. Ren-You, M. Wen-Gan, L. Xiao-Zhou, Z. Yu, and G. Lei, *NLO QCD + NLO EW corrections to  $WZZ$  productions with leptonic decays at the LHC*, [arXiv:1507.03693 \[hep-ph\]](#).
- [608] A. Denner, S. Dittmaier, M. Hecht, and C. Pasold, *NLO QCD and electroweak corrections to  $W+\gamma$  production with leptonic  $W$ -boson decays*, *JHEP* **1504** (2015) 018, [arXiv:1412.7421 \[hep-ph\]](#).
- [609] A. Denner, S. Dittmaier, M. Hecht, and C. Pasold, *NLO QCD and electroweak corrections to  $Z + \gamma$  production with leptonic  $Z$ -boson decays*, *JHEP* **02** (2016) 057, [arXiv:1510.08742 \[hep-ph\]](#).
- [610] G. Bevilacqua, M. Czakon, M. Garzelli, A. van Hameren, A. Kardos, et al., *HELAC-NLO*, [arXiv:1110.1499 \[hep-ph\]](#).
- [611] S. Actis, A. Denner, L. Hofer, A. Scharf, and S. Uccirati, *Recursive generation of one-loop amplitudes in the Standard Model*, *JHEP* **1304** (2013) 037, [arXiv:1211.6316 \[hep-ph\]](#).
- [612] M. Chiesa, N. Greiner, and F. Tramontano, *Automation of electroweak corrections for LHC processes*, *J. Phys.* **G43** (2016) no. 1, 013002, [arXiv:1507.08579 \[hep-ph\]](#).
- [613] A. Denner, L. Hofer, A. Scharf, and S. Uccirati, *Electroweak corrections to lepton pair production in association with two hard jets at the LHC*, *JHEP* **1501** (2015) 094, [arXiv:1411.0916 \[hep-ph\]](#).
- [614] S. Kallweit, J. M. Lindert, P. Maierhöfer, S. Pozzorini, and M. Schönherr, *NLO electroweak automation and precise predictions for  $W$ +multijet production at the LHC*, [arXiv:1412.5157 \[hep-ph\]](#).
- [615] S. Kallweit, J. M. Lindert, P. Maierhöfer, S. Pozzorini, and M. Schönherr, *NLO QCD+EW*

- predictions for V+jets including off-shell vector-boson decays and multijet merging*, [arXiv:1511.08692 \[hep-ph\]](#).
- [616] B. Biedermann, A. Denner, S. Dittmaier, L. Hofer, and B. Jäger, *Electroweak corrections to  $pp \rightarrow \mu^+ \mu^- e^+ e^- + X$  at the LHC – a Higgs background study*, [arXiv:1601.07787 \[hep-ph\]](#).
- [617] E. Accomando, A. Denner, and A. Kaiser, *Logarithmic electroweak corrections to gauge-boson pair production at the LHC*, *Nucl.Phys.* **B706** (2005) 325–371, [arXiv:hep-ph/0409247 \[hep-ph\]](#).
- [618] E. Accomando and A. Kaiser, *Electroweak corrections and anomalous triple gauge-boson couplings in  $W^+W^-$  and  $W^\pm Z$  production at the LHC*, *Phys.Rev.* **D73** (2006) 093006, [arXiv:hep-ph/0511088 \[hep-ph\]](#).
- [619] A. Fuhrer, A. V. Manohar, J.-y. Chiu, and R. Kelley, *Radiative Corrections to Longitudinal and Transverse Gauge Boson and Higgs Production*, *Phys.Rev.* **D81** (2010) 093005, [arXiv:1003.0025 \[hep-ph\]](#).
- [620] T. Becher and X. Garcia i Tormo, *Electroweak Sudakov effects in  $W$ ,  $Z$  and  $\gamma$  production at large transverse momentum*, *Phys.Rev.* **D88** (2013) no. 1, 013009, [arXiv:1305.4202 \[hep-ph\]](#).
- [621] A. Fuhrer, A. V. Manohar, and W. J. Waalewijn, *Electroweak radiative Corrections to Higgs Production via Vector Boson Fusion using Soft-Collinear Effective Theory*, *Phys.Rev.* **D84** (2011) 013007, [arXiv:1011.1505 \[hep-ph\]](#).
- [622] F. Siringo and G. Buccheri, *Electroweak Radiative Corrections to Higgs Production via Vector Boson Fusion using SCET: Numerical Results*, *Phys. Rev.* **D86** (2012) 053013, [arXiv:1207.1906 \[hep-ph\]](#).
- [623] J. M. Campbell and R. Ellis, *MCFM for the Tevatron and the LHC*, *Nucl.Phys.Proc.Suppl.* **205-206** (2010) 10–15, [arXiv:1007.3492 \[hep-ph\]](#).
- [624] J. M. Campbell, D. Wackerath, and J. Zhou, *Electroweak Corrections at the LHC with MCFM*, in *23rd International Workshop on Deep-Inelastic Scattering and Related Subjects (DIS 2015) Dallas, Texas, United States, April 27-May 1, 2015*. 2015. [arXiv:1508.06247 \[hep-ph\]](#). <https://inspirehep.net/record/1389721/files/arXiv:1508.06247.pdf>.
- [625] M. L. Mangano, M. Moretti, F. Piccinini, R. Pittau, and A. D. Polosa, *ALPGEN, a generator for hard multiparton processes in hadronic collisions*, *JHEP* **0307** (2003) 001, [arXiv:hep-ph/0206293 \[hep-ph\]](#).
- [626] A. B. Arbuzov and R. R. Sadykov, *Inverse bremsstrahlung contributions to Drell-Yan like processes*, *J. Exp. Theor. Phys.* **106** (2008) 488–494, [arXiv:0707.0423 \[hep-ph\]](#).
- [627] C. Buttar, S. Dittmaier, V. Drollinger, S. Frixione, A. Nikitenko, et al., *Les houches physics at TeV colliders 2005, standard model and Higgs working group: Summary report*, [arXiv:hep-ph/0604120 \[hep-ph\]](#).
- [628] S. Jadach, B. F. L. Ward, and Z. Was, *KK MC 4.22: Coherent exclusive exponentiation of electroweak corrections for  $f\bar{f}f\bar{f}$  at the LHC and muon colliders*, *Phys. Rev.* **D88** (2013) no. 11, 114022, [arXiv:1307.4037 \[hep-ph\]](#).
- [629] S. A. Yost, V. Halyo, M. Hejna, and B. F. L. Ward, *HERWIRI2: Exponentiated Electroweak Corrections in a Hadronic Event Generator*, *PoS ICHEP2012* (2013) 098.
- [630] N. Davidson, T. Przedzinski, and Z. Was, *PHOTOS Interface in C++: Technical and Physics Documentation*, *Comput. Phys. Commun.* **199** (2016) 86–101, [arXiv:1011.0937 \[hep-ph\]](#).
- [631] P. Golonka and Z. Was, *PHOTOS Monte Carlo: A Precision tool for QED corrections in  $Z$  and  $W$  decays*, *Eur. Phys. J.* **C45** (2006) 97–107, [arXiv:hep-ph/0506026 \[hep-ph\]](#).
- [632] J. H. Kuhn, A. Kulesza, S. Pozzorini, and M. Schulze, *Logarithmic electroweak corrections to hadronic  $Z+1$  jet production at large transverse momentum*, *Phys. Lett.* **B609** (2005) 277–285,

- [arXiv:hep-ph/0408308](#) [hep-ph].
- [633] J. H. Kuhn, A. Kulesza, S. Pozzorini, and M. Schulze, *Electroweak corrections to large transverse momentum production of W bosons at the LHC*, *Phys. Lett.* **B651** (2007) 160–165, [arXiv:hep-ph/0703283](#) [HEP-PH].
- [634] K. Mishra et al., *Electroweak Corrections at High Energies*, in *Community Summer Study 2013: Snowmass on the Mississippi (CSS2013) Minneapolis, MN, USA, July 29-August 6, 2013*. 2013. [arXiv:1308.1430](#) [hep-ph].  
<https://inspirehep.net/record/1246902/files/arXiv:1308.1430.pdf>.
- [635] J. M. Campbell et al., *Working Group Report: Quantum Chromodynamics*, in *Community Summer Study 2013: Snowmass on the Mississippi (CSS2013) Minneapolis, MN, USA, July 29-August 6, 2013*. 2013. [arXiv:1310.5189](#) [hep-ph].  
<https://inspirehep.net/record/1261432/files/arXiv:1310.5189.pdf>.
- [636] P. M. F. Cascioli, J. Lindert and S. Pozzorini. <http://openloops.hepforge.org>.
- [637] S. Kallweit, MUNICH: “*MULTI-chaNNel Integrator at Swiss (CH) precision*”—an automated parton level NLO generator, In preparation.
- [638] F. Caravaglios and M. Moretti, *An algorithm to compute Born scattering amplitudes without Feynman graphs*, *Phys.Lett.* **B358** (1995) 332–338, [arXiv:hep-ph/9507237](#) [hep-ph].
- [639] A. Scharf, *Electroweak corrections to b-jet and di-jet production*, in *Particles and fields. Proceedings, Meeting of the Division of the American Physical Society, DPF 2009, Detroit, USA, July 26-31, 2009*. 2009. [arXiv:0910.0223](#) [hep-ph].  
<https://inspirehep.net/record/832780/files/arXiv:0910.0223.pdf>.
- [640] J. H. Kuhn, A. Scharf, and P. Uwer, *Weak effects in b-jet production at hadron colliders*, *Phys. Rev.* **D82** (2010) 013007, [arXiv:0909.0059](#) [hep-ph].
- [641] S. Dittmaier, A. Huss, and C. Speckner, *Weak radiative corrections to dijet production at the LHC*, *PoS DIS2013* (2013) 283, [arXiv:1306.6298](#) [hep-ph].
- [642] D. Pagani, I. Tsinikos, and M. Zaro, *The impact of the photon PDF and electroweak corrections on  $t\bar{t}$  distributions*, [arXiv:1606.01915](#) [hep-ph].
- [643] G. Marchesini and B. R. Webber, *Simulation of QCD Jets Including Soft Gluon Interference*, *Nucl. Phys.* **B238** (1984) 1–29.
- [644] T. Sjostrand, L. Lonnblad, S. Mrenna, and P. Z. Skands, *Pythia 6.3 physics and manual*, [arXiv:hep-ph/0308153](#) [hep-ph].

## Chapter 2: Higgs and EW Symmetry Breaking Studies

### Editors:

R. Contino<sup>1,2</sup>, D. Curtin<sup>3</sup>, A. Katz<sup>1,4</sup>, M. L. Mangano<sup>1</sup>, G. Panico<sup>5</sup>, M. J. Ramsey-Musolf<sup>6,7</sup>, G. Zanderighi<sup>1</sup>

### Contributors:

C. Anastasiou<sup>8</sup>, W. Astill<sup>9</sup>, G. Bambhaniya<sup>21</sup>, J. K. Behr<sup>10,11</sup>, W. Bizon<sup>9</sup>, P. S. Bhupal Dev<sup>12</sup>, D. Bortoletto<sup>10</sup>, D. Buttazzo<sup>22</sup>, Q.-H. Cao<sup>13,14,15</sup>, F. Caola<sup>1</sup>, J. Chakraborty<sup>16</sup>, C.-Y. Chen<sup>17,18,19</sup>, S.-L. Chen<sup>15,20</sup>, D. de Florian<sup>23</sup>, F. Dulat<sup>8</sup>, C. Englert<sup>24</sup>, J. A. Frost<sup>10</sup>, B. Fuks<sup>25</sup>, T. Gherghetta<sup>26</sup>, G. Giudice<sup>1</sup>, J. Gluza<sup>27</sup>, N. Greiner<sup>28</sup>, H. Gray<sup>29</sup>, N. P. Hartland<sup>10</sup>, V. Hirschi<sup>30</sup>, C. Issever<sup>10</sup>, T. Jeliński<sup>27</sup>, A. Karlberg<sup>9</sup>, J. H. Kim<sup>31,32,33</sup>, F. Kling<sup>34</sup>, A. Lazopoulos<sup>8</sup>, S. J. Lee<sup>35,36</sup>, Y. Liu<sup>13</sup>, G. Luisoni<sup>1</sup>, O. Mattelaer<sup>37</sup>, J. Mazzitelli<sup>23,38</sup>, B. Mistlberger<sup>1</sup>, P. Monni<sup>9</sup>, K. Nikolopoulos<sup>39</sup>, R. N. Mohapatra<sup>3</sup>, A. Papaefstathiou<sup>1</sup>, M. Perelstein<sup>40</sup>, F. Petriello<sup>41</sup>, T. Plehn<sup>42</sup>, P. Reimitz<sup>42</sup>, J. Ren<sup>43</sup>, J. Rojo<sup>10</sup>, K. Sakurai<sup>37</sup>, T. Schell<sup>42</sup>, F. Sala<sup>44</sup>, M. Selvaggi<sup>45</sup>, H.-S. Shao<sup>1</sup>, M. Son<sup>31</sup>, M. Spannowsky<sup>37</sup>, T. Srivastava<sup>16</sup>, S.-F. Su<sup>34</sup>, R. Szafron<sup>46</sup>, T. Tait<sup>47</sup>, A. Tesi<sup>48</sup>, A. Thamm<sup>49</sup>, P. Torrielli<sup>50</sup>, F. Tramontano<sup>51</sup>, J. Winter<sup>52</sup>, A. Wulzer<sup>53</sup>, Q.-S. Yan<sup>54,55,56</sup>, W. M. Yao<sup>57</sup>, Y.-C. Zhang<sup>58</sup>, X. Zhao<sup>54</sup>, Z. Zhao<sup>54,59</sup>, Y.-M. Zhong<sup>60</sup>

<sup>1</sup> CERN, TH Department, CH-1211 Geneva, Switzerland

<sup>2</sup> EPFL, Lausanne, Switzerland

<sup>3</sup> Maryland Center for Fundamental Physics, Department of Physics, University of Maryland, College Park, MD 20742, USA

<sup>4</sup> Université de Genève, Department of Theoretical Physics and Center for Astroparticle Physics, 24 quai E. Ansermet, CH-1211, Geneva 4, Switzerland

<sup>5</sup> IFAE, Universitat Autònoma de Barcelona, E-08193 Bellaterra, Barcelona

<sup>6</sup> Amherst Center for Fundamental Interactions, Physics Department, University of Massachusetts Amherst, Amherst, MA 01003, USA

<sup>7</sup> Kellogg Radiation Laboratory, California Institute of Technology, Pasadena, CA 91125 USA

<sup>8</sup> Institute for Theoretical Physics, ETH Zürich, 8093 Zürich, Switzerland

<sup>9</sup> Rudolf Peierls Centre for Theoretical Physics, 1 Keble Road, University of Oxford, UK

<sup>10</sup> Physics Department, 1 Keble Road, University of Oxford, UK

<sup>11</sup> Deutsches Elektronen-Synchrotron (DESY), Notkestrasse 85, D-22607 Hamburg, Germany

<sup>12</sup> Max-Planck-Institut für Kernphysik, Saupfercheckweg 1, D-69117 Heidelberg, Germany

<sup>13</sup> Department of Physics and State Key Laboratory of Nuclear Physics and Technology, Peking University, Beijing 100871, China

<sup>14</sup> Collaborative Innovation Center of Quantum Matter, Beijing 100871, China

<sup>15</sup> Center for High Energy Physics, Peking University, Beijing 100871, China

<sup>16</sup> Department of Physics, Indian Institute of Technology, Kanpur-208016, India

<sup>17</sup> Department of Physics, Brookhaven National Laboratory, Upton, New York 11973, USA

<sup>18</sup> Department of Physics and Astronomy, University of Victoria, Victoria, British Columbia V8P 5C2, Canada

<sup>19</sup> Perimeter Institute for Theoretical Physics, Waterloo, Ontario N2J 2W9, Canada

<sup>20</sup> Key Laboratory of Quark and Lepton Physics (MoE) and Institute of Particle Physics, Central China Normal University, Wuhan 430079, China

<sup>21</sup> Theoretical Physics Division, Physical Research Laboratory, Ahmedabad-380009, India

<sup>22</sup> Physik-Institut, Universität Zürich, CH-8057 Zürich, Switzerland

- <sup>23</sup> International Center for Advanced Studies (ICAS), UNSAM, Campus Miguelete, 25 de Mayo y Francia, (1650) Buenos Aires, Argentina
- <sup>24</sup> SUPA, School of Physics and Astronomy, University of Glasgow, Glasgow G12 8QQ, UK
- <sup>25</sup> Sorbonne Universités, UPMC Univ. Paris 06, UMR 7589, LPTHE, F-75005 Paris, France CNRS, UMR 7589, LPTHE, F-75005 Paris, France
- <sup>26</sup> School of Physics and Astronomy, University of Minnesota, Minneapolis, MN 55455, USA
- <sup>27</sup> Institute of Physics, University of Silesia, Uniwersytecka 4, 40-007 Katowice, Poland
- <sup>28</sup> Physik Institut, Universität Zürich, Winterthurerstrasse 190, CH-8057 Zürich, Switzerland
- <sup>29</sup> CERN, EP Department, CH-1211 Geneva, Switzerland
- <sup>30</sup> SLAC, National Accelerator Laboratory, 2575 Sand Hill Road, Menlo Park, CA 94025-7090, USA
- <sup>31</sup> Department of Physics, Korea Advanced Institute of Science and Technology, 335 Gwahak-ro, Yuseong-gu, Daejeon 305-701, Korea
- <sup>32</sup> Center for Theoretical Physics of the Universe, IBS, 34051 Daejeon, Korea
- <sup>33</sup> Center for Axion and Precision Physics Research, IBS, 34141 Daejeon, Korea
- <sup>34</sup> Department of Physics, University of Arizona, Tucson, AZ 85721, USA
- <sup>35</sup> Department of Physics, Korea University, Seoul 136-713, Korea
- <sup>36</sup> School of Physics, Korea Institute for Advanced Study, Seoul 130-722, Korea
- <sup>37</sup> IPPP, Department of Physics, University of Durham, Science Laboratories, South Road, Durham, DH1 3LE, UK
- <sup>38</sup> Departamento de Fisica and IFIBA, FCEyN, Universidad de Buenos Aires, (1428) Pabellon 1 Ciudad Universitaria, Capital Federal, Argentina
- <sup>39</sup> School of Physics and Astronomy, University of Birmingham, Birmingham, B15 2TT, UK
- <sup>40</sup> Laboratory for Elementary Particle Physics, Cornell University, Ithaca, NY 14853, USA
- <sup>41</sup> Northwestern University, Department of Physics and Astronomy, 2145 Sheridan Road, Evanston, Illinois 60208-3112, USA
- <sup>42</sup> Institut für Theoretische Physik, Universität Heidelberg, Germany
- <sup>43</sup> Department of Physics, University of Toronto, Toronto, Ontario, Canada M5S1A7
- <sup>44</sup> 2LPTHE, CNRS, UMR 7589, 4 Place Jussieu, F-75252, Paris, France
- <sup>45</sup> Centre for Cosmology, Particle Physics and Phenomenology CP3, Université Catholique de Louvain, Chemin du Cyclotron, 1348 Louvain la Neuve, Belgium
- <sup>46</sup> Department of Physics, University of Alberta, Edmonton, AB T6G 2E1, Canada
- <sup>47</sup> Department of Physics and Astronomy, University of California, Irvine, CA 92697, USA
- <sup>48</sup> Enrico Fermi Institute, University of Chicago, Chicago, IL 60637, USA
- <sup>49</sup> PRISMA Cluster of Excellence and Mainz Institute for Theoretical Physics, Johannes Gutenberg University, 55099 Mainz, Germany
- <sup>50</sup> Dipartimento di Fisica, Università di Torino, and INFN, Sezione di Torino, Via P. Giuria 1, I-10125, Turin, Italy
- <sup>51</sup> Università di Napoli “Federico II” and INFN, Sezione di Napoli, 80126 Napoli, Italy
- <sup>52</sup> Department of Physics and Astronomy, Michigan State University, East Lansing, MI 48824, USA
- <sup>53</sup> Dipartimento di Fisica e Astronomia, Università di Padova and INFN, Sezione di Padova, via Marzolo 8, I-35131 Padova, Italy
- <sup>54</sup> School of Physical Sciences, University of Chinese Academy of Sciences, Beijing 100049, P. R. China
- <sup>55</sup> Center for High-Energy Physics, Peking University, Beijing 100871, P. R. China
- <sup>56</sup> Center for future high energy physics, Chinese Academy of Sciences 100049, P. R. China
- <sup>57</sup> Lawrence Berkeley National Lab (LBNL), One Cyclotron Rd, Berkeley, CA94720, USA
- <sup>58</sup> Service de Physique Théorique, Université Libre de Bruxelles, Boulevard du Triomphe, CP225, 1050 Brussels, Belgium
- <sup>59</sup> Department of Physics, University of Siegen, 57068 Siegen, Germany
- <sup>60</sup> C.N. Yang Institute for Theoretical Physics, Stony Brook University, Stony Brook, New York, USA

**Abstract**

This Chapter summarises the physics opportunities for the study of Higgs bosons and the dynamics of electroweak symmetry breaking at the 100 TeV  $pp$  collider.

**1 Introduction**

Despite its impressive success in accounting for a wide range of experimental observations, the Standard Model (SM) leaves many of our most important questions unanswered:

- Why does the universe contain more matter than anti-matter?
- What is the identity of the dark matter and what are its interactions?
- Why are the masses of neutrinos so much smaller than those of all other known elementary fermions?

The discovery [1, 2] of the Higgs-like scalar [3–8] at the LHC highlights additional theoretical puzzles. The scalar sector is the “obscure” sector of the SM, in the sense that it is the least understood part of the theory. The principles dictating its structure are still unclear. This is to be contrasted with the gauge sector, which logically follows from an elegant symmetry principle and has all the features of a fundamental structure. Not surprisingly, many of the open problems of the SM are connected to the Higgs sector. For example, the stability of the Higgs mass [9] and of the Electroweak (EW) scale in general against UV-sensitive radiative corrections motivates additional symmetry structures near the TeV scale. To address these questions, possible theoretical extensions of the SM have been proposed. Their experimental manifestations can be direct, via the production of new particles, or indirect, via deviations of the Higgs properties from their SM predictions.

With its higher energy and the associated increase in parton luminosity, a 100 TeV  $pp$  collider would provide an unprecedented potential to both detect new particles, and to explore in detail the Higgs boson properties, uniquely complementing the capabilities at the LHC and possible future  $e^+e^-$  colliders. This Chapter is dedicated to a first assessment of this potential.

In the first Section we review what is known today about the production properties of the 125 GeV Higgs boson at 100 TeV. We present evidence that the increased energy does not introduce uncertainties larger than those already established from the studies for the LHC [10–12]. Furthermore, the large production rates available at 100 TeV open new opportunities to optimize the balance between statistical uncertainties, background contamination, and systematic uncertainties of both theoretical and experimental origin. The second Section illustrates these ideas with a few concrete examples of possible precision attainable at 100 TeV. These are not intended to provide a robust and definitive assessment of the ultimate goals; this would be premature, since both the theoretical landscape (higher-order corrections, resummations, PDFs, and event simulation tools in general) and the future detectors’ performance potential are far from being known. Rather, these examples suggest possible new directions, which on paper and in the case of idealized analysis scenarios offer exciting opportunities to push the precision and the reach of Higgs physics into a domain that will hardly be attainable by the LHC (although some of these ideas might well apply to the HL-LHC as well).

The third Section addresses the determination of the Higgs self-coupling and the measurement of the Higgs potential. This is important for several reasons. In the SM, the shape of the Higgs potential is completely fixed by the mass and vacuum expectation value of the Higgs field. Therefore, an independent measurement of the trilinear and quadrilinear Higgs self-interactions provides important additional tests of the validity of the SM. This test is quite non-trivial. Indeed, as discussed in the final Section, in many Beyond-the-SM (BSM) scenarios sizable corrections to the Higgs self-couplings are predicted, which, in some cases, can lead to large deviations in multi-Higgs production processes but not in other observables. In these scenarios, an analysis of the non-linear Higgs couplings can be more sensitive to new-physics

effects than other direct or indirect probes [13, 14]. This Section includes an overview of the production rates for multiple Higgs production, including those of associated production and in the vector-boson fusion channel. This is followed by a detailed up-to-date study of the possible precision with which the triple Higgs coupling can be measured, and a first assessment of the potential to extract information on the quartic coupling.

Determining the structure of the Higgs potential is also important to understand the features of the EW phase transition, whose properties can have significant implications for cosmology. For instance, a strong first order transition could provide a viable scenario to realize baryogenesis at the EW scale (see for example [15] and references therein). In the SM the EW transition is known to be rather weak (for a Higgs mass  $m_h \sim 70 - 80$  GeV, only a cross-over is predicted), so that it is not suitable for a successful baryogenesis. Many BSM scenarios, however, predict modifications in the Higgs potential that lead to first order EW transitions, whose strength could allow for a viable baryogenesis. An additional aspect related to the structure of the Higgs potential is the issue of the stability of the EW vacuum (see for instance Ref. [16]). The final Section of this Chapter will address these questions in great detail. This Section will also study the impact of studies in the Higgs sector on the issue of Dark Matter, on the origin of neutrino masses, and on naturalness. Extensions of the SM affecting the Higgs sector of the theory often call for the existence of additional scalar degrees of freedom, either fundamental or emergent. Such *Beyond the SM (BSM) Higgs sectors* frequently involve new singlet or electroweak-charged fields, making their discovery at the LHC challenging. The prospects for their direct observation at 100 TeV will be presented in the final part of the Section.

The results and observations presented throughout this document, in addition to put in perspective the crucial role of a 100 TeV  $pp$  collider in clarifying the nature of the Higgs boson and electroweak symmetry breaking, can be used as benchmarks to define detector performance goals, or to exercise new analysis concepts (focused, for example, on the challenge of tagging multi-TeV objects such as top and bottom quarks, or Higgs and gauge bosons). Equally important, they will hopefully trigger complete analyses, as well as new ideas and proposals for interesting observables. Higgs physics at 100 TeV will not just be a larger-statistics version of the LHC, it will have the potential of being a totally new ballgame.

## 2 SM Higgs production

We discuss in this Section the 125 GeV SM Higgs boson production properties at 100 TeV, covering total rates and kinematical distributions. Multiple Higgs production is discussed in Section 4.

For ease of reference, and for the dominant production channels, we summarize in Table 1 the central values of the total cross sections that will be described in more detail below. The increases with respect to the LHC energy are very large, ranging from a factor of  $\sim 10$  for the  $VH$  ( $V = W, Z$ ) associated production, to a factor of  $\sim 60$  for the  $t\bar{t}H$  channel. As will be shown in this section, much larger increases are expected for kinematic configurations at large transverse momentum.

With these very large rate increases, it is important to verify that the relative accuracy of the predictions does not deteriorate. We shall therefore present the current estimates of theoretical systematics, based on the available calculations of QCD and electroweak perturbative corrections, and on the knowledge of the proton parton distribution functions (PDFs). With the long time between now and the possible operation of the FCC-hh, the results shown here represent only a crude and conservative picture of the precision that will eventually be available. But it is extremely encouraging that, already today, the typical systematical uncertainties at 100 TeV, whether due to missing higher-order effects or to PDFs, are comparable to those at 14 TeV. This implies that, in perspective, the FCC-hh has a great potential to perform precision measurements of the Higgs boson. A first assessment of this potential will be discussed in the next Section.

In addition to the standard production processes, we document, in the last part of this Section, the rates of rarer channels of associated production (e.g. production with multiple gauge bosons). These processes could allow independent tests of the Higgs boson properties, and might provide channels with improved signal over background, with possibly reduced systematic uncertainties. We hope that the first results shown here will trigger some dedicated phenomenological analysis. For a recent overview of Higgs physics at 33 and 100 TeV, see also [17].

	$gg \rightarrow H$ (Sect 2.1)	$VBF$ (Sect 2.5)	$HW^\pm$ (Sect 2.4)	$HZ$ (Sect 2.4)	$t\bar{t}H$ (Sect 2.6)
$\sigma(\text{pb})$	802	69	15.7	11.2	32.1
$\sigma(100 \text{ TeV})/\sigma(14 \text{ TeV})$	16.5	16.1	10.4	11.4	52.3

**Table 1:** Upper row: cross sections at a 100 TeV collider for the production of a SM Higgs boson in  $gg$  fusion, vector boson fusion, associated production with  $W$  and  $Z$  bosons, and associated production with a  $t\bar{t}$  pair. Lower row: rate increase relative to 14 TeV [18]. The details of the individual processes are described in the relevant subsections.

### 2.1 Inclusive $gg \rightarrow H$ production

In this section we analyse the production of a Standard Model Higgs boson via the gluon fusion production mode at a 100 TeV proton proton collider. As at the LHC with 13 TeV this particular production mode represents the dominant channel for the production of Higgs bosons.

We relate perturbative QFT predictions to the cross section at a  $\sqrt{S} = 100$  TeV collider using the general factorisation formula

$$\sigma = \tau \sum_{ij} \int_{\tau}^1 \frac{dz}{z} \int_{\frac{\tau}{z}}^1 \frac{dx}{x} f_i(x) f_j\left(\frac{\tau}{zx}\right) \frac{\hat{\sigma}_{ij}(z)}{z}, \quad (1)$$

where  $\hat{\sigma}_{ij}$  are the partonic cross sections for producing a Higgs boson from a scattering of partons  $i$  and

$j$ , and  $f_i$  and  $f_j$  are the corresponding parton densities. We have defined the ratios

$$\tau = \frac{m_H^2}{S} \quad \text{and} \quad z = \frac{m_H^2}{s}. \quad (2)$$

Here,  $s$  is the partonic center of mass energy. In the wake of the LHC program tremendous efforts have been made from the phenomenology community to improve the theoretical predictions for the Higgs boson cross section. In this section we want to briefly review the various ingredients for a state of the art prediction for the FCC and discuss the associated uncertainties. To this end we split the partonic cross section as follows.

$$\hat{\sigma}_{ij} \simeq R_{LO} (\hat{\sigma}_{ij,EFT} + \hat{\sigma}_{ij,EW}) + \delta\hat{\sigma}_{ij,ex;t,b,c}^{LO} + \delta\hat{\sigma}_{ij,ex;t,b,c}^{NLO} + \delta_t\hat{\sigma}_{ij,EFT}^{NNLO}. \quad (3)$$

The relatively low mass of the Higgs boson in comparison to the top threshold allows the use of an effective theory in which we regard a limit of infinite top quark mass and only consider the effects of massless five-flavour QCD on the gluon fusion cross section. This effective theory is described by an effective Lagrangian [19–23]

$$\mathcal{L}_{EFT} = \mathcal{L}_{QCD,5} - \frac{1}{3\pi} C H G_{\mu\nu}^a G_a^{\mu\nu}, \quad (4)$$

where the Higgs boson is coupled to the Yang-Mills Lagrangian of QCD via a Wilson coefficient [24–26] and  $\mathcal{L}_{QCD,5}$  is the QCD Lagrangian with five massless quark flavours. The cross section  $\hat{\sigma}_{ij,EFT}$  is the partonic cross section for Higgs production computed in this effective theory. It captures the dominant part of the gluon fusion production mode [27–30]. Recently, it was computed through N<sup>3</sup>LO in perturbation theory [31].

Effects due to the fact that the top mass is finite need to be included in order to make precision predictions for the inclusive Higgs boson production cross section. At LO and NLO in QCD the full dependence on the quark masses is known [32–39].

First, to improve the behaviour of the effective theory cross section we rescale  $\hat{\sigma}_{ij,EFT}$  with the constant ratio

$$R_{LO} \equiv \frac{\sigma_{ex;t}^{LO}}{\sigma_{EFT}^{LO}}, \quad (5)$$

where  $\sigma_{ex;t}^{LO}$  is the leading order cross section in QCD computed under the assumption that only the top quark has a non-vanishing Yukawa coupling.  $\sigma_{EFT}^{LO}$  is the leading order effective theory cross section. In order to also include important effects due to the non-vanishing Yukawa coupling of the bottom and charm quark we correct our cross section prediction at LO with  $\delta\hat{\sigma}_{ij,ex;t,b,c}^{LO}$  and at NLO with  $\delta\hat{\sigma}_{ij,ex;t,b,c}^{NLO}$ . These correction factors account for the exactly known mass dependence at LO and NLO beyond the rescaled EFT. The exact mass dependence at NNLO is presently unknown. However, corrections due to the finite top mass beyond the rescaled EFT have been computed as an expansion in the inverse top mass [40–42]. We account for these effects with the term  $\delta_t\hat{\sigma}_{ij,EFT}^{NNLO}$ .

Besides corrections due to QCD it is important to include electroweak corrections to the inclusive production cross section. The electroweak corrections to the LO cross section at first order in the weak coupling were computed [43, 44] and an approximation to mixed higher order corrections at first order in the weak as well as the strong coupling exists [45]. We account for these corrections with  $\hat{\sigma}_{ij,EW}$ .

Next, we study the numerical impact of the aforementioned contributions on the Higgs boson cross section at 100 TeV and estimate the respective uncertainties. We implemented the effects mentioned above into a soon to be released version of the code `iHixs` [46, 47] and evaluated the cross section with the setup summarised in Table 2. Throughout the following analysis we choose parton distribution functions provided by Ref. [48]. For a detailed analysis of the various sources of uncertainties at 13 TeV we refer the interested reader to Ref. [49].

$\sqrt{S}$	100TeV
$m_h$	125GeV
PDF	PDF4LHC15_nnlo_100
$\alpha_s(m_Z)$	0.118
$m_t(m_t)$	162.7 ( $\overline{MS}$ )
$m_b(m_b)$	4.18 ( $\overline{MS}$ )
$m_c(3GeV)$	0.986 ( $\overline{MS}$ )
$\mu = \mu_R = \mu_F$	62.5 ( $= m_h/2$ )

**Table 2:** Setup

### 2.1.1 Effective Theory

The Higgs boson cross section is plagued by especially large perturbative QCD corrections. The dominant part of these corrections is captured by the effective field theory description of the cross section introduced in Eq. (4). As a measure for the uncertainty of the partonic cross section due to the truncation of the perturbative series we regard the dependence of the cross section on the unphysical scale  $\mu$  of dimensional regularisation. We will choose a central scale  $\mu_{\text{central}} = \frac{m_h}{2}$  for the prediction of the central value of our cross section and vary the scale in the interval  $\mu \in [\frac{m_h}{4}, m_h]$  to obtain an estimate of the uncertainty due to missing higher orders.

First, we investigate the dependence of  $\hat{\sigma}_{ij,EFT}$  computed through different orders in perturbation theory on the hadronic center of mass energy  $S$  as plotted in fig. 1. One can easily see that an increase of

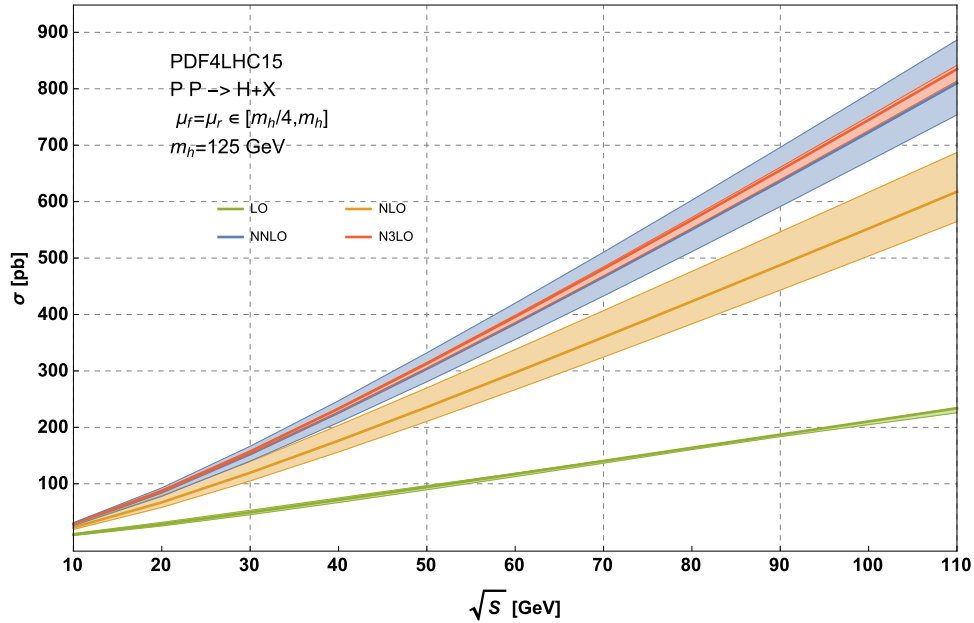


**Fig. 1:** The effective theory gluon fusion cross section at all perturbative orders through N<sup>3</sup>LO in the scale interval  $[\frac{m_h}{4}, m_h]$  as a function of the collider energy  $\sqrt{S}$ .

the center of mass energy leads to a more than linear increase of the production cross section. Furthermore, we observe that higher orders in perturbation theory play an important role for precise predictions for the Higgs boson cross section. The lower orders dramatically underestimate the cross section and particularly the scale uncertainty. Only with the recently obtained N<sup>3</sup>LO corrections [31] the perturbative series finally stabilises and the uncertainty estimate due to scale variations is significantly reduced.

In fig. 2 we plot the effective theory  $K$ -factor for various orders in perturbation theory.

$$K^{(n)} = \frac{\sigma_{\text{EFT}}^{\text{N}^n\text{LO}}}{\sigma_{\text{EFT}}^{\text{LO}}}. \quad (6)$$

Here,  $\sigma_{\text{EFT}}^{\text{N}^n\text{LO}}$  is the hadronic Higgs production cross section based on the effective theory prediction through  $\text{N}^n\text{LO}$ . One can easily see that QCD corrections become slightly more important as we increase the center of mass energy. The relative size of the variation of the cross section due to variation of the common scale  $\mu$  is roughly independent of the center of mass energy of the proton collider.

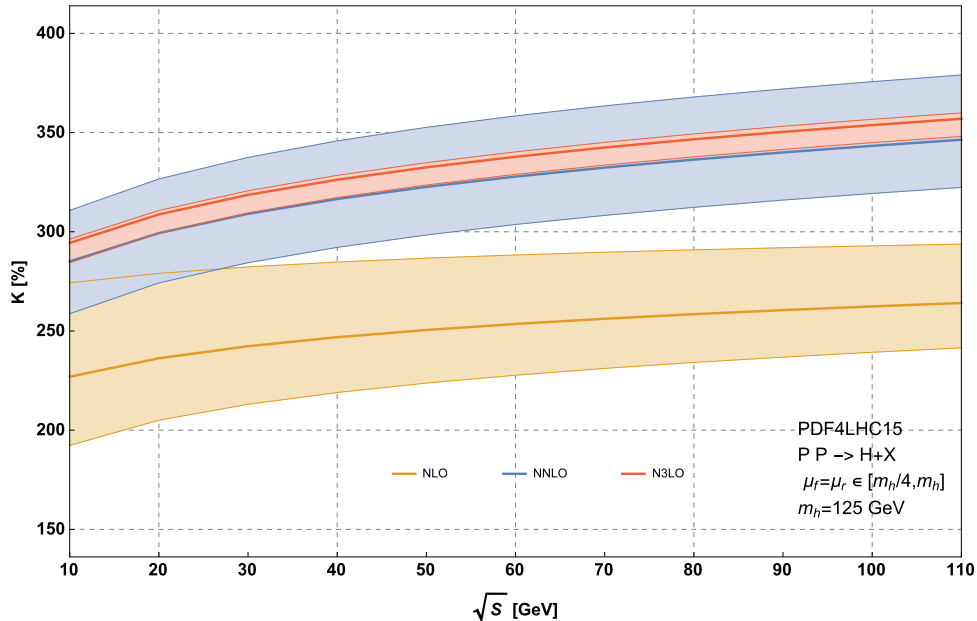


**Fig. 2:** QCD  $K$ -factor for the effective theory Higgs production cross section as a function of the hadronic center of mass energy.

### 2.1.2 Quark Mass Effects

First, let us discuss the quality of the effective theory approach considered above. The cross section obtained with this approach corresponds to the leading term in an expansion of the partonic cross section in  $\delta = \frac{s}{4m_t^2}$ . In fig 3 we plot the gluon luminosity for Higgs production as a function of  $z$ . The area that represents the production of gluons with a partonic center of mass energy larger than  $2m_t$  is shaded in red and in green for the complement. In  $\sim 96\%$  of all events in which a gluon pair has large enough energy to produce a Higgs boson the expansion parameter  $\delta$  is smaller than one and the effective theory can be expected to perform reasonably well. In comparison, at 13 TeV  $\delta$  is smaller than one for  $\sim 98\%$  of all gluon pairs that are produced with a center of mass energy larger than the Higgs boson mass.

Next, let us assess the performance of the rescaled effective theory quantitatively. The rescaling by the ratio  $R_{LO} = 1.063$  provides a reasonable approximation of the cross section with full top mass dependence. If we consider the exact corrections due to the top quark through NLO we find only a mild correction of 2.8% on top of the rescaled effective theory NLO cross section. At NNLO the exact dependence of the QCD cross section on the top quark mass is unknown and only higher order terms in the expansion in  $\delta$  are available. These amount to 1.1% of the total cross section. Following the recommendation of Ref. [40] we assign a matching uncertainty of  $\delta \frac{1}{m_t} = \pm 1\%$  due to the incomplete NNLO corrections.

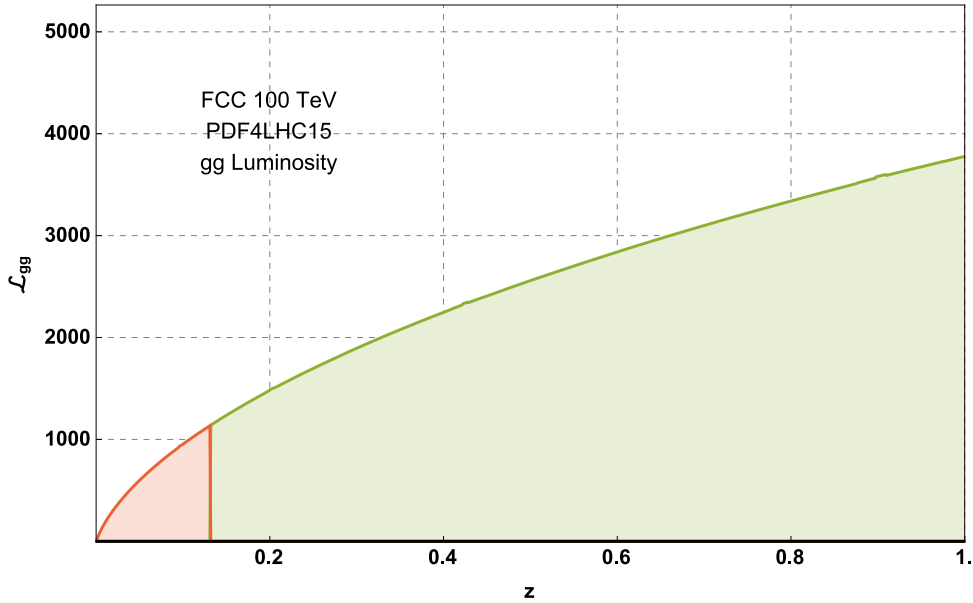


**Fig. 3:** Higgs production gluon luminosity at a 100 TeV proton proton collider. The area shaded in red corresponds to partonic center of mass energy larger than  $2m_t$  and the green area to partonic center of mass energy less than  $2m_t$ .

Of considerable importance are effects due to the interference of amplitudes coupling light quarks to the Higgs and amplitudes with the usual top quark Yukawa interaction. At LO and NLO we find destructive interference of these contributions and we include them as part of  $\hat{\sigma}_{ij,ex;t,b,c}^{NLO}$ . Currently, no computation of interference effects of light and heavy quark amplitudes at NNLO is available and we assess the uncertainty due to these missing contributions via

$$\delta_{tbc} = \pm \left| \frac{\sigma_{ex;t}^{NLO} - \sigma_{ex;t,b,c}^{NLO}}{\sigma_{ex;t}^{NLO}} \right| \frac{R_{LO} \delta \sigma_{EFT}^{NNLO}}{\sigma} = \pm 0.8\%. \quad (7)$$

Here,  $\sigma_{ex;t}^{NLO}$  and  $\sigma_{ex;t,b,c}^{NLO}$  are the hadronic cross sections based on NLO partonic cross sections containing mass effects from the top quark only and mass effects from the top, bottom and charm quark respectively.  $\delta \sigma_{EFT}^{NNLO}$  is the NNLO correction to the cross section resulting from the effective theory partonic cross section.

Parametric uncertainties due to the imprecise knowledge of the quark masses are small and we neglect in all further discussions.

### 2.1.3 Electroweak corrections

Electroweak corrections at  $\mathcal{O}(\alpha)$  were computed in Ref. [43]. These corrections contain only virtual contributions and are thus independent of the energy. We currently include them as

$$\hat{\sigma}_{ij,EW} = \kappa_{EW} \times \hat{\sigma}_{ij,EFT}, \quad (8)$$

where  $\kappa_{EW}$  is the rescaling factor arising due to the electroweak corrections. Electroweak corrections beyond  $\mathcal{O}(\alpha)$  were approximated in Ref. [45]. We also include those effects and assign residual uncertainty of  $\delta_{EW} = \pm 1\%$  on the total cross section due to missing higher order mixed electroweak and QCD corrections [49].

Electroweak corrections for Higgs production in gluon fusion in association with a jet were computed by [50]. These turn out to be negligible for the inclusive cross section.

### 2.1.4 $\alpha_S$ and PDF uncertainties

The strong coupling constant and the parton distribution functions are quantities that are extracted from a large set of diverse measurements. Naturally, there is an uncertainty associated with these quantities that has to be taken into account when deriving predictions for the Higgs boson production cross section. Here, we follow the prescription outlined by the PDF4LHC working group in Ref. [48] to derive the PDF and  $\alpha_S$  uncertainty for the Higgs production cross section. We find

$$\delta_{\text{PDF}} = \pm 2.5\%, \quad \delta_{\alpha_S} = \pm 2.9\%. \quad (9)$$

In Fig. 4 we plot the PDF and  $\alpha_S$  uncertainty for the effective theory cross section as a function of the scale  $\mu$  normalised to its central value.

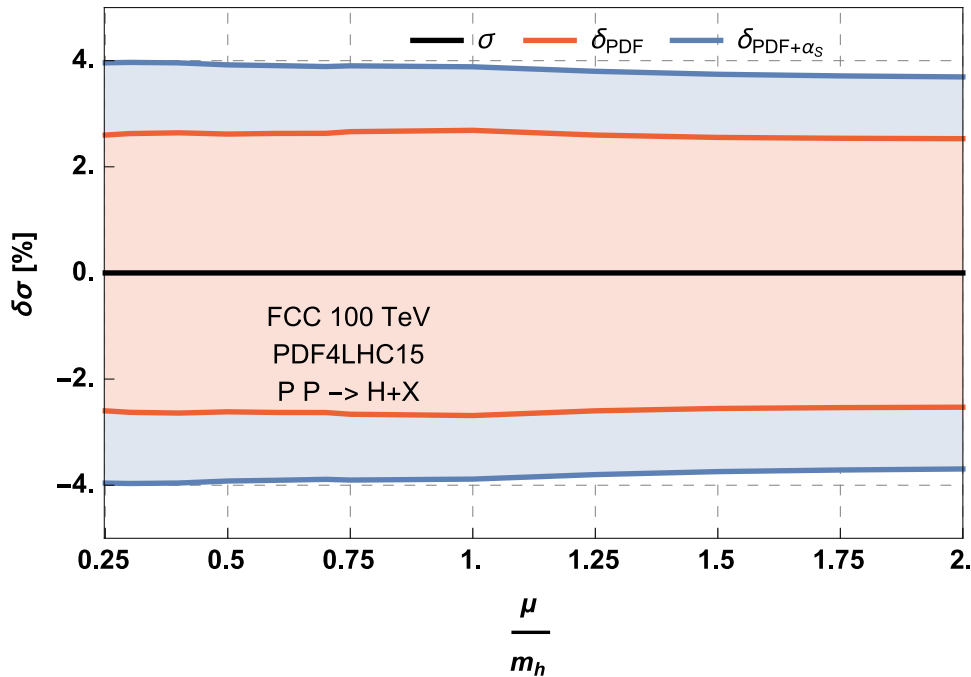


**Fig. 4:** PDF and  $\alpha_S$  uncertainty of the effective theory cross section as a function of the perturbative scale  $\mu$  normalised to the central value of  $\sigma_{\text{EFF}}(\mu)$ .

We want to remark that the predictions obtained here are subject to the choice of the parton distribution functions. Especially choosing parton distribution functions and strong coupling constant according to Ref. [51, 52] results in quantitatively different predictions. This discrepancy is not covered by current uncertainty estimates and should be resolved.

Currently, parton distributions are obtained using cross sections computed up to at most NNLO. As we combine these NNLO parton distribution functions with the effective theory cross section computed at N<sup>3</sup>LO we have to assign an uncertainty for the miss-match. As a measure for this uncertainty  $\delta_{\text{PDF-theo}}$  we use

$$\delta_{\text{PDF-theo}} = \pm \frac{1}{2} \left| \frac{\sigma_{\text{EFT, NNLO}}^{\text{NNLO}} - \sigma_{\text{EFT, NLO}}^{\text{NNLO}}}{\sigma_{\text{EFT, NNLO}}^{\text{NNLO}}} \right| = \pm 2.7\%. \quad (10)$$

Here,  $\sigma_{\text{EFT, N}^n\text{LO}}^{\text{NNLO}}$  is the hadronic cross section resulting from the convolution of the effective theory NNLO partonic cross section with N<sup>n</sup>LO parton distribution functions. For both orders we use PDF sets provided by the PDF4LHC working group [48].

$\delta_{\text{PDF}}$	$\delta_{\alpha_S}$	$\delta_{\text{scale}}$	$\delta_{\text{PDF-theo}}$	$\delta_{\text{EW}}$	$\delta_{\text{tbc}}$	$\delta_{\frac{1}{m_t}}$
$\pm 2.5\%$	$\pm 2.9\%$	$\begin{smallmatrix} +0.8\% \\ -1.9\% \end{smallmatrix}$	$\pm 2.7\%$	$\pm 1\%$	$\pm 0.8\%$	$\pm 1\%$

**Table 3:** Various sources of uncertainties of the inclusive gluon fusion Higgs production cross section at a 100 TeV proton-proton collider.

### 2.1.5 Summary

In this section we have discussed state-of-the-art predictions for the inclusive Higgs boson production cross section via gluon fusion at a 100 TeV proton-proton collider. This inclusive cross section will be accessible experimentally at percent level precision and an in-depth theoretical understanding of this observable is consequently paramount to a successful Higgs phenomenology program at the FCC.

Already now we are in the position to derive high-precision predictions for this cross section. The current state-of-the-art prediction with its associated uncertainties is:

$$\sigma = 802 \text{ pb} \begin{smallmatrix} +6.1\% \\ -7.2\% \end{smallmatrix} (\delta_{\text{theo}}) \begin{smallmatrix} +2.5\% \\ -2.5\% \end{smallmatrix} (\delta_{\text{PDF}}) \begin{smallmatrix} +2.9\% \\ -2.9\% \end{smallmatrix} (\delta_{\alpha_s}). \quad (11)$$

A more detailed summary of all sources of uncertainties we included can be found in Table 3. In Eq. (11) we combined all but the PDF and  $\alpha_S$  uncertainty linearly to obtain one theoretical uncertainty  $\delta_{\text{theo}}$  for the gluon fusion Higgs production cross section at 100 TeV. It is interesting to see how the inclusive cross section is comprised of the different contributions discussed above. The breakdown of the cross section is

$$\begin{aligned} 802 \text{ pb} &= 223.7 \text{ pb} && (\text{LO}, R_{LO} \times \text{EFT}) \\ &+ 363.1 \text{ pb} && (\text{NLO}, R_{LO} \times \text{EFT}) \\ &- 37.2 \text{ pb} && ((t, b, c), \text{exact NLO}) \\ &+ 181.1 \text{ pb} && (\text{NNLO}, R_{LO} \times \text{EFT}) \\ &+ 8.2 \text{ pb} && (\text{NNLO}, 1/m_t) \\ &+ 39.5 \text{ pb} && (\text{Electro-Weak}) \\ &+ 23.6 \text{ pb} && (\text{N3LO}, R_{LO} \times \text{EFT}). \end{aligned} \quad (12)$$

The experimental and theoretical advances in anticipation of a 100 TeV collider will help to elevate the inclusive Higgs production cross section to an unprecedented level of precision that will enable future collider studies to tackle the precision frontier. Improvements of the experimental methods and extraction methods as well as refined theoretical predictions will lead to more precise determinations of the strong coupling constant and of the parton distributions. This will serve to greatly reduce the dominant sources of uncertainty that plague the Higgs cross section at the current level of precision. One of the most important advances for precision in anticipation of a 100 TeV collider will be the extraction of N<sup>3</sup>LO parton distribution functions. This will unlock the full benefit of the N<sup>3</sup>LO calculation of partonic cross section and lead to a significant reduction of the residual uncertainty. Another milestone for theoretical predictions will be computation of the NNLO partonic cross sections with full dependence on the quark masses. This computation would simultaneously shrink the uncertainties due to  $\delta_{\text{tbc}}$  as well as  $\delta_{\frac{1}{m_t}}$ . Furthermore, an improved understanding of electroweak effects will be highly desirable. In particular a full calculation of the mixed QCD and electroweak corrections to Higgs production will lead to a better control of the residual uncertainties and bring the inclusive Higgs cross section to an even higher level of precision.

## 2.2 Higgs plus jet and Higgs $p_T$ spectrum in $gg \rightarrow H$

In this section we study the production of Higgs in gluon fusion in association with one extra jet and more in general we analyze the transverse momentum spectrum of the Higgs. Results in this section are obtained using MCFM [53] and [54].

### 2.2.1 Jet veto efficiencies

At 100 TeV, extra jet radiation is enhanced and a significant fraction of Higgs boson events is produced in association with one or more extra jets. To quantify this statement, in Fig. 5 we plot the jet veto efficiency at 100 TeV, defined as the fraction of exactly 0-jet events in the total Higgs sample

$$\epsilon(p_{t,\text{veto}}) \equiv 1 - \frac{\Sigma_{1\text{-jet, incl}}(p_{t,\text{veto}})}{\sigma_{\text{tot}}}, \quad (13)$$

as well as the one-jet inclusive cross section as a function of the jet transverse momentum requirement,  $\Sigma_{1\text{-jet, incl}}(p_{t,\text{veto}}) \equiv \int_{p_{t,\text{veto}}}^{\infty} \frac{d\sigma}{dp_{t,\text{jet}}} dp_{t,\text{jet}}$ . Throughout this section, jets are reconstructed with the anti- $k_t$

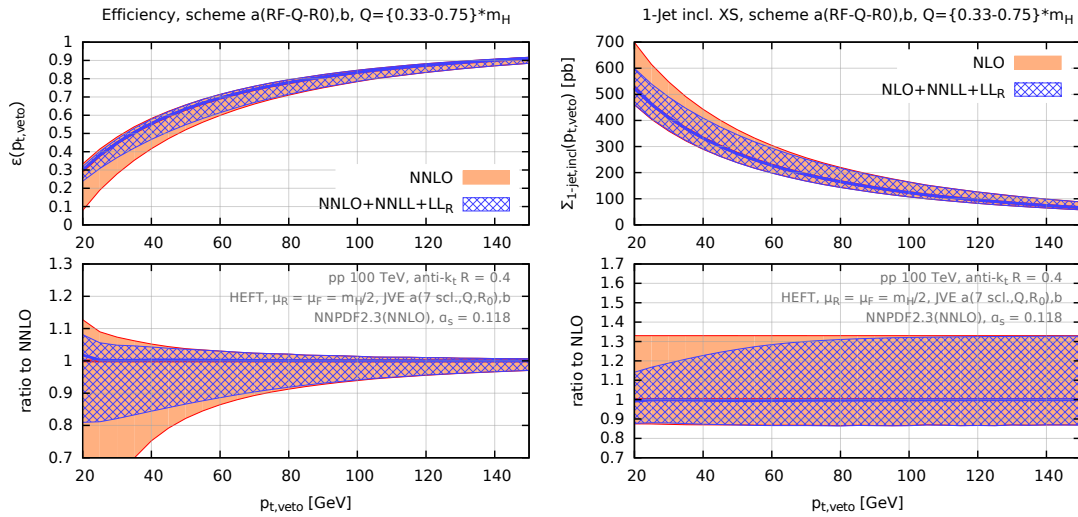


**Fig. 5:** Jet veto efficiency (left) and 1-jet inclusive cross section for Higgs production in gluon fusion at 100 TeV, see text for details.

algorithm with  $R = 0.4$ . No rapidity cut on the jet is applied. The efficiency and one-jet cross section shown in Fig. 5 are computed both in pure fixed-order perturbation theory (red/solid) and matched to NNLL  $\ln m_H/p_{t,\text{veto}}$  and LL jet-radius  $\ln R$  resummation (blue/hatched). The uncertainties are obtained with the Jet-Veto-Efficiency method, see [55] for details. For a jet  $p_t$  of  $\sim 60$  GeV, Fig. 5 shows that about 30% of the total Higgs cross section comes from events with one or more jets. Also, for jet transverse momenta larger than  $\sim 60$  GeV it is also clear from Fig. 5 that pure fixed-order perturbation theory provides an excellent description of the jet efficiencies and cross sections. All-order resummation effects become sizable at smaller transverse momenta, where however soft physics effects like underlying event and MPI may play an important role at the centre-of-mass energies considered in this report.

### 2.2.2 The Higgs $p_T$ spectrum

We now study the Higgs cross-section as a function of a cut on the transverse momentum of the Higgs boson  $\sigma(p_{T,H} > p_{t,\text{cut}})$ . Recently, NNLO predictions for the Higgs transverse momentum spectrum became available [54, 56–59]. Unfortunately, all these computations are performed in the Higgs Effective Theory approximation, where the top quark is integrated out and the Higgs couples directly to gluons

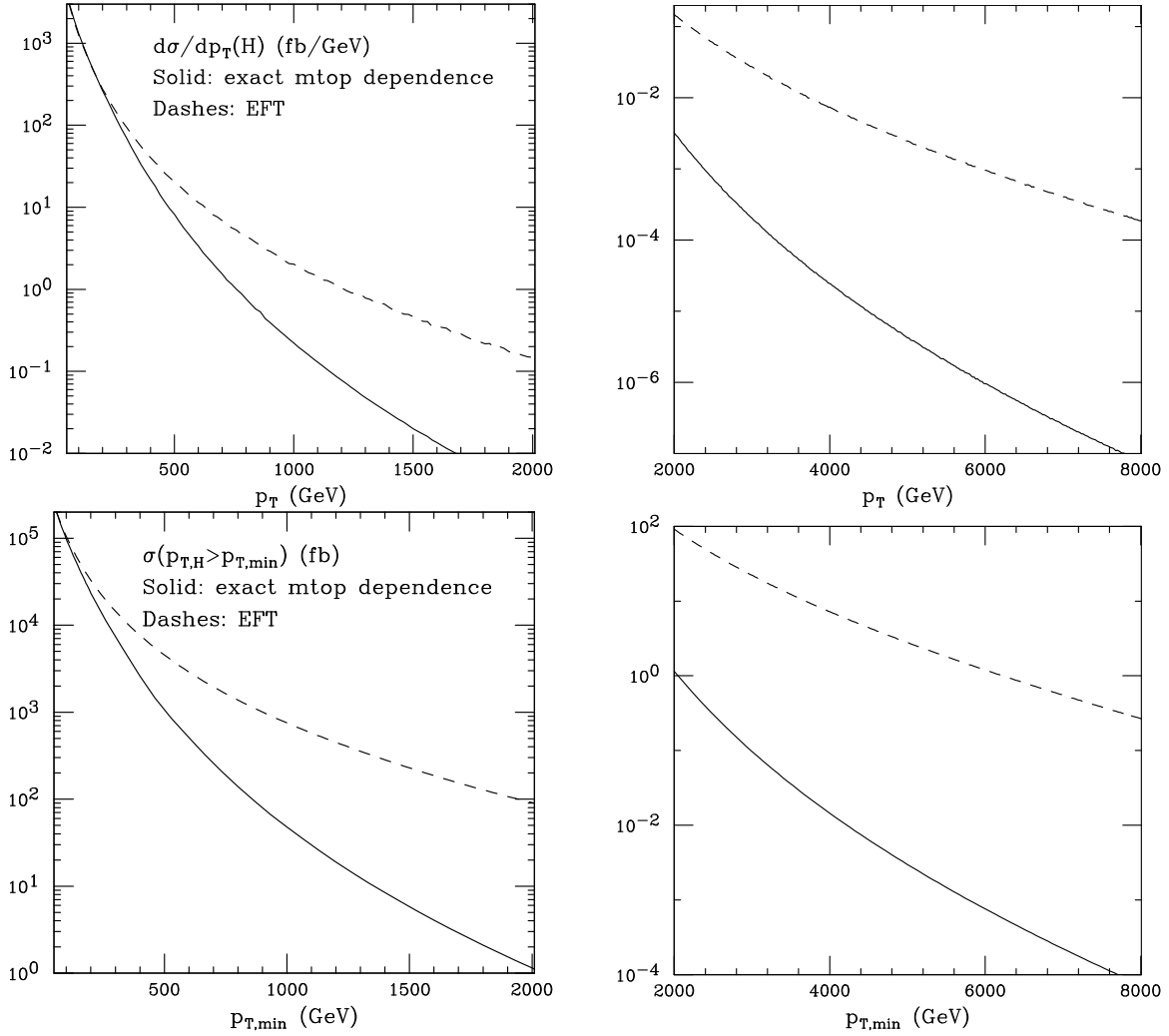


**Fig. 6:** Higgs differential (top) and integrated (bottom)  $p_t$  spectrum, comparing the results of the calculation with the exact  $m_{top}$  dependence, and in the effective field theory (EFT) approximation.

via a point-like effective interaction. As such, they are only reliable for energy scales well below the top mass. In the full theory, the Higgs transverse momentum distribution is only known at leading order. In Fig. 6, we compare the LO distributions for the effective  $m_t \rightarrow \infty$  and full (resolved top) theory. This figure clearly shows the breakdown of the Higgs Effective Theory at high  $p_t$ . Finite top quark effects at high  $p_t$  are more important than perturbative QCD corrections, despite the latter being large. To quantify this statement, we show in the left panel of Fig. 7 the LO, NLO and NNLO predictions for the transverse momentum spectrum in the effective theory. We see that QCD corrections can lead to  $\sim 100\%$  corrections, while Fig. 6 shows that the full theory deviates from the effective one by 1-2 order of magnitudes in the high  $p_t$  regime. Because of this, in this section we will use the LO prediction with full quark mass dependence, which as we already said is the best result available right now. Given its LO nature, these predictions are affected by a very large scale uncertainty. To choose an optimal scale for LO predictions, we study the perturbative convergence in the effective theory. In Fig. 7 we show the impact of higher order corrections for the central scale  $\mu = \sqrt{m_H^2 + p_{t,H}^2}/2$ . With this choice, the impact of higher order corrections is somewhat reduced, and we will use this as a default for all the predictions in this section. Fig. 7 suggests that this should be a good approximation in the whole  $p_t$  range considered here up to a factor of about 2.

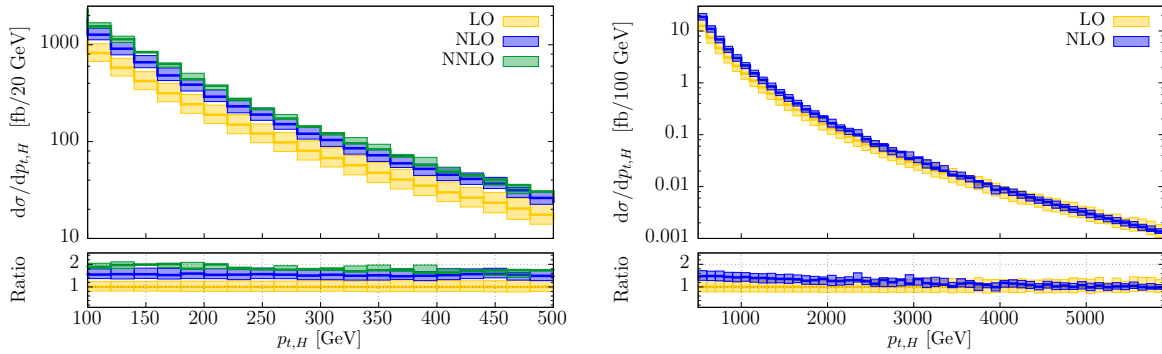


**Fig. 7:** Scale variation study. Note that at high  $p_t$  there is a large uncertainty coming from PDFs.

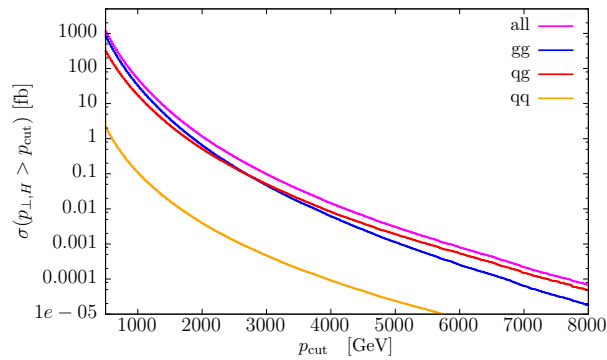


**Fig. 8:** Channel decomposition of the Higgs total cross section, as a function of the Higgs transverse momentum. See text for details.

From the result in Fig. 6 it is clear that even for very large values of the Higgs transverse momentum the cross section is non negligible. This, combined with a projected luminosity target in the  $\text{ab}^{-1}$  range, will allow for detailed studies of Higgs boson production at very high transverse momentum in all the major decay channels. To quantify this statement, in Table 4 we report the value of the transverse momentum cut  $p_{t,\text{cut}}$  for which  $\sigma(p_{t,H} > p_{t,\text{cut}})$  is larger than  $\sim 1 \text{ fb}/1 \text{ ab}$ . Fig. 6 also indicates that at a 100 TeV collider a detailed study of the structure of the  $ggH$  coupling would be possible through an analysis of the Higgs transverse momentum shape. Indeed, it will be possible to investigate the energy dependence of the  $ggH$  coupling from scales  $\sim m_H$  all the way up to the multi-TeV regime. This can provide valuable information on possible BSM effects in the Higgs sector, see e.g. [60] for a general discussion and [61] for a more targeted analysis at a 100 TeV collider. In this context, it may also be interesting to study the channel decomposition of the full result. For our scale choice, this is shown in Fig. 2.2.2. We see a cross-over between a  $gg$ -dominated regime to a  $qg$  dominated regime around  $\sim 2.5$  TeV. We conclude a general analysis of differential distributions for Higgs production in association with one extra jet by showing in Fig. 9 the Higgs and jet rapidity distributions at 100 TeV compared with the same at 13 TeV. It is clear that a wider rapidity coverage is desirable at 100 TeV.

Finally, we consider differential distributions of Higgs decay products. As a case of study, we consider the  $H \rightarrow WW$  channel and study the kinematics distributions of the final state leptons. We consider two scenarios, one with a mild cut  $p_{\perp,H} > 60 \text{ GeV}$  on the Higgs transverse momentum and one with a much harder cut  $p_{\perp,H} > 1 \text{ TeV}$ . For reference, the total cross section for  $pp \rightarrow H \rightarrow WW \rightarrow 2l2\nu$  in the two cases is  $\sigma = 470/0.1 \text{ fb}$  for the low/high cut. Results are shown in Fig. 10. While the di-lepton invariant mass shape is very stable with respect to the  $p_t$  cut, both the di-lepton  $p_t$  and azimuthal separation shapes change significantly. As expected, the  $p_{t,ll}$  spectrum shifts towards higher

	$\sigma(p_t > p_{t,cut}) \times BR = 1 \text{ fb}$	$\sigma(p_t > p_{t,cut}) \times BR = 1 \text{ ab}$
$H \rightarrow b\bar{b}$	$p_{t,cut} = 1860 \text{ GeV}$	$p_{t,cut} = 5380 \text{ GeV}$
$H \rightarrow \tau\bar{\tau}$	$p_{t,cut} = 1240 \text{ GeV}$	$p_{t,cut} = 3950 \text{ GeV}$
$H \rightarrow \mu^+\mu^-$	$p_{t,cut} = 340 \text{ GeV}$	$p_{t,cut} = 1570 \text{ GeV}$
$H \rightarrow c\bar{c}$	$p_{t,cut} = 1070 \text{ GeV}$	$p_{t,cut} = 3520 \text{ GeV}$
$H \rightarrow s\bar{s}$	$p_{t,cut} = 350 \text{ GeV}$	$p_{t,cut} = 1600 \text{ GeV}$
$H \rightarrow gg$	$p_{t,cut} = 1320 \text{ GeV}$	$p_{t,cut} = 4130 \text{ GeV}$
$H \rightarrow \gamma\gamma$	$p_{t,cut} = 620 \text{ GeV}$	$p_{t,cut} = 2350 \text{ GeV}$
$H \rightarrow Z\gamma$	$p_{t,cut} = 570 \text{ GeV}$	$p_{t,cut} = 2200 \text{ GeV}$
$H \rightarrow W^+W^-$	$p_{t,cut} = 1560 \text{ GeV}$	$p_{t,cut} = 4700 \text{ GeV}$
$H \rightarrow ZZ$	$p_{t,cut} = 1050 \text{ GeV}$	$p_{t,cut} = 3470 \text{ GeV}$

**Table 4:** Cross-section times branching ratio as a function of  $p_{t,cut}$ . Each entry corresponds to the  $p_{t,cut}$  value. No  $VV \rightarrow 4l$  branching ratio included.

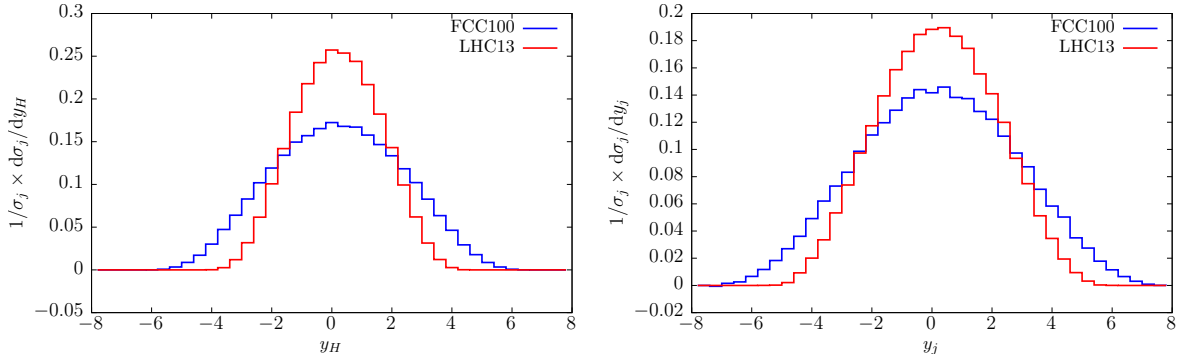


**Fig. 9:** Higgs and leading jet rapidity distributions, normalized to the total cross section.

values of  $p_t$ . The characteristic peak at small  $\phi$  of the lepton azimuthal separation becomes more and more pronounced as the Higgs  $p_t$  increases.

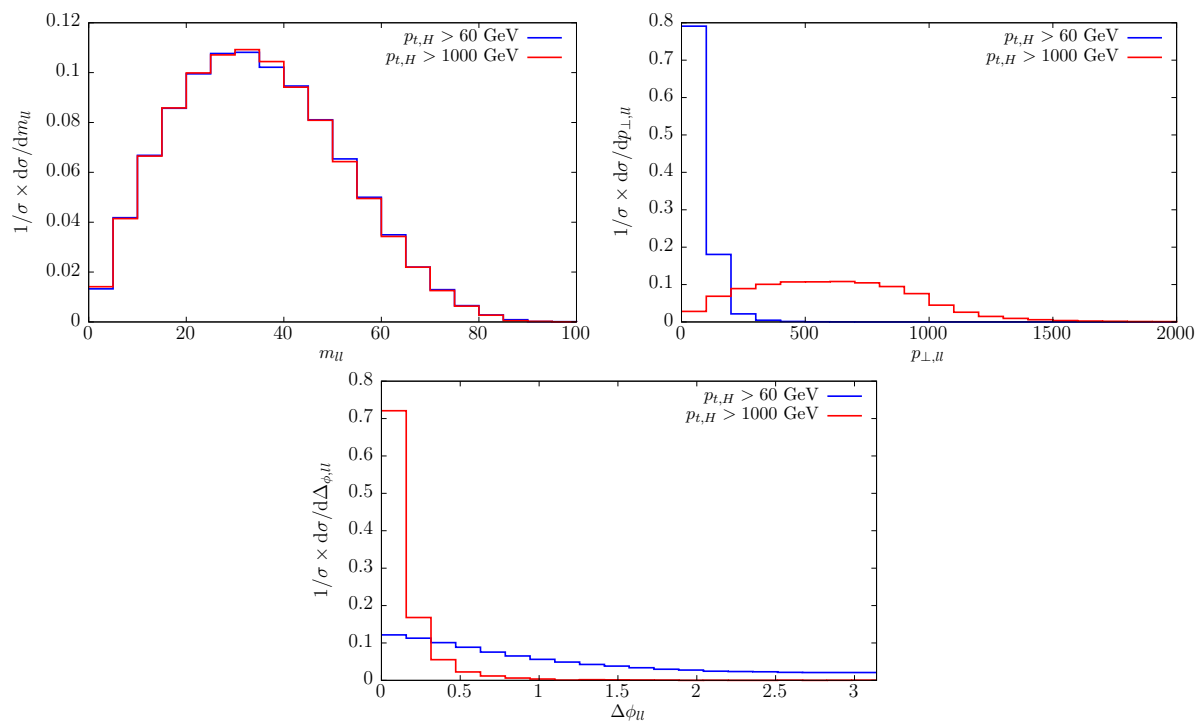


**Fig. 10:** Normalized differential distributions for the  $pp \rightarrow H \rightarrow WW \rightarrow 2l2\nu$  process. Results for two values of cuts on the Higgs transverse momentum are shown, see text for details.

### 2.3 Higgs plus jets production in $gg \rightarrow H$

In this section we present NLO QCD results for the production of a Standard Model Higgs boson in association with up to three jets in gluon-gluon fusion (GGF). If not stated differently, the computations are done in the approximation of an infinitely heavy top quark using the same effective field theory Lagrangian presented in Eq. (4).

Gluon-gluon fusion is not only the largest Higgs boson production channel, but, as already shown in Section 2.1, it is also characterized by very large higher-order corrections. Although less dramatic than in the fully inclusive case of Higgs boson production, the production in association with jets also suffers from large corrections due to NLO effects. In this section we will study how this changes when the center-of-mass energy increases from 14 to 100 TeV.

Gluon fusion is also the largest background for Higgs boson production through vector boson fusion (VBFH). Despite the very peculiar experimental signature of the VBFH channel, whose topology allows to define fiducial cuts which reduce the backgrounds dramatically, the contamination from GGF remains a very important aspect at LHC energies. It is therefore interesting to study the impact of typical VBFH-type selection cuts on the GGF background also at FCC energies.

Another important aspect to keep in mind, is the limited range of validity of the effective field theory description, in which the top quark is integrated out. As already shown for the inclusive case in previous sections, finite top quark and bottom quark mass effects can become large when the transverse energy is large enough to resolve the quark loop that couples the Higgs boson to gluons. At the end of this section, we will investigate the impact of these corrections presenting LO results in the full theory.

#### 2.3.1 Computational setup

The computation is performed using the setup developed for an analogous analysis at 8 and 13 TeV [62], and is based on the automated tools GOSAM [63, 64] and SHERPA [65], linked via the interface defined in the Binoth Les Houches Accord [66, 67].

The one-loop amplitudes are generated with GOSAM, and are based on an algebraic generation of  $d$ -dimensional integrands using a Feynman diagrammatic approach. The expressions for the amplitudes are generated employing QGRAF [68], FORM [69, 70] and SPINNEY [71]. For the reduction of the tensor integrals at running time, we used NINJA [72, 73], which is an automated package carrying out the integrand reduction via Laurent expansion [74], and ONELOOP [75] for the evaluation of the scalar integrals. Unstable phase space points are detected automatically and reevaluated with the tensor integral library GOLEM95 [76–78]. The tree-level matrix elements for the Born and real-emission contribution, and the subtraction terms in the Catani-Seymour approach [79] have been evaluated within SHERPA using the matrix element generator COMIX [80].

Using this framework we stored NLO events in the form of ROOT Ntuples. Details about the format of the Ntuples generated by SHERPA can be found in [81]. The predictions presented in the following were computed using Ntuples at 14 and 100 TeV with generation cuts specified by

$$p_{T,\text{jet}} > 25 \text{ GeV} \quad \text{and} \quad |\eta_{\text{jet}}| < 10,$$

and for which the Higgs boson mass  $m_H$  and the Higgs vacuum expectation value  $v$  are set to  $m_H = 125 \text{ GeV}$  and  $v = 246 \text{ GeV}$ , respectively. To improve the efficiency in performing the VBFH analysis using the selection cuts described below, a separate set of Ntuples was generated. This set includes an additional generation cut on the invariant mass of the two leading transverse momentum jets. To generate large dijet masses from scratch, we require  $m_{j_1 j_2} > 1600 \text{ GeV}$ .

The results reported here are obtained by clustering jets with the anti- $k_T$  algorithm [82, 83] employing a cone radius of  $R = 0.4$ . We utilized the implementation as provided by the FASTJET package [84], and also relied on using the CT14nlo PDF set [85] in the calculations presented here. In order

Numbers in pb	$\sigma_{\text{LO}}^{14\text{ TeV}}$	$\sigma_{\text{NLO}}^{14\text{ TeV}}$	$\sigma_{\text{LO}}^{100\text{ TeV}}$	$\sigma_{\text{NLO}}^{100\text{ TeV}}$	NLO Ratio
H+1 jet					
$p_{T,\text{jet}} > 30\text{ GeV}$	$9.39^{+38\%}_{-26\%}$	$15.4^{+15\%}_{-15\%}$	$217^{+21\%}_{-17\%}$	$336^{+10\%}_{-9\%}$	21.8
$p_{T,\text{jet}} > 50\text{ GeV}$	$5.11^{+39\%}_{-26\%}$	$8.49^{+15\%}_{-15\%}$	$135^{+22\%}_{-18\%}$	$215^{+11\%}_{-10\%}$	25.3
$p_{T,\text{jet}} > 100\text{ GeV}$	$1.66^{+40\%}_{-27\%}$	$2.73^{+15\%}_{-16\%}$	$58.2^{+24\%}_{-19\%}$	$92.1^{+11\%}_{-11\%}$	33.7
$p_{T,\text{jet}} > 300\text{ GeV}$	$0.11^{+43\%}_{-28\%}$	$0.17^{+15\%}_{-16\%}$	$8.51^{+28\%}_{-21\%}$	$13.2^{+11\%}_{-11\%}$	77.6
H+2 jets					
$p_{T,\text{jet}} > 30\text{ GeV}$	$3.60^{+57\%}_{-34\%}$	$5.40^{+12\%}_{-18\%}$	$148^{+40\%}_{-27\%}$	$174^{+2\%}_{-8\%}$	32.2
$p_{T,\text{jet}} > 50\text{ GeV}$	$1.25^{+58\%}_{-34\%}$	$1.96^{+15\%}_{-19\%}$	$65.0^{+41\%}_{-27\%}$	$83.7^{+3\%}_{-11\%}$	42.7
$p_{T,\text{jet}} > 100\text{ GeV}$	$0.22^{+58\%}_{-34\%}$	$0.36^{+17\%}_{-20\%}$	$17.7^{+42\%}_{-28\%}$	$24.6^{+8\%}_{-13\%}$	68.3
$p_{T,\text{jet}} > 300\text{ GeV}$	$6.35 \cdot 10^{-3} \text{ }^{+57\%}_{-34\%}$	$1.03 \cdot 10^{-2} \text{ }^{+17\%}_{-20\%}$	$1.41^{+43\%}_{-28\%}$	$2.07^{+10\%}_{-14\%}$	202.9
H+3 jets					
$p_{T,\text{jet}} > 30\text{ GeV}$	$1.22^{+76\%}_{-40\%}$	$1.77^{+9\%}_{-21\%}$	$89.0^{+58\%}_{-34\%}$	$84.3^{+24\%}_{-5\%}$	47.6
$p_{T,\text{jet}} > 50\text{ GeV}$	$0.29^{+75\%}_{-40\%}$	$0.46^{+15\%}_{-23\%}$	$29.8^{+58\%}_{-34\%}$	$32.9^{+10\%}_{-10\%}$	71.5
$p_{T,\text{jet}} > 100\text{ GeV}$	$3.07 \cdot 10^{-2} \text{ }^{+74\%}_{-40\%}$	$4.95 \cdot 10^{-2} \text{ }^{+19\%}_{-23\%}$	$5.61^{+57\%}_{-34\%}$	$7.04^{+1\%}_{-14\%}$	142.1
$p_{T,\text{jet}} > 300\text{ GeV}$	$2.97 \cdot 10^{-4} \text{ }^{+71\%}_{-39\%}$	$4.86 \cdot 10^{-4} \text{ }^{+20\%}_{-23\%}$	$0.24^{+56\%}_{-34\%}$	$0.34^{+9\%}_{-16\%}$	700.2

**Table 5:** Total inclusive cross sections for the production of a Higgs boson in association with one, two or three jets at LO and NLO in QCD. Numbers are reported for center-of-mass energies of 14 and 100 TeV and four choices of transverse momentum cuts on the jets, namely  $p_{T,\text{jet}} > 30, 50, 100$  and  $300\text{ GeV}$ . The last column shows the ratios between the NLO cross sections at the two center-of-mass energies. The uncertainty estimates are obtained from standard scale variations.

to assess the impact of varying the transverse momentum threshold for the jets, we apply four different cuts at

$$p_{T,\text{jet}} > 30, 50, 100 \text{ and } 300\text{ GeV},$$

and keep the same cut on  $\eta_{\text{jet}}$  as in the Ntuples generation. For the VBFH analysis, we then apply additional cuts as described further below in Section 2.3.3

The renormalization and factorization scales were set equal, and are defined as

$$\mu_{\text{R}} = \mu_{\text{F}} = \frac{\hat{H}'_T}{2} = \frac{1}{2} \left( \sqrt{m_H^2 + p_{T,H}^2} + \sum_i |p_{T,j_i}| \right). \quad (14)$$

The sum runs over all partons accompanying the Higgs boson in the event. Theoretical uncertainties are estimated in the standard way by varying the central scale by factors of 0.5 and 2.

### 2.3.2 Gluon fusion results

We start by summarizing in Table 5 the total inclusive cross sections for the production of a Higgs boson in gluon-gluon fusion accompanied by one, two or three additional jets. We show results at LO and NLO in QCD for  $pp$  collisions at 14 and 100 TeV. Furthermore, the total cross sections are given for four different  $p_{T,\text{jet}}$  cuts on the jets. In the last column we show the ratio of the NLO result for 100 TeV over the NLO result for 14 TeV. This ratio significantly increases when the  $p_{T,\text{jet}}$  cut is tightened, and it also strongly increases as a function of the jet multiplicities. This can be easily understood by the fact that in a 100 TeV environment, the cuts appear much less severe than for 14 TeV; their impact on

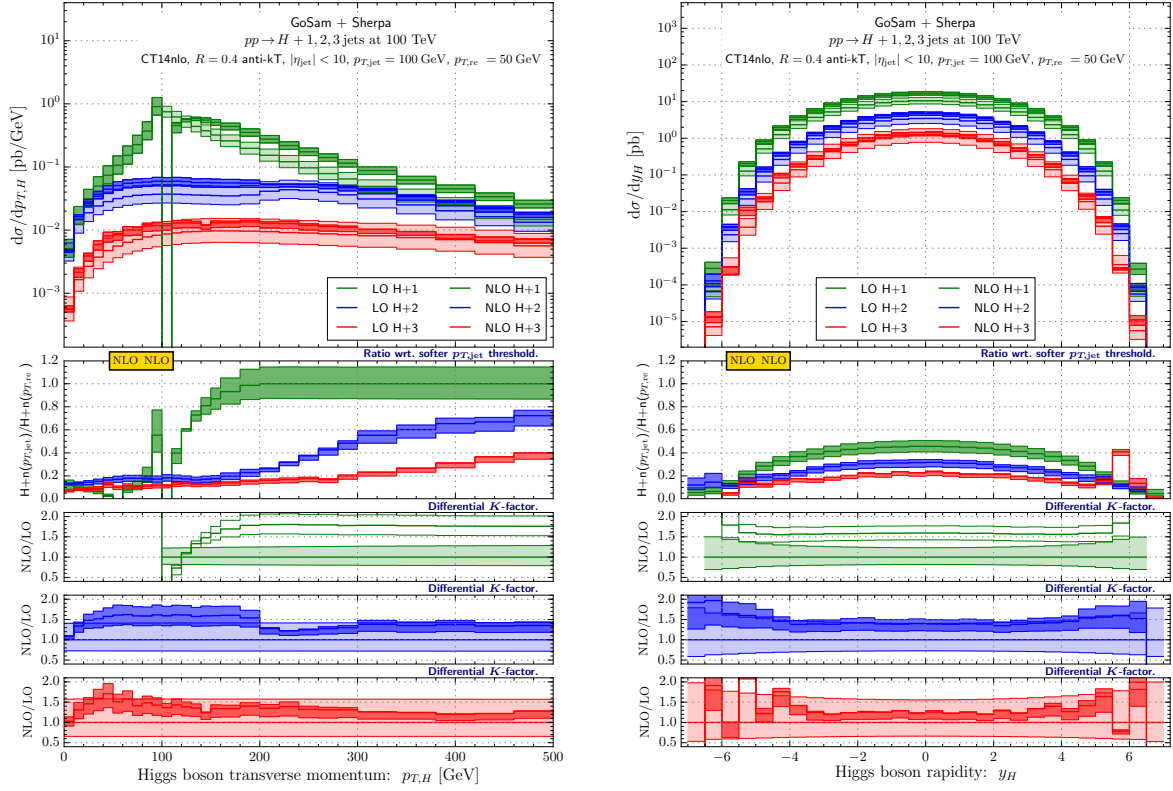


**Fig. 11:** The transverse momentum spectrum  $p_{T,H}$  and the rapidity distribution  $y_H$  of the Higgs boson at 100 TeV for the three production modes H+1, 2, 3 jets. Results are shown at LO and NLO including the effect from standard scale variations and imposing a jet threshold of  $p_{T,\text{jet}} > 100$  GeV. The second panel depicts the NLO ratios taken wrt. reference results obtained with  $p_{T,\text{jet}} > 50$  GeV; the other ratio plot panels display the differential  $K$ -factors for the different jet multiplicities.

the lower energy is therefore larger. For the same reasons, this pattern is also found for the number of jets. With rising center-of-mass energy, it becomes easier to produce additional jets, which leads to the enhancement of the inclusive cross section ratio.

Turning to more exclusive observables, Fig. 11 shows (to the left) the transverse momentum distribution and (to the right) the rapidity distribution of the Higgs boson at 100 TeV with a transverse momentum requirement on the jets of  $p_{T,\text{jet}} > 100$  GeV. The different colours denote the various jet multiplicities. The brighter bands show the LO predictions with their respective uncertainties, whereas the NLO results are displayed by darker bands. As we deal with fixed-order predictions, we observe for the  $p_{T,H}$  distributions – as expected – Sudakov shoulder effects decreasing in their extent at  $p_T \sim 100, 200$  and  $300$  GeV for the one-jet, two-jet and three-jet final states, respectively. The uppermost ratio plot shows the results for  $p_{T,\text{jet}} > 100$  GeV divided by the corresponding results of the same jet multiplicity, but with a  $p_{T,\text{jet}}$  threshold of 50 GeV. As expected this ratio gets smaller for higher jet multiplicities, which means the more jets are present, the more sensitively the cross section changes in response to a jet threshold increase. In the one-jet case we find that the ratio turns one for  $p_{T,H} > 200$  GeV. Below this value, the 50 GeV threshold sample contains event topologies that are absent for  $p_{T,\text{jet}} > 100$  GeV. The ratio will hence be smaller than one. For example, a configuration consisting of a jet with  $p_T = 99.9$  GeV and a real emission of size  $p_T = 99.8$  GeV will be present for 50 GeV thresholds but be missed by the higher  $p_{T,\text{jet}}$  sample. Lastly we note that the size of the  $K$ -factors decreases for jettier final states. We also observe that the 100 TeV environment allows for a wide range of Higgs boson rapidities independent

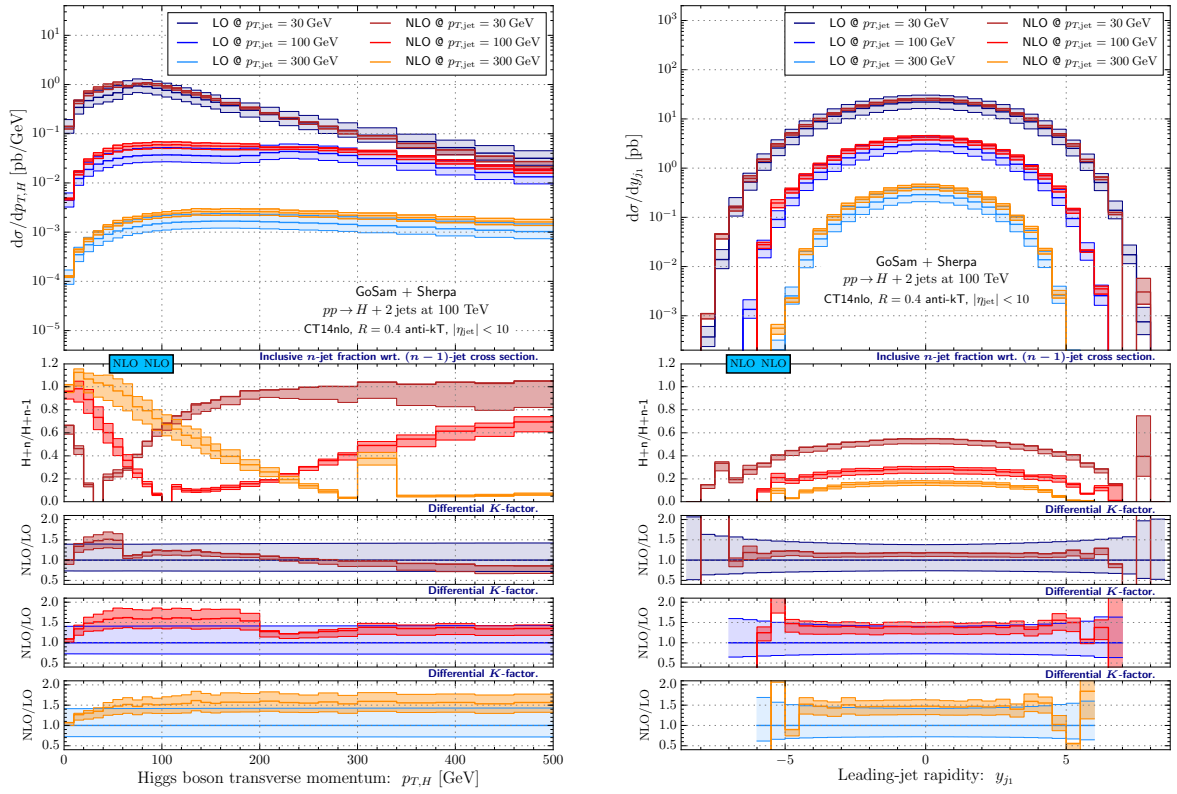


**Fig. 12:** The transverse momentum spectrum  $p_{T,H}$  of the Higgs boson and the rapidity distribution  $y_{j_1}$  of the leading jet, both of which shown at LO and NLO, and for different transverse momentum requirements on the jets in H+2-jet scatterings as produced at a 100 TeV  $pp$  collider. The comparison to the H+1-jet case at NLO is visualized in the first ratio plot, followed by the canonical NLO versus LO ratio plots for the different  $p_{T,jet}$  values. All uncertainty envelopes originate from standard scale variations by factors of two.

of the jet multiplicity. One easily gains two absolute units wrt. the capabilities of the LHC.

The left plot of Fig. 12 shows again transverse momentum distributions of the Higgs boson, however in this case we only consider the curves for H+2 jets at 100 TeV. Here, we examine the impact of tightening the transverse momentum cut on the jets. The typical shoulder present for  $p_{T,jet} > 30$  GeV progressively disappears for increasing values of  $p_{T,jet}$  such that the corresponding distribution for  $p_{T,jet} > 300$  GeV becomes almost flat in the range from 100 to 500 GeV. In the right plot of Fig. 12, the analogous comparison for the rapidity of the leading jet is presented. As expected, the successively harder jet constraints lead to a more central production of the jets reducing the rapidity range where the differential cross section is larger than 1 fb by about six units. In both plots of Fig. 12, the first ratio plot highlights the behaviour of the fraction between the inclusive results for H+2 jets and H+1 jet. While for the Higgs boson transverse momentum, this fraction varies considerably and can reach one in phase space regions of near-zero as well as large  $p_{T,H}$  (earmarking the important two-jet regions), for the leading jet rapidity, the maximum occurs always at  $y_{j_1} = 0$  decreasing from about 0.6 to 0.2 once the jet transverse momentum cut is tightened. This shows that the leading jet tends to be produced more centrally in events of higher jet multiplicity. An increase of the transverse momentum cut also has consequences on the size and shape of the NLO corrections. This is shown in the lower insert plots. In general, for sharper cuts, the higher-order corrections become larger but flatter over the considered kinematical range. Similar results are also obtained for the H+3-jet process.

Figure 13 focuses on the leading jet transverse momentum. The plot on the left hand side compares

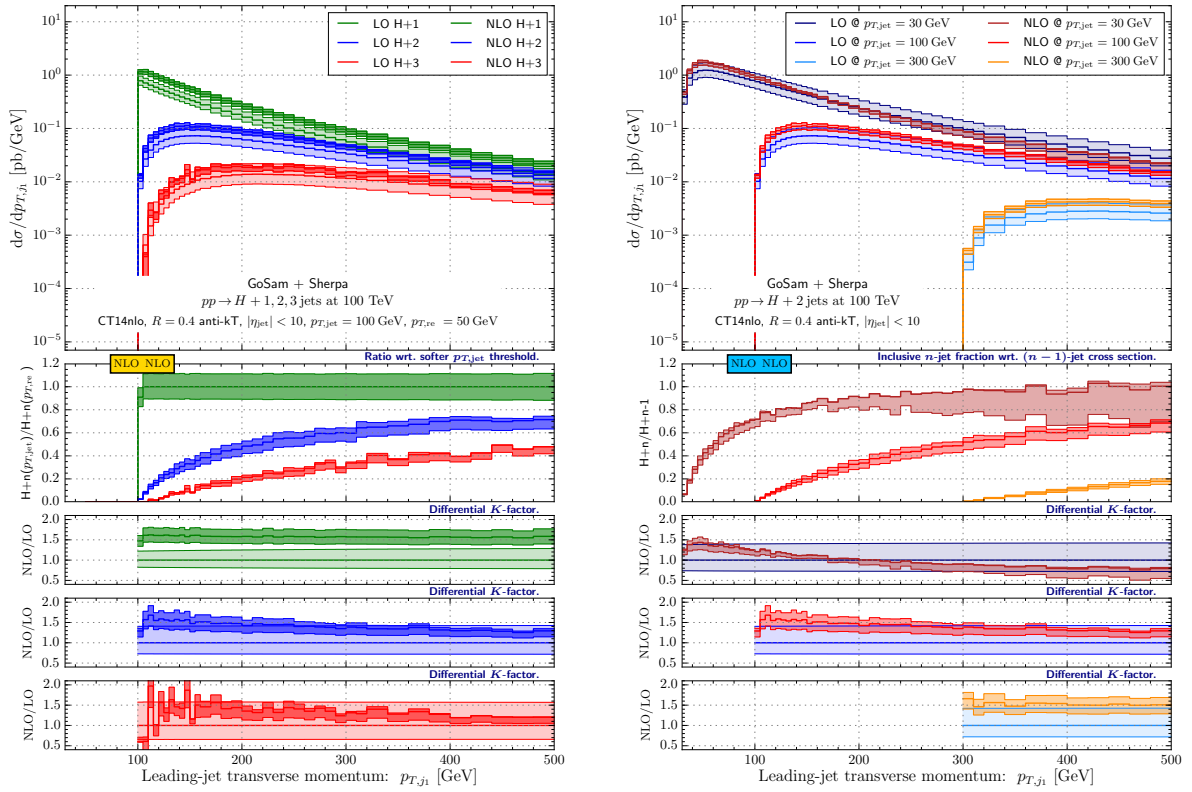


**Fig. 13:** The transverse momentum distribution  $p_{T,j_1}$  of the leading jet at an FCC energy of 100 TeV for the three production modes of H+1, 2, 3 jets (left) and varying jet- $p_T$  thresholds exemplified for the case of H+2-jet production (right). The layout of the plot to the left (right) is the same as used in Figure 11 (Figure 12).

predictions for H+1, 2, 3 jets with one another at LO and NLO for a jet threshold of  $p_{T,jet} > 100$  GeV. The scheme of the lower ratio plots is equal to the one of Fig. 11. For  $p_{T,j_1} \approx 300$  GeV, we see that 60% (30%) of the inclusive two-jet (three-jet) events (using the reference jet threshold) have a second jet at or above a transverse momentum of 100 GeV. The plot on the right hand side instead shows the effect of the different jet transverse momentum constraints for H+2 jets production at 100 TeV, following the colour convention and the scheme of Fig. 12. For lower jet thresholds, the two-jet cross section rises quickly with increasing lead-jet  $p_T$  to the same order of magnitude as the one-jet cross section. We find that an increase of the jet- $p_T$  constraint helps slow down this behavior sufficiently.

The plots of Fig. 14 show the rapidity separation between the Higgs boson and the leading jet (on the left) and between the two leading jets (on the right). In the former case, the distributions show the results for the three different final state multiplicities, whereas in the latter case, the curves refer to the H+3-jet process and compare the impact of the different jet transverse momentum cuts. For both observables, the large production rates and the huge available phase space allow to have differential cross sections, which for separations as large as three units in  $\Delta y$ , are only a factor of two smaller than the ones at zero rapidity separation. Independent of the jet multiplicity, both NLO corrections as well as tighter jet definitions trigger enhancements in the  $\Delta y_{H,j_1}$  distribution (left panel) for configurations where the Higgs boson and the leading jet are close in rapidity. For the  $\Delta y_{j_1,j_2}$  variable (right panel), a rather uniform behaviour is found while changing the jet threshold: the three-jet over two-jet fraction as well as the  $K$ -factors remain rather constant over the entire  $\Delta y$  range.

Additional two-particle observables are presented in Fig. 15. The left plot shows the radial separation between the Higgs boson and the closest jet for H+1, 2 and 3-jet production. As expected, with

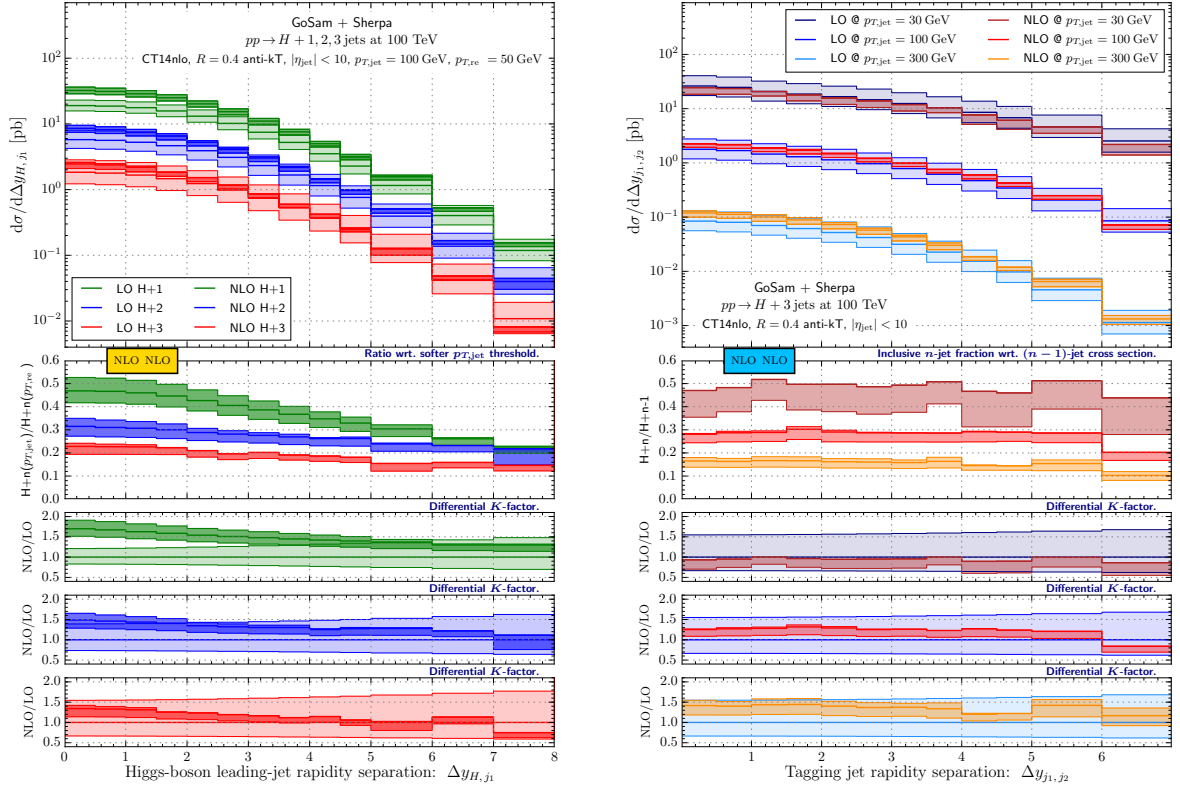


**Fig. 14:** The rapidity separation  $\Delta y_{H,j_1}$  between the Higgs boson and the hardest jet in H+1, 2, 3-jet production and the rapidity separation  $\Delta y_{j_1,j_2}$  between the two hardest jets in H+3-jet production at a 100 TeV proton–proton collider. The spectra for the latter are shown for varying jet- $p_T$  thresholds. Again, the layout of the left and the right plot corresponds to the layout employed in Fig. 11 and 12, respectively.

an increasing number of jets in the final state, the average radial separation between the Higgs boson and the closest jet decreases. As a consequence, for small radius separations, the contributions from all three jet multiplicities are of similar size, whereas for values larger than  $\pi$ , it is the lower multiplicities that dominate for obvious kinematical reasons. We also take from the first ratio plot that a higher jet threshold leads to more centrally produced jets such that there is a small rate increase at low  $\Delta R_{\min}$  for two- and higher jet multiplicities. Furthermore, the NLO corrections can be as large as 100% and in case of H+3 jets, the  $K$ -factor can as well be significantly smaller than one. The right plot presents predictions for the dijet invariant mass of the two leading jets in H+3-jet production for different jet transverse momentum thresholds. It is interesting to observe that because of the vast phase space, the distributions fall off very slowly and for a transverse momentum threshold of  $p_{T,\text{jet}} > 300$  GeV, the maximum of the distribution actually lies above 1 TeV. Looking at the impact of higher-order contributions in the lower three panels, we observe that these corrections slightly increase for larger jet thresholds but for all three choices, the  $K$ -factor remains flat to a good approximation. In the second panel we instead consider the cross section ratios at NLO between successive  $p_{T,\text{jet}}$ . They show that any jet threshold step-up by a factor of three results in a reduction of at least one order of magnitude.

### 2.3.3 Results with vector boson fusion selection criteria

In order to quantify the number of GGF background events passing the VBFH selection criteria, we present results for which we applied the following VBFH-type cuts on top of the baseline set of con-

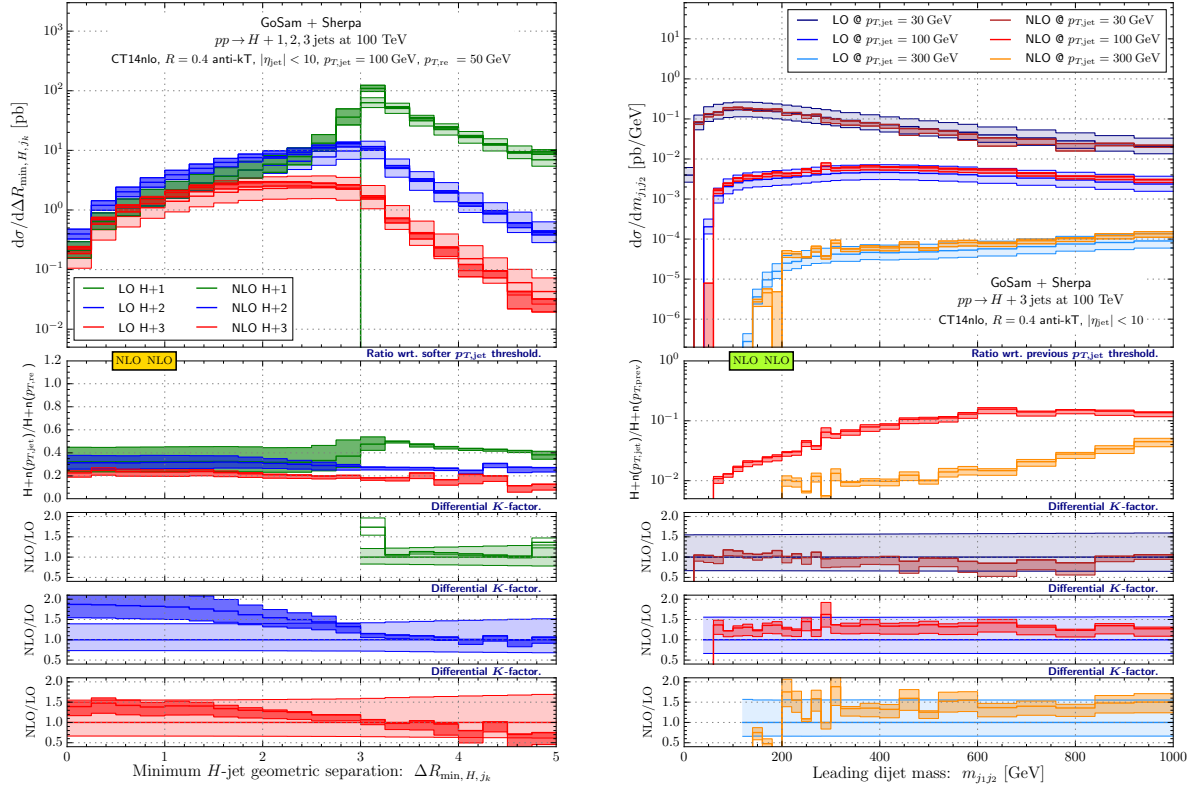


**Fig. 15:** The geometric separation  $\Delta R_{\min, H, j_k}$  between the Higgs boson and the jet closest to it, and the invariant mass distribution of the leading dijet system at a 100 TeV proton–proton collider. For the former, distributions are shown for H+1, 2, 3-jet production, while for the latter, the jet- $p_T$  thresholds are varied to show the corresponding distributions obtained from H+3-jet events. The colour coding and plot layout is as previously described with the only exception that the upper ratios in the left panel are taken between successive  $p_{T, \text{jet}}$  results for the same jet multiplicity.

straints defined in the previous section:

$$m_{j_1 j_2} > 1600 \text{ GeV}, \quad |\Delta y_{j_1, j_2}| > 6.5, \quad y_{j_1} \cdot y_{j_2} < 0. \quad (15)$$

In Table 6 the total cross sections for a center-of-mass energy of 100 TeV are summarized. Differential distributions will be discussed in a slightly different context in one of the later sections, see Section 2.5, together with the results obtained from the VBF@NNLO computations.

### 2.3.4 Finite quark mass effects

It is well known that the infinitely large top quark mass approximation has a restricted validity range, and that for energies large enough to resolve the massive top quark loop, the deviations start to become sizeable. In order to quantify better the effects due to finite quark masses, in the following we compare LO predictions in the effective theory with computations in the full theory. We consider here only massive top quarks running in the loop. The effect of massive bottom quarks for a center-of-mass energy of 100 TeV can be safely neglected. For the top quark mass, we use  $m_t = 172.3 \text{ GeV}$ . Compared to the results shown in the previous section, we now impose a more restrictive cut on the pseudo-rapidity of the jets, demanding  $|\eta_{\text{jet}}| < 4.4$ ; the impact of this cut is however fairly minimal on the observables that we are considering.

Numbers in pb	$\sigma_{\text{LO}}^{100 \text{ TeV}}$	$\sigma_{\text{NLO}}^{100 \text{ TeV}}$
H+2 jets		
$p_{T,\text{jet}} > 30 \text{ GeV}$	$4.60^{+56\%}_{-33\%}$	$4.70^{+17\%}_{-7\%}$
$p_{T,\text{jet}} > 50 \text{ GeV}$	$1.71^{+56\%}_{-34\%}$	$1.98^{+6\%}_{-11\%}$
$p_{T,\text{jet}} > 100 \text{ GeV}$	$0.26^{+57\%}_{-34\%}$	$0.31^{+3\%}_{-13\%}$
$p_{T,\text{jet}} > 300 \text{ GeV}$	$5.10 \cdot 10^{-3} \text{ }^{+58\%}_{-34\%}$	$6.20 \cdot 10^{-3} \text{ }^{-1\%}_{-14\%}$

**Table 6:** Total inclusive cross sections for the production of a Higgs boson in association with two jets at LO and NLO in QCD after the application of the VBF selection criteria stated in Eq. 15. Numbers are reported for a center-of-mass energy of 100 TeV and four choices of transverse momentum cuts, namely  $p_{T,\text{jet}} > 30, 50, 100$  and 300 GeV. The uncertainty envelopes are obtained from standard scale variations.

Before turning to the discussion of a handful of differential cross sections, we compare the predictions for the total inclusive cross section in the effective theory at LO and NLO, and in the full theory at LO; Table 7 lists the results for various jet- $p_T$  thresholds. We also indicate the reduction of the LO cross section induced by the incorporation of finite top quark mass effects. As expected, this reduction becomes more pronounced for increasing values of  $p_{T,\text{jet}}$  turning the finite mass corrections into the dominant effect for  $p_{T,\text{jet}} \gtrsim 100 \text{ GeV}$ . This effect becomes even more dramatic when increasing the multiplicity from H+2 jets to H+3 jets.

Figure 16 shows predictions for the transverse momentum distribution of the Higgs boson (left), and for the leading dijet invariant mass (right). We observe that for the transverse momentum, the finite top mass effects start to become important at values of  $p_{T,H} \approx 300 \text{ GeV}$ . Interestingly, the NLO corrections for the given scale choice show the same qualitative behaviour as the LO contribution in the full theory. In particular for the H+3-jet process, the full theory and the NLO effective theory

Numbers in pb	$\sigma_{\text{LO}}^{100 \text{ TeV}}$	$\sigma_{\text{NLO}}^{100 \text{ TeV}}$	$\sigma_{\text{LO,full}}^{100 \text{ TeV}}$	$\sigma_{\text{LO,full}}^{100 \text{ TeV}} / \sigma_{\text{LO}}^{100 \text{ TeV}}$
H+2 jets				
$p_{T,\text{jet}} > 30 \text{ GeV}$	$124^{+39\%}_{-27\%}$	$156^{+3\%}_{-10\%}$	$120^{+39\%}_{-26\%}$	0.968
$p_{T,\text{jet}} > 50 \text{ GeV}$	$57.3^{+40\%}_{-27\%}$	$76.5^{+6\%}_{-11\%}$	$52.2^{+40\%}_{-27\%}$	0.911
$p_{T,\text{jet}} > 100 \text{ GeV}$	$16.5^{+41\%}_{-28\%}$	$23.3^{+9\%}_{-13\%}$	$13.1^{+41\%}_{-27\%}$	0.794
$p_{T,\text{jet}} > 300 \text{ GeV}$	$1.40^{+43\%}_{-28\%}$	$2.05^{+10\%}_{-14\%}$	$0.62^{+43\%}_{-28\%}$	0.443
H+3 jets				
$p_{T,\text{jet}} > 30 \text{ GeV}$	$70.4^{+56\%}_{-34\%}$	$72.6^{+15\%}_{-8\%}$	$63.0^{+56\%}_{-34\%}$	0.895
$p_{T,\text{jet}} > 50 \text{ GeV}$	$25.2^{+56\%}_{-34\%}$	$29.3^{+5\%}_{-11\%}$	$20.8^{+56\%}_{-34\%}$	0.825
$p_{T,\text{jet}} > 100 \text{ GeV}$	$5.13^{+56\%}_{-34\%}$	$6.57^{+3\%}_{-14\%}$	$3.46^{+57\%}_{-34\%}$	0.674
$p_{T,\text{jet}} > 300 \text{ GeV}$	$0.24^{+56\%}_{-34\%}$	$0.33^{+9\%}_{-16\%}$	$0.07^{+60\%}_{-35\%}$	0.292

**Table 7:** Total inclusive cross sections for the hadro-production of a Higgs boson in association with two as well as three jets at a center-of-mass energy of 100 TeV. The LO results as predicted by the full theory are shown in the next-to rightmost column, and are compared to the results from the effective theory at LO and NLO. Note that all cross section are obtained for the basic gluon fusion selection, however imposing a narrower jet rapidity requirement of  $|\eta_{\text{jet}}| < 4.4$ . Again, rates are calculated for up to four choices of jet- $p_T$  thresholds, namely  $p_{T,\text{jet}} > 30, 50, 100$  and 300 GeV. The last column lists the ratios between the LO predictions of the full and effective theory.

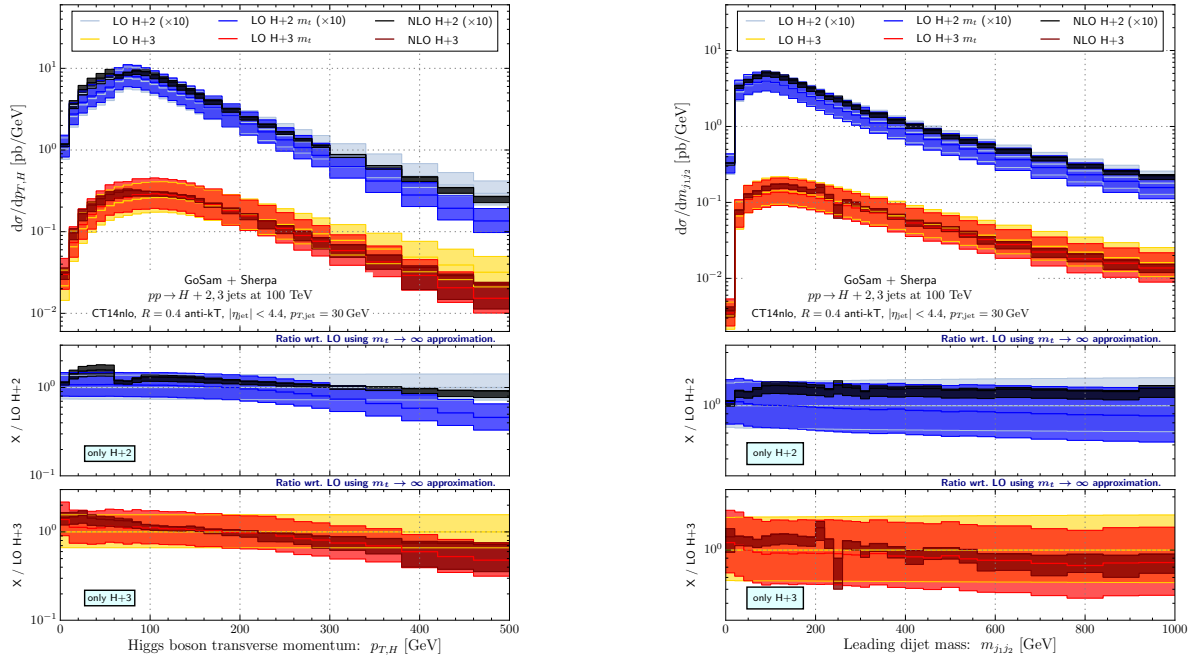


**Fig. 16:** The impact of finite top quark mass effects in the loop-induced emission of a Higgs boson in GGF  $H+n$ -jet production at a 100 TeV proton–proton collider. LO results based on the full and effective theory as well as NLO results using the effective theory are shown (to the left) for the transverse momentum spectrum,  $p_{T,H}$ , of the Higgs boson and (to the right) for the invariant mass distribution,  $m_{j_1 j_2}$ , of the leading dijet system. The  $H+2$ -jet and  $H+3$ -jet predictions are grouped in separate ratio plots using the respective LO results as their reference. Uncertainty bands are derived from standard scale variations.

seem to almost give the same prediction, except for the size of the scale variations. On the contrary the predictions for the invariant mass distributions in the full theory only mildly deviate from the ones computed in the effective theory; again the tails are somewhat softer. For both  $H+2$  jets and  $H+3$  jets, the NLO predictions remain within the respective scale uncertainties of the LO results over the whole range shown in the figure. In addition, the shapes of the NLO effective and LO full theory show a fairly similar behaviour. In the two-jet case there is however a clear rate difference due to the considerably greater-than-one  $K$ -factor.

The last figure exemplifies how severe deviations can become between the full and effective theory description for the hardness of transverse particle/jet production. This is nicely demonstrated by means of the  $H_{T, \text{jets}}$  distribution shown to the left of Fig. 17. The finite top quark mass effects clearly dominate over the NLO corrections calculated in the effective theory. The  $H+2$ -jet case in particular demonstrates the extreme and opposite behaviour of both effects – a large  $K$ -factor on the one side versus an even more effective suppression of the  $H_T$  tail on the other side by about 70-80%. While the finite mass effects always suppress the rate for hard jet production, the NLO corrections can lead to an enhancement as seen for  $H+2$  jets as well as to a reduction as we observe in the  $H+3$ -jet case.

As in the previous figure, we contrast two different types of observables with each other. In the right panel of Fig. 17 we therefore display an angular correlation, more precisely we show the azimuthal angle separation between the leading and subleading jet. This kind of observable is important in precision coupling measurements, and although the corrections tend to be much smaller, they have to be understood in detail to satisfy the demand for high precision. Here, both the NLO corrections and finite mass effects lead to similar shape changes, suppressing small-angle contributions while the back-to-back configurations receive an (effective) enhancement (due to the finite  $m_t$  treatment). This time, we notice

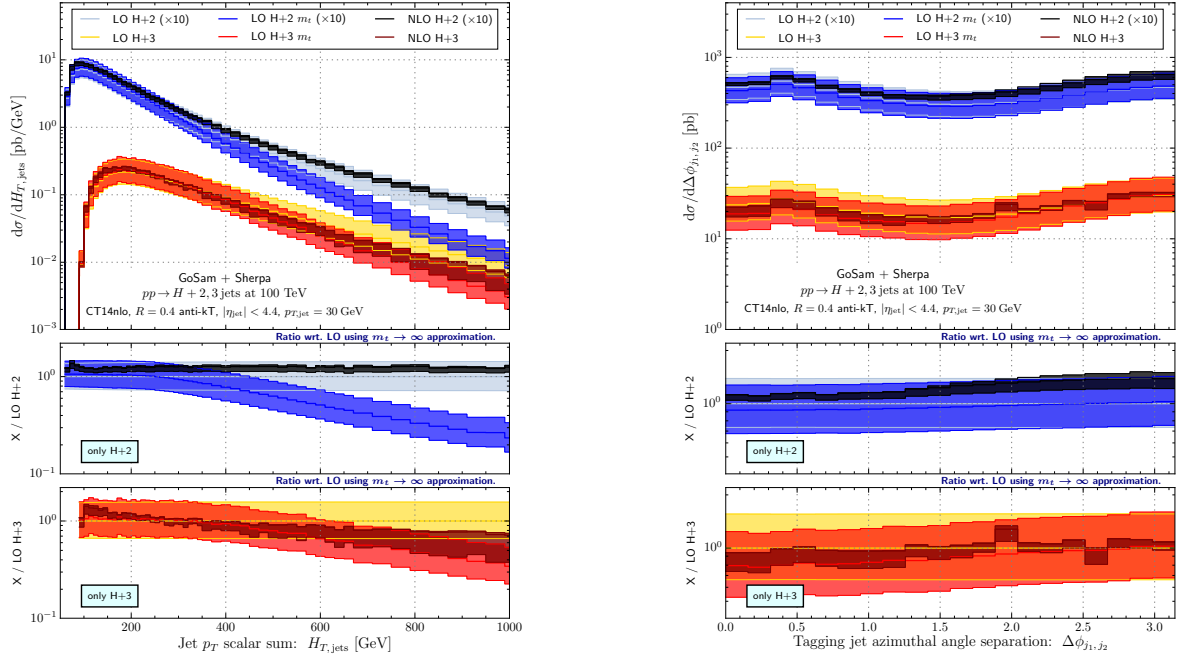


**Fig. 17:** Finite top quark mass effects in GGF-based  $H + n$ -jet production arising from collisions of protons at 100 TeV. The jets-only scalar sum of transverse momenta,  $H_{T,jets}$ , and the azimuthal angle distribution,  $\Delta\phi_{j_1,j_2}$ , between the leading and subleading jet are shown to the left and right, respectively. The differential spectra (and associated uncertainties from scale variations) were obtained from the full theory at LO, and the effective theory at LO (providing the references) and NLO. The upper ratio plot contains the  $H + 2$ -jet predictions while the lower one depicts those for  $H + 3$  jets.

a slight increase of the  $m_t$  effects (from 10% to 20%) for the final states of higher jet multiplicity.

### 2.3.5 Conclusions

In this section we studied the associate production of a Standard Model Higgs boson in association with up to three jets in gluon–gluon fusion. We compared LO and NLO QCD predictions for several different cuts on the transverse momentum of the jets and also produced results with VBFH-type cuts, which are compared with VBF predictions in Section 2.5. Because of the large center-of-mass energy and the huge available phase space, the production rates become much larger compared to LHC energies. This can be observed in particular when comparing the relative size of contributions coming from different multiplicities. In the last part of this section, we studied the impact of finite quark mass effects. For typical jet transverse momentum cuts, which at FCC energies are likely to be of the order of 100 GeV, these corrections are non-negligible and their impact is in general larger than NLO QCD corrections in the effective theory. Moreover, all quantities that are related to measuring the transverse activity of the  $H + n$ -jet processes will receive significant corrections reducing the cross section in the hard regions.

## 2.4 Associated $VH$ production

Associate production of the Higgs and gauge bosons mostly arises from the Higgs-strahlung processes  $q\bar{q} \rightarrow V^* \rightarrow VH$  ( $V = W, Z$ ). These provide direct probes of the  $VVH$  couplings.

Cross sections for  $HV$  associated production in hadron collisions are studied since long. For the inclusive cross sections, up to NNLO QCD corrections are available in the program `vh@nnlo` [86–88]. Furthermore, programs have been developed for the computation of fully differential distributions including NNLO QCD corrections [89–92], the EW corrections [93, 94] and event generators matching and merging NLO QCD corrections for  $VH$ +jets production to parton showers [95–97]. Finally, the computation of NNLO QCD corrections matched with parton shower has been worked out in Ref. [98], reweighting events samples obtained with the code presented in Ref. [95] with the histograms obtained with the program of Ref. [91] and relying for the level of accuracy on the theorems presented in [99]. The results in Table 8 have been obtained using `vh@nnlo` and the `NNPDF30_nnlo_as_0118` [100] pdf set. The central renormalisation and factorisation scales have been set both to the mass of the  $HV$  system. For the estimate of the scale uncertainty reported in the table, we varied them independently up to a factor of 3 with the constraint  $\mu_f \cdot \mu_r \leq 2$ .

	$\sigma_{tot}[\text{pb}]$	$\delta_{PDF}[\text{pb}]$	$\delta_{scale}[\text{pb}]$	$\sigma_{DY}[\text{pb}]$	$\sigma_{ggHV}[\text{pb}]$	$\sigma_{top}[\text{pb}]$
HW	15.710	$\pm 0.024$	$^{+0.010}_{-0.020}$	15.403	–	0.307
HZ	11.178	$\pm 0.022$	$^{+0.062}_{-0.044}$	8.946	2.069	0.163

**Table 8:** Total cross sections  $\sigma(VH)$ , including up to NNLO QCD corrections, and respective PDF and PDF uncertainties.

Figure 9 shows the cross sections for the  $WH$  process, with different selection cuts for the associated jet activity.

$\sigma_{NNLO} [\text{fb}] @ 100 \text{ TeV}$				
$HW^+(\rightarrow He^+\nu_e)$				
no cuts	no jets with $p_T > 100 \text{ GeV}$	at least 1 jet with $p_T > 100 \text{ GeV}$	at least 1 jet with $p_T > 500 \text{ GeV}$	at least 1 jet with $p_T > 1 \text{ TeV}$
539	444	94.7	5.20	0.817
$HW^-(\rightarrow He^-\bar{\nu}_e)$				
no cuts	no jets with $p_T > 100 \text{ GeV}$	at least 1 jet with $p_T > 100 \text{ GeV}$	at least 1 jet with $p_T > 500 \text{ GeV}$	at least 1 jet with $p_T > 1 \text{ TeV}$
425	350.6	74.37	3.718	0.541

**Table 9:**  $HW$  fiducial cross sections in fb at NNLO accuracy for the different selection cuts on the jet activity.

As was the case for the Higgs production processes discussed so far, collisions at 100 TeV allow to extend the kinematic reach of  $VH$  final states to rather extreme configurations, where the  $VH$  pair is produced with huge invariant mass, or at very large  $p_T$ . Production at large invariant mass is of phenomenological interest for several reasons. For example, it provides the leading source of irreducible background for the detection of exotic new particles (e.g. new gauge bosons) decaying to  $VH$ . Furthermore, production at large invariant mass probes the  $VVH$  coupling in the region where the  $Q^2$  of the virtual gauge boson is far off shell. This could exhibit sensitivity to the presence of higher-dimension effective operators, potentially beyond what can be tested from the precise determination of the  $H \rightarrow VV^*$  decay branching ratios. Figure 18 (left panel) shows that, with over  $10 \text{ ab}^{-1}$  of integrated luminosity, the SM rate will extend all the way out to  $M(VH) \sim 20 \text{ TeV}$ . In these configurations, with Higgs and gauge bosons with a transverse momentum of several TeV, it is likely that one will be able to effectively

tag these events through the  $H \rightarrow b\bar{b}$  and  $V \rightarrow$  dijet decay modes, therefore using the largest available branching ratios!

Another interesting, and complementary, kinematical configuration, is the production of the  $VH$  pair at large  $p_T$ . This will be dominated by the recoil against a jet, with the  $VH$  pair maintaining a small invariant mass. As shown in the right panel of Fig. 18, there will be rate out to  $p_T(VH)$  beyond 7 TeV. As we shall see in Section 3.3, and in the case of the abundant  $H \rightarrow b\bar{b}$  decay modes, these configurations enjoy a particularly favourable  $S/B$  ratio, when compared to the otherwise dominant QCD background from associated  $Vb\bar{b}$  production.

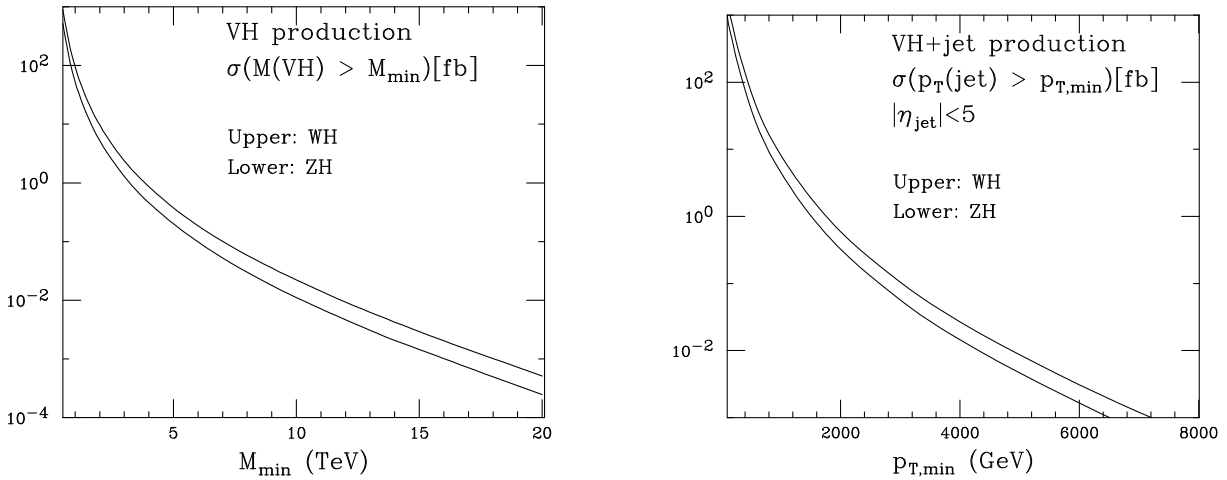


**Fig. 18:** Left panel: integrated invariant mass distribution of  $VH$  pairs, at LO. Right panel: integrated transverse momentum spectrum of the  $VH$  system, recoiling against a jet.

Figure 19 shows the integrated  $p_T$  spectrum of the Higgs produced in association with a  $W^\pm$  boson. The solid line corresponds to the LO process, in which it is the  $W$  that recoils against the Higgs. The dashed and dotted lines show the contribution induced by the  $q\bar{q} \rightarrow WHg$  and  $qg \rightarrow WHq$  processes.

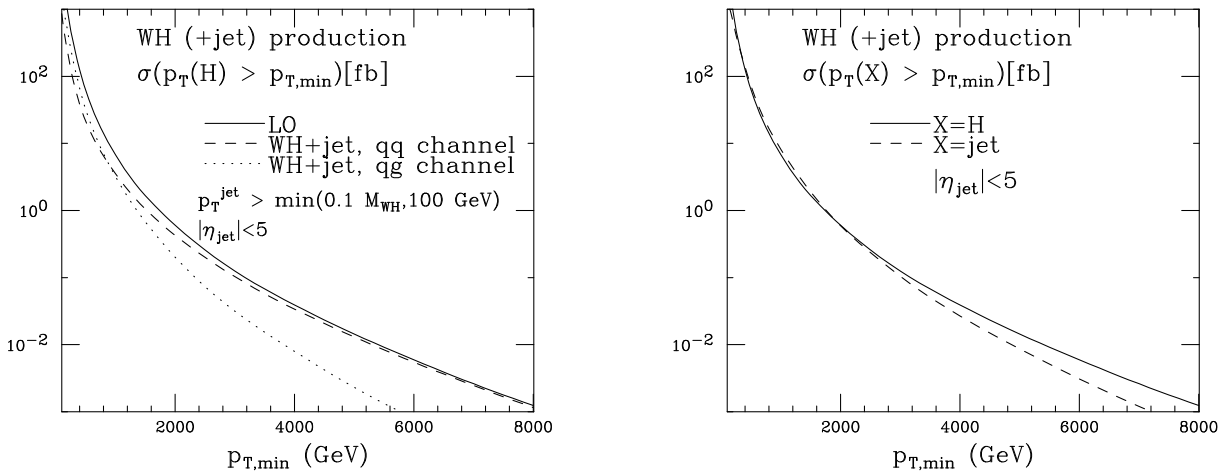


**Fig. 19:** Integrated inclusive  $p_T$  spectrum of the Higgs boson (left panel) and of a jet produced in the  $WH$ +jet process (right panel).

To isolate the hard component of these higher-order corrections, namely to exclude the virtual and soft/collinear  $O(\alpha_s)$  processes that exhibit Born-like kinematics, we require the radiated parton to have  $p_T$  no smaller than 10% of the  $WH$  mass or of 100 GeV. The results show that Higgs production at large  $p_T$  is indeed dominated by Born-like kinematics. This is confirmed in the left panel of Fig. 20, showing

the back-to-back feature of the  $\Delta R(WH)$  distribution (normalized to 1), for various  $p_T(H)$  thresholds. We notice the very different shape of the  $\Delta R(WH)$  distribution when events are tagged by the presence of a large  $p_T$  jet (see central plot of Fig. 20).

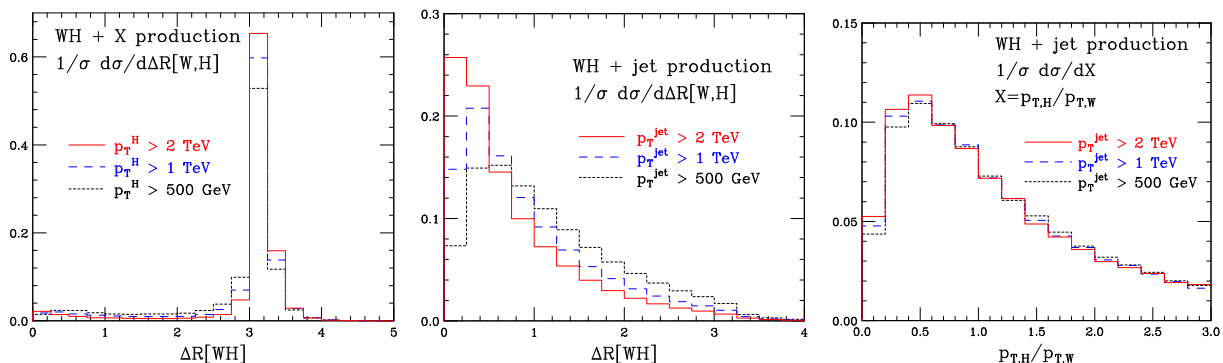


**Fig. 20:**  $\Delta R$  correlation between the  $H$  and  $W$  boson, in events tagged by the presence of a high- $p_T$  Higgs (left) and of a high- $p_T$  jet (central panel). Right panel: transverse momentum of the Higgs boson, relative to that of the  $W$  boson, in events with a high- $p_T$  jet. All distributions are normalized to 1.

## 2.5 VBF Higgs production

In this section we study the production of a Standard Model Higgs through Vector Boson Fusion (VBFH) at a 100 TeV proton-proton collider. As is the case at 13 TeV, VBFH has the second largest Higgs production cross section and is interesting on its own for a multitude of reasons: 1) it is induced already at tree-level; 2) the transverse momentum of the Higgs is non-zero at lowest order which makes it suitable for searches for invisible decays; 3) it can be distinguished from background processes due to a signature of two forward jets. This last property is very important, as the inclusive VBF signal is completely drowned in QCD Hjj production. One of the aims of this section is to study how well typical VBF cuts suppress this background at a 100 TeV proton-proton machine.

### 2.5.1 Generators

Fixed order LO predictions for and QCD corrections to VBFH have been obtained using PROVBFH [101] which is based on POWHEG's fully differential NLO QCD calculation for Higgs production in association with three jets via VBF [102, 103], and an inclusive NNLO QCD calculation [104]. NLO-EW corrections are obtained with HAWK [93, 105]. NLO interfaced to a Parton Shower (NLO+PS) results have been obtained using the POWHEG-BOX [106–109] together with version 6.428 of PYTHIA [110] with the Perugia Tune P12 [111]. QCD Hjj results are obtained as in Section 2.3.

### 2.5.2 Parameters

$\sqrt{S}$	100 TeV
$M_H$	125 GeV
PDF	MMHT2014nnlo68cl & CT14nnlo
$a_s(M_Z)$	0.118
$M_Z$	91.1876 GeV
$M_W$	80.385 GeV
$\Gamma_Z$	2.4952 GeV
$\Gamma_W$	2.085 GeV
$G_F$	$1.16637 \times 10^{-5} \text{GeV}^{-2}$
$n_f$	5
$\mu^2 = \mu_R^2 = \mu_F^2$	$\frac{M_H}{2} \sqrt{\left(\frac{M_H}{2}\right)^2 + p_{t,H}^2}$

**Table 10:** Setup

For the purpose of this study we have used the EW parameters shown in Table 10 together with tree-level electroweak relations to obtain the weak mixing angle,  $\theta_W$ , and the electromagnetic coupling,  $\alpha_{EW}$

$$\sin^2 \theta_W = 1 - M_W^2/M_Z^2, \quad \alpha_{EW} = \sqrt{2}G_F M_W^2 \sin^2 \theta_W/\pi. \quad (16)$$

We include no off-shell effects for the Higgs Boson but include Breit-Wigner propagators for the  $W$  and  $Z$  boson. In order to estimate scale uncertainties we vary  $\mu$  up and down a factor 2 while keeping  $\mu_R = \mu_F$ . We use a diagonal CKM matrix. When reconstructing jets we use the anti- $k_t$  algorithm [82, 83] as implemented in FASTJET [84] with radius parameter  $R = 0.4$ .

For VBFH predictions we have used the MMHT2014NNLO68CL [112] PDF set and for QCD Hjj predictions we have used the CT14NNLO [85] PDF set as implemented in LHAPDF [113]. In order to include photon induced contributions to the NLO-EW corrections we have employed the

NNPDF2.3QED [114] PDF set, which includes a photon PDF. It is worth noticing that the relative EW correction factor only very mildly depends on the PDF set, so that the induced error arising from using different PDFs can be safely assumed to be contained in the other theoretical uncertainties.

### 2.5.3 Inclusive VBF production

Due to the massive vector bosons exchanged in VBFH production the cross section is finite even when both jets become fully unresolved in fixed-order calculations. In Table 11 we present the fully inclusive LO cross section and both NNLO-QCD and NLO-EW corrections. The NNLO-QCD corrections are calculated in the DIS-like approximation (Structure Function Approximation) [115] where there is no cross-talk between the upper and lower quark line in the VBF diagram. This approximation is exact at LO and NLO but formally excludes a number of diagrams at NNLO. These contributions have been shown to be tiny under typical VBF cuts and can therefore safely be neglected [105, 116, 117]. The NLO-EW corrections include both t- and u-channel contributions but exclude the s-channel contributions to be consistent with the Structure Function Approximation. The s-channel contribution should hence be treated as a background to the VBF signal.

**Table 11:** Total VBF cross section including QCD and EW corrections and their uncertainties for a 100 TeV proton-proton collider.  $\sigma^{\text{VBF}}$  is obtained using Eq. (17) where  $\sigma_{\text{NNLOQCD}}^{\text{DIS}}$  is the total VBFH cross section computed to NNLO accuracy in QCD,  $\delta_{\text{EW}}$  is the relative EW induced corrections and  $\sigma_\gamma$  is the cross section induced by incoming photons. For comparison, the LO order cross section,  $\sigma_{\text{LO}}$ , is also shown.

$\sigma^{\text{VBF}}$ [pb]	$\Delta_{\text{scale}}$ [%]	$\sigma_{\text{LO}}$ [pb]	$\sigma_{\text{NNLOQCD}}^{\text{DIS}}$ [pb]	$\delta_{\text{EW}}$ [%]	$\sigma_\gamma$ [pb]
69.0	$^{+0.85}_{-0.46}$	80.6	73.5	-7.3	0.81

In order to compute the VBF cross section we combine the NNLO-QCD and NLO-EW corrections in the following way

$$\sigma^{\text{VBF}} = \sigma_{\text{NNLOQCD}}^{\text{DIS}}(1 + \delta_{\text{EW}}) + \sigma_\gamma, \quad (17)$$

where  $\sigma_{\text{NNLOQCD}}^{\text{DIS}}$  is the NNLO-QCD prediction in the DIS-like approximation,  $\delta_{\text{EW}}$  is the relative EW correction factor and  $\sigma_\gamma$  is the photon induced contribution. The combined corrections to the LO cross section is about 14% with QCD and EW corrections contributing an almost equal amount. The scale uncertainty  $\Delta_{\text{scale}}$  is due to varying  $\mu$  by a factor 2 up and down in the QCD calculation alone keeping  $\mu_F = \mu_R$ . For comparison the total QCD and EW corrections at 14 TeV amount to about 7% and the QCD induced scale variations to about 0.4%.

### 2.5.4 VBF cuts

In order to separate the VBFH signal from the main background of QCD  $Hjj$  production we will extend typical VBF cuts used at the LHC to a 100 TeV proton-proton collider. These cuts take advantage of the fact that VBFH production, and VBF production in general, has a very clear signature of two forward jets clearly separated in rapidity. Examining the topology of a typical VBFH production diagram it becomes very clear that this is the case because the two leading jets are essential remnants of the two colliding protons. Since the  $p_t$  of the jets will be governed by the mass scale of the weak vector bosons and the energy by the PDFs the jets will typically be very energetic and in opposite rapidity hemispheres.

As is clear from Fig. 21 the hardest jet in VBFH production peaks at around 60 GeV. As discussed above this value is set by the mass of the weak vector bosons and hence the  $p_t$  spectra of the two hardest jets are very similar to what one finds at the LHC. From this point of view and in order to

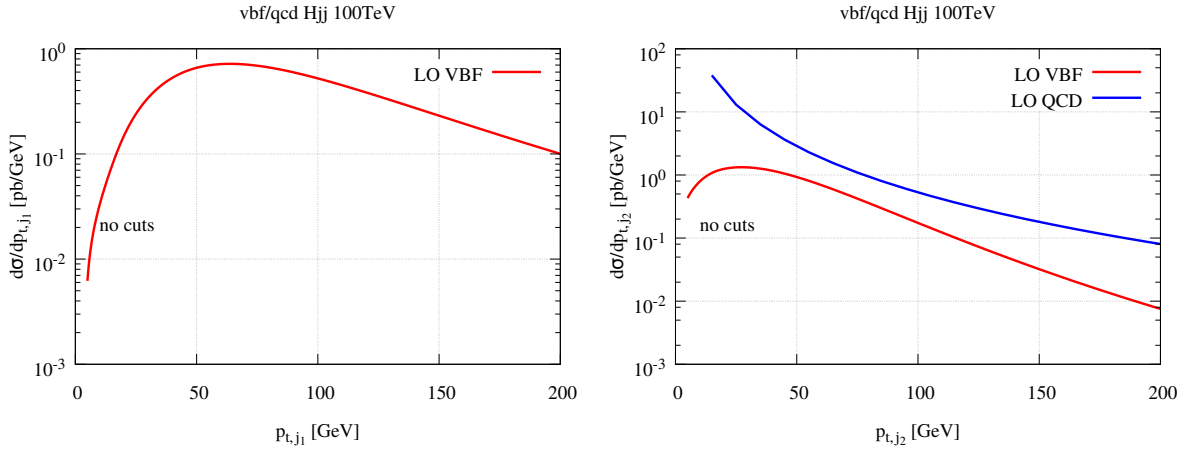


**Fig. 21:** Left panel: The  $p_t$  of the hardest jet in VBFH production at 100 TeV. We require at least two jets in the event but apply no other cuts; right panel: The  $p_t$  of the second hardest jet in VBFH and QCD Hjj production at 100 TeV.

maximise the VBFH cross section one should keep jets with  $p_{t,cut} > 30$  GeV. Here we present results for  $p_{t,cut} = \{30, 50, 100\}$  GeV to study the impact of the jet cut on both the VBFH signal and QCD Hjj background. We only impose the cut on the two hardest jets in the event.

To establish VBF cuts at 100 TeV we first study the variables which are typically used at the LHC. These are the dijet invariant mass,  $M_{jj}$ , the rapidity separation between the two leading jets,  $\Delta y_{jj}$ , the separation between the two leading jets in the rapidity-azimuthal angle plane,  $\Delta R_{jj}$  and the azimuthal angle between the two leading jet  $\phi_{jj}$ . In Fig. 22 we show  $M_{jj}$  and  $\Delta y_{jj}$  after applying a cut on the two leading jets of  $p_t > 30$  GeV and requiring that the two leading jets are in opposite detector hemispheres. This last cut removes around 60% of the background while retaining about 80% of the signal.

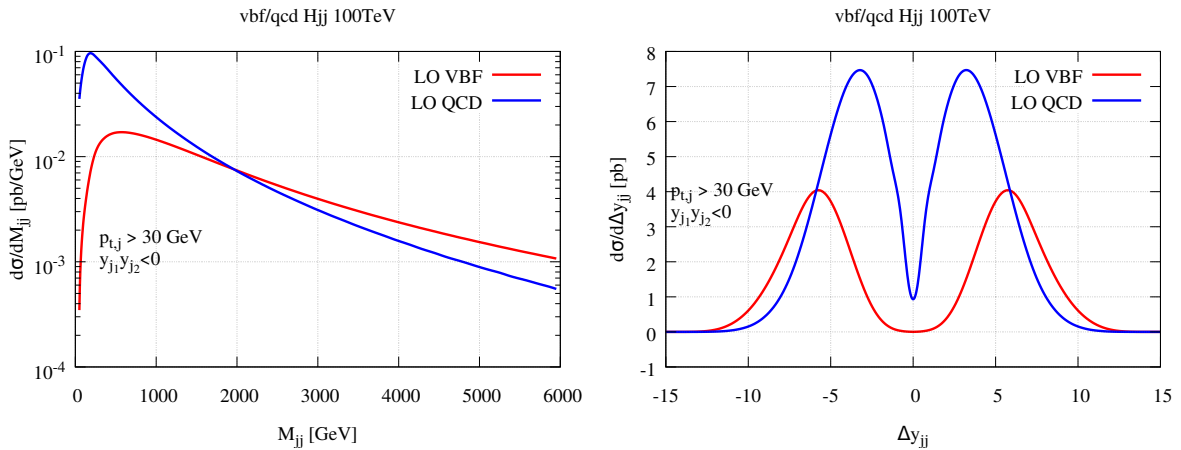


**Fig. 22:** Left panel: The invariant dijet mass  $M_{jj}$  of the two hardest jets in VBFH and QCD Hjj production at 100 TeV. right panel: The rapidity separation of the two hardest jets  $\Delta y_{jj}$  in VBFH and QCD Hjj production at 100 TeV.

In order to suppress the QCD background a cut of  $\Delta y_{jj} > 6.5$  is imposed. This cut also significantly reduces the QCD  $M_{jj}$  peak and shifts the VBF peak to about 2400 GeV. In order to further suppress the QCD background we impose  $M_{jj} > 1600$  GeV. After these cuts have been applied, and

requiring  $p_{t,j} > 30$  GeV, the VBF signal to QCD background ratio is roughly 3 with a total NNLO-QCD VBFH cross section of about 12 pb. From Fig. 23 it is clear that one could also impose a cut on  $\phi_{jj}$  to improve the suppression whereas a cut on  $\Delta R_{jj}$  would not help to achieve that. We hence state the VBF cuts that we will be using throughout this section are

$$M_{j_1 j_2} > 1600 \text{ GeV}, \quad \Delta y_{j_1 j_2} > 6.5, \quad y_{j_1} y_{j_2} < 0. \quad (18)$$

where  $j_1$  is the hardest jet in the event and  $j_2$  is the second hardest jet. At a 13 TeV machine the VBFH cross section is  $\mathcal{O}(1 \text{ pb})$  under typical VBF cuts.

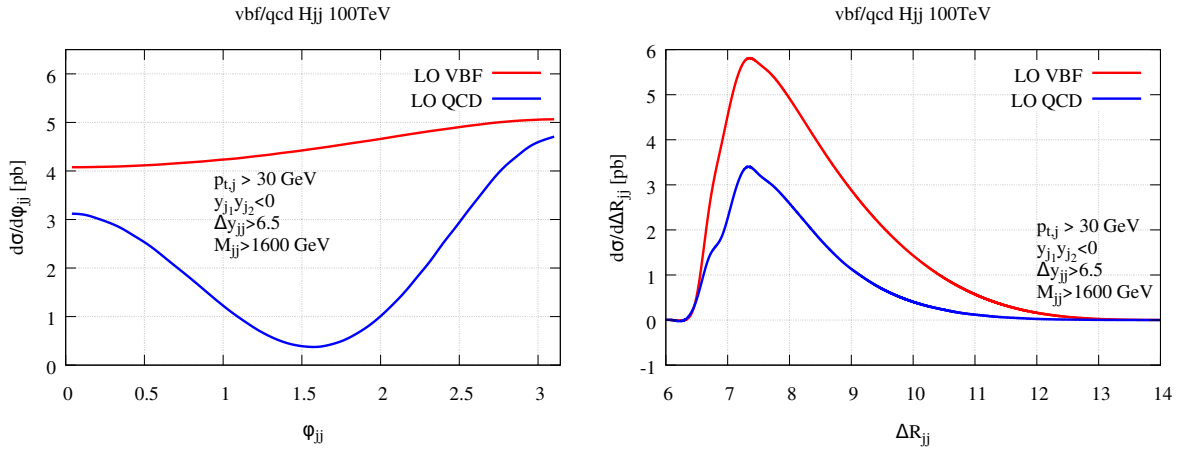


**Fig. 23:** Left panel: The azimuthal angle  $\phi_{jj}$  between the two hardest jets in VBFH and QCD Hjj production at 100 TeV. right panel: The rapidity-azimuthal angle separation of the two hardest jets  $\Delta R_{jj}$  in VBFH and QCD Hjj production at 100 TeV.

In Table 12 we show the fiducial cross section obtained after applying the VBF cuts of Eq. (18) to VBFH and QCD Hjj production. The cross sections are reported at the three different jet  $p_t$  cut values  $\{30, 50, 100\}$  GeV. All numbers are computed at LO. It is clear from the table that requiring a somewhat higher jet  $p_t$  cut than 30 GeV leads to a lower  $S/\sqrt{B}$  ratio. In going from 30 GeV to 50 GeV this reduction is however small.

**Table 12:** Fiducial VBFH and QCD Hjj cross sections for a 100 TeV proton-proton collider at LO under the VBF cuts of Eq. (18). The numbers are obtained using the setup of Table 10 using the CT14nn1o PDF.  $S/\sqrt{B}$  is defined as the ratio between the VBFH signal and the square root of the QCD background at an integrated luminosity of  $20 \text{ ab}^{-1}$ .

	$\sigma(p_{t,j} > 30 \text{ GeV})$ [pb]	$\sigma(p_{t,j} > 50 \text{ GeV})$ [pb]	$\sigma(p_{t,j} > 100 \text{ GeV})$ [pb]
VBFH	14.1	7.51	1.08
QCD Hjj	5.04	1.97	0.331
$S/\sqrt{B}@ (20 \text{ ab}^{-1})$	28100	24200	8500

In Table 13 we show for comparison the cross sections obtained after only applying the three jet  $p_t$  cuts. As expected the VBFH signal is drowned in the QCD background. It is worth noticing that the  $S/\sqrt{B}$  ratio is still very large when one assumes an integrated luminosity of  $20 \text{ ab}^{-1}$  and that it declines as the jet cut is increased.

**Table 13:** Total VBFH and QCD Hjj cross sections for a 100 TeV proton-proton collider at LO with a cut on the two hardest jets. The numbers are obtained using the setup of Table 10 using the CT14nn1o PDF.  $S/\sqrt{B}$  is defined as the ratio between the VBFH signal and the square root of the QCD background at an integrated luminosity of  $20 \text{ ab}^{-1}$ .

	$\sigma(p_{t,j} > 30 \text{ GeV})$ [pb]	$\sigma(p_{t,j} > 50 \text{ GeV})$ [pb]	$\sigma(p_{t,j} > 100 \text{ GeV})$ [pb]
VBFH	51.3	28.5	5.25
QCD Hjj	166	78.6	23.9
$S/\sqrt{B}@ (20 \text{ ab}^{-1})$	17900	14300	4900

### 2.5.5 Perturbative corrections

The results shown in the previous section were all computed at LO. Here we briefly investigate the impact of NNLO-QCD, NLO-EW and parton shower corrections to the VBF cross section computed with  $p_{t,j} > 30 \text{ GeV}$  and under the VBF cuts of Eq. (18) at a 100 TeV collider. We also compare to the NLO-QCD predictions for QCD Hjj production.

In Table 14 we show the best prediction for  $\sigma^{\text{VBF}}$  as obtained by Eq. (17) and compare it to the same cross section obtained by showering POWHEG events with PYTHIA6 but including no effects beyond the parton shower itself. The NLO-EW and NNLO-QCD corrections are found to be of roughly the same order, and amount to a total negative correction of  $\sim 23\%$ . As was the case for the inclusive cross section the corrections are a factor two larger than at 14 TeV. Even though the perturbative corrections to QCD Hjj production are negative, the effect of including higher order corrections is that the  $S/\sqrt{B}$  ratio at an integrated luminosity of  $20 \text{ ab}^{-1}$  is decreased from 28100 to 24300.

**Table 14:** Fiducial VBF cross section including QCD and EW corrections and their uncertainties for a 100 TeV proton-proton collider. For comparison the QCD induced Hjj cross section is also shown. At fixed-order QCD corrections are included at NNLO and EW corrections at NLO.

Process	$\sigma^{\text{fid}}$ [pb]	$\Delta_{\text{scale}}$ [%]	$\sigma_{\text{QCD}}$ [pb]	$\delta_{\text{EW}}$ [%]	$\sigma_{\gamma}$ [pb]
VBFH (NNLO-QCD/NLO-EW)	10.8	$\pm 1.0$	12.1	-12.6	0.22
VBFH (NLO+PS)	11.9	$+0.56$ $-0.41$	11.9	-	-
QCD Hjj (NLO)	4.70	$+0$ $-17$	4.70	-	-

In Figs. 24-27 we show comparisons between VBFH and QCD Hjj production computed at NNLO and NLO in QCD respectively. We have applied the VBF cuts of Eq. (18). Also shown is the k-factor for VBFH production going from LO to NLO and NLO to NNLO. Note that the QCD Hjj predictions have been obtained with the effective theory setup described in Section 2.1 and hence the  $p_t$  spectra should not be trusted beyond  $2M_t$ . Furthermore, in the left plots of Figs. 24 and 25 we notice a large scale dependence of the QCD Hjj predictions for higher values of the transverse momentum of the leading jet and of the Higgs boson. This is probably due to a not optimal choice of scale, which for the downward variation suffers from large cancellations among the different NLO contributions (Born, virtual, integrated subtraction terms and real radiation minus subtraction terms). We observe that increasing the minimum transverse momentum cut improves the behaviour, whereas choosing a fixed scale instead of a dynamical one makes it even worse. The exact origin of this large scale dependence needs further investigation.

As can be seen from the plots the VBF cuts have suppressed the background QCD Hjj production in all corners of phase space. One could still imagine further optimising these cuts, for example by requiring  $\phi_{jj}$  in the vicinity of  $\frac{\pi}{2}$  or a slightly larger invariant dijet mass. We note in particular that requiring that the Higgs Boson has a transverse momentum greater than 40 GeV seems to favour the

VBFH signal. Since a cut on the transverse momentum of the decay products of the Higgs would no matter what have to be imposed, this improves the efficiency of the VBF cuts in realistic experimental setups.

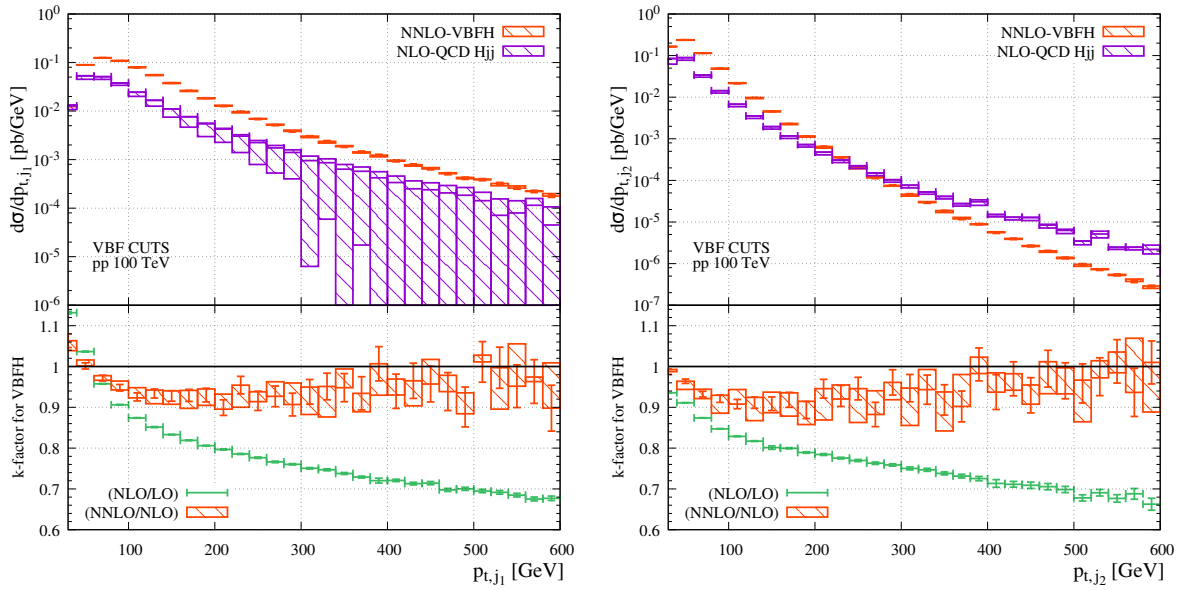


**Fig. 24:** Comparison between NNLO predictions for VBFH production at NLO predictions for QCD Hjj production under the VBF cuts of Eq. (18). The bands represent scale uncertainties obtained by varying  $\mu_F = \mu_R$  by a factor two up and down. For the VBFH production the statistical uncertainty is represented by the vertical line. No statistical uncertainties are shown for the QCD Hjj result. The lower panel shows the k-factor for VBFH production going to LO to NLO and NLO to NNLO. Left panel: Transverse momentum of the leading jet. Right Panel: Transverse momentum of the subleading jet.

### 2.5.6 Differential distributions

In addition to the distributions already presented, we here show a number of distributions to indicate the kinematical reach of the VBFH channel at 100 TeV. Assuming an integrated luminosity of  $20 \text{ ab}^{-1}$  we study how many events will be produced with a Higgs whose transverse momentum exceeds  $p_{t,\min}$ . In Figs. 28 and 29 we show this distribution for various cut configurations. This variable is particularly interesting in the context of anomalous couplings in the weak sector. It can be seen that even under VBF cuts and requiring hard jets, a number of Higgs bosons with transverse momentum of the order 6 TeV will be produced in this scenario.

In Fig. 30 we show the same distribution but fully inclusively and at various perturbative orders. Also shown is the k-factor going from LO to NLO and from NLO to NNLO. The perturbative corrections to this variable are modest as it is not sensitive to real radiation at the inclusive level. After applying VBF cuts and jet cuts the low  $p_{t,H}$ -spectrum receives moderate corrections whereas the corrections at larger values of  $p_{t,H}$  can become very large as indicated in Fig. 25.

In Fig. 31 we show how many events will be produced with a dijet invariant mass exceeding  $M_{\min}$  at various cut configurations. Because the two hardest jets in the VBFH event are typically the proton remnants the invariant dijet mass can become very large. As can be seen from the figure, even after applying VBF cuts and requiring very hard jets hundreds of events with an invariant dijet mass larger than 60 TeV is expected. This is of interest when probing for BSM physics at the very highest scales. It is also worth noticing that the tail of the distribution is almost unaffected by the VBF cuts, as the VBF cuts are optimised to favour high invariant dijet events.

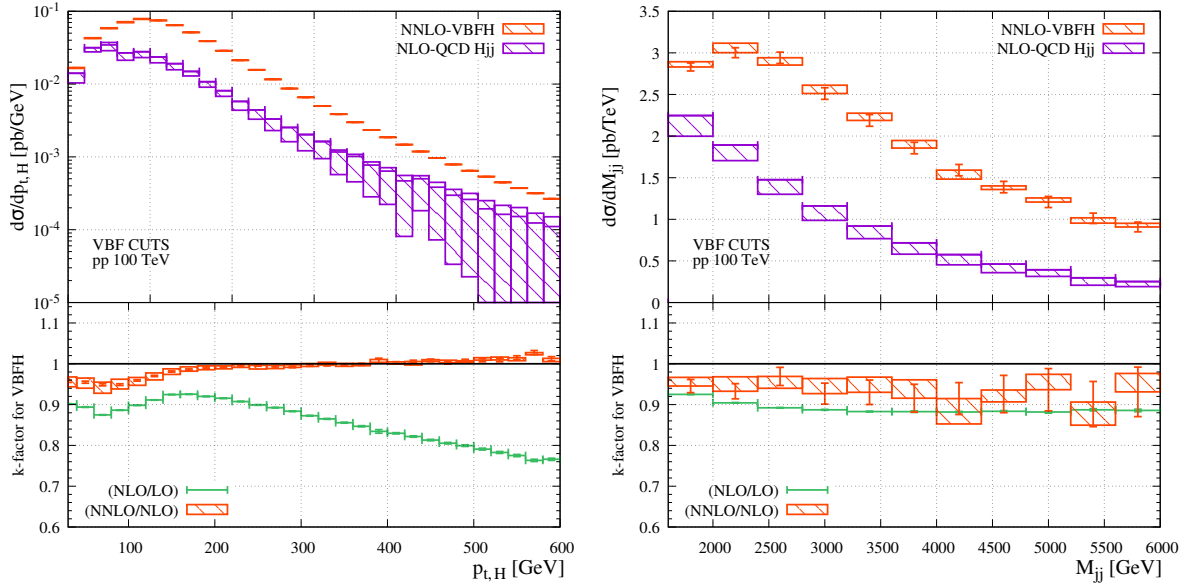


**Fig. 25:** Comparison between NNLO predictions for VBFH production at NLO predictions for QCD Hjj production under the VBF cuts of Eq. (18). The bands represent scale uncertainties obtained by varying  $\mu_F = \mu_R$  by a factor two up and down. For the VBFH production the statistical uncertainty is represented by the vertical line. No statistical uncertainties are shown for the QCD Hjj result. The lower panel shows the k-factor for VBFH production going to LO to NLO and NLO to NNLO. Left panel: Transverse momentum of the Higgs Boson. Right Panel: Invariant mass of the dijet pair.

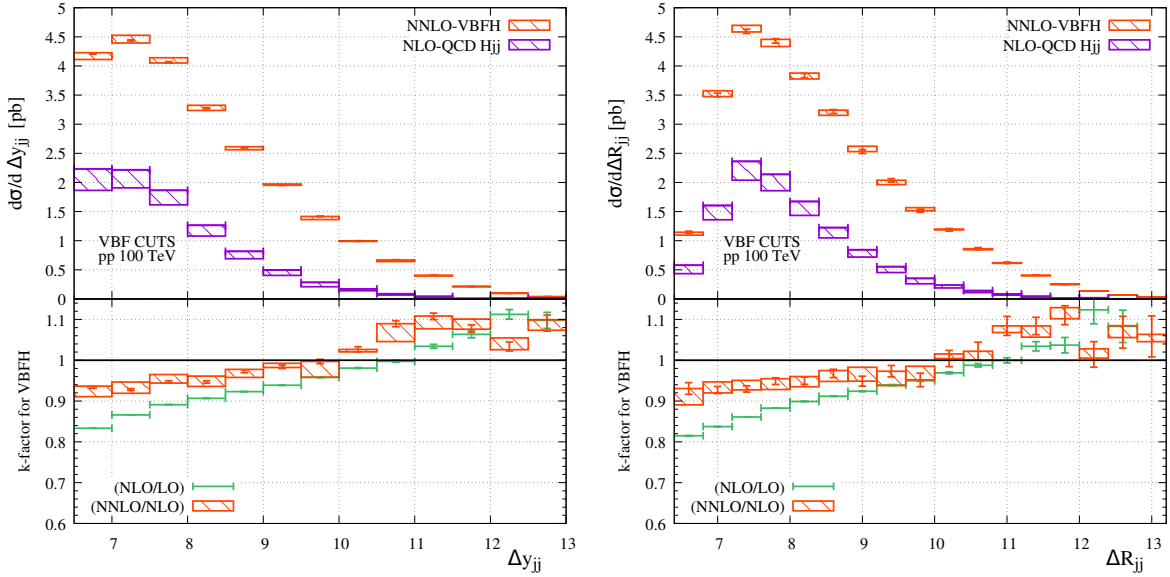


**Fig. 26:** Comparison between NNLO predictions for VBFH production at NLO predictions for QCD Hjj production under the VBF cuts of Eq. (18). The bands represent scale uncertainties obtained by varying  $\mu_F = \mu_R$  by a factor two up and down. For the VBFH production the statistical uncertainty is represented by the vertical line. No statistical uncertainties are shown for the QCD Hjj result. The lower panel shows the k-factor for VBFH production going to LO to NLO and NLO to NNLO. Left panel: Absolute value of the rapidity separation between the two leading jets. Right Panel: Distance between the two leading jets in the rapidity-azimuthal plane.

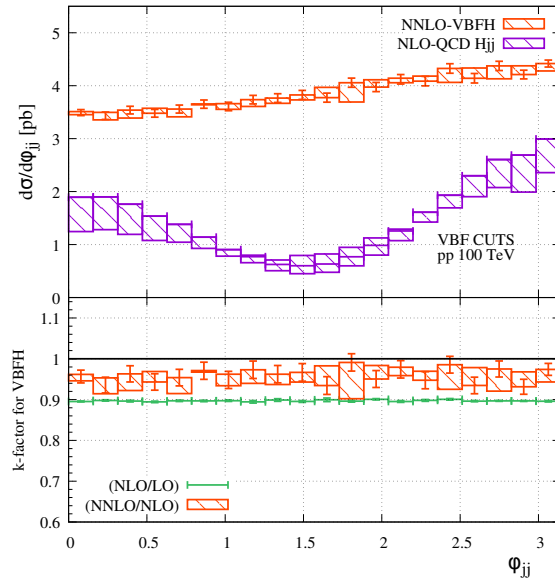


**Fig. 27:** Comparison between NNLO predictions for VBFH production at NLO predictions for QCD Hjj production under the VBF cuts of Eq. (18). The bands represent scale uncertainties obtained by varying  $\mu_F = \mu_R$  by a factor two up and down. For the VBFH production the statistical uncertainty is represented by the vertical line. No statistical uncertainties are shown for the QCD Hjj result. The lower panel shows the k-factor for VBFH production going to LO to NLO and NLO to NNLO. Shown here is the azimuthal angle between the two leading jets.

### 2.5.7 Detector implications

The requirement that the two hardest jets are in opposite detector hemispheres and are separated by at least 6.5 units of rapidity, means that a symmetric detector in the style of ATLAS or CMS must have a rapidity reach well above 3.25. In fact, looking at Fig. 32, which shows the fraction of events which satisfy  $\max(|y_{j1}|, |y_{j2}|) > y_{\min}$  for various cut configurations, it becomes clear that a detector with a rapidity reach of 4.5 would at best only retain 40% of the VBFH events after VBF cuts are applied. Since a jet with  $p_t = 30$  GeV can be produced at a rapidity of  $\sim 8$  whereas a jet with  $p_t = 100$  GeV can only be produced with rapidities up to  $\sim 6.8$ , the required rapidity reach of the detector will also depend on how well soft jets can be measured and controlled at 100 TeV. In all cases a rapidity reach above 6 seems to be desirable.

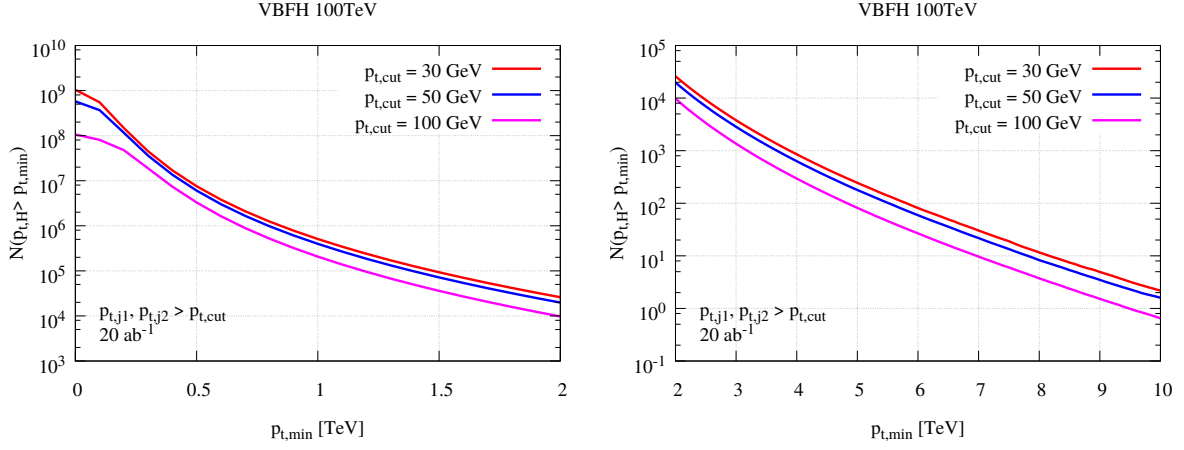


**Fig. 28:** The total number of VBFH events produced with  $p_{t,H} > p_{t,min}$  at a 100 TeV collider with an integrated luminosity of  $20 \text{ ab}^{-1}$  under three different jet  $p_t$  cuts. Left panel:  $p_{t,H}$  in the range 0-2 TeV. Right panel:  $p_{t,H}$  in the range 2-10 TeV.

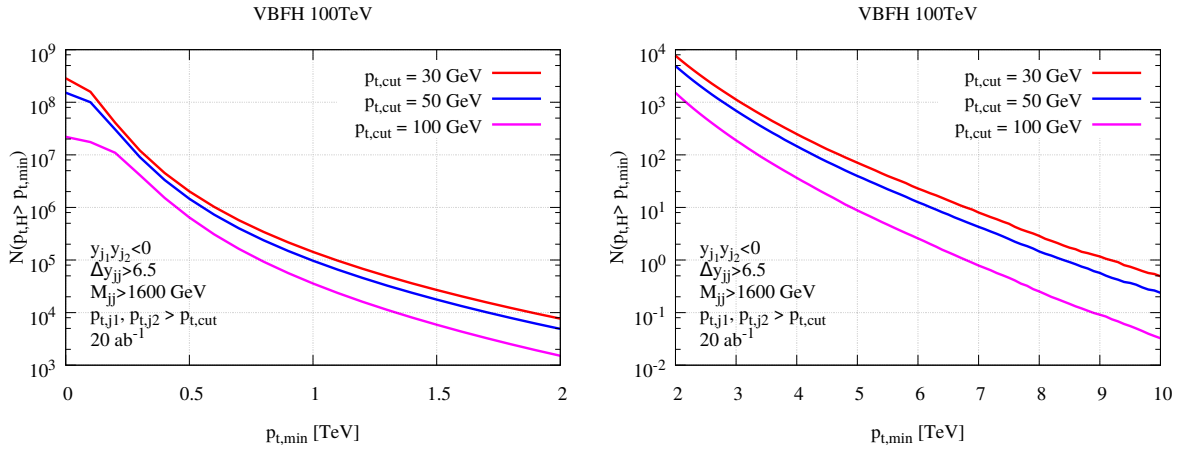


**Fig. 29:** The total number of VBFH events produced with  $p_{t,H} > p_{t,min}$  at a 100 TeV collider with an integrated luminosity of  $20 \text{ ab}^{-1}$  under three different jet  $p_t$  cuts and with the VBF cuts of Eq. (18) applied. Left panel:  $p_{t,H}$  in the range 0-2 TeV. Right panel:  $p_{t,H}$  in the range 2-10 TeV.

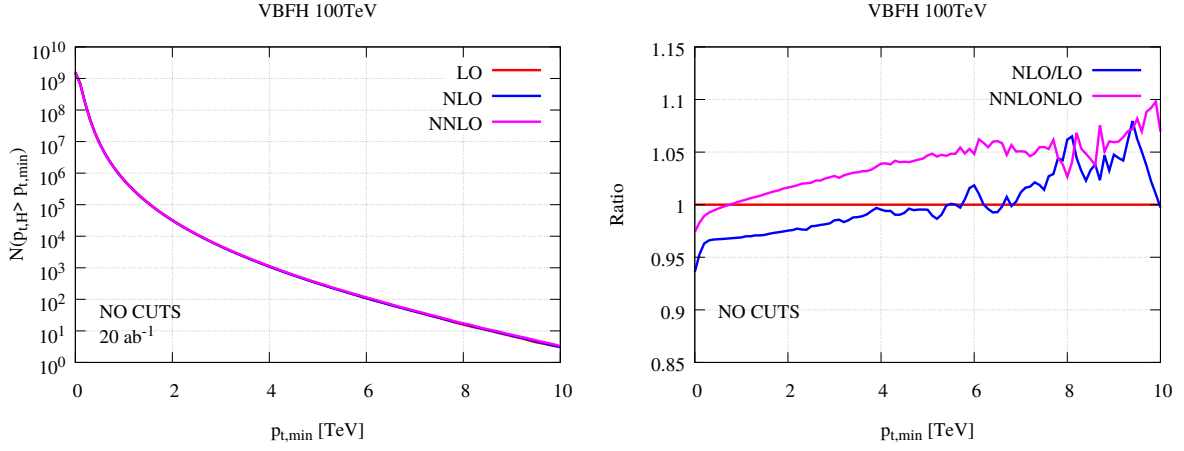


**Fig. 30:** The total number of VBFH events produced with  $p_{t,H} > p_{t,\min}$  at a 100 TeV collider with an integrated luminosity of  $20 \text{ ab}^{-1}$  with no cuts applied. Left panel: Spectrum computed at LO, NLO and NNLO in QCD. Due to the small corrections the difference between the three curves is hard to see by eye. Right panel: The k-factor going from LO to NLO and NLO to NNLO.

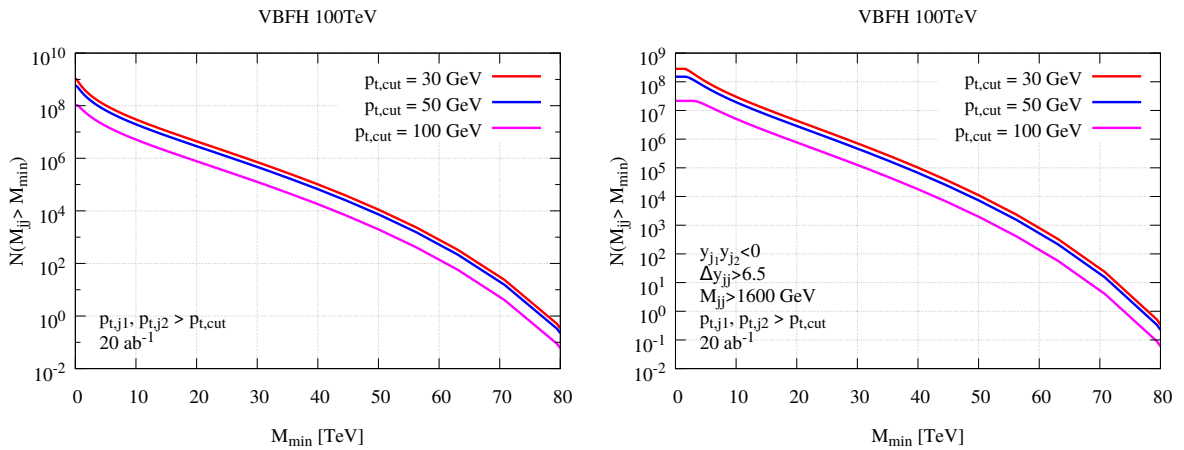


**Fig. 31:** The total number of VBFH events produced with  $M_{j_1 j_2} > M_{\min}$  at a 100 TeV collider with an integrated luminosity of  $20 \text{ ab}^{-1}$ . Left panel: Three different jet  $p_t$  cuts applied but no VBF cuts applied. Right panel: VBF cuts of Eq. (18) and three different jet  $p_t$  cuts applied.

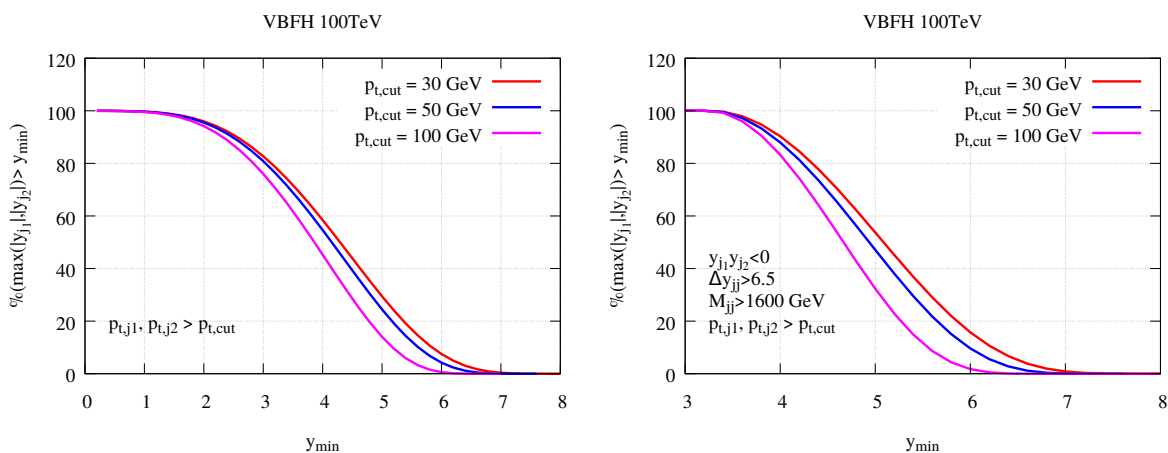


**Fig. 32:** The total fraction of events where  $\max(|y_{j1}|, |y_{j2}|) > y_{\min}$  at a 100 TeV collider. Left panel: Three different jet  $p_t$  cuts applied but no VBF cuts applied. Right panel: VBF cuts of Eq. (18) and three different jet  $p_t$  cuts applied.

## 2.6 Associated $t\bar{t}H$ production

The  $t\bar{t}H$  process provides the most direct probe of the interaction of the Higgs boson with the top quark. Theoretical calculations have been completed including NLO QCD [118,119] and EW [120] corrections. NLO corrections have recently been extended to the case of unstable top quarks, in the dilepton final state [121].

In this section, we collect results for the total production cross sections and for some key kinematical distributions. In particular, we update and extend parts of the study presented in Ref. [122], where it was shown that tight correlations between scale and PDF uncertainties lead to very precise predictions for the ratio of  $t\bar{t}H$  and  $t\bar{t}Z$  production. We focus in this section on the discussion of rate and theoretical systematics, and in Section 3.4 we review the prospects for measurements of  $y_{top}$ .

All results shown here were obtained using the MADGRAPH5\_AMC@NLO code [123], which includes both NLO QCD and EW corrections, in the case of stable top quarks. Additional details, and the results for 13 TeV, can be found in Ref. [122]. The default parameter set used here is given by:

Parameter	value	Parameter	value
$G_\mu$	$1.1987498350461625 \cdot 10^{-5}$	$n_{lf}$	5
$m_t$	173.3	$vy_t$	173.3
$m_W$	80.419	$m_Z$	91.188
$m_H$	125.0	$\alpha^{-1}$	128.930

$\mu_R = \mu_F = \mu_0 = \sum_{f \in \text{final states}} m_{T,f}/2$  is the default for the central choice of renormalization and factorization scales, where  $m_{T,f}$  is the transverse mass of the final particle  $f$ . This scale choice interpolates between the dynamical scales that were shown in Refs. [118,119] to minimize the  $p_T$  dependence of the NLO/LO ratios for the top and Higgs spectra. The scale variation systematics is obtained covering the standard range  $0.5\mu_0 \leq \mu_{R,F} \leq 2\mu_0$ , with  $\mu_R$  and  $\mu_F$  varying independently.

Table 15 shows the total cross section results, at the LO in the EW effects. The first row shows the results of the MSTW2008 NLO [124] sets, which will be used as a default for the other results of this section. The second row uses the more recent PDF4LHC15 [125] recommendation, which combines the systematics from the following NLO PDF sets: NNPDF3.0 [100], MMHT2014 [112] and CT14 [85]. The difference between MSTW2008 and PDF4LHC15 is at the level of 3%, which is compatible with the quoted uncertainty on the  $t\bar{t}H$  cross section.

Here, and in following tables and figures, we include the results for the  $t\bar{t}Z$  process as well, and for the  $t\bar{t}H/t\bar{t}Z$  ratios. As discussed in detail in [122], there are strong correlations among the sources of systematic uncertainty for these two processes, leading to very robust predictions for their ratios. In particular, all the results shown here relative to  $t\bar{t}H/t\bar{t}Z$  ratios will enforce the full correlation of the systematics induced by the PDF variations and by parameters such as  $m_{top,H}$ , and will assume likewise a complete correlation between the scale variations.

Table 15 shows that the scale uncertainty of the individual processes, in the range of  $\pm 9\%$ , is reduced in the ratio to  $\pm 1.5\%$ . The PDF uncertainty on the ratio is at the permille level, and the compar-

	$\sigma(t\bar{t}H)[\text{pb}]$	$\sigma(t\bar{t}Z)[\text{pb}]$	$\frac{\sigma(t\bar{t}H)}{\sigma(t\bar{t}Z)}$
MSTW2008	$33.9^{+7.1\%+2.2\%}_{-8.3\%-2.2\%}$	$57.9^{+8.9\%+2.2\%}_{-9.5\%-2.4\%}$	$0.585^{+1.3\%+0.3\%}_{-2.0\%-0.2\%}$
PDF4LHC15	$32.8^{+6.9\%+1.6\%}_{-8.1\%-1.6\%}$	$56.0^{+8.8\%+1.5\%}_{-9.3\%-1.5\%}$	$0.586^{+1.3\%+0.12\%}_{-2.0\%-0.12\%}$

**Table 15:** Total cross sections  $\sigma(t\bar{t}H)$  and  $\sigma(t\bar{t}Z)$  and the ratios  $\sigma(t\bar{t}H)/\sigma(t\bar{t}Z)$  with NLO QCD. The results include the renormalization/factorization scale and PDF+ $\alpha_s$  uncertainties.

	$\alpha(m_Z)$ scheme			$G_\mu$ scheme		
	$\sigma(t\bar{t}H)$ [pb]	$\sigma(t\bar{t}Z)$ [pb]	$\frac{\sigma(t\bar{t}H)}{\sigma(t\bar{t}Z)}$	$\sigma(t\bar{t}H)$ [pb]	$\sigma(t\bar{t}Z)$ [pb]	$\frac{\sigma(t\bar{t}H)}{\sigma(t\bar{t}Z)}$
NLO QCD	33.9	57.9	0.585	32.9	56.3	0.585
$\mathcal{O}(\alpha_s^2\alpha^2)$ Weak	-0.73	-2.15		0.027	-0.90	
$\mathcal{O}(\alpha_s^2\alpha^2)$ EW	-0.65	-2.0		0.14	-0.77	
NLO QCD+Weak	33.1	55.8	0.594	32.9	55.4	0.594
NLO QCD+EW	33.2	55.9	0.594	33.1	55.6	0.595

**Table 16:** Effect of the EW NLO corrections, in the  $\alpha(m_Z)$  and  $G_\mu$  schemes.

	$\sigma(t\bar{t}H)$ [pb]	$\sigma(t\bar{t}Z)$ [pb]	$\frac{\sigma(t\bar{t}H)}{\sigma(t\bar{t}Z)}$
default	$33.9^{+7.1\%}_{-8.3\%}$	$57.9^{+8.9\%}_{-9.5\%}$	$0.585^{+1.3\%}_{-2.0\%}$
$\mu_0 = m_t + m_{H,Z}/2$	$39.0^{+9.8\%}_{-9.6\%}$	$67.2^{+11\%}_{-11\%}$	$0.580^{+1.2\%}_{-1.8\%}$
$m_t = y_{top}v = 174.1$ GeV	33.9	57.2	0.592
$m_t = y_{top}v = 172.5$ GeV	33.7	58.6	0.576
$m_H = 126.0$ GeV	33.2	57.9	0.575

**Table 17:** Results with NLO QCD corrections at 100 TeV by varying some parameter values. In the first two rows we include the renormalization/factorization scale uncertainties.

ison of the old MSTW2008 result with the most recent PDF4LHC15 one confirms the reliability of this estimate.

The effect of the NLO EW corrections in two different schemes is shown in Table 16. The shift of the individual  $t\bar{t}H$  and  $t\bar{t}Z$  is at the level of few percent, and depends on the EW scheme and on the process. The ratio shifts with respect to the LO EW result by less than 2%, and the EW scheme dependence is at the permille level. This suggests that the residual uncertainty of the cross-section ratio due to higher-order EW corrections should be significantly below the percent level.

We explore further variations in our default parameter set in Table 17. There, we remove the PDF uncertainties, which are practically unaffected by these parameter changes. Choosing the fixed value  $\mu_0 = m_t + m_{H,Z}/2$  for the central choice of the renormalization and factorization scales, modifies the ratio  $\sigma(t\bar{t}H)/\sigma(t\bar{t}Z)$  by 1% – 1.5%, consistent with the range established using the dynamical scale.

For  $m_t$ , we consider a variation in the range of  $m_t = 173.3 \pm 0.8$  GeV. We notice that  $\sigma(t\bar{t}H)$  is practically constant. This is due to the anti-correlation between the increase (decrease) in rate due to pure phase-space, and the decrease (increase) in the strength of  $y_{top}$ , when the top mass is lower (higher). The  $t\bar{t}Z$  process is vice versa directly sensitive to  $m_t$  at the level of  $\pm 1.5\%$  over the  $\pm 0.8$  GeV range, and this sensitivity is reflected in the variation of the cross-section ratio. We notice, however, that if we kept the value of  $y_{top}$  fixed when we change  $m_t$ , the dynamical effect on the rate would be totally correlated, and the ratio would remain constant to within a few permille, as shown in Table 18. This shows that the ratio is only sensitive to the strength of  $y_{top}$ , and only minimally to the precise value of  $m_t$ .

Finally, we observe a  $\sim 2\%$  shift in  $\sigma(t\bar{t}H)$  (and therefore in the ratios) when  $m_H$  is changed by 1 GeV, which is a gross underestimate of the precision with which the Higgs mass is [126] and will soon be known.

	$\sigma(t\bar{t}H)[\text{pb}]$	$\sigma(t\bar{t}Z)[\text{pb}]$	$\frac{\sigma(t\bar{t}H)}{\sigma(t\bar{t}Z)}$
$m_t = 174.1 \text{ GeV}$	23.88	37.99	0.629
$m_t = 172.5 \text{ GeV}$	24.21	38.73	0.625

**Table 18:** LO results for different top masses, keeping the top Yukawa coupling fixed at  $y_{top}v = 173.3 \text{ GeV}$ .

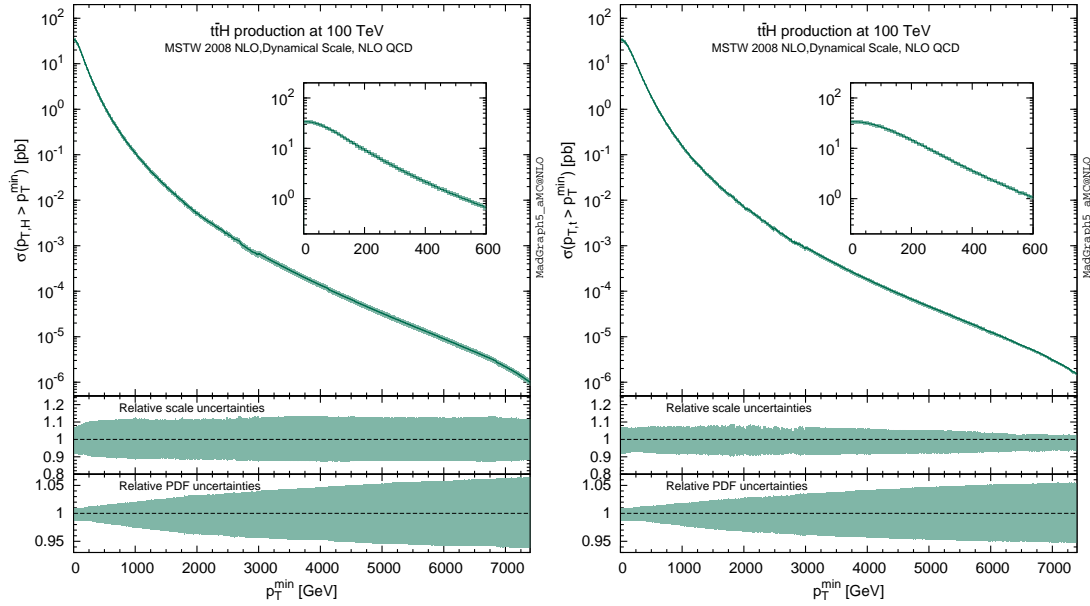


**Fig. 33:** Integrated transverse momentum distributions for the Higgs boson (left) and (anti-)top quark (right), in the  $t\bar{t}H$  process at a 100 TeV collider.

In summary, we quote, as the best estimate for the  $t\bar{t}H$  cross section at 100 TeV (with  $m_H = 125 \text{ GeV}$  and  $m_{top} = 173.3 \text{ GeV}$ ), the following:

$$\sigma(t\bar{t}H)[\text{pb}] = 32.1 \begin{matrix} +6.9\% \\ -8.1\%_{scale} \end{matrix} \pm 1.6\%_{PDF4LHC15} \pm 0.3\%_{m_{top}} \quad (19)$$

This includes the full EW corrections, and accounts for a  $\pm 0.8 \text{ GeV}$  uncertainty in the top mass.

### 2.6.1 Kinematical distributions

As shown in the study of other production processes, one of the key features of the 100 TeV collider is the existence of large production rates even with kinematical configurations at extremely large energy. For the  $t\bar{t}H$  process, this is well illustrated by Fig. 33, which gives the cross sections for production of the Higgs (left) and top quark (right) above a given  $p_T$  threshold. With the expected FCC-hh luminosities, the production will extend well beyond  $p_T \sim 5 \text{ TeV}$ . We note that the spectra are very stable against scale and PDF systematics, the former staying within a 10% window. In Fig. 34 we also plot the integrated cross section for producing  $t$ ,  $\bar{t}$  and  $H$  all above a given  $p_T$  threshold, in configurations in which these three objects are pair-wise separated by  $\Delta R > 1$  and 2.

Any experimental analysis, and in particular the boosted approach that will be used in Section 3.4, will restrict the phase-space available to the final states. To preserve the precision in the theoretical prediction of the ratio of total  $t\bar{t}H$  and  $t\bar{t}Z$  cross sections, it is crucial to ensure that the reduction in systematics uncertainties carries over to the description of final states after kinematical cuts have been

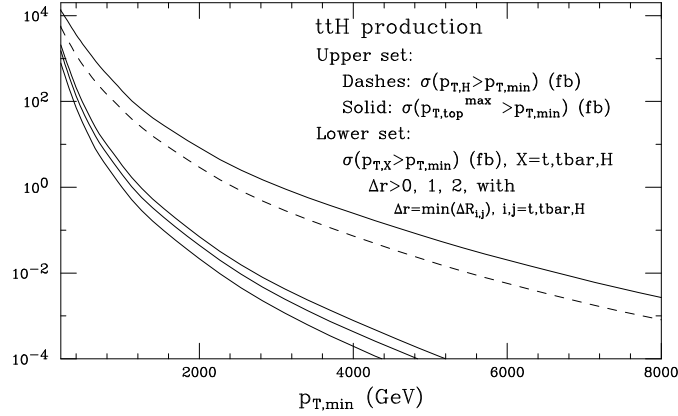


**Fig. 34:** Integrated distributions for the  $p_T$  of the Higgs boson (upper solid line), the maximum  $p_T$  of top and antitop quarks (upper dashed line), and for the minimum  $p_T$  of  $t$ ,  $\bar{t}$  and  $H$ , with different cuts on the  $\Delta R$  separation among different objects.

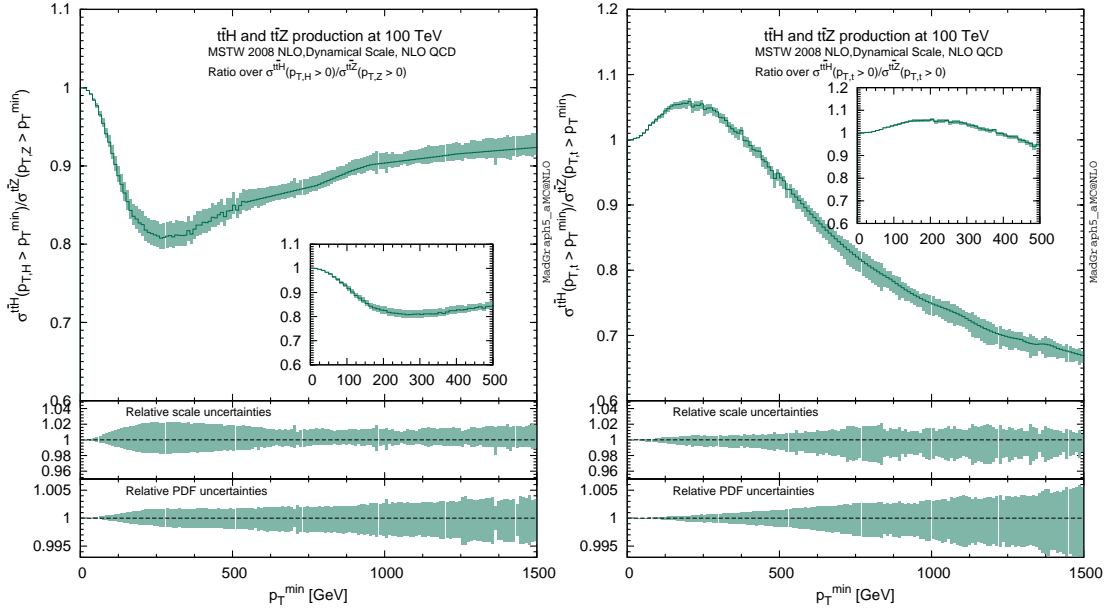


**Fig. 35:** Scale and PDF systematics of ratios of integrated  $p_T$  spectra for different observables, at 100 TeV. From left to right:  $p_T$  of the boson,  $p_T$  of the top quark.

applied. The following results will give some concrete examples, focused on the discussion of scale and PDF systematics.

We show in Fig. 35 the ratio of the integrated  $p_T$  spectra of various final-state objects  $X$ :  $\sigma[t\bar{t}H](p_{T,X} > p_{T,\min})/\sigma[t\bar{t}Z](p_{T,X} > p_{T,\min})$ . On the left,  $X = H(Z)$  for the  $t\bar{t}H$  ( $t\bar{t}Z$ ) process. In the middle,  $X = t$  and on the right  $X$  is the  $t\bar{t}$  system. We normalize the ratios to 1 at  $p_{T,\min} = 0$ , so that the resulting uncertainties correspond to the systematics in the extrapolation of the ratio of differential distributions to the ratio of the total rates. The three upper panels show that the ratios are not a constant, and can change by up to 20% up to  $p_T = 500$  GeV. The relative uncertainties, separately for the scale and PDF variation (MSTW2008 NLO set), are shown in the lower plots. The scale uncertainties reach a value of  $\pm 2\%$  for the boson  $p_T$  spectra,  $\pm 1\%$  for the top, and  $\pm 3\%$  for the  $p_T$  of the  $t\bar{t}$  pair. The PDF uncertainties remain well below the percent level throughout.

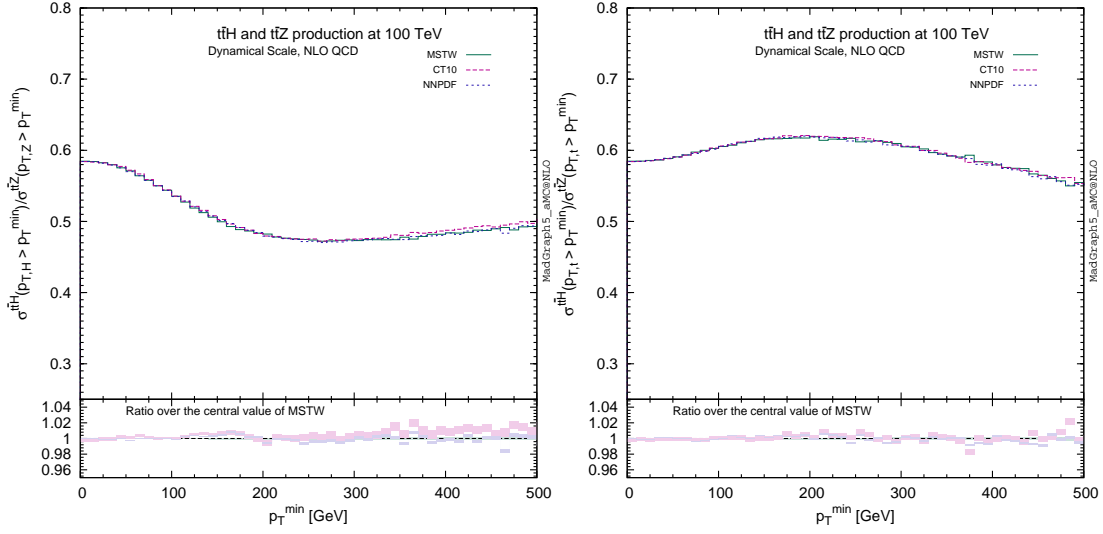


**Fig. 36:** Three PDF sets systematics of ratios of integrated  $p_T$  spectra for different observables, at 100 TeV. From left to right:  $p_T$  of the boson,  $p_T$  of the top quark.

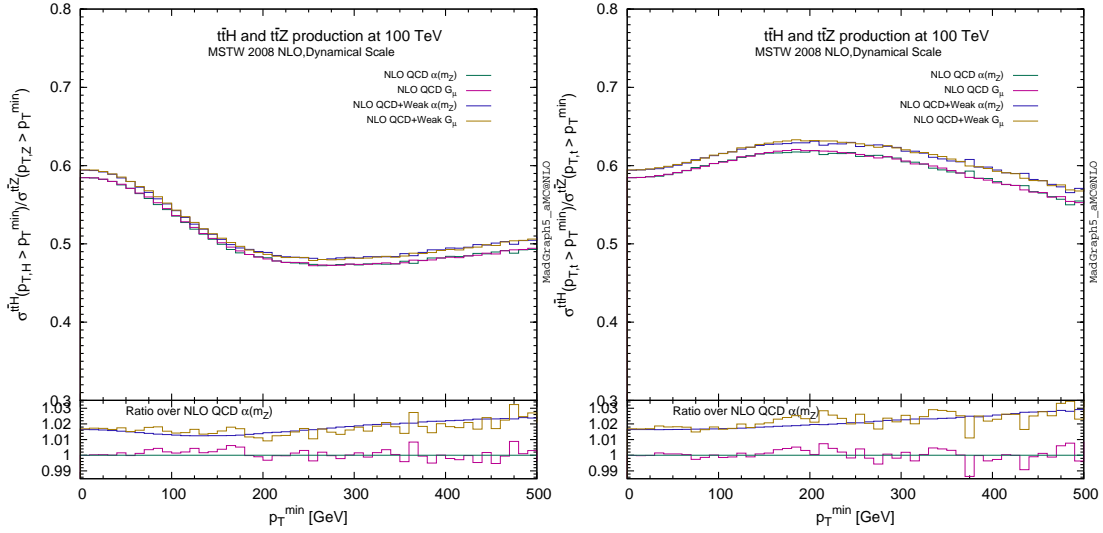


**Fig. 37:** EW scheme dependence and weak corrections of ratios of integrated  $p_T$  spectra for different observables, at 100 TeV. From left to right:  $p_T$  of the boson,  $p_T$  of the top quark.

These results imply that the relative shapes of the  $p_T$  spectra can be controlled with a precision that remains consistent with the overall goal of a percent-level extraction of the relative rates. There is no doubt that future NNLO calculations of both processes will improve this even further. Very precise measurements of the shape of the  $Z$  boson spectra in  $t\bar{t}Z$  events using e.g. the very clean leptonic  $Z$  decay will also help confirming the accuracy of the predicted  $p_T$  spectra and reduce a possible left-over uncertainty.

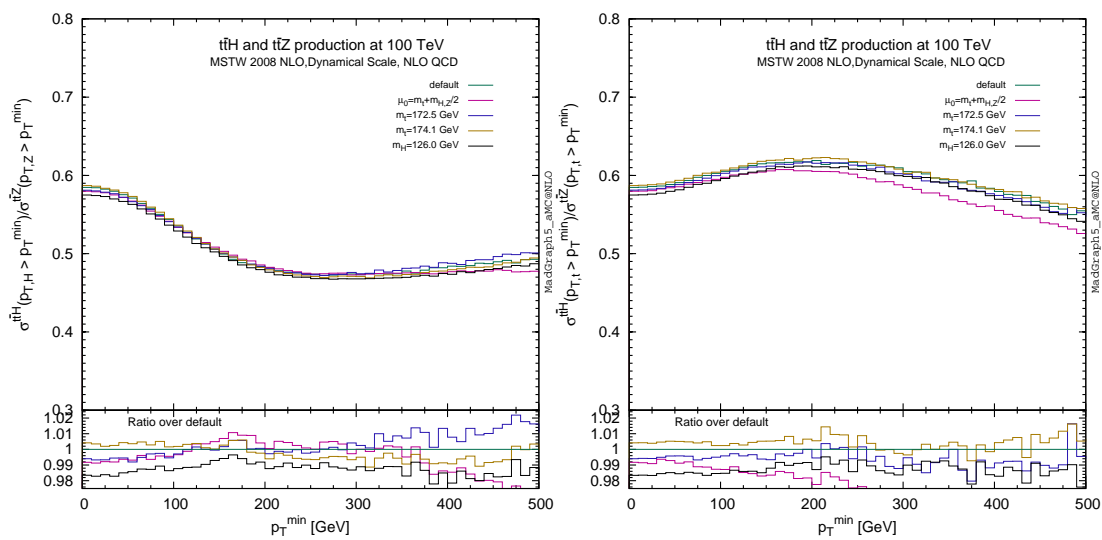


**Fig. 38:** Other systematics of ratios of integrated  $p_T$  spectra for different observables, at 100 TeV. From left to right:  $p_T$  of the boson,  $p_T$  of the top quark.

## 2.7 Rare production modes

The first section of Table 19 [127], obtained with the MadGraph5\_aMC@NLO code [123], reports the rate for associated production of a SM Higgs boson with a single top. The cross section is in excess of 5 picobarns at 100 TeV, and displays a considerable increase with collider energy.

This remarkable growth, together with the sensitivity of this process to the sign of the top Yukawa coupling  $y_t$  [128], makes this reaction a golden channel for a precise measurement of the latter. It has been shown [129] that already at the 14-TeV LHC it is possible to put loose bounds on the sign of  $y_t$ , mainly with a semileptonically decaying top quark, and in the  $H \rightarrow b\bar{b}$  and  $H \rightarrow \gamma\gamma$  decay channels. At 100 TeV the situation will improve considerably: the NLO cross section for the main irreducible background to  $tH(\rightarrow \gamma\gamma)j$  production, namely  $t\gamma\gamma j$  QCD production, has a growth  $\rho$  comparable to that of the signal, hence the significance of the signal, in comparison with the LHC, is expected to scale at least with the square root of the number of events. Moreover, the sensitivity of the signal to  $y_t$  is only slightly reduced at 100 TeV with respect to 8 TeV, as shown explicitly in the left panel of Fig.39.

The second part of Table 19 and the right panel of Fig. 39 [127] detail the cross section for a Higgs in association with a pair of gauge bosons (see also [130] for a recent analysis). Rates for these channels are smaller than for single top, of the order of a few tens of femtobarns at 100 TeV, but still accessible. Theoretical systematics are typically below 10%, and the rate growth with energy is mild, compatibly with the fact that these processes are  $q\bar{q}$ -driven.

These rare channels are interesting as they can add some power to constrain possible anomalous Higgs couplings to vector-boson (and fermion) pairs, which in turn has implications on the analysis of perturbative unitarity at high energy and strong links with the study of anomalous triple-vector-boson vertices [131, 132]. In particular the  $pp \rightarrow HW^+W^-$  process, the one with the largest cross section in this category, has been shown [133] to be promising in this respect already at the high-luminosity LHC, and will considerably benefit from the rate increase of a factor of roughly forty at 100 TeV.

Process	$\sigma_{\text{NLO}}(8 \text{ TeV})$ [fb]	$\sigma_{\text{NLO}}(100 \text{ TeV})$ [fb]	$\rho$
$pp \rightarrow Htj$	$2.07 \cdot 10^1$ $^{+2\%}_{-1\%}$ $^{+2\%}_{-2\%}$	$5.21 \cdot 10^3$ $^{+3\%}_{-5\%}$ $^{+1\%}_{-1\%}$	252
$pp \rightarrow HW^+W^-$ (4FS)	$4.62 \cdot 10^0$ $^{+3\%}_{-2\%}$ $^{+2\%}_{-2\%}$	$1.68 \cdot 10^2$ $^{+5\%}_{-6\%}$ $^{+2\%}_{-1\%}$	36
$pp \rightarrow HZW^\pm$	$2.17 \cdot 10^0$ $^{+4\%}_{-4\%}$ $^{+2\%}_{-2\%}$	$9.94 \cdot 10^1$ $^{+6\%}_{-7\%}$ $^{+2\%}_{-1\%}$	46
$pp \rightarrow HW^\pm\gamma$	$2.36 \cdot 10^0$ $^{+3\%}_{-3\%}$ $^{+2\%}_{-2\%}$	$7.75 \cdot 10^1$ $^{+7\%}_{-8\%}$ $^{+2\%}_{-1\%}$	33
$pp \rightarrow HZ\gamma$	$1.54 \cdot 10^0$ $^{+3\%}_{-2\%}$ $^{+2\%}_{-2\%}$	$4.29 \cdot 10^1$ $^{+5\%}_{-7\%}$ $^{+2\%}_{-2\%}$	28
$pp \rightarrow HZZ$	$1.10 \cdot 10^0$ $^{+2\%}_{-2\%}$ $^{+2\%}_{-2\%}$	$4.20 \cdot 10^1$ $^{+4\%}_{-6\%}$ $^{+2\%}_{-1\%}$	38

**Table 19:** Production of a Higgs boson at 8 and 100 TeV. The rightmost column reports the ratio  $\rho$  of the 100-TeV to the 8-TeV cross sections [127]. Theoretical uncertainties are due to scale and PDF variations, respectively. Processes  $pp \rightarrow Htj$  does not feature any jet cuts.

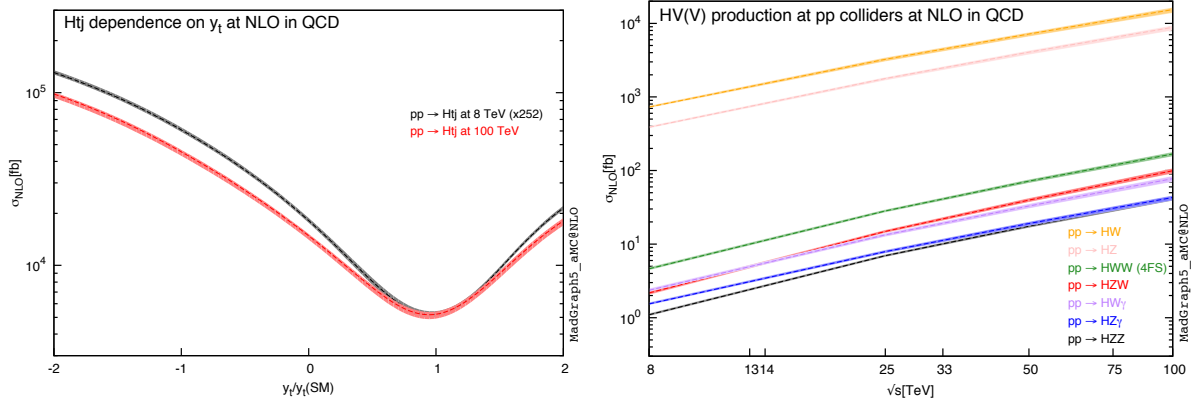


**Fig. 39:** Left panel: sensitivity of  $pp \rightarrow Htj$  to  $y_t$  at 8 and 100 TeV; right panel: cross section for associated production of a Higgs and up to two electroweak vector bosons [127].

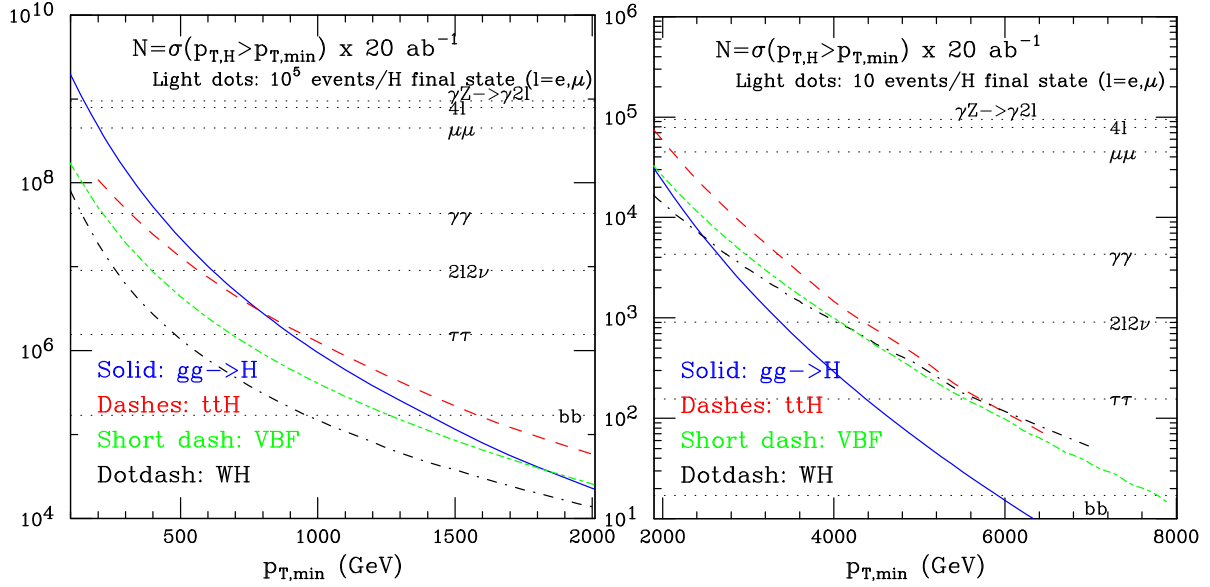


**Fig. 40:** Integrated Higgs transverse momentum rates, for various production channels, with  $20 \text{ ab}^{-1}$ . The light-dotted horizontal lines in the left (right) panel correspond to the production of  $10^5$  ( $10$ ) events with a Higgs decay to the indicated final states.

### 3 Prospects for measurements of SM Higgs properties

Table 20 shows the number of Higgs bosons produced at 100 TeV with an integrated luminosity of  $20 \text{ ab}^{-1}$ . For reference, we compare these rates to what was available at the end of the LHC run 1, and what will be available at the end of the full HL-LHC programme, namely  $3 \text{ ab}^{-1}$  at 14 TeV.

	$N_{100}$	$N_{100}/N_8$	$N_{100}/N_{14}$
$gg \rightarrow H$	$16 \times 10^9$	$4 \times 10^4$	110
VBF	$1.6 \times 10^9$	$5 \times 10^4$	120
$WH$	$3.2 \times 10^8$	$2 \times 10^4$	65
$ZH$	$2.2 \times 10^8$	$3 \times 10^4$	85
$t\bar{t}H$	$7.6 \times 10^8$	$3 \times 10^5$	420

**Table 20:** Indicative total event rates at 100 TeV ( $N_{100}$ ), and statistical increase with respect to the statistics of the LHC run 1 ( $N_8$ ) and the HL-LHC ( $N_{14}$ ), for various production channels. We define here  $N_{100} = \sigma_{100 \text{ TeV}} \times 20 \text{ ab}^{-1}$ ,  $N_8 = \sigma_{8 \text{ TeV}} \times 20 \text{ fb}^{-1}$ ,  $N_{14} = \sigma_{14 \text{ TeV}} \times 3 \text{ ab}^{-1}$ .

Naive scaling leads to a potential for improvements in the statistical precision in the range of few hundreds w.r.t to run 1, and of order 10-20 w.r.t. HL-LHC. As is well known, the HL-LHC itself will already be systematics dominated for several measurements. But with such a huge increase in rate and, as we shall see, in kinematic reach, one can envisage new approaches to both precision measurements and to the exploration of new phenomena in the production dynamics. Furthermore, these rates will push the search for rare or forbidden Higgs decays well beyond the LHC reach.

The most remarkable feature of Higgs production at 100 TeV is not just the rate increase w.r.t. the LHC, but the extreme kinematical range over which the Higgs bosons are distributed. Figure 40 shows the integrated  $p_H$  spectra for the dominant production processes, and prompts several important remarks.

To start with, we highlight the remarkable statistics. Horizontal light-dotted lines in the figures show the  $p_T(H)$  values corresponding to samples of  $10^5$  (left) and 10 (right) events, for various final

states. The former statistics are possibly suitable for percent-level measurements, the latter indicate the most extreme  $p_T$  values at which measurements of Higgs production dynamics are in principle possible. This could have relevance, for example, in the context of searches for new physics, where Higgses could either be part of a signal, or a background.

Secondly, we note that the hierarchy of rates among the different processes, shown for example in Table 20, is only valid for the bulk of the production. As  $p_T(H)$  grows above  $\sim 500$  GeV,  $t\bar{t}H$  emerges as the most abundant source of large- $p_T$  Higgses. Moving to yet larger  $p_T$ , even VBF and eventually associated  $VH$  production come to be more important than  $gg \rightarrow H$ . The key reason for this is the form-factor-like suppression of the  $ggH$  vertex at large virtuality, when the finite- $m_{top}$  effects are properly accounted for.

This observation has important implications for the measurements. For example, while dedicated cuts are needed to extract the VBF Higgs-production signal from the inclusive  $gg \rightarrow H + X$  Higgs sample, at large  $p_T$  the dominant source of irreducible background is top production. The separation of  $t\bar{t}H$  from VBF when  $p_T(H) > 1$  TeV can rely on kinematic and event-shape discriminators, which are likely more powerful and efficient than the usual VBF cuts. This may also have important implications on the detector, since optimal acceptance to VBF cuts requires instrumentation in the very difficult forward  $\eta$  region.

Large Higgs  $p_T$  values, furthermore, make it possible to consider using the otherwise disfavoured  $H \rightarrow b\bar{b}$  decay mode, thanks to the higher and higher discrimination power of jet-structure techniques. The ability to use this high-BR decay, extends considerably the accessible  $p_T(H)$  range. Lower-BR final states, such as  $H \rightarrow \gamma\gamma, ZZ^*, Z\gamma$  or  $\mu^+\mu^-$ , remain nevertheless usable for precision measurements (i.e. event rates in excess of  $10^4$ ), over a broad range of  $p_T$ .

In this Section we shall elaborate in some more detail on these ideas. One could organize the discussion according to final state (e.g. addressing the issue of how to best measure a given BR from a global fit of several production channels), or according to production channel (e.g. to compare different decays in the same channel, in order to remove possible production systematics from the precise determination of BR ratios). We shall adopt a mixed approach and, as emphasized above, we shall not analyze in quantitative terms all sources of theoretical and experimental uncertainties. Several of the studies shown here were done including only the leading relevant order of perturbation theory. We include the dominant sources of backgrounds, and make crude, and typically optimistic, assumptions about the relevant detector performance issues. The key purpose is to show what is in principle possible, and postpone more rigorous studies to future work.

### 3.1 Higgs acceptance

We present here some reference results to document the detector acceptance for Higgs decay final states, as a function of the pseudorapidity coverage and of the minimum  $p_T$  thresholds. These results can orient the choices in the optimal detector layout.

Figure 41 shows the detector acceptance, for different  $p_T$  thresholds, for 2-body Higgs decays (e.g.  $H \rightarrow b\bar{b}, H \rightarrow \gamma\gamma, H \rightarrow \mu^+\mu^-$ ). Each box corresponds to Higgs bosons produced in  $gg$  fusion, at various fixed values of the Higgs transverse momentum ( $p_T(H) = 0, 50, 100, 200, 500$  and  $1000$  GeV). For each  $p_T(H)$  value we consider a minimum  $p_T$  cut ( $p_{T,min}$ ) for the two decay products (0, 20, 30 and 40 GeV), and show the acceptance as a function of the largest  $|\eta|$  ( $\eta_{max}$ ). The acceptance is defined with respect to the total sample of events produced at the given value of  $p_T(H)$ .

The largest sensitivity to  $p_{T,min}$  is present for values of  $p_T(H)$  around 50 – 100 GeV, since the boost in this range will suppress the acceptance for the decay particle produced in the backward direction with respect to the Higgs direction. For the largest values of  $p_T(H)$ , the acceptance is much less sensitive to  $p_{T,min}$ , and is well optimized in the central region  $|\eta| < 2.5$ .

Figure 42 shows similar results, for the 3-body decay  $H \rightarrow Z\gamma \rightarrow \mu^+\mu^-\gamma$ . The  $p_{T,min}$  and  $\eta$

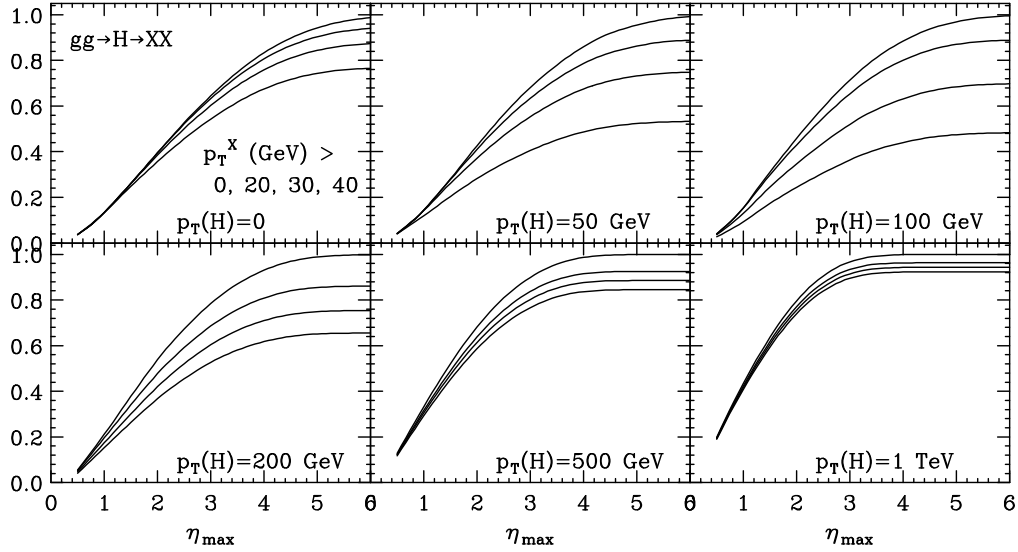


**Fig. 41:** Detector acceptance, as a function of the maximal pseudorapidity coverage  $\eta_{max}$ , for the 2-body decay of Higgs bosons produced in  $gg$  fusion at various  $p_T$  values (this applies, e.g., to  $H \rightarrow b\bar{b}, \gamma\gamma$  or  $\mu^+\mu^-$ ). The different lines refer to different thresholds in the minimum  $p_T$  of the decay particles.

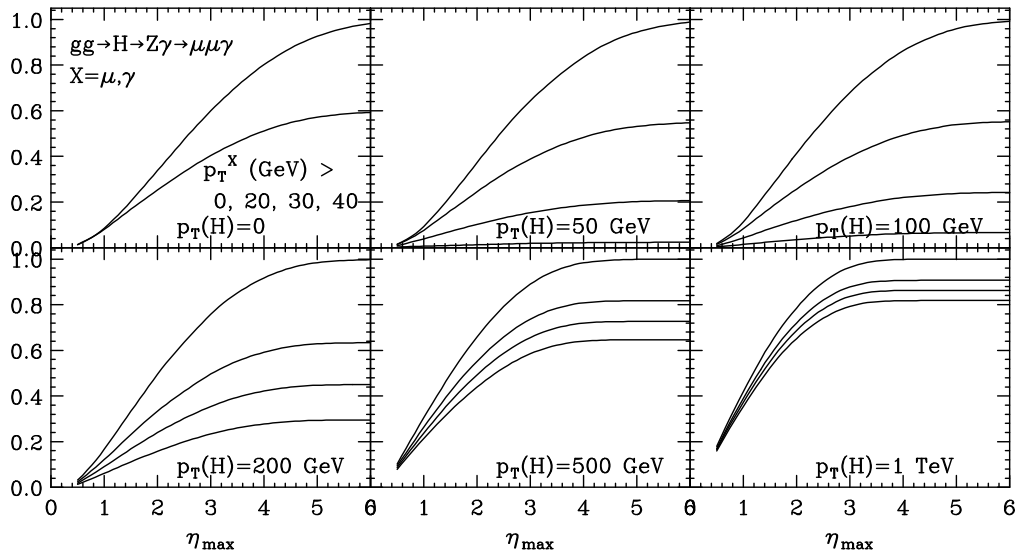


**Fig. 42:** Same as Fig. 41, for the decay  $H \rightarrow Z\gamma \rightarrow \mu^+\mu^-\gamma$ . The  $p_T$  and  $\eta_{max}$  cuts apply to both muons and to the photon.

cuts here are applied to all decay products. At  $p_T(H) = 0$  there is no acceptance for  $p_{T,min} \geq 30$  GeV, since the photon energy in the  $H$  rest frame is of order 30 GeV (up to a negligible effect due to the finite  $Z$  width). For these decays, the overall loss in acceptance due to the  $p_T$  threshold is always significant, as shown by the large- $\eta$  limit of the distributions.

The strong  $p_{T,min}$  dependence is emphasized even more in the 4-body decays, such as  $H \rightarrow WW^* \rightarrow 2\ell 2\nu$  and  $H \rightarrow ZZ^* \rightarrow 4\ell$ , whose acceptance plots are shown in Figs. 43 and 44. For 4-lepton decays, we consider also the acceptance of asymmetric cuts, such as those used at the LHC. They appear as absolutely necessary, at least for  $p_T(H)$  values below  $\sim 500$  GeV, since the decay kinematics

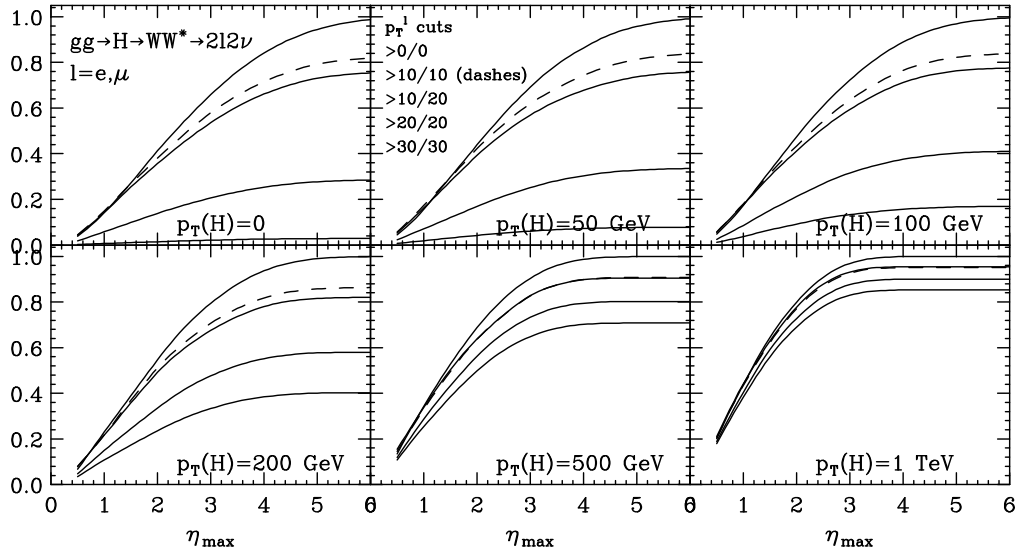


**Fig. 43:** Same as Fig. 41, for the decay  $H \rightarrow WW^* \rightarrow \ell^+ \ell^- 2\nu$ . The  $p_T^\ell$  cuts shown in the second inset apply to the softest and the hardest of the two charged leptons.

$H$ decay	$p_T(H)$	$ \eta  < 2.5$	$< 4$	$< 5$	$H$ decay	$p_T(H)$	$ \eta  < 2.5$	$< 4$	$< 5$
2-body	0	0.5	0.76	0.84	$Z\gamma \rightarrow \ell\ell\gamma$	0	0.33	0.51	0.57
$p_T^{min} = 30$	50	0.48	0.68	0.74	$p_T^{min} = 20$	50	0.32	0.49	0.53
	500	0.72	0.87	0.88		500	0.66	0.81	0.82
$WW^* \rightarrow 2\ell 2\nu$	0	0.17	0.25	0.28	$ZZ^* \rightarrow 4\ell$	0	0.20	0.33	0.38
$p_T^{min} = 20$	50	0.21	0.30	0.33	$p_T^{min} = 10$	50	0.23	0.36	0.40
	500	0.66	0.79	0.80		500	0.63	0.77	0.79

**Table 21:** Acceptances for various Higgs decay modes, in  $gg \rightarrow H + X$  production, as function of Higgs  $p_T$ . All final state products (except the neutrinos in the  $WW^*$  mode) are required to have  $p_T > p_{T,min}$ .

enhances the spectral asymmetry, and a uniform cut for all leptons at 20 GeV would lead to an acceptance at the percent level.

For example, ATLAS [134] requires the three leading leptons to have  $p_T$  larger than 10, 15 and 20 GeV, and the fourth lepton to exceed 6 (if muon) or 7 (if electron) GeV. CMS [135] requires the two leading leptons to have  $p_T$  larger than 10 and 20 GeV, and the others to exceed 5 (if muon) or 7 (if electron) GeV. We consider here similar cuts, namely the thresholds (5, 10, 15, 20) or (10, 10, 15, 20). We note that, for  $p_T(H)$  below few hundred GeV, the difference between 5 and 10 GeV for the softest lepton is almost a factor of 2 in acceptance. We also notice that the acceptance of the fully symmetric cut (10, 10, 10, 10) is almost identical to that of (10, 10, 15, 20). This is a result of the decay kinematics. We stress that for these processes the low- $p_T$  acceptance is far more important than rapidity coverage, and must be preserved.

In case of  $WW^* \rightarrow 2\ell 2\nu$  decays, the fiducial regions selected by ATLAS [136] and CMS [137] require the thresholds of 10 GeV for the softer lepton, and 20 (CMS) or 22 (ATLAS) for the leading one. For 100 TeV, we show here the options (10, 10), (20, 20) and (10, 20).

The results for some reference  $p_T$  and  $|\eta|$  thresholds are collected in Table 21.

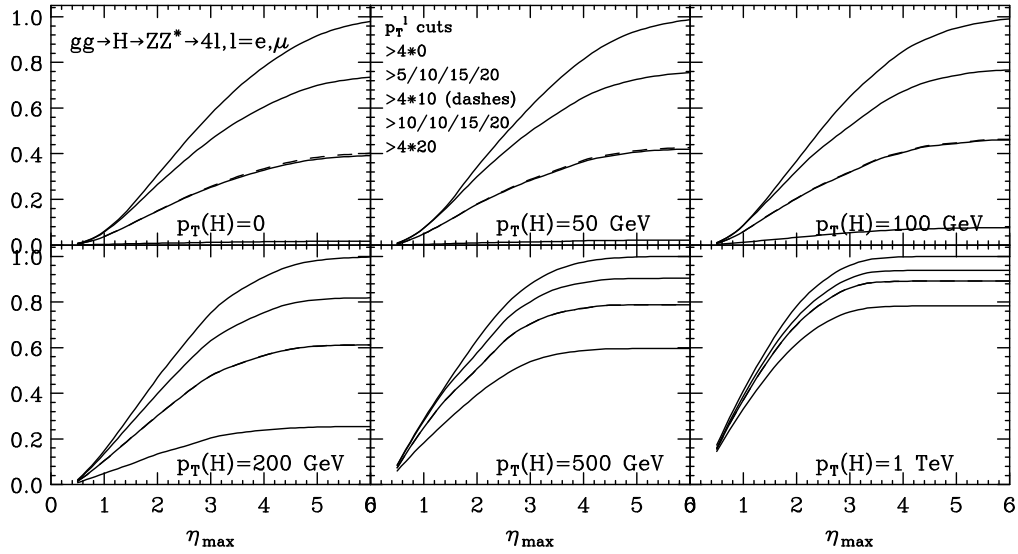


**Fig. 44:** Same as Fig. 41, for the decay  $H \rightarrow ZZ^* \rightarrow 4$  charged leptons. The  $p_T^\ell$  cuts shown in the second inset apply to the softest through the hardest of the four charged leptons.

### 3.2 Small-BR $H$ final states at intermediate $p_T$

We consider here  $H$  decays with BRs in the range of  $10^{-3} - 10^{-4}$ , such as  $H \rightarrow \gamma\gamma$ ,  $H \rightarrow \gamma Z$ ,  $H \rightarrow 4\ell$  and  $\mu^+\mu^-$ . At a fully inclusive level, these events are produced by the millions; a thorough analysis of the potential for precise measurements from these large samples requires a detailed understanding of the experimental environment, starting from the consideration of the impact of hundreds, if not thousands, of pileup events. This is work for future studies.

We discuss here instead the possible interest to study these final states in decays of Higgs bosons produced with  $p_T$  values of a few 100 GeV, where rates are still large, but  $S/B$  ratios are typically better than for the inclusive samples, and the experimental environment is possibly easier (e.g. production is more central than for the fully inclusive Higgs sample, and the higher  $p_T$ 's can improve the reconstruction of the primary vertex and the resolution of multiple pileup events). A possible target of such studies is a very precise (percent level of better) measurement of the relative decay BRs: the production ratio between different final states will in fact remove several of the dominant systematics intrinsic in the absolute rate measurements, such as the integrated luminosity or the theoretical production rate uncertainty.

#### 3.2.1 $H \rightarrow \gamma\gamma$

Figure 45 (left plot) shows the  $p_T$  spectrum of diphotons from  $H$  decays ( $BR = 2.3 \times 10^{-3}$ ), and from the dominant irreducible background, namely QCD  $\gamma\gamma$  production (for a discussion of  $pp \rightarrow \gamma\gamma$ , see the Volume “Standard Model physics at 100 TeV” of this report). The QCD contribution is constrained by an invariant mass cut,  $|m(\gamma\gamma) - 125 \text{ GeV}| < 4 \text{ GeV}$ . This is rather conservative even by today standards, where current analyses point at resolutions in this channel of about 1-2 GeV. But the energy resolution will degrade at the values of photon energies considered in the regime of large  $p_T(H)$ , so we take 4 GeV as an indicative benchmark. The size of the background, for a reasonable range of resolution, scales linearly.

The background considered in this plot includes all sources ( $q\bar{q}$ ,  $qg$  and  $gg$  initial states), and is subject to an isolation constraint, which plays however a negligible role, since the diphoton pair at large  $p_T$  at this order of perturbation theory mostly recoils against the partons. We note that the  $S/B$  ratio is of  $O(1)$  in this region, much larger than for the low  $p_T(H)$  sample, where it drops well below 1/10. The

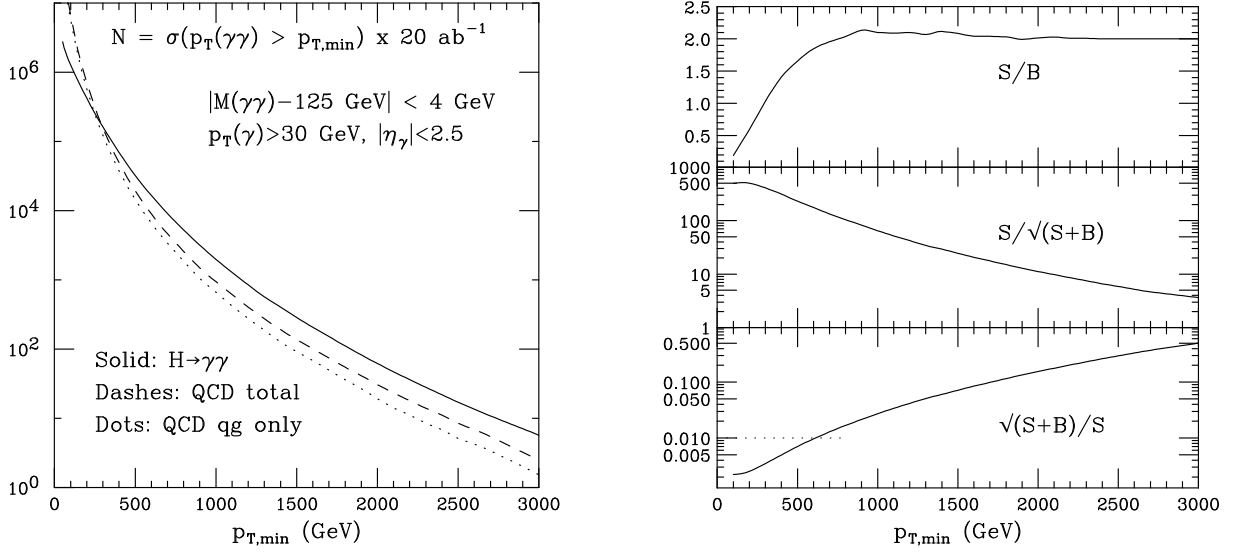


**Fig. 45:** Left: Integrated transverse momentum rates ( $20 \text{ ab}^{-1}$ ) for a photon pair with mass close to the Higgs mass: signal and QCD background. Right:  $S/B$ , significance of the signal, and potential statistical accuracy of the sample.

statistical precision, in presence of this background, remains below 1% up to  $p_T(H) \sim 600 \text{ GeV}$ .

### 3.2.2 $H \rightarrow \mu^+ \mu^-$

Figure 46 (left plot) shows the  $p_T$  spectrum of dimuons from  $H$  decays ( $BR = 2.2 \times 10^{-4}$ ), and from the leading irreducible background, namely Drell-Yan (DY)  $\mu^+ \mu^-$  production, dominated by the tail of the  $Z^*/\gamma$  distribution (see e.g. the ATLAS [138] and CMS [139] analyses).

The DY contribution is constrained by an invariant mass cut,  $|m(\gamma\gamma) - 125 \text{ GeV}| < 1 \text{ GeV}$ . This is better than the resolution of today's LHC experiments: the signal full width at half maximum estimated by CMS for events with one central muon, for example, varies in the range 4-5 GeV [139]), but 1 GeV is consistent with the improvement in the muon  $p_T$  resolution by a factor of  $O(5)$ , projected for the 100 TeV detectors.

The DY background includes  $q\bar{q}$  and  $qg$  initial states. Contrary to the  $\gamma\gamma$  decay, the  $S/B$  for dimuons deteriorates at larger  $p_T(H)$ , but still allows for a precision in the rate measurement better than 2% for  $p_T(H)$  up to  $\sim 200 \text{ GeV}$ . This could allow for a 1% determination of the muon Yukawa coupling,  $y_\mu$ , relative to the  $H\gamma\gamma$  coupling.

### 3.2.3 $H \rightarrow ZZ^*$ and $H \rightarrow Z\gamma$

We consider here  $H \rightarrow ZZ^*$  and  $H \rightarrow Z\gamma$ , with leptonic decays of the  $Z$  boson to electron or muon pairs ( $BR = 1.3 \times 10^{-4}$  and  $BR = 1.1 \times 10^{-4}$ , respectively). The rates for signals and leading irreducible backgrounds are given in Figs. 47 and 48.

We considered for these plots the following acceptance cuts:

- $H \rightarrow ZZ^* \rightarrow 4\ell$ :  $p_T(\ell) > 10 \text{ GeV}, |\eta(\ell)| < 2.5$
- $H \rightarrow Z\gamma \rightarrow 2\ell\gamma$ :  $p_T(\ell, \gamma) > 20 \text{ GeV}, |\eta(\ell, \gamma)| < 2.5$

We notice that, as shown in the acceptance plots of Fig. 44, at large  $p_T(H)$  the cut  $p_T(\ell) > 10 \text{ GeV}$  for all 4 leptons has an acceptance almost identical to that of the asymmetric cut 10/10/15/20 GeV. With

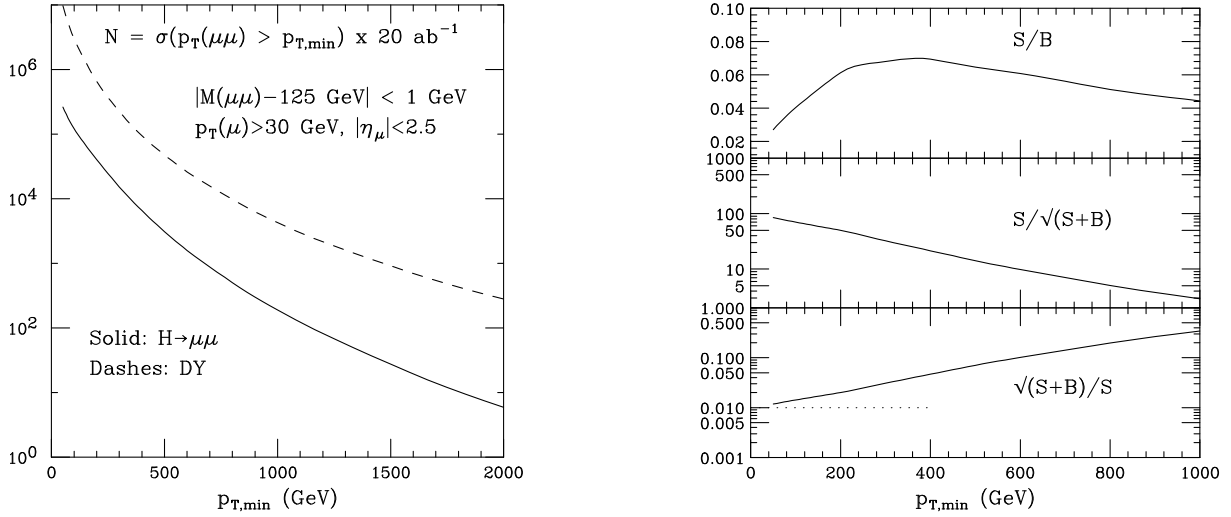


**Fig. 46:** Left: Integrated transverse momentum rates ( $20 \text{ ab}^{-1}$ ) for a muon pair with mass close to the Higgs mass: signal and  $DY$  background. Right:  $S/B$ , significance of the signal, and potential statistical accuracy of the sample.

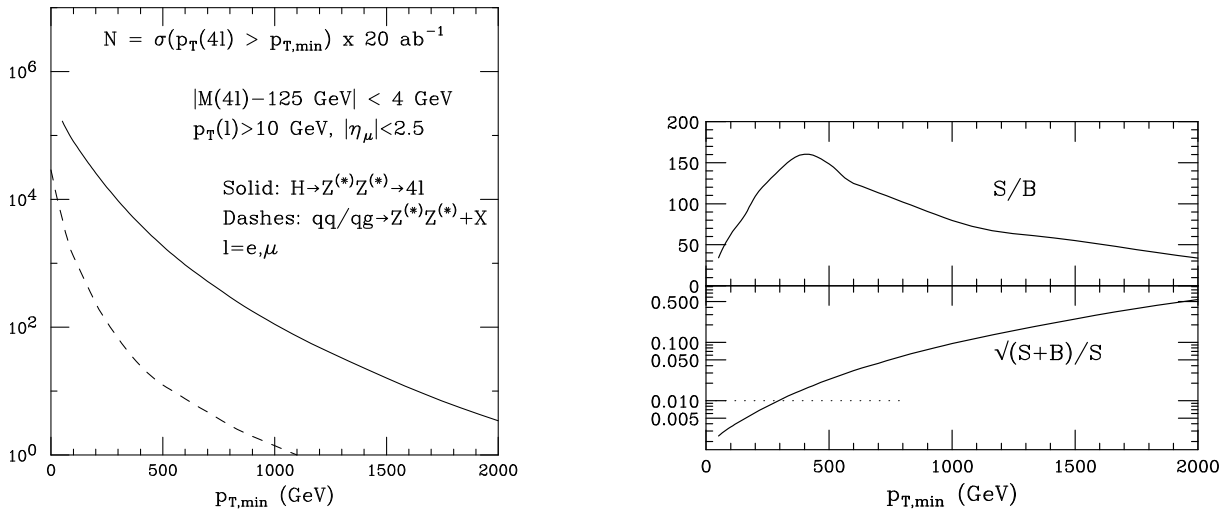


**Fig. 47:** Integrated transverse momentum rates ( $20 \text{ ab}^{-1}$ ) for a four-lepton final state ( $\ell = e, \mu$ ), with mass close to the Higgs mass: signal and QCD background.

reference to that figure, we also point out that increasing the  $\eta$  range and reducing the threshold for the  $p_T$  of the softest lepton, would each increase the signal rate by a factor of 2.

We assume here once again 4 GeV as mass resolution for both the 3- and 4-body final states. For the 4-lepton final state, the  $S/B$  ratio was already larger than 1 in the 8 TeV run of the LHC; due to greater increase in the gluon PDF relative to the quark one, the QCD background at 100 TeV becomes negligible. A 1% determination of the rate is statistically possible for  $p_T(H) \lesssim 300 \text{ GeV}$ . Likewise, the  $S/B$  ratio for  $Z\gamma$  improves significantly as  $p_T(H)$  is increased, and becomes larger than 0.5 above  $\sim 300 \text{ GeV}$ . In this region the statistical precision is better than 2%, allowing for a percent-level measurement of the  $HZ\gamma$  coupling relative to  $H\gamma\gamma$ .

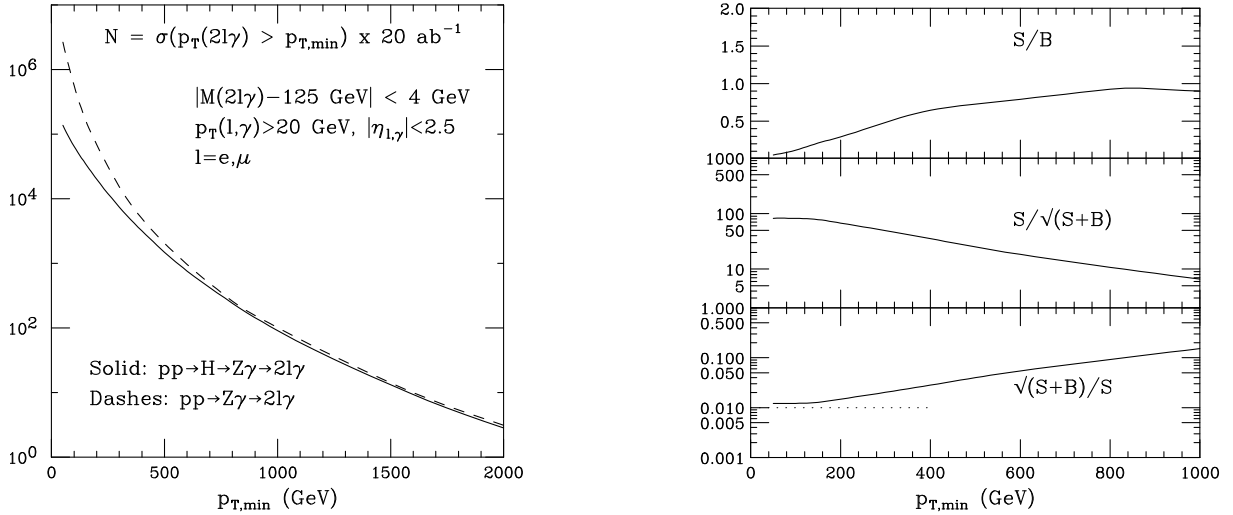


**Fig. 48:** Left: Integrated transverse momentum rates ( $20 \text{ ab}^{-1}$ ) for a dimuon+photon pair system with mass close to the Higgs mass: signal and QCD background. Right:  $S/B$ , significance of the signal, and potential statistical accuracy of the sample.

### 3.3 Associated $VH$ production

We consider here some examples of possible measurements of  $WH$  production, in the  $H \rightarrow b\bar{b}$  final state. As in the previous discussion, we do not attempt to optimize the detection of the fully inclusive sample, but examine the opportunities offered by production in kinematical configuration that are unconventional at the LHC, and where the 100 TeV collider could offer prospects for interesting new measurements.

We start by the case of  $WH$  production at large invariant mass. As shown before, this is dominated by the Born-level topologies, with the  $W$  and  $H$  recoiling against each other. The largest backgrounds to the  $H \rightarrow b\bar{b}$  decay are the QCD associated production of  $Wb\bar{b}$ , and the large-mass tail of the  $Z$  boson in  $WZ^*$ , with  $Z^* \rightarrow b\bar{b}$ . For these kinematics, top quark production is not an important background. The integrated mass spectra of signal and backgrounds are shown in the left panel of Fig. 49. We model the background with a parton-level calculation, require the  $b\bar{b}$  pair to have an invariant mass in the range of 100–150 GeV, and both  $W$  and  $b\bar{b}$  system are in the region  $|\eta| < 2.5$ . The rates include the branching ratio for the decays  $W \rightarrow \ell\nu$  ( $\ell = e, \mu$ ).

Of course the invariant mass on the  $b\bar{b}$  pair provides only a very crude picture of the potential to suppress the QCD  $Wb\bar{b}$  background. The application of the standard  $H \rightarrow b\bar{b}$  tagging techniques [140], developed for boosts in the range of few hundred GeV, may require important adaptations and optimization in the multi-TeV regime, where the whole Higgs-jet is contained within a cone of radius smaller than  $R = 0.1$ . In the accompanying SM Volume of this Report [141], the tagging of multi-TeV gauge bosons from the decay of resonances with masses in the 5–40 TeV range is discussed. Gauge boson hadronic decays can be tagged with efficiencies in the range of 80%, with suppression factors of order 20–100 for normal QCD jets of comparable  $p_T$ . This performance is comparable to the effectiveness of the naive  $m_{bb}$  cut we applied: the dotted line in Fig. 49 shows in fact the background level obtained by requesting the  $b\bar{b}$  pair to be contained within a jet of radius  $R = 1$ , without any mass cut. The reduction due to the mass cut is a factor of order 10–20. The very large  $S/B$  shown in Fig. 49 shows that there is plenty of room to cope with the challenge of identifying these hyper-boosted  $H \rightarrow b\bar{b}$  jets and rejecting their backgrounds.

As a further example of possible applications, we consider the other kinematical configurations of interest, namely  $WH$  production in presence of a high- $p_T$  jet. For the signal, the dominant process is

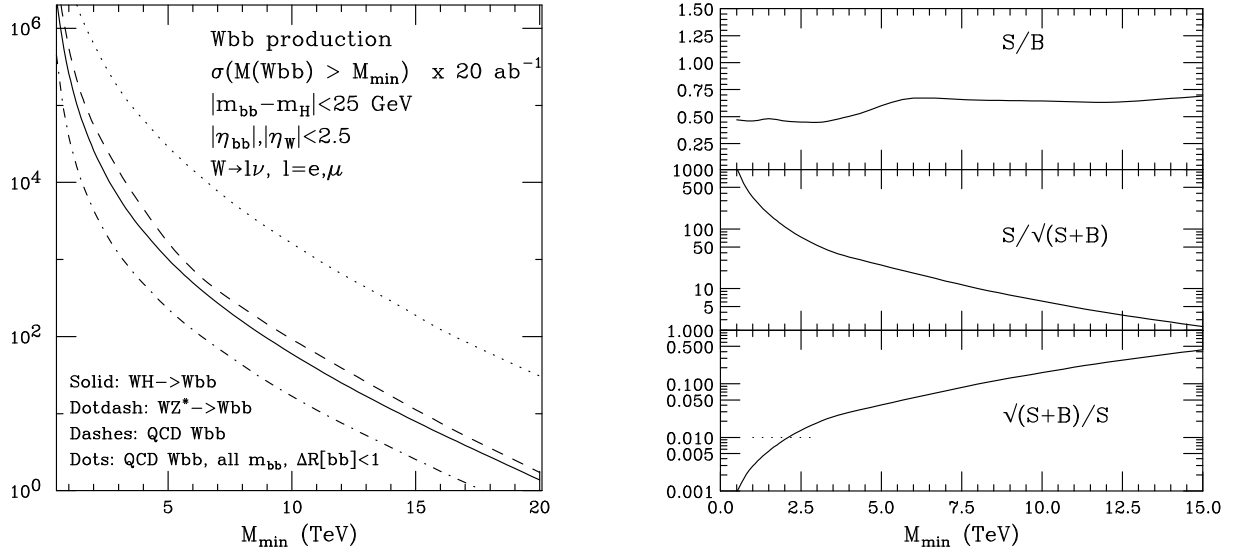


**Fig. 49:** Left: Integrated invariant mass rate ( $20 \text{ ab}^{-1}$ ) for a  $Wb\bar{b}$  pair, with  $W \rightarrow \ell\nu$  ( $\ell = e, \mu$ ) and  $|m_{bb} - m_H| < 25 \text{ GeV}$ : signal and QCD background. Right:  $S/B$ , significance of the signal, and potential statistical accuracy of the sample.

$q\bar{q} \rightarrow gW^* \rightarrow gWH$ , where the Higgs is simply radiated off the high- $p_T$   $W$  that recoils against the jet. As shown in Section 2.4, this leads to a strong correlation between the  $W$  and  $H$  direction, resulting in a  $\Delta R(WH)$  distribution peaked at small values. For the background, on the other hand, the dominant production dynamics is given by the process  $qg \rightarrow q(g \rightarrow b\bar{b})$ , with the  $W$  radiated from the initial or final state quarks. In this case, there is no strong correlation between the  $b\bar{b}$  and the  $W$ : if anything, they much prefer to be produced back to back.

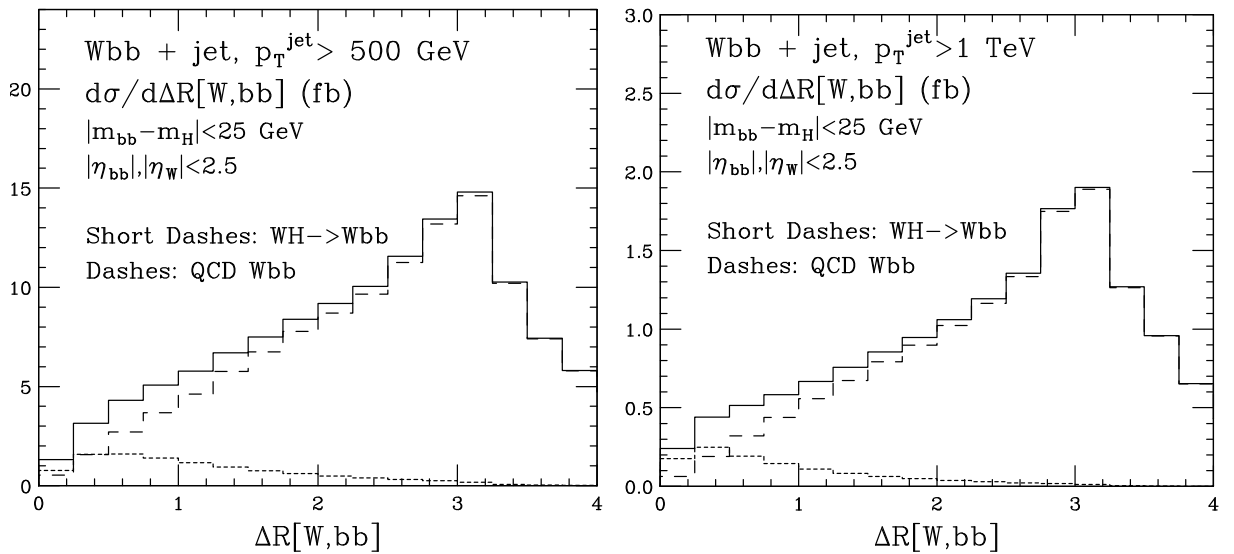


**Fig. 50:** Angular correlation between the  $W$  boson and the  $b\bar{b}$  pair for signal (short dashes) and QCD background (dashes) in final states with a jet of  $p_T > 500 \text{ GeV}$  (left) and  $1 \text{ TeV}$  (right). The solid curve denotes the sum of signal and QCD background. No  $W$  branching ratio is included.

This is shown very clearly in Fig. 50, which shows the  $\Delta R(WH)$  distribution for the background (dashed histograms) and for the Higgs signal (short-dashed histograms), for different thresholds on the jet  $p_T$ . A simple cut on  $\Delta R(WH) < 1$  leads to an order of magnitude reduction of the background,

while maintaining the largest fraction of the signal. This is shown in the second panel of Fig. 51, where the two dashed (continuous, red) lines give the background (signal) before and after the  $\Delta R$  cut. The cut brings the  $S/B$  ratio to the level of 1, with sufficient statistics to exceed the percent level precision in the signal extraction. Further background rejection can likely be obtained by cutting on the  $W$  boson transverse momentum, which is harder for the signal.

It is clear that more work is needed for a reliable assessment of the potential for interesting and precise measurements using the associated  $VH$  production channels. The application and extension of  $H \rightarrow b\bar{b}$  tagging and background rejection techniques will certainly also lead to valuable input to the detector design process, both in the calorimeter and tracker areas. There is also room for the use of final states other than  $b\bar{b}$ . We trust that these topics will be picked up for the studies towards the FCC-hh Conceptual Design Report.

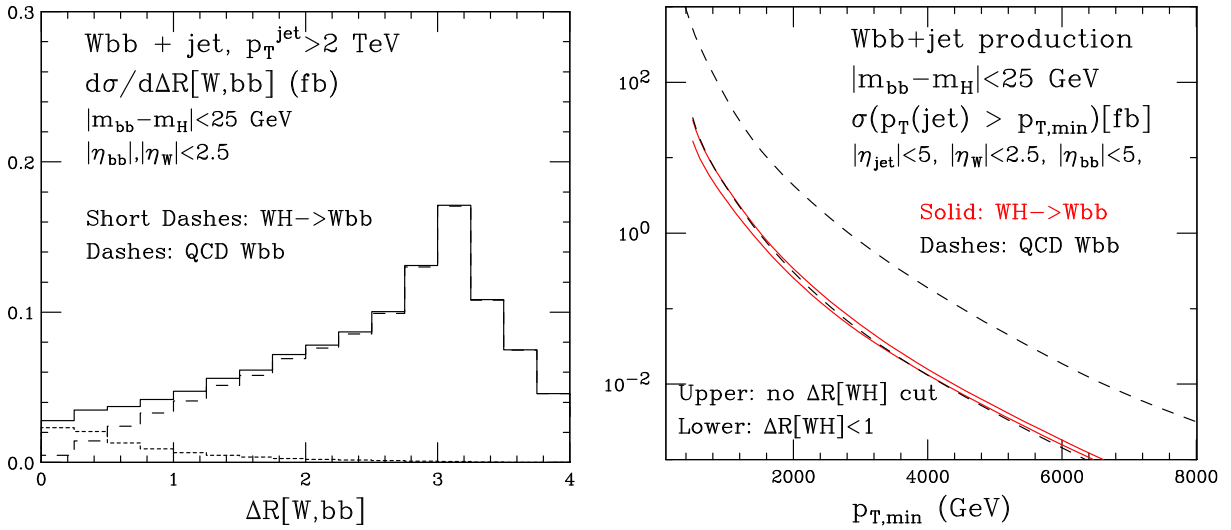


**Fig. 51:** Left panel: same as the previous Figure, with  $p_T > 2$  TeV. Right: Signal and background rates, as a function of the jet  $p_T$  threshold, before and after a  $\Delta R(WH) < 1$  cut. No  $W$  branching ratio included.

### 3.4 Measurement of top Yukawa coupling from the $t\bar{t}H/t\bar{t}Z$ ratio

The  $t\bar{t}H$  production process can be studied for a variety of Higgs decay channels. We collect in Table 22 the event rates for potentially interesting Higgs decays combined with  $t\bar{t}H$  production, for an integrated luminosity of  $20 \text{ ab}^{-1}$  at 100 TeV. These numbers include the branching ratio for the mixed lepton-hadron  $t\bar{t} \rightarrow \ell\nu_\ell + \text{jets}$  decay ( $\ell = e, \mu$ ), in addition to the relevant Higgs branching ratios.

Since analysis cuts and efficiencies will further reduce these rates, the otherwise very clean  $H \rightarrow 4\ell$  will hardly meet the target of the 1% precision. In the case of  $H \rightarrow \gamma\gamma$ , basic parton level cuts such as:

$$\begin{aligned} p_{T,\gamma,b,j} > 25 \text{ GeV} & \quad , & |\eta_{\gamma,b,j}| < 2.5 & \quad , & \Delta R_{jj,bb,bj} > 0.4 \\ p_{T,\ell} > 20 \text{ GeV} & \quad , & |\eta_\ell| < 2.5 & & \end{aligned} \quad (20)$$

leave around  $5 \cdot 10^4$  events with  $20 \text{ ab}^{-1}$ , while the  $t\bar{t}\gamma\gamma$  background, subject to a  $|m_{\gamma\gamma} - 125| < 5 \text{ GeV}$  cut, is almost a factor of 10 smaller. The  $H \rightarrow 2\ell 2\nu$  final state has also a potentially interesting rate, which will deserve a dedicated study.

The large rate for  $H \rightarrow b\bar{b}$  decays allows to consider boosted topologies, placing tight cuts on the emerging jets, and drastically reducing the various sources of backgrounds. Figure 33 shows, for example, that requesting  $p_{T,H} > 500 \text{ GeV}$  gives a rate of  $\mathcal{O}(1)$  pb, or 10M events with  $10 \text{ ab}^{-1}$ . This improved statistics also allows us to rely on a well-measured and similarly peaked  $t\bar{t}Z \rightarrow t\bar{t}b\bar{b}$  signal to reduce systematic and theoretical uncertainties, as anticipated in Section 2.6, and discussed in detail in Ref. [122]. We summarize here these findings, and update the results of that work to a broader range of Higgs  $p_T$ . We refer to Ref. [122] for the details.

The analysis models the first HEPTOPTAGGER application to  $t\bar{t}H$  production with  $H \rightarrow b\bar{b}$  [142], and builds on the recent improvements in the HEPTOPTAGGER2 [143] and in the BDRS Higgs tagger [140], which reduce background sculpting and increase the signal statistics.

We consider the final states:

$$pp \rightarrow t\bar{t}H \rightarrow (bjj) (\bar{b}\ell\bar{\nu}) (b\bar{b}), (b\ell\nu) (\bar{b}jj) (b\bar{b}) . \quad (21)$$

and the leading backgrounds:

- $pp \rightarrow t\bar{t}b\bar{b}$ , the main irreducible QCD background
- $pp \rightarrow t\bar{t}Z$ , including the  $Z$ -peak in the  $m_{bb}$  distribution
- $pp \rightarrow t\bar{t} + \text{jets}$  with fake-bottoms tags

The analysis requires:

1. an isolated lepton with  $|y_\ell| < 2.5$  and  $p_{T,\ell} > 15 \text{ GeV}$ .
2. a tagged top ( $R = 1.8$ ,  $p_{T,j} > 200 \text{ GeV}$ ,  $|y_j^{(t)}| < 4$ ) without any  $b$ -tag requirement
3. a tagged Higgs jet with two  $b$ -tags inside ( $R = 1.2$ ,  $p_{T,j} > 200 \text{ GeV}$ ,  $|y_j^{(H)}| < 2.5$ )
4. a  $b$ -tagged jet ( $R = 0.6$ ,  $p_{T,j} > 30 \text{ GeV}$ ,  $|y_b| < 2.5$ ) outside the top and Higgs fat jets, corresponding to the top decaying semileptonically.

$H \rightarrow 4\ell$	$H \rightarrow \gamma\gamma$	$H \rightarrow 2\ell 2\nu$	$H \rightarrow b\bar{b}$
$2.6 \cdot 10^4$	$4.6 \cdot 10^5$	$2.0 \cdot 10^6$	$1.2 \cdot 10^8$

**Table 22:**  $t\bar{t}H$  event rates for various Higgs decay modes, with  $20 \text{ ab}^{-1}$  at 100 TeV, assuming  $t\bar{t} \rightarrow \ell\nu + \text{jets}$ . Here and for Higgs decays,  $\ell$  can be either an electron or a muon.

The  $m_{bb}$  distribution provides the sidebands to control the  $t\bar{t}b\bar{b}$  and  $t\bar{t}$ +jets backgrounds, and a second mass peak from the  $t\bar{t}Z$  mass peak. All Monte Carlo event samples are generated at leading order, using MadGraph5 [144] with NNPDF2.3 parton densities [145], showering and hadronization via Pythia8 [146] and the fast detector simulation with Delphes3 [147, 148]. The jet clustering and the analysis are done with FastJet3 [84], a modified BDRS Higgs tagger [140, 142] and the HEPTOPTAGGER2 [143]. All  $b$ -tags require a parton-level  $b$ -quark within  $\Delta R < 0.3$  and assume a  $b$ -tagging efficiency of 50% and a mis-tagging probability of 1%.

Figure 52 shows the reconstructed  $m_{bb}$  spectrum for the signal and the backgrounds, varying the  $p_T$  threshold of the top and Higgs tagged fat jets in steps of 100 GeV from 200 up to 500 GeV.

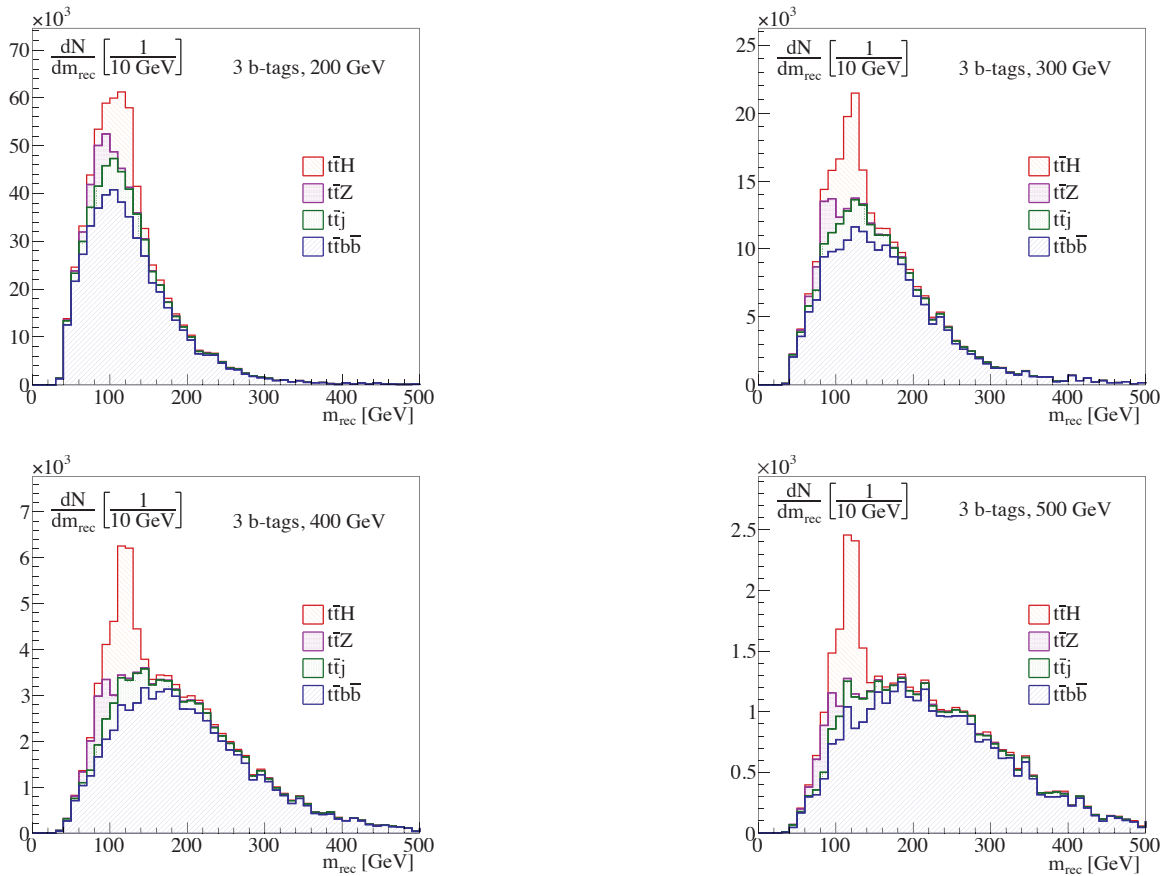


**Fig. 52:** Reconstructed  $m_{bb}$  for a  $p_T$  threshold from 200 GeV to 500 GeV (the roughness of the distributions is a consequence of limited MC statistics).

For the 200 GeV cut, and the signal region  $m_{bb} \in [104, 136]$  GeV, we arrive at a signal-to-background ratio around  $S/B \approx 1/3$  and a Gaussian significance  $S/\sqrt{B} = 120$ , assuming an integrated luminosity of  $\mathcal{L} = 20 \text{ ab}^{-1}$ . The error on the number of nominally  $N_S = 44700$  signal events is given by two terms. First, we assume that we can determine  $N_S$  from the total number of events  $N_S + N_B$  using a perfect determination of  $N_B$  from the side bands. Second, the side band  $m_{bb} \in [160, 296]$  GeV with altogether  $N_{\text{side}} = 135000$  events and a relative uncertainty of  $1/\sqrt{N_{\text{side}}}$  introduces a statistical uncertainty  $\Delta N_B$ , altogether leading to

$$\Delta N_S = \left[ \left( \sqrt{N_S + N_B} \right)^2 + (\Delta N_B)^2 \right]^{1/2}$$

$$= \left[ \left( \sqrt{N_S + N_B} \right)^2 + \left( \frac{N_B}{\sqrt{N_{\text{side}}}} \right)^2 \right]^{1/2} = 0.013 N_S . \quad (22)$$

For the Yukawa coupling this translates into a relative error of around 1%. The first term alone would give  $\Delta N_S = 0.010 N_S$ .

The analysis for larger  $p_T$  cuts leads to the numbers in the following table:

$p_{T,\text{min}}[\text{GeV}]$	$N_S$	$N_B$	$N_S + N_B$	$N_{\text{Sideband}}$	$\Delta N_S/N_S$	$N_S/N_B$	$N_S/\sqrt{N_B}$
250	29400	74700	104000	155000	0.013	0.39	107
300	18800	39000	57900	116000	0.014	0.48	95
350	13300	27500	40800	79800	0.017	0.48	80
400	8970	16700	25600	50300	0.020	0.54	69
450	5950	9810	15800	35100	0.023	0.61	60
500	3830	5730	9560	24400	0.027	0.67	51

For the signal region we count  $N_S$  in the region with  $N_S/N_B > 1/5$ , for the sideband region we require  $N_S/N_B < 1/10$ . The corresponding  $m_{bb}$  distribution is binned in steps of 10 GeV.  $N_B$  is the sum of all  $t\bar{t}b\bar{b}$ ,  $t\bar{t} + \text{jets}$  and  $t\bar{t}Z$  events combined. We notice that the precision on the number of extracted signal events,  $\Delta N_S/N_S$ , remains at the level of 1-2% over a broad range transverse momenta, providing an important validation of the robustness of the analysis.

More details, and the results of the combined Crystal Ball fit of the  $Z$  and  $H$  signals, are given in Ref. [122]. The continuum side band and the second peak offer two ways to control the backgrounds as well as the translation of the  $t\bar{t}b\bar{b}$  rate into a measurement of the Yukawa coupling. We therefore find that  $y_{\text{top}}$  could be measured to around 1% with a 100 TeV collider and an integrated luminosity of  $20 \text{ ab}^{-1}$ . This is an order of magnitude improvement over the expected LHC reach, with significantly improved control over the critical uncertainties.

There exist additional, complementary opportunities offered by the  $t\bar{t}H$  study. For example, the  $H \rightarrow \gamma\gamma$  decay could allow a direct measurement of the ratio of branching ratios  $B(H \rightarrow \gamma\gamma)/B(H \rightarrow b\bar{b})$ . It would serve as a complementary, although indirect, probe of the  $t\bar{t}H$  coupling. Furthermore,  $H \rightarrow 2\ell 2\nu$  could also be interesting, since there is enough rate to explore the regime  $p_{T,H} \gg m_H$ , which, especially for the  $e^\pm \mu^\mp \nu \bar{\nu}$  final state, could be particularly clean.

### 3.5 Combined determination of $y_t$ and $\Gamma(H)$ from $t\bar{t}H$ vs $t\bar{t}t\bar{t}$ production

Precise information of Higgs boson, e.g. its mass, width, spin, parity, and couplings, should shed light on new physics beyond the Standard Model. In this section we discuss the measurements of two important properties of the Higgs boson, the total width ( $\Gamma_H$ ) and its coupling to top-quark ( $y_{Ht\bar{t}}$ ), through the  $t\bar{t}H$  and  $t\bar{t}t\bar{t}$  productions at a 100 TeV  $pp$  collider. The top Yukawa-coupling can be measured in the  $t\bar{t}H$  production. An ultimate precision of about 1% is expected at a 100 TeV  $pp$  collider in the channel of  $pp \rightarrow t\bar{t}H \rightarrow t\bar{t}b\bar{b}$  with an integrated luminosity ( $\mathcal{L}$ ) of  $20 \text{ ab}^{-1}$ , assuming the  $H \rightarrow b\bar{b}$  branching ratio is the same as in the SM. However, this assumption may not be valid in NP models; for example,  $\Gamma_H$  might differ from the SM value ( $\Gamma_H^{\text{SM}}$ ) in the case that the Higgs boson decays into a pair of invisible particles. It is important to find a new experimental input to relax the assumption. Four top-quark ( $t\bar{t}t\bar{t}$ ) production provides a powerful tool to probe the top-quark Yukawa coupling, and in addition, combining the  $t\bar{t}H$  and  $t\bar{t}t\bar{t}$  productions also determines  $\Gamma_H$  precisely [149].

Under the narrow width approximation, the production cross section of  $pp \rightarrow t\bar{t}H \rightarrow t\bar{t}b\bar{b}$  is

$$\begin{aligned} \sigma(pp \rightarrow t\bar{t}H \rightarrow t\bar{t}b\bar{b}) &= \sigma^{\text{SM}}(pp \rightarrow t\bar{t}H \rightarrow t\bar{t}b\bar{b}) \times \kappa_t^2 \kappa_b^2 \frac{\Gamma_H^{\text{SM}}}{\Gamma_H} \\ &\equiv \sigma^{\text{SM}}(pp \rightarrow t\bar{t}H \rightarrow t\bar{t}b\bar{b}) \times \mu_{t\bar{t}H}^{b\bar{b}}, \end{aligned} \quad (23)$$

where  $\kappa_t \equiv y_{Htt}/y_{Htt}^{\text{SM}}$  and  $\kappa_b \equiv y_{Hbb}/y_{Hbb}^{\text{SM}}$  are the Higgs coupling scaling factors. The signal strength  $\mu_{t\bar{t}H}^{bb}$ , defined as

$$\mu_{t\bar{t}H}^{bb} = \frac{\kappa_t^2 \kappa_b^2}{R_\Gamma} \quad \text{with} \quad R_\Gamma \equiv \frac{\Gamma_H}{\Gamma_H^{\text{SM}}}, \quad (24)$$

is expected to be measured with 1% precision,  $\mu_{t\bar{t}H}^{bb} = 1.00 \pm 0.01$  [122]. Since the  $\kappa_t$ ,  $\kappa_b$  and  $\Gamma_H$  parameters are independent in  $\mu_{t\bar{t}H}^{bb}$ , one cannot determine them from the  $t\bar{t}H$  production alone. Bounds on the  $\kappa_t$ ,  $\kappa_b$  and  $R_\Gamma$  can be derived from a global analysis of various Higgs production channels. The bottom Yukawa coupling would be measured precisely at electron-positron colliders. Once  $\kappa_b$  is known, a correlation between  $\kappa_t$  and  $R_\Gamma$  is obtained as following

$$\frac{\kappa_t^2}{R_\Gamma} = \mu_{t\bar{t}H}. \quad (25)$$

If the top-quark Yukawa coupling could be directly measured in a single channel, then one can probe  $R_\Gamma$  from Eq. 25.

In the SM the  $t\bar{t}\bar{t}\bar{t}$  production occurs either through a gluon mediator [150] or by an off-shell Higgs mediator; see Fig. 53 for the representative Feynman diagrams. Interferences between the QCD diagrams ( $t\bar{t}\bar{t}\bar{t}_g$ ) and the Higgs diagrams ( $t\bar{t}\bar{t}\bar{t}_H$ ) are absent at the tree level. We thus name the cross section of the QCD induced channel as  $\sigma(t\bar{t}\bar{t}\bar{t})_g$  and the cross section of the Higgs induced channel as  $\sigma(t\bar{t}\bar{t}\bar{t})_H$ . There are two advantages of the Higgs-induced  $t\bar{t}\bar{t}\bar{t}$  production: i) no dependence on the Higgs boson width; ii) the cross section proportional to the top quark Yukawa coupling to the fourth power, i.e.

$$\sigma(t\bar{t}\bar{t}\bar{t})_H \propto \kappa_t^4 \sigma^{\text{SM}}(t\bar{t}\bar{t}\bar{t})_H, \quad (26)$$

where  $\sigma^{\text{SM}}(t\bar{t}\bar{t}\bar{t})_H$  denotes the SM production cross section. The not-so-small interferences among the three kinds of Feynman diagrams are also accounted. Since the QCD and electroweak gauge interactions of top quarks have been well established, we consider only the top Yukawa coupling might differ from the SM value throughout this section. As a result, the cross section of  $t\bar{t}\bar{t}\bar{t}$  production is

$$\sigma(t\bar{t}\bar{t}\bar{t}) = \sigma^{\text{SM}}(t\bar{t}\bar{t}\bar{t})_{g+Z/\gamma} + \kappa_t^2 \sigma^{\text{SM}}(t\bar{t}\bar{t}\bar{t})_{\text{int}} + \kappa_t^4 \sigma^{\text{SM}}(t\bar{t}\bar{t}\bar{t})_H, \quad (27)$$

where

$$\begin{aligned} \sigma^{\text{SM}}(t\bar{t}\bar{t}\bar{t})_{g+Z/\gamma} &\propto |\mathcal{M}_g + \mathcal{M}_{Z/\gamma}|^2, \\ \sigma^{\text{SM}}(t\bar{t}\bar{t}\bar{t})_H &\propto |\mathcal{M}_H|^2, \\ \sigma^{\text{SM}}(t\bar{t}\bar{t}\bar{t})_{\text{int}} &\propto \mathcal{M}_{g+Z/\gamma} \mathcal{M}_H^\dagger + \mathcal{M}_{g+Z/\gamma}^\dagger \mathcal{M}_H. \end{aligned} \quad (28)$$

We use MadEvent [151] to calculate the leading order cross section of  $t\bar{t}\bar{t}\bar{t}$  production in the SM. The numerical results are summarized as follows:

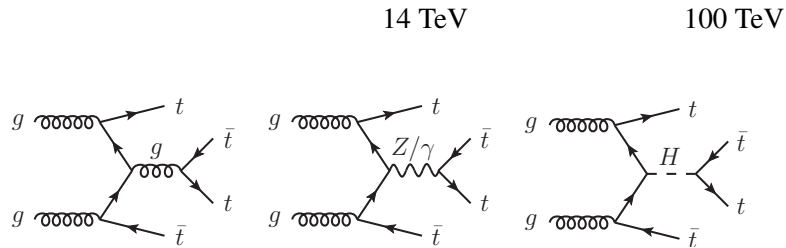


**Fig. 53:** Representative Feynman diagrams of the  $t\bar{t}\bar{t}\bar{t}$  production through the QCD interaction and the Higgs boson mediation.

$$\begin{aligned}
 \sigma^{\text{SM}}(t\bar{t}\bar{t})_{g+Z/\gamma} &: & 12.390 \text{ fb}, & & 3276 \text{ fb}, \\
 \sigma^{\text{SM}}(t\bar{t}\bar{t})_H &: & 1.477 \text{ fb}, & & 271.3 \text{ fb}, \\
 \sigma^{\text{SM}}(t\bar{t}\bar{t})_{\text{int}} &: & -2.060 \text{ fb}, & & -356.9 \text{ fb}.
 \end{aligned} \tag{29}$$

The numerical results shown above are checked with CalcHEP [152]. The NLO QCD corrections to the  $t\bar{t}\bar{t}_g$  background is calculated in Ref. [153], which is about 4934 fb with 25% uncertainty. Unfortunately, as the QCD corrections to the interference and electroweak contributions is not available yet, a tree-level simulation of the signal process is used to estimate the accuracy of Higgs width measurement.

A special signature of the four top-quark events is the same-sign charged leptons (SSL) from the two same-sign top quarks. The ATLAS and CMS collaborations have extensively studied the same sign lepton pair signal at the LHC [154, 155]. The other two top quarks are demanded to decay hadronically in order to maximize the production rate. Therefore, the topology of the signal event consists of two same-sign charged leptons, four  $b$ -quarks, four light-flavor quarks, and two invisible neutrinos. In practice it is challenging to identify four  $b$ -jets. Instead, we demand at least 5 jets are tagged and three of them are identified as  $b$ -jets. The two invisible neutrinos appear as a missing transverse momentum ( $\cancel{E}_T$ ) in the detector. Thus, the collider signature of interests to us is two same-sign leptons, at least five jets and three of them tagged as  $b$ -jets, and a large  $\cancel{E}_T$ .

The SM backgrounds for same-sign leptons can be divided into three categories: i) prompt same-sign lepton pair from SM rare process, including di-boson and  $W^\pm W^\pm jj$ ; ii) fake lepton, which comes from heavy quark jet, namely  $b$ -decays, and the dominant one is the  $t\bar{t} + X$  events [156]; iii) charge misidentification. As pointed out by the CMS collaboration [155], the background from charge misidentification is generally much smaller and stays below the few-percent level. We thus ignore this type of backgrounds in our simulation and focus on those non-prompt backgrounds  $t\bar{t} + X$  and rare SM processes contributions. For four top quark production process another feature worthy being specified is that multiple  $b$ -jets decay from top quark appear in the final state. Same-sign lepton plus multiple  $b$ -jets has a significant discrimination with the backgrounds. From above analysis, it is clear that the major backgrounds are  $t\bar{t} + X$  and  $W^\pm W^\pm jj$ . Another SM processes can contribute the same-sign lepton are di-boson, while it can be highly suppressed by the request of multiple jets in the final state. Therefore we focus on the  $t\bar{t} + X$ ,  $W^\pm W^\pm jj$  and  $t\bar{t}\bar{t}(g)$  backgrounds below. The cross section of the  $t\bar{t}$  production is calculated with the next-to-leading-order(NLO) QCD correction using MCFM package [53]. The NLO QCD corrections to the  $t\bar{t}Z$  and  $t\bar{t}W$  background are taken into account by multiplying the leading order cross sections with a constant  $K$ -factor; for example,  $K_F = 1.17$  for the  $t\bar{t}Z$  and  $K_F = 2.20$  for the  $t\bar{t}W$  production [141].

Both the signal and background events are generated at the parton level using MadEvent [151] at the 100 TeV proton-proton collider. We use Pythia [146] to generate parton showering and hadronization effects. The Delphes package [147] is used to simulate detector smearing effects in accord to a fairly standard Gaussian-type detector resolution given by  $\delta E/E = \mathcal{A}/\sqrt{E/\text{GeV}} \oplus \mathcal{B}$ , where  $\mathcal{A}$  is a sampling term and  $\mathcal{B}$  is a constant term. For leptons we take  $\mathcal{A} = 5\%$  and  $\mathcal{B} = 0.55\%$ , and for jets we take  $\mathcal{A} = 100\%$  and  $\mathcal{B} = 5\%$ . We require the charged lepton has a transverse momentum  $p_T^\ell$  greater than 20 GeV, rapidity  $|\eta_\ell| \leq 2.5$  and its overlap with jets  $\Delta R_{j\ell} = \sqrt{(\Delta\eta)^2 + (\Delta\phi)^2} \geq 0.4$ . The  $\cancel{E}_T$  is then defined to balance the total transverse momentum of visible objects.

Figure 54 displays the numbers of reconstructed jets (a) and  $b$ -tagged jets (b) in the signal and background processes. It is clear that the signal event exhibits often five or more jets. Demanding at least three identified  $b$ -jets would efficiently reject those SM backgrounds. In the simulation we impose a set of kinematics cuts as follows:

$$\begin{aligned}
 p_T^{j,\ell} &\geq 20 \text{ GeV}, & |\eta^{j,\ell}| &< 2.5, & \cancel{E}_T &\geq 150 \text{ GeV}, \\
 N_{\ell^\pm} &= 2, & N_{\text{jets}} &\geq 6, & N_{b\text{-jets}} &\geq 3, \\
 m_T &\geq 100 \text{ GeV}, & H_T &\geq 800 \text{ GeV}.
 \end{aligned} \tag{30}$$

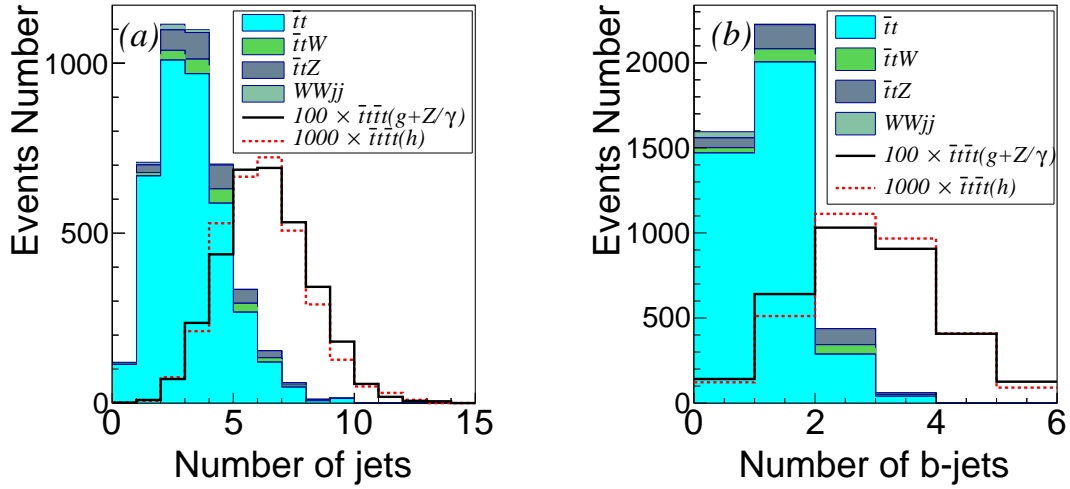


**Fig. 54:** The numbers of the reconstructed jets (a) and  $b$ -tagged jets (b) in the signal and background events at the 100 TeV collider with an integrated luminosity of  $1 \text{ fb}^{-1}$ . To better character the signal distribution the cross section has been rescaled to 1000 times. No cuts except for same-sign lepton pair have been applied.

**Table 23:** Number of the signal and background events at the 100 TeV  $pp$  collider with an integrated luminosity of  $1 \text{ ab}^{-1}$ . The kinematics cuts listed in each row are applied sequentially.

	Basic	SSL	Jets	$\cancel{E}_T$	$m_T$	$H_T$
$t\bar{t}t\bar{t}_H$	271300	3227.1	1010.6	412.4	242.8	222.5
$t\bar{t}t\bar{t}_{g+Z/\gamma}$	3276000	32366.9	11056.5	4193.3	2620.8	2407.9
$t\bar{t}t\bar{t}_{\text{int}}$	-356900	-4040.1	-1275.9	-467.5	-273.0	-253.4
$t\bar{t}$	$3.22 \times 10^{10}$	3802170	33411	0	0	0
$t\bar{t}W^+$	2596250	91917.4	1222.2	509.2	356.5	356.5
$t\bar{t}W^-$	1810460	81234.8	1585.5	629.4	399.4	387.3
$t\bar{t}Z$	4311270	306908	3995.6	1109.9	665.9	621.5
$W^\pm W^\pm jj$	275500	39097.4	2.188	0	0	0

Here  $m_T$  denotes the transverse mass of the leading charged lepton ( $\ell_1$ ) and the  $\cancel{E}_T$ , defined as

$$m_T = \sqrt{2p_T^{\ell_1} \cancel{E}_T (1 - \cos \Delta\phi)}, \quad (31)$$

where  $\Delta\phi$  is the azimuthal angle between the  $\ell_1$  lepton and the  $\cancel{E}_T$ . The  $m_T$  cut is to remove those backgrounds involving leptonically decayed  $W$  bosons. The  $H_T$  is the the scalar sum of the transverse momenta of all the visible particles and the missing energy  $\cancel{E}_T$ .

Table 23 shows the numbers of the signal and the background events after a series of kinematics cuts at the 100 TeV proton-proton collider with an integrated luminosity of  $1 \text{ ab}^{-1}$ . The  $t\bar{t}t\bar{t}$  production through the QCD interaction and the production through the Higgs boson mediator share similar kinematics, therefore, both the QCD and Higgs mediated productions exhibit similar efficiencies for each cut shown in Table 23; see the second and third columns. It might be possible to distinguish the two contributions using the so-called color pull technique [157]. The major backgrounds in the SM are from the  $t\bar{t}W^\pm$  and  $t\bar{t}Z$  productions.

After applying the cuts given in Eq. 30, the  $t\bar{t}t\bar{t}$  production from the QCD and electroweak gauge interactions dominates over the SM backgrounds; see Table. 23. The  $t\bar{t}t\bar{t}$  production in the SM can be

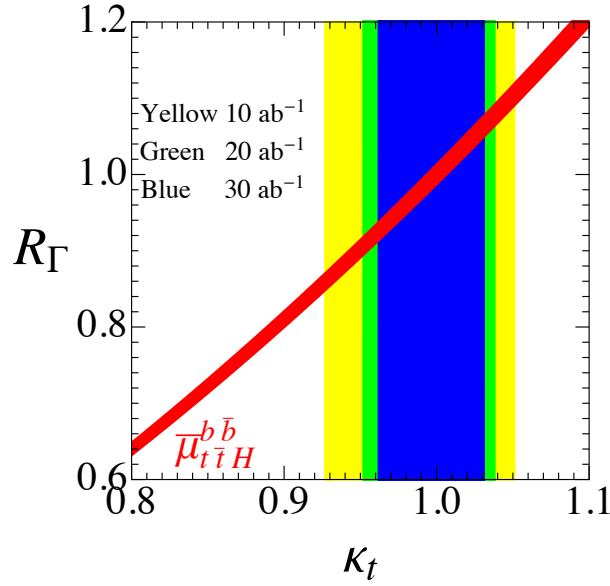


**Fig. 55:** Relative uncertainty on the signal strength  $\mu_{t\bar{t}H}$  projected in the plane  $\kappa_t$  and  $R_\Gamma$  at a 100 TeV hadron collider with  $20 \text{ ab}^{-1}$  for the Higgs decay modes  $H \rightarrow b\bar{b}$  (red band). The yellow (green, blue) vertical band denotes the limit  $0.927 \leq \kappa_t \leq 1.051$  ( $0.952 \leq \kappa_t \leq 1.038$ ,  $0.962 \leq \kappa_t \leq 1.031$ ) corresponding to the  $1\sigma$  signal uncertainty with the integrated luminosity of  $10 \text{ ab}^{-1}$  ( $20 \text{ ab}^{-1}$ ,  $30 \text{ ab}^{-1}$ ).

measured at a  $5\sigma$  confidence level with an integrated luminosity of  $8.95 \text{ fb}^{-1}$ . We thus expect the  $t\bar{t}t\bar{t}$  production to be discovered soon after the operation of the 100 TeV machine. The great potential enables us to discuss the precision of measuring the top Yukawa coupling in the  $t\bar{t}t\bar{t}$  production. We estimate the signal statistical fluctuation as

$$\Delta N_S = \sqrt{N_S + N_B}, \quad (32)$$

assuming that the events number satisfies the Gaussian distribution. The signal uncertainty is  $\Delta N_S = 0.0095 N_S$  for  $\mathcal{L} = 10 \text{ ab}^{-1}$ ,  $\Delta N_S = 0.0067 N_S$  for  $\mathcal{L} = 20 \text{ ab}^{-1}$ , and  $\Delta N_S = 0.0055 N_S$  for  $\mathcal{L} = 30 \text{ ab}^{-1}$ , respectively. We interpret the uncertainty of the signal event as the uncertainty of the top Yukawa coupling, i.e.

$$\Delta N_S = \delta\kappa_t \left[ 2\sigma^{\text{SM}}(t\bar{t}t\bar{t})_{\text{int}} + 4\sigma^{\text{SM}}(t\bar{t}t\bar{t})_H \right] \times \mathcal{L} + \mathcal{O}(\delta\kappa_t^2), \quad (33)$$

where  $\delta\kappa_t \equiv \kappa_t - 1$  and the SM cross sections refer to the values after all the cuts shown in the last column in Table 23. It yields a precision of  $\kappa_t$  measurement as follows:  $0.927 \leq \kappa_t \leq 1.051$  for  $\mathcal{L} = 10 \text{ ab}^{-1}$ ,  $0.952 \leq \kappa_t \leq 1.038$  for  $\mathcal{L} = 20 \text{ ab}^{-1}$ , and  $0.962 \leq \kappa_t \leq 1.031$  for  $\mathcal{L} = 30 \text{ ab}^{-1}$ , respectively.

Figure 55 displays the correlation between  $R_\Gamma$  and  $\kappa_t$  imposed by the projected  $\overline{\mu}_{t\bar{t}H}^{b\bar{b}}$  measurement [122]; see the red band. The expectations of the  $\kappa_t$  measurement in the  $t\bar{t}t\bar{t}$  production are also plotted where the yellow (green, blue) contour region denotes the uncertainty of  $\kappa_t$  with  $\mathcal{L} = 10 \text{ ab}^{-1}$  ( $20 \text{ ab}^{-1}$ ,  $30 \text{ ab}^{-1}$ ), respectively. Combining both the  $t\bar{t}H$  and  $t\bar{t}t\bar{t}$  productions imposes a tight bound on the Higgs boson width; for example,  $0.85 \Gamma_H^{\text{SM}} \leq \Gamma_H \leq 1.12 \Gamma_H^{\text{SM}}$  for  $\mathcal{L} = 10 \text{ ab}^{-1}$ ,  $0.89 \Gamma_H^{\text{SM}} \leq \Gamma_H \leq 1.09 \Gamma_H^{\text{SM}}$  for  $\mathcal{L} = 20 \text{ ab}^{-1}$ , and  $0.91 \Gamma_H^{\text{SM}} \leq \Gamma_H \leq 1.08 \Gamma_H^{\text{SM}}$  for  $\mathcal{L} = 30 \text{ ab}^{-1}$ , respectively.

### 3.6 Rare SM Exclusive Higgs decays

The measurement of the rare exclusive decays  $H \rightarrow V\gamma$ , where  $V$  denotes a vector meson, would allow a unique probe of the Higgs coupling to light quarks. While the absolute value of the bottom-quark

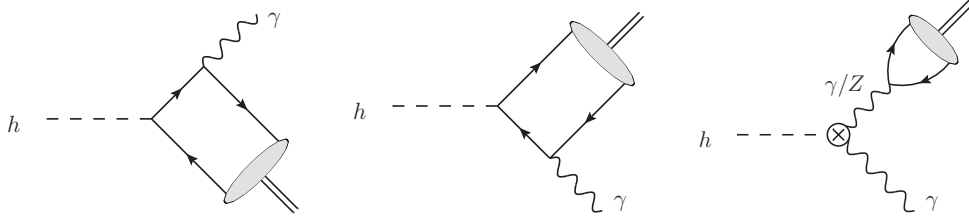


**Fig. 56:** Direct (left and center) and indirect (right) contributions to the  $H \rightarrow V\gamma$  decay amplitude. The blob represents the non-perturbative meson wave function. The crossed circle in the third diagram denotes the off-shell  $H \rightarrow \gamma\gamma^*$  and  $H \rightarrow \gamma Z^*$  amplitudes, which in the SM arise first at one-loop order.

Yukawa coupling can be accessed by measuring  $b$ -tagged jets in the associated production of the Higgs boson with a  $W$  or  $Z$  boson, this method becomes progressively more difficult for the lighter-quark couplings. Advanced charm-tagging techniques may allow some access to the charm-quark Yukawa coupling [158], but no other way of directly measuring even lighter-quark couplings is currently known. The small branching ratios for these exclusive decays renders them inaccessible at future  $e^+e^-$  colliders. The program of measuring these decay modes is therefore unique to hadron-collider facilities. The large Higgs boson production rate at a proposed 100 TeV collider makes this facility an ideal place to measure these otherwise inaccessible quantities.

The possibility of measuring rare exclusive Higgs decays was first pointed out in [159, 160], and the theoretical framework for their prediction was further developed in [161–163]. Our discussion follows closely the techniques introduced in these works, and we only summarize the salient features here. We begin our discussion of the theoretical predictions for these modes by introducing the effective Yukawa Lagrangian

$$\mathcal{L} = - \sum_q \kappa_q \frac{m_q}{v} H \bar{q}_L q_R - \sum_{q \neq q'} \frac{y_{qq'}}{\sqrt{2}} H \bar{q}_L q'_R + h.c., \quad (34)$$

where in the SM  $\kappa_q = 1$  while the flavor-changing Yukawa couplings  $y_{qq'}$  vanish. The effective Lagrangian leads to two categories of exclusive Higgs decays: flavor-conserving decays involving the  $\kappa_q$  couplings, where  $V = \rho, \omega, \phi, J/\psi, \Upsilon(nS)$ , and flavor-violating decays involving the  $y_{qq'}$  couplings, where  $V = B_s^{*0}, B_d^{*0}, K^{*0}, D^{*0}$ . In view of the very strong indirect bounds on flavor off-diagonal Higgs couplings to light quarks [164], the flavor-violating decays  $H \rightarrow V\gamma$  are bound to be very strongly suppressed. We will therefore restrict our discussion here to flavor-conserving processes.

The exclusive decays  $H \rightarrow V\gamma$  are mediated by two distinct mechanisms, which interfere destructively.

- In the *indirect process*, the Higgs boson decays (primarily through loops involving heavy top quarks or weak gauge bosons) to a real photon  $\gamma$  and a virtual  $\gamma^*$  or  $Z^*$  boson, which then converts into the vector meson  $V$ . This contribution only occurs for the flavor-conserving decay modes. The effect of the off-shellness of the photon and the contribution involving the  $H\gamma Z^*$  coupling are suppressed by  $m_V^2/M_H^2$  and hence are very small [163].
- In the *direct process*, the Higgs boson decays into a pair of a quark and an antiquark, one of which radiates off a photon. This mechanism introduces the dependence of the decay amplitude on the  $\kappa_q$  parameters. The formation of the vector meson out of the quark-antiquark pair involves some non-trivial hadronic dynamics.

The relevant lowest-order Feynman diagrams contributing to the direct and indirect processes are shown in Figure 56.

We begin by outlining the calculation of the indirect amplitude. The virtual photon of  $Z$  boson couples to the vector meson through the matrix element of a local current, which can be parameterized in terms of a single hadronic parameter: the vector-meson decay constant  $f_V$ . This quantity can be obtained directly from experimental data. In particular, the leptonic decay rate of the vector meson can be written as

$$\Gamma(V \rightarrow l^+ l^-) = \frac{4\pi Q_V^2 f_V^2}{3m_V} \alpha^2(m_V), \quad (35)$$

where  $Q_V$  is the relevant combination of quark electric charges. The effective couplings  $H\gamma\gamma^*$  and  $H\gamma Z^*$  vertices, which appear in the indirect amplitude, can be calculated with high accuracy in the SM. The by far dominant contributions involve loop diagrams containing heavy top quarks or  $W$  bosons. The two-loop electroweak and QCD corrections to this amplitude are known, and when combined shift the leading one-loop expression by less than 1% for the measured value of the Higgs boson mass [165]. However, physics beyond the SM could affect these couplings in a non-trivial way, either through modifications of the  $Ht\bar{t}$  and  $HW^+W^-$  couplings or by means of loops containing new heavy particles. The measurement of the light-quark couplings to the Higgs should therefore be considered together with the extraction of the effective  $H\gamma\gamma$  coupling. As pointed out in [163], by taking the ratio of the  $H \rightarrow V\gamma$  and  $H \rightarrow \gamma\gamma$  branching fractions one can remove this sensitivity to unknown new contributions to the  $H\gamma\gamma$  coupling.

We now consider the theoretical prediction for the direct amplitude. This quantity cannot be directly related to data, unlike the indirect amplitude. Two theoretical approaches have been used to calculate this contribution. The hierarchy  $M_H \gg m_V$  implies that the vector meson is emitted at very high energy  $E_V \gg m_V$  in the Higgs-boson rest frame. The partons making up the vector meson can thus be described by energetic particles moving collinear to the direction of  $V$ . This kinematic hierarchy allows the QCD factorization approach [166, 167] to be utilized. Up to corrections of order  $(\Lambda_{\text{QCD}}/M_H)^2$  for light mesons, and of order  $(m_V/M_H)^2$  for heavy vector mesons, this method can be used to express the direct contribution to the  $H \rightarrow V\gamma$  decay amplitude as a perturbatively calculable hard-scattering coefficient convoluted with the leading-twist light-cone distribution amplitude (LCDA) of the vector meson. This approach was pursued in [163], where the full next-to-leading order (NLO) QCD corrections were calculated and large logarithms of the form  $[\alpha_s \ln(M_H/m_V)]^n$  were resummed at NLO, and in [160], where an initial LO analysis was performed. The dominant theoretical uncertainties remaining after this calculation are parametric uncertainties associated with the non-perturbative LCDAs of the vector mesons. Thanks to the high value  $\mu \sim M_H$  of the factorization scale, however, the LCDAs are close to the asymptotic form  $\phi_V(x, \mu) = 6x(1-x)$  attained for  $\mu \rightarrow \infty$ , and hence the sensitivity to yet not well known hadronic parameters turns out to be mild. For the heavy vector mesons  $V = J/\psi, \Upsilon(nS)$ , the quark and antiquark which form the meson are slow-moving in the  $V$  rest frame. This allows the non-relativistic QCD framework (NRQCD) [168] to be employed to facilitate the calculation of the direct amplitude. This approach was pursued in [161], where the NLO corrections in the velocity  $v$  of the quarks in the  $V$  rest frame, the next-to-leading order corrections in  $\alpha_s$ , and the leading-logarithmic resummation of collinear logarithms were incorporated into the theoretical predictions. The dominant theoretical uncertainties affecting the results for  $H \rightarrow J/\psi\gamma$  and  $H \rightarrow \Upsilon(nS)\gamma$  after the inclusion of these corrections are the uncalculated  $\mathcal{O}(v^4)$  and  $\mathcal{O}(\alpha_s v^2)$  terms in the NRQCD expansion.

Table 24 collects theoretical predictions for the various  $H \rightarrow V\gamma$  branching fractions in the SM. The inclusion of NLO QCD corrections and resummation help to reduce the theoretical uncertainties. There is in general good agreement between the results obtained by different groups. The  $H \rightarrow \phi\gamma$  branching ratio obtained in [163] is lower than that found in [160] because of an update of the  $\phi$ -meson decay constant performed in the former work. Also, in [163] the effects of  $\rho$ - $\omega$ - $\phi$  mixing are taken into account. One observes that the  $H \rightarrow V\gamma$  branching fractions are typically of order few times  $10^{-6}$ , which makes them very challenging to observe. The most striking feature of the results shown in the table concerns the  $H \rightarrow \Upsilon(nS)\gamma$  modes, whose branching fractions are very strongly suppressed. This suppression results from an accidental and almost perfect cancellation between the direct and indirect

Mode Method	Branching Fraction [ $10^{-6}$ ]		
	NRQCD [161]	LCDA LO [160]	LCDA NLO [163]
$\text{Br}(H \rightarrow \rho^0 \gamma)$	–	$19.0 \pm 1.5$	$16.8 \pm 0.8$
$\text{Br}(H \rightarrow \omega \gamma)$	–	$1.60 \pm 0.17$	$1.48 \pm 0.08$
$\text{Br}(H \rightarrow \phi \gamma)$	–	$3.00 \pm 0.13$	$2.31 \pm 0.11$
$\text{Br}(H \rightarrow J/\psi \gamma)$	$2.79^{+0.16}_{-0.15}$	–	$2.95 \pm 0.17$
$\text{Br}(H \rightarrow \Upsilon(1S) \gamma)$	$(0.61^{+1.74}_{-0.61}) \cdot 10^{-3}$	–	$(4.61^{+1.76}_{-1.23}) \cdot 10^{-3}$
$\text{Br}(H \rightarrow \Upsilon(2S) \gamma)$	$(2.02^{+1.86}_{-1.28}) \cdot 10^{-3}$	–	$(2.34^{+0.76}_{-1.00}) \cdot 10^{-3}$
$\text{Br}(H \rightarrow \Upsilon(3S) \gamma)$	$(2.44^{+1.75}_{-1.30}) \cdot 10^{-3}$	–	$(2.13^{+0.76}_{-1.13}) \cdot 10^{-3}$

**Table 24:** Theoretical predictions for the  $H \rightarrow V\gamma$  branching ratios in the SM, obtained using different theoretical approaches.

amplitudes, as first pointed out in [159]. In the case of  $H \rightarrow \Upsilon(1S)\gamma$  the cancellation is so perfect that the small imaginary part of the direct contribution induced by one-loop QCD corrections gives the leading contribution to the decay amplitude. The fact that this imaginary part was neglected in [161] explains why a too small branching fraction for this mode was obtained there.

### 3.6.1 Experimental prospects

The considered rare exclusive Higgs boson decays to a quarkonium and a photon, are – currently – the only available means to probe the quark Yukawa coupling in the first and second generation. The only exception being, as pointed out earlier, the possibility to implement advanced charm-tagging techniques, specifically to probe the charm-quark Yukawa coupling. As a result, these Higgs boson decays are particularly interesting from an experimental perspective, both as signatures unique to the hadron collider programme and as experimental topologies. Furthermore, similar rare and exclusive decays of the  $W^\pm$  and  $Z$  bosons have also attracted interest [162, 169, 170], offering a physics programme in precision quantum chromodynamics (QCD), electroweak physics, and physics beyond the SM.

Using  $20.3 \text{ fb}^{-1}$  of 8 TeV proton-proton collision data, the ATLAS Collaboration has performed a search for Higgs and  $Z$  boson decays to  $J/\psi \gamma$  and  $\Upsilon(nS) \gamma$  ( $n = 1, 2, 3$ ) [171]. No significant excess has been observed and 95% confidence level upper limits were placed on the respective branching ratios. In the  $J/\psi \gamma$  final state the limits are  $1.5 \times 10^{-3}$  and  $2.6 \times 10^{-6}$  for the Higgs and  $Z$  boson decays, respectively, while in the  $\Upsilon(1S, 2S, 3S) \gamma$  final states the limits are  $(1.3, 1.9, 1.3) \times 10^{-3}$  and  $(3.4, 6.5, 5.4) \times 10^{-6}$ , respectively. The CMS Collaboration has placed a 95% C.L. upper limit of  $1.5 \times 10^{-3}$  on the  $h \rightarrow J/\psi \gamma$  branching ratio [172]. In all cases, the SM production rate for the observed Higgs boson is assumed. Currently, no other direct experimental constraint on these decays is available.

The scope of these early experimental investigations is two-fold: On one hand to provide the first direct experimental constraints on these quantities, and on the other hand to map the experimental challenges involved in such searches. Looking to the future, the ATLAS Collaboration estimated the expected sensitivity for Higgs and  $Z$  boson decays to a  $J/\psi$  and a photon, assuming up to  $3000 \text{ fb}^{-1}$  of data collected with the ATLAS detector at the centre-of-mass energy of 14 TeV, during the operation of the High Luminosity LHC (HL-LHC). The expected sensitivity for the  $h \rightarrow J/\psi \gamma$  branching ratio, assuming 300 and  $3000 \text{ fb}^{-1}$  at 14 TeV, is  $153 \times 10^{-6}$  and  $44 \times 10^{-6}$ , respectively [173]. The corresponding sensitivities for the  $Z \rightarrow J/\psi \gamma$  branching ratios are  $7 \times 10^{-7}$  and  $4.4 \times 10^{-7}$ , respectively [173]. In this analysis, the same overall detector performance as in LHC Run 1 is assumed, while an analysis optimisation has been performed and a multivariate discriminant using the same kinematic information as the published analysis [171] has been introduced. The main limiting factor in reaching SM sensitivity was identified to be the number of expected signal events, where only about 3 events were expected following

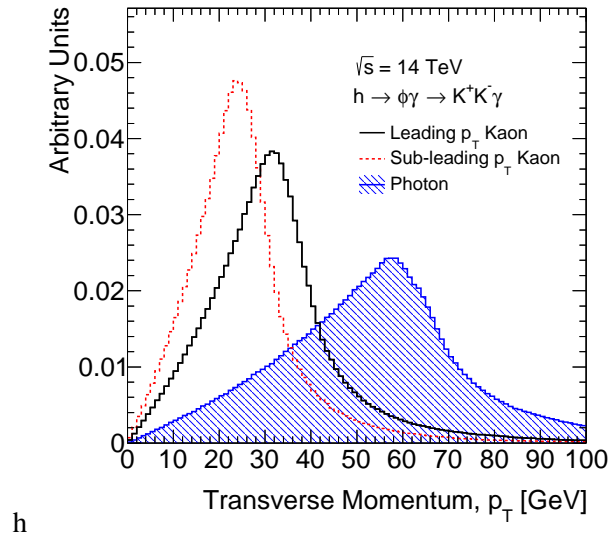


**Fig. 57:** Transverse momentum distribution of decay products in  $h \rightarrow \phi\gamma \rightarrow K^+K^-\gamma$  decays [174].

the complete event selection for the complete HL-LHC. Moreover, as the search sensitivity approaches the SM expectation for the  $h \rightarrow J/\psi\gamma$  branching ratio, the contribution from  $h \rightarrow \mu\mu\gamma$  decays, with a non-resonant dimuon pair, needs to be included. These can be separated efficiently from the  $h \rightarrow J/\psi\gamma$  signal, using dimuon mass information.

Moving to the lighter quarks, the Higgs boson coupling to the strange-quark can be probed through the  $h \rightarrow \phi\gamma$  decay. The subsequent  $\phi \rightarrow K^+K^-$  decay features a large branching ratio of about 49% and gives access to a simple final state of a hard photon recoiling against two collimated high transverse momentum tracks, as can be seen in Fig. 57. With the SM branching ratio prediction presented in Table 24, about 6.5 events are expected to be produced with  $100 \text{ fb}^{-1}$  at 14 TeV. For the first generation quarks, the  $h \rightarrow \omega\gamma$  and  $h \rightarrow \rho\gamma$  are being considered, followed by the  $\omega \rightarrow \pi^+\pi^-\pi^0$  and  $\rho \rightarrow \pi^+\pi^-$  decays, both with large branching ratios of about 89% and 100%, respectively. The corresponding expected number of events, assuming the SM branching ratios for these decays, are about 7.6 and 96, respectively. The experimental acceptance for these decays, assuming reasonable geometrical acceptance and transverse momentum requirements, is expected to range between 40 and 70% [174]. It is noted that the search for  $\omega\gamma$  and  $\rho\gamma$  final states is further complicated due to the large natural width of the  $\rho$  meson and the  $\omega$ - $\rho$  interference.

These rare decays to a vector meson and a photon feature very interesting and experimentally challenging boosted topologies. The signature is distinct, but the QCD backgrounds require careful consideration. A primary challenge arises from the trigger availability to collect the required datasets. In the considered cases, the decay signature is a photon of large transverse momentum that is isolated from hadronic activity, recoiling against a narrow hadronic jet. It is important to consider such signatures, early on in designing the trigger system. Fast track finding and reconstruction in the inner detector, available at an early stage in the trigger could help suppress backgrounds.

At the FCC-hh environment, the large production cross-section for the signal and the large expected integrated luminosity alleviates the main issue confronted by the studies at the LHC and the HL-LHC, namely the small expected yields. With  $20 \text{ ab}^{-1}$  at the centre-of-mass energy of 100 TeV, a factor 100 increase in the produced Higgs boson, with respect to HL-LHC, is expected. This substantial increase in the signal yield, will also allow for more effective event categorisation to further suppress the backgrounds. Production based signatures, like the vector-boson-fusion or production in association with a leptonically decaying  $W$  or  $Z$  boson will be exploited. Furthermore, enhancement in the sensitivity can

be expected by exploiting the boosted regime, where the Higgs boson is produced with substantial transverse momentum. Early studies on this have been performed at the LHC [171], and careful evaluation of the potential at 100 TeV is needed.

## 4 Multi-Higgs production

In the previous sections we focused on processes involving the production of a single Higgs boson, which allow one to test with high accuracy the linear Higgs interactions, most noticeably those involving gauge bosons and third-generation SM fermions. These processes, however, cannot be used to directly probe interactions containing two or more Higgs fields, whose determination is of primary importance for analyzing the Higgs potential. Non-linear Higgs vertices can be accessed by looking at channels in which multiple Higgs bosons are produced either alone or in association with additional objects. In this section we will consider these channels with the aim of understanding the precision with which the Higgs potential could be determined at a future 100 TeV hadron collider.

### 4.1 Parametrizing the Higgs interactions

As we already mentioned, the main aim of the analyses that we will present in this section is to estimate the precision with which the Higgs potential can be probed through the exploitation of multi-Higgs production processes. It is thus useful to parametrize the relevant Higgs self-interactions in a general form. In the language of an effective field theory, we can write the Higgs self-interaction Lagrangian as

$$\mathcal{L} = -\frac{1}{2}m_h^2 h^2 - \lambda_3 \frac{m_h^2}{2v} h^3 - \lambda_4 \frac{m_h^2}{8v^2} h^4, \quad (36)$$

where  $v = 246$  GeV denotes the Higgs vacuum expectation value. The SM Lagrangian is obtained by setting  $\lambda_3 = \lambda_4 = 1$ ; in this case the terms in Eq. (36) provide the whole Higgs potential. On the contrary, in BSM scenarios, higher-order operators are in general also present, as for instance contact interactions involving higher-powers of the Higgs field or additional derivatives.

The use of the parametrization in Eq. (36) can be fully justified in an effective-field-theory framework in which an expansion in powers of the momenta is valid. Namely, we assume that each additional derivative in the effective Lagrangian is accompanied by a factor  $1/m_*$ , where  $m_*$  is a mass scale that broadly characterizes a possible new-physics dynamics. In this way the contribution of higher-derivative terms to low-energy observables is suppressed by additional powers of  $E^2/m_*^2$ , guaranteeing that the effective theory is valid for energy scales  $E \ll m_*$ . For most of the processes we are going to consider the kinematic distributions are peaked mostly at threshold. Hence an analysis focusing on the total cross section can be interpreted in the effective-field-theory context provided that the new physics is at the TeV scale or beyond ( $m_* \gtrsim 1$  TeV).<sup>1</sup> It is important to stress that the parametrization in Eq. (36) does not rely on any expansion in powers of the Higgs field. Operators involving more than four powers of  $h$  are in fact irrelevant for the processes we are considering and can be safely neglected.

In the case in which, in addition to the derivative expansion, we can also rely on an expansion in powers of the Higgs field, the most relevant new-physics effects can be described in terms of dimension-6 operators [175–177]. If the Higgs is part of an  $SU(2)_L$  doublet  $H$ , only two effective operators contribute to the modification of the Higgs self-interactions, namely<sup>2</sup>

$$\Delta\mathcal{L}_6 \supset \frac{\bar{c}_H}{2v^2} \partial_\mu (H^\dagger H) \partial^\mu (H^\dagger H) - \frac{\bar{c}_6}{v^2} \frac{m_h^2}{2v^2} (H^\dagger H)^3, \quad (37)$$

where  $H$  denotes the Higgs doublet. These operators induce corrections to the trilinear and quadrilinear Higgs interactions, whose size is given by

$$\lambda_3 = 1 - \frac{3}{2}\bar{c}_H + \bar{c}_6, \quad \lambda_4 = 1 - \frac{25}{3}\bar{c}_H + 6\bar{c}_6. \quad (38)$$

<sup>1</sup>Possible issues with the effective description can instead arise in analyses focused on the high-energy tails of the invariant mass distributions.

<sup>2</sup>We neglect a third operator  $\mathcal{O}_T = (H^\dagger \overleftrightarrow{D}_\mu H)(H^\dagger \overleftrightarrow{D}^\mu H)$ , since it breaks the custodial symmetry and is constrained by the EW precision measurements to have a very small coefficient.

It is important to stress that the operator  $\mathcal{O}_H$  modifies several observables that can be also tested in single-Higgs processes. For instance, it induces an overall rescaling of the linear couplings of the Higgs field to the SM gauge bosons and to the fermions. The present LHC data already constrain these corrections not to exceed the  $\sim 10\%$  level. Moreover future lepton colliders could test these effects with very high accuracy, reaching a precision of the order of a few percent [178]. The operator  $\mathcal{O}_6$ , on the other hand, modifies only the Higgs self-interactions, and it can thus be tested directly only in collider processes involving multiple Higgs production. Notice that, if the relevant new-physics effects are entirely due to  $\mathcal{O}_6$ , the deviations in the trilinear and quadrilinear Higgs couplings are correlated.

Analogously to the parametrization of the Higgs potential, possible deviations in the Higgs couplings to the gauge bosons can be parametrized by

$$\mathcal{L} = \left( m_W^2 W_\mu W^\mu + \frac{m_Z^2}{2} Z_\mu Z^\mu \right) \left( 1 + 2c_V \frac{h}{v} + c_{2V} \frac{h^2}{v^2} \right). \quad (39)$$

These interactions are relevant for interpreting double Higgs production in the VBF channel. The SM Lagrangian is recovered for  $c_V = c_{2V} = 1$ .

#### 4.1.1 Estimate of the size of new-physics corrections

As we already mentioned, the measurement of multi-Higgs production processes can provide a significant test of the validity of the SM. It is however also important to assess its impact in context of BSM scenarios. In this case, multi-Higgs processes can be used to discover new-physics effects or, in the case of a good agreement with the SM prediction, can be translated into exclusions on the parameter space of BSM models. Obviously the impact on the various BSM scenarios crucially depends on the size of the expected deviations in the Higgs potential and in the other Higgs couplings and on the possibility of disentangling these effects from other possible corrections due to the presence of new resonances. In the following we will provide some estimates of these effects in a few motivated BSM contexts.<sup>3</sup>

As a preliminary observation, notice that in BSM scenarios multiple Higgs production can be modified in different ways. A first obvious effect comes from non-standard Higgs interactions, that is modified couplings already present in the SM or new (non-renormalizable) interactions.<sup>4</sup> An additional effect can arise from the presence of new resonances, which can contribute through tree-level or loop diagrams. In particular, if the new-physics is light, multi-Higgs production can receive resonant contributions from the on-shell production of one or more resonances which afterwards decay into multi-Higgs final states. Obviously, in the latter case a different search strategy must be employed to study the direct production of new states, either through multi-Higgs production channels or in related processes. Searches for resonant double-Higgs production have already been performed at the LHC [181–183].

If the new physics is relatively heavy, it is still useful to perform a non-resonant search for multi-Higgs production using a parametrization in terms of effective Higgs couplings. Indeed, since multi-Higgs production cross sections are typically peaked not far from the kinematic threshold, a new-physics scale  $m_* \gtrsim 1$  TeV is high enough to ensure that resonant production gives a subleading contribution to the total rates. Therefore, the impact of the new physics on the total cross section can be reliably described in terms of effective operators.

Let us now discuss the expected size of the corrections to the Higgs vertices. For definiteness we will concentrate on the effects relevant for Higgs pair production (triple Higgs production can be analyzed along the same lines). The set of Higgs interactions relevant for the various production channels

<sup>3</sup>For additional details see Ref. [179].

<sup>4</sup>For example, new multi-Higgs interactions are typically present in theories where the Higgs boson is a composite state of new strongly-coupled dynamics. In these scenarios the non-linear Higgs dynamics implies the presence of new non-renormalizable Higgs interactions (see for instance Ref. [180]).

is [184, 185]

$$\begin{aligned} \mathcal{L} \supset & \left( m_W^2 W_\mu W^\mu + \frac{m_Z^2}{2} Z_\mu Z^\mu \right) \left( 1 + 2c_V \frac{h}{v} + c_{2V} \frac{h^2}{v^2} \right) - \lambda_3 \frac{m_h^2}{2v} h^3 \\ & - m_t \bar{t} t \left( 1 + c_t \frac{h}{v} + c_{2t} \frac{h^2}{2v^2} \right) + \frac{g_s^2}{4\pi^2} \left( c_g \frac{h}{v} + c_{2g} \frac{h^2}{2v^2} \right) G_{\mu\nu}^a G^{a\mu\nu}, \end{aligned} \quad (40)$$

where the SM corresponds to  $c_V = c_{2V} = 1$ ,  $c_t = 1$ ,  $\lambda_3 = 1$  and  $c_{2t} = c_g = c_{2g} = 0$ . Notice that, in addition to the dependence on the Higgs trilinear interaction, Higgs pair production is influenced by several other vertex modifications. In particular, the gluon fusion process is also sensitive to corrections to the Yukawa coupling of the top quark (and, in a much milder way, of the bottom quark), as well as to the presence of new contact interactions with gluons, which could arise from loop contributions of new heavy states. In the case of Vector Boson Fusion (VBF), modified Higgs couplings to the gauge fields are also relevant.

In generic new-physics scenarios, corrections to all these couplings are present and can have comparable size. Let us start by estimating these corrections in theories where the Higgs arises as a Nambu-Goldstone boson (NGB) from some new strongly-coupled dynamics. In this case the SILH power counting implies [176, 180]

$$\delta\lambda_3, \delta c_V, \delta c_{2V}, \delta c_t, c_{2t} \sim \frac{v^2}{f^2}, \quad \delta c_g, c_{2g} \sim \frac{v^2}{f^2} \frac{\lambda^2}{g_*^2}, \quad (41)$$

where  $g_*$  denotes the typical coupling strength of the strong dynamics, while  $f$  is defined as  $f = m_*/g_*$ . The corrections to couplings that are forbidden by the Goldstone symmetry are suppressed if the latter is broken by a small amount. In particular, contact interactions with gluons are generated proportional to (the square of) some weak spurion coupling  $\lambda$ , while corrections to the top Yukawa coupling and to the trilinear Higgs coupling are suppressed respectively by the factors  $y_t$  and  $m_h^2/2v^2$  (notice that these factors have been already included in the definition of Eq. (40)).

It is apparent from Eq. (41) that in theories respecting the SILH power counting the corrections to the various Higgs couplings are all of comparable order. Higgs pair production is thus affected by all these effects simultaneously. In order to disentangle them and extract the Higgs self-interactions one thus needs to use additional measurements (as for instance single-Higgs production channels) and to adopt a more refined analysis strategy which makes use of kinematic distributions [179].

There are however other new-physics scenarios where the corrections to the Higgs self-couplings can be enhanced and become larger than those to the other couplings. One scenario of this kind is obtained by assuming that the Higgs is a generic composite state (not a NGB as assumed before) from a new strongly-coupled dynamics. In this case the corrections to the Higgs self-interactions are enhanced by a factor  $2v^2 g_*^2/m_h^2$  compared to the SILH case. One thus expects  $\delta\lambda_3 \sim g_*^2 v^4/f^2 m_h^2$ , which can be sizable even if  $v^2/f^2 \ll 1$  (in which case the corrections to the linear Higgs couplings are small). The price to pay for this enhancement, however, is an additional tuning that is required to keep the higgs mass small, since one would naturally expect  $m_h^2 \sim m_*^2$ .

Another scenario which leads to large corrections mainly to the Higgs self-couplings is obtained by considering a new strong dynamics coupled to the SM through a Higgs portal [179]:  $\mathcal{L}_{int} = \lambda H^\dagger H O$ , where  $O$  is a composite operator and  $\lambda$  is the coupling strength. In this case one finds

$$\delta c_V \sim \delta c_{2V} \sim \delta c_t \sim c_{2t} \sim \frac{\lambda^2 v^2}{g_*^4 f^2}, \quad \delta\lambda_3 \sim \frac{2v^2 \lambda \lambda^2 v^2}{m_h^2 g_*^4 f^2}. \quad (42)$$

The corrections to the Higgs trilinear self-coupling can be dominant if  $\lambda > m_h^2/(2v^2) \simeq 0.13$ . In this scenario it is thus possible to obtain  $\delta\lambda_3 \sim 1$ , while keeping the corrections to the other Higgs couplings at the few percent level.

For other possible new physics giving rise to a modified Higgs potential see also Section 5 of this report.

process	$\sigma(14 \text{ TeV})$ (fb)	$\sigma(100 \text{ TeV})$ (fb)	accuracy
$HH$ (ggf)	$45.05^{+4.4\%}_{-6.0\%} \pm 3.0\% \pm 10\%$	$1749^{+5.1\%}_{-6.6\%} \pm 2.7\% \pm 10\%$	NNLL matched to NNLO
$HHjj$ (VBF)	$1.94^{+2.3\%}_{-2.6\%} \pm 2.3\%$	$80.3^{+0.5\%}_{-0.4\%} \pm 1.7\%$	NLO
$HHZ$	$0.415^{+3.5\%}_{-2.7\%} \pm 1.8\%$	$8.23^{+5.9\%}_{-4.6\%} \pm 1.7\%$	NNLO
$HHW^+$	$0.269^{+0.33\%}_{-0.39\%} \pm 2.1\%$	$4.70^{+0.90\%}_{-0.96\%} \pm 1.8\%$	NNLO
$HHW^-$	$0.198^{+1.2\%}_{-1.3\%} \pm 2.7\%$	$3.30^{+3.5\%}_{-4.3\%} \pm 1.9\%$	NNLO
$HHt\bar{t}$	$0.949^{+1.7\%}_{-4.5\%} \pm 3.1\%$	$82.1^{+7.9\%}_{-7.4\%} \pm 1.6\%$	NLO
$HHtj$	$0.0364^{+4.2\%}_{-1.8\%} \pm 4.7\%$	$4.44^{+2.2\%}_{-2.6\%} \pm 2.4\%$	NLO
$HHH$	$0.0892^{+14.8\%}_{-13.6\%} \pm 3.2\%$	$4.82^{+12.3\%}_{-11.9\%} \pm 1.8\%$	NLO

**Table 25:** Cross sections for production of two or three SM Higgs bosons, including associated production channels, at a 14 TeV and 100 TeV hadron collider [18]. The cross sections are computed by choosing  $\mu = M_{hh}/2$  ( $\mu = M_{hhh}/2$  in the case of triple production). The error intervals correspond to scale variation and PDF +  $\alpha_s$  uncertainty. In  $HH$  production in the gluon-fusion channel a conservative 10% uncertainty is included to take into account the effects of the infinite top-mass approximation (see Section 4.2.1).

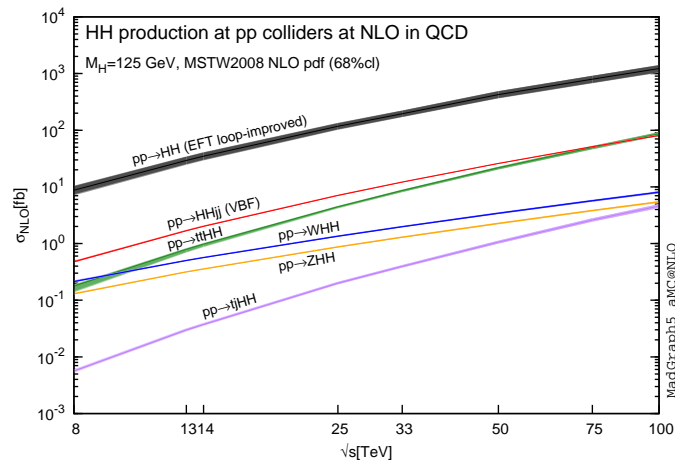


**Fig. 58:** Cross sections as a function of the collider COM energy. From ref. [186].

#### 4.1.2 Production cross sections and summary of results

To conclude this introduction, we present an overview of the various multi-Higgs production channels and we quickly summarize the results of the analyses that will be presented in details in the following subsections.

Table 25, extracted from the results of Ref. [18], reports the rates for SM Higgs pair and triple production, including channels of associated production with jets, gauge bosons and top quarks. The dependence of the production rates on the center-of-mass (COM) energy of the collider is shown in Fig. 58. As for single-Higgs production, the dominant channel for Higgs pair production is gluon fusion, with a rate of 1750 fb, which constitutes more than 90% of the total production rate. With respect to the 14 TeV LHC, the gluon-fusion rate is enhanced by a factor  $\sim 40$ . The second more significant channel is pair production in association with a top pair, whose cross section is 82 fb, closely followed by VBF with a rate of 80 fb. Notice that the relative importance of these two channels is reversed with respect to the 14 TeV LHC case, where VBF was about twice larger than  $HHt\bar{t}$ . The remaining pair production

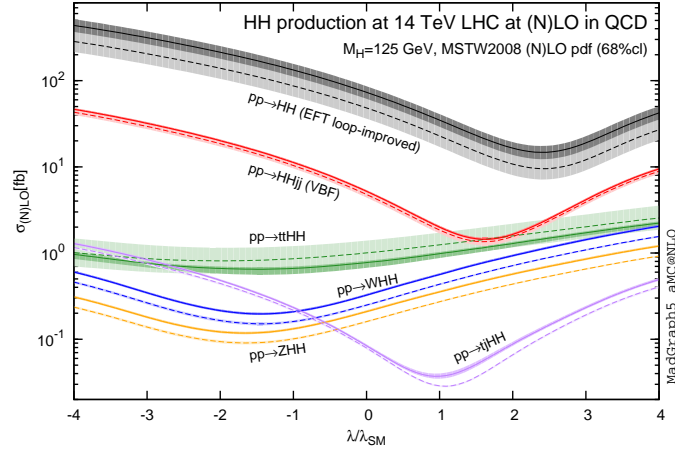


**Fig. 59:** Dependence of total cross sections on the Higgs trilinear coupling at 14 TeV. From ref. [186].

process	precision on $\sigma_{SM}$	68% CL interval on Higgs self-couplings
$HH \rightarrow b\bar{b}\gamma\gamma$	3%	$\lambda_3 \in [0.97, 1.03]$
$HH \rightarrow b\bar{b}b\bar{b}$	5%	$\lambda_3 \in [0.9, 1.5]$
$HH \rightarrow b\bar{b}4\ell$	$O(25\%)$	$\lambda_3 \in [0.6, 1.4]$
$HH \rightarrow b\bar{b}\ell^+\ell^-$	$O(15\%)$	$\lambda_3 \in [0.8, 1.2]$
$HH \rightarrow b\bar{b}\ell^+\ell^-\gamma$	—	—
$HHH \rightarrow b\bar{b}b\bar{b}\gamma\gamma$	$O(100\%)$	$\lambda_4 \in [-4, +16]$

**Table 26:** Expected precision (at 68% CL) on the SM cross section and 68% CL interval on the Higgs trilinear and quartic self-couplings (in SM units). All the numbers are obtained for an integrated luminosity of  $30 \text{ ab}^{-1}$  and do not take into account possible systematic errors.

modes, in association with a gauge boson or with  $tj$ , play a secondary role, since their cross section is at most  $\sim 8 \text{ fb}$ . Finally, triple Higgs production has a cross section around  $5 \text{ fb}$ .

As we already mentioned, the main aim of the analyses reported in this section is to determine the precision with which the SM production rates and the Higgs self-couplings can be measured. It is thus important to analyze the dependence of the cross section on the Higgs self-couplings. The production rates for the Higgs pair production channels are shown in Fig. 59 as a function of the trilinear Higgs coupling  $\lambda_3$ . Although the plot shows the rates for the 14 TeV LHC, it is approximately valid also at 100 TeV. One can see that for  $\lambda_3 \sim 1$ , *i.e.* for values close to the SM one, a significant reduction in the cross section is present in the gluon-fusion and VBF channels and, even more, in the  $HHtj$  channel. This feature decreases the signal significance for the SM case. However, it allows one to more easily differentiate scenarios with a modified trilinear coupling (especially if  $\lambda_3 < 1$ ), since in these cases a large increase in the cross section is present.

In the following we will present a few analyses focused on the most important multi-Higgs production channels. Here we summarize the main results. In particular, the expected precisions on the extraction of the SM signal cross section and the Higgs self-couplings are listed in Table 26.

Due to the sizable cross section, the gluon-fusion mode lends itself to the exploitation of several final states. As at the 14 TeV LHC, the  $b\bar{b}\gamma\gamma$  final state remains the “golden” channel, since it retains a significant signal rate and allows one to efficiently keep the backgrounds under control. From this

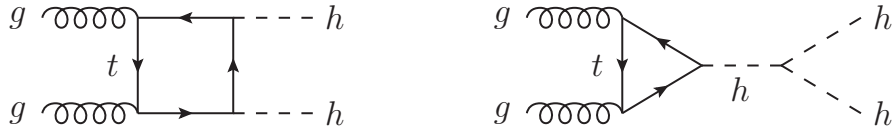


**Fig. 60:** Diagrams contributing to the Higgs pair production process through gluon fusion (an additional diagram obtained by crossing the box one is not shown).

channel a statistical precision of the order of  $1 - 2\%$  is expected on the SM signal cross section, while the Higgs trilinear coupling could be determined with a precision of order  $3 - 4\%$ . These numbers have to be compared with the precision expected at a possible future high-energy lepton collider, at which the Higgs trilinear coupling is expected to be measurable with a precision  $\sim 16\%$  for a COM energy  $\sim 1$  TeV and  $2 \text{ ab}^{-1}$  integrated luminosity [187–189]. A better precision, of around  $12\%$ , is only achievable with a 3 TeV collider and  $2 \text{ ab}^{-1}$  integrated luminosity [190, 191]. Other final states, namely  $b\bar{b}b\bar{b}$  and final states containing leptons, can also lead to a measurement of the SM signal, although in these cases the expected significance is lower than in the  $b\bar{b}\gamma\gamma$  channel.

Finally, the Higgs quartic self-coupling can be probed through the triple Higgs production channel. In this case the most promising final state seems to be  $b\bar{b}b\bar{b}\gamma\gamma$ , whose cross section is however small. This channel could allow an order-one determination of the SM production rate and could constrain the quartic coupling in the range  $\lambda_4 \in [-4, +16]$ .

## 4.2 Double Higgs production from gluon fusion

We start the presentation of the analyses of the various Higgs pair production channels by considering the gluon-fusion process, which, as we saw, provides the dominant contribution to the total rate. At 100 TeV, the gluon fusion cross section computed at NNLL (matched to NNLO) accuracy is  $1750 \text{ fb}$  [18]. At present, this result is affected by a significant uncertainty (of the order of  $10\%$ ) due to the fact that the NLO and NNLO contributions are only known in the infinite top mass limit. A discussion of the current status of the computations and of the sources of uncertainties will be provided in Subsection 4.2.1.

In the SM the gluon fusion process receives contributions from two types of diagrams (see Fig. 60). The box-type diagrams, which depend on the top Yukawa couplings, and the triangle-type one, which in addition to the top Yukawa also includes the trilinear Higgs self-interaction. In the SM a partial cancellation between these two kinds of diagrams is present, which leads to a  $\sim 50\%$  suppression of the total cross section. The behavior of the box and the triangle diagrams at high  $\sqrt{\hat{s}} = m_{hh} \gg m_t, m_h$  is quite different however. The corresponding amplitudes scale as

$$\mathcal{A}_{\square} \sim \frac{\alpha_s}{4\pi} y_t^2, \quad \mathcal{A}_{\triangle} \sim \lambda_3 \frac{\alpha_s}{4\pi} y_t^2 \frac{m_h^2}{\hat{s}} \left( \log \frac{m_t^2}{\hat{s}} + i\pi \right)^2. \quad (43)$$

From these equations it is apparent that, due to the presence of the off-shell Higgs propagator, the triangle diagram is suppressed for high  $\hat{s}$ . This implies that the Higgs trilinear coupling affects the  $m_{hh}$  distribution mostly at threshold, while the tail at large invariant mass is mostly determined by the box contribution.

The shape of the Higgs pair invariant mass distribution for the SM signal is shown in Fig. 61 [192]. The central line corresponds to the choice  $\mu_F = \mu_R = M_{hh}/2$  for the factorization and renormalization scales, and the band illustrates the scale uncertainty, evaluated by varying independently the above scales in the range  $\mu_0/2 \leq \mu_R, \mu_F \leq 2\mu_0$  with the constraint  $1/2 \leq \mu_R/\mu_F < 2$ , where  $\mu_0$  is the central scale. The lower panel shows the ratio with respect to the central value, and it can be seen that the scale uncertainty is roughly constant in the whole range, being of the order of  $\pm 5\%$ . One can see that the peak of the distribution is at  $m_{hh} \sim 400 \text{ GeV}$  and some suppression is present close to threshold. The

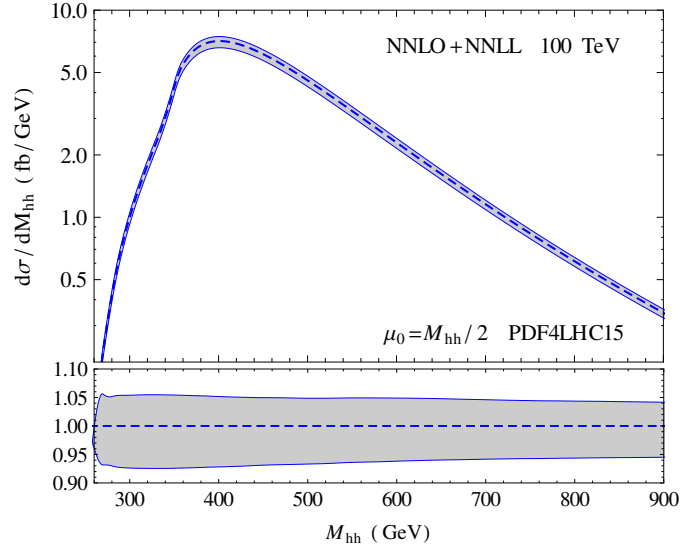


**Fig. 61:** The invariant mass distribution at NNLO+NNLL [192] for a 100 TeV collider, with the corresponding scale uncertainty. The lower panel shows the ratio with respect to the central prediction.

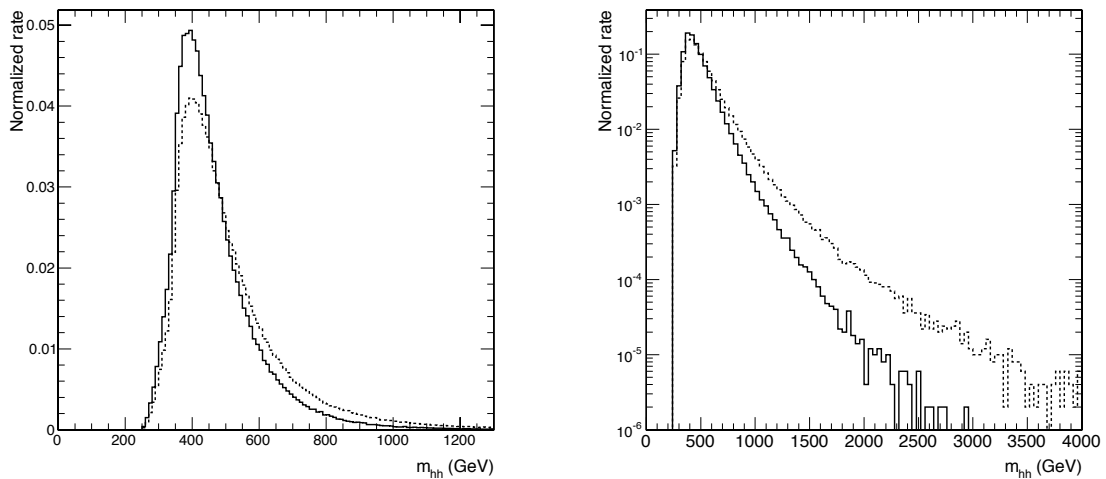


**Fig. 62:** Comparison between the normalized  $m_{hh}$  distributions for the SM signal. The solid and dotted lines correspond to  $\sqrt{s} = 14$  TeV and  $\sqrt{s} = 100$  TeV respectively. The distributions have been computed at LO retaining the full top mass dependence. The plots are taken from Ref. [179].

suppression is a consequence of the partial cancellation between the box and triangle diagrams that, as we already mentioned, is present in the SM.

The invariant mass distribution at a 14 TeV collider is similar to the one at 100 TeV. The comparison between the two distributions is shown in Fig. 62. The position of the peak and the threshold behavior is unchanged. The tail of the distribution, on the other hand, is significantly larger at a 100 TeV collider, starting from  $m_{hh} \gtrsim 700$  GeV. This modification of the tail, however, has only a small impact on the total production rate, which is still dominated by the peak region  $300 \text{ GeV} \lesssim m_{hh} \lesssim 600 \text{ GeV}$ .

Non-standard Higgs interactions, in particular the couplings with the top (either a modified Yukawa or the non-renormalizable interaction  $hht\bar{t}$ ) and the contact interactions with the gluons (see Eq. (40)), lead to corrections that are not suppressed at high  $m_{hh}$ . Therefore they can significantly change the tail of the kinematic distribution at large invariant mass. An analysis exploiting the differential  $m_{hh}$

distribution can thus be helpful to disentangle possible corrections to the various Higgs couplings [179]. This kind of analysis goes however beyond the scope of the present report. Here we will analyze only the inclusive total signal rate and focus on scenarios in which the Higgs trilinear coupling is significantly modified, while the corrections to the other couplings are negligible.

As already mentioned, the sizable production cross section via gluon fusion allows one to consider various decay channels for an experimental search. In the following we will describe some preliminary analyses that focus on the most relevant final states with the aim of determining the precision with which the SM signal can be extracted. In particular the  $b\bar{b}\gamma\gamma$  channel will be presented in Subsection 4.2.2, the  $b\bar{b}b\bar{b}$  channel in Subsection 4.2.3 and finally the rare final states containing leptons in Subsection 4.2.4.

Before discussing the details of the analyses we briefly discuss in the next subsection the present status of the computation of the SM Higgs pair production in gluon fusion, pointing out, in particular, the various sources of theoretical uncertainty.

#### 4.2.1 Status of SM gluon fusion cross section computation

In the last years, a lot of effort has been devoted towards the improvement of the theoretical prediction of the SM Higgs pair production cross section via gluon fusion. Even though this loop-induced process is known in an exact way only at LO in the QCD perturbative expansion [193–195], very useful approximations are available for the higher-order corrections.

One main approach, exploited extensively for the calculation of the single-Higgs production cross section, consists in working in the large top-mass approximation, in which the Higgs has a direct effective coupling to gluons. Within this approximation, the LO becomes a tree-level contribution, and higher-order corrections can be computed. In this way, both the NLO [196] and NNLO [197] corrections have been obtained, together with threshold resummation effects at NNLL accuracy [192, 198]. The QCD corrections were found to be large, resulting in about a 50% increase from LO to NLO, and a still sizeable  $\sim 20\%$  increment from NLO to NNLO at a collider center-of-mass energy of 100 TeV (corrections are even larger for lower energies). Of course, in order to use these results, an estimate of the accuracy of the approximation is needed.

Two different approaches have been used to estimate the finite top-mass effects at NLO. In Refs. [199, 200] the analysis was performed through the computation of subleading terms in the  $1/m_t$  expansion. By evaluating the deviation of the results containing powers of  $1/m_t$  from the infinite top-mass prediction, the authors estimate that the effective theory is accurate to  $\pm 10\%$  at NLO [200]. On the other hand, in Ref. [201] the exact one-loop real emission contributions were included via a reweighting technique, finding in this way that the NLO total cross section decreases by about 10%. The pure EFT result reproduces well the shape of the Higgs pair invariant mass distribution obtained retaining the exact real contributions. It is worth mentioning that this is not the case for all the distributions, and for instance the EFT fails to reproduce the region where the Higgs pair system has a large transverse momentum. Based on the two studies described above, it is possible to estimate the current accuracy of the large top-mass approximation to be  $\pm 10\%$  for the total cross section.<sup>5</sup>

The final result for the SM cross section for hadron colliders with center-of-mass energy  $E_{cm} = 14$  TeV and  $E_{cm} = 100$  TeV are listed in Table 25 together with the size of the different theoretical uncertainty. These results are computed at NNLO+NNLL accuracy using the PDF4LHC recommendation for the parton flux [125], and the values  $m_h = 125$  GeV and  $m_t = 172.5$  GeV for the Higgs and top quark masses. The scale uncertainty at NNLO+NNLL is quite small, as it is also the case for the PDF and  $\alpha_S$  uncertainty. Therefore, theoretical uncertainties are currently driven by the use of the large top-mass approximation. It is worth noticing that, once the exact NLO becomes available, the remaining

<sup>5</sup>Recently the complete computation of the NLO cross section including the finite-top-mass corrections has been performed [202]. The results are at present available only for the 14 TeV LHC and show a  $\sim 10\%$  reduction of the cross section with respect to the approximate results.

EFT uncertainty at NNLO is expected to be at most  $\pm 5\%$  [200].

#### 4.2.2 The $HH \rightarrow b\bar{b}\gamma\gamma$ channel

In this section we analyze the  $HH \rightarrow b\bar{b}\gamma\gamma$  channel, which has been singled out in the literature as the process that can lead to the highest SM signal significance and highest precision in the measurement of the Higgs trilinear coupling. This channel has a relatively small branching ratio ( $BR \simeq 0.264\%$  in the SM), which somewhat limits the signal yield (in the SM the total rate for this channel at a 100 TeV pp collider is  $\simeq 4.6$  fb). The presence of two photons, however, allows one to efficiently keep the background under control while preserving a fair fraction of the signal events.

Various studies included an analysis of this channel at future high-energy hadron colliders, focusing mainly on the extraction of the Higgs trilinear coupling [203–205], or performing a global analysis of the impact of the modifications of the various Higgs couplings [179]. The differences among these analyses stem mainly from different assumptions about the detector performance, a different treatment of the backgrounds and the choice of benchmark integrated luminosity. In the following we will present (in a summarized form) the results of a new analysis of the  $HH \rightarrow b\bar{b}\gamma\gamma$  final state, specifically focused on the extraction of the trilinear Higgs coupling in a SM-like scenario [206]. Differently from most of the previous ones, this new analysis is tailored specifically on a 100 TeV future hadron collider, with the primary purpose of estimating how much the achievable precision is influenced by the detector performance.

##### 4.2.2.1 Simulation setup

The parton-level generation of the signal and the backgrounds is performed by using MadGraph5\_aMC@NLO (version 2.3.3) [144] and the parton density functions ctEq611 [207]. The signal is generated at LO retaining the finite-top-mass effects and afterwards rescaled by a k-factor in order to match the NNLL gluon-fusion SM cross section (see Table 25). The analysis includes the following main backgrounds: the non-resonant processes  $b\bar{b}\gamma\gamma$ ,  $b\bar{b}j\gamma$  (with one fake photon),  $bj\gamma\gamma$  and  $jj\gamma\gamma$  (respectively with one and two fake  $b$ -jets),<sup>6</sup> and the resonant processes  $b\bar{b}h$  and  $t\bar{t}h$ . The cross sections for each background process after the acceptance cuts of Table 27 are given in Table 29. The  $b\bar{b}\gamma\gamma$  and  $bj\gamma\gamma$  samples are generated by matching up to one extra parton at the matrix-element level.<sup>7</sup> In the case of  $b\bar{b}\gamma\gamma$ , matching accounts for the bulk of the NLO correction to the cross section, as virtual effects are small for this process, see Ref. [179]. The remaining backgrounds are instead generated at LO without matching and rescaled by the following k-factors to take into account higher-order effects:  $k = 1.08$  for  $b\bar{b}j\gamma$ ,  $k = 1.3$  for  $t\bar{t}h$ ,  $k = 0.87$  for  $b\bar{b}h$  and  $k = 1.43$  for  $\gamma\gamma jj$ .

Showering and hadronization effects are included for the signal and background samples by using the pythia6 package [110]. The simulation of the underlying event has been found to have a minor impact on the analysis and, therefore, has been omitted for simplicity. Detector simulation effects are included by using the Delphes package (version 3.3.1) [147] with a custom card that describes the FCC-hh detector parametrization. A more detailed discussion of the benchmarks used for the calorimeters performance parametrization will be given in the next subsection.

The tagging of  $b$ -jets and photons is performed by using the Delphes flavor tagging information that associates each jet with a parton after showering. Events are then re-weighted according to the  $b$ - and photon-tagging probabilities. The following benchmark efficiencies are considered: The  $b$ -tagging probabilities are chosen to be constant throughout the detector and independent of the transverse momenta, with values  $p_{b \rightarrow b} = 0.75$ ,  $p_{c \rightarrow b} = 0.1$  and  $p_{j \rightarrow b} = 0.01$ , for  $b$ ,  $c$  and light jet tagging to  $b$ -jets

<sup>6</sup>Here  $j$  denotes a jet initiated by a gluon or a light quark  $u$ ,  $d$ ,  $s$ ,  $c$ . For simplicity  $bj\gamma\gamma$  denotes the sum of the processes where the  $b$ -jet is initiated by either a  $b$  quark or an anti- $b$  quark.

<sup>7</sup>The  $k_T$ -MLM matching scheme has been used with matching scale 35 GeV and matching parameter  $x_{\text{qcut}} = 25$  GeV.

Acceptance cuts	Final selection
$\gamma$ isolation $R = 0.4$	$\gamma$ isolation $R = 0.4$
$(p_T(had)/p_T(\gamma) < 0.15)$	$(p_T(had)/p_T(\gamma) < 0.15)$
jets: anti- $k_T$ , parameter $R = 0.4$	jets: anti- $k_T$ , parameter $R = 0.4$
$ \eta_{b,\gamma,j}  < 6$	$ \eta_{b,\gamma}  < 4.5$
$p_T(b), p_T(\gamma), p_T(j) > 35$ GeV	$p_T(b_1), p_T(\gamma_1) > 60$ GeV
	$p_T(b_2), p_T(\gamma_2) > 35$ GeV
$m_{bb} \in [60, 200]$ GeV	$m_{bb} \in [100, 150]$ GeV
$m_{\gamma\gamma} \in [100, 150]$ GeV	$ m_{\gamma\gamma} - m_h  < 2.0, 2.5, 4.5$ GeV
	$p_T(bb), p_T(\gamma\gamma) > 100$ GeV
	$\Delta R(bb), \Delta R(\gamma\gamma) < 3.5$
	no isolated leptons with $p_T > 25$ GeV

**Table 27:** List of cuts at the acceptance level (left column) and final cuts (right column) used for the analysis. The final cuts are optimized to increase the precision on the trilinear Higgs self-coupling. The three values listed for the final cuts on the  $m_{\gamma\gamma}$  invariant mass are used in the “low”, “medium” and “high” detector performance scenarios.

respectively. The light-jet-to-photon mis-tagging probability is parametrized via the function

$$p_{j \rightarrow \gamma} = \alpha \exp(-p_{T,j}/\beta), \quad (44)$$

where  $\alpha$  and  $\beta$  are parameters whose benchmark values are set to  $\alpha = 0.01$  and  $\beta = 30$  GeV. Photons are assumed to be reconstructed with an efficiency that depends on  $\eta$ , namely

$$\begin{cases} 95\% & \text{for } |\eta| \leq 1.5 \\ 90\% & \text{for } 1.5 < |\eta| \leq 4 \\ 80\% & \text{for } 4 < |\eta| \leq 6 \end{cases}, \quad (45)$$

provided that they have a transverse momentum  $p_T(\gamma) > 10$  GeV.

#### 4.2.2.2 Benchmark scenarios for the detector performance

In the analysis three benchmark scenarios for the detector performance are considered, denoted in the following as “Low”, “Medium” and “High” performance scenarios. These three benchmarks are simulated through Delphes by implementing different choices for the energy resolution in the electromagnetic and hadronic calorimeters cells. For this purpose the variance of the energy distribution in a single cell is parametrized by the following formula

$$\Delta E = \sqrt{a^2 E^2 + b^2 E}, \quad (46)$$

where  $E$  is measured in GeV and the values of the  $a$  and  $b$  parameters are listed in Table 28. The energy output is then assumed to follow a log-normal distribution, namely the  $\log E$  variable follows a Gaussian distribution. The advantage of this distribution lies in the fact that it tends asymptotically to the usual normal distribution for large  $E$  and provides only positive values for the energy. For a more detailed discussion about the setup used for the Delphes simulation we refer the reader to Ref. [206].

	ECAL				HCAL			
	$ \eta  \leq 4$		$4 <  \eta  \leq 6$		$ \eta  \leq 4$		$4 <  \eta  \leq 6$	
	$a$	$b$	$a$	$b$	$a$	$b$	$a$	$b$
Low	0.02	0.2	0.01	0.1	0.05	1.0	0.05	1.0
Medium	0.01	0.1	0.01	0.1	0.03	0.5	0.05	1.0
High	0.007	0.06	0.01	0.1	0.01	0.3	0.03	0.5

**Table 28:** Parameters defining the energy resolution in the electromagnetic (ECAL) and hadronic (HCAL) calorimeter cells for the “Low”, “Medium” and “High” detector performance benchmarks.

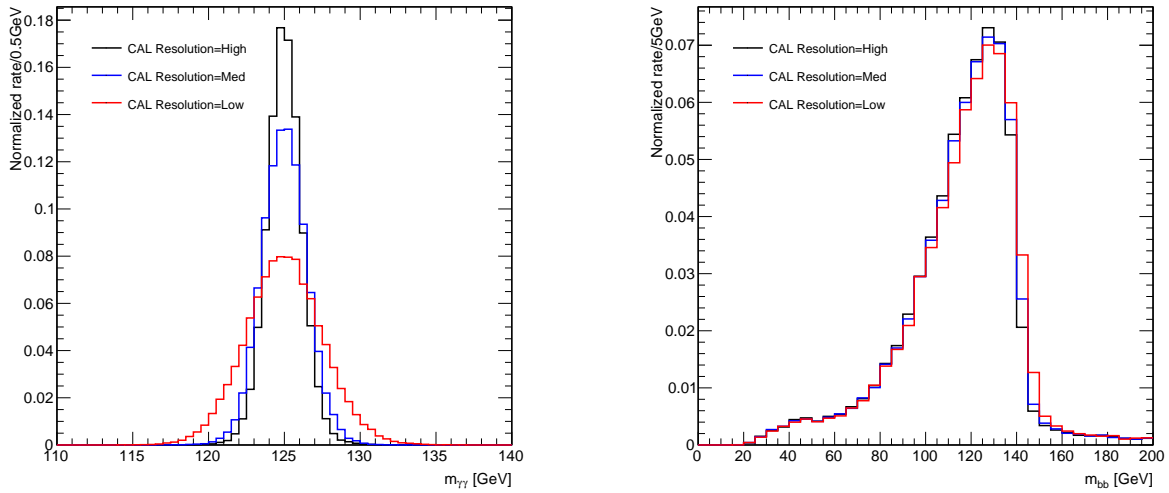


**Fig. 63:** Distribution of the reconstructed invariant mass of the photon pair (left panel) and bottom pair (right panel) for the signal. The plots show how the distributions vary in the “Low” (red curve), “Medium” (blue curve) and “High” (black curve) detector performance benchmarks.

As it will be discussed later on, the detector performance can have a significant impact on the analysis and on the achievable precision in the measurements of the signal cross section and Higgs self-couplings. The finite energy resolution of the calorimeter induces a smearing in the reconstruction of the photon- and bottom-pair invariant masses, which are crucial observables for differentiating signal and background events. The distributions of the reconstructed invariant masses  $m_{\gamma\gamma}$  and  $m_{bb}$  are shown in Fig. 63, for the three detector performance benchmarks. One can see that the impact on the photon invariant mass can be sizable. In the “Low” performance benchmark the width of the distribution is  $\Delta m_{\gamma\gamma} \simeq 3$  GeV, while it decreases to  $\simeq 2$  GeV and  $\simeq 1.5$  GeV in the “Medium” and “High” benchmarks respectively. This means that a cut on the  $m_{\gamma\gamma}$  invariant mass can be twice more effective in the “High” benchmark than in the “Low” one in reducing backgrounds containing non-resonant photons (as for instance the non-resonant  $b\bar{b}\gamma\gamma$  background).

The reconstruction of the bottom pair invariant mass  $m_{bb}$  is instead only marginally affected by the calorimeters energy resolution, as can be seen from the right panel of Fig. 63. In all cases the distribution is peaked at the Higgs mass and at half-height it is contained in the region  $\sim [100, 145]$  GeV. The reconstruction of the  $m_{bb}$  invariant mass, on the other hand, is highly affected in the presence of a strong magnetic field in the detector. In order to be able to bend very energetic charge particles, indeed, a very intense magnetic field is needed. As a benchmark value,  $B = 6$  T has been chosen in the analysis. The problem with such a magnetic field is the fact that low-energy charged particles (with a transverse

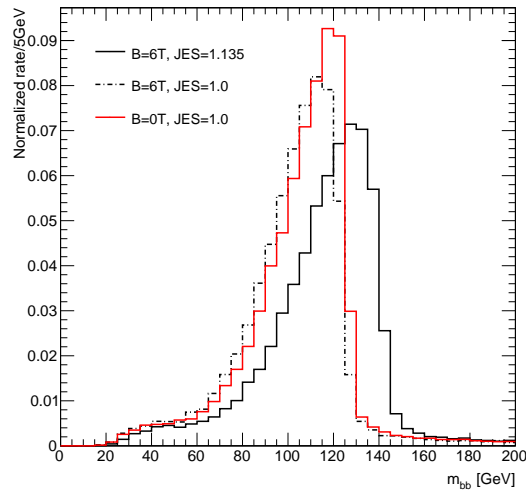


**Fig. 64:** Distribution of the reconstructed bottom pair invariant mass for different values of the detector magnetic field  $B$  and of the JES correction. The red curve corresponds to the case with no magnetic field  $B = 0$  T and no JES correction  $r_{\text{JES}} = 1$ , the dot-dashed black curve corresponds to  $B = 6$  T and  $r_{\text{JES}} = 1$ , and the solid black curve corresponds to  $B = 6$  T and  $r_{\text{JES}} = 1.135$ .

momentum  $p_T \lesssim 5$  GeV) do not reach the electromagnetic calorimeter, so that it is difficult to reconstruct their energy. This effect can be significant in processes that happen dominantly at “low-energy”, as in the case of double Higgs production where the bulk of the cross section comes from the threshold region. Figure 64 shows that a strong magnetic field can distort the  $m_{bb}$  distribution and shift its peak (by roughly 5 GeV for  $B = 6$  T). Such shift, together with the energy loss in the reconstruction of the  $b$  momenta, can be partially compensated by a rescaling of the jet energy scale (JES).<sup>8</sup> As shown in the figure, a rescaling of the jets’ four-momentum by a factor  $r_{\text{JES}} = 1.135$  is sufficient to shift back the distribution and move its peak to the value  $m_{bb} \simeq m_h$ .

#### 4.2.2.3 Analysis strategy

As discussed in the introduction, the main aim of the analysis described here is to determine the achievable precision on the SM signal cross section and on the Higgs trilinear coupling. For this purpose a simple cut-and-count strategy focused on the inclusive event rate can be used. More sophisticated analysis strategies, as for instance an exclusive one that also takes into account the differential distributions, could be useful in disentangling different new-physics effects (see for instance Ref. [179]).

In optimizing the selection cuts two different strategies can in principle be used: one can either maximize the precision on the SM signal or that on the Higgs trilinear coupling. The two procedures lead to significantly different sets of cuts. The effect of a change in the Higgs self-coupling mostly affects the threshold behavior, thus “looser” cuts aimed at preserving a large fraction of the threshold events improve the precision on  $\lambda_3$ . On the other hand, the threshold region is also the one that has a larger background, hence harder cuts might be convenient to improve the precision on the SM signal rate.

For the analysis presented here, cuts have been optimized to maximize the precision on  $\lambda_3$ . This choice is motivated by the fact that the SM signal significance is always quite high, and optimizing for the extraction of the Higgs trilinear coupling does not degrade significantly the precision on the signal

<sup>8</sup>Actual experimental analyses adopt more sophisticated jet calibration procedures and particle flow techniques are usually used to cope with these effects. The simple rescaling applied in the analysis discussed here should be thus considered as a rough approximation of a more accurate experimental procedure.

Process	Acceptance cuts [fb]	Final selection [fb]	Events ( $L = 30 \text{ ab}^{-1}$ )
$h(b\bar{b})h(\gamma\gamma)$ (SM)	0.73	0.40	12061
$bbj\gamma$	132	0.467	13996
$jj\gamma\gamma$	30.1	0.164	4909
$t\bar{t}h(\gamma\gamma)$	1.85	0.163	4883
$b\bar{b}\gamma\gamma$	47.6	0.098	2947
$b\bar{b}h(\gamma\gamma)$	0.098	$7.6 \times 10^{-3}$	227
$bj\gamma\gamma$	3.14	$5.2 \times 10^{-3}$	155
Total background	212	1.30	27118

**Table 29:** Cross section for SM signal and main backgrounds after the acceptance and final cuts of Table 27. The last column shows the number of signal and background events after the final cuts for an integrated luminosity of  $30 \text{ ab}^{-1}$ .

cross section. In fact, the sensitivity to the signal cross section depends mildly on the choice of the cuts (provided they do not vary dramatically). On the contrary, the precision on the Higgs trilinear is much more sensitive to variations of the cuts.

The set of benchmark cuts are listed in Table 27. Mild  $p_T$  cuts are imposed on the photons and  $b$ -quarks, namely  $p_T(b_1), p_T(\gamma_1) > 60 \text{ GeV}$  and  $p_T(b_2), p_T(\gamma_2) > 35 \text{ GeV}$ , where  $b_{1,2}, \gamma_{1,2}$  denote the hardest/softest  $b$ -quark and photon. Stronger cuts are imposed on the transverse momentum of the photon and  $b$  pair,  $p_T(bb), p_T(\gamma\gamma) > 100 \text{ GeV}$ . All the reconstructed objects are required to be within a rapidity  $|\eta_{b,\gamma}| < 4.5$ , while the separation between the two photons and the two  $b$ -quarks is required to be not too large, namely  $\Delta R(bb), \Delta R(\gamma\gamma) < 3.5$ . Notice that the angular cuts imposed on  $\Delta R$  are milder than the ones typically used in the previous literature [179, 203–205]. The invariant mass of the  $b$  pair is required to be in the window  $m_{bb} \in [100, 150] \text{ GeV}$ . For the invariant mass of the photon pair, three different windows are used optimized for each detector performance scenario:  $|m_{\gamma\gamma} - m_h| < 2.0, 2.5, 4.5 \text{ GeV}$  for the “High”, “Medium” and “Low” performance benchmarks respectively. As discussed in Subsection 4.2.2.2, these choices of invariant mass windows allow one to retain a sufficiently large fraction of the signal events.

The signal and background cross sections after the acceptance and final selection cuts are given in Table 29. One can see that the most significant background after all cuts is  $b\bar{b}j\gamma$ , followed by  $jj\gamma\gamma$  and  $t\bar{t}h$ . Another non-negligible contribution comes from the irreducible process  $b\bar{b}\gamma\gamma$ . The backgrounds  $b\bar{b}h$  and  $bj\gamma\gamma$  turn out to be negligible instead.

Notice that other double Higgs production channels, in particular  $t\bar{t}HH$  and VBF, provide an additional contribution to the signal of the order of 10%. Given the high precision on the SM signal rate and on the Higgs trilinear coupling, these contributions should be taken into account in a full experimental analysis. However, the inclusion of these effects is not expected to change significantly the estimated precision on the Higgs trilinear coupling presented in the following.

#### 4.2.2.4 Results

The results in Table 29 suggest that, with an integrated luminosity of  $L = 30 \text{ ab}^{-1}$ , a precision on the SM signal of the order of 1.6% can be obtained, corresponding to  $S/\sqrt{S+B} \simeq 61$ . By a simple rescaling, one can see that already with  $L = 500 \text{ fb}^{-1}$  a 13% determination of the cross section is possible. Notice that these results, as well as those presented in the following, include only the statistical uncertainties and are obtained by neglecting the theoretical error on the prediction of the signal and the systematic uncertainty on the overall determination of the background rates. Anticipating the size of these effects

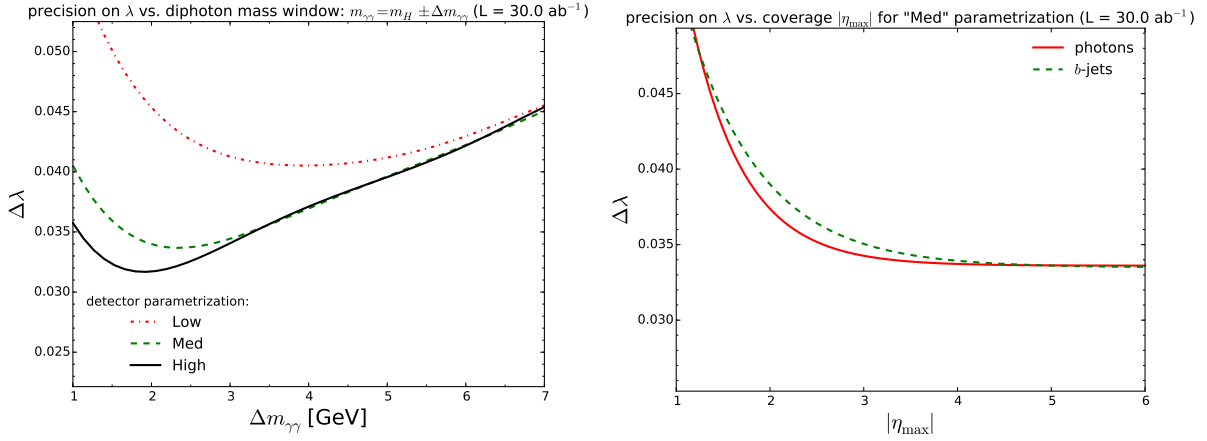


**Fig. 65:** Estimated precision on the measurement of the Higgs trilinear self-coupling. The left panel shows the result as a function of the cut on the invariant mass of the photon pair  $\Delta m_{\gamma\gamma}$  for the three detector benchmark scenarios, “Low” (dot-dashed red), “Medium” (dashed green) and “High” (solid black). In the right panel the result is shown as a function of the cut on the maximal rapidity of the reconstructed objects  $\eta_{\max}$  assuming the “Medium” detector benchmark (the solid red and dashed green curves correspond to a variation of the photon and  $b$ -jets acceptances respectively). All the results have been obtained for an integrated luminosity of  $30 \text{ ab}^{-1}$ .

for a future 100 TeV collider is a difficult task. An estimate of the impact of some of the possible systematic errors and of the geometry and performances of the detector is provided in the following.

As illustrated by the left panel of Fig. 65, a maximal precision on the Higgs trilinear coupling of the order of 3.4% can be obtained in the “Medium” detector performance benchmark. The figure shows that this value crucially depends on the size of the photon invariant mass window used to select the events. If the size of the window is modified, the precision on the Higgs trilinear can be substantially degraded (especially for smaller sizes of the window, which reduce the amount of reconstructed signal events). In the “Low” and “High” scenarios a precision of respectively 4.1% and 3.2% seems to be achievable.

Let us now discuss how the precision changes by varying the most important parameters related to the detector geometry and performances, namely the  $\eta$  coverage, the  $b$ -tagging efficiencies and the photon mis-tagging rate. For this purpose the “Medium” performance scenario will be taken as a reference and each parameter varied separately.

The precision on  $\lambda_3$  is shown in the right panel of Fig. 65 as a function of the maximal rapidity coverage  $\eta_{\max}$  for photons and  $b$ -jets. One can see that extending the coverage beyond  $|\eta_{\max}| \sim 3.5$  does not lead to any substantial improvement. In other words, having a larger coverage in rapidity does not seem a crucial feature for the extraction of the Higgs self coupling, and a reach up to  $|\eta_{\max}| = 2.5 - 3$  could be considered to be an acceptable compromise.

A more crucial role is instead played by the  $b$ -tagging efficiencies and rejection rates, as shown in Fig. 66. The reconstruction efficiency for the  $b$ -jets is the most important parameter, since it directly controls the signal reconstruction rate. A minimal efficiency  $p_{b \rightarrow b} \simeq 0.75$  is necessary to achieve a good precision on the Higgs trilinear coupling. A value  $p_{b \rightarrow b} \simeq 0.6$  already degrades the achievable precision to  $\simeq 4.0\%$ . The mistag rates for charm-jets  $p_{c \rightarrow b}$  plays a marginal role and does not affect too much the precision on  $\lambda_3$  as long as  $p_{c \rightarrow b} \lesssim 0.2$ . The impact of the light-quark and gluon jets mistag rate  $p_{j \rightarrow b}$  is even milder and does not influence the result as long as  $p_{j \rightarrow b} \lesssim 0.05$ . Finally, the lower right panel of Fig. 66 shows how the precision on  $\lambda_3$  changes when the mistag rate of fake photons from jets is modified. The curve is obtained by varying the overall coefficient  $\alpha$  in Eq. (44) (values on the horizontal axis) and keeping fixed the functional dependence on  $p_{T,j}$  with  $\beta = 30 \text{ GeV}$ . One can see that high

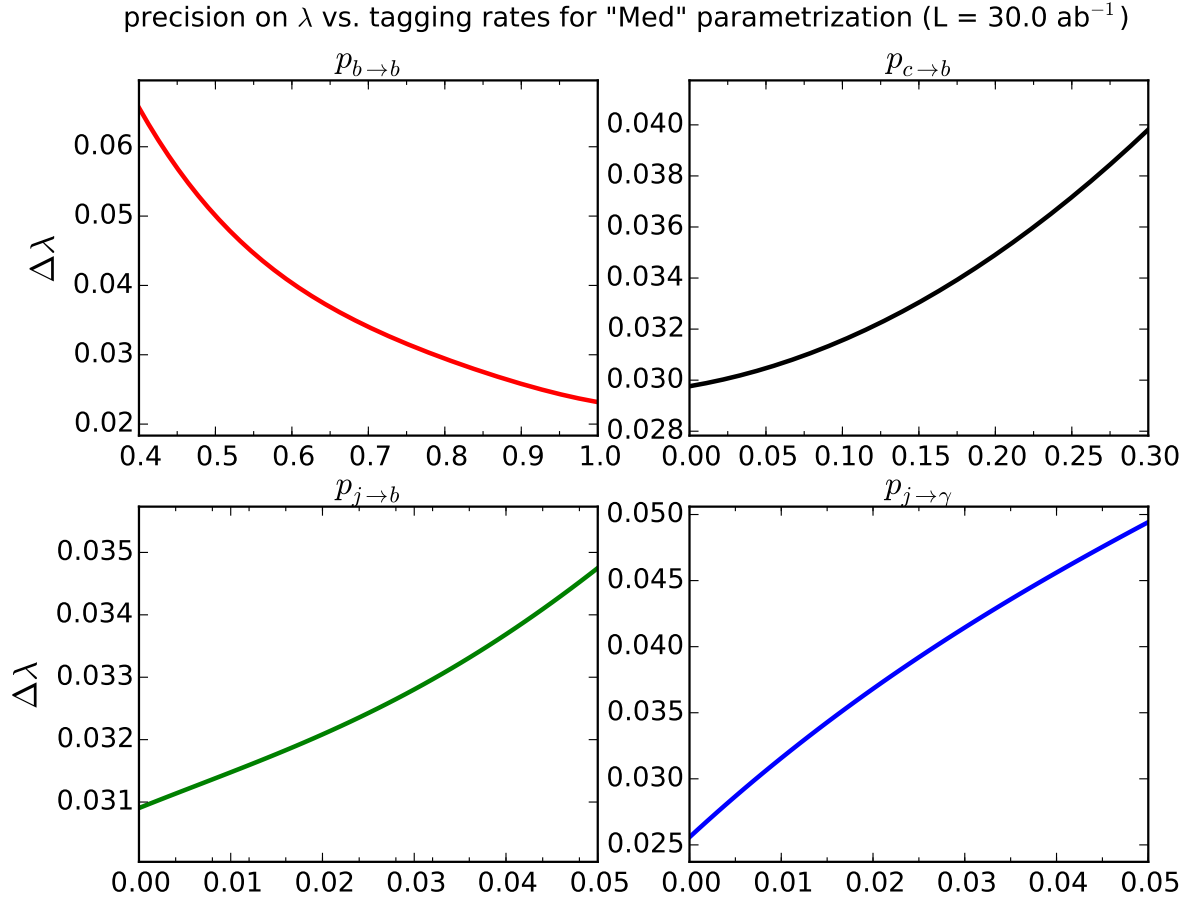


**Fig. 66:** Estimated precision on the measurement of the Higgs trilinear self-coupling as a function of the  $b$ -tagging efficiency. Each plot shows how the precision changes by varying only one parameter, namely the  $b$  reconstruction efficiency  $p_{b \rightarrow b}$  (upper left), the  $c \rightarrow b$  mistag rate (upper right), the  $j \rightarrow b$  mistag rate (lower left) and the  $j \rightarrow \gamma$  mistag rate (lower right). In the case of the  $j \rightarrow \gamma$  mistag, on the horizontal axis we give the coefficient  $\alpha$  of the mistag function in Eq. (44). All the results have been obtained in the “Medium” detector performance scenario with an integrated luminosity of  $30 \text{ ab}^{-1}$ .

mistag rates ( $\alpha \sim 0.05$ ) can significantly affect the achievable precision. This is a consequence of the fact that the main background,  $b\bar{b}j\gamma$ , contains one fake photon from jet mis-tagging. Keeping  $\alpha$  below 0.02 is enough not to affect significantly the precision on  $\lambda_3$ .

To conclude, we briefly comment on the possible impact of the theoretical error on the signal cross section and of the systematic uncertainties on the overall background rate. Table 30 shows how the precision on the Higgs trilinear coupling varies as a function of the relative error on the signal cross section,  $\Delta_S \equiv \Delta\sigma(pp \rightarrow hh)/\sigma(pp \rightarrow hh)$ , and of an overall rescaling of the total background by a factor  $r_B$ . Notice that an actual experimental analysis will most likely extract the background rate directly from the data (by fitting for instance the  $m_{\gamma\gamma}$  distribution away from the Higgs peak, as done for the diphoton channel in single-Higgs production). The rescaling factor  $r_B$  should be thus considered as a way to assess the impact of the error associated with the MonteCarlo calculation of the background rate in Table 29. The actual systematic uncertainty on the background rate in an experimental analysis will likely be much smaller, and possibly negligible. In the limit in which the systematic uncertainty (theory error + pdfs uncertainty) on the signal cross section becomes larger than its statistical error, the precision on the Higgs trilinear measurement saturates to  $\simeq 2\Delta_S$ . Since the statistical error on the signal rate is expected to be small (of the order of 3 – 4%), the systematic uncertainty can easily become the

	$\Delta_S = 0.00$	$\Delta_S = 0.01$	$\Delta_S = 0.015$	$\Delta_S = 0.02$	$\Delta_S = 0.025$
$r_B = 0.5$	2.7%	3.4%	4.1%	4.9%	5.8%
$r_B = 1.0$	3.4%	3.9%	4.6%	5.3%	6.1%
$r_B = 1.5$	3.9%	4.4%	5.0%	5.7%	6.4%
$r_B = 2.0$	4.4%	4.8%	5.4%	6.0%	6.8%
$r_B = 3.0$	5.2%	5.6%	6.0%	6.6%	7.3%

**Table 30:** Impact of the systematic uncertainties on the precision on the trilinear Higgs coupling. The precision on  $\lambda_3$  is shown for different values of the systematic uncertainty on the signal,  $\Delta_S$ , and of the rescaling factor for the total background rate  $r_B$ . The “Medium” detector performance scenario and an integrated luminosity of  $30 \text{ ab}^{-1}$  have been assumed.

main limitation in the extraction of  $\lambda_3$ . At present, as already discussed, the computation of the signal has a  $\sim 10\%$  uncertainty due to the use of the infinite top mass approximation. It is highly probable that finite-mass computations will become available in the near future. The remaining uncertainty from scale variation at NNLL order is still  $\sim 5\%$ , while the pdf error is  $\sim 3\%$ . Without further improvements on these two issues, the systematic uncertainty will be the main limiting factor in the determination of  $\lambda_3$  and the maximal precision would be limited to  $\delta\lambda_3/\lambda_3 \sim 10\%$ .

### 4.2.3 The $HH \rightarrow b\bar{b}b\bar{b}$ channel

In the analysis of the  $b\bar{b}\gamma\gamma$  final state presented in the previous subsection, a large fraction of the double Higgs production cross section was sacrificed in order to select a clean final state, for which the background levels can be easily kept under control. In this subsection a different strategy is considered which makes use of the final state with the largest branching ratio, namely  $b\bar{b}b\bar{b}$ . The total cross section for this final state is 580 fb at a hadronic 100 TeV collider, which is two order of magnitude larger than the  $b\bar{b}\gamma\gamma$  one. The level of backgrounds one needs to cope with, however, is much larger thus severely complicating the signal extraction.

One of the possible advantages of the  $b\bar{b}b\bar{b}$  final state is the fact that it provides a reasonable number of events in the tail at large invariant masses of the Higgs pair. This, in principle, allows one to analyse the high-energy kinematic regime much better than other final states with smaller cross sections. As we discussed before, the tail of the  $m_{hh}$  distribution is not particularly sensitive to the change of the trilinear Higgs coupling, which mostly affects the kinematic distribution at threshold. However it can be more sensitive to other new-physics effects, such as deviations induced by dimension-6 and dimension-8 effective operators that induce a contact interaction between the Higgs and the gluons (see for instance the discussion in Ref. [179]). The analysis of these effects, although interesting and worth studying further, goes beyond the scope of the present report. In the following we will concentrate only on the SM case and on the extraction of the Higgs trilinear coupling and we will discuss an analysis based on a recent feasibility study at the 14 TeV LHC [208],<sup>9</sup> with suitable modifications for the 100 TeV case.

#### 4.2.3.1 Monte Carlo samples generation

Higgs pair production in the gluon-fusion channel is simulated at LO through MadGraph5\_aMC@NLO [123, 201] by using the recently developed functionalities for loop-induced processes [211]. The calculation is performed in the  $n_f = 4$  scheme and the renormalization and factorization scales are taken to be  $\mu_F = \mu_R = H_T/2$ . The NNPDF 3.0  $n_f = 4$  LO set [100] is adopted with  $\alpha_s(m_Z^2) = 0.118$ , interfaced via LHAPDF6 [113]. To achieve the correct higher-order value of the integrated cross-section, the LO signal sample is rescaled to match the NNLO+NNLL inclusive calculation [192, 197]. Parton level

<sup>9</sup>Other studies of Higgs pair production in the same final state at the LHC can be found in Refs. [209, 210].

signal events are then showered with Pythia8 [146, 212] (version v8.201) using the Monash 2013 tune [213], based on the NNPDF2.3LO PDF set [114, 145]. Background samples are generated at LO with SHERPA [65] (v2.1.1) and rescaled to known higher-order results, using the same  $K$ -factors as in [208]. The input PDFs and scales are the same as for the signal samples. In order to keep the analysis simple enough, only the irreducible QCD  $4b$  background is included. This background is one of the most important at the LHC, together with  $b\bar{b}jj$ , and is thus expected to provide a rough estimate of the total background also at 100 TeV. Single Higgs production processes and electroweak backgrounds are much smaller and are also neglected.

#### 4.2.3.2 Analysis strategy

After the parton shower, final state particles are clustered using the jet reconstruction algorithms of FastJet [82, 84] (v3.1.0). First of all, *small- $R$  jets* are reconstructed with the anti- $k_T$  algorithm [83] with  $R = 0.4$ , and required to have transverse momentum  $p_T \geq 40$  GeV and pseudo-rapidity  $|\eta| < 2.5$ . In addition *large- $R$  jets* are defined, reconstructed with anti- $k_T$  with  $R = 1.0$ . These are required to have  $p_T \geq 200$  GeV, lie in the  $|\eta| < 2.0$  region and satisfy the BDRS mass-drop tagger (MDT) [140]. Finally, *small- $R$  subjets* are constructed by clustering all final-state particles with anti- $k_T$  with  $R = 0.3$ , that are then ghost-associated to the large- $R$  jets [214]. These are required to satisfy the condition  $p_T > 50$  GeV and  $|\eta| < 2.5$ . For the boosted and intermediate categories, which involve large- $R$  jets, a number of jet substructure variables [215, 216] are used in the analysis: the  $k_T$ -splitting scale [140, 217], the ratio of 2-to-1 subjettiness  $\tau_{21}$  [218, 219], and the ratios of energy correlation functions (ECFs)  $C_2^{(\beta)}$  [220] and  $D_2^{(\beta)}$  [221].

For each jet definition a different  $b$ -tagging strategy is adopted. A *small- $R$  jet* is tagged as a  $b$ -jet with probability  $f_b$  if it contains at least one  $b$ -quark among its constituents with  $p_T \geq 15$  GeV [222]. If no  $b$ -quarks are found among its constituents, a jet with  $p_T \geq 15$  GeV can be still be tagged as a  $b$ -jet with a mistag rate of  $f_l$  ( $f_c$ ) in the case of a light (charm) jet constituent. *Large- $R$  jets* are  $b$ -tagged by ghost-associating anti- $k_T$   $R = 0.3$  (AKT03) subjets to the original large- $R$  jets [214, 216, 223, 224]. A large- $R$  jet is considered to be  $b$ -tagged if the leading and subleading AKT03 subjets are both individually  $b$ -tagged, with the same criteria as for the small- $R$  jets. The treatment of the  $b$ -jet mis-identification from light and charm jets is the same as for the small- $R$  jets. For the  $b$ -tagging probability  $f_b$ , along with the  $b$ -mistag probability of light ( $f_l$ ) and charm ( $f_c$ ) jets, the following values are used:  $f_b = 0.8$ ,  $f_l = 0.01$  and  $f_c = 0.1$ .

The analysis strategy follows the scale-invariant resonance tagging method of Ref. [225]. Rather than restricting to a specific event topology, it consistently combines the information from three possible topologies: boosted, intermediate and resolved, with the optimal cuts for each category being determined separately. The three categories are defined as follows. Events are classified in the *boosted category* if they contain at least two large- $R$  jets, with the two leading jets being  $b$ -tagged. They are classified in the *intermediate category* if there is exactly one  $b$ -tagged, large- $R$  jet, which is assigned to be the leading Higgs candidate. In addition, at least two  $b$ -tagged small- $R$  jets are required, which must be separated with respect to the large- $R$  jet by  $\Delta R \geq 1.2$ . Finally, events are assigned to the *resolved category* if they contain at least four  $b$ -tagged small- $R$  jets. The two Higgs candidates are reconstructed out of the leading four small- $R$  jets in the event by minimizing the relative difference of dijet masses. In all categories, once a Higgs boson candidate has been identified, its invariant mass is required to lie within a fixed window of width 80 GeV, symmetric around the nominal Higgs boson mass of  $m_h = 125$  GeV. The object and event selection are deliberately loose since their optimization is performed through a Multivariate Analysis (MVA) strategy.

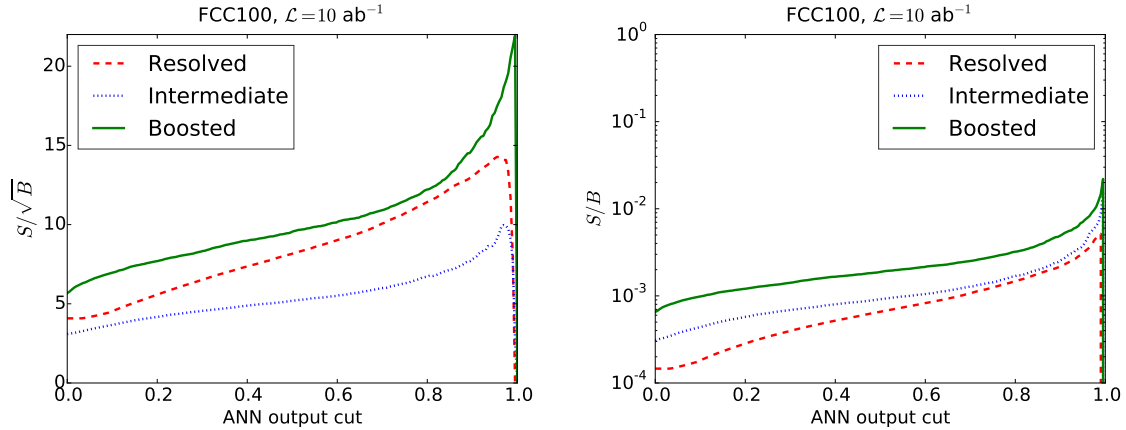


**Fig. 67:** The values of the signal significance,  $S/\sqrt{B}$ , and of the signal over background ratio,  $S/B$ , for the boosted, intermediate and resolved categories as a function of the cut  $y_{\text{cut}}$  in the ANN output. Only the  $4b$  QCD background is considered here. The  $y_{\text{cut}} = 0$  results are those at the end of the cut-based analysis.

Category		$N_{\text{ev}} \text{ signal}$	$N_{\text{ev}} \text{ back}$	$S/\sqrt{B}$	$S/B$
Boosted	$y_{\text{cut}} = 0$	$5 \cdot 10^4$	$8 \cdot 10^7$	6	$6 \cdot 10^{-4}$
	$y_{\text{cut}} = 0.99$	$2 \cdot 10^4$	$1 \cdot 10^6$	22	$2 \cdot 10^{-2}$
Intermediate	$y_{\text{cut}} = 0$	$3 \cdot 10^4$	$1 \cdot 10^8$	3	$3 \cdot 10^{-4}$
	$y_{\text{cut}} = 0.98$	$2 \cdot 10^4$	$2 \cdot 10^6$	10	$7 \cdot 10^{-3}$
Resolved	$y_{\text{cut}} = 0$	$1 \cdot 10^5$	$8 \cdot 10^8$	4	$1 \cdot 10^{-4}$
	$y_{\text{cut}} = 0.95$	$6 \cdot 10^4$	$2 \cdot 10^7$	15	$4 \cdot 10^{-3}$

**Table 31:** Post-MVA results, for the optimal value of the ANN discriminant  $y_{\text{cut}}$  in the three categories, compared with the corresponding pre-MVA results ( $y_{\text{cut}} = 0$ ). We quote the number of signal and background events expected for  $\mathcal{L} = 10 \text{ ab}^{-1}$ , the signal significance  $S/\sqrt{B}$  and the signal over background ratio  $S/B$ . In this table, only the irreducible QCD  $4b$  background has been considered.

#### 4.2.3.3 Results

Following Ref. [208], a preliminary cut-based analysis is performed, followed by a MVA procedure aimed at the optimization of the separation between signal and backgrounds. The specific type of MVA that it is used is a multi-layer feed-forward artificial neural network (ANN), known as *perceptron* or *deep neural network*. The MVA inputs are the set of kinematic variables describing the signal and background events which satisfy the requirements of the cut-based analysis, including the jet substructure variables. The output of the trained ANNs allows for the identification, in a fully automated way, of the most relevant variables for the discrimination between signal and background.

The results for the signal significance  $S/\sqrt{B}$  and the signal-over-background ratio  $S/B$  at a 100 TeV collider are shown in Fig. 67 as a function of the ANN output cut  $y_{\text{cut}}$  for the three categories. A total integrated luminosity of  $\mathcal{L} = 10 \text{ ab}^{-1}$  is assumed, and only the irreducible QCD  $4b$  background is included. The values for  $y_{\text{cut}} = 0$  correspond to those at the end of the loose cut-based analysis. One can observe how in the three categories there is a marked improvement both in signal significance and in the signal over background ratio as compared to the pre-MVA results. In Table 31 the post-MVA results are given for the optimal value of the ANN discriminant  $y_{\text{cut}}$  in the three categories, compared with the corresponding pre-MVA results ( $y_{\text{cut}} = 0$ ). The number of signal and background events expected for an integrated luminosity of  $\mathcal{L} = 10 \text{ ab}^{-1}$  is also quoted.

From Fig. 67 and Table 31 one can observe that the statistical significance of the three categories

is very large, with a post-MVA value of  $S/\sqrt{B} \simeq 20$  in the boosted category. However, one also finds that, as compared to the LHC case, the QCD  $4b$  multijet background increases more rapidly than the signal and thus  $S/B$  is actually smaller than at 14 TeV [208]. Achieving percent values in  $S/B$  requires very hard cuts on the value of the ANN output  $y_{\text{cut}}$ . At 100 TeV the boosted category is the most promising one: not only it benefits from the highest signal significances, it also exhibits the best signal over background ratio. The result is analogous to the one found at 14 TeV [208], where the significance of the three categories was quite similar, with the boosted one being the best without pile-up, and the resolved one exhibiting the higher significance in the simulations with pile-up. Unfortunately, as it was already mentioned and will be further discussed below, the boosted category is the less sensitive to the Higgs self-coupling, and thus a measurement of the trilinear will depend to good extent on the resolved category. The smallness of  $S/B$  indicates that at a 100 TeV collider, even more than at 14 TeV, the feasibility of the measurement of the  $\sigma(hh \rightarrow b\bar{b}b\bar{b})$  cross-section will depend strongly on how small the systematic uncertainties will be, in particular those associated to the background determination.

#### 4.2.3.4 Extracting the Higgs self-coupling.

The extraction of the trilinear coupling  $\lambda_3$  from the corresponding cross-section is complicated by the destructive interference between diagrams that depend on  $\lambda_3$  and those that do not. Here a first estimate is provided of the accuracy on the Higgs self-coupling that can be obtained from the  $b\bar{b}b\bar{b}$  final state. A robust estimate would require a careful study of the impact of experimental systematic uncertainties, which is beyond the scope of this report. Therefore, a number of simplifying assumptions will be used, in particular a very simple estimate of the total systematic uncertainty in the cross-section measurement, which is the limiting factor in the extraction of  $\lambda_3$ .

The sensitivity in the Higgs self-coupling is defined by the  $\chi^2$  estimator

$$\chi^2(\lambda_3) \equiv \frac{[\sigma(hh, \lambda_3) - \sigma(hh, \lambda_{3\text{SM}})]^2}{(\delta_{\text{stat}}\sigma)^2 + (\delta_{\text{sys}}\sigma)^2}, \quad (47)$$

where  $\lambda_3$  is the Higgs self-coupling,  $\lambda_{3\text{SM}} = 1$  is its SM value,  $\sigma(hh, \lambda_3)$  is the post-MVA signal cross-section for a given value of  $\lambda_3$ , and  $\delta_{\text{stat}}\sigma$  and  $\delta_{\text{sys}}\sigma$  are respectively the statistical and systematic uncertainties in the cross-section measurement. Signal samples for a range of  $\lambda_3$  values have been processed by the same analysis chain, including the MVA (which is not re-trained), as for the SM samples. The 68% CL range for the extraction of  $\lambda_3$  is found using the usual parameter-fitting criterion to determine the values  $\pm\delta\lambda_3$  for which the cross-section satisfies

$$\chi^2(\lambda_{3\text{SM}} \pm \delta\lambda_3) = \chi^2(\lambda_{3\text{SM}}) + 1. \quad (48)$$

Figure 68 shows the  $\sigma(hh \rightarrow b\bar{b}b\bar{b})$  cross-section at various steps of the cut-flow: generator level, after kinematical cuts [208], after  $b$ -tagging and finally after the MVA. The results in the resolved (left plot) and boosted (right plot) categories are shown as a function of the Higgs self-coupling  $\lambda_3$ . For the MVA cut, a representative value of  $y_{\text{cut}} \simeq 0.7$  has been used. One finds that, although the MVA is only trained on the SM sample, the signal selection efficiency of the MVA is relatively flat when  $\lambda_3$  is varied, reflecting the fact that the signal kinematics do not change dramatically. From the plots one can also see that the resolved category (low and medium Higgs  $p_T$ ) is more sensitive to variations of  $\lambda$  than the boosted one (large Higgs  $p_T$ ), as indicated by the shallower minimum of the latter after the  $b$ -tagging and MVA cuts. This reflects the fact that the triangle diagram (which depends on the Higgs self-coupling) is dominant near the threshold region.

Imposing the condition Eq. (48), 68% confidence level intervals are derived on the Higgs self-coupling  $\lambda_3$  in the boosted, resolved and intermediate categories, for different assumptions on the total systematic error in the measured cross-section. The ranges that are found are reported in Table 32. As expected, the results depend strongly on the assumption for the systematic uncertainty on the measured

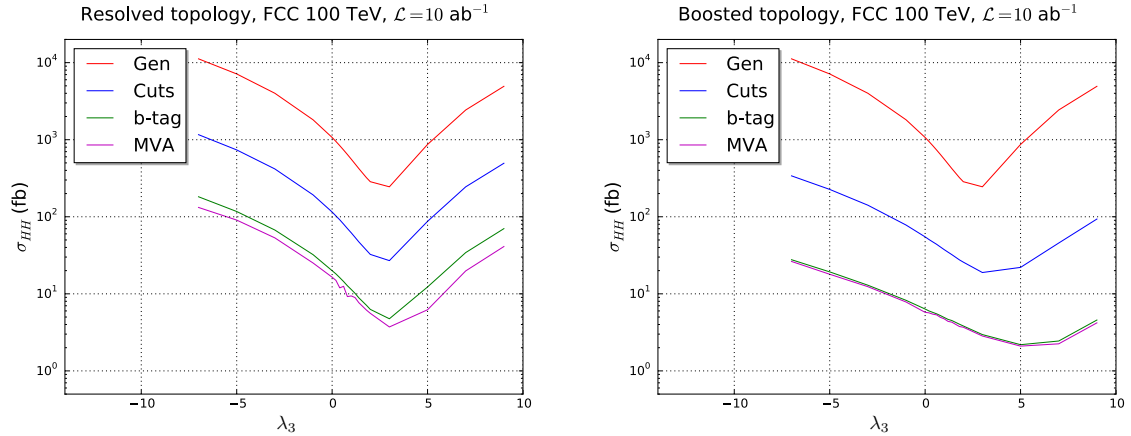


**Fig. 68:** The  $\sigma(hh \rightarrow b\bar{b}b\bar{b})$  cross-section at various steps of the cut-flow: generator level, after kinematical cuts, after  $b$ -tagging and finally after the MVA. We show the results in the resolved (left plot) and boosted (right plot) categories, as a function of the Higgs self-coupling  $\lambda_3$ . For the MVA, a representative value of the ANN output of  $y_{\text{cut}} \simeq 0.7$  has been used in this plot.

cross-section. In the optimistic scenario of a measurement with  $\delta_{\text{sys}}\sigma = 25\%$ , the best performance comes from the resolved category, where at the 68% CL the trilinear can be determined to lie in the interval  $\lambda_3 \in [0.9, 1.5]$ . Looser constraints are derived from the intermediate and from the boosted category. On the other hand, for  $\delta_{\text{sys}}\sigma = 100\%$ , the constraints in all three categories degrade substantially, especially for  $\lambda_3 \geq 1$ , due to the negative interference effects.

	$\delta_{\text{sys}}\sigma = 25\%$	$\delta_{\text{sys}}\sigma = 100\%$
Boosted	$\lambda_3 \in [-0.1, 2.2]$	$\lambda_3 \in [-1.5, > 9]$
Intermediate	$\lambda_3 \in [0.7, 1.6]$	$\lambda_3 \in [-0.4, > 9]$
Resolved	$\lambda_3 \in [0.9, 1.5]$	$\lambda_3 \in [-0.1, 7]$

**Table 32:** The 68% confidence level intervals on the Higgs self-coupling  $\lambda_3$  obtained from the condition Eq. (48) in the boosted, resolved and intermediate categories. We consider two different assumptions on the total systematic error in the measured cross-section,  $\delta_{\text{sys}} = 25\%$  and  $\delta_{\text{sys}} = 100\%$ .

#### 4.2.4 Additional modes with leptons

Due to the considerable increase of the Higgs pair production cross section at 100 TeV, it is conceivable that rare, but potentially cleaner, final states become accessible [226]. This is for instance the case for decay channels including leptons. In the following we will examine the final states containing a pair of  $b$ -jets and 2 or more leptons, namely  $hh \rightarrow (b\bar{b})(ZZ^*) \rightarrow (b\bar{b})(4\ell)$ ,  $hh \rightarrow (b\bar{b})(WW^*)/(\tau^+\tau^-) \rightarrow (b\bar{b})(\ell^+\ell^-)$ ,  $hh \rightarrow (b\bar{b})(\mu^+\mu^-)$  and  $hh \rightarrow (b\bar{b})(Z\gamma) \rightarrow (b\bar{b})(\ell^+\ell^-\gamma)$ .

##### 4.2.4.1 Simulation setup and detector performance

The signal events are generated at LO using the Herwig++ event generator [227, 228] interfaced with the OpenLoops package for the one-loop amplitudes [229, 230]. The backgrounds are generated with the MadGraph 5/aMC@NLO package [123, 231, 232], at NLO QCD. The only exception is the  $t\bar{t}$  background, which is generated at LO and merged with the Herwig++ parton shower using the MLM algorithm, including  $t\bar{t} + 1$  parton matrix elements. For the latter, the cross section is normalized to the total

NLO result. All simulations include modelling of hadronization as well as the underlying event through multiple parton interactions, as they are available in Herwig++. No simulation of additional interacting protons (pile-up) is included in this study. The CT10n1o pdf set [233] is used for all simulations.

The detector effects are included by smearing the momenta of all reconstructed objects and introducing suitable reconstruction efficiencies. The smearing and efficiency parameters for jets and muons are taken from Ref. [234], while for electrons follow Ref. [235]. Jets are reconstructed by using the anti- $k_t$  algorithm available in the FastJet package [82, 84], with a radius parameter  $R = 0.4$ . Only jets with  $p_T > 40$  GeV and  $|\eta| < 3$  are considered in the analysis. The jet-to-lepton mis-identification probability is taken to be  $p_{j \rightarrow \ell} = 0.0048 \times \exp(-0.035 p_{Tj}/\text{GeV})$ , following Ref. [204]. A transverse momentum cut  $p_T > 20$  GeV is applied on all the leptons, which are also required to lie in the pseudorapidity range  $|\eta| < 2.5$ . An isolation criterion is also applied by considering a lepton isolated if it has  $\sum_i p_{T,i}$  less than 15% of its transverse momentum in a cone of  $\Delta R = 0.2$  around it. The tagging of  $b$  jets is simulated by looking for jets containing  $B$ -hadrons in the range  $|\eta| < 2.5$ . The tagging efficiency is assumed to be 70%, with a mis-tagging probability of 1% for light-flavor jets. Mis-tagged  $c$ -jets are not included in the analysis, since their contributions is estimated to be negligible. Finally no smearing is applied to the missing transverse energy.<sup>10</sup>

In addition to the previous parametrization of the detector effects (denoted as ‘LHC’ parametrization in the following), an ‘ideal’ parametrization is also considered obtained by setting all efficiencies to 100% (within the same acceptance regions for jets and leptons) and by removing all momentum smearing effects. The mis-tagging rates for  $b$ -jets, leptons and photon are kept identical in both parametrizations. However, additional backgrounds due to mis-tagging are not particularly important for the channels considered here, provided that they remain at the levels estimated for the high-luminosity LHC.

#### 4.2.4.2 The $hh \rightarrow (b\bar{b})(4\ell)$ channel

At a 100 TeV collider, the cross section for the final state  $hh \rightarrow (b\bar{b})(4\ell)$  increases to about 0.26 fb. The analysis strategy is focused on the reconstruction of all the relevant objects in the hard process, namely the two  $b$ -jets and the 4 leptons. The events are selected by demanding the presence of two pairs of leptons of opposite charge and same flavor, as well as two identified  $b$ -jets. To simulate a possible 4-lepton trigger, the following staggered cuts are imposed on the leptons:  $p_{T,\ell_{\{1,2,3,4\}}} > \{35, 30, 25, 20\}$  GeV.

Since the signal is not expected to possess a large amount of missing transverse energy, a further cut  $\cancel{E}_T < 100$  GeV is imposed. To further reduce the background it is also useful to add a cut on the lepton separations. Since the distance between all leptons in the  $hh$  signal is substantially smaller than in most of the background processes, a cut  $\Delta R(\ell_1, \ell_j) < 1.0$ , with  $j = \{2, 3, 4\}$ , is imposed. The backgrounds coming from processes with multiple  $Z$  bosons can be reduced by rejecting events with two on-shell  $Z$ 's, namely rejecting the event if there are two combinations of same-flavor opposite-sign leptons with an invariant mass  $m_{\ell^+\ell^-} \in [80, 100]$  GeV. No single pair of same-flavor opposite-sign leptons is allowed with a mass above 120 GeV. Finally, the mass windows for the reconstruction of the two Higgs bosons are chosen as

$$M_{b\bar{b}} \in [100, 150] \text{ GeV}, \quad M_{4\ell} \in [110, 140] \text{ GeV}, \quad (50)$$

and no cut on the total invariant mass of all the reconstructed objects is imposed.

After the cuts, the most relevant backgrounds are the ones coming from top pair production in association with an Higgs or a  $Z$  boson. The cross section and event yield of all the analyzed backgrounds

<sup>10</sup>Due to the large cross section, in order to generate the  $t\bar{t}$  samples the following generation-level cuts are applied on the final-state objects  $(\ell^+ b\nu_\ell)(\ell'^- \bar{b}\bar{\nu}_{\ell'})$ :

$$p_{T,b} > 40 \text{ GeV}, \quad p_{T,\ell} > 30 \text{ GeV}, \quad |\eta_\ell| < 2.5, \quad 0.1 < \Delta(b, b), \Delta(\ell, \ell) < 2.0. \quad (49)$$

are listed, together with the signal, in Table 33. For simplicity, only the mis-tagging of a single lepton are considered, with the dominant process in this case being  $W^\pm Zh$ . Processes with multiple mis-tagged leptons are estimated to be totally negligible.

channel	$\sigma(100 \text{ TeV})$ (fb)	$N_{30 \text{ ab}^{-1}}$ (ideal)	$N_{30 \text{ ab}^{-1}}$ (LHC)
$hh \rightarrow (b\bar{b})(\ell^+\ell^-\ell'^+\ell'^-)$	0.26	130	41
$t\bar{t}h \rightarrow (\ell^+b\nu_\ell)(\ell'^-\bar{b}\bar{\nu}_{\ell'}) (2\ell)$	193.6	304	109
$t\bar{t}Z \rightarrow (\ell^+b\nu_\ell)(\ell'^-\bar{b}\bar{\nu}_{\ell'}) (2\ell)$	256.7	66	25
$Zh \rightarrow (b\bar{b})(4\ell)$	2.29	$\mathcal{O}(1)$	$\mathcal{O}(1)$
$ZZZ \rightarrow (4\ell)(b\bar{b})$	0.53	$\mathcal{O}(1)$	$\mathcal{O}(1)$
$b\bar{b}h \rightarrow b\bar{b}(4\ell) \quad (p_{T,b} > 15 \text{ GeV})$	0.26	$\mathcal{O}(10)$	$\mathcal{O}(1)$
$ZZh \rightarrow (4\ell)(b\bar{b})$	0.12	$\mathcal{O}(10^{-2})$	$\mathcal{O}(10^{-2})$
$ZZjj \rightarrow (4\ell) + \text{fake } b\bar{b}$	781.4	$\mathcal{O}(10^{-1})$	$\mathcal{O}(10^{-1})$
$hZjj \rightarrow (4\ell) + \text{fake } b\bar{b}$	68.2	$\mathcal{O}(10^{-2})$	$\mathcal{O}(10^{-2})$
$W^\pm ZZj \rightarrow (\ell\nu_\ell)(\ell^+\ell^-)(b\bar{b}) + \text{fake } \ell$	7.5	$\mathcal{O}(10^{-1})$	$\mathcal{O}(10^{-1})$
$W^\pm Zhj \rightarrow (\ell\nu_\ell)(\ell^+\ell^-)(b\bar{b}) + \text{fake } \ell$	1.4	$\mathcal{O}(10^{-1})$	$\mathcal{O}(10^{-2})$

**Table 33:** Signal and relevant backgrounds for the  $(b\bar{b})(\ell^+\ell^-\ell'^+\ell'^-)$  channel. The second column reports the cross section after the generation cuts (for the  $b\bar{b}h$  channel the additional cut listed in the table is imposed at generation level). The third and fourth columns show the number of events,  $N_{30 \text{ ab}^{-1}}$ , after the cuts for the ‘ideal’ and ‘LHC’ detector parametrizations obtained by assuming an integrated luminosity of  $30 \text{ ab}^{-1}$ .

As a result of the analysis one gets that, for the SM signal in the ideal detector parametrization,  $S/\sqrt{B+S} \simeq 5.8$  (with  $S/B \simeq 0.35$ ). This corresponds to an estimated precision of  $\mathcal{O}(20\%)$  on the SM cross section, which roughly corresponds to a precision of  $\mathcal{O}(30\%)$  on the Higgs trilinear coupling. In the case of the LHC parametrization one instead has  $S/\sqrt{B+S} \simeq 3.1$  (with  $S/B \simeq 0.31$ ), which corresponds to a precision of  $\mathcal{O}(30\%)$  on the SM cross section and of  $\mathcal{O}(40\%)$  on the Higgs trilinear.<sup>11</sup>

#### 4.2.4.3 The $hh \rightarrow (b\bar{b})(\ell^+\ell^-)(+\cancel{E}_T)$ channel

As a second channel we consider the final state that includes a  $b\bar{b}$  and two oppositely-charged leptons. This final state receives contributions from three different  $hh$  decay modes. The largest one comes from  $hh \rightarrow (b\bar{b})(W^+W^-)$  with the  $W$ ’s decaying (either directly, or indirectly through taus) to electrons or muons. The second-largest contribution comes from  $hh \rightarrow (b\bar{b})(\tau^+\tau^-)$ , with both taus decaying to electrons or muons. Both these channels include final-state neutrinos, and hence are associated with large missing energy. A third, smaller contribution comes from  $hh \rightarrow (b\bar{b})(\mu^+\mu^-)$ , i.e. through the direct decay of one Higgs boson to muons.

Due to the different origin of the leptons in the three processes, the kinematics varies substantially. As already mentioned, in  $(b\bar{b})(W^+W^-)$  and  $(b\bar{b})(\tau^+\tau^-)$  large missing energy is expected. In the  $(b\bar{b})(\tau^+\tau^-)$  channel, the  $\tau$  leptons are light compared to the Higgs boson, hence the leptons and the neutrinos in their decays are expected to be collimated. On the contrary, in  $(b\bar{b})(W^+W^-)$  both  $W$ ’s are heavy, one being most of the time on-shell and the other off-shell with  $M_{W^*}$  peaking at  $\sim 40 \text{ GeV}$ . In order to take into account the different kinematics of the various sub-processes, two separate signal regions are constructed. The first aims at capturing events containing rather large missing energy, targeting the  $(b\bar{b})(W^+W^-)$  and  $(b\bar{b})(\tau^+\tau^-)$  channels, whereas the second is aimed towards events with minimal missing energy that are expected to characterize the  $(b\bar{b})(\mu^+\mu^-)$  channel.

The object reconstruction strategy in the two signal regions is similar. Events with two tagged  $b$ -jets and two isolated leptons are considered, with isolation criteria equal to those used in the  $hh \rightarrow$

<sup>11</sup>In order to estimate the precision on the trilinear Higgs coupling  $\lambda_3$  it is assumed that the dependence of the total cross section on  $\lambda_3$  is the same as the one before the cuts.

observable	$\text{SR}_{\cancel{E}}$	$\text{SR}_{\mu}$
$\cancel{E}_T$	$> 100 \text{ GeV}$	$< 40 \text{ GeV}$
$p_{T,\ell_1}$	$> 60 \text{ GeV}$	$> 90 \text{ GeV}$
$p_{T,\ell_2}$	$> 55 \text{ GeV}$	$> 60 \text{ GeV}$
$\Delta R(\ell_1, \ell_2)$	$< 0.9$	$\in (1.0, 1.8)$
$M_{\ell\ell}$	$\in (50, 80) \text{ GeV}$	$\in (120, 130) \text{ GeV}$
$p_{T,b_1}$	$> 90 \text{ GeV}$	$> 90 \text{ GeV}$
$p_{T,b_2}$	$> 80 \text{ GeV}$	$> 80 \text{ GeV}$
$\Delta R(b_1, b_2)$	$\in (0.5, 1.3)$	$\in (0.5, 1.5)$
$M_{bb}$	$\in (110, 140) \text{ GeV}$	$\in (110, 140) \text{ GeV}$
$M_{bb\ell\ell}$	$> 350 \text{ GeV}$	$> 350 \text{ GeV}$
$M_{\text{reco.}}$	$> 600 \text{ GeV}$	none

**Table 34:** Cuts defining the two signal regions constructed in the analysis of the  $hh \rightarrow (\bar{b}b)(\ell^+\ell^-)(+\cancel{E}_T)$  channel. The signal regions  $\text{SR}_{\cancel{E}}$  and  $\text{SR}_{\mu}$  are optimized for the channels with and without missing transverse energy respectively.

$(\bar{b}\bar{b})(4\ell)$  analysis of Subsection 4.2.4.2. In addition to the standard observables characterizing the final state objects, it is useful to introduce a further quantity,  $M_{\text{reco.}}$ , aimed at reconstructing the invariant mass of the Higgs decaying into leptons and neutrinos.  $M_{\text{reco.}}$  is constructed by assuming that the missing energy arising from neutrinos in the decays of the  $\tau$  leptons is collinear to the observed leptons:

$$M_{\text{reco.}} = [p_{b_1} + p_{b_2} + (1 + f_1)p_{\ell_1} + (1 + f_2)p_{\ell_2}]^2, \quad (51)$$

where  $p_{b_i}, p_{\ell_i}$  are the observed momenta of the  $i$ -th  $b$ -jet and  $i$ -th lepton and  $f_{1,2}$  are constants of proportionality between the neutrino and lepton momenta from the decay of the two  $\tau$  leptons, namely  $p_{\nu_i} = f_i p_{\ell_i}$ . The latter can be calculated from the observed missing transverse energy by inverting the missing transverse momentum balance relation  $L \cdot \mathbf{f} = \cancel{E}$ , where  $L$  is the matrix  $L_i^j = p_{\ell_i}^j$ , in which the superscript denotes the component of the  $i$ -th lepton momentum,  $j = \{x, y\}$  and  $E$  and  $\mathbf{f}$  are the vectors  $\cancel{E} = (\cancel{E}^x, \cancel{E}^y)$  and  $\mathbf{f} = (f_1, f_2)$ .

The two signal regions are denoted by  $\text{SR}_{\cancel{E}}$  and  $\text{SR}_{\mu}$ . The former is optimized for a signal with significant missing transverse energy and is aimed at the decay modes  $(\bar{b}\bar{b})(W^+W^-)$ ,  $(\bar{b}\bar{b})(\tau^+\tau^-)$ . The second region  $\text{SR}_{\mu}$  is instead focused on events with minimal missing energy, as in the  $(\bar{b}\bar{b})(\mu^+\mu^-)$  channel. The cuts defining the two signal regions are listed in Table 34.

The main irreducible backgrounds for the  $(\bar{b}\bar{b})(\ell^+\ell^-)(+\cancel{E}_T)$  final state include the following processes:  $t\bar{t}$  with subsequent semi-leptonic decays of both top quarks;  $\bar{b}\bar{b}Z$  with decays of the  $Z$  boson to leptons;  $\bar{b}\bar{b}h$  with subsequent decays of the Higgs boson to two leptons; and the resonant  $hZ$  and  $ZZ$  backgrounds. The two largest reducible backgrounds are also considered, coming from the mis-tagging of a jet to a single lepton in the  $\bar{b}\bar{b}W^\pm$  channel and the mis-tagging of a  $\bar{b}\bar{b}$  pair in the  $\ell^+\ell^- + \text{jets}$  background.<sup>12</sup> As before, no mis-identification of  $c$ -jets to  $b$ -jets is included.

The signal and background cross section are shown in Table 35, where the expected number of signal and background events in the signal region  $\text{SR}_{\cancel{E}}$  is also reported for the ‘LHC’ and the ‘ideal’ detector parametrizations. Notice that, since the same set of cuts is used for both parametrizations, the ‘ideal’ case does not necessarily provide a substantial improvement in the signal efficiency. This happens in particular for the  $(\bar{b}\bar{b})(W^+W^-)$  sample. The high signal yield in this channel allows one to determine the SM-like  $hh$  production with fair accuracy. In the ‘ideal’ case, with  $30 \text{ ab}^{-1}$  integrated luminosity, a

<sup>12</sup>This last background has been estimated by simulating  $\ell^+\ell^- + 1$  parton at NLO.

channel	$\sigma(100 \text{ TeV}) \text{ (fb)}$	$N_{30 \text{ ab}^{-1}} \text{ (ideal)}$	$N_{30 \text{ ab}^{-1}} \text{ (LHC)}$
$hh \rightarrow (b\bar{b})(W^+W^-) \rightarrow (b\bar{b})(\ell^+\nu_{\ell'}\ell^-\bar{\nu}_{\ell'})$	27.16	209	199
$hh \rightarrow (b\bar{b})(\tau^+\tau^-) \rightarrow (b\bar{b})(\ell^+\nu_{\ell'}\bar{\nu}_{\tau}\ell^-\bar{\nu}_{\ell'}\nu_{\tau})$	14.63	385	243
$t\bar{t} \rightarrow (\ell^+b\nu_{\ell})(\ell'^-\bar{b}\bar{\nu}_{\ell'})$ (cuts as in Eq. 49)	$25.08 \times 10^3$	$343_{-94}^{+232}$	$158_{-48}^{+153}$
$b\bar{b}Z \rightarrow b\bar{b}(\ell^+\ell^-)$ ( $p_{T,b} > 30 \text{ GeV}$ )	$107.36 \times 10^3$	$2580_{-750}^{+2040}$	$4940_{-1130}^{+2250}$
$ZZ \rightarrow b\bar{b}(\ell^+\ell^-)$	356.0	$\mathcal{O}(1)$	$\mathcal{O}(1)$
$hZ \rightarrow b\bar{b}(\ell^+\ell^-)$	99.79	498	404
$b\bar{b}h \rightarrow b\bar{b}(\ell^+\ell^-)$ ( $p_{T,b} > 30 \text{ GeV}$ )	26.81	$\mathcal{O}(10)$	$\mathcal{O}(10)$
$b\bar{b}W^{\pm} \rightarrow b\bar{b}(\ell^{\pm}\nu_{\ell}) + \text{fake } \ell$ ( $p_{T,b} > 30 \text{ GeV}$ )	1032.6	$\mathcal{O}(10^{-1})$	$\mathcal{O}(10^{-1})$
$\ell^+\ell^- + \text{jets} \rightarrow (\ell^+\ell^-) + \text{fake } b\bar{b}$	$2.14 \times 10^3$	$\mathcal{O}(10^{-1})$	$\mathcal{O}(10^{-1})$

**Table 35:** Signal and background cross sections for the  $(b\bar{b})(\ell^+\ell^- + \cancel{E})$  channel. Due to the limited MonteCarlo statistics, the estimated number of events for the  $t\bar{t}$  and  $b\bar{b}Z$  backgrounds has a rather limited precision (the  $1\sigma$  interval is given in the table together with the central value).

channel	$\sigma(100 \text{ TeV}) \text{ (fb)}$	$N_{30 \text{ ab}^{-1}} \text{ (ideal)}$	$N_{30 \text{ ab}^{-1}} \text{ (LHC)}$
$hh \rightarrow (b\bar{b})(\mu^+\mu^-)$	0.42	86	18
$t\bar{t} \rightarrow (\ell^+b\nu_{\ell})(\ell'^-\bar{b}\bar{\nu}_{\ell'})$ (cuts as in Eq. 49)	$25.08 \times 10^3$	$480_{-140}^{+1100}$	$158_{-48}^{+150}$
$b\bar{b}Z \rightarrow b\bar{b}(\ell^+\ell^-)$ ( $p_{T,b} > 30 \text{ GeV}$ )	$107.36 \times 10^3$	$< 740$	$490_{-140}^{+1130}$
$ZZ \rightarrow b\bar{b}(\ell^+\ell^-)$	356.0	$\mathcal{O}(1)$	$\mathcal{O}(1)$
$hZ \rightarrow b\bar{b}(\ell^+\ell^-)$	99.79	$\mathcal{O}(1)$	25
$b\bar{b}h \rightarrow b\bar{b}(\ell^+\ell^-)$ ( $p_{T,b} > 30 \text{ GeV}$ )	26.81	$\mathcal{O}(10)$	$\mathcal{O}(10)$
$b\bar{b}W^{\pm} \rightarrow b\bar{b}(\ell^{\pm}\nu_{\ell}) + \text{fake } \ell$ ( $p_{T,b} > 30 \text{ GeV}$ )	1032.6	$\mathcal{O}(10^{-1})$	$\mathcal{O}(10^{-1})$
$\ell^+\ell^- + \text{jets} \rightarrow (\ell^+\ell^-) + \text{fake } b\bar{b}$	$2.14 \times 10^3$	$\mathcal{O}(10^{-1})$	$\mathcal{O}(10^{-1})$

**Table 36:** Signal and background cross sections for the  $(b\bar{b})(\mu^+\mu^-)$  channel. Due to the limited MonteCarlo statistics, the estimated number of events for the  $t\bar{t}$  and  $b\bar{b}Z$  backgrounds has a rather limited precision. The  $1\sigma$  interval is given in the table together with the central value. For the case of  $b\bar{b}Z$  in the ‘ideal’ parametrization, we list the  $1\sigma$ -equivalent region, since no events were left after the cuts.

large statistical significance  $S/\sqrt{B+S} \sim 9.4$  is expected with  $S/B \sim 0.17$ , allowing a determination of the total SM cross section with a precision of  $\mathcal{O}(10\%)$ . This corresponds to an estimated precision on the Higgs trilinear coupling of  $\mathcal{O}(10\%)$ . In the ‘LHC’ parametrization, the statistical significance remains fairly high,  $S/\sqrt{B+S} \sim 5.7$  with  $S/B \sim 0.08$ , leading to a precision of  $\mathcal{O}(20\%)$  on the SM cross section and  $\mathcal{O}(20\%)$  on the Higgs trilinear.

On the other hand, the prospects for the  $(b\bar{b})(\mu^+\mu^-)$  channel after the  $\text{SR}_{\mu}$  cuts are applied are rather bleak: with  $30 \text{ ab}^{-1}$  of integrated luminosity, only a handful of events are expected with the ‘LHC’ detector parametrization with a few hundred background events, even imposing hard transverse momentum cuts on the muons and a tight mass window on the di-muon invariant mass around the Higgs boson mass. Because of the latter cut, turning to the ‘ideal’ situation improves the signal efficiency substantially, since the smearing of the muon momenta is absent. Despite this, only  $\mathcal{O}(80)$  events would be obtained with  $30 \text{ ab}^{-1}$  integrated luminosity with a similar number of background events as for the ‘LHC’ parametrization. Hence, barring any significant enhancements of the rate due to new physics, the  $(b\bar{b})(\mu^+\mu^-)$  contribution to the  $hh \rightarrow (b\bar{b})(\ell^+\ell^-)$  final state is not expected to provide significant information.

#### 4.2.4.4 The $hh \rightarrow (b\bar{b})(\ell^+\ell^-\gamma)$ channel

The  $hh \rightarrow (b\bar{b})(\ell^+\ell^-\gamma)$  channel in the SM has a cross section  $\sigma_{SM} \simeq 0.21$  fb, only slightly lower than the  $hh \rightarrow (b\bar{b})(4\ell)$  one. The backgrounds are, however, substantially larger. An estimate of the relevance of this channel can be obtained by including only the most significant irreducible backgrounds, namely those from  $b\bar{b}Z\gamma$ ,  $t\bar{t}\gamma$ , and  $hZ\gamma$ , as well as the dominant reducible ones, where a photon is mis-tagged in  $b\bar{b}Z$  or  $t\bar{t}$  production.

Events are selected by requiring two leptons of the same flavor with  $p_{T,\ell_{\{1,2\}}} > \{40, 35\}$  GeV, two anti- $k_t$   $R = 0.4$   $b$ -jets with  $p_{T,b_{\{1,2\}}} > \{60, 40\}$  GeV,  $\cancel{E}_T < 80$  GeV and a photon with  $p_{T,\gamma} > 40$  GeV. No isolation requirements are imposed on the photon. The additional cuts are imposed:  $\Delta R(\ell_1, \ell_2) < 1.8$ ,  $\Delta R(\ell_1, \gamma) < 1.5$  and  $0.5 < \Delta R(b_1, b_2) < 2.0$ . The invariant mass of the  $b$ -jet pair is required to be in the range  $100 < M_{b\bar{b}} < 150$  GeV, while the system of the two leptons and the photon must have an invariant mass lying in the range  $100 \text{ GeV} < M_{\ell^+\ell^-\gamma} < 150 \text{ GeV}$ .

Even after these cuts, the  $b\bar{b}Z\gamma$  background dominates the final sample, giving a signal-to-background ratio of  $\mathcal{O}(0.02 - 0.03)$  with only  $\mathcal{O}(100)$  signal events with  $30 \text{ ab}^{-1}$  integrated luminosity. Therefore, this channel is not expected to provide significant information on the double Higgs production process at a 100 TeV pp collider, unless a significant alteration of the  $hh$  channel is present due to new physics effects.

### 4.3 Triple Higgs production and the quartic Higgs self-coupling

In this section we discuss the prospects for the measurement of the triple-Higgs production process. The main relevance of this channel lies in the possibility of directly accessing the quadrilinear Higgs self-coupling. The very small production cross section, however, makes the measurement of  $\lambda_4$  extremely challenging.

Early work on triple-Higgs production showed that lepton colliders can not access this channel. For instance, at an  $e^+e^-$  machine with a center-of-mass energy of  $\sqrt{s} = 1$  TeV, the cross section of the process  $e^+e^- \rightarrow ZHHH$  is only 0.4 ab [236], leading to just 1.2 signal events when assuming the designed integrated luminosity of  $3 \text{ ab}^{-1}$ .

The situation can instead be more favorable at high-energy hadron colliders. In this case the main production channel is gluon fusion, while production modes in association with a gauge bosons, namely  $WHHH + X$  and  $ZHHH + X$ , have a negligible cross section [237]. At the 14 TeV LHC the total SM production cross section is of the order of 0.1 fb [201, 238, 239], which is too small to be observed with the current designed luminosity. On the other hand, at a 100 TeV hadron collider, similarly to what happens for double-Higgs production, the gluon fusion cross section increases by almost two orders of magnitude with respect to the LHC value, reaching about 5 fb (see Table 25). This leads to a reasonable amount of signal events to perform a dedicated analysis.

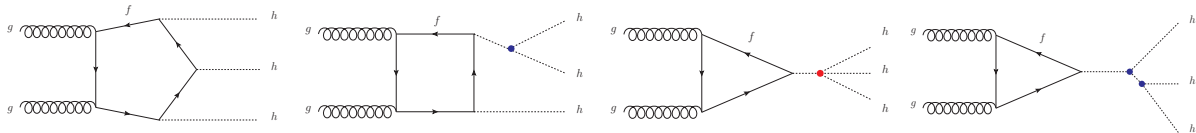


**Fig. 69:** Example Feynman diagrams contributing to Higgs boson triple production via gluon fusion in the Standard Model. The vertices highlighted with blobs indicate either triple (blue) or quartic (red) self-coupling contributions.

The main diagrams contributing to the gluon fusion channel are shown in Fig. 69. It turns out that, exactly as in the double-Higgs process, the main contribution to the amplitude comes from the diagrams that do not contain the multi-Higgs interactions, namely the pentagon ones. The diagrams with a trilinear and a quadrilinear Higgs coupling, on the other hand, are significantly suppressed. The dependence of the total cross section on the Higgs self couplings is thus expected to be quite mild. This expectation

is indeed confirmed by Fig. 70, which shows the total cross section as a function of the Higgs quartic coupling. A modification of the Higgs quartic self-coupling has also a marginal impact on the kinematic distributions, as shown in Fig. 71. These results suggest that the extraction of the  $\lambda_4$  coupling is a very challenging task, and can be problematic unless the triple-Higgs production channel can be measured with quite good accuracy.

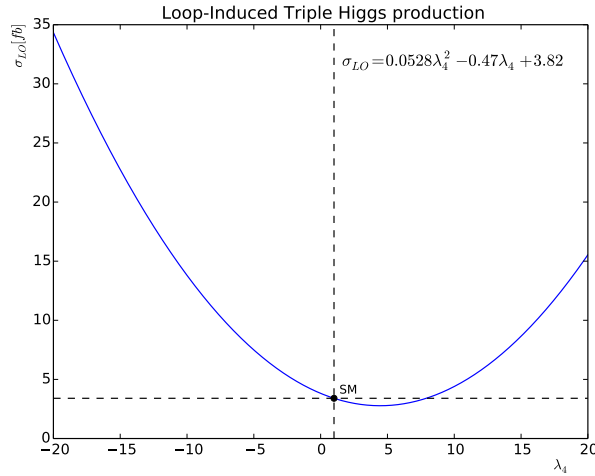


**Fig. 70:** Inclusive LO cross-section for  $gg \rightarrow HHH$  as a function of the  $\lambda_4$  parameter. Details on the computation can be found in Ref. [240].

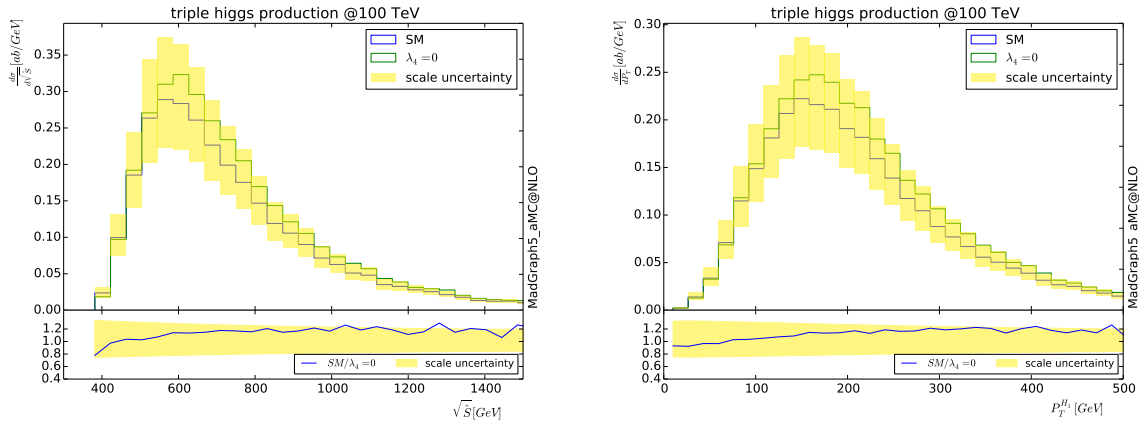


**Fig. 71:** Dependence of the differential cross-section for the triple Higgs production channel on the Higgs quartic self-coupling. The left and right panels show the  $\sqrt{s}$  and  $p_T^{H_1}$  distributions for the benchmark points  $\lambda_4 = 1$  (SM) and  $\lambda_4 = 0$ .

One of the most promising decay channel to observe the triple-Higgs production process is  $pp \rightarrow HHH \rightarrow b\bar{b}b\bar{b}\gamma\gamma$ . This channel combines a clear enough final state, which can be used discriminate the signal against the various backgrounds, and a relatively large cross section. In the following subsections we will describe the three analyses of Refs. [240–242], which focus on scenarios with different  $b$ -tagging efficiency, namely 60%, 70% and 80%. The 60%  $b$ -tagging benchmark can be considered as a pessimistic scenario since it assumes the current  $b$ -tagging working point at the LHC. The other two analyses, on the other hand, give an idea of how much the prospects for measuring triple-Higgs production can improve with a higher detector performance.

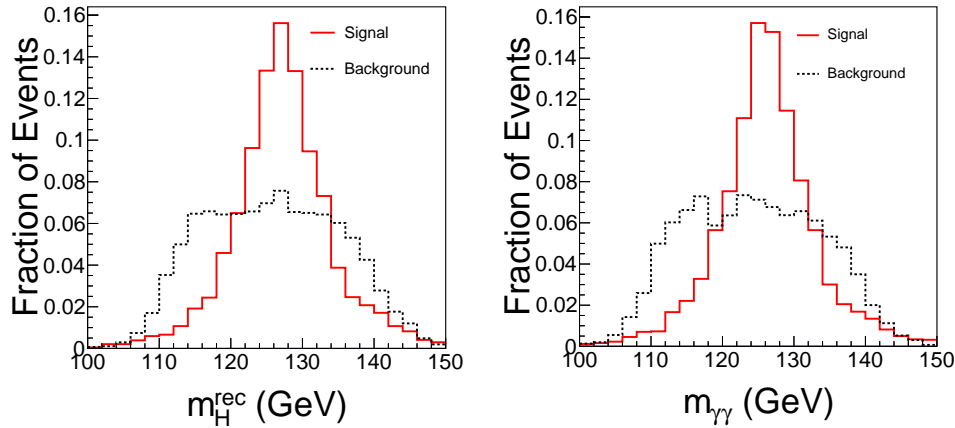


**Fig. 72:** Distributions of the reconstructed Higgs mass  $m_H^{rec}$  and invariant mass of the di-photon system  $m_{\gamma\gamma}$  for the signal and background events.

#### 4.3.1 Pessimistic hypothesis: 60% $b$ -tagging efficiency

Let us first consider a “pessimistic” scenario in which the  $b$ -tagging efficiency is 60% [240]. The signal events are generated at LO (using the MadLoop/aMC@NLO [243] and GoSam [64] packages) and the NLO effects are taken into account through a rescaling by a  $k$ -factor  $k = 2$ . Two types of backgrounds are considered, namely  $pp \rightarrow b\bar{b}jj\gamma\gamma$  and  $pp \rightarrow Ht\bar{t}$ . Parton shower and hadronization effects for the signal events are also included by using PYTHIA [110, 146], while detector effects are taken into account through DELPHES 3.0 [147, 244]. In all the simulations the PDF set CTEQ6L1 [245] is used.

Jets are clustered using the anti- $k_t$  algorithm [83] as implemented in FASTJET [84] with a cone of radius  $R = 0.5$  and minimum  $p_T(j) = 30$  GeV. For photon identification, the maximum reconstruction efficiency is assumed to be 95%, for transverse momentum  $p_T(\gamma) > 10$  GeV and rapidity  $|\eta(\gamma)| \leq 2.5$ , whereas it decreases to 85% for  $2.5 < |\eta(\gamma)| \leq 5.0$ . Pile-up effects are neglected. The  $b$ -tagging procedure is implemented by mimicking the 60%  $b$ -jet efficiency LHC working point. The (mis-)tagging efficiencies vary as a function of the transverse momentum  $p_T$  and rapidity  $\eta$  of the jets. For a transverse momentum of  $p_T(j) = 120$  GeV, the  $b$ -tagging efficiencies for ( $b$ ,  $c$ , light) jets are (0.6, 0.1, 0.001), while they drop to (0.28, 0.046, 0.001) at  $p_T(j) = 30$  GeV.

In order to suppress the large background and select the most relevant events, several preselection cuts are introduced.

1. Only events with 4 or 5 jets are considered, including at least 2 tagged  $b$ -jets. The transverse momenta of the jets are required to be  $p_T(j) > 30$  GeV.
2. The events are required to contain exactly 2 isolated photons with  $p_T(\gamma) > 30$  GeV.
3. The total number of jets reconstructed by the detector is required to be  $\leq 5$  (this cut aims at suppressing the  $pp \rightarrow t\bar{t}H$  background with fully hadronic  $t\bar{t}$  decays, where  $t \rightarrow bW^+$ ).
4. Events with MET  $> 50$  GeV are vetoed (this cut aims at decreasing the  $pp \rightarrow t\bar{t}H$  background).

In order to cope with the combinatoric issues, a “Higgs reconstructed mass”  $m_H^{rec}$  is constructed by considering all possible jet pairings and selecting the permutation that minimizes the  $\chi$ -squared fit to three decaying particles with a mass  $m_H^{rec}$ . Events with large  $\chi$ -square ( $\chi^2 > 6.1$ ) are discarded. The reconstructed Higgs mass is then required to be in the window  $|m_H^{rec} - 126 \text{ GeV}| < 5.1 \text{ GeV}$ . A similar chi-square technique [246] is used to look for the presence of a top final state and reject those type of events. The distribution of the reconstructed mass  $m_H^{rec}$  and of the photons invariant mass  $m_{\gamma\gamma}$  is shown in Fig. 72 for the signal and backgrounds events.

	Signal	$b\bar{b}jj\gamma\gamma$	$Ht\bar{t}$	$S/B$	$S/\sqrt{B}$
preselection	50	$2.3 \times 10^5$	$2.2 \times 10^4$	$2.5 \times 10^{-4}$	0.14
$\chi^2_{H,min} < 6.1$	26	$4.6 \times 10^4$	$9.9 \times 10^3$	$5.0 \times 10^{-4}$	0.14
$ m_H^{rec} - 126 \text{ GeV}  < 5.1 \text{ GeV}$	20	$1.7 \times 10^4$	$7.0 \times 10^3$	$8.1 \times 10^{-4}$	0.15

**Table 37:** Signal sensitivity in the “pessimistic” scenario after each group of selection cuts is imposed. The integrated luminosity is assumed to be  $30 \text{ ab}^{-1}$ .

The impact of the various cuts listed before is shown in Table 37. The ratio  $S/B$  can be enhanced by almost one order of magnitude, but the signal significance  $S/\sqrt{S+B} \simeq 0.15$  remains quite poor. The small size of the signal cross section, combined with the smearing induced by the finite detector resolution, prevents an efficient suppression of the background. More sophisticated analysis strategies (multivariate approaches and boosted decision trees) or the variation of the number of tagged  $b$ -jets do not substantially modify the results and only allow a marginal improvement in the signal significance. With such low sensitivity and weak dependence of the cross-section on the Higgs quartic self-coupling, the analysis considered in this subsection is expected to lead to a determination of  $\lambda_4$  in the range  $[-20, 30]$  with an integrated luminosity of  $30 \text{ ab}^{-1}$ .

### 4.3.2 Intermediate hypothesis: 70% $b$ -tagging efficiency

The second scenario considered is an “intermediate” one in which the  $b$ -tagging efficiency is assumed to be 70% [242]. For this analysis the signal and background events are generated by convoluting the LO hard-scattering matrix elements (calculated by MADGRAPH5\_AMC@NLO) with the NNPDF 2.3 set of parton densities [114]. To take into account NLO effects the background samples are conservatively rescaled by including a  $k$ -factor of 2. All generated final-state particles are required to have a transverse-momentum  $p_T > 15 \text{ GeV}$ , a pseudorapidity  $|\eta| < 5$  and to be isolated from each other by an angular distance, in the transverse plane, of  $\Delta R > 0.4$ . Parton shower, hadronization, underlying event and pile-up effects are not included. Detector effects are taken into account by including generic reconstruction features based on the ATLAS detector performances, namely a smearing of the momentum and energy of the photons and jets [235, 247]. In particular, photons can be remarkably well reconstructed with a resolution that only weakly depends on the energy. One consequently expects that a relatively narrow peak, centered on the true Higgs-boson mass value, will emerge in the diphoton invariant-mass spectrum. As already mentioned, the  $b$ -tagging efficiency is assumed to be 70% and the related mistagging rates for a  $c$ -jet and a light jet are taken to be 18% and 1% respectively [248].

Events are preselected by demanding that they contain at least four central jets and exactly two central photons with  $|\eta| < 2.5$ . The transverse momenta of the four leading jets are required to be greater than 50, 30, 20 and 15 GeV, and the ones of the two photons to satisfy  $p_T^{\gamma_1} > 35 \text{ GeV}$  and  $p_T^{\gamma_2} > 15 \text{ GeV}$ . In order to reduce the signal contamination from jets misidentified as photons, isolation constraints on the photons are imposed, namely the transverse energy lying in a cone of radius  $R = 0.3$  centered on each photon is required to be smaller than 6 GeV [249]. After the preselection, the two Higgs bosons originating from the four jets are reconstructed and their invariant masses  $m_{jjk}$  (with  $k = 1, 2$ ) are required to satisfy  $|m_h - m_{jjk}| < 15 \text{ GeV}$ . In order to solve possible combinatorics issues, the correct two dijet systems are selected as the combination of jets that minimizes the mass asymmetry

$$\Delta_{jj_1, jj_2} = \frac{m_{jj_1} - m_{jj_2}}{m_{jj_1} + m_{jj_2}}. \quad (52)$$

The third Higgs boson is reconstructed from the diphoton system whose invariant mass  $m_{\gamma\gamma}$  is required to be in a window  $|m_h - m_{\gamma\gamma}| < M$  with  $M \in [1, 5] \text{ GeV}$ . For the minimal number of  $b$ -tagged jets,

Selection step	Signal	$\gamma\gamma b\bar{b}jj$	$\gamma\gamma Z_{bb}jj$	$\gamma\gamma t\bar{t}$	Significance
Preselection	2.6 ab	$4.2 \times 10^6$ ab	$5.3 \times 10^4$ ab	$1.1 \times 10^5$ ab	$6 \times 10^{-3} \sigma$
$ m_h - m_{jj1,2}  < 15$ GeV	2.0 ab	$1.7 \times 10^5$ ab	$1.8 \times 10^3$ ab	$1.1 \times 10^4$ ab	$0.021 \sigma$
$ m_h - m_{\gamma\gamma}  < 5$ GeV	2.0 ab	$6.9 \times 10^3$ ab	68 ab	500 ab	$0.1 \sigma$
$m_{jjjj} < 600$ GeV	1.7 ab	$6.9 \times 10^3$ ab	68 ab	280 ab	$0.089 \sigma$
$N_b^{\min} = 2$	1.4 ab	$1.3 \times 10^3$ ab	27 ab	74 ab	$0.17 \sigma$
$N_b^{\min} = 3$	1.1 ab	160 ab	3.5 ab	12 ab	$0.37 \sigma$
$N_b^{\min} = 4$	0.42 ab	1.3 ab	0.27 ab	0.26 ab	$1.3 \sigma$
$ m_h - m_{\gamma\gamma}  < 2$ GeV	2.0 ab	$2.9 \times 10^3$ ab	34 ab	210 ab	$0.16 \sigma$
$m_{jjjj} < 600$ GeV	1.7 ab	$2.9 \times 10^3$ ab	34 ab	120 ab	$0.14 \sigma$
$N_b^{\min} = 2$	1.3 ab	890 ab	17 ab	25 ab	$0.19 \sigma$
$N_b^{\min} = 3$	1.1 ab	76 ab	0.33 ab	5.2 ab	$0.54 \sigma$
$N_b^{\min} = 4$	0.40 ab	0.62 ab	$1.7 \times 10^{-3}$ ab	0.15 ab	$1.7 \sigma$
$ m_h - m_{\gamma\gamma}  < 1$ GeV	1.5 ab	$1.2 \times 10^3$ ab	34 ab	94 ab	$0.18 \sigma$
$m_{jjjj} < 600$ GeV	1.3 ab	$1.2 \times 10^3$ ab	34 ab	54 ab	$0.16 \sigma$
$N_b^{\min} = 2$	1.0 ab	590 ab	17 ab	17 ab	$0.18 \sigma$
$N_b^{\min} = 3$	0.84 ab	59 ab	0.33 ab	1.7 ab	$0.48 \sigma$
$N_b^{\min} = 4$	0.31 ab	0.54 ab	$1.7 \times 10^{-3}$ ab	0.065 ab	$1.5 \sigma$

**Table 38:** Effects of the selection strategy in the “intermediate” analysis for the SM case. The signal and background cross sections after each of the selection steps is shown. The last column shows the signal significance computed for a luminosity  $20 \text{ ab}^{-1}$ .

$N_b^{\min}$ , different options are considered, namely  $N_b^{\min} \in [2, 4]$ . Finally the invariant mass of the four-jet system is required to be smaller than 600 GeV. This cut has the advantage of significantly reducing the  $\gamma\gamma t\bar{t}$  background without affecting the signal since jets arising from a top quark decay are generally harder. As a result, the dominant sources of background consist of  $\gamma\gamma b\bar{b}jj$ ,  $\gamma\gamma Z(\rightarrow bb)jj$  and  $\gamma\gamma t\bar{t}$ .<sup>13</sup>

The effects of the selection strategy for the SM case are shown in Table 38. In the table the results are given for different choices of the diphoton invariant-mass resolution  $M$  and of the minimum number of required  $b$ -tagged jets  $N_b^{\min}$ . For all  $M$  values, a requirement of four  $b$ -tagged jets is needed in order to achieve a fair sensitivity to the signal. With this choice a significance around  $1.7 \sigma$  can be obtained. The signal significance  $\sigma$  as a function of the Higgs trilinear and quartic self-couplings is shown in Fig. 73 for a luminosity of  $20 \text{ ab}^{-1}$ . In the figure two benchmarks with  $M = 5$  GeV and  $M = 2$  GeV are shown. In both benchmarks 4 tagged  $b$ -jets are required, since this choice maximizes the significance.<sup>14</sup>

A strong dependence on the Higgs trilinear coupling  $\kappa_3 \equiv \lambda_3 - 1$  is found due to the jet and photon  $p_T$  distributions that are harder when  $\kappa_3$  is large and positive, while the analysis turns out to be less sensitive to the quartic Higgs coupling  $\kappa_4 \equiv \lambda_4 - 1$ . For the benchmark value  $M = 2$  GeV,  $N_b^{\min} = 4$  (left panel of Fig. 73), a good fraction of the parameter space is covered at the  $3\sigma$  level for negative  $\kappa_3$  values. On the other hand, in the SM case ( $\kappa_3 = \kappa_4 = 0$ ) a signal significance of at most  $\sim 2\sigma$  can be obtained. In all studied setups, the significance isolines closely follow the total cross section and thus it is very challenging to get any sensitivity for positive shifts in the Higgs self couplings ( $\kappa_{3,4} > 0$ ).

<sup>13</sup>The additional backgrounds  $h(\rightarrow \gamma\gamma)h(\rightarrow bb)Z(\rightarrow bb)$  and  $h(\rightarrow \gamma\gamma)b\bar{b}b\bar{b}$  are also considered in the analysis, but are found to give a negligible contribution.

<sup>14</sup>Analogous plots for  $M = 1$  GeV and for a different number of tagged  $b$ -jets can be found in the original paper [242].

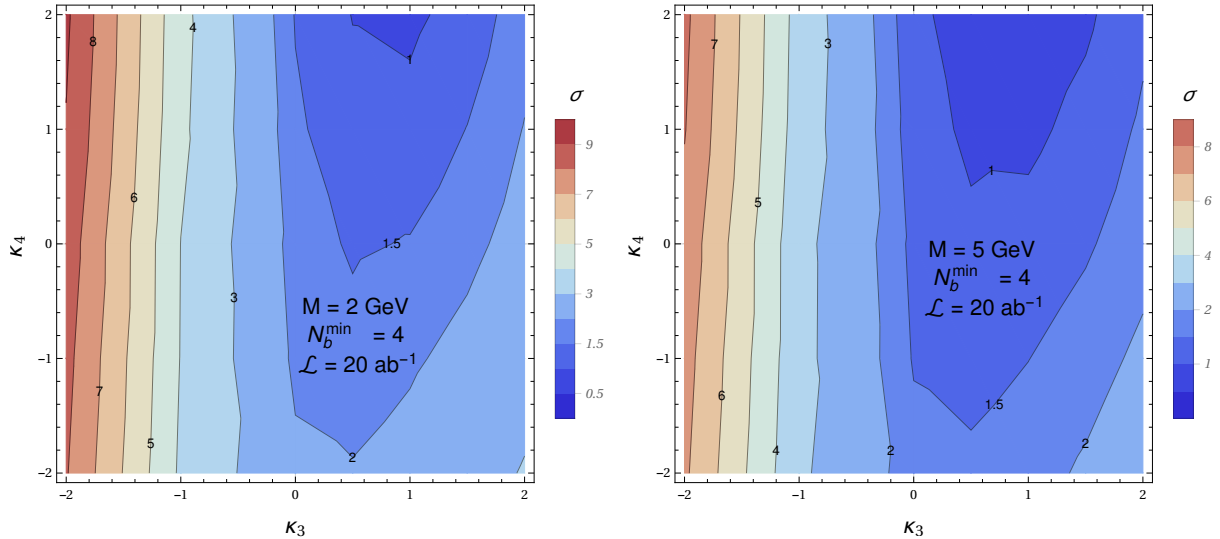


**Fig. 73:** Sensitivity of the FCC to the production of a triple-Higgs system decaying into a  $\gamma\gamma\bar{b}b\bar{b}$  final state for two different choices of the  $M$  in the “intermediate” scenario.

### 4.3.3 Optimistic hypothesis: 80% $b$ -tagging efficiency

As a final case consider the “optimistic” scenario with a  $b$ -tagging efficiency of 80% [241]. In this analysis a cut of  $|\eta| < 5$  and  $p_T > 400$  MeV is introduced on all particles of all event samples considered. Jets are reconstructed from hadrons using the anti- $k_t$  algorithm [82, 84], with a radius parameter of  $R = 0.4$ . Only jets with  $p_T > 40$  GeV and  $|\eta| < 3.0$  are kept (this includes  $b$ -jets). An ideal reconstruction efficiency of 100% is assumed for the photons, which are required to satisfy the conditions  $|\eta| < 3.5$  and  $p_T > 40$  GeV. A crude estimate of the detector effects is included through jet-to-photon mis-identification probability and an heavy flavour (mis-)tagging efficiency. The jet-to-photon mis-identification probability is set to  $p_{j \rightarrow \gamma} = 10^{-3}$  and is assumed to be constant in the whole kinematic range considered. A flat  $b$ -jet identification rate of 80% is assumed, while the mis-tagging of a light jet to bottom-quark-initiated jet is set to be 1%. All photons are required to be isolated, namely in a cone of radius  $\Delta R = 0.2$  around the photon, the sum of the transverse momenta of particles, *i.e.*  $\sum_i p_{T,i}$ , should be less than 15% of the photon transverse momentum. The jet momenta are not smeared since a large (60 – 80 GeV) invariant  $b\bar{b}$  mass window is considered in the analysis. The photon momenta are also not smeared, reflecting the fact that the photon momentum resolution at LHC is already at the  $\sim 1\%$  level.

Given the large cross sections of processes with high-multiplicity final states at a 100 TeV collider, the only processes fully generated at parton level are those that include true photons and true  $b$ -quarks. This implies that light extra jets are generated only at the parton shower level, which is included via HERWIG++ [227, 228, 250–252].<sup>15</sup> Additional phase-space cuts applied to the samples  $b\bar{b}b\bar{b}$ ,  $b\bar{b}b\bar{b}\gamma$ ,  $b\bar{b}b\bar{b}\gamma\gamma$  and  $b\bar{b}\gamma\gamma$  are shown in Table 39.

As a requirement for the signal sample, four  $b$ -jets, or light jets mis-identified as  $b$ -jets, are required with  $|\eta| < 3.0$ , with transverse momenta  $p_{T,b_{\{1,2,3,4\}}} > \{80, 50, 40, 40\}$  GeV, where the subscripts 1, 2, 3, 4 denote the first, second, third and fourth hardest  $b$ -jets respectively. Two photons, or jets mis-identified as photons, are required with  $|\eta| < 3.0$  and  $p_{T,\gamma_{\{1,2\}}} > \{70, 40\}$  GeV. Due to the fact that it is impossible for the majority of  $b$ -jets to identify whether they originated from a  $b$ -quark or an anti- $b$ -quark, there exists a 3-fold combinatorial ambiguity in combining  $b$ -jets into the two Higgs boson candidates. As a simple choice, the highest- $p_T$   $b$ -jet is paired with its closest  $b$ -jet in  $\Delta R = \sqrt{\Delta\eta^2 + \Delta\phi^2}$ , while

<sup>15</sup>HERWIG++ is also used to simulate hadronization and underlying event effects. Pile-up events, instead, are not considered.

observable	PS cut
$p_{T,b}$	$> 35$ GeV, at least one $> 70$ GeV
$ \eta_b $	$< 3.2$
$p_{T,\gamma}$	$> 35$ GeV, at least one $> 70$ GeV
$ \eta_\gamma $	$< 3.5$
$\Delta R_{\gamma\gamma}$	$> 0.2$
$m_{\gamma\gamma}$	$\in [90, 160]$ GeV

**Table 39:** The phase-space cuts imposed on the background samples  $b\bar{b}b\bar{b}$ ,  $b\bar{b}b\bar{b}\gamma$ ,  $b\bar{b}b\bar{b}\gamma\gamma$ ,  $b\bar{b}\gamma\gamma$  in the “optimistic” scenario.

other two remaining  $b$ -jets are paired together.<sup>16</sup> The invariant masses of the  $b$ -jet paired are constructed,  $m_{bb}^{\text{close},1}$  and  $m_{bb}^{\text{close},2}$  respectively, which are required to be  $m_{bb}^{\text{close},1} \in [100, 160]$  GeV and  $m_{bb}^{\text{close},2} \in [90, 170]$  GeV. The rather large mass windows are chosen so as to retain most of the already rare signal. Moreover, the distance between the highest- $p_T$   $b$ -jet and the corresponding paired one is constructed and restricted to be within  $\Delta R_{bb}^{\text{close},1} \in [0.2, 1.6]$ .<sup>17</sup> The invariant mass of the photon pair is required to be in a small window around the measured Higgs boson mass  $m_{\gamma\gamma} \in [124, 126]$  GeV.<sup>18</sup> Finally, the distance between the two photons is required to be within  $\Delta R_{\gamma\gamma} \in [0.2, 4.0]$ . The selection cuts are summarized in Table 40.

observable	selection cut
$p_{T,b_{\{1,2,3,4\}}}$	$> \{80, 50, 40, 40\}$ GeV
$ \eta_b $	$< 3.0$
$m_{bb}^{\text{close},1}$	$\in [100, 160]$ GeV
$m_{bb}^{\text{close},2}$	$\in [90, 170]$ GeV
$\Delta R_{bb}^{\text{close},1}$	$\in [0.2, 1.6]$
$\Delta R_{bb}^{\text{close},2}$	no cut
$p_{T,\gamma_{\{1,2\}}}$	$> \{70, 40\}$ GeV
$ \eta_\gamma $	$< 3.5$
$\Delta R_{\gamma\gamma}$	$\in [0.2, 4.0]$
$m_{\gamma\gamma}$	$\in [124, 126]$ GeV

**Table 40:** Final selection cuts imposed in the “optimistic” analysis of the  $(b\bar{b})(b\bar{b})(\gamma\gamma)$  final state.

The signal cross section after the cuts as well as the list of background processes considered in the analysis is given in Table 41. The most significant backgrounds are the QCD production of  $b\bar{b}b\bar{b}\gamma\gamma$ , along with all processes involving the production of only two Higgs boson in association with extra jets of QCD origin. More precisely, the latter class of processes closely reproduces the kinematic distribution of the signal, since in this case the tight di-photon mass window is of no help. Moreover, the Higgs bosons in di-Higgs production processes are harder on average than those in  $hhh$ , thus passing transverse momentum cuts easily. This background could be tackled in future studies with a  $h \rightarrow b\bar{b}$  tagging algorithm based on the jet substructure analysis techniques that exploit the differences between the energy spread of fat

<sup>16</sup>An alternative method based on the minimization of the squared sum of  $(m_{bb} - m_h)$  from each  $b$ -jet combination yields results that differ by only  $\mathcal{O}(1\%)$  compared to the simpler  $\Delta R$  method.

<sup>17</sup>The distance between the other paired  $b$ -jets was not found to have significant discriminating power.

<sup>18</sup>This cut implies that the di-photon resolution must be better than  $\sim 1$  GeV at the FCC-hh. The current resolution at the LHC is  $1 - 2$  GeV, [253, 254] and thus it is not unreasonable to expect a marginally improved resolution at the detectors of the future collider.

process	$\sigma_{\text{LO}}$ (fb)	$\sigma_{\text{NLO}} \times \text{BR} \times \mathcal{P}_{\text{tag}}$ (ab)	$\epsilon_{\text{analysis}}$	$N_{30 \text{ ab}^{-1}}^{\text{cuts}}$
$hhh \rightarrow (b\bar{b})(b\bar{b})(\gamma\gamma)$ , SM	2.89	5.4	0.06	9.7
$b\bar{b}b\bar{b}\gamma\gamma$	1.28	1050	$2.6 \times 10^{-4}$	8.2
$hZZ$ , (NLO) ( $ZZ \rightarrow (b\bar{b})(b\bar{b})$ )	0.817	0.8	0.002	$\ll 1$
$hhZ$ , (NLO) ( $Z \rightarrow (b\bar{b})$ )	0.754	0.8	0.007	$\ll 1$
$hZ$ , (NLO) ( $Z \rightarrow (b\bar{b})$ )	$8.02 \times 10^3$	1130	$\mathcal{O}(10^{-5})$	$\ll 1$
$b\bar{b}b\bar{b}\gamma$ + jets	$2.95 \times 10^3$	2420	$\mathcal{O}(10^{-5})$	$\mathcal{O}(1)$
$b\bar{b}b\bar{b}$ + jets	$5.45 \times 10^3$	4460	$\mathcal{O}(10^{-6})$	$\ll 1$
$b\bar{b}\gamma\gamma$ + jets	98.7	4.0	$\mathcal{O}(10^{-5})$	$\ll 1$
$hh$ + jets, SM	275	593	$7 \times 10^{-4}$	12.4

**Table 41:** List of the various processes considered in the “optimistic” analysis of the  $(b\bar{b})(b\bar{b})(\gamma\gamma)$  final state. The parton-level cross section, including the cuts given in the main text is presented as well as the analysis efficiency and the expected number of events at  $30 \text{ ab}^{-1}$ . A flat  $k$ -factor of  $k = 2.0$  has been applied to all tree-level processes (including  $hh$ +jets) as an estimate of the expected increase in cross section from LO to NLO. The  $hZZ$ ,  $hhZ$  and  $hZ$  processes have been produced at NLO and hence no  $k$ -factor is applied.

$b$ -jets originating from Higgs decay and the one of fat  $b$ -jets from QCD gluon splitting<sup>19</sup>. The expected sensitivity to triple Higgs production in the SM obtained with this analysis is  $S/\sqrt{B} \sim 2.1$  for  $30 \text{ ab}^{-1}$ , with  $S/B \sim 0.5$ . Finally, assuming that the trilinear Higgs coupling is not modified from the SM value, it can be estimated that the  $\lambda_4$  parameter can be constrained to the range  $\lambda_4 \in [\sim -4, \sim +16]$  at 95% confidence level with an integrated luminosity of  $30 \text{ ab}^{-1}$ .

#### 4.3.4 Prospects of measuring the Higgs quartic self-coupling

The comparison among the three analyses presented in this section allows one to draw some general conclusions about the possibility to measure the triple-Higgs production cross section and to extract the Higgs quadrilinear self-coupling.

A crucial element that determines the experimental sensitivity are the efficiency and the fake rejection rates of the  $b$ -tagging procedure. The “pessimistic” and “intermediate” analyses indeed show that two and even three  $b$ -tags are not sufficient to efficiently suppress the large backgrounds. In particular, as it can be seen from Table 38, the  $\gamma\gamma b\bar{b}jj$  background can only be kept under control with 4  $b$ -tags, a choice that allows one to reduce it to a level comparable with the SM signal yield. In this situation the overall efficiency of the  $b$ -tagging procedure becomes an essential ingredient to determine the sensitivity of the search. An increase in the reconstruction efficiency from the 60% level assumed in the “pessimistic” analysis to the 70% used in the “intermediate” one already implies an enhancement of the signal by almost a factor two. An 80% efficiency would instead increase the number of reconstructed signal events by a factor three. A minimal  $b$ -tagging efficiency of 70% seems thus necessary to achieve some sensitivity to the signal.

It must be however noticed that an increase in the  $b$ -tagging efficiency can be effective only if it can be achieved by keeping the fake rejection rates to an acceptable level (namely at most  $\sim 1\%$  for the light jets and 10 – 20% for  $c$ -jets). Indeed, in all the analyses the main backgrounds include some with fake  $b$ -jets (e.g.  $\gamma\gamma b\bar{b}jj$  in the “pessimistic” and “intermediate” analyses and  $hhjj$  in the “optimistic” one).

Another element that can significantly affect the analysis is the experimental resolution in the

<sup>19</sup>Note that the additional two  $b$ -jets in  $hh$ +jets and  $hZ$ +jets have been generated by gluon splitting into  $b\bar{b}$  performed by the shower Monte Carlo program.

reconstruction of the invariant mass of the di-photon system,  $m_{\gamma\gamma}$ . This resolution affects linearly the size of the backgrounds containing two photons not coming from an Higgs boson decay, as in the case of the  $\gamma\gamma b\bar{b}j\bar{j}$  and  $\gamma\gamma b\bar{b}b\bar{b}$  non-resonant backgrounds. As it can be seen from the “pessimistic” and “intermediate” analyses (see in particular the cut-flow in Table 38) a resolution around 1 – 2 GeV is a minimal requirement for the analysis to be effective.

An important ingredient to be further investigated is the relevance of the various backgrounds in the analysis when showering and detector effects are included. From the available analyses, it seems that different choices for the cut strategy can be used, which lead to comparable sensitivity to the signal, but significantly change the relevance of the various backgrounds.

Summarizing the results of the “intermediate” and “optimistic” analyses, it seems that in a realistic situation a signal comparable to the SM one would lead to a significance around  $2\sigma$ . This would allow an  $\mathcal{O}(1)$  determination of the production cross section. The situation could get better if a modification of the trilinear Higgs coupling is present. In particular a negative shift in  $\lambda_3$  would lead to a significant increase in the signal cross section allowing for a higher significance as shown in Fig. 73.

The prospects for extracting the quartic Higgs self-coupling, unfortunately, are not very promising. As mentioned before, the dependence of the  $HHH$  production cross section on  $\lambda_4$  is very mild (see Fig. 71) and an order-one change in the signal can only be obtained for large deviations ( $|\delta\lambda_4| \gtrsim 5$ ) with respect to the SM value. As a reference result we can quote the one obtained in the “optimistic” scenario, in which the quartic self-coupling, in the absence of modifications of the other Higgs couplings, is expected to be constrained in the range  $\lambda_4 \in [\sim -4, \sim +16]$  with an integrated luminosity of  $30 \text{ ab}^{-1}$ .

## 5 BSM aspects of Higgs physics and EWSB

### 5.1 Introduction

In this chapter, we explore the discovery potential of BSM Higgs sectors at a 100 TeV collider. In doing so we draw upon a rich literature, as well as several original studies. An overview is provided in Section 5.2, where we briefly review some of the motivations for BSM Higgs sectors which are explored in more detail in later sections. We also identify the most important unique physics opportunities at a 100 TeV collider, especially in connection to Higgs physics. These represent measurements or insights into BSM scenarios that are qualitatively impossible to glean from the LHC or a lepton collider program. Finally, we argue that a 100 TeV collider is uniquely versatile as a tool for exploring BSM Higgs sectors, since it acts as both a high-energy direct production machine as well as an intensity-frontier precision tool for exploring the uncolored TeV scale. This perspective provides guidance for future detector design, especially regarding the reconstruction of soft or exotic objects, to ensure that the full discovery potential of a 100 TeV collider is realized.

More detail is provided in Sections 5.3 - 5.6. We outline the motivation for BSM Higgs sectors in the context of several unresolved mysteries: the dynamics of the electroweak phase transition and its possible connection to baryogenesis, the nature of dark matter, the origins of neutrino masses, and solutions to the Hierarchy Problem. In each case, we identify the most promising signatures at a 100 TeV collider, and outline the vital role such a machine would play in testing these extensions of the SM via its exploration of BSM Higgs sectors.

Finally, we examine the reach of a 100 TeV collider for general BSM Higgs sectors in Section 5.7, with particular attention paid to the mass reach of heavy Higgs direct production in 2HDM and singlet extensions of the SM scalar sector. Such extensions are relevant in their own right, but also occur as part of more complete theories which address the above-mentioned mysteries. The high mass reach of a 100 TeV collider makes direct production of new Higgs states one of the most important and promising physics goals.

### 5.2 Overview

#### 5.2.1 Motivations for BSM Higgs Sectors

Here we briefly summarize the most important motivations for the existence of BSM Higgs sectors, both experimentally and theoretically. This is explored in more detail in Sections 5.3 - 5.6. Additional details on the cosmological implications of BSM Higgs sectors and their phenomenological consequences may be found in Refs. [255, 256].

##### 5.2.1.1 The Electroweak Phase Transition and Baryogenesis

It is well-known that the SM cannot explain the origin of the matter-antimatter asymmetry, characterized by the tiny baryon-to-photon ratio [257]:

$$Y_B = \frac{n_B}{s} = (8.59 \pm 0.11) \times 10^{-11} \quad (\text{Planck}) \quad (53)$$

where  $n_B$  ( $s$ ) is the baryon number (entropy) density. This tiny baryon asymmetry of the universe (BAU) nevertheless comprises roughly 5% of the present cosmic energy density. Explaining why it is not significantly smaller is a key challenge for BSM physics. While it is possible that the universe began with a non-zero BAU, the inflationary paradigm implies that the survival of any appreciable BAU at the end of inflation would have been highly unlikely. Thus, one looks to the particle physics of the post-inflationary universe to account for the observed value of  $Y_B$ .

The necessary particle physics ingredients, identified by Sakharov [258] nearly half a century ago, include:

1. baryon number violation;

2. C- and CP-violation; and
3. either departure from equilibrium dynamics or CPT-violation.

While the SM contains the first ingredient in the guise of electroweak sphalerons, it fails with respect the second and third. The known CP-violation associated with the SM CKM matrix is too feeble to have produced an appreciable  $Y_B$ , and the SM universe was never sufficiently out-of-equilibrium to have preserved it, even if it had been sufficiently large. Consequently, BSM interactions are needed to remedy these shortcomings.

A number of theoretically attractive BSM baryogenesis scenarios have been developed over the years, with greater or lesser degrees of testability. From the high energy collider standpoint one of the most interesting possibilities is electroweak baryogenesis (EWBG) (for a recent review, see Ref. [259]). EWBG requires that electroweak symmetry breaking (EWSB) occur *via* a strong, first order electroweak phase transition (EWPT). For the SM universe, lattice studies indicate EWSB takes place through a cross over transition, as the observed mass of the Higgs-like scalar is too heavy to allow for a first order transition. Nevertheless, the presence of additional scalar fields in BSM Higgs scenarios could allow for a first order transition in a variety of ways, as discussed in detail in Section 5.3.

Present measurements of Higgs properties imply that these new scalars are unlikely to be charged under  $SU(3)_C$ . Since they must couple to the SM Higgs scalar in order to affect the thermal history of EWSB, they necessarily also contribute to the Higgs production cross section in gluon-gluon fusion if they are charged under  $SU(3)_C$ . Recent model-independent studies as well as analyses of the “light stop” catalyzed EWPT in the MSSM and simple extensions [260–262], indicate that a strong first order EWPT is usually incompatible with Higgs signal data if the new scalar is colored. Consequently, any new scalars that enable a first order EWPT are likely to be  $SU(3)_C$  singlets.

Present data still allow for first order EWPT-viable scalar sector extensions to contain  $SU(2)_L \times U(1)_Y$  non-singlets as well as scalars that carry no SM charges and that interact with the Higgs solely via Higgs portal interactions. In either case, discovery at the LHC and possibly future  $e^+e^-$  is possible, but probing the landscape of possible scenarios will require a higher energy pp collider, given the generically small production cross sections. A detailed discussion appears in Section 5.3.

In considering the EWPT, several additional observations are worth bearing in mind. First, the existence of a strong first order EWPT is a necessary condition for successful EWBG, but not a guarantee that the BAU was produced during the era of EWSB. The CP-violation associated with the BSM Higgs sectors may still have been too feeble. In this respect, probes of BSM CP-violation with searches for permanent electric dipole moments of atoms, molecules, nucleons and nuclei provide a powerful probe, as do studies of CP-violating observables in heavy flavor systems under certain circumstances. Second, there exist well-motivated weak scale baryogenesis scenarios that do not rely on a first order EWPT, such as the recently introduced “WIMPY baryogenesis” paradigm [263]. Nevertheless, since our emphasis in this section falls on BSM Higgs, we will concentrate on the implications for EWBG.

Against this backdrop, understanding the thermal history of EWSB is interesting in its own right, independent from the EWBG implications. For example, it could have implications for the generation of primordial gravitational waves [264]. By analogy, we note that exploring the phase diagram of QCD has been a topic of intense theoretical and experimental effort for several decades, involving a combination of lattice QCD studies and experiments at the Relativistic Heavy Ion Collider and ALICE detector at the LHC. With the additional motivations for BSM Higgs sectors to be discussed below, it is interesting to ask about the implications of these SM extensions for the phase diagram of the electroweak sector of the more complete theory that enfolds the SM. Both discovery of new scalars as well as detailed probes of the scalar potential will in principle allow us to flesh out the thermal history of EWSB.

### 5.2.1.2 Dark Matter

The astrophysical and cosmological evidence for the existence of Dark Matter is overwhelming. However, these observations almost entirely rely on DM's gravitational interactions, revealing little information about its identity or interactions with the SM. Determining just what constitutes the DM, how it interacts, and why it comprises roughly 27% of the energy density of the present universe is one of the key challenges at the interface of particle physics and cosmology. From a particle physics standpoint, many BSM theories admit a variety of DM candidates of various types (cold DM, axions, etc.) but the lack of a signal to date leaves all possibilities open.

Experimentally, a host of dark matter direct detection experiments are looking for nuclear recoils from collisions with ambient DM, under the assumption that interactions are not too weak. The sensitivity of these searches has increased tremendously, and one expects that they will enter the neutrino-background dominated regime in the next few decades. If a signal is detected, additional measurements from either astrophysics or collider experiments would not only corroborate the existing evidence for dark matter but would help reveal its particle nature and interactions. Indeed, recent astrophysical observations, such as the positron excess observed by the Pamela, Fermi-LAT, and AMS-02, or the excess of gamma rays at 2.2 GeV from the galactic center, provide tantalizing clues and have inspired a flurry of particle physics model-building. Even if these indirect signatures prove to be entirely of astrophysical origin and direct detection experiments continue yield null results,<sup>20</sup> cosmological constraints like the DM relic abundance and its effect on large-scale structure formation could still point towards certain interactions with the SM.

Colliders can probe dark matter through direct production of pairs of dark matter particles,  $\chi$ . Since dark matter is stable on cosmological timescales, the process  $pp \rightarrow \chi\chi$  is unobservable since  $\chi$  leaves no visible trace in the detector. Consequently, one must look for a visible signature arising from production of additional visible particles in association with  $\chi$  pairs. The standard collider search strategy involves  $pp \rightarrow \chi\chi + X$ , where  $X$  may be a jet, SM gauge boson, or even the SM Higgs boson – the so-called “mono- $X$  plus missing energy” signature. Depending on the specific dark matter model, the reach in  $M_\chi$  anticipated by the end of the LHC high luminosity phase is projected to be a few TeV.

Dark matter can either be a part of the scalar sector, or connected to the SM via a scalar portal. Furthermore, it is possible that the dark matter mass and nature of its interactions would make observation in the mono- $X$  plus MET channel inaccessible at the LHC. For example, if the Higgs sector is extended in inert-doublet models [265] to include a dark matter candidate, which is very hard to detect at the LHC for masses heavier than a few hundred GeV. The situation is even more severe for scalars in non-doublet electroweak representations, which typically requires a mass in the 2-3 TeV range in order to saturate the observed relic abundance under a thermal dark matter scenario (lighter states would annihilate away too quickly due to gauge interactions). The corresponding production cross section can be far too small to be LHC accessible, but with the higher energy and associated parton luminosity, a 100 TeV  $pp$  collider could allow for discovery. The extended scalar sector associated with such a scenario would also provide rich opportunities for discovery and characterization.

The conclusions are similar for scenarios where scalars are responsible for the interactions of DM with the SM. For example, if the DM is part of a hidden sector, it may communicate solely to the SM Higgs sector through the exchange of a SM gauge singlet scalar, making the Higgs sector our only portal to the dark sector. Direct searches for this mediator or for dark matter production through the mediator are complementary to direct detection experiments. The high mass reach and luminosity of a 100 TeV collider allows it to probe TeV-scale mediator and dark matter masses [266, 267], a feat which is very difficult to accomplish for most scenarios at the LHC. This will be discussed in more detail in Section 5.4.

<sup>20</sup>While a few direct detection experiments have reported positive signals, they remain inconclusive

### 5.2.1.3 *Origins of Neutrino Mass*

Explaining the origin of the small scale of neutrino masses, relative to the masses of the other known elementary fermions, remains a forefront challenge for particle and nuclear physics. While the Higgs mechanism thus far appears to account for the non-vanishing masses of the charged fermions and electroweak gauge bosons, the significantly smaller scale of the active neutrino masses, as inferred from neutrino oscillation and nuclear  $\beta$ -decay, suggests that an alternate mechanism may be responsible in this sector. The longstanding, theoretically favored explanation, the see saw mechanism, postulates the existence of additional fields whose interactions with the SM lepton doublets violates total lepton number. The fields may be right-handed, electroweak gauge singlet neutrinos; scalars that transform as triplets under  $SU(2)_L$ ; or fermions that transform as electroweak triplets. These three possibilities correspond to the Type I, II, and III see-saw mechanisms, respectively (for a recent review, see, *e.g.*, Ref. [268]).<sup>21</sup> The light neutrino masses are inversely proportional to the mass scale  $\Lambda$  of the new fields, with

$$m_\nu \sim \frac{Cv^2}{\Lambda} \quad (54)$$

where  $v = 246$  GeV is the weak scale and  $C$  involves one or more of the coupling constants in the specific realization.

For  $C \sim \mathcal{O}(1)$  one has  $\Lambda \sim \mathcal{O}(10^{14} - 10^{15})$  GeV, a scale that is clearly inaccessible to terrestrial experiments. However, there exist a well-motivated variations on the conventional see-saw mechanism in which  $\Lambda$  may be at the TeV scale, such as low-scale see-saw scenarios or radiative neutrino mass models. In this case, direct production of the new fields may be accessible in high-energy  $pp$  collisions. Of particular interest to this chapter are situations involving new scalars, as in the Type II see-saw mechanism or radiative neutrino mass models. A discussion of the opportunities for discovery of these new scalars and their neutrino mass-related properties with a 100 TeV  $pp$  collider appears in Section 5.5.

### 5.2.1.4 *Naturalness*

The SM can be viewed as a Wilsonian effective field theory with a finite momentum cutoff  $\Lambda$ , parameterizing the scale at which new degrees of freedom appear. In that case, the EW scale is not stable with respect to quantum corrections from the UV. This *Hierarchy Problem* is most transparent in the expression for the physical Higgs mass parameter in the SM Lagrangian, which sets the electroweak scale:

$$\mu^2 = \mu_0^2 + \frac{3y_t^2}{4\pi^2}\Lambda^2 + \dots, \quad (55)$$

where the first term is the bare Higgs mass term and the second term is the dominant radiative contribution, which arises from top quarks at one-loop. If  $\Lambda$  is much higher than a TeV these loop corrections are much larger than the physical Higgs mass, meaning the EW scale is *tuned*. Naturalness, as a guiding principle for BSM model building, suggests one of the following:<sup>22</sup>

- (a) New degrees of freedom appear at the TeV scale to regulate this quadratic divergence, thereby protecting the Higgs mass from large UV contributions. This motivates supersymmetric solutions to the hierarchy problem, where stops below a TeV cancel the top loop.
- (b) The Higgs ceases to be a sensible degree of freedom above the TeV scale. This is the case for technicolor, or more recently Composite Higgs type solutions to the Hierarchy Problem.

<sup>21</sup>Note that in left-right symmetric models, the Type II see-saw mechanism contains a parallel structure involving  $SU(2)_R$  scalars.

<sup>22</sup>The only known counterexample to this reasoning is the so-called “dynamical solution” to the hierarchy problem, the relaxion [269]. The minimal relaxion scenario has no interesting predictions for the collider experiments. However, it is not yet clear that a full consistent relaxion model, consistent with the cosmological constraints, exists.

There is, at least naively, some tension between the expectations of Naturalness and null results from recent LHC searches. Even so, standard supersymmetric or composite theories could still show up at LHC run 2. Some scenarios, including more exotic theoretical realizations of naturalness, could escape detection at the LHC all-together. This makes it vital to study their signatures at a 100 TeV collider.

Given the direct connection between the Higgs boson and the Hierarchy Problem, it is not surprising that Naturalness is strongly connected to BSM Higgs sectors. This is explored in detail in Section 5.6.

For example, supersymmetric theories feature larger Higgs sectors than the single SM doublet in order to cancel anomalies; the MSSM realizes a particular subset of Type 2 Two-Higgs Doublet models. Direct production of additional TeV-scale Higgs states will therefore be an important physics goal of a 100 TeV collider. The existence of top partners or the composite nature of the Higgs can also change the Higgs couplings to SM particles at loop- and tree-level respectively. Additional light states can be part of these extended Higgs sectors. This makes exotic Higgs decays an attractive signature, given the huge production rates for the SM-like Higgs boson at a 100 TeV collider. Finally, the full structure of the natural theory implies the existence of additional EW-charged states at or near the TeV scale, such as vector resonances in Composite Higgs theories or EWinos in supersymmetry.

An especially enticing scenario for the 100 TeV collider are theories of Neutral Naturalness, like the Twin Higgs [270] or Folded SUSY [271]. In these theories, the quadratically divergent top contribution to the Higgs mass is cancelled at one-loop by *colorless* top partner states, which only carry EW quantum numbers or can even be SM singlets. While there are some very attractive discovery avenues for the LHC, many cases can only be probed at future lepton and hadron colliders. This can lead to a plethora of signatures, including exotic Higgs decays to long-lived particles, direct production of uncolored top partners through the Higgs portal, and Higgs coupling deviations or direct production of new singlet states due to mixing effects. Perhaps the most exciting possibility is discovering many states carrying SM charges with masses in the 5 - 10 TeV range, which are predicted by all known UV completions of Neutral Naturalness. The 100 TeV collider is the only machine that would allow us to explore the full symmetry underlying these theories.

#### 5.2.1.5 BSM Scalar Sectors

We discussed above several theories or frameworks which address the strength of the electroweak phase transition, the hierarchy problem, dark matter, and the origin of neutrino masses. All of them involve extended scalar sectors. However, the list of scenarios we study is not exhaustive, and no matter where we turn, BSM model building often involves modifying the Higgs sector. For example, *Flavor* is usually seen as a problem in theories with more elaborate Higgs sectors because heavy Higgs mass eigenstates are not necessarily aligned in flavor space, leading to unacceptable tree-level contributions to FCNC processes. This problem could turn into a virtue, as the richer Higgs-induced flavor structure may be used to explain the pattern of quark and lepton masses. Examples are the extension of the flavor symmetry to the Higgs sector [272], the gauging of the flavor group [273], the Froggatt-Nielsen scheme [274], or higher-dimensional Yukawa couplings [275, 276]. The purported *instability of the SM scalar potential* [16, 277, 278] may also motivate extended scalar sectors. It can be interpreted as indicating the existence of new particles, and introducing new Higgs bosons is the most economical solution [279–285].

These considerations suggest that maybe the right question is not why additional Higgs bosons should exist, but rather why they shouldn't exist. The argument in favor of the SM Higgs structure is usually based on an Occam's razor criterion: simplicity and minimality. But are simplicity and minimality really conceptual ingredients of the SM? Wouldn't logical simplicity prefer a gauge structure for EW breaking (such as technicolor) rather than the introduction of scalar particles with new non-gauge interactions? Are *three* generations of quarks and leptons the choice preferred by minimality? Indeed, the existence of an enlarged Higgs sector is an almost inescapable consequence of theoretical constructions that address the naturalness problem with new dynamics. As an extreme conclusion, one could say

that an enlarged scalar sector is a good discriminator between theories with or without dynamical explanations of the hierarchy at the weak scale. The discovery of new Higgs bosons would strike a mortal blow to the logical arguments in favor of an anthropic explanation of the hierarchy. Also cosmological relaxation mechanisms [269] would be disfavored by the uncovering of an extended Higgs sector.

All of this provides ample motivation to study extended scalar sectors as theoretical structures in their own right. The possibilities include EW sterile scalars (e.g. in models motivated by EWSB or Neutral Naturalness), or more complicated landscape of the scalar particles, like, for example, in theories of partial compositeness. Probably one of most famous scenarios of the extended Higgs sector is a so-called two-Higgs doublets model (2HDM). A particular version of the 2HDM is inevitably a part of the supersymmetrized version of the SM, motivated by naturalness. However, 2HDM is an attractive scenario of its own, not necessarily motivated by naturalness and any other BSM scenario.

For this reason, we pay special attention to the direct production reach of a 100 TeV collider for new scalar states. Previous studies [286] indicate a multi-TeV reach for new Higgs doublets and TeV-reach for new singlet scalar states in most scenarios. We discuss this in more detail, in Section 5.7. We also provide a theoretical overview of the 2HDM and explain the parts of parameter space that are still relevant in light of LHC results.

## 5.2.2 *Unique Opportunities at 100 TeV*

Here we summarize the most important Higgs-related measurements for which a 100 TeV collider is uniquely suited, compared to the LHC or planned future lepton colliders.

### 5.2.2.1 *Measurement of the Higgs self-coupling*

The Higgs cubic coupling reveals direct information about the shape of the Higgs potential near our vacuum, and can be determined from measurements of non-resonant di-Higgs production. Unfortunately, such a measurement is extremely difficult. The HL-LHC can only determine this cubic coupling with  $\mathcal{O}(100\%)$  precision (see [287–289] and [179, 203, 290, 291]), and proposed lepton colliders with sub-TeV center-of-mass energies are expected to have similar or slightly better precisions (see [189, 292]). A 1 TeV ILC program with  $2 \text{ ab}^{-1}$  of luminosity could yield one-sigma precision of 16% [187–189].

Fortunately, the 100 TeV collider is the ultimate machine for measuring the self-interaction of the Higgs boson. The study in Section 4 found that 3 – 4% statistical precision is achievable with  $30 \text{ ab}^{-1}$  of luminosity, see Table 26. Inclusion of systematic errors could lead to a precision of about 5 – 6% with the same luminosity, see Table 30 and the discussions in [179, 203, 204].

Higgs self-coupling measurements with  $\lesssim 5\%$  precision are required to exclude a strong electroweak phase transition in  $\mathbb{Z}_2$  symmetric singlet scalar extensions of the SM, and provide an important probe of mixed singlet scenarios that is orthogonal to precision Higgs coupling measurements (to other SM particles) at lepton colliders. Such precision is also required to exclude certain neutral top partner scenarios, which can provide additional probes of neutral naturalness [293], and may also provide sensitivity for low-scale neutrino see-saws.

Regardless of any BSM motivation, measuring the shape of the Higgs potential around our vacuum is a worthy goal of precision Higgs physics in itself, and one which can only be carried out with any real precision at a 100 TeV machine.

### 5.2.2.2 *Direct production of new electroweak states*

A 100 TeV collider would be sensitive to EW-charged BSM states with masses of 5 – 10 TeV. This chapter contains or summarizes several studies of direct Higgs production in scenarios with extended scalar sectors that demonstrate this point, but even for squeezed fermion spectra like EWinos in split SUSY, a 100 TeV collider can have sensitivity to multi-TeV masses [294–296].

This has crucial implications for many fundamental questions in particle physics. Many models of new physics contain additional Higgs doublets or triplets, including supersymmetry, or possible mechanisms for generating the neutrino mass or inducing a strong EWPT. A reach for multi-TeV EW states also has relevance for naturalness: it could allow EWinos in split-SUSY to be detected [295], and it would allow direct production of states that are part of the UV completion for theories of neutral naturalness. Most such UV completions also contain heavy colored states around 5-10 TeV, which are an obvious target for a 100 TeV collider, but even in models where such colored states might be avoided, it seems difficult to avoid new EW states. Therefore, the capability of probing heavy EW states allows the 100 TeV machine to probe theories of naturalness, possibly exhaustively [293].

### 5.2.2.3 Direct production of new singlet states

A 100 TeV collider allows us to probe the most challenging aspect of the TeV-scale: SM singlets. Singlets with sub-TeV masses occur in many BSM extensions, motivated by Neutral Naturalness, a strong EWPT, the NMSSM, etc. These states are notoriously hard to probe at the LHC, and too heavy to produce at most proposed lepton colliders. Searches for di-higgs or di- $Z$  final states at 100 TeV are sensitive to singlet scalar masses up to about a TeV, and in some cases significantly above a TeV, depending on the model. A  $pp$  center-of-mass energy of 100 TeV with  $30\text{ab}^{-1}$  is needed to exhaustively probe a sub-TeV singlet that induces a strong phase transition, both with and without Higgs mixing. For heavier mixed singlets, the FCC-hh could extend the discovery reach up to several TeV and down to Higgs-singlet mixing angles below 0.001.

### 5.2.2.4 Ultra-rare exotic Higgs decays

A 100 TeV collider with  $\mathcal{O}(10\text{ab}^{-1})$  of luminosity produces  $\sim 10^{10}$  SM-like Higgs bosons. Even when accounting for triggering requirements (which may well be absent at such a machine) this enormous rate allows for the detection of exotic Higgs decays with tiny branching fractions smaller than  $10^{-8}$ , as long as the final states are conspicuous enough to stand out from the SM background. Exotic Higgs decays are motivated for a myriad of reasons in many BSM scenarios (see e.g. [297]). For example, the Higgs portal is the lowest-dimensional interaction one can add between the SM sector and a hidden sector. This makes exotic Higgs decays a prime discovery channel of new physics, as long as the new states are relatively light. This was demonstrated for dark photons in [298] and for displaced decays in the context of Neutral Naturalness by [299], but applies to any theory which produces ultra-rare exotic Higgs decays with conspicuous final states.

### 5.2.2.5 High-Precision High-Energy Measurements

A somewhat under-appreciated capability of the 100 TeV collider is the potential for high-energy high-precision measurements. A good example was studied by [300], which showed that dilepton measurements of Drell-Yan production at 100 TeV can be sensitive to new states with EW charges around a TeV. This is especially important since such a measurement is almost completely model-independent, depending only on the masses and gauge charges of new particles, and being completely independent of decay modes etc, which could in some scenarios serve to hide the signatures of new states. This measurement is complementary to another high-precision measurement that is possible at the 100 TeV collider: the determination of the  $h\gamma\gamma$  coupling with percent-level precision, see Section 3.2.1.

An important application of this model-independent measurement is to theories of Neutral Naturalness, which includes scenarios with electroweak-charged top partners that are neutral under SM color. The results of [300] were used in [293] to argue that such EW-charged top partners would be detectable at a 100 TeV collider with masses of at least 2 TeV or more, depending on multiplicity. This exhausts the natural range of top partner masses in an untuned theory, and essentially guarantees discovery if the hierarchy problem is solved by such states.

Another application are theories of a strong EWPT, which can be induced by new light bosons with masses around a few hundred GeV. If these new degrees of freedom carry SM gauge charges, detecting their effect in the DY spectrum would be an orthogonal, model-independent way to guarantee their discovery.

### 5.2.2.6 Searches for invisible states

There is ample motivation to search for new invisible (stable) states at colliders, the most obvious one being Dark Matter. Such searches are notoriously difficult at the LHC, but the 100 TeV collider will be sensitive to scalar mediators as well as dark matter masses of more than a TeV using for mono-X + MET or dijet+MET searches.

Another important motivation is the  $\mathbb{Z}_2$  symmetric singlet extension of the SM, which can induce a strong EWPT. A VBF jets + MET search, exploiting pair production of the singlets, is vital in excluding the entire EWBG-viable parameter space of this model, and requires  $30\text{ab}^{-1}$  of luminosity at a 100 TeV collider.

### 5.2.3 Probing the Intensity Frontier at 100 TeV

The study of new physics opportunities in general, and BSM Higgs physics in particular, leads us to an important complementary perspective on the role of a 100 TeV collider. Of course, one of the most important reasons for increasing the center-of-mass energy is to increase the reach for direct production of heavy new states. However, an equally important reason is the huge increase in the production rate of light states like the 125 GeV Higgs. In producing  $\sim 10^{10}$  Higgs bosons the 100 TeV collider has no equal in measuring certain Higgs-related processes, such as rare decays and the self-coupling. Similarly, relatively light states near a TeV (compared to  $\sqrt{s}$ ) with sufficiently weak interactions can only be discovered at a 100 TeV collider. This includes some singlet scalar states, or an electroweak multiplet whose neutral component contributes substantially to the dark matter relic density.

In that sense, the 100 TeV collider acts as an *intensity frontier experiment* for uncolored physics near the TeV-scale. This has several important implications for detector design. It is vital to maintain sensitivity for relatively soft final states, which may arise from the decay of e.g. the SM-like Higgs. The ability to reconstruct soft  $b$ -jets with  $p_T \sim \mathcal{O}(20\text{GeV})$  and long-lived particle decays that decay (ideally) only  $\mathcal{O}(50\mu\text{m})$  from the interaction point are important for realizing the full discovery potential of such a machine. Triggers might also be a concern: at such high center-of-mass energies, trigger strategies analogous to current LHC operation would miss many important low-mass processes. This provides powerful motivation to realize *trigger-less* operation (or at least, full event reconstruction at low trigger level so that interesting soft physics can be directly selected for).

## 5.3 Electroweak Phase Transition and Baryogenesis

As indicated in the Overview, determining the thermal history of EWSB is both interesting in its own right and relevant to the possibility of electroweak baryogenesis (EWBG). The latter requires a strong first order EWPT. From this standpoint, the object of interest is the finite-temperature effective action  $S_{\text{eff}}$  whose space-time independent component is the effective potential  $V_{\text{eff}}(T, \varphi)$ . Here,  $\varphi$  denotes the vevs of the scalar fields in the theory and  $T$  is the temperature. A first order EWPT can arise when  $V_{\text{eff}}(T, \varphi)$  contains a barrier between the electroweak symmetric minimum (vanishing vevs for all fields that carry SM gauge charges) and the EWSB minimum. In principle, such a situation could have pertained to the SM universe, as thermal gauge boson loops induce a barrier between the broken and symmetric phases. In practice, the effect is too feeble to lead to a first order EWPT. More specifically, the character of the SM EWSB transition depends critically on the Higgs quartic self-coupling,  $\lambda \propto m_h^2/v^2$ . The maximum value for this coupling that is compatible with a first order phase transition corresponds to an upper bound on  $m_h$  between 70 and 80 GeV [301–303], clearly well below the experimental value. For a 125

GeV Higgs, lattice studies indicate that the EWSB transition in the SM is of a cross-over type with no potential for baryon number generation.

Nevertheless, well-motivated BSM scenarios can lead to a first order phase transition that may provide the necessary conditions for EWBG. The barrier between the two phases can arise from a number of effects, either singly or in combination:

1. finite-temperature loops involving BSM degrees of freedom;
2. large zero-temperature loop effects from new BSM states with sizable Higgs couplings;
3. new tree-level interactions;
4. additional contributions to  $m_h$  that allow  $\lambda$  to be smaller than its SM value.

In addition, the presence of such effects may lead to a richer thermal history than in a purely SM universe. One of the most compelling opportunities for the FCC-hh is to explore as fully as possible the set of possibilities for the finite-temperature EWSB dynamics. In what follows, we briefly review the present theoretical situation, followed by a discussion of representative scenarios that may be particularly interesting for a 100 TeV proton-proton collider. More detailed discussions may be found in two white papers [255, 256].

### 5.3.1 Theoretical Studies

Here we classify BSM scenarios according to the dynamics by which they generate a strong, first order EWPT.

*First order transitions induced by BSM thermal loops.* The MSSM represents the most widely-considered BSM scenario that, in principle, could give rise to a loop-induced, strong first order EWPT (SFOEWPT). The effect relies on contributions to  $V_{\text{eff}}(T, \varphi)$  from stops, whose coupling to the Higgs field is  $\mathcal{O}(1)$  and whose contribution is  $N_C$ -enhanced. Generation of a SFOEWPT requires that at least one of the stop mass eigenstates be relatively light, with mass  $m_{\tilde{t}} \sim \mathcal{O}(100 \text{ GeV})$  in our vacuum [304]. Such a light stop requires a tachyonic soft mass-squared parameter, and allowing for the possibility of a stable color- and charge-breaking vacuum associated with a non-vanishing stop vev. Recent theoretical work indicates that for the “light stop scenario” the universe may undergo a SFOEWPT transition to the color-symmetric Higgs phase and that the latter is metastable with respect to a deeper color-breaking phase. However, the lifetime of the Higgs phase is longer than the age of the universe, so once the universe lands there at high- $T$ , it stays there [305].

Unfortunately, LHC Higgs data now preclude this interesting possibility within the MSSM [260, 261], even if one augments the scalar potential by “hard” SUSY-breaking operators beyond the MSSM [262]. On the other hand, in a more general framework, loop-induced SFOEWPT remains a viable possibility. The reason is that supersymmetry rigidly relates the stop-Higgs coupling to the SM top Yukawa; without this assumption, new scalar fields may have stronger couplings to the Higgs, and hence have a stronger effect on the EWPT dynamics through loops. If the new scalar field responsible for the SFOEWPT is colored, the deviations in the Higgs coupling to gluons induced by its loops will be sufficiently large to be discovered in the upcoming runs of the LHC and HL-LHC, unless some cancellation mechanism is operational [306]. However, the scalar responsible for the SFOEWPT may also be charged only under electroweak interactions, or in fact be a complete SM-gauge singlet. (In the latter case, both tree-level and loop-level modifications of the potential may be important; see below.) In these scenarios, the LHC Higgs program alone will not be sufficient to conclusively probe the parameter space where the SFOEWPT occurs, leaving this important task for future colliders. Among the most important measurements that will constrain such scenarios are the precision measurements of the  $h\gamma\gamma$  and  $hZZ$  couplings at the HL-LHC and electron-positron Higgs factories, and the measurement of the Higgs cubic coupling at the 100 TeV proton-proton collider [306, 307].

*Zero-temperature loop effects.* It is possible for thermal loops from  $W$  and  $Z$  bosons to generate a SFOEWPT even for a 125 GeV Higgs mass, so long as the shape of the potential differs from the SM case. This can be realized if there are relatively large (but still perturbative) couplings between the Higgs and some new degrees of freedom. Non-analytical zero-temperature loop corrections can then lift the EWSB minimum, effectively reducing the depth of the potential well and allowing SM thermal contributions to generate the potential energy barrier required for a strong first order transition. Note that unlike in the above scenario of BSM thermal loops, the new degrees of freedom generating these zero-temperature loop corrections do not have to be so light as to be in thermal contact with the plasma during the phase transition. This has been studied in many contexts, most recently in [308] with a focus on 100 TeV signatures, most importantly  $\mathcal{O}(10\%)$  deviations in the Higgs cubic coupling.

*Tree-level barriers.* A promising avenue appears to entail BSM scenarios that contain gauge singlet scalars or scalars carrying only electroweak gauge charges. The former class has received the most attention in recent years, both in the context of the NMSSM and in non-supersymmetric singlet extensions. For these scenarios the phase transition dynamics may rely on a tree-level barrier between the electroweak symmetric and broken phases. (Tree-level effects can also generate a strong phase transition in the 2HDM, though this mechanism has not yet been fully explored.<sup>23</sup>) Thermal loops, of course, also contribute to  $V_{\text{eff}}(T, \varphi)$ , and they are essential for symmetry restoration at high  $T$ . It is important to note that both the electroweak symmetric and broken phases may involve non-vanishing vevs for the singlet fields. The transition to the EWSB phase may, thus, proceed first through a “singlet phase” [308–310], a possibility that can lead to a stronger first order EWPT than if the transition to a joint Higgs-singlet phase occurs in a single step [309]. The possibilities of a SFOEWPT associated with a tree-level barrier in singlet extensions have been studied extensively in both supersymmetric and non-supersymmetric contexts. As we discuss below, work completed to date indicates that there exist interesting opportunities to probe this class of scenarios with a 100 TeV  $pp$  collider.

*Combinations.* Within the context of the singlet extension, one may also encounter a SFOEWPT even in the absence of a tree-level barrier. The presence of a quartic singlet-Higgs operator may reduce the effective quartic coupling at high- $T$ . In conjunction with the gauge loop-induced barrier, a SFOEWPT may arise [309]. A possibility of more recent interest is multi-step EWSB that involves a combination of thermal loop- and tree-level dynamics [311–313]. Multi-step transitions may arise in BSM scenarios involving new electroweak scalar multiplets, generically denoted here as  $\phi$ . For non-doublet representations, a SFOEWPT to a phase of non-vanishing  $\langle\phi\rangle$  may occur as a result of a loop-induced barrier, followed by a first order transition to the Higgs phase associated with a tree-level barrier generated by a  $\phi^\dagger\phi H^\dagger H$  interaction. The baryon asymmetry may be produced during the first step, assuming the presence of appropriate sources of CP-violation [313], and transferred to the Higgs phase during the second step provided that electroweak sphalerons are not re-excited and that the entropy injection associated with the second transition is sufficiently modest. Measurements of Higgs diphoton decay signal strength provide an important probe of this possibility if the new scalar masses are relatively light. For heavier new scalars, direct production may provide an interesting avenue for a 100 TeV collider.

### 5.3.2 Representative Scenarios

Here, we concentrate in more detail on those scenarios for which dedicated studies have been performed for a 100 TeV  $pp$  collider. In doing so, we emphasize that exploration of the EWPT with a 100 TeV collider is a relatively new area of investigation and that there exists considerable room for additional theoretical work. Thus, our choice of representative scenarios is not intended to be exhaustive but rather is dictated by the presence of existing, quantitative studies. For purely organizational purposes, we group these scenarios according to the transformation properties of the BSM scalars under SM gauge symmetries.

<sup>23</sup>Private Communication with Jose Miguel No.

*Scalar singlet extensions.* The simplest extension of the SM scalar sector entails the addition of a single, real gauge singlet  $S$ . In the NMSSM, of course, the new singlet must be complex, but many of the generic EWPT features of well-motivated singlet extensions can be studied using the real singlet extension, the “xSM”. The most general, renormalizable potential has the form<sup>24</sup>

$$V(H, S) = -\mu^2 (H^\dagger H) + \lambda (H^\dagger H)^2 + \frac{a_1}{2} (H^\dagger H) S + \frac{a_2}{2} (H^\dagger H) S^2 + \frac{b_2}{2} S^2 + \frac{b_3}{3} S^3 + \frac{b_4}{4} S^4 . \quad (56)$$

The presence of the cubic operators implies that  $S$  will have a non-vanishing vev at  $T = 0$ . Diagonalizing the resulting mass-squared matrix for the two neutral scalars leads to the mass eigenstates

$$\begin{pmatrix} h_1 \\ h_2 \end{pmatrix} = \begin{pmatrix} \cos \theta & \sin \theta \\ -\sin \theta & \cos \theta \end{pmatrix} \begin{pmatrix} h \\ s \end{pmatrix} \quad (57)$$

The mixing angle  $\theta$  and  $h_{1,2}$  masses  $m_{1,2}$  are functions of the parameters in Eq. (56) and of the doublet and singlet vevs, once the minimization conditions are imposed.

For positive  $b_2$ , the cubic operator  $H^\dagger H S$  will induce a barrier between the origin and the EWSB minimum wherein both  $\langle H^0 \rangle$  and  $\langle S \rangle$  are non-vanishing<sup>25</sup>. For an appropriate range of the potential parameters the transition to the EWSB can be strongly first order. For  $b_2 < 0$ , a minimum along the  $S$ -direction will occur with singlet vev  $\langle S \rangle = x_0$ . It is possible that the Higgs portal operator  $H^\dagger H S^2$  can generate a barrier between the  $(\langle H^0 \rangle, \langle S \rangle = (0, x_0))$  minimum and an EWSB minimum wherein  $\langle H^0 \rangle \neq 0$ , even in the absence of cubic terms in Eq. (56). The thermal history in the latter case involves a two-step transition to the EWSB vacuum, with a first step to the  $(0, x_0)$ , followed by a second transition to the EWSB vacuum [308, 309]. Under suitable conditions, the latter transition may also be strongly first order. Studies carried out to date indicate [308, 309, 314] that a SFOEWPT can arise when the mass  $m_2$  of the singlet-like scalar is less than one TeV for perturbative values of the couplings in in Eq. (56). The phenomenological probes for this scenario are discussed in Section 5.3.3 below.

For much larger masses, it is appropriate to integrate the singlet out of the theory, leading to additional terms in the effective Higgs Lagrangian of the form [315]

$$\mathcal{L}_{\text{eff}} \supset \frac{a_1^2}{m_S^4} \mathcal{O}_H - \left( \frac{a_1^2 a_2}{m_S^4} - \frac{2a_2^3 b_3}{m_S^6} \right) \mathcal{O}_6 \quad (58)$$

where

$$\mathcal{O}_H = \frac{1}{2} \left( \partial_\mu H^\dagger H \right)^2 \quad (59)$$

$$\mathcal{O}_6 = (H^\dagger H)^3 . \quad (60)$$

A SFOEWPT can arise if

$$\frac{2v^4}{m_H^2} < \frac{m_S^2}{a_1^2 a_2} < \frac{6v^4}{m_H^2} . \quad (61)$$

Precision Higgs studies, such as a measurement of  $\sigma(e^+ e^- \rightarrow Zh)$  or the Higgs cubic coupling, could probe this regime.

An instructive special case of the xSM is obtained by imposing a  $\mathbb{Z}_2$  symmetry on the potential in Eq. (56). The number of free parameters in this scenario, which was studied in detail by the authors of ref. [308], is reduced to just three (singlet mass, quartic coupling and Higgs portal coupling), making

<sup>24</sup>We eliminate a term linear in  $S$  by a linear shift in the field by a constant.

<sup>25</sup>In the region where  $S > 0$  one must have  $a_1 < 0$  for this to occur.

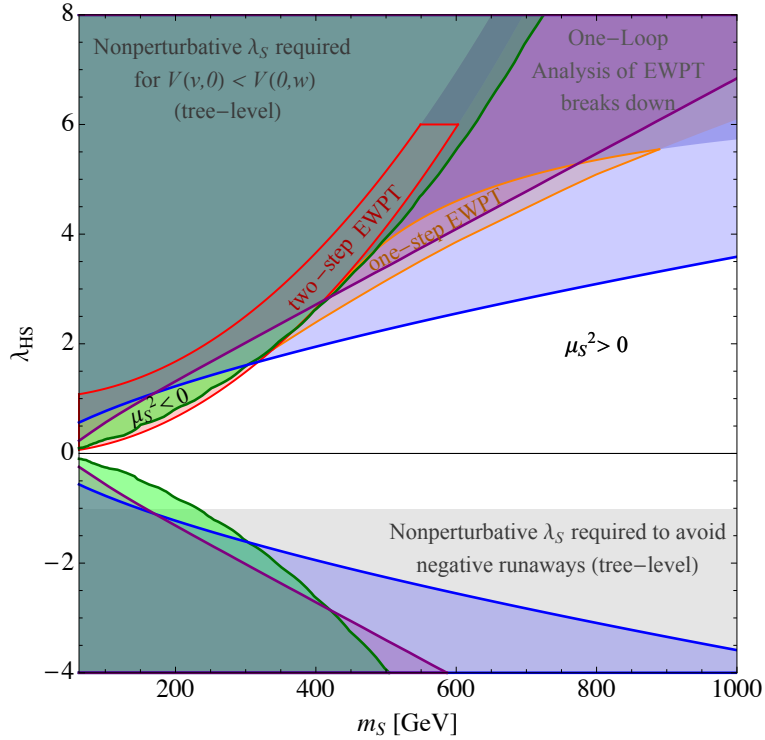


**Fig. 74:** Summary of the  $\mathbb{Z}_2$ -symmetric singlet’s parameter space for a strong EWPT, from [308].  $m_S$  is the physical singlet mass at the EWSB vacuum, while  $\lambda_{HS} = a_2/2$ ,  $\mu_S^2 = b_2$  and  $\lambda_S = b_4$  in the notation of Eq. (56). All 100 TeV sensitivity projections assume  $30\text{ab}^{-1}$  of luminosity. **Gray** shaded regions require non-perturbative  $\lambda_S > 8$  and are not under theoretical control. **Red** shaded region with red boundary: a strong two-step PT from tree-effects is possible for some choice of  $\lambda_S$ . **Orange** shaded region with orange boundary: a strong one-step PT from zero-temperature loop-effects is possible. Gray-Blue shading in top-right corner indicates the one-loop analysis becomes unreliable for  $\lambda_{HS} \gtrsim 5(6)$  in the one-step (two-step) region. In the **blue** shaded region, higgs triple coupling is modified by more than 10% compared to the SM, which could be excluded at the  $2\sigma$  [204] or better, see Table 26. In the **green** shaded region, a simple collider analysis yields  $S/\sqrt{B} \geq 2$  for VBF production of  $h^* \rightarrow SS$ . (Confirmed in later collider study by [316].) In the **purple** shaded region,  $\delta\sigma_{Zh}$  is shifted by more than 0.6%, which can be excluded by TLEP. Note that both EWBG preferred regions are excludable by XENON1T if  $S$  is a thermal relic.

it amenable to full exploration via analytical methods. It also serves as a useful “experimental worst-case” benchmark scenario of a SFOEWPT, since the the  $\mathbb{Z}_2$  symmetry turns off most of the signatures of generic singlet extensions by precluding doublet-singlet mixing.

In the  $\mathbb{Z}_2$ -symmetric xSM, a SFOEWPT can occur in two ways. For  $b_2 < 0$ , a two-step transition via the vacuum with a singlet vev can be made very strong for some range of self-couplings  $b_4$ . For  $b_2 > 0$  and large Higgs-portal couplings, zero-temperature loop effects lift the EWSB vacuum, allowing SM thermal loops to generate the necessary potential barrier. This is illustrated as the red and orange shaded/outlined regions in Fig. 74.

This scenario is almost completely invisible at the LHC, and only part of the relevant parameter space can be probed at lepton colliders. However, as we will review in Section 5.3.3 below, a 100 TeV collider can probe the entire EWBG-viable parameter space in this scenario, via either direct singlet pair production or measurements of the Higgs cubic coupling. This demonstrates the tremendous discovery potential for EWBG contributed by such a machine.

*Electroweak scalar multiplets.* Extensions of the SM scalar sector containing new color neutral, elec-

troweak multiplets arise in a variety of contexts, including type-II see-saw models, GUTs, and simple dark matter scenarios. The most widely-considered possibility is likely the two-Higgs doublet model (2HDM). In the general case where the origins of the 2HDM operators are not constrained by SUSY, it has been shown that a SFOEWPT can arise through a suitable choice of potential parameters. The precise dynamics responsible are not yet fully understood, but one likely candidate are tree-level effects that generate a barrier<sup>26</sup>. However, it has been found [317, 318] that a phenomenological consequence is the existence of the exotic decay channel for the CP-odd neutral scalar:  $A^0 \rightarrow ZH^0$ . It appears likely that this scenario will be well-probed through LHC  $A^0$  searches using this decay mode. Consequently, we will not consider it further here.

For non-doublet electroweak multiplets, denoted here  $\phi$ , the  $\rho$ -parameter constrains the  $T = 0$  neutral vev to be rather small. As a result, the tree-level barriers associated with cubic operators are not pronounced. On the other hand, it is possible the EWSB occurs twice: first along the  $\phi^0$  direction with vanishing  $H^0$ , and subsequently to the non-zero Higgs vacuum with small or vanishing  $\phi^0$  vev. The first transition may be strongly first order, leading to the conditions needed for EWBG. The resulting baryon asymmetry will be transferred to the Higgs phase during the second step if the entropy injection is not too large. Studies of the phase transition dynamics and phenomenological tests have been reported in Ref. [311] for a concrete illustration with a real triplet, and general considerations outlined in the subsequent work of Ref. [312]. The corresponding CP-violating dynamics needed for baryon asymmetry generation have been discussed in general terms in Ref. [313] along with a concrete illustration of its viability. To date, no work has been completed on the probes using a 100 TeV  $pp$  collider. However, the new electroweak states must generally be pair produced. The corresponding phase space considerations, along with the electroweak scale cross sections, make this class of scenarios an interesting opportunity for a next generation hadronic collider.

While the signal associated with direct production is highly model dependent, the deviations of the Higgs boson couplings from the SM values more generic in the presence of the EW scalar. One of the most important observables in this case is  $h\gamma\gamma$  coupling, which is necessarily affected due to the new light EW charged states running in the loop. In the next subsection we will estimate the deviations and comment on the prospects of the 100 TeV machine.

### 5.3.3 Prospective signatures

While there exist a number of studies analyzing the prospects for LHC probes of the EWPT (for a review and references, see, *e.g.* Ref. [259]), relatively few have focused on the prospects for a next generation high energy  $pp$  collider. Here, we review work completed to date, following the same organization as in Section 5.3.2.

*Gauge Singlets.* We start by considering the  $\mathbb{Z}_2$ -symmetric xSM, which was studied in detail by the authors of Ref. [308]. Remarkably, despite the fact that this model represents an experimental worst-case scenario for EWBG, *all parameter regions with a SFOEWPT can be probed at a 100 TeV collider.*

Unlike the general xSM, this scenario has only a handful of signatures. The singlet can only be pair-produced via the  $H^\dagger HS^2$  operator through the processes  $pp \rightarrow h^* \rightarrow SS$  and  $pp \rightarrow h^* \rightarrow SSjj$ , where the former corresponds to gluon fusion production of the off-shell Higgs and the latter to VBF production. A search for VBF-tagged dijets + MET can be sensitive to  $SS$  production, though mono-jet analyses are also worth exploring in more detail. Singlet loops will modify the Higgs cubic coupling and  $Zh$  coupling at the  $\sim 10\%$  and  $\sim 0.5\%$  level respectively. The former are best measured at the 100 TeV collider, see [204] and Table 26, while the latter can be detected at lepton colliders like FCC-ee [178, 319–321]. As Fig. 74 shows, direct singlet pair production (green region) is sensitive to the two-step phase transition, while measurements of the Higgs cubic coupling (blue region) are sensitive to the one-step region. This allows the 100 TeV collider to achieve full coverage of the parameter space

<sup>26</sup>Private Communication with Jose Miguel No.

viable for EWBG.

The authors of Ref. [308] observe that since  $S$  is stable, it constitutes a dark matter candidate, a possibility that has been considered widely by other studies, most recently [322]. The XENON 1T direct detection search could probe the entire SFOEWPT-viable region, well in advance of the initiation of the FCC-hh program. Non-observation of a direct detection signal, however, would not preclude this scenario. In principle, introduction of small  $Z_2$ -breaking terms would render the singlet-like state unstable, thereby evading DM direct detection searches. For a sufficiently long decay length,  $SS$  would nevertheless appear as MET, leaving the VBF channel as the only viable probe under these conditions. Furthermore, even if a dark matter signal is detected, collider studies will be necessary to determine the nature of the new particles, and their possible connection to the EWPT.

The general xSM has many more signatures, since the presence of  $Z_2$  breaking operators in the potential can lead to non-negligible doublet-singlet mixing. In this case, one may directly produce the singlet-like state  $h_2$ , with reduction in production cross section by  $\sin^2\theta$  compared to the SM Higgs production cross section. For a given  $m_2$ , it will decay the same final states as would a pure SM Higgs of that mass. However, for  $m_2 > 2m_1$ , the decay  $h_2 \rightarrow h_1 h_1$  becomes kinematically allowed, leading to the possibility of resonant di-Higgs production. Studies of this possibility have been carried out for the LHC [323–326], and there exist promising possibilities for both discovery and exclusion if  $h_2$  is relatively light. The resonant di-Higgs cross section can be significantly larger than the non-resonant SM di-Higgs cross section, so observation of this process could occur as early as Run II of the LHC.

Nonetheless, we are again led to the conclusion that a full probe of the SFOEWPT-viable xSM *via* resonant di-Higgs production will likely require a 100 TeV  $pp$  collider. Recently, the authors of Ref. [327] have investigated the discovery reach for the LHC and future  $pp$  colliders for the SFOEWPT-viable parameter space of the xSM. After scanning over the parameters in the potential (56) and identifying choices that lead to a SFOEWPT, the authors selected points yielding the maximum and minimum  $\sigma(pp \rightarrow h_2) \times \text{BR}(h_2 \rightarrow h_1 h_1)$ . Results were grouped by  $m_{h_2}$  in bins 50 GeV-wide, and a set of 22 benchmark parameter sets chosen (11 each for the minimum and maximum resonant di-Higgs signal strength). Two sets of final states were considered:  $b\bar{b}\gamma\gamma$  and  $4\tau$ . After taking into account SM backgrounds and combining the prospective reach for the two channels, the significance  $N_\sigma$  for each benchmark point was computed using a boosted decision tree analysis. Results are shown in Fig. 75. The left panel compares the reach of the high-luminosity phase of the LHC with that of a 100 TeV  $pp$  collider with 3 and 30  $\text{ab}^{-1}$ , respectively. It is apparent that under this “best case” study, wherein no pile up or detector effects have been included, *the discovery reach of a 100 TeV  $pp$  collider could cover nearly all of the SFOEWPT-viable parameter space with 30  $\text{ab}^{-1}$* . For the LHC, the reach with these two channels is more limited. We note that inclusion of pile up and detector effects will likely degrade the discovery potential. However, for this best case analysis, the significance lies well above  $5\sigma$  for nearly all of the SFOEWPT-viable parameter space. Thus, we expect this discovery potential to persist even with a more realistic analysis.

In this context, it is also interesting to ask whether 100 TeV is the optimal energy for this probe. To address this question, the authors of Ref. [327] performed a similar study for  $\sqrt{s} = 50$  and 200 TeV as well. The results are given in the right panel of Fig. 75. Unsurprisingly, the reach of a 200 TeV collider would exceed that of a 100 TeV machine, with the advantage being particularly pronounced for the higher mass region. On the other hand, for lower  $\sqrt{s}$ , one would begin to lose discovery potential in the high mass region and face less room for degradation of the significance once pile up and detector performance are considered.

Measurements of the Higgs trilinear self-coupling provide an alternate probe of the EWPT [307]. In the absence of a  $Z_2$  symmetry, this coupling will be modified by a combination of the parameters in the potential and the non-zero mixing angle. The opportunities for probing this effect at the LHC and various prospective future colliders are illustrated in Fig. 76, where the critical temperature for the EWPT is plotted vs. the trilinear self coupling  $g_{111}$ . The SM value corresponds to the solid vertical black

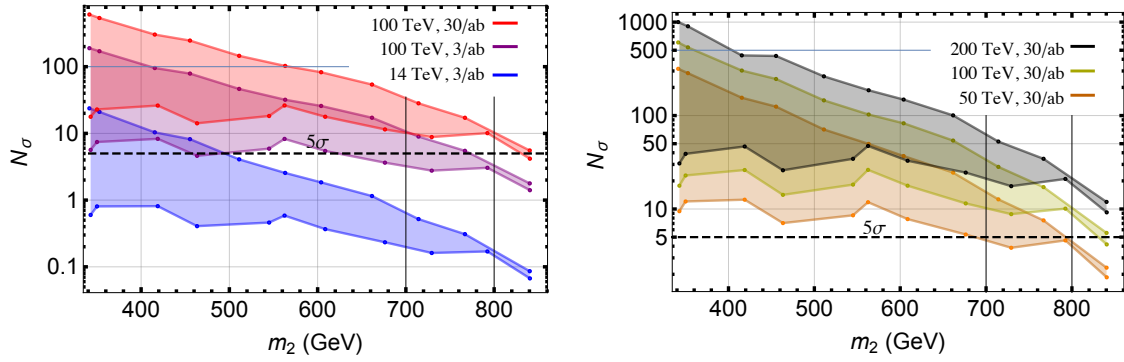


**Fig. 75:** Physics reach for a SFOEWPT in the xSM with the LHC and a higher energy  $pp$  collider, considering resonant di-Higgs production in the  $b\bar{b}\gamma\gamma$  and  $4\tau$  channels [327]. For each panel, vertical axis gives the significance  $N_\sigma$  for each of the 22 SFOEWPT-viable benchmark points (see text), combining the significance of the two channels. For a given colored band, the upper (lower) edges give the maximum (minimum)  $\sigma(pp \rightarrow h_2) \times \text{BR}(h_2 \rightarrow h_1 h_1)$ . Left panel: comparison of the reach for the high luminosity phase of the LHC with a 100 TeV  $pp$  collider at two different integrated luminosities. Right panel: comparison of the reach with 30  $\text{ab}^{-1}$  at three different center of mass energies.

line. The colored vertical bands indicate the prospective sensitivities of the LHC and future colliders. The black dots indicate results of a scan over the parameters in Eq. (56) that lead to a SFOEWPT, taking into account present LHC, electroweak precision, and LEP Higgs search constraints. It is clear that significant modifications of the self-coupling can occur. Moreover, even in the absence of an observed deviation at the LHC or future  $e^+e^-$  colliders, there exists significant opportunities for discovery with a next generation  $pp$  collider.

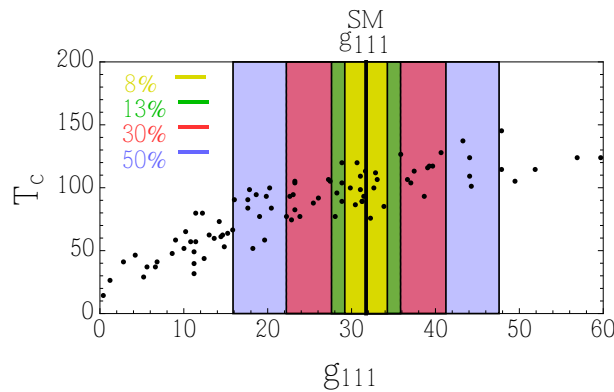


**Fig. 76:** Correlation between the critical temperature and SM-like Higgs scalar self-coupling in the singlet-extended SM with a strong first-order electroweak phase transition, adapted from Ref. [314]. Colors indicate prospective sensitivities of the HL-LHC (purple), CEPC/FCC-ee (red), ILC (green), and SPPC/FCC-hh (yellow). The latter was assumed to be 8%, but the precision may be as good as 3%, see Table 26.

*Non-trivial representations of the SM.* In this case, where the strong EWPT is induced by thermal loops of the new degrees of freedom, we expect strong deviations of the higgs couplings to  $gg$ ,  $\gamma\gamma$  and  $\gamma Z$  are expected. These couplings are the most important, because at the SM these couplings show up at one-loop at the LO, and therefore any new light state might potentially lead to strong deviations from the SM. We will focus here on the first two couplings, namely  $gg$  and  $\gamma\gamma$ . While the latter can be relatively precisely probed at hadron colliders via appropriate decay mode of the higgs, the former affects the

dominant higgs production mode.

The expected deviations of the coupling to the  $gg$  in the case of the colored scalars is appreciable. We illustrate this on an example of the  $SU(3)_c$  triplet with the EW quantum numbers  $1_{-4/3}$  on Fig. 77. In this example we overlay the contours of the deviations from the SM higgs couplings on the strength of the EWPT, which we parametrize as

$$\xi \equiv \frac{v_c}{T_c} \quad (62)$$

where  $v_c$  stands for the higgs VEV at the temperature of the PT, and  $T_c$  is the temperature of the PT.<sup>27</sup> The value of  $\xi$  is calculated in the one-loop approximation. In principle one demands  $\xi \gtrsim 1$  for the strong 1st order PT, however, given the order one uncertainties one usually gets in thermal loops calculation, even nominally smaller values of  $\xi$  in this approximation might be viable. As we clearly see from here most of the valid parameter space for the triplet has either been already probed at the LHC, or will be probed in LHC13 or VLHC.

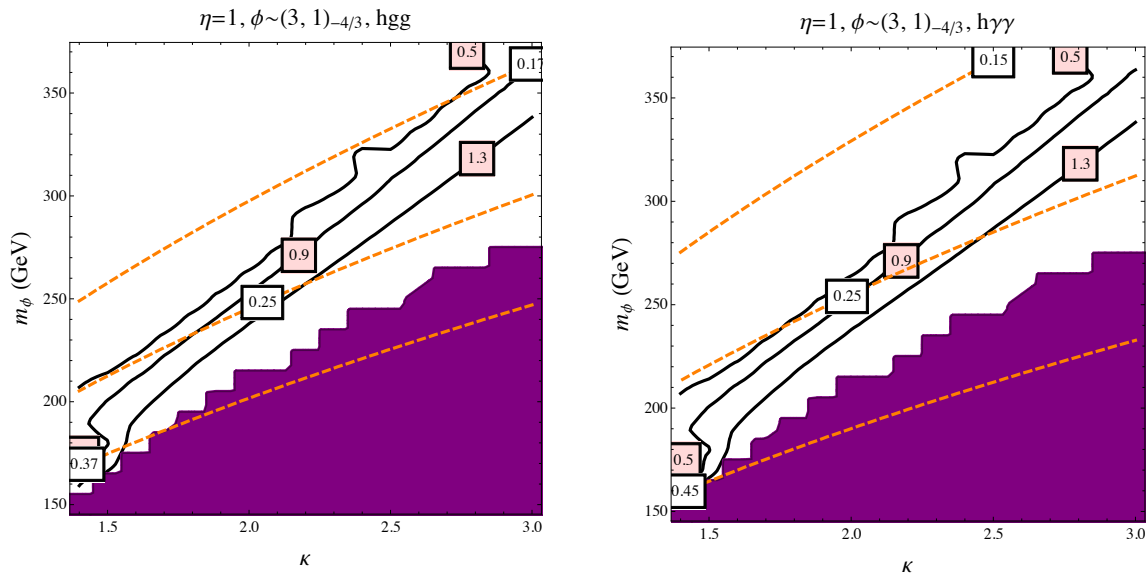


**Fig. 77:** Orange contours: deviations (in percent from SM) of the  $hgg$  and  $h\gamma\gamma$  couplings from the SM values in the presence of the diquark with the quantum numbers  $1_{-4/3}$ . In the shaded region there is no one-step transition to the EW vacuum. The black solid lines stand for the strength of the EW phase transition  $\xi$ . The plots are from Ref. [306].

The situation is different one we consider EW-charged colorless states. Here the main deviations are in  $\gamma\gamma$  and  $\gamma Z$  channels. We will show the deviations in the first channel, to the best of our knowledge the deviations in  $\gamma Z$  have not yet been explored in the context. On the other hand, deviations of  $h\gamma\gamma$  couplings can be as small as 5% in the relevant part of parameter space. While the HL-LHC may be sensitive to diphoton decay branching ratio at the few percent level, the FCC-pp will be able to make important gains in addressing this option, see Section 3.2.1. We illustrate this point on Fig. 78. Although it is not clear whether the HL-LHC will be able to achieve the absolute sensitivity required to completely probe this possibility (better than 5%), substantial gains can be made by measuring the ratios of the various cross sections, for example the BRs of  $\gamma\gamma$  relative to  $ZZ^*$  [329, 330].

<sup>27</sup>The quantity  $\xi$  is not, in general, gauge invariant [328]. A more rigorous, gauge invariant characterization of the strength of the EWPT requires computation of the sphaleron energy and a careful treatment of  $T_c$ . These computations are also subject to additional theoretical uncertainties. For a detailed, discussion, see [328]. In what follows, we will treat it as a rough “rule of thumb”, deferring a gauge invariant analysis to future studies.

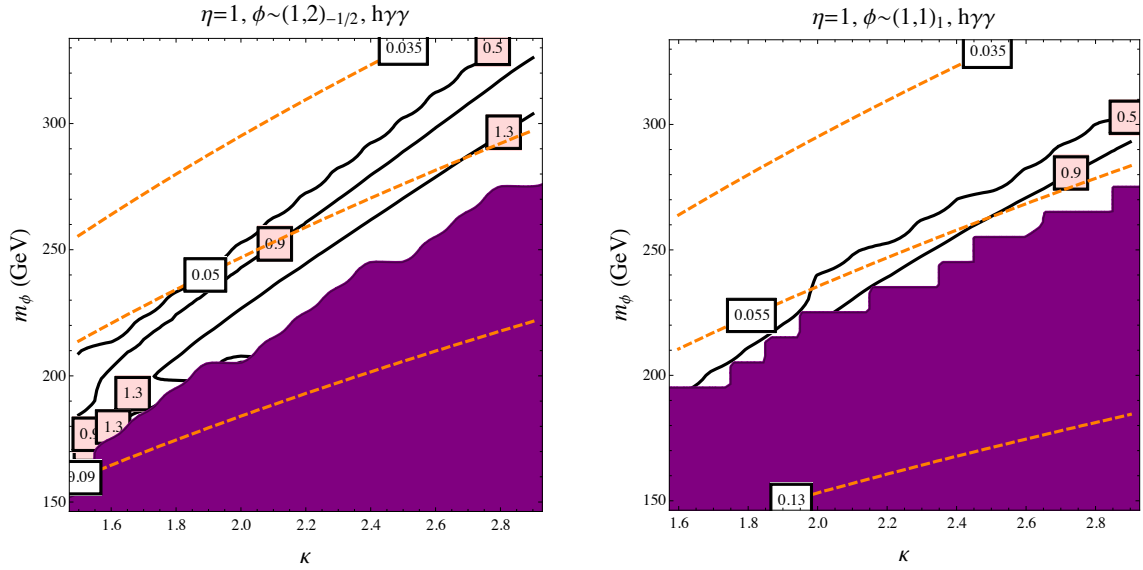


**Fig. 78:** Expected deviation of  $h\gamma\gamma$  couplings in case of EW-charged scalars with quantum numbers 1, 2,  $-1/2$  (left panel) and 1, 1, 1 (right panel) from Ref. [306]. Same labeling as Fig. 77.

### 5.3.4 EWPT: The discovery landscape

Given the relatively small set of studies dedicated to probes of the EWPT at a 100 TeV collider, it would be premature to draw far-reaching conclusions about the range of opportunities for the FCC-hh. Indeed, the importance of engaging the community in performing these investigations was one of the key conclusions to the recent ACFI workshop that focused on this physics [256]. Nonetheless, the work performed to date points to what is likely a rich opportunity. As indicated in Fig. 75, for the simplest BSM scenario yielding a SFOEWPT, the LHC will begin to “scratch the surface”, whereas the FCC-hh would provide an essentially exhaustive probe, which is also illustrated by Fig. 74. Moreover,  $\sqrt{s} = 100$  TeV appears to be close to the minimum needed for discovery.

Of course, it is possible that if this scenario is realized in nature, the parameters will put it in an LHC-accessible region. In this case, the FCC-hh could provide confirmation relatively early in its operation, and could then be used to explore additional signatures, such as small deviations of the Higgs trilinear coupling from its SM value (see Fig. 76). Importantly, these observables provide an orthogonal probe of EWBG compared to, for example, measurements of Higgs mixing at lepton colliders through Higgs coupling measurements, since the Higgs self coupling and mixing angle are not correlated in xSM scenarios with a SFOEWPT [314]. While the 100 TeV collider may be able to probe EWBG exhaustively, it seems especially unlikely that such new physics could escape detection at both the 100 TeV *and* a lepton collider. This complementarity provides a strong argument for the construction of both machines.

## 5.4 Dark Matter

An extended Higgs sector offers new possibilities for dark matter candidates and new avenues for the dark matter to communicate with the Standard Model states. In general, there is a wide variety of theoretical constructs exhibiting this feature, including models where the dark matter is a scalar, fermion, or vector particle, and constructions where it is either an electroweak singlet or part of an SU(2) multiplet, charged under the electroweak interaction. Similarly, there are a variety of possibilities for the SU(2) representations of the extended Higgs sector. If the couplings are large enough, this class of theories results in potentially visible phenomena resulting from dark matter annihilation, scattering with heavy nuclei, and production at high energy colliders. Colliders offer a particular opportunity when the interac-

tions between the dark matter and the standard model are suppressed at low momentum transfer, which suppresses its annihilation and/or scattering with heavy nuclei, because the ambient dark matter in the galaxy is highly non-relativistic, with  $v \sim 10^{-4}$ .

### 5.4.1 Landscape of Current Models

In the limit in which the mediator particles are heavy compared to all energies of interest, all theories flow to a universal effective field theory (EFT) consisting of the Standard Model plus the dark matter, and residual non-renormalizable terms in the form of contact interactions which connect them [331–336]. The EFT limit has been widely studied using data from run I of the LHC. At the same time, it is recognized that theories in which the mediators are light enough to play an active role in collider phenomenology are of great interest, and simplified model descriptions including such particles have been widely discussed [337–339].

We can discriminate between various classes of simplified models using scalar particles to communicate with a secluded sector:

#### 5.4.1.1 Inert multiplet models

In inert models, the Standard Model is extended by a scalar multiplet in a certain electroweak representation:

$$\mathcal{L} = \mathcal{L}_{\text{SM}} + \frac{1}{2} \partial_\mu \phi \partial^\mu \phi - \frac{1}{2} m_\phi^2 \phi^2 - c_\phi |H^2| |\phi^2| - \lambda_\phi |\phi^2|^2, \quad (63)$$

where  $H$  is the SM-like Higgs doublet, and  $\phi$  is the additional scalar field that may be a SM gauge singlet or charged under SM electroweak symmetry. Note that this construction contains a  $\mathbb{Z}_2$  symmetry  $\phi \rightarrow -\phi$ , such that (provided  $\phi$  does not develop a vacuum expectation value, and thus mix with the SM Higgs) its lightest component is stable. Cases in which  $\phi$  is an even-dimensional  $\text{SU}(2)$  representation are generically in tension with null searches for scattering with nuclei, but odd-dimensional  $\text{SU}(2)$  representations remain relatively unconstrained [340, 341]. For recent studies for the case when  $\phi$  transforms non-trivially under SM electroweak symmetry, see, *e.g.* [342, 343]. Scenarios wherein  $\phi$  is a gauge singlet (real or complex) correspond to setting the  $\mathbb{Z}_2$ -breaking coefficients  $a_1 = b_3 = 0$  in Eq. (56) and identifying  $b_2 \rightarrow m_\phi^2$ ,  $a_2 \rightarrow 2c_\phi$ , and  $b_4 \rightarrow 4\lambda_\phi$ . This scenario has been studied extensively in Refs. [279, 280, 308, 310, 322, 344–349]. An extension to the 2HDM plus a real singlet has been considered in Refs. [347, 350].

#### 5.4.1.2 Higgs-multiplet mixing models

If the  $\mathbb{Z}_2$  symmetry is broken, either explicitly by including a trilinear interaction such as  $\phi |H|^2$ , or spontaneously by engineering a potential for  $\phi$  which results in it obtaining a vacuum expectation value, it will mix with the SM Higgs. In general, this removes the possibility that  $\phi$  itself will play the role of dark matter, but it may nonetheless serve as the portal to the dark sector if it couples to the dark matter. For example, if  $\phi$  and the dark matter  $\chi$  are both electroweak singlets, the only renormalizable interactions of  $\chi$  respecting a  $\mathbb{Z}_2$  are with  $\phi$ . Through mixing with the Higgs,  $\phi$  picks up coupling to the Standard Model, and thus serves as the bridge between the two sectors (as does the SM Higgs) [344, 351, 352].

An special case occurs when  $\phi$  is a complex singlet [280, 310, 346]. In this scenario, if the potential contains a global  $\text{U}(1)$  symmetry that is both spontaneously and softly broken, the massive Goldstone mode can serve as a dark matter candidate while the remaining degree of freedom mixes with the SM Higgs boson.

#### 5.4.1.3 Vector mediators

While scalar mediators can be directly related to Higgs phenomenology, either by mixing additional scalar degrees of freedom with the Standard Model Higgs field, or by involving the Higgs boson in

the production of new scalar particles, spin-1 mediators connecting the visible and dark sector is an interesting alternative. A vector mediator can arise from extended or additional gauge sectors to the Standard Model gauge group. Often a second Higgs boson is needed for the vector mediator to acquire a mass in a gauge invariant way. Such scenarios can for example arise from radiative symmetry breaking in the dark sector [353, 354].

#### 5.4.1.4 Fermionic Dark Matter

Fermionic dark matter can communicate with the Standard Model through the Higgs portal provided the dark matter is charged under the electroweak group. Coupling to the SM Higgs requires a combination of a  $n$ -dimensional representation with an  $n + 1$ -dimensional one, and an appropriate choice of hypercharge. Given current constraints, this is a region of particular interest in the MSSM, and can also be represented by simplified models, including the “singlet-doublet” [355–357], “doublet-triplet” [358], and “triplet-quadruplet” [359] implementations. The generic feature in such models is electroweak-charged matter, which the relic abundance suggests typically has TeV scale masses. In the absence of additional ingredients, this is a regime which is difficult or impossible to probe effectively at LHC energies, but is typically within reach of a 100 TeV future collider.

#### 5.4.2 Signatures

When the mediators are heavy compared to the typical parton energies, all theories flow to a universal set of effective field theories, and lead to signatures in which the dark matter is produced directly (with additional radiation to trigger) through contact interactions. Projections for the limits on such interactions at 100 TeV were derived in [360].

For models discussed in Section 5.4.1.1, a neutral scalar of the multiplet  $\phi$  could act as DM candidate. If then  $m_\phi < m_H/2$  the decay  $H \rightarrow \phi\phi$  contributes to the total Higgs width  $\Gamma_H$  and can be probed in searches for invisible Higgs decays [361]. If realised within the Higgs portal model of Eq. 63, with only two free parameters, this scenario is very predictive. We show the branching ratio of the Higgs boson into the stable particle  $\phi$  in Fig. 79 (left). Current LHC limits [362–364] reach as low as  $\text{BR}(H \rightarrow \text{inv}) \lesssim 30\%$ , while an extrapolation to  $3000 \text{ fb}^{-1}$  yields  $\text{BR}(H \rightarrow \text{inv}) \lesssim 5\%$  [365] if systematic uncertainties scale with  $1/\sqrt{\mathcal{L}}$ .

It has been pointed out that off-shell Higgs measurements can set an indirect limit on the total Higgs width [366], which could in turn result in a limit on Higgs decays into dark matter candidates, however such an interpretation is highly model-dependent [367] and can only be invoked on a case-by-case basis [368].

If  $m_\phi > m_H/2$   $2\phi$ -production in association with one or two jets or a pair of heavy quarks can be probed at future hadron colliders. The authors of [316, 369] find the VBF configuration to be most promising to limit  $m_\phi$  and  $c_\phi$  of Eq. 63. For a combined limit on  $m_\phi$  and  $c_\phi$  in the mono-jet,  $t\bar{t}h$  and VBF channel see Fig. 79 (middle). Increasing the collision energy from  $\sqrt{s} = 14 \text{ TeV}$  to  $\sqrt{s} = 100 \text{ TeV}$  and the integrated luminosity from  $3 \text{ ab}^{-1}$  to  $30 \text{ ab}^{-1}$  extends the testable parameter range significantly, e.g. for  $m_\phi = 200 \text{ GeV}$  from  $c_\phi = 2.7$  to  $c_\phi \leq 0.7$  at 95% C.L. Requesting  $\phi$  to contribute to a certain fraction of the relic dark matter density results in the contours of Fig. 79 (right).

In the context of models of Sections 5.4.1.2 and 5.4.1.3 possible signatures at future colliders can be far more diverse than modified Higgs branching ratios or final states with missing energy. Depending on the particle content and their representations mixing between scalars and gauge bosons, e.g. via kinetic mixing, can result in a rich phenomenology. Not only can  $\phi$  be probed effectively in an indirect way by global Higgs fits [371, 372] but also in direct searches without involvement of the Higgs boson. In addition, for models wherein  $\phi$  transforms nontrivially under SM electroweak symmetry, Drell-Yan pair production that includes at least one electrically charged component of the multiplet may lead to the appearance of a disappearing charged track, providing an additional probe of this class of scenarios [342].

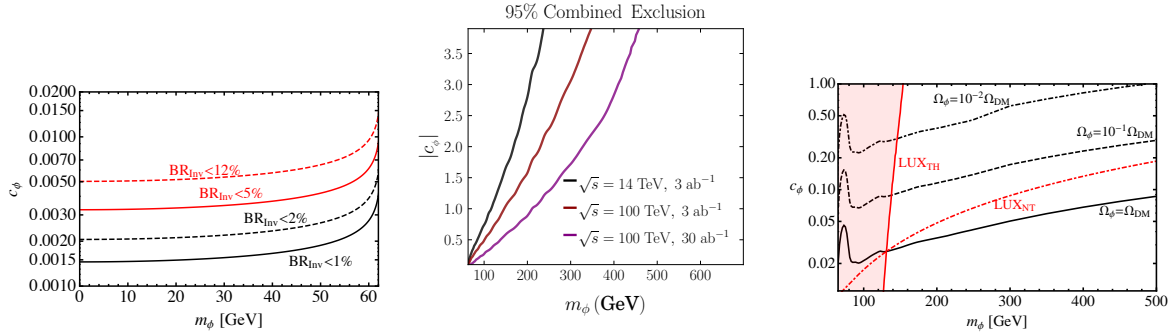


**Fig. 79:** The left figure shows the branching ratio of the decay  $H \rightarrow \phi\phi$  [370] for  $m_\phi \leq m_H/2$ . The figure in the middle shows the expected improvement on the Higgs portal coupling  $c_\phi$  against  $m_\phi$  when increasing the collision energy from  $\sqrt{s} = 14$  TeV to  $\sqrt{s} = 100$  TeV and the integrated luminosity from  $3 \text{ ab}^{-1}$  to  $30 \text{ ab}^{-1}$ . The fraction of the relic dark matter density  $\Omega_{DM}$  is shown in the right figure. More information on middle and right figures can be found in [316].

In [266] predictions for searches for scalar and vector mediators at a possible 100 TeV have been obtained, see Fig. 80. They show strong complementarity between the reach of hadron colliders, indirect and direct detection experiments. Further, it has been shown that the mediator mass and CP property can be inferred from jet distributions in VBF topologies [267].

Striking signatures, with little Standard Model background, are displaced vertices or even displaced jets. They can arise if the mediator has a sufficiently long lifetime and decays back into electrically charged Standard Model particles [297, 375] or mesons of a dark sector which in turn decay into Standard Model mesons, e.g. if the Standard Model gauge group is extended by a dark  $SU(N_d)$  [376]. In the latter case, if the mediator is pair-produced, resulting in more than one so-called "emerging jets", the QCD background can be rejected completely. All scenarios with rare but rather clean Higgs decays benefit greatly from the enhanced Higgs production rate and increased integrated luminosity of a 100 TeV collider.

## 5.5 The Origins of Neutrino Mass and Left-right symmetric model

The neutrino oscillation data have unambiguously established that neutrinos have tiny but non-zero masses, as well as mixing between different flavors. Understanding these necessarily requires physics beyond the Standard Model (SM). Since the origin of masses for all the SM charged fermions has now been clarified by the discovery of the Higgs boson [1, 2], an important question is what physics is behind neutrino masses. If we simply add three right-handed (RH) neutrinos  $N_R$  to the SM, one can write Yukawa couplings of the form  $\mathcal{L}_{\nu,Y} = h_\nu \bar{L} H N_R$ , where  $H$  is the SM Higgs doublet and  $L$  the lepton doublet. After electroweak symmetry breaking by the vacuum expectation value (VEV) of the neutral component of the SM Higgs, i.e.  $\langle H^0 \rangle = v_{ew}$ , this gives a Dirac mass to neutrinos of magnitude  $m_D = h_\nu v_{ew}$ . To get sub-eV neutrino masses, however, we need  $h_\nu \lesssim 10^{-12}$ , which is an "unnaturally" small number, as compared to the Yukawa couplings involving other SM fermions. So the strong suspicion is that there is some new physics beyond just the addition of RH neutrinos, as well as new Higgs bosons associated with this, which is responsible for neutrino mass generation.

A simple paradigm is the (type-I) seesaw mechanism [377–380] where the RH neutrinos alluded to above have Majorana masses, in addition to having Yukawa couplings like all charged fermions. Neutrinos being electrically neutral allows for this possibility, making them different from the charged fermions and suggesting that this might be at the root of such diverse mass and mixing patterns for leptons compared to quarks. The crux of this physics is the seesaw matrix with the generic form in the

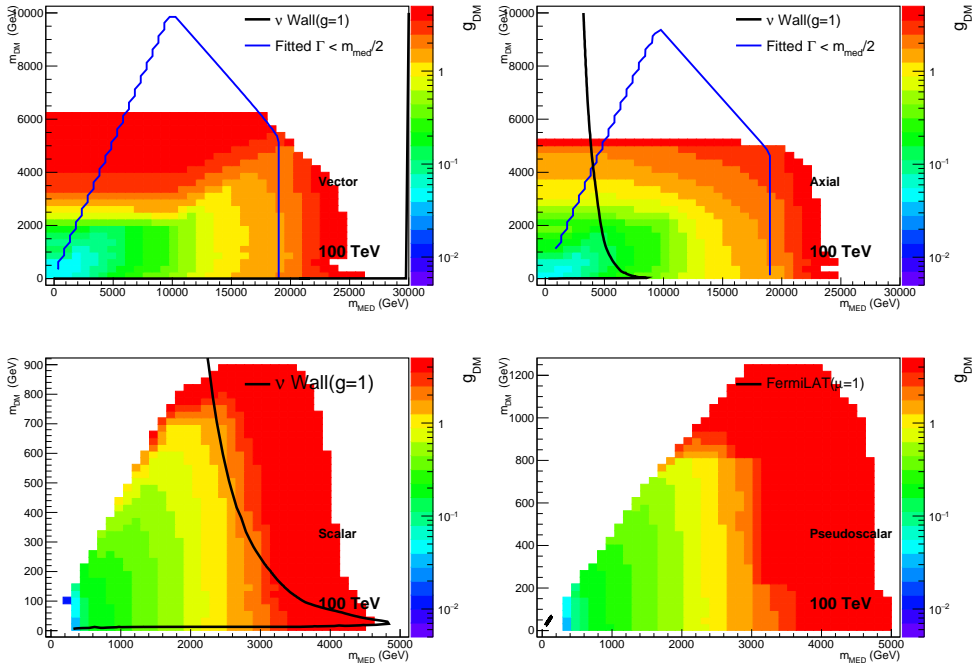


**Fig. 80:** 100 TeV limits for vector (upper left), axial-vector (upper right), scalar (lower left) and pseudoscalar (upper right) mediators. The blue curves on the figures for the vector and axial-vector depict the regions inside which the width of the mediator is smaller than its mass, i.e.  $\Gamma_{\text{MED}} < m_{\text{MED}}$ . The black lines for the vector, axial-vector and scalar cases show the limits obtained if cross sections down to the neutrino wall [373] can be probed. For the pseudoscalar the black line shows the limit from FermiLAT [374]. More information on these figures can be found in [267].

$(\nu_L, N_R)$  space:

$$\mathcal{M}_\nu = \begin{pmatrix} 0 & m_D \\ m_D^T & M_N \end{pmatrix} \quad (64)$$

where  $M_N$  is the Majorana mass for  $N_R$  which embodies the new neutrino mass physics, along with the mixing between the light ( $\nu_L$ ) and heavy ( $N_R$ ) neutrinos governed by the parameter  $V_{\ell N} \sim m_D M_N^{-1}$ . The mass of light neutrinos is given by the seesaw formula

$$M_\nu \simeq -m_D M_N^{-1} m_D^T. \quad (65)$$

The question that one is led to ask is what is the origin of  $N_R$  and the associated Majorana masses which represents the seesaw scale. We require that the new physics should naturally provide the key ingredients of the seesaw mechanism, i.e. the RH neutrinos and a symmetry origin of their masses  $M_N$ . This will necessarily involve new Higgs bosons, whose collider signals are discussed in this article for a future collider with center-of-mass  $\sqrt{s} = 100$  TeV. Clearly for the seesaw scale to be accessible at such colliders, it must be below the multi-TeV regime, which implies that there will exist new Higgs bosons with TeV masses. A look at the seesaw formula makes it clear that with a multi-TeV seesaw scale, a sub-eV neutrino mass is quite compatible with Yukawa couplings similar to electron Yukawa of the SM (i.e.  $h_\nu \sim h_e$ ), thus obviating the need for any ultra-small Yukawas (as for example in the pure Dirac case).

### 5.5.1 Left-Right Symmetric models (LRSM)

An appealing UV-complete model for the TeV-scale seesaw is the left-right symmetric model (LRSM) which extends the SM electroweak gauge group to  $SU(2)_L \times SU(2)_R \times U(1)_{B-L}$  [381–383]. The fermions are assigned to the LR gauge group as follows: denoting  $Q \equiv (u \ d)^T$  and  $\psi \equiv (\nu \ e)^T$  as the quark and lepton doublets respectively, we assign  $Q_L$  and  $\psi_L$  as the doublets under the  $SU(2)_L$  group and  $Q_R$  and  $\psi_R$  as the doublets under the  $SU(2)_R$  group. The Higgs sector of the model consists of one or several of the following multiplets, that go the beyond the SM Higgs doublet:

$$\phi \equiv \begin{pmatrix} \phi_1^0 & \phi_2^+ \\ \phi_1^- & \phi_2^0 \end{pmatrix}, \quad \Delta_L \equiv \begin{pmatrix} \Delta_L^+/\sqrt{2} & \Delta_L^{++} \\ \Delta_L^0 & -\Delta_L^+/\sqrt{2} \end{pmatrix}, \quad \Delta_R \equiv \begin{pmatrix} \Delta_R^+/\sqrt{2} & \Delta_R^{++} \\ \Delta_R^0 & -\Delta_R^+/\sqrt{2} \end{pmatrix}. \quad (66)$$

There are versions of the model where parity and  $SU(2)_R$  gauge symmetry scales are decoupled so that  $\Delta_L$  fields are absent from the low energy theory [384]. An important practical implication of the parity decoupling is that it suppresses the type-II seesaw contribution to neutrino masses and thus provides a natural way to realize the TeV-scale type-I seesaw mechanism, as in Eq. (65).

It has also been pointed out recently that the class of minimal left-right models discussed here provide a natural setting for new fermions or scalars that are stable without the need for extra symmetries and therefore become candidates for dark matter of the universe [385–388]. We do not elaborate on these issues here since they do not affect our considerations reported here.

The gauge symmetry  $SU(2)_R \times U(1)_{B-L}$  is broken by the VEV  $\langle \Delta_R^0 \rangle = v_R$  to the group  $U(1)_Y$  of the SM. So  $v_R$  will be the seesaw scale as we see below and is chosen to be in the multi-TeV range. The VEV of the  $\phi$  field,  $\langle \phi \rangle = \text{diag}(\kappa, \kappa' e^{i\alpha})$ , breaks the SM gauge group to  $U(1)_{\text{em}}$ , with  $\alpha$  being a CP-violating phase. We will work in the limit that  $\kappa' \ll \kappa$ , so that  $\kappa \simeq v_{\text{ew}}$ .

To see how the fermions pick up mass and how the seesaw mechanism arises, we write down the Yukawa Lagrangian of the model:

$$\begin{aligned} \mathcal{L}_Y = & h_{ij}^{\ell,a} \bar{\psi}_{L_i} \phi_a \psi_{R_j} + \tilde{h}_{ij}^{\ell,a} \bar{\psi}_{L_i} \tilde{\phi}_a \psi_{R_j} + h_{ij}^{q,a} \bar{Q}_{L_i} \phi_a Q_{R_j} + \tilde{h}_{ij}^{q,a} \bar{Q}_{L_i} \tilde{\phi}_a Q_{R_j} \\ & + f(\psi_{R_i} \Delta_R \psi_{R_j} + \psi_{L_i} \Delta_L \psi_{L_j}) + \text{H.c.} \end{aligned} \quad (67)$$

where  $i, j$  stand for generations and  $a$  for labeling Higgs bi-doublets, and  $\tilde{\phi} = \tau_2 \phi^* \tau_2$  ( $\tau_2$  being the second Pauli matrix). After symmetry breaking, the quark and charged lepton masses are given by the generic formula  $M_f = h^f \kappa + \tilde{h}^f \kappa' e^{-i\alpha}$  for up-type quarks, while for down-type quarks and charged leptons, it is the same formula with  $\kappa$  and  $\kappa'$  interchanged and  $\alpha \rightarrow -\alpha$ . The above Yukawa Lagrangian leads to the Dirac mass matrix for neutrinos,  $m_D = h^\ell \kappa + \tilde{h}^\ell \kappa' e^{-i\alpha}$ , and the Majorana mass matrix for the heavy RH neutrinos,  $M_N = f v_R$ , which go into the seesaw formula (65) for calculating the light neutrino masses.

### 5.5.2 Scalar Potential

The most general renormalizable scalar potential for the bidoublet and triplet fields, which is invariant under parity, is given by

$$\begin{aligned} \mathcal{V} = & -\mu_1^2 \text{Tr}(\phi^\dagger \phi) - \mu_2^2 \left[ \text{Tr}(\tilde{\phi} \phi^\dagger) + \text{Tr}(\tilde{\phi}^\dagger \phi) \right] - \mu_3^2 \text{Tr}(\Delta_R \Delta_R^\dagger) \\ & + \lambda_1 \left[ \text{Tr}(\phi^\dagger \phi) \right]^2 + \lambda_2 \left\{ \left[ \text{Tr}(\tilde{\phi} \phi^\dagger) \right]^2 + \left[ \text{Tr}(\tilde{\phi}^\dagger \phi) \right]^2 \right\} \\ & + \lambda_3 \text{Tr}(\tilde{\phi} \phi^\dagger) \text{Tr}(\tilde{\phi}^\dagger \phi) + \lambda_4 \text{Tr}(\phi^\dagger \phi) \left[ \text{Tr}(\tilde{\phi} \phi^\dagger) + \text{Tr}(\tilde{\phi}^\dagger \phi) \right] \\ & + \rho_1 \left[ \text{Tr}(\Delta_R \Delta_R^\dagger) \right]^2 + \rho_2 \text{Tr}(\Delta_R \Delta_R) \text{Tr}(\Delta_R^\dagger \Delta_R^\dagger) \\ & + \alpha_1 \text{Tr}(\phi^\dagger \phi) \text{Tr}(\Delta_R \Delta_R^\dagger) + \left[ \alpha_2 e^{i\delta_2} \text{Tr}(\tilde{\phi}^\dagger \phi) \text{Tr}(\Delta_R \Delta_R^\dagger) + \text{H.c.} \right] + \alpha_3 \text{Tr}(\phi^\dagger \phi \Delta_R \Delta_R^\dagger). \end{aligned} \quad (68)$$

Due to the left-right symmetry, all 12 parameters  $\mu_{1,2,3}^2$ ,  $\lambda_{1,2,3,4}$ ,  $\rho_{1,2}$ ,  $\alpha_{1,2,3}$  are real, except for the CP violating phase  $\delta_2$ , as explicitly stated in Eq. (68). If the  $v_R$  is in the multi-TeV range, the parity symmetric theory above leads to an unacceptably large contribution to neutrino masses from the  $\Delta_L$  VEV (the so-called type-II seesaw contribution). In order to make the TeV-scale LRSM an acceptable and natural theory for small neutrino masses (without invoking any fine-tuning or cancellations between the type-I and type-II terms), one needs to suppress the type-II contribution. This can be done simply by decoupling parity and  $SU(2)_R$  breaking scales, in which case in the low energy spectrum (and hence, in the scalar potential), the  $\Delta_L$  field is absent [384]. In this section, we will consider this class of TeV-scale LRSM (unless otherwise specified) and study its implications in the Higgs sector.

### 5.5.3 New Higgs bosons in LRSM

In the minimal LRSM with the left-handed triplet  $\Delta_L$  decoupled, there are 14 degrees of freedom in the scalar sector, of which two neutral components and two pairs of singly-charged states are eaten by the six massive gauge bosons ( $W^\pm$ ,  $W_R^\pm$ ,  $Z$ ,  $Z_R$ ), thus leaving 8 physical scalar fields, namely, three CP-even ( $h$ ,  $H_{1,3}^0$ ), one CP-odd ( $A_1^0$ ), two singly-charged ( $H_1^\pm$ ) and RH doubly-charged fields ( $H_2^{\pm\pm}$ ) ( $h$  being the SM Higgs boson).<sup>28</sup> Their mass eigenvalues are given by (with  $\xi \equiv \kappa'/\kappa$ )

$$M_h^2 = \left(4\lambda_1 - \frac{\alpha_1^2}{\rho_1}\right) \kappa^2, \quad (69)$$

$$M_{H_1^0}^2 = \alpha_3(1 + 2\xi^2)v_R^2 + 4 \left(2\lambda_2 + \lambda_3 + \frac{4\alpha_2^2}{\alpha_3 - 4\rho_1}\right) \kappa^2, \quad (70)$$

$$M_{H_3^0}^2 = 4\rho_1 v_R^2 + \left(\frac{\alpha_1^2}{\rho_1} - \frac{16\alpha_2^2}{\alpha_3 - 4\rho_1}\right) \kappa^2, \quad (71)$$

$$M_{A_1^0}^2 = \alpha_3(1 + 2\xi^2)v_R^2 + 4(\lambda_3 - 2\lambda_2) \kappa^2, \quad (72)$$

$$M_{H_1^\pm}^2 = \alpha_3 \left( (1 + 2\xi^2)v_R^2 + \frac{1}{2}\kappa^2 \right), \quad (73)$$

$$M_{H_2^{\pm\pm}}^2 = 4\rho_2 v_R^2 + \alpha_3 \kappa^2. \quad (74)$$

Note that prior to symmetry breaking, there are two distinct types of Higgs bosons in the minimal version of the model [cf. Eq. (66)]: the bi-fundamental Higgs field  $\phi(\mathbf{2}, \mathbf{2}, 0)$  that is responsible for breaking the SM electroweak gauge symmetry and generating Dirac fermion masses, and the triplet field  $\Delta_R(\mathbf{1}, \mathbf{3}, 2)$  that is responsible for breaking the  $SU(2)_R \times U(1)_{B-L}$  symmetry and generating the seesaw scale. Apart from their interactions with the gauge bosons and the bi-doublet fields, the triplet fields are hadrophobic, i.e. couple exclusively to leptons in the limit of  $\kappa \ll v_R$ . After symmetry breaking, these Higgs fields mix among themselves, but in the limit  $\epsilon \equiv \kappa/v_R$ ,  $\xi \equiv \kappa'/\kappa \ll 1$ , they can be considered almost pure states. With this approximation, we find the predominantly bi-fundamental Higgs mass eigenstates at the TeV-scale to be

$$\begin{aligned} H_1^0 &= \text{Re } \phi_2^0 - \xi \text{Re } \phi_1^0 - \beta\epsilon \text{Re } \Delta_R^0, \\ A_1^0 &= \text{Im } \phi_2^0 + \xi \text{Im } \phi_1^0, \\ H_1^\pm &= \phi_2^\pm + \xi \phi_1^\pm + \frac{\epsilon}{\sqrt{2}} \Delta_R^\pm. \end{aligned} \quad (75)$$

Similarly, the predominantly hadrophobic Higgs mass eigenstates at the TeV-scale are

$$\begin{aligned} H_3^0 &= \text{Re } \Delta_R^0 + \beta\epsilon \text{Re } \phi_1^0 + \beta'\epsilon \text{Re } \phi_2^0, \\ H_2^{\pm\pm} &= \Delta_R^{\pm\pm}, \end{aligned} \quad (76)$$

<sup>28</sup>The physical scalars from  $\Delta_L$  are labeled respectively as  $H_2^0$ ,  $A_2^0$ ,  $H_2^\pm$  and  $H_1^{\pm\pm}$ , and are decoupled from the low-energy spectrum.

where  $\beta, \beta'$  are some combinations of the scalar couplings in the Higgs potential and are expected to be of order  $\sim 1$ . The hadrophobic Higgs masses are typically of order  $\beta v_R$ . Since our goal is to explore the Higgs sector of the minimal LRSM at the  $\sqrt{s} = 100$  TeV collider, we will assume that the  $SU(2)_R$ -symmetry breaking scale is in the multi-TeV range, which generally means that the new Higgs fields are also in the multi-TeV range. For an earlier discussion of the Higgs mass spectrum in this model, see Refs. [389, 390]. A recent detailed study at the future 100 TeV collider, including the relevant couplings, production and decay modes of these new Higgs bosons, can be found in Ref. [391].

### 5.5.3.1 Bidoublet Higgs Sector

We identify the lightest CP-even Higgs boson (denoted by  $h$ ) as the SM-like Higgs field and fix its mass to be 125 GeV by appropriately choosing the parameters of the scalar potential. Its trilinear coupling is then related in the same way as in the SM in the limit of  $\xi \ll 1$ :

$$\lambda_{hhh} = \frac{1}{2\sqrt{2}} \left( 4\lambda_1 - \frac{\alpha_1^2}{\rho_1} \right) \kappa + \sqrt{2} \left( 4\lambda_4 - \frac{\alpha_1\alpha_2}{\rho_1} \right) \xi\kappa, \quad (77)$$

but differs from this prediction once  $\kappa'$  becomes comparable to  $\kappa$ . So any observed deviation of the  $m_h - \lambda_{hhh}$  relation of the SM would be a measure of the ratio  $\kappa'/\kappa$  in the LRSM.

Turing now to the heavier fields, namely  $H_1^0, A_1^0$  and  $H_1^\pm$ , being in the same bidoublet, they are expected to have similar masses. The scale of their masses is severely constrained in the minimal version of the model by low energy flavor changing neutral current (FCNC) processes, such as  $K_L - K_S$  mass difference,  $B - \bar{B}$  mixing etc [392–395] and is known to imply  $M_{H^0} \geq 8 - 10$  TeV. These fields are therefore not accessible at the LHC but ripe for searches at the 100 TeV collider.

### 5.5.3.2 Hadrophobic Higgs Sector

The second set of Higgs fields in this model consists of the hadrophobic scalars  $H_3^0$  and  $H_2^{\pm\pm}$  that are part of  $\Delta_R(\mathbf{1}, \mathbf{3}, 2)$  which is responsible for giving Majorana mass to the RH neutrinos. Prior to symmetry breaking, they do not couple to quarks, as is evident from Eq. (67).

## 5.5.4 Production of the Heavy Higgs Bosons

Using the relevant couplings given in [391], we can read off the main collider signals of the heavy Higgs sector in the minimal LRSM. As noted above, we require  $M_{H_1^0}, M_{A_1^0}, M_{H_1^\pm} \gtrsim 10$  TeV to satisfy the FCNC constraints, whereas  $M_{H_3^0}, M_{H_2^{\pm\pm}}$  can be much lighter, since there are no such stringent low energy flavor constraints on them. The doubly-charged scalars must be above a few hundred GeV to satisfy the existing LHC constraints [396].

The productions of the heavy CP-even/odd Higgs fields  $H_1^0/A_1^0$  are mainly through the  $b$ -parton content of the proton, i.e.  $b\bar{b} \rightarrow H_1^0/A_1^0$ . This is due to the fact that the couplings of  $H_1^0$  and  $A_1^0$  to light quarks are Yukawa-suppressed and to top-quark is suppressed by  $\kappa'/\kappa$ , while the gluon fusion channel is highly suppressed by the loop factor in the chiral limit of small  $m_b^2/M_{H_1^0}^2 \rightarrow 0$ . The parton-level cross sections for  $pp \rightarrow H_1^0/A_1^0$  and other relevant sub-dominant processes at  $\sqrt{s} = 100$  TeV are shown in Fig. 81 (left). Here we have computed the leading order (LO) cross sections using CalcHEP3.6.25 event generator [152] and CT14 [85] parton distribution functions (PDFs). We also include the NLO and NNLO QCD corrections estimated using an appropriately modified version of SuSHi [397] and find that the NNLO  $K$ -factor is sizable  $\sim 2.6 - 2.8$ .

For the singly-charged Higgs field  $H_1^\pm$ , the dominant production process is via associated production with a highly boosted top quark jet, e.g.  $\bar{b}g \rightarrow H_1^+\bar{t}$ . This is mainly due to the large gluon-content (and sizable bottom content) of the proton and the large Yukawa coupling of  $H_1^\pm$  to third-generation fermions. The NLO corrections, e.g. the process with an extra  $b$ -quark jet, are found to be about 1.6.

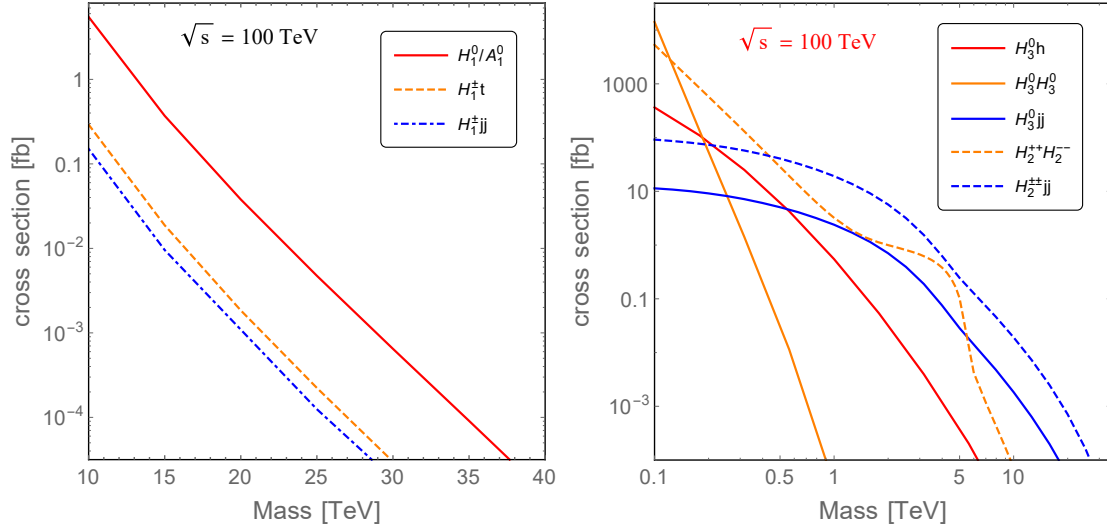


**Fig. 81:** Dominant production cross sections for the heavy bidoublet Higgs bosons  $H_1^0$ ,  $A_1^0$  and  $H_1^\pm$  (left) and hadrophobic Higgs bosons  $H_3^0$  and  $H_2^{\pm\pm}$  (right) in the minimal LRSM at a  $\sqrt{s} = 100$  TeV FCC-hh. Reproduced from [391].

The associated production with two light quark jets is also important, which is predominantly via the SM  $W$  boson:  $pp \rightarrow H_1^\pm W^\mp \rightarrow H_1^\pm jj$ , with subleading contribution from heavy  $W_R$  vector boson fusion (VBF) process. Without imposing any specialized selection cuts on the light and heavy quark jets and just using the basic trigger cuts  $p_{T_j} > 50$  GeV and  $\Delta R_{jj} > 0.4$ , we show the parton-level cross sections in these three channels for  $H_1^\pm$  production as a function of its mass in Figure 81 (left).

For the hadrophobic Higgs sector, the dominant production mode for  $H_3^0$  is either via the VBF process involving RH gauge bosons in  $t$ -channel:  $pp \rightarrow H_3^0 jj$  (with potentially important contribution from Higgsstrahlung processes  $pp \rightarrow H_3^0 V_R \rightarrow H_3^0 jj$  where  $V_R = W_R, Z_R$ ) or via associated production with the SM Higgs or pair-production of  $H_3^0$ :  $pp \rightarrow h^*/H_1^{0(*)} \rightarrow H_3^0 h/H_3^0 H_3^0$ , depending on the mass spectrum. The VBF processes are guaranteed by the gauge couplings, while the other two channels depend on the quartic couplings, mainly  $\alpha_1$  and  $\alpha_2$ . The  $H_1^0$  portal in the  $H_3^0 h$  and  $H_3^0 H_3^0$  channels is highly suppressed by the large bidoublet mass in most of the parameter space of interest, and we switch it off by setting  $\alpha_2 = 0$ . Regarding the SM Higgs portal, from the masses of the SM Higgs  $h$  and  $H_3^0$  [cf. Eq. (69) and (71)], one can easily obtain that  $\lambda_1 = M_h^2/4\kappa^2 + \alpha_1^2 v_R^2/M_{H_3^0}^2$ . To prevent an unacceptably large  $\lambda_1$  when  $H_3^0$  is light below the TeV scale, we set a small value of  $\alpha_1 = 0.01$ . For the VBF channel, we set explicitly the gauge coupling  $g_R = g_L$ <sup>29</sup> and the RH scale  $v_R = 10$  TeV to fix the masses of heavy gauge bosons, and apply the same basic cuts on the light quark jets as above. The corresponding production cross sections in the three dominate channels are shown in Fig. 81 (right). For the Higgs portal, we include the NLO QCD  $k$ -factor, which is known to be large  $\sim 2$  for the top-quark loop [12]. It is obvious that when  $H_3^0$  is light, say  $M_{H_3^0} \lesssim 500$  GeV, the Higgs portal dominates, otherwise the VBF process takes over as the dominant channel.

For the doubly-charged Higgs sector, the dominant production mode is either via the Drell-Yan (DY) mechanism:  $pp \rightarrow \gamma^*/Z^*/Z_R^{(*)} \rightarrow H_2^{++}H_2^{--}$  (with potentially sub-leading contribution from the SM Higgs or resonant enhancement from the heavy  $H_1^0$  or  $H_3^0$ ) or via the VBF process  $pp \rightarrow H_2^{\pm\pm} jj$  mediated by RH gauge bosons  $W_R^\pm$  in the  $t$ -channel (with potentially important contribution from the Higgsstrahlung process  $pp \rightarrow H_2^{\pm\pm} W_R^\mp \rightarrow H_2^{\pm\pm} jj$ ). The LO cross sections are shown in Fig. 81 (right), where we have chosen the same set of parameters and cuts given above, as well as  $M_{H_3^0} = 5$  TeV to

<sup>29</sup>Note that the parameter  $g_R/g_L$  has significant effect on the  $H_3^0$  production in the VBF channel [391].

**Table 42:** Dominant decay channels of the heavy bidoublet and hadrophobic Higgs bosons in the minimal LRSM and their corresponding branching fractions. See text and Ref. [391] for more details.

scalar	channels	BR / comments
$H_1^0$	$b\bar{b}$ $hH_3^0 \rightarrow hhh \rightarrow 6b/4b2\gamma$ $WW_R \rightarrow 4j/\ell^\pm\ell^\pm 4j$	The BRs of the three channels are comparable in most of the parameter space of interest, with the exact values depending on the parameters in LR model.
$A_1^0$	$b\bar{b}$ $WW_R \rightarrow 4j/\ell^\pm\ell^\pm 4j$	The two channels are comparable, depending on the parameters. $\Gamma(A_1^0 \rightarrow b\bar{b}) \simeq \Gamma(H_1^0 \rightarrow b\bar{b})$ $\Gamma(A_1^0 \rightarrow WW_R) \simeq \Gamma(H_1^0 \rightarrow WW_R)$
$H_1^\pm$	$t\bar{b}(\bar{t}b) \rightarrow bbjj/bb\ell\nu$ $ZW_R \rightarrow 4j/\ell^\pm\ell^\mp\ell^\pm\ell^\pm jj$ $hW_R \rightarrow bbjj/\ell^\pm\ell^\pm bbjj$	The three channels are comparable, depending on the parameters. $\Gamma(H_1^+ \rightarrow t\bar{b}) \simeq \frac{1}{2}\Gamma(H_1^+ \rightarrow b\bar{b})$ $\Gamma(H_1^+ \rightarrow ZW_R) \simeq \Gamma(H_1^+ \rightarrow hW_R) \simeq \frac{1}{2}\Gamma(H_1^+ \rightarrow WW_R)$
$H_3^0$	$hh \rightarrow 4b/2b2\gamma$ $N_R N_R \rightarrow \ell^\pm\ell^\pm 4j$ $W_R^\pm W_R^\mp \rightarrow 4j/\ell^\pm\ell^\pm 4j$ $Z_R Z_R \rightarrow 4j/\ell^\pm\ell^\mp jj$ $H_2^{++} H_2^{--} \rightarrow \ell^+ \ell^+ \ell^- \ell^-$	$\sim 100\%$ (if the heavy particle channels are not open ) sizable if the four heavy particle channels are open
$H_2^{\pm\pm}$	$\ell^\pm\ell^\pm$ $W_R^\pm W_R^\pm \rightarrow 4j/\ell^\pm\ell^\pm 4j$	$\sim 100\%$ (if $W_R W_R$ channel is not open ) sizable if kinematically allowed

completely fix the coupling  $hH_2^{++}H_2^{--}$  [cf. Table 5 in Ref. [391]]. We find that for  $M_{H_2^{\pm\pm}} \lesssim 400$  GeV, the DY process is dominant, whereas for relatively larger  $M_{H_2^{\pm\pm}}$ , this is suppressed, compared to the VBF process, due to kinematic reasons. The bump in the DY channel around 5 TeV is due to the resonant  $Z_R$  contribution with  $M_{Z_R} \simeq 2M_{H_2^{\pm\pm}}$ .

### 5.5.5 Decays of the heavy Higgs bosons

For the bidoublet scalar  $H_1^0$ , the dominant decay channels are  $b\bar{b}$ ,  $hH_3^0$  and  $WW_R$  (if kinematically allowed) which almost saturate the total decay width. The branching fractions are comparable, depending on the top Yukawa coupling  $y_t$  and the quartic couplings  $\alpha_2$  and  $\alpha_3$  (relevant to the mass of  $H_1^0$ ). It is remarkable that for all the heavy Higgs bosons in the LRSM at LO all the dependence on the gauge coupling  $g_R$  is cancelled out (except for the dependence through the heavy gauge bosons), and the decay widths are proportional to the RH scale  $v_R$ , as that is the only relevant energy scale in the high-energy limit. The other channels are suppressed by the relatively smaller couplings (e.g.  $hh$  and  $t\bar{t}$ ) or the phase space (e.g.  $W_R W_R$  and  $Z_R Z_R$ ). Given the three dominant channels with large couplings, the total decay width of  $H_1^0$  is generally very large in most of the parameter space, up to a TeV or even larger.

The decay of  $A_1^0$  is somewhat similar to  $H_1^0$ , and is dominated by  $b\bar{b}$  and  $WW_R$ , with the partial decay widths the same as that for  $H_1^0$  at the leading order. This implies that the bi-doublet CP-even and odd scalars in the LRSM will appear as wide resonances at the FCC-hh.

For the singly-charged sector, since  $H_1^\pm$  comes from the same doublet as  $H_1^0$  and  $A_1^0$ , its decay is closely related to the two neutral scalars. From the couplings in Table 3 of Ref. [391], it is easily found that  $H_1^\pm$  decays dominantly to  $t\bar{b}$  ( $\bar{t}b$ ),  $ZW_R^\pm$  and  $hW_R^\pm$ , with the partial widths half of those corresponding to the two neutral scalars, cf. Table 42. The latter two decay modes are related via the Goldstone equivalence theorem before symmetry breaking at the RH scale. These partial decay width relations among  $H_1^0$ ,  $A_1^0$  and  $H_1^\pm$  could be used as a way to distinguish the LRSM Higgs sector from other beyond SM Higgs sectors, such as in the MSSM.

For the hadrophobic scalar  $H_3^0$ , if it is not heavy enough to produce  $N_R N_R$ ,  $W_R W_R$ ,  $Z_R Z_R$  or  $H_2^{++}H_2^{--}$ , it can decay only to  $hh$ , since the  $t\bar{t}$  and  $b\bar{b}$  channels are suppressed by the small mixing

parameter  $\epsilon$ . In this case the width depends on the quartic parameter  $\alpha_1$  which is directly related to the SM Higgs mass and trilinear coupling  $\lambda_{hhh}$  [cf. Eqs. (69) and (77)]. Due to the theoretical and experimental constraints, the decay width of  $H_3^0$  in this case could possibly be very small, around 10 GeV scale. If the decays to heavy particles are open, the width would be largely enhanced, as none of those couplings are suppressed; see Table 4 of Ref. [391]. An interesting case is the decay into a pair of doubly-charged Higgs, which decays further into four leptons. In this case we can study the two scalars simultaneously in one chain of production and decay processes. Note that in this channel, the trilinear coupling for the vertex  $H_3^0 H_2^{++} H_2^{--}$  is directly related to the masses of the two particles [cf. Eqs. (73) and (74) and Table 5 of Ref. [391]].

For the doubly-charged scalar  $H_2^{\pm\pm}$ , the dominant decay channel is to two same-sign leptons. If its mass is larger than twice the  $W_R$  mass, the  $W_R W_R$  channel is also open and contributes sizably to the total width. As stated above, the  $W_R$  channel depends on the gauge coupling  $g_R$  only through the  $W_R$  boson mass.

More details of the dominant decay channels can be found in Ref. [391], including the analytic formulae for all the partial decay widths at LO. There are also rare lepton number violating Higgs decays that could provide additional signals for the LRSM at colliders [398].

### 5.5.6 Key discovery channels at the 100 TeV collider

Given the dominant production and decay modes of heavy Higgs states in the minimal LRSM demonstrated above, we list here the key discovery channels at the FCC-hh. For concreteness, we mainly focus on the channels with least dependence on the hitherto unknown model parameters.

Since the production of bidoublet Higgs bosons is solely determined by their Yukawa couplings to the third generation quarks, their signal sensitivities depend only their masses but not on the RH scale  $v_R$  or the gauge coupling  $g_R$ . For the bidoublet neutral scalars  $H_1^0/A_1^0$ , the main discovery channel is  $pp \rightarrow H_1^0/A_1^0 \rightarrow b\bar{b}$ . Due to the high center-of-mass energy and large masses of  $H_1^0/A_1^0$ , as required by FCNC constraints, the  $b$ -jets are highly boosted, which could help to distinguish them to some extent from the SM  $b\bar{b}$  background, for instance with a large invariant mass cut of  $M_{bb} > 10$  TeV. With the additional basic transverse momentum and jet separation cuts, it is found that the neutral bi-doublet scalars  $H_1^0/A_1^0$  can be probed in the  $b\bar{b}$  channel up to 15.2 TeV at  $3\sigma$  C.L., assuming an optimistic integrated luminosity of  $30 \text{ ab}^{-1}$  [391].

For the CP-even  $H_1^0$ , there is an additional key channel, i.e.  $pp \rightarrow H_1^0 \rightarrow hH_3^0 \rightarrow hhh$  [cf. Table 42]. If  $H_3^0$  is not very heavy, e.g. at the TeV scale, this is a viable channel for both  $H_1^0$  and  $H_3^0$  discovery, by examining the triple Higgs production, for instance with the distinct final state of  $6b$  or  $4b + \gamma\gamma$ . The LO  $gg \rightarrow hhh$  production cross section in the SM is 3 fb at  $\sqrt{s} = 100$  TeV, with a large NLO  $K$ -factor of  $\sim 2$  [240, 241]. However, this large background can be suppressed effectively by applying  $M_{bb} > 10$  TeV. Assuming a branching ratio of 10% for  $H_1^0$  decaying into  $hH_3^0$ , it is found that the sensitivity in this channel is comparable to the  $b\bar{b}$  mode, reaching up to 14.7 TeV for  $H_1^0$  [391].

For the singly charged  $H_1^\pm$ , the key discovery channel is  $pp \rightarrow H_1^\pm t \rightarrow t\bar{t}b$ . Again, due to the large mass of  $H_1^\pm$ , both  $t$  and  $b$ -jets will be highly boosted, which will be a key feature to extract the signal from the irreducible QCD  $t\bar{t}b$  background. In particular, jet substructure analysis of the heavy quark jets and the kinematic observables could help to suppress the SM background and also to distinguish the LRSM model from other scenarios such as the MSSM. With solely a simple cut on the bottom jets  $M_{bb} > 5$  TeV, as well as the basic cuts, it is found that the singly-charged scalar  $H_1^\pm$  can be probed only up to 7.1 TeV at the C.L. level of  $3\sigma$ , mainly due to the small production cross section and the large QCD background [391].

The situation is more intricate for the hadrophobic scalars, as the dominant production channels depend on the RH scale  $v_R$ , either through the vertices or through the RH gauge boson propagators, as well as the gauge coupling  $g_R$ . For  $H_3^0$ , the key channel is  $pp \rightarrow H_3^0 jj \rightarrow hhjj$ , which can be searched

for in either  $4b + jj$  or  $bb\gamma\gamma jj$  channels. The dominant SM backgrounds are from VBF production of SM Higgs pair and  $ZZW$  processes [17, 127]. For smaller  $H_3^0$  masses, the triple Higgs channel  $pp \rightarrow H_3^0 h \rightarrow hhh$  becomes important, which can be readily distinguished from the same final state due to  $H_1^0$  decay, because of the different invariant masses and due to the fact that the  $H_3^0$  resonance width is rather small, say  $\sim$  few times 10 GeV, as compared to the broad resonance of order TeV for  $H_1^0$ .

Regarding the doubly-charged scalars  $H_2^{\pm\pm}$ , the key channels are (i) for low masses, the DY process  $pp \rightarrow H_2^{++} H_2^{--} \rightarrow \ell^+ \ell^+ \ell^- \ell^-$ , where some of the leptons could in principle be of different flavor, thus probing lepton flavor violation, with the dominant SM  $ZZ$  background [399], and (ii) for high masses, the VBF process  $pp \rightarrow H_2^{\pm\pm} jj \rightarrow \ell^\pm \ell^\pm jj$ , which is a high-energy analog of the neutrinoless double beta decay, thus probing lepton number violation at FCC-hh. The leptonic channels are rather clean and the backgrounds are mostly from the SM  $ZZ$  and  $WZ$  leptonic decays with one of the signs of leptons wrongly reconstructed. As demonstrated in Section 5.5.7 the VBF process  $H_2^{++} H_2^{--} jj$  is also promising at the FCC-hh. It is interesting to note that this channel could also stem from  $pp \rightarrow H_3^0 jj \rightarrow H_2^{++} H_2^{--} jj$  with on-shell VBF production of  $H_3^0$ , provided  $M_{H_3^0} > 2M_{H_2^{\pm\pm}}$ , which could significantly enhance this signal.

Adopting the benchmark values of parameters given in Section 5.5.4, we show the projected sensitivities for  $H_3^0$  and  $H_2^{\pm\pm}$  in all the dominant channels in Fig. 82 for an integrated luminosity of 30  $\text{ab}^{-1}$ . In all the channels, we choose only the decay modes with the largest significance: for  $H_3^0$ , it is the decay chain  $H_3^0 \rightarrow hh \rightarrow 4b$ , while for the doubly-charged scalar  $H_2^{\pm\pm}$  it is the final states of  $\ell^\pm \ell^\pm$  with  $\ell = e, \mu$ . All the corresponding SM backgrounds have been taken into consideration in a conservative manner; see Ref. [391] for more details. The sensitivities in the SM Higgs portal  $H_3^0$  production channels ( $H_3^0 h$  and  $H_3^0 H_3^0$ ) increase for a larger  $v_R$  and in these two channels  $H_3^0$  can be probed up to multi-TeV range. In the DY channel,  $H_2^{\pm\pm}$  is produced predominately through the SM  $\gamma/Z$  mediators and thus the sensitivity is almost independent of  $v_R$ , except a resonance-like enhancement due to a heavy  $Z_R$  boson with mass  $M_{Z_R} \simeq 2M_{H_2^{\pm\pm}}$ . In the VBF channel, both  $H_3^0$  and  $H_2^{\pm\pm}$  can be probed up to the few TeV range when  $v_R$  is small; when  $v_R$  becomes larger, due to the increasing  $W_R$  (and  $Z_R$ ) mass, the sensitivities drop rapidly, especially when the heavy gauge bosons can not be pair produced on-shell. Even when  $v_R$  is in the range of few times 10 TeV, a TeV-scale hadrophobic scalar in the minimal LRSM can still be seen at the 100 TeV collider. The Higgsstrahlung sensitivities are lower for both  $H_3^0$  and  $H_2^{\pm\pm}$  compared to the VBF channels, and are not shown in Fig. 82.

More details of the sensitivity studies can be found in Ref. [391]. This parton-level analysis is intended to serve as a guideline for more sophisticated and accurate simulations in future, including optimized selection acceptance and cut efficiencies, and other experimental issues, such as jet energy calibration, boosted top and bottom quark tagging efficiencies, etc. For a full detector-level case study of the pair-production of doubly-charged scalars in association with two jets, see Section 5.5.7.

### 5.5.7 Case study: $pp \rightarrow H_{1,2}^{++} H_{1,2}^{--} jj$

As stated in Section 5.5.4, the dominant production channel for the RH doubly-charged scalars  $H_2^{\pm\pm}$  is via the DY pair-production or VBF single production, depending on the model parameters. Another interesting possibility in the VBF scenario is the pair-production  $H_{1,2}^{++} H_{1,2}^{--} jj$  (where  $H_{1,2}^{\pm\pm}$  is the LH triplet counterpart of  $H_2^{\pm\pm}$ ), which has been studied in great detail in Ref. [400]. In this section, we summarize the main results for this case study. One should be aware that in presence of the left-handed triplet  $\Delta_L$ , not all charged scalars are *always* simultaneously light; however, there are parameter domains where it is possible [400–402]. In general, the doubly-charged scalars decay to either a pair of same-sign charged leptons or a pair of  $SU(2)_{L,R}$  charged gauge bosons. The decay branching ratios are controlled by their respective VEVs. See Table 1 of [401] for more details. In this case study, it is assumed that the doubly-charged scalars dominantly decay to a pair of same-sign charged leptons, thus leading to the signal of four leptons associated with two forward jets, i.e.,  $pp \rightarrow H_{1,2}^{++} H_{1,2}^{--} jj \rightarrow 4\ell + 2j$ .

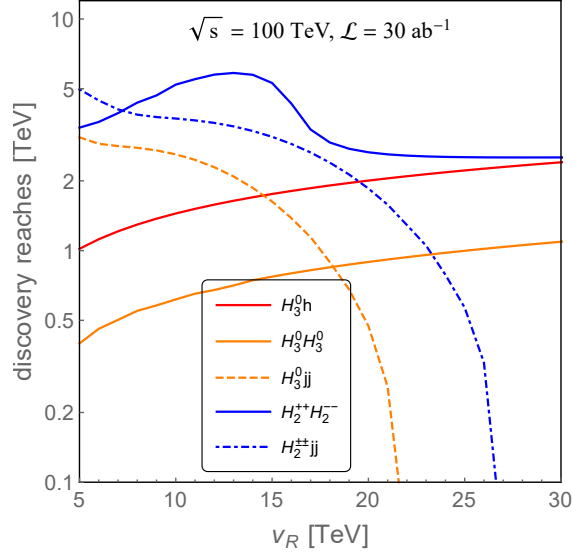


**Fig. 82:** Projected sensitivities of the heavy hadrophobic Higgs bosons  $H_3^0$  and  $H_2^{\pm\pm}$  in the dominant channels in the minimal LRSM at  $\sqrt{s} = 100$  TeV FCC-hh for an integrated luminosity of  $30 \text{ ab}^{-1}$ . Reproduced from [391]. See text for more details.

To perform the analysis, we have imported our own implemented minimal LRSM files in Madgraph [123] using FeynRules [403]. In Ref. [400], two benchmark points consistent with experimental and theoretical constraints were shown which lead to two different sets of scalar spectra, where the common mass of the doubly-charged scalars was 500 GeV and 1000 GeV, respectively. In this case, the LO production cross-sections are

$$\begin{aligned}\sigma(pp \rightarrow H_1^{\pm\pm} H_1^{\mp\mp} jj) &= 599.70 [73.28] \times 10^{-2} \text{ fb}, \\ \sigma(pp \rightarrow H_2^{\pm\pm} H_2^{\mp\mp} jj) &= 401.40 [37.43] \times 10^{-2} \text{ fb},\end{aligned}\quad (78)$$

for  $\sqrt{s}=100$  TeV with  $M_{H_{1,2}^{\pm\pm}} = 500$  [1000] GeV respectively [400]. Then we have allowed  $H_{1,2}^{\pm\pm}$  to decay leptonically within Madgraph and that has been interfaced with DELPHES [147] to isolate the leptons and jets. For lepton/jet identifications and construction we have used default FCC-hh card in DELPHES which also includes the basic isolation and selection criteria. We have also incorporated the following VBF cuts [400, 404] within DELPHES-root signal analysis code:  $p_{Tj_1}, p_{Tj_2} > 50$  GeV,  $|\eta_{j_1} - \eta_{j_2}| > 4$ ,  $m_{j_1 j_2} > 500$  GeV and  $\eta_{j_1} * \eta_{j_2} < 0$ . After implementing VBF cuts and hard  $p_T$  cuts ( $p_{T\ell_1} > 30$  GeV,  $p_{T\ell_2} > 30$  GeV,  $p_{T\ell_3} > 20$  GeV,  $p_{T\ell_4} > 20$  GeV) for four leptons in DELPHES-root code [147], we find signal cross section to be:

$$\sigma(pp \rightarrow 4l + jj)_{\text{sig.}} = 48.92 [5.5146] \times 10^{-2} \text{ fb},\quad (79)$$

for  $\sqrt{s}=100$  TeV with  $M_{H_{1,2}^{\pm\pm}} = 500$  [1000] GeV, respectively. In the analysis without DELPHES FCC-hh cards [400], this cross section is  $37.01 [3.54] \times 10^{-2}$  fb. The departures in the signal cross sections are quite large – around 32% and 56 % respectively for first and second benchmark points. It shows that the implementation of dedicated DELPHES cards which take care of the lepton and jet reconstructions, and isolations, is promising and worth of further development for FCC-hh.

The dominant SM background comes from  $ZZjj$  final state. We have computed and estimated this background using same set of selection criteria, hard  $p_T$  and VBF cuts for leptons and jets, at parton level using Madgraph [144], and at hadron level using PYTHIA [110] after incorporating showering and hadronization:

$$\sigma(pp \rightarrow 4l + jj)_{\text{bkg.}} = 479.4 [3.8] \times 10^{-2} \text{ fb}.\quad (80)$$

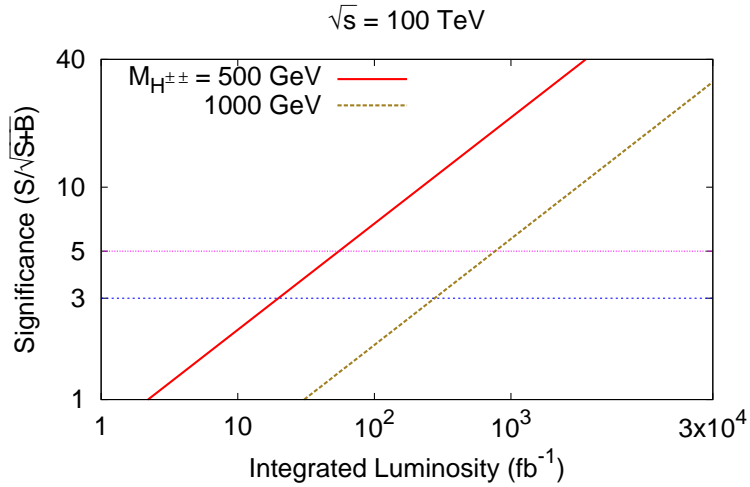


**Fig. 83:** Significance vs integrated luminosity for  $pp \rightarrow H_{1,2}^{++} H_{1,2}^{--} jj \rightarrow 4\ell + 2j$  with doubly-charged scalar masses of 500 GeV (solid-red line) and 1000 GeV (dotted-yellow) and center of mass energy at  $\sqrt{s}=100$  TeV. Here the left- and right-handed doubly-charged scalar contributions are summed up, and the two horizontal lines represent the significances at the level 5 and 3 respectively.

For the suggested benchmark points with  $M_{H_{1,2}^{\pm\pm}}=500$  and 1000 GeV we have also analyzed the significances of the signal events for different set of integrated luminosities, see Fig. 83. We have defined the significance as  $S/\sqrt{S+B}$ , where  $S$  and  $B$  are the signal and background events (cross section $\times$ luminosity). It is interesting to note that below a luminosity of  $100 \text{ fb}^{-1}$  it is possible to adjudge the signal strength with significance level 5 (magenta dotted line) for  $M_{H_{1,2}^{\pm\pm}}=500$  GeV. To make a definite comment on the other benchmark points with larger doubly-charged scalar masses we need to wait till we collect enough data with integrated luminosity  $\sim \mathcal{O}(1000) \text{ fb}^{-1}$ .

### 5.5.8 Distinguishing from the MSSM Higgs Sector

One of the key features which distinguishes the LRSM Higgs sector from other popular beyond SM Higgs sectors, such as the 2HDM, is the presence of the doubly-charged scalars. Thus, a positive signal for any of the doubly-charged scalars discussed here will be a strong evidence for the LRSM. Another distinction is due to the  $H_3^0 \rightarrow hh$  decay mode of the neutral hadrophobic scalar in LRSM, which is absent in generic 2HDM scenarios in the so-called *alignment limit*, since the  $Hhh$  coupling identically vanishes [405–407].

As for the bidoublet Higgs sector in the LRSM, this is similar to the MSSM Higgs sector, which also contains two SM Higgs doublets. However there is a profound difference between the two models, since in the LR case, the second Higgs, in the limit of  $\kappa' = 0$  does not contribute to fermion masses and therefore the decay properties are very different, as illustrated in Table 43. In particular, the  $\tau^+\tau^-$  final state is suppressed by either the Dirac Yukawa coupling or the left-right mixing for the neutral bi-doublet scalars  $H_1^0/A_1^0$  in the LRSM [cf. Table 12 of Ref. [391]], whereas this is one of the cleanest search channels for the MSSM heavy Higgs sector in the large  $\tan\beta$  limit. Furthermore, due to the presence of extra gauge fields in our case i.e.  $W_R^\pm, Z_R$ , new modes appear, e.g.  $H_1^0 \rightarrow W_R^\pm W^\mp$  and  $H_1^\pm \rightarrow W_R^\pm Z$ , which have no MSSM analog. These modes can lead to distinguishing signals in leptonic channels e.g.  $\ell^\pm\ell^\pm 4j$  with  $\sim 5\%$  branching ratio. With  $30 \text{ ab}^{-1}$  data, this can lead to about 1000 events before cuts, while the SM background for these sign-sign dilepton processes is expected to be very small. One can also use the relations between the various partial decay widths as shown in Table 42 to distinguish the

**Table 43:** A comparison of the dominant collider signals of neutral and charged scalars in the minimal LRSM and MSSM.

Field	MSSM	LRSM
$H_1^0, A_1^0$	$b\bar{b}, \tau^+\tau^-$ (high $\tan\beta$ )	$b\bar{b}$
	$t\bar{t}$ (low $\tan\beta$ )	$WW_R \rightarrow \ell^\pm\ell^\pm 4j$
$H^+$	$t\bar{b}t\bar{b}, t\bar{b}\tau^+\nu$	$\bar{t}_L b_R$

LRSM Higgs sector from other scenarios.

If a positive signal is observed, one can also construct various angular and kinematic observables to distinguish the LRSM scenario from other models giving similar signals [408–410]. For instance, we find from Table 43 that  $\bar{t}_L b_R$  final states are preferred over the  $\bar{t}_R b_L$  final states for the  $H_1^+$  production, which can be utilized to distinguish it from other 2HDM scenarios, including the MSSM.

### 5.5.9 How would this fit into the discovery landscape?

Discovery of any of the signals of the LRSM, and in particular its Higgs sector, would bring about a fundamental change in our thinking about neutrino masses and will change our perspective on supersymmetry and grand unification. This will also affect the discussion of the origin of matter via leptogenesis in a profound manner. For instance, if the  $W_R$  gauge boson is discovered below  $9(g_R/g_L)$  TeV, it will rule out the whole leptogenesis approach [411–415]. Discussions of issues such as naturalness will have to assume the low energy group to be the left-right symmetric group rather than the SM gauge group. This has implications for the stability of the electroweak vacuum [416, 417].

## 5.6 Naturalness

### 5.6.1 Supersymmetry

In spite of the stringent bounds, which have been put on superpartners' masses by the ATLAS and CMS collaborations, supersymmetry (SUSY) is still an attractive candidate for physics beyond the SM. It can successfully address the big hierarchy problem, although with some (potentially mild) residual fine tuning.

The superpartners, and most importantly stops, gauginos and higgsinos play a crucial role in restoring the naturalness, and their masses are directly related to the fine tuning of the supersymmetric extension of the SM [418–421]. Summaries of the search program can be found, for example, in Ref. [422]. However, SUSY also necessarily modifies the higgs sector of the SM, and we will mostly concentrate on these modifications here.

The modifications of the higgs sector in SUSY are twofold. First, low masses superpartners, required by naturalness might significantly affect the higgs couplings at the loop level. Given that the leading-order higgs coupling to the photons and gluons show up in the SM at the one-loop level, light stops and, to a lesser extent, light gauginos might affect these couplings appreciably. These effects have been extensively studied in the literature, see for example Refs. [423, 424]. In particular, Ref. [423] found that stops with mass of order  $\sim 250$  GeV imply a deviation in the higgs couplings of order  $r_g \equiv g_{hgg}/g_{hgg}^{SM} \approx 1.25$ , triggering an order one deviation in the higgs gluon fusion production rate. In general, the contributions of the stops to the gluon coupling in the small mixing limit is approximately given by the very well known formula

$$r_g - 1 \approx \frac{1}{4} \left( \frac{m_t^2}{m_{\tilde{t}_1}^2} + \frac{m_t^2}{m_{\tilde{t}_2}^2} - \frac{X_t^2 m_t^2}{m_{\tilde{t}_1}^2 m_{\tilde{t}_2}^2} \right), \quad (81)$$

with  $X_t \equiv A_t - \mu \cot\beta$  being the left-right mixing between the stops. One can derive a very similar formula for  $r_\gamma \equiv g_{h\gamma\gamma}/g_{h\gamma\gamma}^{SM}$ . The modifications due to the stops are large as long as they are light (with

mass around  $\sim 200$  GeV) and have small mixing, while the effect rapidly decreases for larger masses and becomes negligible for  $m_{\tilde{t}} \gtrsim 400$  GeV. Of course, exclusions based on these considerations are never completely robust because of the so-called “funnel region” where the left-right mixing completely cancels out the contribution to the  $hgg$  coupling, but this regime is also less interesting from the point of view of naturalness considerations.

Although these modifications to the higgs couplings are interesting and helped until now to rule out certain SUSY scenarios, most of the parameter space with light stops has been already excluded by the direct searches at the LHC. Higgs couplings are currently superior to direct searches only for the challenging case of compressed spectra. If such squeezed stops are the cause of higgs coupling deviations and escape detection at the LHC, the vastly superior sensitivity of a 100 TeV collider to weak scale colored states makes discovery extremely likely. Precision high-energy measurements of DY production at a 100 TeV collider are also likely to model-independently detect such states via their effect on EW RG evolution [300].

The charginos (winos and higgsinos) might also have an interesting effect on the  $h\gamma\gamma$  coupling. This effect is much more modest than that from stops, but it can still be important because of the challenges that the EWeakinos searches usually pose: small cross sections and relatively soft signatures. This point has been first emphasized in [425, 426]. In practice, the effect becomes important only for relatively small  $\tan\beta$ . This region of parameter space is somewhat disfavored by naturalness, at least if one restricts to more minimalistic scenarios, but it can still be important if a larger degree of residual fine-tuning is tolerated. At  $\tan\beta \approx 1$  the contribution to the higgs couplings can be approximated as

$$r_\gamma \approx 1 + 0.41 \frac{m_W^2}{M_{2\mu} - m_W^2} \quad (82)$$

Practically for  $\tan\beta \approx 1$  this value varies between 0.7 and 1.13, while for  $\tan\beta > 2$  the allowed range further shrinks to  $0.8 < r_\gamma < 1.1$ . The effect also decouples quickly with increasing gaugino mass. The precision of a  $h\gamma\gamma$  coupling measurement might be below percent-level at a 100 TeV collider, see Section 3.2.1, which corresponds to a limit  $M_{2\mu} \gtrsim (500 \text{ GeV})^2$  from Eq. (82). The generic EWino reach through direct production is in the TeV range or above [294–296], but it would be interesting to understand in which scenarios a  $h\gamma\gamma$  coupling measurement could provide superior sensitivity.

Another effect, which has an important impact on the SUSY higgs sector, has to do with the fact that SUSY necessarily involves 2HDM of type II. Moreover, if one insists on naturalness, the heavy higgses cannot be arbitrarily heavy. Naturalness considerations imply upper bounds on their masses [427–429], which are however much milder than those on stops or higgsinos. In particular, Ref. [429] showed that in order not to exacerbate the fine-tuning of the supersymmetrized SM one would plausibly expect to see the heavy higgses of the 2HDM at masses of 1 – 3 TeV. Needless to say, such a range of masses is far beyond the reach of the LHC, while it represents a promising opportunity for a 100 TeV collider. We will elaborate on the reach on these new states in Section 5.7, where it will be also discussed in the more generic context of the 2HDM.

## 5.6.2 Composite Higgs

### 5.6.2.1 Higgs compositeness – General Overview

In the past decade a realistic framework has emerged [176, 430–436] (for a recent review see [180]) in which the Higgs boson arises as a pseudo-Nambu-Goldstone Boson (pNGB) from the spontaneous breaking of a global symmetry  $G \rightarrow G'$  of a new strongly interacting sector. These theories have two crucial advantages over plain technicolor models. Firstly, the presence of a light Higgs boson allows a parametric separation between the  $G \rightarrow G'$  breaking scale  $f$  and the electroweak symmetry breaking scale  $v$ . This alleviates the tension of technicolor models with electroweak precision tests. Secondly, the flavor problem of technicolor can be greatly improved by the implementation of partial compositeness [437, 438].

The simplest realistic realization of the composite Higgs idea is represented by  $G = SO(5) \times U(1)_X$  and  $G' = SO(4) \times U(1)_X$  and called the Minimal Composite Higgs Model (MCHM) [432, 433]. The  $U(1)_X$  factor is needed to obtain the correct hypercharge,  $Y \equiv T_R^3 + X$ , for the SM fermions. This breaking pattern satisfies the conditions of a viable model: the SM vector bosons gauge a subgroup  $SU(2)_L \times U(1)_Y \subset G$  and  $G/G'$  contains an  $SU(2)_L$  doublet which can be identified with the Higgs doublet. The coset space of the MCHM contains four NGBs transforming as a 4 of  $SO(4)$ , three of which are eaten by the SM gauge bosons while the fourth is the physical Higgs boson. Larger cosets give rise to more NGBs, including, for example, extra singlets and doublets [439–441]. Interestingly, an additional singlet could be interpreted as a Dark Matter candidate [439, 441–446].

At low energy, below the mass scale of the heavy resonances of the strong dynamics, the theory is described by an effective Lagrangian involving the composite Higgs doublet and the SM fields. Effects induced by the virtual exchange of the heavy modes are encoded by local operators whose relative importance can be estimated by assuming a power counting. For example, under the assumption that the new strongly-coupled dynamics is described by a single mass scale  $m_*$  and a single coupling strength  $g_*$ , the effective Lagrangian has the form [176]

$$\mathcal{L}_{\text{eff}} = \frac{m_*^4}{g_*^2} \mathcal{L} \left( \frac{D_\mu}{m_*}, \frac{g_* H}{m_*}, \frac{\lambda \Psi}{m_*^{3/2}} \right). \quad (83)$$

One naively expects a typical coupling strength among the bound states of order  $g \lesssim g_* \leq 4\pi$ , where values  $g_* < 4\pi$  allow a perturbative expansion in the effective theory. The mass scale of the heavy resonances,  $m_*$ , represents the cutoff of the effective theory and sets its range of validity. Equation (83) describes the low-energy dynamics of the light composite Higgs  $H$  with elementary SM fermions  $\Psi$ , as first discussed in Ref. [176]. The coupling  $\lambda$  controls the strength of the interaction between the elementary and composite fermions, where the latter have been integrated out. If the Higgs is strongly coupled, a simple yet crucial observation is that any additional power of  $H$  costs a factor  $g_*/m_* \equiv 1/f$ ,<sup>30</sup> while any additional derivative is suppressed by a factor  $1/m_*$ . Note that extra powers of the gauge fields are also suppressed by  $1/m_*$  as they can only appear through covariant derivatives in minimally coupled theories. If the light Higgs interacts strongly with the new dynamics,  $g_* \gg 1$ , then the leading corrections to low-energy observables arise from operators with extra powers of  $H$  rather than derivatives. This remark greatly simplifies the list of important operators.

Composite Higgs models predict various new physics effects that can be probed at current and future colliders. In particular, new heavy vectors and fermions (the top partners) are expected and can be directly searched for. In addition, the composite nature of the pNGB Higgs implies deviations of the Higgs couplings from their SM value by an amount proportional to  $\xi = v^2/f^2$ , where  $v$  is the scale of EWSB and  $f$  the decay constant of the pNGB. In the MCHM, and more in general in theories with coset  $SO(5)/SO(4)$ , the following prediction holds for the couplings of one and two Higgs bosons to gauge bosons:

$$\frac{g_{hVV}^{MCHM}}{g_{hVV}^{SM}} = \sqrt{1 - \xi}, \quad \frac{g_{hhVV}^{MCHM}}{g_{hhVV}^{SM}} = 1 - 2\xi, \quad (84)$$

where  $g_{hVV}^{SM}$  and  $g_{hhVV}^{SM}$  represent the SM couplings, while  $g_{hVV}^{MCHM}$  and  $g_{hhVV}^{MCHM}$  stand for the couplings in the MCHM. At low energy, virtual effects of the heavy resonances can be parametrized in terms of local operators, which also lead to anomalous Higgs couplings (such as, for example, derivative interactions between the Higgs and gauge bosons). Precision measurements of the Higgs couplings thus constraint the compositeness scale and indirectly probe the heavy resonances. In fact, direct and indirect measurements represent complementary strategies to test the parameter space of a composite Higgs models.

<sup>30</sup>Note that a weakly-coupled, elementary Higgs would cost a factor  $g/m_*$ .

As discussed in detail in the Volume of this report dedicated to BSM physics [447], the parameter space of the MCHM can be described by the mass of the heavy vectors,  $m_\rho$ , and their coupling strength,  $g_\rho$  (to be identified with  $m_*$  and  $g_*$  respectively). These two parameters are related through the relation  $\xi \sim g_\rho^2 v^2 / m_\rho^2$ . In a recent study [448, 449], the expected direct reach of a 100 TeV collider was compared to the indirect reach on  $\xi$  of various lepton colliders. Indirect searches are sensitive to  $\xi$  through precision measurements of the Higgs couplings: a high-luminosity upgrade of the LHC can probe values down to  $\xi \geq 0.1$  [450, 451], while lepton colliders like TLEP and CLIC are expected to reach the sub-percent level [178, 191]. Direct resonance searches for heavy vector particles at 100 TeV with  $10 \text{ ab}^{-1}$ , on the contrary, are sensitive to masses between 10 and 20 TeV for coupling strengths between  $g_\rho \sim 8$  and 2. Masses up to 35 TeV become accessible for  $g_\rho \lesssim 1.5$ . Note that this corresponds to values of  $\xi$  of the order  $O(10^{-4})$ . This illustrates the complementarity of the two searches strategies: indirect searches are more powerful for large couplings, while direct searches can access considerably larger masses for small coupling values.

### 5.6.2.2 Unnatural (or Split) Composite Higgs

Composite Higgs models must satisfy a number of indirect constraints that arise from flavor and precision electroweak observables. While the precision electroweak constraints from the  $T$  parameter are avoided with a custodial symmetry and those from the  $S$  parameter are ameliorated with  $g_\rho \gtrsim 3$ , the most stringent constraints actually arise from flavor observables which gives rise to an approximate lower bound on the scale of spontaneous symmetry breaking  $f \gtrsim 10 \text{ TeV}$  [180, 452]. It is therefore clear that composite Higgs models require additional flavor structure in order to satisfy these constraints. Instead, if a more minimal approach is taken, one can simply assume that  $f \gtrsim 10 \text{ TeV}$ . Of course this simplicity comes at the price of a tuning in the Higgs potential of order  $v^2/f^2 \sim 10^{-4}$ . This meso-tuning is still a many orders of magnitude improvement compared to that encountered in the Standard Model with a Planck scale cutoff and leads to an unnatural (or split) version of composite Higgs models.

Interestingly, even though the resonances are now very heavy these models can still give rise to distinctive experimental signals. The crucial requirement involves preserving gauge coupling unification due to a composite right-handed top quark [453]. The minimal coset preserving this one-loop result together with a discrete symmetry needed for proton and dark matter stability is  $SU(7)/SU(6) \times U(1)$  [454]. This coset contains twelve Nambu-Goldstone bosons, forming a complex  $\mathbf{5}$  containing the usual Higgs doublet,  $H$ , with a color triplet partner,  $T$ , and a complex singlet,  $S$  which can be a stable dark matter candidate. In addition, the composite right-handed top quark, needed for gauge coupling unification, is part of a complete  $SU(6)$  multiplet containing extra exotic states,  $\chi^c$ , that will be degenerate with the top quark. These states can be decoupled by pairing them with top companions,  $\chi$  to form a Dirac mass of order  $f$ .

Interestingly the split compositeness can possess a rich non-minimal higgs sector. The unnatural or split spectrum will consist of the pseudo Nambu-Goldstone bosons,  $H, T$  and  $S$  with masses  $\ll f$ , which are split from the resonances with masses  $> f$ , while the top companions  $\chi$  have Dirac masses of order  $f$ . Thus for  $f \gtrsim 10 \text{ TeV}$ , the color triplet partner  $T$  of the Higgs doublet and the top companion states  $\chi$ , crucial for gauge coupling unification, will be accessible at a future 100 TeV collider.<sup>31</sup>

In the model of Ref. [454], the color triplet partner  $T$  of the Higgs doublet will be the lightest colored state. Its dominant decay mode is  $T \rightarrow t^c b^c S S$  which arises from a dimension-six term, where  $t^c, b^c$  are Standard Model quarks and  $S$  is the singlet scalar. The decay length is given by

$$c\tau = 0.6 \text{ mm} \left( \frac{1}{c_3^T} \right)^2 \left( \frac{8}{g_\rho} \right)^3 \left( \frac{3 \text{ TeV}}{m_T} \right)^5 \left( \frac{f}{10 \text{ TeV}} \right)^4 \frac{1}{J(m_t, m_S)}, \quad (85)$$

where  $c_3^T$  is an order one constant,  $m_T(m_S)$  is the color triplet (singlet scalar) mass and  $J(m_t, m_S)$  is a

<sup>31</sup>In fact the top companions cannot be made arbitrarily heavy because this will worsen the unification and therefore there is an approximate upper bound  $f \lesssim 500 \text{ TeV}$  [454].

phase space factor (see Ref. [455] for details). Thus, since the scale  $f \gtrsim 10$  TeV, the color triplet is long-lived and can decay via displaced vertices or outside the detector. This signal at a 100 TeV collider was analyzed in Ref. [455]. When  $f = 10$  TeV, displaced vertex and collider stable searches are sensitive to triplet masses in the range 3-10 TeV, while for heavier triplet masses, prompt decay searches are sensitive to color triplet masses in the range 4-7 TeV. For  $f = 100$  TeV there are no accessible prompt decays and the displaced vertex and collider stable searches can now cover color triplet masses up to 10 TeV. These results are depicted in Fig. 84.

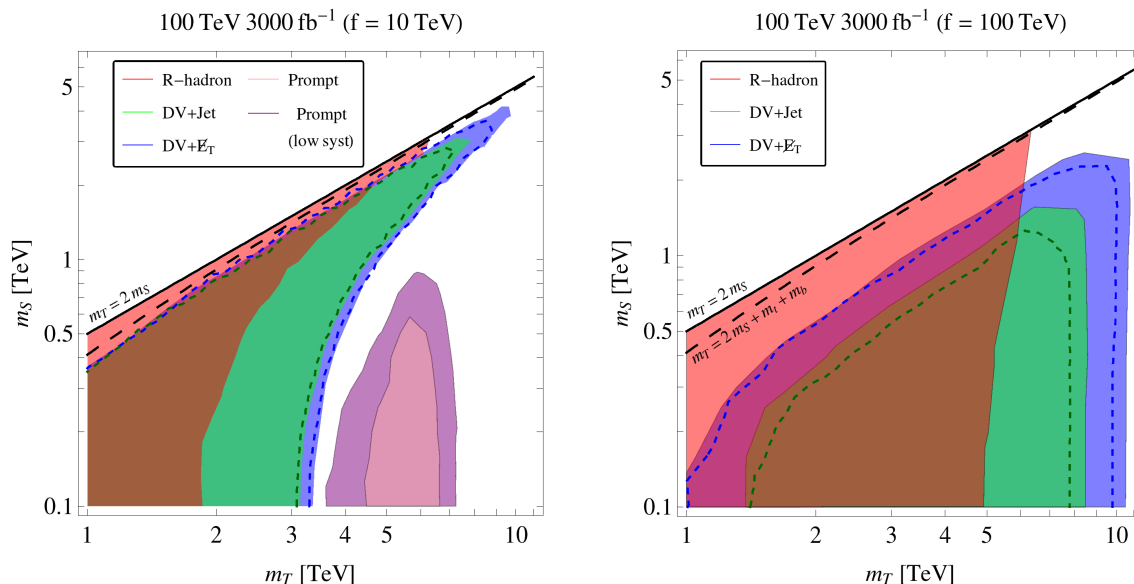


**Fig. 84:** Projections for a 100 TeV collider with  $3 \text{ ab}^{-1}$  of integrated luminosity as functions of the scalar mass  $m_S$  and triplet mass  $m_T$ . The shaded regions show the  $5\sigma$  discovery reach (95% CLs exclusion limit) for the R-hadron/displaced (prompt) searches. The dashed lines include an additional factor of two reduction in the signal efficiency for DV searches to account for the impact of more stringent experimental cuts. The left and right panels correspond to  $f = 10$  and 100 TeV respectively. This figure is taken from Ref. [455].

The top companions are the next heaviest states and have  $SU(3) \times SU(2) \times U(1)_Y$  quantum numbers:

$$\chi \equiv \tilde{q}^c \oplus \tilde{e} \oplus \tilde{d}^c \oplus \tilde{l} = (\bar{\mathbf{3}}, \mathbf{2})_{-\frac{1}{6}} \oplus (\mathbf{1}, \mathbf{1})_{-1} \oplus (\bar{\mathbf{3}}, \mathbf{1})_{\frac{1}{3}} \oplus (\mathbf{1}, \mathbf{2})_{-\frac{1}{2}} \quad (86)$$

These states are similar to excited Standard Model quarks and leptons and will decay promptly at a 100 TeV collider. Assuming a scale  $f \gtrsim 10$  TeV the top companions will have masses in the 10 – 20 TeV range. The colored top companions  $\tilde{q}^c, \tilde{d}^c$  will have unsuppressed decays to quarks and the color triplet  $T$ , whereas the  $SU(2)$  singlet,  $\tilde{e}$  has a three-body decay into a bottom quark and two scalar triplets and the  $SU(2)$  doublet,  $\tilde{l}$  decays to a quark, a color triplet and a scalar singlet [454]. A further study of top companion mass limits from these decays at a 100 TeV collider will be useful.

In summary, at a 100 TeV collider color triplet scalars give rise to distinctive signals and together with the top companions provide a smoking-gun signal for unnaturalness in composite Higgs models.

### 5.6.3 Neutral Naturalness

Here we briefly discuss the signatures of *Neutral Naturalness*, with emphasis on the Higgs-related measurements most suited for a 100 TeV collider. We anchor the discussion by referring to two concrete benchmark models, *Folded SUSY* (FSUSY) [271] which features EW-charged scalar top partners, and the *Twin Higgs* [270] featuring SM-singlet fermionic top partners. However, some aspects of the phenomenology can also be derived more model-independently [293, 456]. The phenomenology of Neutral

Naturalness is rich, and includes potentially measurable Higgs coupling deviations, exotic Higgs decays, and direct production of partner states, additional Higgs states, or multi-TeV SM-charged states that are part of the more complete protective symmetry that ultimately underlies the model.

### 5.6.3.1 Theory overview

In perturbative extensions of the SM, the hierarchy problem can be solved by introducing top partners. The coupling of these states to the Higgs is related to the top Yukawa by some symmetry (like supersymmetry, or a discrete symmetry in Little Higgs models [457–460]) such that the partner’s quadratically divergent one-loop Higgs mass contribution cancels that of the top quark. In most theories, this symmetry ensures that the top partners carry SM color charge, allowing copious production at hadron colliders as long as their mass is in the natural  $\lesssim$  TeV range.

It is possible to devise concrete models in which the symmetry which protects the Higgs includes a discrete group like  $\mathbb{Z}_2$ , and does not commute with SM color. This leads to the possibility of color-neutral top partners. Such theories of *Neutral Naturalness* feature very different phenomenology from theories like the MSSM.

We anchor our discussion by referring to two archetypical theory examples of Neutral Naturalness. The first is *Folded SUSY* (FSUSY) [271] which features a mirror sector of sparticles carrying SM EW quantum numbers. This mirror sector is charged under its own copy of QCD, which confines at a few – 10 GeV. This leads to *Hidden Valley* phenomenology [375, 461–463]: since LEP limits forbid light EW-charged particles below  $\sim 100$  GeV, the lightest new particles are mirror glueballs. Because the only interactions between the mirror sector and the SM proceed via the EW-scale particles, the lifetimes of the glueballs are necessarily suppressed by powers of  $\frac{\Lambda}{E_{EW}}$ , leading to the above mentioned hidden valley scenarios. Top partner loops couple the Higgs to mirror gluons, allowing for mirror glueball production in exotic Higgs decays, and displaced glueball decay via mixing with the SM-like Higgs.

Our second theory benchmark is the *Twin Higgs* [270], which features SM-singlet fermionic top partners. These are part of a mirror sector containing copies of all SM particles and gauge forces. The original mirror Twin Higgs model has several cosmological problems due to an abundance of light invisible mirror states. One simple modification, which satisfies all cosmological constraints [464, 465], is the Fraternal Twin Higgs (FTH) [466], which only duplicates the third generation in the mirror sector. In that case, the hadrons of mirror QCD can be made up of mirror glueballs, mirror quarkonia, or a mixture of both.

A common feature of these theories is the existence of a *mirror QCD* gauge group under which the top partners (and other fields in the mirror sector) are charged. From a top-down perspective this mirror QCD arises as a consequence of the discrete symmetry relating the SM and mirror sector. At some high scale, the mirror  $g_S^B$  and  $y_t^B$  are (almost) equal the SM  $g_S^A, y_t^A$ . From a bottom-up perspective [466], the existence of a mirror QCD force is expected, since otherwise  $y_t^B$  would run very differently from  $y_t^A$ , ruining the cancellation between the top loop and the top partner loop in the Higgs mass at a scale of a few TeV. As we see below, this mirror QCD, and the associated low-energy hadron states, have important phenomenological consequences. Of course, the discrete symmetry usually has to be broken in some way (otherwise the two sectors would be identical), and it is possible to break mirror QCD as well [467, 468]. In natural versions of these models, new SM-charged states appear at a few TeV, which is in line with the above bottom-up expectation.

There are several features of Neutral Naturalness that are even more model-independent. Top partners, by their very nature, have to couple to the SM through the Higgs-portal, which leads to loop-level deviations in the  $Zh$  production cross section that is potentially detectable at future lepton colliders [456]. Other possibilities include tree-level Higgs coupling deviations can also arise due to mixing effects, modifications of the Higgs cubic coupling due to top partner loops, electroweak precision observables [293], and direct top partner production via off-shell Higgs bosons [308, 316]. Crucially, it seems very chal-

lenging to construct a model of Neutral Naturalness which does not lead to detectable signatures at a 100 TeV collider, lepton colliders, or both [293]. This lends additional motivation for Higgs-related measurements at a 100 TeV collider.

Models of Neutral Naturalness solve the Little Hierarchy problem via a one-loop cancellation between top and top partner Higgs mass contributions. This cancellation is not enforced at two-loop order, necessitating a full solution to the hierarchy problem to become apparent in a UV completion at scales of  $\sim 5 - 10\text{TeV}$  [469–477]. In all known examples, these UV completions involve BSM states carrying SM charges, allowing for direct production at a 100 TeV collider. This will not be our focus here, but since the UV completion scale is connected to the degree of tuning in the theory, the ability of a 100 TeV collider to probe the full theory is complementary to Higgs-related measurements.

### 5.6.3.2 Higgs coupling deviations

In the minimal Folded SUSY model, the electroweak and Higgs sectors are identical to the MSSM. Realistically there is significant uncertainty as to the exact structure of the scalar sector: the MSSM itself favors a light Higgs below 125 GeV, motivating extensions like non-decoupling  $D$ -terms [478], while Folded SUSY needs some additional structure for viable electroweak symmetry breaking [479]. Even so, the required features of FSUSY imply the existence of additional Higgs bosons, leading to measurable Higgs coupling deviations if the decoupling limits is not satisfied. However, given that the naturalness limits, which are similar to the SUSY case, discussed in Section 5.6.1, the deviations might potentially be too small not only for LHC, but also for the future leptonic collider.

The electroweak charge of the top partners in FSUSY implies loop-corrections to  $\text{Br}(h \rightarrow \gamma\gamma)$ , which can be percent-level for top partner masses below 500 GeV [480]. This represents a significant opportunity for lepton colliders [178], but the LHC or a 100 TeV collider is more likely to produce the EW-charged top partners directly than to see deviations in the diphoton rate.

In all known Twin Higgs models, a soft mass which breaks the discrete symmetry between SM- and mirror-Higgs has to be balanced against  $f$ , the vev of the mirror Higgs (or, more generally, the scale at which the higher symmetry which protects the light Higgs from quadratically divergent corrections is spontaneously broken) in order to achieve SM-like couplings of the 125 GeV Higgs to SM states. This leads to a tree-level tuning in the model, which is of order  $v^2/f^2$ , which is also the size of the mixing between the SM-like Higgs and the mirror Higgs. Therefore, in natural models where  $v^2/f^2$  is not too small, there are detectable universal Higgs coupling deviations of the same order due to this tree-level mixing effect. These deviations can be detected at the percent-level at future lepton colliders [178], which are the smoking gun of Twin Higgs theories. Such a deviation, if detected at lepton colliders, would greatly motivate 100 TeV searches for additional signals of the Twin Higgs, such as SM-charged multi-TeV states.

In principle, it is possible to imagine Neutral Naturalness scenarios from a bottom-up perspective without measurable Higgs coupling deviations [293]. However, avoiding this smoking-gun-signature at lepton colliders comes at the cost of larger couplings in the hidden sector, reducing the required scale of the UV completion in the absence of strong tuning. The 100 TeV collider would then be able to produce the states of the UV completion directly, assuming they carry SM charge. This is the strongest demonstration of the important complementarity between the two types of possible future colliders.

### 5.6.3.3 Exotic Higgs decays

Exotic Higgs decays are one of the best-motivated signatures of Neutral Naturalness. As outlined above, most theories of Neutral Naturalness feature a mirror-QCD gauge symmetry under which the top partners are charged. The Higgs therefore couples to mirror-gluons via a top partner loop in analogy to its coupling to SM-gluons through the top loop. This means the Higgs can decay to mirror gluons, and therefore into light states in the mirror sector. The size of the exotic branching fraction is related to the

top mass, and therefore to the naturalness of the theory itself, with less tuned scenarios giving higher exotic decay rates. The specific phenomenology of these exotic Higgs decays depends on the structure of the mirror QCD sector.

The mirror QCD sector could be SM-like, with quarks that are light compared to the confinement scale. This would allow the Higgs to decay to hidden pions and other hadrons, making it a classical Hidden Valley scenario [375, 461–463], realized for example by the original mirror Twin Higgs. If the exotic Higgs decays proceed through Yukawa couplings comparable to  $y_b \sim 0.02$ , exotic branching ratios could easily be as large as 10%, which is detectable at the LHC and future colliders even if the decay products are detector-stable and hence invisible. On the other hand, if the decay proceeds through a top loop to mirror gluons only, the exotic branching fraction is of order  $\lesssim 10^{-3}$  (see below). A high-luminosity lepton collider like TLEP/FCC-ee [481] is sensitive to exotic Higgs decays with branching fractions  $\sim 10^{-5}$  ( $10^{-3}$ ) if the decay products are very conspicuous with very little background (invisible or inconspicuous with sizable backgrounds). Therefore, depending on the detailed final state, discovering such a decay may be challenging even at lepton colliders.

In studying exotic Higgs decays, the clean environment of lepton colliders makes them superior if the final states are not very distinctive, e.g.  $\bar{b}b + \text{MET}$  or only MET. On the other hand, the huge Higgs production rates make the LHC and the 100 TeV collider vastly superior to lepton colliders when studying exotic Higgs decays with *highly distinctive* final states, allowing access to much lower branching fractions. Few final states are more distinctive than long-lived particles that decay within the detector with measurable displacement from the interaction point. Neutral Naturalness strongly motivates exotic Higgs decays to displaced final states.

The simplest scenario is a mirror sector without any light matter charged under mirror QCD. This is guaranteed in FSUSY, where LEP limits constrain the mass of the EW-charged mirror sector. It can occur in Fraternal Twin Higgs scenarios, if the mirror  $b$ -quark is not too light. In that case, the mirror hadrons are *glueballs*. There are  $\sim 12$  stable glueball states in pure  $SU(3)$  gauge theory [482], with masses ranging from  $m_0 \approx 7\Lambda_{\text{QCD}}^B$  for the lightest  $G_0 \equiv 0^{++}$  state, to  $\sim 2.7m_0$  for the heaviest state. In the presence of top partners much heavier than  $\Lambda_{\text{QCD}}^B$ , some of these states can decay via a top partner loop to SM particles via an off-shell Higgs boson [483]. We concentrate on the  $0^{++}$  state, since it has one of the shortest lifetimes and, as the lightest glueball, presumably produced commonly by mirror-hadronization.<sup>32</sup> For  $m_0 \gtrsim 2m_b$  (in the FTH case) and top partner mass  $m_T$ , the decay length of  $G_0$  is approximately

$$c\tau \approx \left(\frac{m_T}{400\text{GeV}}\right)^4 \left(\frac{20\text{GeV}}{m_0}\right)^7 \times \begin{cases} (35\text{cm}) & \text{[FSUSY]} \\ (8.8\text{cm}) & \text{[FTH]} \end{cases} \quad (87)$$

where we assume  $m_T \gg m_t/2$  for FTH and degenerate unmixed stops for FSUSY. For natural theories, these decay lengths are in the  $\mu\text{m}$  - km decay range. This leads to displaced signals at hadron colliders, with some glueballs decaying dominantly to 3<sup>rd</sup> generation SM fermion pairs.

RG arguments favor masses for  $G_0$  in the  $\sim 10 - 60\text{GeV}$  range (though model-dependent effects can easily shift that range) [299]. The same top partner loop which allows glueballs to decay also allows the Higgs boson to decay to mirror gluons, which then hadronize to yield mirror glueballs, see Fig. 85. The rate for *inclusive* production of mirror glueballs from exotic Higgs decays can be estimated by rescaling  $\text{Br}(h \rightarrow \text{gluons}) \sim 8\%$  in the SM:

$$\text{Br}(h \rightarrow \text{mirror glue}) \approx 10^{-3} \left(\frac{400\text{GeV}}{m_T}\right)^4 \times \begin{cases} 1 & \text{[FSUSY]} \\ 4 & \text{[FTH]} \end{cases} \quad (88)$$

Non-perturbative or RG effects on the mirror QCD coupling can change this by an order 1 factor [299, 466]. The *exclusive* branching fraction to the unstable  $0^{++}$  glueballs can be parameterized as the above

<sup>32</sup>Thermal estimates [484] suggest that roughly half of all produced glueballs are in the  $0^{++}$  state, but given our ignorance about pure-gauge hadronization, this estimate is highly uncertain.

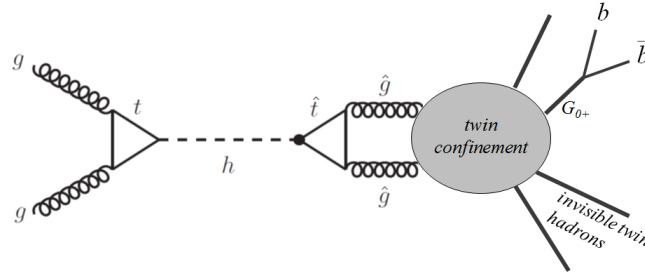


**Fig. 85:** Production of mirror hadrons in exotic Higgs decays, and their decay back to the SM, in the Fraternal Twin Higgs model. Figure from [466].

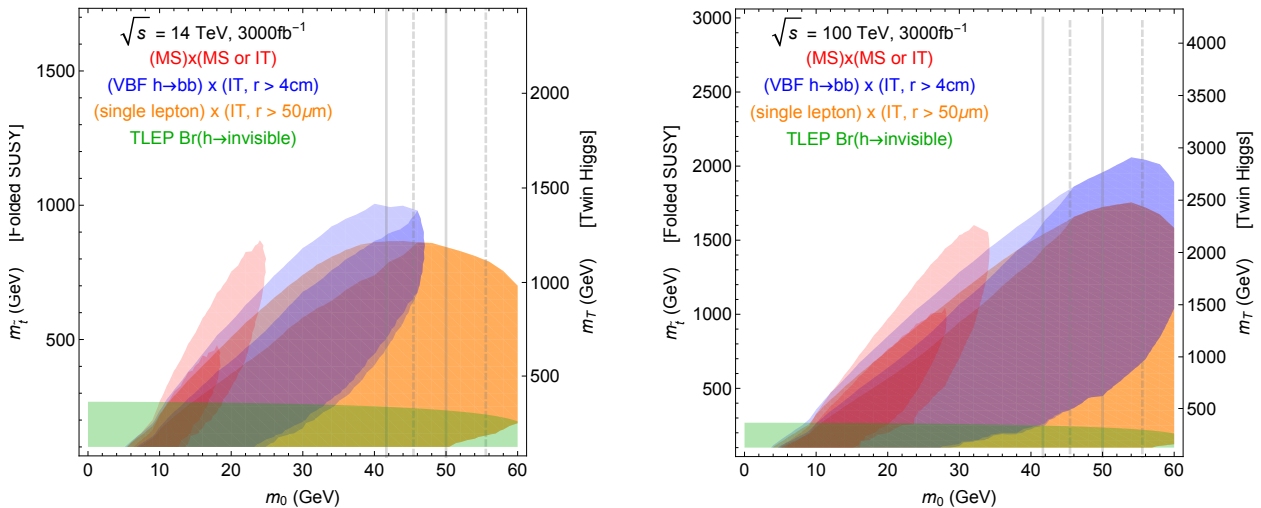


**Fig. 86:** Summary of discovery potential for the simplified model of Neutral Naturalness with light mirror glueballs at LHC14 and 100 TeV collider with  $3000 \text{ fb}^{-1}$ , from looking for (i) one DV in the muon system (MS) and one additional DV in either the MS or the inner tracker (IT), (ii) one DV at least 4 cm from beam line and VBF jets (blue) and (iii) one DV with at least  $50 \mu\text{m}$  from beam line and a single lepton (orange). Assuming negligible backgrounds and 10 events for discovery. See [299] for details. Note different scaling of vertical axes. For comparison, the inclusive TLEP  $h \rightarrow$  invisible limit, as applied to the perturbative prediction for  $\text{Br}(h \rightarrow \text{all glueballs})$ , is shown for future searches as well, which serves as a pessimistic estimate of TLEP sensitivity. Lighter and darker shading correspond to the optimistic (pessimistic) estimates of exclusive  $0^{++}$  yield, under the assumption that  $h$  decays dominantly to two glueballs. Effect of glueball lifetime uncertainty is small and not shown.  $m_0$  is the mass of the lightest glueball  $G_0$ ; the vertical axes correspond to mirror stop mass in FSUSY and mirror top mass in FTH and Quirky Little Higgs. Vertical solid (dashed) lines show where  $\kappa$  might be enhanced (suppressed) due to non-perturbative mixing effects [466].

inclusive branching fraction multiplied by a nuisance factor  $\kappa$  which ranges from  $\sim 0.1 - 1$  when there is phase space available to produce heavier glueballs. This simple approach was used by the authors of [299], who estimated the reach of various displaced searches at the LHC using ATLAS reconstruction efficiencies for displaced vertices (DV). A very conservative estimate of 100 TeV reach was derived by simply repeating the analysis for higher energy. Top partner mass reach, which is  $\sim 1.5\text{TeV}$  for TH top partners at the HL-LHC and  $\sim 3\text{TeV}$  at the 100 TeV collider with  $3\text{ab}^{-1}$  of luminosity, is shown in Fig. 86 as a function of glueball mass. Light shading indicates estimated uncertainties due to unknown details of mirror hadronization. Different search strategies are required to cover the entire range of glueball masses and lifetimes, most importantly searches for single displaced vertices together with VBF jets of leptons from Higgs production (see [299] for details, and [485] for other possibilities involving displaced triggers). This sensitivity projection is highly conservative, since the exotic Higgs decay was assumed to be 2-body, which underestimates the displaced vertex signal yield for light glueballs. Even so, the reach is impressive and provides good coverage for the natural regime of these theories. It also underlines that the detector of a 100 TeV collider needs to be able to reconstruct soft and displaced objects stemming from Higgs decays to maximize its potential for new physics discoveries. The reach could also be dramatically improved if a future detector could trigger on displaced decays, or indeed operate without a trigger.

Another possible scenario is a mirror QCD sector containing only light mirror bottom quarks  $B$ . This is one possible outcome of the Fraternal Twin Higgs (see [466] for a detailed discussion). If the mirror bottom quark mass satisfies  $m_0 \lesssim m_B < m_h/2$ , then the Higgs can decay to  $\bar{B}B$ , which forms a mirror bottomonium state and annihilates into mirror glueballs. This enhances the inclusive twin glueball rate to

$$\text{Br}(h \rightarrow \text{mirror glue}) \approx \text{Br}(h \rightarrow \bar{B}B) \approx 0.15 \left( \frac{m_B}{12\text{GeV}} \right)^2 \left( \frac{400\text{GeV}}{m_T} \right)^4, \quad (m_B < m_h/2). \quad (89)$$

which can be as large as  $\sim 10\%$ .

Alternatively, in the FTH, exotic Higgs decays can produce long-lived mirror bottomonium states if they are the lightest mirror hadrons. The rate is equal to that shown in Eq. (89). The bottomonium spectrum also contains an unstable  $0^{++}$  state that decays via the top partner loop. The lifetime of this state is

$$\Gamma_{\chi \rightarrow YY} \sim 2 \times 10^{-3} \left( \frac{v}{f} \right)^4 \frac{m_\chi^{11/3} m_0^{10/3}}{v^2 m_h (m_h^2 - m_\chi^2)^2} \Gamma_{h \rightarrow YY}(m_h), \quad (90)$$

assuming there are no light twin neutrinos which could short-circuit this decay mode. This leads to similar phenomenology as the pure glueball scenario described above, however in this case the lifetime can depend very differently on the  $0^{++}$  mass, which motivates the search for relatively short decay lengths  $\sim 10\mu\text{m}$  even for unstable particle masses near 15 GeV.

Finally, it is important to point out that in all of the above scenarios, the lifetime can be shorter than  $\sim 10\mu\text{m}$  (for very heavy glueballs with light top partners, or for bottomonia), which motivates searches for non-displaced  $b$ -rich final states of exotic Higgs decays.

#### 5.6.3.4 Direct production of top partners

The Higgs portal guarantees that neutral top partners can be produced at the 100 TeV colliders via an intermediate off-shell Higgs boson. Measurement of the top partner masses or couplings via direct production could serve as a powerful diagnostic of Neutral Naturalness to distinguish it from generic Hidden Valleys, which can also lead to displaced exotic Higgs decays.

Let us first consider the FTH scenario. In that case, any produced top partner pair will quickly mirror-beta-decay to mirror-bottoms, which then either decay to light glueballs or bottomonia, leading to

displaced vertices in the detector. Higgs portal direct production, however, has a very low cross section, making direct production measurements unfeasible at the LHC for top partners heavier than a few 100 GeV [486]. The 100 TeV collider with  $3\text{ab}^{-1}$ , on the other hand, will produce hundreds of top partner pairs with potentially multiple displaced vertices, even if  $m_T = 1\text{TeV}$  [293].

Top partner direct production is most spectacular for EW-charged partners, as for FSUSY. In that case, DY-like pair production leads to large signal rates. Since there is no light mirror-QCD-charged matter, the top partner pairs form a quirky bound state which de-excites via soft glueball and photon emission [487–490] before annihilating dominantly into mirror gluon jets, which hadronize to mirror glueballs [486]. This can lead to spectacular “emerging jet” [376] type signatures with many displaced vertices for top partner masses in the TeV range at the LHC and multi-TeV range at the 100 TeV collider. This has been recently studied in [486], which also addresses how to parameterize the unknown hadronization of the pure-gluon mirror sector. It is shown that exotic Higgs decays and direct top partner pair production have complementary sensitivity to EW-charged partners in different regions of parameter space. At a 100 TeV collider, the mass reach provided by both channels extends to several TeV or more.

The most challenging scenario is a scenario with neutral top partners but without mirror QCD. In that case, top partner production proceeds through the Higgs portal but without producing displaced vertices in the final state. This has been studied by [308, 316], which found that  $jj + \text{MET}$  searches for VBF  $h^* \rightarrow \bar{T}T$  production was the most promising channel. Even so, the production rate is so low that now meaningful bounds are derived at the LHC. A 100 TeV collider is necessary to achieve sensitivity to top partner masses of a few 100 GeV, which is the naturally preferred range.

In all of the above cases, direct production of neutral top partners is complementary to direct production of SM-charged BSM states at the 5-10 TeV scale, which are expected in the UV completion of Neutral Naturalness theories. The latter was recently explored in [491], which found reach for masses up to about 10 TeV. Both direct production measurements generally require a 100 TeV collider (especially for the Twin Higgs) and would provide valuable information on the structure of the theory.

## 5.7 BSM Higgs Sectors

In this section we will overview the direct reach for the new BSM higgs states at 100 TeV machine. We first review the two-Higgs doublet model (2HDM), which is relevant both as a standalone scenario and as an integral part of SUSY, models that explain the neutrino mass, etc. There have been a variety of studies studying the mass reach of a 100 TeV colliders to probe these new states by direct production. Singlet extensions are another highly relevant scenario, which occur in models of Neutral Naturalness, electroweak baryogenesis, and supersymmetry as the NMSSM and its derivatives, and we summarize recent work on the reach of future colliders for these states. Of course, this exploration of possibilities for BSM scalar sectors is not exhaustive, covering two of the most representative classes of scenarios. Particular examples of higgs triplet models are studied in the context of generating the neutrino mass in Section 5.5, and more work on general extensions at 100 TeV is needed.

### 5.7.1 Two-Higgs Doublet Models

#### 5.7.1.1 Higgs couplings

Two-doublet models are one of the most common extensions of the SM Higgs sector and are naturally realised in supersymmetry. Besides the ordinary Goldstones eaten by the gauge bosons, such models describe two CP-even ( $h^0$  and  $H^0$ ), one CP-odd ( $A^0$ ) and one charged ( $H^\pm$ ) physical states. Let us consider, for simplicity, the type-II structure that arises in supersymmetry.

The physical content of the models can be described in terms of two angles. The angle  $\beta$ , which defines the direction of the Higgs vev in the plane of the two neutral CP-even current eigenstates (usually denoted by  $H_d^0$  and  $H_u^0$ ). And the angle  $\alpha$ , which defines the direction of the lightest CP-even state ( $h^0$ ) in the same plane. Following the usual convention for the definition of these angles, the directions of the

Higgs vev and  $h^0$  coincide when  $\beta - \alpha = \pi/2$ . In the literature, the condition that these two directions coincide is usually referred to as *alignment*. When alignment holds,  $h^0$  behaves as the SM Higgs and the orthogonal state does not participate in the process of EW breaking.

Present LHC measurements tell us that the observed Higgs boson is SM-like at the level of about 20–30% while the full LHC program will be able to make tests in the range between a few to 10%. Assuming that no deviation is observed, it is a good starting point to take the Higgs as approximately SM-like. This situation is automatically obtained in the limit in which we take all new states ( $H^0$ ,  $A^0$ ,  $H^\pm$ ) much heavier than  $h^0$ , which corresponds to  $m_A \rightarrow \infty$  and which is usually referred to as the *decoupling limit*.

Since the Higgs couplings can be written in terms of the angles  $\alpha$  and  $\beta$ , we can easily obtain their expression in the decoupling limit ( $m_A \rightarrow \infty$ )

$$g_{hVV} = \sin(\beta - \alpha) \approx 1 - \frac{2(1-t^{-2})^2}{t^2(1+t^{-2})^4} \left(\frac{m_Z}{m_A}\right)^4 \quad (91)$$

$$g_{htt} = \frac{\cos \alpha}{\sin \beta} \approx 1 - \frac{2(1-t^{-2})}{t^2(1+t^{-2})^2} \left(\frac{m_Z}{m_A}\right)^2 \quad (92)$$

$$g_{hbb} = -\frac{\sin \alpha}{\cos \beta} \approx 1 + \frac{2(1-t^{-2})}{(1+t^{-2})^2} \left(\frac{m_Z}{m_A}\right)^2, \quad (93)$$

where  $t \equiv \tan \beta$  and  $g_{hXX}$  denote the couplings of the SM-like Higgs to weak gauge bosons ( $X = V$ ), top ( $X = t$ ), and bottom ( $X = b$ ), in units of the corresponding SM couplings. Equations (91)–(93) show explicitly how  $h$  behaves exactly as the SM Higgs in the decoupling limit. Note that the  $h$  coupling to gauge bosons becomes SM-like very rapidly, since deviations scale as  $(m_Z/m_A)^4$ . The convergence becomes even more rapid for large  $\tan \beta$ , since deviations scale as  $1/t^2$ .

To summarise: decoupling implies alignment, since  $m_A \rightarrow \infty$  implies  $\beta - \alpha \rightarrow \pi/2$ . Moreover, decoupling implies a special pattern of deviations from the SM predictions

$$\delta g_{hVV} \approx 0.02\% \left(\frac{10}{t}\right)^2 \left(\frac{300 \text{ GeV}}{m_A}\right)^4 \quad (94)$$

$$\delta g_{htt} \approx 0.2\% \left(\frac{10}{t}\right)^2 \left(\frac{300 \text{ GeV}}{m_A}\right)^2 \quad (95)$$

$$\delta g_{hbb} \approx 18\% \left(\frac{300 \text{ GeV}}{m_A}\right)^2. \quad (96)$$

In the decoupling limit, the couplings of the heavy states are also simply determined. For instance, for the heavy CP-even state  $H^0$ , one finds

$$g_{HVV} = \cos(\beta - \alpha) \approx -\frac{2}{t} \left(\frac{m_Z}{m_A}\right)^2, \quad g_{Htt} \approx -\frac{1}{t}, \quad g_{Hbb} \approx t. \quad (97)$$

This means that the coupling of a single heavy Higgs to gauge bosons vanishes in the decoupling limit. Moreover, at large  $\tan \beta$ , the coupling to bottom quarks is enhanced. The production of heavy Higgses is dominated by  $gg \rightarrow H^0/A^0$  via loops of top or bottom quarks,  $b\bar{b} \rightarrow H^0/A^0$ , or associated production with  $H^0/A^0$  emitted from a top or bottom quark line.

If the observed Higgs boson is confirmed to be nearly SM-like, we must conclude that the alignment condition is approximately satisfied. We have shown that decoupling implies alignment. So one may now wonder: does alignment imply decoupling? The answer is no. In a general two-Higgs doublet model it is possible to satisfy  $\beta - \alpha \approx \pi/2$ , while still keeping light the new Higgs states [405, 407, 492, 493]. Although this cannot be achieved in the most minimal version of supersymmetric models, alignment without decoupling can occur in supersymmetry with new singlet or triplet states [494] or for extreme values of radiative corrections [406].

As in the case of decoupling, also *alignment without decoupling* predicts a well-defined pattern of Higgs couplings. Using  $\epsilon \equiv \cos(\beta - \alpha) \tan \beta$  as expansion parameter, one finds

$$g_{hVV} \approx 1 - \frac{\epsilon^2}{2t^2}, \quad g_{htt} \approx 1 + \frac{\epsilon}{t^2}, \quad g_{hbb} \approx 1 - \epsilon, \quad (98)$$

$$g_{HVV} \approx \frac{\epsilon}{t}, \quad g_{Htt} \approx -\frac{1}{t}(1 - \epsilon), \quad g_{Hbb} \approx t \left(1 + \frac{\epsilon}{t^2}\right). \quad (99)$$

Comparing this result with Eqs. (91)–(93) and (97), one finds the same result as decoupling once we identify  $\epsilon \rightarrow -2(m_Z/m_A)^2$ . Yet, the two cases do not lead to the same phenomenological predictions, since in alignment without decoupling  $\epsilon$  can take either sign.

To summarise, there are two cases in which a two-Higgs doublet model can predict a nearly SM-like Higgs boson, such that Higgs coupling measurements can be satisfied to an arbitrary degree of precision. The two cases are decoupling and alignment without decoupling. Each case leads to a well-defined pattern for the couplings of the light and heavy Higgses, which can be expressed in terms of two parameters:  $m_A$  and  $\tan \beta$  for decoupling, or  $\cos(\beta - \alpha)$  and  $\tan \beta$  for alignment without decoupling. The important difference, from the phenomenological point of view, is that the new Higgs bosons must be heavy for decoupling, but can be arbitrarily light for alignment without decoupling. Furthermore, while standard decay channels of heavy Higgs bosons, like  $H/A \rightarrow WW, ZZ$ ,  $A \rightarrow Zh$ ,  $H \rightarrow hh$ ,  $H^\pm \rightarrow Wh$  are important in the decoupling limit, they become strongly suppressed in the alignment limit, where decays to SM fermions or photons become dominant [495]. This significantly affects the strategy of direct searches, as discussed below.

### 5.7.1.2 Direct Searches for Heavy Higgs Bosons in 2HDM

At the 100 TeV  $pp$  collider the heavy Higgses of the 2HDM are dominantly produced via gluon fusion  $gg \rightarrow H^0/A$ , with dominant top and bottom (for large  $\tan \beta$ ) loops, as well as  $bbH^0/A$  associated production.  $ttH^0/A$  associated production could be important as well. The dominant production process for the charged Higgses is  $tbH^\pm$  associated production. In Fig. 87 we show the production cross sections for  $A$ ,  $H^0$  and  $H^\pm$  at 100 TeV  $pp$  collider in the Type II 2HDM with  $\cos(\beta - \alpha) = 0$ . For neutral Higgses, gluon fusion production dominates at low  $\tan \beta$  while  $bbH^0/A$  associated production dominates at large  $\tan \beta$ . The  $tbH^\pm$  production cross section gets enhanced at both small and large  $\tan \beta$ .

Comparing to the 14 TeV LHC, the production rates can be enhanced by about a factor of 30 – 50 for gluon fusion and  $bb$  associated production, and about a factor of 90 for the charged Higgs for Higgs mass of about 500 GeV, and even more for heavier Higgses, resulting in great discovery potential for heavy Higgses at a 100 TeV  $pp$  colliders.

At the LHC, most of the current searches for non-SM neutral Higgs bosons focus on the conventional Higgs search channels with a  $WW$ ,  $ZZ$ ,  $\gamma\gamma$ ,  $\tau\tau$  and  $bb$  final state [501–507]. These decay modes are characteristic to the 2HDM in the decoupling limit, where we in general do not expect big splittings between the various heavy Higgses. Typically, the production rate of the extra Higgses is suppressed, compared to that of the SM Higgs, either due to its larger mass or its suppressed couplings to the SM particles. The decay of the heavy neutral Higgses to the  $WW$  and  $ZZ$  final states, which provided a large sensitivity for SM Higgs searches, is absent for the CP-odd Higgs, and could be highly suppressed for the non-SM like CP-even Higgs, especially in the alignment limit [495], in which case SM fermion and photon final states become more important. The decay modes into  $\tau\tau$  or  $bb$  suffer from either suppressed branching fraction once the top pair mode opens up or large SM backgrounds, and are therefore only relevant for regions of the parameter space with an enhanced  $bb$  or  $\tau\tau$  coupling. If the non-SM neutral Higgs is heavy enough, the decay mode into top pairs becomes important. However, when the Higgs is produced in gluon fusion, such decay suffers from large  $t\bar{t}$  background and a possible destructive interference with the SM background [495, 508]. Direct searches for charged Higgs bosons are even more difficult at the LHC. For  $m_{H^\pm} > m_t$ , the cross section for the dominant production channel of

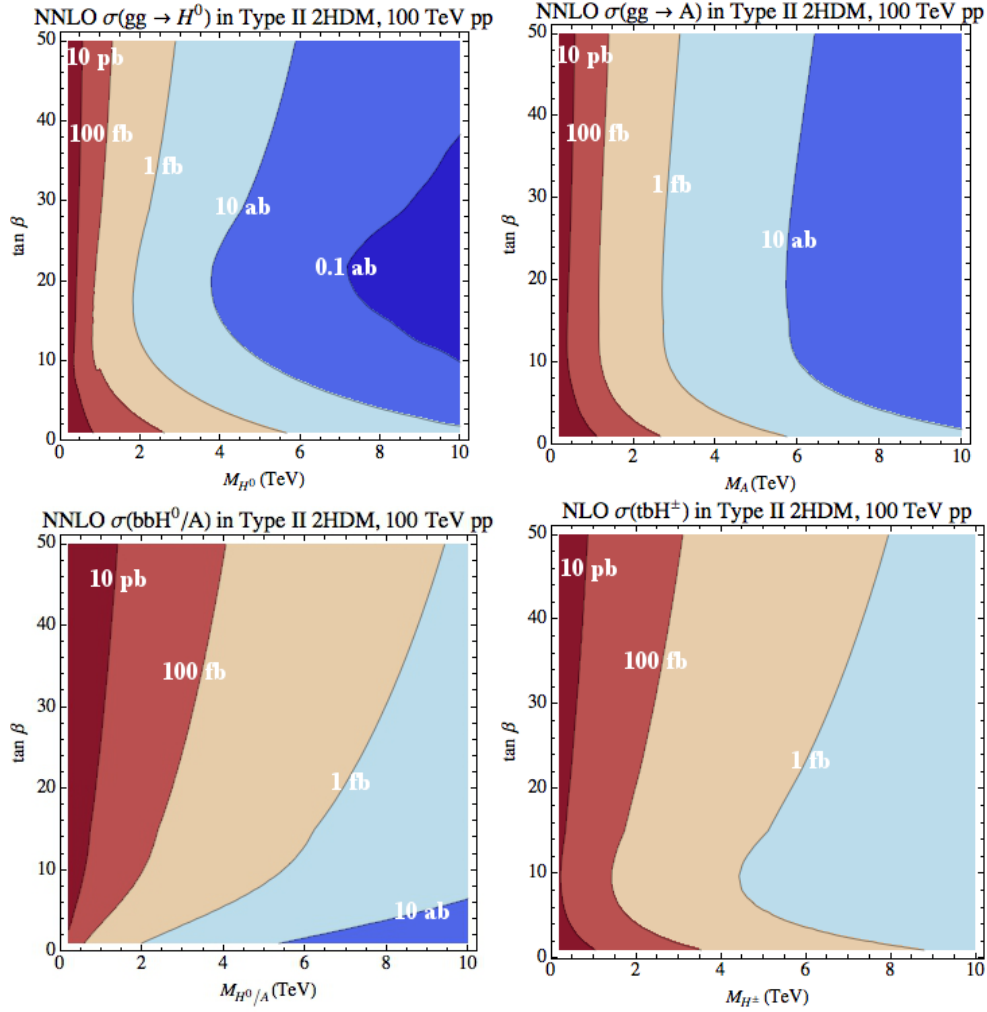


**Fig. 87:** Dominant production cross sections for non-SM like Higgses in the Type II 2HDM at the 100 TeV  $pp$  collider: NNLO cross section for  $gg \rightarrow H^0$  or  $A$  (top left and top right panel, calculated using HIGLU [496] with the NNPDF2.3 parton distribution functions [114]), NNLO cross section for bottom-associated production  $bbH^0/A$  (lower left panel, calculated using SusHi [397, 497, 498]).  $bbH^0$  and  $bbA$  cross sections are the same in the alignment limit), NLO cross section for  $tbH^\pm$  (lower right panel, calculated in Prospino [499, 500]).

$tbH^\pm$  is typically small. The dominant decay mode  $H^\pm \rightarrow tb$  is hard to identify given the large  $tt$  and  $ttbb$  background, while the subdominant decay of  $H^\pm \rightarrow \tau\nu$  has suppressed branching fraction. In the MSSM, even at the end of the LHC running, there is a “wedge region” [178] in the  $m_A - \tan\beta$  plane for  $\tan\beta \sim 7$  and  $m_A \gtrsim 300$  GeV in which only a SM-like Higgs can be discovered at the LHC. Similarly, the reach for the non-SM Higgses in other models with an extended Higgs sector is limited as well.

The situation is very different at a 100 TeV collider. Two recent studies [286, 509] estimated the reach of Higgs production searches in the MSSM at 100 TeV, where the heavy bosons are produced in association with and decay into SM fermions. The reach, shown in Fig. 88, is impressive. Heavy Higgs masses up to 5-10 TeV will be probed with  $3 \text{ ab}^{-1}$  for all values of  $\tan\beta$ . This also shows that the wedge region could be covered by making use of new kinematic features of such signal events at a 100 TeV  $pp$  collider, in this case top tagging in the boosted region. At low  $\tan\beta$ , the greatest sensitivity to neutral Higgs bosons is achieved with a same-sign dilepton search for Higgses produced in association with one or two top quarks, which subsequently decay to  $\bar{t}t$ . The associated production channel avoids the difficult interference issues of a  $pp \rightarrow H^0 \rightarrow \bar{t}t$  search.

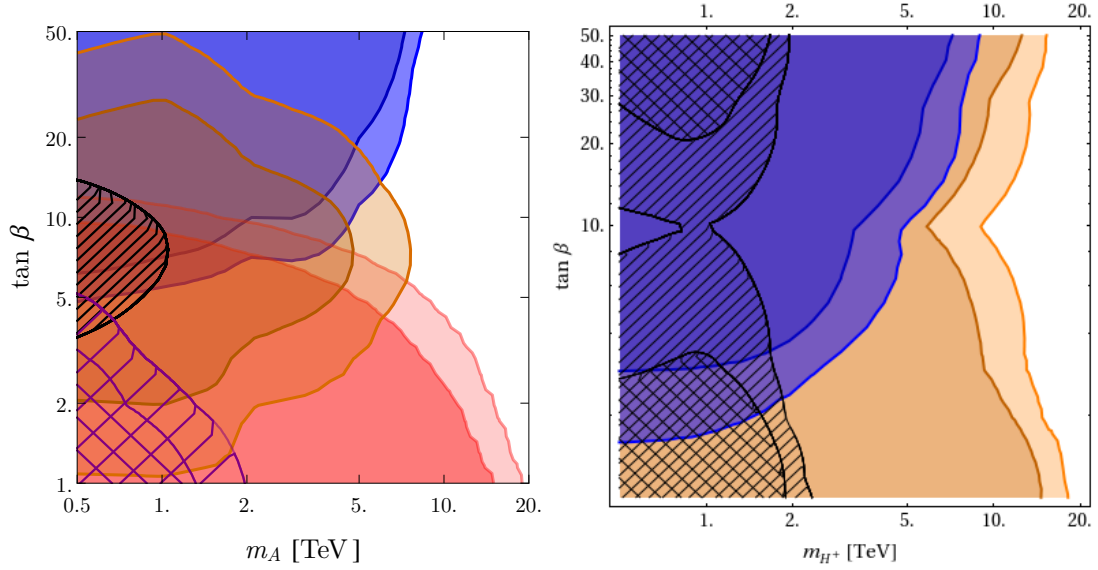


**Fig. 88:** 95% C.L. exclusion bounds for neutral (left panel, from [509]) and charged (right panel, from [286]) Higgses of the MSSM at a 100 TeV collider. The blue and orange regions are probed by the channels  $pp \rightarrow bbH^0/A \rightarrow bb\tau\tau$  and  $pp \rightarrow bbH^0/A \rightarrow bbt\bar{t}$  for the neutral Higgses and  $pp \rightarrow tbH^\pm \rightarrow tb\tau\nu$  and  $pp \rightarrow tbH^\pm \rightarrow tbt\bar{b}$  for the charged Higgses, respectively. The red region is probed by heavy Higgs production in association with one or two top quarks, with subsequent decay to  $\bar{t}t$ , yielding a same-sign dilepton signature. Given the same channel or the same color, the two different opacities indicate the sensitivities w.r.t. a luminosity of  $3 \text{ ab}^{-1}$  and  $30 \text{ ab}^{-1}$  at a 100 TeV  $pp$  collider, respectively. The cross-hatched and diagonally hatched regions are the predicted exclusion contours for associated Higgs production at the LHC for  $0.3 \text{ ab}^{-1}$ , and  $3 \text{ ab}^{-1}$ , respectively.

Parent Higgs	Decay	Possible Final States	Channels in 2HDM
Neutral Higgs $H^0, A$	$HH$ type	$(bb/\tau\tau/WW/ZZ/\gamma\gamma)(bb/\tau\tau/WW/ZZ/\gamma\gamma)$	$H^0 \rightarrow AA, h^0 h^0$
	$HZ$ type	$(\ell\ell/qq/\nu\nu)(bb/\tau\tau/WW/ZZ/\gamma\gamma)$	$H^0 \rightarrow AZ, A \rightarrow H^0 Z, h^0 Z$
	$H^+H^-$ type	$(tb/\tau\nu/cs)(tb/\tau\nu/cs)$	$H^0 \rightarrow H^+H^-$
	$H^\pm W^\mp$ type	$(\ell\nu/qq')(\ell\nu/qq')$	$H^0/A \rightarrow H^\pm W^\mp$
Charged Higgs	$HW^\pm$ type	$(\ell\nu/qq')(bb/\tau\tau/WW/ZZ/\gamma\gamma)$	$H^\pm \rightarrow h^0 W, H^0 W, AW$

**Table 44:** Summary of exotic decay modes for non-SM Higgs bosons. For each type of exotic decays (second column), we present possible final states (third column) and relevant channels in 2HDM. Note that  $H$  in column two refers to any of the neutral Higgs, e.g.  $h^0, H^0$  or  $A$  in 2HDM.

In addition to their decays to the SM particles, non-SM Higgses can decay via exotic modes, i.e., heavier Higgs decays into two light Higgses, or one light Higgs plus one SM gauge boson. Clearly this happens in the case when the splitting between the various heavy higgses is not small. This can happen in the alignment limit of the 2HDM without decoupling. As outlined above, this limit is less generic than the decoupling limit, but still worth a detail study.

Five main exotic decay categories for Higgses of the 2HDM are shown in Table 44. Once these decay modes are kinematically open, they typically dominate over the conventional decay channels. Recent studies on exotic decays of heavy Higgs bosons can be found in Refs. [510–521].

Theoretical and experimental constraints restrict possible mass hierarchies in 2HDM. At high Higgs mass and close to the alignment limit, unitarity imposes a relation between the soft  $Z_2$ -breaking term and the heavy CP-even neutral Higgs mass  $m_{12}^2 = m_{H^0}^2 s_\beta c_\beta$ <sup>33</sup>. In this limit, the decay branching fraction  $H^0 \rightarrow h^0 h^0, AA, H^+H^-$  vanishes and vacuum stability further requires the CP-even non-SM

<sup>33</sup>Note that this is automatically fulfilled in the MSSM.

Higgs  $H^0$  to be the lightest non-SM like Higgs. In addition, electroweak precision measurements require the charge Higgs mass to be close to either of the neutral non-SM Higgs masses. This leaves us with only two possible mass hierarchies permitting exotic Higgs decays:  $m_{H^0} \approx m_{H^+} < m_A$  and  $m_{H^0} < m_A \approx m_{H^+}$ . At high Higgs masses, unitarity further requires the mass splitting between the non-SM Higgses to be small and therefore imposes an upper bound on the Higgs mass permitting exotic Higgs decays around  $m_H \sim 1.5 - 2$  TeV. These restrictions can be significantly relaxed at lower Higgs mass, allowing a larger spectrum of mass hierarchies including those permitting the decays  $H^0 \rightarrow AA, H^+H^-$ . Considering the limited reach of the LHC around the “wedge region”, exotic Higgs decay channels in the low Higgs mass region,  $m_{H^0} \lesssim 500$  GeV, might still provide discovery potential at a 100 TeV  $pp$  collider. In Fig. 89 we show the branching fraction of non-SM Higgs bosons in Type II 2HDM for  $\sin(\beta - \alpha) = 1$  and a mass hierarchy containing a 1 TeV parent Higgs and a 850 GeV daughter Higgs.

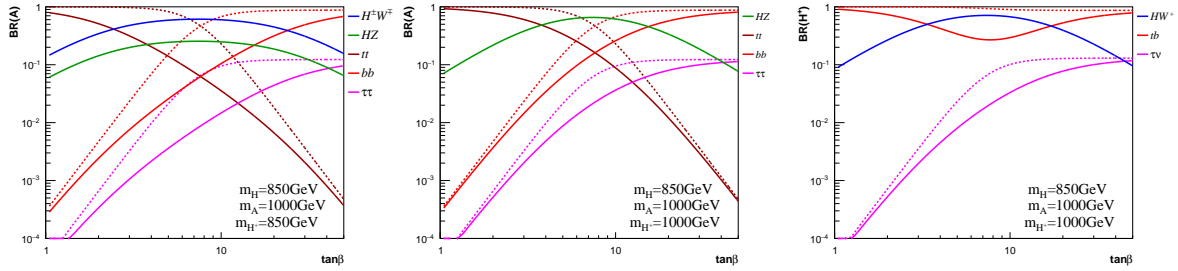


**Fig. 89:** Branching fractions for  $A$  (left and center panel) and  $H^+$  (right panel) in the Type II 2HDM with  $\sin(\beta - \alpha) = 1$  and  $m_{12}^2 = m_{H^0}^2 s_\beta c_\beta$ . We show the two allowed mass hierarchies  $m_{H^0} = m_{H^+} < m_A$  (left panel) and  $m_{H^0} < m_A = m_{H^+}$  (center and right panel). The parent and daughter Higgs masses are chosen to be 1 TeV and 850 GeV, respectively. Dashed curves are the branching fractions when exotic decay modes are kinematically forbidden. All decay branching fractions are calculated using the program 2HDMC [522].

Note that most of the current experimental searches for the non-SM Higgs assume the absence of exotic decay modes. Once there are light Higgs states such that these exotic modes are kinematically open, the current search bounds can be greatly relaxed given the suppressed decay branching fractions into SM final states [511, 513, 515]. Furthermore, exotic Higgs decays to final states with two light Higgses or one Higgs plus one SM gauge boson provide complementary search channels. Here, we list such exotic Higgs decays and consider potential search strategies.

$$- H^0 \rightarrow AA \text{ or } H^0 \rightarrow h^0 h^0$$

With the final state Higgs decaying via  $bb, \gamma\gamma, \tau\tau, WW^*$ , final states of  $bbbb, bb\tau\tau, bb\gamma\gamma$  and  $\gamma\gamma WW^*$  can be used to search for resonant Higgs decay to two light neutral Higgses. Current searches at the LHC 8 TeV with about  $20 \text{ fb}^{-1}$  luminosity gave observed limits of 2.1 pb at 260 GeV and about 0.018 pb at 1000 GeV [523]. While  $bb\gamma\gamma$  and  $bb\tau\tau$  have comparable sensitivities at low mass,  $bbbb$  mode dominates at high mass.

$$- H^0 \rightarrow AZ \text{ or } A \rightarrow H^0 Z$$

With  $Z \rightarrow \ell\ell$  and  $H^0/A \rightarrow bb, \tau\tau$ , the final states of  $bb\ell\ell, \tau\tau\ell\ell$  can be obtained with gluon fusion production, or in the  $bb$  associated production with two additional  $b$  jets [510–512]. Recent searches from ATLAS and CMS have shown certain sensitivity in this channel [524–527]. In parameter regions where  $\text{Br}(A \rightarrow H^0 Z) \times \text{Br}(H^0 \rightarrow ZZ)$  is not completely suppressed,  $ZZZ$  final states with two  $Z$  decaying leptonically and one  $Z$  decaying hadronically can also be useful [511]. Other channels with top final states could be explored as well.

Note that the decay  $A \rightarrow ZH^0$  has been identified as a particular signature of a SFOEWPT in the 2HDM [317]. As discussed below, the prospects for observing this channel in the  $\ell\ell b\bar{b}$  and  $\ell\ell W^+W^-$  model have been analyzed in Ref. [318].

$$- H^0 \rightarrow H^+H^-$$

With both  $H^\pm$  decaying via  $\tau\nu$  final states, the signal of  $\tau\tau\nu\nu$  can be separated from the SM  $W^+W^-$  background since the charged tau decay product in the signal typically has a hard spectrum compared to that of the background [515].

$$- H^0/A \rightarrow H^\pm W^\mp$$

Similar to the  $H^+H^-$  case,  $H^\pm \rightarrow \tau\nu, tb$  and  $W \rightarrow \ell\nu$  with  $\ell\tau\nu\bar{\nu}$  or  $tb\ell\nu$  could be used to search for  $H^0/A \rightarrow H^\pm W^\mp$ . Note that for the CP-even Higgs  $H^0$ , the branching fraction of  $H^0 \rightarrow H^\pm W^\mp$  is mostly suppressed comparing to  $H^0 \rightarrow H^+H^-$  as long as the latter process is kinematically open and not accidentally suppressed [515]. However, for the CP-odd Higgs  $A$ , this is the only decay channel with a charged Higgs in the decay products.

$$- H^\pm \rightarrow H^0W, AW$$

This is the only exotic decay channel for the charged Higgs in the 2HDM. Given the associated production of  $tbH^\pm$ , and the decay of  $H^0, A$  into the  $bb$  or  $\tau\tau$  channel,  $\tau\tau bbWW$  or  $bbbbWW$  can be used to probe this channel [513].  $H^0/A \rightarrow t\bar{t}$  could also be used given the boosted top in the high energy environment.

Note that while  $H^\pm \rightarrow WZ$  is absent in 2HDM type extension of the SM Higgs sector, it could appear, however, in the real triplet models extension of the SM once the triplet obtains a vev [342].

### 5.7.2 Singlet Extensions of the Higgs Sector<sup>34</sup>

The simplest example of an extended Higgs sector consists in the addition of a real scalar field, singlet under all the gauge groups, to the SM. Despite its great simplicity, this scenario arises in many of the most natural extensions of the SM – e.g. the Next-to-Minimal Supersymmetric SM (NMSSM, see Section 5.7.2.1), Twin Higgs (see Section 5.7.2.2), some Composite Higgs models – and is therefore of considerable physical interest.

In general, a CP-even scalar singlet will mix with the Higgs boson at a renormalizable level. As a consequence, both physical scalar states can be produced at colliders through their couplings to SM particles, and be observed by means of their visible decays.

Let us denote by  $h$  and  $\phi$  the physical mass eigenstates, and by  $\gamma$  the mixing angle. In a weakly interacting theory, the couplings of  $h$  and  $\phi$  are just the ones of a SM Higgs, rescaled by a universal factor of  $\cos\gamma$  or  $\sin\gamma$ , respectively. Hence, assuming no invisible decays, the signal strengths  $\mu_{h,\phi}$  into SM particles are

$$\mu_h = \mu_{\text{SM}}(m_h) \times c_\gamma^2, \quad (100)$$

$$\mu_{\phi \rightarrow VV, ff} = \mu_{\text{SM}}(m_\phi) \times s_\gamma^2 \times (1 - \text{BR}_{\phi \rightarrow hh}), \quad (101)$$

$$\mu_{\phi \rightarrow hh} = \sigma_{\text{SM}}(m_\phi) \times s_\gamma^2 \times \text{BR}_{\phi \rightarrow hh}, \quad (102)$$

where  $\mu_{\text{SM}}(m)$  is the corresponding signal strength of a standard Higgs with mass  $m$ , and  $\text{BR}_{\phi \rightarrow hh}$  is the branching ratio of  $\phi$  into two Higgses – an independent parameter at this level. The phenomenology

<sup>34</sup>Contribution by Dario Buttazzo, Filippo Sala and Andrea Tesi

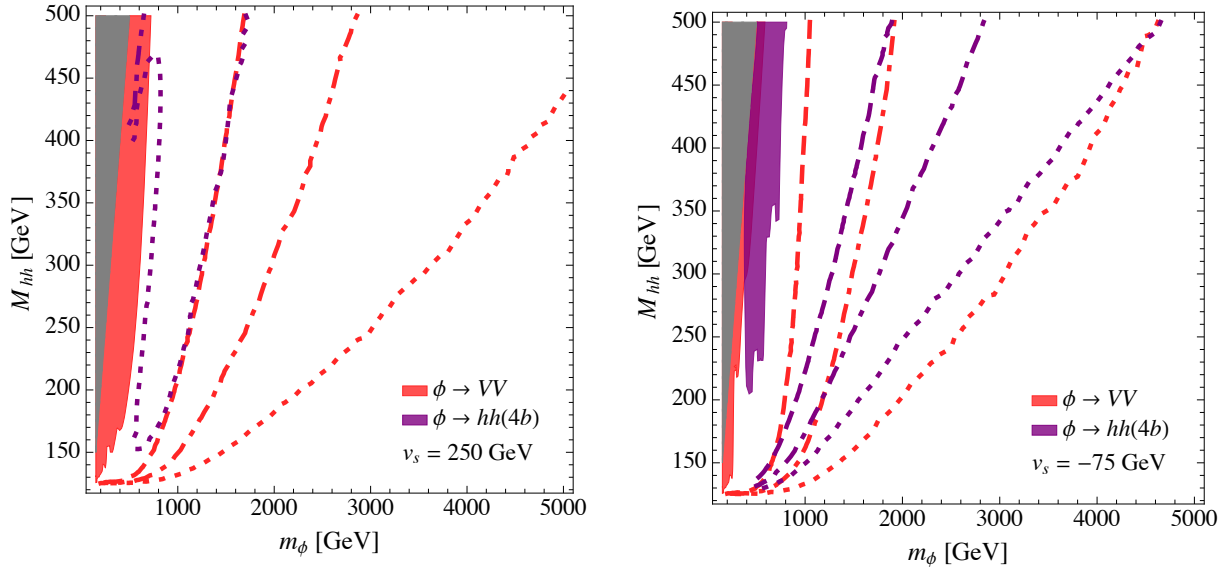


**Fig. 90:** Reach of direct searches for generic singlet extensions of the SM in the  $m_\phi$ - $M_{hh}$  plane, see Eq. (103). The singlet vev is  $v_s = 250$  GeV (left) and  $v_s = -75$  GeV (right). Searches using the  $VV$  and  $hh$  final state are shown in red and purple. The solid colored regions are excluded at 95% CL by the 8 TeV LHC. Lines represent the expected bounds for FCC-hh (dotted), high-luminosity LHC (dashed), and high-energy LHC (dot-dashed), all with a luminosity of  $3 \text{ ab}^{-1}$ . Taken from Ref. [528].

of the Higgs sector is therefore completely described by three parameters:  $m_\phi$ ,  $s_\gamma$ , and  $\text{BR}_{\phi \rightarrow hh}$ . The second state  $\phi$  behaves like a heavy SM Higgs boson, with reduced couplings and an additional decay width into  $hh$ .

The mixing angle  $\gamma$  and  $m_\phi$  are not independent quantities, but are related via

$$\sin^2 \gamma = \frac{M_{hh}^2 - m_h^2}{m_\phi^2 - m_h^2}, \quad (103)$$

where  $M_{hh}^2 \propto v^2$  is the first diagonal entry of the Higgs squared mass matrix, in the gauge eigenstate basis. In the following we will often use  $M_{hh}$  as a parameter, instead of  $\gamma$ , to avoid considering unnatural regions of the parameter space with high mass and large mixing angle.

Given the singlet nature of  $\phi$ , its main decay channels are into pairs of  $W$ ,  $Z$ , and Higgs bosons. In the large- $m_\phi$  limit, the equivalence theorem implies that

$$\text{BR}_{\phi \rightarrow hh} = \text{BR}_{\phi \rightarrow ZZ} = \frac{1}{2} \text{BR}_{\phi \rightarrow WW}. \quad (104)$$

The leading corrections to this relation<sup>35</sup> for finite masses depend only on the vacuum expectation value of the singlet,  $v_s$  [528]. Therefore, to a good approximation  $m_\phi$ ,  $M_{hh}$ , and  $v_s$  constitute a set of independent parameters that describe the phenomenology.

The FCC reach for a generic resonance in these channels has been discussed in Ref. [528], where it has been obtained through a parton luminosity rescaling from the 8 TeV LHC results [448]. Figure 90 shows the combined reach from all the  $VV$  final states, compared with the one in the  $hh$  channel from the  $4b$  final state, again for two different values of  $v_s$ . The reach of the high-luminosity (14 TeV,  $3 \text{ ab}^{-1}$ ) and high-energy (33 TeV,  $3 \text{ ab}^{-1}$ ) upgrades of the LHC are also shown for comparison. It can be seen

<sup>35</sup>The exact expressions for the triple couplings  $g_{\phi hh}$  and  $g_{hhh}$  depend on the details of the scalar potential, and can be found in ref. [528].

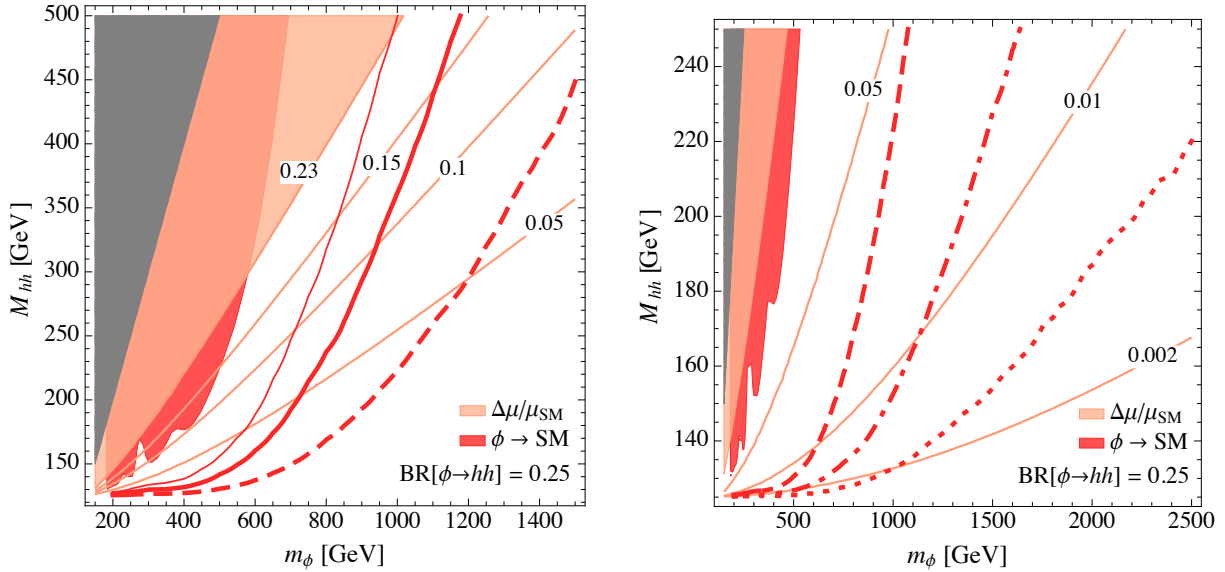


**Fig. 91:** Comparison between direct and indirect searches in the singlet model, and for  $\text{BR}_{\phi \rightarrow hh} = 0.25$ . Left: region relevant for the LHC (thin lines: 13 TeV, thick lines: 14 TeV, dashed: high luminosity). Right: projections for future colliders (dot-dashed: 33 TeV LHC, dotted: FCC-hh with  $3 \text{ ab}^{-1}$ ). Coloured isolines of  $s_\gamma^2$ . The colored region is excluded at 95% CL. Taken from Ref. [528].

that the  $VV$  searches are always dominant at FCC. Moreover, the detection of a  $hh$  resonance in the multi-TeV range is possible only for values of  $v_s$  related also to very large modifications (a factor of two or even larger) in the triple Higgs coupling  $g_{hhh}$ . Moderate to large deviations in such a coupling are a generic prediction of a singlet mixed with the Higgs, contrarily for example to the case of 2HDM, and the very high energy of the FCC-hh appear to provide a unique opportunity to test this possibility.

Finally, Fig. 91 compares the reach of direct and indirect searches, for fixed  $\text{BR}_{\phi \rightarrow hh} = 0.25$ , and for two regions relevant for the LHC and for FCC, respectively. The deviation in Higgs signal strengths, shown as colored isolines, are proportional to  $s_\gamma^2$ . Given the universal rescaling of all the couplings, the power of Higgs coupling measurements in the singlet case is rather limited, as compared e.g. to a 2HDM (see Section 5.7.1). It is interesting to note that direct searches at FCC-hh are more powerful than indirect measurements at FCC-ee for resonance masses below about 1 TeV.

The results of the simple scenario presented in this Section apply in general to any singlet scalar, and can easily be applied to more concrete cases, as we discuss below for the NMSSM and the Twin Higgs.

### 5.7.2.1 NMSSM

The NMSSM constitutes a particularly interesting physics case for several reasons. In particular, since the extra Higgs bosons could be the first new degrees of freedom to be detected, it is important to quantify the reach of LHC and future colliders for scalar states in this scenario.

The NMSSM consists in the MSSM with the addition of an extra gauge singlet  $S$ , so that the superpotential reads

$$W_{\text{NMSSM}} = W_{\text{MSSM}} + \lambda S H_u H_d + V(S), \quad (105)$$

where  $V$  is a polynomial up to order three in the new field  $S$ . This addition is relevant from the point of view of naturalness for large enough  $\lambda$ , since the different dependence of the weak scale  $v$  in the high energy parameters allows, for a given amount of tuning, to raise the stop and gluino masses by a factor  $\sim \lambda/g$  with respect to the MSSM. The Higgs mass value  $m_h$  is also less constraining in the NMSSM

than in the MSSM, thanks to the extra SUSY-preserving contribution of the form  $\sin^2 2\beta \lambda v^2/2$ . The drawback of this last feature is that, for a too large  $\lambda$ , a tuning is reintroduced to lower the Higgs mass to 125 GeV. These considerations have been made precise in the analysis of Ref. [529], that identified  $\lambda \sim 1$  as a region of minimal tuning, capable of accommodating stops and gluinos as heavy as 1.2 and 2.5 TeV respectively. The loss of perturbativity before the GUT scale, implied by a value of  $\lambda \gtrsim 0.75$ , is avoidable without spoiling unification, see *e.g.* the model proposed in [530] and references therein.

The Higgs sector of the NMSSM consists of six particles: three CP-even ones,  $h$ ,  $H$  and  $\phi$ , two CP-odd ones  $A$  and  $A_s$ , and a charged state  $H^\pm$ . We mostly concentrate on the CP-even ones, and identify  $h$  with the 125 GeV state discovered at the LHC,  $H$  with the mostly doublet mass eigenstate, and  $\phi$  with the mostly singlet one. Three mixing angles, to be called  $\delta$ ,  $\gamma$ , and  $\sigma$ , control the rotation between the mass eigenstates and the gauge eigenstates where one doublet takes all the vev.

It has been shown in Ref. [530] that the phenomenology of the three CP-even states, with the exception of the trilinear couplings among the Higgses, can be described in terms of only six parameters, which we find convenient to choose as:

$$m_\phi^2, \quad m_H^2, \quad m_{H^\pm}^2, \quad \tan \beta, \quad \lambda, \quad \Delta^2, \quad (106)$$

where with  $\Delta^2$  we denote all the radiative contributions to the Higgs mass, which sums up the contributions from the rest of the superpartner spectrum.<sup>36</sup> Radiative corrections to other elements of the scalar mass matrix are assumed to be small. The mixings angles can be expressed in terms of the parameters in (106), see Refs. [530, 531] for the full analytical formulae.

Deviations in the Higgs couplings,

$$\frac{g_{h\bar{u}u}}{g_{h\bar{u}u}^{\text{SM}}} = c_\gamma \left( c_\delta + \frac{s_\delta}{\tan \beta} \right), \quad \frac{g_{h\bar{d}d}}{g_{h\bar{d}d}^{\text{SM}}} = c_\gamma (c_\delta - s_\delta \tan \beta), \quad \frac{g_{hVV}}{g_{hVV}^{\text{SM}}} = c_\gamma c_\delta, \quad (107)$$

(where  $s_\theta, c_\theta = \sin \theta, \cos \theta$ ) constrain only the two mixing angles  $\delta$  and  $\gamma$  that involve  $h$ . While a fit to the Higgs couplings leaves space for a sizable mixing  $\gamma$ , at the level of  $\sin \gamma \sim 0.45$ , it leaves little space for two mixed doublets. Perhaps more important than that, the LHC14 with  $300 \text{ fb}^{-1}$  is not expected to probe substantially the  $h$ - $S$  mixing  $\gamma$ , while the opposite is true for  $\delta$ , which will be constrained to the few percent level [531].

Since the purpose of this document is to set a general strategy for searching for BSM Higgses, for convenience we now summarize the phenomenology in two limiting cases, identified by their relevant degrees of freedom<sup>37</sup>.

- ◇  $h$  and a singlet-like state  $\phi$  in the low-energy spectrum, with  $H$  decoupled and  $\delta = 0$ . The generic parameter  $M_{hh}$  of Section 5.7.2 is now identified with the upper bound on the Higgs boson mass

$$M_{hh}^2 = c_{2\beta}^2 m_Z^2 + s_{2\beta}^2 \lambda^2 v^2/2 + \Delta^2, \quad (108)$$

and the total number of free parameters decreases from six to four,  $m_\phi$ ,  $\lambda$ ,  $\tan \beta$  and  $\Delta$ . Since  $\Delta$  has little impact on the phenomenology of the model (unless it is very large), it is convenient to fix it to some reference value, typical of stops in the TeV range.

- ◇  $h$  and a second doublet  $H$  in the low-energy spectrum, with  $\phi$  decoupled and  $\gamma = 0$ . The Higgs sector now realizes a particular type-II 2HDM. Here the total number of free parameters is three,  $m_H$ ,  $\tan \beta$  and  $\Delta$ , and also the charged scalar  $H_\pm$  is predicted with a mass close to that of the CP-even one  $H$ . The MSSM is a particular realization of this case, where  $\lambda = 0$  and  $\Delta$  is fixed to reproduce the correct value of the Higgs mass. However, for generic values of  $\Delta$ ,  $\lambda \neq 0$  and the realized 2HDM will be different from the MSSM.

<sup>36</sup>We will choose values representative of TeV-scale stops, but the phenomenology does not sensitively depend on  $\Delta^2$  unless the value is much larger than what we assume.

<sup>37</sup>For a discussion with the same logic and more details, we refer the reader to the short review [532].

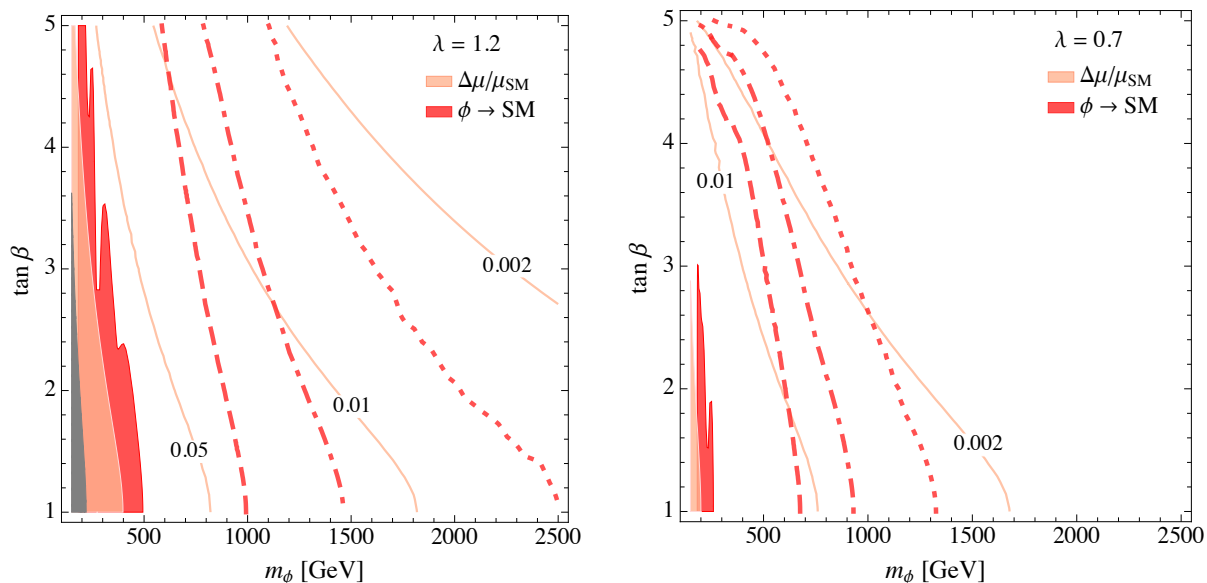


**Fig. 92:** Parameter space of the NMSSM scenario in the limit of decoupled heavy doublet  $H$ . Shaded areas: 95% CL exclusions from Higgs signal strengths (pink) and direct searches for  $\phi \rightarrow \text{SM}$  (red) at LHC8. Lines: contours of  $s_\gamma^2$  (pink), expected reach of direct searches at HL-LHC (dashed), HE-LHC (dot-dashed), and FCC-hh with  $3 \text{ ab}^{-1}$  (dotted). Grey: unphysical regions.  $\text{BR}_{\phi \rightarrow hh}$  fixed to its asymptotic value  $1/4$ . Left:  $\Delta = 70 \text{ GeV}$  and  $\lambda = 1.2$ ; right:  $\Delta = 80 \text{ GeV}$  and  $\lambda = 0.7$ . Taken from Ref. [528].

Let us summarize the phenomenology of these two cases. In the  $h$ -singlet mixing scenario, Higgs coupling measurements will leave much of the parameter space unexplored, unless a per-mille precision is reached, as expected at the FCC-ee (or CEPC). Direct searches for the extra Higgs is therefore the most powerful probe of the Higgs sector in this case. The impact of current and future searches is shown in Fig. 92, for the values of  $\lambda = 1.2$  and  $0.7$ , respectively. For simplicity we have fixed  $\text{BR}(\phi \rightarrow hh)$  to its asymptotic value of  $1/4$ , a case where  $VV$  searches dominate over  $hh$  ones<sup>38</sup>. From Fig. 92 one reads that direct searches are expected to dominate the reach in the parameter space of the model. At a 100 TeV  $pp$  collider they will be complementary with Higgs coupling measurements of a leptonic collider like the FCC-ee or the CEPC. No matter how we look for BSM in the Higgs sector, the region of smaller  $\lambda$  will be more difficult to probe than that of a larger one, giving more importance to other SUSY searches (like stop and gluino ones). In each scenario, singlet scalar masses in excess of a TeV can be probed, depending on the value of  $\tan \beta$ .

We now move to the second case, where the relevant degrees of freedom are  $h$  and the doublet-like state  $H$ . This scenario is best probed via measurements of the Higgs signal strengths into SM particles, as evident from Fig. 93. A region of “alignment without decoupling” of the state  $H$  survives for  $\lambda \simeq 0.65$  and  $\tan \beta \simeq 2.5$ , corresponding to a zero of the mixing angle  $\delta$ . That region – which is already constrained by the bounds on  $m_{H^\pm}$  coming from flavour measurements like  $\text{BR}(B \rightarrow X_s \gamma)$  – needs direct searches for the new states in order to be probed. The discussion follows that of two Higgs doublet models of Section 5.7.1. We recall here the main features for convenience, following the recent study of Ref. [495]: exact alignment  $\delta = 0$  implies  $\text{BR}_{H \rightarrow hh} = \text{BR}_{H \rightarrow VV} = \text{BR}_{A \rightarrow Zh} = \text{BR}_{H^\pm \rightarrow W^\pm h} = 0$ , but contrary to the  $h$ - $\phi$  singlet case some couplings to SM fermions survive, allowing to probe the existence of  $H$  in resonant searches in  $t\bar{t}$ ,  $b\bar{b}$ ,  $l^+l^-$  and  $\gamma\gamma$ . For larger values of  $m_H$ , the  $t\bar{t}$  channel opens and dominates the branching ratio. The 100 TeV studies of heavy Higgs production in association

<sup>38</sup>“Small” values of  $v_s$  can make resonant di-Higgs production more important, a case which we do not discuss here.

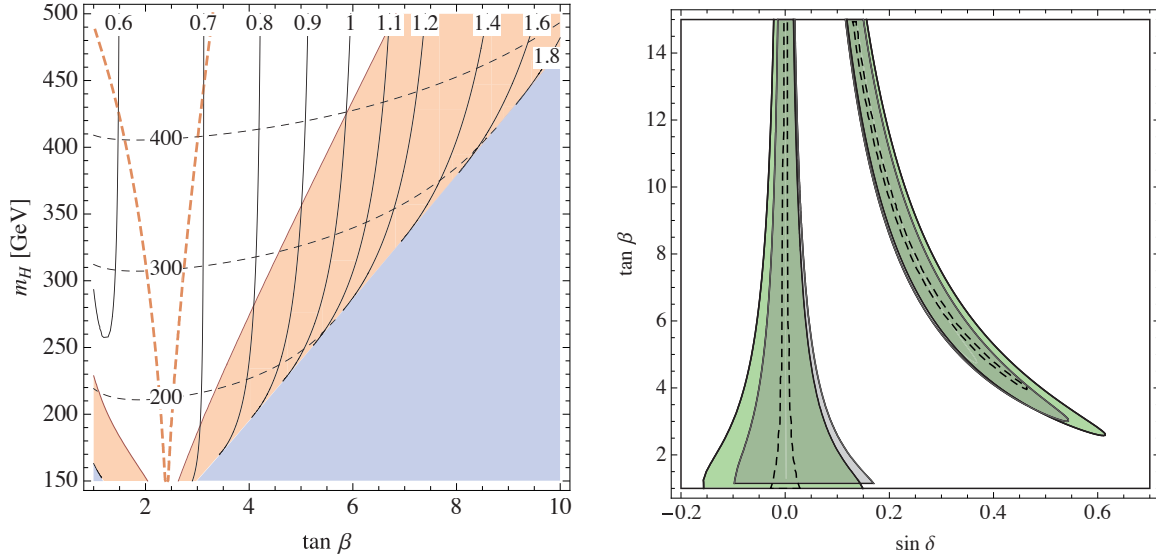


**Fig. 93:** Left: parameter space of the NMSSM scenario with a decoupled scalar  $S$ , with radiative corrections to the Higgs mass fixed at  $\Delta = 75 \text{ GeV}$ . Isolines of  $\lambda$  (solid black), and of  $m_{H^\pm}$  (dashed black). 95% CL exclusions from Higgs coupling measurements at LHC8 (shaded pink), expected reach at LHC14 with  $300 \text{ fb}^{-1}$  (pink dashed). Blue: unphysical regions. The entire shown parameter space is likely to be excluded by direct searches for heavy Higgs doublets at 100 TeV, see Fig. 88. Right: Higgs couplings fit (95% CL allowed regions) for  $\sin^2 \gamma = 0$  (green) and  $\sin^2 \gamma = 0.15$  (grey) from the LHC run 1, and projection for LHC14 (dashed,  $\gamma = 0$ ). Taken from Ref. [533].

with SM fermions [286, 509] indicates that 5-10 TeV masses can be probed, which likely applies to this NMSSM scenario as well, see Fig. 88.

Going back to a fully mixed situation, where all the states  $h$ ,  $H$  and  $\phi$  are kept in the spectrum, demands to work with more parameters. Numerical scans are usually employed for this purpose, and they allow to interconnect the phenomenology of the Higgs scalar sector with that of other SUSY particles. We do not explore this case further, and refer the reader to the recent studies [534, 535] for a discussion. Also, in case some signal is observed, it will be important to explain it in a fully mixed situation. For this purpose, analytical relations such as the ones presented in Refs. [530, 531] would provide a useful guidance.

Finally, we mention that the case of an extra Higgs lighter than 125 GeV is motivated and still partially unexplored. This is true especially for a singlet like state  $\phi$ , since flavour bounds on  $m_{H^\pm}$  pose serious challenges to having  $m_H < 125 \text{ GeV}$ .

### 5.7.2.2 Twin Higgs

Another motivated scenario where we expect a scalar singlet at accessible energies is the Twin Higgs model (TH). As discussed in Section 5.6.3, the TH is a well-motivated solution to the Hierarchy problem with uncolored top partners and many possible discovery channels. Here we discuss how the extended Higgs sector may be directly probed.

Amongst the twin states the mirror Higgs, which is a SM singlet, can be singly produced via its mixing with the SM Higgs, and accessible at present and future colliders. In order to describe the main phenomenology, we focus on the linearised TH model [466], where the scalar potential consists of only two degrees of freedom, the 125 GeV Higgs and the mirror Higgs  $\sigma$ . Notice that the presence of this extra singlet is a feature of any TH construction, and therefore it constitutes a natural signature. Using

the label A for our SM sector and B for the twin sector, we have

$$V(H_A, H_B) = \kappa(|H_A|^4 + |H_B|^4) + m^2(|H_A|^2 - |H_B|^2) + \lambda_* \left( |H_A|^2 + |H_B|^2 - \frac{f_0^2}{2} \right)^2. \quad (109)$$

The first term in the potential breaks the SU(4) global symmetry but leaves  $Z_2$  intact, the second term softly breaks  $Z_2$  as needed to achieve a separation between the two VEVs. The last one parametrises a spontaneous symmetry breaking SU(4)/SU(3). It is a combination of the spontaneous symmetry breaking and the soft breaking of the  $Z_2$  symmetry that realises the TH mechanism.

From a phenomenological point of view, the relevant parameters are  $\lambda_*$  and  $f_0$ , where the size of  $\lambda_*$  is required to be small, or the mirror Higgs will get a mass ( $m_\sigma \sim \sqrt{\lambda_*} f_0$ ) of the order of the cut-off of the model invalidating our phenomenological picture. The particle  $\sigma$  is often called the radial-mode of the corresponding symmetry breaking pattern.

The two Higgs doublets  $H_A$  and  $H_B$  are charged under the SM and twin weak interactions, respectively. Therefore, in the unitary gauge, six Goldstone bosons are eaten by the gauge bosons of the two sectors, leaving only two scalar degrees of freedom the SM Higgs,  $h$ , and  $\sigma$ . In the interaction basis they have a mass mixing. Trading two of the four parameters for the electro-weak VEV and Higgs mass, one can compute the mixing parameter between the two states

$$\sin^2 \gamma = \frac{v^2}{f^2} - \frac{m_h^2}{m_\sigma^2 - m_h^2} \left( 1 - 2 \frac{v^2}{f^2} \right), \quad (110)$$

where  $m_h$  and  $m_\sigma$  are the physical masses, while in terms of the parameters in Eq. (109),  $v^2 = \frac{\kappa \lambda_* f_0^2 - (\kappa + 2\lambda_*) m^2}{\kappa(\kappa + 2\lambda_*)}$ ,  $f^2 = f_0^2 \frac{2\lambda_*}{2\lambda_* + \kappa}$ .

This is very similar to the spectrum of a simple singlet-extension of the SM, given that the mixing angle enters the  $\sigma$  signal strengths, and it also controls the leading and model independent contributions to the electro-weak  $S$  and  $T$  parameters. Differently from the NMSSM or other weakly coupled extensions, however, in this case the mixing angle does not vanish in the large- $m_\sigma$  regime, but it approaches a constant proportional to  $v^2/f^2$ . This is reminiscent of the pNGB nature of the Higgs in the Twin Higgs model. This simple scenario can be meaningfully constrained by means of indirect and direct measurement. While precision Higgs measurements are only sensitive to  $\sin \gamma$  in (110), the direct searches of  $\sigma$  depend also on the branching ratios in its possible decay channels.

We now discuss direct searches for the radial mode  $\sigma$ . Through the mixing (110),  $\sigma$  inherits all the decay mode of a SM Higgs with mass  $m_\sigma$ . However,  $\sigma$  has model independent couplings to the twin electro-weak gauge bosons. We expect  $\sigma$  to have a mass that scales with the parameter  $f$ , therefore in the  $O(500 - 1000 \text{ GeV})$  range, where all the decay channels are practically open. It mostly decays to vector bosons of the SM and twin sector, the latter contribute to the invisible decay width. In the large mass limit, the branching ratios of  $\sigma$  are fixed by the equivalence theorem to be

$$\text{BR}_{\text{twin-VV}} \simeq \frac{3}{7}, \quad \text{BR}_{hh} \simeq \text{BR}_{ZZ} \simeq \frac{1}{2} \text{BR}_{WW} \simeq \frac{1}{7}. \quad (111)$$

The above equation has two immediate consequences: *i*) the dominant decay channel is diboson (including double Higgs), as expected for an electro-weak singlet in the TeV region; *ii*) the additional invisible decay channel to twin dibosons dilutes the branching fractions for the visible channels, and contributes to the widening of the width (especially in the large mass limit). *i*) and *ii*), together with the scaling of  $m_\sigma$ , then suggest that the largest impact of direct searches is expected for weakly coupled scenarios, with  $m_\sigma \sim f$ , in a region of moderate  $f$ .

These considerations are reflected in Fig. 94, where, in the plane of the only two free parameters,  $(f, m_\sigma)$ , we show the impact of Higgs coupling determination and recast of direct searches in the diboson channel. For reference, we fix the invisible branching ratio to its asymptotic value of 3/7. As expected,

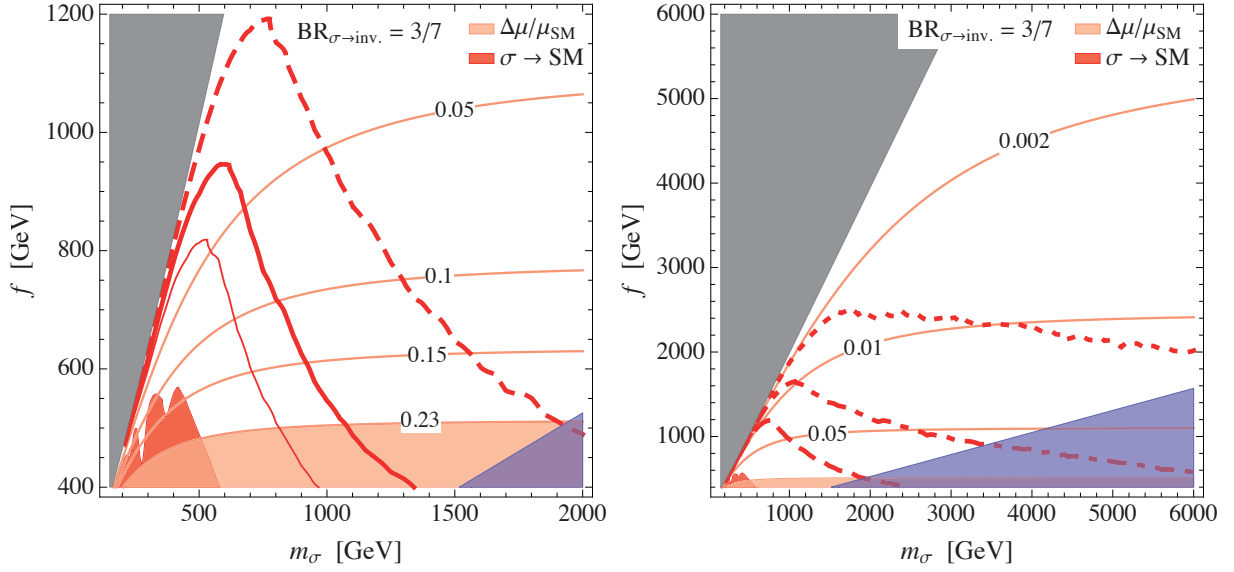


**Fig. 94:** Parameter space of the scalar singlet in Twin Higgs scenarios in the plane of the mass of the radial mode  $m_\sigma$  and the mirror Higgs vev  $f$ . Pink lines: contours of  $s_\gamma^2$ . A lepton collider like ILC250 (TLEP) will likely be able to exclude  $s_\gamma^2$  at the 0.05 (0.008) level [178, 481]. Red lines: expected reach of the LHC13 (continuous thin), LHC14 (continuous), HL-LHC (dashed), HE-LHC (dot-dashed), and FCC-hh with  $3 \text{ ab}^{-1}$  (dotted). Shaded regions: excluded at 95% C.L. by direct searches (red), excluded by Higgs couplings (pink),  $\Gamma_\sigma > m_\sigma$  (blue), unphysical parameters (grey).  $\text{BR}_{\phi \rightarrow hh}$  fixed to its asymptotic value  $3/7$  for reference. Figure taken from Ref. [528].

direct searches will provide a strong probe of the scenario considered for  $m_\sigma \sim f$ , while for much higher values indirect constraints are expected to dominate<sup>39</sup>. This is an important example of complementarity between proposed future lepton and hadron colliders, which together will be able to probe the natural Twin Higgs parameter space with TeV-scale mirror Higgs vevs and masses.

<sup>39</sup>In this Twin Higgs model, the trilinear Higgs coupling  $g_{hhh}$  is fixed in terms of  $m_\sigma$  and  $f$ , and does not substantially deviate from its SM value.

**Acknowledgements**

The research of D. Buttazzo was supported in part by the Swiss National Science Foundation (SNF) under contract 200021-159720. The work of C.-Y.C is supported by NSERC, Canada. Research at the Perimeter Institute is supported in part by the Government of Canada through NSERC and by the Province of Ontario through MEDT. D.C. is supported by National Science Foundation grant No. PHY-1315155 and the Maryland Center for Fundamental Physics. The work of Q.-H.C. is supported in part by the National Science Foundation of China under Grand No. 11175069, No. 11275009 and No. 11422545. NG was supported by the Swiss National Science Foundation under contract PZ00P2\_154829. TG is supported by the DOE grant DE-SC0011842 at the University of Minnesota. AK is supported by the British Science and Technology Facilities Council and by the Buckee Scholarship at Merton College. The work of M.L.M. is supported by the European Research Council advanced grant 291377 “*LHCtheory*”: *Theoretical predictions and analyses of LHC physics: advancing the precision frontier*. The work of R.N.M. is supported in part by the US National Science Foundation Grant No. PHY-1315155. F.P. is supported by the U.S. DOE grants DE-FG02-91ER40684 and DE-AC02-06CH11357. MP is supported by the U.S. National Science Foundation grant PHY-1316222. M.J.R.-M. was supported in part under U.S. Department of Energy contract DE-SC0011095. F.S. is supported by the European Research Council (ERC) under the EU Seventh Framework Programme (FP7/2007-2013)/ERC Starting Grant (agreement n. 278234 — ‘NEWDARK’ project). The work of M.S. is supported by the National Fund for Scientific Research (F.R.S.-FNRS Belgium), by the IISN “MadGraph” convention 4.4511.10, by the IISN “Fundamental interactions” convention 4.4517.08, and in part by the Belgian Federal Science Policy Office through the Interuniversity Attraction Pole P7/37. The work of P.T. has received funding from the European Union Seventh Framework programme for research and innovation under the Marie Curie grant agreement N. 609402-2020 researchers: Train to Move (T2M). The work of TMPT is supported in part by NSF Grant No. PHY-1316792. The work of P.S.B.D. was supported by the DFG with grant RO 2516/5-1. Y.C.Z. would like to thank the IISN and Belgian Science Policy (IAP VII/37) for support. The work of G.B., J.C., J.G., T.J., T.S., R.S. is supported by Department of Science & Technology, Government of INDIA under the Grant Agreement number IFA12-PH-34 (INSPIRE Faculty Award), Polish National Center of Science (NCN) under the Grant Agreement number DEC-2013/11/B/ST2/04023 and Science and Engineering Research Canada (NSERC). The work of S.-F.S. and F.K. was supported by US Department of Energy under Grant DE-FG02-04ER-41298. F.K. also acknowledges support from the Fermilab Graduate Student Research Program in Theoretical Physics operated by Fermi Research Alliance, LLC under Contract No. DE-AC02-07CH11359 with the United States Department of Energy. The work of J.K.B. is supported by a Rhodes Scholarship. D.B., J.A.F. and C.I. are supported by the STFC. J.Rojo and N. H. are supported by an European Research Council Starting Grant “PDF4BSM”. J.Rojo is supported by an STFC Rutherford Fellowship and Grant ST/K005227/1 and ST/M003787/1. The research of WA, WB, and GZ is supported by the ERC consolidator grant 614577 “HICCUP: High Impact Cross Section Calculations for Ultimate Precision”. For part of this research the computing resources from the Rechenzentrum Garching were used.

**References**

- [1] ATLAS Collaboration, G. Aad et al., *Observation of a new particle in the search for the Standard Model Higgs boson with the ATLAS detector at the LHC*, *Phys. Lett.* **B716** (2012) 1–29, [arXiv:1207.7214 \[hep-ex\]](#).
- [2] CMS Collaboration, S. Chatrchyan et al., *Observation of a new boson at a mass of 125 GeV with the CMS experiment at the LHC*, *Phys. Lett.* **B716** (2012) 30–61, [arXiv:1207.7235 \[hep-ex\]](#).
- [3] F. Englert and R. Brout, *Broken Symmetry and the Mass of Gauge Vector Mesons*, *Phys. Rev. Lett.* **13** (1964) 321–323.
- [4] P. W. Higgs, *Broken symmetries, massless particles and gauge fields*, *Phys. Lett.* **12** (1964) 132–133.

- [5] P. W. Higgs, *Broken Symmetries and the Masses of Gauge Bosons*, *Phys. Rev. Lett.* **13** (1964) 508–509.
- [6] G. S. Guralnik, C. R. Hagen, and T. W. B. Kibble, *Global Conservation Laws and Massless Particles*, *Phys. Rev. Lett.* **13** (1964) 585–587.
- [7] P. W. Higgs, *Spontaneous Symmetry Breakdown without Massless Bosons*, *Phys. Rev.* **145** (1966) 1156–1163.
- [8] T. W. B. Kibble, *Symmetry breaking in nonAbelian gauge theories*, *Phys. Rev.* **155** (1967) 1554–1561.
- [9] V. F. Weisskopf, *On the Self-Energy and the Electromagnetic Field of the Electron*, *Phys. Rev.* **56** (1939) 72–85.
- [10] LHC Higgs Cross Section Working Group Collaboration, S. Dittmaier et al., *Handbook of LHC Higgs Cross Sections: 1. Inclusive Observables*, [arXiv:1101.0593](https://arxiv.org/abs/1101.0593) [hep-ph].
- [11] S. Dittmaier et al., *Handbook of LHC Higgs Cross Sections: 2. Differential Distributions*, [arXiv:1201.3084](https://arxiv.org/abs/1201.3084) [hep-ph].
- [12] LHC Higgs Cross Section Working Group Collaboration, J. R. Andersen et al., *Handbook of LHC Higgs Cross Sections: 3. Higgs Properties*, [arXiv:1307.1347](https://arxiv.org/abs/1307.1347) [hep-ph].
- [13] R. Gröber and M. Mühlleitner, *Composite Higgs Boson Pair Production at the LHC*, *JHEP* **06** (2011) 020, [arXiv:1012.1562](https://arxiv.org/abs/1012.1562) [hep-ph].
- [14] R. Contino, M. Ghezzi, M. Moretti, G. Panico, F. Piccinini, and A. Wulzer, *Anomalous Couplings in Double Higgs Production*, *JHEP* **08** (2012) 154, [arXiv:1205.5444](https://arxiv.org/abs/1205.5444) [hep-ph].
- [15] M. Trodden, *Electroweak baryogenesis*, *Rev.Mod.Phys.* **71** (1999) 1463–1500, [arXiv:hep-ph/9803479](https://arxiv.org/abs/hep-ph/9803479) [hep-ph].
- [16] G. Degrandi, S. Di Vita, J. Elias-Miro, J. R. Espinosa, G. F. Giudice, G. Isidori, and A. Strumia, *Higgs mass and vacuum stability in the Standard Model at NNLO*, *JHEP* **08** (2012) 098, [arXiv:1205.6497](https://arxiv.org/abs/1205.6497) [hep-ph].
- [17] J. Baglio, A. Djouadi, and J. Quevillon, *Prospects for Higgs physics at energies up to 100 TeV*, [arXiv:1511.07853](https://arxiv.org/abs/1511.07853) [hep-ph].
- [18] *Higgs Cross Section Working Group*, <https://cern.ch/twiki/bin/view/LHCPhysics/LHCHXSWG>.
- [19] H. M. Georgi, S. L. Glashow, M. E. Machacek, and D. V. Nanopoulos, *Higgs Bosons from Two-Gluon Annihilation in Proton-Proton Collisions*, *Physical Review Letters* **40** (1978) no. 11, 692–694. <http://inspirehep.net/record/122052>.
- [20] F. Wilczek, *Decays of Heavy Vector Mesons into Higgs Particles*, *Physical Review Letters* **39** (1977) no. 21, 1304–1306.
- [21] M. Shifman, A. Vainshtein, and V. Zakharov, *Remarks on Higgs-boson interactions with nucleons*, *Physics Letters B* **78** (1978) no. 4, 443–446.
- [22] *Effective Gauge Theory and the Effect of Heavy Quarks*, *Zeitschrift für Physik C* **18** (1983) 69.
- [23] V. P. Spiridonov and K. G. Chetyrkin, *Nonleading mass corrections and renormalization of the operators  $m\bar{\psi}\psi$  and  $G_{\mu\nu}G^{\mu\nu}$* , *Sov. J. Nucl. Phys.* **47** (1988) 522–527. <http://inspirehep.net/record/275481>.
- [24] K. G. Chetyrkin, B. A. Kniehl, and M. Steinhauser, *Decoupling Relations to  $O(\alpha_s^3)$  and their Connection to Low-Energy Theorems*, *Nucl. Phys.* **B510** (1998) 61–87, [arXiv:hep-ph/9708255](https://arxiv.org/abs/hep-ph/9708255) [hep-ph].
- [25] K. Chetyrkin, J. Kühn, and C. Sturm, *QCD decoupling at four loops*, *Nuclear Physics B* **744** (2006) no. 1-2, 121–135. <http://inspirehep.net/record/699609>.
- [26] Y. Schröder and M. Steinhauser, *Four-loop decoupling relations for the strong coupling*, *Journal of High Energy Physics* **2006** (jan, 2006) 051–051. <http://inspirehep.net/record/699607>.

- [27] S. Dawson, *Radiative corrections to Higgs boson production*, Nuclear Physics B **359** (1991) no. 2-3, 283–300. <http://inspirehep.net/record/302911>.
- [28] R. V. Harlander and W. B. Kilgore, *Next-to-next-to-leading order Higgs production at Hadron Colliders.*, Physical review letters **88** (may, 2002) 201801. <http://inspirehep.net/record/582006>.
- [29] V. Ravindran, J. Smith, and W. van Neerven, *NNLO corrections to the total cross section for Higgs boson production in hadron-hadron collisions*, Nuclear Physics B **665** (aug, 2003) 325–366. <http://inspirehep.net/record/613462>.
- [30] C. Anastasiou and K. Melnikov, *Higgs boson production at hadron colliders in NNLO QCD*, Nuclear Physics B **646** (dec, 2002) 220–256, arXiv:0207004 [hep-ph]. <http://arxiv.org/abs/hep-ph/0207004>.
- [31] C. Anastasiou, C. Duhr, F. Dulat, F. Herzog, and B. Mistlberger, *Higgs boson gluon-fusion production in QCD at three loops.*, Physical review letters **114** (may, 2015) 212001, arXiv:1503.06056. <http://arxiv.org/abs/1503.06056>.
- [32] U. Aglietti, R. Bonciani, G. Degrossi, and A. Vicini, *Analytic results for virtual QCD corrections to Higgs production and decay*, Journal of High Energy Physics **2007** (jan, 2007) 021–021. <http://inspirehep.net/record/732276>.
- [33] M. Spira, a. Djouadi, D. Graudenz, and P. M. Zerwas, *Higgs boson production at the LHC*, Nuclear Physics B **453** (1995) no. February, 17, arXiv:9504378 [hep-ph].
- [34] R. V. Harlander and P. Kant, *Higgs production and decay: analytic results at next-to-leading order QCD*, Journal of High Energy Physics **2005** (2005) no. 12, 15, arXiv:0509189 [hep-ph].
- [35] C. Anastasiou, S. Bucherer, and Z. Kunszt, *HPro: A NLO Monte-Carlo for Higgs production via gluon fusion with finite heavy quark masses*, Journal of High Energy Physics **2009** (oct, 2009) 068–068. <http://inspirehep.net/record/825632>.
- [36] A. Djouadi, M. Spira, and P. Zerwas, *Production of Higgs bosons in proton colliders. QCD corrections*, Physics Letters B **264** (1991) no. 3-4, 440–446. <http://inspirehep.net/record/315069>.
- [37] D. Graudenz, M. Spira, and P. M. Zerwas, *QCD corrections to Higgs boson production at proton proton colliders*, Phys. Rev. Lett. **70** (1993) no. 10, 1372–1375. <http://link.aps.org/abstract/PRL/v70/p1372>.
- [38] R. Bonciani, G. Degrossi, and A. Vicini, *Scalar Particle Contribution to Higgs Production via Gluon Fusion at NLO*, Journal of High Energy Physics **2002** (2007) no. 11, 20, arXiv:0709.4227 [hep-ph]. <http://arxiv.org/abs/0709.4227>.
- [39] C. Anastasiou, S. Beerli, S. Bucherer, A. Daleo, and Z. Kunszt, *Two-loop amplitudes and master integrals for the production of a Higgs boson via a massive quark and a scalar-quark loop*, Journal of High Energy Physics **2007** (jan, 2007) 082–082. <http://inspirehep.net/record/732077>.
- [40] R. V. Harlander, H. Mantler, S. Marzani, and K. J. Ozeren, *Higgs production in gluon fusion at next-to-next-to-leading order QCD for finite top mass*, The European Physical Journal C **66** (2010) no. 3-4, 359–372, arXiv:0912.2104.
- [41] A. Pak, M. Rogal, and M. Steinhauser, *Finite top quark mass effects in NNLO Higgs boson production at LHC*, Journal of High Energy Physics **2010** (feb, 2010) 25. <http://inspirehep.net/record/837783>.
- [42] R. V. Harlander and K. J. Ozeren, *Finite top mass effects for hadronic Higgs production at next-to-next-to-leading order*, Journal of High Energy Physics **2009** (nov, 2009) 088–088. <http://inspirehep.net/record/831613>.
- [43] S. Actis, G. Passarino, C. Sturm, and S. Uccirati, *NLO Electroweak Corrections to Higgs Boson*

- Production at Hadron Colliders*, eprint arXiv **0809** (2008) 1301, arXiv:0809.1301.
- [44] U. Aglietti, R. Bonciani, G. Degrossi, and A. Vicini, *Two-loop light fermion contribution to Higgs production and decays*, *Phys. Lett. B* **595** (2004) no. 1-4, 432–441, arXiv:0404071 [hep-ph]. <http://inspirehep.net/record/647789>.
- [45] C. Anastasiou, R. Boughezal, and F. J. Petriello, *Mixed qcd-electroweak corrections to Higgs boson production in gluon fusion*, *JHEP* **0904** (2009) no. 04, 003, arXiv:0811.3458. <http://inspirehep.net/record/803217>.
- [46] C. Anastasiou, S. Buehler, F. Herzog, and A. Lazopoulos, *Total cross-section for Higgs boson hadroproduction with anomalous Standard-Model interactions*, *Journal of High Energy Physics* **2011** (2011) no. 12, 44, arXiv:1107.0683. <http://arxiv.org/abs/1107.0683>.
- [47] C. Anastasiou, S. Buehler, F. Herzog, and A. Lazopoulos, *Inclusive Higgs boson cross-section for the LHC at 8 TeV*, arXiv.org **hep-ph** (2012) , arXiv:1202.3638.
- [48] J. Rojo, A. Accardi, R. D. Ball, A. Cooper-Sarkar, A. de Roeck, S. Farry, J. Ferrando, S. Forte, J. Gao, L. Harland-Lang, J. Huston, A. Glazov, M. Gouzevitch, C. Gwenlan, K. Lipka, M. Lisovsky, M. Mangano, P. Nadolsky, L. Perrozzi, R. Placakyte, V. Radescu, G. P. Salam, and R. Thorne, *The PDF4LHC report on PDFs and LHC data: Results from Run I and preparation for Run II*, arXiv:1507.0556.
- [49] C. Anastasiou, C. Duhr, F. Dulat, E. Furlan, T. Gehrmann, F. Herzog, A. Lazopoulos, and B. Mistlberger, *High precision determination of the gluon fusion Higgs boson cross-section at the LHC*, arXiv:1602.00695 [hep-ph].
- [50] W.-Y. Keung and F. J. Petriello, *Electroweak and finite quark-mass effects on the Higgs boson transverse momentum distribution*, *Physical Review D* **80** (jul, 2009) 013007. <http://inspirehep.net/record/820705>.
- [51] S. Alekhin, J. Blümlein, and S. Moch, *The ABM parton distributions tuned to LHC data*, *Physical Review D* **89** (mar, 2014) 054028. <http://inspirehep.net/record/1258127>.
- [52] S. Alekhin, J. Blümlein, and S. Moch, *Parton distribution functions and benchmark cross sections at next-to-next-to-leading order*, *Physical Review D* **86** (sep, 2012) 054009. <http://inspirehep.net/record/1088724>.
- [53] J. M. Campbell and R. K. Ellis, *MCFM for the Tevatron and the LHC*, *Nucl. Phys. Proc. Suppl.* **205-206** (2010) 10–15, arXiv:1007.3492 [hep-ph].
- [54] F. Caola, K. Melnikov, and M. Schulze, *Fiducial cross sections for Higgs boson production in association with a jet at next-to-next-to-leading order in QCD*, *Phys. Rev.* **D92** (2015) no. 7, 074032, arXiv:1508.02684 [hep-ph].
- [55] A. Banfi, F. Caola, F. A. Dreyer, P. F. Monni, G. P. Salam, G. Zanderighi, and F. Dulat, *Jet-vetoed Higgs cross section in gluon fusion at N<sup>3</sup>LO+NNLL with small-R resummation*, arXiv:1511.02886 [hep-ph].
- [56] R. Boughezal, F. Caola, K. Melnikov, F. Petriello, and M. Schulze, *Higgs boson production in association with a jet at next-to-next-to-leading order*, *Phys. Rev. Lett.* **115** (2015) no. 8, 082003, arXiv:1504.07922 [hep-ph].
- [57] R. Boughezal, C. Focke, W. Giele, X. Liu, and F. Petriello, *Higgs boson production in association with a jet at NNLO using jetiness subtraction*, *Phys. Lett.* **B748** (2015) 5–8, arXiv:1505.03893 [hep-ph].
- [58] X. Chen, T. Gehrmann, E. W. N. Glover, and M. Jaquier, *Precise QCD predictions for the production of Higgs + jet final states*, *Phys. Lett.* **B740** (2015) 147–150, arXiv:1408.5325 [hep-ph].
- [59] X. Chen, T. Gehrmann, N. Glover, and M. Jaquier, *Higgs plus one jet production at NNLO*, in *Proceedings, 12th International Symposium on Radiative Corrections (Radcor 2015) and LoopFest XIV (Radiative Corrections for the LHC and Future Colliders)*. 2016.

- [arXiv:1604.04085](https://arxiv.org/abs/1604.04085) [hep-ph].  
<http://inspirehep.net/record/1446990/files/arXiv:1604.04085.pdf>.
- [60] C. Arnesen, I. Z. Rothstein, and J. Zupan, *Smoking Guns for On-Shell New Physics at the LHC*, *Phys. Rev. Lett.* **103** (2009) 151801, [arXiv:0809.1429](https://arxiv.org/abs/0809.1429) [hep-ph].
- [61] C. Grojean, E. Salvioni, M. Schlaffer, and A. Weiler, *Very boosted Higgs in gluon fusion*, *JHEP* **05** (2014) 022, [arXiv:1312.3317](https://arxiv.org/abs/1312.3317) [hep-ph].
- [62] N. Greiner, S. Hoeche, G. Luisoni, M. Schoenherr, J.-C. Winter, and V. Yundin, *Phenomenological analysis of Higgs boson production through gluon fusion in association with jets*, *JHEP* **01** (2016) 169, [arXiv:1506.01016](https://arxiv.org/abs/1506.01016) [hep-ph].
- [63] G. Cullen, N. Greiner, G. Heinrich, G. Luisoni, P. Mastrolia, et al., *Automated One-Loop Calculations with GoSam*, *Eur.Phys.J.* **C72** (2012) 1889, [arXiv:1111.2034](https://arxiv.org/abs/1111.2034) [hep-ph].
- [64] G. Cullen et al., *GOSAM-2.0: a tool for automated one-loop calculations within the Standard Model and beyond*, *Eur. Phys. J.* **C74** (2014) no. 8, 3001, [arXiv:1404.7096](https://arxiv.org/abs/1404.7096) [hep-ph].
- [65] T. Gleisberg, S. Hoeche, F. Krauss, M. Schonherr, S. Schumann, F. Siegert, and J. Winter, *Event generation with SHERPA 1.1*, *JHEP* **02** (2009) 007, [arXiv:0811.4622](https://arxiv.org/abs/0811.4622) [hep-ph].
- [66] T. Binoth, F. Boudjema, G. Dissertori, A. Lazopoulos, A. Denner, et al., *A Proposal for a standard interface between Monte Carlo tools and one-loop programs*, *Comput.Phys.Commun.* **181** (2010) 1612–1622, [arXiv:1001.1307](https://arxiv.org/abs/1001.1307) [hep-ph].
- [67] S. Alioli, S. Badger, J. Bellm, B. Biedermann, F. Boudjema, et al., *Update of the Binoth Les Houches Accord for a standard interface between Monte Carlo tools and one-loop programs*, *Comput.Phys.Commun.* **185** (2014) 560–571, [arXiv:1308.3462](https://arxiv.org/abs/1308.3462) [hep-ph].
- [68] P. Nogueira, *Automatic Feynman graph generation*, *J.Comput.Phys.* **105** (1993) 279–289.
- [69] J. A. M. Vermaseren, *New features of FORM*, [math-ph/0010025](https://arxiv.org/abs/math-ph/0010025).
- [70] J. Kuipers, T. Ueda, J. Vermaseren, and J. Vollinga, *FORM version 4.0*, *Comput.Phys.Commun.* **184** (2013) 1453–1467, [arXiv:1203.6543](https://arxiv.org/abs/1203.6543) [cs.SC].
- [71] G. Cullen, M. Koch-Janusz, and T. Reiter, *Spinney: A Form Library for Helicity Spinors*, *Comput.Phys.Commun.* **182** (2011) 2368–2387, [arXiv:1008.0803](https://arxiv.org/abs/1008.0803) [hep-ph].
- [72] H. van Deurzen, G. Luisoni, P. Mastrolia, E. Mirabella, G. Ossola, et al., *Multi-leg One-loop Massive Amplitudes from Integrand Reduction via Laurent Expansion*, *JHEP* **1403** (2014) 115, [arXiv:1312.6678](https://arxiv.org/abs/1312.6678) [hep-ph].
- [73] T. Peraro, *Ninja: Automated Integrand Reduction via Laurent Expansion for One-Loop Amplitudes*, *Comput.Phys.Commun.* **185** (2014) 2771–2797, [arXiv:1403.1229](https://arxiv.org/abs/1403.1229) [hep-ph].
- [74] P. Mastrolia, E. Mirabella, and T. Peraro, *Integrand reduction of one-loop scattering amplitudes through Laurent series expansion*, *JHEP* **1206** (2012) 095, [arXiv:1203.0291](https://arxiv.org/abs/1203.0291) [hep-ph].
- [75] A. van Hameren, *OneLoop: For the evaluation of one-loop scalar functions*, *Comput.Phys.Commun.* **182** (2011) 2427–2438, [arXiv:1007.4716](https://arxiv.org/abs/1007.4716) [hep-ph].
- [76] G. Heinrich, G. Ossola, T. Reiter, and F. Tramontano, *Tensorial Reconstruction at the Integrand Level*, *JHEP* **10** (2010) 105, [arXiv:1008.2441](https://arxiv.org/abs/1008.2441) [hep-ph].
- [77] T. Binoth, J. P. Guillet, G. Heinrich, E. Pilon, and T. Reiter, *Golem95: A Numerical program to calculate one-loop tensor integrals with up to six external legs*, *Comput. Phys. Commun.* **180** (2009) 2317–2330, [arXiv:0810.0992](https://arxiv.org/abs/0810.0992) [hep-ph].
- [78] G. Cullen, J. P. Guillet, G. Heinrich, T. Kleinschmidt, E. Pilon, et al., *Golem95C: A library for one-loop integrals with complex masses*, *Comput.Phys.Commun.* **182** (2011) 2276–2284, [arXiv:1101.5595](https://arxiv.org/abs/1101.5595) [hep-ph].
- [79] S. Catani and M. H. Seymour, *A general algorithm for calculating jet cross sections in NLO QCD*, *Nucl. Phys.* **B485** (1997) 291–419, [arXiv:hep-ph/9605323](https://arxiv.org/abs/hep-ph/9605323).
- [80] T. Gleisberg and S. Hoeche, *Comix, a new matrix element generator*, *JHEP* **12** (2008) 039,

- [arXiv:0808.3674 \[hep-ph\]](#).
- [81] Z. Bern, L. J. Dixon, F. Febres Cordero, S. Hoeche, H. Ita, D. A. Kosower, and D. Maitre, *Ntuples for NLO Events at Hadron Colliders*, *Comput. Phys. Commun.* **185** (2014) 1443–1460, [arXiv:1310.7439 \[hep-ph\]](#).
- [82] M. Cacciari and G. P. Salam, *Dispelling the  $N^3$  myth for the  $k_t$  jet-finder*, *Phys. Lett.* **B641** (2006) 57–61, [arXiv:hep-ph/0512210 \[hep-ph\]](#).
- [83] M. Cacciari, G. P. Salam, and G. Soyez, *The Anti- $k(t)$  jet clustering algorithm*, *JHEP* **04** (2008) 063, [arXiv:0802.1189 \[hep-ph\]](#).
- [84] M. Cacciari, G. P. Salam, and G. Soyez, *FastJet User Manual*, *Eur. Phys. J.* **C72** (2012) 1896, [arXiv:1111.6097 \[hep-ph\]](#).
- [85] S. Dulat, T. J. Hou, J. Gao, M. Guzzi, J. Huston, P. Nadolsky, J. Pumplin, C. Schmidt, D. Stump, and C. P. Yuan, *The CT14 Global Analysis of Quantum Chromodynamics*, [arXiv:1506.07443 \[hep-ph\]](#).
- [86] O. Brein, R. V. Harlander, and T. J. Zirke, *vh@nnlo - Higgs Strahlung at hadron colliders*, [arXiv:1210.5347 \[hep-ph\]](#).
- [87] R. V. Harlander, S. Liebler, and T. Zirke, *Higgs Strahlung at the Large Hadron Collider in the 2-Higgs-Doublet Model*, *JHEP* **02** (2014) 023, [arXiv:1307.8122 \[hep-ph\]](#).
- [88] O. Brein, R. Harlander, M. Wiesemann, and T. Zirke, *Top-Quark Mediated Effects in Hadronic Higgs-Strahlung*, *Eur. Phys. J.* **C72** (2012) 1868, [arXiv:1111.0761 \[hep-ph\]](#).
- [89] G. Ferrera, M. Grazzini, and F. Tramontano, *Associated WH production at hadron colliders: a fully exclusive QCD calculation at NNLO*, *Phys. Rev. Lett.* **107** (2011) 152003, [arXiv:1107.1164 \[hep-ph\]](#).
- [90] G. Ferrera, M. Grazzini, and F. Tramontano, *Higher-order QCD effects for associated WH production and decay at the LHC*, *JHEP* **04** (2014) 039, [arXiv:1312.1669 \[hep-ph\]](#).
- [91] G. Ferrera, M. Grazzini, and F. Tramontano, *Associated ZH production at hadron colliders: the fully differential NNLO QCD calculation*, *Phys. Lett.* **B740** (2015) 51–55, [arXiv:1407.4747 \[hep-ph\]](#).
- [92] J. M. Campbell, R. K. Ellis, and C. Williams, *Associated production of a Higgs boson at NNLO*, [arXiv:1601.00658 \[hep-ph\]](#).
- [93] A. Denner, S. Dittmaier, S. Kallweit, and A. Mück, *HAWK 2.0: A Monte Carlo program for Higgs production in vector-boson fusion and Higgs strahlung at hadron colliders*, *Comput. Phys. Commun.* **195** (2015) 161–171, [arXiv:1412.5390 \[hep-ph\]](#).
- [94] A. Denner, S. Dittmaier, S. Kallweit, and A. Mück, *Electroweak corrections to Higgs-strahlung off W/Z bosons at the Tevatron and the LHC with HAWK*, *JHEP* **03** (2012) 075, [arXiv:1112.5142 \[hep-ph\]](#).
- [95] G. Luisoni, P. Nason, C. Oleari, and F. Tramontano, *HW $^\pm$ /HZ + 0 and 1 jet at NLO with the POWHEG BOX interfaced to GoSam and their merging within MiNLO*, *JHEP* **1310** (2013) 083, [arXiv:1306.2542 \[hep-ph\]](#).
- [96] R. Frederix and S. Frixione, *Merging meets matching in MC@NLO*, *JHEP* **12** (2012) 061, [arXiv:1209.6215 \[hep-ph\]](#).
- [97] B. Hespel, F. Maltoni, and E. Vryonidou, *Higgs and Z boson associated production via gluon fusion in the SM and the 2HDM*, *JHEP* **06** (2015) 065, [arXiv:1503.01656 \[hep-ph\]](#).
- [98] W. Astill, W. Bizon, E. Re, and G. Zanderighi, *NNLOPS accurate associated HW production*, [arXiv:1603.01620 \[hep-ph\]](#).
- [99] K. Hamilton, P. Nason, E. Re, and G. Zanderighi, *NNLOPS simulation of Higgs boson production*, *JHEP* **10** (2013) 222, [arXiv:1309.0017 \[hep-ph\]](#).
- [100] NNPDF Collaboration, R. D. Ball et al., *Parton distributions for the LHC Run II*, *JHEP* **04**

- (2015) 040, [arXiv:1410.8849 \[hep-ph\]](#).
- [101] M. Cacciari, F. A. Dreyer, A. Karlberg, G. P. Salam, and G. Zanderighi, *Fully Differential Vector-Boson-Fusion Higgs Production at Next-to-Next-to-Leading Order*, *Phys. Rev. Lett.* **115** (2015) no. 8, 082002, [arXiv:1506.02660 \[hep-ph\]](#).
- [102] T. Figy, V. Hankele, and D. Zeppenfeld, *Next-to-leading order QCD corrections to Higgs plus three jet production in vector-boson fusion*, *JHEP* **02** (2008) 076, [arXiv:0710.5621 \[hep-ph\]](#).
- [103] B. Jäger, F. Schissler, and D. Zeppenfeld, *Parton-shower effects on Higgs boson production via vector-boson fusion in association with three jets*, *JHEP* **07** (2014) 125, [arXiv:1405.6950 \[hep-ph\]](#).
- [104] P. Bolzoni, F. Maltoni, S.-O. Moch, and M. Zaro, *Higgs production via vector-boson fusion at NNLO in QCD*, *Phys. Rev. Lett.* **105** (2010) 011801, [arXiv:1003.4451 \[hep-ph\]](#).
- [105] M. Ciccolini, A. Denner, and S. Dittmaier, *Electroweak and QCD corrections to Higgs production via vector-boson fusion at the LHC*, *Phys. Rev.* **D77** (2008) 013002, [arXiv:0710.4749 \[hep-ph\]](#).
- [106] P. Nason and C. Oleari, *NLO Higgs boson production via vector-boson fusion matched with shower in POWHEG*, *JHEP* **02** (2010) 037, [arXiv:0911.5299 \[hep-ph\]](#).
- [107] P. Nason, *A New method for combining NLO QCD with shower Monte Carlo algorithms*, *JHEP* **11** (2004) 040, [arXiv:hep-ph/0409146 \[hep-ph\]](#).
- [108] S. Frixione, P. Nason, and C. Oleari, *Matching NLO QCD computations with Parton Shower simulations: the POWHEG method*, *JHEP* **11** (2007) 070, [arXiv:0709.2092 \[hep-ph\]](#).
- [109] S. Alioli, P. Nason, C. Oleari, and E. Re, *A general framework for implementing NLO calculations in shower Monte Carlo programs: the POWHEG BOX*, *JHEP* **06** (2010) 043, [arXiv:1002.2581 \[hep-ph\]](#).
- [110] T. Sjostrand, S. Mrenna, and P. Z. Skands, *PYTHIA 6.4 Physics and Manual*, *JHEP* **0605** (2006) 026, [arXiv:hep-ph/0603175 \[hep-ph\]](#).
- [111] P. Z. Skands, *Tuning Monte Carlo Generators: The Perugia Tunes*, *Phys. Rev.* **D82** (2010) 074018, [arXiv:1005.3457 \[hep-ph\]](#).
- [112] L. A. Harland-Lang, A. D. Martin, P. Motylinski, and R. S. Thorne, *Parton distributions in the LHC era: MMHT 2014 PDFs*, *Eur. Phys. J.* **C75** (2015) no. 5, 204, [arXiv:1412.3989 \[hep-ph\]](#).
- [113] A. Buckley, J. Ferrando, S. Lloyd, K. Nordström, B. Page, M. Rüfenacht, M. Schönherr, and G. Watt, *LHAPDF6: parton density access in the LHC precision era*, *Eur. Phys. J.* **C75** (2015) 132, [arXiv:1412.7420 \[hep-ph\]](#).
- [114] R. D. Ball, V. Bertone, S. Carrazza, C. S. Deans, L. Del Debbio, et al., *Parton distributions with LHC data*, *Nucl.Phys.* **B867** (2013) 244–289, [arXiv:1207.1303 \[hep-ph\]](#).
- [115] T. Han, G. Valencia, and S. Willenbrock, *Structure function approach to vector boson scattering in  $p p$  collisions*, *Phys. Rev. Lett.* **69** (1992) 3274–3277, [arXiv:hep-ph/9206246 \[hep-ph\]](#).
- [116] P. Bolzoni, F. Maltoni, S.-O. Moch, and M. Zaro, *Vector boson fusion at NNLO in QCD: SM Higgs and beyond*, *Phys. Rev.* **D85** (2012) 035002, [arXiv:1109.3717 \[hep-ph\]](#).
- [117] J. R. Andersen, T. Binoth, G. Heinrich, and J. M. Smillie, *Loop induced interference effects in Higgs Boson plus two jet production at the LHC*, *JHEP* **02** (2008) 057, [arXiv:0709.3513 \[hep-ph\]](#).
- [118] W. Beenakker, S. Dittmaier, M. Kramer, B. Plumper, M. Spira, and P. M. Zerwas, *NLO QCD corrections to  $t$  anti- $t$   $H$  production in hadron collisions*, *Nucl. Phys.* **B653** (2003) 151–203, [arXiv:hep-ph/0211352 \[hep-ph\]](#).
- [119] S. Dawson, C. Jackson, L. H. Orr, L. Reina, and D. Wackerroth, *Associated Higgs production with top quarks at the large hadron collider: NLO QCD corrections*, *Phys. Rev.* **D68** (2003) 034022,

- [arXiv:hep-ph/0305087 \[hep-ph\]](#).
- [120] S. Frixione, V. Hirschi, D. Pagani, H. S. Shao, and M. Zaro, *Weak corrections to Higgs hadroproduction in association with a top-quark pair*, *JHEP* **09** (2014) 065, [arXiv:1407.0823 \[hep-ph\]](#).
- [121] A. Denner and R. Feger, *NLO QCD corrections to off-shell top-antitop production with leptonic decays in association with a Higgs boson at the LHC*, *JHEP* **11** (2015) 209, [arXiv:1506.07448 \[hep-ph\]](#).
- [122] M. Mangano, T. Plehn, P. Reimitz, T. Schell, and H.-S. Shao, *Measuring the Top Yukawa Coupling at 100 TeV*, [arXiv:1507.08169 \[hep-ph\]](#).
- [123] J. Alwall, R. Frederix, S. Frixione, V. Hirschi, F. Maltoni, et al., *The automated computation of tree-level and next-to-leading order differential cross sections, and their matching to parton shower simulations*, *JHEP* **1407** (2014) 079, [arXiv:1405.0301 \[hep-ph\]](#).
- [124] A. D. Martin, W. J. Stirling, R. S. Thorne, and G. Watt, *Parton distributions for the LHC*, *Eur. Phys. J.* **C63** (2009) 189–285, [arXiv:0901.0002 \[hep-ph\]](#).
- [125] J. Butterworth et al., *PDF4LHC recommendations for LHC Run II*, *J. Phys.* **G43** (2016) 023001, [arXiv:1510.03865 \[hep-ph\]](#).
- [126] ATLAS, CMS Collaboration, G. Aad et al., *Combined Measurement of the Higgs Boson Mass in pp Collisions at  $\sqrt{s} = 7$  and 8 TeV with the ATLAS and CMS Experiments*, *Phys. Rev. Lett.* **114** (2015) 191803, [arXiv:1503.07589 \[hep-ex\]](#).
- [127] P. Torrielli, *Rare Standard Model processes for present and future hadronic colliders*, [arXiv:1407.1623 \[hep-ph\]](#).
- [128] M. Farina, C. Grojean, F. Maltoni, E. Salvioni, and A. Thamm, *Lifting degeneracies in Higgs couplings using single top production in association with a Higgs boson*, *JHEP* **05** (2013) 022, [arXiv:1211.3736 \[hep-ph\]](#).
- [129] J. Chang, K. Cheung, J. S. Lee, and C.-T. Lu, *Probing the Top-Yukawa Coupling in Associated Higgs production with a Single Top Quark*, *JHEP* **05** (2014) 062, [arXiv:1403.2053 \[hep-ph\]](#).
- [130] J. Baglio, *Next-To-Leading Order QCD Corrections to Associated Production of a SM Higgs Boson with a Pair of Weak Bosons in the POWHEG-BOX*, [arXiv:1512.05787 \[hep-ph\]](#).
- [131] T. Corbett, O. J. P. Éboli, J. Gonzalez-Fraile, and M. C. Gonzalez-Garcia, *Determining Triple Gauge Boson Couplings from Higgs Data*, *Phys. Rev. Lett.* **111** (2013) 011801, [arXiv:1304.1151 \[hep-ph\]](#).
- [132] N. Liu, J. Ren, and B. Yang, *Next-to-leading order QCD corrections to  $HZW^\pm$  production at 14 TeV LHC*, *Phys. Lett.* **B731** (2014) 70–73, [arXiv:1310.6192 \[hep-ph\]](#).
- [133] E. Gabrielli, M. Heikinheimo, L. Marzola, B. Mele, C. Spethmann, and H. Veermae, *Anomalous Higgs-boson coupling effects in  $HW+W\tilde{L}\tilde{S}$  production at the LHC*, *Phys. Rev.* **D89** (2014) no. 5, 053012, [arXiv:1312.4956 \[hep-ph\]](#).
- [134] ATLAS Collaboration, G. Aad et al., *Fiducial and differential cross sections of Higgs boson production measured in the four-lepton decay channel in pp collisions at  $\sqrt{s}=8$  TeV with the ATLAS detector*, *Phys. Lett.* **B738** (2014) 234–253, [arXiv:1408.3226 \[hep-ex\]](#).
- [135] CMS Collaboration, V. Khachatryan et al., *Measurement of differential and integrated fiducial cross sections for Higgs boson production in the four-lepton decay channel in pp collisions at  $\sqrt{s} = 7$  and 8 TeV*, [arXiv:1512.08377 \[hep-ex\]](#).
- [136] ATLAS Collaboration, G. Aad et al., *Observation and measurement of Higgs boson decays to  $WW^*$  with the ATLAS detector*, *Phys. Rev.* **D92** (2015) no. 1, 012006, [arXiv:1412.2641 \[hep-ex\]](#).
- [137] CMS Collaboration, C. Collaboration, *Measurement of the transverse momentum spectrum of the Higgs boson produced in pp collisions at  $\sqrt{s} = 8$  TeV using the  $H \rightarrow WW$  decays*, .

- [138] ATLAS Collaboration, G. Aad et al., *Search for the Standard Model Higgs boson decay to  $\mu^+\mu^-$  with the ATLAS detector*, *Phys. Lett.* **B738** (2014) 68–86, [arXiv:1406.7663 \[hep-ex\]](#).
- [139] CMS Collaboration, V. Khachatryan et al., *Search for a standard model-like Higgs boson in the  $\mu^+\mu^-$  and  $e^+e^-$  decay channels at the LHC*, *Phys. Lett.* **B744** (2015) 184–207, [arXiv:1410.6679 \[hep-ex\]](#).
- [140] J. M. Butterworth, A. R. Davison, M. Rubin, and G. P. Salam, *Jet substructure as a new Higgs search channel at the LHC*, *Phys. Rev. Lett.* **100** (2008) 242001, [arXiv:0802.2470 \[hep-ph\]](#).
- [141] M. Mangano, G. Zanderighi, et al., *Physics at a 100 TeV pp collider: Standard Model processes*, CERN-TH-2016-112, 2016.
- [142] T. Plehn, G. P. Salam, and M. Spannowsky, *Fat Jets for a Light Higgs*, *Phys. Rev. Lett.* **104** (2010) 111801, [arXiv:0910.5472 \[hep-ph\]](#).
- [143] G. Kasieczka, T. Plehn, T. Schell, T. Strebler, and G. P. Salam, *Resonance Searches with an Updated Top Tagger*, *JHEP* **06** (2015) 203, [arXiv:1503.05921 \[hep-ph\]](#).
- [144] J. Alwall, M. Herquet, F. Maltoni, O. Mattelaer, and T. Stelzer, *MadGraph 5 : Going Beyond*, *JHEP* **1106** (2011) 128, [arXiv:1106.0522 \[hep-ph\]](#).
- [145] NNPDF Collaboration, R. D. Ball, V. Bertone, S. Carrazza, L. Del Debbio, S. Forte, A. Guffanti, N. P. Hartland, and J. Rojo, *Parton distributions with QED corrections*, *Nucl. Phys.* **B877** (2013) 290–320, [arXiv:1308.0598 \[hep-ph\]](#).
- [146] T. Sjostrand, S. Ask, J. R. Christiansen, R. Corke, N. Desai, P. Ilten, S. Mrenna, S. Prestel, C. O. Rasmussen, and P. Z. Skands, *An Introduction to PYTHIA 8.2*, *Comput. Phys. Commun.* **191** (2015) 159–177, [arXiv:1410.3012 \[hep-ph\]](#).
- [147] DELPHES 3 Collaboration, J. de Favereau et al., *DELPHES 3, A modular framework for fast simulation of a generic collider experiment*, *JHEP* **1402** (2014) 057, [arXiv:1307.6346 \[hep-ex\]](#).
- [148] J. Anderson, A. Avetisyan, R. Brock, S. Chekanov, T. Cohen, et al., *Snowmass Energy Frontier Simulations*, [arXiv:1309.1057 \[hep-ex\]](#).
- [149] Q.-H. Cao, S.-L. Chen, and Y. Liu, *Probing Higgs Width and Top Quark Yukawa Coupling from  $t\bar{t}H$  and  $t\bar{t}t\bar{t}$  Productions*, [arXiv:1602.01934 \[hep-ph\]](#).
- [150] V. D. Barger, A. L. Stange, and R. J. N. Phillips, *Four heavy quark hadroproduction*, *Phys. Rev.* **D44** (1991) 1987–1996.
- [151] J. Alwall, P. Demin, S. de Visscher, R. Frederix, M. Herquet, F. Maltoni, T. Plehn, D. L. Rainwater, and T. Stelzer, *MadGraph/MadEvent v4: The New Web Generation*, *JHEP* **09** (2007) 028, [arXiv:0706.2334 \[hep-ph\]](#).
- [152] A. Belyaev, N. D. Christensen, and A. Pukhov, *CalcHEP 3.4 for collider physics within and beyond the Standard Model*, *Comput. Phys. Commun.* **184** (2013) 1729–1769, [arXiv:1207.6082 \[hep-ph\]](#).
- [153] F. Maltoni, D. Pagani, and I. Tsirikos, *Associated production of a top-quark pair with vector bosons at NLO in QCD: impact on  $t\bar{t}H$  searches at the LHC*, [arXiv:1507.05640 \[hep-ph\]](#).
- [154] ATLAS Collaboration, *Search for strongly produced superpartners in final states with two same sign leptons with the ATLAS detector using 21 fb-1 of proton-proton collisions at  $\sqrt{s}=8$  TeV*, ATLAS-CONF-2013-007, CERN, Geneva, Mar, 2013. <https://cds.cern.ch/record/1522430>.
- [155] CMS Collaboration, S. Chatrchyan et al., *Search for new physics in events with same-sign dileptons and jets in pp collisions at  $\sqrt{s} = 8$  TeV*, *JHEP* **01** (2014) 163, [arXiv:1311.6736](#). [Erratum: JHEP01,014(2015)].
- [156] ATLAS Collaboration, *Search for Supersymmetry in final states with two same-sign leptons, jets and missing transverse momentum with the ATLAS detector in pp collisions at  $\sqrt{s}=8$  TeV*,

- ATLAS-CONF-2012-105, CERN, Geneva, Aug, 2012.  
<https://cds.cern.ch/record/1472674>.
- [157] J. Gallicchio and M. D. Schwartz, *Seeing in Color: Jet Superstructure*, *Phys. Rev. Lett.* **105** (2010) 022001, [arXiv:1001.5027](https://arxiv.org/abs/1001.5027) [hep-ph].
- [158] G. Perez, Y. Soreq, E. Stamou, and K. Tobioka, *Prospects for measuring the Higgs boson coupling to light quarks*, *Phys. Rev.* **D93** (2016) no. 1, 013001, [arXiv:1505.06689](https://arxiv.org/abs/1505.06689) [hep-ph].
- [159] G. T. Bodwin, F. Petriello, S. Stoynev, and M. Velasco, *Higgs boson decays to quarkonia and the  $H\bar{c}c$  coupling*, *Phys. Rev.* **D88** (2013) no. 5, 053003, [arXiv:1306.5770](https://arxiv.org/abs/1306.5770) [hep-ph].
- [160] A. L. Kagan, G. Perez, F. Petriello, Y. Soreq, S. Stoynev, and J. Zupan, *Exclusive Window onto Higgs Yukawa Couplings*, *Phys. Rev. Lett.* **114** (2015) no. 10, 101802, [arXiv:1406.1722](https://arxiv.org/abs/1406.1722) [hep-ph].
- [161] G. T. Bodwin, H. S. Chung, J.-H. Ee, J. Lee, and F. Petriello, *Relativistic corrections to Higgs boson decays to quarkonia*, *Phys. Rev.* **D90** (2014) no. 11, 113010, [arXiv:1407.6695](https://arxiv.org/abs/1407.6695) [hep-ph].
- [162] Y. Grossman, M. König, and M. Neubert, *Exclusive Radiative Decays of W and Z Bosons in QCD Factorization*, *JHEP* **04** (2015) 101, [arXiv:1501.06569](https://arxiv.org/abs/1501.06569) [hep-ph].
- [163] M. König and M. Neubert, *Exclusive Radiative Higgs Decays as Probes of Light-Quark Yukawa Couplings*, *JHEP* **08** (2015) 012, [arXiv:1505.03870](https://arxiv.org/abs/1505.03870) [hep-ph].
- [164] R. Harnik, J. Kopp, and J. Zupan, *Flavor Violating Higgs Decays*, *JHEP* **03** (2013) 026, [arXiv:1209.1397](https://arxiv.org/abs/1209.1397) [hep-ph].
- [165] G. Degrossi and F. Maltoni, *Two-loop electroweak corrections to the Higgs-boson decay  $H \rightarrow \gamma\gamma$* , *Nucl. Phys.* **B724** (2005) 183–196, [arXiv:hep-ph/0504137](https://arxiv.org/abs/hep-ph/0504137) [hep-ph].
- [166] G. P. Lepage and S. J. Brodsky, *Exclusive Processes in Perturbative Quantum Chromodynamics*, *Phys. Rev.* **D22** (1980) 2157.
- [167] A. V. Efremov and A. V. Radyushkin, *Factorization and Asymptotical Behavior of Pion Form-Factor in QCD*, *Phys. Lett.* **B94** (1980) 245–250.
- [168] G. T. Bodwin, E. Braaten, and G. P. Lepage, *Rigorous QCD analysis of inclusive annihilation and production of heavy quarkonium*, *Phys. Rev.* **D51** (1995) 1125–1171, [arXiv:hep-ph/9407339](https://arxiv.org/abs/hep-ph/9407339) [hep-ph]. [Erratum: *Phys. Rev.* **D55**, 5853(1997)].
- [169] M. Mangano and T. Melia, *Rare exclusive hadronic W decays in a  $t\bar{t}$  environment*, *Eur. Phys. J.* **C75** (2015) no. 6, 258, [arXiv:1410.7475](https://arxiv.org/abs/1410.7475) [hep-ph].
- [170] T.-C. Huang and F. Petriello, *Rare exclusive decays of the Z-boson revisited*, *Phys. Rev.* **D92** (2015) no. 1, 014007, [arXiv:1411.5924](https://arxiv.org/abs/1411.5924) [hep-ph].
- [171] ATLAS Collaboration, G. Aad et al., *Search for Higgs and Z Boson Decays to  $J/\psi\gamma$  and  $\Upsilon(nS)\gamma$  with the ATLAS Detector*, *Phys. Rev. Lett.* **114** (2015) no. 12, 121801, [arXiv:1501.03276](https://arxiv.org/abs/1501.03276) [hep-ex].
- [172] CMS Collaboration, V. Khachatryan et al., *Search for a Higgs boson decaying into  $\gamma^*\gamma \rightarrow \ell\ell\gamma$  with low dilepton mass in pp collisions at  $\sqrt{s} = 8$  TeV*, *Phys. Lett.* **B753** (2016) 341–362, [arXiv:1507.03031](https://arxiv.org/abs/1507.03031) [hep-ex].
- [173] *Search for the Standard Model Higgs and Z Boson decays to  $J/\psi\gamma$ : HL-LHC projections*, ATL-PHYS-PUB-2015-043, CERN, Geneva, Sep, 2015.  
<http://cds.cern.ch/record/2054550>.
- [174] A. Chisholm and K. Nikolopoulos. Generator level study of the  $H \rightarrow \phi\gamma$ ,  $H \rightarrow \rho\gamma$  and  $H \rightarrow \omega\gamma$  decays.
- [175] W. Buchmuller and D. Wyler, *Effective Lagrangian Analysis of New Interactions and Flavor Conservation*, *Nucl. Phys.* **B268** (1986) 621–653.
- [176] G. F. Giudice, C. Grojean, A. Pomarol, and R. Rattazzi, *The Strongly-Interacting Light Higgs*,

- JHEP **06** (2007) 045, [arXiv:hep-ph/0703164](#) [hep-ph].
- [177] B. Grzadkowski, M. Iskrzynski, M. Misiak, and J. Rosiek, *Dimension-Six Terms in the Standard Model Lagrangian*, JHEP **10** (2010) 085, [arXiv:1008.4884](#) [hep-ph].
- [178] S. Dawson et al., *Working Group Report: Higgs Boson*, in *Community Summer Study 2013: Snowmass on the Mississippi (CSS2013) Minneapolis, MN, USA, July 29-August 6, 2013*. 2013. [arXiv:1310.8361](#) [hep-ex].
- [179] A. Azatov, R. Contino, G. Panico, and M. Son, *Effective field theory analysis of double Higgs boson production via gluon fusion*, Phys. Rev. **D92** (2015) no. 3, 035001, [arXiv:1502.00539](#) [hep-ph].
- [180] G. Panico and A. Wulzer, *The Composite Nambu-Goldstone Higgs*, Lect. Notes Phys. **913** (2016) pp.1–316, [arXiv:1506.01961](#) [hep-ph].
- [181] CMS Collaboration, V. Khachatryan et al., *Search for resonant pair production of Higgs bosons decaying to two bottom quark-antiquark pairs in proton-proton collisions at 8 TeV*, Phys. Lett. **B749** (2015) 560–582, [arXiv:1503.04114](#) [hep-ex].
- [182] CMS Collaboration, *Search for resonant pair production of Higgs bosons decaying to  $b\bar{b}$  and  $\tau^+\tau^-$  in proton-proton collisions at  $\sqrt{s} = 8$  TeV*, CMS-PAS-EXO-15-008, CERN, Geneva, 2015. <https://cds.cern.ch/record/2125293>.
- [183] *A search for resonant Higgs-pair production in the  $b\bar{b}b\bar{b}$  final state in pp collisions at  $\sqrt{s} = 8$  TeV*, ATLAS-CONF-2014-005, CERN, Geneva, Mar, 2014. <https://cds.cern.ch/record/1666518>.
- [184] R. Contino, M. Ghezzi, C. Grojean, M. Mühlleitner, and M. Spira, *Effective Lagrangian for a light Higgs-like scalar*, JHEP **07** (2013) 035, [arXiv:1303.3876](#) [hep-ph].
- [185] G. Panico, *Prospects for double Higgs production*, in *Physics Prospects for Linear and other Future Colliders after the Discovery of the Higgs (LFC15) Trento, Italy, September 7-11, 2015*. 2015. [arXiv:1512.04316](#) [hep-ph].
- [186] R. Frederix, S. Frixione, V. Hirschi, F. Maltoni, O. Mattelaer, P. Torrielli, E. Vryonidou, and M. Zaro, *Higgs pair production at the LHC with NLO and parton-shower effects*, Phys. Lett. **B732** (2014) 142–149, [arXiv:1401.7340](#) [hep-ph].
- [187] J. Tian, *Study of Higgs self-coupling at the ILC based on the full detector simulation at  $\sqrt{s} = 500$  GeV and  $\sqrt{s} = 1$  TeV*, 2013. <http://www-flc.desy.de/lcnotes/notes/LC-REP-2013-003.pdf>.
- [188] M. Kurata et al., *The Higgs Self Coupling Analysis Using the Events Containing  $H \rightarrow WW^*$  Decay*, 2013. <http://www-flc.desy.de/lcnotes/notes/LC-REP-2013-025.pdf>.
- [189] K. Fujii et al., *Physics Case for the International Linear Collider*, [arXiv:1506.05992](#) [hep-ex].
- [190] L. Linssen, *CLIC: physics and detectors at a future TeV-scale  $e^+e^-$  linear collider*, [https://edms.cern.ch/file/1465497/1/Linssen\\_CLIC\\_Ghent\\_seminar\\_Jan2015\\_compressed.pdf](https://edms.cern.ch/file/1465497/1/Linssen_CLIC_Ghent_seminar_Jan2015_compressed.pdf), 2015. Seminar at Ghent University (on behalf of the CLICdp collaboration).
- [191] CLIC Detector and Physics Study Collaborations, H. Abramowicz et al., *Physics at the CLIC  $e^+e^-$  Linear Collider – Input to the Snowmass process 2013*, in *Community Summer Study 2013: Snowmass on the Mississippi (CSS2013) Minneapolis, MN, USA, July 29-August 6, 2013*. 2013. [arXiv:1307.5288](#) [hep-ex].
- [192] D. de Florian and J. Mazzitelli, *Higgs pair production at next-to-next-to-leading logarithmic accuracy at the LHC*, JHEP **09** (2015) 053, [arXiv:1505.07122](#) [hep-ph].
- [193] E. W. N. Glover and J. J. van der Bij, *Higgs boson pair production via gluon fusion*, Nucl. Phys. **B309** (1988) 282.
- [194] O. J. P. Eboli, G. C. Marques, S. F. Novaes, and A. A. Natale, *Twin Higgs boson production*,

- Phys. Lett.* **B197** (1987) 269.
- [195] T. Plehn, M. Spira, and P. Zerwas, *Pair production of neutral Higgs particles in gluon-gluon collisions*, *Nucl.Phys.* **B479** (1996) 46–64, [arXiv:hep-ph/9603205 \[hep-ph\]](#).
- [196] S. Dawson, S. Dittmaier, and M. Spira, *Neutral Higgs boson pair production at hadron colliders: QCD corrections*, *Phys. Rev.* **D58** (1998) 115012, [arXiv:hep-ph/9805244 \[hep-ph\]](#).
- [197] D. de Florian and J. Mazzitelli, *Higgs Boson Pair Production at Next-to-Next-to-Leading Order in QCD*, *Phys. Rev. Lett.* **111** (2013) 201801, [arXiv:1309.6594 \[hep-ph\]](#).
- [198] D. Y. Shao, C. S. Li, H. T. Li, and J. Wang, *Threshold resummation effects in Higgs boson pair production at the LHC*, *JHEP* **07** (2013) 169, [arXiv:1301.1245 \[hep-ph\]](#).
- [199] J. Grigo, J. Hoff, K. Melnikov, and M. Steinhauser, *On the Higgs boson pair production at the LHC*, *Nucl. Phys.* **B875** (2013) 1–17, [arXiv:1305.7340 \[hep-ph\]](#).
- [200] J. Grigo, J. Hoff, and M. Steinhauser, *Higgs boson pair production: top quark mass effects at NLO and NNLO*, *Nucl. Phys.* **B900** (2015) 412–430, [arXiv:1508.00909 \[hep-ph\]](#).
- [201] F. Maltoni, E. Vryonidou, and M. Zaro, *Top-quark mass effects in double and triple Higgs production in gluon-gluon fusion at NLO*, *JHEP* **11** (2014) 079, [arXiv:1408.6542 \[hep-ph\]](#).
- [202] S. Borowka, N. Greiner, G. Heinrich, S. P. Jones, M. Kerner, J. Schlenk, U. Schubert, and T. Zirke, *Higgs boson pair production in gluon fusion at NLO with full top-quark mass dependence*, [arXiv:1604.06447 \[hep-ph\]](#).
- [203] W. Yao, *Studies of measuring Higgs self-coupling with  $HH \rightarrow b\bar{b}\gamma\gamma$  at the future hadron colliders*, [arXiv:1308.6302 \[hep-ph\]](#).
- [204] A. J. Barr, M. J. Dolan, C. Englert, D. E. Ferreira de Lima, and M. Spannowsky, *Higgs Self-Coupling Measurements at a 100 TeV Hadron Collider*, *JHEP* **1502** (2015) 016, [arXiv:1412.7154 \[hep-ph\]](#).
- [205] H.-J. He, J. Ren, and W. Yao, *Probing New Physics of Cubic Higgs Interaction via Higgs Pair Production at Hadron Colliders*, [arXiv:1506.03302 \[hep-ph\]](#).
- [206] R. Contino, C. Englert, R. Jing, G. Panico, A. Papaefstathiou, M. Selvaggi, M. Son, M. Spannowsky, and W.-M. Yao, *in preparation*, .
- [207] D. Stump, J. Huston, J. Pumplin, W.-K. Tung, H. L. Lai, S. Kuhlmann, and J. F. Owens, *Inclusive jet production, parton distributions, and the search for new physics*, *JHEP* **10** (2003) 046, [arXiv:hep-ph/0303013 \[hep-ph\]](#).
- [208] J. K. Behr, D. Bortoletto, J. A. Frost, N. P. Hartland, C. Issever, and J. Rojo, *Boosting Higgs pair production in the  $b\bar{b}b\bar{b}$  final state with multivariate techniques*, [arXiv:1512.08928 \[hep-ph\]](#).
- [209] D. Wardrope, E. Jansen, N. Konstantinidis, B. Cooper, R. Falla, and N. Norjoharuddeen, *Non-resonant Higgs-pair production in the  $b\bar{b}b\bar{b}$  final state at the LHC*, *Eur. Phys. J.* **C75** (2015) no. 5, 219, [arXiv:1410.2794 \[hep-ph\]](#).
- [210] D. E. Ferreira de Lima, A. Papaefstathiou, and M. Spannowsky, *Standard model Higgs boson pair production in the  $(b\bar{b})(b\bar{b})$  final state*, *JHEP* **08** (2014) 030, [arXiv:1404.7139 \[hep-ph\]](#).
- [211] V. Hirschi and O. Mattelaer, *Automated event generation for loop-induced processes*, *JHEP* **10** (2015) 146, [arXiv:1507.00020 \[hep-ph\]](#).
- [212] T. Sjostrand, S. Mrenna, and P. Z. Skands, *A Brief Introduction to PYTHIA 8.1*, *Comput.Phys.Commun.* **178** (2008) 852–867, [arXiv:0710.3820 \[hep-ph\]](#).
- [213] P. Skands, S. Carrazza, and J. Rojo, *Tuning PYTHIA 8.1: the Monash 2013 Tune*, *Eur. Phys. J.* **C74** (2014) no. 8, 3024, [arXiv:1404.5630 \[hep-ph\]](#).
- [214] ATLAS Collaboration, G. Aad et al., *Search for Higgs boson pair production in the  $b\bar{b}b\bar{b}$  final state from  $pp$  collisions at  $\sqrt{s} = 8$  TeV with the ATLAS detector*, [arXiv:1506.00285 \[hep-ex\]](#).
- [215] G. P. Salam, *Towards Jetography*, *Eur. Phys. J.* **C67** (2010) 637–686, [arXiv:0906.1833](#)

- [hep-ph].
- [216] ATLAS Collaboration, G. Aad et al., *Performance of jet substructure techniques for large- $R$  jets in proton-proton collisions at  $\sqrt{s} = 7$  TeV using the ATLAS detector*, *JHEP* **09** (2013) 076, [arXiv:1306.4945 \[hep-ex\]](#).
- [217] J. M. Butterworth, B. E. Cox, and J. R. Forshaw, *WW scattering at the CERN LHC*, *Phys. Rev.* **D65** (2002) 096014, [arXiv:hep-ph/0201098 \[hep-ph\]](#).
- [218] J. Thaler and K. Van Tilburg, *Identifying Boosted Objects with  $N$ -subjettiness*, *JHEP* **03** (2011) 015, [arXiv:1011.2268 \[hep-ph\]](#).
- [219] J. Thaler and K. Van Tilburg, *Maximizing Boosted Top Identification by Minimizing  $N$ -subjettiness*, *JHEP* **02** (2012) 093, [arXiv:1108.2701 \[hep-ph\]](#).
- [220] A. J. Larkoski, G. P. Salam, and J. Thaler, *Energy Correlation Functions for Jet Substructure*, *JHEP* **06** (2013) 108, [arXiv:1305.0007 \[hep-ph\]](#).
- [221] A. J. Larkoski, I. Mould, and D. Neill, *Power Counting to Better Jet Observables*, *JHEP* **12** (2014) 009, [arXiv:1409.6298 \[hep-ph\]](#).
- [222] ATLAS Collaboration, G. Aad et al., *Performance of  $b$ -Jet Identification in the ATLAS Experiment*, [arXiv:1512.01094 \[hep-ex\]](#).
- [223] M. Cacciari and G. P. Salam, *Pileup subtraction using jet areas*, *Phys. Lett.* **B659** (2008) 119–126, [arXiv:0707.1378 \[hep-ph\]](#).
- [224] *Calibration of  $b$ -tagging using dileptonic top pair events in a combinatorial likelihood approach with the ATLAS experiment*, ATLAS-CONF-2014-004, CERN, Geneva, Feb, 2014. <https://cds.cern.ch/record/1664335>.
- [225] M. Gouzevitch, A. Oliveira, J. Rojo, R. Rosenfeld, G. P. Salam, and V. Sanz, *Scale-invariant resonance tagging in multijet events and new physics in Higgs pair production*, *JHEP* **07** (2013) 148, [arXiv:1303.6636 \[hep-ph\]](#).
- [226] A. Papaefstathiou, *Discovering Higgs boson pair production through rare final states at a 100 TeV collider*, *Phys. Rev.* **D91** (2015) no. 11, 113016, [arXiv:1504.04621 \[hep-ph\]](#).
- [227] M. Bahr et al., *Herwig++ Physics and Manual*, *Eur. Phys. J.* **C58** (2008) 639–707, [arXiv:0803.0883 \[hep-ph\]](#).
- [228] J. Bellm et al., *Herwig 7.0 / Herwig++ 3.0 Release Note*, [arXiv:1512.01178 \[hep-ph\]](#).
- [229] F. Cascioli, P. Maierhofer, and S. Pozzorini, *Scattering Amplitudes with Open Loops*, *Phys. Rev. Lett.* **108** (2012) 111601, [arXiv:1111.5206 \[hep-ph\]](#).
- [230] Maierhöfer, Philipp and Papaefstathiou, Andreas, *Higgs Boson pair production merged to one jet*, *JHEP* **03** (2014) 126, [arXiv:1401.0007 \[hep-ph\]](#).
- [231] S. Frixione, F. Stoeckli, P. Torrielli, and B. R. Webber, *NLO QCD corrections in Herwig++ with MC@NLO*, *JHEP* **01** (2011) 053, [arXiv:1010.0568 \[hep-ph\]](#).
- [232] R. Frederix, S. Frixione, V. Hirschi, F. Maltoni, R. Pittau, and P. Torrielli, *Scalar and pseudoscalar Higgs production in association with a top<sup>?</sup>antitop pair*, *Phys. Lett.* **B701** (2011) 427–433, [arXiv:1104.5613 \[hep-ph\]](#).
- [233] H.-L. Lai, M. Guzzi, J. Huston, Z. Li, P. M. Nadolsky, J. Pumplin, and C. P. Yuan, *New parton distributions for collider physics*, *Phys. Rev.* **D82** (2010) 074024, [arXiv:1007.2241 \[hep-ph\]](#).
- [234] *Performance assumptions based on full simulation for an upgraded ATLAS detector at a High-Luminosity LHC*, ATL-PHYS-PUB-2013-009, CERN, Geneva, Sep, 2013. <http://cds.cern.ch/record/1604420>.
- [235] *Performance assumptions for an upgraded ATLAS detector at a High-Luminosity LHC*, ATL-PHYS-PUB-2013-004, CERN, Geneva, Mar, 2013. <http://cds.cern.ch/record/1527529>.
- [236] A. Djouadi, W. Kilian, M. Mühlleitner, and P. M. Zerwas, *Testing Higgs selfcouplings at  $e^+ e^-$*

- linear colliders*, *Eur. Phys. J.* **C10** (1999) 27–43, [arXiv:hep-ph/9903229 \[hep-ph\]](#).
- [237] D. A. Dicus, C. Kao, and W. W. Repko, *Self Coupling of the Higgs boson in the processes  $pp \rightarrow ZHHH + X$  and  $pp \rightarrow WHHH + X$* , [arXiv:1602.05849 \[hep-ph\]](#).
- [238] T. Plehn and M. Rauch, *The quartic higgs coupling at hadron colliders*, *Phys. Rev.* **D72** (2005) 053008, [arXiv:hep-ph/0507321 \[hep-ph\]](#).
- [239] T. Binoth, S. Karg, N. Kauer, and R. Ruckl, *Multi-Higgs boson production in the Standard Model and beyond*, *Phys. Rev.* **D74** (2006) 113008, [arXiv:hep-ph/0608057 \[hep-ph\]](#).
- [240] C.-Y. Chen, Q.-S. Yan, X. Zhao, Y.-M. Zhong, and Z. Zhao, *Probing triple-Higgs productions via  $4b2\gamma$  decay channel at a 100 TeV hadron collider*, *Phys. Rev.* **D93** (2016) no. 1, 013007, [arXiv:1510.04013 \[hep-ph\]](#).
- [241] A. Papaefstathiou and K. Sakurai, *Triple Higgs boson production at a 100 TeV proton-proton collider*, [arXiv:1508.06524 \[hep-ph\]](#).
- [242] B. Fuks, J. H. Kim, and S. J. Lee, *Probing Higgs self-interactions in proton-proton collisions at a center-of-mass energy of 100 TeV*, [arXiv:1510.07697 \[hep-ph\]](#).
- [243] V. Hirschi, R. Frederix, S. Frixione, M. V. Garzelli, F. Maltoni, et al., *Automation of one-loop QCD corrections*, *JHEP* **1105** (2011) 044, [arXiv:1103.0621 \[hep-ph\]](#).
- [244] S. Ovin, X. Rouby, and V. Lemaître, *DELPHES, a framework for fast simulation of a generic collider experiment*, [arXiv:0903.2225 \[hep-ph\]](#).
- [245] J. Pumplin, D. Stump, J. Huston, H. Lai, P. M. Nadolsky, et al., *New generation of parton distributions with uncertainties from global QCD analysis*, *JHEP* **0207** (2002) 012, [arXiv:hep-ph/0201195 \[hep-ph\]](#).
- [246] S. Yang and Q.-S. Yan, *Searching for Heavy Charged Higgs Boson with Jet Substructure at the LHC*, *JHEP* **02** (2012) 074, [arXiv:1111.4530 \[hep-ph\]](#).
- [247] ATLAS Collaboration, G. Aad et al., *Electron and photon energy calibration with the ATLAS detector using LHC Run 1 data*, *Eur. Phys. J.* **C74** (2014) no. 10, 3071, [arXiv:1407.5063 \[hep-ex\]](#).
- [248] *b-tagging in dense environments*, ATL-PHYS-PUB-2014-014, CERN, Geneva, Aug, 2014. <https://cds.cern.ch/record/1750682>.
- [249] *Centrality, rapidity and  $p_T$  dependence of isolated prompt photon production in lead-lead collisions at  $\sqrt{s_{NN}} = 2.76$  TeV with the ATLAS detector at the LHC*, ATLAS-CONF-2014-026, CERN, Geneva, May, 2014. <https://cds.cern.ch/record/1702992>.
- [250] S. Gieseke et al., *Herwig++ 2.5 Release Note*, [arXiv:1102.1672 \[hep-ph\]](#).
- [251] K. Arnold et al., *Herwig++ 2.6 Release Note*, [arXiv:1205.4902 \[hep-ph\]](#).
- [252] J. Bellm, S. Gieseke, D. Grellscheid, A. Papaefstathiou, S. Platzer, et al., *Herwig++ 2.7 Release Note*, [arXiv:1310.6877 \[hep-ph\]](#).
- [253] CMS Collaboration, S. Chatrchyan et al., *Search for the standard model Higgs boson decaying into two photons in  $pp$  collisions at  $\sqrt{s} = 7$  TeV*, *Phys. Lett.* **B710** (2012) 403–425, [arXiv:1202.1487 \[hep-ex\]](#).
- [254] ATLAS Collaboration, G. Aad et al., *Measurement of Higgs boson production in the diphoton decay channel in  $pp$  collisions at center-of-mass energies of 7 and 8 TeV with the ATLAS detector*, *Phys. Rev.* **D90** (2014) no. 11, 112015, [arXiv:1408.7084 \[hep-ex\]](#).
- [255] K. Assamagan et al., *The Higgs Portal and Cosmology*, 2016. [arXiv:1604.05324 \[hep-ph\]](#). <http://inspirehep.net/record/1449094/files/arXiv:1604.05324.pdf>.
- [256] *ACFI Workshop Probing the Electroweak Phase Transition with a Next Generation PP Collider*, <http://www.physics.umass.edu/acfi/seminars-and-workshops/probing-the-electroweak-phase-transition-with-a-next-generation-pp-collider>. September 2015.

- [257] Planck Collaboration, P. Ade et al., *Planck 2013 results. XVI. Cosmological parameters*, *Astron.Astrophys.* (2014) , [arXiv:1303.5076 \[astro-ph.CO\]](#) .
- [258] A. Sakharov, *Violation of CP Invariance, c Asymmetry, and Baryon Asymmetry of the Universe*, *Pisma Zh.Eksp.Teor.Fiz.* **5** (1967) 32–35.
- [259] D. E. Morrissey and M. J. Ramsey-Musolf, *Electroweak baryogenesis*, *New J.Phys.* **14** (2012) 125003, [arXiv:1206.2942 \[hep-ph\]](#) .
- [260] D. Curtin, P. Jaiswal, and P. Meade, *Excluding Electroweak Baryogenesis in the MSSM*, *JHEP* **08** (2012) 005, [arXiv:1203.2932 \[hep-ph\]](#) .
- [261] T. Cohen, D. E. Morrissey, and A. Pierce, *Electroweak Baryogenesis and Higgs Signatures*, *Phys. Rev.* **D86** (2012) 013009, [arXiv:1203.2924 \[hep-ph\]](#) .
- [262] A. Katz, M. Perelstein, M. J. Ramsey-Musolf, and P. Winslow, *Stop-Catalyzed Baryogenesis Beyond the MSSM*, [arXiv:1509.02934 \[hep-ph\]](#) .
- [263] Y. Cui, L. Randall, and B. Shuve, *A WIMPy Baryogenesis Miracle*, *JHEP* **04** (2012) 075, [arXiv:1112.2704 \[hep-ph\]](#) .
- [264] C. Caprini et al., *Science with the space-based interferometer eLISA. II: Gravitational waves from cosmological phase transitions*, [arXiv:1512.06239 \[astro-ph.CO\]](#) .
- [265] R. Barbieri, L. J. Hall, and V. S. Rychkov, *Improved naturalness with a heavy Higgs: An Alternative road to LHC physics*, *Phys.Rev.* **D74** (2006) 015007, [arXiv:hep-ph/0603188 \[hep-ph\]](#) .
- [266] P. Harris, V. V. Khoze, M. Spannowsky, and C. Williams, *Closing up on Dark Sectors at Colliders: from 14 to 100 TeV*, *Phys. Rev.* **D93** (2016) no. 5, 054030, [arXiv:1509.02904 \[hep-ph\]](#) .
- [267] V. V. Khoze, G. Ro, and M. Spannowsky, *Spectroscopy of scalar mediators to dark matter at the LHC and at 100 TeV*, *Phys. Rev.* **D92** (2015) no. 7, 075006, [arXiv:1505.03019 \[hep-ph\]](#) .
- [268] P. Fileviez Perez, *New Paradigm for Baryon and Lepton Number Violation*, *Phys. Rept.* **597** (2015) 1–30, [arXiv:1501.01886 \[hep-ph\]](#) .
- [269] P. W. Graham, D. E. Kaplan, and S. Rajendran, *Cosmological Relaxation of the Electroweak Scale*, [arXiv:1504.07551 \[hep-ph\]](#) .
- [270] Z. Chacko, H.-S. Goh, and R. Harnik, *The Twin Higgs: Natural electroweak breaking from mirror symmetry*, *Phys. Rev. Lett.* **96** (2006) 231802, [arXiv:hep-ph/0506256 \[hep-ph\]](#) .
- [271] G. Burdman, Z. Chacko, H.-S. Goh, and R. Harnik, *Folded supersymmetry and the LEP paradox*, *JHEP* **02** (2007) 009, [arXiv:hep-ph/0609152 \[hep-ph\]](#) .
- [272] S. Weinberg, *Using quark and lepton masses to guess the scalar spectrum*, in *In \*Islamabad 1990, Proceedings, High energy physics and cosmology\* 1-12*. 1991. <http://alice.cern.ch/format/showfull?sysnb=0132168>.
- [273] B. Grinstein, M. Redi, and G. Villadoro, *Low Scale Flavor Gauge Symmetries*, *JHEP* **11** (2010) 067, [arXiv:1009.2049 \[hep-ph\]](#) .
- [274] C. D. Froggatt and H. B. Nielsen, *Hierarchy of Quark Masses, Cabibbo Angles and CP Violation*, *Nucl. Phys.* **B147** (1979) 277.
- [275] K. S. Babu and S. Nandi, *Natural fermion mass hierarchy and new signals for the Higgs boson*, *Phys. Rev.* **D62** (2000) 033002, [arXiv:hep-ph/9907213 \[hep-ph\]](#) .
- [276] G. F. Giudice and O. Lebedev, *Higgs-dependent Yukawa couplings*, *Phys. Lett.* **B665** (2008) 79–85, [arXiv:0804.1753 \[hep-ph\]](#) .
- [277] D. Buttazzo, G. Degrassi, P. P. Giardino, G. F. Giudice, F. Sala, et al., *Investigating the near-criticality of the Higgs boson*, *JHEP* **1312** (2013) 089, [arXiv:1307.3536](#) .
- [278] A. V. Bednyakov, B. A. Kniehl, A. F. Pikelner, and O. L. Veretin, *Stability of the Electroweak Vacuum: Gauge Independence and Advanced Precision*, *Phys. Rev. Lett.* **115** (2015) no. 20,

- 201802, [arXiv:1507.08833 \[hep-ph\]](#).
- [279] M. Gonderinger, Y. Li, H. Patel, and M. J. Ramsey-Musolf, *Vacuum Stability, Perturbativity, and Scalar Singlet Dark Matter*, *JHEP* **01** (2010) 053, [arXiv:0910.3167 \[hep-ph\]](#).
- [280] M. Gonderinger, H. Lim, and M. J. Ramsey-Musolf, *Complex Scalar Singlet Dark Matter: Vacuum Stability and Phenomenology*, *Phys.Rev.* **D86** (2012) 043511, [arXiv:1202.1316 \[hep-ph\]](#).
- [281] O. Lebedev, *On Stability of the Electroweak Vacuum and the Higgs Portal*, *Eur. Phys. J.* **C72** (2012) 2058, [arXiv:1203.0156 \[hep-ph\]](#).
- [282] J. Elias-Miro, J. R. Espinosa, G. F. Giudice, H. M. Lee, and A. Strumia, *Stabilization of the Electroweak Vacuum by a Scalar Threshold Effect*, *JHEP* **06** (2012) 031, [arXiv:1203.0237 \[hep-ph\]](#).
- [283] W. Chao, M. Gonderinger, and M. J. Ramsey-Musolf, *Higgs Vacuum Stability, Neutrino Mass, and Dark Matter*, *Phys. Rev.* **D86** (2012) 113017, [arXiv:1210.0491 \[hep-ph\]](#).
- [284] C. Cheung, M. Papucci, and K. M. Zurek, *Higgs and Dark Matter Hints of an Oasis in the Desert*, *JHEP* **07** (2012) 105, [arXiv:1203.5106 \[hep-ph\]](#).
- [285] P. Ferreira, H. E. Haber, and E. Santos, *Preserving the validity of the Two-Higgs Doublet Model up to the Planck scale*, *Phys. Rev.* **D92** (2015) 033003, [arXiv:1505.04001 \[hep-ph\]](#).
- [286] J. Hajer, Y.-Y. Li, T. Liu, and J. F. H. Shiu, *Heavy Higgs Bosons at 14 TeV and 100 TeV*, *JHEP* **11** (2015) 124, [arXiv:1504.07617 \[hep-ph\]](#).
- [287] *Prospects for measuring Higgs pair production in the channel  $H(\rightarrow \gamma\gamma)H(\rightarrow b\bar{b})$  using the ATLAS detector at the HL-LHC*, ATL-PHYS-PUB-2014-019, CERN, Geneva, Oct, 2014. <http://cds.cern.ch/record/1956733>.
- [288] *Higgs Pair Production in the  $H(\rightarrow \tau\tau)H(\rightarrow b\bar{b})$  channel at the High-Luminosity LHC*, ATL-PHYS-PUB-2015-046, CERN, Geneva, Nov, 2015. <http://cds.cern.ch/record/2065974>.
- [289] CMS Collaboration, *Higgs pair production at the High Luminosity LHC*, CMS-PAS-FTR-15-002, 2015. <http://cms-results.web.cern.ch/cms-results/public-results/preliminary-results/FTR-15-002/>.
- [290] A. J. Barr, M. J. Dolan, C. Englert, and M. Spannowsky, *Di-Higgs final states augMT2ed – selecting  $hh$  events at the high luminosity LHC*, *Phys. Lett.* **B728** (2014) 308–313, [arXiv:1309.6318 \[hep-ph\]](#).
- [291] F. Goertz, A. Papaefstathiou, L. L. Yang, and J. Zurita, *Higgs Boson self-coupling measurements using ratios of cross sections*, *JHEP* **1306** (2013) 016, [arXiv:1301.3492 \[hep-ph\]](#).
- [292] H. Baer, T. Barklow, K. Fujii, Y. Gao, A. Hoang, S. Kanemura, J. List, H. E. Logan, A. Nomerotski, M. Perelstein, et al., *The International Linear Collider Technical Design Report - Volume 2: Physics*, [arXiv:1306.6352 \[hep-ph\]](#).
- [293] D. Curtin and P. Saraswat, *Towards a No-Lose Theorem for Naturalness*, [arXiv:1509.04284 \[hep-ph\]](#).
- [294] M. Low and L.-T. Wang, *Neutralino Dark Matter at 100 TeV*, [arXiv:1404.0682 \[hep-ph\]](#).
- [295] S. Gori, S. Jung, L.-T. Wang, and J. D. Wells, *Prospects for Electroweakino Discovery at a 100 TeV Hadron Collider*, *JHEP* **12** (2014) 108, [arXiv:1410.6287 \[hep-ph\]](#).
- [296] J. Bramante, P. J. Fox, A. Martin, B. Ostdiek, T. Plehn, T. Schell, and M. Takeuchi, *Relic neutralino surface at a 100 TeV collider*, *Phys. Rev.* **D91** (2015) 054015, [arXiv:1412.4789 \[hep-ph\]](#).
- [297] D. Curtin et al., *Exotic decays of the 125 GeV Higgs boson*, *Phys. Rev.* **D90** (2014) no. 7, 075004, [arXiv:1312.4992 \[hep-ph\]](#).
- [298] D. Curtin, R. Essig, S. Gori, and J. Shelton, *Illuminating Dark Photons with High-Energy*

- Colliders*, *JHEP* **1502** (2015) 157, [arXiv:1412.0018 \[hep-ph\]](#).
- [299] D. Curtin and C. B. Verhaaren, *Discovering Uncolored Naturalness in Exotic Higgs Decays*, [arXiv:1506.06141 \[hep-ph\]](#).
- [300] D. S. M. Alves, J. Galloway, J. T. Ruderman, and J. R. Walsh, *Running Electroweak Couplings as a Probe of New Physics*, *JHEP* **02** (2015) 007, [arXiv:1410.6810 \[hep-ph\]](#).
- [301] M. Gurtler, E.-M. Ilgenfritz, and A. Schiller, *Where the electroweak phase transition ends*, *Phys. Rev.* **D56** (1997) 3888–3895, [arXiv:hep-lat/9704013 \[hep-lat\]](#).
- [302] M. Laine and K. Rummukainen, *What’s new with the electroweak phase transition?*, *Nucl. Phys. Proc. Suppl.* **73** (1999) 180–185, [arXiv:hep-lat/9809045 \[hep-lat\]](#).
- [303] F. Csikor, Z. Fodor, and J. Heitger, *Endpoint of the hot electroweak phase transition*, *Phys. Rev. Lett.* **82** (1999) 21–24, [arXiv:hep-ph/9809291 \[hep-ph\]](#).
- [304] M. S. Carena, M. Quiros, and C. Wagner, *Electroweak baryogenesis and Higgs and stop searches at LEP and the Tevatron*, *Nucl.Phys.* **B524** (1998) 3–22, [arXiv:hep-ph/9710401 \[hep-ph\]](#).
- [305] M. Carena, G. Nardini, M. Quiros, and C. E. Wagner, *The Effective Theory of the Light Stop Scenario*, *JHEP* **0810** (2008) 062, [arXiv:0806.4297 \[hep-ph\]](#).
- [306] A. Katz and M. Perelstein, *Higgs Couplings and Electroweak Phase Transition*, *JHEP* **1407** (2014) 108, [arXiv:1401.1827 \[hep-ph\]](#).
- [307] A. Noble and M. Perelstein, *Higgs self-coupling as a probe of electroweak phase transition*, *Phys.Rev.* **D78** (2008) 063518, [arXiv:0711.3018 \[hep-ph\]](#).
- [308] D. Curtin, P. Meade, and C.-T. Yu, *Testing Electroweak Baryogenesis with Future Colliders*, *JHEP* **1411** (2014) 127, [arXiv:1409.0005 \[hep-ph\]](#).
- [309] S. Profumo, M. J. Ramsey-Musolf, and G. Shaughnessy, *Singlet Higgs Phenomenology and the Electroweak Phase Transition*, *JHEP* **0708** (2007) 010, [arXiv:0705.2425 \[hep-ph\]](#).
- [310] M. Jiang, L. Bian, W. Huang, and J. Shu, *Impact of a complex singlet: From dark matter to baryogenesis*, [arXiv:1502.07574 \[hep-ph\]](#).
- [311] H. H. Patel and M. J. Ramsey-Musolf, *Stepping Into Electroweak Symmetry Breaking: Phase Transitions and Higgs Phenomenology*, *Phys.Rev.* **D88** (2013) 035013, [arXiv:1212.5652 \[hep-ph\]](#).
- [312] N. Blinov, J. Kozaczuk, D. E. Morrissey, and C. Tamarit, *Electroweak Baryogenesis from Exotic Electroweak Symmetry Breaking*, *Phys. Rev.* **D92** (2015) no. 3, 035012, [arXiv:1504.05195 \[hep-ph\]](#).
- [313] S. Inoue, G. Ovanessian, and M. J. Ramsey-Musolf, *Two-Step Electroweak Baryogenesis*, [arXiv:1508.05404 \[hep-ph\]](#).
- [314] S. Profumo, M. J. Ramsey-Musolf, C. L. Wainwright, and P. Winslow, *Singlet-Catalyzed Electroweak Phase Transitions and Precision Higgs Studies*, [arXiv:1407.5342 \[hep-ph\]](#).
- [315] B. Henning, X. Lu, and H. Murayama, *What do precision Higgs measurements buy us?*, [arXiv:1404.1058 \[hep-ph\]](#).
- [316] N. Craig, H. K. Lou, M. McCullough, and A. Thalappilil, *The Higgs Portal Above Threshold*, *JHEP* **02** (2016) 127, [arXiv:1412.0258 \[hep-ph\]](#).
- [317] G. Dorsch, S. Huber, and J. No, *A strong electroweak phase transition in the 2HDM after LHC8*, *JHEP* **1310** (2013) 029, [arXiv:1305.6610 \[hep-ph\]](#).
- [318] G. Dorsch, S. Huber, K. Mimasu, and J. No, *Echoes of the Electroweak Phase Transition: Discovering a second Higgs doublet through  $A_0 \rightarrow H_0 Z$* , [arXiv:1405.5537 \[hep-ph\]](#).
- [319] M. E. Peskin, *Comparison of LHC and ILC Capabilities for Higgs Boson Coupling Measurements*, [arXiv:1207.2516 \[hep-ph\]](#).
- [320] A. Blondel, M. Koratzinos, R. Assmann, A. Butterworth, P. Janot, et al., *LEP3: A High Luminosity  $e^+e^-$  Collider to study the Higgs Boson*, [arXiv:1208.0504 \[physics.acc-ph\]](#).

- [321] M. Klute, R. Lafaye, T. Plehn, M. Rauch, and D. Zerwas, *Measuring Higgs Couplings at a Linear Collider*, *Europhys.Lett.* **101** (2013) 51001, [arXiv:1301.1322 \[hep-ph\]](#).
- [322] J. M. Cline, K. Kainulainen, P. Scott, and C. Weniger, *Update on scalar singlet dark matter*, *Phys. Rev.* **D88** (2013) 055025, [arXiv:1306.4710 \[hep-ph\]](#). [Erratum: *Phys. Rev.* **D92**,no.3,039906(2015)].
- [323] M. J. Dolan, C. Englert, and M. Spannowsky, *New Physics in LHC Higgs boson pair production*, *Phys. Rev.* **D87** (2013) no. 5, 055002, [arXiv:1210.8166 \[hep-ph\]](#).
- [324] J. M. No and M. Ramsey-Musolf, *Probing the Higgs Portal at the LHC Through Resonant di-Higgs Production*, *Phys.Rev.* **D89** (2014) 095031, [arXiv:1310.6035 \[hep-ph\]](#).
- [325] C.-Y. Chen, S. Dawson, and I. M. Lewis, *Exploring resonant di-Higgs boson production in the Higgs singlet model*, *Phys. Rev.* **D91** (2015) no. 3, 035015, [arXiv:1410.5488 \[hep-ph\]](#).
- [326] V. Barger, L. L. Everett, C. B. Jackson, A. D. Peterson, and G. Shaughnessy, *New physics in resonant production of Higgs boson pairs*, *Phys. Rev. Lett.* **114** (2015) no. 1, 011801, [arXiv:1408.0003 \[hep-ph\]](#).
- [327] A. V. Kotwal, M. J. Ramsey-Musolf, J. M. No, and P. Winslow, *Singlet-Catalyzed Electroweak Phase Transitions in the 100 TeV Frontier*, [arXiv:1605.06123 \[hep-ph\]](#).
- [328] H. H. Patel and M. J. Ramsey-Musolf, *Baryon Washout, Electroweak Phase Transition, and Perturbation Theory*, *JHEP* **1107** (2011) 029, [arXiv:1101.4665 \[hep-ph\]](#).
- [329] L. G. Almeida, S. J. Lee, S. Pokorski, and J. D. Wells, *Study of the standard model Higgs boson partial widths and branching fractions*, *Phys. Rev.* **D89** (2014) no. 3, 033006, [arXiv:1311.6721 \[hep-ph\]](#).
- [330] A. Djouadi, J. Quevillon, and R. Vega-Morales, *Into the multi-TeV scale with a Higgs golden ratio*, [arXiv:1509.03913 \[hep-ph\]](#).
- [331] M. Beltran, D. Hooper, E. W. Kolb, and Z. C. Krusberg, *Deducing the nature of dark matter from direct and indirect detection experiments in the absence of collider signatures of new physics*, *Phys. Rev.* **D80** (2009) 043509, [arXiv:0808.3384 \[hep-ph\]](#).
- [332] Q.-H. Cao, C.-R. Chen, C. S. Li, and H. Zhang, *Effective Dark Matter Model: Relic density, CDMS II, Fermi LAT and LHC*, *JHEP* **08** (2011) 018, [arXiv:0912.4511 \[hep-ph\]](#).
- [333] M. Beltran, D. Hooper, E. W. Kolb, Z. A. C. Krusberg, and T. M. P. Tait, *Maverick dark matter at colliders*, *JHEP* **09** (2010) 037, [arXiv:1002.4137 \[hep-ph\]](#).
- [334] J. Goodman, M. Ibe, A. Rajaraman, W. Shepherd, T. M. P. Tait, and H.-B. Yu, *Constraints on Dark Matter from Colliders*, *Phys. Rev.* **D82** (2010) 116010, [arXiv:1008.1783 \[hep-ph\]](#).
- [335] Y. Bai, P. J. Fox, and R. Harnik, *The Tevatron at the Frontier of Dark Matter Direct Detection*, *JHEP* **12** (2010) 048, [arXiv:1005.3797 \[hep-ph\]](#).
- [336] J. Goodman, M. Ibe, A. Rajaraman, W. Shepherd, T. M. P. Tait, and H.-B. Yu, *Constraints on Light Majorana dark Matter from Colliders*, *Phys. Lett.* **B695** (2011) 185–188, [arXiv:1005.1286 \[hep-ph\]](#).
- [337] J. Abdallah et al., *Simplified Models for Dark Matter and Missing Energy Searches at the LHC*, [arXiv:1409.2893 \[hep-ph\]](#).
- [338] S. A. Malik et al., *Interplay and Characterization of Dark Matter Searches at Colliders and in Direct Detection Experiments*, *Phys. Dark Univ.* **9-10** (2015) 51–58, [arXiv:1409.4075 \[hep-ex\]](#).
- [339] G. Busoni et al., *Recommendations on presenting LHC searches for missing transverse energy signals using simplified s-channel models of dark matter*, [arXiv:1603.04156 \[hep-ex\]](#).
- [340] C. P. Burgess, M. Pospelov, and T. ter Veldhuis, *The Minimal model of nonbaryonic dark matter: A Singlet scalar*, *Nucl. Phys.* **B619** (2001) 709–728, [arXiv:hep-ph/0011335 \[hep-ph\]](#).
- [341] M. Cirelli, N. Fornengo, and A. Strumia, *Minimal dark matter*, *Nucl. Phys.* **B753** (2006)

- 178–194, [arXiv:hep-ph/0512090](#) [hep-ph].
- [342] P. Fileviez Perez, H. H. Patel, M. Ramsey-Musolf, and K. Wang, *Triplet Scalars and Dark Matter at the LHC*, *Phys.Rev.* **D79** (2009) 055024, [arXiv:0811.3957](#) [hep-ph].
- [343] T. Hambye, F. S. Ling, L. Lopez Honorez, and J. Rocher, *Scalar Multiplet Dark Matter*, *JHEP* **07** (2009) 090, [arXiv:0903.4010](#) [hep-ph]. [Erratum: JHEP05,066(2010)].
- [344] V. Barger, P. Langacker, M. McCaskey, M. J. Ramsey-Musolf, and G. Shaughnessy, *LHC Phenomenology of an Extended Standard Model with a Real Scalar Singlet*, *Phys. Rev.* **D77** (2008) 035005, [arXiv:0706.4311](#) [hep-ph].
- [345] X.-G. He, T. Li, X.-Q. Li, J. Tandean, and H.-C. Tsai, *Constraints on Scalar Dark Matter from Direct Experimental Searches*, *Phys. Rev.* **D79** (2009) 023521, [arXiv:0811.0658](#) [hep-ph].
- [346] V. Barger, P. Langacker, M. McCaskey, M. Ramsey-Musolf, and G. Shaughnessy, *Complex Singlet Extension of the Standard Model*, *Phys.Rev.* **D79** (2009) 015018, [arXiv:0811.0393](#) [hep-ph].
- [347] X.-G. He and J. Tandean, *Low-Mass Dark-Matter Hint from CDMS II, Higgs Boson at the LHC, and Darkon Models*, *Phys. Rev.* **D88** (2013) 013020, [arXiv:1304.6058](#) [hep-ph].
- [348] L. Feng, S. Profumo, and L. Ubaldi, *Closing in on singlet scalar dark matter: LUX, invisible Higgs decays and gamma-ray lines*, *JHEP* **03** (2015) 045, [arXiv:1412.1105](#) [hep-ph].
- [349] F. Kahlhoefer and J. McDonald, *WIMP Dark Matter and Unitarity-Conserving Inflation via a Gauge Singlet Scalar*, *JCAP* **1511** (2015) no. 11, 015, [arXiv:1507.03600](#) [astro-ph.CO].
- [350] A. Drozd, B. Grzadkowski, J. F. Gunion, and Y. Jiang, *Extending two-Higgs-doublet models by a singlet scalar field - the Case for Dark Matter*, *JHEP* **11** (2014) 105, [arXiv:1408.2106](#) [hep-ph].
- [351] M. R. Buckley, D. Feld, and D. Goncalves, *Scalar Simplified Models for Dark Matter*, *Phys. Rev.* **D91** (2015) 015017, [arXiv:1410.6497](#) [hep-ph].
- [352] S. Baek, P. Ko, M. Park, W.-I. Park, and C. Yu, *Beyond the Dark matter effective field theory and a simplified model approach at colliders*, *Phys. Lett.* **B756** (2016) 289–294, [arXiv:1506.06556](#) [hep-ph].
- [353] R. Foot, A. Kobakhidze, K. L. McDonald, and R. R. Volkas, *A Solution to the hierarchy problem from an almost decoupled hidden sector within a classically scale invariant theory*, *Phys. Rev.* **D77** (2008) 035006, [arXiv:0709.2750](#) [hep-ph].
- [354] C. Englert, J. Jaeckel, V. V. Khoze, and M. Spannowsky, *Emergence of the Electroweak Scale through the Higgs Portal*, *JHEP* **04** (2013) 060, [arXiv:1301.4224](#) [hep-ph].
- [355] T. Cohen, J. Kearney, A. Pierce, and D. Tucker-Smith, *Singlet-Doublet Dark Matter*, *Phys. Rev.* **D85** (2012) 075003, [arXiv:1109.2604](#) [hep-ph].
- [356] L. Calibbi, A. Mariotti, and P. Tziveloglou, *Singlet-Doublet Model: Dark matter searches and LHC constraints*, *JHEP* **10** (2015) 116, [arXiv:1505.03867](#) [hep-ph].
- [357] S. Banerjee, S. Matsumoto, K. Mukaida, and Y.-L. S. Tsai, *WIMP Dark Matter in a Well-Tempered Regime: A case study on Singlet-Doublets Fermionic WIMP*, [arXiv:1603.07387](#) [hep-ph].
- [358] A. Dedes and D. Karamitros, *Doublet-Triplet Fermionic Dark Matter*, *Phys. Rev.* **D89** (2014) no. 11, 115002, [arXiv:1403.7744](#) [hep-ph].
- [359] T. M. P. Tait and Z.-H. Yu, *Triplet-Quadruplet Dark Matter*, *JHEP* **03** (2016) 204, [arXiv:1601.01354](#) [hep-ph].
- [360] N. Zhou, D. Berge, L. Wang, D. Whiteson, and T. Tait, *Sensitivity of future collider facilities to WIMP pair production via effective operators and light mediators*, [arXiv:1307.5327](#) [hep-ex].
- [361] A. Djouadi, O. Lebedev, Y. Mambrini, and J. Quevillon, *Implications of LHC searches for*

- Higgs-portal dark matter*, *Phys. Lett.* **B709** (2012) 65–69, [arXiv:1112.3299 \[hep-ph\]](#).
- [362] CMS Collaboration, S. Chatrchyan et al., *Search for invisible decays of Higgs bosons in the vector boson fusion and associated ZH production modes*, *Eur. Phys. J.* **C74** (2014) 2980, [arXiv:1404.1344 \[hep-ex\]](#).
- [363] ATLAS Collaboration, G. Aad et al., *Constraints on new phenomena via Higgs boson couplings and invisible decays with the ATLAS detector*, *JHEP* **11** (2015) 206, [arXiv:1509.00672 \[hep-ex\]](#).
- [364] CMS Collaboration, *Search for invisible decays of a Higgs boson produced via vector boson fusion at  $\sqrt{s} = 13$  TeV*, CMS-PAS-HIG-16-009, CERN, Geneva, 2016. <https://cds.cern.ch/record/2142460>.
- [365] J. Brooke, M. R. Buckley, P. Dunne, B. Penning, J. Tamanas, and M. Zgubic, *Vector Boson Fusion Searches for Dark Matter at the LHC*, [arXiv:1603.07739 \[hep-ph\]](#).
- [366] F. Caola and K. Melnikov, *Constraining the Higgs boson width with ZZ production at the LHC*, *Phys. Rev.* **D88** (2013) 054024, [arXiv:1307.4935 \[hep-ph\]](#).
- [367] C. Englert and M. Spannowsky, *Limitations and Opportunities of Off-Shell Coupling Measurements*, *Phys. Rev.* **D90** (2014) 053003, [arXiv:1405.0285 \[hep-ph\]](#).
- [368] C. Englert, Y. Soreq, and M. Spannowsky, *Off-Shell Higgs Coupling Measurements in BSM scenarios*, *JHEP* **05** (2015) 145, [arXiv:1410.5440 \[hep-ph\]](#).
- [369] M. Endo and Y. Takaesu, *Heavy WIMP through Higgs portal at the LHC*, *Phys. Lett.* **B743** (2015) 228–234, [arXiv:1407.6882 \[hep-ph\]](#).
- [370] M. McCullough, *Talk given at FERMILAB: Higgs Portal at 100 TeV*, , Fermilab, 2015.
- [371] D. Lopez-Val, T. Plehn, and M. Rauch, *Measuring extended Higgs sectors as a consistent free couplings model*, *JHEP* **10** (2013) 134, [arXiv:1308.1979 \[hep-ph\]](#).
- [372] G. M. Pruna and T. Robens, *Higgs singlet extension parameter space in the light of the LHC discovery*, *Phys. Rev.* **D88** (2013) no. 11, 115012, [arXiv:1303.1150 \[hep-ph\]](#).
- [373] P. Cushman et al., *Working Group Report: WIMP Dark Matter Direct Detection*, in *Community Summer Study 2013: Snowmass on the Mississippi (CSS2013) Minneapolis, MN, USA, July 29-August 6, 2013*. 2013. [arXiv:1310.8327 \[hep-ex\]](#). <https://inspirehep.net/record/1262767/files/arXiv:1310.8327.pdf>.
- [374] Fermi-LAT Collaboration, M. Ackermann et al., *Constraining Dark Matter Models from a Combined Analysis of Milky Way Satellites with the Fermi Large Area Telescope*, *Phys. Rev. Lett.* **107** (2011) 241302, [arXiv:1108.3546 \[astro-ph.HE\]](#).
- [375] M. J. Strassler and K. M. Zurek, *Discovering the Higgs through highly-displaced vertices*, *Phys. Lett.* **B661** (2008) 263–267, [arXiv:hep-ph/0605193 \[hep-ph\]](#).
- [376] P. Schwaller, D. Stolarski, and A. Weiler, *Emerging Jets*, *JHEP* **05** (2015) 059, [arXiv:1502.05409 \[hep-ph\]](#).
- [377] P. Minkowski,  *$\mu \rightarrow e\gamma$  at a Rate of One Out of  $10^9$  Muon Decays?*, *Phys. Lett.* **B67** (1977) 421–428.
- [378] R. N. Mohapatra and G. Senjanovic, *Neutrino Mass and Spontaneous Parity Violation*, *Phys. Rev. Lett.* **44** (1980) 912.
- [379] M. Gell-Mann, P. Ramond, and R. Slansky, *Complex Spinors and Unified Theories*, *Conf. Proc.* **C790927** (1979) 315–321, [arXiv:1306.4669 \[hep-th\]](#).
- [380] T. Yanagida, *Horizontal symmetry and masses of neutrinos*, *Conf. Proc.* **C7902131** (1979) 95–99. [*Conf. Proc.*C7902131,95(1979)].
- [381] R. N. Mohapatra and J. C. Pati, *Left-Right Gauge Symmetry and an Isoconjugate Model of CP Violation*, *Phys. Rev.* **D11** (1975) 566–571.
- [382] R. N. Mohapatra and J. C. Pati, *A Natural Left-Right Symmetry*, *Phys. Rev.* **D11** (1975) 2558.

- [383] G. Senjanovic and R. N. Mohapatra, *Exact Left-Right Symmetry and Spontaneous Violation of Parity*, *Phys. Rev.* **D12** (1975) 1502.
- [384] D. Chang, R. N. Mohapatra, and M. K. Parida, *Decoupling Parity and  $SU(2)$ -R Breaking Scales: A New Approach to Left-Right Symmetric Models*, *Phys. Rev. Lett.* **52** (1984) 1072.
- [385] J. Heeck and S. Patra, *Minimal Left-Right Symmetric Dark Matter*, *Phys. Rev. Lett.* **115** (2015) no. 12, 121804, [arXiv:1507.01584 \[hep-ph\]](#).
- [386] P. Ko and T. Nomura,  *$SU(2)_L \times SU(2)_R$  minimal dark matter with 2 TeV  $W'$* , *Phys. Lett.* **B753** (2016) 612–618, [arXiv:1510.07872 \[hep-ph\]](#).
- [387] C. Garcia-Cely and J. Heeck, *Phenomenology of left-right symmetric dark matter*, [arXiv:1512.03332 \[hep-ph\]](#).
- [388] N. Nagata, K. A. Olive, and J. Zheng, *Weakly-Interacting Massive Particles in Non-supersymmetric  $SO(10)$  Grand Unified Models*, *JHEP* **10** (2015) 193, [arXiv:1509.00809 \[hep-ph\]](#).
- [389] J. F. Gunion, B. Kayser, R. N. Mohapatra, N. G. Deshpande, J. Grifols, A. Mendez, F. I. Olness, and P. B. Pal, *Production and detection at ssc of higgs bosons in left-right symmetric theories*, in *Physics of the Superconducting Supercollider: Proceedings, 1986 Summer Study, June 23 - July 11, 1986, Snowmass, Colorado*. 1986. [http://lss.fnal.gov/cgi-bin/find\\_paper.pl?other/PRINT-86-1324.pdf](http://lss.fnal.gov/cgi-bin/find_paper.pl?other/PRINT-86-1324.pdf).
- [390] J. F. Gunion, J. Grifols, A. Mendez, B. Kayser, and F. I. Olness, *Higgs Bosons in Left-Right Symmetric Models*, *Phys. Rev.* **D40** (1989) 1546.
- [391] P. S. B. Dev, R. N. Mohapatra, and Y. Zhang, *Probing the Higgs Sector of the Minimal Left-Right Symmetric Model at Future Hadron Colliders*, [arXiv:1602.05947 \[hep-ph\]](#).
- [392] G. Beall, M. Bander, and A. Soni, *Constraint on the Mass Scale of a Left-Right Symmetric Electroweak Theory from the  $K(L)$   $K(S)$  Mass Difference*, *Phys. Rev. Lett.* **48** (1982) 848.
- [393] Y. Zhang, H. An, X. Ji, and R. N. Mohapatra, *General CP Violation in Minimal Left-Right Symmetric Model and Constraints on the Right-Handed Scale*, *Nucl. Phys. B* **802** (2008) 247–279, [arXiv:0712.4218 \[hep-ph\]](#).
- [394] A. Maiezza, M. Nemevsek, F. Nesti, and G. Senjanovic, *Left-Right Symmetry at LHC*, *Phys. Rev.* **D82** (2010) 055022, [arXiv:1005.5160 \[hep-ph\]](#).
- [395] S. Bertolini, A. Maiezza, and F. Nesti, *Present and Future  $K$  and  $B$  Meson Mixing Constraints on TeV Scale Left-Right Symmetry*, *Phys. Rev.* **D89** (2014) no. 9, 095028, [arXiv:1403.7112 \[hep-ph\]](#).
- [396] ATLAS Collaboration, G. Aad et al., *Search for anomalous production of prompt same-sign lepton pairs and pair-produced doubly charged Higgs bosons with  $\sqrt{s} = 8$  TeV  $pp$  collisions using the ATLAS detector*, *JHEP* **03** (2015) 041, [arXiv:1412.0237 \[hep-ex\]](#).
- [397] R. V. Harlander, S. Liebler, and H. Mantler, *SusHi: A program for the calculation of Higgs production in gluon fusion and bottom-quark annihilation in the Standard Model and the MSSM*, *Comput.Phys.Commun.* **184** (2013) 1605–1617, [arXiv:1212.3249 \[hep-ph\]](#).
- [398] A. Maiezza, M. Nemevsek, and F. Nesti, *Lepton Number Violation in Higgs Decay at LHC*, *Phys. Rev. Lett.* **115** (2015) 081802, [arXiv:1503.06834 \[hep-ph\]](#).
- [399] D. Rathlev, *Vector pair cross sections at 100 TeV*, 2015. <https://indico.cern.ch/event/437912/session/1/contribution/6/attachments/1166328/1681749/talk.pdf> (2015).
- [400] G. Bambhaniya, J. Chakraborty, J. Gluza, T. Jelinski, and R. Szafron, *Search for doubly charged Higgs bosons through vector boson fusion at the LHC and beyond*, *Phys. Rev.* **D92** (2015) no. 1, 015016, [arXiv:1504.03999 \[hep-ph\]](#).
- [401] G. Bambhaniya, J. Chakraborty, J. Gluza, M. Kordiaczynska, and R. Szafron, *Left-Right Symmetry and the Charged Higgs Bosons at the LHC*, *JHEP* **05** (2014) 033, [arXiv:1311.4144](#)

- [hep-ph].
- [402] G. Bambhaniya, J. Chakraborty, J. Gluza, T. Jelinski, and M. Kordiaczynska, *Lowest limits on the doubly charged Higgs boson masses in the minimal left-right symmetric model*, *Phys. Rev. D* **90** (2014) no. 9, 095003, [arXiv:1408.0774 \[hep-ph\]](#).
- [403] C. Degrande, C. Duhr, B. Fuks, D. Grellscheid, O. Mattelaer, and T. Reiter, *UFO - The Universal FeynRules Output*, *Comput. Phys. Commun.* **183** (2012) 1201–1214, [arXiv:1108.2040 \[hep-ph\]](#).
- [404] B. Dutta, R. Eusebi, Y. Gao, T. Ghosh, and T. Kamon, *Exploring the doubly charged Higgs boson of the left-right symmetric model using vector boson fusionlike events at the LHC*, *Phys. Rev. D* **90** (2014) 055015, [arXiv:1404.0685 \[hep-ph\]](#).
- [405] J. F. Gunion and H. E. Haber, *The CP conserving two Higgs doublet model: The Approach to the decoupling limit*, *Phys. Rev. D* **67** (2003) 075019, [arXiv:hep-ph/0207010 \[hep-ph\]](#).
- [406] M. Carena, I. Low, N. R. Shah, and C. E. M. Wagner, *Impersonating the Standard Model Higgs Boson: Alignment without Decoupling*, *JHEP* **04** (2014) 015, [arXiv:1310.2248 \[hep-ph\]](#).
- [407] P. S. Bhupal Dev and A. Pilaftsis, *Maximally Symmetric Two Higgs Doublet Model with Natural Standard Model Alignment*, *JHEP* **12** (2014) 024, [arXiv:1408.3405 \[hep-ph\]](#). [Erratum: *JHEP*11,147(2015)].
- [408] T. Han, I. Lewis, R. Ruiz, and Z.-g. Si, *Lepton Number Violation and  $W'$  Chiral Couplings at the LHC*, *Phys. Rev. D* **87** (2013) no. 3, 035011, [arXiv:1211.6447 \[hep-ph\]](#). [Erratum: *Phys. Rev. D*87,no.3,039906(2013)].
- [409] C.-Y. Chen, P. S. B. Dev, and R. N. Mohapatra, *Probing Heavy-Light Neutrino Mixing in Left-Right Seesaw Models at the LHC*, *Phys. Rev. D* **88** (2013) 033014, [arXiv:1306.2342 \[hep-ph\]](#).
- [410] P. S. B. Dev, D. Kim, and R. N. Mohapatra, *Disambiguating Seesaw Models using Invariant Mass Variables at Hadron Colliders*, [arXiv:1510.04328 \[hep-ph\]](#).
- [411] J.-M. Frere, T. Hambye, and G. Vertongen, *Is leptogenesis falsifiable at LHC?*, *JHEP* **01** (2009) 051, [arXiv:0806.0841 \[hep-ph\]](#).
- [412] F. F. Deppisch, J. Harz, and M. Hirsch, *Falsifying High-Scale Leptogenesis at the LHC*, *Phys. Rev. Lett.* **112** (2014) 221601, [arXiv:1312.4447 \[hep-ph\]](#).
- [413] P. S. B. Dev, C.-H. Lee, and R. N. Mohapatra, *Leptogenesis Constraints on the Mass of Right-handed Gauge Bosons*, *Phys. Rev. D* **90** (2014) no. 9, 095012, [arXiv:1408.2820 \[hep-ph\]](#).
- [414] P. S. B. Dev, C.-H. Lee, and R. N. Mohapatra, *TeV Scale Lepton Number Violation and Baryogenesis*, *J. Phys. Conf. Ser.* **631** (2015) no. 1, 012007, [arXiv:1503.04970 \[hep-ph\]](#).
- [415] M. Dhuria, C. Hati, R. Rangarajan, and U. Sarkar, *Falsifying leptogenesis for a TeV scale  $W_R^\pm$  at the LHC*, *Phys. Rev. D* **92** (2015) no. 3, 031701, [arXiv:1503.07198 \[hep-ph\]](#).
- [416] R. N. Mohapatra, *Limits on the Mass of the Right-handed Majorana Neutrino*, *Phys. Rev. D* **34** (1986) 909.
- [417] A. Maiezza, M. Nemevsek, and F. Nesti, *Perturbativity and mass scales of Left-Right Higgs bosons*, [arXiv:1603.00360 \[hep-ph\]](#).
- [418] S. Dimopoulos and G. Giudice, *Naturalness constraints in supersymmetric theories with nonuniversal soft terms*, *Phys. Lett.* **B357** (1995) 573–578, [arXiv:hep-ph/9507282 \[hep-ph\]](#).
- [419] A. G. Cohen, D. B. Kaplan, and A. E. Nelson, *The More minimal supersymmetric standard model*, *Phys. Lett.* **B388** (1996) 588–598, [arXiv:hep-ph/9607394 \[hep-ph\]](#).
- [420] M. Papucci, J. T. Ruderman, and A. Weiler, *Natural SUSY Endures*, *JHEP* **09** (2012) 035, [arXiv:1110.6926 \[hep-ph\]](#).
- [421] C. Brust, A. Katz, S. Lawrence, and R. Sundrum, *SUSY, the Third Generation and the LHC*,

- [JHEP 03 \(2012\) 103](#), [arXiv:1110.6670 \[hep-ph\]](#).
- [422] N. Craig, *The State of Supersymmetry after Run I of the LHC*, in *Beyond the Standard Model after the first run of the LHC Arcetri, Florence, Italy, May 20-July 12, 2013*. 2013. [arXiv:1309.0528 \[hep-ph\]](#). <http://inspirehep.net/record/1252552/files/arXiv:1309.0528.pdf>.
- [423] K. Blum, R. T. D’Agnolo, and J. Fan, *Natural SUSY Predicts: Higgs Couplings*, [JHEP 01 \(2013\) 057](#), [arXiv:1206.5303 \[hep-ph\]](#).
- [424] J. R. Espinosa, C. Grojean, V. Sanz, and M. Trott, *NSUSY fits*, [JHEP 12 \(2012\) 077](#), [arXiv:1207.7355 \[hep-ph\]](#).
- [425] A. Djouadi, V. Driesen, W. Hollik, and J. I. Illana, *The Coupling of the lightest SUSY Higgs boson to two photons in the decoupling regime*, [Eur. Phys. J. C1 \(1998\) 149–162](#), [arXiv:hep-ph/9612362 \[hep-ph\]](#).
- [426] M. A. Diaz and P. Fileviez Perez, *Can we distinguish between  $h(SM)$  and  $h_0$  in split supersymmetry?*, [J. Phys. G31 \(2005\) 563–569](#), [arXiv:hep-ph/0412066 \[hep-ph\]](#).
- [427] L. J. Hall, D. Pinner, and J. T. Ruderman, *A Natural SUSY Higgs Near 126 GeV*, [JHEP 04 \(2012\) 131](#), [arXiv:1112.2703 \[hep-ph\]](#).
- [428] T. Gherghetta, B. von Harling, A. D. Medina, and M. A. Schmidt, *The price of being SM-like in SUSY*, [JHEP 04 \(2014\) 180](#), [arXiv:1401.8291 \[hep-ph\]](#).
- [429] A. Katz, M. Reece, and A. Sajjad, *Naturalness,  $b \rightarrow s\gamma$ , and SUSY heavy Higgses*, [JHEP 10 \(2014\) 102](#), [arXiv:1406.1172 \[hep-ph\]](#).
- [430] R. Contino, Y. Nomura, and A. Pomarol, *Higgs as a holographic pseudoGoldstone boson*, [Nucl.Phys. B671 \(2003\) 148–174](#), [arXiv:hep-ph/0306259 \[hep-ph\]](#).
- [431] K. Agashe, R. Contino, and A. Pomarol, *The Minimal composite Higgs model*, [Nucl.Phys. B719 \(2005\) 165–187](#), [arXiv:hep-ph/0412089 \[hep-ph\]](#).
- [432] K. Agashe and R. Contino, *The Minimal composite Higgs model and electroweak precision tests*, [Nucl. Phys. B742 \(2006\) 59–85](#), [arXiv:hep-ph/0510164 \[hep-ph\]](#).
- [433] R. Contino, L. Da Rold, and A. Pomarol, *Light custodians in natural composite Higgs models*, [Phys.Rev. D75 \(2007\) 055014](#), [arXiv:hep-ph/0612048 \[hep-ph\]](#).
- [434] G. Panico, M. Serone, and A. Wulzer, *A Model of electroweak symmetry breaking from a fifth dimension*, [Nucl. Phys. B739 \(2006\) 186–207](#), [arXiv:hep-ph/0510373 \[hep-ph\]](#).
- [435] R. Barbieri, B. Bellazzini, V. S. Rychkov, and A. Varagnolo, *The Higgs boson from an extended symmetry*, [Phys. Rev. D76 \(2007\) 115008](#), [arXiv:0706.0432 \[hep-ph\]](#).
- [436] R. Contino, *The Higgs as a Composite Nambu-Goldstone Boson*, in *Physics of the large and the small, TASI 09, proceedings of the Theoretical Advanced Study Institute in Elementary Particle Physics, Boulder, Colorado, USA, 1-26 June 2009*, pp. 235–306. 2011. [arXiv:1005.4269 \[hep-ph\]](#). <http://inspirehep.net/record/856065/files/arXiv:1005.4269.pdf>.
- [437] D. B. Kaplan, *Flavor at SSC energies: A New mechanism for dynamically generated fermion masses*, [Nucl. Phys. B365 \(1991\) 259–278](#).
- [438] R. Contino, T. Kramer, M. Son, and R. Sundrum, *Warped/composite phenomenology simplified*, [JHEP 05 \(2007\) 074](#), [arXiv:hep-ph/0612180 \[hep-ph\]](#).
- [439] B. Gripaios, A. Pomarol, F. Riva, and J. Serra, *Beyond the Minimal Composite Higgs Model*, [JHEP 04 \(2009\) 070](#), [arXiv:0902.1483 \[hep-ph\]](#).
- [440] J. Mrazek, A. Pomarol, R. Rattazzi, M. Redi, J. Serra, and A. Wulzer, *The Other Natural Two Higgs Doublet Model*, [Nucl. Phys. B853 \(2011\) 1–48](#), [arXiv:1105.5403 \[hep-ph\]](#).
- [441] M. Chala,  *$h \rightarrow \gamma\gamma$  excess and Dark Matter from Composite Higgs Models*, [JHEP 01 \(2013\) 122](#), [arXiv:1210.6208 \[hep-ph\]](#).
- [442] M. Frigerio, A. Pomarol, F. Riva, and A. Urbano, *Composite Scalar Dark Matter*, [JHEP 07 \(2012\) 015](#), [arXiv:1204.2808 \[hep-ph\]](#).

- [443] D. Marzocca and A. Urbano, *Composite Dark Matter and LHC Interplay*, **JHEP** **07** (2014) 107, [arXiv:1404.7419 \[hep-ph\]](#).
- [444] N. Fonseca, R. Z. Funchal, A. Lessa, and L. Lopez-Honorez, *Dark Matter Constraints on Composite Higgs Models*, **JHEP** **06** (2015) 154, [arXiv:1501.05957 \[hep-ph\]](#).
- [445] A. Carmona and M. Chala, *Composite Dark Sectors*, **JHEP** **06** (2015) 105, [arXiv:1504.00332 \[hep-ph\]](#).
- [446] M. Kim, S. J. Lee, and A. Parolini, *WIMP Dark Matter in Composite Higgs Models and the Dilaton Portal*, [arXiv:1602.05590 \[hep-ph\]](#).
- [447] T. Golling et al., *Physics at a 100 TeV pp collider: beyond the Standard Model phenomena*, [arXiv:1606.00947 \[hep-ph\]](#).
- [448] A. Thamm, R. Torre, and A. Wulzer, *Future tests of Higgs compositeness: direct vs indirect*, **JHEP** **07** (2015) 100, [arXiv:1502.01701 \[hep-ph\]](#).
- [449] A. Andreazza et al., *What Next: White Paper of the INFN-CSNI*, *Frascati Phys. Ser.* **60** (2015) 1–302. [[Inspire](#)].
- [450] CMS Collaboration, *CMS at the High-Energy Frontier: Contribution to the Update of the European Strategy for Particle Physics*, CMS-NOTE-2012-006. CERN-CMS-NOTE-2012-006, CERN, Geneva, Oct, 2012. <https://cds.cern.ch/record/1494600>.
- [451] *Projections for measurements of Higgs boson signal strengths and coupling parameters with the ATLAS detector at a HL-LHC*, ATL-PHYS-PUB-2014-016, CERN, Geneva, Oct, 2014. <http://cds.cern.ch/record/1956710>.
- [452] B. Bellazzini, C. Csaki, and J. Serra, *Composite Higgses*, **Eur. Phys. J.** **C74** (2014) no. 5, 2766, [arXiv:1401.2457 \[hep-ph\]](#).
- [453] K. Agashe, R. Contino, and R. Sundrum, *Top compositeness and precision unification*, **Phys. Rev. Lett.** **95** (2005) 171804, [arXiv:hep-ph/0502222 \[hep-ph\]](#).
- [454] J. Barnard, T. Gherghetta, T. S. Ray, and A. Spray, *The Unnatural Composite Higgs*, **JHEP** **01** (2015) 067, [arXiv:1409.7391 \[hep-ph\]](#).
- [455] J. Barnard, P. Cox, T. Gherghetta, and A. Spray, *Long-Lived, Colour-Triplet Scalars from Unnaturalness*, [arXiv:1510.06405 \[hep-ph\]](#).
- [456] N. Craig, C. Englert, and M. McCullough, *New Probe of Naturalness*, **Phys. Rev. Lett.** **111** (2013) no. 12, 121803, [arXiv:1305.5251 \[hep-ph\]](#).
- [457] N. Arkani-Hamed, A. G. Cohen, and H. Georgi, *Electroweak symmetry breaking from dimensional deconstruction*, **Phys.Lett.** **B513** (2001) 232–240, [arXiv:hep-ph/0105239 \[hep-ph\]](#).
- [458] N. Arkani-Hamed, A. G. Cohen, T. Gregoire, and J. G. Wacker, *Phenomenology of electroweak symmetry breaking from theory space*, **JHEP** **08** (2002) 020, [arXiv:hep-ph/0202089 \[hep-ph\]](#).
- [459] N. Arkani-Hamed, A. Cohen, E. Katz, A. Nelson, T. Gregoire, et al., *The Minimal moose for a little Higgs*, **JHEP** **0208** (2002) 021, [arXiv:hep-ph/0206020 \[hep-ph\]](#).
- [460] M. Schmaltz and D. Tucker-Smith, *Little Higgs review*, **Ann.Rev.Nucl.Part.Sci.** **55** (2005) 229–270, [arXiv:hep-ph/0502182 \[hep-ph\]](#).
- [461] M. J. Strassler and K. M. Zurek, *Echoes of a hidden valley at hadron colliders*, **Phys.Lett.** **B651** (2007) 374–379, [arXiv:hep-ph/0604261 \[hep-ph\]](#).
- [462] M. J. Strassler, *Possible effects of a hidden valley on supersymmetric phenomenology*, [arXiv:hep-ph/0607160 \[hep-ph\]](#).
- [463] T. Han, Z. Si, K. M. Zurek, and M. J. Strassler, *Phenomenology of hidden valleys at hadron colliders*, **JHEP** **0807** (2008) 008, [arXiv:0712.2041 \[hep-ph\]](#).
- [464] I. G. García, R. Lasenby, and J. March-Russell, *Twin Higgs WIMP Dark Matter*,

- [arXiv:1505.07109 \[hep-ph\]](#).
- [465] N. Craig and A. Katz, *The Fraternal WIMP Miracle*, [arXiv:1505.07113 \[hep-ph\]](#).
- [466] N. Craig, A. Katz, M. Strassler, and R. Sundrum, *Naturalness in the Dark at the LHC*, [arXiv:1501.05310 \[hep-ph\]](#).
- [467] D. Poland and J. Thaler, *The Dark Top*, *JHEP* **11** (2008) 083, [arXiv:0808.1290 \[hep-ph\]](#).
- [468] B. Batell and M. McCullough, *Neutrino Masses from Neutral Top Partners*, [arXiv:1504.04016 \[hep-ph\]](#).
- [469] P. Batra and Z. Chacko, *A Composite Twin Higgs Model*, *Phys.Rev.* **D79** (2009) 095012, [arXiv:0811.0394 \[hep-ph\]](#).
- [470] R. Barbieri, D. Greco, R. Rattazzi, and A. Wulzer, *The Composite Twin Higgs scenario*, [arXiv:1501.07803 \[hep-ph\]](#).
- [471] M. Low, A. Tesi, and L.-T. Wang, *Twin Higgs mechanism and a composite Higgs boson*, *Phys.Rev.* **D91** (2015) no. 9, 095012, [arXiv:1501.07890 \[hep-ph\]](#).
- [472] M. Geller and O. Telem, *A Holographic Twin Higgs Model*, *Phys.Rev.Lett.* **114** (2015) no. 19, 191801, [arXiv:1411.2974 \[hep-ph\]](#).
- [473] N. Craig and K. Howe, *Doubling down on naturalness with a supersymmetric twin Higgs*, *JHEP* **1403** (2014) 140, [arXiv:1312.1341 \[hep-ph\]](#).
- [474] N. Craig and H. K. Lou, *Scherk-Schwarz Supersymmetry Breaking in 4D*, *JHEP* **1412** (2014) 184, [arXiv:1406.4880 \[hep-ph\]](#).
- [475] S. Chang, L. J. Hall, and N. Weiner, *A Supersymmetric twin Higgs*, *Phys. Rev.* **D75** (2007) 035009, [arXiv:hep-ph/0604076 \[hep-ph\]](#).
- [476] N. Craig, S. Knapen, P. Longhi, and M. Strassler, *The Vector-like Twin Higgs*, [arXiv:1601.07181 \[hep-ph\]](#).
- [477] R. Harnik, K. Howe, and J. Kearney, *Tadpole-Induced Electroweak Symmetry Breaking and pNGB Higgs Models*, [arXiv:1603.03772 \[hep-ph\]](#).
- [478] P. Batra, A. Delgado, D. E. Kaplan, and T. M. P. Tait, *The Higgs mass bound in gauge extensions of the minimal supersymmetric standard model*, *JHEP* **02** (2004) 043, [arXiv:hep-ph/0309149 \[hep-ph\]](#).
- [479] T. Cohen, N. Craig, H. K. Lou, and D. Pinner, *Folded Supersymmetry with a Twist*, [arXiv:1508.05396 \[hep-ph\]](#).
- [480] G. Burdman, Z. Chacko, R. Harnik, L. de Lima, and C. B. Verhaaren, *Colorless Top Partners, a 125 GeV Higgs, and the Limits on Naturalness*, *Phys.Rev.* **D91** (2015) 055007, [arXiv:1411.3310 \[hep-ph\]](#).
- [481] TLEP Design Study Working Group Collaboration, M. Bicer et al., *First Look at the Physics Case of TLEP*, *JHEP* **01** (2014) 164, [arXiv:1308.6176 \[hep-ex\]](#).
- [482] C. J. Morningstar and M. J. Peardon, *The Glueball spectrum from an anisotropic lattice study*, *Phys.Rev.* **D60** (1999) 034509, [arXiv:hep-lat/9901004 \[hep-lat\]](#).
- [483] J. E. Juknevich, *Pure-gluon hidden valleys through the Higgs portal*, *JHEP* **1008** (2010) 121, [arXiv:0911.5616 \[hep-ph\]](#).
- [484] J. Juknevich, *Phenomenology of pure-gauge hidden valleys at Hadron colliders*. PhD thesis, Rutgers U., Piscataway. <https://rucore.libraries.rutgers.edu/rutgers-lib/30125/>.
- [485] C. Csaki, E. Kuflik, S. Lombardo, and O. Slone, *Searching for displaced Higgs boson decays*, *Phys. Rev.* **D92** (2015) no. 7, 073008, [arXiv:1508.01522 \[hep-ph\]](#).
- [486] Z. Chacko, D. Curtin, and C. B. Verhaaren, *A Quirky Probe of Neutral Naturalness*, [arXiv:1512.05782 \[hep-ph\]](#).
- [487] J. Kang and M. A. Luty, *Macroscopic Strings and 'Quirks' at Colliders*, *JHEP* **0911** (2009) 065, [arXiv:0805.4642 \[hep-ph\]](#).

- [488] G. Burdman, Z. Chacko, H.-S. Goh, R. Harnik, and C. A. Krenke, *The Quirky Collider Signals of Folded Supersymmetry*, *Phys.Rev.* **D78** (2008) 075028, [arXiv:0805.4667 \[hep-ph\]](#).
- [489] R. Harnik and T. Wizansky, *Signals of New Physics in the Underlying Event*, *Phys.Rev.* **D80** (2009) 075015, [arXiv:0810.3948 \[hep-ph\]](#).
- [490] R. Harnik, G. D. Kribs, and A. Martin, *Quirks at the Tevatron and Beyond*, *Phys.Rev.* **D84** (2011) 035029, [arXiv:1106.2569 \[hep-ph\]](#).
- [491] H.-C. Cheng, S. Jung, E. Salvioni, and Y. Tsai, *Exotic Quarks in Twin Higgs Models*, *JHEP* **03** (2016) 074, [arXiv:1512.02647 \[hep-ph\]](#).
- [492] I. F. Ginzburg and M. Krawczyk, *Symmetries of two Higgs doublet model and CP violation*, *Phys. Rev.* **D72** (2005) 115013, [arXiv:hep-ph/0408011 \[hep-ph\]](#).
- [493] N. Craig, J. Galloway, and S. Thomas, *Searching for Signs of the Second Higgs Doublet*, [arXiv:1305.2424 \[hep-ph\]](#).
- [494] A. Delgado, G. Nardini, and M. Quiros, *A Light Supersymmetric Higgs Sector Hidden by a Standard Model-like Higgs*, *JHEP* **07** (2013) 054, [arXiv:1303.0800 \[hep-ph\]](#).
- [495] N. Craig, F. D’Eramo, P. Draper, S. Thomas, and H. Zhang, *The Hunt for the Rest of the Higgs Bosons*, *JHEP* **06** (2015) 137, [arXiv:1504.04630 \[hep-ph\]](#).
- [496] M. Spira, *HIGLU: A program for the calculation of the total Higgs production cross-section at hadron colliders via gluon fusion including QCD corrections*, [arXiv:hep-ph/9510347 \[hep-ph\]](#).
- [497] R. V. Harlander and W. B. Kilgore, *Higgs boson production in bottom quark fusion at next-to-next-to leading order*, *Phys.Rev.* **D68** (2003) 013001, [arXiv:hep-ph/0304035 \[hep-ph\]](#).
- [498] R. V. Harlander and W. B. Kilgore, *Next-to-next-to-leading order Higgs production at hadron colliders*, *Phys.Rev.Lett.* **88** (2002) 201801, [arXiv:hep-ph/0201206 \[hep-ph\]](#).
- [499] T. Plehn, *Charged Higgs boson production in bottom gluon fusion*, *Phys.Rev.* **D67** (2003) 014018, [arXiv:hep-ph/0206121 \[hep-ph\]](#).
- [500] W. Beenakker, R. Hopker, and M. Spira, *PROSPINO: A Program for the production of supersymmetric particles in next-to-leading order QCD*, [arXiv:hep-ph/9611232 \[hep-ph\]](#).
- [501] ATLAS Collaboration, G. Aad et al., *Search for neutral Higgs bosons of the minimal supersymmetric standard model in pp collisions at  $\sqrt{s} = 8$  TeV with the ATLAS detector*, *JHEP* **1411** (2014) 056, [arXiv:1409.6064 \[hep-ex\]](#).
- [502] CMS Collaboration, C. Collaboration, *Search for charged Higgs bosons with the  $H^+$  to tau nu decay channel in the fully hadronic final state at  $\sqrt{s} = 8$  TeV*, .
- [503] CMS Collaboration, S. Chatrchyan et al., *Search for a Higgs boson decaying into a b-quark pair and produced in association with b quarks in proton-proton collisions at 7 TeV*, *Phys.Lett.* **B722** (2013) 207–232, [arXiv:1302.2892 \[hep-ex\]](#).
- [504] ATLAS Collaboration, G. Aad et al., *Search for Higgs bosons in Two-Higgs-Doublet models in the  $H \rightarrow WW \rightarrow e\nu\mu\nu$  channel with the ATLAS detector*, ATLAS-CONF-2013-027, CERN, Geneva, Mar, 2013.
- [505] CMS Collaboration, V. Khachatryan et al., *Searches for heavy Higgs bosons in two-Higgs-doublet models and for t to ch decay using multilepton and diphoton final states in pp collisions at 8 TeV*, *Phys.Rev.* **D90** (2014) no. 11, 112013, [arXiv:1410.2751 \[hep-ex\]](#).
- [506] G. Aad et al., *Search for charged Higgs bosons in the  $\tau$ +jets final state with pp collision data recorded at  $\sqrt{s} = 8$  TeV with the ATLAS experiment*, ATLAS-CONF-2013-090, CERN, Geneva, Aug, 2013.
- [507] CMS Collaboration, S. Chatrchyan et al., *Higgs to tau tau (MSSM)*, CMS-PAS-HIG-13-021, CERN, Geneva, 2013.

- [508] D. Dicus, A. Stange, and S. Willenbrock, *Higgs decay to top quarks at hadron colliders*, *Phys. Lett.* **B333** (1994) 126–131, [arXiv:hep-ph/9404359](#) [hep-ph].
- [509] N. Craig, J. Hajer, Y.-Y. Li, T. Liu, and H. Zhang, *Heavy Higgs Bosons at Low  $\tan\beta$ : from the LHC to 100 TeV*, [arXiv:1605.08744](#) [hep-ph].
- [510] B. Coleppa, F. Kling, and S. Su, *Exotic Higgs Decay via AZ/HZ Channel: a Snowmass Whitepaper*, [arXiv:1308.6201](#) [hep-ph].
- [511] B. Coleppa, F. Kling, and S. Su, *Exotic Decays Of A Heavy Neutral Higgs Through HZ/AZ Channel*, *JHEP* **1409** (2014) 161, [arXiv:1404.1922](#) [hep-ph].
- [512] E. Brownson, N. Craig, U. Heintz, G. Kukartsev, M. Narain, et al., *Heavy Higgs Scalars at Future Hadron Colliders (A Snowmass Whitepaper)*, [arXiv:1308.6334](#) [hep-ex].
- [513] B. Coleppa, F. Kling, and S. Su, *Charged Higgs search via  $AW^\pm/HW^\pm$  channel*, *JHEP* **1412** (2014) 148, [arXiv:1408.4119](#) [hep-ph].
- [514] F. Kling, A. Pyarelal, and S. Su, *Light Charged Higgs Bosons to AW/HW via Top Decay*, *JHEP* **11** (2015) 051, [arXiv:1504.06624](#) [hep-ph].
- [515] T. Li and S. Su, *Exotic Higgs Decay via Charged Higgs*, *JHEP* **11** (2015) 068, [arXiv:1504.04381](#) [hep-ph].
- [516] U. Maitra, B. Mukhopadhyaya, S. Nandi, S. K. Rai, and A. Shivaji, *Searching for an elusive charged Higgs boson at the Large Hadron Collider*, *Phys.Rev.* **D89** (2014) no. 5, 055024, [arXiv:1401.1775](#) [hep-ph].
- [517] L. Basso, A. Lipniacka, F. Mahmoudi, S. Moretti, P. Osland, et al., *Probing the charged Higgs boson at the LHC in the CP-violating type-II 2HDM*, *JHEP* **1211** (2012) 011, [arXiv:1205.6569](#) [hep-ph].
- [518] R. Dermisek, J. P. Hall, E. Lunghi, and S. Shin, *A New Avenue to Charged Higgs Discovery in Multi-Higgs Models*, *JHEP* **1404** (2014) 140, [arXiv:1311.7208](#) [hep-ph].
- [519] B. Mohn, N. Gollub, and K. A. Assamagan, *The ATLAS discovery potential for a heavy Charged Higgs boson in a large mass splitting MSSM scenario*, ATL-PHYS-PUB-2005-017. ATL-COM-PHYS-2005-021. CERN-ATL-COM-PHYS-2005-021, CERN, Geneva, 2005.
- [520] K. Assamagan, *Signature of the charged Higgs decay  $H^{+-}$  to  $Wh_0$  with the ATLAS detector*, *Acta Phys.Polon.* **B31** (2000) 881–893.
- [521] K. A. Assamagan, Y. Coadou, and A. Deandrea, *ATLAS discovery potential for a heavy charged Higgs boson*, *Eur.Phys.J.direct* **C4** (2002) 9, [arXiv:hep-ph/0203121](#) [hep-ph].
- [522] D. Eriksson, J. Rathsman, and O. Stal, *2HDMC: Two-Higgs-Doublet Model Calculator Physics and Manual*, *Comput.Phys.Commun.* **181** (2010) 189–205, [arXiv:0902.0851](#) [hep-ph].
- [523] ATLAS Collaboration, G. Aad et al., *Searches for Higgs boson pair production in the  $hh \rightarrow bb\tau\tau, \gamma\gamma WW^*, \gamma\gamma bb, bbbb$  channels with the ATLAS detector*, [arXiv:1509.04670](#) [hep-ex].
- [524] CMS Collaboration, *Search for a pseudoscalar boson  $A$  decaying into a  $Z$  and an  $h$  boson in the  $llbb$  final state*, CMS-PAS-HIG-14-011, CERN, Geneva, 2014. <https://cds.cern.ch/record/1969698>.
- [525] CMS Collaboration, *2HDM scenario,  $H$  to  $hh$  and  $A$  to  $Zh$* , CMS-PAS-HIG-13-025, CERN, Geneva, 2013. <https://cds.cern.ch/record/1637776>.
- [526] ATLAS Collaboration, G. Aad et al., *Search for a CP-odd Higgs boson decaying to  $Zh$  in  $pp$  collisions at  $\sqrt{s} = 8$  TeV with the ATLAS detector*, *Phys.Lett.* **B744** (2015) 163–183, [arXiv:1502.04478](#) [hep-ex].
- [527] CMS Collaboration, *Search for  $H/A$  decaying into  $Z+A/H$ , with  $Z$  to  $ll$  and  $A/H$  to fermion pair*, CMS-PAS-HIG-15-001, CERN, Geneva, 2015. <https://cds.cern.ch/record/2014119>.
- [528] D. Buttazzo, F. Sala, and A. Tesi, *Singlet-like Higgs bosons at present and future colliders*, *JHEP*

- 11** (2015) 158, [arXiv:1505.05488 \[hep-ph\]](#).
- [529] T. Gherghetta, B. von Harling, A. D. Medina, and M. A. Schmidt, *The Scale-Invariant NMSSM and the 126 GeV Higgs Boson*, *JHEP* **02** (2013) 032, [arXiv:1212.5243 \[hep-ph\]](#).
- [530] R. Barbieri, D. Buttazzo, K. Kannike, F. Sala, and A. Tesi, *Exploring the Higgs sector of a most natural NMSSM*, *Phys. Rev.* **D87** (2013) no. 11, 115018, [arXiv:1304.3670 \[hep-ph\]](#).
- [531] R. Barbieri, D. Buttazzo, K. Kannike, F. Sala, and A. Tesi, *One or more Higgs bosons?*, *Phys. Rev.* **D88** (2013) 055011, [arXiv:1307.4937 \[hep-ph\]](#).
- [532] F. Sala, *Higgs and flavour as doors to new physics*, [arXiv:1509.08655 \[hep-ph\]](#).
- [533] D. Buttazzo, *Natural scalars in the NMSSM*, in *Proceedings, 49th Rencontres de Moriond on Electroweak Interactions and Unified Theories*, pp. 369–374. 2014. [arXiv:1405.3321 \[hep-ph\]](#). <http://inspirehep.net/record/1296087/files/arXiv:1405.3321.pdf>.
- [534] S. F. King, M. Mühlleitner, R. Nevzorov, and K. Walz, *Discovery Prospects for NMSSM Higgs Bosons at the High-Energy Large Hadron Collider*, *Phys. Rev.* **D90** (2014) no. 9, 095014, [arXiv:1408.1120 \[hep-ph\]](#).
- [535] M. Carena, H. E. Haber, I. Low, N. R. Shah, and C. E. M. Wagner, *On the Alignment Limit of the NMSSM Higgs Sector*, [arXiv:1510.09137 \[hep-ph\]](#).



## Chapter 3: Beyond the Standard Model Phenomena

### Editors:

*T. Golling*<sup>1</sup>, *M. Hance*<sup>2</sup>, *P. Harris*<sup>3</sup>, *M.L. Mangano*<sup>4</sup>, *M. McCullough*<sup>4</sup>, *F. Moortgat*<sup>3</sup>, *P. Schwaller*<sup>5</sup>, *R. Torre*<sup>6</sup>,

### Contributors:

*P. Agrawal*<sup>7</sup>, *D.S.M. Alves*<sup>8,9</sup>, *S. Antusch*<sup>10,11</sup>, *A. Arbey*<sup>4,12</sup>, *B. Auerbach*<sup>13</sup>, *G. Bambhaniya*<sup>14</sup>, *M. Battaglia*<sup>2</sup>, *M. Bauer*<sup>15</sup>, *P.S. Bhupal Dev*<sup>16,17</sup>, *A. Boveia*<sup>3</sup>, *J. Bramante*<sup>18</sup>, *O. Buchmueller*<sup>19</sup>, *M. Buschmann*<sup>20</sup>, *J. Chakraborty*<sup>21</sup>, *M. Chala*<sup>5</sup>, *S. Chekanov*<sup>13</sup>, *C.-Y. Chen*<sup>22,23</sup>, *H.-C. Cheng*<sup>24</sup>, *M. Cirelli*<sup>25</sup>, *M. Citron*<sup>19</sup>, *T. Cohen*<sup>26</sup>, *N. Craig*<sup>27</sup>, *D. Curtin*<sup>28</sup>, *R.T. D'Agnolo*<sup>29</sup>, *C. Doglioni*<sup>30</sup>, *J.A. Dror*<sup>31</sup>, *T. du Pree*<sup>3</sup>, *D. Dylewsky*<sup>32</sup>, *J. Ellis*<sup>33,4</sup>, *S.A.R. Ellis*<sup>34</sup>, *R. Essig*<sup>35</sup>, *J.J. Fan*<sup>36</sup>, *M. Farina*<sup>37</sup>, *J.L. Feng*<sup>38</sup>, *P.J. Fox*<sup>39</sup>, *J. Galloway*<sup>8</sup>, *G. Giudice*<sup>4</sup>, *J. Gluza*<sup>40</sup>, *S. Gori*<sup>23,41</sup>, *S. Guha*<sup>42</sup>, *K. Hahn*<sup>43</sup>, *T. Han*<sup>44,45</sup>, *C. Helsen*<sup>3</sup>, *A. Henriques*<sup>3</sup>, *S. Iwamoto*<sup>46</sup>, *T. Jeliński*<sup>40</sup>, *S. Jung*<sup>45,47</sup>, *F. Kahlhoefer*<sup>5</sup>, *V.V. Khoze*<sup>48</sup>, *D. Kim*<sup>49</sup>, *J. Kopp*<sup>20</sup>, *A. Kotwal*<sup>50</sup>, *M. Krämer*<sup>51</sup>, *J.M. Lindert*<sup>52</sup>, *J. Liu*<sup>20</sup>, *H.K. Lou*<sup>9</sup>, *J. Love*<sup>13</sup>, *M. Low*<sup>29</sup>, *P.A.N. Machado*<sup>54</sup>, *F. Mahmoudi*<sup>4,12</sup>, *J. Marrouche*<sup>19</sup>, *A. Martin*<sup>18</sup>, *K. Mohan*<sup>55</sup>, *R.N. Mohapatra*<sup>28</sup>, *G. Nardini*<sup>56</sup>, *K.A. Olive*<sup>57</sup>, *B. Ostdiek*<sup>26</sup>, *G. Panico*<sup>58</sup>, *T. Plehn*<sup>15</sup>, *J. Proudfoot*<sup>13</sup>, *Z. Qian*<sup>44</sup>, *M. Reece*<sup>7</sup>, *T. Rizzo*<sup>47</sup>, *C. Roskas*<sup>60</sup>, *J. Ruderman*<sup>8</sup>, *R. Ruiz*<sup>48</sup>, *F. Sala*<sup>25</sup>, *E. Salvioni*<sup>24</sup>, *P. Saraswat*<sup>28,61</sup>, *T. Schell*<sup>15</sup>, *K. Schmidt-Hoberg*<sup>5</sup>, *J. Serra*<sup>4</sup>, *Y. Shadmi*<sup>46</sup>, *J. Shelton*<sup>61</sup>, *C. Solans*<sup>3</sup>, *M. Spannowsky*<sup>48</sup>, *T. Srivastava*<sup>21</sup>, *D. Stolarski*<sup>62</sup>, *R. Szafron*<sup>63</sup>, *M. Taoso*<sup>54</sup>, *S. Tarem*<sup>46</sup>, *A. Thalapillil*<sup>37</sup>, *A. Thamm*<sup>20</sup>, *Y. Tsai*<sup>24</sup>, *C. Verhaaren*<sup>64</sup>, *N. Vignaroli*<sup>55,65</sup>, *J.R. Walsh*<sup>53,66</sup>, *L.T. Wang*<sup>67,68</sup>, *C. Weiland*<sup>48</sup>, *J. Wells*<sup>34</sup>, *C. Williams*<sup>69</sup>, *A. Wulzer*<sup>3</sup>, *W. Xue*<sup>70</sup>, *F. Yu*<sup>20</sup>, *B. Zheng*<sup>34</sup>, *J. Zheng*<sup>57</sup>

<sup>1</sup> University of Geneva, Geneva, Switzerland

<sup>2</sup> University of California, Santa Cruz, Santa Cruz, CA, USA

<sup>3</sup> CERN, EP Department, CH-1211 Geneva, Switzerland

<sup>4</sup> CERN, TH Department, CH-1211 Geneva, Switzerland

<sup>5</sup> DESY, Notkestr. 85, D-22607 Hamburg, Germany

<sup>6</sup> Institut de Théorie des Phénomènes Physiques, EPFL, CH1015 Lausanne, Switzerland

<sup>7</sup> Department of Physics, Harvard University, Cambridge, MA 02138, USA

<sup>8</sup> Center for Cosmology and Particle Physics, Department of Physics, New York University, New York, NY 10003, USA

<sup>9</sup> Department of Physics, Princeton University, Princeton, NJ 08544, USA

<sup>10</sup> Department of Physics, University of Basel, Klingelbergstr. 82, CH-4056 Basel, Switzerland

<sup>11</sup> Max-Planck-Institut für Physik, Föhringer Ring 6, D-80805 München, Germany

<sup>12</sup> Univ Lyon, Univ Lyon 1, ENS de Lyon, CNRS, Centre de Recherche Astrophysique de Lyon UMR5574, F-69230 Saint-Genis-Laval, France

<sup>13</sup> High Energy Physics Division, Argonne National Laboratory, Argonne IL, USA

<sup>14</sup> Theoretical Physics Division, Physical Research Laboratory, Ahmedabad-380009, India

<sup>15</sup> Institut für Theoretische Physik, Universität Heidelberg, Germany

<sup>16</sup> Physik-Department T30d, Technische Universität München, James-Franck-Strasse 1, D-85748 Garching, Germany

<sup>17</sup> Max-Planck-Institut für Kernphysik, Saupfercheckweg 1, D-69117 Heidelberg, Germany

<sup>18</sup> Department of Physics, University of Notre Dame, IN, USA

<sup>19</sup> High Energy Physics Group, Blackett Lab., Imperial College, Prince Consort Road, London SW7 2AZ, UK

- <sup>20</sup> PRISMA Cluster of Excellence and Mainz Institute for Theoretical Physics, Johannes Gutenberg University, 55099 Mainz, Germany
- <sup>21</sup> Department of Physics, Indian Institute of Technology, Kanpur-208016, India
- <sup>22</sup> Department of Physics and Astronomy, University of Victoria, Victoria, BC V8P 5C2, Canada
- <sup>23</sup> Perimeter Institute for Theoretical Physics, 31 Caroline St. N, Waterloo, Ontario, Canada
- <sup>24</sup> Department of Physics, University of California, Davis, Davis, CA 95616, USA
- <sup>25</sup> LPTHE, CNRS, UMR 7589, 4 Place Jussieu, F-75252, Paris, France
- <sup>26</sup> Institute of Theoretical Science, University of Oregon, Eugene, OR 97403
- <sup>27</sup> University of California, Santa Barbara, CA, USA
- <sup>28</sup> Maryland Center for Fundamental Physics and Department of Physics, University of Maryland, College Park, MD 20742, USA
- <sup>29</sup> School of Natural Sciences, Institute for Advanced Study, Princeton, NJ 08540, USA
- <sup>30</sup> Fysiska institutionen, Lunds universitet, Lund, Sweden
- <sup>31</sup> LEPP, Department of Physics, Cornell University, Newman Laboratory, Ithaca, NY 14853, USA
- <sup>32</sup> Department of Physics, University of Washington, Seattle WA, USA
- <sup>33</sup> Theoretical Particle Physics and Cosmology Group, Dept. of Physics, King's College London, London WC2R 2LS, UK
- <sup>34</sup> Michigan Center for Theoretical Physics (MCTP), Physics Department, University of Michigan, Ann Arbor, MI 48104 USA
- <sup>35</sup> C.N. Yang Institute for Theoretical Physics, Stony Brook University, Stony Brook, NY 11794, USA
- <sup>36</sup> Department of Physics, Brown University, Providence, RI 02912, USA
- <sup>37</sup> New High Energy Theory Center, Department of Physics, Rutgers University, 136 Frelinghuisen Road, Piscataway, NJ 08854, USA
- <sup>38</sup> Department of Physics and Astronomy, University of California, Irvine, CA 92697, USA
- <sup>39</sup> Theoretical Physics Department, Fermilab, Batavia, IL 60510, USA
- <sup>40</sup> Institute of Physics, University of Silesia, Uniwersytecka 4, 40-007 Katowice, Poland
- <sup>41</sup> Department of Physics, University of Cincinnati, Cincinnati, Ohio 45221, USA
- <sup>42</sup> Mitchell Physics Building, Texas A&M, College Station, TX 77843, USA
- <sup>43</sup> Northwestern University, Evanston IL, USA
- <sup>44</sup> Pittsburgh Particle Physics, Astronomy, and Cosmology Center (Pitt-PACC) Department of Physics and Astronomy, University of Pittsburgh, Pittsburgh, PA 15260, USA
- <sup>45</sup> Korea Institute for Advanced Study (KIAS), Seoul 130-012, Korea
- <sup>46</sup> Physics Department, Technion, Israel Institute of Technology, Haifa 32000, Israel
- <sup>47</sup> SLAC National Accelerator Laboratory, Menlo Park, CA 94025, USA
- <sup>48</sup> Institute for Particle Physics Phenomenology (IPPP), Department of Physics, Durham University, Durham, DH1 3LE, UK
- <sup>49</sup> Department of Physics, University of Florida, Gainesville, FL 32611, USA
- <sup>50</sup> Department of Physics, Duke University, Durham NC, USA
- <sup>51</sup> Institute for Theoretical Particle Physics and Cosmology, RWTH Aachen University, D-52056 Aachen, Germany
- <sup>52</sup> Physik-Institut, Universität Zürich, CH-8057 Zürich, Switzerland
- <sup>53</sup> Center for Theoretical Physics, University of California, Berkeley, CA 94720, USA
- <sup>54</sup> IFT UAM-CSIC, Cantoblanco, 28049, Madrid, Spain
- <sup>55</sup> Department of Physics and Astronomy, Michigan State University, East Lansing, MI 48824, USA
- <sup>56</sup> Institute for Theoretical Physics, Albert Einstein Center, University of Bern, Sidlerstr. 5, CH-3012 Bern, Switzerland
- <sup>57</sup> William I. Fine Theoretical Physics Institute, School of Physics and Astronomy, Univ. of Minnesota, Minneapolis, MN 55455, USA
- <sup>58</sup> IFAE, Universitat Autònoma de Barcelona, E-08193 Bellaterra, Barcelona, Spain
- <sup>59</sup> Nikhef, Science Park Amsterdam, Netherlands

<sup>60</sup> Department of Physics and Astronomy, Johns Hopkins University, Baltimore, MD 21218, USA

<sup>61</sup> Dept of Physics, University of Illinois at Urbana-Champaign, 1110 West Green Street Urbana, IL 61801, USA

<sup>62</sup> Ottawa-Carleton Institute for Physics, Carleton University, 1125 Colonel By Drive, Ottawa, Ontario K1S 5B6, Canada

<sup>63</sup> Department of Physics, University of Alberta, Edmonton, AB T6G 2E1, Canada

<sup>64</sup> Maryland Center for Fundamental Physics, Department of Physics, University of Maryland, College Park, MD 20742, USA

<sup>65</sup> CP3-Origins and DIAS, University of Southern Denmark, Campusvej 55, 5230 Odense M, Denmark

<sup>66</sup> Ernest Orlando Lawrence Berkeley National Laboratory, University of California, Berkeley, CA 94720, USA

<sup>67</sup> Department of Physics, The University of Chicago, Chicago, IL 60637, USA

<sup>68</sup> Enrico Fermi Institute and Kavli Institute for Cosmological Physics, The University of Chicago, Chicago, IL 60637, USA

<sup>69</sup> Department of Physics, University at Buffalo, The State University of New York, Buffalo, NY 14260-1500, USA

<sup>70</sup> Center for Theoretical Physics, Massachusetts Institute of Technology, Cambridge, MA 02139, USA

### Abstract

This Chapter summarises the physics opportunities in the search and study of physics beyond the Standard Model at the 100 TeV  $pp$  collider.

## 1 Introduction

Experimental measurements at a 100 TeV collider would cover previously unexplored territory at energies never before reached in a laboratory environment. Standard Model calculations will enable precise predictions for the phenomenology of the known particles and forces in this new frontier. The comparison of observations against predictions will allow for the structure of the Standard Model to be tested at unprecedented energies and with unparalleled precision. If observations and predictions agree within estimated uncertainties then this would provide a stunning confirmation of our present understanding of nature. If, on the other hand, observations do not agree with theoretical predictions this would mark a breakdown of the Standard Model of particle physics and the rise of new physical processes. In this way, amongst its many roles, a 100 TeV collider may discover new laws of nature.

In its significance for our understanding of nature, the discovery of new physics at the energies accessible to a 100 TeV collider would be unrivaled, but it would not necessarily be unheralded. There are a number of reasons to believe that a new physical description of nature beyond the Standard Model may be required at these energies. In this section we will summarise the landscape beyond the Standard Model accessible to a 100 TeV collider.

At the deepest level, one may discover new symmetries of spacetime at 100 TeV, for which a leading candidate is supersymmetry. Supersymmetry as a new high energy symmetry of spacetime is theoretically motivated from a number of perspectives, covering dark matter, unification of the forces, and the electroweak hierarchy problem. In Section 2 we will summarise these motivations in detail. Section 2 will then go on to systematically consider the rich phenomenology of the various new particles predicted in supersymmetric theories, with an aim to connect this phenomenology with concrete supersymmetric scenarios to provide a clear context for the interpretation of measurements.

One hint of new physical effects that may be unearthed at a new energy scale come from presence of dark matter. It is now well established that dark matter is prevalent throughout the universe. To explain its large abundance, many different mechanisms of new effects beyond the Standard Model have been proposed. This spectra of models extend from supersymmetric models to other exotic models that go beyond the basic precepts of supersymmetry. A remarkable aspect of dark matter models is that with

a loose set of assumptions, many of these models give concrete predictions of the current dark matter abundance originating from the early universe. In many cases, coverage of the allowed parameter space can be obtained with a 100 TeV machine. In Section 3, we review the different classes of dark matter models and the characteristic searches both at a hadronic collider and beyond that drive the sensitivity to these models.

In Section 4 we will discuss the reach for a future 100 TeV collider on a variety of new physics signatures that are not typical of supersymmetric and Dark Matter models. Most of these signatures originate from the decay of heavy resonances to Standard Model particles, but also indirect probes of new physics based on the measurement of the production of Standard Model particles at high invariant masses will be discussed. To make quantitative the assessment of the 100 TeV collider reach for these signatures, different benchmark models will be considered, related to some of the main issues of the SM, among which the hierarchy problem and the origin of neutrino masses. The list of studies that we present are at a very preliminary level and the list itself is far from being complete. However, they constitute a solid starting point that allows to identify the main experimental issues associated to the different signatures and that are essential for the design of the future facilities, i.e. both the collider and the detectors.

It is clear that the exploration of physics beyond the Standard Model using proton-proton collisions with a center-of-mass energy of 100 TeV bears unprecedented challenges. Energy ranges with dynamic scales ranging from the sub GeV to 10s of TeV become a necessity to maximize the capability demanded to study different physical effects. High instantaneous luminosity will require exquisite techniques to mitigate pileup. Such techniques include standard techniques at the LHC such as charged particle vertexing studies, but also more advanced approaches such as neutral vertex association through fast timing or with hadron fragmentation structure [1–3]. In order to contain the highest  $p_T$  jets (of tens of TeV) fully in the hadronic calorimeter a depth of at least 12 nuclear interaction lengths ( $\lambda_I$ ) is necessary.

To identify highly boosted hadronically decaying top quarks,  $W$ ,  $Z$  and  $H$  bosons with transverse momenta in the multi-TeV range a very fine hadronic calorimeter lateral segmentation in  $\eta \times \phi$  of at least  $0.025 \times 0.025$  is needed. This allows for the measurement of the boson jet substructure. Even this segmentation might limit the identification of these objects for the highest accessible  $p_T$  objects. Tracker or tracker+ECAL based jet substructure methods might offer a solution [4–6]. However, the increasing presence of long-lived neutral hadrons at higher  $p_T$  represents a difficult challenge in jet substructure that may have limitations [7]. This will also affect the capability to measure the polarisation of these objects.

Reconstructing leptonic decays of the top quark and  $W$ ,  $Z$  and  $H$  bosons will be limited in the highly boosted regime: the small opening angles, e.g. between the lepton and the  $b$ -jet in a  $t \rightarrow W(\rightarrow \ell\nu)b$  decay result in non-isolated leptons which are very hard to distinguish from e.g. a lepton from a  $b$ -hadron decay.

Another challenge is the momentum resolution for multi-TeV muons. The size of the ATLAS detector [8], for instance, is driven by the size of the muon system with the goal to measure the transverse momentum of muons with  $p_T = 1$  TeV with a 10% uncertainty, resulting in a diameter of ATLAS of about 25 m. Scaling this up to muons of  $p_T = 10$  TeV with a similar resolution pushes the size of the detector and of the magnetic field to unfeasible dimensions, and alternative strategies are needed and are currently under study.

The tracking system will also be challenged to efficiently reconstruct multi-TeV objects. Identification of  $b$  jets or  $\tau$  leptons with a  $p_T$  well above 1 TeV is largely unexplored, even at the LHC. The  $b$ -tagging performance of the current ATLAS and CMS detector deteriorate dramatically in the  $p_T$  range between a few hundred GeV and 1 TeV. The  $\tau$  lepton identification and the decay components of the tau suffer from similar limitations of resolution in the tracker and calorimeters in the highly boosted regime. More generally, the high boost of Standard Model particles results in very collimated objects and makes high demands on tracking capabilities in very dense environments. Charge particle angular separation can currently go to a level roughly  $0.01 \times 0.01$  in  $\eta \times \phi$ , which has an impact for  $b$ -quark jets

at roughly 1 TeV. Preserving consistent performance for a 100 TeV detector would require separation in part of the detector at angles roughly 10 times smaller.

Even as much of the discussion of the beyond the Standard Model (BSM) physics potential of a 100 TeV collider focuses on the high- $p_T$  regime, reconstruction of low- $p_T$  and displaced objects will also be critical to discover many new physics scenarios. BSM models with weak couplings or compressed mass spectra may lead to low- $p_T$  final states. Such events may only be distinguished above backgrounds by tagging soft or displaced decay products, such as soft leptons, kinked or disappearing tracks, highly-displaced vertices, or even measuring the charged particle  $dE/dx$ . Tracking and calorimetry must therefore be hermetic for prompt, high- $p_T$  objects in addition to soft and/or displaced objects.

In addition to the challenges of resolving high  $p_T$  objects, data rates and detector readout will have to be sufficiently fast to correspond with the high collision rate. The high collision rates and demands for high granularity will significantly increase the data rate coming out of the detector. Triggering of both low energy anomalous objects, such as disappearing tracks, and high  $p_T$  objects demands more sophisticated high data volume readouts and high speed pattern recognition, especially under the onset of pileup.

While the design of a new detector poses interesting and difficult problems, many of the technologies currently being investigated for HL-LHC already go in the direction of improving the granularity and data rate of the detectors. Additionally, much of the interesting BSM physics requires high  $p_T$  objects, for which the demands on basic calorimetric resolution, tracking performance for simple objects such as quark or gluon jets or missing transverse energy can be met with existing technologies. Nevertheless, a clear need for more information is present.

All the BSM physics benchmarks discussed in this section are used to identify the most relevant features needed by the new detectors. This should lead to a compromise between the feasibility of the desired detector and the coverage of the largest possible spectrum of new physics signatures. A realistic fast simulation of different detector configurations and a close collaboration between theorists and experimentalists is crucial in this phase of the study to assess the limitations and to study solutions for them.

## 2 Supersymmetry

### 2.1 Introduction

As the detailed theoretical study of quantum field theory progressed in the 1970's it slowly emerged, in various respects, that a new symmetry of spacetime was possible. Under the known spacetime symmetries the fields we observe, such as scalars (spin-0), fermions (spin-1/2), and vectors (spin-1), all form different representations of the Lorentz group and they transform under the known spacetime symmetries in their own way, independently. However, it was realised that under the new hypothetical spacetime symmetry these different representations may themselves transform into one another and would together be combined into a larger representation of a larger symmetry, a supersymmetry [9, 10]. These larger representations are called superfields, since they contain multiple component fields. Perhaps the most economical superfield, known as a chiral superfield, contains a complex scalar boson and a Weyl fermion. Supersymmetry imposes specific relations between the interactions and masses of these component fields. If gravitational interactions are to respect this symmetry, which they must if the symmetry is realised at a fundamental level, then the supersymmetry manifests as a gravitational theory, known as supergravity [11, 12]. This theory contains, in addition to the spin-2 graviton, a spin-3/2 partner fermion known as the gravitino which again has interactions purely dictated by the supersymmetry.

What would the discovery of supersymmetry mean for our understanding of nature? It would be nothing short of the discovery of an entirely new spacetime symmetry. The discovery of any symmetry signifies a fundamental shift in our perspective on fundamental physics and such discoveries are rare. Examples include the early  $U(1)_{EM}$  symmetry of electromagnetism, the  $SU(3)_C$  symmetry of QCD and more recently the embedding of electromagnetism into the full  $U(1)_Y \times SU(2)_W$  symmetry of the electroweak sector, of which the W and Z bosons are the additional force carriers and the Higgs serves as the final cornerstone in the theory. However, the last time a new spacetime symmetry was discovered harks back to the work of Einstein and the discovery of the diffeomorphism invariance of the laws of physics. The discovery of supersymmetry would thus mark a monumental shift in how we perceive nature at its most fundamental level.

If supersymmetry is realised in nature, how could we tell? As already stated, in supersymmetry every field is inextricably tied to its superpartner. This means that if supersymmetry were an exact symmetry of nature every particle we know would have a superpartner: every boson would have a fermion partner, with the suffix 'ino', every fermion a boson partner, with the prefix 's'. Thus the Higgs boson would have a fermion 'Higgsino' partner, the photon a 'photino', and the gluon a 'gluino'. The electron would have a scalar 'selectron' partner, the top quark a 'stop squark' partner and so forth. Exact supersymmetry would require that all superpartners have equal mass to their observed counterpart and hence practically all of the superpartners would have been discovered already. However, it turns out that the fundamental, high-energy, supersymmetry may persist if the masses of the partners are split from their known counterparts by an amount known as the soft mass. The term 'soft' is used as this form of supersymmetry breaking preserves the supersymmetric features of the theory at high energies. The soft mass may lift the mass of, for example, the selectron by an amount  $\tilde{m}$  above the electron mass. At energies  $E \gg \tilde{m}$  the theory will still be supersymmetric and maintain all of its appealing features, although the partner will not be directly apparent at energies  $E \ll \tilde{m}$ , essentially hiding supersymmetry from low-energy observers.<sup>1</sup>

If one simply takes the Standard Model of particle physics and supersymmetrizes it, then in the simplest variant, known as the MSSM, the only complication beyond the adding of superpartners is that two separate Higgs doublets are required, for reasons related to anomaly cancellation.<sup>2</sup> Each doublet obtains a vacuum expectation value. The vev for the Higgs doublet coupling to the up-type fermions is  $v_u$ , and the one coupling to down-type fermions is  $v_d$ . The ratio of these parameters arises frequently

<sup>1</sup>Besides the mass terms, for the scalars there are also scalar trilinear couplings which mimic the matter Yukawa couplings. These couplings are known as 'A-terms' and, while they break supersymmetry, this breaking is soft.

<sup>2</sup>In renormalizable models two Higgs doublets are also required as a result of holomorphicity of the superpotential.

and is commonly known as  $\tan \beta = v_u/v_d$ . Thus, all told, the number of fields is a mite greater than a simple doubling of fields.

The couplings of the additional superpartners to the known fields is predicted by supersymmetry itself. Thus in many cases once the mass of the superpartners are chosen it is possible to predict the collider production rate for a specific superfield.<sup>3</sup> Because of this predictability, in this supersymmetry section the experimental prospects for discovering supersymmetry at a 100 TeV collider can be broken down for each particular superpartner. In Section 2.2 predictions for the production cross sections of different particles are presented, and following this search strategies and projections for stop squarks (Section 2.3), gluinos (Section 2.4), the first two generations of squarks (Section 2.5), and electroweakinos such as winos, binos, and higgsinos (Section 2.6) are presented. However, before considering the experimental sensitivity it is useful to explore further the theoretical aspects of supersymmetry, to inform our interpretation of the search projections with regard to expectations for well-motivated mass ranges.

The goal of this section is not to promote supersymmetry for any of its particular virtues, nor is it to use supersymmetry to provide a precise physics motivation for a 100 TeV collider, however it is pragmatic to consider the superpartner mass ranges suggested by certain theoretical perspectives to provide a reference point for experimental projections. For the sake of a broad discussion, the various superpartner soft masses may be broken down into three categories. We may also use symmetries to understand their expected proximity to one another. Since the Higgs mass has been measured we will keep it separate; however, although they are not strictly related to each other, all of the other scalar masses may be broadly described with a generic parameter  $\tilde{m}_0$ . The symmetry broken by the scalar soft masses is supersymmetry, and it may be naturally small. In isolation, the Higgsino mass  $\mu$  pairs the up-type Higgsino  $\tilde{H}_u$  with the down-type Higgsino  $\tilde{H}_d$  to form a Dirac mass. This parameter respects supersymmetry, but breaks a Peccei-Quinn symmetry of the MSSM, thus it can be naturally small and is not a priori connected with the scale of supersymmetry breaking. Also the three gaugino masses are not strictly related to each other, however in many models they are not hierarchically different. Thus, for the purposes of broad discussion, we may lump them into one parameter  $\tilde{M}_{1/2}$ . This parameter breaks supersymmetry and a continuous R-symmetry, thus it may also be naturally small.

With these considerations in mind it is clearly possible to have hierarchies amongst these parameters. In particular, it is natural to have  $\tilde{M}_{1/2} \ll \tilde{m}_0$  and/or  $\mu \ll \tilde{m}_0$ , or it may be that they are all comparable  $\tilde{M}_{1/2} \sim \mu \sim \tilde{m}_0$ . We will now consider in detail some of the theoretical and phenomenological features of supersymmetry with a specific view towards motivating certain mass ranges for the different types of superpartner.

### 2.1.1 Dark Matter

When the SM is supersymmetrized some remarkable features arise. The first is that if an additional  $Z_2$  global symmetry known as ‘R-parity’ is imposed, to help avoid potentially phenomenologically unacceptable features such as fast proton decay, then the theory contains not one, but a number of fields that are compelling candidates for explaining the dark matter. Most importantly, these fields have the required masses and couplings to satisfy the required ingredients for the so-called ‘WIMP Miracle’, which naturally generates a dark matter abundance in the region of the observed abundance for stable weak-scale particles [13, 14]. The main candidates are the so-called ‘neutralinos’, comprising the neutral Higgsinos, Wino, and Bino, which may all mix under electroweak symmetry breaking. There are also the sneutrinos, which are a priori interesting dark matter candidates [15–17], although as the simplest incarnations are already in tension with direct detection searches we will not consider sneutrinos further here. As the dark matter searches are covered in Section 3 we will not consider the dark matter candidates in any more detail, however it is worth keeping in mind throughout this section that the provision of good dark matter

<sup>3</sup>In some cases additional soft terms may also enter, such as scalar trilinear couplings, thus these may need to be chosen to make predictions for some sparticles.

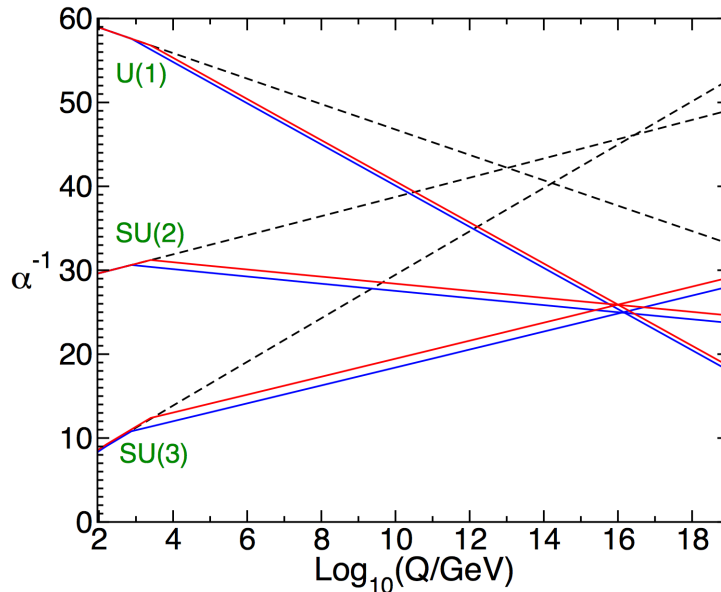


**Fig. 1:** Renormalization group evolution of gauge couplings up to high energies, taken from [20]. The Standard Model gauge couplings are shown in dashed black and the gauge couplings with superpartners added, with masses in the range  $0.75 \rightarrow 2.5$  TeV, are shown in red and blue. Unification of the forces at high energies is clearly apparent in the supersymmetric case.

candidates remains a strong motivation for considering supersymmetric theories. Neutralino dark matter thus motivates the mass range  $\mu, \tilde{M}_{1/2} \lesssim \mathcal{O}(\text{few TeV})$ , otherwise it would not be possible to obtain the correct relic density and they would overclose the Universe. This clearly points to a mass range that is within kinematic reach of a 100 TeV collider.

### 2.1.2 Gauge Coupling Unification

An unexpected surprise that arises whenever the Standard Model is supersymmetrized connects the behaviour of the Standard Model gauge couplings to a deep idea concerning the nature of the forces at extremely high energies. When the superpartners are added, it was found that upon evolving the  $U(1)_Y$ ,  $SU(2)_W$ , and  $SU(3)_C$  gauge couplings up to high energies they appeared to unify at energies close to  $E \sim 10^{16}$  GeV [18, 19]. This is shown in Fig. 1. Of course, that two lines will cross is almost guaranteed, however three lines crossing almost at a point is strongly suggestive of a deeper structure.

Ever since the unification of the electroweak forces, it has been believed that further unification of all gauge forces, now including  $SU(3)_C$ , may occur at very high energies. A variety of larger gauge groups into which they may unify have been proposed, however the simplest is arguably an  $SU(5)$  gauge symmetry [21].<sup>4</sup> It is deeply compelling that the Standard Model matter gauge representations neatly fall into multiplets of a larger symmetry, such as  $SU(5)$ , as this need not have been the case. A key feature which must arise at the unification scale in such a theory is that the gauge couplings must themselves become equal. Thus supersymmetric gauge coupling unification is strongly suggestive that supersymmetry may go hand-in-hand with the unification of the forces and, if discovered, the superpartners would provide a low energy echo of physics at extremely high energies.

When considering the role of the superpartners in supersymmetric unification one finds that some are more relevant than others. The reason is that since the matter fermions of the Standard Model fill out

<sup>4</sup>It is also possible that the gauge forces unify with gravity, in the context of String Theory, however we will not discuss this possibility here.

complete unified representations, so must their partners, the squarks and the sleptons. Thus although the masses of squarks and sleptons may change the scale at which unification occurs they do not significantly alter whether or not the couplings will unify, unless they are split by large mass differences themselves. This means that the most important superpartners for gauge coupling unification are the fermions: the gauginos and the Higgsinos.

Studies of supersymmetric gauge coupling unification generally find that for successful unification it is necessary to have gauginos and higgsinos not too far from the weak scale. If the gaugino and Higgsino mass parameters are taken equal, then unification requires  $\mu, \widetilde{M}_{1/2} \lesssim \mathcal{O}(10 \text{ TeV})$  with some uncertainty due to unknown threshold corrections at the unification scale [22]. The scalar soft masses,  $\widetilde{m}_0$ , may be arbitrarily heavy while preserving successful gauge coupling unification. This realization led to the consideration of so-called ‘Split-Supersymmetry’ theories [23–25], in which the main motivations for the mass spectrum are taken from gauge coupling unification and dark matter, as discussed previously.

The fact that, in addition to the gauge forces, also the matter particles are unified in representations of the unified gauge symmetry group, can imply relations between the Yukawa couplings of quarks and leptons at the unification scale [21, 26–30]. To compare such predictions with the measured values of the fermion masses, one has to take into account the supersymmetric loop threshold corrections at the soft breaking mass scale [31–36], which depend on the masses of the superpartners. Including them in the analysis, and using the measured fermion masses and Higgs mass as constraints, unified theories are even capable of predicting the complete sparticle spectrum [36, 37]. An example from a recent analysis is shown in Fig. 2. The superpartner masses are found to be  $\lesssim \mathcal{O}(5 \text{ TeV})$ , testable at a 100 TeV pp collider. Similar upper limits, in the range of  $\mathcal{O}(20 \text{ TeV})$ , are discussed in [38].

To summarize, as with dark matter, gauge coupling unification and the unification of matter particles in representations of the unifying gauge symmetry group motivate the existence of superpartners of the Standard Model particles with masses  $\lesssim \mathcal{O}(10 \text{ TeV})$ , once again suggesting that much of the parameter space motivated by this consideration should be within reach of a 100 TeV collider.

### 2.1.3 The Higgs Mass

As is common in physics, when new symmetries are introduced to a theory, the predictive power often increases. Because supersymmetry is softly broken, many new parameters associated with this breaking are introduced and certain aspects of the increased predictivity are lost. However, some predictability beyond the SM remains and the Higgs boson mass is a prime example.

In the Standard Model, when the theory is written in the unbroken electroweak phase there are only two fundamental parameters in the scalar potential, the doublet mass  $m_H$ , and the quartic coupling  $\lambda$ . In the broken electroweak vacuum this translates to two fundamental parameters, the Higgs vacuum expectation value  $v = 246 \text{ GeV}$ , and the Higgs scalar mass  $m_h$ . Once these two parameters are set, all other terms, such as the Higgs self-couplings, are determined. Supersymmetric theories take this one step further as supersymmetry relates the Higgs scalar potential quartic coupling to the electroweak gauge couplings in a fixed manner. The story is complicated a little relative to the Standard Model by the two Higgs doublets required in supersymmetric theories, however since the quartic couplings in the scalar potential are no longer free parameters, once the vacuum expectation value is set  $v = \sqrt{v_u^2 + v_d^2} = 246 \text{ GeV}$ , the Higgs mass is now also predicted by the theory. At tree level, this prediction is

$$m_h = M_Z |\cos 2\beta| . \quad (1)$$

Clearly for any value of  $\beta$  this prediction is at odds with the observed value of  $m_h \approx 125 \text{ GeV}$  and thus for consistency additional contributions to the Higgs doublet quartic terms are required. Within the MSSM the only potential source is from radiative corrections at higher orders in perturbation theory. The dominant corrections arise from loops of particles with the greatest coupling to the Higgs, the stop squarks [39, 40]. If the soft mass splitting between the top-quark and stop squarks is large enough then

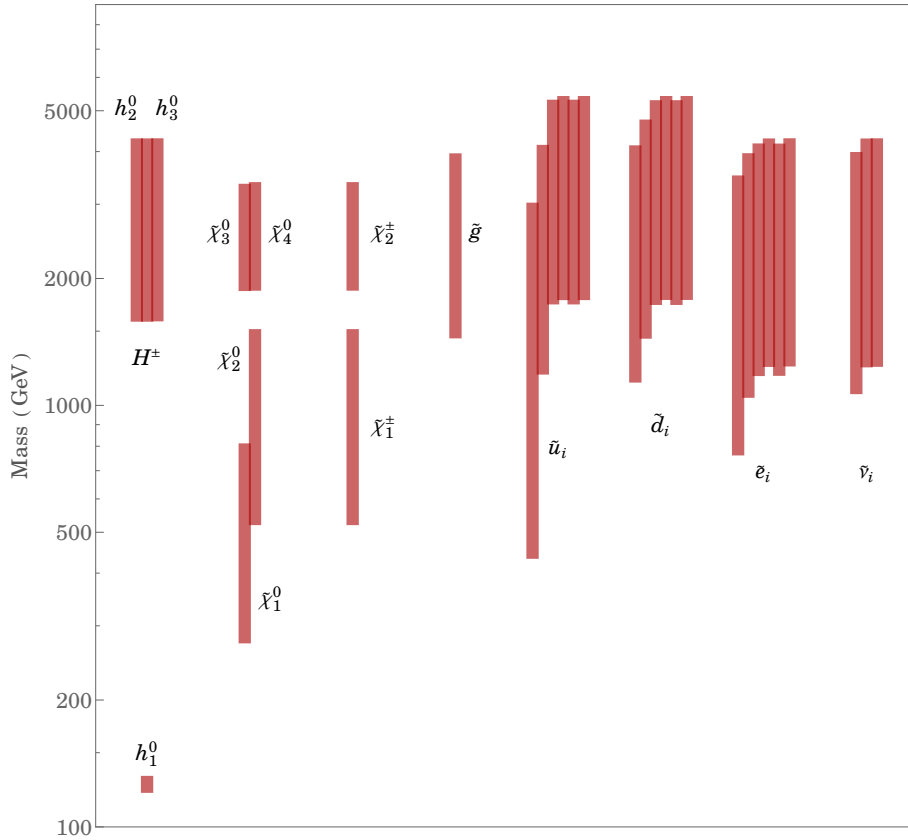


**Fig. 2:** Prediction for the superpartner and Higgs boson masses ( $1\sigma$  HPD intervals) in classes of SU(5) unified theories with the unification scale relations  $\frac{y_\tau}{y_b} = -\frac{3}{2}$ ,  $\frac{y_\mu}{y_s} = 6$ ,  $\frac{y_e}{y_d} = -\frac{1}{2}$  and universal (CMSSM) boundary conditions for the soft breaking parameters [36].

radiative corrections which are sensitive to this supersymmetry breaking may spoil the supersymmetric prediction for the Higgs quartic couplings and allow for contributions that may bring the Higgs boson mass within the observed window.

In Fig. 3 we show the expected soft mass parameter scales which reproduce the observed Higgs mass. Clearly, within the MSSM the observed Higgs mass may be reproduced for scalar masses in the range  $1 \text{ TeV} \lesssim \tilde{m}_0 \lesssim 10^8 \text{ TeV}$ .<sup>5</sup> Furthermore, if we consider the range  $\tan\beta > 4$ , then scalar masses below  $\mathcal{O}(10\text{'s TeV})$  are required. This is the first upper bound we have encountered for the scalar soft masses, resulting directly from the Higgs mass measurements. Theoretically, this has given rise to a reduction in the allowed parameter space of supersymmetric theories and in the context of Split SUSY, where previously scalar masses could take almost any value, now the Higgs mass measurements have led to the so-called ‘Mini-Split’ scenario [22, 43], where there is an upper bound on the value of the scalar soft masses.

There are variants of the MSSM in which the Higgs mass may also be raised above the MSSM tree-level prediction by utilizing additional effects deriving from couplings to new fields. If the coupling is to new fields in the superpotential then such theories are typically variants of the NMSSM, in which the Higgs doublets couple to an additional gauge singlet. Alternatively, the corrections may arise from coupling to new gauge fields, due to additional contributions to the quartic scalar potential predicted by supersymmetric gauge interactions. Importantly, in these scenarios the additional enhancements of the

<sup>5</sup>In fact, if the soft scalar trilinear term  $\tilde{A}_t$  is chosen so as to maximise the shift in the Higgs mass, the lightest stop squark could be as light as  $\sim 500 \text{ GeV}$  [42].

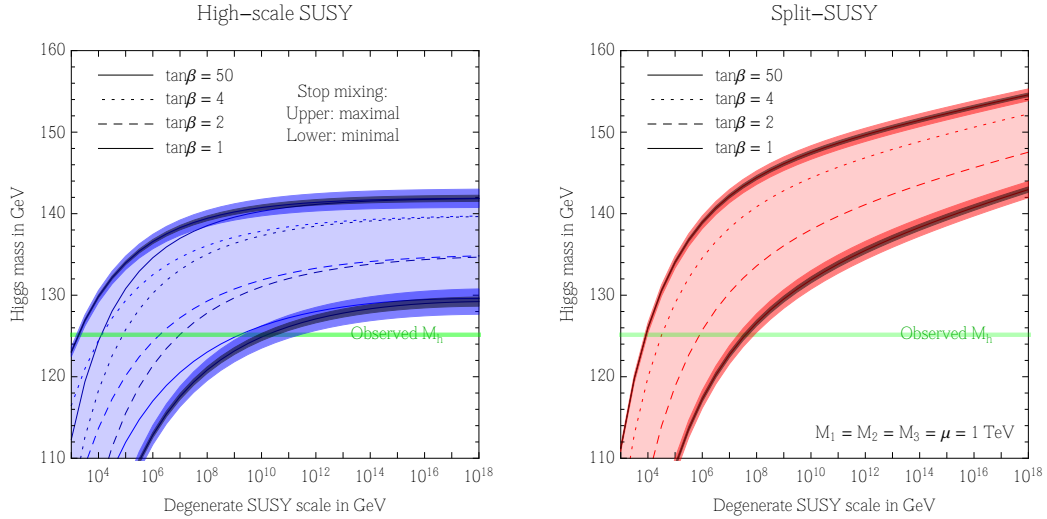


**Fig. 3:** Higgs mass predictions as a function of the supersymmetry breaking soft mass scale and the Higgs sector parameter  $\tan\beta$ , taken from [41]. In the High-Scale scenario all soft masses  $\mu, \widetilde{M}_{1/2}, \widetilde{m}_0$  are varied together, whereas in the Split SUSY scenario  $\mu, \widetilde{M}_{1/2}$  are kept at 1 TeV and only the scalar soft masses  $\widetilde{m}_0$  are varied.

Higgs mass only serve to reduce the required value of the radiative corrections, and hence the required value of the scalar soft masses. Thus the required scalar soft mass values shown in Fig. 3 serve as an approximate upper limit for theories beyond the MSSM.

To summarize, the measurement of the Higgs mass has now provided information that is key to understanding the expected mass ranges of superpartners relevant to a 100 TeV collider, particularly for the stop squarks. Although scalar masses may be as large as  $\widetilde{m}_0 \sim 10^8$  TeV, for a broad range of parameter space, if it is the case that  $\tan\beta > 4$  this upper bound is reduced significantly to  $\widetilde{m}_0 \lesssim \mathcal{O}(10\text{'s TeV})$ . All told, the observed Higgs mass may in some cases already point towards scalar superpartners within the expected reach of a 100 TeV collider.

It should also be noted that an appealing feature of supersymmetric models is that electroweak symmetry breaking may be driven radiatively upon RG evolution from high to low scales [44–48]. This attractive feature may not be possible in all scenarios, including the Mini-Split models, depending on parameter choices.

#### 2.1.4 Naturalness and the Hierarchy Problem

Finally, we arrive at a question that has been a driving force within fundamental physics research, and we find a supersymmetric answer to this question in which one of the most magical aspects of supersymmetry comes to the fore. Briefly, before considering the hierarchy problem in detail, it is worthwhile to explain why this central feature of supersymmetric theories has been left to the end of this section. The reason is twofold. First, as we will see, a total supersymmetric resolution of the hierarchy problem looks increasingly under tension from LHC measurements, hence this motivation for supersymmetry is perhaps waning relative to the others, at least in its purest form, and this trend may continue with additional LHC data. Secondly, this discussion was deliberately left until the end to reinforce the notion that it is not necessary to rely on naturalness arguments in order to discuss supersymmetry as a well-motivated new spacetime symmetry, or as an interesting phenomenological framework which may lie at the core of deep questions in fundamental physics concerning dark matter and the unification of the forces.

If the Standard Model of particle physics could be taken in isolation it would be a well-defined quantum field theory with the Higgs mass as a renormalized input parameter, which could in principle

take any value desired. However, this is not the case and the Standard Model must itself be viewed as a low energy effective description of some more fundamental theory at higher energy scales, as there are numerous reasons to expect new physics at energies  $M_{\text{New}}$  far above the weak scale. We will discuss a sample here. The most obvious example is the theory which UV-completes QFT at the Planck scale  $M_{\text{New}} = M_P \sim 10^{18}$  GeV to provide a consistent unification of quantum mechanics and general relativity, i.e. the theory of quantum gravity. This may be preceded, at lower energies, by the grand unified theory of the gauge forces, at the scale  $M_{\text{New}} = M_{GUT} \sim 10^{16}$  GeV. This may be preceded by the Peccei-Quinn breaking scale  $M_{\text{New}} = f_a \gtrsim 10^9$  GeV associated with the axion solution of the strong CP-problem, or by the right-handed neutrino mass scale  $M_{\text{New}} = M_N \gtrsim 10^{11}$  GeV. In any of these cases there should exist new fields with mass characterized by the relevant energy scale, coupled to the Higgs. Even in the absence of new physics at these energies, hypercharge exhibits a Landau pole and becomes strongly coupled at very high energies, thus even within the SM there is reason to believe in the existence of new physics at extremely high energies, although realistically quantum gravitational effects will have entered before that scale, rendering an unambiguous discussion of this feature difficult.

The possibility of new physics at high energies is not a problem in itself, rather the problem is concerned with how the weak scale may be so far below  $M_{\text{New}}$ . The reason is that even if we were to set the tree-level Higgs mass to a value hierarchically below  $M_{\text{New}}$ , this situation would not be stable at the quantum level. Radiative corrections, most often depicted through one-loop diagrams, will in general give corrections to the Higgs mass, and hence the weak scale, of  $\delta M_H \sim \mathcal{O}(M_{\text{New}})$ . One could choose to finely tune parameters such that all contributions contrive to cancel at low energies, leading to  $M_H \ll M_{\text{New}}$  when all corrections are included. However, in arguments elucidated by Wilson, t' Hooft [49], and specifically quoting Susskind [50], “observable properties of a system should not depend sensitively on variations in the fundamental parameters”. This is the core of the hierarchy problem: a finely-tuned scenario for the weak scale is unnatural, seemingly implausible, although still possible.

The supersymmetric solution to this problem is straightforward to sketch. All fermions enjoy a chiral symmetry acting on their individual Weyl components. A fermion mass, whether Dirac or Majorana, breaks this chiral symmetry. This means that if the mass, and hence breaking of the chiral symmetry, is small then a fermion may remain naturally smaller than other mass scales in the theory and this will remain true at the quantum level. In fact, we are already familiar with this in the Standard Model. While we may wonder at the origin of the huge hierarchy between the electron mass and the tau mass, we do not puzzle over the quantum stability of this mass difference. This lies at the core of the supersymmetric resolution of the hierarchy problem. Supersymmetry ties the mass of a scalar field to the mass of its fermionic superpartner, and since supersymmetry does not break the chiral symmetry enjoyed by the fermion, and the chiral symmetry protects the fermion mass from large quantum corrections, so too must the mass of its scalar partner be protected, by proxy.

This means that in a supersymmetric theory it is perfectly natural for the mass of the individual components of a superfield to be hierarchically below other mass scales in the theory, even if two superfields with vastly separated masses are coupled to each other with  $\mathcal{O}(1)$  couplings. This is extraordinary and is quite at odds with naive intuition, which is what makes this property of supersymmetry so magical. In practice it means that in a supersymmetric theory the weak scale could be comfortably below new physics at a scale  $M_{\text{New}}$ , even if this is identified with the Planck scale. Thus supersymmetry may provide a concrete foundation for the Standard Model fields all the way up to the scale of quantum gravity.

Of course in nature supersymmetry must be broken and once the symmetry is broken at a scale  $\tilde{m}$ , which represents the soft mass scale, the Higgs mass is no longer protected from quantum corrections. Thus supersymmetry is effective in protecting the Higgs mass all the way down from a high mass scale to the supersymmetry breaking scale  $M_{\text{New}} \rightarrow \tilde{m}$ , however from the soft mass scale down to the weak scale,  $\tilde{m} \rightarrow m_h$  supersymmetry is no longer present. This means that for a natural theory without tuning we must expect  $\tilde{m} \sim m_h$ , and conversely if  $\tilde{m} \gg m_h$  there must be some fine tuning to realize the weak scale below the soft mass scale. These qualitative arguments may be made quantitative. A well motivated

measure for the degree of tuning in the weak scale with respect to a given fundamental parameter in the theory,  $a$ , is [51, 52]

$$\Delta[a] = \frac{\partial \log M_Z^2}{\partial \log a^2} . \quad (2)$$

By minimising the weak scale potential at large  $\tan \beta$  we find

$$M_Z^2 = -2(m_{H_u}^2 + |\mu|^2) , \quad (3)$$

where  $m_{H_u}^2$  is the soft mass for the up-type Higgs which includes all radiative corrections. Let us consider the tree-level contribution from the  $\mu$ -term, along with the one-loop contributions from stop squarks and the winos, and the two-loop contribution from gluinos, which are given by

$$\delta m_{H_u}^2(\tilde{t}) = -\frac{3y_t^2}{4\pi^2} m_{\tilde{t}}^2 \log(\Lambda/m_{\tilde{t}}) \quad (4)$$

$$\delta m_{H_u}^2(\tilde{W}) = -\frac{3g^2}{8\pi^2} (m_{\tilde{W}}^2 + m_h^2) \log(\Lambda/m_{\tilde{W}}) \quad (5)$$

$$\delta m_{\tilde{t}}^2 = \frac{2g_s^2}{3\pi^2} m_{\tilde{g}}^2 \log(\Lambda/m_{\tilde{g}}) , \quad (6)$$

where  $\Lambda$  is a UV-cutoff at which the full UV-completion of supersymmetry kicks in, and the last term may be inserted into the first to obtain an estimate of the tuning from gluinos. Conservatively taking  $\Lambda = 10$  TeV we arrive at the following expectations for a theory which is only tuned at the 10% level [53]:

$$\mu \lesssim 200 \text{ GeV} , \quad m_{\tilde{t}} \lesssim 400 \text{ GeV} , \quad m_{\tilde{W}} \lesssim 1 \text{ TeV} , \quad m_{\tilde{g}} \lesssim 800 \text{ GeV} , \quad (7)$$

This picture is clearly at odds with the stop mass values required to achieve the observed Higgs mass in the MSSM, shown in Fig. 3. However it may be that non-minimal structure beyond the MSSM lifts the Higgs mass without requiring large stop masses, thus this constraint is not too significant. More importantly, current constraints on the Higgs boson couplings, which would typically be modified if the stop squarks were light, already place stringent constraints on light stop scenarios. Furthermore, direct searches for stops and gluinos, already show that significant portions of this parameter space are in tension with LHC 8 TeV data (for a thorough overview see [53]). Finally, in many (but not all) concrete scenarios it is expected that the first two generation squarks should not be significantly heavier than the stop squarks and, as the production cross section is enhanced due to valence quarks in the initial state, constraints on first two generation squarks are very strong, indirectly placing strong constraints on the naturalness of many supersymmetric theories.

Where do these strong constraints leave the supersymmetric solution to the hierarchy problem? As we are on the brink of a paradigm shift in our understanding of electroweak naturalness a number of possibilities are plausible.

It could be that the weak scale is meso-tuned, as in Mini-Split supersymmetry, and the aesthetic motivations for supersymmetry as a new spacetime symmetry are justified, whereas the naturalness arguments were misguided, to at least some degree, since supersymmetry does solve the big hierarchy problem and we are instead left with a relatively small tuning of the weak scale up to energies as high as  $\mathcal{O}(10^8)$  TeV. This scenario is in some sense quite successful. A fundamental Higgs boson of mass  $m_h \lesssim 135$  GeV is predicted, gauge coupling unification and successful dark matter candidates are realized, all at the cost of accepting some meso-tuning. Although not necessarily guaranteed, the gauginos should be below mass scales of  $\sim \mathcal{O}(\text{few TeV})$ , mostly driven by the dark matter requirement.

Another possibility which has only recently been explored is that the Mini-Split spectrum is realized in nature, with all of the above successes, however the theory is not actually tuned due to a hidden dynamical mechanism which renders the hierarchy from the weak scale to the soft mass scale natural [54]. This can be achieved by employing the cosmological relaxation mechanism of [55] in a

supersymmetric context. In this case both the aesthetic arguments for supersymmetry and the naturalness arguments for the weak scale were well founded, however the two may have manifested in an entirely unexpected manner, with a cocktail of symmetries and dynamics protecting the naturalness of the weak scale up to the highest energies. As before, the gauginos should be below mass scales of  $\sim \mathcal{O}(10\text{'s TeV})$ , however this expectation comes from the fact that a loop factor suppression between scalars and gauginos is expected in this model and in addition the scalars cannot be arbitrarily heavy due to the finite cutoff of the cosmological relaxation mechanism.

Alternatively, a reevaluation of the fine-tuning in the infrared may be required if a spectrum with heavy squarks is made natural due to correlations between soft mass UV-boundary conditions and the infrared value of the Higgs mass, as in ‘Focus Point’ supersymmetry [56] or in the recently proposed ‘Radiatively-Driven’ natural Supersymmetry [57]. In these cases gauginos, Higgsinos, and most likely also stop and sbottom squarks are expected to still be in the sub-10 TeV range. The first two generation squarks may be somewhat heavier.

Finally, it is still possible that the weak scale is relatively natural due to supersymmetry, however the sparticles have evaded detection until now. If this is the case it is likely the stop squarks are still relatively light, in the range of a few 100’s of GeV, and the Higgs mass is raised by an additional tree-level term. For the stop squarks to evade detection there are a number of possible scenarios. We will discuss just a few here. One is an example of a so-called ‘compressed’ spectrum (see e.g. [58]), where the mass splitting between the stop and the stable neutralino is so small that the tell-tale missing energy signature carried away by the neutralino is diminished to the point of being unobservable. Another possibility is ‘Stealth Supersymmetry’ [59, 60], where again the missing energy signatures are diminished, however in this case from sparticle decays passing through a hidden sector. Yet another possibility is for R-parity violating decays of the superpartners [61], since in this case missing-energy signatures are removed and the collider searches must contend with larger backgrounds (see e.g. [62] for models and collider phenomenology). For a natural spectrum the first two generations of squarks must also have evaded detection. One possibility is to raise their mass above experimental bounds, which is compatible with naturalness if they stay within an order of magnitude or so of the gluinos and stops [63–65]. Dirac gauginos also offer opportunities for suppressing collider signatures, at no cost to the naturalness of the theory [66, 67], as Dirac gauginos may naturally be heavier than their Majorana counterparts. This scenario allows not only for the suppression of gluino signatures at the LHC, but also suppresses the t-channel gluino exchange production of the first two generation squarks.

In summary, if we wish for supersymmetry to provide a comprehensive solution to the electroweak hierarchy problem, then the full cohort of sparticles should lie below  $\mathcal{O}(\text{few TeV})$ . Otherwise we are forced into considering at least some fine tuning of the weak scale or alternatively the introduction of an additional mechanism, beyond supersymmetry, to enable a natural weak scale.

### 2.1.5 Summary

Having whetted our appetite with a variety of theoretical considerations we are now well placed to understand the connection between theoretically motivated mass ranges in supersymmetry and the experimental reach of a 100 TeV collider for supersymmetry. A brief summary of the theory motivation for superpartner mass ranges is as follows.

- Supersymmetric dark matter leads us to expect electroweak fermions comprising some admixture of the bino, wino, and/or Higgsino, with mass below  $\sim \text{few TeV}$ . If the bino and wino masses are not hierarchically separated from the gluino mass then we may also expect gluinos below  $\mathcal{O}(10\text{'s TeV})$ .
- Expectations from gauge coupling unification and the unification of matter particles in representations of the unifying gauge symmetry group are similar, and motivate the existence of superpartners of the Standard Model particles with masses  $\lesssim \mathcal{O}(10 \text{ TeV})$ . More detailed predictions for the

superpartner masses are possible in the context of specific unified models.

- The measured Higgs mass points towards scalar superpartners below  $\sim 10^8$  TeV, and in many well-motivated cases the upper limit may be as low as  $\mathcal{O}(10^3)$  TeV. Strictly speaking this applies mostly to the stop squarks, however in many models they are within an order of magnitude of the first two generation squarks as well.
- Naturalness points towards superpartners that are as light as can be possible given current experimental constraints. With stops ideally below  $\sim 400$  GeV, gluinos below  $\sim$  few TeV, and first two generation squarks below  $\sim$  few TeV. Relaxing the naturalness criterion raises the masses at the price of increased fine tuning. If the weak scale is natural then it is likely that supersymmetry has been hidden by an exotic scenario, that may require specialized techniques to dig the signal out from background.

Let us now consider the experimental prospects for supersymmetry at 100 TeV. Numerous studies have already shown that a potential proton-proton collider operating at  $\sqrt{s} = 100$  TeV greatly extends the kinematic reach for superpartners, into the many-TeV range [68–77]. Previous studies have focused primarily on pair production of superpartners, both strongly-interacting [68, 69, 71] and weakly-interacting [70, 73–76]. In Section 2.2 we will consider the pair production cross sections for various superpartners at 100 TeV, including NLO corrections. In Sections 2.3 to 2.6 we will focus on searches specific to particular superpartners, often employing simplified models. In Section 2.7 we discuss the exotic signatures of long-lived charged superpartners and in Section 2.8 potential indirect constraints on stop squarks from modifications of Higgs pair production. In Section 2.9 potential measurements at a 100 TeV collider are interpreted in the context of two specific supersymmetric models, the ‘constrained MSSM’ and Mini-Split Supersymmetry. Section 2.10 discusses the next steps to be made after discovering supersymmetry at a 100 TeV collider. Finally, in Section 2.11 we summarize, focussing on a broad characterization of the expected reach of a 100 TeV collider and the potential implications for our understanding of supersymmetry.

## 2.2 Cross Sections for Production of SUSY Particles

In this section we present reference cross sections for the production of SUSY particles at 100 TeV.

We first focus on the pair production of squarks and gluinos,

$$pp \rightarrow \tilde{q}\tilde{q}, \tilde{q}\tilde{q}^*, \tilde{q}\tilde{g}, \tilde{g}\tilde{g} + X, \quad (8)$$

where the charge conjugated processes  $pp \rightarrow \tilde{q}^*\tilde{q}$  etc. are included. We assume 10 mass-degenerate squark flavours,  $\tilde{q} \in \{u_{L/R}, d_{L/R}, c_{L/R}, s_{L/R}, b_{L/R}\}$  and have suppressed the chirality labels in Eq.(8) and below. The production of stops is treated separately, as the large Yukawa coupling between top quarks, stops and Higgs fields gives rise to potentially large mixing effects and mass splitting. Thus, for stop production we consider the pair production of the lighter mass eigenstate,  $\tilde{t}_1$ ,

$$pp \rightarrow \tilde{t}_1\tilde{t}_1^* + X. \quad (9)$$

First, in Fig. 4 we show cross section predictions for the various squark and gluino production processes, assuming degenerate squark and gluino masses. For squark/gluino masses near 2 TeV the inclusive cross section is of the order 100 pb. The relative size of the various production channels depends on the squark/gluino masses and is driven by the corresponding parton luminosities. The cross sections include NLO SUSY-QCD corrections [78, 79] and the resummation of threshold logarithms at next-to-leading logarithmic (NLL) accuracy [80, 81], as described in Ref. [82].

We will now consider individual production processes in more detail, starting with gluino pair production in a simplified model with the squarks decoupled. In Fig. 5 we show the NLO+NLL cross section,  $pp \rightarrow \tilde{g}\tilde{g}$ , including the theoretical uncertainty from scale variation and the parton distribution

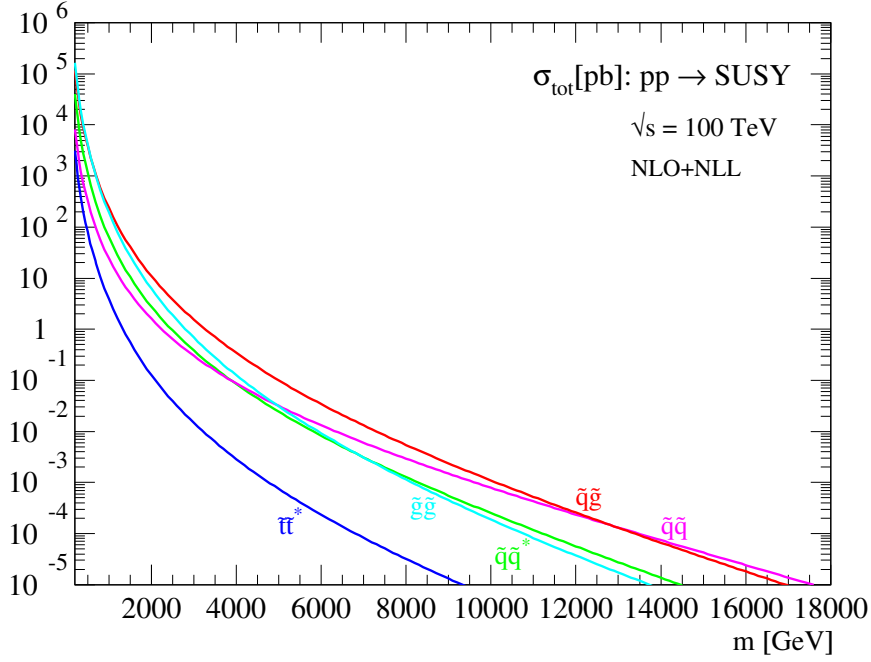


**Fig. 4:** NLO+NLL cross sections for squark and gluino pair-production,  $pp \rightarrow \tilde{q}\tilde{q}, \tilde{q}\tilde{q}^*, \tilde{q}\tilde{g}, \tilde{g}\tilde{g}, \tilde{t}_1\tilde{t}_1^* + X$ , at  $\sqrt{S} = 100$  TeV, as a function of the degenerate squark and gluino mass  $m_{\tilde{q}} = m_{\tilde{g}} = m$ . From Ref. [82].

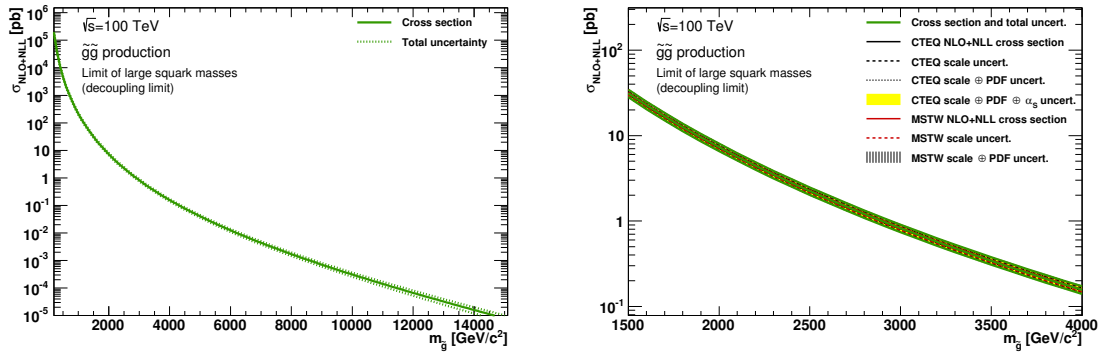


**Fig. 5:** NLO+NLL cross section for gluino pair-production,  $pp \rightarrow \tilde{g}\tilde{g} + X$ , at  $\sqrt{S} = 100$  TeV, as a function of the gluino mass with squarks decoupled. The black (red) lines correspond to the cross section and scale uncertainties predicted using the CTEQ6.6 [83] (MSTW2008 [84]) pdf set. The yellow (dashed black) band corresponds to the total CTEQ6.6 (MSTW2008) uncertainty, as described in [82]. The green lines show the final cross section and its total uncertainty. From Ref. [82].

functions, as determined following the procedure described in Ref. [82]. The individual sources of the uncertainty are shown in the lower plot for the mass range  $1 \text{ TeV} \leq m_{\tilde{g}} \leq 4 \text{ TeV}$ . Fig. 6 shows the corresponding results for squark-antisquark production,  $pp \rightarrow \tilde{q}\tilde{q}^*$ , with gluinos decoupled.

Finally, in Fig. 7 we show the cross section for the pair production of the lighter stop mass eigenstate in a model where all other sparticles are decoupled. Note that these cross sections are approximately equal to the cross section for the lighter sbottom mass eigenstate, assuming that the rest of the coloured SUSY spectrum is decoupled.

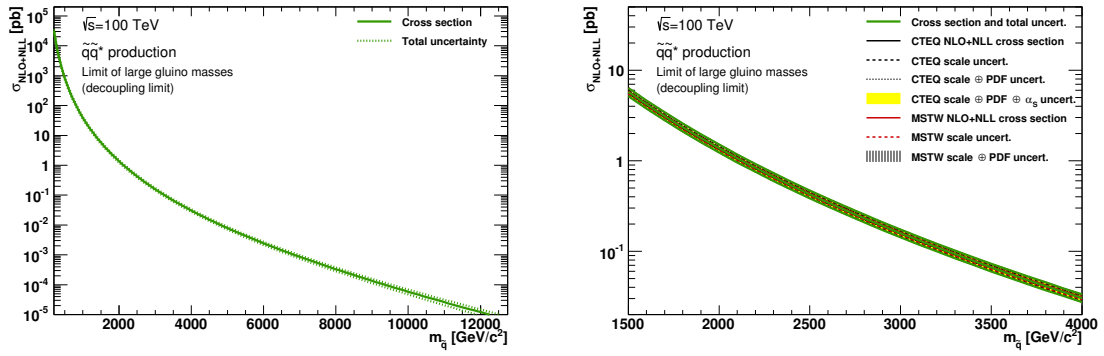


**Fig. 6:** NLO+NLL cross section for squark-antisquark production,  $pp \rightarrow \tilde{q}\tilde{q}^* + X$ , at  $\sqrt{S} = 100$  TeV, as a function of the squark mass with gluinos decoupled. The black (red) lines correspond to the cross section and scale uncertainties predicted using the CTEQ6.6 [83] (MSTW2008 [84]) pdf set. The yellow (dashed black) band corresponds to the total CTEQ6.6 (MSTW2008) uncertainty, as described in [82]. The green lines show the final cross section and its total uncertainty. From Ref. [82].

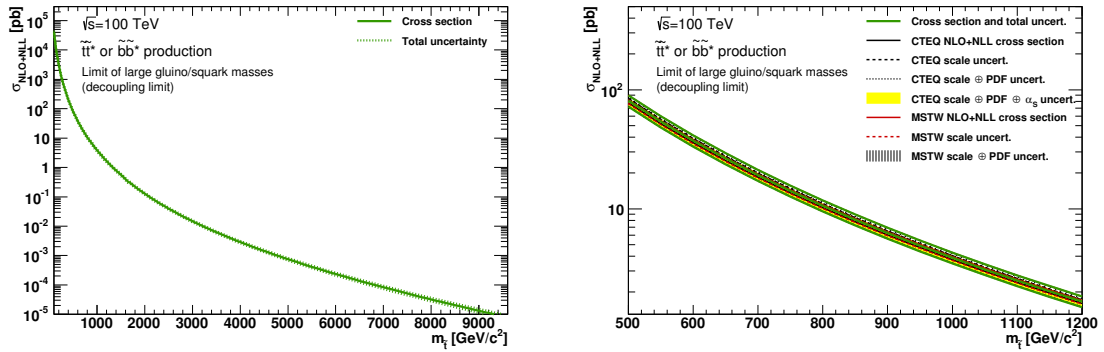


**Fig. 7:** NLO+NLL cross section for stop-antistop production,  $pp \rightarrow \tilde{t}_1\tilde{t}_1^* + X$ , at  $\sqrt{S} = 100$  TeV, as a function of the stop mass with all other coloured sparticles decoupled. The black (red) lines correspond to the cross section and scale uncertainties predicted using the CTEQ6.6 [83] (MSTW2008 [84]) pdf set. The yellow (dashed black) band corresponds to the total CTEQ6.6 (MSTW2008) uncertainty, as described in [82]. The green lines show the final cross section and its total uncertainty. From Ref. [82].

Besides higher-order QCD corrections, the production of squarks and gluinos receives Born-level [85] and higher-order electroweak (EW) contributions [86–92]. These EW corrections are enhanced well above the TeV scale due to large logarithms of Sudakov type. For  $\sqrt{\hat{s}} \gg M_W$ , NLO EW corrections can be at the level of several tens of percent of the LO cross section. In Fig. 8 we illustrate the effect of such EW corrections for the case of squark-antisquark (left) and stop-antistop (right) production, where for squark-antisquark production we separate different chirality combinations (LL, RR, LR+RL). The production of left-handed squark-antisquark pairs receives NLO EW corrections with respect to the LO predictions of up to  $-30\%$ , while for the other production modes and for stop-antistop production NLO EW corrections are smaller. These large NLO EW corrections are partly compensated (or even overcompensated) by the contribution from photon-induced production. However, these contributions are accompanied by very large intrinsic PDF uncertainties [92], which may substantially alter the size of the electroweak corrections. Overall, any precision study of SUSY particle production in the multi-TeV range should include higher-order EW corrections and photon-induced production.

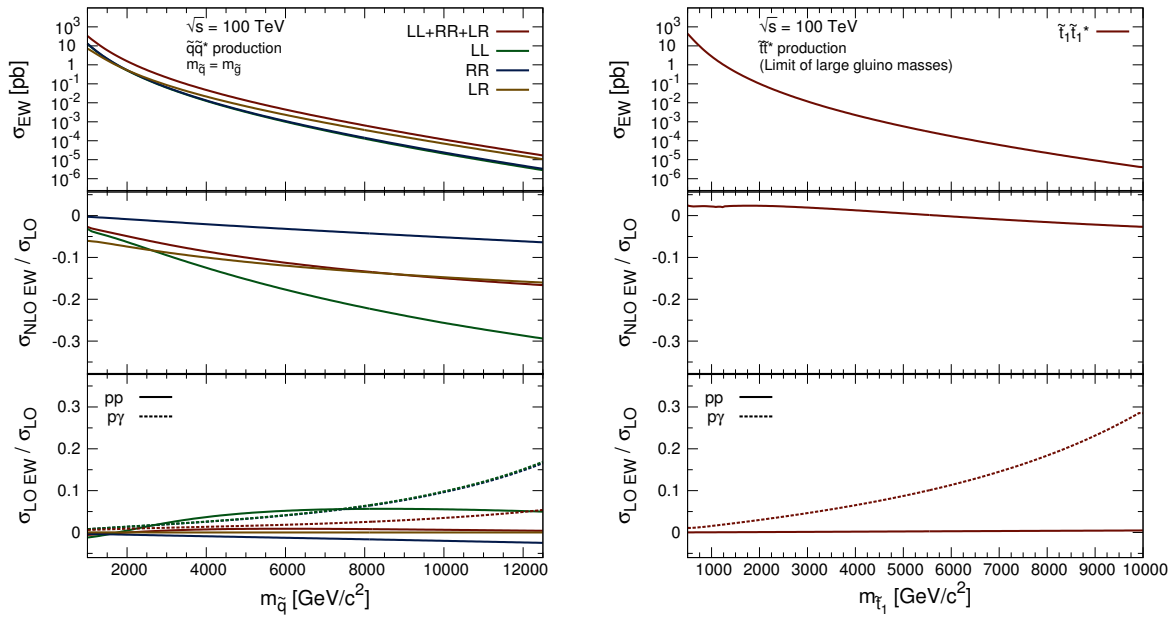


**Fig. 8:** Cross sections for squark-antisquark production,  $pp \rightarrow \tilde{q}\tilde{q}^* + X$ , and stop-antistop production,  $pp \rightarrow \tilde{t}_1\tilde{t}_1^* + X$ , at  $\sqrt{s} = 100$  TeV including EW corrections  $\sigma_{\text{EW}} = \sigma_{\text{LO}} + \sigma_{\text{LO EW}} + \sigma_{\text{NLO EW}}$ , as a function of the produced squark/stop mass. In the case of squark-antisquark production all squarks and the gluino have the same mass  $m_{\tilde{q}} = m_{\tilde{g}}$ , while in the case of stop-antistop production the gluino is decoupled and all light-flavor squark masses are set to  $m_{\tilde{q}} = 5000$  GeV. All cross sections are obtained using NNPDF2.3QED [93].

The associated production of neutralinos with squarks and gluinos provides a complementary probe of SUSY particle production. In Fig. 9 we present the (leading-order) cross section for  $pp \rightarrow \tilde{\chi}_1^0 + \tilde{q}$  in a simplified model with degenerate squarks of the first two generations and a bino  $\tilde{\chi}_1^0$ . All other SUSY particles are decoupled. The cross section for  $pp \rightarrow \tilde{\chi}_1^0 + \tilde{g}$  is shown in Fig. 10. Again, we consider a pure bino  $\tilde{\chi}_1^0$ , and set the gluino and the squarks of the first two generations to a common mass. The cross sections have been obtained with MadGraph5 [94].

### 2.3 Stop Squarks

The largest radiative correction to the Higgs potential arises from top loops, thus the scalar partner of the top (stop) is of critical importance for understanding if supersymmetry solves the hierarchy problem. In this section, we will study the reach for stops at a future 100 TeV hadron collider.

Motivated by dark matter and proton decay, we consider  $R$ -parity to be a good symmetry and imagine a neutral lightest supersymmetric particle (LSP) that is stable on collider time scales. We will refer to the LSP as a neutralino ( $\tilde{\chi}_1^0$ ), but it could have quantum numbers which differ from the usual MSSM neutralinos. Thus we take a simplified model which consists of a stop and a much lighter neutralino, and, in this model, the decay  $\tilde{t} \rightarrow t\tilde{\chi}_1^0$  occurs 100% of the time.

#### 2.3.1 Leptonic Decays

The LHC experiments have performed many searches for stops [95, 96], and such searches will be an important piece of the LHC and HL-LHC physics programs. However, the kinematic regime accessible at  $\sqrt{s} = 100$  TeV is completely different from that of the LHC, and will require new search strategies. From the cross sections shown in Section 2.2 we see that a 100 TeV machine will easily produce multi-

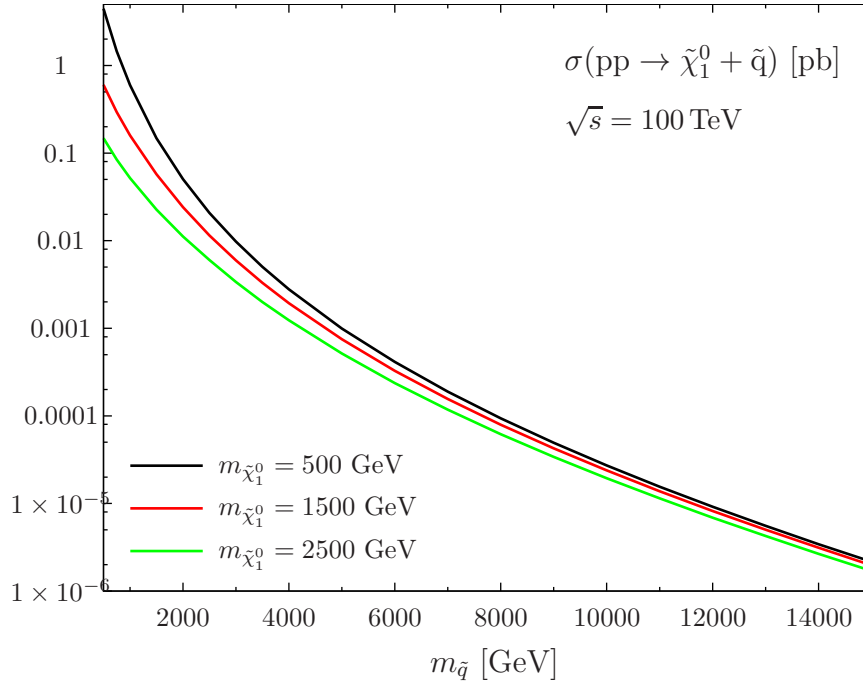


**Fig. 9:** LO cross section for neutralino-squark associate production,  $pp \rightarrow \tilde{\chi}_1^0 + \tilde{q}$ , at  $\sqrt{s} = 100$  TeV, as a function of the squark mass for three different values of the neutralino mass. We assume a simplified model with degenerate masses for the squarks of the first two generations, a pure bino  $\tilde{\chi}_1^0$ , and all other SUSY particles decoupled.

TeV stops, so we expect a large fraction of the parameter space to contain multi-TeV top quarks.

LHC techniques fail at higher energies precisely because the top quarks are highly boosted. In Fig. 11 we show the top quark  $p_T$  and the average  $\Delta R$  between its decay products as a function of the stop and neutralino masses. In most of the parameter space accessible at  $\sqrt{s} = 100$  TeV the top decay products are contained in a cone of the same size of an LHC jet:  $\Delta R \lesssim 0.5$ . In some cases the separation between them is even smaller than the size of LHC calorimeter cells. For example, an 8 TeV stop and a light neutralino give a large fraction of top quarks with  $p_T^t \approx 5$  TeV. This corresponds to a separation between the  $W$  and the  $b$  from the top decay of  $\Delta R \approx 0.07$ , to be compared with a tower of the CMS hadronic calorimeter in the barrel  $\Delta\eta \times \Delta\phi \sim \mathcal{O}(0.1 \times 0.1)$  [97].

It is clear that traditional LHC searches, which aim to reconstruct the top quark from its decay products, will be ineffective, unless detector granularities improve considerably. The same is true for algorithms specifically designed to tag top quarks [98,99], as was shown in Ref [71]. Therefore we avoid relying on substructure techniques, and instead build our search around the requirement of a muon inside a jet. This greatly reduces the SM backgrounds while making the analysis almost insensitive to the future detector design. Similar techniques are already in use at hadron colliders to tag  $b$ -jets [100–109].

The analysis was performed with the Snowmass background samples [110] for the  $t\bar{t}$ +jets, single  $t$ +jets,  $t\bar{t}V$ +jets, and  $V$ +jets ( $V = W, Z$ ) background processes. An  $H_T$ -binned QCD multijet sample was also produced, following the same prescription as the Snowmass samples. Signal samples were produced unbinned in  $H_T$ . All samples were generated with MadGraph5 [111] and showered with Pythia6 [112]. The detector simulation was implemented using Delphes [113] with the Snowmass combined detector card [114]. The signal cross-section was computed at NLL + NLO in [82], consistent with the calculations presented in Section 2.2.

Our selection requirements are (applied in the order in which they are listed):

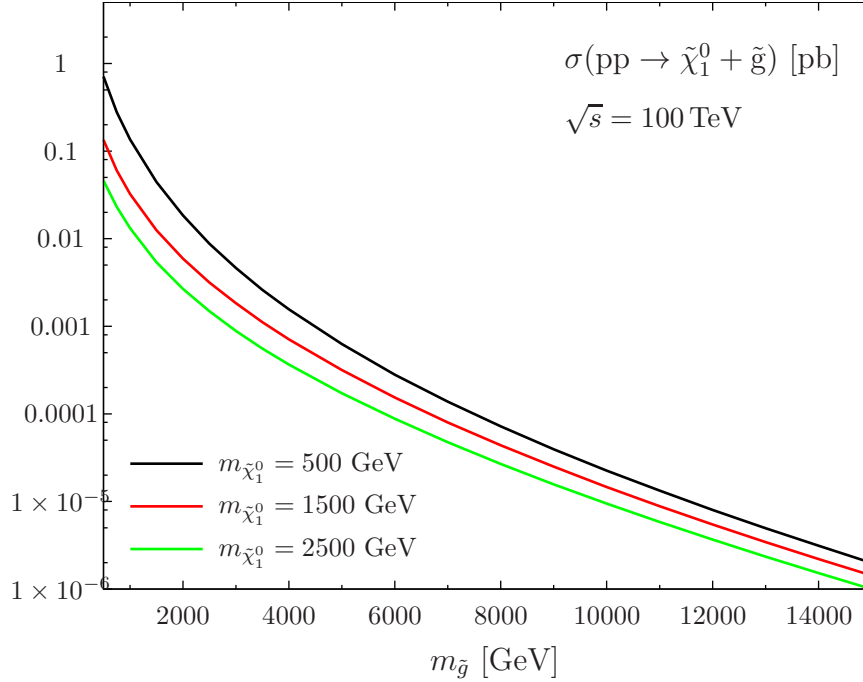


**Fig. 10:** LO cross section for neutralino-gluino associate production,  $pp \rightarrow \tilde{\chi}_1^0 + \tilde{g}$ , at  $\sqrt{S} = 100$  TeV, as a function of the gluino mass for three different values of the neutralino mass. We assume a simplified model with degenerate masses for the gluino and the squarks of the first two generations, a pure bino  $\tilde{\chi}_1^0$ , and all other SUSY particles decoupled.

1. At least two  $\Delta R = 0.5$  anti- $k_t$  jets [115] with  $|\eta| < 2.5$  and  $p_T > 1$  TeV must be present in the event.
2. We require at least one muon with  $p_T^\mu > 200$  GeV inside a  $\Delta R = 0.5$  cone centered around the axis of one of the leading two jets.
3. Events in which at least one isolated lepton (either an electron or a muon) with  $p_T > 35$  GeV and  $|\eta| < 2.5$  is present are rejected. Our isolation criterion requires that the total  $p_T$  of all particles within a  $\Delta R < 0.5$  cone around the lepton be less than 10% of its  $p_T$ .
4.  $\Delta\phi_{\cancel{E}_T, J} > 1.0$ , where  $\Delta\phi_{\cancel{E}_T, J}$  is the minimum  $|\Delta\phi|$  between missing energy ( $\cancel{E}_T$ ) and any jet in the event with  $p_T > 200$  GeV and  $|\eta| < 2.5$ .
5. After the previous cuts are applied we define three signal regions:  $\cancel{E}_T > 3, 3.5$  or 4 TeV.

This set of cuts is designed to optimize the stop mass reach for light neutralinos. As we approach the diagonal of the  $m_{\tilde{t}} - m_{\tilde{\chi}_1^0}$  plane, the top gets a smaller fraction of the initial energy, and its decay products become more separated. In addition, the total visible energy and  $\cancel{E}_T$  in the event are considerably reduced. In this compressed region of parameter space the natural candidate to recover sensitivity is a dilepton search [71]. This leads us to consider also the signal region defined by the following set of requirements:

1. At least two  $\Delta R = 0.5$  anti- $k_T$  jets with  $|\eta| < 2.5$  and  $p_T > 500$  GeV in the event.
2. The presence of two isolated leptons (either electrons or muons) with  $p_T^\ell > 35$  GeV is required. The isolation criterion is the same described for the boosted signal region.
3.  $\cancel{E}_T > 2$  TeV.

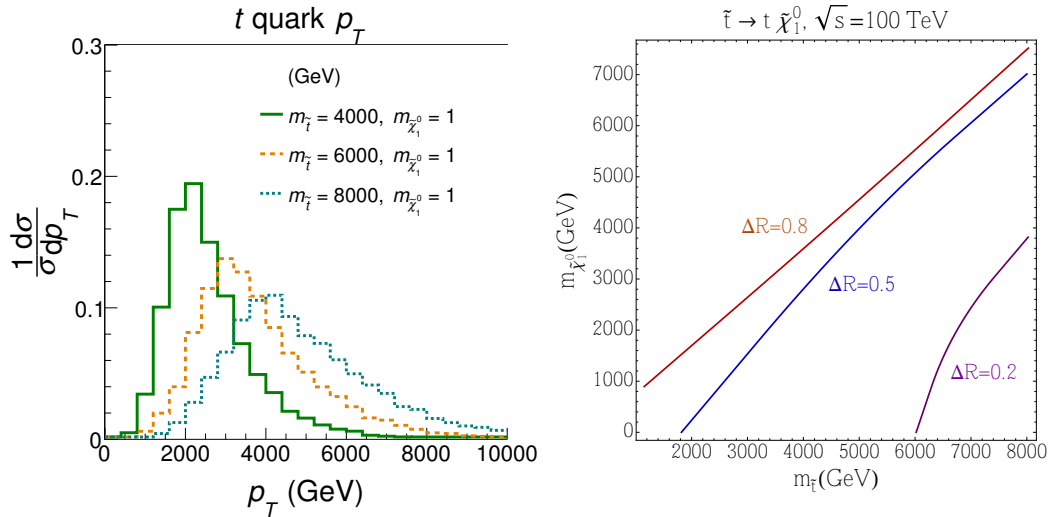


**Fig. 11:** Left: The  $p_T$  distribution of the leading top quark for  $m_{\tilde{t}} = 4, 6, 8$  TeV, setting  $m_{\tilde{\chi}_1^0} = 1$  GeV. Right: Average  $\Delta R$  between  $W$  and  $b$  from top decays as a function of  $m_{\tilde{t}}$  and  $m_{\tilde{\chi}_1^0}$ .

4.  $\Delta\phi_{\cancel{E}_T, J, \ell} > 1.0$ , where  $\Delta\phi_{\cancel{E}_T, J, \ell}$  is the minimum  $|\Delta\phi|$  between  $\cancel{E}_T$  and any jet with  $p_T > 200$  GeV and  $|\eta| < 2.5$ , and any isolated lepton with  $p_T^\ell > 35$  GeV and  $|\eta| < 2.5$ .

The expected mass reach of the compressed and boosted searches is shown in Fig. 12 for  $3000 \text{ fb}^{-1}$  of integrated luminosity. We assume a 20% systematic uncertainty on both signal and background. Exclusion is defined at 95% confidence level, and the significance for discovery is  $5\sigma$ . Background and signal are modeled as Poisson distributions with Gaussian systematics. Exclusion limits are computed using a modified Frequentist procedure ( $CL_s$ ) computed using ROOSTATS [116]. We find that stops with masses of  $\approx 5.5(8)$  TeV can be discovered (excluded) if the neutralino is massless. In most of the parameter space we can exclude neutralino masses up to 2 TeV. In the compressed region we can discover stops up to 1.5 TeV. The impact of larger systematic uncertainties on both signal and background is discussed in [71].

Another conclusion of the study is that an integrated luminosity of  $3000 \text{ fb}^{-1}$  does not saturate the potential of a 100 TeV collider. A factor of 10 more in integrated luminosity would extend the discovery reach on the stop mass up to 8 TeV (for a massless neutralino) and the exclusion to 10 TeV [71].

### 2.3.2 Hadronic Decays

In this section we consider fully hadronic decays using strategies inspired by [98, 117–121]. Experimental searches for this channel from the 8 TeV run of the LHC are reviewed in [96, 122] with a current bound of about 700 GeV for very light neutralinos. The limit weakens with increasing neutralino mass, disappearing completely for a neutralino heavier than about 300 GeV.

The fully hadronic channel has two advantages over leptonic searches. The first is that it has the largest branching fraction for the top decays. The second is that it has no inherent missing energy from neutrinos, so all the missing energy comes from the neutralinos. This allows many backgrounds to be reduced by vetoing events with leptons.

Here we will present a very crude estimate of the reach at a future 100 TeV collider. We will choose stringent cuts to get a very pure signal sample, and then compute the signal efficiency using literature and simplified parton level simulations. The results, presented in Ref. [121], are summarized in Table 1 for  $\sqrt{s} = 100$  TeV, and for other future collider scenarios. Those results use tree-level cross sections given by MadGraph 5 [111], but for our 100 TeV study we use NLL+NLO results from [82].

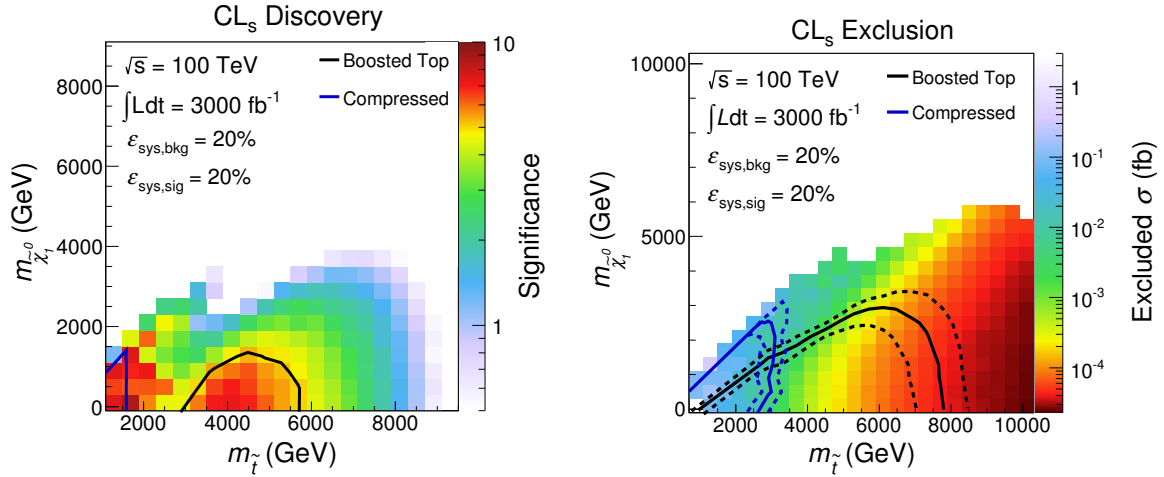


**Fig. 12:** Left: Discovery potential and Right: Projected exclusion limits for  $3000 \text{ fb}^{-1}$  of total integrated luminosity at  $\sqrt{s} = 100 \text{ TeV}$ . The solid lines show the expected discovery or exclusion obtained from the boosted top (black) and compressed spectra (blue) searches. In the boosted regime we use the  $\cancel{E}_T$  cut that gives the strongest exclusion for each point in the plane. The dotted lines in the left panel show the  $\pm 1\sigma$  uncertainty band around the expected exclusion.

Collider	Energy	Luminosity	Cross Section	Mass
LHC8	8 TeV	$20.5 \text{ fb}^{-1}$	10 fb	650 GeV
LHC	14 TeV	$300 \text{ fb}^{-1}$	3.5 fb	1.0 TeV
HL LHC	14 TeV	$3 \text{ ab}^{-1}$	1.1 fb	1.2 TeV
HE LHC	33 TeV	$3 \text{ ab}^{-1}$	91 ab	3.0 TeV
FCC-hh	100 TeV	$1 \text{ ab}^{-1}$	200 ab	5.7 TeV

**Table 1:** The first line gives the current bound on stops from the LHC 8 TeV data [96, 122]. The remaining lines give the estimated  $5\sigma$  discovery reach in stop pair production cross section and mass for different future hadron collider runs (from [121]). At 100 TeV, NLL+NLO cross sections can be used to extend the reach.

We use top tagging [4, 98, 99, 123–126] to distinguish signal from background. Since highly boosted top tagging may suffer from intrinsic limitations due to the nature of calorimeters [7], the search presented here avoids specialized substructure variables and instead uses top-tagging techniques established at the LHC. This is applied to stop searches in theory studies in [98, 117–121]. Top tagging has been used by experiments at the LHC [127, 128] in other types of searches, and from [127] we take the efficiency of top tagging to be 50% for tops with  $p_T > 500 \text{ GeV}$ . From the same search we take the fake rate to be 5% for the same  $p_T$  range. There is very little data for  $p_T > 800 \text{ GeV}$ , but we will use these efficiencies throughout our study, even at very high energy. The HPTTopTagger [4] study focuses on  $p_T > 1 \text{ TeV}$  and finds somewhat lower tagging efficiency but also lower fake rates.

Therefore, we make the following cuts taking the efficiency from the literature:

- Require both tops decay hadronically (46%),
- Require one  $b$ -tag (70%) [129, 130],
- Require both tops pass a top tagger (25%).

We also simulate pair production of 6 TeV stops decaying to a nearly massless (1 GeV) neutralino at a 100 TeV machine. The simulation is done at parton level with MadGraph 5 [111] and is used to compute the efficiency for the following two cuts:

Energy	Luminosity	Cross Section	Mass
100 TeV	1 ab <sup>-1</sup>	200 ab	6.2 TeV
100 TeV	30 ab <sup>-1</sup>	36 ab	7.9 TeV

**Table 2:** Discovery reach at a 100 TeV collider using NLL+NLO cross sections for two different luminosity benchmarks.

- Require that both tops have  $p_T > 500$  GeV (97%),
- Require missing transverse energy bigger than 4 TeV (38%).

The first cut justifies the efficiency of the top tagger cut from above. The efficiency of the second cut is computed after the first cut is applied, and the total efficiency of all cuts is 3.0%.

In order to estimate the size of the backgrounds, we use the same combination of cut efficiencies obtained from the literature and parton level Monte Carlo. Because of our requirement of  $b$  and top tags, the dominant backgrounds will be those with on-shell tops. In searches at the LHC, the dominant background is  $t\bar{t}$  production where one of the tops decays to a hadronic  $\tau$ . At 100 TeV, however, this background is made negligibly small by the large missing energy cut. Therefore, the dominant background is  $t\bar{t}Z$  where the  $Z$  decays to neutrinos and is highly boosted to pass the missing energy cut.

The production cross section at 100 TeV is 46 pb. Applying just the 4 TeV missing energy cut reduces the effective cross section to 130 ab. Applying the requirement of both tops having  $p_T > 500$ , as well as branching ratios and  $b$  and top tags reduces the effective cross section to 1.4 ab, so with these hard cuts, even this potentially large background can be reduced to be essentially negligible until extremely high luminosity is reached. Other more exotic backgrounds such as four top and  $t\bar{t}ZZ$  production are not considered here, but they are expected to be subdominant.

Our results are summarized in Table 1. We estimate the  $\sigma$ -significance as number of signal events divided by the square root of the number of background events. This can be rewritten as a discovery of  $N_\sigma$  being achieved with the following signal cross section

$$\sigma_s = \frac{N_\sigma}{\varepsilon_s} \sqrt{\frac{\varepsilon_b \sigma_b}{L}} \quad (10)$$

where  $\varepsilon_s$  is the signal efficiency computed in Section 2.3.2,  $\varepsilon_b \sigma_b$  is the effective background cross section, and  $L$  is the integrated luminosity of the collider run. Our cuts are such that the expected number of background events is  $\mathcal{O}(1)$ , so we need  $\mathcal{O}(5)$  events for a  $5\sigma$  discovery. In this regime, Eq. (10) is not strictly correct, but will suffice as a reasonable approximation here. We find that at 100 TeV machine with 1 ab<sup>-1</sup> of luminosity can discover stops with pair production cross section of 200 ab. Using leading order cross sections from Madgraph 5, this corresponds to a discovery reach of 5.7 TeV.

Using the cross sections in Section 2.2 to estimate the mass reach leads to slightly stronger limits, albeit with higher-order corrections included for signal while background is still treated at leading order. With these caveats, we can use Eq. 10 and Fig. 7 to estimate the reach. The final results are shown in Table 2. Going from leading order to the more precise calculation extends the reach by about 10%.

The analysis here is a very naive estimate of the reach, and there many things that could be done to make it more precise including implementing top decays and hadronization as well as a realistic detector simulation. One can also consider more sophisticated cuts which vary for the different stop masses. It would also be interesting to see what the top tagging efficiency and fake rates look like at even higher top momenta. These and other issues are left for future study.

## 2.4 Gluinos

Gluinos are a critical component of supersymmetric theories. With regard to the hierarchy problem they only enter the Higgs potential at two loops embedded within a stop loop. However, due to the large top Yukawa, and reasonably large QCD gauge coupling, these corrections can be large, thus gluinos are still important for understanding the role of supersymmetry in addressing the hierarchy problem.

In this section we study the reach of a 100 TeV collider for gluinos in the context of several simplified models. The gluino and LSP will always be considered to be relatively light, sometimes along with light-flavor squarks. The LSP is assumed to be stable, and all decays are assumed to be prompt. Depending on the spectrum of heavy scalar sparticle masses, gluino decays can be mediated by light-flavor squarks or by stops. When the decays are mediated by light-flavor squarks, the gluino effectively undergoes a three-body decay to two quarks and the invisible  $\tilde{\chi}_1^0$ . For decays mediated by stops, the gluino decays to  $t\bar{t} + \tilde{\chi}_1^0$ . In cases where light-flavor squarks are also accessible, the gluinos and squarks can be produced in association with each other, leading to a third class of signatures. The three signatures considered in this section, along with the analysis strategies used to confront them, are shown below:

Simplified Model	Decay Channel	Search Strategy
Gluino-neutralino (light flavor)	$\tilde{g} \rightarrow q\bar{q}\tilde{\chi}_1^0$	jets+ $\cancel{E}_T$ , mono-jet
Gluino-neutralino (heavy flavor)	$\tilde{g} \rightarrow t\bar{t}\tilde{\chi}_1^0$	Same-sign dilepton
Gluino-squark with a massless neutralino	$\tilde{g} \rightarrow (q\bar{q}\tilde{\chi}_1^0/q\tilde{q}^*);$ $\tilde{q} \rightarrow (q\tilde{\chi}_1^0/q\tilde{g})$	jets+ $\cancel{E}_T$

### 2.4.1 Pair Production

Models of split and mini-split SUSY can have scalar superpartner masses well above the masses of the gauginos [22–25, 43]. In this case, the gluino ( $\tilde{g}$ ) and LSP ( $\tilde{\chi}_1^0$ ) are left as the only accessible superpartners at a  $\sqrt{s} = 100$  TeV collider. However, the large cross section for gluino production, as shown in Section 2.2, makes this a likely discovery channel for SUSY at present and future colliders. A full description of all analyses summarized here is available in Refs. [68, 71].

Parton level events for all searches were generated using Madgraph5 v1.5.10 [111]. All signals involve the pair production of SUSY particles and are matched using MLM matching up to 2 additional jets. The  $k_t$ -ordered shower scheme with a matching scale of  $q_{\text{cut}}=x_{\text{qcut}}=100$  GeV was used. We do not account for any possible inadequacies inherent in the current Monte Carlo technology, *e.g.* electroweak gauge bosons are not included in the shower.

The gluinos and squarks were treated as stable at the parton level. These events were subsequently decayed and showered using Pythia6 [112] and passed through the Delphes detector simulation [113] using the “Snowmass” detector parameter card [114]. Total production cross sections were computed at NLO using a modified version of Prospino v2.1 [78, 79, 131], and stop cross sections were computed at NLL using [82], consistent with the results shown in Section 2.2.

#### 2.4.1.1 Gluino-neutralino with light flavor decays

In a simplified gluino-neutralino model with decays to light flavor quarks, the gluino is the only kinematically accessible colored particle. The squarks are completely decoupled and do not contribute to gluino production diagrams. The gluino undergoes a prompt three-body decay through off-shell squarks,  $\tilde{g} \rightarrow q\bar{q}\tilde{\chi}_1^0$ , where  $q$  is one of the light quarks and  $\tilde{\chi}_1^0$  is a neutralino LSP. The only two relevant parameters are the gluino mass  $m_{\tilde{g}}$  and the neutralino mass  $m_{\tilde{\chi}_1^0}$ .

The background is dominated by  $W/Z + \text{jets}$ , with subdominant contributions from  $t\bar{t}$  production. Single top events and  $W/Z$  events from vector boson fusion processes are negligible. In all cases, there

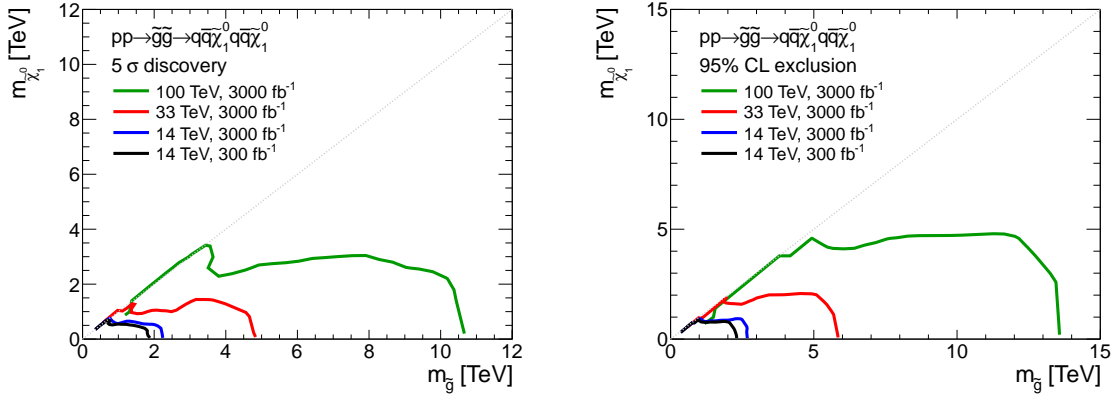


**Fig. 13:** Results for the gluino-neutralino model with light flavor decays. The left [right] panel shows the  $5\sigma$  discovery reach [95% CL exclusion] for the four collider scenarios studied here. A 20% systematic uncertainty is assumed and pile-up is not included.

are decay modes which lead to multi-jet signatures. The  $\cancel{E}_T$  can come from a variety of sources, such as neutrinos, jets/leptons that are lost down the beam pipe, and energy smearing effects.

The first analysis used to confront such signals is inspired by an ATLAS upgrade study [132]. After an event preselection, rectangular cuts on one or more variables are optimized at each point in parameter space to yield maximum signal significance. Specifically, we simultaneously scan a two-dimensional set of cuts on  $\cancel{E}_T$  and  $H_T$ , where  $\cancel{E}_T$  is the magnitude of the missing transverse momentum and  $H_T$  is defined as the scalar sum of jet  $p_T$ . Following a standard four-jet pre-selection, the following cuts are applied:

- $\cancel{E}_T/\sqrt{H_T} > 15 \text{ GeV}^{1/2}$
- The leading jet  $p_T$  must satisfy  $p_T^{\text{leading}} < 0.4 H_T$
- $\cancel{E}_T > (\cancel{E}_T)_{\text{optimal}}$
- $H_T > (H_T)_{\text{optimal}}$

The discovery reach and limits for all several future collider scenarios in the full  $m_{\tilde{g}}$  versus  $m_{\tilde{\chi}_1^0}$  plane can be seen in Fig. 13. For a 100 TeV collider with  $3000 \text{ fb}^{-1}$ , the limit with massless neutralinos is projected to be 13.5 TeV (corresponding to 60 events). The 100 TeV proton collider with  $3000 \text{ fb}^{-1}$  could discover a gluino as heavy as 11 TeV if the neutralino is massless, while for  $m_{\tilde{\chi}_1^0} \gtrsim 1 \text{ TeV}$  the gluino mass reach rapidly diminishes.

A separate analysis is used to target the compressed region of parameter space of this simplified model, where:

$$m_{\tilde{g}} - m_{\tilde{\chi}_1^0} \equiv \Delta m \ll m_{\tilde{g}}. \quad (11)$$

For models with this spectrum, the search strategy of the previous section does not provide the optimal reach. With compressed spectra the gluino decays only generate soft partons, thereby suppressing the  $H_T$  signals and reducing the efficiency for passing the 4 jet requirement. A more effective strategy for compressed spectra searches relies instead on events with hard initial state radiation (ISR) jets to discriminate signal from background.

The dominant background is the production of a  $Z$  boson in association with jets, where the  $Z$  boson decays into a pair of neutrinos ( $Z \rightarrow \nu\nu$ ), leading to events with jets and a significant amount of missing transverse energy. Subleading backgrounds are the production of a  $W$  boson which decays leptonically ( $W \rightarrow \ell\nu$ ) in association with jets, where the charged lepton is not reconstructed properly.

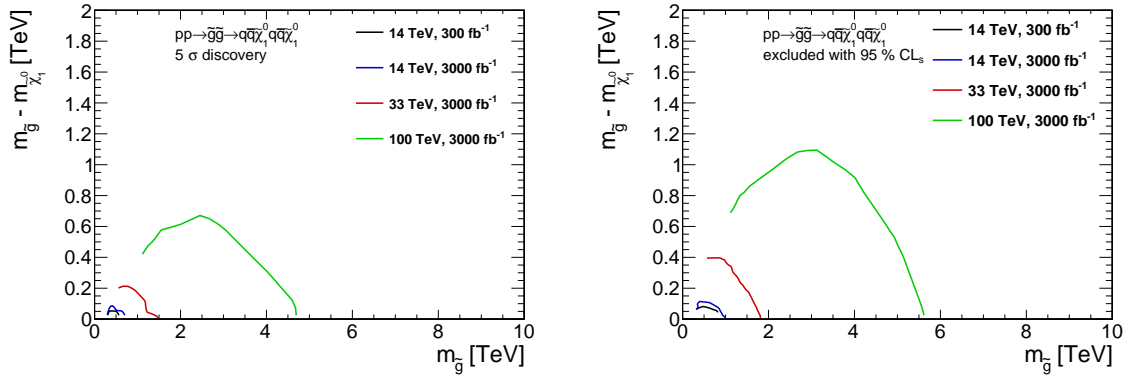


**Fig. 14:** Results for the gluino-neutralino model with light flavor decays for the analyses that target the compressed region of parameter space. The left [right] panel shows the  $5\sigma$  discovery reach [95% CL exclusion] for the four collider scenarios studied here. A 20% systematic uncertainty is assumed and pile-up is not included.

Finally, when considering events with a significant number of jets,  $t\bar{t}$  production in the fully hadronic decay channel ( $t \rightarrow b q q'$ ) can be relevant.

In this study, we will apply two different search strategies that are optimized for this kinematic configuration and will choose the one that leads to the most stringent bound on the production cross section for each point in parameter space. Some of the cuts chosen below are inspired by recent public results from ATLAS [133] and CMS [134] on monojet searches. Following a standard pre-selection, we first define a search strategy that selects events with a very hard leading jet

- at most 2 jets
- leading jet must have  $p_T > (\text{leading jet } p_T)_{\text{optimal}}$  and  $|\eta| < 2.0$
- second jet is allowed if  $\Delta\varphi(j_2, \cancel{E}_T) > 0.5$
- $\cancel{E}_T > (\cancel{E}_T)_{\text{optimal}}$

where both  $(\cancel{E}_T)_{\text{optimal}}$  and  $(\text{leading jet } p_T)_{\text{optimal}}$  are determined simultaneously by taking the values in the range 1 – 10 TeV that yields the strongest exclusion.

The second search strategy targeting the compressed regime uses a  $\cancel{E}_T$ -based selection with no jet veto:

- leading jet with  $p_T > 110$  GeV and  $|\eta| < 2.4$
- $\cancel{E}_T > (\cancel{E}_T)_{\text{optimal}}$

with  $\cancel{E}_T$  varied in the range (1, 10) TeV. No requirement is placed on a maximum number of jets. Note that for higher jet multiplicities the production of top quark pairs in the fully hadronic decay mode starts to dominate over  $W/Z$  + jets production.

The discovery reach and limits for the compressed searches for all four collider scenarios in the full  $m_{\tilde{g}}$  versus  $m_{\tilde{\chi}_1^0}$  plane are shown in Fig. 14.

For a 100 TeV proton collider with  $3000 \text{ fb}^{-1}$  of data, the exclusion reach for a mass difference of 5 GeV covers gluino masses of up to approximately 5.7 TeV, with reduced reach for larger mass differences. For very small mass differences discoveries could be made for gluino masses up to 4.8 TeV. This search improves the exclusion (discovery) reach near the degenerate limit by roughly 1.7 TeV (1.3 TeV) compared to the  $H_T + \cancel{E}_T$ -based analysis; the  $H_T + \cancel{E}_T$ -based searches do not begin to set stronger limits until  $\Delta \gtrsim 500$  GeV.

### 2.4.1.2 Gluino-neutralino with heavy flavor decays

In a gluino-neutralino model with decays to heavy flavour quarks, the gluino is the only kinematically accessible colored particle. The squarks are completely decoupled and do not contribute to gluino production diagrams. The gluino undergoes a prompt three-body decay through off-shell stops,  $\tilde{g} \rightarrow t\bar{t}\tilde{\chi}_1^0$ , where  $t$  is the top quark and  $\tilde{\chi}_1^0$  is a neutralino LSP. The only two relevant parameters are the gluino mass  $m_{\tilde{g}}$  and the neutralino mass  $m_{\tilde{\chi}_1^0}$ .

The model produces two  $t\bar{t}$  pairs along with considerable  $\cancel{E}_T$  (away from the compressed region of parameter space), and therefore provides an interesting benchmark scenario for searches involving a combination of hadronic activity, leptonic signatures and  $b$ -tagging. A search which requires same-sign di-leptons (SSDL) is one viable approach to eliminating the SM background since this final state is highly suppressed in the SM. A SSDL pair is required and any remaining leptons are not allowed to form a  $Z$ -boson, inspired by the CMS collaboration in [135]. We note that this was the only channel explored in this scenario; it would be interesting to investigate how an all hadronic final state search would perform at the higher energy machines.

The analysis used to derive the results below requires an SSDL pair, which is very efficient at eliminating backgrounds. The dominant background is top pair production, where both tops decay leptonically (the di-leptonic channel). There are subdominant backgrounds from  $Wb\bar{b}$ , which are accounted for by including the  $BJ$  Snowmass particle container [110]. All backgrounds simulated for Snowmass are included and their rates are found to be negligible. Since the SSDL requirement is very effective at suppressing backgrounds, only a mild cut on  $\cancel{E}_T$  is necessary to observe this model. This implies that this search will also be very effective in the compressed regions of parameter space where  $m_{\tilde{g}} \simeq m_{\tilde{\chi}_1^0}$ .

After preselection, the following are used as discriminating variables. Eight model points, three with very low LSP mass, three with medium LSP mass, and two with high LSP mass are used to define eight signal regions, which rely on some combination of the following cuts.

- Symmetric  $M_{T2} > (\text{symmetric } M_{T2})_{\text{optimal}}$
- $p_T > (p_T)_{\text{optimal}}$  for the hardest lepton
- $\cancel{E}_T > (\cancel{E}_T)_{\text{optimal}}$
- $N_{\text{jets}} > (N_{\text{jets}})_{\text{optimal}}$
- $N_{b\text{-jets}} > (N_{b\text{-jets}})_{\text{optimal}}$
- $m_{\text{eff}} > (m_{\text{eff}})_{\text{optimal}}$
- $(H_T)_{\text{jets}} > ((H_T)_{\text{jets}})_{\text{optimal}}$

Symmetric  $M_{T2}$  is defined in the canonical way [136–138], where the SSDL pair is used for the visible signal and the invisible particle test mass is assumed to be zero;  $m_{\text{eff}}$  is defined as the scalar sum of the  $p_T$  of all visible objects and  $\cancel{E}_T$ .

The results for the gluino-squark-neutralino model are given in Fig. 15. The 14 TeV 300 fb<sup>-1</sup> limit is projected to be 1.9 TeV (corresponding to 73 events), and the 3000 fb<sup>-1</sup> limit is projected to be 2.4 TeV (corresponding to 67 events). The 14 TeV LHC with 3000 fb<sup>-1</sup> could discover a gluino (with  $\tilde{g} \rightarrow t\bar{t}\tilde{\chi}_1^0$ ) as heavy as 2.0 TeV if the neutralino is massless. The 33 TeV 3000 fb<sup>-1</sup> limit is projected to be 4.0 TeV (corresponding to 243 events). A 33 TeV proton collider with 3000 fb<sup>-1</sup> could discover a gluino (with  $\tilde{g} \rightarrow t\bar{t}\tilde{\chi}_1^0$ ) as heavy as 3.4 TeV if the neutralino is massless. The 100 TeV 3000 fb<sup>-1</sup> limit is projected to be 8.8 TeV (corresponding to 224 events). A 100 TeV proton collider with 3000 fb<sup>-1</sup> could discover a gluino (with  $\tilde{g} \rightarrow t\bar{t}\tilde{\chi}_1^0$ ) as heavy as 6.4 TeV if the neutralino is massless. Note that due to the relatively weak cuts that can be placed on  $\cancel{E}_T$ , the SSDL signal is robust against models with almost degenerate gluino and neutralino.

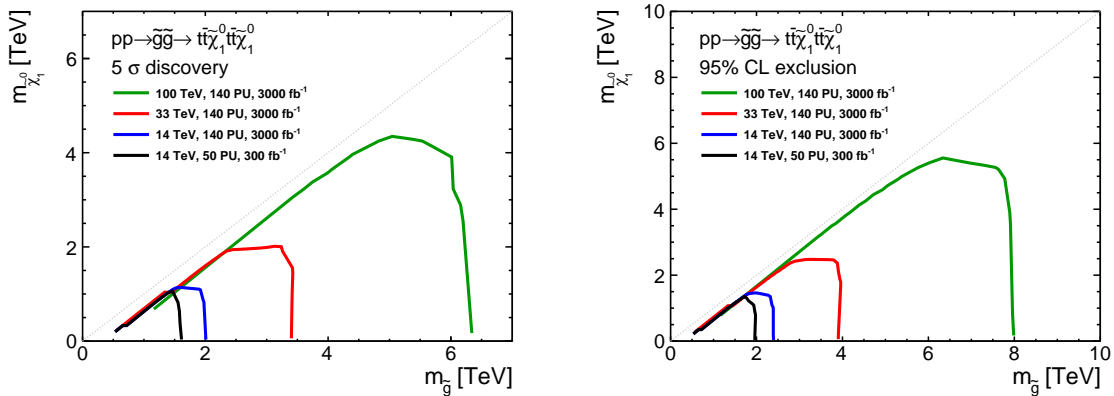


**Fig. 15:** Results for the gluino-squark-neutralino model. The neutralino mass is taken to be 1 GeV. The left [right] panel shows the  $5\sigma$  discovery reach [95% CL exclusion] for the four collider scenarios studied here. A 20% systematic uncertainty is assumed and pile-up is included.

## 2.4.2 Associated Production

In gluino-squark neutralino models, the gluino, the first and second generation squarks, and the LSP are all kinematically accessible. The only relevant parameters are the squark mass  $m_{\tilde{q}}$ , which is taken to be universal for the first two generations, the gluino mass  $m_{\tilde{g}}$ , and the neutralino mass  $m_{\tilde{\chi}_1^0}$ . We consider two scenarios: one in which the neutralino is massless, and the gluino and squark have similar masses; and another in which the neutralino is also light, but the squark mass is substantially above that of the gluino mass.

### 2.4.2.1 Associated production with $m_{\tilde{q}} \sim m_{\tilde{g}}$

For this study we fix the neutralino mass  $m_{\tilde{\chi}_1^0} = 1$  TeV, which captures the relevant kinematics for  $m_{\tilde{g}}, m_{\tilde{q}} \gg m_{\tilde{\chi}_1^0}$ . The decay mode is chosen depending on the mass hierarchy.

This model is a good proxy for comparing the power of searches that rely on the traditional jets and  $\cancel{E}_T$  style hadron collider search strategy to discriminate against background. The final state ranges from two to four (or more) hard jets from the decay (depending on the production channel) and missing energy. The current preliminary limits on this model using  $20 \text{ fb}^{-1}$  of 8 TeV data are  $m_{\tilde{g}} = 1750$  GeV and  $m_{\tilde{q}} = 1600$  GeV (ATLAS [139]) assuming a massless neutralino.

Following an identical analysis strategy as for the gluino-neutralino model, described in Section 2.4.1, the results for the gluino-squark-neutralino model are given in Fig. 16 and in Table 3. A 100 TeV collider can exclude up to 16 TeV in mass for  $m_{\tilde{g}} \sim m_{\tilde{q}}$ .

### 2.4.2.2 Associated production with $m_{\tilde{q}} > m_{\tilde{g}}$

The gluino-squark-neutralino model in the previous section was probed in a region where  $m_{\tilde{g}} \sim m_{\tilde{q}}$ . In this section, we consider squark-gluino associated production in a region of parameter space in which the gluinos are relatively light, while the squarks are heavier, but not completely decoupled. This work is documented more completely in [140], where we have analysed the prospects for squark-gaugino associated production at a 100 TeV collider.

Squark-gluino associated production is interesting because it has the potential to probe much higher squark masses than those reached in pair production. Spectra with a hierarchy between the gluino and the first two generation squarks are predicted in many scenarios, such as anomaly-mediated SUSY breaking [141, 142], or in “mini-split”-type models [22, 143, 144].

We consider two simplified models for squark-gluino associated production. In both, the particle

$\sqrt{s}$ [TeV]	$\int \mathcal{L} dt$ [fb $^{-1}$ ]	95% CL Exclusion	
		Mass Reach [TeV]	$N$ produced
14	300	2.8	155
14	3000	3.2	293
33	3000	6.8	132
100	3000	16	136

**Table 3:** 95% CL exclusion limits on associated gluino-squark production for various collider scenarios. The last column indicates the total number of squark pairs produced at a squark mass at the 95% CL exclusion limit for the given collider scenario.

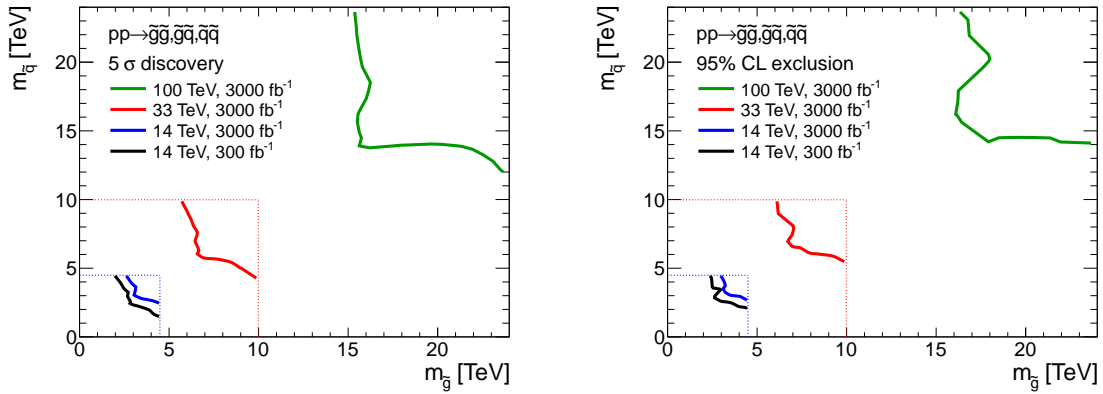


**Fig. 16:** Results for the gluino-squark-neutralino model. The neutralino mass is taken to be 1 GeV. The left [right] panel shows the  $5\sigma$  discovery reach [95% CL exclusion] for the four collider scenarios studied here. A 20% systematic uncertainty is assumed and pile-up is not included.

content consists only of first and second generation squarks, gluino, and a Bino LSP ( $\tilde{\chi}_1^0 = \tilde{B}$ ). The two models correspond to different choices of the LSP mass:

- Non-compressed:  $M_1 = 100$  GeV (results in Fig. 18(a))
- Compressed:  $m_{\tilde{g}} - m_{\tilde{\chi}_1^0} = 15$  GeV (results in Fig. 18(b))

where we take the first and second generation squarks to be degenerate in mass, and decouple all other superpartners. Our results are insensitive to the choice of  $M_1 = 100$  GeV in the non-compressed spectra, as the LSP is effectively massless for  $m_{\tilde{\chi}_1^0} \ll m_{\tilde{g}}$ . The compressed spectra are consistent with the gluino-neutralino dark matter (DM) coannihilation region [145, 146].

Events from squark-gluino associated production have distinctive event topologies, with a hard leading jet and significant  $\cancel{E}_T$ . Both arise primarily from the decay of the heavy squark, since the gluino is produced at relatively low  $p_T$ . As in the gluino simplified models above, the dominant sources of background are top pair production and production of an SM boson + jets [68]. However, both of these backgrounds fall off rapidly both with increasing  $p_T(j_1)$ ,  $\cancel{E}_T$ , and  $\cancel{E}_T \sqrt{H_T}$  (where  $H_T$  is the scalar sum of the jet transverse energies). This can be seen for an example spectrum point in Fig. 17.

The leading jet typically has a  $p_T(j_1) \sim m_{\tilde{q}}/2$ , while the decay of the squark into the LSP  $\tilde{q} \rightarrow q\tilde{g} \rightarrow 3q\tilde{\chi}_1^0$  results in a highly boosted neutralino and large  $\cancel{E}_T$ . As such, heavy squark - light gluino associated production events have a striking collider signature with very low SM backgrounds.

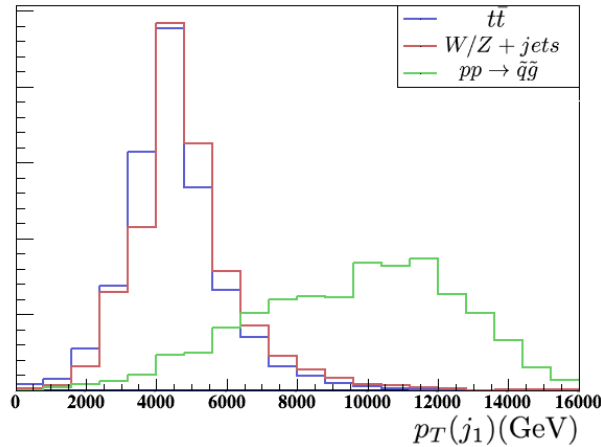


**Fig. 17:** Example distribution of the leading jet  $p_T$  for  $pp \rightarrow \tilde{q}\tilde{g}$ , showing that the leading jet  $p_T$  of the signal (green) is a good discriminatory variable. Shown here is the spectrum with  $m_{\tilde{q}} \simeq 26$  TeV and  $m_{\tilde{g}} \simeq 4$  TeV. All events shown satisfy  $\cancel{E}_T > 2$  TeV.

We impose the following baseline cuts for both spectra:

$$H_T > 10 \text{ TeV}, \quad \cancel{E}_T / \sqrt{H_T} > 20 \text{ TeV}^{1/2}.$$

For the non-compressed spectra we impose the additional cut:

$$8 \text{ jets with } p_T > 50 \text{ (150) GeV}$$

where the softer cut is optimized for heavier squarks and lighter gluinos, while the harder cut is optimized for lighter squarks and heavier gluinos. We then scan over leading jet  $p_T$  and  $\cancel{E}_T$  cuts in order to maximize the significance,  $\sigma$ :

$$\sigma \equiv \frac{S}{\sqrt{1 + B + \lambda^2 B^2 + \gamma^2 S^2}}, \quad (12)$$

where  $S$  ( $B$ ) is the number of signal (background) events passing all cuts, and  $\gamma$  ( $\lambda$ ) parameterize systematic uncertainties associated with signal (background) normalization. We have verified that the optimal cuts render any “background” from gluino pair production subdominant to the SM background.

Our results are shown in Figs. 18(a) and 18(b) for the non-compressed and compressed spectra, respectively. We have assumed a conservative  $3 \text{ ab}^{-1}$  integrated luminosity [147].

The solid, long-dashed and short-dashed lines correspond respectively to assuming systematic uncertainties of 5, 10 and 15% in the signal normalisation, while keeping the background systematic uncertainty fixed at 20%. The number of background events is quite low due to the hard leading jet  $p_T$  and  $\cancel{E}_T$  cuts, so the projected reach is relatively insensitive to background systematic uncertainties.

The increased reach for the compressed spectra is due to the additional  $\cancel{E}_T$  resulting from the heavier LSP. We note that the entire neutralino-gluino coannihilation region (whose upper endpoint lies at  $m_{\tilde{g}} \approx m_{\tilde{\chi}_1^0} \approx 8$  TeV [146]) can be excluded if the squark masses are  $\lesssim 28$  TeV.

The results of the previous sections imply that gluino pair production is likely to be the discovery channel for coloured superpartners provided  $m_{\tilde{g}} \lesssim 14$  TeV. However, for the compressed spectra, gluino pair production searches rapidly lose sensitivity. As such, squark-gluino associated production could be a potential discovery channel for spectra where the gluino and LSP are nearly degenerate.

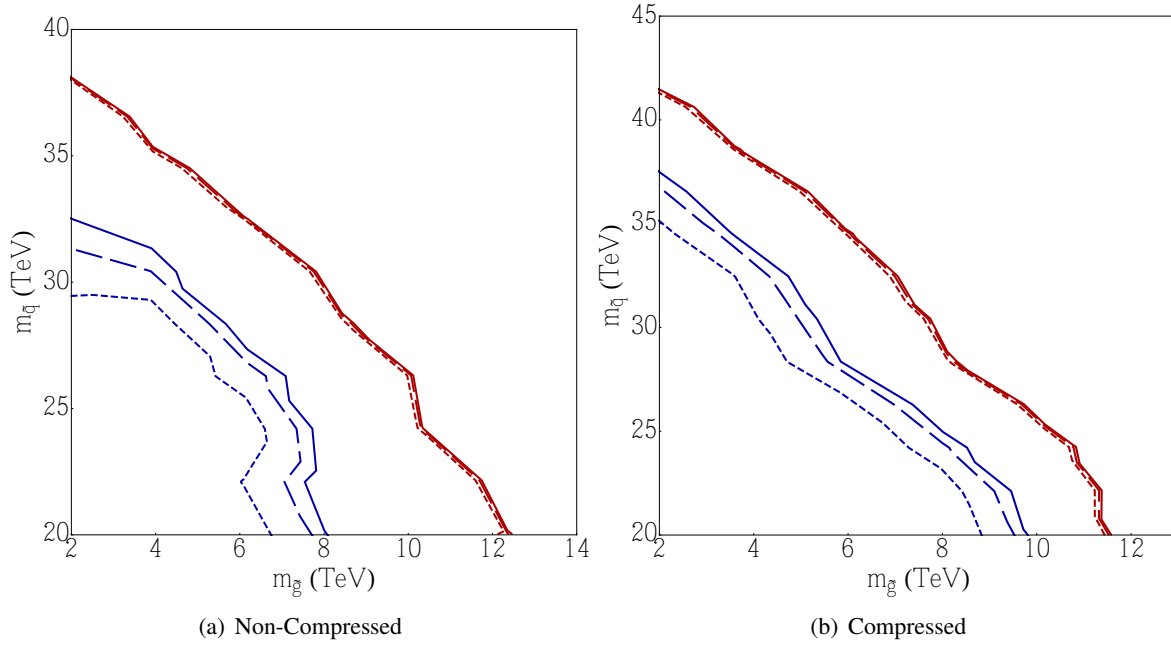


**Fig. 18:** Experimental reach for squark-gluino associated production at a 100 TeV collider with  $3 \text{ ab}^{-1}$  integrated luminosity. Left panel: Experimental reach for spectra with a  $\sim 100$  GeV LSP mass. Right panel: Experimental reach for spectra with  $m_{\tilde{q}} - m_{\tilde{\chi}_1^0} = 15$  GeV. The solid, long dashed and short dashed lines are for 5, 10, 15% systematic uncertainty for the signal respectively. Blue lines indicate  $5\sigma$  discovery reach and red lines indicate 95% exclusion limits. We assume 20% systematic uncertainty in the background.

## 2.5 Squarks

While naturalness considerations motivate light stops, discussed in Section 2.3, and light gluinos, discussed in Section 2.4, supersymmetric partners of light-flavor quarks can have significantly larger masses at little extra fine-tuning cost. However, models that include Dirac gluinos [148] can accommodate light squark masses in a way that makes them a discovery mode for BSM physics at hadron colliders.

This section summarizes the “squark-neutralino” simplified model discussed in [68, 71], in which the first and second generation squarks  $\tilde{q} = \tilde{u}_L, \tilde{u}_R, \tilde{d}_L, \tilde{d}_R, \tilde{c}_L, \tilde{c}_R, \tilde{s}_L, \tilde{s}_R$  are the only kinematically accessible colored states. All other SUSY particles are decoupled. The relevant parameters of the model are the squark mass  $m_{\tilde{q}}$ , which is taken to be universal for the first two generations, and the neutralino mass  $m_{\tilde{\chi}_1^0}$ . Squarks are pair-produced via strong interactions, and the only allowed decay is to a light-flavor quark and the neutralino LSP.

Squark-neutralino simplified models have been probed at the LHC, operating at  $\sqrt{s} = 8$  TeV, by the CMS [149] and ATLAS [150] collaborations. No significant excesses have been observed, and limits on squark masses are approaching 1 TeV for neutralinos with masses up to 400 GeV.

The final state for the model under study is two high- $p_T$  jets with significant  $\cancel{E}_T$ . Thus, as with the gluino and associated gluino-squark searches in Section 2.4, this model is probed with a simple “jets+ $\cancel{E}_T$ ” search strategy, inspired by [132].

Parton-level signal events were generated using Madgraph5 v1.5.10 [111]. All signals involve the pair production of SUSY particles and are matched using MLM matching up to 2 additional jets. The  $k_t$ -ordered shower scheme with a matching scale of  $q_{\text{cut}}=x_{\text{qcut}}=100$  GeV was used. Note that we do not account for any possible inadequacies inherent in the current Monte Carlo technology, *e.g.* electroweak gauge bosons are not included in the shower.

The gluinos and squarks were treated as stable at the parton level. These events were subsequently

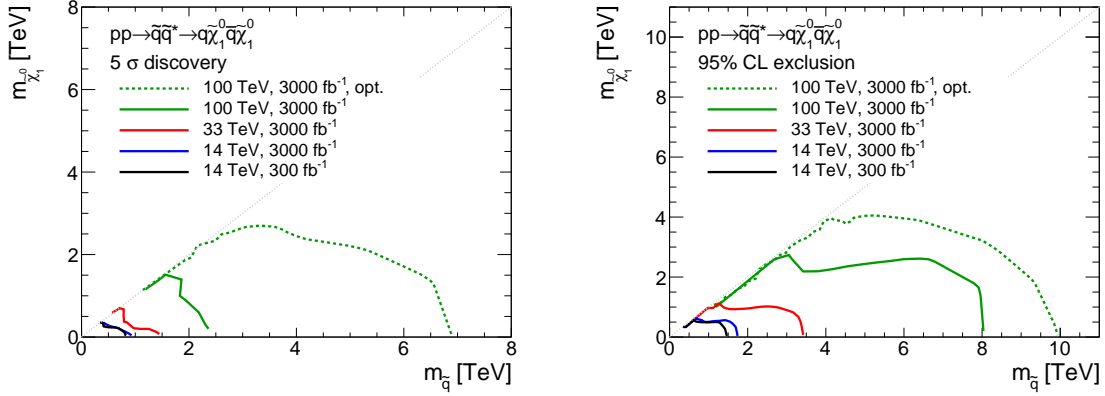


**Fig. 19:** Results for the squark-neutralino model. The left [right] panel shows the  $5\sigma$  discovery reach [95% CL exclusion] for the four collider scenarios studied here. A 20% systematic uncertainty is assumed and pile-up is not included. The dashed green line shows the results of a re-tuned search at  $\sqrt{s} = 100$  TeV.

decayed and showered using Pythia6 [112] and passed through the Delphes detector simulation [113] using the “Snowmass” detector parameter card [114]. Total production cross sections were computed at NLO using a modified version of Prospino v2.1 [78, 79, 131].

Background estimates are made using the “Snowmass 2013” background samples [110]. Generated processes include  $W/Z$ +jets,  $t\bar{t}$ , single-top, diboson,  $t + V$  and  $t\bar{t} + V$ , and Higgs. QCD multijet backgrounds were not generated, thus the analysis makes stringent cuts on  $\cancel{E}_T$  and related quantities to ensure that QCD multijet backgrounds will be negligible.

The squark search is optimized in two different regions of the squark-neutralino mass plane. The first search targets high-mass squarks with relatively-light LSPs using a straightforward jets+ $\cancel{E}_T$  strategy. The second search targets the “compressed” region where  $m_{\tilde{q}} \approx m_{\tilde{\chi}_1^0}$ .

As with the jets+ $\cancel{E}_T$  search for gluinos presented in Section 2.4, a standard event pre-selection is defined by the following requirements:

- $\cancel{E}_T/\sqrt{H_T} > 15 \text{ GeV}^{1/2}$
- The leading jet  $p_T$  must satisfy  $p_T^{\text{leading}} < 0.4 H_T$

After pre-selection, rectangular cuts on  $\cancel{E}_T$  and  $H_T$  are simultaneously optimized to yield maximum signal significance. The resulting requirements on  $H_T$  and  $\cancel{E}_T$  are typically a substantial fraction of the squark mass for low values of  $m_{\tilde{\chi}_1^0}$ . After optimization, the background is dominated by  $W/Z$  + jets, with smaller contributions from  $t\bar{t}$  production. All other backgrounds are negligible.

The results of the squark search are shown in the solid lines in Fig. 19 for four different collider scenarios. The 14 TeV  $300 \text{ fb}^{-1}$  limit with massless neutralinos is projected to be 1.5 TeV (corresponding to 1022 events), while the 14 TeV  $3000 \text{ fb}^{-1}$  limit is projected to be 1.7 TeV (corresponding to 3482 events). The 14 TeV LHC with  $3000 \text{ fb}^{-1}$  could discover a squark as heavy as 800 GeV if the neutralino is massless. The 33 TeV  $3000 \text{ fb}^{-1}$  limit with massless neutralinos is projected to be 3.4 TeV (corresponding to 3482 events), with discovery reach up to 1.4 TeV for massless neutralinos.

The 100 TeV  $3000 \text{ fb}^{-1}$  limit with massless neutralinos is projected to be 8.0 TeV (corresponding to 849 events), with discovery reach up to 2.4 TeV if the neutralino is massless. Compared to the 14 and 33 TeV searches, the squark reach degrades less rapidly as the neutralino mass is increased from the massless limit. The reduced cross section for light-squark production and the lower jet multiplicity of the final state combine to reduce the mass reach for this model relative to the stop or gluino searches.

The poor performance of the search at 100 TeV motivated a re-analysis of this model for the 100

TeV scenario. In the re-optimized analysis, the pre-selection requirements, which were optimized for the gluino-neutralino model described earlier, are removed. Events are required to have four jets with  $p_T > 500$  GeV, and must satisfy the following topological selection requirements, motivated by the analysis in Ref. [149]:

- $(\vec{p}_T^{\text{miss}} - \sum_{\ell,j} \vec{p}_T) < 100$  GeV
- $\min \Delta\phi(p_T^{\text{miss}}, \text{leading 4 jets}) < 0.6$

Requirements on  $H_T$  and  $\cancel{E}_T$  are then simultaneously optimized, as described earlier. The results of the re-optimized search are shown in the dashed green line of Fig. 19. The exclusion limits improve modestly, but the discovery contours improve significantly, due partially to the increased signal acceptance of the new selection compared to the previous jets+ $\cancel{E}_T$  studies. Further improvements are expected by implementing other analysis techniques demonstrated in Ref. [149], such as  $H_T$ -binning and the use of variables like  $M_{T,2}$ .

The second analysis strategy targets the compressed region of the squark-neutralino plane, where:

$$m_{\tilde{q}} - m_{\tilde{\chi}_1^0} \equiv \Delta m \ll m_{\tilde{q}}. \quad (13)$$

Due to the large LSP masses in this scenario, signal events often do not contain substantial  $H_T$ , making a simple jets+ $\cancel{E}_T$  search ineffective. In this case we rely on initial state radiation to boost the SUSY system, creating a monojet+ $\cancel{E}_T$  final state.

The compressed analysis is described in detail in Section 2.4, and the results of the search for four collider scenarios are shown in Fig. 20. For all four colliders, the  $\cancel{E}_T$ -based strategy has the best performance and is used to quantify the sensitivity.

At a 14 TeV collider, it is possible to exclude (discover) squarks in the degenerate limit with mass less than  $\sim 650$  GeV (500 GeV) with  $300 \text{ fb}^{-1}$  of data. Increasing the integrated luminosity by a factor of 10 has a minimal impact on the discovery reach for compressed squark models. This search improves the exclusion (discovery) reach near the degenerate limit by roughly 300 GeV (150 GeV) compared to the jets+ $\cancel{E}_T$ -based analysis described above; the jets+ $\cancel{E}_T$  searches do not begin to set stronger limits until  $\Delta m \gtrsim 50$  GeV.

For a 33 TeV collider, it is possible to exclude (discover) squarks in the degenerate limit with mass less than  $\sim 1.2$  (0.7) TeV with  $3000 \text{ fb}^{-1}$  of data. This does not substantially improve the discovery reach near the degenerate limit compared to the jets+ $\cancel{E}_T$  analysis, but does improve the exclusion reach by roughly 200 GeV for  $\Delta m \lesssim 100$  GeV.

Finally, for the 100 TeV collider, it is possible to exclude (discover) squarks in the degenerate limit with mass less than  $\sim 4$  TeV (3 TeV) with  $3000 \text{ fb}^{-1}$  of data. This improves the exclusion (discovery) reach near the degenerate limit compared to the jets+ $\cancel{E}_T$  analysis targeted at the non-compressed region described above by roughly 1.5 TeV (1.8 TeV) for  $\Delta m \lesssim 200$  GeV.

## 2.6 Electroweakinos

This section describes the discovery prospects for electroweakinos – Wino, Bino and Higgsino – at a 100 TeV  $pp$  collider. For studies focussing on the dark matter aspect of electroweakinos, see Sec. 3. We focus on supersymmetric scenarios where electroweakinos have a mass at around the electroweak-TeV scale, and all other superparticles are much heavier and beyond the collider reach. We specifically consider scenarios in which the mass parameters of the electroweakinos are not too close to each other. In this case, electroweakinos generally do not mix significantly with each other, leaving neutral and charged components of Winos and Higgsinos almost degenerate and different kinds of electroweakinos well-separated in mass. We call these nearly degenerate sets of states collectively the Lightest Supersymmetric

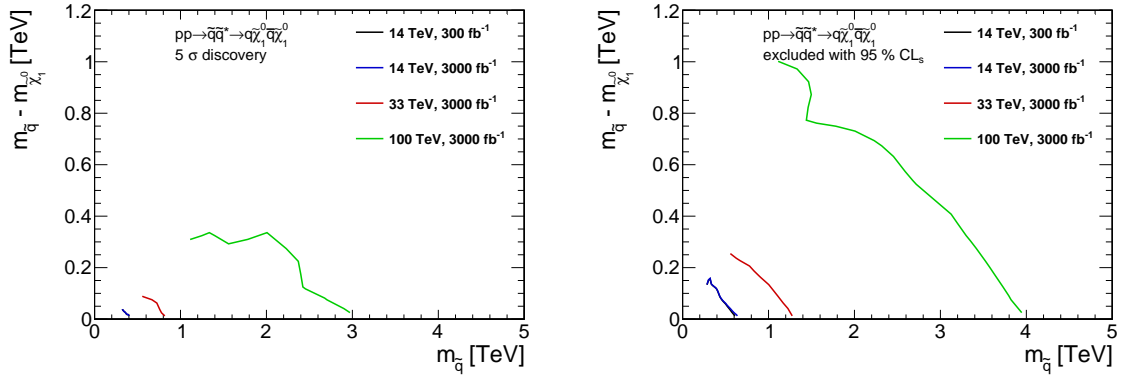


**Fig. 20:** Results for the squark-neutralino model with light flavor decays for the analyses that target the compressed region of parameter space. The left [right] panel shows the  $5\sigma$  discovery reach [95% CL exclusion] for the four collider scenarios studied here. A 20% systematic uncertainty is assumed and pile-up is not included.

Particle (LSP) ( $\chi_1^{0,\pm}$ ) or Next-to-Lightest Supersymmetric Particle NLSP ( $\chi_2^{0,\pm}$ )<sup>6</sup>.

Here we very briefly summarize the work in Ref. [74]<sup>7</sup> and focus on the direct production of NLSP pairs – neutralino pair, chargino pair and neutralino-chargino pair – and their subsequent decays to the LSP and a boson, either the Higgs boson  $h$  or  $W, Z$  gauge bosons, producing a multiple lepton and missing transverse energy signature.

$$\chi_2^{0,\pm} \rightarrow \chi_1^{0,\pm} Z/h, \quad \chi_2^{0,\pm} \rightarrow \chi_1^{\pm,0} W, \quad (14)$$

$$W \rightarrow \ell\nu, \quad Z \rightarrow \ell^+\ell^-, \quad h \rightarrow ZZ^*, \quad WW^* \rightarrow 4\ell, 2\ell 2\nu \quad (15)$$

Although final states involving hadronic jets are possible, multilepton signals typically provide the strongest discovery channels. We divide multilepton signals into two opposite-sign leptons of any flavor (OSDL), two same-sign leptons of any flavor (SSDL), three leptons ( $3\ell$ ), and four leptons ( $4\ell$ ), where leptons can be either electrons or muons.

For each simulated benchmark, we optimize the cuts on the following variables to maximize the statistical significance with an assumed luminosity of  $3 \text{ ab}^{-1}$ :

- $\cancel{E}_T$
- $p_T(\ell_2)/p_T(\ell_1)$
- $H_T(\text{jets})/M_{\text{eff}}$
- $M'_{\text{eff}} = M_{\text{eff}} - p_T(\ell_1)$
- $M_T(E_T^{\text{miss}}, \ell\ell)$ , the transverse masses between missing energy and various combinations of leptons
- $E_T^{\text{miss}}/M_{\text{eff}}$

where  $H_T(\text{jets})$  is the scalar sum of all jet  $p_T$  (we do not veto any jets if present) and  $M_{\text{eff}}$  is the scalar  $p_T$  sum of all jets, leptons and missing energy. We refer the reader to Ref. [74] for more detailed discussions of the variables, cut optimization, and other selection criteria that were considered.

We present results for the following cases:

- Higgsino NLSP and Bino LSP (Higgsino-Bino) :  $M_2 \gg \mu > M_1$ .
- Higgsino NLSP and Wino LSP (Higgsino-Wino) :  $M_1 \gg \mu > M_2$ .

<sup>6</sup>In some work they are called the co-NLSP.

<sup>7</sup>See also [73] for a related work in the framework of a future 100 TeV collider.

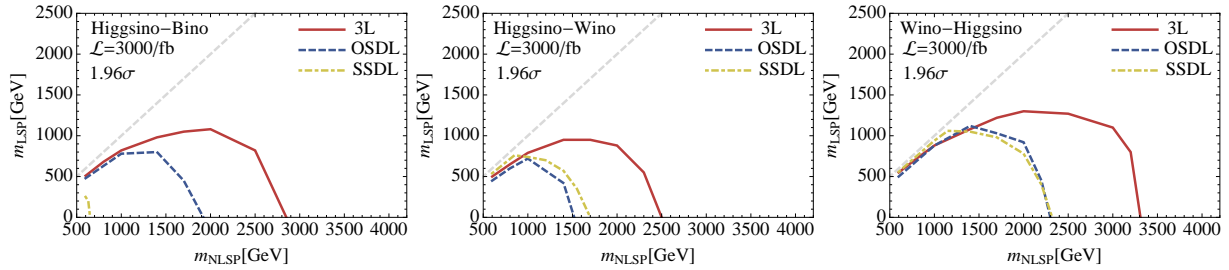


**Fig. 21:**  $2\sigma$  exclusion bounds of NLSP electroweakinos via  $3\ell$  (red-solid), OSDL (blue-dashed) and SSDL (yellow-dotdashed) searches at a 100 TeV  $pp$  collider with  $3000 \text{ fb}^{-1}$ . Three figures are for different NLSP-LSP combinations: Higgsino-NLSP and Bino-LSP (left), Higgsino-NLSP and Wino-LSP (middle), and Wino-NLSP and Higgsino-LSP (right). For the  $5\sigma$  reach, see Ref. [74].

- Wino NLSP and Higgsino LSP (Wino-Higgsino) :  $M_1 \gg M_2 > \mu$ .
- Wino NLSP and Bino LSP (Wino-Bino) :  $\mu \gg M_2 > M_1$ .

The mass of the heaviest electroweakino is fixed to be 5 TeV. Instead of following the simplified model approach, we take into account all predicted branching ratios of the NLSP to gauge bosons and the Higgs with various  $\tan \beta$  and signs of electroweakino masses. Notably, for the first three cases with Higgsino as either the NLSP or the LSP, the branching ratios do not depend sensitively on those parameters; and the branching ratios to the  $Z$  and the Higgs boson are always the same [151]. This is because the Higgsino system consists of two nearly degenerate neutralinos indistinguishable at colliders and summing their individual decays (only the sum is observable) leads to such a simple branching ratio relation. This can be derived from the Goldstone equivalence theorem, that holds generically in these scenarios as their mass separations are much larger than the electroweak scale, and from the Higgs alignment limit that we know from Higgs precision data. For the case of Wino-Bino, instead, the branching ratio of the NLSP depends sensitively on  $\tan \beta$  and on the signs of mass parameters.

We collect the  $2\sigma$  exclusion bounds for the first three cases, with Higgsinos either LSP or NLSP, in Fig. 21. We do not specify the value of  $\tan \beta$  and signs of mass parameters since the results almost do not depend on them. The  $3\ell$  search (in red) provides the best overall sensitivity, but the SSDL (in yellow) can provide complementary sensitivity for the region with small mass-splitting. Maximum discovery reaches on the NLSP mass are between 1.5 and 2.3 TeV for massless LSP. The Wino-Higgsino case shows the best reach among the three cases because the Wino NLSP production rate is twice bigger than that of the Higgsino NLSP (see the right panel of the figure).

The results can also be interpreted to address whether thermal Dark Matter (DM) candidates of 1 TeV Higgsino or 3 TeV Wino [152–154] can be discovered or excluded via electroweakino searches at a 100 TeV collider with  $3 \text{ ab}^{-1}$  of integrated luminosity. The right panel demonstrates that an LSP Higgsino at 1 TeV can be excluded if the Wino has a mass lighter than  $\sim 3$  TeV and not too close to 1 TeV. Wino DM, instead, cannot be probed with  $3 \text{ ab}^{-1}$  luminosity (see the middle panel of the figure). Unfortunately, the discovery of the 1 TeV Higgsino (and 3 TeV Wino) DM with  $3 \text{ ab}^{-1}$  data will be challenging (see the corresponding plots in [74]).

The discovery and exclusion reach for the last case of Wino-Bino are collected in Fig. 22. Four representative choices of additional parameters –  $\tan \beta$  and signs of mass parameters – are considered. The four representative results differ significantly in the reach of the NLSP mass, in the shape of the reach curve, and in the relative importance of  $Z$  and  $h$  boson contributions, primarily due to variations in the NLSP branching ratios as the additional parameters change.

The upper-right panel of Fig. 22 demonstrates the importance of the Higgs boson contribution for small  $\tan \beta$  and  $\mu M_2 > 0$ ; for other choices, there can be a (partial) cancellation between  $\mu \sin 2\beta$  and  $M_2$  terms for the Higgs partial width. In other words, if the Higgsino is much heavier than the Wino,

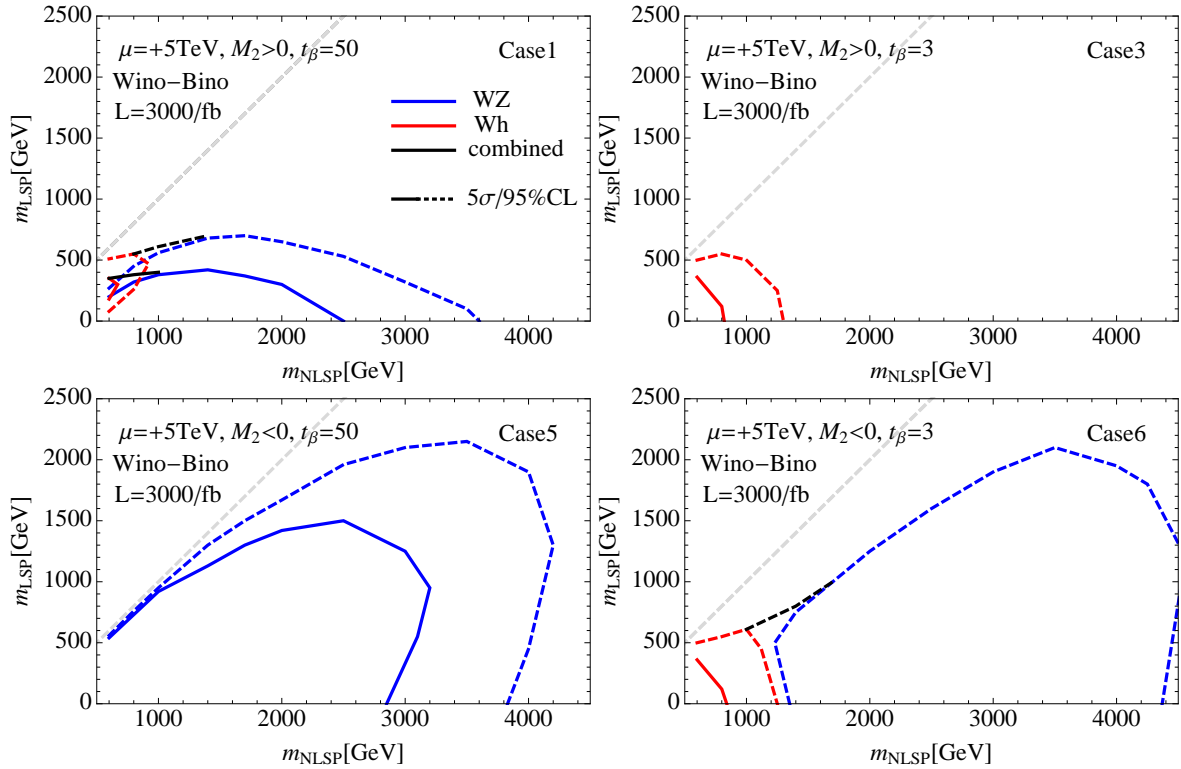


**Fig. 22:**  $5\sigma$  discovery reach (solid) and 95%CL exclusion (dashed) for the case of Wino-NLSP and Bino-LSP with  $3 \text{ ab}^{-1}$  at a 100 TeV  $pp$  collider. Four representative choices of  $\tan\beta$  and signs of mass parameters are shown. All multilepton channels are combined, but the  $3\ell$  search contributes most. The contributions from intermediate  $Z$  (blue) or  $h$  (red) are separately shown to see the effects of NLSP branching ratios. For more results with different choices of the parameters, see Ref. [74].

such cancellation does not occur, making the decay to the Higgs boson always dominate, and the result becomes similar to the upper-right panel. This effect is studied more extensively in Ref. [155–157]. When the branching ratio to the Higgs boson dominates, the reach is relatively low because multi-lepton signals via the Higgs boson are suppressed by the small  $\text{Higgs} \rightarrow WW/ZZ \rightarrow \text{multileptons}$  branching ratios.

Other features of the curves in Fig. 22 are driven by the branching ratio to  $Z$  bosons, which depends on mass and other model parameters. A detailed discussion of the reach is provided in Ref. [74]. In the optimal case, with almost 100% branching ratio to the  $Z$  boson, as in the lower-left panel, multilepton signals can enable the discovery of NLSPs with mass up to about 3 TeV for massless LSP with  $3 \text{ ab}^{-1}$ .

Multilepton events with small angular separation between the leptons is a common feature of multi-TeV electroweakino production. Such events are outside of the acceptance for isolated-lepton searches, but relaxing the requirements on lepton separation in  $R$  can significantly improve the acceptance for high-mass signals. For example, the luminosity needed to probe a 3.5 TeV Wino is reduced by a factor of two for  $\Delta R(\ell, \ell) > 0.05$  compared to  $\Delta R(\ell, \ell) > 0.1$ . Searches for an NLSP heavier than 3 TeV, which often produces collimated leptons, are also significantly improved by retaining events with near-by leptons. This should be an important consideration for the design of the detectors at future  $pp$  colliders.

In summary, a 100 TeV  $pp$  collider, even with just  $3 \text{ ab}^{-1}$  of integrated luminosity, can significantly improve the reach for electroweakinos compared to the LHC. This provides an important probe of SUSY even in the difficult scenario in which the colored superpartners are heavy. Of course, even if SUSY is discovered in other search channels, the discovery and studies of electroweakinos are crucial

in understanding the nature of SUSY breaking. Finally, even though the study presented here is in the context of SUSY, the general lesson is applicable to a broader range of possible new physics particles with only electroweak quantum numbers.

## 2.7 Long-lived Charged Particles

Due to low backgrounds and increased production cross sections at 100 TeV, exotic processes may be a promising avenue for discovering new physics. These exotic processes could include displaced vertices and long-lived charged or coloured objects. In this section we focus on a particular example motivated in supersymmetry: long-lived charged sleptons.

We study the prospects for long-lived charged particle (LLCP) searches at a 100 TeV  $pp$  collider, compared to the 14 TeV LHC, using time-of-flight measurements. We use Drell–Yan pair-produced long-lived sleptons as an example. A novel feature of 100 TeV collisions is the significant energy loss of energetic muons in detectors, which we utilize to discriminate against fake LLCPs. We find that the 14 TeV LHC with an integrated luminosity of  $3 \text{ ab}^{-1}$  is sensitive to LLCP sleptons with  $m \lesssim 1.2 \text{ TeV}$ , and a 100 TeV  $pp$  collider with  $3 \text{ ab}^{-1}$  is sensitive up to  $\sim 4 \text{ TeV}$ , probing interesting dark matter scenarios, including in particular slepton–neutralino co-annihilating WIMP dark matter, and superWIMP dark matter.

Long-lived charged particles (LLCPs), which are stable on collider–detector timescales, require specific methods for triggering, reconstruction, and detection. Thus they provide interesting, model-independent benchmarks for future collider experiments. Furthermore, their discovery will have profound implications for particle physics as well as for cosmology, where their long lifetime may affect the thermal history of the Universe.

Many extensions of the Standard Model predict LLCPs. Supersymmetry contains LLCPs in large portions of its parameter space. In the slepton–neutralino co-annihilation scenario [158–161], dark matter (DM) consists of the lightest supersymmetric particle (LSP), which is the neutralino  $\tilde{\chi}_1^0$ . A charged slepton  $\tilde{\ell}$  is the next-to-lightest SUSY particle (NLSP), and is almost degenerate with the LSP. The slepton NLSP is then long-lived because its decay to the LSP is phase-space suppressed. In the early Universe, the slepton remains in thermal equilibrium almost until the DM freezes-out, and the DM relic abundance is diluted through co-annihilations with the NLSP slepton. The correct relic abundance is obtained for slepton masses  $m_{\tilde{\ell}} \lesssim 600 \text{ GeV}$ .

Another scenario of interest is superweakly-interacting massive (superWIMP) DM [162, 163]. This scenario is naturally realized in gauge-mediated SUSY breaking, where the gravitino  $\tilde{G}$  is the LSP [164–166] and a charged slepton is often the NLSP. The NLSP slepton has a mass  $m_{\tilde{\ell}} \sim 1 \text{ TeV}$ , and decays to the LSP with a lifetime

$$\tau(\tilde{\ell} \rightarrow l\tilde{G}) = 0.59 \text{ sec} \left( \frac{\text{TeV}}{m_{\tilde{\ell}}} \right)^5 \left( \frac{m_{\tilde{G}}}{\text{GeV}} \right)^2 \left( 1 - \frac{m_{\tilde{G}}^2}{m_{\tilde{\ell}}^2} \right)^{-4}. \quad (16)$$

The NLSP freezes out in the early Universe with a relic density larger than the observed value  $\Omega h^2 \simeq 0.12$ , and later decays to the LSP. The relic density is then diluted by the mass ratio  $m_{\tilde{G}}/m_{\tilde{\ell}}$ . Assuming that the NLSPs are right-handed sleptons ( $\tilde{\ell}_R$ ), and that  $N_{\text{gen;LL}}$  of them are co-NLSP ( $1 \leq N_{\text{gen;LL}} \leq 3$ ), i.e. degenerate and long-lived, the gravitino relic density is numerically given by [167]

$$\Omega_{\tilde{G}} h^2 = N_{\text{gen;LL}} \cdot 0.12 \frac{m_{\tilde{\ell}_R} m_{\tilde{G}}}{M^2}, \quad (17)$$

where  $M$  varies from 650 TeV to 1.0 TeV as the Bino mass varies from  $m_{\tilde{B}} = \infty$  to  $m_{\tilde{\ell}_R}$ . Figure 23 shows the relic abundance and NLSP lifetime in this scenario in the slepton–LSP mass plane. The NLSP slepton with  $m_{\tilde{\ell}_R} \gtrsim 650 \text{ GeV}$  is cosmologically viable, and they are observed as LLCPs at collider if

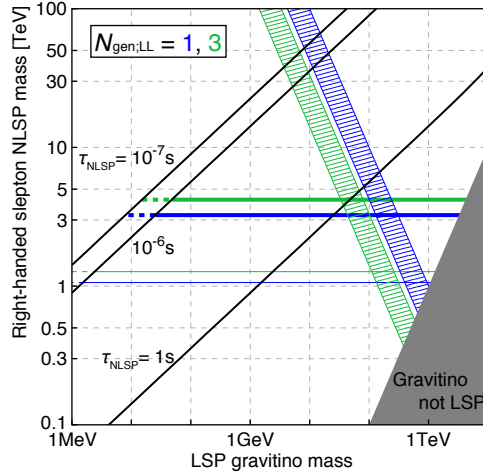


**Fig. 23:** An overview of the parameter space in superWIMP scenarios with  $\tilde{\ell}_R$ -NLSP. In the blue (green) hatched region, gravitinos may saturate, depending on  $m_{\tilde{B}}$ , the DM relic density if  $N_{\text{gen};LL} = 1$  (3), i.e., one (three) among  $\tilde{e}_R$ ,  $\tilde{\mu}_R$ , and  $\tilde{\tau}_R$  is long-lived. The black lines illustrate the lifetime of the NLSP slepton, and the horizontal lines are the expected exclusion limits of right-handed long-lived slepton searches: the thinner (thicker) lines are the 14 TeV LHC (a 100 TeV collider) with an integrated luminosity of  $3 \text{ ab}^{-1}$ .

$m_{\tilde{\ell}_R} \lesssim 40 \text{ TeV}$ . We also show in this figure the expected reach of the 14 TeV LHC and of a 100 TeV collider, which are the main results of Ref. [167].

For collider experiments, muons constitute the main background to LLCP searches. The only difference between a hypothetical LLCP and a muon is the (assumed) large mass of the former. Because of their large mass, LLCPs will typically be produced with a smaller value of relativistic  $\beta$ . This velocity can be measured using the time-of-flight (ToF) to the outer detectors, or through the ionization energy loss,  $dE/dx$ , typically in the innermost layers of a silicon tracking detector. Searches in 100 TeV collisions can exploit a new handle for discriminating LLCPs from muons [167]. Energetic muons with  $p \gtrsim 100 \text{ GeV}$  lose energy through radiative processes, i.e., bremsstrahlung, electron pair-production, and photo-nuclear interactions [168], in addition to the ionization process, while LLCP's, with lower values of  $\beta$ , will radiate significantly less. Therefore, by measuring the energy loss  $E_{\text{loss}}$  along the track of LLCP candidates, we can reduce the number of muon fakes.

We consider a  $\tilde{\ell}_R$  LLCP with  $N_{\text{gen};LL} = 1$  as a benchmark model, and assume a worst-case scenario in which the only production process available is the Drell–Yan direct pair-production  $pp \rightarrow (\gamma, Z) \rightarrow \tilde{\ell}_R \tilde{\ell}_R^*$ . For this scenario, the CMS (ATLAS) collaboration obtained a lower bound  $m > 346$  (286) GeV on the LLCP mass [169, 170], where the LLCP sleptons are identified by ToF and  $dE/dx$  measurements. Note that this is the most pessimistic limit; if heavier SUSY particles can be produced, LLCPs coming from their cascade decays will also contribute to the signal, leading to more stringent limits.

The capabilities of future LHC runs and a 100 TeV  $pp$  collider are studied in Ref. [167], utilizing the detector design and background samples from the Snowmass 2013 Community Summer Study [110, 114, 171]. Figure 24 summarizes the results. The 14 TeV LHC is expected to probe the slepton–neutralino co-annihilation scenario with an integrated luminosity  $\int \mathcal{L} = 0.3 \text{ ab}^{-1}$ , and a high-luminosity run will discover or exclude 1 TeV slepton LLCPs. Meanwhile, a 100 TeV  $pp$  collider will access 3 TeV with  $\int \mathcal{L} = 3 \text{ ab}^{-1}$ .

In the 100 TeV analysis, a qualitatively new event selection is introduced based on the energy deposit of a candidate LLCP in the calorimeter,  $E_{\text{loss}}$ . The energy loss of muons in matter, simulated with Geant 4.10 [172], is shown in Fig. 25. Based on this, the signal LLCPs, which are initially selected

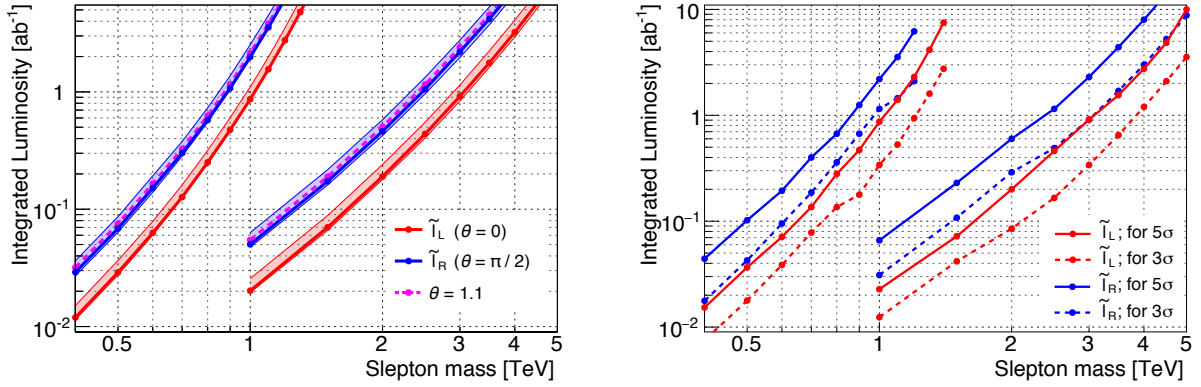


**Fig. 24:** (left) Expected capabilities of the 14 TeV LHC and a 100 TeV  $pp$  collider on searches for long-lived sleptons with  $N_{\text{gen};\text{LL}} = 1$ , plotted in terms of the integrated luminosity required for 95% CL exclusion. Only the Drell–Yan pair-production of the LLCs is assumed, and three values of the slepton left–right mixing angle  $\theta$  are used. Note that, for a fixed  $m_{\tilde{\ell}}$ , the Drell–Yan production cross section is maximized (minimized) at  $\theta \simeq 0$  ( $\theta \simeq 1.1$ ). The lines for  $\tilde{\ell}_L$  ( $\theta = 0$ ) and  $\tilde{\ell}_R$  ( $\pi/2$ ) are drawn as bands, which show the 68% statistical uncertainty of the expectation. (right) The integrated luminosity required for discovery. Solid (dashed) lines are for 5 $\sigma$ - (3 $\sigma$ -) discoveries.

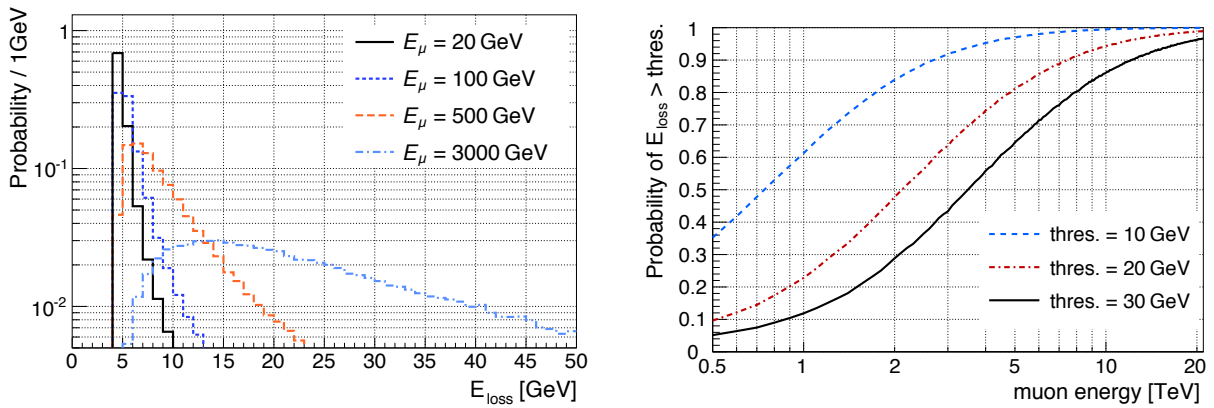


**Fig. 25:** (left) Energy deposit of a muon in the calorimeter, which is modeled as 3.0 m iron. Note that this includes the ionization energy loss, which is 4.8–6.0 GeV for  $E_\mu = 20$ –3000 GeV. (right) The probability that the energy loss of a muon in the calorimeter exceeds certain thresholds as a function of the muon energy.

by  $0.4 < \beta < 0.95$  and  $P_T > 500$  GeV, are further required to have  $E_{\text{loss}} \leq 30$  GeV. The calorimeter is approximated as iron of 3 m thickness. The  $E_{\text{loss}}$  requirement removes 18% of fake LLCs. If each event is required to have two LLCs, the muon-fake background is reduced by 34%. We note that pile-up may degrade the calorimeter resolution, and encourage a careful study of this issue when designing future detectors. Note that the  $E_{\text{loss}}$  cut is not introduced in the 14 TeV LHC analysis, which has a looser requirement of  $p_T > 100$  TeV.

The resolution of the LLC mass measurement is also discussed in [167]. Good momentum resolution is essential to measure the mass of LLCs. We parameterize the momentum resolution of high- $p_T$  tracks by:

$$\Delta p_T = A \oplus B \cdot p_T \oplus C \cdot p_T^2 \approx C \cdot p_T^2. \quad (18)$$

The relevant parameter  $C$  in the ATLAS experiment was measured to be  $C = 0.168(16)/\text{TeV}$  for the barrel region of the muon spectrometer in early 7 TeV data [173]. Stronger magnetic fields in the tracker, as well as larger detector dimensions, will improve the momentum resolution, so we assume a value of

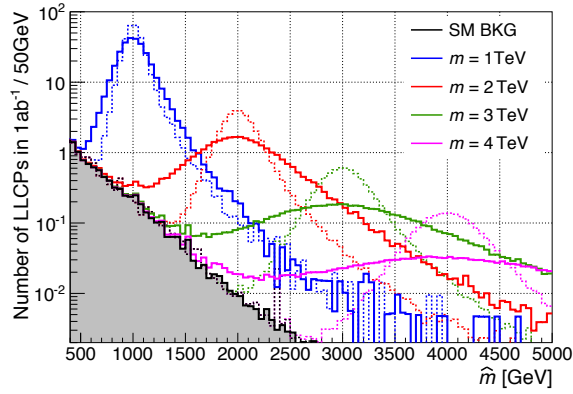


**Fig. 26:** Distribution of the reconstructed LLCP mass in the 100 TeV analysis. Solid lines are with  $C = 0.1/\text{TeV}$ , while dotted lines with  $C = 0$  is drawn as a reference.

$C = 0.1/\text{TeV}$  for the 100 TeV analysis, which gives the result in Fig. 26.

In summary, even for the most pessimistic scenario in which only the channel  $pp \rightarrow (\gamma, Z) \rightarrow \tilde{\ell}_R \tilde{\ell}_R^*$  is available, a 100 TeV  $pp$  collider with  $\int \mathcal{L} = 3 \text{ ab}^{-1}$  has the capability to discover or exclude LLCP sleptons with  $m \lesssim 3 \text{ TeV}$ .

## 2.8 Indirect Probes

At the 100 TeV collider it would also be possible to search for the indirect effects of supersymmetry on SM processes. Two important factors for indirect probes of new physics are precision and energy. Precision could be delivered at the 100 TeV collider due to the large number of SM events possible thanks to the large integrated luminosity. For many processes this would render systematic uncertainties as the dominant limitation in indirect tests of new physics. The high energy that can be achieved at the 100 TeV collider would also enhance the indirect constraints on new physics. Indirect constraints on a multitude of new physics processes are possible, however we will focus here on a particular example in supersymmetry.

While light stop squarks would likely be directly observed at a 100 TeV collider, it may also be useful to search for their indirect effects. In particular precision Higgs coupling constraints, particularly on the Higgs-gluon-gluon coupling, would provide a powerful probe of light stop scenarios. In addition, as a 100 TeV collider would also be able to observe Higgs boson pair production, it is interesting to consider searching for the indirect effects of light stop squarks on Higgs pair production, as will be considered in this section.

As with single Higgs production, the dominant production mode for Higgs pairs is gluon fusion. The stop loop contributes to deviations from the SM di-Higgs rate that can be a powerful indirect signal of SUSY. The much larger di-Higgs cross section at a 100 TeV collider improves the sensitivity of such searches compared to the LHC.

The di-Higgs rate also constrains the Higgs potential, so considerable effort has gone into projecting collider sensitivity. Current LHC searches have used several final states [174–179] and high luminosity projections for several channels have also been completed [180, 181]. Phenomenological studies considering a 100 TeV machine have been done for the  $bb\gamma\gamma$  [182, 183],  $4W$  [184], and  $bb + \text{leptons}$  [185] channels.

Of course, as detailed in Section 2.3, there also exist very powerful direct searches for superpartners, stops featuring prominently. However, these searches depend on particular assumptions about  $R$ -parity [186–188] or where the stop lies in the particle spectrum. Work on these limits include the cases of stops nearly degenerate with the top [59, 60, 189–192], part of a compressed spectrum [58, 193–199],

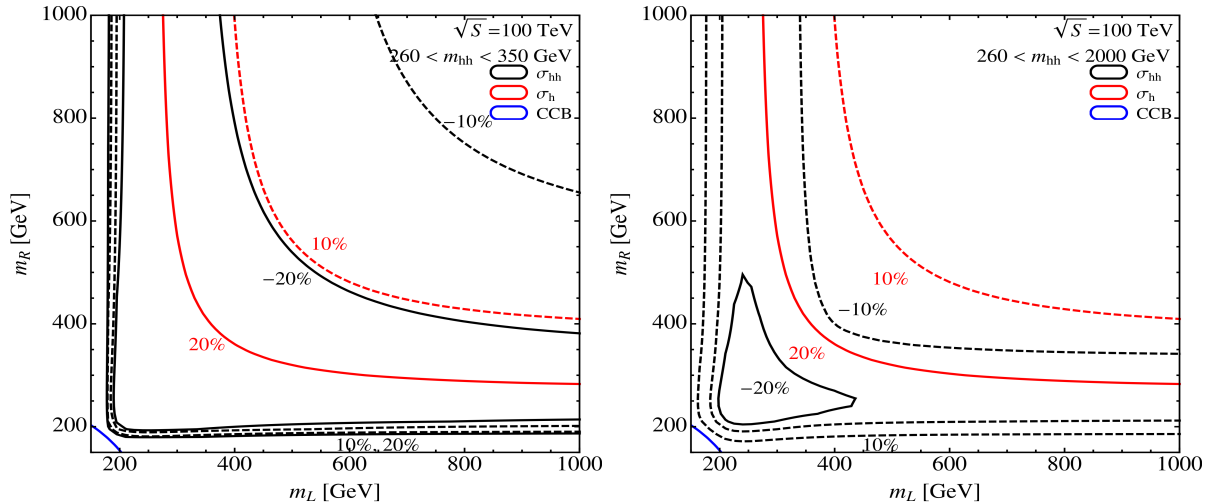


**Fig. 27:** Percentage corrections, relative to the SM, of the single Higgs (red) and di-Higgs (black) production cross sections at  $\sqrt{s} = 100$  TeV in a low energy bin with invariant masses  $260 < m_{hh} < 350$  GeV (left) and  $260 < m_{hh} < 2000$  GeV (right). Vanishing  $A$ -terms have been assumed and the physical left- and right-handed stop masses have been varied through the soft masses. The blue contour gives the approximate contour of color breaking vacuum constraint.

or which decay into light superpartners like staus [200, 201]. Clearly, the insensitivity of the di-Higgs rate to these types of assumptions make it a valuable complementary search.

This is not to say that the di-Higgs approach is unconstrained. A simple EFT analysis [202] demonstrates that constraints on single Higgs production limit the deviation due to new colored particles in the di-Higgs rate (and that the two rates are anticorrelated). However, this analysis is inapplicable when one or both of the stops are light. Even within the constraints imposed by single Higgs production, the shape of the di-Higgs distribution can reveal new physics. The SM di-Higgs rate experiences a cancellation at threshold, so new colored particles, like stops, can have large effects there. This motivates considering the differential cross section (in invariant mass or  $p_T$  for example) close to threshold to see the greatest deviations.

The calculated MSSM di-Higgs cross section [203–206] has been used to explore this idea in [202]. We consider contours of 10 and 20 percent deviation from the SM in the single Higgs and di-Higgs production at a 100 TeV collider. The deviations are considered in a small invariant mass bin close to threshold as well as the more usual large mass bin. The large bin analysis not only makes contact with previous studies, but highlights features in the spectrum at high invariant mass. These have greater effect on the total rate at a 100 TeV collider where the gluon luminosity at large masses are significantly increased.

To demonstrate the mass ranges in which observable effects in di-Higgs production could be observed at 100 TeV, we show contours of constant deviation in the pair production cross section at 100 TeV. In Fig. 27 the stop mixing is set to zero while the soft masses are varied. Figure 28 sets the left- and right-handed soft masses equal and then varied while the mixing parameter is also varied. In regions where both stops are heavy and single Higgs production is SM-like the di-Higgs production is also SM-like. However, when the mass bin close to threshold is considered the fractional change in the di-Higgs rate increases dramatically, so that there are regions where the effects of the stops are seen in the di-Higgs rate close to threshold even while single Higgs deviations are small.

When one or both of the stops are light there are regions wherein the single Higgs production is SM-like, but the di-Higgs rate shows large deviations. This complementarity at low mass enables light stops to be detected even when direct searches fail and the single Higgs production appears SM-like do

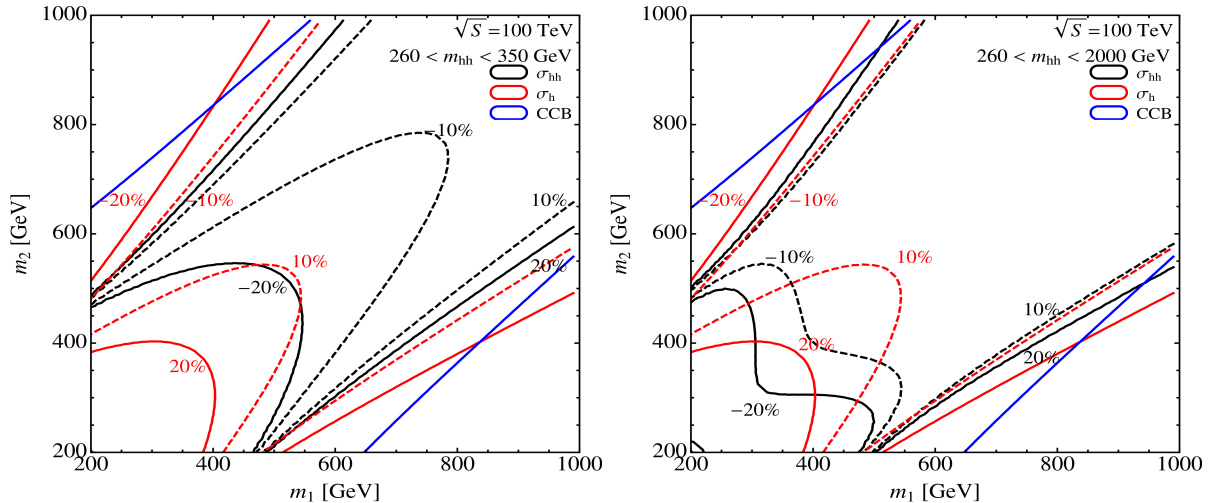


**Fig. 28:** Percentage corrections, relative to the SM, of the single Higgs (red) and di-Higgs (black) production cross sections at  $\sqrt{s} = 100$  TeV in a low energy bin with invariant masses  $260 < m_{hh} < 350$  GeV (left) and  $260 < m_{hh} < 2000$  GeV (right). Degenerate soft masses have been assumed, while the  $A$ -term is varied. The blue contour gives the approximate contour of color breaking vacuum constraint.

to a cancellation. The discriminating power of these studies depends on the high di-Higgs cross section at a 100 TeV collider. This can be easily seen by comparing these results to the 14 TeV results in [202].

## 2.9 Model-Specific Interpretations

Whereas the previous sections have focussed on a more model-independent approach, focussing on specific superpartners and in some cases simplified models, it is also worthwhile to consider 100 TeV measurements in the context of complete supersymmetric models. The number of free parameters in the MSSM is too large to study in its entirety, thus we will consider two well-motivated scenarios that make specific predictions for the pattern of parameters, the ‘CMSSM’ and ‘Mini-Split’ supersymmetry.

### 2.9.1 Constrained Minimal Supersymmetric Standard Model

The ‘CMSSM’ [207–216] assumes four input parameters, a universal scalar mass at the grand unification scale  $m_0$ , a universal gaugino mass  $m_{1/2}$ , a universal scalar trilinear soft term  $A_0$ , the usual Higgs mixing parameter  $\tan\beta$ , and also the sign of the  $\mu$ -term. This framework is especially appealing from a phenomenological standpoint as it predicts the full set of soft parameters at the weak scale from these input parameters, after RG evolution, and this allows for the calculation and combination of diverse experimental constraints, from colliders to dark matter experiments. The power of this approach is that successful phenomenological predictions in one area, for example dark matter, may be tested by constraining the predictions made from the same parameter set, in this case with colliders. In particular, we will focus on testing regions of parameter space that predict the observed dark matter abundance by searching for the coloured particles whose masses are predicted once the parameters are set.

This material is based on [217]. We analyze the nature of the CMSSM parameter space for large values of  $m_0$  and  $m_{1/2}$ , considering the dark matter density prediction and the measurement of the Higgs boson mass, which are the only constraints capable of imposing upper limits on  $m_0$  and  $m_{1/2}$ . Generally, bringing the relic dark matter density within the measured range when the mass parameters are large requires some specific features in the sparticle spectrum such as near-degeneracy between the LSP, the NLSP and perhaps other sparticles, as this suppresses the relic dark matter density by introducing new coannihilation channels during thermal freeze-out. One such possibility is the narrow stop coannihilation

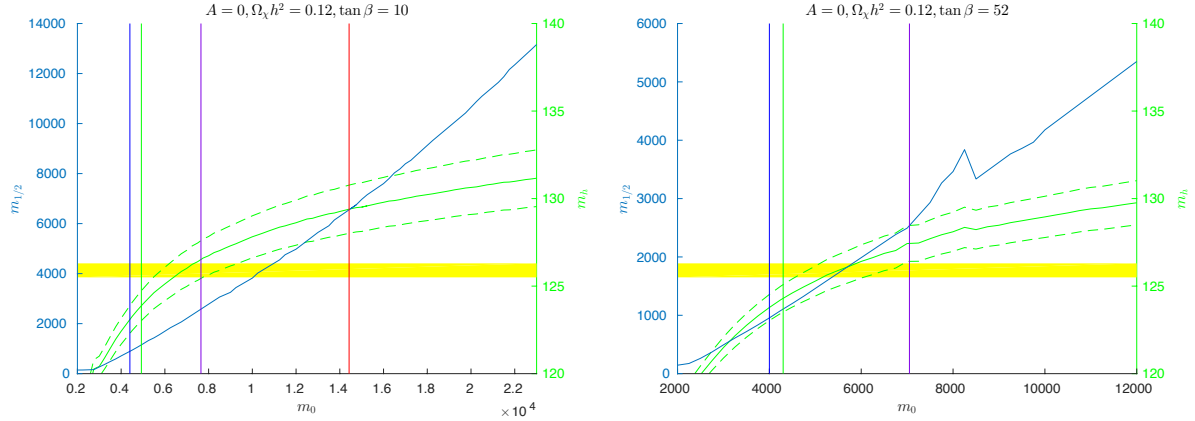


**Fig. 29:** The solid blue lines are the profiles in the  $(m_0, m_{1/2})$  plane of the focus-point strips for  $A_0 = 0$  and  $\tan \beta = 10$  (left panel), and  $A_0 = 0$  and  $\tan \beta = 52$  (right panel). The blue, green, purple and red lines are particle exclusion reaches for particle searches at the LHC with 300 and 3000/fb at 14 TeV, 3000/fb with HE-LHC at 33 TeV and 3000/fb at 100 TeV, respectively. The solid lines are for generic  $\cancel{E}_T$  searches. The solid (dashed) green lines are central values (probable ranges) of  $m_h$  calculated using FeynHiggs 2.10.0, and the yellow band represents the experimental value of  $m_h$ .

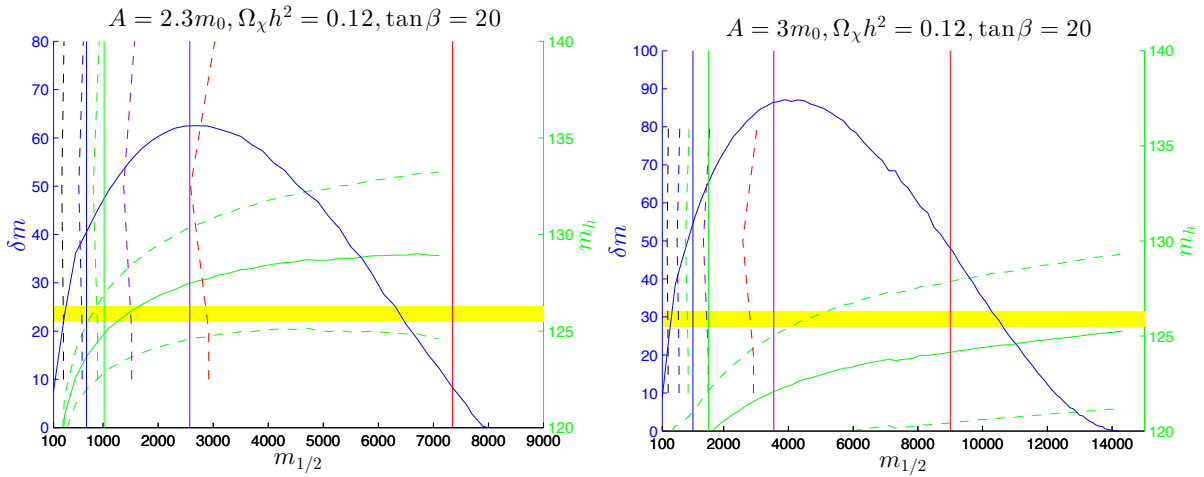


**Fig. 30:** The solid blue lines are the profiles in the  $(m_{1/2}, \delta m \equiv m_{\tilde{t}_1} - m_\chi)$  plane of the stop coannihilation strips for  $A_0/m_0 = 2.3$  and  $\tan \beta = 20$  (left panel), and  $A_0/m_0 = 3.0$  and  $\tan \beta = 20$  (right panel). The solid lines are for generic  $\cancel{E}_T$  searches and the dashed lines are for dedicated stop searches, using the same colours as in Fig. 29 (the dashed black line is for the LHC at 8 TeV).

strip [218–224] where  $\delta m = m_{\tilde{t}_1} - m_\chi$  is small.

Another possibility is the focus-point strip of parameter space [56, 225–229], appearing at larger values of  $m_0/m_{1/2}$ , beside the boundary of the region where radiative electroweak symmetry breaking is consistent. Along the focus-point strip, the Higgsino component of the neutralino LSP is enhanced, and its annihilations and coannihilations with heavier neutralinos and charginos are enhanced. Various studies have shown that the focus-point strip may extend to very large values of  $m_0$  and  $m_{1/2}$ , with  $m_0/m_{1/2} \sim 3$  and  $A_0 \lesssim m_0$ .<sup>8</sup>

Figures 29 and 30 display the profiles of the focus-point strip and of the stop coannihilation strip, along their full lengths. Both pairs of plots show the Higgs mass values calculated using SSARD [217] as

<sup>8</sup>However, it does not extend to arbitrarily large values of  $m_0$  as the Higgs mass measurement constrains  $m_0$ .

inputs to FeynHiggs 2.10.0 (solid green lines). Uncertainty estimates of  $\pm 3$  GeV are also shown. Only portions of the focus-point strips are compatible with the measured Higgs mass (yellow bands) within these uncertainties, whereas for the stop coannihilation strips there are significant additional uncertainties from RGE running, and all of the strips are compatible with the measured Higgs mass. In the cases of the stop coannihilation strips in the lower panels of Fig. 29, we also display as blue lines the mass difference  $\delta m \equiv m_{\tilde{t}_1} - m_\chi$  along the strips. In the examples shown, this mass difference is generally  $< m_W + m_b$ , so that the branching ratio for two-body  $\tilde{t}_1 \rightarrow \chi + c$  decay usually dominates over that for four-body  $\tilde{t}_1 \rightarrow \chi + W + b + \nu$  decay. However, this is not always the case, as illustrated by examples in [224]. The branching ratio for  $\tilde{t}_1 \rightarrow \chi + W + b + \nu$  decay may dominate when  $m_{\tilde{t}_1} - m_\chi > m_W + m_b$ , as seen in the right panel of Fig. 30. Thus, a complete search for supersymmetry at 100 TeV should include searches for both the  $\tilde{t}_1 \rightarrow \chi + c$  and  $\tilde{t}_1 \rightarrow \chi + W + b + \nu$  decay signatures.

The (near-)vertical lines in Figs. 29 and 30 mark estimates from Ref. [217] of the sensitivities of the LHC (black - 8 TeV, blue - 300/fb at 14 TeV, green - 3000/fb at 14 TeV), 3000/fb at HE-LHC (purple) and 3000/fb at 100 TeV (red) along the stop coannihilation strips. The solid lines represent the extrapolated reaches of the generic jets +  $\cancel{E}_T$  searches, and the dashed lines in the lower panels represent the extrapolated reaches of dedicated searches for  $\tilde{t}_1 \rightarrow c + \chi$  decays, which lose some sensitivity as  $\delta m$  increases because of the increase in the  $\tilde{t}_1 \rightarrow \chi + W + b + \nu$  decay branching ratio. We see that the 100 TeV collider would be sensitive to the full extents of the focus-point strips and of the stop coannihilation strip for  $A_0 = 2.3 m_0$ , but not all the stop coannihilation strip for  $A_0 = 3.0 m_0$ : this is true in general for  $A_0/m_0 \gtrsim 2.5$ . We note also that, as discussed in [217], high-precision measurements of electroweak and Higgs observables could constrain the location along the dark matter strip, providing a potential consistency test of the supersymmetric model.

### 2.9.2 Mini-Split Supersymmetry

The spectrum of split supersymmetry (SUSY) contains lighter gauginos (bino, winos, gluinos) and heavier scalars (sfermions and Higgs bosons) [23–25, 143]. Among the gauginos, gluino production can be a useful way to search for split SUSY at hadron colliders. Pure wino production is smaller by electroweak couplings. Pure bino production is very small since it has no direct couplings to gauge bosons. Unless gluinos are much heavier than other gauginos, gluino production can be the dominant production mode of split SUSY particles. In this section, we study gluino search prospects at a 100 TeV  $pp$  collider in split SUSY models [68, 69].

Gluinos are pair produced at  $pp$  colliders. Once produced, each gluino subsequently decays to the lightest gauginos (LSP) – winos or binos – via off-shell squarks as

$$\tilde{g} \rightarrow \chi_1^0 j j. \quad (19)$$

Pair production of gluinos then yields  $\tilde{g}\tilde{g} \rightarrow \chi_1^0 \chi_1^0 j j j j$ . This channel can be searched using an effective mass variable,  $M_{\text{eff}}$ . The effective mass is defined as a scalar sum

$$M_{\text{eff}} = \sum_i p_T(i) + E_T^{\text{miss}}, \quad (20)$$

where the sum runs over all jets with  $p_T > 50$  GeV and  $\eta < 5.0$ . Cuts on the data that aid selecting signal over background include (see also [230]):

- At least two jets with  $p_T > 0.1 M_{\text{eff}}$ .
- Lepton veto.
- $E_T^{\text{miss}} > 0.2 M_{\text{eff}}$  and  $p_T(j_1) < 0.35 M_{\text{eff}}$ .
- $\Delta\phi(j_1, E_T^{\text{miss}}) < \pi - 0.2$  and  $\Delta\phi(j_1, j_2) < 2\pi/3$
- $M_{\text{eff}} > 1.5 M_{\tilde{g}}$ .

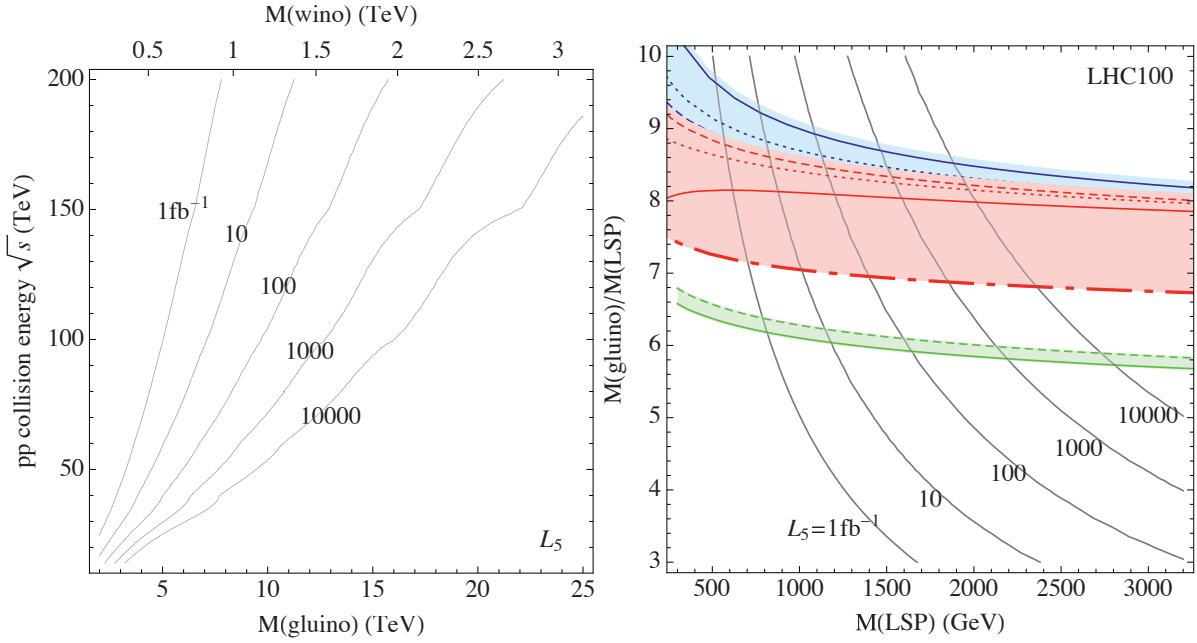


**Fig. 31:** Left panel: The integrated luminosity ( $\text{fb}^{-1}$ ) needed to discover gluino pairs in split SUSY models with  $5\sigma$  statistical significance is contour plotted [69]. It is assumed that the gluino is more than 3 times heavier than the LSP so that the  $M_{\text{eff}}$  analysis is valid. In the upper horizontal axis, the wino mass with the minimal AMSB relation is also shown. Right panel: The result at a 100 TeV  $pp$  collider is shown in terms of the gluino-to-LSP mass ratio in split SUSY [69]. Blue and red regions are predictions of AMSB models with squark masses and  $\tan\beta$  varied. See text and Ref. [69] for more details.

The  $M_{\text{eff}}$  spectrum depends only on the gluino mass and not on the LSP mass, as long as the gluino is more than 3 times heavier than the LSP [69]. The discovery prospect in terms of the gluino mass is shown in Fig. 31; the integrated luminosity needed for  $5\sigma$  statistical significance is shown.

The results can be interpreted in three ways. First, at a 100 TeV  $pp$  collider, up to about 7 (13) TeV gluinos can be discovered with 10 (1000)  $\text{fb}^{-1}$  of data. This result applies to any split SUSY models as long as the gluino is 3 times heavier than the LSP and the decay mode in eq.(19) is dominant; for a smaller mass difference between the gluino and the LSP, the  $M_{\text{eff}}$  becomes a less useful observable for discovery and other strategies may be needed.

Second, if the minimal anomaly-mediated SUSY breaking (AMSB) model [141, 142] is considered as a particular example of split SUSY models, the reach on the gluino mass can be interpreted simultaneously as a reach on the mass of the wino dark matter candidate. In the minimal AMSB model, the wino is the LSP; squarks are one-loop factor heavier than the gluino and out of reach for the collider. The gluino-to-wino mass ratio, which is key to this interpretation of an indirect wino bound, is almost fixed, but varies from 8 to 9.5 for the wino mass between 3 TeV and 200 GeV, respectively [69]. The variation is almost entirely due to the running of gauge couplings, and the Higgsino contribution to the quantum correction can be ignored. The wino mass corresponding to the gluino mass in this model is also shown in the upper horizontal axis in left panel of Fig. 31. A 100 TeV  $pp$  collider can probe wino mass up to 900 GeV (1.4 TeV) with 10 (1000)  $\text{fb}^{-1}$  of integrated luminosity. It is known that the  $\sim 3$  TeV pure wino can be a thermal dark matter contributing to full dark matter density [152], but astrophysical constraints may rule out this possibility [153, 154]. In any event, this very large wino mass is too heavy to be probed at a 100 TeV collider, yet a smaller wino mass, perhaps as a non-thermal dark matter source, can be indirectly probed to mass scales above a TeV as seen by this analysis.

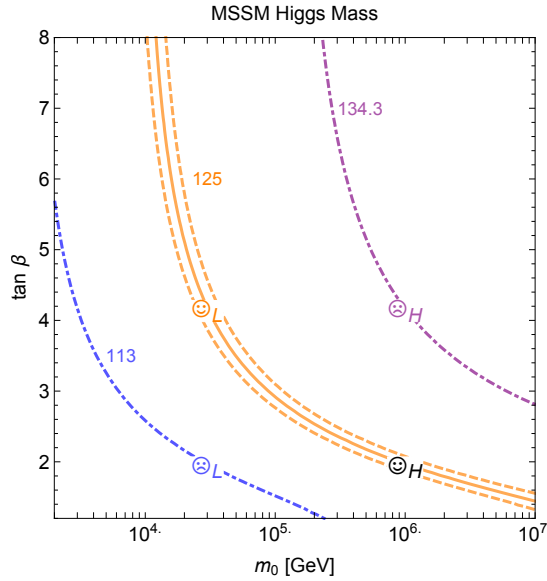


**Fig. 32:** The MSSM Higgs boson mass as computed with SusyHD [231], taking  $A_t = 0$  and fermion masses  $m_{1/2} = 1$  TeV. (Dependence on the details of fermion masses is mild.) The orange solid curve and the dashed orange curves show where the central value and the  $\pm 1\sigma$  variations around it give a 125 GeV Higgs mass. The dot-dashed purple and blue lines show where the Higgs mass is 134.3 and 113 GeV, respectively. We have marked four points, two giving the correct Higgs mass (smiling faces) and two giving an incorrect one (frowning faces), for a closer study.

Finally, the result can be interpreted more generally in terms of the reach on the gluino-to-LSP mass ratio. This is done in the right panel of Fig. 31. The aforementioned minimal AMSB relation of the gluino and wino masses can be modified in general split SUSY models. The variations of sfermion masses between  $1 \leq m_{\tilde{f}}/m_{\tilde{g}} \leq 4\pi\alpha_S$  and  $3 \leq \tan \beta \leq 50$  with  $|\mu| = 4$  TeV lead to the blue and red regions; heavy squarks and Higgsinos modify the gluino mass and the wino mass at one-loop order, respectively. The dependence on the renormalization scale is much smaller. The region of  $M_{\tilde{LSP}}$  and  $M_{\tilde{g}}/M_{\tilde{LSP}}$  probed is under the integrated luminosity contours in the figure. For more details of each curve, we refer to Ref. [69]. This interpretation is most useful when a certain split SUSY model predicts a certain gaugino mass ratio.

## 2.10 Supersymmetry Post-Discovery at 100 TeV

After any discovery of new particles at the LHC or at 100 TeV, we will want to undertake a detailed study of their properties. As one example, suppose that a gluino is discovered with a mass at the TeV scale, which decays through cascades to lighter electroweakinos. A 100 TeV collider would be an effective gluino factory:  $3 \text{ ab}^{-1}$  of data would lead to  $2 \times 10^7$  gluino pair production events if  $m_{\tilde{g}} = 2$  TeV and  $10^5$  events if  $m_{\tilde{g}} = 5$  TeV [82]. Hence, a gluino discovery would be followed up by an extensive program of measuring gluino branching ratios and couplings. In this section, we will outline one particular aspect of such studies: a test of the MSSM prediction of the Higgs mass in split SUSY scenarios where the scalars are significantly heavier than the gluino.

The MSSM at tree level predicts that the Higgs mass is less than the  $Z$  mass, but loop effects can lift it [232–235]. This has led to extensive effort toward high-precision theoretical calculations of the Higgs mass in the MSSM, recently reviewed in [236]. The result primarily depends on the stop mass matrix and  $\tan \beta$ . For relatively low stop masses, large values of  $\tan \beta$  and a sizable mixing parameter  $A_t$  can achieve a 125 GeV Higgs mass, and the stops could be directly probed at 100 TeV. Here we will

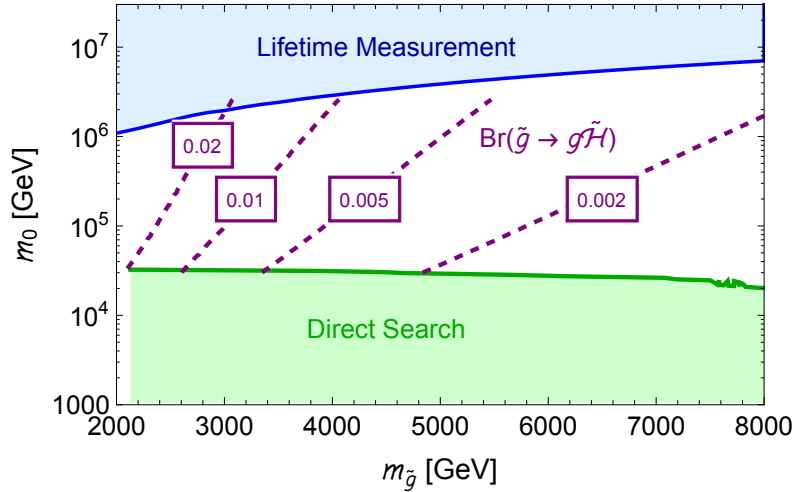


**Fig. 33:** Strategies for probing the SUSY scalar mass scale. The green region can be probed through associated squark-gluino production [140]. The blue region leads to gluino lifetimes above 100 microns [22, 24, 43]. In the intermediate region, the scalar mass can be indirectly probed through gluino branching ratios (which are shown here for the choice of  $\tan\beta$  that achieves a 125 GeV Higgs mass for the given  $m_0$ ) [238].

focus on the case of heavy scalars with small mixing ( $A_t \approx 0$ ), which achieve a 125 GeV Higgs mass at relatively low values of  $\tan\beta$ . Taking all scalars to have mass  $m_0$  and all gauginos to have mass 1 TeV, contours of Higgs boson masses in the  $(m_0, \tan\beta)$  plane are shown in Fig. 32. The orange curves show the region consistent with the measured Higgs mass. We have singled out two points on this curve, one with 30 TeV scalars and  $\tan\beta \approx 4$  marked  $\text{☺}_L$  (the  $L$  for “low mass” scalars, though they are still quite heavy!) and one with 1000 TeV scalars and  $\tan\beta \approx 2$  marked  $\text{☺}_H$  (the  $H$  for “high mass”), for special attention. For comparison, we have also selected two other points at the vertices of a rectangle,  $\text{☹}_L$  and  $\text{☹}_H$ , which predict a Higgs mass differing from the true value by about 10 GeV.

A future study should thoroughly explore the whole parameter space, but for now we highlight the low scalar mass at 30 TeV and high scalar mass at 1000 TeV as benchmarks, for both collider physics and model-building reasons. From the collider physics viewpoint, scalars that are modestly heavier than the gluino can be searched for directly in  $\tilde{q}\tilde{g}$  associated production events [237]. Preliminary estimates for 100 TeV suggest that direct searches for this signal will probe first-generation squarks up to about 30 TeV [140]. On the other hand, scalars that are *much* heavier than the gluino would imply measurably long gluino lifetimes [22, 24, 43]. For a 2 TeV gluino, the threshold at which lifetimes are measurable is roughly  $m_0 \approx 1000$  TeV, corresponding to a 100 micron lifetime. Improved detector technology might push to lower lifetimes, but the lifetime goes as the fourth power of the scalar mass, so dramatic improvements in scalar mass reach are unlikely. Thus, the region of scalar masses  $30 \text{ TeV} \lesssim m_0 \lesssim 1000 \text{ TeV}$  must be probed in a different way. The gluino branching ratio to gluon plus higgsino has been discussed as a key probe in this region [238] due to its logarithmic sensitivity to scalar masses [239, 240]. The parameter space and the possible probes are summarized in Figure 33.

There is also a theoretical case for why the 30 TeV and 1000 TeV scalar mass scales are of particular interest. Many theories predict that scalars are roughly a loop factor heavier than gauginos, among them anomaly mediation without sequestered scalars [141–143] and some moduli mediation scenarios [144, 241–243]. For weak-scale gauginos, these models predict scalars not far from the 30 TeV scale. A SUSY breaking scale near 30 TeV also allows gravitino or moduli decays just before BBN [244–248]. The higher 1000 TeV scale could be appealing from the point of view of flavor physics [23, 249, 250]. It is predicted in certain sequestered scenarios [251–253] that rely on approximate no-scale structure [254–257]. These theories provide a strong motivation for distinguishing between the

low and high scalar mass benchmarks when the scalars are neither light enough to directly produce nor heavy enough to cause the gluino lifetime to be measurable.

### 2.10.0.1 Gluino observables sensitive to scalar masses and $\tan\beta$

Figure 32 makes it clear that we must probe both the scalar mass scale (especially the stop mass scale) and  $\tan\beta$  in order to compare experimental results with the MSSM Higgs mass prediction. An earlier study has discussed the determination of the scalar mass in some detail, albeit at the LHC rather than 100 TeV [238]; we are not aware of a similarly detailed study on the determination of  $\tan\beta$ . We will assume that  $M_3 > M_1, M_2, \mu$ , so that the gluino can decay to any of the neutralinos and charginos. With a reasonable theoretical prior, this is at least an order-one fraction of the interesting parameter space. Any of the neutralinos and charginos will cascade promptly to the LSP. Gluino decays arise only from dimension-six operators generated by integrating out squarks.

### 2.10.0.2 Scalar mass measurement

In the absence of a lifetime measurement, ratios of tree-level gluino decays probe the ratios of different squark masses but not the overall mass scale. However, the one-loop decay  $\tilde{g} \rightarrow g\tilde{H}_{1,2}^0$  of a gluino to a gluon and a neutral higgsino has an additional *logarithmic* sensitivity to the scalar mass scale. This results from a loop diagram that begins with the four-fermion operator responsible for decaying a gluino to a higgsino, a top quark, and an anti-top quark; closes up the top loop; and adds a radiated gluon. As a result, the ratio of two- to three-body decays is a clean probe of the scalar mass scale, with the approximate dependence [239]:

$$\frac{\Gamma(\tilde{g} \rightarrow g\tilde{H}^0)}{\Gamma(\tilde{g} \rightarrow t\bar{t}\tilde{H}^0)} \propto \frac{m_t^2}{m_{\tilde{g}}^2} \log^2 \frac{m_{\tilde{t}}^2}{m_t^2}. \quad (21)$$

We will assume that the decay widths to the two neutral higgsinos are summed over, because they can be difficult to distinguish from one another experimentally. Resummation flattens out the scalar mass dependence at large  $m_{\tilde{t}}$ , but over the range we are interested in this is a relatively small effect [240]. Furthermore, because both the numerator and the denominator depend in the same way on the stop mass and the top Yukawa coupling, this ratio is relatively insensitive to flavor-dependent physics (e.g. the stop mass compared to the first- and second-generation squarks) or to the value of  $\tan\beta$ .

### 2.10.0.3 Measurement of $\tan\beta$

To measure  $\tan\beta$  we can exploit Yukawa couplings  $Y_u \propto 1/\sin\beta$  and  $Y_d \propto 1/\cos\beta$  appearing in higgsino couplings. One probe is the rate of a gluino decay to higgsino relative to the rate to gauginos:

$$\frac{\Gamma(\tilde{g} \rightarrow t\bar{t}\tilde{H}^0)}{\Gamma(\tilde{g} \rightarrow t\bar{t}\tilde{B}^0)}, \frac{\Gamma(\tilde{g} \rightarrow t\bar{t}\tilde{H}^0)}{\Gamma(\tilde{g} \rightarrow t\bar{t}\tilde{W}^0)} \propto \frac{1}{\sin^2\beta}. \quad (22)$$

If the left- and right-handed stop masses are very different, measuring decays to both binos and winos can help to resolve the underlying physics. A disadvantage of this observable is that the dependence on  $\tan\beta$  is mild over the range we are most interested in: systematic uncertainties in efficiencies at colliders of order 10% could prevent us from drawing conclusions.

An observable with a steeper  $\tan\beta$  dependence is the decay rate of the gluino to bottom quarks and a higgsino. In particular, if we can measure the ratio between two decays to higgsinos, we can obtain

$$\frac{\Gamma(\tilde{g} \rightarrow b\bar{b}\tilde{H}^0)}{\Gamma(\tilde{g} \rightarrow t\bar{t}\tilde{H}^0)} \propto \tan^2\beta. \quad (23)$$

The disadvantage is that the decay rate in the numerator is very small for the  $\tan\beta$  values we are interested in. We could, alternatively, measure the ratio  $\Gamma(\tilde{g} \rightarrow b\bar{b}\tilde{H}^0)/\Gamma(\tilde{g} \rightarrow g\tilde{H}^0)$ . This has the same

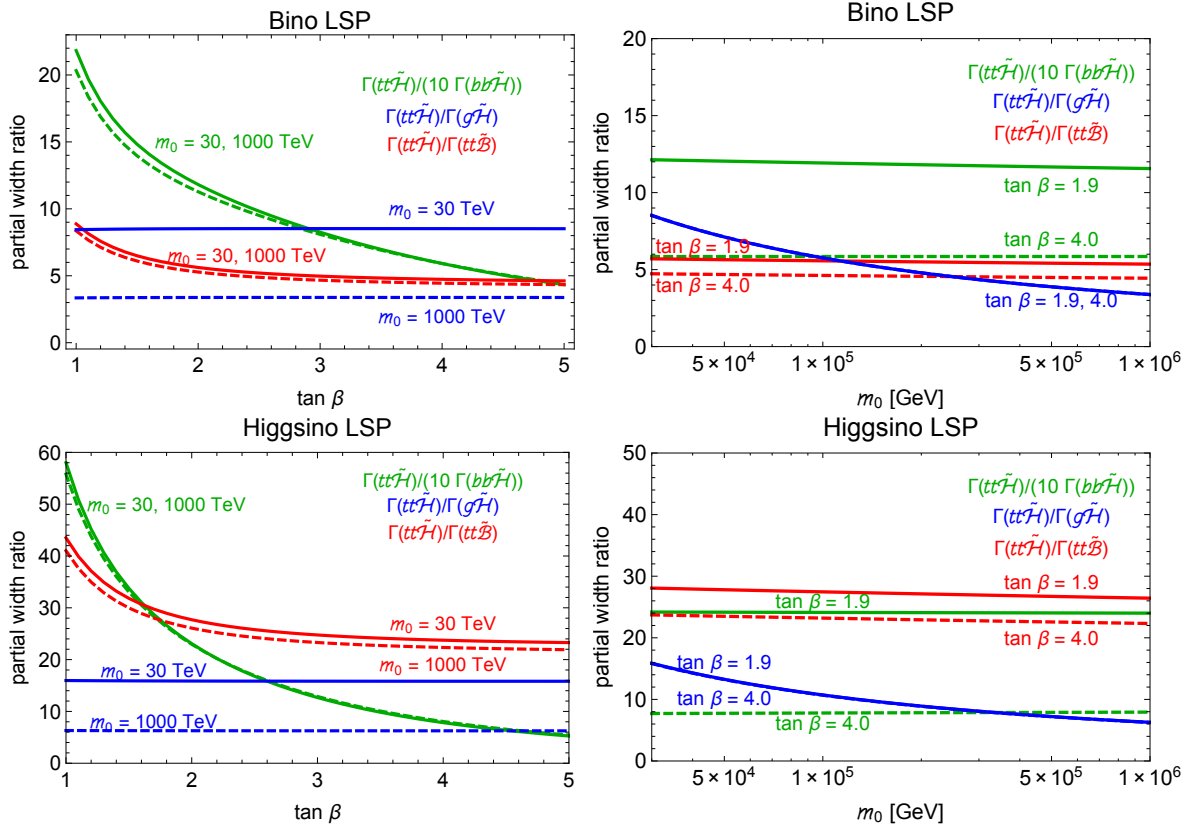


**Fig. 34:** Gluino branching ratios as probes of the SUSY scalar mass scale and  $\tan \beta$ . Top row:  $M_1 = 200$  GeV,  $M_2 = 400$  GeV,  $\mu = 800$  GeV, and  $M_3 = 2$  TeV. Bottom row:  $M_1 = 700$  GeV,  $M_2 = 1$  TeV,  $\mu = 200$  GeV, and  $M_3 = 2$  TeV. Notice that the  $b\bar{b}$  width has been rescaled by a factor of 10 so that the green curve fits in the plot.

$\tan \beta$  dependence, is a larger ratio, and the events being compared may be more similar kinematically. The denominator is sensitive to the scalar mass scale, as noted above, but if this dependence has already been measured we can separate out the  $\tan \beta$  dependence.

The observables  $\Gamma(t\bar{t}\tilde{H}^0)/\Gamma(g\tilde{H}^0)$ ,  $\Gamma(t\bar{t}\tilde{H}^0)/\Gamma(b\bar{b}\tilde{H}^0)$ , and  $\Gamma(t\bar{t}\tilde{H}^0)/\Gamma(t\bar{t}\tilde{B}^0)$ , including resummation effects, are shown in Fig. 34. From the plot we see that, as expected, the first observable (in blue) is sensitive to the scalar mass scale but independent of  $\tan \beta$ , while the latter two observables (in green and red) are sensitive to  $\tan \beta$  but only weakly depend on the scalar mass scale. (This very mild dependence is due to renormalization group mixing among the different dimension-six operators.) Notice that the  $b\bar{b}\tilde{H}^0$  width has a much stronger sensitivity to  $\tan \beta$  but is small—the curve has been rescaled by a factor of 10 to fit in the plot.

#### 2.10.0.4 Electroweak observables sensitive to $\tan \beta$

We can also measure  $\tan \beta$  through purely electroweak physics. The obvious place to look is decays purely in the electroweakino sector. See [258] for a recent detailed discussion of branching ratios in this sector. Depending on the relative ordering of masses, some decays may be effectively absent or inaccessible, so different strategies are necessary. A less obvious probe of  $\tan \beta$  arises from precision measurements of the Higgs boson.

### 2.10.0.5 Higgsino LSPs

If higgsinos are at the bottom of the spectrum, binos and winos will both promptly decay to higgsinos directly through the supersymmetric gauge interaction. In this case, the branching ratios carry very little information on  $\tan\beta$ . However, if events can be found (for instance in wino or gluino pair production) in which the decay  $\tilde{H}_2^0 \rightarrow \ell^+ \ell^- \tilde{H}_1^0$  occurs (through an off-shell  $Z$ -boson), the dilepton invariant mass spectrum is sensitive to the higgsino mass difference, which is dependent on  $\tan\beta$ . However, this is a small effect: the leading mass splitting is  $\sim m_Z^2/M_{1,2}$  and independent of  $\tan\beta$ , with a small subleading term of order  $\mu m_Z^2/M_{1,2}^2 \sin(2\beta)$  (see e.g. [20]). The fraction of events in which this  $Z^*$  decay is observed is also weakly sensitive to  $\tan\beta$ .

### 2.10.0.6 Higgsinos heavier than gauginos

Given a spectrum with  $\mu > M_{1,2}$ , decays of winos to binos (or vice versa if  $M_1 > M_2$ ) may be observable, either in cascades from gluinos or higgsinos or from direct wino production when  $M_2 > M_1$ . The branching ratios in these decays depend on  $\tan\beta$ . To understand this, integrate out the higgsino:

$$\mathcal{L}_{\text{eff}} \supset \frac{gg'}{\mu} \tilde{B} \tilde{W}^i H_u \cdot T^i H_d + \frac{gg'}{2\mu^2} \tilde{B} \tilde{\sigma}^\mu \tilde{W}^{i\dagger} \left( H_d^\dagger i \overleftrightarrow{D}_\mu \sigma^i H_d - H_u^\dagger i \overleftrightarrow{D}_\mu T^i H_u \right) + \text{h.c.} \quad (24)$$

With  $M_2 > M_1$  for concreteness, the first term leads only to  $\tilde{W}^0 \rightarrow h \tilde{B}$  while the second leads to  $\tilde{W}^0 \rightarrow Z \tilde{B}$ . Because the first term involves  $H_u H_d$  and the second involves  $|H_d|^2, |H_u|^2$ , the  $\tan\beta$  dependence of these widths will be different. In the limit  $M_2/\mu \rightarrow 0, (m_h, m_Z)/M_2 \rightarrow 0$ , and  $M_1/M_2$  fixed, the ratio of decay widths scales as

$$\frac{\Gamma(\tilde{W}^0 \rightarrow h \tilde{B}^0)}{\Gamma(\tilde{W}^0 \rightarrow Z \tilde{B}^0)} \approx \frac{4 \tan^2(2\beta) \mu^2}{M_2^2} \left( \frac{1 + M_1/M_2}{1 - M_1/M_2} \right)^2. \quad (25)$$

This is potentially an interesting probe of  $\tan\beta$ .

### 2.10.0.7 Higgsinos in the middle

Now consider the spectrum  $M_2 > \mu > M_1$ . (The case  $M_1 > \mu > M_2$  has similar physics, but binos are not directly produced, so the physics would have to be probed in gluino cascades.) Because winos decay to binos only through mixing with the higgsino, the overwhelming majority of decays will involve a two-step cascade  $\tilde{W} \rightarrow \tilde{H} \rightarrow \tilde{B}$ . The summed decay rates  $\Gamma(\tilde{W}^0 \rightarrow Z \tilde{H}_1^0) + \Gamma(\tilde{W}^0 \rightarrow Z \tilde{H}_2^0)$  are independent of  $\tan\beta$  at tree-level, but the individual amplitudes for these two processes go approximately as  $\sin\beta \mp \cos\beta$ . As a result, when  $\tan\beta = 1$ , some decays are entirely shut off: we find that  $\tilde{W}^0 \rightarrow Z \tilde{H}_2^0, h \tilde{H}_1^0$  occur and  $\tilde{W}^0 \rightarrow Z \tilde{H}_1^0, h \tilde{H}_2^0$  do not. A similar statement is true for the neutral higgsino decays to bino. Hence, for small  $\tan\beta$ , two-step decays involving two Higgses or two  $Z$  bosons occur much more often than mixed decays with one  $Z$  and one  $h$ . That is:

$$\frac{\Gamma(\tilde{W}^0 \rightarrow Zh \tilde{B}^0)}{\Gamma(\tilde{W}^0 \rightarrow ZZ \tilde{B}^0) + \Gamma(\tilde{W}^0 \rightarrow hh \tilde{B}^0)} \propto \left( \frac{\sin\beta - \cos\beta}{\sin\beta + \cos\beta} \right)^2 \quad (26)$$

is a probe of how much  $\tan\beta$  deviates from 1.

### 2.10.0.8 Higgs boson branching ratios

In split SUSY scenarios there is one light Standard Model-like Higgs boson. Its decays are affected only by loops of electroweakinos, which primarily modify the partial width to two photons (since this is already a small loop effect in the Standard Model). The deviation from the Standard Model width is given by

$$\frac{\Gamma(h \rightarrow \gamma\gamma)}{\Gamma(h \rightarrow \gamma\gamma)_{\text{SM}}} \approx 1 + \frac{0.84 m_W^2 \sin(2\beta)}{\mu M_2 - m_W^2 \sin(2\beta)}. \quad (27)$$

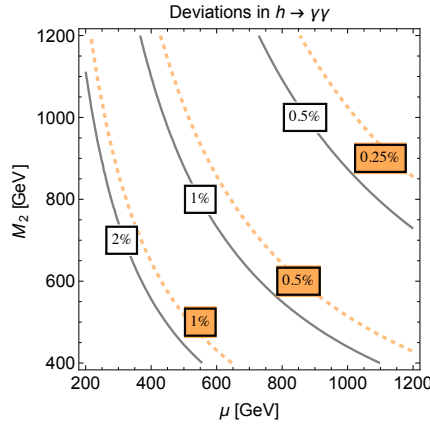


**Fig. 35:** Deviation in  $h \rightarrow \gamma\gamma$  branching ratio from loops of charginos. Solid curves:  $\tan\beta = 2$ . Dashed orange curves:  $\tan\beta = 4$ .

This is a small effect: only about a 2% increase in the branching ratio when  $\mu \approx M_2 \approx 500$  GeV and  $\tan\beta \approx 2$ , as illustrated in Fig. 35. Neither the HL-LHC nor FCC-ee will measure the Higgs coupling to photons accurately enough to make use of this probe. However, there is a chance that 100 TeV can make a very precise measurement of the ratio  $\Gamma(h \rightarrow \gamma\gamma)/\Gamma(h \rightarrow ZZ^*)$ . Many systematics (e.g. involving luminosity and production cross section) cancel in this ratio, so that hadron colliders can cleanly measure it [259, 260]. If a sub-percent-level measurement of this ratio can be made, this could be an interesting alternative probe of  $\tan\beta$  provided that the two charginos are not too heavy.

#### 2.10.0.9 Collider physics: measuring the observables

We will present some preliminary collider studies here, focusing mainly on SUSY backgrounds (i.e. confusion among different decay modes). Of course, Standard Model backgrounds must be assessed, but cuts on missing  $p_T$  and  $H_T$  can help to reduce them, and in any case distinguishing different SUSY processes is a necessary step in measuring relative decay widths. A more extended study is in progress. In simulating events we use Pythia [261] supplied with a decay table computed by SUSY-HIT [262] and modified to include gluino decays as computed in [240]. Jets are clustered using FastJet [263, 264]. For these preliminary studies we forego detector simulation.

#### 2.10.0.10 Measuring the scalar mass scale: an example with higgsino LSPs

First we focus on a spectrum with  $M_3 = 2$  TeV,  $M_2 = 1$  TeV,  $M_1 = 700$  GeV, and  $\mu = 200$  GeV. For this spectrum, due to phase space factors, gluinos decay dominantly to third-generation quarks and higgsinos: depending on our choices of  $m_0$  and  $\tan\beta$ , we have roughly 33 – 36%  $t\bar{t}\tilde{H}^0$  decays and 34 – 38%  $t\bar{b}\tilde{H}^-$  or  $\bar{t}b\tilde{H}^+$  decays. Our first task is to measure  $m_0$  via two-body decays as discussed in Section 2.10.0.2:  $\text{Br}(\tilde{g} \rightarrow g\tilde{H}^0) \approx 5\%$  ( $\odot_H, \ominus_H$ ) or 2% ( $\odot_L, \ominus_L$ ).

We attempt to identify events with a two-body decay on one side and a three-body decay on the other. Our final states, then, are

$$\tilde{g}\tilde{g} \rightarrow g + (t\bar{t} \text{ or } t\bar{b} \text{ or } \bar{t}b) + p_T^{\text{missing}} + \text{soft} + \text{ISR/FSR}. \quad (28)$$

We take advantage of the fact that, neglecting events with hard ISR, if we remove the gluon from the event we expect all other visible objects to have an invariant mass less than  $M_{\tilde{g}}$ . We find that the gluon is typically one of the two hardest jets in the event, so we select events in which removing one of the leading jets leaves a system with relatively low invariant mass. Then we attempt to test if the leading jet we

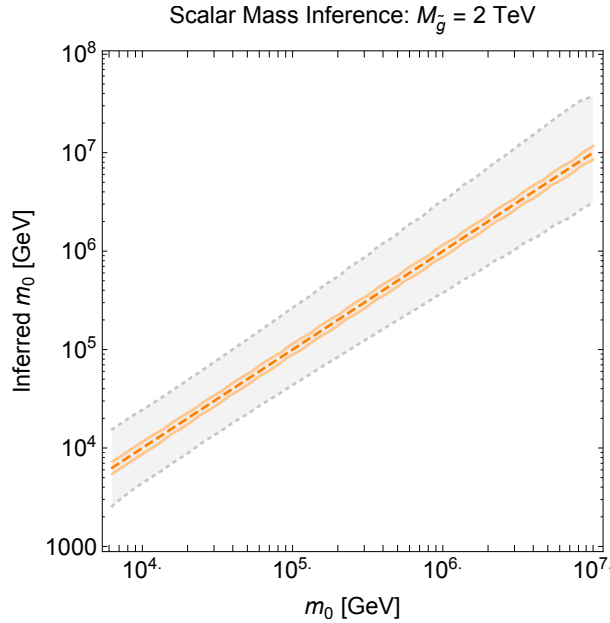


**Fig. 36:** Inference of the scalar mass scale  $m_0$  from the measurement of the rate of 2-body decays  $\tilde{g} \rightarrow g\tilde{H}^0$ . The parameters are  $M_3 = 2$  TeV,  $\mu = 200$  GeV,  $M_1 = 700$  GeV, and  $M_2 = 1000$  GeV. The orange band represents  $1\sigma$  statistical uncertainty with  $3 \text{ ab}^{-1}$  of data, while the grey band corresponds to a 10% systematic uncertainty on cut efficiencies times cross section times luminosity.

removed is actually a gluon by requiring it to have little hard substructure as measured by  $N$ -subjettiness ratio variables  $\tau_N/\tau_{N-1}$  [125, 265] (computed with the winner-take-all axis and  $\beta = 1$  [266]).

We have found a set of cuts with efficiency  $\epsilon_{2\text{body}} \approx 1.5 \times 10^{-3}$  on events containing a 2-body gluino decay but only  $\epsilon_{3\text{body}} \approx 1.3 \times 10^{-4}$  on other events:

$$H_T > 2 \text{ TeV}, \quad p_T^{\text{missing}} > 1.6 \text{ TeV}, \quad p_T(j_1) > 1 \text{ TeV}, \quad (29)$$

$$N_{\text{jet}} < 4, \quad \left| \Delta\phi(j_2, p_T^{\text{missing}}) \right| > 1.8, \quad M(j_{\text{gluon removed}}) < 1.2 \text{ TeV}, \quad (30)$$

$$\tau_2/\tau_1(j_{\text{gluon}}) > 0.65, \quad \tau_3/\tau_2(j_{\text{gluon}}) > 0.65, \quad \text{muons near } j_{\text{gluon}} \text{ vetoed.} \quad (31)$$

Here  $j_{\text{gluon}}$  is either the first or second highest  $p_T$  jet in the event, chosen so that removing this jet and computing the mass of the others—denoted  $M(j_{\text{gluon removed}})$ —gives the smallest result. We define  $N_{\text{jet}}$  as the number of jets with  $|\eta| < 2.5$  and  $p_T > 100$  GeV and  $H_T$  as the scalar sum of the  $p_T$  of those jets. We veto events with any muon of  $p_T > 25$  GeV near our gluon candidate, which helps reduce the number of  $b$ - or  $t$ -jets faking our leading gluon. After these cuts, we can obtain samples that contain a significant fraction of 2-body decays: roughly 30% for the points  $\textcircled{L}$  and  $\textcircled{L}$  and 60% for the points  $\textcircled{H}$  and  $\textcircled{H}$ . In  $3 \text{ ab}^{-1}$  of data, these samples will contain somewhere around 3000 to 6000 events (depending on the two-body decay rate), so despite the relatively low efficiency, statistical uncertainties can be small.

The estimated performance of a simple cut-and-count analysis is presented in Fig. 36. The orange band shows that statistical uncertainty alone can be quite small. The gray band represents a 10% systematic uncertainty in the event rate. This corresponds to about a factor of 2 to 3 uncertainty in the scalar mass scale, bracketing  $\textcircled{L}$  to the range 13 – 74 TeV and  $\textcircled{H}$  to 400 – 3200 TeV. As we have emphasized above, measuring ratios (rather than simply counting events as we have done here) can help to cancel the sizable uncertainties in luminosity and production cross section. However, it may not be possible to eliminate other uncertainties, for instance in the efficiencies of some cuts. We emphasize that

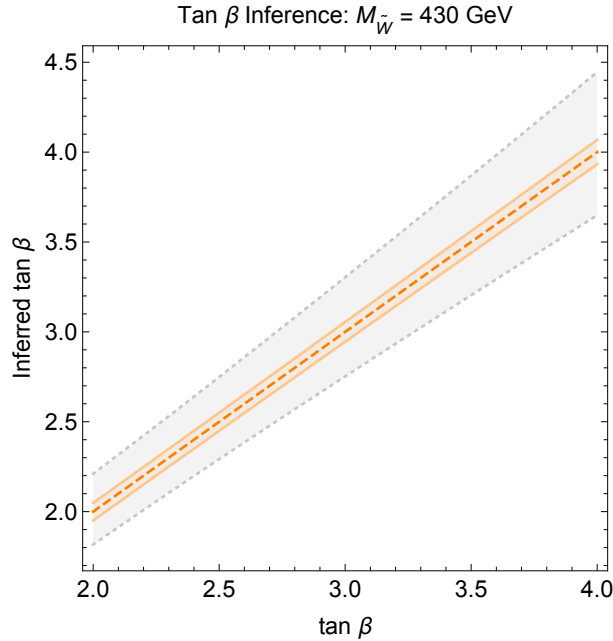


**Fig. 37:** Inference of  $\tan \beta$  from the measurement of the rate of  $\tilde{W}^0 \rightarrow Z\tilde{B}^0$  decays. The parameters are  $M_3 = 2$  TeV,  $M_1 = 200$  GeV,  $M_2 = 400$  GeV, and  $\mu = 800$  GeV. The orange band represents  $1\sigma$  statistical uncertainty with  $3 \text{ ab}^{-1}$  of data, while the grey band corresponds to a 10% systematic uncertainty on cut efficiencies times cross section times luminosity.

this is a preliminary analysis; the cuts can be further optimized, and a more sophisticated multivariate analysis would likely be effective. On the other hand, we have been somewhat optimistic in choosing a 2 TeV gluino mass, as both the production rate and the two-body branching fraction decrease for heavier gluinos. Further study will be required to optimize cuts in different kinematic regions and map out the expected statistical precision.

#### 2.10.0.11 Measuring $\tan \beta$ : an example with heavy higgsinos

Now we turn to a spectrum with  $M_3 = 2$  TeV but  $M_1 = 200$  GeV,  $M_2 = 400$  GeV, and  $\mu = 800$  GeV. In this case, as discussed in Section 2.10.0.6, the relative decay rate of neutral winos to  $Z$  bosons and Higgs bosons can probe  $\tan \beta$ . We examine the case of electroweakino production: in  $3 \text{ ab}^{-1}$  we expect about  $7 \times 10^6$  wino pair production events (including both charged/charged and neutral/charged).

We search for  $\tilde{W}^0 \rightarrow Z\tilde{B}^0$  in events with  $Z \rightarrow \ell^+\ell^-$ , by requiring two opposite-sign same-flavor isolated leptons with  $80 \text{ GeV} < m_{\ell\ell} < 100 \text{ GeV}$ , two jets with  $p_T > 30 \text{ GeV}$ , and  $p_T^{\text{missing}} > 200 \text{ GeV}$ . Opposite-sign opposite-flavor pairs in the  $Z$  mass window are subtracted to eliminate contributions from  $W$  bosons on both sides of the event. The efficiencies of the cuts are  $\epsilon_{\tilde{W} \rightarrow Z\tilde{B}} \approx 8.7 \times 10^{-3}$  on events containing a neutral wino decaying to a  $Z$  boson and bino but only  $\epsilon_{\text{other}} \approx 1.6 \times 10^{-4}$  on other events. After these cuts, we can obtain samples that contain a significant fraction of wino decaying to a  $Z$  boson for  $\tan \beta \approx 4$ : roughly 55% for the points  $\text{☺}_L$  and  $\text{☹}_H$ . In  $3 \text{ ab}^{-1}$  of data, these samples will contain somewhere around 1500 to 3000 events after the cuts, so again despite the relatively low efficiency, statistical uncertainties can be small.

The estimated performance of a simple cut-and-count analysis is presented in Fig. 37. Analogous to Fig. 36, the orange band represents the small statistical uncertainty while the gray band represents a 10% systematic uncertainty in the event rate. This corresponds to about a factor of 10% variation in determining the value of  $\tan \beta$ . In our analysis, we only considered the SUSY background and didn't

take into account of the SM background. The result should be taken as a rough estimate to motivate a further refined analysis.

### 2.10.0.12 Conclusions

A 100 TeV hadron collider has tremendous potential to address many deep fundamental questions in particle physics, such as the underlying mechanism that generates the observed Higgs mass. In this section, we have discussed how to use precision measurements of gluino and neutralino decays at a 100 TeV collider to test the Higgs mass explanation in the MSSM with gauginos at around a TeV. In the MSSM, the Higgs mass is raised from the tree-level prediction by the loop contribution of heavy stops to the observed value. Direct searches and lifetime measurements, which have been discussed already in the literature, still leave untouched a large and interesting region of parameter space with scalar mass in the range (30–1000) TeV and  $\tan\beta$  between 2 and 4. Among all observables in gaugino decays, the two-body decays of gluinos are loop-induced and logarithmically sensitive to the scalar mass scale. We have demonstrated that in a scenario with a higgsino LSP, the scalar mass could be inferred from measuring the gluino two-body decays with a factor of 2 to 3 uncertainty at a 100 TeV collider with  $3 \text{ ab}^{-1}$  data. There are several different approaches to measure  $\tan\beta$  from either gluino decay or wino or higgsino decays. We use winos decaying to a  $Z$  boson in a scenario with a bino LSP and wino lighter than higgsino as an example to demonstrate the potential of determining  $\tan\beta$  with a 10% uncertainty. All the studies are still preliminary, yet they demonstrate the great potential of a 100 TeV collider in precision measurements of SUSY particles at around TeV scale or below and unraveling the mystery of the Higgs mass. A more thorough and refined analysis will be implemented and presented soon [267].

## 2.11 Summary of Phenomenological Studies

The supersymmetric aspect of an experimental program at 100 TeV is very rich. While comprising just the tip of the iceberg, the phenomenological studies of Sections 2.2 to 2.10 demonstrate a varied frontier of exciting signatures. In Fig. 38 we summarise the results of these studies in the context of simplified models assuming  $30 \text{ ab}^{-1}$  of integrated luminosity.

Let us revisit the broadly motivated mass ranges outlined in Section 2.1. While supersymmetry may exist as a new spacetime symmetry at any energy, various considerations converge towards particular mass ranges for superpartners. Dark matter considerations point towards gauginos and/or Higgsinos in the  $\lesssim \mathcal{O}(10 \text{ TeV})$  range. Gauge coupling unification is similarly suggestive for the gauginos, although the upper bound on gaugino masses is less robust than for thermal dark matter. The Higgs mass points towards a range of scalar masses, however for  $\tan\beta \gtrsim 4$ , squarks, in particular stop squarks, should be expected below  $\lesssim \mathcal{O}(10\text{'s TeV})$ . If naturalness is desired, all coloured sparticles should be within  $\lesssim \mathcal{O}(\text{few TeV})$ , and the stops and gluinos as light as granted by current bounds.

Comparing these expectations with the results in Fig. 38 we see that much of the supersymmetric parameter space relevant to core puzzles in high energy physics, such as dark matter, grand unification, the Higgs mass, and naturalness, can be covered. Let us now consider the context of such measurements in light of our current picture of fundamental physics at the LHC, particularly with respect to naturalness of the weak scale. We will then look towards the future potential impact these measurements could have on our understanding of fundamental physics.

The primary goal of the LHC is the exploration of physics at the weak scale. Hence, testing the naturalness principle in the Higgs sector is a central issue. At the time this document is written, the LHC verdict on naturalness is not yet final. Admittedly, data at  $\sqrt{s} = 8 \text{ TeV}$  and preliminary results at 13 TeV strongly disfavour the most straightforward implementations of natural low-energy supersymmetry, which favoured new weakly-interacting particles in the 100 GeV domain and strongly-interacting particles well below the TeV scale.

If the LHC reveals new phenomena, these discoveries will redesign the priorities of future high-

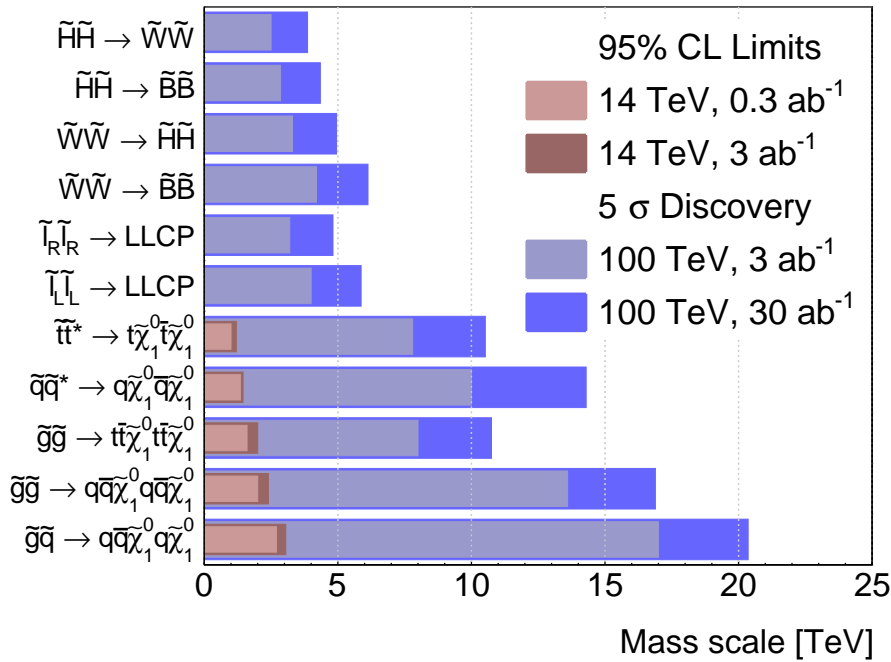


**Fig. 38:** Sensitivity for simplified models considered in this section for the LHC, HL-LHC, and a  $pp$  collider at  $\sqrt{s} = 100$  TeV with data samples of  $3 \text{ ab}^{-1}$  and  $30 \text{ ab}^{-1}$ . The reach for strong-production at 14 TeV is quantified by 95% confidence level upper mass limits on the mass of squarks or gluinos (or both) when the LSP is massless, and is taken from ATLAS and CMS projections [132, 268–271], or from this document in the case of the  $\tilde{g}\tilde{g} \rightarrow t\tilde{\chi}_1^0 t\tilde{\chi}_1^0$  model. Sensitivity for  $\sqrt{s} = 100$  TeV and  $3 \text{ ab}^{-1}$  is quantified by the  $5\sigma$  discovery reach presented in this document. The  $30 \text{ ab}^{-1}$  reach is from this document when available, otherwise it is projected from the  $3 \text{ ab}^{-1}$  reach using the Collider Reach web tool [272].

energy physics. Although today it is impossible to say what those priorities will be, it is hard to imagine a new-physics scenario, supersymmetric or not, which will not motivate us to continue explorations towards energies higher those those of the LHC. As illustrated in this document, the physics program at 100 TeV is rich enough to provide an excellent tool to carry out such explorations at high energies.

If no discoveries are made at the LHC, the simplest versions of low-energy supersymmetry would be ruled out. This would be a momentous result, as supersymmetry has played a central role in the conceptual development of our field for decades. In this sense, the era of natural supersymmetry would come to an end. However, in such an instance it would be incorrect to conclude that the naturalness principle is misguided. Excluding new dynamics at the weak scale would mean ruling out our favoured solutions to the naturalness problem, but not the problem itself, and knowing how nature deals with Higgs naturalness will remain a standing issue. This reframing of the naturalness question would imply the loss of the logical connection between Higgs naturalness and new phenomena at the TeV scale. If this connection is lost, what would be so special about the energy scale explored by a 100 TeV collider and why should we expect new phenomena in that range?

In spite of its virtues at a more fundamental level, supersymmetry may not be the answer to Higgs naturalness. Speculations have been made about logical schemes that deal with Higgs naturalness without dynamics at the weak scale, such as the anthropic principle or cosmological relaxation. Intriguingly, even within these very different schemes, motivations for supersymmetry emerge, although at a scale different than the weak scale and also for different reasons. In the context of unnatural setups, considerations discussed in Section 2.1 about dark matter, gauge coupling unification, or the Higgs mass, or the limited

cutoff that can be achieved in cosmological relaxation scenarios call for supersymmetry with a certain preference for the  $\mathcal{O}(10^{\prime}s)\text{TeV}$  range. Figure 38 demonstrates that this energy range is prime territory for a 100 TeV collider.

To summarise, speculations about the role of supersymmetry in ‘unnatural’ theories suggest that a future physics program should not be regarded as an extension of LHC searches, but rather as conceptually different. If the LHC is the machine of the *naturalness era*, future colliders would become the machine of the *post-naturalness era*. An era in which we are forced to change the focus of our basic questions about particle physics, in which we contemplate partly unnatural theories or theories where naturalness is realised in unconventional ways, and in which supersymmetry may enter in a new guise.

### 3 Dark Matter

#### 3.1 Introduction

Today there is an overwhelming amount of evidence from astrophysical observations that a large fraction of the observed matter density in the universe is invisible to us. This so called Dark Matter (DM) makes up 26% of the total energy density in the universe, and more than 80% of the total matter [273]. Despite numerous observations of the astrophysical properties of DM, not much is known about its particle nature. The main constraints on a particle DM candidate  $\chi$  are that it (see e.g. [274] for a more detailed discussion)

- should gravitate like ordinary matter
- should not carry color or electromagnetic charge
- is massive and non-relativistic at the time the CMB forms
- are long lived enough to be present in the universe today ( $\tau \gg \tau_{\text{universe}}$ )
- does not have too strong self-interactions ( $\sigma/M_{\text{DM}} \lesssim 100 \text{ GeV}^{-3}$ ).

While no SM particles satisfy these criteria, they do not pose very strong constraints on the properties of new particles to play the role of DM. In particular the allowed range of masses spans almost 80 orders of magnitude. Particles with mass below  $10^{-22}$  eV would have a wave length so large that they wipe out structures on the kPc (kilo-Parsec) scale and larger [275], disagreeing with observations, while on the other end of the scale micro-lensing and MACHO (Massive Astrophysical Compact Halo Objects) searches put an upper bound of  $2 \times 10^{-9}$  solar masses or  $10^{48}$  GeV on the mass of the dominant DM component [276–278].

Clearly we can not hope that any future collider will probe the full mass range allowed by astrophysical observations. However there is a very broad class of models for which theory motivates the GeV - TeV mass scale, and which therefore could be in range of a future hadron collider operating at a centre-of-mass energy around 100 TeV. If at any point in the history of the early universe the DM is in thermal equilibrium with the SM particles, then we can estimate its relic density today by studying how it decouples from the SM, the so called freeze-out. For particles which are held in equilibrium by pair creation and annihilation processes, ( $\chi\chi \leftrightarrow \text{SM}$ ) one finds the simple relation that [279]

$$\Omega_{\text{DM}} h^2 \sim \frac{10^9 \text{ GeV}^{-1}}{M_{\text{pl}}} \frac{1}{\langle \sigma v \rangle}, \quad (32)$$

where  $\langle \sigma v \rangle$  is the velocity averaged annihilation cross section of the DM candidate  $\chi$  into SM particles,  $\Omega_{\text{DM}} h^2 \approx 0.12$  is the observed relic abundance of DM [273],  $M_{\text{pl}}$  is the Planck scale and order one factors have been neglected.

For a particle annihilating through processes which do not involve any larger mass scales, the annihilation cross section scales as  $\langle \sigma v \rangle \sim g_{\text{eff}}^4 / M_{\text{DM}}^2$ , where  $g_{\text{eff}}$  is the effective coupling strength which parameterises the process. It follows that

$$\Omega_{\text{DM}} h^2 \sim 0.12 \times \left( \frac{M_{\text{DM}}}{2 \text{ TeV}} \right)^2 \left( \frac{0.3}{g_{\text{eff}}} \right)^4, \quad (33)$$

i.e. that a DM candidate with a mass at or below the TeV scale and which couples to the SM with a strength similar to the weak interactions naturally has a relic density in agreement with observations. There are several variations of this simple approximation which modify the preferred mass range, e.g. when the annihilation processes involve heavier states, when it is velocity suppressed, assisted by co-annihilation or increased through a resonance [158]. Including these effects, one finds that weakly interacting massive particles (WIMPs) can reproduce the observed relic abundance when their mass is in the 10s of GeV to few TeV range. On one side this is the main reason why we hope to find evidence for

DM at the LHC, but on the other hand it already tells us that a higher energy collider will be necessary to efficiently probe the WIMP paradigm for DM.

As the mass of DM increases, Eq. (32) tells us that to maintain the observed relic abundance the annihilation cross section also has to increase. This becomes inconsistent with unitarity of the annihilation amplitudes at  $M_{\text{DM}} \lesssim 110$  TeV, the so called unitarity bound on the mass of DM [280, 281]. Most well motivated models of WIMP DM do not saturate this bound, but rather have upper limits on the DM mass in the few TeV range. One main aspect of this document is to determine how well these models can be probed currently and with a future collider experiment.

For DM masses at the lower end of the WIMP spectrum, one typically expects that annihilation proceeds through a mediator with  $M_{\text{med}} > 2M_{\text{DM}}$ . Then the annihilation cross section is suppressed by  $(M_{\text{DM}}^4/M_{\text{med}}^4)$ . Assuming that no mediator particle exists with a mass below the Higgs mass, then this puts a lower bound of a few GeV on the mass of the WIMP DM candidate, while an even wider range of DM masses becomes accessible if the mediator is lighter but very weakly coupled to the SM.

In the first part of this report, we will focus on WIMP scenarios where the relic density of DM is set by non-relativistic annihilation (freeze-out) to SM particles, either through a SM portal or through new mediators. Obviously if new mediators are present, searching for or constraining them directly might be possible before the DM itself becomes discoverable, and we will discuss how this interplay evolves when going to higher energies.

There are DM models which do not fall into the WIMP category as defined above, but which are still relevant for DM searches at hadron colliders. Mainly these are models where the DM is in thermal equilibrium with the SM at some point, but the relic abundance is not determined by the usual freeze out mechanism. The best known examples are models of asymmetric DM (ADM), where the relic abundance is determined by an asymmetry in DM versus anti-DM in the early universe [282, 283], possibly related to the baryon asymmetry of the universe, and models where the DM annihilates to an additional (lighter) state in the dark sector first, which later decay to SM particles:

$$\chi\chi \rightarrow aa \quad \text{followed by} \quad a \rightarrow \text{SM}. \quad (34)$$

Necessary ingredients in both cases are first an interaction to bring the dark sector into thermal equilibrium with the SM at early times, and furthermore a way to transfer entropy from the dark sector back to the visible sector after the relic abundance is set. For the ADM scenario this means that the symmetric abundance has to annihilate efficiently, either to SM particles as in the WIMP scenario (but with a cross section somewhat larger than in the WIMP case), or an annihilation into lighter, unstable particles of the dark sector.

The entropy transfer must happen before the onset of big bang nucleosynthesis (BBN) at temperatures around 10 MeV. This puts an upper bound on the lifetime of the unstable dark sector particle of  $\tau_a \ll 1$  s. From the collider perspective this means that the dark sector particles can either decay promptly, with a displaced vertex, or could be collider stable, and all three regimes need to be probed to say something conclusive about these non-WIMP scenarios.

In the following introductory chapters, we will review the current bounds on DM from direct and indirect searches, from cosmology and from collider experiments, as well as how the sensitivity is expected to evolve in the next 20 to 30 years. Then we will discuss the prospects of a 100 TeV collider to probe the thermal WIMP scenario, starting with minimal and simplified models and moving on to some examples of UV complete models. Following that we discuss examples of non-WIMP DM scenarios which can be probed at hadron colliders and the possible benefit of a 100 TeV machine, before presenting our conclusions.

### 3.2 Experimental searches for DM

Searches for DM can be split into three separate classes: Direct detection, indirect detection, and collider based searches. Direct detection consists of the search for DM using a nuclear recoil. Indirect detection consists of the class of searches looking for annihilation of DM in galactic collisions. This class of experiments consists of the set of satellite and ground based telescope experiments which search for excesses of either photons or antiparticles in space. Finally, there are collider searches, where production of DM is searched for via its missing energy signature. The two non-collider set of experiments can be compared to the collection of collider searches. For the case of a 100 TeV proton collider, the ultimate bounds of these searches are considered so as to put into context the comparative reach of the colliders.

#### 3.2.1 Direct Detection

Conventional direct detection probes the rate of DM nucleon interactions in earth based experiments. This is done through low rate, high sensitivity searches of low energy DM nucleon recoils. The searches yield a bound on the matter DM cross section  $\sigma$ . This cross section relies on two fundamental ingredients, the type of interaction, and the relative density of DM in the solar system. The searches compute the rate of DM nucleon collisions for a given recoil energy  $E$ , denoted  $dR/dE$ . This we can write as,

$$\frac{dR}{dE} = \frac{\rho_{DM}}{m_N m_{DM}} \int_{v > v_{min}} v f(v) \frac{d\sigma(v, E)}{dE} dv \quad (35)$$

where  $\rho_{DM}$  is the local DM density,  $f(v)$  is the local DM velocity profile for DM velocity  $\vec{v}$ ,  $m_N$  is the recoiling nucleus mass,  $m_{DM}$  is the DM mass and  $\frac{d\sigma}{dE}$  is the differential DM nucleus interaction cross section. The rate measurement can be translated to a cross section bound for a given DM mass through the fact that all parameters are known with the exception of the DM mass,  $m_{DM}$ , and the DM cross section. The other parameters, in particular the DM density,  $\rho_{DM}$  and velocity profile,  $f(v)$ , are inferred from local galactic measurements combined with galactic simulations. The current measurements for the DM density and velocity profile have a level of variability that is expected to improve over the coming years. However the variability itself motivates the use of a collider search to allow for precise determination of the DM properties.

Direct detection searches can be split into two classes of DM interactions, spin-independent and spin-dependent interactions. Spin independent interactions consist of DM nucleon interactions that do not have any dependence on the spin structure of the mediator nucleon interaction. This includes interactions involving a scalar mediator or a vector mediator without an axial coupling. Spin-dependent DM occurs when the interaction model is sensitive to the spin structure of the nucleus. Direct detection has a much larger sensitivity to spin independent interactions due to the coherent enhancement of the cross section proportional to the square of the nucleus mass.

An ultimate bound for direct detection comes from neutrino interactions in the detectors. This background cannot be distinguished from DM interactions and thus is irreducible [284]. This bound has served as a benchmark for DM searches and represents an ultimate goal for the next generation of direct detection experiments. This bound exists for both spin-dependent and spin-independent interactions, as shown in Fig. 39. Recently, the directional DM detection has demonstrated the capability to extend beyond the neutrino wall [285]. However, there is currently no plan to build an experiment large enough to reach this boundary.

The searches for direct detection have greatly improved over the past few years. This has been largely from the development of two technologies, low energy cryogenic detectors, and large scale liquid noble gas detectors. Both these technologies are going through major upgrades in the detector size; further allowing for enhanced sensitivity. In particular, the CDMS detector is expected to extend the sensitivity to low mass DM to the sensitivity threshold near the neutrino wall. For high mass DM, the extension of the LUX detector (LZ and Darwin) [286, 287], and future extensions of liquid argon detectors can potentially cross the neutrino wall [288], see Fig. 39. The same liquid noble gas detectors are

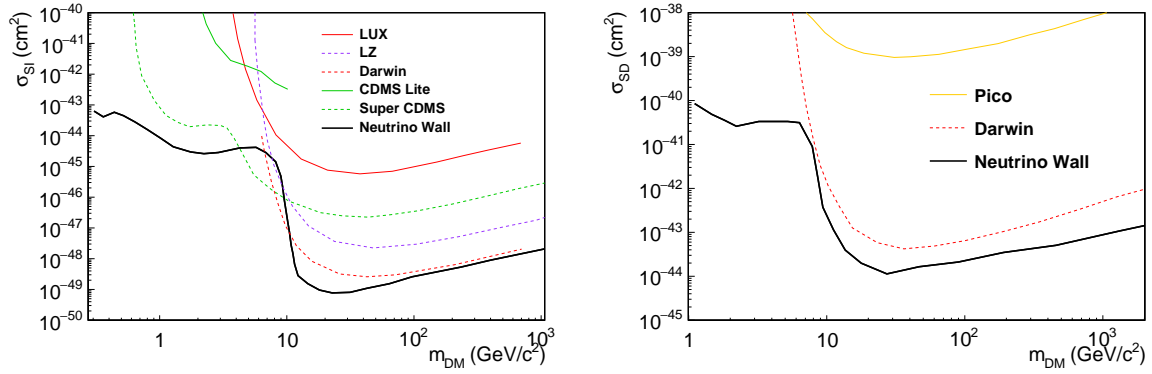


**Fig. 39:** Comparison of the current best bound (solid line) with upcoming experiments (dashed line), and the neutrino wall for spin independent(left) and spin dependent detection (right). For spin dependent interactions additional lines potentially exist for the LZ however they are currently not publicly available.

sensitive to spin dependent DM [289, 290]. Thus, allowing for the the extension of DM searches to the neutrino wall for all DM masses with both spin independent and spin dependent DM.

### 3.2.2 Indirect Detection

Indirect detectors consist of space- and ground-based telescopes, which look for the products of DM induced interactions in and beyond the galaxy. Essentially, these searches consist in looking for the presence, on top of the ordinary cosmic rays, of possible anomalous fluxes of high energy photons, positrons, anti-protons and neutrinos which could be attributed to DM annihilations or decays. Further discrimination can be done by directional searches; explicitly searching for particles from dwarf galaxies or the center of the galaxy. Currently, the experiments can be divided into two sets of experiments: particle based detectors, such as AMS, and photon based detectors, such as the FermiLAT satellite. In both cases, the quoted bound is on the interaction rate of particles at a given energy ( $dN/dE$ ). For the case of photons, this can be written as

$$\frac{dN}{dE} = \frac{1}{4\pi} \frac{\langle\sigma v\rangle}{2m_{DM}^2} F(q^2) \rho'_{DM}, \quad (36)$$

$$\rho'_{DM} = \int_{\Delta\Omega} d\Omega \int_{los} \rho_{DM}^2(r(l, \phi)) dl(r, \phi). \quad (37)$$

Here  $\rho'_{DM}$  is the integral over the line of sight (*los*) of the square of the DM density  $\rho_{DM}$ ,  $F(q^2)$  is the resulting fragmented particle distribution considering the initial particle produced, and  $m_{DM}$  is the DM mass. As with direct detection, the DM mass profile  $\rho_{DM}$  is a necessary input into the calculation. These measurements also suffer from large uncertainties since the rates depend quadratically on  $\rho_{DM}$  and the integral often runs over regions where the density is poorly constrained.

Photon bounds coming from annihilating DM interactions consist of two classes of searches: continuum photon excess searches, and direct photon line searches. Continuum photon searches consist of searches of a broad excesses of photons over the predicted photon background. These searches have relatively large uncertainties since they require a precise knowledge of the photon background. When DM annihilates to a final state that is direct photons, photon line searches can be performed. These searches can exclude much smaller production cross sections since they consist of a classic bump hunt on top of the photon continuum background [153, 154]. In both cases, the current results are driven by two experiments: FermiLAT, a low energy gamma ray satellite, and HESS, a high energy gamma ray telescope.

The FermiLAT satellite dominates bounds for photon energies up to 1 TeV and the HESS telescope array is the dominant bound for energies above 1 TeV.

Figure 40 shows the current bounds for the experiments. Both of the search regions are expected to improve with the upcoming launch of DAMPE [291] and Gamma-400 [292]. Further improvements at high energy will come with the Cherenkov Telescope Array (CTA) [293]. These further extensions are shown in Fig. 40. The goal is to cover the model independent calculation of the relic density shown in Fig. 40. This allows for an exclusion/discovery benchmark of a large class of models. The relic density line can be avoided through models with p-wave annihilation or co-annihilation. In some models, direct photon line searches are more sensitive than broad spectrum searches. In Fig. 40, we also show the direct photon bounds searches and the extrapolated improvements [294, 295] given a consistent level of improvement as that projected with the future continuum searches.

The AMS anti-proton results are also shown 40, along with the band of variations coming from different astrophysical hypotheses. The AMS anti-proton results are already comparable to the existing FermiLAT bounds, and are expected to improve further. It is expected that AMS will continue to run for another 10 years. There are currently no projected upgrades of the AMS detector.

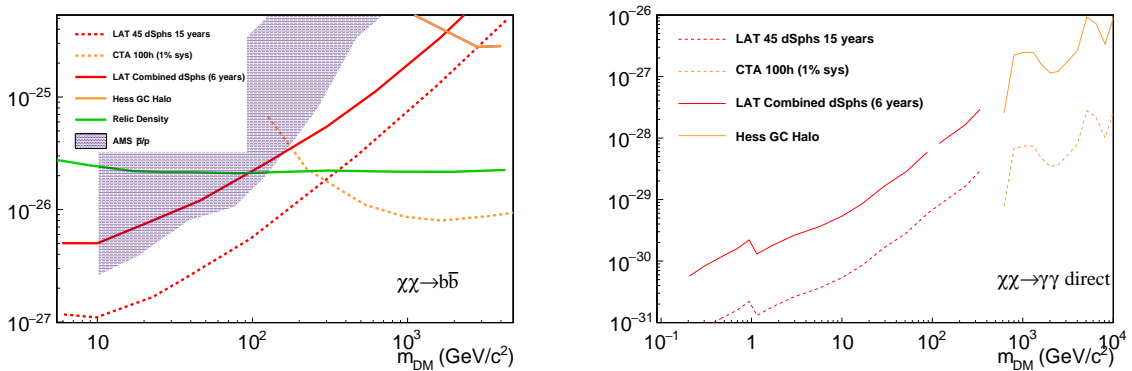


**Fig. 40:** Indirect bounds coming from current AMS [296, 297], FermiLAT [298], and HESS [299] results. Additionally, projected bounds based on 15 life years of FermiLAT and the CTA [293] experiment. Bounds are shown for  $b\bar{b}$  final state for the continuum search(left) and for the direct photon search(right).

### 3.2.3 Relic Density

The current measured relic density from cosmic microwave background(CMB) is  $\Omega_{DM}h^2 = 0.1198 \pm 0.0026$  [273]. This sets a benchmark for which models and constraints for DM can be compared. The annihilation cross section corresponding to the observed relic density is show in Fig. 40. For light DM the required values can be excluded by indirect detection for a number of relevant annihilation channels.

For a large class of models, relic density constraints have the ability bound the allowed space of dark matter models. To illustrate the impact of the relic density, we consider the relic density bound for 4 types of mediators, a scalar, a pseudoscalar, a vector mediator and an axial mediator. These mediators are further discussed in the section on simplified models 3.4.1. For scalar and pseudo-scalar mediators the couplings to quarks are taken to be proportional to the corresponding Higgs Yukawa couplings,  $y_q$  as in models with minimal flavour violation [300, 301], and vector/axial mediators we take flavor universal couplings to all quarks. For simplicity's sake, we take the couplings to the quarks  $g_q$  and the DM particles  $g_{DM}$  to be unity ( $g_q = g_{DM} = 1$ ). This assumption is a bit naive given that for vector and axial mediators, the couplings are on the threshold of being physical. However, the large coupling also opens

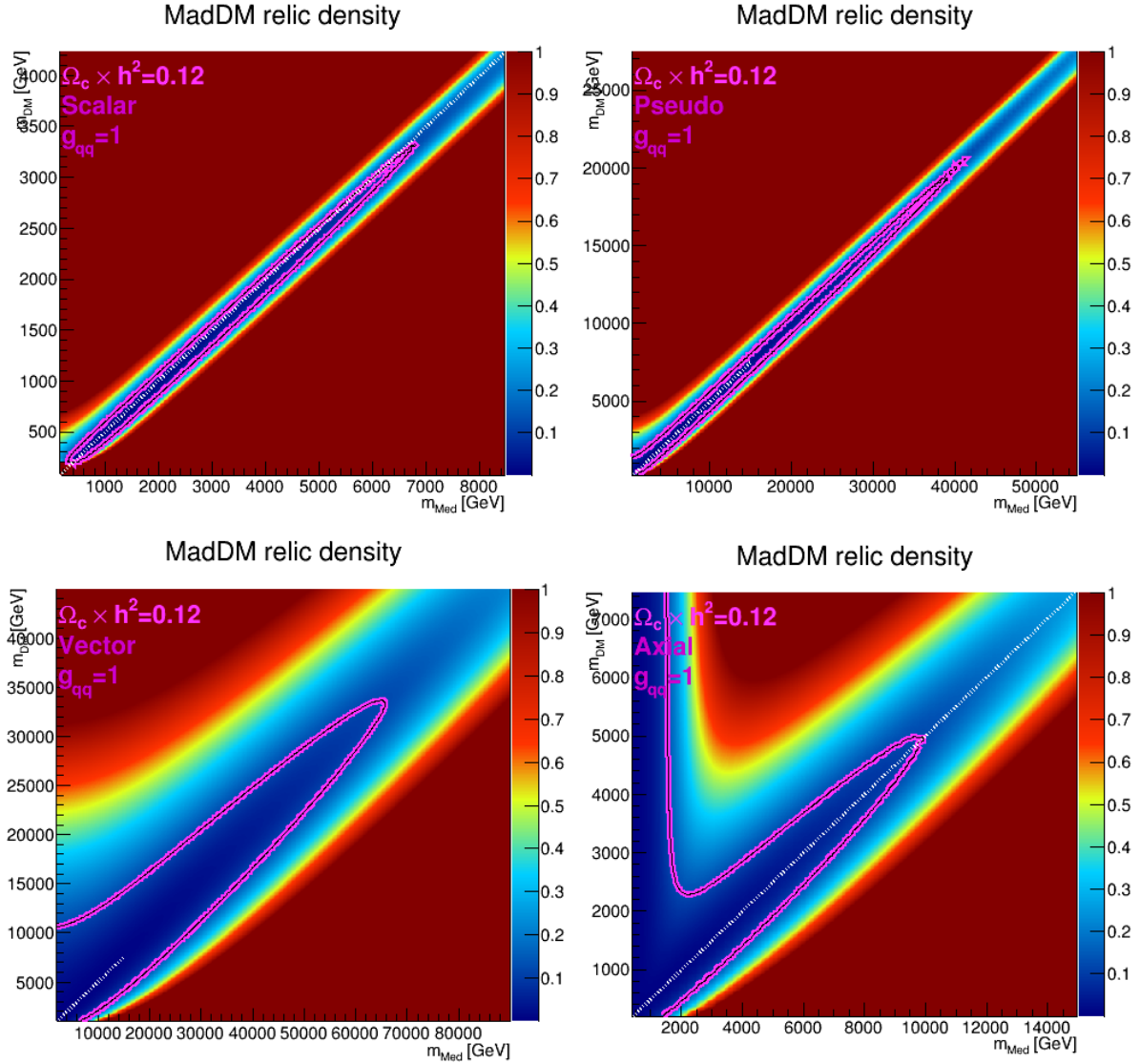


**Fig. 41:** Relic density bound for the simplified models using a Scalar mediator (top-left), Pseudoscalar mediator (top-right), Vector mediator (bottom-left), and Axial mediator (bottom-right).

the allowed region of phase space of the DM models. In the sense that larger coupling means larger DM annihilation cross section, which means smaller DM density at the time of freeze out. This allows us to quote the resulting upper bounds on the DM production as conservative upper bounds.

Figure 41, shows the DM bounds for the four sets of mediators computed using the MadDM [302] program. The reach of the vector mediator is roughly 80 TeV, axial mediator is 8 TeV, scalar mediator is 6 TeV and pseudoscalar mediator is 40 TeV. The bounds all have a similar feature in that the reach in mediator is strongest for DM masses which are close to half the mediator mass (the resonant regime). These bounds can further be modified by the presence of additional particles that couple to the mediator.

### 3.2.4 Collider Production

In many models DM production at colliders proceeds via an additional particle, the so called mediator, which couples to both SM states and DM. This can be an s-channel mediator such as a new scalar particle or a vector boson, or a t-channel mediator such as a squark. Thus, excluding a Z or Higgs mediator, the

search for DM at colliders consists of looking for the DM itself and at least one additional particle.

When DM is produced directly, it will not interact with the detector and thus leaves a missing energy signature. The class of direct searches consist of missing energy signature along with an additional signature. In the case of proton-proton collisions, missing energy results as missing transverse energy due to the lack of conservation of the momentum in the collision axis. The most generic of these searches is the monojet DM search. The search consists of the selection of one or more jets and missing transverse energy recoiling against the jets. Additional missing energy searches consist of replacing the jet with another signature, such as as vector boson, photon or the Higgs boson (so called MET+X final state).

For every MET+X collider search, the dominant background comes from  $Z+X$ , where the  $Z$  boson decays to neutrinos  $Z \rightarrow \nu\nu$ . The current modelling uncertainty of the  $Z+X$  production is theoretically limited by the order of calculation precision for most regions of phase space. However, this can be overcome by modelling the  $Z \rightarrow \nu\nu$  production through a combination of control regions where no DM is present. The most advanced approach involves a simultaneous fit of  $Z \rightarrow \ell\ell, \gamma + X$  control regions, with the theoretical predictions for the  $Z+X/\gamma+X$  production ratio as an additional constraint. The full fit has been shown to model the distribution of  $Z+X$  differential production down to the percent level. This sets a benchmark for the level of precision considered in the rest of the document. It is likely that further development of these approaches in the ensuing years will allow for the preservation of such high precision out to high energies. This ensures that the DM searches will remain statistically limited.

MET+X searches can be greatly enhanced by additional signatures that may occur in specific scenarios. For highly degenerate particles (in the co-annihilation regime), one can have long lived charged particles that decay into DM. This gives the classic MET+X signature with an additional signature: such as a short track resulting from the charged particle before it decayed. These additional tags have the ability to greatly reduce the background and further enhance the sensitivity of collider based searches.

Since DM at the LHC involves additional non-Standard Model particles, one can indirectly search for DM by observing these additional new particles. For example, vector mediators will decay to quarks. Thus, one can search for vector mediators directly by looking for resonant di-jet production [303]. While indirect searches implicitly require that all final states be probed at the LHC, a few final states stand out as particularly complementary. These include the di-jet resonant search and resonant diphoton searches.

Given that there is roughly 20-30 years of development before the 100 TeV collisions, it is likely that some of the current detector complications will be resolved. In particular, the triggering of events is expected to improve with time. To illustrate the expected level of improvement, consider the current MET triggers at the LHC. They are currently able to trigger MET with a threshold above 200 GeV. It has been predicted that at high luminosity running, MET triggers will become ineffective due the large amount additional collisions (pileup) that degrade the overall event resolution. However, this prediction will very likely become invalid due to new developments in track triggering [304, 305] and advances in understanding the MET in dense environments [3]. In this respect, the current LHC benchmarks for future sensitivity are likely to be over conservative with respect to future developments.

### 3.2.5 Current DM Related Excesses

At the moment there are a few hints for new physics from astrophysics and collider experiments. First, the Fermi collaboration has confirmed an excess in gamma rays from the galactic center [306] which, as shown in several previous studies [307–310], can be consistent with DM annihilating in the galactic center. In particular WIMP DM annihilating to massive SM particles in the mass range between 35 GeV and 310 GeV can successfully fit the excess [311]. Since indirect observations of DM often remain inconclusive, a verification of the DM origin of this signal at a collider is desirable. The models discussed in [311] are similar to the benchmark models that are considered in the following sections, and the preferred mass range should be testable at a collider. Currently, strong evidence exists already that

the pseudoscalar interpretation is ruled out by the LHC [312]. Further interpretations are likely to be tested with a 100 TeV collider, if not already at the CERN-LHC.

Furthermore the LHC experiments have recently reported an excess of events in the diphoton channel near 750 GeV, consistent with a new resonance [313, 314]. The possibility that this resonance provides a window to DM was discussed for example in [315–322]. Within half a year from now the LHC should confirm or rule out the presence of this resonance, however it will be important to find out whether it will be sufficient to determine a connection to the dark sector, or whether a 100 TeV collider is necessary.

Other long standing, potentially DM related excesses are the cosmic positron excess [323, 324] and the annual modulation signal observed by the DAMA collaboration [325]. The former suffers from the usual problem that an astrophysical origin of the signal is difficult to exclude, while the latter has not been confirmed by any other DM direct detection experiment so far, and is more and more in tension with constraints from these direct searches.

### 3.3 WIMP Dark Matter, Standard Model Mediators

DM that interacts with known particles through Standard Model mediators is the simplest and most minimal implementation of the WIMP scenario. Since the DM candidate has to be neutral and uncoloured, the most compact models introduce a single multiplet of the electroweak  $SU(2) \times U(1)$  which should contain at least one neutral state. The smallest nontrivial, viable  $SU(2)$  representations are a doublet with hypercharge 1/2, a triplet and a fiveplet [326]. These models introduce only one new parameter, the mass of the multiplet, such that their parameter space can be fully explored, as discussed in Sections 3.3.1 - 3.3.3. Generically, for the correct abundance of thermal DM the mass of these WIMPs should be at the TeV scale [326].

In principle models with more than one multiplet are also conceivable and motivated as low energy limits of more complicated BSM scenarios like the MSSM. The simplest such model consists of a  $SU(2)$  singlet and a doublet [327–332], with other combinations also possible [333]. In Section 3.3.4 a model with a singlet, doublet and triplet is considered instead since this particle content is motivated by the chargino/neutralino sector of the MSSM.

Maybe the simplest model in terms of particle content is that of a scalar  $SU(2)$  singlet with a  $Z_2$  parity symmetry, which couples to the SM only through a renormalizable coupling with the Higgs boson. The prospects for probing this model at a 100 TeV collider are discussed in Section 3.3.5.

#### 3.3.1 Weak Gauge Bosons 1: Wino, Higgsino DM

The smallest multiplet is an  $SU(2)_L$  doublet (also called the higgsino in the context of supersymmetry). To have an electrically neutral state requires two doublets with hypercharges  $Y = \pm 1/2$ , thus we have two neutral Majorana states  $\chi_1^0, \chi_2^0$ , and one charged Dirac state  $\chi^\pm$ .<sup>9</sup> The various states are nearly mass degenerate with a small splitting arising from electroweak symmetry breaking effects. In the high mass limit the charged fermions are heavier by  $\Delta m \simeq 355$  MeV [334].

The neutral and charged states interact in pairs with the Standard Model via  $W$ 's and  $Z$ 's resulting in the interactions  $\chi_1^0 \chi_2^0 Z$ ,  $\chi_{1,2}^0 \chi^\pm W^\mp$ ,  $\chi^\pm \chi^\mp Z$ , and  $\chi^\pm \chi^\mp \gamma$ . At a hadron collider they are pair produced via Drell-Yan resulting in final states of pairs of invisible particles. Even when a charged  $\chi^\pm$  is produced the signal still looks like two invisible particles because the charged  $\chi^\pm$  decays via  $\chi^\pm \rightarrow \chi_1^0 + \pi^\pm$  and the  $\pi^\pm$  has momentum  $\sim \Delta m$  and is thus often undetectable.

At a hadron collider, one needs additional objects in the event other than missing energy. There are several possibilities: the initial state radiation of a jet (or a gauge boson), production in vector boson

<sup>9</sup>We assume the presence of additional operators to slightly split the neutral masses otherwise they would combine into a Dirac fermion which would be ruled out by direct detection.

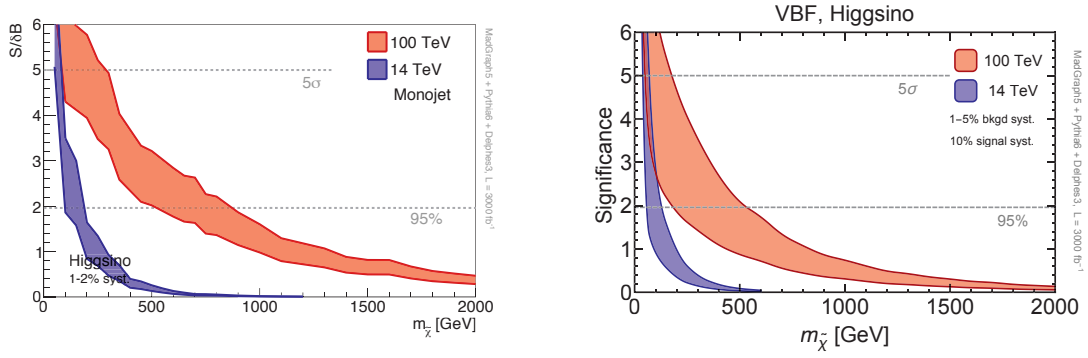


**Fig. 42:** Reach for higgsinos ( $SU(2)_L$  doublets) in the monojet channel (left) and in the vector boson fusion channel (right).

fusion, or tagging on the soft Standard Model objects in the final state. Requiring the initial state radiation of a hard jet is called the monojet channel and looks for a high  $p_T$  jet and large missing energy. This scenario was studied in [70] and found to have a mass reach from 550 GeV to 850 GeV depending on the level of systematic uncertainty assumed, as shown in Fig. 42 (left). Recasts of 8 TeV monojet searches have been performed and show that the mass reach at 8 TeV is less than 100 GeV [335]. In the vector boson fusion channel, one looks for two forward jets and missing energy. This process typically has a lower rate than the monojet channel but one may have smaller backgrounds so it is not obvious a priori how the reach will compare to monojet. This was studied in [76] and was found to have a mass reach of 150 GeV to 500 GeV, also shown in Fig. 42 (right).

The next case is an  $SU(2)_L$  triplet with  $Y = 0$  (also called the wino in the context of supersymmetry). Now there is one neutral state  $\chi^0$  and one charged state  $\chi^\pm$  with a mass splitting of  $\Delta m \simeq 166$  MeV [336]. Both the monojet search and vector boson fusion searches can be performed and the mass reach is 0.9 TeV to 1.4 TeV, shown in Fig. 43. Again, the monojet channel is more sensitive than vector boson fusion.

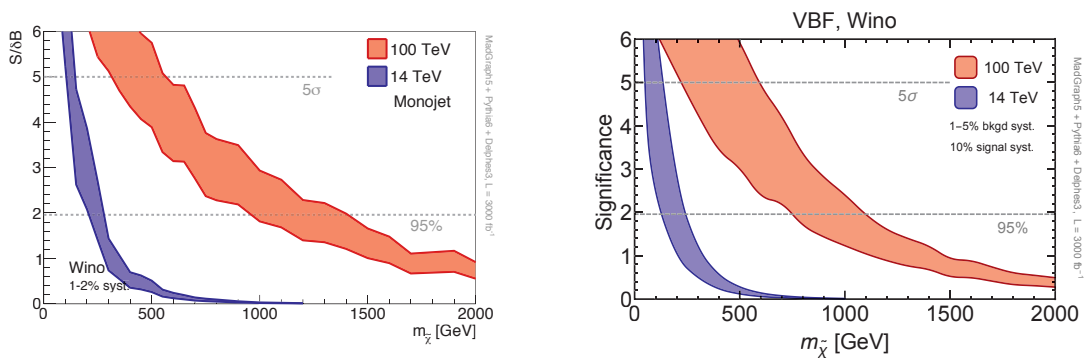


**Fig. 43:** Reach for winos ( $SU(2)_L$  doublets) in the monojet channel (left) and in the vector boson fusion channel (right).

An additional search that can be effectively utilized for the triplet case is the disappearing tracks search where one looks for a track from the charged state that suddenly disappears when it decays into the neutral state and a soft pion. The triplet mass splitting of 166 MeV results in a lifetime of the  $\chi^\pm$  of  $c\tau \sim 6$  cm which is long enough that some of the  $\chi^\pm$ 's will decay in the region where the detector is likely to have a tracker. There are no physics backgrounds to this search, but there are a number of backgrounds arising from detector effects. At the LHC, this is the most sensitive search for the pure wino

and already sets limits of 270 GeV with  $20 \text{ fb}^{-1}$  [337, 338]. One can extrapolate the LHC backgrounds to a 100 TeV collider, though it is important to keep in mind that the estimate is rough as the backgrounds could be much different at a future detector. The extrapolation was performed in [70] and found to have a reach of 2.9 TeV. This is shown in Fig. 44 (left) with bands varying the background normalization up and down by a factor of 5. See also [339] for similar studies on triplets. Due to the shorter lifetime, this is typically not a useful channel for the doublet unless there is UV physics that decreases the splitting between the charged and neutral states, as shown in Fig. 44 (right).

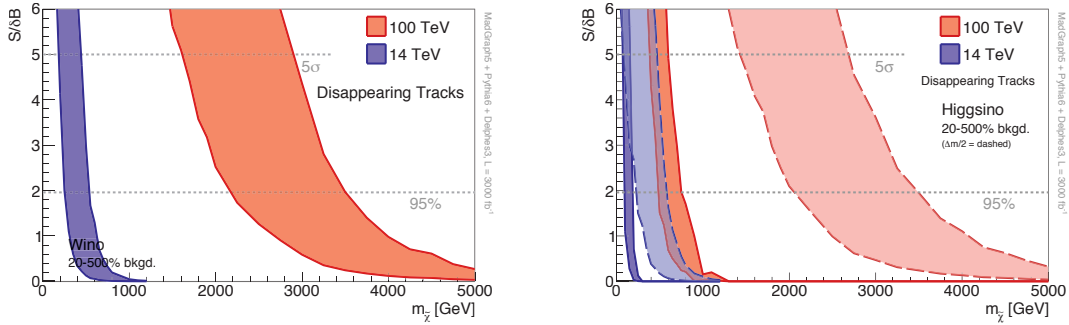


**Fig. 44:** Reach for winos ( $SU(2)_L$  triplets) in the disappearing tracks channel (left) and for higgsinos in the disappearing tracks channel (right).

For both the monojet and vector boson fusion searches the projections were also computed for the 14 TeV LHC and it was found that a 100 TeV collider improves by about a factor of 5 (using an integrated luminosity of  $3 \text{ ab}^{-1}$  at both 14 TeV and 100 TeV). Performing these searches at 100 TeV would not be qualitatively different than at the LHC. One search that offers the chance for a qualitative improvement is the disappearing tracks search, because this is very dependent on the yet-to-be-designed detector properties. Given the high sensitivity of this channel one can envisage designing the detector to optimize this channel. Concretely, current searches require a hard recoiling jet in disappearing track events to trigger on, but if one could trigger on the disappearing track itself, the rates would be increased. Additionally, maintaining a high efficiency to select disappearing tracks is crucial.

Note that the study has been performed for  $\sqrt{s} = 100 \text{ TeV}$ . To properly evaluate the mass reach at other collision energies would require dedicated studies, but simple estimates can be made. By comparing parton luminosities one can see that the mass reach is linear (in center of mass energy) when the luminosity increases quadratically. For a fixed luminosity, the mass reach increase is more mild and in some cases seen to be closer to 40% for a factor of 2 in energy [340].

For the pure states described here there is an interesting complementarity with both direct detection and indirect detection. Let us first consider the higgsino. In order to have the correct thermal relic abundance, the higgsino mass should be 1 TeV. In direct detection the rate vanishes at tree level because the coupling of neutralinos to Higgses arise from the mixing between higgsinos and binos or winos. At one loop the rate is still suppressed due to an accidental cancellation [341]. As shown above unless colliders can achieve systematic uncertainties below 1% one is unable to exclude (not even discover) higgsinos. For winos, 3 TeV is the mass to satisfy the thermal relic abundance. In direct detection the rates are again very small, but lie just above the neutrino coherent scattering rate, at  $\sim 1.3 \times 10^{-47} \text{ cm}^2$  [341], as discussed in more detail in the next section.

One can also consider DM state that are mixtures of binos, higgsinos, and winos. The collider signatures depend strongly on the mass difference between the lightest neutralino and the other states. For mass splittings of  $\sim 20 - 50 \text{ GeV}$ , the reach is studied in [70] while for mass splittings of  $\gtrsim 100 \text{ GeV}$  the reach is studied in [74]. This scenario is studied in more detail in Section 3.3.4. A summary of

the constraints on the pure, mixed and co-annihilating scenarios (c.f. Section 3.5.1) is given in Fig. 45.

These scenarios represent the worst possible cases in the sense that there are very few handles in the events. Future directions that deserve more careful study are considering other particles in the spectrum that could increase the electroweakino rate or yield jets or leptons in their decays providing increased discrimination power.

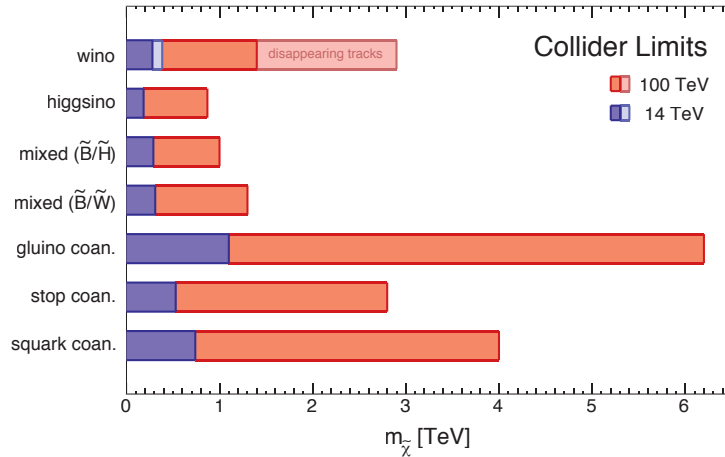


**Fig. 45:** Summary of reach for DM with SM mediators and through co-annihilation at 100 TeV.

### 3.3.2 Weak Gauge Bosons 2: Wino DM

As discussed above, an electroweak triplet with zero hypercharge is one of the most minimal DM models one can imagine [326, 342], and is further motivated in models of high-scale supersymmetry [22, 24, 25, 143, 343–346] and other new physics scenarios [25, 347–349].

We now summarise the status and prospects for the searches of an extra stable fermion triplet, focusing of course on the 100 TeV proton collider, but making explicit the comparison with other future colliders, as well as with direct and indirect DM detection experiments. Our discussion is based on Ref. [339] for the collider reaches, and it is updated with more recent results for DD [350], as well as with preliminary ones for ID [351].

**The model.** The Lagrangian for the minimal Wino DM model reads

$$\mathcal{L} = \mathcal{L}_{\text{SM}} + \frac{1}{2} \bar{\chi} (i \not{D} - M_{\chi}) \chi, \quad (38)$$

so that the only new parameter of this model is the  $\chi$  mass  $M_{\chi}$ . If one demands  $\chi$  to constitute 100% of the DM via thermal freeze out, then also  $M_{\chi}$  is fixed, to roughly 3 TeV [352]. We will also consider different values of  $M_{\chi}$ , to allow for different production mechanisms and for the possibility that  $\chi$  does not constitute 100% of the observed DM.

While at tree level the neutral and charged components of the triplet have the same mass, higher order corrections split the neutral Majorana fermion  $\chi_0$  from the charged  $\chi^{\pm}$ . This mass splitting has been computed at the two-loop level in the SM [336], yielding to  $M_{\chi^{\pm}} - M_{\chi_0} \simeq 165$  MeV (stable to the level of 1 MeV for  $M_{\chi} \gtrsim 1$  TeV)<sup>10</sup>.

The direct pair production of DM particles receive contribution, in this model, not only from production of  $\chi_0$ , but also from that of  $\chi^{\pm}$ . In fact, the small mass splitting causes  $\chi^{\pm}$  to decay into

<sup>10</sup>Possible heavy New Physics contributions to  $M_{\chi^{\pm}} - M_{\chi_0}$  are very suppressed, since the first effective operator contributing to a splitting arises at dimension 7.

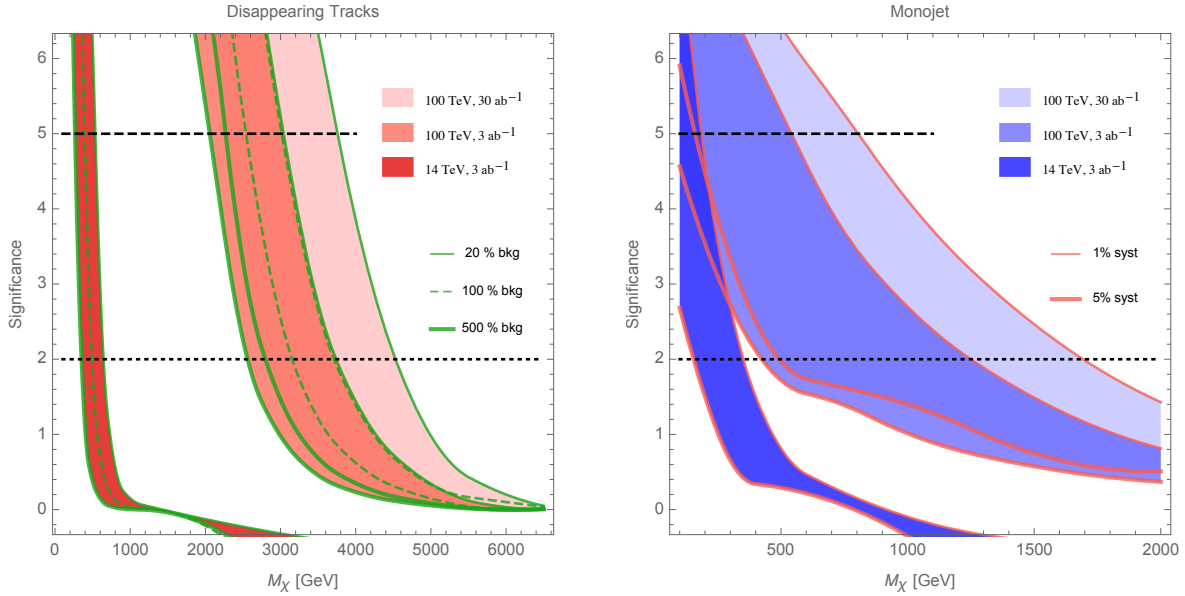


**Fig. 46:** Reach of disappearing tracks (left) and monojet (right) searches [339].

$\chi_0$  plus very soft pions, which are not reconstructed at the LHC, with a decay length at rest of  $\sim 6$  cm. Since current detectors do not reconstruct tracks shorter than  $O(30)$  cm, the bulk of the produced  $\chi^\pm$  contributes to missing transverse energy in the same way of  $\chi_0$ . Still, a fraction of the  $\chi^\pm$  can travel far enough to leave a track in the detector, and then decay to  $\chi_0$  plus soft pions within it, thus yielding a *disappearing track* signal that has no background within the SM [353].

The current best probe of this model at colliders is indeed given by the ATLAS [337] and CMS [338] searches for disappearing tracks, which obtained the bound

$$M_\chi > (260 - 270) \text{ GeV}. \quad (39)$$

In Ref. [339], the reach of the ATLAS search for disappearing tracks is extrapolated to the HL-LHC, as well as to the 100 TeV proton collider, for both 3 and  $30 \text{ ab}^{-1}$  of integrated luminosity (see also Ref. [70]). The result of this procedure is shown in the left-hand plot of Fig. 46. The background to this search comes from detector effects, and the red bands in the reach, for any given future benchmark, correspond to a conservative quantification of the uncertainty coming from our extrapolation. In the right-hand plot we show, for comparison, the expected reach in the “standard” monojet channel. Here the blue bands represent how the reach is expected to change according to the control that will be achieved over the systematics. The reach of other channels like vector boson fusion [76, 339] and monophoton [339] is somehow weaker, but it will provide a useful complementarity. Both for disappearing tracks and for the monojet searches we find a very good agreement with the results of Ref. [70], and we refer the reader to Ref. [339] for more details.

While the region interesting for thermal WIMP DM is out of reach at any conceived future LHC stage, the 100 TeV collider has largely the potential to probe it, and say a final word over the existence of a pure-Wino (independently of DM). The only channel with the potential to discover thermal DM Winos is that of disappearing tracks, and it would benefit, at any future collider, from the capability of reconstructing tracks below the current length of  $O(30)$  cm.

**Relation with future lepton colliders.** Given that  $\chi$  is a full EW multiplet, its contributions to EWPT are very suppressed, at the level of  $W, Y \sim 10^{-7}$  [326]: this sensitivity target is not touched by LEP2 [354], and looks out of reach at any proposed future lepton collider (see Ref. [355] for the expected reaches of high energy positron collider and CPEC).

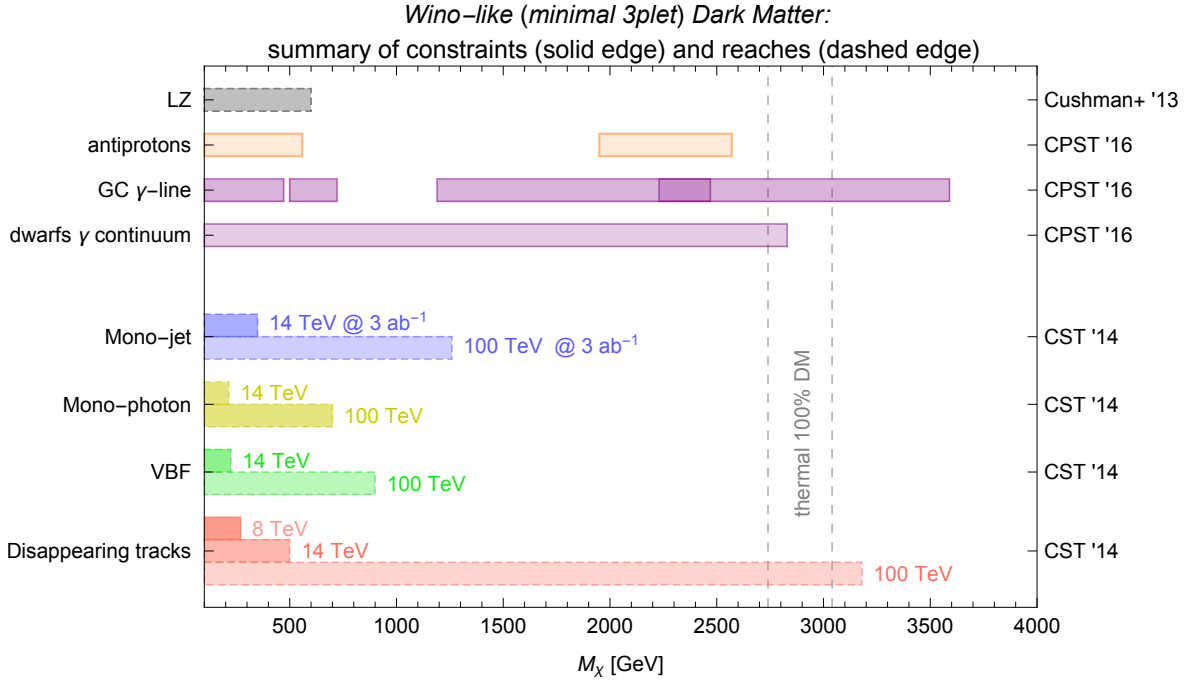


**Fig. 47:** For the GC gamma ray line search of HESS [294], the lighter shading is the exclusion assuming a NFW profile, the darker one assuming a Burkert profile. The FERMI bound from a gamma continuum from dwarf spheroidal galaxies [356] also suffer from some astrophysical uncertainties [357], so the lighter shading.

**Direct and Indirect DM detection.** The most recent cross section computation for the spin independent scattering of an EW fermion triplet with a nucleon gives [350]  $\sigma_{SI} = (2.3 \pm 0.5) \times 10^{-47} \text{ cm}^2$ . This value is out of reach at any current and planned experiment [284], for masses larger than 500 GeV.

Concerning indirect detection, gamma rays from the Galactic Center (as first recognized in [153, 154] for lines) and dwarf spheroidal galaxies are, at present, the most promising probes. We show the reach of two most relevant searches of this kind in Fig. 47, also to compare them with the previously discussed collider and DD reaches. We show there also the weaker reach of antiprotons from AMS-02 [351], for comparison. As far as we know today, a very promising (gamma-ray) telescope to probe this model in the future appears to be CTA, expected to start taking data in 2018 [358]. Whether it will exclude or not a pure-Wino, as 100% of the DM, depends mostly on the control on the astrophysical uncertainties that will be achieved by then.

### 3.3.3 Weak Gauge Bosons 3: Fiveplet DM

While the doublet and triplet DM models discussed so far can decay to the SM through dimension 5 operators, a fiveplet of  $SU(2)$  can only decay through a dimension 6 operator, thus guaranteeing a sufficiently long lifetime of the DM even if the global  $Z_2$  symmetry which makes it stable is broken at the Planck scale.

We define the fiveplet,  $\chi$  as  $\chi = (\chi^{++}, \chi^+, \chi^0, \chi^-, \chi^{--})$ . At the renormalizable level, the size of the representation restricts the Lagrangian to

$$\mathcal{L} = \mathcal{L}_{SM} + c\bar{\chi}(i\not{D} - M)\chi, \quad (40)$$

where  $M$  is the mass of the fiveplet and the constant,  $c$ , is 1/2 or 1 depending on whether  $\chi^0$  is Majorana or Dirac, respectively. The mass degeneracy of the multiplet is broken at one loop by the gauge bosons. For masses of the multiplet  $M \gg m_W$  the singly charged component lies  $\sim 166 \text{ MeV}$  above the neutral component; the doubly charged state is heavier than the neutral state by  $\sim 664 \text{ MeV}$ . These small mass

splittings between the states of the multiplet leave little phase space for decays down to the neutral component. This implies that the charged states can have fairly long lifetimes and travel macroscopic distances at collider experiments. This will be the basis of our search strategy.

As providing a DM candidate is the motivation for this model, we want the neutral component to make up a significant portion of the observed abundance. The large quantum number of the fiveplet, along with the large number of states, allows for very efficient annihilations. This implies that in order to quench the observed relic abundance of DM through thermal freeze-out, the mass of the fiveplet must be heavy; nearly 9.6 TeV if the Sommerfeld enhancement is included [152, 342]. If the mass of the fiveplet is less than 9.6 TeV, the amount of DM left after freeze-out is less than the observed abundance, which leaves room for other sources of DM. There are also other mechanism that would allow for a lighter fiveplet to fulfill the relic abundance [359–362], such that we can treat the mass of the fiveplet as a free parameter with an upper bound of 9.6 TeV.

Direct detection and indirect detection searches are able to constrain the model. A recent reevaluation of the nuclear matrix element was found to be lower than originally thought, leading to a spin independent cross section of  $1.0 \times 10^{-46} \text{ cm}^2$  [349, 363]. In this case, Xenon1T and LZ are projected to have a reach to  $\sim 350 \text{ GeV}$  and  $\sim 4000 \text{ GeV}$ , respectively [284]. Signals (or lack there of) of DM annihilations place the strongest bounds on the model. The Sommerfeld enhancement has a very large effect for the fiveplet and increases the cross section for annihilations into vector bosons [342, 362, 364–367]. With the non-observation of sharp gamma ray spectral features by H.E.S.S., a fermionic fiveplet can only make up all of the DM abundance for a small range of masses around 2.5 TeV and 10 TeV, or be completely excluded, depending on the DM profile [294]. CTA will be able to exclude almost the entire mass range, even for an isothermal profile [358, 366, 367].

The projected direct detection results depend on the DM abundance while indirect detection signals depends on both the abundance and the profile. However, collider bounds do not depend on astrophysical results. To this end, it is important study how the MDM fiveplet can be bounded by collider experiments. In Ref. [368], the disappearing track searches done by ATLAS and CMS [337, 338] are used to show the LHC has excluded a fiveplet below a mass of 267 (293) GeV depending on whether it is Majorana (Dirac). Additionally, it was determined a Majorana (Dirac) fiveplet could be excluded at the 14 TeV LHC up to a mass of 410-670 GeV (465-745 GeV). In the following we review the disappearing track search strategy and extend the method to a 100 TeV collider for the MDM fiveplet.

There have been a few other studies which extrapolate the ATLAS search [337] to future colliders [70, 339, 368, 369]. The optimised cuts presented in [339] are used, which look for

$$\begin{aligned}
 p_{T,j_1} > 1 \text{ TeV}, \quad \cancel{E}_T > 1.4 \text{ TeV}, \quad \Delta\phi_{j,\cancel{E}_T}^{\min} > 1.5, \\
 p_{T,\text{track}} > 2.1 \text{ TeV}, \quad 0.1 < |\eta_{\text{track}}| < 1.9, \quad \text{and} \\
 30 \text{ cm} < \text{transverse track length} < 80 \text{ cm}.
 \end{aligned}
 \tag{41}$$

The variable  $\Delta\phi_{j,\cancel{E}_T}^{\min}$  is the azimuthal angle between the any jet with  $p_T > 500 \text{ GeV}$  and the missing energy. The requirements on the transverse track length and  $\eta_{\text{track}}$  come from the ATLAS search and are used in the future collider extensions as a method to estimate the background. There is no obvious Standard Model process which mimics this signal; the background comes from  $p_T$ -mis-measured tracks and hadrons with large momentum transfer interactions with pieces of the detector. The measured signal and background thus depend heavily on the specifics of the detector. In their search, ATLAS gives the observed shape of the  $p_T$ -mis-measured tracks as  $d\sigma/dp_T^{\text{track}} = (p_T^{\text{track}})^{-a}$  where  $a = 1.78 \pm 0.05$ . This shape is normalized to the background at  $\sqrt{s} = 8 \text{ TeV}$  reported in [337] and then scaled to the ratio of the  $Z(\nu\bar{\nu}) + \text{jets}$  cross section passing initial cuts on  $p_{T,j_1}$ ,  $\cancel{E}_T$ , and  $\Delta\phi_{j,\cancel{E}_T}^{\min}$  at  $\sqrt{s} = 8$  and 100 TeV. There is much inherent uncertainty in this method of extrapolating the background. Measuring the spectrum of the  $p_T$ -mis-measured tracks at the current run of the LHC could help in this regard. To be conservative, we allow for a range of the background cross section, larger or smaller by a factor of 5.

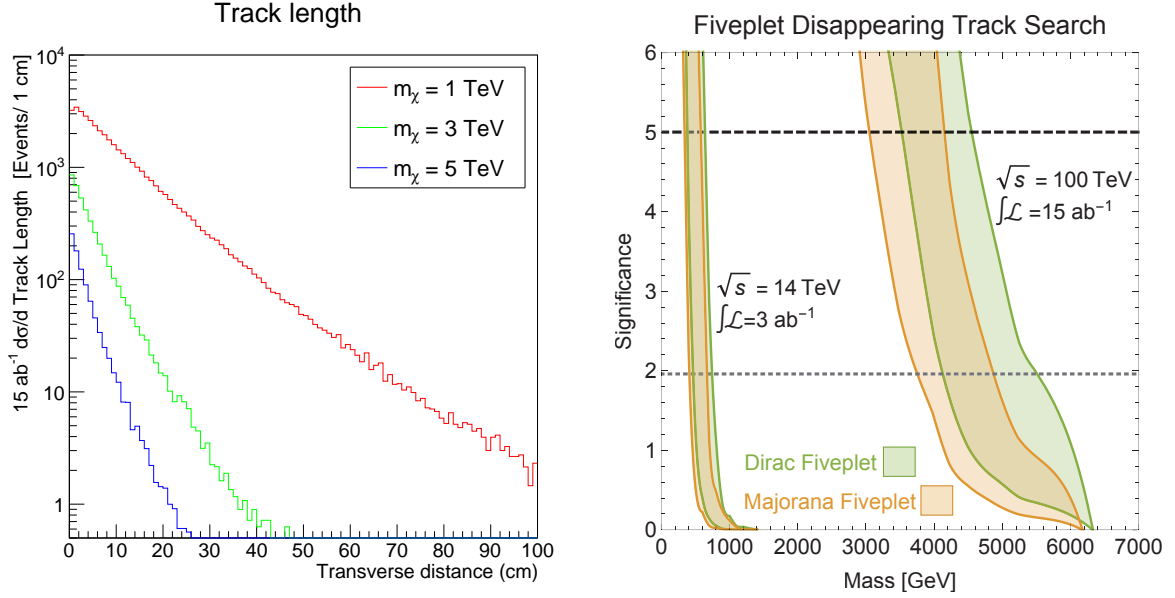


**Fig. 48:** Left: The number of events passing the cuts in Eq. (41) as a function of transverse track length. The different colors are for different masses of a Majorana Fiveplet. The larger masses have lower production cross section and do not receive as large of a boost from the jet, so do not travel as far. The expected background for track lengths between 30 and 80 cm is around 2 events. Right: Reach for the  $\sqrt{s} = 14$  TeV LHC and a future  $\sqrt{s} = 100$  TeV collider. The bands are generated by varying the background between 20% and 500% of the extrapolated value.

The model is implemented using FEYNRULES2.0 [370], and generated events using MADGRAPH5\_AMC@NLO [94] for  $\chi\bar{\chi}$  production with up to two extra partons. The events were matched with the MLM scheme, hadronized, and showered using PYTHIA 6.4 [112], and fast detector simulation was done with DELPHES [113] using FASTJET [263, 264] to cluster the jets with the anti- $k_T$  algorithm [115]. The default ATLAS card was used for DELPHES, modified so the neutral component of  $\chi$  would add to the missing energy. See Refs. [368] and [369] for more details about the analysis.

Our results are summarized in Fig. 48 assuming  $15 \text{ ab}^{-1}$  of integrated luminosity. The left panel shows the expected number of events passing the cuts as a function of the transverse distance travelled by the track. This shows that the heavier mass points are harder to find not just because the production cross section decreases, but also because the tracks do not travel as far. For a given jet momentum that the  $\chi\bar{\chi}$  system recoils off, the heavier DM points do not get as much of a boost. In order to travel between 30 and 80 cm (with a decay length of a few cm) the system needs to be quite boosted.

In the right panel, we plot the significance as a function of the fiveplet mass. This is computed using

$$\text{Significance} = \frac{S}{\sqrt{B + \alpha^2 B^2 + \beta^2 S^2}} \quad (42)$$

where  $S$  and  $B$  are the number of signal and background events. The background and signal systematics are incorporated into  $\alpha$  and  $\beta$  and are conservatively given values of  $\alpha = 20\%$  and  $\beta = 10\%$  [70, 339]. The bands in the plot are generated by varying the number of background events between 20% and 500% of the  $\sim 2$  events expected from the extrapolation.

A 100 TeV collider can greatly extend the search for minimal DM. The discovery reach of the Majorana fiveplet is between 3.1–4.2 TeV while the exclusion reach is 3.8–4.9 TeV. For the case of the Dirac fiveplet, the discovery and exclusion reaches are 3.5–4.5 TeV and 4.1–5.5 TeV. These results are

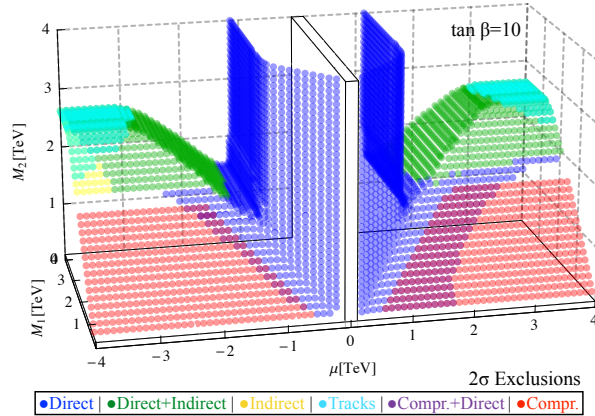


**Fig. 49:** Relic neutralino surface defined by a thermal primordial freeze-out to abundance  $\Omega h^2 \simeq 0.12$ , with all non-neutralino superpartners decoupled, and including Sommerfeld-enhancements to freeze-out annihilation cross-sections. Regions inside the central boxes are excluded by LEP II [372]. We also show future direct detection and indirect detection prospects. The compressed and charged track collider studies referred to as “Compr.” and “Tracks” are described in the text [369, 371].

about a factor of 7 higher than the estimated reach at the LHC. These mass reaches are important in terms of complementarity with the other DM experiments. Depending on the DM profile, there is a possible gap in coverage in the indirect detection experiments for a fiveplet mass of  $\sim 2.5$  TeV, which will be covered by a 100 TeV collider. In addition, the projected LZ results could reach a fiveplet with a mass up to 4 TeV. With a possible higher mass reach than this, the 100 TeV collider can exceed direct detection results without the question of the current relic abundance.

### 3.3.4 Weak Gauge Bosons 4: Thermal Relic Neutralino DM

Weakly interacting DM are one of the few physics scenarios which can feature an *upper* limit on the particle masses. This argument is based mostly on a combination of the experimentally observed relic density constraint and on the fact that the DM states interact weakly. In that spirit, the neutralino/chargino sector of the MSSM is a way to interpolate between singlet, doublet, and triplet  $SU(2)$  representations of the DM state. The question is to what degree a 100 TeV proton-proton collider, together with future direct and indirect detection experiments, can cover the relic neutralino surface with all scalar superpartners, *i.e.* squarks, sleptons, and the heavy Higgs boson decoupled to masses above 8 TeV. The main challenge to collider searches are nearly mass degenerate ( $\lesssim 5\%$  mass difference) states in the neutralino/chargino sector which lead us to a dedicated analysis with very soft leptons and photons combined with extremely hard initial state radiation jets at a 100 TeV hadron collider.

In Refs. [369, 371] it is for example demonstrated how nearly pure bino DM, which freezes out to the observed relic abundance through co-annihilation, can be uncovered by a 100 TeV hadron collider. Figure 49 shows the main collider-related result: for almost pure wino DM as well as for bino-like co-annihilating DM with small couplings to the Standard Model, a future 100 TeV hadron collider allows for full coverage of the relic neutralino surface.

To define the relic neutralino surface the thermal relic abundances were calculated using DarkSE [373], which incorporates Sommerfeld-enhancements to the relic abundance code of DarkSUSY [374]. In addition, the annihilation cross-section to nearly-pure wino freeze-out were checked with MicrOMEGAs [375], modified to include Sommerfeld enhancement. MSSM mass spectra were generated with SuSpect [376], where loop corrections from decoupled SUSY particles were turned off, but electroweakino charged-neutral electroweak custodial mass splittings were set before matrix diagonalization, as described in Ref. [369].

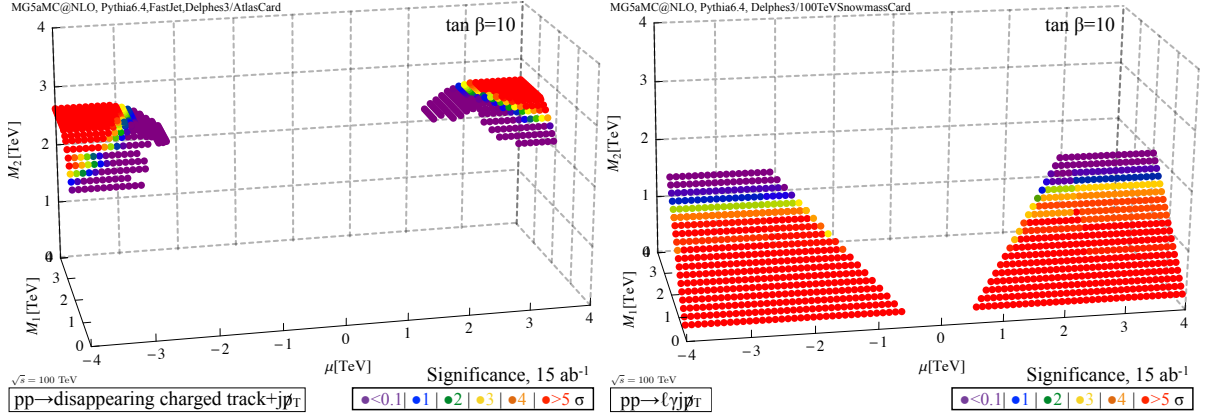


**Fig. 50:** The significance reach over thermal relic neutralino parameter space is shown, for both charged tracks and compressed ( $\gamma + \ell + j + \text{MET}$ ) searches at a 100 TeV collider, after  $15 \text{ ab}^{-1}$  of data. In the case of compressed searches, a larger parameter space can be probed than what is shown above (see [371]).

In Fig. 49 we show the parameter space probed at a 100 TeV hadron collider, alongside the  $2\sigma$  relic neutralino reach of future direct and indirect detection experiments. On the collider side, it first includes a study of sensitivity to disappearing charged tracks for thermal relic neutralinos. In SUSY parameter space with a predominantly wino LSP, the mass splitting between the LSP and lightest chargino becomes as small as 160 MeV. With such a small inter-state mass splitting, decays of the chargino to LSP through an off-shell  $W$  boson are suppressed and can leave  $\mathcal{O}(10 \text{ mm})$  long charged tracks in the detector that vanish to missing transverse energy (MET). To estimate the background to a disappearing charged track search, Ref. [369] matched the data-driven background of an ATLAS charged tracks study [337], by simulating  $pp \rightarrow Z(\nu\bar{\nu}) + \text{jets}$  events at center-of-mass energies 8 TeV and 100 TeV. The ratio of these events passing kinematic cuts on missing transverse momentum and jet momentum were used along with the number of background events found by ATLAS, to project the number of background events at a 100 TeV collider. Signal events featuring at least one chargino paired with a partner electroweakino and jets, were simulated using MG5aMC@NLO [94] with MLM matching [377], combined with Pythia6.4 [112] and DELPHES3 [113]. A dedicated set of cuts makes use of the strengths of a 100 TeV hadron collider with excellent detector performance [369]:

1. at least two jets with  $|\eta| < 2.5$  and  $p_T$  greater than 1 TeV and 0.5 TeV, respectively;
2. at least one disappearing track with  $p_T > 2.1 \text{ TeV}$ ,  $0.1 < |\eta| < 1.9$ , and length 30-80 cm;
3. MET in excess of 1.4 TeV.

The significance shown in Fig. 50 after  $15 \text{ ab}^{-1}$  is based on the estimate  $S/\sqrt{B + \alpha^2 B^2 + \beta^2 S^2}$  with  $\alpha = 2$  and  $\beta = 0.1$  setting the signal and background uncertainty. We see that the charged track search indeed covers the wino LSP region of the relic neutralino surface.

A second parameter region which needs to be targeted by a 100 TeV collider is nearly pure gauge singlet DM, which freezes out to the observed relic abundance by co-annihilating with a heavier partner. Such a nearly-pure bino LSP arises in relic neutralino parameter space where  $M_2 < 2 \text{ TeV}$  and  $\mu > 1 \text{ TeV}$  [369, 371]. Compressed electroweakino searches target the production of electroweakinos 5 – 50 GeV heavier than lighter electroweakino states. As the heavier electroweakinos decay to the LSP, they emit soft state leptons and photons with  $p_T \sim 5 - 50 \text{ GeV}$ . Such soft leptons and photons as part of the collider signature allow for a smaller MET cut than traditional “jet + MET” DM searches, boosting the mass reach of compressed DM searches [70, 74, 335, 371, 378–388]. In Ref. [369], signal events of the type  $pp \rightarrow \chi^\pm \chi^0 + \text{jets}$  were simulated along with the dominant background  $pp \rightarrow \gamma W^\pm + \text{jets}$ . The cuts applied in this study, which employed MG5aMC@NLO, Pythia6.4, and DELPHES3, with the default-valued

Snowmass future detector card [114] were:

1. exactly one photon and exactly one lepton with  $p_T = [10 - 60]$  GeV and  $|\eta| < 2.5$ , separated by  $\Delta R > 0.5$ , and a photon-lepton MT2 [369] of  $M_{T2}^{(\gamma,\ell)} < 10$  GeV;
2. at least one jet, with  $|\eta| < 2.5$  and  $p_T > 0.8$  TeV, but no more than 2 jets with  $p_T > 0.3$  TeV;
3. MET in excess of 1.2 TeV.

A 10-50 GeV size mass splitting between the LSP and NLSP guarantees that leptons and photons emitted in NLSP to LSP decays will be soft. This should be contrasted with the expected transverse momentum of leptons and photons coming from SM  $pp \rightarrow \gamma W^\pm j$  events, which is the dominant background at a 100 TeV collider. The requirement that the  $W$  boson produce  $\sim$  TeV of MET suppresses low- $p_T$  phase space for the accompanying lepton. For similar reasons, because background events are boosted, emitted photons will also tend to have high  $p_T$ . Thus the increased energy of the 100 TeV environment makes this search particularly incisive.

The significance found in this study is shown in Fig. 50, where the background and signal systematic uncertainties were taken to be  $\alpha = \beta = 0.05$ . Its mass reach extends to nearly  $m_\chi \sim 2$  TeV, as shown in Fig. 50, exactly complementing indirect and direct searches. This complementarity is a consequence of the MSSM thermal relic DM LSPs flipping from being nearly pure bino to nearly pure wino around  $M_2 \approx 2$  TeV. For  $M_2 \lesssim 2$  TeV, the NLSP wino is inaccessible by direct and indirect searches, but would be produced at a 100 TeV collider.

To illustrate the complementarity of 100 TeV collider searches and direct as well as indirect detection experiments we illustrate the parameter space excludable by future liquid xenon direct detection searches, and by the Cerenkov Telescope Array's search for gamma ray lines emitted from the central kiloparsecs of the Milky Way galaxy [389] in Fig. 51. We also show present bounds from LUX [390], XENON100 [289], and HESS [294]. Future direct detection constraints were set using MicrOMEGAs output along with the Xenon direct detection reach projected for the next decade [284]. Constraints from indirect detection of DM annihilation in the galactic center were determined with MicrOMEGAs and the one-loop, Sommerfeld-enhanced annihilation rates of Ref. [373]. The projected indirect reach is calculated using the sensitivity forecasted in [389], assuming a standard Einasto DM density profile in the Milky Way.

The picture in all three fields of DM searches turns out to be similar: current experiments, including the LHC, are able to significantly cut into the relic neutralino surface. However, a full coverage of the surface, along with a comprehensive test of weakly interacting DM, is only guaranteed by the next generation of experiments: a 100 TeV hadron collider combined with  $n$ -ton xenon detectors and CTA. This complementarity, which requires two dedicated collider search strategies, is the central message of Fig. 49.

### 3.3.5 Higgs Portal

The Higgs boson provides a unique low-dimension portal between the Standard Model and a dark sector via interactions of the form  $|H|^2 \mathcal{O}$ , where  $\mathcal{O}$  is a gauge-invariant operator with  $\Delta_{\mathcal{O}} \lesssim 2$ . The classic example is  $\mathcal{O} = \phi^2$  where  $\phi$  is neutral under the SM but enjoys a  $Z_2$  symmetry [391–395]. Here we will consider such a scalar Higgs Portal with interactions

$$\mathcal{L} = \mathcal{L}_{SM} - \frac{1}{2} \partial_\mu \phi \partial^\mu \phi - \frac{1}{2} M^2 \phi^2 - c_\phi |H|^2 \phi^2 \quad (43)$$

where  $H$  is the SM-like Higgs doublet and  $\phi$  is a scalar neutral under the Standard Model. After electroweak symmetry breaking the theory consists of

$$\mathcal{L} = \mathcal{L}_{SM} - \frac{1}{2} \partial_\mu \phi \partial^\mu \phi - \frac{1}{2} m_\phi^2 \phi^2 - c_\phi v h \phi^2 - \frac{1}{2} c_\phi h^2 \phi^2 \quad (44)$$

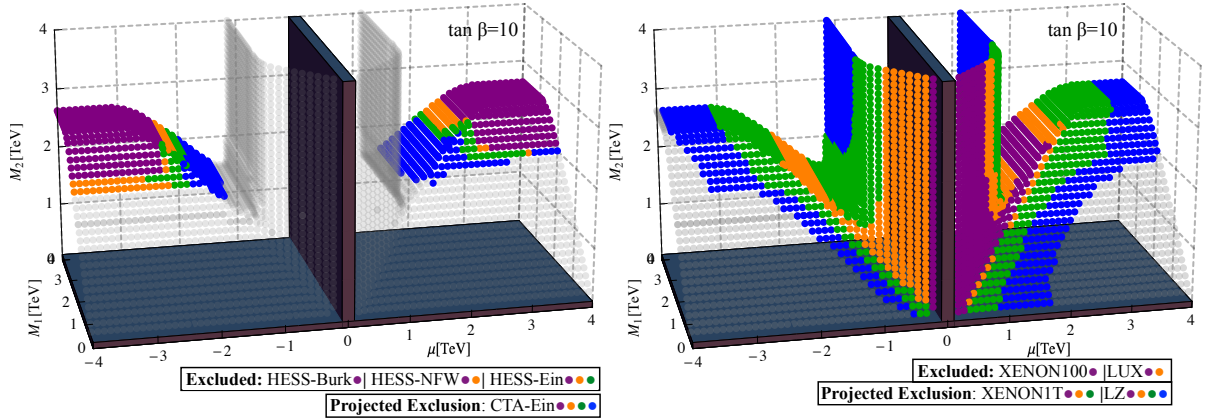


**Fig. 51:** Present indirect and direct detection limits on thermal relic neutralinos are shown, along with future constraints. Codes and calculations employed in the production of this plot are described in the caption of Fig. 49.

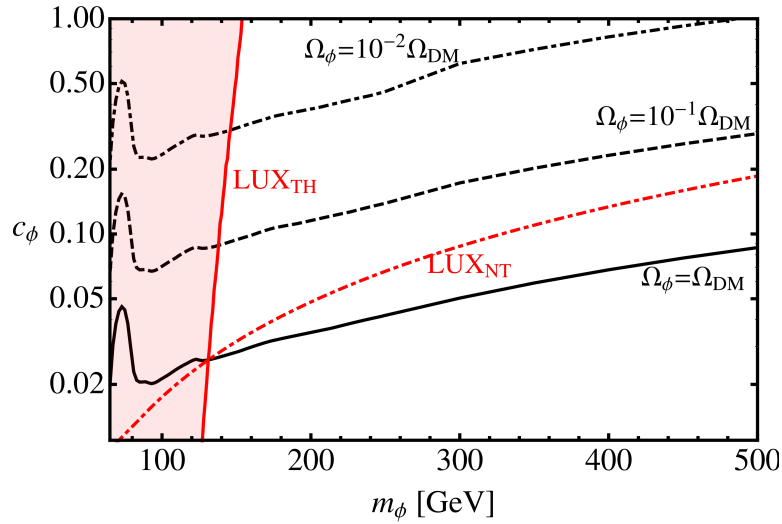


**Fig. 52:** Contours of relic DM density from freeze-out through the Higgs Portal. Constraints on the parameter space from the LUX direct detection experiment [390] are shown in dotted-dashed red ( $LUX_{NT}$ ) where we assume non-thermal processes give the observed DM relic abundance in regions where thermal freeze-out over- or under-produces DM. The solid red line ( $LUX_{TH}$ ) and shaded region show the parameter space excluded given a standard thermal history, where  $\phi$  may comprise only a fraction of DM.

where  $m_\phi^2 = M^2 + c_\phi v^2$  in units where  $v = 246$  GeV.

This portal interaction respects an unbroken  $Z_2$  symmetry  $\phi \rightarrow -\phi$ . If the  $Z_2$  symmetry is exact the Higgs Portal furnishes a DM candidate [391–394, 396]. Higgs Portal DM is highly predictive in the sense that the coupling  $c_\phi$  is determined as a function of  $m_\phi$  if  $\phi$  is required to provide the entirety of the observed DM abundance, as illustrated in Fig. 52. While thermal abundance corresponds to small values of  $c_\phi$ , larger values are allowed if  $\phi$  only accounts for some fraction of the DM or is produced non-thermally in the early Universe.

Although it only communicates with the SM via the Higgs sector, current direct detection experiments are already sensitive to Higgs Portal DM. Current bounds on  $c_\phi$  from the LUX experiment [390] are shown in Fig. 52, both in the case that  $\phi$  comprises the entirety of the observed DM abundance (assuming late-time dilution or production in regions of parameter space where thermal freeze-out over- or under-produces DM) and in the case where  $\phi$  simply has a thermal abundance (in which case it typically

comprises only a fraction of the observed DM abundance). Significantly, when Higgs Portal DM has a thermal history, predicted direct detection rates are almost independent of the Higgs Portal coupling, and the predicted rate largely becomes a function of the mass alone. This raises the prospect of strong complementarity between direct detection and collider probes of Higgs Portal DM, where rates for  $\phi$  production scale with positive powers of  $c_\phi$ .

When  $m_\phi < m_h/2$  this scenario may be very efficiently probed at colliders via the Higgs invisible width [397–405], since the Higgs can decay on-shell into  $\phi\phi$  and the smallness of the SM Higgs width ensures the rate for  $pp \rightarrow h + X \rightarrow \phi\phi + X$  is large for a wide range of  $c_\phi$ . When  $m_\phi > m_h/2$ , however, the Higgs cannot decay on-shell to  $\phi\phi$ , and  $\phi$  pair production instead proceeds through an off-shell Higgs,  $pp \rightarrow h^* + X \rightarrow \phi\phi + X$ . The cross section for this process is then suppressed by an additional factor of  $|c_\phi|^2$  as well as two-body phase space. In this regime,  $pp$  colliders such as the LHC and a 100 TeV proton collider can provide the best means of probing Higgs Portal DM.

With this in mind we assess the reach of  $pp$  colliders at  $\sqrt{s} = 14$  & 100 TeV, with an eye towards constraining the region  $m_\phi > m_h/2$  where hadron machines provides sensitivity complementary to electron-positron colliders and direct detection experiments. We implement the Higgs Portal in FeynRules with  $m_h = 125$  GeV, generating signal and background events at leading order using MadGraph5 v1.5.8 [111], showering with Pythia 8.186 [406] tune 4C, and simulating detector effects in Delphes v3.1.2 with the default CMS detector card (for 14 TeV) and the Snowmass detector card [114] (for 100 TeV). We consider various channels, including vector boson fusion, gluon fusion with an associated jet, and  $t\bar{t}$  associated production. In the case of gluon fusion with an associated jet, events generated with MadGraph are re-weighted to more accurately reflect the  $p_T$  spectrum of the associated jet.

The pre-selection and analysis cuts used in these channels are detailed in [407]. A simple cut-and-count analysis is performed, determining the exclusion significance of a search in terms of signal events  $S$  and background events  $B$  passing cuts via  $S/\sqrt{S+B}$ , and the discovery significance via  $S/\sqrt{S}$ . For  $\sqrt{s} = 14$  TeV an integrated luminosity of  $3 \text{ ab}^{-1}$  is assumed, while for  $\sqrt{s} = 100$  TeV scenarios with  $3 \text{ ab}^{-1}$  and  $30 \text{ ab}^{-1}$  are considered, respectively. Systematic uncertainties in the signal and background estimates are neglected; systematic uncertainties in background determination could have a substantial impact at  $\sqrt{s} = 100$  TeV since  $S/B$  is quite small, but one expects data-driven determination of  $Z$ +jets and other backgrounds to substantially lower systematic uncertainties by the 100 TeV era.

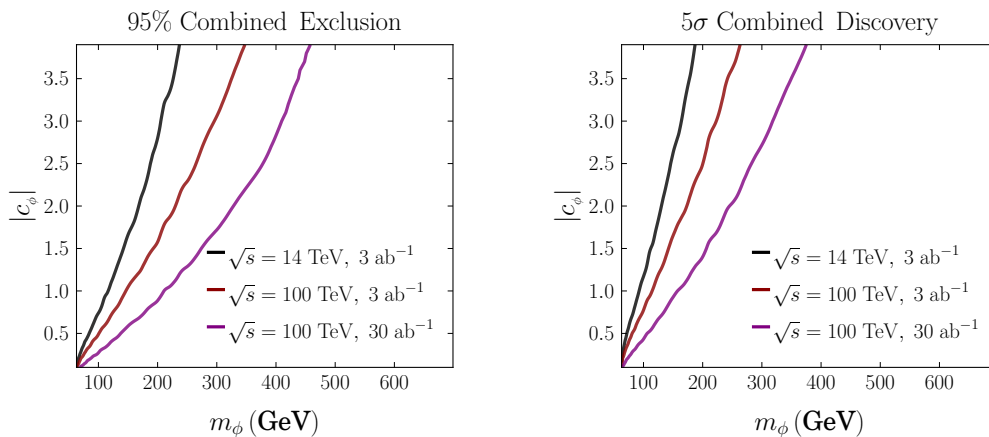


**Fig. 53:** Left: Approximate 95% exclusion reach from the combination of VBF,  $ggH$  and  $t\bar{t}H$  channels with  $3 \text{ ab}^{-1}$  at  $\sqrt{s} = 14$  and  $3, 30 \text{ ab}^{-1}$  at  $\sqrt{s} = 100$  TeV determined from  $S/\sqrt{B} = 1.96$ , neglecting systematic errors and correlations between channels. Right: Approximate  $5\sigma$  discovery reach from the same combination at  $\sqrt{s} = 14, 100$  TeV.

To estimate the reach of a concerted Higgs Portal search program, we present the approximate combined reach of VBF, monojet, and  $t\bar{t}$  searches at  $\sqrt{s} = 14$  and 100 TeV in Fig. 53. We obtain the combination by adding the significance of the VBF, monojet, and  $t\bar{t}$  channels in quadrature, neglecting possible correlations between the two channels. As the cross section is suppressed at high center-of-mass energies by the off-shell Higgs propagator, the improvement in limits between  $\sqrt{s} = 14$  TeV and 100 TeV at comparable integrated luminosity is due in part to improved separation of signal from Standard Model backgrounds.

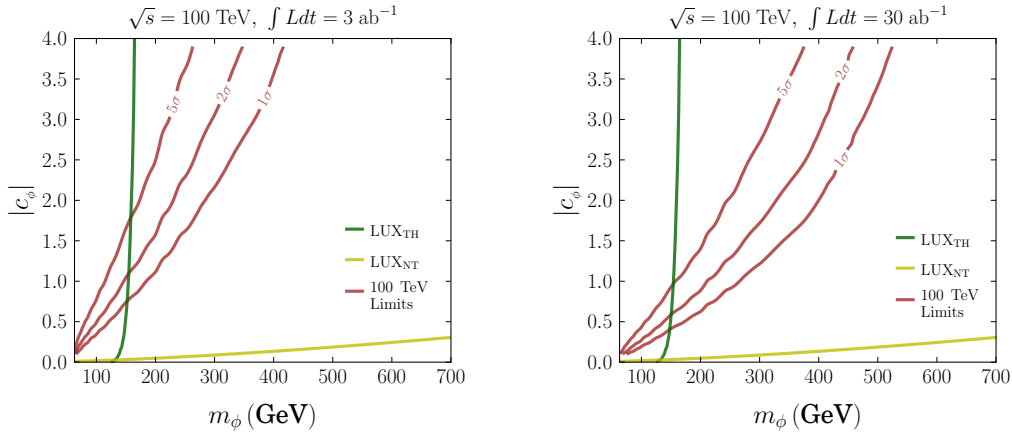


**Fig. 54:** Combined reach of direct searches in VBF,  $ggH$  and  $t\bar{t}H$  channels at  $\sqrt{s} = 100$  TeV for  $3 \text{ ab}^{-1}$  (left) and  $30 \text{ ab}^{-1}$  (right) compared to DM direct detection. In each plot the red lines denotes the  $1\sigma$  exclusion,  $2\sigma$  exclusion, and  $5\sigma$  discovery reach from direct searches at  $\sqrt{s} = 100$  TeV. The region to the left of the green (yellow) line denotes the LUX exclusion for Higgs Portal DM with thermal (non-thermal) abundance given by  $c_\phi, m_\phi$ .

The complementarity between collider searches at 100 TeV and direct detection experiments is illustrated in Fig. 54. Collider searches are not competitive with DM direct detection for small couplings, but at  $c_\phi \gtrsim 1$  can exceed the exclusion and discovery reach of the LUX direct detection experiment when the Higgs portal state possesses its natural thermal abundance. In the event of a signal in future direct detection experiments, this also suggests that direct evidence for Higgs Portal states may be obtained through searches at colliders. In summary,

- If the  $Z_2$  symmetry is exact and the Higgs Portal DM saturates the observed DM density (which may require a non-thermal history), then direct detection probes are likely to be most sensitive.
- If the  $Z_2$  symmetry is exact and a standard thermal history is assumed then in regions where  $\Omega_\phi \leq \Omega_{DM}$  colliders and direct detection experiments provide complementary probes, sensitive to different parameter regions due to a different scaling behavior with the portal coupling  $c_\phi$ .
- If the  $Z_2$  symmetry is approximate and only stabilizes  $\phi$  on the timescale  $\tau \gtrsim 10^{-8}\text{s}$  but is allowed to decay in the early Universe, or if the  $Z_2$  symmetry is exact but  $\phi$  has hidden sector decays to other neutral states then colliders are the only probes of the Higgs Portal coupling, with electron-positron colliders constraining  $m_\phi > m_h/2$  and proton-proton colliders constraining  $m_\phi \geq m_h/2$

### 3.4 WIMP Dark Matter, BSM Mediators (Simplified Models)

For a large class of models, the search for DM can be simplified to a search for a generic mediator that couples to Standard Model particles [303, 408–416]. The choice of mediator can be used to span the class of different experiments that search for DM. The simplest split of the mediator class is between spin 0 and spin 1 mediators. For spin 0 mediators, the couplings of the mediator to Standard Model particles are assumed to be yukawa. The production modes thus resemble the Higgs production. This complements

the searches for heavy scalar mediators. Additionally, in the case where electroweak symmetry breaking is present, the search directly parallels the heavy higgs searches. For spin 1 mediators, the couplings are flavor universal with equal coupling strength to each of the quarks. Production modes of these resemble Standard Model  $Z$  boson production and searches with this model parallel  $Z'$  production.

The mediators can further be split by the type of coupling structure. In the case of spin 0 mediators, this can be split into scalar and pseudoscalar couplings. While the production cross sections, and sensitivity do not change by much at the collider. Pseudoscalar mediators are velocity suppressed with direct detection, and enhanced with indirect detection. This significantly changes the sensitivity of these experiments. Furthermore, the bounds from relic density can also change significantly. For spin 1 type mediators, the split in coupling structure yields vector and axial-vector mediators. Again, the sensitivity for collider experiments does not change by a large amount; however, the sensitivity with direct detection changes drastically in direct detection. Axial-vector mediators can only be probed with spin-dependent direct detection, whereas vector mediators can be probed with spin-independent direct detection. Mixed coupling structures are not considered, since they can often be determined from reinterpreted bounds of the purely coupled mediator searches; Section 3.4.3 explicitly considers interesting combinations of vector and axial-vector mediators. The full lagrangians for these simplified models are described in 3.4.1.

For all mediator types, no mixing with Standard Model particles is assumed. Mixing of additional particles, such as a heavy scalar with the Higgs boson, can lead to additional constraints coming from precision measurements of the Higgs couplings. Mixing parameters typically require a completed model and are thus ignored so as to be generic.

### 3.4.1 Simplified Model Collider Bounds

In DM searches at hadron colliders, the putative dark particles are pair-produced in collisions of the visible sector particles – the Standard Model quarks and gluons. In the set-up studied here [417], there are no direct interactions between the SM sector and the DM particles. Instead these interactions are mediated by an intermediate degree of freedom – the mediator field. In general, one can expect four types of mediators, scalar  $S$ , pseudo-scalar  $P$ , vector  $Z'$  or axial-vector  $Z''$ . The corresponding four classes of simplified models describing elementary interactions of these four mediators with the SM quarks and with the dark sector fermions  $\chi$  are

$$\mathcal{L}_{\text{scalar}} \supset -\frac{1}{2}m_{\text{MED}}^2 S^2 - g_{\text{DM}} S \bar{\chi}\chi - \sum_q g_{\text{SM}}^q S \bar{q}q - m_{\text{DM}} \bar{\chi}\chi, \quad (45)$$

$$\mathcal{L}_{\text{pseudo-scalar}} \supset -\frac{1}{2}m_{\text{MED}}^2 P^2 - ig_{\text{DM}} P \bar{\chi}\gamma^5\chi - \sum_q ig_{\text{SM}}^q P \bar{q}\gamma^5 q - m_{\text{DM}} \bar{\chi}\chi, \quad (46)$$

$$\mathcal{L}_{\text{vector}} \supset \frac{1}{2}m_{\text{MED}}^2 Z'_\mu Z'^\mu - g_{\text{DM}} Z'_\mu \bar{\chi}\gamma^\mu\chi - \sum_q g_{\text{SM}}^q Z'_\mu \bar{q}\gamma^\mu q - m_{\text{DM}} \bar{\chi}\chi, \quad (47)$$

$$\mathcal{L}_{\text{axial}} \supset \frac{1}{2}m_{\text{MED}}^2 Z''_\mu Z''^\mu - g_{\text{DM}} Z''_\mu \bar{\chi}\gamma^\mu\gamma^5\chi - \sum_q g_{\text{SM}}^q Z''_\mu \bar{q}\gamma^\mu\gamma^5 q - m_{\text{DM}} \bar{\chi}\chi. \quad (48)$$

The coupling constant  $g_{\text{DM}}$  characterizes the interactions of the messengers with the dark sector particles, which for simplicity we take to be Dirac fermions  $\chi, \bar{\chi}$ , the case of scalar DM particles is a straightforward extension of these results.

The coupling constants linking the messengers to the SM quarks are collectively described by  $g_{\text{SM}}^q$ ,

$$\text{scalar \& pseudo-scalar messengers :} \quad g_{\text{SM}}^q \equiv g_q y_q = g_q \frac{m_q}{v}, \quad (49)$$

$$\text{vector \& axial-vector messengers :} \quad g_{\text{SM}}^q = g_{\text{SM}}. \quad (50)$$

For scalar and pseudo-scalar messengers the couplings to quarks are taken to be proportional to the corresponding Higgs Yukawa couplings,  $y_q$  as in models with minimal flavour violation [300], and we keep the scaling  $g_q$  flavour-universal for all quarks. For axial and vector mediators  $g_{SM}$  is a gauge coupling in the dark sector which we also take to be flavour universal. The coupling parameters which we can vary are thus  $g_{DM}$  plus either  $g_q$  or  $g_{SM}$ , the latter choice depending on the messengers.<sup>11</sup>

In general, the simplified model description of the dark sector is characterised by five parameters: the mediator mass  $m_{MED}$ , the mediator width  $\Gamma_{MED}$ , the dark particle mass  $m_{DM}$ , and the mediator-SM and the mediator-Dark sector couplings,  $g_{SM}$ ,  $g_{DM}$ . Out of these, the mediator width  $\Gamma_{MED}$ , does not appear explicitly in the simplified model Lagrangians (45)-(48) and should be specified separately.  $\Gamma_{MED}$  accounts for the allowed decay modes of a given mediator particle into other particles from the visible and the dark sector. In a complete theory,  $\Gamma_{MED}$  can be computed from its Lagrangian, but in a simplified model we can instead determine only the so-called minimal width  $\Gamma_{MED,min}$ , i.e. the mediator width computed using the mediator interactions with the SM quarks and the  $\bar{\chi}$ ,  $\chi$  DM particles defined in Eqs. (45)-(48). Importantly  $\Gamma_{MED,min}$  does not take into account the possibility of the mediator to decay into e.g. other particles of the dark sector, beyond  $\bar{\chi}$ ,  $\chi$ , which would increase the value of  $\Gamma_{DM}$ . In Ref. [413] the role of  $\Gamma_{MED}$  is investigated as an independent parameter in the simplified models characterisation of dark sectors by using a simple grid for  $\Gamma_{DM} = \{1, 2, 5, 10\} \times \Gamma_{MED,min}$ , it is known that this can reduce the sensitivity substantially. We instead adopt a reduced simplified description where the width is set to its minimal computed value  $\Gamma_{MED,min}$  which amounts to larger signal cross-sections (we will also check that  $\Gamma_{MED,min} < m_{MED}/2$ ). For our simplified models we have

$$\Gamma_{MED,min} = \Gamma_{\chi\bar{\chi}} + \sum_{i=1}^{N_f} N_c \Gamma_{q_i\bar{q}_i} \quad (51)$$

where  $\Gamma_{\chi\bar{\chi}}$  is the mediator decay rate into two DM fermions, and the sum is over the SM quark flavours. Depending on the mediator mass, decays to top quarks may or may not be open i.e.  $m_{MED}$  should be  $> 2m_t$  for an open decay. The partial decay widths of vector, Axial-vector, scalar and pseudo-scalar mediators into fermions are given by,

$$\Gamma_{ff}^V = \frac{g_f^2(m_{MED}^2 + 2m_f^2)}{12\pi m_{MED}} \sqrt{1 - \frac{4m_f^2}{m_{MED}^2}}, \quad \Gamma_{ff}^A = \frac{g_f^2(m_{MED}^2 - 4m_f^2)}{12\pi m_{MED}} \sqrt{1 - \frac{4m_f^2}{m_{MED}^2}} \quad (52)$$

$$\Gamma_{ff}^S = \frac{g_f^2}{8\pi} m_{MED} \left(1 - \frac{4m_f^2}{m_{MED}^2}\right)^{\frac{3}{2}}, \quad \Gamma_{ff}^P = \frac{g_f^2}{8\pi} m_{MED} \left(1 - \frac{4m_f^2}{m_{MED}^2}\right)^{\frac{1}{2}} \quad (53)$$

where  $m_f$  denotes masses of either SM quarks  $q$  or DM fermions  $\chi$  and the coupling constant  $g_f$  denotes either  $g_{SM}$  or  $g_{DM}$ .

For the simplified DM searches, the most universal DM search can be done by performing the jets+MET search (so-called monojet search) [418–430]. Depending on the choice for the mediator field different production mechanisms will contribute. For vectors and axial-vectors the dominant mechanism is the quark-antiquark annihilation at tree-level. For scalars and pseudo-scalars on the other hand, the loop-level gluon fusion processes are more relevant. The representative Feynman diagrams for both channels are shown in Fig. 55. In comparing DM collider searches with direct and indirect detection experiments it is important to keep in mind that our collider processes and limits continue to be applicable

<sup>11</sup>In Ref. [413],  $g_{DM}$  is parameterised for (pseudo-)scalar messengers as  $g_{DM} = g_\chi m_{DM}/v$  to look symmetric w.r.t. (49), and  $g_\chi$  is treated as a free parameter. Here we do not impose this requirement and leave  $g_{DM}$  as the free parameter.

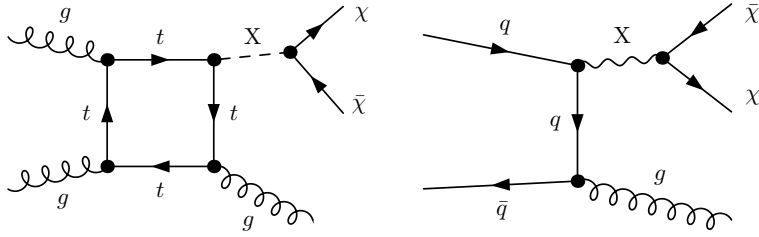


**Fig. 55:** Representative Feynman diagrams for gluon and quark induced mono-jet plus MET processes. The mediator  $X$  can be a scalar, pseudo-scalar, vector or axial-vector particle. The gluon fusion process involves the heavy quark loop which we compute in the microscopic theory, while the quark-anti-quark annihilation is a tree-level process at leading order.

for discovery of any dark sector particles escaping the detector. Hence dark particles produced at colliders do not have to be the cosmologically stable DM.

Regarding the possible origin and the UV consistency of the simplified models (45)-(48), the scalar and pseudo-scalar messenger fields in our simplified models (45)-(46) are singlets under the Standard Model. The simplified models (45)-(46) can arise from two types of the more fundamental theories. The simplest theories of the first type are the two-Higgs-doublet models [431]. In this case the mediators would originate from the second Higgs doublet. The other type of models giving rise to our simplified models are even simpler in the sense that scalar mediators (and the dark sector particles they are coupled to) can be genuinely neutral under the SM but mix with the neutral component of the Higgs [391,394,432,433]. These models provide a direct connection of the dark sector with Higgs physics and can link the origin of the electroweak and the DM scales [402,434–436]. The simplified dark sector models with vector and axial-vector mediators in Eqs. (47)-(48) can also be derived from appropriate first-principles theories. Since the mediators are spin-one particles, these UV models would necessarily require the mediators to be gauge fields and the DM to be charged under these gauge transformations. A classification of anomaly-free extensions of the Standard Model Abelian  $U(1)'$  factor was given in [437] and can be used for constructing an example of a consistent gauge-invariant vector and axial theories of the type (48).

### 3.4.1.1 Dark matter projections

Difficulty exists in correctly modeling the production of the backgrounds at 100 TeV. In particular, the knowledge of the gluon pdfs, the influence of higher order QCD effects, and corrections coming from the electroweak Sudakovs. At 100 TeV collider energies, emission of additional radiation will result in copious jet-production around the Electroweak scale. This will require delicate handling with respect to matching and merging of parton shower and matrix element emissions. Given the likely timescale of construction, and the rapid improvement in theoretical tools, none of the above issues should be regarded as significantly likely to negatively affect the physics program at a 100 TeV collider. For this study, we probe the sensitivity of the monojet search at the 100 TeV collider. The dominant backgrounds for events in either the LHC or the future collider will come from  $Z \rightarrow \nu\bar{\nu}$ ,  $W \rightarrow \ell\nu$ , and  $t\bar{t}$  production. To simulate a hypothetical study, all samples are done using aMC@NLO [94] with 0,1,2 jets merged with the exception  $W$ +jets, where the second jet was not produced.

For the signal we use MadGraph for the Vector/Axial simplified models and a combination of MCFM [438, 439] and VBFNLO [440–442] for the production of Scalar/Pseudoscalar mediators in association with one and two-jets. The output LHE events are then merged using the CKKW-L interface of Pythia 8 [406]. NNPDF3.0 [443] PDF's are used for the generation of all Monte-Carlo samples. This scheme of generation allows for the full use of the second jet in the discrimination of signal and background.

The signal extraction is performed with a full shape analysis of the MET distribution following a selection of the monojet final state. The dominant backgrounds combine from  $Z \rightarrow \nu\bar{\nu}$  production. The second largest background is comes from the  $W$  boson production where a lepton is either fails the lepton identification or is out of the acceptance of the detector. The third largest background comes from  $t\bar{t}$  production where again a lepton from one of the  $W$  boson decays is outside of the detector volume. For the  $Z \rightarrow \nu\bar{\nu}$  background, the  $Z \rightarrow \mu^+\mu^-$  control region is used to model the background. For the  $W \rightarrow \ell\nu$ , top and diboson backgrounds, we use the single lepton control region. For each of these control regions the full statistical uncertainty on the shape is propagated per bin on each of the backgrounds with an additional one percent uncertainty uncorrelated per bin to account for additional modelling uncertainties. For all but the tail bins of the shape uncertainties on the  $\cancel{E}_T$  spectrum are roughly 1% with the dominant uncertainty resulting from the additional one percent modelling uncertainty. The signal is profiled using the standard limit extraction (CL<sub>s</sub>) [444, 445]. Additional nuisances are placed on the background normalization for lepton efficiencies and luminosity. The overall uncertainty setup is extremely conservative since more advanced approaches are in use at the LHC. Also, it is likley that advances in the understanding of higher order electroweak and QCD corrections will be able to further constrain these backgrounds to sub-percentage precision.

Detector effects for a pseudo future high energy detector, and LHC detector are simulated requiring the same jet and MET resolutions as the CMS detector with the one exception that the detector has an added lepton acceptance extended up to  $|\eta| < 4.0$  and  $|\eta| < 5.5$  for the 14 TeV and 100 TeV detectors respectively [305, 446, 447]. Effects from pileup are taken to account to match the expected conditions for high luminosity running at the LHC.

Kinematic distributions for our simplified models of dark sectors alongside the main SM backgrounds are shown in Fig. 56. The distributions are shown as functions of two kinematic variables,  $p_T$  of the leading jet, and missing energy  $\cancel{E}_T$ . The event selection cuts imposed for the distributions in Fig. 56 are  $\cancel{E}_T \geq 200$  GeV and  $\min(\Delta\phi_{\cancel{E}_T, j_i}) \geq 0.5$ , where  $i$  runs over all jets in each event.

### 3.4.1.2 Direct and Indirect Detection Limits

Comparisons for direct and indirect detection cross sections be determined from the Lagrangians Eq. (45)-(48) giving,

$$\sigma_{\text{XP}}^V = \frac{9}{\pi} \frac{g_{\text{DM}}^2 g_{\text{SM}}^2 \rho^2}{m_{\text{MED}}^4} \quad (54)$$

and

$$\sigma_{\text{XP}}^A = \frac{3}{\pi} \frac{g_{\text{DM}}^2 g_{\text{SM}}^2 a^2 \rho^2}{m_{\text{MED}}^4}, \quad (55)$$

with  $a \simeq 0.43$  [410, 448] and the reduced mass  $\rho = m_{\text{DM}} m_p / (m_{\text{DM}} + m_p)$ , for the cross section of a DM particle scattering spin-independently (vector mediator) or spin-dependently (axial-vector mediator) from a proton.

The cross section for a DM particle scattering from a nuclei via a scalar mediator of Eq. (45) is given by [449–451]

$$\sigma_{\text{XP}}^S = \frac{\rho^2}{\pi} \left| \sum_{q=u,d,s} f_q^p \frac{m_p}{m_q} \left( \frac{g_{\text{DM}} g_q y_q}{m_{\text{MED}}^2} \right) + \frac{2}{27} f_{\text{TG}} \sum_{q=c,b,t} \frac{m_p}{m_q} \left( \frac{g_{\text{DM}} g_q y_q}{m_{\text{MED}}^2} \right) \right|^2, \quad (56)$$

where  $f_u^{p(n)} = 0.021(0.019)$ ,  $f_d^{p(n)} = 0.041(0.045)$ ,  $f_s^p = 0.043$  and  $f_{\text{TG}} \simeq 1 - \sum_{q=u,d,s} f_q^n$  [363, 452, 453] and  $m_p$  is the proton mass.

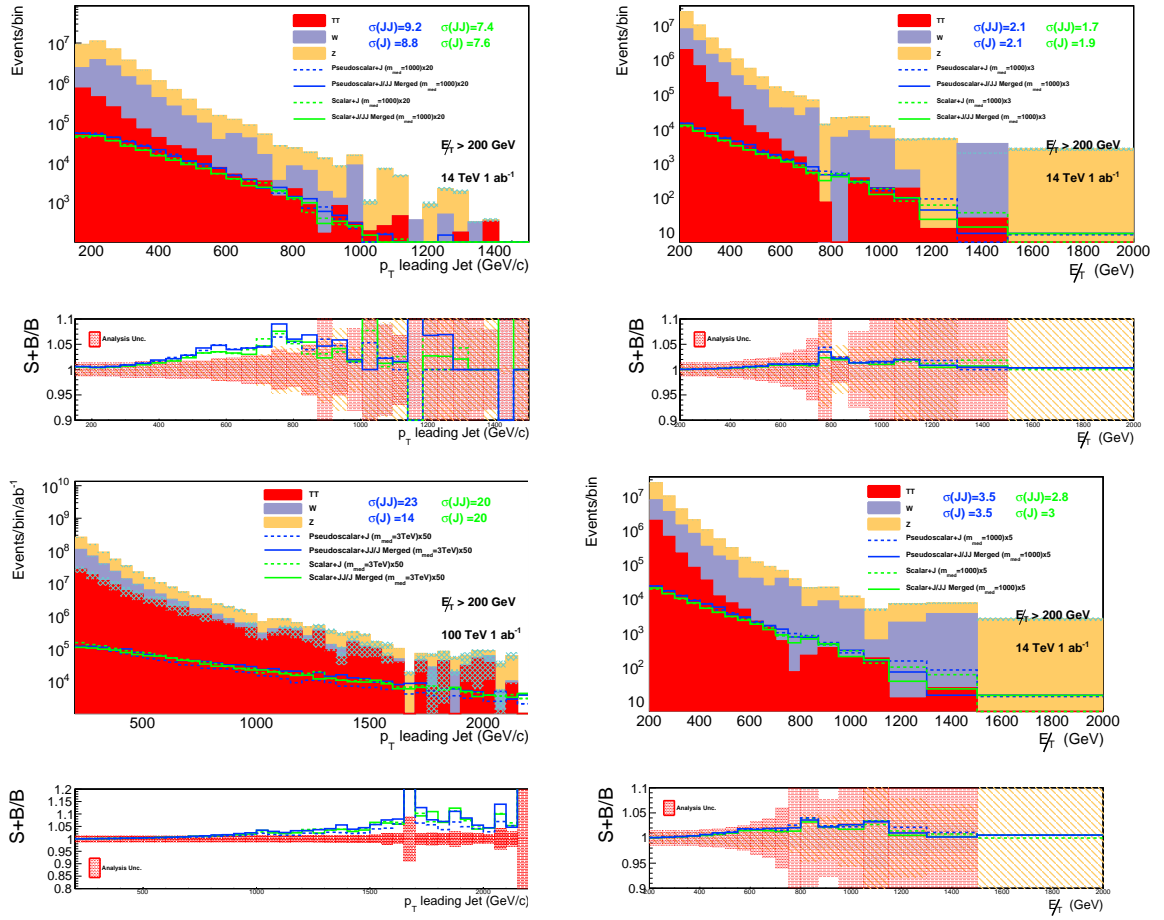


**Fig. 56:** Kinematic distributions for signal scalar and mediator models and the SM backgrounds at 14 TeV(top) and 100 TeV(bottom) assuming  $1 \text{ ab}^{-1}$  of integrated luminosity. We show four kinematic variables:  $p_T$  of the leading jet (left) and the missing energy  $\cancel{E}_T$  (right). Ratios of  $(S + B)/B$  are shown for each observable. The red bands indicate the uncertainties on the background distributions. The accordingly color-coded numbers for  $\text{sig}(\text{JJ})$  and  $\text{sig}(\text{J})$  give the statistical significance to disfavour the presence of the signal using the  $\text{CL}_s$  method.

When comparing the expected sensitivity for the LHC and a 100 TeV collider for DM searches to those of Direct Detection it is interesting to compare the expected impact of the neutrino wall [284, 411]. We take their interaction cross section to be indicative for the ultimate reach of DD experiments [284, 411]. For a pseudo-scalar mediator, taking existing limits into account [454, 455], indirect detection experiments can result in stronger limits than direct detection experiments [456, 457]. For the simplified model of Eq. (46), we use the velocity-averaged DM annihilation cross section into  $\bar{b}b$ ,

$$\langle \sigma v \rangle_{\bar{b}b}^P = \frac{N_C}{2\pi} \frac{(y_b g_b)^2 g_{DM}^2 m_{DM}^2}{(m_{MED}^2 - 4m_{DM}^2)^2 + m_{MED}^2 \Gamma_{MED}^2} \sqrt{1 - \frac{m_b^2}{m_{DM}^2}}, \quad (57)$$

which allows us to derive a limit on the parameters in the  $\bar{b}b$  channel [454].

### 3.4.1.3 Results

Results are obtained scanning over a spectrum of signal models at 14 TeV and 100 TeV. A predicted luminosity of  $1 \text{ ab}^{-1}$  is used for both analyses, so the sensitivity can be compared directly. We note that this amount of integrated luminosity is a rather modest amount compared to what is likely to be collected

at a future collider, the LHC bounds on the other hand represent a qualitative upper bound given the run plans over the next 10 years.

Figure 57 presents the total cross section which the analysis excludes for each of the four mediator types defined in Eqs. (45)-(48). We define our cross sections by setting  $g_{DM} = g_{SM} = 1$  and select the mediator mass as indicated in the legend of each figure respectively. As an illustrative example we have chosen a relatively small characteristic value of 100 GeV, although the results obtained for other kinematically accessible values of DM mass were found to be similar. The kinematics of the process are then completely specified once the couplings  $g_{DM}$  and  $g_{SM}$  are set, since this fixes the minimal width of the mediator [413]. The excluded cross section is then related to the predicted cross section as follows,

$$\sigma = \mu \sigma(g_{DM} = 1, g_{SM} = 1, m_{MED}), \tag{58}$$

With the kinematics of the model fixed we set a limit on  $\mu$  defined above using the  $CL_s$ -method, again assuming  $1 \text{ ab}^{-1}$  of data. Values with  $\mu < 1$  indicate the excluded couplings and width are smaller than the tested model, and the point is then excluded. In Fig. 57 we also distinguish between the mono-jet (shown in green) and the multi-jet-based analyses (shown in yellow). It can be seen that the new multi-jet-based analysis is more powerful and provides a considerable improvement at 14 and at 100 TeV.

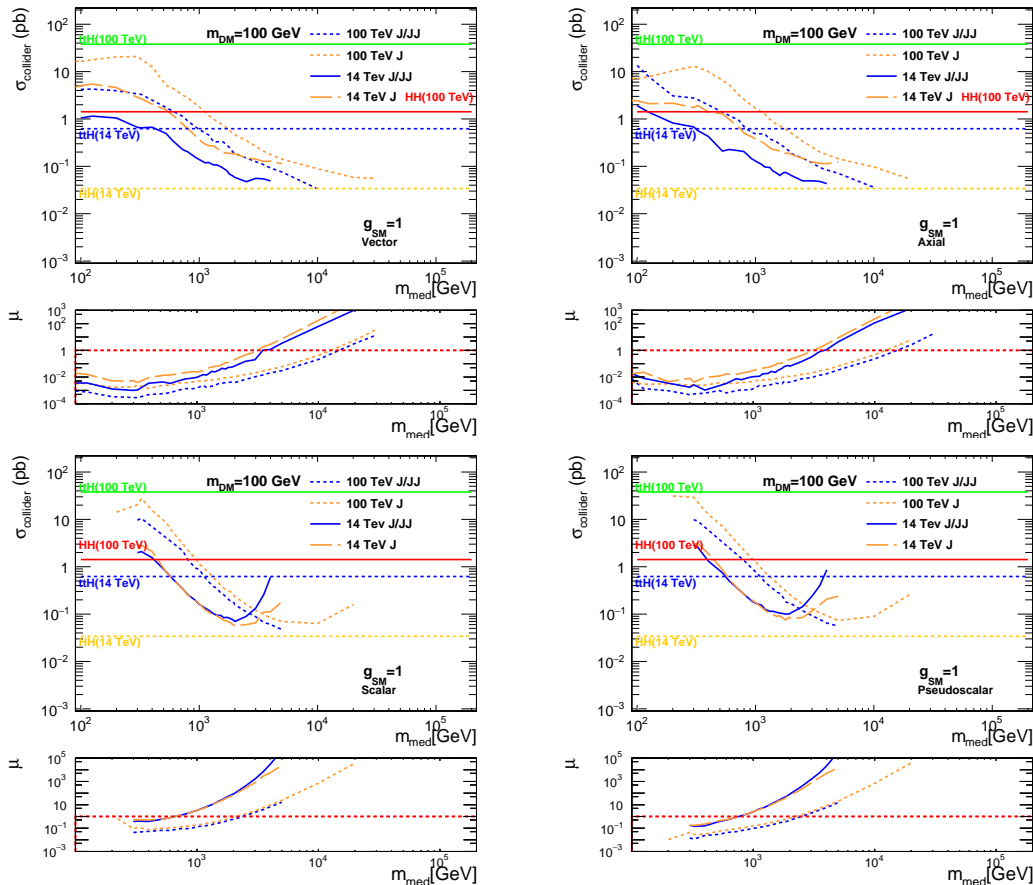


**Fig. 57:** Cross section exclusion limits as a function of mediator mass for a fixed DM mass at a given coupling. We show results for vector (upper left panel), axial-vector (upper right panel), scalar (lower left panel) and pseudoscalar (lower right panel)

For the case of scalar and pseudo-scalar mediators at 14 TeV there is a cross-over for mediators heavier than  $\simeq 1$  TeV, which is absent at 100 TeV. This corresponds to exactly the regions of phase space in which the off-shell effects dominate. The one-jet sample has access to the significant cross section which arises from the tails of the Breit-Wigner distribution, whereas the multileg sample does not. This region therefore has large theory errors using the multi-leg sample. However, we note that the region of phase space for which the multi-leg sample breaks down is far from the values of  $\mu = 1$ , so this region of phase space is of limited importance in regards to setting limits on model parameters. Finally we note that Fig. 57 also includes cross sections for interesting SM predictions which the 100 TeV collider and Run II of the LHC will investigate. We present the cross sections for  $t\bar{t}H$  and  $HH$  and show their relative size compared to our DM predictions.

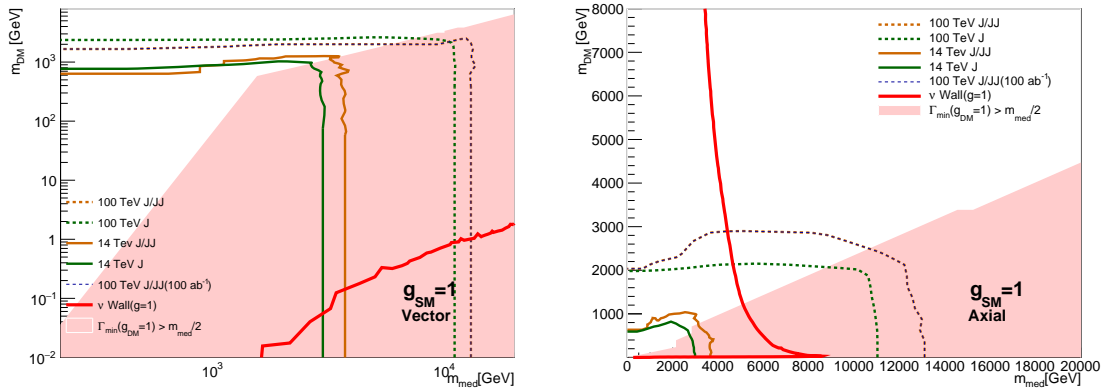


**Fig. 58:** Mass limits for vector mediator models (left panel) and axial-vector models (right panel) at 14 and 100 TeV colliders using the multi-leg and a single-leg analysis. We also show the neutrino wall limit of the direct detection.

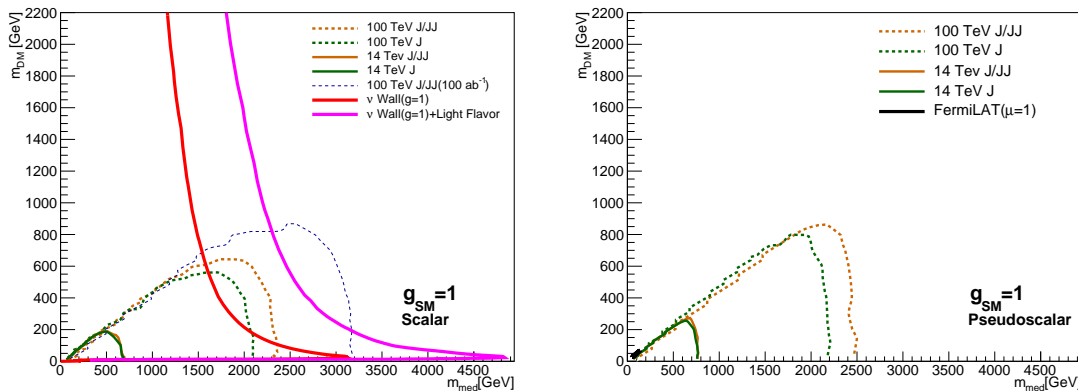


**Fig. 59:** Mass limits for scalar mediator models (left panel) and pseudo-scalar models (right panel) at 14 and 100 TeV colliders using the multi-leg and a single-leg analysis. The neutrino wall affecting the direct detection experiments is shown in the left plot and the indirect detection limit for pseudo-scalars using FERMI-LAT data [454] is shown as a tiny speck in the lower left of the plot on the right.

In Figs. 58 and 59 we show these exclusion contours for the simplified model analysis using a fixed value of the mediator couplings,  $g_{\text{DM}} = g_{\text{SM}} = 1$  for all 4 mediator models of Eqs. (45)-(48). To enable the direct comparison between different experiments/techniques, these figures show all five exclusion contours – the 14 TeV and the 100 TeV limits, using both the one-jet and the multi-jet analysis, together with the DD/ID non-collider limits/projections.

It is interesting to note the dependence of the DD limits in the scalar mediator case on the number of quark degrees of freedom it couples to. Unlike the production mechanism at collider searches which is sensitive only to the heavy top quark, the DD limits are sensitive also to light degrees of freedom thanks to the cancellation of the quark mass in the  $y_q/m_q$  factor in Eq. (56). Thus, the DD limits are quite sensitive to choice of flavors that mediator couples to in the simplified model. The magenta contour in Fig. 58 represents the inclusion of interactions with all quark flavors (as in the simplified model in Eq. (45)). For a different choice of the simplified model, for example with only the top quark couplings to the mediator, the DD contour is shown in red. The difference between the red and magenta contours in the scalar mediator case in Fig. 58 shows the sensitivity of the DD limits to a range of simplified models; at the same time the collider searches are primarily sensitive to the scalar-to-top couplings<sup>12</sup>. For this parameter choice we note that the collider constraints lie below the neutrino wall for  $1 \text{ ab}^{-1}$ , as the 100 TeV collider collects more data the wall can be breached. As an example we plot the expected limit given  $100 \text{ ab}^{-1}$  of 100 TeV data for the scalar mediator.

### 3.4.2 Comparison with Relic Density

Finally, in the context of simplified models, we can compare the sensitivity of the four mediator types with the relic density bounds. The relic density bound serves as a qualitative upper bound for the simplified models [458]. If full coverage can be obtained over the range of the allowed space given the relic constraints, the simplified model can probe all allowed space consistent with the relic density. Such models can be modified to circumvent the relic density constraint. However, most modifications of the simplified model which embed them in more realistic models lead to tighter constraints on the relic density.

The bounds from a 100 TeV collider, the neutrino wall, and the projected bounds from indirect detection are shown in Fig. 60. From these bounds, we observe that the allowed mediator masses that preserve the relic density are excluded by direct detection for vector mediators. The axial mediators are nearly excluded by the collider bounds, and with additional data will be excluded. The allowed scalar region is excluded up to roughly 3 TeV, and the pseudoscalar is excluded up to 3.5 TeV. The allowed regions for both the scalar are not completely covered. The pseudoscalar, in particular, poses the largest challenge to be constrained by either indirect detection or collider constraints. It should be noted that both the direct photon line and indirect Fermi and HESS projections are shown for the indirect bounds in Fig. 60.

### 3.4.3 Probing Thermal DM with Monojets and Dijets

Simplified models offer a useful framework to focus on the interactions of the DM particles, while at the same time being flexible enough to allow for a rich phenomenology [301]. As pointed out in Refs. [303, 459, 460], one of the central implications of assuming the presence of a new mediator is that one can probe the model not only with collider searches based on missing energy in association with SM particles, but also with dedicated searches for the mediator particles themselves, which make use of the fact that any mediator produced from SM particles in the initial state can also decay back into SM states. Combining both kinds of searches it is possible to constrain the visible and invisible decay modes of the assumed mediator and hence probe a wide range of mediator masses.

In the present study we demonstrate this complementarity for a 100 TeV circular proton collider

<sup>12</sup>We note that in the previous figures the  $\nu$ -wall curve corresponds to the magenta curve.

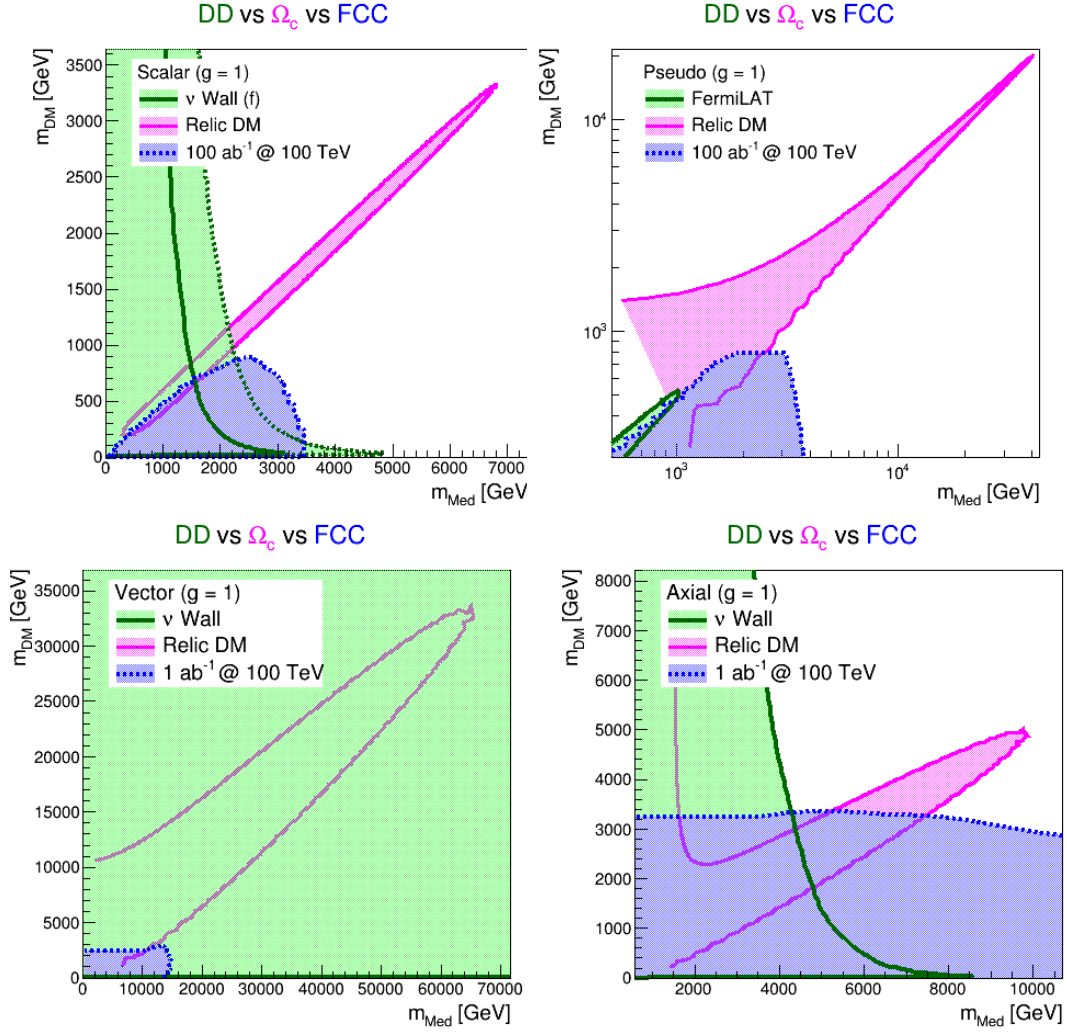


**Fig. 60:** Mass limits for scalar mediator models (top left panel), pseudo-scalar models (top right panel), vector models (bottom left panel), and axial models (bottom right panels) at 100 TeV colliders. The neutrino wall affecting the direct detection experiments is green for all plots excluding the pseudo-scalar mediator, where the projected indirect detection limit using FERMI-LAT and HESS projections data [299] is shown. The relic density is additionally computed all allowed mediator and DM masses are contained within the relic density lines.

and compare the resulting constraints to the parameter space compatible with WIMP freeze-out. For concreteness, we consider the case of a spin-1 mediator, which could e.g. be the massive gauge boson of an additional broken  $U(1)'$  gauge symmetry. As discussed in [461], it is important that the couplings of the mediator are chosen in a way that preserves gauge invariance and that perturbative unitarity is not violated in the parameter regions under consideration. Following [461], we therefore assume that the WIMP is a Majorana fermion and that the mediator has only vectorial couplings to SM quarks:

$$\mathcal{L} \supset -g_q \sum_q Z'^{\mu} \bar{q} \gamma_{\mu} q - \frac{g_{\text{DM}}}{2} Z'^{\mu} \bar{\chi} \gamma_{\mu} \gamma^5 \chi. \quad (59)$$

This choice suppresses constraints from electroweak precision observables, searches for dilepton resonances and DM direct detection experiments, which would otherwise rule out most of the parameter space compatible with thermal freeze-out. In other words, we focus on a typical case that the 100 TeV collider will have to tackle if no DM detection arises in the next decade.

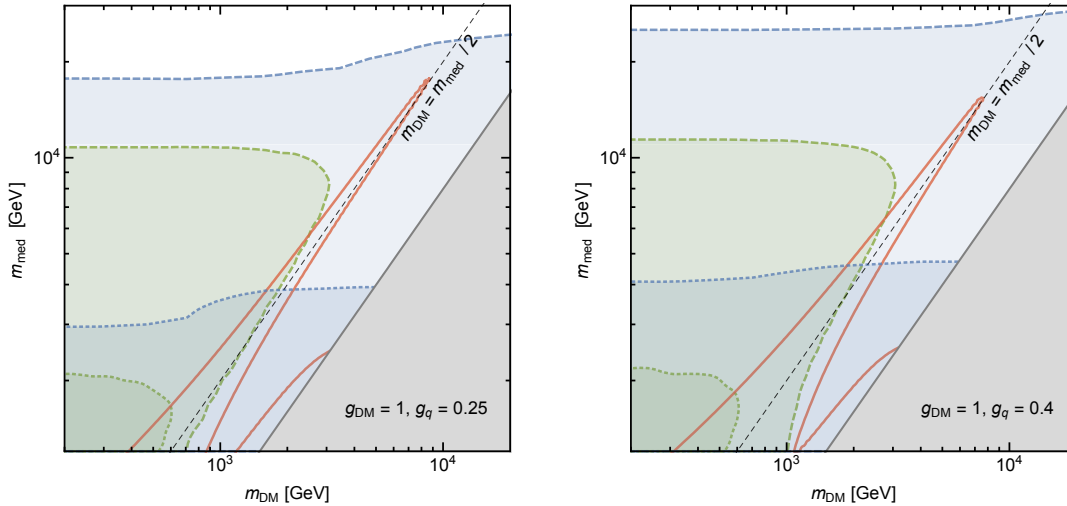


**Fig. 61:** Expected sensitivity of monojet (green) and dijet resonance (blue) searches at the 100 TeV collider (dashed lines) compared to the expected sensitivity of the LHC at 14 TeV (dotted lines) and the parameter values that reproduce the observed relic abundance (red, solid). The grey regions are excluded by perturbative unitarity (cf. [461]).

**Constraining simplified models.** To calculate the expected sensitivity of the 100 TeV collider for simplified models we assume an integrated luminosity of  $\mathcal{L} = 10 \text{ ab}^{-1}$  at a centre-of-mass energy of 100 TeV. For comparison, we also show the reach of the Large Hadron Collider with  $\mathcal{L} = 300 \text{ fb}^{-1}$  at 14 TeV (LHC14).

**Monojets:** We implement the analysis strategy suggested in [462], which essentially corresponds to a scaled-up version of the most recent CMS analysis [422]. Most importantly, the analysis cuts require missing transverse energy ( $\cancel{E}_T$ ) in excess of 2.6 TeV. We simulate the expected signal using MadGraph v5 [94] and Pythia v6 [112]. In existing monojet searches, detector effects play a rather small role, leading to a modest reduction of the monojet cross section by about 20% [463], and we assume that these effects are of similar size in future colliders.

We also simulate the dominant SM background, which arises from invisibly decaying  $Z$ -bosons,  $pp \rightarrow j + Z(\rightarrow \nu\bar{\nu})$ . In addition to statistical uncertainties, we include 1% systematic uncertainties, implying that statistical and systematic uncertainties are of comparable magnitude. Denoting the expected number of background events by  $B$ , we can then potentially exclude a given set of parameters at 95% CL if the predicted number of signal events  $S$  violates the inequality  $S^2 / (S + B + (0.01 B)^2) < 3.84$  [429]. We find that the 100 TeV collider can probe any physics contributions in excess of  $\sigma_{\text{crit}} = 0.15 \text{ fb}$ .

For the LHC we implement the analysis strategy proposed in [464], which requires  $\cancel{E}_T > 800 \text{ GeV}$ . For the cuts that we employ, and assuming 2% systematic uncertainties, we find that the LHC will be able to probe monojet cross section larger than  $\sigma_{\text{crit}} = 0.6 \text{ fb}$ .

**Dijets:** The search for dijet events coming from the  $pp \rightarrow Z' \rightarrow jj$  process probes the large- $m_{\text{DM}}$  parameter region [303]. We simulate this signal by means of MadGraph v5, Pythia v6 and Delphes v3 [113]. The background expectations after imposing the cuts adopted in the CMS dijet analysis [465] are extracted from [466]. We apply these cuts to the signal using MadAnalysis [467]. The reach of the 100 TeV collider to this signal is then estimated by applying the  $\text{CL}_s$  method to the distribution of the dijet invariant mass  $m_{jj}$ , neglecting systematic uncertainties. This approach allows us to probe even broad resonances. We proceed in the same way for LHC14.

**Combination:** In Fig. 61 we show several examples for the expected sensitivity of the 100 TeV collider compared to the projection for LHC14 TeV and the parameters that reproduce the observed DM relic

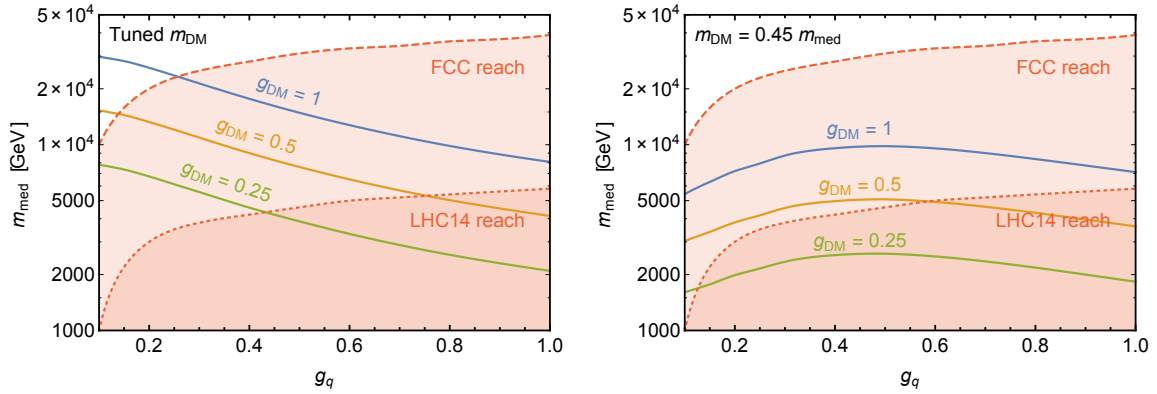


**Fig. 62:** Largest value of  $m_{\text{med}}$  compatible with the observed relic abundance (for several values of  $g_{\text{DM}}$ ; solid lines) in comparison with the largest mediator mass that can be probed by the 100 TeV collider (dashed lines) and LHC14 (dotted lines) as a function of the quark coupling  $g_q$ . In the left panel we tune  $m_{\text{DM}}$  in such a way that the resonant enhancement is maximised, whereas in the right panel we fix  $m_{\text{DM}} = 0.45 m_{\text{med}}$ .

abundance ( $\Omega_{\text{DM}}/h^2 = 0.119$ ) as calculated with `micrOMEGAs v4` [468]. Note that we do not display direct detection bounds, which are strongly suppressed for the coupling combinations that we consider and therefore turn out not to be competitive to the bounds from colliders. Theoretical constraints from perturbative unitarity (cf. [461]) are also shown.

**Probing the resonance region.** For the cases considered in Fig. 61, the 100 TeV collider is sensitive to all parameter points compatible with the observed DM relic abundance. However, for small couplings and  $m_{\text{DM}} \approx m_{\text{med}}/2$  there is a strong enhancement of the DM annihilation cross section due to the mediator going on-shell in the process  $\chi\chi \rightarrow q\bar{q}$ . As a result, very large mediator masses can still be compatible with the observed DM relic abundance. This is quantified in Fig. 62, which displays the maximal  $m_{\text{med}}$  allowed by  $\Omega_{\text{DM}}/h^2 \leq 0.119$  as a function of  $g_q$  for several values of  $g_{\text{DM}}$  (solid lines). In the left panel we tune  $m_{\text{DM}}$  for each value of  $g_q$  and  $g_{\text{DM}}$  to maximise the resonant enhancement during thermal freeze-out, which typically requires  $m_{\text{DM}}$  slightly below  $m_{\text{med}}/2$  due to the kinetic energy of the annihilating DM particles. For small couplings, the resonance is very narrow and the resonant enhancement is possible only at the expense of a large fine-tuning on  $m_{\text{DM}}$ . In the right panel we therefore show an example without excessive tuning (setting  $m_{\text{DM}} = 0.45 m_{\text{med}}$ ) such that the effect of the resonance is reduced rather than enhanced for very narrow resonances and smaller mediator masses are required to reproduce the observed relic abundance.

The crucial observation is that dijet resonance searches at the 100 TeV collider potentially possess the sensitivity to probe even the resonance region. Figure 62 also shows the maximum mediator mass that can be probed by the 100 TeV collider (dashed curve) and LHC14 (dotted curve). We conclude that for most of the values of  $g_{\text{DM}}$  and  $g_q$  that we consider, the 100 TeV collider can probe *all* mediator masses and DM masses compatible with thermal freeze-out. This conclusion is made explicit in Fig. 63, where we show the potential reach of the 100 TeV collider and LHC14 as a function of the two couplings  $g_q$  and  $g_{\text{DM}}$ . We observe that only highly-tuned corners of parameter space (with  $m_{\text{DM}} \approx m_{\text{med}}/2$  and  $g_q \ll g_{\text{DM}}$ ) can potentially evade detection at a 100 TeV collider. In the largest fraction of the allowed parameter space, on the other hand, the 100 TeV collider will be able to probe the assumption of thermal freeze-out for the simplified model that we consider. Notably, this conclusion applies even to the scenario where the analyzed DM particle constitutes only a fraction of the total relic density, which requires even smaller mediator masses.

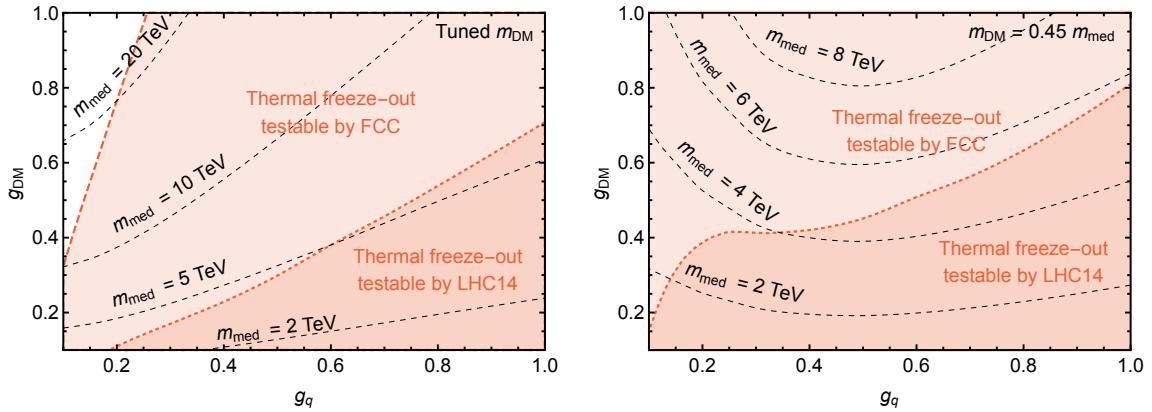


**Fig. 63:** Expected sensitivity at a 100 TeV collider (dashed) and LHC14 (dotted) for thermal WIMPs in the  $g_q$ - $g_{DM}$  parameter plane, when setting  $m_{\text{med}}$  to the largest value compatible with the observed relic abundance (as indicated by the black dashed lines). In the left panel we tune  $m_{DM}$  in such a way that the resonant enhancement is maximised, in the right panel, we fix  $m_{DM} = 0.45 m_{\text{med}}$ .

### 3.4.4 Light Mediators: Dark Photons at a 100 TeV collider

A 100 TeV collider extends the mass reach of direct searches for new physics over the LHC and other lower-energy colliders. There are also precision studies that can only be performed at such a high energy machine, such as high-invariant-mass measurements of the Drell-Yan (DY) spectrum. These allow for model-independent searches for new TeV-scale electroweakly charged states through their effect on the RG evolution of SM gauge couplings [469]. A somewhat less appreciated possibility is that the 100 TeV collider can discover new physics that produces only low-energy objects, such as certain exotic Higgs decays [470] or low-mass hidden sectors. One might think that lepton colliders are better suited to discover such new physics, since reconstruction of low- $p_T$  events with multiple soft objects is greatly aided by the much cleaner final state compared to hadron colliders. However, if the final state is conspicuous enough, e.g. by producing multiple leptons and/or photons, then the enormous production rate and luminosity at a 100 TeV collider (and to a lesser extent the HL-LHC) can easily outweigh this advantage, and allow access to Beyond the Standard Model (BSM) couplings that are several orders of magnitude smaller than what is possible at the statistically limited lepton collider experiments.

The 100 TeV collider can therefore act as an *intensity frontier experiment* for the study of, for example, light hidden sectors. One of the best examples to demonstrate this capability are BSM theories with dark photons [471–474]. This will also demonstrate the complementarity of future lepton and hadron colliders in offering different experimental probes of the same BSM scenario. Here we very briefly summarize the work in [474], which studied the experimental reach of current and future lepton and hadron colliders to study BSM sectors with dark photons.

The minimal benchmark model for dark photons features a dark  $U(1)_D$  gauge symmetry that mixes with hypercharge via a small kinetic mixing  $\epsilon$ :

$$\mathcal{L} \supset -\frac{1}{4} \hat{B}_{\mu\nu} \hat{B}^{\mu\nu} - \frac{1}{4} \hat{Z}_{D\mu\nu} \hat{Z}_D^{\mu\nu} + \frac{1}{2} \frac{\epsilon}{\cos\theta} \hat{Z}_{D\mu\nu} \hat{B}^{\mu\nu} + \frac{1}{2} m_{D,0}^2 \hat{Z}_D^\mu \hat{Z}_{D\mu}. \quad (60)$$

Here  $\hat{B}$ ,  $\hat{Z}_D$  are the hypercharge and  $U(1)_D$  gauge bosons with non-canonical kinetic terms. The kinetic mixing can be eliminated via a field redefinition to make the kinetic terms canonical. This results in fields charged under SM hypercharge effectively acquiring a “milli-charge” under the  $U(1)_D$  gauge interaction. This gives rise to an effective mass mixing between the dark photon  $Z_D$  and the SM  $Z$ -boson through the acquired milli-charge of the SM Higgs. Diagonalizing the gauge boson mass matrix yields a Lagrangian containing  $Z_D f \bar{f}$  and  $h Z_D Z$  couplings of  $\mathcal{O}(\epsilon)$ . In the absence of other hidden-sector states lighter than the dark photon,  $Z_D$  decays dominantly to SM fermion pairs with gauge-like branching ratios. This

results in sizable branching fractions to SM leptons, and should be contrasted with e.g. new scalar states that couple to SM fermions with Yukawa-like interactions and decay dominantly to third generation fermions.<sup>13</sup>

The dark photon mass term  $m_{D,0}^2$  in Eq. (60) arises most simply by introducing a “dark Higgs”  $S$  that breaks  $U(1)_D$  via a vacuum expectation value in analogy to the SM Higgs mechanism. This expands the scalar sector of the SM as follows:

$$V_0(H, S) = -\mu^2|H|^2 + \lambda|H|^4 - \mu_S^2|S|^2 + \lambda_S|S|^4 + \kappa|S|^2|H|^2, \quad (61)$$

where the renormalizable coupling  $\kappa$  induces mixing between the SM Higgs and  $S$ , and is assumed to be small so as not to greatly modify the properties of the observed SM-like Higgs boson. Apart from Higgs coupling modifications, this mixing also induces  $hZ_D Z_D$  terms of  $\mathcal{O}(\kappa)$ . (This term is also generated by kinetic mixing, but only at  $\mathcal{O}(\epsilon^2)$ .)

Historically, most of the effort in searching for dark photons has been devoted to masses in the range  $\text{MeV} \lesssim m_{Z_D} \lesssim 10 \text{ GeV}$ , through techniques as diverse as precision QED measurements, rare meson decays, supernova cooling, collider experiments, and beam dumps [475–510]. However there is no theory reason not to extend the searches to the entire experimentally accessible range [470, 470, 495, 496, 511–515]. Generation of dark photon masses in natural theories has been studied in [477, 516–519], and in many cases can allow for natural dark photons above 10 GeV equally well.

In our study of dark photon signatures, it is useful to distinguish the *hypercharge portal*, i.e. the kinetic mixing  $\epsilon$  in Eq. (60), from the *Higgs portal*, i.e. the Higgs mixing  $\kappa$  in Eq. (61). Both refer to renormalizable operators connecting the SM to a hidden BSM sector, and both generate distinct leading signals that may be observed at future lepton and hadron colliders. Note that while some aspects of the Higgs portal coupling were studied already above, that study was restricted to the case where the Higgs is the only mediator to the DM sector, while here the mediator couples to the Higgs portal, thus allowing for mixing with the Higgs and a vast range of complementary signatures not studied above.

The most promising signatures of the hypercharge portal that were studied in [474] are 1. electroweak precision observables (EWPOs) sensitive to the hypercharge portal, 2. the process  $pp \rightarrow Z_D \rightarrow \ell^+ \ell^-$  production via DY-like direct production and 3. exotic Higgs decays via the hypercharge portal,  $h \rightarrow Z Z_D \rightarrow 4\ell$ . Their reach is compared in the plane of dark photon mass vs. kinetic mixing in Fig. 64. Ideally, detection in all three channels, at both future 100 TeV and lepton colliders, would allow for a detailed diagnosis of the dark sector.

If there is non-negligible mixing between the SM-like and the dark Higgs, additional measurements are possible via the Higgs portal. It is useful to define the effective mixing parameter

$$\kappa' = \kappa \frac{m_h^2}{|m_h^2 - m_s^2|}. \quad (62)$$

The most promising Higgs portal signature is the exotic Higgs decay  $h \rightarrow Z_D Z_D$ , with branching fraction that scales as  $\mathcal{O}(\kappa'^2)$ . As long as the  $Z_D$  are produced on-shell, they decay via the hypercharge portal without  $\epsilon$  affecting the  $Z_D Z_D$  production cross section. As Fig. 65 makes clear, this is the scenario where the advantages of the 100 TeV collider as an intensity frontier experiment are most apparent. Branching ratios as low as  $\text{Br}(h \rightarrow Z_D Z_D) \sim 10^{-7}(10^{-8})$  can be probed with  $300 \text{ fb}^{-1}$  ( $3 \text{ ab}^{-1}$ ) when  $Z_D$  decays promptly, since the search for the  $4\ell$  final state with two  $m_{Z_D}$  resonances and one  $m_h$  resonance is practically background-free.

Prompt  $Z_D$  decay implies  $\epsilon \gtrsim 10^{-5}$ . Detection of prompt  $h \rightarrow Z_D Z_D \rightarrow 4\ell$  is therefore already sensitive to kinetic mixings much smaller than what can be probed directly. That sensitivity is greatly extended when expanding the search to include *long-lived particles* produced in exotic Higgs decays.

<sup>13</sup>See [474] for a MadGraph [111] implementation, as well as tables of branching ratios and decay widths.

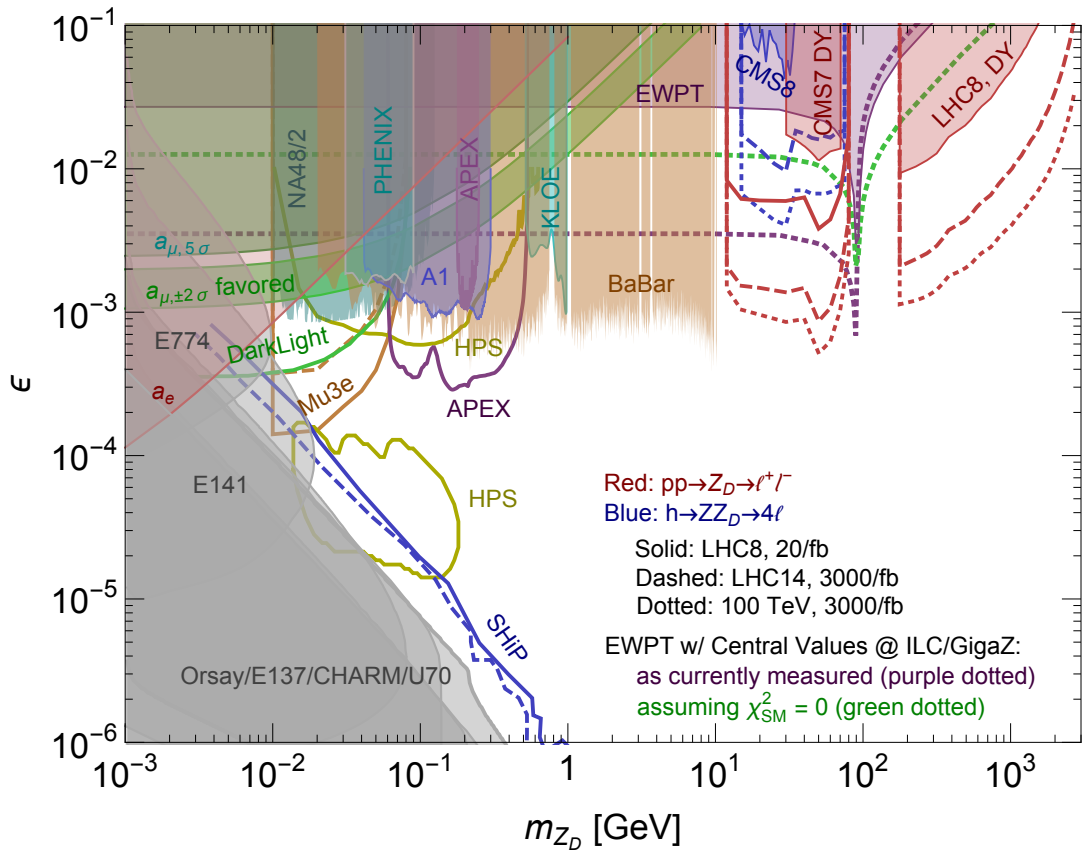


**Fig. 64:** Summary of dark photon constraints and prospects (see [474] for references). High-energy colliders (LHC14, 100 TeV, ILC/GigaZ) are uniquely sensitive to dark photons with  $m_{Z_D} \gtrsim 10$  GeV, while precision QED observables and searches at  $B$ - and  $\Phi$ -factories, beam dump experiments, and fixed target-experiments probe lower masses. Dark photons can be detected at high-energy colliders in a significant part of open parameter space in the exotic decay of the 125 GeV Higgs boson,  $h \rightarrow ZZ_D \rightarrow 4\ell$ , (blue curves) in Drell-Yan events,  $pp \rightarrow Z_D \rightarrow \ell\ell$ , (red curves) and through improved measurements of electroweak precision observables (green/purple dashed curves). Note that all constraints and prospects assume that the dark photon decays directly to SM particles, except for the precision measurements of the electron/muon anomalous magnetic moment and the electroweak observables. Figure taken from [474]. Drell-Yan projections are rescaled from the LHC results of [514, 515], and we anticipate some further improvement at high masses may be possible.

This is separately motivated in theories of Neutral Naturalness [523, 524] and more generally in Hidden Valleys [525–528], of which the dark photon scenario is a particular example.

Figure 66 illustrates the sensitivity to kinetic mixing achievable if dark photon decays within a 1 or 10m detector volume could be reconstructed at the LHC or a 100 TeV collider (assuming prompt lepton efficiencies and expected signal-to-background). Different contours indicate different assumptions made for the exotic Higgs decay branching ratio  $\text{Br}(h \rightarrow Z_D Z_D)$ , which can be relatively large even if kinetic mixing is tiny. The enormous rate of Higgs production at a 100 TeV collider compensates for the overwhelming fraction of dark photons that escape the detector for very small kinetic mixing, allowing  $\epsilon$  as small as  $\sim 10^{-10}$  to be probed. This opens a window onto a broad swath of otherwise inaccessible parameter space, and relies on having available a production mechanism for dark sector states that is separate to the coupling which controls their decay to SM particles. Searches with sensitivity to the displaced dilepton final state are already underway at the LHC [529, 530].

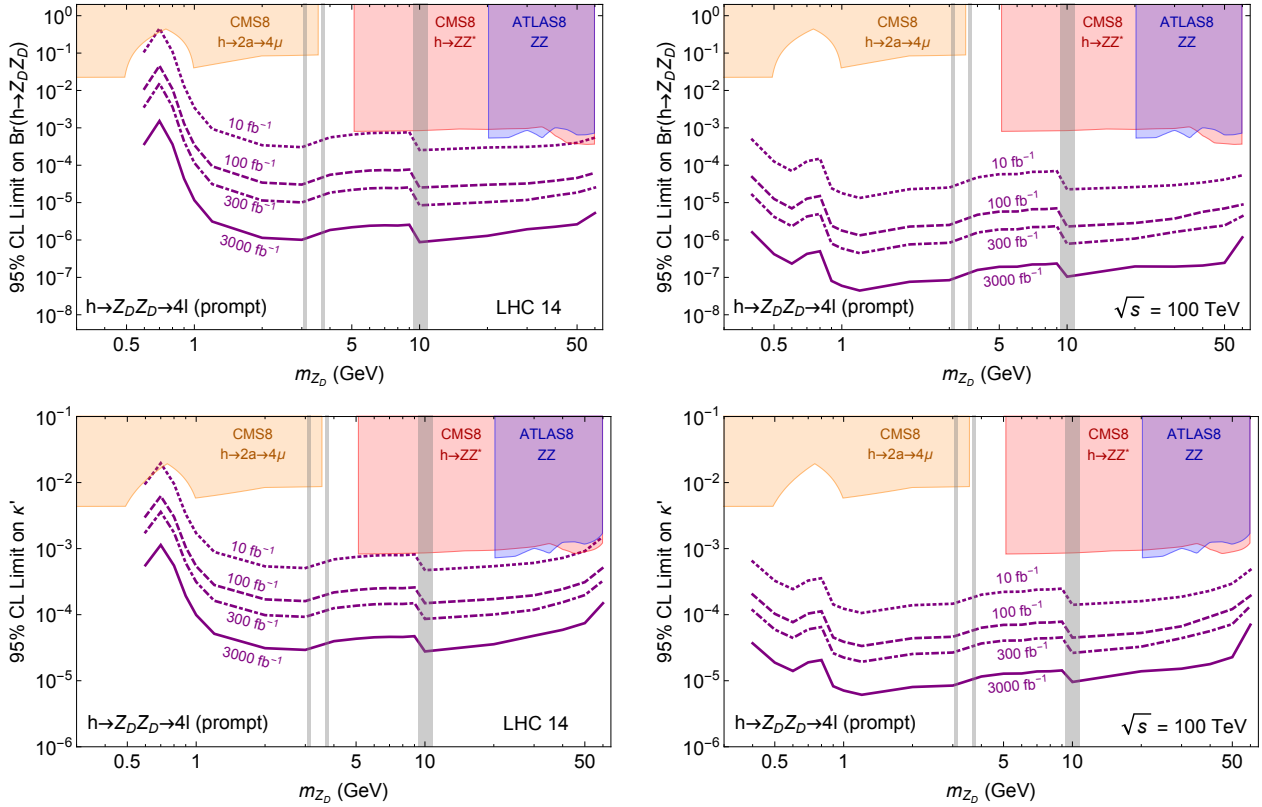


**Fig. 65:** Expected 95% CLs limits on the total exotic Higgs decay branching ratio,  $\text{Br}(h \rightarrow Z_D Z_D)$  (top), and the effective Higgs mixing parameter  $\kappa'$  (bottom) at the LHC (left) and a 100 TeV pp collider (right). Gray bands correspond to regions where quarkonium background may invalidate these projections. The limits obtained in [470] from a recast of LHC Run 1 results are shown in red ( $h \rightarrow ZZ^* \rightarrow 4\ell$  search by CMS [520]) and blue (ATLAS  $ZZ$  cross section measurement [521]) shaded regions. The limit from the CMS 8 TeV  $h \rightarrow 2a \rightarrow 4\mu$  search [522] is shaded in orange, assuming the efficiencies for pseudoscalar and dark photon decay to muons are the same. Figure from [474].

For the Higgs portal, important complementarities with the capabilities of future lepton colliders can also be identified.

- A sizable  $\text{Br}(h \rightarrow Z_D Z_D)$  is generated through non-negligible mixing of the SM-like Higgs with the dark Higgs  $S$ . This leads to potentially detectable Higgs coupling deviations at lepton colliders.
- Direct production of the SM-singlet dark Higgs  $s$  is possible at both lepton and hadron colliders, either directly or through exotic decays of the SM-like Higgs boson. If  $s$  can only decay via its mixing with the Higgs, the dominant final state will be third-generation fermion pairs  $\bar{b}b$ ,  $\tau^+\tau^-$  and  $\bar{c}c$ . If  $s$  is light enough to be produced at lepton colliders, the energy of its decay products may be so low that reconstruction of these final states without resonances of light leptons is difficult at a 100 TeV hadron collider. In that case, the clean environment of a lepton collider could prove invaluable in searching for  $s \rightarrow \bar{b}b, \tau^+\tau^-$  signals.

Finally, the potentially stunning sensitivity of a 100 TeV collider to dark photon signatures is only possible if future detector designs allow for the recording and reconstruction of relatively soft objects, with  $p_T \sim \mathcal{O}(20 \text{ GeV})$ , as well as low-mass  $\sim \mathcal{O}(10 \text{ GeV})$  displaced decays. If these requirements are satisfied, a 100 TeV collider could easily discover hidden sector signatures that cannot be probed by any other means.

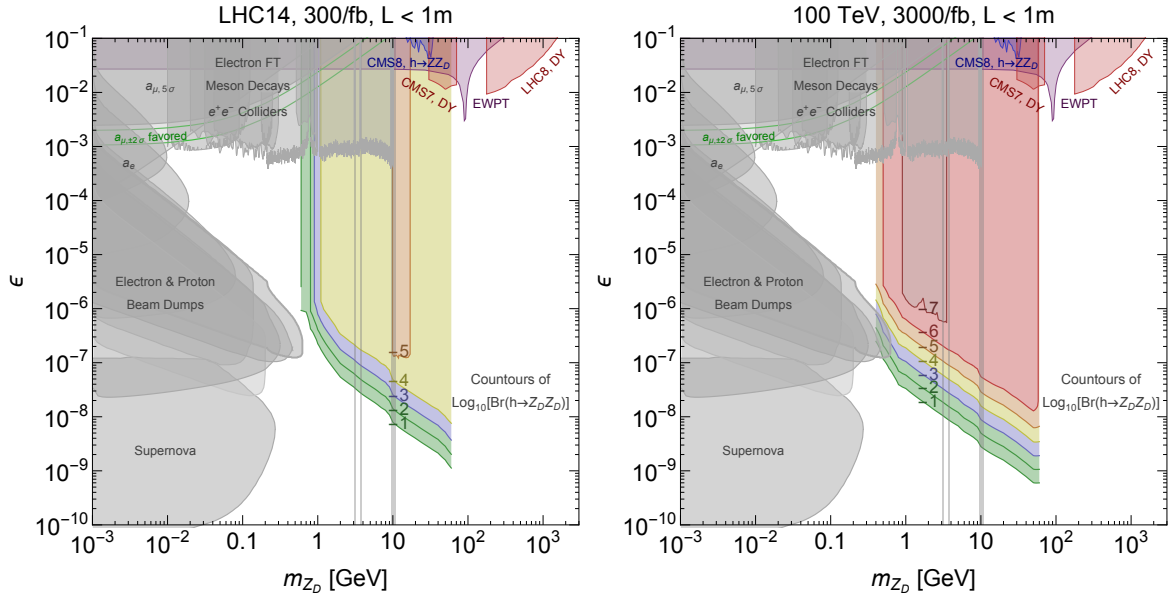


**Fig. 66:** Estimate of expected 95% CLs limits on  $\epsilon$  for different  $\text{Br}(h \rightarrow Z_D Z_D)$  at the LHC (*left*) and a 100 TeV collider (*right*), assuming a displaced lepton jet search has the same sensitivity to decays within the given distance from the interaction point as a prompt  $Z_D Z_D$  search (see Fig. 65). A detector size  $L$  of 1 m is assumed for all plots. Gray shaded regions show current constraints (see [474] for references).

### 3.5 WIMP, Non-Minimal Models

#### 3.5.1 Gluino, Stop Coannihilation

A non-minimal scenario that can thermally produce the correct relic abundance and may be testable at a future collider is co-annihilation. For concreteness we consider the DM to be a bino (electroweak singlet) and the co-annihilator to be a colored sparticle with a mass  $m = 1.05 m_{\tilde{\chi}}$  where  $m_{\tilde{\chi}}$  is the bino mass. The near mass degeneracy allows the bino annihilation rate (with the co-annihilator) to increase which decreases the relic abundance. The mass that gives the correct relic abundance depends on the splitting between the bino and co-annihilator. The collider rate, on the other hand, is determined by the mass of the co-annihilator.

The first co-annihilator we consider is the gluino which is a color octet fermion. At 100 TeV one finds a reach for the bino of 5.8 TeV to 6.2 TeV.<sup>14</sup> The reach is shown in Fig. 67 (left). In this figure the upper  $x$ -axis shows the bino mass assuming  $m_{\tilde{g}} = 1.05 m_{\tilde{\chi}}$  while the lower  $x$ -axis shows the  $m_{\tilde{g}} - m_{\tilde{\chi}}$  value for which one finds the correct relic abundance [531]. In this projection the gluinos are pair produced and assumed to decay via  $\tilde{g} \rightarrow \tilde{\chi} + \text{undetected}$ . The most effective search is in the monojet channel.

The second co-annihilator we consider is the right handed stop which is a color triplet scalar. The expected exclusion for the bino is 2.4 TeV to 2.8 TeV and in fact the discovery reach is 1.7 TeV to 2.1 TeV and is shown in Fig. 67 (right). The  $x$ -axes, the same as in the gluino case, show the bino mass assuming  $m_{\tilde{t}} = 1.05 m_{\tilde{\chi}}$  and the  $m_{\tilde{t}} - m_{\tilde{\chi}}$  value for the relic abundance [531, 532]. The stops are pair produced and assumed to decay via  $\tilde{t} \rightarrow \tilde{\chi} + \text{undetected}$  so the monojet channel is used.

Relative to 14 TeV, the increase in reach is about a factor of 5. Importantly, however, the factor of 5 is enough to cover the thermal relic region for stops and come fairly close to covering the region for gluinos.

<sup>14</sup>Actually the reach is 6.1 TeV to 6.5 TeV on the gluino and is not too sensitive to the bino mass.

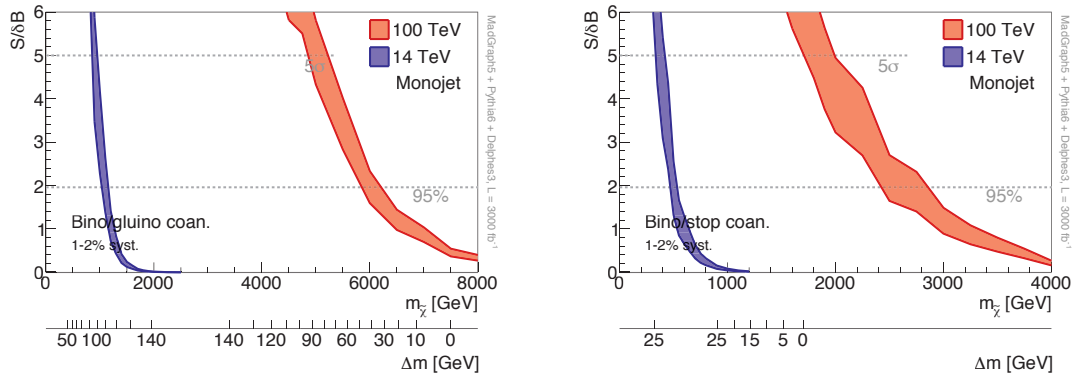


**Fig. 67:** Reach for bins that co-annihilate with gluinos (left) and bins that co-annihilate with stops (right).

One obvious direction for future study is to consider also looking for the decay products of the gluino or stop. This may be challenging because the most likely decays are  $\tilde{g} \rightarrow \tilde{\chi}jj$  via an offshell squark and  $\tilde{t} \rightarrow \tilde{\chi}bjj$  or  $\tilde{t} \rightarrow \tilde{\chi}bl\nu$  via an offshell top, where the jets and leptons will have a momentum  $\sim \Delta m$  which is  $\mathcal{O}(10)$  GeV in the preferred parameter region. It is not clear how feasible it will be to tag such low  $p_T$  objects at 100 TeV. On the other hand, in the monojet channel the  $\tilde{g}\tilde{g}$  or  $\tilde{t}\tilde{t}^*$  system recoils against a hard jet, so one can expect more energetic decay products when using certain selection criteria.

### 3.5.2 MSSM Dark Matter

A crucial question in the development of a new collider program is whether, beyond increasing our sensitivity and mass reach to new phenomena, the design energy and luminosity can provide us with definite answers to our most pressing questions. DM motivated SUSY is a very compelling framework to ask ourselves this question for a high energy hadron collider project, such as the 100 TeV proton collider. SUSY is one of the best motivated theories of physics beyond the SM. The DM relic density provides us with well-defined constraints on the mass and the nature of the WIMP candidate. In the MSSM with neutralino LSP,  $\chi_1^0$  masses above 3.5-4 TeV are strongly disfavoured by the universe overclosure bounds, thus defining a mass scale well within the reach of the 100 TeV collider energy. In addition, direct DM searches set constraints probing more and more in depth into the MSSM parameter space, in particular for values of the  $\mu$  parameter below 1-1.5 TeV. These constraints are complementary to those derived from direct searches at the LHC and indirect sensitivity from the Higgs sector.

For this report, the sensitivity of an 100 TeV  $pp$  collider to DM-motivated MSSM has been studied by scans of the 19-parameters pMSSM where the SUSY particle masses have been independently varied up to 20 TeV. The pMSSM has been extensively used to assess the current and projected coverage of the MSSM parameter space by the LHC searches [533–536]. Generated pMSSM points have been checked against low-energy and flavour physics constraints and the lightest Higgs boson mass has been required to be in the range  $119 < M_{h^0} < 129$  GeV. In addition, we require the neutralino relic density not to exceed the PLANCK CMB result, when accounting for systematic uncertainties. This allows for additional, non-SUSY contributions to the relic density from CMB. For each accepted pMSSM point, sets of inclusive SUSY events have been generated and the physics objects computed after a parametric detector simulation.

Searches in jets+MET, leptons+MET, monojets and monoW/Z+MET have been evaluated using analysis strategies derived from those currently performed on the LHC data, but re-optimising the kinematical cuts. Results have been obtained in terms of the fraction of pMSSM points that could be excluded in case no excess of events is observed with a given integrated luminosity of 100 TeV  $pp$  data and when combining with current and future DM direct detection data. Results are summarised in Fig. 68 and

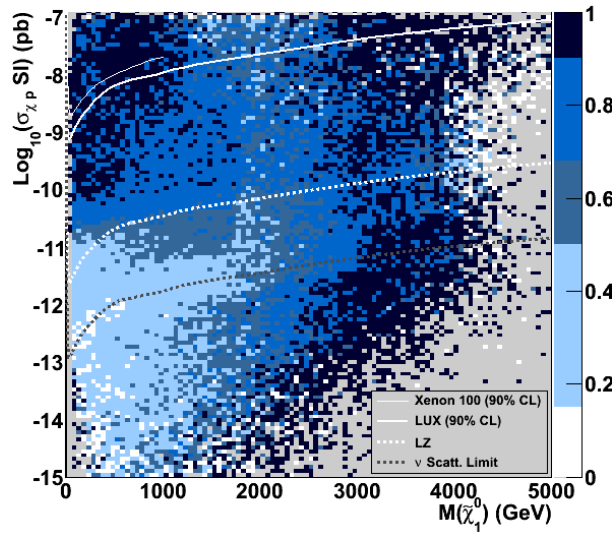


**Fig. 68:** Fraction of DM-motivated pMSSM points with neutralino LSP and SUSY masses up to 20 TeV excluded by searches at a 100 TeV  $pp$  collider in the neutralino scattering cross section vs. neutralino mass plane. Current and projected limits from DM direct detection experiments are overlaid.

$\sqrt{s}$ (TeV)	$L$ ( $\text{ab}^{-1}$ )	Collider (MET)	+LUX DM	+LX DM	+3rd Gen. DM
100	1.0	0.63	0.65	0.73	0.90
100	3.0	0.67	0.69	0.75	0.91
100	5.0	0.69	0.72	0.76	0.92

**Table 4:** Fraction of DM-motivated pMSSM points with neutralino LSP and SUSY masses up to 20 TeV excluded by searches at a 100 TeV  $pp$  collider and DM direct searches.

Table 4 showing how the combination of 100 TeV collider and future DM direct detection experiments can virtually saturate the MSSM parameter space, if SUSY is responsible for (at least part of) DM.

In gravitino DM models with thermal leptogenesis, the interplay of gravitino relic density, reheating temperature of the Universe after the inflationary phase,  $T_{RH}$  and the gluino mass,  $M_{\tilde{g}}$ , determine an upper bound on the gluino mass relevant to the HL-LHC and also a high energy hadron collider [537]. With a sensitivity to the gluino mass up to  $\sim 10$  TeV, the 100 TeV collider can fully probe these models for  $T_{RH} > 3 \times 10^8$  GeV (see Fig. 69).

### 3.6 Beyond WIMP DM

As mentioned in the introduction, there is a variety of DM models where the observed relic density is obtained by a mechanism different from WIMP freeze-out, but which nevertheless are testable in collider experiments.

Here we will discuss an example of an asymmetric DM (ADM) model, a scenario with a composite hidden sector, a model of super-WIMPs and a variation of supersymmetry where the abundance of the DM candidate, the gravitino, is set by decays of the next-to lightest supersymmetric particle. All these

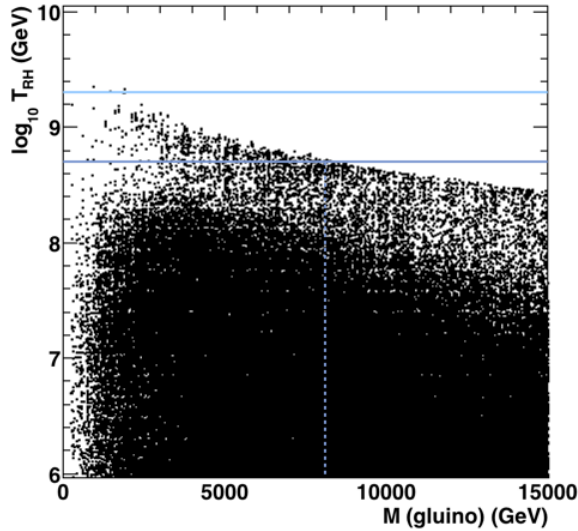


**Fig. 69:** Distribution of DM-motivated pMSSM points with gravitino LSP, neutralino NLSP and SUSY masses up to 20 TeV in the re-heating temperature vs. gluino mass plane. A constraint on the gluino mass can exclude gravitino LSP models with thermal leptogenesis requiring re-heating temperatures above  $\sim 5 \times 10^8$  GeV.

models lead to collider signatures that could be detectable at a hadron collider but which are different from the usual DM search channels. Their detectability should therefore also be taken into account when discussing future collider experiments.

What this section is not, but what would be highly desirable for the future, is a full classification of beyond-WIMP DM signatures which are relevant for colliders. In particular the testability of the ADM paradigm (and not just particular models) at a future collider should be analyzed further.

### 3.6.1 Asymmetric DM through the Higgs Portal

The Higgsogenesis scenario introduced in Ref. [538] is one of the most compact ADM models. The DM sector consists of a pair of a vector-like  $SU(2)$  doublet of fermions  $X_2$  and a neutral fermionic singlet  $X_1$  (the DM candidate), and is thus similar to the singlet doublet models mentioned above and to the Bino/Higgsino scenario, which can be probed at a 100 TeV collider up to masses of order 1.2 TeV, see Fig. 45 and Ref. [70] for more details.

The basic idea is to use the chemical potential of the Higgs to transfer an asymmetry between the SM and the DM sector. After an asymmetry is generated in the visible sector, but before electroweak symmetry breaking, the Higgs carries a nonzero charge asymmetry, which is transferred to the DM sector by an operator

$$\mathcal{L} \supset \frac{1}{\Lambda_2} (H^\dagger X_2)^2 + \text{h.c.}, \quad (63)$$

which is possible for values of  $\Lambda_2$  up to the GUT scale. A small Yukawa coupling  $y_H \bar{X}_2 X_1 H$  allows  $X_2 \rightarrow X_1 H$  decays, which transfer the asymmetry to  $X_1$  once the temperature drops below  $M_{X_2}$ , and which should happen after the transfer operator freezes out. The inverse process, where an asymmetry generated in the dark sector is transferred to the SM, is also possible with this mechanism.

In Ref. [538] it was shown that this mechanism can give the correct DM relic abundance for a range of DM masses from 10 GeV to 10 TeV, which should at least partially be in range of a future hadron collider. A more detailed study would be welcome.

Note that while the Higgsogenesis mechanism is minimal in the sense that no complicated transfer sector is possible, the problem of annihilating the symmetric component is not yet addressed. Indeed Ref. [538] introduces an auxiliary mediator  $\phi$  such that the DM can annihilate through the process  $X_1\bar{X}_1 \rightarrow \phi\phi$ , with  $\phi$  later decaying to SM particles. In this case the constraints from light mediator searches (see Section 3.4.1) become relevant, and additional studies for light scalar portals at 100 TeV are needed.

Instead if one demands that the symmetric component of DM in ADM models annihilates directly into SM particles, then one can use a similar approach as for WIMP particles, namely by either classifying the annihilation channels using effective operators or, as done in the WIMP section above, using the particles that mediate the annihilation. The main difference is that now the annihilation has to be **stronger** than in the WIMP case, since the relic abundance should be dominated by the asymmetric contribution, otherwise it would just be another WIMP scenario. For ADM annihilating to SM quarks, this was studied in [539, 540] using effective operators to parameterise the interactions. An update of this study using the simplified model approach discussed above, and including projections to 100 TeV hadron colliders, would be useful.

Alternatively if the ADM candidate is part of a complex, possibly composite dark sector, then the fast annihilation of the symmetric component into unstable dark sector states can be a natural consequence of the model, and such an example is discussed in the next section.

### 3.6.2 Dark QCD, Hidden Valley DM

Models where the DM candidate is a stable composite state of a QCD like dark sector are well motivated, simply by comparison with the case of the proton in QCD. Stability of DM would be guaranteed by global DM number conservation, and the mass scale can be generated through dimensional transmutation from a small coupling at a high scale.

Such models were originally considered in the context of parity symmetric "mirror world" scenarios [541–544], where the DM would be composed of mirror protons. However in those scenarios the only interactions of the visible world with the dark sector are gravitational, such that they are not relevant for collider phenomenology (and indeed are difficult to verify overall).

In [525, 528] so called Hidden Valley were introduced where a QCD like confining hidden sector communicates with the SM through heavy mediators, and DM models based on this general construction were introduced e.g. in [545–548]. The main idea is that the DM candidate is a composite baryonic bound state made out of dark quarks of a "dark QCD" which, similar to the proton in the SM, is stable because it carries a conserved DM number, and with a mass of order of the GeV scale set by the dark QCD confinement scale  $\Lambda_D$ . A heavy TeV scale mediator  $X$  is responsible for sharing the asymmetry between the SM and the dark sector. Fast annihilation of the symmetric DM component is now guaranteed by the equivalent of proton anti-proton annihilations into pions in QCD, i.e. the DM annihilates to dark pions. The heavy mediators itself can allow the dark pions to decay back to SM particles, therefore no additional light mediators have to be introduced by hand.

Observability of such a dark sector is mainly determined by whether the mediator particle can be produced at a collider. If this is the case, the phenomenology can be quite spectacular, since the strong dynamics in the hidden sector can produce dark jets, events with many displaced vertices, final states with many heavy flavours, and more [528, 549].

Let us first consider one characteristic signature dubbed "emerging jets" in [550], where the mediator  $X$  is pair produced and decays to quarks and dark quarks. While each quark will undergo a regular shower and hadronization process and give rise to jets, the dark quarks will shower in the dark sector first and produce dark jets made out of mostly dark pions. These dark pions naturally have lifetimes of order millimeters to meters, and therefore decay back to SM particles throughout the detector, collimated within a "dark jet". The strategy proposed in [550] is to reconstruct regular multi-jet events and then

search for emerging jets, i.e. jets with few or no tracks pointing back to the interaction point, in the multi-jet sample. It was found that requiring two emerging jets in one event almost fully removes the QCD backgrounds, which mostly come from long lived neutral mesons decaying in the detector. At the 14 TeV LHC this class of models can be probed for mediator masses up to 1.5 TeV which, by applying naive parton luminosity scaling<sup>15</sup>, implies a reach of up to 9 TeV at a 100 TeV machine with  $3 \text{ ab}^{-1}$ .

A variation of the above scenario occurs when the dark pions in the shower have different lifetimes, ranging from prompt decays to particles stable enough to escape the detector. In this case one gets a jets plus missing energy signal, with the missing energy correlated with the jet directions. Reference [551] proposes a search for such events coming from the decay of a  $Z'$  mediator into hidden sector particles, which utilises the transverse mass computed from the jets and missing energy to distinguish from QCD backgrounds. At the LHC the projected reach is 3.5 TeV, which should scale up to 20 TeV at a 100 TeV collider.

Finally if the hidden sector communicates with the SM mainly through the Higgs portal, then exotic Higgs decays involving displaced vertices might be the leading tool to probe such dark sectors [470, 526]. A 100 TeV machine is an ideal tool to search for exotic Higgs decays, simply due to the large amount of Higgs bosons produced there (this is discussed in the accompanying Higgs at 100 TeV document).

The main point of this section is to introduce some examples of DM models which give rise to signatures which are different from the well known missing energy searches and also different from standard mediator searches. Detectability at a hadron collider in these cases is mainly due to particles associated with the DM sector, but not the DM itself<sup>16</sup>, and this is also the reason why new search strategies are possible and necessary.

A possible classification of signatures should be possible in two steps: First, one specifies how the dark sector communicates with the SM. This is very similar to the WIMP case, so the classification of SM and BSM mediators done above can be applied here as well. The second step is to classify the dynamics in the dark sector itself. This includes distinguishing perturbative and non-perturbative dark sectors, and a classification of additional symmetries which could for example give rise to a hierarchy of lifetimes or further constrain the interactions of the mediator.

### 3.6.3 Radiating DM

**Radiation in the Dark Sector** At the spectacular partonic center of mass energies afforded by a 100 TeV collider, radiative processes reach unprecedented levels. This is true not only for QCD and electroweak interactions, but also for any new physics sector that contains light particles with appreciable couplings. A particularly well-motivated example is self-interacting DM [552, 553], which could potentially resolve shortcomings of our present understanding of cosmic structure formation on dwarf galaxy scales (see also [554, 555]). Moreover, DM self-interactions can also lead to Sommerfeld enhancement in DM annihilation [556–558], and possibly even to the formation of DM bound states [559, 560].

Perhaps the leading candidate for the mediator of DM self-interactions is a dark photon  $A'$ —the gauge boson of a corresponding to a new local  $U(1)'$  symmetry in the dark sector. To be phenomenologically relevant,  $A'$  is typically light (MeV–GeV), has relatively strong couplings to DM ( $\alpha' \sim 0.01$ – $0.1$ ), and tiny couplings to the SM sector through kinetic mixing with the photon. The dark sector Lagrangian in such a scenario reads

$$\mathcal{L}_{\text{dark}} \equiv \bar{\chi}(i\not{\partial} - m_{\chi} + ig_{A'}A')\chi - \frac{1}{4}F'_{\mu\nu}F'^{\mu\nu} + \frac{1}{2}m_{A'}^2 A'_\mu A'^\mu - \frac{\epsilon}{2}F'_{\mu\nu}F^{\mu\nu}. \quad (64)$$

Here,  $\chi$  is the fermionic DM particle with mass  $m_{\chi}$ ,  $g_{A'} = \sqrt{4\pi\alpha'}$  is the  $U(1)'$  gauge coupling,  $m_{A'}$  is the dark photon mass, and  $\epsilon$  is the kinetic mixing parameter, which is typically  $< 10^{-3}$ . We remain ag-

<sup>15</sup><http://collider-reach.web.cern.ch>

<sup>16</sup>This is also true e.g. for the disappearing track search which is crucial for the Wino scenario discussed above.

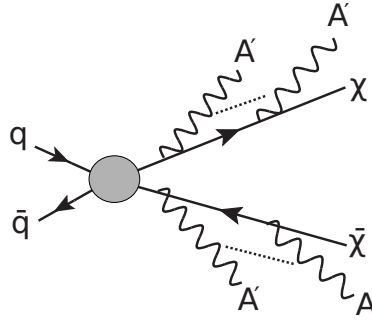


**Fig. 70:** The process that gives radiating DM its name: production of two DM particles  $\chi$ , followed by the emission of several soft or collinear dark photons  $A'$  [561].

nostic about the origin of the dark photon mass—it could originate from a dark sector Higgs mechanism or from the Stückelberg mechanism.

When DM is produced with a large boost at a collider, there is a high probability that additional collinear  $A'$  bosons are radiated (see Fig. 70) [561]. This is particularly true if the DM itself and the dark photon are rather light, for instance on the order of GeV, where direct detection bounds are weak. The higher the center of mass energy of the process, the more  $A'$  bosons are radiated, as illustrated in Fig. 71. These  $A'$  bosons eventually decay to observable SM particles through the kinetic mixing term in Eq. (64), with the exact branching ratios depending sensitively on  $m_{A'}$  (see Fig. 2 in Ref. [561]). Depending on the value of  $\epsilon$ , the decays can be either prompt or displaced. Phenomenologically, the final state of the process  $pp \rightarrow \bar{\chi}\chi + nA'$  thus consists of two “jets” of collimated  $A'$  decay products, plus missing energy.

**Phenomenology of Radiating Dark Matter** Depending on the decay modes, these  $A'$  jets can be classified into one of the following categories:

- **Lepton Jets.** If all  $A'$  bosons radiated by a DM particle decay leptonically, a large number of collimated leptons is expected. Such lepton jets have been discussed previously for instance in Refs. [470, 516, 518, 564–570]. Experimentally, lepton jets have been searched for in Refs. [530, 571]. SM backgrounds to these searches are extremely low, making them a particularly sensitive probe of new physics. This is especially true for  $m_{A'} \lesssim 2m_\pi$ , where all  $A'$  bosons decay leptonically. At larger  $m_{A'}$ , the branching ratio for  $A' \rightarrow \ell^+\ell^-$  varies between 20% and 70%.
- **Mixed Jets.** If some of the  $A'$  in the dark photon jet decay leptonically and others decay hadronically, we expect a QCD-like jet with anomalously large lepton content. This signature can be distinguished from ordinary QCD jets by looking for an anomalously large energy deposit in the electromagnetic calorimeter and/or the muon system. Moreover, for displaced  $A'$  decays, the occurrence of displaced vertices is a smoking gun signature.
- **Hadronic Jets.** If all collimated  $A'$  bosons decay to hadrons, they closely resemble a QCD jet. Nevertheless, if the kinetic mixing parameter  $\epsilon$  is so small that  $A'$  decays are displaced, a separation from SM backgrounds is possible.

**Why go to 100 TeV** It is clear from Fig. 71 that a search for radiating DM could greatly benefit from the increased center of mass energy afforded by a 100 TeV collider: at higher  $\sqrt{\hat{s}}$ , the probability that a DM particle radiates at least one  $A'$  is much higher than at the LHC, and in many events, several  $A'$  bosons will be emitted per DM particle, making the signature even more spectacular. Of course, the relation between the partonic center of mass energy  $\sqrt{\hat{s}}$  and the collider energy  $\sqrt{s}$  depends on the details of the DM production process. If DM is produced through an  $s$ -channel mediator with mass at the

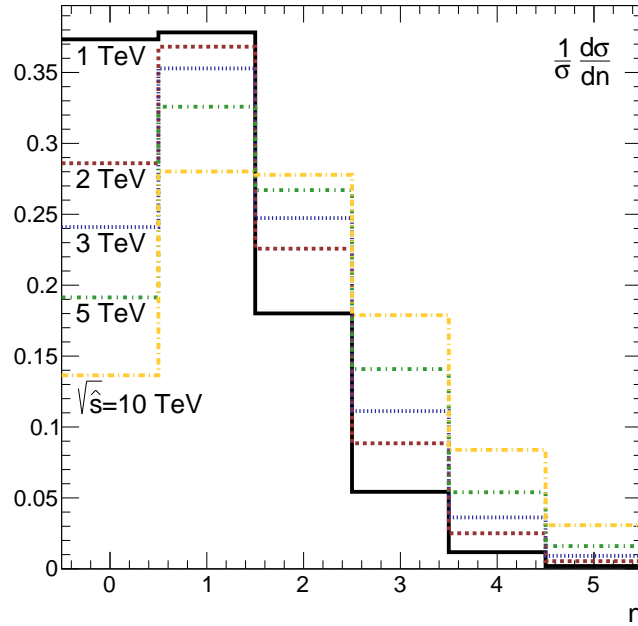


**Fig. 71:** The distribution of the number of dark photons  $A'$  radiated in each DM pair production process  $pp \rightarrow \bar{\chi}\chi$  for several values of the partonic center of mass energy  $\sqrt{\hat{s}}$ . We have used a dark fine structure constant of  $\alpha' = 0.05$ , a DM mass of  $m_\chi = 4$  GeV, and a dark photon mass  $m_{A'} = 1.5$  GeV. The computation was carried out in Pythia 8 [261, 562, 563], using the hidden valley model implemented therein. See Ref. [561] for an analytic treatment of dark radiation.

electroweak scale,  $\sqrt{\hat{s}}$  is typically similar to the mediator mass if that mass is kinematically accessible. Naturally, at a 100 TeV collider, much heavier mediators can be probed than at the LHC. For off-shell production, e.g. through colored  $t$ -channel mediators such as squarks,  $\sqrt{\hat{s}}$  is determined by the valence quark PDFs. Once again, a 100 TeV machine would have a significant edge over the LHC. In fact, dark radiation cannot be probed in such  $t$ -channel scenarios at the LHC at all. At 100 TeV, such restrictions are removed, allowing a 100 TeV collider to probe radiating DM in all of the most important electroweak-scale production channels.

**Some Thoughts on Search Strategies and Detector Design** The sensitivity of a search for radiating DM hinges crucially on the analysis cuts imposed. Questions to consider in designing a search for radiating DM are

- **Is there a signal in the tracking detector?** Most prompt  $A'$  decays will lead to such signals, but for displaced decays of longer lived  $A'$  bosons, it will usually be absent. Moreover, some subdominant decay modes ( $A' \rightarrow K^0 \bar{K}^0$  and  $A' \rightarrow \pi^0 \gamma$ ) do not yield a tracker signal.
- **Is there a signal in the calorimeters?** Once again, the presence of such a signal depends on the  $A'$  decay mode:  $A' \rightarrow \mu^+ \mu^-$  is not visible to the calorimeters, while all other decay modes are.
- **What fraction of the decay energy is deposited in the electromagnetic calorimeter?** (as opposed to the hadronic calorimeter). For short-lived  $A'$ , this fraction allows to distinguish different decay modes. For displaced decays, however, even a decay like  $A' \rightarrow e^+ e^-$  can deposit its energy mostly in the hadronic calorimeter.

It is clear from these considerations that the sensitivity of a search for radiating DM depends sensitively on the detector design. In particular, the values of the kinetic mixing parameter  $\epsilon$  that can

be probed efficiently in the search for displaced decays change with the radial size of the detector. This statement can be quantified by considering that the  $A'$  decay rate to leptons is given by

$$\Gamma(A' \rightarrow \ell^+ \ell^-) = \frac{1}{3} \alpha \epsilon^2 m_{A'} = \frac{1}{8 \times 10^{-6} \text{ cm}} \left( \frac{\epsilon}{10^{-3}} \right)^2 \left( \frac{m_{A'}}{\text{GeV}} \right) \quad (65)$$

in the limit  $m_\ell \ll m_{A'}$  (see Ref. [561] for a more detailed discussion of  $A'$  decays). For this reason, it may be useful, for instance, to have one rather compact detector and one fairly large one (like at the LHC). Thinking even further, a dedicated search for radiating DM in the small  $\epsilon$  region might benefit from dedicated muon detectors placed far away  $\gtrsim 10$  m from the interaction point. Of course, with such a system it would be difficult to achieve good angular coverage.

### 3.6.4 SuperWIMPs and Gravitino DM

Many extensions of the SM introduce additional particles which are only very weakly coupled to the SM, and which are potential DM candidates. Prime examples are the axion as a solution of the strong CP problem, and the gravitino which arises in supersymmetric models involving gravity. In some cases the mechanism that sets the relic density of such particles is accessible at colliders, and we will discuss one such example now, following [424] (see also [572–575]).

Consider a super-WIMP (SWIMP) with mass  $m_{\text{SWIMP}}$  which is stable on cosmological time scales, but which is not thermalized in the early universe, and furthermore a weakly interacting particle  $L$  which freezes out with relic abundance  $\Omega_L$ . If  $L$  decays to the SWIMP with a lifetime short enough to not upset nucleosynthesis, then the super-WIMP can be the DM candidate with abundance set by

$$\Omega_{\text{SWIMP}} h^2 = \frac{m_{\text{SWIMP}}}{m_L} \Omega_L. \quad (66)$$

The difference from a WIMP scenario is that now  $L$  can be charged, and this is the case for example in supersymmetric models where  $L$  can be a charged slepton, or a KK-lepton in extra-dimensional models. Signatures of these scenarios now include heavy stable charged particles travelling through the collider and displaced decays of  $L$  in the detector which can give rise to either displaced vertices or kinked tracks. Since  $L$  is the natural end product of any new particle which is produced and which carries the DM symmetry, these signatures will also appear in combination with jets and leptons. Another exciting possibility is that  $L$ , if charged, can lose energy rapidly and therefore might get stuck in the detector or in the surrounding material [573], where it can be trapped and analyzed before it decays.

The reach for these signatures should scale with the center of mass energy, since they are free from SM backgrounds. Therefore a 100 TeV collider can certainly probe  $m_L$  in the multi-TeV range, maybe even reach 10s of TeV, provided that future detectors have at least the same capabilities as the LHC experiments.

## 3.7 DM Summary

In this section, the reach of a 100 TeV collider for large classes of DM models was explored and compared to the reach of the 14 TeV LHC, indirect and direct DM detection experiments and other collider and laboratory experiments. As one would have expected, a 100 TeV machine vastly increases the mass range up to which DM models can be probed, and in several cases the upper mass limit indicated by the observed DM density is reached. In other words:

- There are well defined DM models whose parameter space can be fully probed at a 100 TeV collider.

Maybe the simplest example is the Wino (SU(2) triplet) scenario studied in Sections 3.3.1, 3.3.2, 3.3.4. Here one important aspect is that monojet searches alone can not cover the theoretically motivated DM

Final State	Analysis	Section
jet+MET	Wino, Higgsino DM	<a href="#">3.3.1 - 3.3.4</a>
jet+MET	Higgs Portal	<a href="#">3.3.5</a>
jet+MET	Simplified Vector/Axial	<a href="#">3.4.1 - 3.4.3</a>
jet+MET	Simplified Scalar/Pseudo	<a href="#">3.4.1 - 3.4.3</a>
jet+MET	Gluon/stop coannihilation	<a href="#">3.5.1</a>
VBF jets +MET	Wino, Higgsino DM	<a href="#">3.3.1 - 3.3.2</a>
VBF jets +MET	Higgs Portal	<a href="#">3.3.5</a>
photon+MET	Wino	<a href="#">3.3.2</a>
Disappearing tracks	Wino,Higgsino	<a href="#">3.3.1 - 3.3.2</a>
Disappearing tracks	Fiveplet DM	<a href="#">3.3.3</a>
Disappearing tracks	Relic-Neutralino	<a href="#">3.3.4</a>
lepton+ $\gamma$ +MET	Relic-Neutralino	<a href="#">3.3.4</a>
$Z_D \rightarrow ll+(Z_D \rightarrow ll)$	Dark Photons	<a href="#">3.4.4, 3.6.3</a>
displaced jets	Dark QCD/Hidden Valley	<a href="#">3.6.2</a>
long lived charged particle	Super-WIMPS/Gravitino	<a href="#">3.6.4</a>
dijet	Simplified Vector/Axial	<a href="#">3.4.1 - 3.4.3</a>

**Table 5:** Overview of the final states and the associated model, with a link to the respective section.

mass range, however the combination with either indirect detection or with disappearing track searches is sufficient to fully probe the viable parameter space.

Monojet and related missing energy searches are essential to establishing the presence (or absence) of DM at a collider, and in many scenarios they extend the reach beyond parameter space accessible in direct detection, as can be nicely seen for example in Figs. 58, 59. However also here it is important to notice that full coverage of the viable parameter space is often only possible by combining these searches with other channels. A nice example is provided in Fig. 62, where the search for the mediator in the dijet channel is necessary to probe the tuned region of parameter space where resonant annihilation allows for very large DM and mediator masses.

Fortunately a hadron collider allows the study of many signal channels in parallel, and standard multijet + MET searches can easily be combined with disappearing track or displaced object searches. The importance of those more exotic signatures is not only highlighted by their ability to close of the parameter space of some of the minimal models discussed in Sections 3.3.1-3.3.4, but also because they give access to a broader range of DM models which might not easily show up in missing energy signatures, like some of the examples discussed in Section 3.6.

A list of final states which are relevant for DM searches at a 100 TeV collider is given in Table 5. Here information is provided which models are probed by which final states and, for models which are testable in several final states, which ones are the most sensitive. It should be emphasised that this list is not complete but instead based on the models and channels for which studies are available, and in particular scenarios for which only one channel is sensitive would benefit from further studies.

While the overall prospects for observing DM at a 100 TeV hadron collider are promising, one should not forget that there are models which are notoriously difficult to probe. The worst offender is one of the simplest models, namely the Higgs portal with a singlet scalar DM candidate, discussed in Section 3.3.5. The good news here is that this model also has a clear prediction for the direct detection rate, which is accessible in the next generation of experiments. Further studies of such a DM candidate might then require a linear collider, so this should be seen as additional motivation to study the complementarity of high energy lepton colliders with a 100 TeV hadron collider.

## 4 Other BSM Signatures

This section is devoted to the assessment of the potentials of a future circular hadron collider at 100 TeV (to which we will sometimes refer simply as FCC) in terms of BSM signature that are not “typical” of supersymmetric and dark matter models. Of course, most of the signatures discussed here can be relevant for certain such models, however they do not constitute their key ingredient nor their smoking gun signatures in a way clarified in the following discussion. In particular the goal of this section can be summarized in two points:

- Study motivated and generic signatures that allow to test new physics. With motivated and generic we mean signatures that are shared by large classes of new physics scenarios.
- Define collider and detector benchmarks that allow the highest possible sensitivity to these motivated and generic signatures and that can help in a concrete assessment of the needed design of the future facilities.

The results will be presented as a list of more or less detailed studies of concrete BSM models, which predict a particular signature, shared by broad BSM scenarios. The cases presented in what follows generally fall into three broad categories:

- Single production of new particles;
- Pair production of new particles;
- Precision measurement aimed at constraining NP indirectly.

However, since single and pair production can constitute, in some cases, like for instance fermionic top partners, inseparable signatures of motivated BSM scenarios, we prefer to separate the results into three sections devoted to new bosonic resonances, which are signatures typically interesting for single production and new fermionic resonances, which, depending on the scenario can be interesting both in the single production (in association with other SM particles) and pair production. Finally we will devote a last section to the non-resonant signatures, which are aimed at constraining new physics indirectly. We can already get a preliminary idea, which will be refined in the following sections, of the reach of a 100 TeV collider on high invariant mass objects, by considering the single production of a general heavy resonance  $R$ . For the production of a narrow resonance  $R$ , which can be described as a  $2 \rightarrow 1$  processes, the inclusive tree level production cross-section can be written as

$$\sigma(pp \rightarrow R + X) = \sum_{i,j \in p} \frac{\Gamma_{R \rightarrow ij}}{M_V} \frac{16\pi^2(2J_R + 1)}{N_{\text{pol}}} \frac{C_R}{C_i C_j} \frac{dL_{ij}}{d\hat{s}} \Big|_{\hat{s}=M_R^2}, \quad (67)$$

where  $\Gamma_{R \rightarrow ij}$  represent the partial widths of the corresponding decay process  $R \rightarrow ij$ ,  $i, j = \{g, q, \bar{q}, W_{L,T}, Z_{L,T}, \gamma\}$  are the colliding partons in the two protons, and  $dL_{ij}/d\hat{s}|_{\hat{s}=M_R^2}$  is the corresponding parton luminosity evaluated at the resonance mass. The factor  $J_R$  is the spin of the resonance,  $C_R$  the dimension of its color representation,  $C_{i,j}$  are the dimensions of the color representations of the two partons and  $N_{\text{pol}}$  is the number of polarization states of the incoming partons contributing to the production. This last quantity is equal or smaller than the sum over polarization  $(2s_i + 1)(2s_j + 1)$ , where  $s_i, s_j$  are the spins of the incoming partons. For instance, in the case of a scalar produced by gluon fusion, like the Higgs boson,  $N_{\text{pol}} = 2$ , since only the  $(+-)$  and  $(-+)$  polarization configurations of the initial gluons contribute to the production of a  $J = 0$  state. If needed, the cross-section in Eq. (67) can be corrected by a  $k$ -factor to take into account higher order radiative corrections. In Fig. 72 the parton luminosities  $dL_{ij}/d\hat{s}$  as function of  $\hat{s}$  are shown for quark and gluon partonic initial states, and in particular for  $gg, gq, q\bar{q}$  and  $qq$  configurations. There are two kind of corrections to the expression of the production cross section in Eq. (67), which come from width effects, suppressed by  $\Gamma/M$  and from the effect of parton luminosities varying too fast, within a region corresponding to the resonance

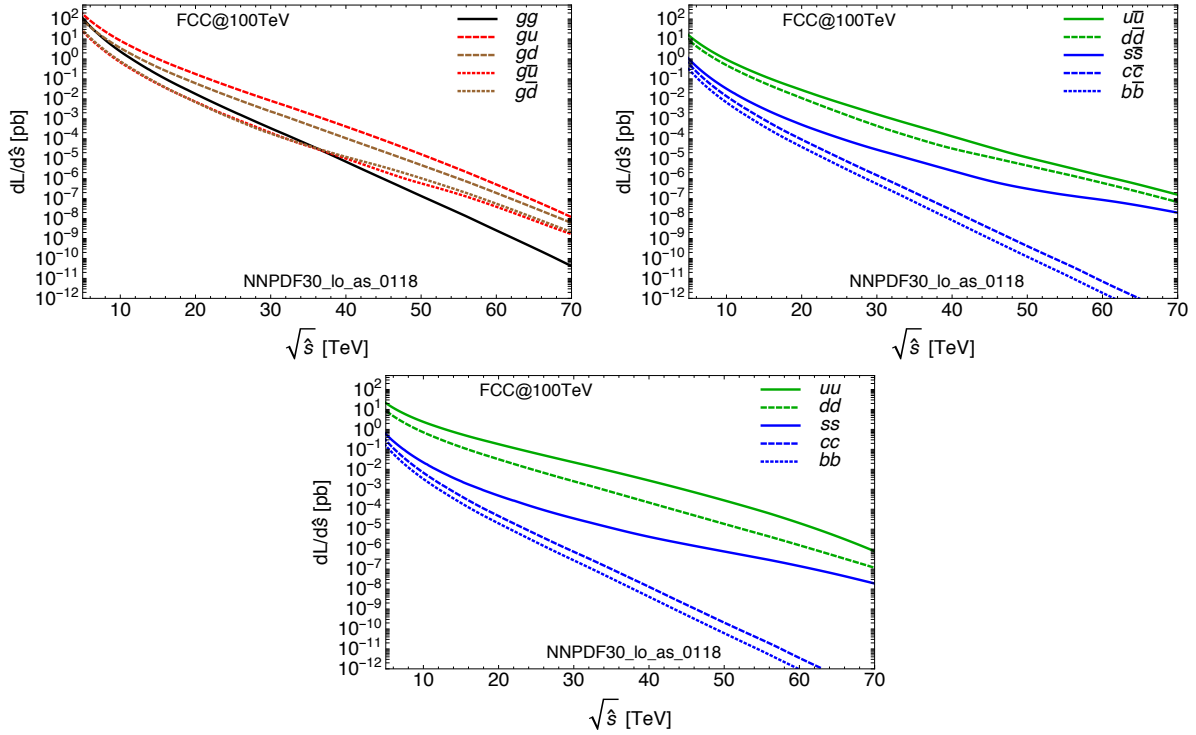


**Fig. 72:** Parton luminosities  $d\mathcal{L}/d\hat{s}$  as functions of the partonic center of mass energy  $\sqrt{\hat{s}}$  for a 100 TeV proton-proton collider, computed using the NNPDF30\_LO\_as\_0118 PDF set [443]. *Upper left:*  $gg$ ,  $qg$  and  $q\bar{q}$  initial states; *Upper right:*  $q\bar{q}$  initial states; *Lower:*  $qq$  initial states.

width, to be considered constant. In this latter case, approximating the integral over the parton luminosities with their value at the resonance mass fails, generating a large off-shell tail at low masses. This threshold effect usually corresponds to the region where the parton luminosities start to decrease faster than exponentially, which roughly corresponds, in Fig. 72, to the point where the curves change their convexity.

A simple application of the formula in Eq. (67) for the production of new resonances is given by the production of exotic color resonances. In Fig. 73 we show the production cross sections<sup>17</sup> for some different colored resonances corresponding to charged and neutral color-octet vectors, charged color-sextet vectors with fractional charge and excited quarks with spin 3/2. From the figure it is clear that production cross sections of the order of fb or hundreds of ab are expected for colored states in the mass range 25-50 TeV. Considering the large integrated luminosity planned for a 100 TeV collider, of several inverse ab, some of these states should be accessible up to masses even above 50 TeV, depending on their production mechanism. As it is clear from Fig. 72, the color-octet vectors, being produced by  $q\bar{q}$  have the lowest production cross section, followed by the excited quark, produced by  $qg$  and the diquark sextets, produced by  $qq$ . In general, all these colored resonances are expected to decay back to di-jets. Assuming an integrated luminosity of several inverse ab a 100 TeV collider should be able to extend the reach on colored resonances of the LHC from a few TeV, to the 30-60 TeV region.

Another interesting possibility is the production of new gauge bosons, such as  $Z'$  and  $W'$  vectors. These are typically produced by Drell-Yan  $q\bar{q}$  annihilation and decay to two leptons or lepton-neutrino depending on the charge, leading to final states that are effectively zero background in the multi-TeV

<sup>17</sup>The widths relevant to compute these production cross sections using Eq. (67) are set to the value corresponding to interactions fixed by a (model-dependent) dimensionless coupling that we have set to one for illustration [576].

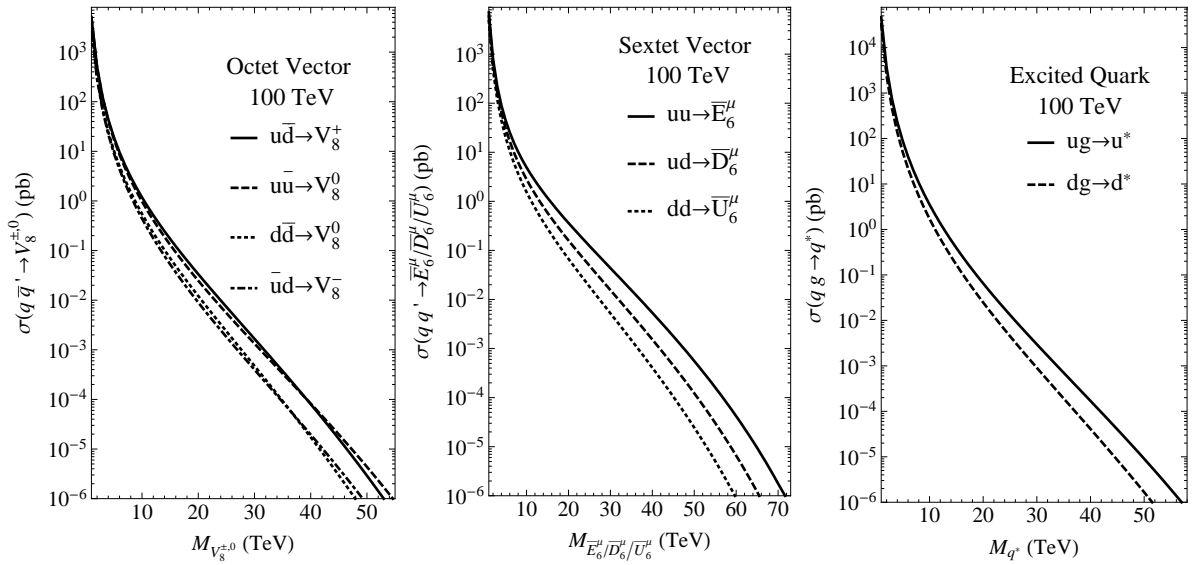


**Fig. 73:** Production cross sections for exotic colored resonances at 14 TeV and 100 TeV. *Left:* charged and neutral color-octet vector states; *Center:* fractionally charged color-sextet vector states (di-quark-like); *Right:* spin-3/2 excited quark states.

region. The typical cross sections of different  $Z'$  and  $W'$  models [577] are shown in Fig. 74. Again the reach of the LHC, which is around 5 TeV for such states, can be significantly extended at a 100 TeV collider, up to 25-35 TeV. The case of new vector bosons arising as composite resonances is also very interesting. In Fig. 75 we show the cross section of a  $\rho$ -like state arising in minimal composite Higgs models [578] for typical values of the parameters. In this case decays to two electroweak gauge bosons are typically enhanced compared to di-lepton and lepton-neutrino final states, corresponding to a reach that extends up to about 20 TeV. Scenarios presenting new  $Z'$  and  $W'$  bosons are studied in more detail in Sections 4.1.1, 4.1.2, 4.1.4, respectively in the di-lepton and lepton neutrino, di-jet and  $t\bar{t}$  final states. Resonances arising from a strong sector responsible for electroweak symmetry breaking (EWSB) are discussed in Section 4.1.5, where the reach from direct searches in DY production is compared with the indirect reach of leptonic colliders and in Section 4.1.7, where the VBF production is studied in the  $t\bar{b}$  final state.

Up to now we have given some examples of the reach of a 100 TeV collider on single resonance production. Of course also pair productions are extremely favored by the large available center of mass energy. Some of the very well know candidates for pair production searches are the so-called top partners, which can be either scalar, fermions or even vectors [579], depending on the model, whose role is compensating the large sensitivity of the Higgs mass parameter to the top loop contribution responsible for the hierarchy problem of the electroweak scale. On top of these particles, other states with different quantum numbers can be related to naturalness, like for instance color octet fermions, as the gluino in SUSY. All these states related to naturalness will be discussed extensively in this BSM part of the report, both in the SUSY section, focusing, for what concerns colored particles, on stops, sbottoms and gluinos, and in this section, focusing on fermionic partners of the top, usually referred to as just top partners. In order to give a preliminary idea of the reach of a 100 TeV collider on these particles, we show in Fig. 76 the typical production cross sections for both color-triplets [580] and color-octets [581] scalars, fermions and vectors. In the case of color-triplet particles, the spin-0, 1/2, and 1, refer to stop-like,  $T'$ -like and color-triplet vector top partners respectively. In the case of color-octet they correspond to states that are techni-meson-like, gluino-like (both Majorana or Dirac) and KK-gluon-like. Differently to what happens for the single production of resonances, which essentially depend on a free coupling of the new

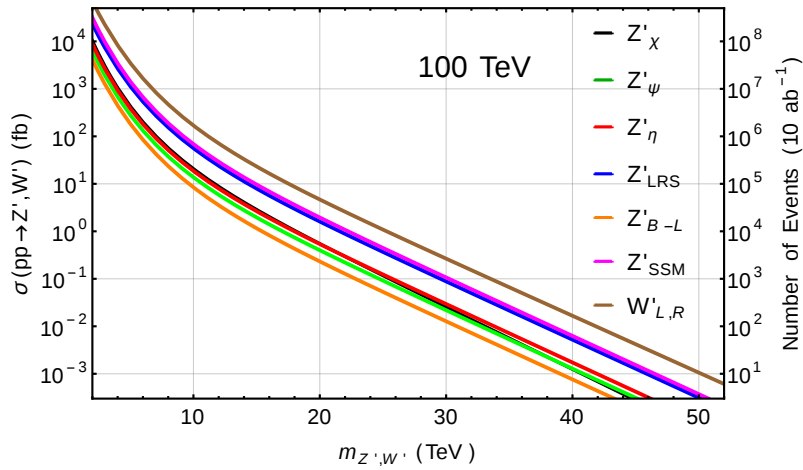


**Fig. 74:** Production cross section of  $W'$  and  $Z'$  gauge bosons in various models [577] at 100 TeV.

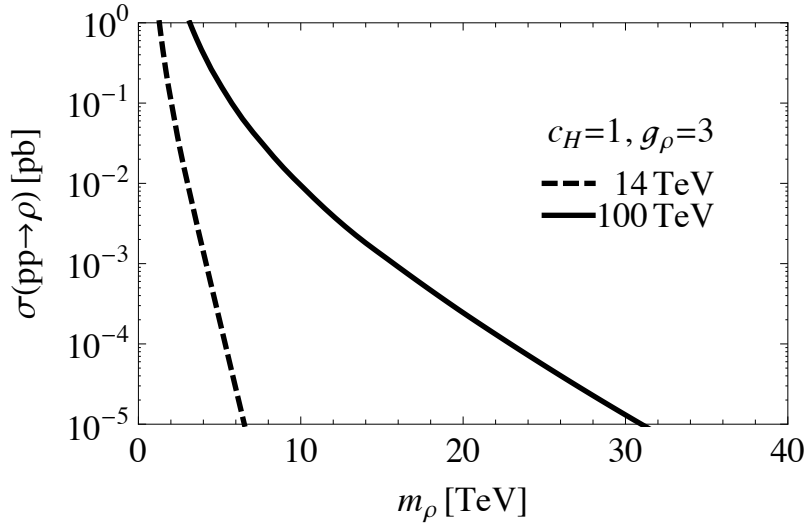


**Fig. 75:** Production cross section of a  $\rho$ -like vector resonance arising in minimal composite Higgs models [578] at 100 TeV. Typical values of the relevant parameters have been chosen.

theory, the pair productions are completely fixed by QCD interactions and, once the quantum numbers under the color gauge group are fixed, their production rate can be determined model independently. Of course, the bigger the color charge and the spin, the bigger the pair production cross section. Provided that the decay channels can be efficiently discriminated from background, the large rates are expected to lead to mass reach that extend from about 5 TeV for color-triplet scalars, to about 15 TeV for color-octet vectors. Concerning colored resonances, fermionic top-partners are discussed in more details in Section 4.2.2, where both single and pair production are considered and in Section 4.2.3, where the top-partners arising in Twin Higgs models are studied in signatures involving displaced decays with a prompt  $t\bar{t}$  pair.

In order to compare the reach on colored resonances produced in pairs, with un-colored ones, we consider the pair production of new heavy leptons. These particles may be motivated in BSM scenarios related to the mechanism of neutrino mass generation. In Fig. 77 we show the heavy leptons pair production cross section. We consider both a triplet [582] and a singlet of  $SU(2)_L$ , denoted by  $T$  and  $N$ . In the case of the triplet, analogously to what happens for the colored particles, the pair production cross section

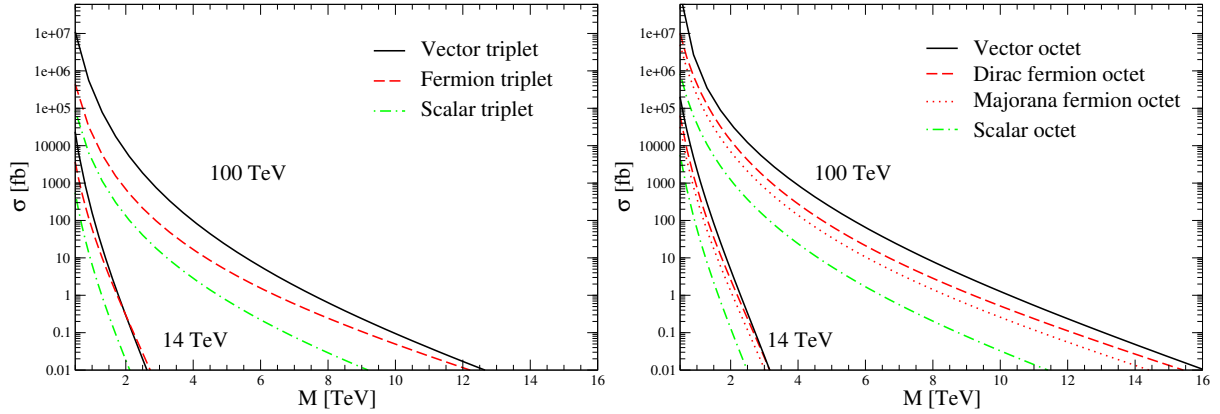


**Fig. 76:** Pair production cross sections of new colored states. *Left:* color-triplets; *Right:* color-octets. The different dashing represent spin-1 (solid), 1/2 (dashed), and 0 (dot-dashed).

is entirely fixed by electroweak interactions [583, 584]. The states in the triplet are expected to be almost degenerate in mass and typically decay into the  $T^\pm \rightarrow W^\pm \nu, Z \ell^\pm, h \ell^\pm$  and  $T^0 \rightarrow W^\pm \ell^\mp, Z \nu, h \nu$  final states, as discussed in Section 4.2.1. From the Figure, we see that depending on the decay channel the reach on these particles, which at the LHC is limited to around the TeV, can be extended at a 100 TeV collider in the range of 5–8 TeV. Concerning the SM singlet  $N$ , we consider its production in association with a SM lepton, which depends on the details of the mixing matrix between  $N$  and the SM neutrinos. In the Figure we show the  $N \ell^\pm$  production cross section normalized to a mixing matrix equal to the identity, which would correspond to the production cross section of a doublet of  $SU(2)$ . Some of these signatures involving heavy leptons are discussed in detail in Section 4.2.1.

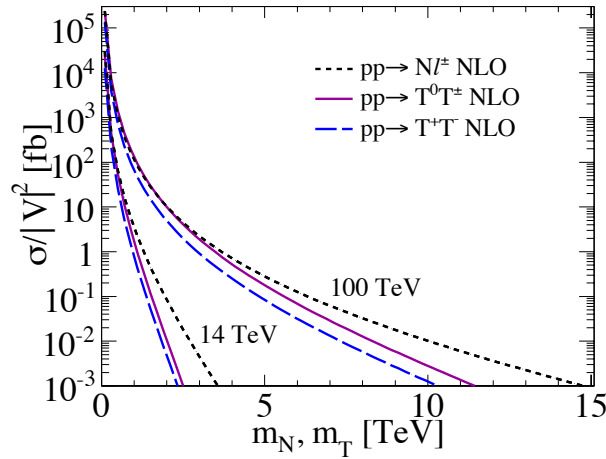


**Fig. 77:** Pair production of new heavy leptons at 14 and 100 TeV, for an  $SU(2)$  triplet ( $T^{\pm,0}$ ) and for a singlet state  $N \ell^\pm$  via mixing. See Section 4.2.1 for details.

## 4.1 New Bosonic Resonances

### 4.1.1 New Gauge Bosons in Dilepton Final States

If a new gauge boson is discovered the next step will be to identify its origins within some underlying UV theory. A necessary step along this road is the determination of the new gauge boson couplings to

Model	1 ab <sup>-1</sup>	10 ab <sup>-1</sup>	100 ab <sup>-1</sup>
SSM	23.8	33.3	41.3
LRM	22.6	31.5	39.5
$\psi$	20.1	29.1	37.2
$\chi$	22.7	30.6	38.2
$\eta$	20.3	29.8	38.0
I	22.4	29.2	36.2

**Table 6:** Discovery reach in the leptonic decay mode for various  $Z'$  models [577] in TeV at  $\sqrt{s} = 100$  TeV for different integrated luminosities. Exclusion reach are roughly  $\simeq 3.5$  TeV larger in all cases.

the various fields of the Standard Model. Here we discuss a set of measurements that have been proposed to access this information and their potential use at a 100 TeV hadron collider.

“Identification” is the first step after a new discovery, i.e., the determination of what it is that has been found. We have been experiencing an example of this procedure in action in the ongoing program to probe the detailed nature of the 125 GeV Higgs boson. In going from the LHC to a 100 TeV collider, the window for the discovery of new gauge bosons is enormously increased as is summarized for the usual canonical scenarios in both Table 6 and Fig. 78. While discovery in the clean Drell-Yan leptonic channels will only require order 10’s of events, the determination of the various couplings necessitates event statistics which are order 10 – 100 times larger. This implies that only new gauge bosons with masses about 10 TeV or more below their corresponding discovery reach will be amenable to coupling extractions for a given value of the integrated luminosity.

Frequently, to simplify the situation as much as possible in the case of a new  $Z'$ , it is assumed that the couplings are generation independent, that  $Z - Z'$  mixing can be neglected (which is a very good assumption for large masses) and that the gauge charge to which the  $Z'$  couples commutes with the corresponding SM generators. Under these assumptions the couplings of the  $Z'$  to the SM fermions are given in terms of only 5 independent parameters corresponding to the SM fermion representations:  $Q_L$ ,  $L_L$ ,  $u_R$ ,  $d_R$  and  $e_R$ . Surrendering any of these simplifying assumptions enlarges the set of independent parameters that need to be determined. On the other hand, in the case of a  $W'$ , the most important quantity to determine is the helicity of its couplings to the SM fermions, which separates potential models into two broad categories.

In order to extract the values of the  $Z'$  couplings in as model-independent of a way as possible we cannot assume that the new gauge bosons will only decay into the known SM particles. This implies that measurements which depend on the new gauge bosons width, such as the production cross section times leptonic branching fraction,  $\sigma B_\ell$ , cannot be used for this purpose. Several of these decay-independent observables (which mostly employ high  $p_T$  lepton triggers) have been proposed and were discussed in detail in Ref. [585], which we will summarize below. First we consider those observables that employ the dilepton discovery mode to extract coupling information.

- The most obvious way to by-pass the shortfall of  $\sigma B_\ell$  as a useful observable is to rescale it by the  $Z'$  width, e.g.,  $\sigma B_\ell \Gamma_{Z'}$  so that it only depends on the couplings above in the narrow width approximation (NWA). The typical values of  $\Gamma_{Z'}/M_{Z'}$  in the models in Table 6 are of the order of 1% or so. One finds that this observable,  $\sigma B_\ell \Gamma_{Z'}$ , varies by a factor of about 20 for just these six familiar sample models thus showing its strong coupling sensitivity. Since this quantity makes use of the discovery channel, only a few hundred events are necessary to obtain a reasonably reliable

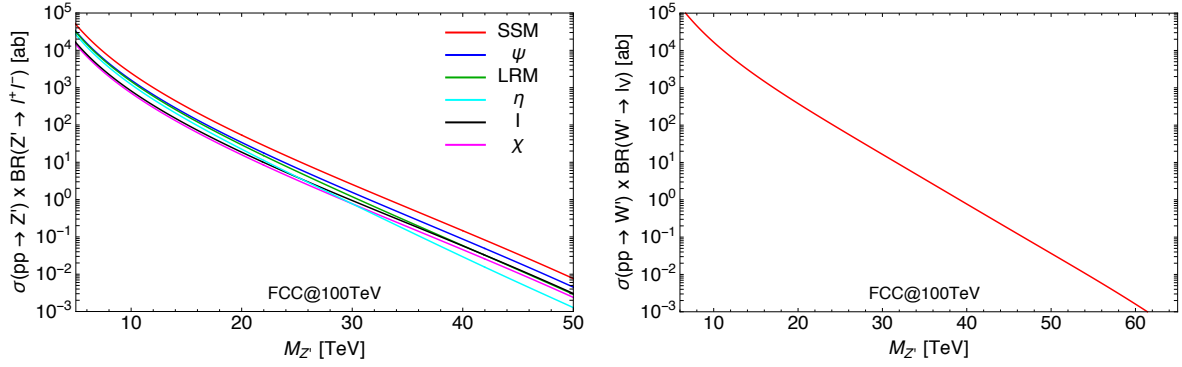


**Fig. 78:** *Left:* Cross section times leptonic branching fraction,  $\sigma(pp \rightarrow Z') \times \text{BR}(Z' \rightarrow l^+l^-)$ , as functions of the mass for the  $Z'$  models indicated in the legend at  $\sqrt{s} = 100$  TeV. The legend is ordered following the order of the curves at  $M_{Z'} = 20$  TeV; *Right:* same quantity for the SSM/LRM  $W'$  (with  $g_R = g_L$  and Dirac neutrinos).

determination with small (statistical) errors.<sup>18</sup> The main difficulty with employing this observable occurs when the  $Z'$  width is substantially smaller than the dilepton mass resolution so that the value of  $\Gamma_{Z'}$  cannot be trivially determined.

- A familiar observable is the leptonic forward-backward asymmetry,  $A_{FB}$ , which can be obtained from the lepton's angular distribution. In the  $Z'$  rest frame, with  $z = \cos \theta^*$  being defined between the initial quark,  $q$ , and outgoing  $l^-$  direction, this distribution is given by  $\sim 1 + z^2 + 8A_{FB}z/3$ . Note that a non-zero value of  $A_{FB}$  requires vector and axial-vector couplings of the  $Z'$  to both the quarks and leptons. A problem arises in that the  $q$  direction cannot always be identified with the boost direction of the  $Z'$ , which itself is not always cleanly defined (without applying a suitable cut). Similarly, the rapidity coverage for the leptons can be critical especially if it more restricted than the typical ATLAS/CMS value of  $|\eta_\ell| < 2.5$  as larger scattering angles, which show the greatest sensitivity, will have a reduced contribution. All this results in a dilution of  $A_{FB}$  which can be partially compensated for using Monte Carlo. Again, only a few hundred events are needed to obtain a reasonable estimate of  $A_{FB}$  but this increase in required statistics for a fixed luminosity implies a significant reduction in the reach for coupling information extraction. Since both  $u\bar{u}$  and  $d\bar{d}$  initial states will, in general, contribute to  $Z'$  production the knowledge of the PDFs (and their evolution) will be important in the use of  $A_{FB}$  to extract  $Z'$  coupling information. Going beyond NWA it is possible that information on  $A_{FB}$  can be obtained in the interference region below the  $Z'$  peak but this will also require a significant increase in integrated luminosity.
- The last observable that makes direct use of the  $\ell = e, \mu$  discovery channel is the central rapidity ratio ( $r_y$ ), i.e., the fraction of events with lepton rapidities below some cut value compared to those above that same value.  $r_y$  is sensitive to the  $u\bar{u}/d\bar{d}$  admixture in the  $Z'$  couplings and so is also quite sensitive to the  $Z'$  mass due to the running of the PDFs. However, in comparison to the previously discussed observables,  $r_y$  provides somewhat weaker information on the  $Z'$  couplings.
- The  $Z' \rightarrow \tau^+\tau^-$  mode is also potentially powerful, particularly in the case of generation-independent couplings, as the  $\tau$  polarization,  $P_\tau$ , (as can be determined in single-prong decays) can be used to extract the coupling ratio  $v_\ell/a_\ell$ . Even in the 1-parameter  $E_6$  models,  $P_\tau$  can take on values over its entire allowed range  $-1 \leq P_\tau \leq 1$ . However, this mode suffers from the obvious  $\tau$  identification issues in this highly boosted regime and its possible effectiveness for coupling extraction at 100 TeV will require further study.

<sup>18</sup>30 times the events needed for discovery corresponds to roughly a reduction of at least 10 TeV in mass from the discovery reach for the same integrated luminosity.

To get a rough idea of the separation of the various models en route to coupling extraction provided by these observables, consider the top two panels in Fig. 79 which assumes  $L = 5 \text{ ab}^{-1}$  and  $M_{Z'} = 15 \text{ TeV}$ . We see that these six models are all distinguishable from each other except for the two  $E_6$  models,  $\psi$  and  $\eta$ , using just these variables alone.

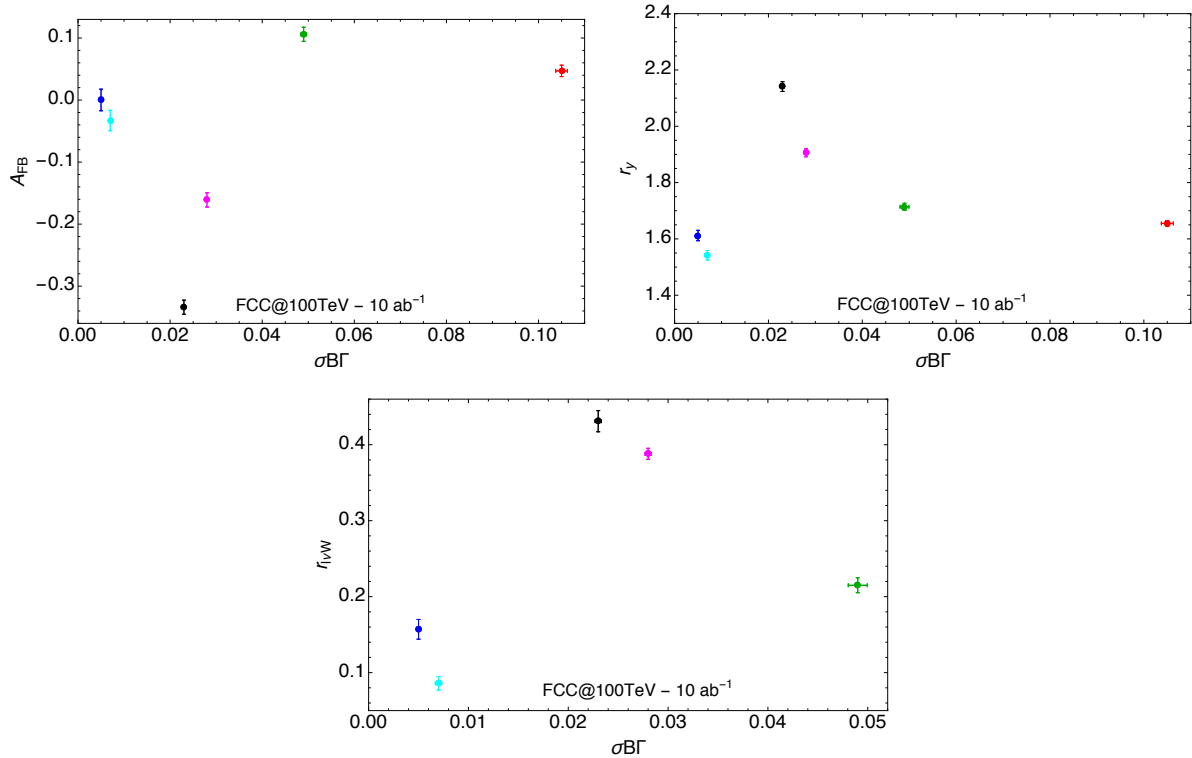


**Fig. 79:** Comparisons of the values of the observables  $A_{FB}$ ,  $r_\gamma$  and  $r_{l\nu W}$  for  $L = 10 \text{ ab}^{-1}$  and  $M_{Z'} = 15 \text{ TeV}$  for the six models shown in Table 6 and Fig. 78 above with the same color coding (from left to right: blue, cyan, black, magenta, green and red, see Fig. 78 for the corresponding models).

Once we go beyond the dilepton channel, numerous possibilities to obtain coupling information are available each with their own strengths and weaknesses.

- Still restricting ourselves to 2-body decays to SM fermions,  $Z' \rightarrow t\bar{t}$  (using boosted top techniques) may be useful if the top polarization can be measured as it is sensitive to the ratio of the LH- and RH-couplings at the  $Z't\bar{t}$  vertex. The use of this variable at 100 TeV requires further study. See Section 4.1.4 for a study of resonances decaying into the  $t\bar{t}$  final state.
- 3-body decays of the  $Z'$  can be useful, e.g., in the absence of  $Z - Z'$  mixing the decay  $Z' \rightarrow \ell\nu W$  occurs by  $W$  emission off of a lepton leg. The  $W$ , being coupled to the leptons in a LH manner, projects out the LH  $Z'$  coupling to leptons as well. Although this decay rate suffers from both 3-body phase space and coupling factors in comparison to  $Z' \rightarrow \ell^+\ell^-$ , it is also  $\log^2(M_{Z'}/M_W)$  enhanced due to the infrared and collinear singularities in the relevant diagrams. This enhancement can be quite important for mass ratios of order 200 that we are considering here. For example, for a  $Z'$  mass of 15 TeV in the LRM the cross section for the  $l^\pm\nu W^\mp$  final state is about 50 ab. One difficulty at these energies is the rather large boost of the final state  $W, Z$  and its small opening angle with respect to the lepton from which it was emitted, i.e., isolation issues. Further, if the  $W, Z$  are found through their dijet decay modes (for statistical reasons) this will not easily allow for  $W, Z$  separation and will likely appear as a fat single jet. However, this final state deserves

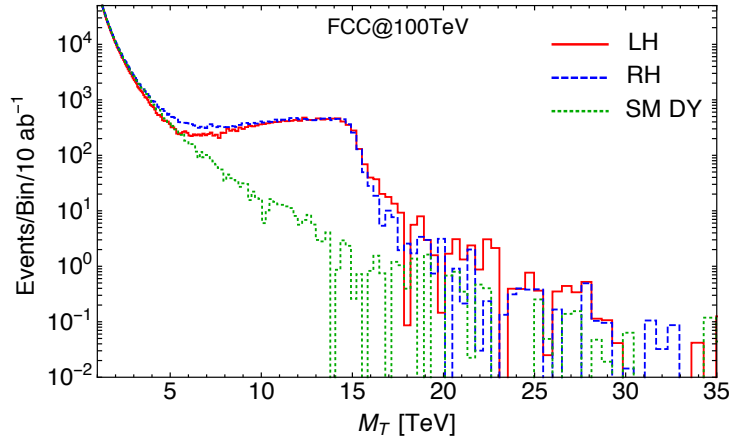


**Fig. 80:** Comparison of the  $W'$  leptonic transverse mass distribution for LH(red,solid) or RH(blue,dashed) couplings assuming a mass of 15 TeV and an integrated luminosity of  $10 \text{ ab}^{-1}$ . The Drell-Yan SM background appears in green(dotted).

further study since the ratio  $r_{\ell\nu W} = \Gamma(Z' \rightarrow \ell\nu W)/\Gamma(Z' \rightarrow \ell^+\ell^-)$  can provide reasonable coupling information as shown in Fig. 79.

- The  $Z'$  can be produced in association with another SM state, e.g.,  $Z'W^\pm$ , by “initial state radiation”. This additional gauge boson can be used as a probe to again “project out” certain combinations of the leptonic  $Z'$  couplings. These channels suffer from some of the same issues as in the case of  $r_{\ell\nu W}$  as  $W^\pm$  and  $Z$  final states will be essentially impossible to distinguish in their dijet decay modes while employing their leptonic decays will require increased luminosity to compensate for the smaller branching fractions. More study is needed.

Now let us very briefly mention the case of a new  $W'$ . If the  $W'$  couples LH and/or neutrinos are Dirac states then the  $W' \rightarrow \ell\nu$  mode is the standard discovery channel (the case of  $W'$  decays involving RH neutrinos will be discussed in Section 4.1.9). For integrated luminosities of 1(10,100)  $\text{ab}^{-1}$  the discovery reach is found to be 31.6(39.1, 46.7) TeV. As mentioned above, the main issue here is whether the  $W'$  couples in a LH or RH manner. Employing *only* this mode in the NWA, however, a purely LH or RH  $W'$  are indistinguishable. One possibility to get around this, similar to that discussed above, is to make use of the  $W' \rightarrow t\bar{b}$  mode and then determine the polarization of the top. Another is to go off-resonance in the transverse mass ( $M_T$ ) region below the  $W'$  Jacobian peak and examine the  $W - W'$  interference; this interference is absent(destructive) if the  $W'$  is RH(LH). This is particularly noticeable when  $M_T \simeq 0.4M_{W'}$ , as can be seen in Fig. 80, even for low integrated luminosities. Using this technique the  $W'$  coupling helicity can be determined for masses up to roughly 10 TeV below the discovery reach. Of course if the neutrinos are Majorana fields and the  $W'$  couples in a RH manner as in the LRM then  $W' \rightarrow \ell N$  is the discovery channel where the heavy  $N$  itself decays to dijets and a charged lepton. This signature will be studied in details in Section 4.1.9.

#### 4.1.2 Di-jet Resonances and Calorimeter Requirements

In this preliminary stage of the design of a future 100 TeV collider, we seek to estimate the necessary specifications of detection devices that will be able to accommodate the planned high energies and provide suitably precise measurements of any new phenomena that occur. In this subsection we discuss the kinematic properties of resonant processes involving jets, with particular attention to the performance of hadronic jets and to the calorimeter containment of very energetic particles. The benchmark model chosen for this study is a resonant new particle coupling to quarks and gluons, that would manifest as a

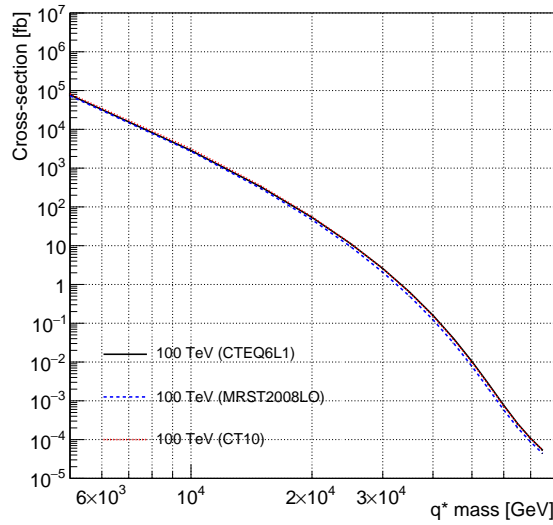


**Fig. 81:** Excited quark production cross-sections as a function of mass.

local excess over the QCD background.

The sensitivity of a new physics search for a resonant process is linked to an accurate measurement of the jet energy, and therefore to the calorimeter resolution. Broader local excesses are more difficult to distinguish over the QCD background. In this contribution we use simulations of new physics events (specifically, decays of excited quarks) and modify the calorimeter energy resolution in the detector simulation, in order to observe the effect of the smearing on the width of the signal excess in the dijet invariant mass. Firstly we give an overview of the simulation and software used for this study, including an overview of the benchmark model chosen. Then we include further detail on the calorimeter smearing and the event selection. The last part of this contribution contains the results of this study and conclusions towards future studies.

The benchmark model used in this study is quark compositeness [586, 587]: excited up and down quarks, and relative antiparticles, are simulated from proton-proton collisions at 100 TeV. Only gauge interactions are included in the benchmark model. The excited quark masses are assumed to be 10 and 40 TeV. Cross sections for this model at 100 TeV as a function of the  $q^*$  mass are shown in Fig. 81 for different parton distribution functions [84, 588–590]. The Pythia event generator [406] using the MRST2008LO [84] and the default tune for parton shower, interfaced to the Sacrifice steering software [591], are used for the event generation. Following the event generation, Delphes 3.1.2 [113] is used to apply detector effects using the standard FCC detector card to the signal and perform jet finding, using the anti-kt algorithm [263] with radius 0.5. The events were analysed in MadAnalysis [592] and ROOT 5.34.18 [593].

The energy resolution for a calorimeter in this study is parameterized as:

$$\frac{[\sigma]}{E} = \frac{50}{E} \oplus c\%, \quad (68)$$

where  $c$  is the constant term that is varied in this study to model possible effects e.g. from calorimeter punch-through, using the Delphes SimpleCalorimeter module. Events were selected according to the following criteria [594]:

- Leading and subleading jets must have  $p_T > 50$  GeV and rapidity  $|y| < 2.8$ ;

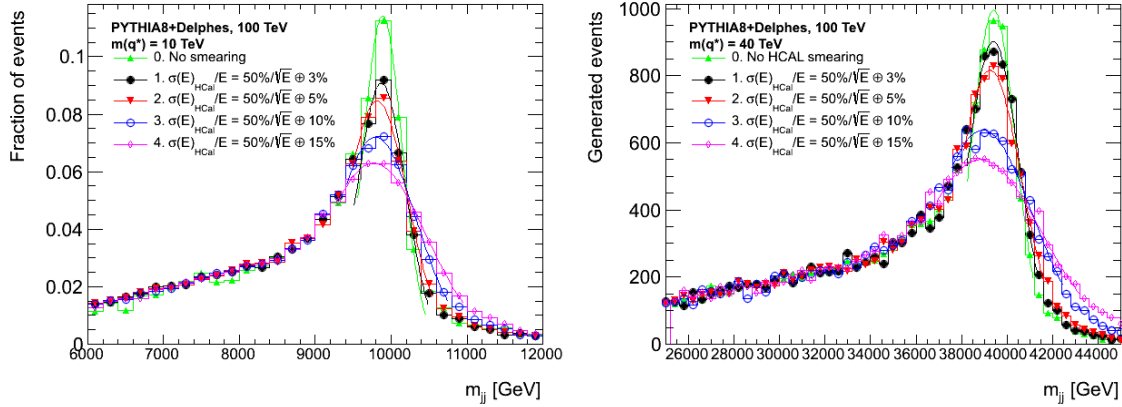


**Fig. 82:** Dijet invariant mass peak for a  $q^*$  after event selection, fitted using a Gaussian shape, after smearing with different values of the constant term of the jet energy resolution. *Left:* 10 TeV  $q^*$ ; *Right:* 40 TeV  $q^*$ .

- Half the rapidity separation ( $y^*$ ) of leading and subleading jets must be below 0.6.

Analysis of data from simulated 10 TeV  $q^*$  decays smeared with Delphes indicates that an increase in the constant term of the jet energy resolution broadens the width of the dijet invariant mass signal. To quantify the broadening, the core of the dijet mass distribution after smearing and event selection is fitted using a Gaussian as shown in Figs. 82. The width of the Gaussian is then divided by the dijet mass to obtain a relative resolution, and plotted as a function of the constant term broadening in Fig. 83. The relative mass resolution ranges from 2.5% without any smearing to approximately 7% in the case of a 15% constant term, for a  $q^*$  with a mass of 40 TeV .

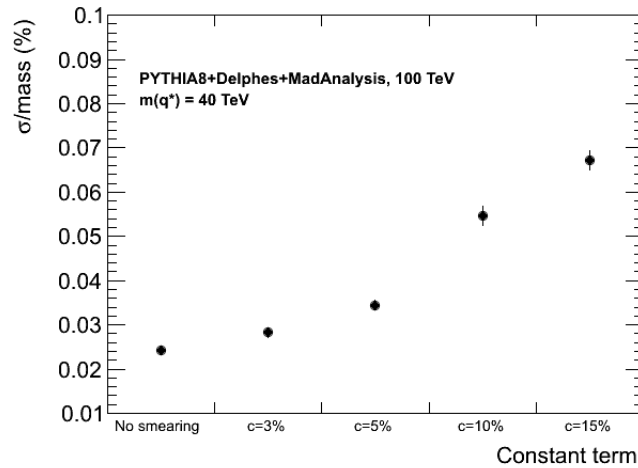


**Fig. 83:** Relative mass resolution as a function of jet energy resolution constant term for a 40 TeV  $q^*$ .

Figure 82 show that a Gaussian shape does not provide a good description of the signal peak. The broadening of the dijet mass peak is driven by both PDF effects, dominant in the higher mass samples, and by the choice of the jet algorithm. Although initially informative, this study should be extended to a more systematic analysis of different effects that broaden the dijet invariant mass peak in order to improve the peak parameterisation, and to the study of the impact of this broadening on the search sensitivity.

### 4.1.3 Resonances in the $jj$ Final State

Estimates for the sensitivity of a 100 TeV  $pp$  collider to color singlet  $Z'_B$  and color octet  $G'$  vector boson dijet resonances have been performed in Ref. [466], while studies of other resonant and non-resonant scenarios are performed in Refs. [595–597]. The color singlet  $Z'_B$  particle is a dijet resonance predicted in models with gauged baryon number [598], whose phenomenology is encapsulated by a flavor-universal coupling to quarks  $g_B/6$  and the  $Z'_B$  mass. The coloron  $G'$  arises in extended  $SU(3)_C$  color models as a heavy cousin of the SM gluon, and also couples universally to quarks with a coupling  $g_s \tan \theta$ . The two models also exhibit different dijet resonance peak structures as a result of different final state radiation, and serve to complement the discussion in the previous section regarding broadening effects and peak sensitivity via explicit simulation of color-singlet and color-octet resonance models.

We simulate QCD continuum background and  $Z'_B$  and  $G'$  signals using MadGraph 5 [111] and passed to PYTHIA [112] for parton showering and hadronization: we use MLM [599] matching between QCD two-jet and three-jet final states. Events are clustered using FASTJET v.3.0.2 [264] by the anti- $k_T$  algorithm [115] with distance parameter  $R = 0.5$  and basic detector simulation effects are used to smear the jet energies and momentum reconstruction. We do not include any interference between signal and background for the resonance searches, and so the background sample is identical for each of the BSM searches. The dijet invariant mass is constructed following the CMS 8 TeV analysis [600], where the two leading  $p_T$  jets are used as seed jets. Then, subleading jets within  $\Delta R = 1.1$  are added to the closest seed jet to form two wide jets.

We analyze the dijet search sensitivity at the 100 TeV  $pp$  collider. Using our samples for QCD background and signal, we conduct a resonance search using a Crystal Ball fit on the signal distribution to identify the peak structure of the resonance [598]. To estimate the statistical significance  $\sigma = N_S/\sqrt{N_S + N_B}$  of this signal peak, we compare the number of signal events within 3 standard deviations of the Gaussian core of the Crystal Ball fit to the number of QCD events in the same mass window: we do not include systematic uncertainties, though these are certainly important when the resonance becomes very weakly coupled.

The results for the  $Z'_B$  and coloron resonances are shown in Fig. 84 for  $5\sigma$  discovery sensitivity using  $3 \text{ ab}^{-1}$  and  $10 \text{ ab}^{-1}$  integrated luminosity. We have reproduced the current exclusion limits from Ref. [598] in the gray region. For the right panel, the coloron has a total width larger than 15% of its mass above the curve marked “Wide resonance,” while for couplings below the line labeled “Non-minimal models,” the ultraviolet completion of the extended color sector requires additional particles, such as vectorlike quarks or a second coloron, to retain perturbative gauge couplings.

We see that a  $Z'_B$  boson can be discovered as heavy as 32 TeV, depending on its coupling to quarks  $g_B$ , while the 100 TeV  $pp$  collider also have discovery sensitivity to couplings as small as  $g_B \sim 0.2$  for lighter  $Z'_B$  resonances. Colorons can be discovered as heavy as 42 TeV, and couplings as small as  $\tan \theta \sim 0.02$  can also be seen. The sensitivity prospects of the 100 TeV  $pp$  machine for low  $\mathcal{O}(\text{TeV})$  resonance masses, however, strongly depend on the dijet trigger threshold, which in turn depends on improvements in trigger bandwidth and limits from detector hardware.

### 4.1.4 Resonances in $t\bar{t}$ Final State

The sensitivity of a 100 TeV  $pp$  collider to heavy particles decaying to top-antitop ( $t\bar{t}$ ) final states has been studied in Ref. [601]. The existence of such particles was discussed in the framework of a generic Randall-Sundrum model [602]. This model predicts a number of heavy particles, such as an extra  $Z'$  gauge boson (see Ref. [577] for a review) or Kaluza-Klein (KK) excitation of the gluon  $g_{KK}$  [603]. The studies used a complete suite of leading-order and next-to-leading order Monte Carlo samples from the HepSim repository [604] to understand the backgrounds expected for top decays for transverse energies above 3 TeV. No detector simulation was used. The KK signal was generated at leading-order (NLO predictions at 100 TeV are presented in [605]).

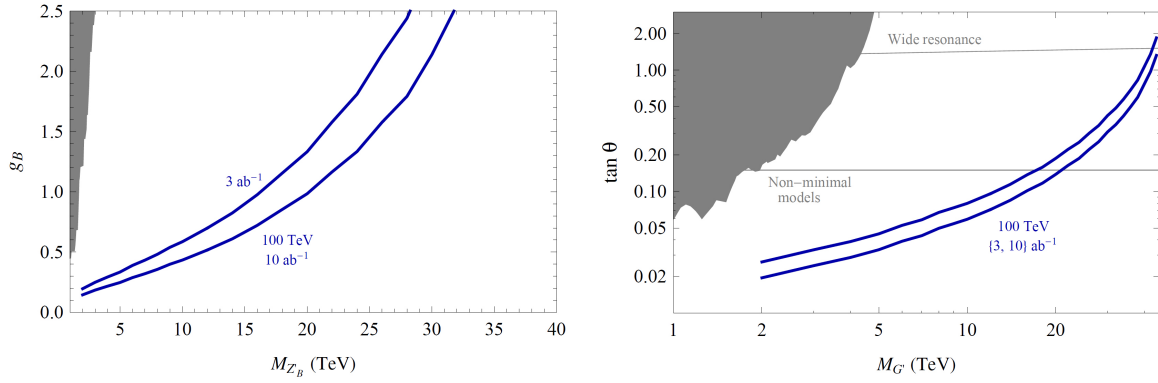


**Fig. 84:** Projected  $5\sigma$  discovery sensitivity for (left)  $Z'_B$  and (right) coloron dijet resonances, where the current exclusion bounds are shaded gray.

The studies used dijet invariant mass distributions to extract  $t\bar{t}$  resonance signals above 8 TeV. The dijet masses were reconstructed using the anti- $k_T$  algorithm [115] with a distance parameter of 0.5. The studies of the sensitivity were performed in a fully boosted regime, i.e. by looking at the invariant mass of two jets arising from the  $t\bar{t}$  system. This approach is challenging due to large collimation of decay products from top quarks, and large background expected from the SM jets. It should also be noted that even leptonic top-quark decays is a challenge at such transverse momentum, since leptons from  $W$  decays are often within the vicinity of boosted  $b$ -quark jets.

The analysis used several popular discriminating variables that reduce SM backgrounds, such as  $N$ -subjettiness characteristics [265,606], the jet  $k_T$  splitting scales [607], jet eccentricity [608], the effective radius of jets and jet masses. In addition,  $b$ -tagging was used assuming a 70%  $b$ -tagging efficiency.

Figure 85 shows the dijet masses after double  $b$ -tagging and jet shape cuts optimized to increase the signal-over-background ratios. This figure was used to estimate sensitivity, which is equivalent to “ $2\sigma$  evidence” value of  $\sigma \times \text{BR}$  for the signal calculated using the  $CL_b$  method as implemented in the MCLIMIT program [609]. Figure 86 shows the sensitivity limits for  $Z'$  and  $g_{KK}$  particles simulated using the PYTHIA8 model [112]. It should be noted that PYTHIA8 generates the boosted  $t\bar{t}$  topology similarly, but the decay widths and the production rates of  $Z'$  and  $g_{KK}$  are different. The width of the  $Z'$  boson was set to  $\Gamma/M = 3\%$ , while the width of  $g_{KK}$  is substantially larger,  $\Gamma/M = 16\%$ . The  $g_{KK}$  production rate is more than a factor of ten larger than that of  $Z'$  boson.

The discriminating variables based on jet substructure and  $b$ -tagging can increase the signal-over-background ratio by several orders of magnitude, as shown in Table 7. This increases the sensitivity on the  $\sigma \times \text{BR}$  of  $Z'$  and  $g_{KK}$  bosons by more than a factor of ten. A requirement for a high-momentum muon inside boosted jets can improve the signal-over-background ratio as shown in Table 7, but it significantly reduces statistics, thus it does not lead to a competitive limit compared to the selection based on a combination of  $b$ -tagging and jet substructure variables. Figure 87 illustrates the rejection factor for QCD background events as a function of the efficiency of top-quark reconstruction [601]. Identifying top quarks with a cut on a high-momentum muon near or inside a jet is less performant compared to jet substructure techniques once branching ratios are taken into account. Even simple jet substructure techniques, such as a cut on  $\tau_{32}$  (the ratio of the  $N$ -subjettiness variables  $\tau_3/\tau_2$  [265, 606]) and the splitting scale  $\sqrt{d_{12}}$  [607], can overperform the leptonic channel in terms of the background rejection and signal efficiency.

It should be pointed out that the 95% CL sensitivity estimates for a 100 TeV collider with the integrated luminosity of  $10 \text{ ab}^{-1}$  are rather general, as long as the widths of the  $t\bar{t}$  resonances are similar to those discussed in this analysis. Table 8 shows the values of  $\sigma \times \text{BR}$  for theory and experimental

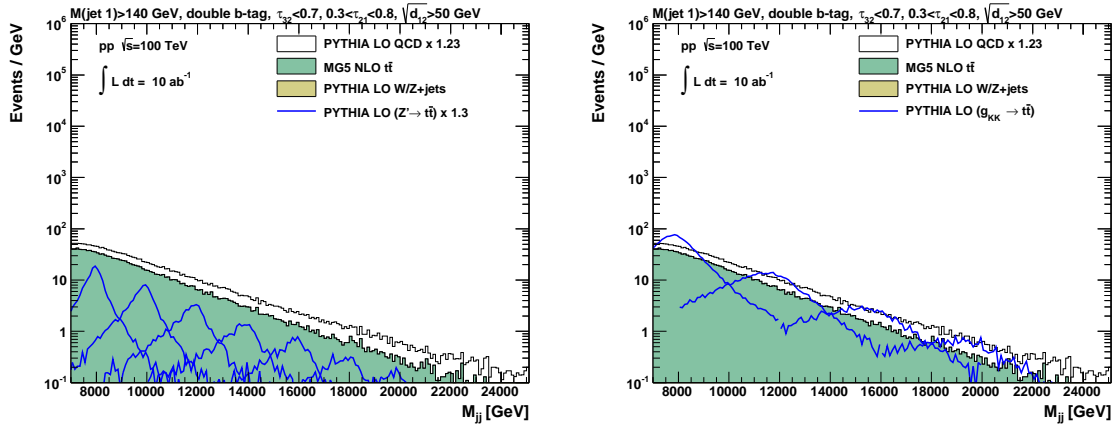


**Fig. 85:** Dijet mass distributions after jet shape and  $b$ -tagging requirements on both jets (see Ref. [601] for details). No subjet requirements were imposed on the second jet. The expectations for resonant processes are shown with the lines. The background histograms are stacked. *Left:* Dijet mass distribution with  $Z' \rightarrow t\bar{t}$  signal; *Right:* Dijet mass distribution with  $g_{KK} \rightarrow t\bar{t}$  signal.

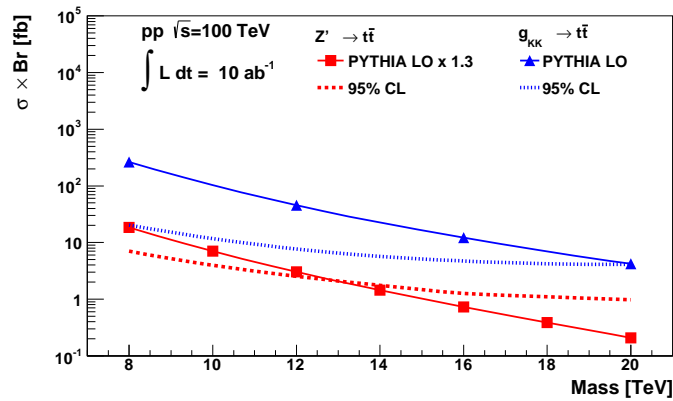


**Fig. 86:** 95% CL sensitivity estimates for a 100 TeV collider with an integrated luminosity of  $10 \text{ ab}^{-1}$  for  $Z'$  and  $g_{KK}$  bosons decaying to  $t\bar{t}$  using the “fully-boosted” regime without resolving separate decay products of top quarks. Details of the selection cuts are given in Ref. [601]. The sensitivities are given after applying jet substructure selections [601] and double  $b$ -tagging.

sensitivity as a function of resonance masses used in Fig. 86 for different values of integrated luminosity. It can be seen that a 100 TeV collider with an integrated luminosity of  $10 \text{ ab}^{-1}$  can be sensitive to a  $g_{KK}$  resonance with a mass of 17 TeV, assuming the LO QCD cross section for the  $g_{KK}$  production. The study also shows that the assumed integrated luminosity is sufficient to be sensitive to  $Z' \rightarrow t\bar{t}$  decays with mass of 13 TeV.

It is useful to estimate how the sensitivity would improve with integrated luminosity. The results discussed above were extrapolated to higher values of luminosity using a similar technique. For an integrated luminosity of  $30 \text{ ab}^{-1}$ , the  $Z'$  mass reach would increase to 16 TeV, while the mass reach for  $g_{KK}$  would increase to 19.5 TeV. More details on this analysis can be found in Ref. [601].

No cuts	JS2	$b$ -tag	$b$ -tag+JS1	$b$ -tag+JS2	$b$ -tag+JS1+ $\mu$
0.0007	0.007	0.16	0.19	0.21	0.36

**Table 7:** The signal-over-background (S/B) ratio for a  $Z'$  with mass 10 TeV for different combinations of the selection cuts [601]. The abbreviation "JS2" indicates the jet substructure cuts applied for both jets, while "JS1" indicates the jet substructure cuts for a single jet. The last column shows a combination of  $b$ -tagging, jet substructure selection and a reconstruction of a high-momentum muon that carries more than 35% of jet transverse momentum. Although the S/B ratio is the largest for the last column, the statistics expected for  $10 \text{ ab}^{-1}$  is not sufficient to obtain a competitive 95% CL sensitivity compared to other selections.

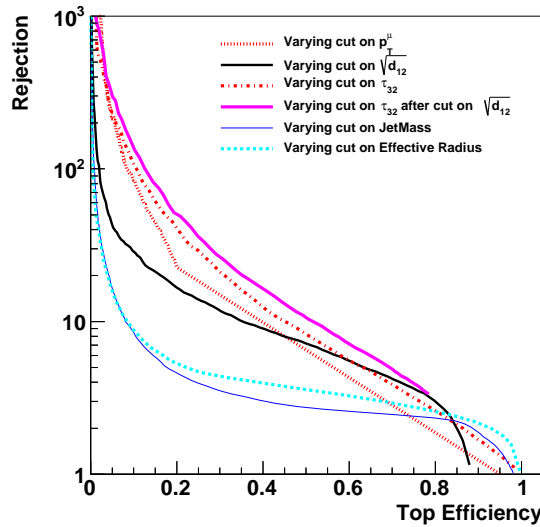


**Fig. 87:** Rejection factor for QCD jets versus efficiency of reconstruction of top quarks for different variables used to select top jets.

#### 4.1.5 Composite Resonances: Direct vs Indirect Probes

In this subsection, we study the expected direct reach of a 100 TeV collider on heavy vector triplets [610] and compare it to the expected indirect reach of various proposed future lepton colliders in a minimal composite Higgs model [611].

The comparison of the discovery and exclusion prospects of a 100 TeV collider and various proposed lepton colliders is crucial to gain a deeper understanding of the expected impact of these experiments. It is most conveniently done within a small parameter space of an explicit model. Here we choose a minimal composite Higgs model [612–614]. This is not only a theoretically well-motivated scenario but also predicts direct and indirect signs of new physics which can be studied at the different colliders. All new physics effects are comprehensively discussed in Ref. [611] and we refer the reader to this reference for further details. Here we report a brief summary of this study.

The strongest indirect constraints on composite Higgs models come from electroweak precision tests. However, their impact depends heavily on the details of the model. In order to remain as much as possible agnostic on these details and therefore more model independent, we do not focus, when considering indirect effects, on electroweak precision tests, measured both at LEP (with some improvement from Tevatron and LHC) and possibly improved at future leptonic machines. Instead we concentrate on

mass (TeV)	$\sigma \times \text{BR}$ (fb)			
	$Z'$ (th.)	$Z'$ (exp.)	$g_{KK}$ (th.)	$g_{KK}$ (exp.)
8	18.46	7.00	262.3	20.2
10	7.03	3.97		
12	3.02	2.54	45.4	7.7
14	1.44	1.75		
16	0.73	1.27	12.2	4.7
18	0.39	1.10		
20	0.21	0.98	4.2	4.1

**Table 8:** Values of  $\sigma \times \text{BR}$  for theory and experimental sensitivity as a function of resonance mass shown in Fig. 86.

indirect effects originating from the modification of the Higgs couplings because they are largely model-independent. In fact, for all models based on the minimal coset  $SO(5)/SO(4)$ , the Higgs coupling to electroweak gauge bosons is universally predicted to deviate from the SM expectation by  $k_V = \sqrt{1 - \xi}$ , where  $\xi = v^2/f^2$ ,  $f$  is the decay constant of the pseudo-Nambu-Goldstone boson Higgs and  $v$  is the scale of EWSB. We will thus take the sensitivity of future lepton colliders to  $k_V$  as a good model-independent measure of their reach on composite Higgs models.

Direct signatures stem from top partners and electroweak vector resonances. Top partners are generally more model-dependent: their mass controls the generation of the Higgs potential and thus the level of fine tuning required to achieve EWSB and a light Higgs boson [615]. The prospect for top partner searches at a 100 TeV collider are discussed in Section 4.2.2. In the analysis we perform here, aiming at being as much as possible model independent, we focus on vector resonances which are associated with the current operators of the SM gauge group. In particular, we study a colorless triplet under  $SU(2)_L$  with zero hypercharge. The simplified model for the heavy vector triplet, studied in detail in model B of Ref. [610], depends on only two parameters: the mass  $m_\rho$  of the vector triplet and the new coupling  $g_\rho$  which describes the self interactions of the heavy vector and parameterizes the couplings to SM particles. The two parameters are related to  $\xi$  by

$$\xi = \frac{g_\rho^2 v^2}{m_\rho^2}. \quad (69)$$

Thus the indirect reach on  $\xi$  can be compared to the direct reach on  $m_\rho$ , and exclusion bounds are set in the  $(m_\rho, \xi)$  or, analogously, in the  $(m_\rho, g_\rho)$  plane.

Figure 88 shows the LHC bounds on  $\sigma \times \text{BR}$  at 8 TeV with  $20 \text{ fb}^{-1}$ , expected limits at the 14 TeV LHC with  $300 \text{ fb}^{-1}$  (LHC) and  $3 \text{ ab}^{-1}$  (HL-LHC) and at a 100 TeV collider with  $1 \text{ ab}^{-1}$  and  $10 \text{ ab}^{-1}$ . Blue curves represent CMS bounds on  $WZ$  in a fully leptonic final state [617], while the more sensitive orange curves depict CMS limits from opposite sign di-lepton searches [616]. We verified that the corresponding ATLAS searches in Refs. [618] and [619] yield similar results. The current bounds have been extrapolated to larger center-of-mass energies and different integrated luminosities with the procedure described in Ref. [611]. As it can be seen from the figures, the limits approach a constant value at high invariant masses. This is expected as the region corresponds to the zero background regime. An increase of the integrated luminosity by a factor of 10 at a constant center-of-mass energy improves the exclusion bound by a factor of 10 for large masses and by a factor  $\sqrt{10} \sim 3$  for intermediate masses where

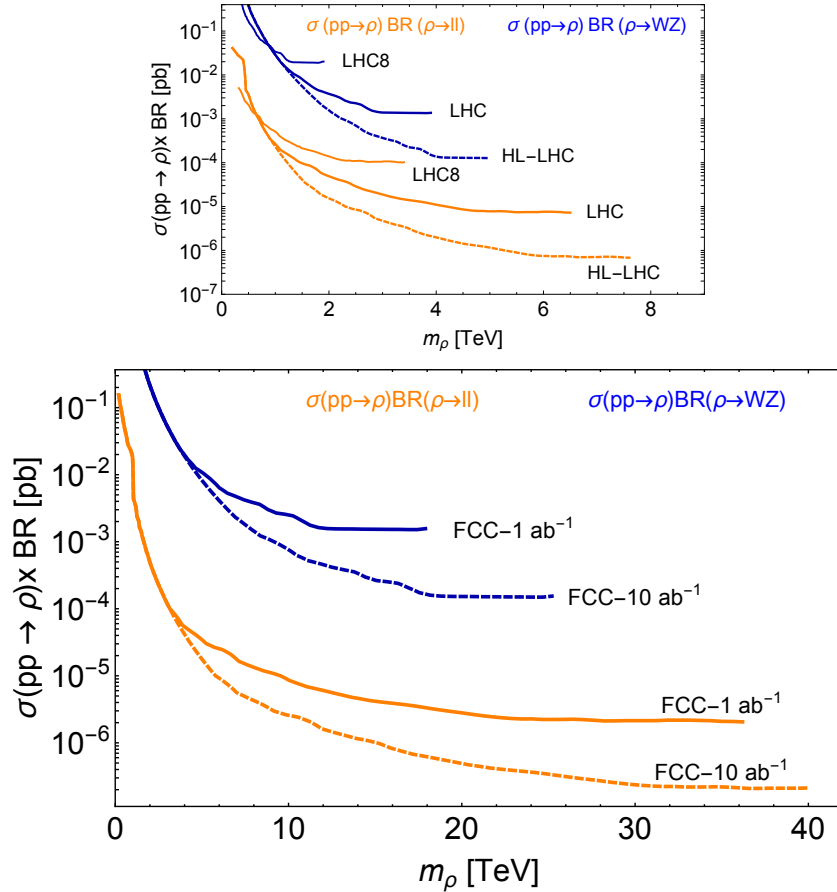


**Fig. 88:** *Left:* Bounds on  $\sigma \times \text{BR}$  from LHC at 8 TeV (LHC8) with  $20 \text{ fb}^{-1}$  (solid) and corresponding extrapolations to LHC at 14 TeV with  $300 \text{ fb}^{-1}$  (solid) (LHC) and  $3 \text{ ab}^{-1}$  (dashed) (HL-LHC); *Right:* extrapolation of LHC8 to a 100 TeV collider with  $1 \text{ ab}^{-1}$  (solid) and  $10 \text{ ab}^{-1}$  (dashed). The two analyses of refs. [616] (CMS di-leptons, orange, lower curves) and [617] (CMS fully leptonic di-bosons, blue, upper curves) are considered.

the background becomes sizeable, and the limit scales as the square root of the number of background events. At very low masses, the bounds become unreliable due to a subtlety in the extrapolation procedure which gives a conservative, but not strongest, bound (see Ref. [611] for details). Finally note in the low mass limit, that bounds from the 14 TeV LHC are weaker than at 8 TeV, and a similar feature can be observed when comparing a 100 TeV collider to the LHC at 14 TeV. This is due to the larger background expected at higher center-of-mass energies. The growing cross-section at higher energy colliders will compensate for this effect, however, and will eventually result in stronger limits on the model parameters in the entire mass range.

These bounds on  $\sigma \times \text{BR}$  can be translated into excluded regions in the  $(m_\rho, g_\rho)$  and  $(m_\rho, \xi)$  parameter space shown in the left and right panels of Fig. 89 respectively. Both plots show the relevant parameter space for a 100 TeV collider. The strong coupling  $g_\rho$  is constrained to be larger than the SM couplings but still within the perturbative regime,  $1 \leq g_\rho \leq 4\pi$ , and  $\xi \leq 1$ . Regions which violate these conditions are theoretically excluded and shaded in grey in the exclusion plots. Current direct limits for 8 TeV are shown in dark violet, while extrapolated bounds from the 14 TeV LHC and a 100 TeV collider are depicted in medium and light colours. The 100 TeV collider bound refers to an integrated luminosity of  $10 \text{ ab}^{-1}$ , while the dashed violet line shows the bound at  $1 \text{ ab}^{-1}$ .

The shape of the direct bounds can be understood as follows. The coupling of the heavy triplet to SM fermions scales as  $g^2/g_\rho$ , where  $g$  is the SM  $SU(2)_L$  gauge coupling. Since the dominant production

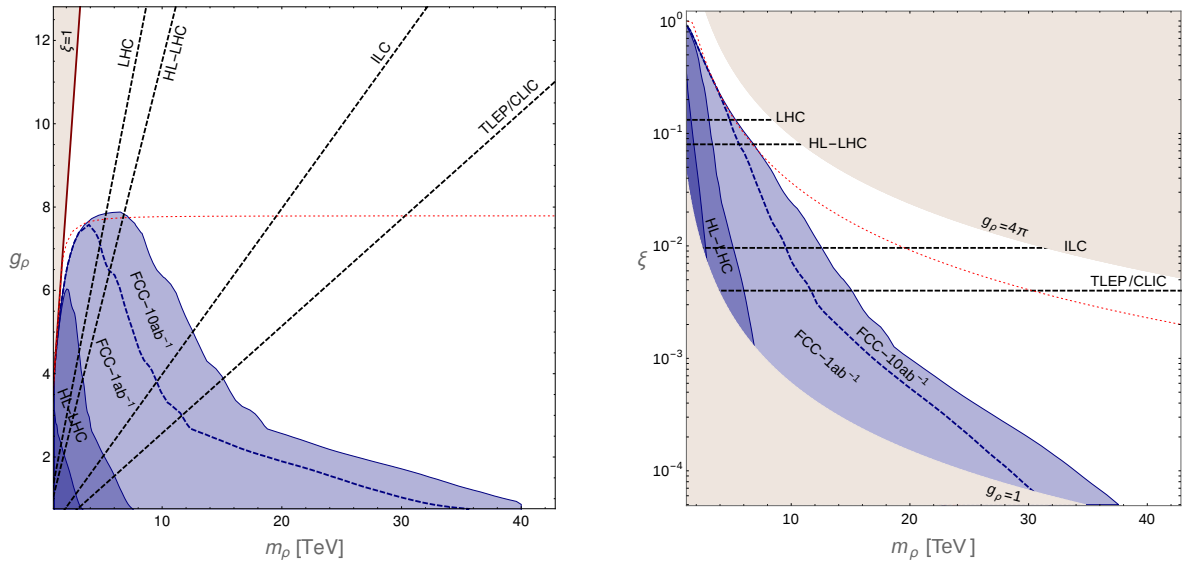


**Fig. 89:** Comparison of direct and indirect searches in the parameter space of the MCHM. *Left:* comparison in the  $(m_\rho, g_\rho)$  plane; *Right:* comparison in the  $(m_\rho, \xi)$  plane. See the text for details.

mode is Drell-Yan, we see that the vector becomes effectively weakly coupled for large values of  $g_\rho$ . This explains the weaker mass reach at large couplings. Furthermore, the scaling behaviour accounts for the far mass reach of the di-lepton channel for low couplings. The kink at intermediate masses is due to the transition between the regions where di-boson searches dominate the exclusion (low masses, large coupling) and where di-lepton searches dominate the exclusion (high masses, low coupling). The triplet coupling to SM bosons goes as  $g_\rho$  and hence di-boson channels are more sensitive for larger values of  $g_\rho$ .

From the plots we can infer, as expected, that an increase in the center-of-mass energy of the collider enhances the mass reach significantly. In fact, only a 100 TeV collider has the capability to access the multi-TeV region. An increase in luminosity improves the mass reach only slightly but is considerably more effective in the reach for larger  $g_\rho$ .

Note that resonances become broad for large  $g_\rho$  because their coupling to longitudinal vector bosons and the Higgs grows which increases the intrinsic width as  $g_\rho^2$ . Broad resonances are harder to detect and since a narrow resonance has been assumed in our analysis we expect the actual limits to be even weaker than ours in the large coupling regime. To estimate the region where finite width effects should start to become relevant we included the fine red dotted curves which depict the boundary to the region where the widths exceeds 20% of the mass. In the region above the red line the width is even larger and our bounds are no longer reliable (see Ref. [610] for details).

Indirect constraints are depicted as black dashed lines and show the expected  $2\sigma$  errors on  $\xi$ , corresponding to twice the error on  $k_V \simeq 1 - \xi/2$ , obtained from single Higgs production. The values are taken from Refs. [620–622]. In the  $(m_\rho, \xi)$  plane, the limits simply corresponds to horizontal lines and translate into straight lines with varying inclination in the  $(m_\rho, g_\rho)$  plane. In particular, the plots show the LHC reach with  $300 \text{ fb}^{-1}$  and  $3 \text{ ab}^{-1}$  corresponding to  $\xi > 0.13$  and  $\xi > 0.08$  respectively, and the expected reach of the ILC and a leptonic FCC at  $\sqrt{s} = 500 \text{ GeV}$  and  $\sqrt{s} = 350 \text{ GeV}$  corresponding to  $\xi > 0.01$  and  $\xi > 0.004$ . Note that CLIC with  $2 \text{ ab}^{-1}$  is expected to have a sensitivity comparable to the leptonic FCC.

In conclusion, the plots demonstrate that direct and indirect searches are complementary and probe the parameter space of a composite Higgs model from different directions. While direct searches are more powerful in the low coupling regime, indirect searches win for large couplings.

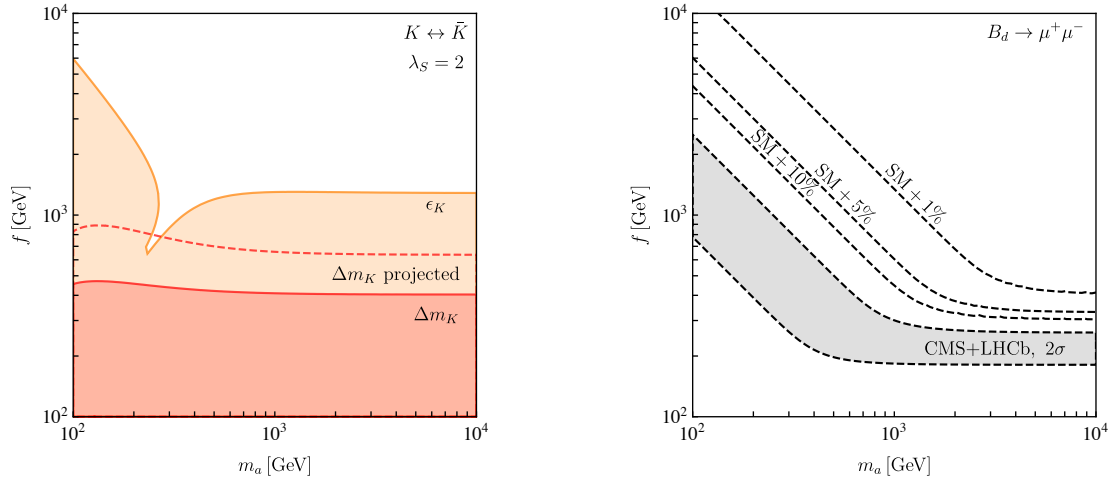


**Fig. 90:** Left: regions in the  $m_a - f$  plane excluded by flavon contributions to  $\epsilon_K$  (orange) and  $\Delta m_K$  (red) for our benchmark point and  $\lambda_S = 2$ . The dashed red contour corresponds to the excluded region based on projected improvements in  $\Delta m_K$ . Right: parameter space where the branching ratio for  $B_d \rightarrow \mu^+ \mu^-$  stays within the  $2\sigma$  confidence interval (shaded gray), as well as contours of 1%, 5% and 10% enhancement with respect to the SM prediction. Figure from Ref. [637].

#### 4.1.6 Hunting the Flavon

In spite of a major effort in theoretical and experimental particle physics over many decades, the hierarchies in the quark and lepton masses and mixing angles is not explained by the Standard Model. A high-energy collider going significantly beyond LHC energies will, for the first time, have the chance to systematically probe a dynamic origin of this flavor structure. We know various theories, which address the flavor structure for example through abelian flavor symmetries [623–626], loop-suppressed couplings to the Higgs [627], partial compositeness [628], or wave-function localization [629–633]. All of these mechanisms introduce flavor-violating couplings and new, heavy degrees of freedom, which are usually expected to be too heavy to be produced at the LHC. For instance, partial compositeness or warped extra dimensions predict vector-like heavy quarks and colored spin-one resonances with large cross sections, as discussed elsewhere in this report. Unfortunately, these resonance features are often not uniquely pointing to flavor models.

A 100 TeV machine will for the first time directly probe parameter space not excluded by quark flavor experiments. For low flavor breaking scales, which are well motivated if the flavor sector is related to electroweak symmetry breaking [634, 635] or dark matter [636], the FCC-hh has the potential to discover the dynamical degree of freedom of flavor symmetry breaking. In our discussion following Ref. [637] we focus on flavon couplings directly related to the flavor breaking mechanism induced by a minimal Froggatt-Nielsen model.

Before we discuss potential FCC searches, we briefly review the current and future indirect constraints in the quark and lepton sectors. On the quark side, the flavon mass and couplings are constrained by the non-observation of new physics in meson mixing and semi-leptonic meson decays. Future improvements in meson mixing analyses are unlikely to significantly change the typical current constraints [638], and CP-violation in  $K - \bar{K}$  mixing will remain the strongest bound. We show its impact on the flavon parameter space in the left panel of Fig. 90. In the semi-leptonic decay  $B_d \rightarrow \mu^+ \mu^-$  possible per-cent deviations from the SM prediction could hint at a flavon, while current limits from  $B_d$  and  $B_s$  decays from CMS and LHCb measurements [639–641, 641] are weaker than bounds from meson mixing. In the right panel of Fig. 90, we show the current best fit point as well as contours of constant deviation from flavon exchange in  $B_d \rightarrow \mu^+ \mu^-$  searches.

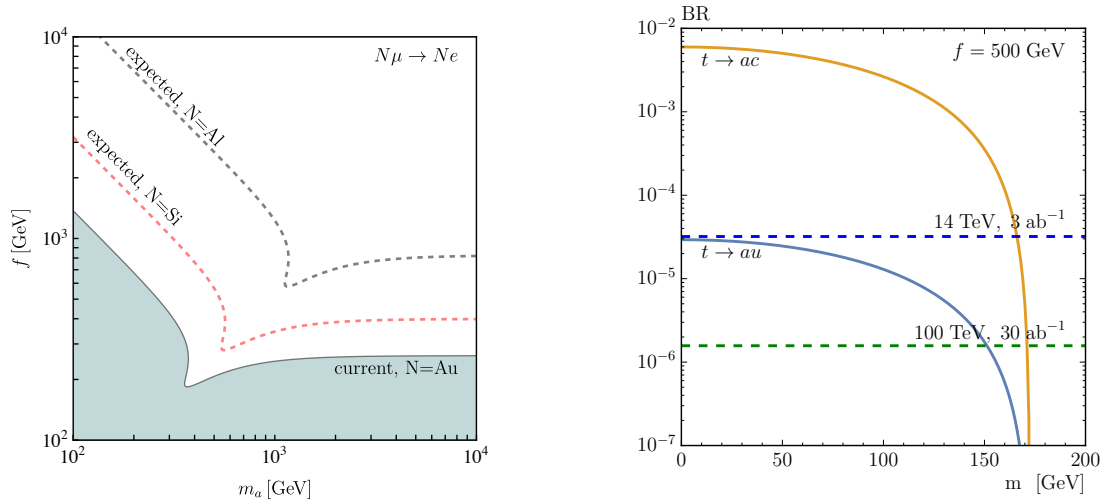


**Fig. 91:** Left: Regions in the  $m_a - f$  plane excluded by flavon contributions to the conversion  $N\mu \rightarrow Ne$ . Right: top branching ratios into a flavon and a jet as a function of the flavon mass, assuming a fixed VEV of  $f = 500$  GeV. Figure from Ref. [637].

In contrast to the quark sector, the next generation of experiments measuring lepton flavor violation will gain immense sensitivity over the current experiments. The current bound from the radiative decay  $\mu \rightarrow e\gamma$  will be improved by an order of magnitude by the MEG II experiment [642]. In addition, the DeeMe [643], COMET [644], and Mu2e [645] experiment project an improvement of up to four orders of magnitude in  $\mu \rightarrow e$  conversion. Finally, the bound on  $\text{Br}(\mu \rightarrow 3e)$  should be improved by five orders of magnitude by the Mu3e experiment [646]. To illustrate this improvement we choose a benchmark point where the flavor structures in the quark and lepton sectors are generated by the same minimal parameter setup. On the one hand, this allows us to directly assess the different experimental projections. Given that this link is a strong assumption, we should aim at an independent coverage of the flavon parameter space through leptonic and hadronic observables. In the left panel of Fig. 91, we show the current constraint and impact of future limits from  $\mu \rightarrow e$  conversion for which we find the strongest future limits. At least for relatively small flavon masses the experimental test of the lepton sector will soon surpass the flavor physics reach.

Collider searches at the FCC will complement the quark flavor reach in particular in the weak regime where the scalar flavon effects are partly cancelled by the additional pseudo-scalar contributions. Such searches are particularly challenging due to the absence of flavon couplings to electroweak gauge bosons and top quarks (in our simple setup).

For our collider signatures we rely on flavon-specific flavor off-diagonal coupling to charm and top quarks. In the light-flavon region, the LHC sets a bound from rare top decays, which will be significantly improved at the FCC-hh, as discussed in the SM part of this report [647]. The corresponding branching ratios and projected limits are shown in the right panel of Fig. 91. The small production cross sections at the LHC, shown in the left panel of Fig. 92, make it impossible to probe flavons heavier than the top quark even at high LHC luminosities. Flavon production cross sections at the 100 TeV collider are typically larger by two orders of magnitude. In particular flavon production with heavy initial-state sea quarks become gain relevance. Still, we find that  $s$ -channel resonance searches at 100 TeV are barely sensitive due to top and QCD backgrounds [637].

We therefore propose to search for flavons in associated production with a top quark. For the leading flavon decay  $a \rightarrow t + \text{jet}$  we arrive at a same-sign top pair signature with an additional jet,

$$pp \rightarrow t_\ell a \rightarrow t_\ell t_\ell \bar{c}, \quad (70)$$

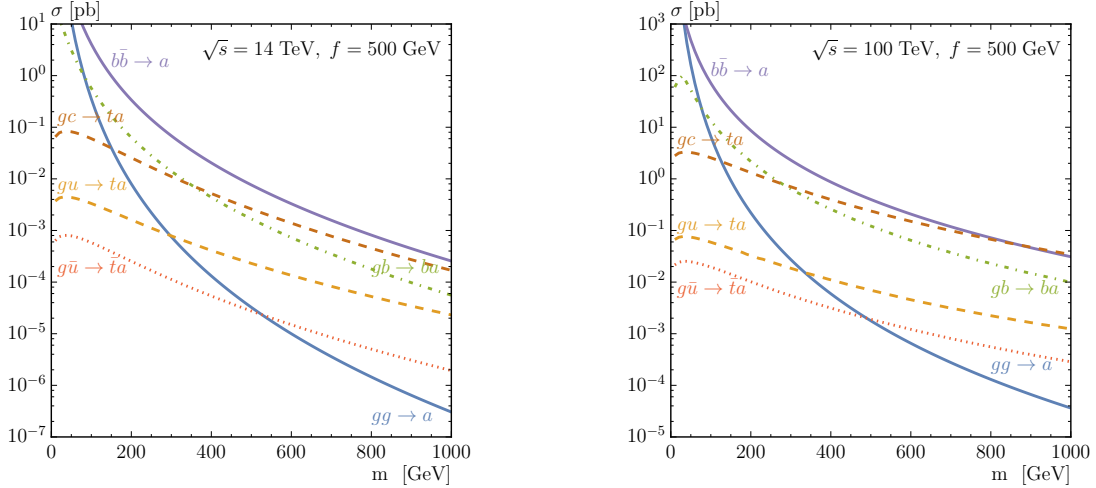


**Fig. 92:** Flavon production cross sections in the different channels for the 14 TeV LHC and a 100 TeV hadron collider using the MSTW2008 PDF set [84]. Couplings are evaluated at  $\mu = m_a$  or  $\mu = m_a + m_t$  with CRUNDEC [649]. Figure from Ref. [637].

with a partonic  $gc$  initial state. It leads to two same-sign leptons, two  $b$ -jets, and one additional jet. We simulate the hard process with MADGRAPH5+PYTHIA8+DELPHES3 [94, 113, 261, 263, 264] and find a signal rate of  $5.4 \times 10^{-3} \text{ pb} \times (500 \text{ GeV}/f)^2$  for  $m_a = 500 \text{ GeV}$ . The irreducible SM background,

$$pp \rightarrow bbW^+W^+j \quad (71)$$

has a leading order cross section of  $5.7 \cdot 10^{-7} \text{ pb}$  and is therefore negligible. Instead, we need to consider  $t_\ell \bar{t} Z j$  and  $t_\ell \bar{t} W^+ j$  production, with at least one leptonic top decay and a leptonically decaying weak boson. These backgrounds are significantly larger,  $\sigma_{t_\ell \bar{t} W^+ j} = 0.33 \text{ pb}$  and  $\sigma_{t_\ell \bar{t} Z j} = 0.48 \text{ pb}$ . To isolate the signal, we

- require two isolated same-sign leptons with

$$R_{\text{iso}} = 0.2, \quad I_{\text{iso}} = 0.1, \quad p_{T,\ell} > 10 \text{ GeV}, \quad |\eta_\ell| < 2.5; \quad (72)$$

- veto a third lepton with any opposite-sign combination giving  $|m_{\ell^+\ell^-} - m_Z| < 15 \text{ GeV}$ ;
- identify the hardest anti- $k_T$  jet [648] ( $p_T > 40 \text{ GeV}$ , and  $|\eta_j| < 2.5$ ) jet with  $p_{T,j} > 100 \text{ GeV}$  as our  $c$ -candidate;
- require, among the non- $c$  jets, at least two  $b$ -tags with a parton-level  $b$ -quark within  $R < 0.3$  and an assumed tagging efficiency 50 %;
- require  $\cancel{p}_T > 50 \text{ GeV}$ ;
- require  $m_t < m_{T2} < m_a$ ;
- consider two  $b$ -jet charge tagging efficiencies, as described below.

Since the missing transverse momentum has to be distributed between the flavon decay and the top decay, we define two branches by assigning each  $b$ -quark to the leptons and minimizing  $\Delta R_{\ell_1 b_i} + \Delta R_{\ell_2 b_j}$ . We further assign the hard  $c$ -jet to the top candidate with the smaller  $\Delta y_{(\ell b),j}$ . For most signal events we expect  $m_t < m_{T2} < m_a$ , which allows us to search for an excess of events over the background that provides side-bands at high value of  $m_{T2}$  [136, 137]. We show the corresponding distribution in the left panel of Fig. 93.

A final, distinctive feature of the signal is that both leptons originate from tops, so the two  $b$ -jets should be tagged with the same charge [650]. Recent ATLAS studies [651] show that a  $b\bar{b}$  distinction is

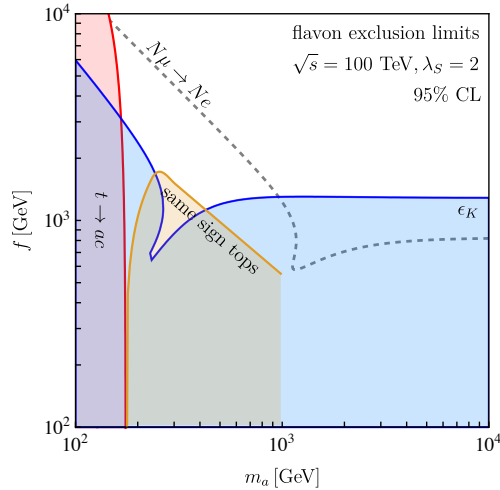


**Fig. 93:** Regions in the  $m_a - f$  plane which can be probed by quark flavor physics ( $\epsilon_K$ ), by lepton flavor physics ( $\mu \rightarrow e$  conversion), and by a 100 TeV hadron collider. For the latter we show the reach of anomalous top decays and same-sign top production. Figure from Ref. [637].

possible with  $\epsilon_S = 0.2$  and  $\epsilon_B = 0.06$ . For our analysis we assume two scenarios: a conservative estimate based on these ATLAS efficiencies, and a more optimistic case for which we assume an improved mis-tagging rate of  $\epsilon_B = 0.01$  and an overall  $b$ -tagging efficiency of 70 %.

To summarize our findings and illustrate the competitive reach of a 100 TeV collider, we show its projected 95% CL reach in the associated production channel in Fig. 93. In addition, we show the projected reach of indirect quark flavor and lepton flavor experiments. We see that experiments sensitive to the quark and lepton sectors nicely overlap in the parameter space of our universally challenging benchmark model. The combination of direct and indirect searches in the quark and lepton sectors will for the first time give us the opportunity to test the dynamic nature of the flavor structure in the Standard Model. Just like any collider search, the FCC-hh will provide us with conclusive information about the nature of the flavon up to TeV-scale flavon masses.

#### 4.1.7 $W' \rightarrow tb$ in Weak Boson Fusion

In this section we discuss the motivations, summarize the main results and suggest possible improvements of the study presented in Ref. [652], where a first estimate of the reach of a 100 TeV collider on a  $W'$  vector resonance produced via weak-boson-fusion and decaying dominantly into  $tb$  was presented. As we pointed out in the previous subsection, vector resonances  $V$  are a general prediction of many BSM scenarios and in particular of compelling models of Higgs compositeness [653], where they emerge from new strongly interacting dynamics which also generates the Higgs. Naturally, one thus expects a strong interaction of the vector resonances with the Higgs and the would-be Goldstone bosons, *i.e.* the longitudinal  $W_L, Z_L$  bosons. The mass hierarchy of the SM quarks can indeed be explained through variations in the size of the mixing of SM quarks with the strong sector. Consequently, the interaction of vector resonances with SM light quarks is typically small. Heavier quarks, such as the top and bottom, have a sizable mixing with their composite partners in the strong sector and are partially composite particles [628]. The light generations have instead a negligible degree of compositeness. The light quark couplings to vector resonances is thus small and is inversely proportional to the  $V$  coupling to the  $W_L/Z_L$  bosons, which we denote as  $g_V$  [610, 654, 655]. This implies that for larger  $g_V$  couplings, corresponding to the regime of a more strongly coupled BSM dynamics, the vector resonance production via Drell-Yan, which is the main production mechanism at the LHC, is suppressed by  $\sim g^2/g_V^2$ . In the large  $g_V$  regime, the alternative vector-boson-fusion (VBF) production mechanism, which is instead enhanced

by  $g_V^2$ , becomes thus relevant (as shown in Fig. 94) and can allow to directly test a strongly-coupled (but yet perturbative) regime that could otherwise be difficult to test via the DY channel. The sensitivity of the VBF production, due to its t-channel nature, increases considerably with the center-of-mass energy of a  $pp$  collider (Fig. 94). A future 100 TeV collider, as we estimated in Ref. [652], can give a unique opportunity to test a wide range of vector resonance masses for large  $g_V$  coupling. As it is clear from the previous subsection, this particular choice of parameter space cannot be easily probed at the LHC<sup>19</sup>, even with  $3000 \text{ fb}^{-1}$  [611].

For our analysis of the channel in Fig. 95 at a 100 TeV collider, we have considered a two-site effective description of a Minimal Composite Higgs Model (MCHM) [653] with partial compositeness (see Ref. [652] for details on the model). The relevant terms of the Lagrangian read as follows:

$$\begin{aligned}
 \mathcal{L}_V = & -g_2 M_W \cot \theta_2 W_\mu'^+ W^{-\mu} h \\
 & + i \frac{g_2}{c_W} \cot \theta_2 \frac{M_W^2}{M_{W'}^2} \left[ Z^\mu W^{+\nu} \left( \partial_\mu W_\nu'^- - \partial_\nu W_\mu'^- \right) \right. \\
 & \left. + Z^\mu W'^{+\nu} \left( \partial_\mu W_\nu^- - \partial_\nu W_\mu^- \right) + W'^{+\mu} W^{-\nu} \left( \partial_\mu Z_\nu - \partial_\nu Z_\mu \right) \right] \\
 & - \frac{g_2}{\sqrt{2}} \tan \theta_2 W_\mu'^+ \left( \bar{q}_L^u \gamma^\mu q_L^d + \bar{\nu}_{lL} \gamma^\mu l_L^- \right) \\
 & + \frac{g_2}{\sqrt{2}} W_\mu'^+ \left( \bar{t}_L \gamma^\mu b_L \right) \left( s_L^2 \cot \theta_2 - c_L^2 \tan \theta_2 \right) + \text{H. c.}
 \end{aligned} \tag{73}$$

where  $g_2 = e/\sin \theta_W$ ,  $s_W(c_W) \equiv \sin \theta_W(\cos \theta_W)$  and  $q = (q^u, q^d)$  represents a doublet of the first or second generation of quarks. The parameter  $s_L$  ( $c_L = \sqrt{1 - s_L^2}$ ) represents the degree of compositeness of the 3rd generation ( $t_L, b_L$ ) doublet. Motivated by the partial compositeness scenario, we have considered a relatively large value  $s_L = 0.7$ . For such a value the  $W' \rightarrow tb$  BR is about 0.6 in the regime  $g_V \gtrsim 3$ , relevant to this analysis. The  $\theta_2$  parameter in the Lagrangian determines the rotation which diagonalizes the mixing between a composite  $W^*$  resonance from the strong sector and an elementary  $W$  boson, which leads to the  $W'$  and to the SM  $W$  mass-eigenstates.  $\theta_2$  controls the interactions of the vector resonances. In particular, the  $V$  coupling to  $W_L/Z_L$  bosons is given by  $g_V = g_2 \cot \theta_2$ .

We have performed a search analysis, based on Monte Carlo simulations, of the VBF  $W' \rightarrow tb$  signal depicted in Fig. 95 at a 100 TeV collider. Signal and background events have been simulated at LO with MadGraph 5 [111] and passed to PYTHIA [264] for showering and hadronization. We have also applied a smearing to the jet energy in order to mimic detector effects [656]. The main backgrounds include the  $WWbb$ , which is mainly made of  $t\bar{t}$  events with a minor contribution from single-top  $Wt$  events, the  $Wbb$ +jets and the t-channel single top  $tb$ +jets. This latter, which has a t-channel topology similar to the signal, represents the dominant background after applying our selection. We focused on the final state:

$$e/\mu + n_{jet} \text{ jets}, \quad n_{jet} \geq 4 \text{ (2 b-tag)}. \tag{74}$$

and we applied the following isolation criteria and  $p_T$  acceptance cuts on the lepton and jets:

$$p_T j > 30 \text{ GeV}, \quad p_T l > 40 \text{ GeV}, \quad \Delta R(l - j) > 0.2, \quad |\eta_j| < 5, 6 \tag{75}$$

We explored a region at high  $W'$  masses, where the top is boosted and, as a consequence, the lepton tends to be harder and at a lower  $R$  separation from the b-jet, which also comes from the top decay. The relatively hard acceptance cut on the lepton  $p_T$  has been chosen in order to obtain a better distinction from the b-jet [657].

<sup>19</sup>Also considering that  $V$  resonances become typically broad in this regime.

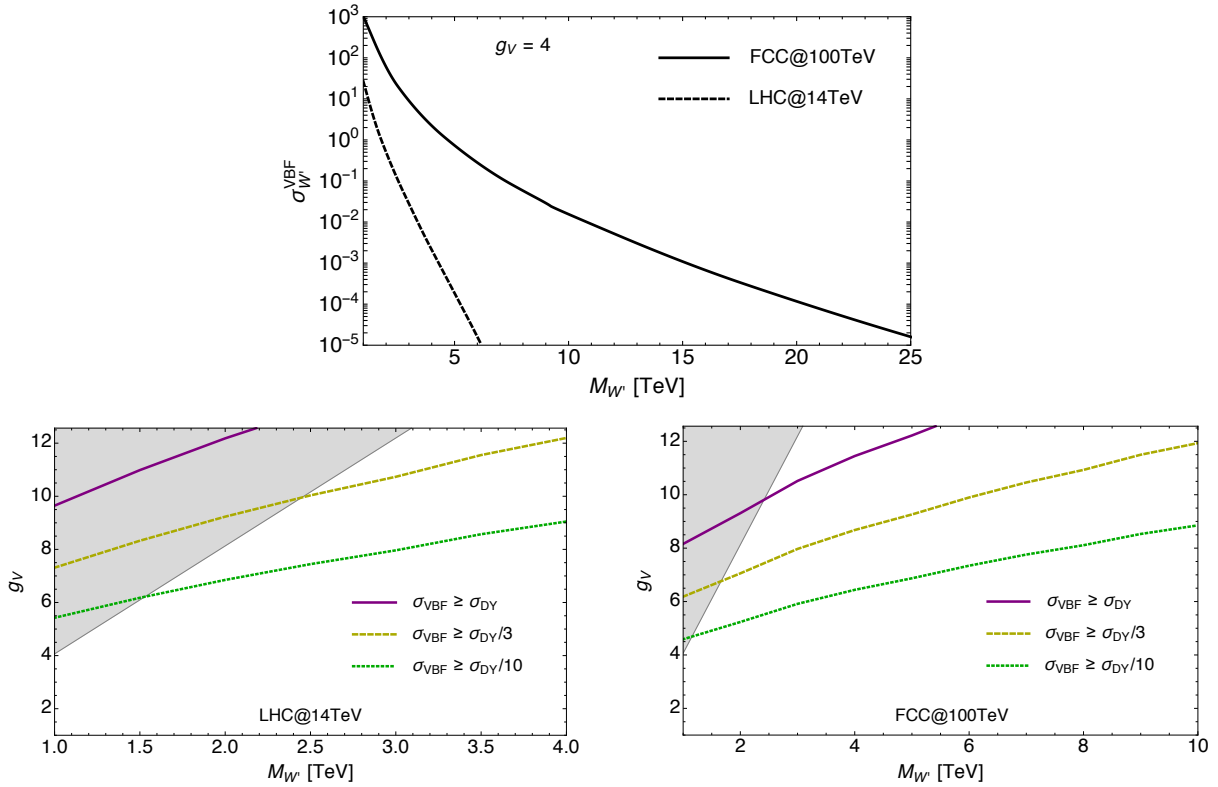


**Fig. 94:** *Upper:* cross section for the  $W'$  VBF production at the LHC-14 (dashed curve) and at a futuristic 100 TeV pp collider (thick curve) for a coupling  $g_V = 4$ . Cross sections scale as  $g_V^2$  with the coupling. We have applied a 30 GeV cut on the jet  $p_T$  and a rapidity acceptance  $|\eta_j| < 5$ . *Lower left:* contours of different ratios of the VBF over DY  $W'$  production cross sections on the  $(M_{W'}, g_V)$  parameter space at the LHC-14; *Lower right:* same quantity at a 100 TeV collider. The shaded areas in the upper-left corner of the parameter space correspond to values  $g_V v / M_V > 1$  which are indicative of a theoretically excluded region (where  $v/f \gtrsim 1$ ) in MCHM.

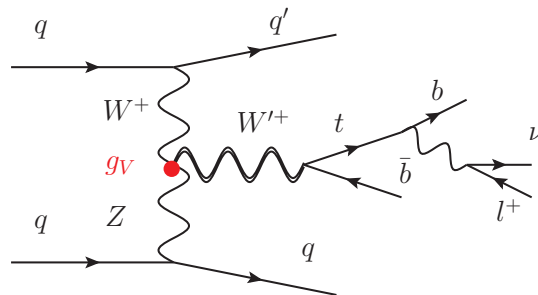


**Fig. 95:** Feynman diagram for the VBF  $W' \rightarrow tb$  process. Both the  $W'^+$  and the  $W'^-$  processes are considered in the analysis.

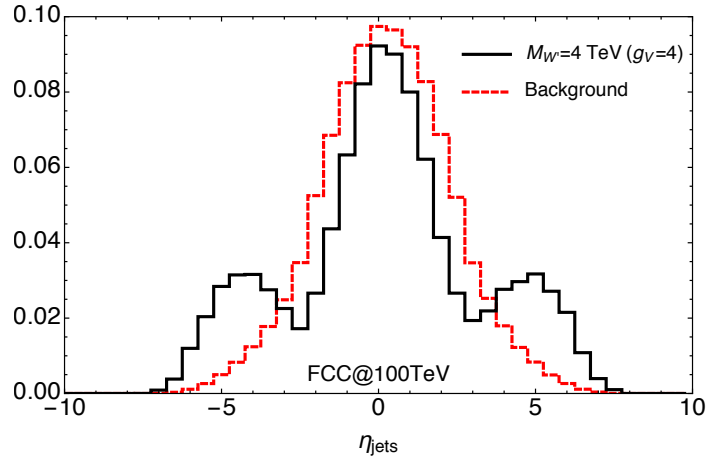


**Fig. 96:** Normalized rapidity distribution of all of the final jets which have passed the acceptance requirements in Eq. (75), with the exception of the  $|\eta_j|$  restriction, for the total background (red dashed curve) and the signal with  $m_{W'} = 4$  TeV,  $g_V = 4$  (black curve) at a 100 TeV collider.

We have employed a simple search strategy which relies on the main characteristics of the signal: the distinctive VBF topology with the two final forward-backward jets emitted at high rapidity and with a large  $\eta$  separation (see Fig. 96) and the presence of a heavy resonance which leads to hard final states. We have thus imposed a first cut on  $HT_2$ , defined as the scalar sum on the  $p_T$  of the leading and second-leading jet,  $HT_2 > 800$  GeV, which already reduces significantly the background and we have then imposed a forward-backward jet tagging, by requiring that at least one signal jet had  $\eta > 2.5$  and at least one jet  $\eta < -2.5$  and that the forward-backward jets had a rapidity separation  $|\Delta\eta_{FJ,BJ}| > 8$ . We found that at a 100 TeV collider, the signal is really boosted and, for a significant fraction of the events, the two final forward-backward jets have a rapidity larger than 6, as shown in Fig. 96. We thus point out that it would be advantageous to extend the rapidity acceptance of a future  $pp$  collider to the forward region up to values  $\sim 6$ .

The subsequent steps of the analysis consist on a simple reconstruction procedure of the top and the bottom in the final state which allow the  $W'$  resonance reconstruction. We have thus imposed a bound on the reconstructed  $W'$  invariant mass,  $m_{W'}$ , and on the  $p_T$  of the top and of the bottom:

$M_{W'}$ (TeV)	2	3	4	5	6
$m_{W'} >$ (TeV)	1.5	2.5	3.5	4.0	5.0
$p_T b, t >$ (TeV)	0.75	0.9	1.5	1.5	1.5

(76)

The final results of our selection are shown on Table 9. We used these results to extract the discovery/exclusion reach on the  $W'$  (mass, coupling) parameter space of a 100 TeV collider. We found that while the 14 TeV LHC can access only a small portion of the MCHM parameter space (the high-luminosity LHC, with  $3 \text{ ab}^{-1}$  can exclude a  $W'$  vector resonance up to about 2.1 TeV), a future 100 TeV  $pp$  collider has a much wider sensitivity. The left plot in Fig. 97 shows that at a 100 TeV collider a  $5\sigma$  discovery is achieved for a  $W'$  in the VBF channel with masses up to 5.1 (4) TeV with 10 (1)  $\text{ab}^{-1}$  of integrated luminosity in the large  $g_V$  coupling region. The exclusion potential of a 100 TeV collider, as shown in the lower plot of Fig. 97, extends up to  $W'$  masses of 6.1 (5.1) TeV with 10 (1)  $\text{ab}^{-1}$ . These values refer to a jet-rapidity acceptance  $|\eta_j| < 6$ . As we anticipated, we found that the reach of a 100 TeV collider is significantly enhanced, by about a 10% in the  $W'$  mass reach, if the rapidity acceptance on the jets can be increased from 5, the present LHC rapidity coverage, up to 6.

100 TeV $(M_{W'} \text{ (TeV)}, g_V)$	signal		bckg	
	$ \eta_j  < 5$	$ \eta_j  < 6$	$ \eta_j  < 5$	$ \eta_j  < 6$
(2, 4)	0.56	1.1	70	100
(3, 4)	0.13	0.25	31	45
(4, 4)	0.022	0.042	4.8	7.2
(4, 8)	0.082	0.15	4.8	7.2
(5, 8)	0.028	0.051	3.6	4.9
(6, 12)	0.013	0.022	1.4	1.8

**Table 9:** Signal and background cross sections, in fb, at a 100 TeV collider after the complete selection.

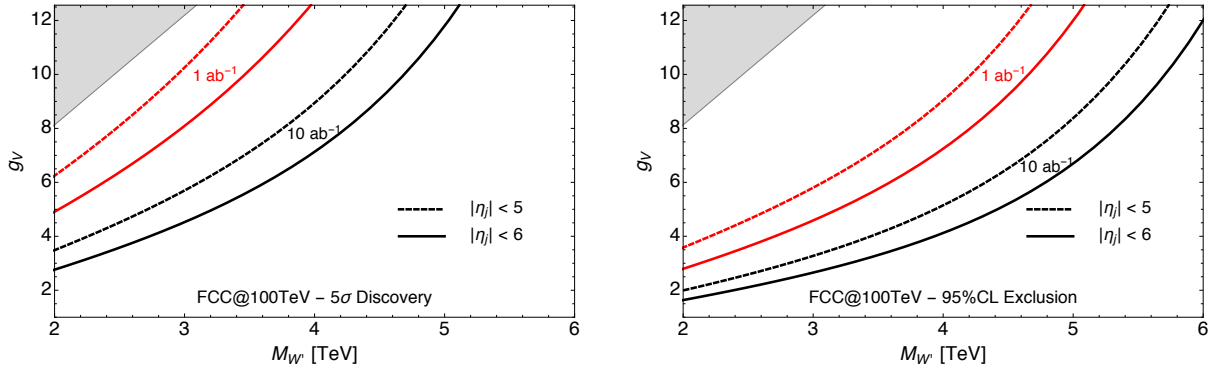


**Fig. 97:** The 100 TeV pp collider reach, with 1 and 10  $\text{ab}^{-1}$ , on a  $W'$  produced via VBF in the  $tb$  channel. *Left:*  $5\sigma$  discovery potential. *Right:* 95% CL exclusion reach. The continuous (dotted) curves are obtained for a jet rapidity acceptance  $|\eta_j| < 6$  (5). The shaded areas in the upper-left corner of the parameter space correspond to values  $g_V v/M_V > 1$  which are indicative of a theoretically excluded region (where  $v/f \gtrsim 1$ ) in MCHM.

In conclusion, we have shown that a future 100 TeV  $pp$  collider offers the possibility to test, using the VBF channel, a wide range of a vector resonance mass and coupling parameter space and, most importantly, that the reach of a 100 TeV collider in VBF extends up to the more strongly-coupled regime of composite Higgs models, which is not within the reach of LHC.

Motivated by MCHM with partially composite 3rd generation quarks, we have focused on the  $W' \rightarrow tb$  channel and have outlined a simple signal-selection strategy which mainly relies on the distinctive VBF topology. Several improvements and extensions to our analysis are possible. Firstly, one could further exploit the boosted nature of the final states to apply more refined top-reconstruction techniques (as for example explained in Section 4.1.4). It could be also interesting, in this case, to consider a different final state, for example a totally hadronic final state, which would lead to a larger signal cross section compared to the semileptonic channel considered in our analysis. A natural extension of our study is then to consider different  $W'$  decay channels. In the case, for example, where the top degree of compositeness is relatively small ( $s_L \lesssim 0.5$ ) the dominant decay channels become  $W' \rightarrow WZ/Wh$ . Finally, in our analysis we have neglected the possible contributions of vector-like quarks, which could lead to spectacular new signatures [655] at a 100 TeV collider.

#### 4.1.8 Photon Cascade Decay of the Warped Graviton

The warped Randall-Sundrum models, where Standard Model gauge fields [658,659] and fermions [630] are allowed to propagate in the 5-dimensional bulk, provides an excellent framework to address both the Planck-weak and flavor hierarchy problems of the SM [629,660,661]. In this class of models, the Kaluza-Klein (KK) gravitons (as well as gauge and fermion KK states) mostly interact with heavy SM fields such as the top quark, Higgs, and longitudinal modes of  $Z/W$  gauge bosons because all the particles involved in the relevant couplings are localized near the TeV/IR brane. Hence, once produced, they give rise to interesting collider signatures, and various aspects of collider phenomenology (mostly in the context of the LHC) have been studied in, for example, in Refs. [603,662–672].

At the same time, future colliders beyond the LHC could not only offer discovery opportunities for the KK particles but also allow their precision studies. Given this situation, it is opportune and interesting to examine potential signals from KK particles in more detail and explore other non-conventional decay modes especially if they can provide independent information on the underlying model parameters. With this goal in mind, we investigate here a novel signature coming from the cascade decay of KK gravitons, i.e., those with final states having other KK particles. We particularly focus on the “photon cascade” decay mode, for which the original study was presented in Ref. [673],

$$pp \rightarrow G_1 \rightarrow \gamma_1 \gamma, \quad (77)$$

where  $G_1$  and  $\gamma_1$  denote the first KK states of the graviton and photon, respectively. This channel could potentially be a good cross-check of the conventional search channels accompanying two heavy SM states. Moreover, in the post-discovery and precision study phase, the specific dependence of the rate on the volume factor for the process in Eq. (77) – which differs from that in conventional ones – may enable us to extract the underlying model parameters *separately* in conjunction with information from other channels. In this context, we emphasize that, in general, this new decay mode is *complementary* to the ones that were previously investigated.

A rough sketch of particle profiles in the model under consideration is given as follows: 1) *all* KK states are localized near the TeV/IR brane, 2) left-handed top and bottom quarks are either localized near TeV brane or have a (roughly) flat profile; for concreteness we choose this latter option, with the  $t_R$  localized near the TeV brane, 3) SM photon and gluon have flat profiles, and 4) light SM fermions are localized near the UV brane (to suppress their couplings with the Higgs). We then find the following features of the KK graviton coupling, in particular, for their production and decay: i) the couplings to  $t_R/h/W_L/Z_L$  are the largest, i.e.,  $\mathcal{O}(1)$ , ii) the coupling to the SM gluon, relevant for production, is suppressed by a “volume factor”  $\sim 1/(k\pi R)$ , and iii) the coupling of  $\gamma_1$  with  $\gamma$  is “in-between” the previous two. Here,  $k$  and  $R$  are the curvature scale and the compactification radius of the RS background, respectively; the Planck-weak hierarchy is generated for  $kR \simeq 11$ .

The couplings relevant to vertices  $G_1 gg$  and  $G_1 \gamma_1 \gamma$  have been studied in Ref. [662], and it turns out that they are proportional to  $1/(k\pi R)$  and  $1/\sqrt{k\pi R}$ . Therefore, the total rate for  $gg \rightarrow G_1 \rightarrow WW, ZZ$  etc., goes like  $\sim 1/(k\pi R)^2$ , whereas that for  $gg \rightarrow G_1 \rightarrow \gamma_1 \gamma$  scales with  $\sim 1/(k\pi R)^3$ . Roughly speaking, we then anticipate that the ratio between conventional channels and photon cascade channel should scale as  $k\pi R$ , enabling us to extract information on the 5D parameter  $kR$ . Hence, a measurement of the process proposed here after potential discovery made in the conventional heavy SM channels can shed light on the parameters of warped models.

The signal process that we consider is  $pp \rightarrow G_1 \rightarrow \gamma_1 \gamma$  followed by  $\gamma_1 \rightarrow W^+ W^- \rightarrow (jj)\ell\nu$ . We adopted the KK photon couplings and model parameter values in Ref. [668], which motivated the choice  $\text{BR}(\gamma_1 \rightarrow W^+ W^-) \simeq 0.44$  as a typical value. Basically, the signal process is characterized by a three-step cascade decay of  $G_1$  into  $\gamma$ , (hadronic)  $W$ , and  $\ell$  ( $e$  or  $\mu$ ) along with an (invisible) neutrino:

$$G_1 \rightarrow \gamma \gamma_1 \rightarrow \gamma W^\pm W^\mp \rightarrow \gamma W^\pm (\rightarrow jj) \ell^\mp \nu \quad (78)$$

Since all visible particles (including the hadronic  $W$ ) are fully distinguishable, many distinctive kinematic features can be easily applied without any combinatorial issues. We first expect a hard photon due to a sizable mass gap between  $G_1$  and  $\gamma_1$ . A large mass hierarchy between  $\gamma_1$  and  $W$  again enables us to have hard jets, lepton, and missing transverse momentum. In particular, the  $W$  is so significantly boosted that the two jets are highly collimated, demanding us to employ the boosted object techniques to tag merged two-prong  $W$  jets while suppressing the single-prong QCD jet background.

On top of the cuts motivated by the hardness of final state objects, the two invariant masses defined by  $G_1$  and  $\gamma_1$  and the associated invariant mass cuts play a crucial role in suppressing backgrounds. In order to reconstruct them, we first obtain the energy-momentum of the invisible neutrino using the missing transverse momentum constraint and  $\nu/W$  mass-shell conditions. Although there arise two solutions, we consider the event of interest as accepted in our analysis if either of the resulting solutions pass the two invariant mass window cuts:

$$m_1^\gamma - \Gamma_1^\gamma < m_{\ell jj\nu} < m_1^\gamma + \Gamma_1^\gamma, \quad (79)$$

$$m_1^G - \Gamma_1^G < m_{\gamma\ell jj\nu} < m_1^G + 2\Gamma_1^G, \quad (80)$$

where  $\Gamma_1^G$  and  $\Gamma_1^\gamma$  are the widths of  $G_1$  and  $\gamma_1$ , respectively. Here the asymmetric form of the latter criteria considers the possibility of skewed Breit-Wigner distributions for KK gravitons having a large  $c$  ( $\equiv k/\bar{M}_P$ ) parameter. More quantitatively, it turns out that the KK graviton with a large  $c$  value (e.g.,  $\sim 2$ ) has a particle width larger than  $\sim 20\%$  of its mass. Moreover, the  $G_1 gg$  coupling emerges from a dim-5 operator (in turn, due to its spin-2 nature) which grows with energy, and therefore, larger  $m_{\gamma\ell jj\nu}$  values are preferred. In particular, at higher energy colliders such as a 100 TeV collider, the KK graviton mass of a few TeV is in the regime of low  $x$ , so that we expect that the associated invariant mass distribution is not significantly affected by the gluon parton distribution function, i.e., the skewness becomes manifest. The left panel of Fig. 98 demonstrates the shift of the peak position for three different KK photon masses with the  $c$  parameter fixed to 2. We observe that the peak position is shifted by about half  $\Gamma_1^G$  in all cases, comparing with relevant theory expectations denoted by the black dashed vertical lines.

When it comes to the selection process in regard to  $m_{\ell jj\nu}$  and  $m_{\gamma\ell jj\nu}$ , we introduce a new *weighted* measure  $\mathcal{W}$  defined as

$$\mathcal{W} = \frac{|m_{\ell jj\nu} - m_1^\gamma|}{\Gamma_1^\gamma} + \frac{|m_{\gamma\ell jj\nu} - (m_1^G + 0.5\Gamma_1^G)|}{1.5\Gamma_1^G}, \quad (81)$$

in order to capture the events where one of the invariant mass windows is marginally not satisfied while the other is satisfied. The right panel of Fig. 98 shows the performance of the  $\mathcal{W}$  measure. The signal events typically give a small  $\mathcal{W}$ , whereas background events are peaked at a larger value of  $\mathcal{W}$ . This is because it is rather unlikely for the reconstructed  $m_{G_1}$  and  $m_{\gamma_1}$  in background events to be within both invariant mass windows simultaneously.

Given that the collider signature of our signal process is characterized by  $\gamma\ell jj + \cancel{E}_T$ , several SM processes should be taken into consideration as potential backgrounds. Obviously, the irreducible SM background is from  $WW\gamma$  production. Due to the existence of merged  $jj$  in the signal, we expect that the most important reducible background comes from  $Wj\gamma$ , which contains a (single-prong) QCD jet. It turns out that this reducible background dominates over the irreducible one from  $WW\gamma$ . Several other backgrounds such as  $WWj$  (by a photon fake),  $ZZ\gamma$ , and  $Wjj\gamma$  can be considered, but they can be sufficiently suppressed by a set of cuts that we impose.

We next discuss the discovery opportunity of the KK graviton based on the cuts listed in Table 10. To this end, we take a couple of representative study points (SPs) at  $\sqrt{s} = 100$  TeV: 1) SP1 with  $m_1^\gamma = 2.5$  TeV and  $c = 2$  and 2) SP2 with  $m_1^\gamma = 3$  TeV and  $c = 2$ . As mentioned before, the dominant SM background is  $Wj\gamma$ . For the distributions of the transverse momenta of the leading jet  $P_T^j$  and

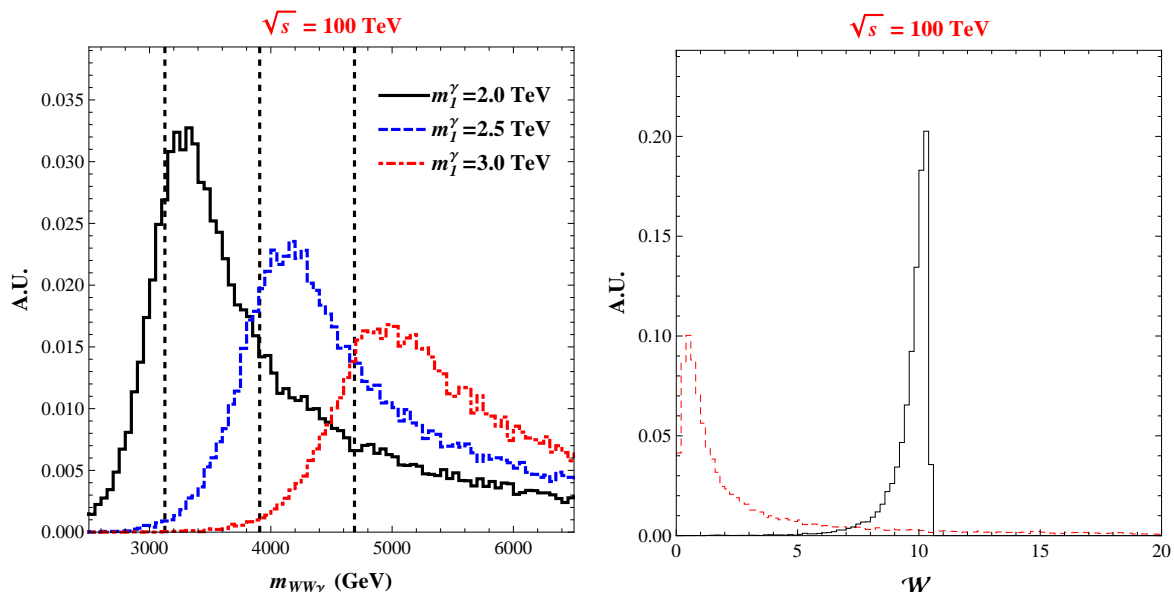


**Fig. 98:** Left panel: unit-normalized  $m_{WW\gamma}$  distributions for three different  $m_{\gamma_1}$  values with  $c = 2$ .  $\sqrt{s}$  is set to be 100 TeV. The vertical dashed lines indicate the relevant theory expectations. Right panel: unit-normalized distributions of the  $W$  variable for the dominant background  $Wj\gamma$  (black solid histogram) and the signal (red dashed histogram) events at  $\sqrt{s} = 100$  TeV.

the photon  $P_T^\gamma$ , the background peaks in the low  $P_T$  region while the signal events tend to have larger values of  $P_T$  above 150 GeV and 600 GeV for the jets and photon, respectively. Therefore, we find that  $P_T^j > 150$  GeV and  $P_T^\gamma > 600$  GeV are very powerful in reducing the background. Furthermore, the invariant mass constructed with the two  $W$ 's and the photon can provide a powerful handle for the signal-background separation. As discussed above, we implement this observation as the  $W$  measure and confirm its performance (see the right panel of Fig. 98).

We make our parton-level Monte Carlo simulation for both signal and background processes, using MG5\_aMC@NLO [94] and CalcHEP3.4 [674] using the parton distribution functions NNPDF23 [675]. To implement the warped hierarchy/flavor model under consideration appropriately, we first take existing model files in Ref. [676]. As the model files do not contain the vertex of  $G_1\gamma_1\gamma$ , we add the relevant vertex structure based on the corresponding one encoded in  $G_1\gamma\gamma$  as previously explained. In addition, various decay modes of  $\gamma_1$  are written by modifying the existing vertices in the model files. We obtain the total number of signal (defined as  $S$ ) and background (defined as  $B$ ) events to calculate the significance  $S/\sqrt{B}$  as follows:

$$S = \epsilon_W \times N_S, \quad (82)$$

$$B = \epsilon_W \times N_{WW\gamma} + 2 \times (1 - \epsilon_j) \times N_{Wj\gamma}, \quad (83)$$

where  $N_S$ ,  $N_{WW\gamma}$ , and  $N_{Wj\gamma}$  are numbers of events after all cuts, i.e., the numbers in the second and third last rows in Table 10, for the signal (either SP1 or SP2),  $WW\gamma$ , and  $Wj\gamma$  backgrounds, respectively. Here the tagging efficiency  $\epsilon_W$  (rejection rate  $\epsilon_j$ ) for a two-prong  $W$ -jet (single-prong QCD jet) is set to be 0.5 (0.95) [677]. For a more conservative analysis, we include a factor of two for the  $Wj\gamma$  background to account for the next-to-leading order corrections.

Table 10 shows signal (SP1 and SP2) and background ( $WW\gamma$  and  $Wj\gamma$ ) cross sections in fb according to a set of cuts at a  $pp$  collider of  $\sqrt{s} = 100$  TeV. We find that  $m_{\gamma_1}^\gamma = 2.5$  TeV (or equivalently,  $m_{\gamma_1}^G \sim 3.7$  TeV) can allow a  $5\sigma$  discovery of our photon cascade decay signal with an integrated luminosity of  $3 \text{ ab}^{-1}$ . This scale of the KK graviton mass is in a fairly good agreement with precision

	SP1	SP2	$WW\gamma$	$Wj\gamma$
No cut	0.4	0.13	–	–
Basic cuts	0.35	0.12	(391)	$(1.68 \times 10^5)$
$p_T^\gamma > 600$	0.31	0.11	1.81	132.0
$p_T^{j/\ell} > 150$	0.26	0.10	0.28	42.5
$ \eta^{\text{all}}  < 2.0$	0.21	0.08	0.19	29.6
$E_T^{\text{miss}} > 150$	0.20	0.077	0.10	13.1
$\Delta R_{jj} < 0.4$	0.19	0.077	0.09	–
$60 < m_{jj} < 100$	0.19	0.077	0.09	–
$\mathcal{W} < 0.9(\text{SP1})$	0.03	–	0.0025	0.29
$\mathcal{W} < 2.0(\text{SP2})$	–	0.014	0.0055	1.19
$\mathcal{L}$ (ab <sup>-1</sup> )	3	3	3	3
Number of events (SP1)	90	–	7.5	870
Number of events (SP2)	–	42	16.5	3570
$S/\sqrt{B}$	$5.0\sigma$	$1.1\sigma$	–	–

**Table 10:** Signal and background cross sections in fb according to a sequence of cuts for two study points, SP1:  $m_1^\gamma = 2.5$  TeV with  $c = 2$  and SP2:  $m_1^\gamma = 3$  TeV with  $c = 2$ , and two dominant SM backgrounds at a  $pp$  collider of  $\sqrt{s} = 100$  TeV. To evaluate the background cross sections as leading order (in parentheses) without introducing any possible divergence, we require basic selection cuts such as  $p_T^j > 20$  GeV,  $p_T^{\gamma/\ell} > 10$  GeV,  $|\eta^j| < 5$ ,  $|\eta^{\gamma/\ell}| < 2.5$ , and  $\Delta R_{jj/j\gamma} > 0.01$ . All momenta and masses are in the unit of GeV.

electroweak constraints [678, 679] as well as the current bounds inferred from a null observation of KK gluons [680, 681].

To summarize, we have studied an unconventional search channel of the KK graviton featured by a novel ‘‘cascade decay’’ into a photon and an on-shell KK photon  $\gamma_1$  which subsequently decays into a semi-leptonic  $W$  pair. The highly energetic photon due to the mass gap between  $G_1$  and  $\gamma_1$  provides a distinct and elementary final state signature which can be detected efficiently. Although the photon coupling is suppressed by a 5D ‘‘volume factor’’, the strong coupling between  $G_1$  and  $\gamma_1$  renders this mode merely semi-suppressed. Consequently, we pointed out that the different dependence of the total rate on the volume factor from that of conventional search channels could enable us to determine the underlying model parameters. We found that the discovery reach of the KK graviton at future colliders such as a 100 TeV collider would be roughly  $m_1^G = 4$  TeV at an integrated luminosity of  $3 \text{ ab}^{-1}$ . Finally, we emphasize that the proposed search strategy with regard to  $\gamma\ell jj + \cancel{E}_T$  signature can be straightforwardly applied to other BSM models containing processes yielding the same final state.

#### 4.1.9 Seesaw Models and Resonances with Cascade Decays Involving RH Neutrinos

A widely discussed paradigm for neutrino masses is the so-called type-I seesaw mechanism [682–685] which postulates the existence of heavy right-handed (RH) neutrinos  $N$  with Majorana masses. The mass scale of the RH neutrinos, synonymous with the seesaw scale, is *a priori* unknown, and its determination would play a big role in vindicating the seesaw mechanism as the new physics responsible for neutrino

mass generation. In a bottom-up approach, the seesaw scale could be anywhere ranging from the left-handed (LH) neutrino mass scale of sub-eV all the way up to the grand unification theory (GUT) scale. However, there are arguments based on naturalness of the Higgs mass which suggest the seesaw scale to be below  $10^7$  GeV or so [686, 687]. It is therefore of interest to focus on the seesaw scale being in the multi-TeV range which can be accessed at the current and foreseeable future collider energies. In particular, hadron colliders can probe TeV-scale seesaw through the “smoking gun” lepton number violating (LNV) signal of same-sign dilepton plus dijet final states:  $pp \rightarrow W^* \rightarrow N\ell^\pm \rightarrow \ell^\pm\ell^\pm jj$  [688] and other related processes, such as the collinear-enhanced  $t$ -channel photon exchange processes [689–691]. In addition, there are many kinds of complementary low energy searches for rare processes, such as neutrinoless double beta decay ( $0\nu\beta\beta$ ) [692], lepton flavor violation (LFV) [693], anomalous Higgs decays [694–697] and so on which are sensitive to TeV-scale models of neutrino mass. It is important to emphasize that the collider probe of the seesaw is truly complementary to the low-energy searches of LNV and LFV at the intensity frontier. For a recent review on the collider aspects of TeV-scale seesaw, see e.g., Ref. [698].

In the simplest seesaw extension of the SM, i.e. with the minimal addition of the heavy Majorana neutrinos while keeping the SM gauge group unchanged, there are two key aspects that can be tested experimentally, namely, the Majorana mass  $M_N$  of the mostly sterile neutrinos and their mixing  $V_{\ell N}$  with the active neutrinos. In the traditional “vanilla” seesaw mechanism [682–685], the left-right neutrino mixing is suppressed by the light neutrino mass  $M_\nu \lesssim 0.1$  eV:

$$V_{\ell N} \simeq \sqrt{\frac{M_\nu}{M_N}} \lesssim 10^{-6} \sqrt{\frac{100 \text{ GeV}}{M_N}}. \quad (84)$$

Thus for a TeV-scale seesaw, the experimental effects of the light-heavy neutrino mixing are expected to be too small, unless the RH neutrinos have additional interactions, e.g. when they are charged under a  $U(1)$  or  $SU(2)$  gauge group. There exists a class of low-scale Type-I seesaw scenarios [699–708], where  $V_{\ell N}$  can be sizable due to specific textures of the Dirac and Majorana mass matrices in the seesaw formula  $M_\nu \simeq -M_D M_N^{-1} M_D^T$ . However, the constraints of small neutrino masses usually suppress the LNV  $\ell^\pm\ell^\pm jj$  signals [702, 707, 709] in these models.

Another natural realization of a low-scale seesaw scenario with large light-heavy neutrino mixing is the inverse seesaw model [710, 711]. In this case, the magnitude of the neutrino mass becomes decoupled from the heavy neutrino mass, thus allowing for a large mixing

$$V_{\ell N} \simeq \sqrt{\frac{M_\nu}{\mu_S}} \approx 10^{-2} \sqrt{\frac{1 \text{ keV}}{\mu_S}}, \quad (85)$$

where  $\mu_S$  is the small LNV parameter in the theory, whose smallness is “technically natural”, i.e. in the limit of  $\mu_S \rightarrow 0$ , lepton number symmetry is restored and the LH neutrinos are massless to all orders in perturbation theory, as in the SM.

As for the LNV signature at colliders, in a natural seesaw scenario with approximate lepton number conservation, the LNV amplitude for the on-shell production of heavy neutrinos at average four-momentum squared  $\bar{s} = (M_{N_1}^2 + M_{N_2}^2)/2$  can be written as

$$\mathcal{A}_{\text{LNV}}(\bar{s}) = -V_{\ell N}^2 \frac{2\Delta M_N}{\Delta M_N^2 + \Gamma_N^2} + \mathcal{O}\left(\frac{\Delta M_N}{M_N}\right), \quad (86)$$

for  $\Delta M_N \lesssim \Gamma_N$ , i.e. for small mass difference  $\Delta M_N = |M_{N_1} - M_{N_2}|$  between the heavy neutrinos compared to their average decay width  $\Gamma_N \equiv (\Gamma_{N_1} + \Gamma_{N_2})/2$ . Thus, the LNV amplitude in (86) will be suppressed by the small mass splitting, except for the case  $\Delta M_N \simeq \Gamma_N$  when it can be resonantly enhanced [712]. In general, whether the dilepton signal can be of same-sign or mostly of opposite-sign depends on how degenerate the RH neutrinos are and to what extent they satisfy the coherence

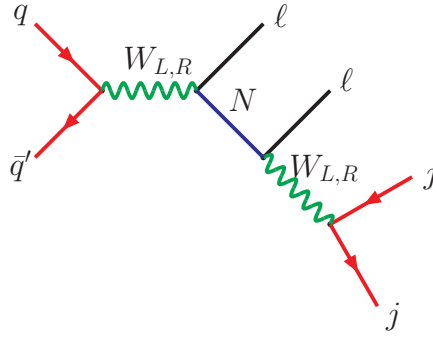


**Fig. 99:** Feynman diagram for the “smoking gun” collider signal of seesaw in the LRSM.

condition [713]. For seesaw models with suppressed same-sign dilepton signal, one can use the opposite-sign dilepton signal [714] and rely on the specific kinematic features to distill the signal from the huge SM background. Another option is to use the trilepton channel:  $pp \rightarrow W^* \rightarrow N\ell^\pm \rightarrow \ell^\pm\ell^\mp\ell^\pm + \cancel{E}_T$  [715–720], which has a relatively smaller SM background.

The current direct search limits using the same-sign dilepton channel with  $20 \text{ fb}^{-1}$  data at  $\sqrt{s} = 8$  TeV LHC [721, 722] range from  $|V_{\ell N}|^2 \lesssim 10^{-2} - 1$  for  $M_N = 100 - 500$  GeV for  $\ell = e, \mu$ . These limits could be improved by roughly an order of magnitude and extended for heavy neutrino masses up to a TeV or so with the Run-II phase of the LHC [698] or with a future lepton collider [723, 724]. On the other hand, with the currently allowed mixing, a  $5\sigma$  discovery can be made for a TeV-scale heavy Majorana neutrino at a 100 TeV collider with  $1 \text{ ab}^{-1}$  of integrated luminosity [691]. We should note here that the  $W\gamma$  vector boson fusion processes [690, 691, 698] become increasingly important at these energies and must be taken into account, along with the usual Drell-Yan production mechanism so far considered in analyzing the LHC data.

On the theory front, a natural framework which could provide a TeV-scale renormalizable theory of the seesaw mechanism is the Left-Right (L-R) Symmetric extension of the SM (LRSM) [725–728], see also Section 4.5 of Volume 2 of this report. The two essential ingredients of seesaw, i.e., the existence of the RH neutrinos (and exactly three of them) and the seesaw scale, emerge naturally in LRSM – the former as the parity gauge partners of the LH neutrinos and the latter as the scale of parity restoration. There also exist examples [729] where the small neutrino masses via type-I seesaw at TeV-scale can arise without excessive fine tuning of the LRSM parameters. In addition, the discovery of the RH gauge bosons below 10 TeV could falsify the popular mechanism of leptogenesis as a viable explanation of the observed matter-antimatter asymmetry in our Universe [730–733]. There are therefore considerable theoretical motivations to search for TeV-scale L-R seesaw signatures at the LHC and future colliders. It is worth emphasizing that in the LRSM, the Majorana nature of the RH neutrinos inevitably leads to the LNV signature of  $\ell^\pm\ell^\pm jj$  [585, 688, 717, 734–741], irrespective of the light-heavy neutrino mixing parameter  $V_{\ell N}$ . A RH charged gauge boson mass up to  $\sim 5.5$  TeV with  $300 \text{ fb}^{-1}$  of data at the 14 TeV LHC [734] or up to  $\sim 32$  TeV with  $1 \text{ ab}^{-1}$  of data at a 100 TeV collider [585, 741] can be probed using the same-sign dilepton channel.

For  $M_{W_R} > M_N > M_W$ , there are *four* different sources in the LRSM for the origin of the  $\ell\ell jj$  signal at the LHC [739, 742] (see Fig. 99):

$$LL: \quad pp \rightarrow W_L^* \rightarrow \ell N \rightarrow \ell\ell W_L \rightarrow \ell\ell jj, \quad (87)$$

$$RR: \quad pp \rightarrow W_R \rightarrow \ell N \rightarrow \ell\ell W_R^* \rightarrow \ell\ell jj, \quad (88)$$

$$RL: \quad pp \rightarrow W_R \rightarrow \ell N \rightarrow \ell\ell W_L \rightarrow \ell\ell jj, \quad (89)$$

$$LR: \quad pp \rightarrow W_L^* \rightarrow \ell N \rightarrow \ell\ell W_R^* \rightarrow \ell\ell jj, \quad (90)$$

where the first ( $LL$ ) mode is the only one that arises in the SM seesaw via  $s$ -channel exchange of the SM  $W$ -boson, whereas all the four modes can arise in L-R models. These signals are uniquely suited to probe the Majorana and Dirac flavor structure of the neutrino seesaw and are therefore an important probe of the detailed nature of the seesaw mechanism. To this end, it is important to disambiguate the different mechanisms (87)-(90) in case of a positive collider signal in future. This can be done systematically [741] by determining the kinematic endpoints of different invariant mass distributions, e.g.,  $m_{\ell\ell}$ ,  $m_{\ell jj}$ ,  $m_{\ell\ell j}$  etc., irrespectively of the dynamical details. This general kinematic strategy is equally applicable to both same and opposite-sign dilepton signals. In this sense, its efficacy is not just limited to the type-I seesaw models, but also to many of its variants, such as the inverse [710, 711], linear [743] and generalized [704, 744–746] seesaw models, which typically predict a dominant opposite-sign dilepton signal. Some of these variants might indeed be relevant in the potential discovery of parity restoration, if the recent observations from both CMS [714] and ATLAS [722] indicating a paucity of  $\ell^\pm \ell^\pm jj$  events is confirmed in future collider data.

Let us consider pure right-handed current (RHC) signals for the process of Eq. (88). Here we try to be as model independent as possible and we assume and discuss general left and right gauge couplings  $g_L, g_R$ . We are testing effects of a heavy particle sector neglecting small heavy neutrino and  $W_2^\pm$  mixings with corresponding light SM states. In this way pure effects coming from right-handed sector on the  $pp \rightarrow lljj$  process are discussed [747]. It is also shown when mixings of heavy neutrino states can be factored out.

RHC Lagrangian includes general couplings  $g_L, g_R$ , which are important for gauge couplings unification [745, 748]

$$\mathcal{L}_L + \mathcal{L}_R = \frac{g_L}{\sqrt{2}} \bar{\nu}_a \gamma^\mu P_L (U_{PMNS})_{aj} l_j W_{1\mu}^+ + \frac{g_R}{\sqrt{2}} \bar{N}_a \gamma^\mu P_R (K_R)_{aj} l_j W_{2\mu}^+ + \text{h.c.} \quad (91)$$

$\mathcal{L}_L$  describes the SM physics of charged currents. It includes the neutrino mixing matrix  $U_{PMNS}$ , responsible for neutrino oscillations phenomena.  $\mathcal{L}_R$  is responsible for non-standard effects connected with heavy neutrinos  $N_a$  and right-handed currents mediated by an additional heavy charged gauge boson  $W_2$ .  $K_R$  defines a mixing matrix between flavour and massive heavy neutrino states. We assume it unitary, for a discussion, see Ref. [747].

The main RHC Feynman diagram which gives the  $pp \rightarrow lljj$  process comes through two  $W_2$  gauge bosons and heavy neutrinos  $N_a$  in intermediate states, i.e.  $pp \rightarrow W_2 \rightarrow N_a l \rightarrow ll W_2 \rightarrow lljj$ . For literature, see Refs. [688, 715, 729, 735–737, 739, 740, 745–747, 749–758]. This signal mimics the signature of neutrinoless double beta decay when the two leptons are same-sign electrons.

To account lepton number violation, which might come if Majorana neutrinos are involved, we use the following notation:

$$\sigma_{ij}^{\pm\pm} = \sigma(pp \rightarrow l_i^\pm l_j^\pm jj), \quad (92)$$

$$\sigma_{ij}^{\pm\mp} = \sigma(pp \rightarrow l_i^\pm l_j^\mp jj). \quad (93)$$

We collectively denote all these cross-sections by  $\sigma_{ij}$ . The process depends on the gauge couplings  $g_L$  and  $g_R$ , the quark mixing matrices  $U_{CKM}^{L,R}$ , which can be chosen of the same form [759, 760], the Parton Distribution Functions (PDFs)  $f_\alpha(x, Q^2)$  and the heavy neutrino mixing matrix  $(K_R)_{aj}$ , see Eq. (91). The mass scales which are important for the process are:  $M_{W_2}$ ,  $M_{N_a}$  and  $\sqrt{s}$ . It can be shown, that quite generally we have  $\Gamma(W_2)/M_{W_2}$ ,  $\Gamma(N_a)/M_{N_a} \ll 1$  and the NWA can be used to compute  $\sigma_{ij}$  [747, 761]. When masses of heavy neutrinos are degenerate then dependence on the mixing matrix elements  $(K_R)_{aj}$  can be factorized from the whole expression in the following way:

$$\sigma_{ij}^{\pm\pm} = \hat{\sigma}^{\pm\pm} \left| \sum_a (K_R^\dagger)_{ia} (K_R^*)_{aj} \right|^2, \quad (94)$$

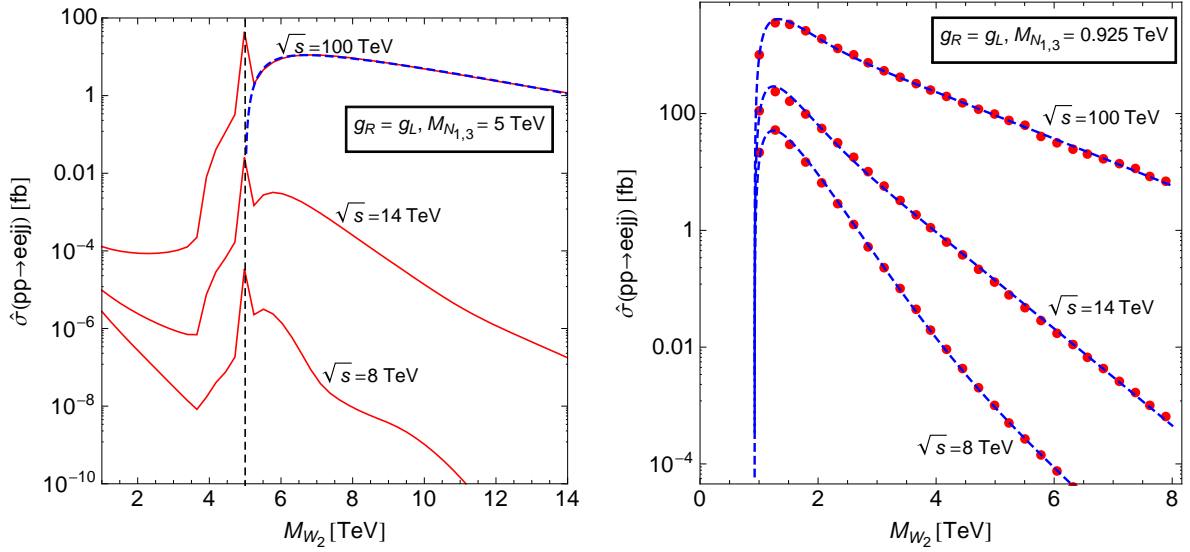


**Fig. 100:** Examples of the neutrino mixing  $K_R$  independent analysis. *Left:* The dependence of the total cross-section  $\hat{\sigma}_{ee} = \hat{\sigma}_{ee}^{+-} + \hat{\sigma}_{ee}^{++} + \hat{\sigma}_{ee}^{--}$  on  $M_{W_2}$  derived with the help of the MADGRAPH for  $\sqrt{s} = 8, 14, 100$  TeV. Heavy neutrino masses are  $M_{N_{1,3}} = 5$  TeV and  $M_{N_2} = 10$  TeV, while  $g_L = g_R$ . NWA is valid only in the region in which  $M_{W_2} > M_{N_{1,3}}$  and  $M_{W_2}$  is neither close to  $M_{N_a}$  nor to  $\sqrt{s}$  (where the distance is measured in  $\Gamma(W_2)$  units). *Right:* An example of fitting analytical formula (102) (blue dashed curves) to the numerical results (red dots) obtained for  $\sqrt{s} = 8, 14$  and 100 TeV,  $M_{N_{1,3}} = 0.925$  TeV,  $M_{N_2} = 10$  TeV with the help of the MadGraph 5 [111]. Values of the fitted parameters  $a, b, c$  and  $d$  are given in the main text, see eqs. (103)-(105).

$$\sigma_{ij}^{\pm\mp} = \hat{\sigma}^{\pm\mp} \left| \sum_a (K_R^\dagger)_{ia} (K_R)_{aj} \right|^2, \quad (95)$$

where  $\hat{\sigma}^{\pm\pm}, \hat{\sigma}^{\pm\mp}$  are “bare” cross-sections calculated for  $(K_R)_{aj} = \delta_{aj}$ , and

$$\hat{\sigma}^{\pm\pm} = \sigma(pp \rightarrow W_2^\pm) \times \text{BR}(W_2^\pm \rightarrow N_1 l_1^\pm) \text{BR}(N_1 \rightarrow l_1^\pm jj), \quad (96)$$

$$\hat{\sigma}^{+-} = [\sigma(pp \rightarrow W_2^+) + \sigma(pp \rightarrow W_2^-)] \times \text{BR}(W_2^+ \rightarrow N_1 l_1^+) \text{BR}(N_1 \rightarrow l_1^- jj). \quad (97)$$

These can be written as

$$\hat{\sigma} = \sum_{\alpha\beta} \int_{M_{N_1}^2/s}^1 dx \int_{M_{N_1}^2/xs}^1 dy f_\alpha(y, Q^2) f_\beta(x, Q^2) \hat{\sigma}_{\alpha\beta}(xys), \quad (98)$$

where  $f_\alpha(x, Q^2)$  are PDFs of partons  $\alpha$ , while  $Q$  is a characteristic scale of partonic process. Finally,  $\hat{\sigma}_{\alpha\beta}$  stands for partonic cross-section. Using the NWA one can write the “bare” cross sections in the following form [761]:

$$\hat{\sigma} = \frac{g_R^2 \pi}{18s} \frac{F_W(x_1)}{[18 + \sum_b F_W(x_b)]} \sum_{\alpha\beta} \Phi_{\alpha\beta} \left( \frac{M_{W_2}^2}{s}, M_{W_2}^2 \right). \quad (99)$$

Here, we have used differential parton-parton luminosities  $\Phi_{\alpha\beta}(\tau)$ , see e.g. [762], defined as:

$$\Phi_{\alpha\beta}(\tau, Q^2) = \frac{1}{1 + \delta_{\alpha\beta}} \int_\tau^1 \frac{dx}{x} f_\alpha(x, Q^2) f_\beta\left(\frac{\tau}{x}, Q^2\right) \quad (100)$$

and

$$F_W(x) = (2 - 3x + x^3)\theta(1 - x). \quad (101)$$

Let us shortly comment on the form of eq. (99). First, the typical asymptotic  $\sim 1/s$  is clearly visible. Second, note that  $\hat{\sigma} \sim g_R^2$  while one would rather expect  $\hat{\sigma} \sim g_R^8$  from counting powers of gauge couplings entering matrix element corresponding to the process  $pp \rightarrow l_i l_j j j$ . That difference is no longer surprising when one recalls that dominant contributions to the cross-section come from configurations in which  $W_2$  and  $N_a$  are nearly on-shell, what precisely corresponds to NWA. Finally, let us also remark that the simple consequence of  $\hat{\sigma} \sim g_R^2$  is that the cross-section scales like  $(g_R/g_L)^2 g_L^2$ .

It turns out that one can estimate the total cross-section  $\hat{\sigma}_{ee} = \hat{\sigma}_{ee}^{+-} + \hat{\sigma}_{ee}^{++} + \hat{\sigma}_{ee}^{--}$  under investigation using naive approximation:

$$\hat{\sigma}_{ee} = \frac{F_W(x_1)}{1 + \frac{1}{18} \sum_b F_W(x_b)} P(\mu), \quad (102)$$

where  $\mu = M_{W_2}/(1 \text{ TeV})$  while  $P(\mu) = a(e^{-b\mu} + ce^{-d\mu})$ . For example, in the scenario in which  $M_{N_{1,3}} = 0.925 \text{ TeV}$ , the values of fitted parameters  $a, b, c$  and  $d$  are (see Fig. 100):

$$(8 \text{ TeV}) \quad a = 0.18 \times 10^5 \text{ fb}, \quad b = 3.62, \quad c = 0.002, \quad \text{and} \quad d = 2.17, \quad (103)$$

$$(14 \text{ TeV}) \quad a = 1.32 \times 10^5 \text{ fb}, \quad b = 3.97, \quad c = 0.016, \quad \text{and} \quad d = 1.92, \quad (104)$$

$$(100 \text{ TeV}) \quad a = 5.40 \times 10^5 \text{ fb}, \quad b = 3.04, \quad c = 0.020, \quad \text{and} \quad d = 0.94. \quad (105)$$

Heavy neutrino masses are taken as in Ref. [747], though here the cross sections in Fig. 100 is general and independent of the  $K_R$  mixing matrix parametrization. For  $M_N = 10 \text{ TeV}$  the cross section is already very small, at the  $\sim \text{ab}$  level in a whole range of considered  $M_{W_2}$  masses.

From this analysis we see that the  $pp \rightarrow lljj$  process signal coming from right-handed currents (RHC) is about two order of magnitudes larger at a 100 TeV collider compared to the LHC at 14 TeV and the process can be parametrized in a simple way for  $M_{W_2} \geq M_{N_i}$  independently of the heavy neutrino mixing scenarios. The background for the process depends on charges of dileptons. For the same  $l^\pm l^\pm$  (LNV) and opposite  $l^\pm l^\mp$  (LNC) signal cases see, e.g., the discussions in Refs. [735, 741, 763, 764]. Further studies are needed to assess the potential for extracting signal from background at a 100 TeV collider.

## 4.2 New Fermionic Resonances

### 4.2.1 Seesaw Leptons at Future Hadron Collider Experiments

As we already stressed in Section 4.1.9, collider tests of neutrino mass-generating offer a high degree of complementarity to low energy probes like neutrinoless double-beta decay, and precision lepton experiments. In particular, low energy realizations of fermionic Seesaw mechanisms predict EW- and TeV-scale  $SU(2)_L$  singlets ( $N$ ) and triplets ( $T^\pm, T^0$ ) that couple to gauge bosons through mixing (singlet) or directly via gauge quantum numbers (triplet).

If kinematically accessible, these particles can be resonantly produced in hadron collisions through a variety of mechanisms. Fig. 101 shows LO and NLO production rates of a singlet neutrino for  $m_N > M_W$  [765, 766]. While Drell-Yan (DY) largely dominates at 14 TeV, the situation is qualitatively different at 100 TeV, where the gluon fusion (GF) process

$$g g \rightarrow N \nu_\ell^{(-)} \quad (106)$$

is the leading production mode for  $m_N \lesssim 1.5 \text{ TeV}$  [765]. Beyond this, vector boson fusion (VBF)

$$q \gamma \xrightarrow{W\gamma \text{ Fusion}} N \ell^\pm q' \quad (107)$$

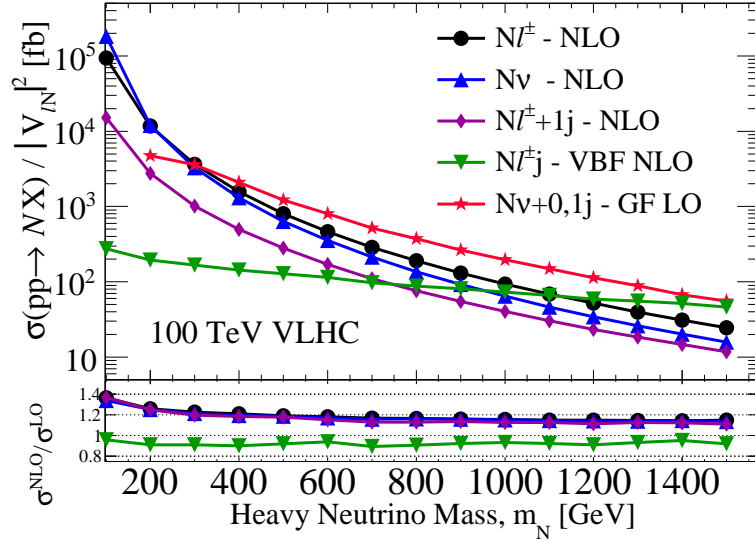


**Fig. 101:** 100 TeV pair production rates of a singlet seesaw lepton [765] as a function of mass.

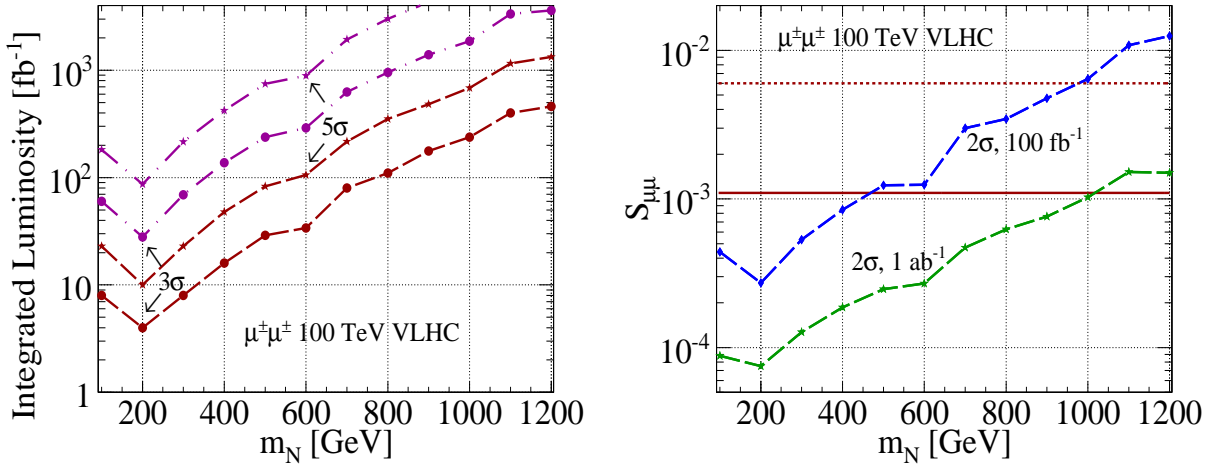


**Fig. 102:** *Left:* required luminosity for 3 ( $5$ ) $\sigma$  evidence (discovery) at a 100 TeV collider as a function of heavy neutrino mass  $m_N$  in the  $\mu^\pm\mu^\pm$  final state assuming optimistic (dash) and pessimistic (dash-dot) mixing scenarios [691]; *Right:* sensitivity to  $N - \mu$  mixing at a 100 TeV collider [691]. Both plots are in the Type-I Seesaw model.

is dominant. For  $m_N \approx 1$  TeV, the GF, DY, and VBF mechanisms all share cross sections of the order of 100 fb. In Fig. 77 we have already shown the NLO triplet pair production rates for both the charged current and neutral current Drell-Yan processes [767, 768]

$$q \bar{q}' \rightarrow W^* \rightarrow T^0 T^\pm \quad \text{and} \quad q \bar{q} \rightarrow \gamma \rightarrow T^+ T^-. \quad (108)$$

Compared to the 14 TeV LHC, the reach of a 100 TeV  $pp$  collider grows considerably from  $\sigma_{14 \text{ TeV}} = 1$  ab for triplet masses  $m_T \approx 2.5$  TeV to  $\sigma_{100 \text{ TeV}} = 1$  ab for  $m_T \approx 10 - 11$  TeV.

We now briefly summarize preliminary discovery potential of Seesaw leptons at 100 TeV. We note that model-independent benchmark searches are rather robust since it is straightforward to reinterpret collider results for a particular neutrino flavor model.

A key prediction of Type I-based scenarios is the existence of lepton number violating interactions,  $N \rightarrow \ell^\pm W^\mp$ , which implies the same-sign leptons collider signature [688] already discussed in Section

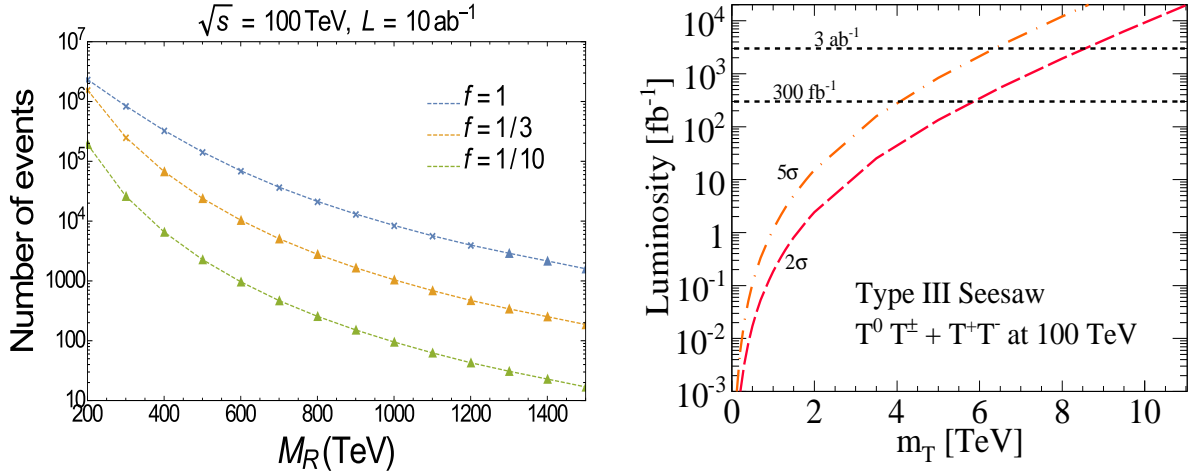


**Fig. 103:** *Left:* in ISS, number of  $\mu^\pm\tau^\mp jj$  events at a 100 TeV collider as a function of the seesaw scale  $M_R$  for representative scaling factors  $f$  [769]. Triangles respect constraints from LFV radiative decays while crosses do not respect the  $\tau \rightarrow \mu\gamma$  BaBar upper limit [770]. *Right:* in Type III Seesaw, required luminosity for 2 (5) $\sigma$  sensitivity (discovery) at a 100 TeV collider versus heavy lepton mass  $m_T$  with fully reconstructible final states [767].

#### 4.1.9

$$q\bar{q}' \rightarrow N\ell_1^\pm \rightarrow \ell_1^\pm \ell_2^\pm W^\mp \rightarrow \ell_1^\pm \ell_2^\pm jj. \quad (109)$$

The largeness of the  $N\ell^\pm$  VBF production cross section relative to the charged current DY process offers considerable gain to inclusive searches for heavy Majorana neutrinos. Assuming currently allowed mixing, a 5 $\sigma$  discovery can be made via the  $\mu^\pm\mu^\pm$  channel for  $m_N = 1070$  GeV at 100 TeV after 1  $\text{ab}^{-1}$ ; conversely,  $N - \mu$  mixing as small as  $S_{\mu\mu} \approx |V_{\mu N}|^2 \lesssim 8 \times 10^{-5}$  may be probed [691]. In the same-sign muon final state, the left panel of Fig. 102 shows the required luminosity for 3 (5) $\sigma$  evidence (discovery) as a function of  $m_N$  assuming an optimistic (dash) and pessimistic (dash-dot) mixing scenario; in the right panel of Fig. 102 the sensitivity to mixing between heavy neutrinos and muons flavor states is shown. The Inverse Seesaw relies on an approximately conserved lepton number symmetry to suppress the light neutrino masses and lower the seesaw scale while keeping large Yukawa couplings. As a consequence, heavy neutrinos form pseudo-Dirac pairs and lepton number violating processes such as the one in Eq. (109) are suppressed. In Ref. [769], a search relying on lepton flavor violating (LFV) final states

$$q\bar{q}' \rightarrow N\ell_1^\pm \rightarrow \ell_1^\pm \ell_2^\mp W^\mp \rightarrow \ell_1^\pm \ell_2^\mp jj, \quad (110)$$

was proposed. The left panel of Fig. 103 shows the number of expected events for inclusive  $\mu^\pm\tau^\mp jj$  production. Similar numbers would be expected for the  $e^\pm\tau^\mp$  analogue, while experimental limits on  $\mu \rightarrow e\gamma$  [771, 772] severely limit the  $e^\pm\mu^\mp jj$  event rate. This assumes only the lightest pseudo-Dirac pair is kinematically accessible, and uses the  $\mu_X$ -parametrization [773] with a neutrino Yukawa coupling

$$Y_\nu = f \begin{pmatrix} -1 & 1 & 0 \\ 1 & 1 & 0.9 \\ 1 & 1 & 1 \end{pmatrix}. \quad (111)$$

$M_R$  is defined as in Ref. [769] and can be interpreted as the seesaw scale. The mass of the heavy neutrinos is equal to  $M_R$  up to corrections proportional to  $Y_\nu v/M_R$ , explaining the difference at low  $M_R$ .

For masses well above the EW scale, triplet fermions preferentially decay to the Higgs and longitudinal polarizations of the  $W$  and  $Z$  bosons, a manifestation of the Goldstone Equivalence Theorem. For

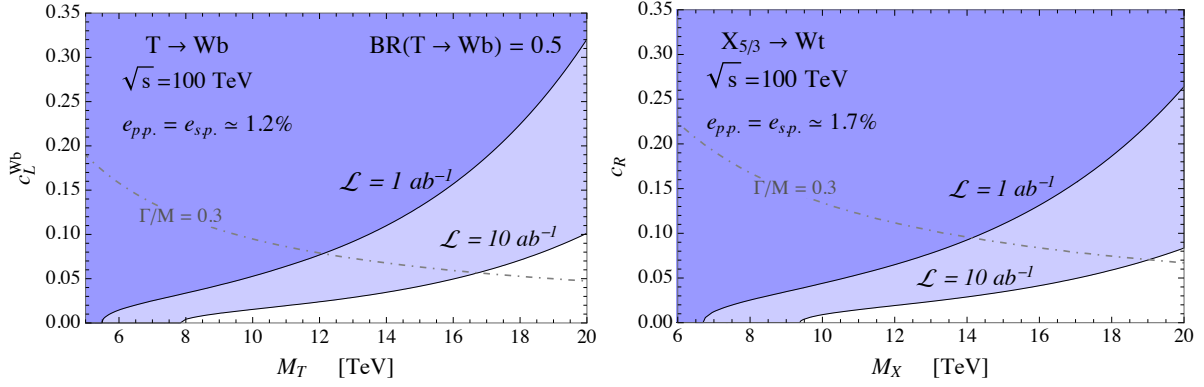


**Fig. 104:** *Left:* Exclusion reach for a top partner  $T$  of electric charge  $2/3$ ; *Right:* same plot for an  $X_{5/3}$  of charge  $5/3$ . The plots are obtained by assuming that future searches at 100 TeV will be sensitive to the same number of signal events as the current 8 TeV ones. Namely, excluded signal yields  $S_{exc} \simeq 25$  and  $S_{exc} \simeq 10$  are assumed for the  $T$  and the  $X_{5/3}$ . Signal selection efficiencies are also extracted from 8 TeV results. In the case of the single production mode, for which no dedicated searches are currently available, the efficiency ( $e_{s.p.}$ ) is taken equal to the pair production one for simplicity. Further details can be found in Ref. [774].

EW boson decays to jets or charged lepton pairs, heavy lepton pairs can decay into fully reconstructible final-states with four jets and two high- $p_T$  leptons that scale like  $p_T^\ell \sim m_T/2$ :

$$T^0 T^\pm \rightarrow \ell \ell' + WZ/Wh \rightarrow \ell \ell' + 4j / 2j + 2b, \quad (112)$$

$$T^+ T^- \rightarrow \ell \ell' + ZZ/Zh/hh \rightarrow \ell \ell' + 4j / 2j + 2b / 4b. \quad (113)$$

Assuming a nominal detector acceptance and efficiency of  $\mathcal{A} = 0.75$ , at 100 TeV and after  $10 \text{ fb}^{-1}$ , a  $5\sigma$  discovery can be achieved for  $m_T \approx 1.4 - 1.6 \text{ TeV}$  [767]. Taking instead  $\mathcal{A} = 1.0$ , The right panel of Fig. 103 shows the discovery potential of the combined charged current and neutral current processes. After  $3 \text{ ab}^{-1}$ , there is  $5 (2)\sigma$  discovery (sensitivity) up to  $m_T \approx 6 (8) \text{ TeV}$ .

#### 4.2.2 Fermionic Top Partners in Composite Higgs Models

An 100 TeV collider can probe models with a terrific amount of Electro-Weak fine tuning. Even if none of these models had to be discovered, the result will be extremely informative as it will strongly disfavour (or exclude) a Natural origin of the Electro-Weak scale, pushing us towards the investigation of alternatives. We illustrate this point by estimating the reach, in terms of exclusions, for vector-like coloured fermions with a sizeable coupling to third-generation quarks, the so-called “top partners”. Top partners are a common prediction of composite Higgs models in which the partial compositeness paradigm is assumed for the generation of fermion masses (see, e.g., Refs. [613,614] for a review). In these models, their mass  $M$  is directly related to the amount of fine-tuning  $\Delta$  according to the approximate formula

$$\Delta \sim \left( \frac{M}{500 \text{ GeV}} \right)^2. \quad (114)$$

Top partners are coloured, thus they are unmistakably produced in pair by QCD interactions. They are also endowed with a sizeable coupling to third generation quarks and SM vector bosons or Higgs. The latter coupling is responsible for their decay, but also for their single production in association with a forward jet and a third generation quark. Exclusion contours are displayed in Fig. 104, in the plane defined by the top partner mass and its single production coupling. Top partners of electric charge  $2/3$  (and  $\text{BR}(Wb) = 0.5$ , which is typical for a SM singlet) and  $5/3$  are shown, respectively, in the left and

right plots. The results are based on a rough extrapolation based on current LHC Run-I limits and details are reported in the figure caption and, more extensively, in Ref. [774]. A partial confirmation of the validity of the extrapolation, based on 100 TeV simulations, can be found in Ref. [775].

The result is that top partner masses of around 9 TeV can be excluded at an 100 TeV collider with  $10 \text{ ab}^{-1}$  luminosity in a completely model-independent way (i.e., for vanishing single-production coupling). According to Eq. (114), this corresponds to  $\Delta \sim 300$ . For composite Higgs models that cannot be excluded at the LHC, namely for  $\xi = v^2/f^2 = 0.05$  or  $\xi = 0.01$ , single production couplings of order  $c \simeq 0.2$  or  $c \simeq 0.1$  are expected [774] and the reach considerably increases.

### 4.2.3 Exotic Quarks in Twin Higgs Models: Displaced Decays in Association with a Prompt $t\bar{t}$ Pair

Models of “neutral naturalness”, where the top partners do not carry SM color, provide a new set of signatures at hadron collider experiments. Since the low-energy connection between the SM and the sector that stabilizes the weak scale is feeble, the decays of the lightest BSM particles into the SM typically have macroscopic lifetimes, leading to displaced signatures. These challenging signals, combined with the low production rates of uncolored particles, imply that it is not unconceivable that a neutrally natural theory with a fine-tuning of  $O(10)\%$  may completely escape detection at the LHC. However, a general feature of this class of models is that they only solve the little hierarchy problem, and thus require UV completion at a relatively low scale of at most  $\sim 10$  TeV. The particles belonging to the UV theory would likely become accessible at a future 100 TeV collider, thanks to the high partonic energies available, allowing the future collider to probe an entirely new set of experimental signals. In this subsection, following Ref. [776], we begin the identification of the signatures of UV completions of neutral naturalness, by considering its prime example, the Twin Higgs [777], as benchmark model.

In the Twin Higgs, all the new particles lighter than about a TeV are complete SM singlets. However, the model requires to be extended below  $\sim 10$  TeV, to remove residual logarithmic divergences. In non-supersymmetric UV completions, new exotic fermions charged under both the SM and the twin gauge symmetries must accompany the top quark. Their masses are expected to be in the 1-10 TeV range. Some of these new fermions carry SM color, and would therefore be pair produced with large rates at a 100 TeV collider. Once produced, each of these “exotic quarks” decays into a SM top quark plus twin particles. Some of the twin particles can decay back to the SM with long lifetimes, giving rise to spectacular displaced vertices in combination with the prompt  $t\bar{t}$  pair. Therefore, the signatures we consider are, labeling the exotic quarks as  $\mathcal{T}, \mathcal{B}$ ,

$$\begin{aligned} pp &\rightarrow (\mathcal{T} \rightarrow t\hat{Z})(\bar{\mathcal{T}} \rightarrow \bar{t}\hat{Z}) \rightarrow t\bar{t} + \text{twin hadrons}, & \text{twin hadron} &\rightarrow \text{displaced signal}, \\ pp &\rightarrow (\mathcal{B} \rightarrow t\hat{W})(\bar{\mathcal{B}} \rightarrow \bar{t}\hat{W}) \rightarrow t\bar{t} + \text{twin leptons}, & \text{twin lepton} &\rightarrow \text{displaced signal}, \end{aligned} \quad (115)$$

where  $\hat{Z}, \hat{W}$  are the twin gauge bosons (we denote all the twin particles with a hat).

We consider the “fraternal” version of the Twin Higgs, inspired by naturalness, where only the third generation SM fermions acquire a twin partner [523]. Therefore the twin hadrons in eq. (115) are produced by the  $\hat{Z} \rightarrow \hat{b}\bar{b}$  decay, followed by twin hadronization. Depending on the parameters, the long-lived twin hadron can be either a  $CP$ -even scalar meson  $\hat{\chi}_{b0}$ , a vector meson  $\hat{Y}$  or a glueball  $\hat{G}_{0^{++}}$ . The  $\hat{\chi}_{b0}$  and  $\hat{G}_{0^{++}}$  decay through mixing with the 125 GeV Higgs and therefore primarily into  $b\bar{b}$ , whereas the  $\hat{Y}$  decays via photon kinetic mixing and thus almost democratically into all the SM electrically charged particles. The corresponding proper decay lengths are [523, 776]

$$\begin{aligned} c\tau_{\hat{\chi}_{b0}} &\simeq 3.8 \text{ cm} \left( \frac{m_b}{m_{\hat{b}}} \right)^2 \left( \frac{f}{1 \text{ TeV}} \right)^4 \left( \frac{5 \text{ GeV}}{\Lambda} \right)^5, \\ c\tau_{\hat{Y}} &\simeq 1.3 \text{ cm} \left( \frac{m_{\hat{A}}}{100 \text{ GeV}} \right)^4 \left( \frac{10^{-3}}{\epsilon} \right)^2 \left( \frac{5 \text{ GeV}}{\Lambda} \right)^5, \end{aligned} \quad (116)$$

$$c\tau_{\hat{G}_{0^{++}}} \simeq 1 \text{ cm} \left( \frac{5 \text{ GeV}}{\Lambda} \right)^7 \left( \frac{f}{1 \text{ TeV}} \right)^4,$$

where the benchmark value of the  $Z_2$ -breaking scale  $f$  ensures that Higgs coupling deviations are too small to be detected at the LHC. The choice of twin-QCD confinement scale  $\Lambda$  is instead motivated by naturalness arguments [523]. For  $\epsilon$ , which determines the size of the kinetic mixing between the twin photon (with mass  $m_{\hat{A}}$ ) and SM photon, we use the value naturally generated by exotic quark loops. In our study we kept most of the above parameters fixed to the benchmark values of Eq. (116), except for the mass of the  $\hat{b}$  quark. As a consequence, the typical decay lengths that we consider are as follows: the proper lifetime of  $\hat{\chi}_{b0}$  approximately varies from 1 cm to 10 m, whereas the  $\hat{Y}$  and  $\hat{G}_{0^{++}}$  have centimeter-scale decays.

For the hadronic ( $b\bar{b}$ ) displaced decay search, the detector is modeled, following the ATLAS searches of refs. [778, 779], as the sum of two annuli with radii  $1 < r < 28$  cm and  $200 < r < 750$  cm, representing the inner detector (ID) and hadronic calorimeter plus muon spectrometer, respectively, with an efficiency for displaced vertex (DV) identification equal to a constant 10%. In the search for  $\hat{Y}$  decays we concentrate on dimuon DVs in the ID, which is modeled, following the CMS search of Ref. [529], as an annulus with radii  $1 < r < 50$  cm and efficiency for DV identification equal to a constant 50%. In addition, simple cuts are applied directly on the twin hadrons, to roughly reproduce reasonable experimental requirements.

The combination of the prompt  $t\bar{t}$  and displaced signal ensures a straightforward triggering, and is expected to remove completely the SM background. Then, assuming no events are observed, a signal hypothesis can be excluded at 95% if it would predict more than 3 events. The projected reach of the displaced twin hadron +  $t\bar{t}$  search at a 100 TeV collider is shown in Fig. 105, assuming an integrated luminosity of  $1 \text{ ab}^{-1}$ . The sensitivity extends up to  $m_{\mathcal{T}} \sim 11$  TeV. For comparison, we also show the estimated reach obtained from the search for direct stop production [780], which is sensitive to the exotic quarks if all the produced twin particles leave the detector as missing energy. We find that the potential of the search for  $t\bar{t}$ +displaced signals can be significantly superior. Estimates for luminosities different from  $1 \text{ ab}^{-1}$  can be obtained by assuming that the signal rate scales with the partonic luminosities. This is a reasonable first approximation, because at large  $m_{\mathcal{T}}$  the exotic quark branching ratios are approximately independent of the mass, and the variation of the typical twin hadron boost factor gives subdominant effects.

The twin leptons are produced in the decay of the twin  $W$  boson,  $\hat{W} \rightarrow \hat{\ell}\hat{\ell}$  (since we assume twin electromagnetism is broken, for our purposes the distinction between twin tau and twin neutrino is irrelevant, so we simply denote all twin leptons by  $\hat{\ell}$ ). The twin leptons can mix with the SM neutrinos and thus effectively behave as sterile neutrinos, decaying into either three SM leptons or one SM lepton and a pair of quarks. As a consequence, both hadronic and leptonic displaced decay searches are relevant. The proper decay length is given by

$$c\tau_{\hat{\ell}} = 10 \text{ cm} \left( \frac{10^{-3}}{\sin \theta_\nu} \right)^2 \left( \frac{m_{\hat{\ell}}}{6 \text{ GeV}} \right)^5. \quad (117)$$

where  $\sin \theta_\nu$  controls the  $\hat{\ell}$ - $\nu$  mixing. In the range of parameters we consider, the lifetime varies from 1 cm to 10 m. The simulation of the twin lepton signals is described in detail in Ref. [776]. Here we only observe that the twin leptons are very boosted, and thus their decay products are very collimated, with typical angular separation of  $\Delta R \sim O(0.01)$ . Therefore searches for lepton jets [530] play an important role.

The projected reach of the displaced twin lepton +  $t\bar{t}$  search at a 100 TeV collider with  $1 \text{ ab}^{-1}$  is shown in Fig. 106, again under the assumption of zero SM background. The sensitivity extends up to  $m_{\mathcal{B}} \sim 11$  TeV, with hadronic displaced signals more promising due to the larger branching ratio of  $\hat{\ell}$  into quarks. To compare the reach of the twin hadron and twin lepton signals, it is useful to recall that

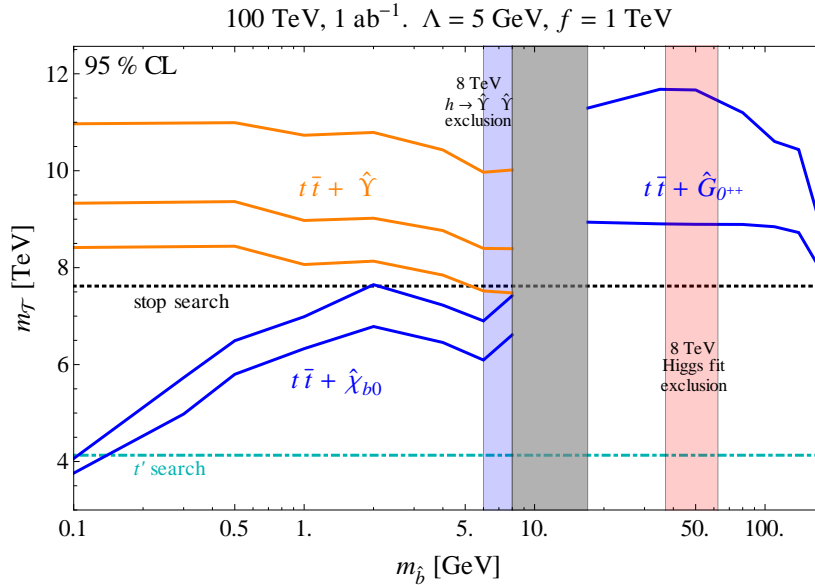


**Fig. 105:** Projected bounds on the mass of the exotic quark  $\mathcal{T}$  from the twin hadron displaced signal at a 100 TeV collider. The orange and blue curves correspond to the  $t\bar{t}$ +displaced twin hadron signals. Also shown are the bounds from top partner (dot-dashed light blue lines) and stop (dotted black lines) searches.

$m_{\mathcal{T}} \simeq (m_{\mathcal{B}}^2 + y_t^2 f^2/2)^{1/2}$ , therefore the  $\mathcal{T}$  and  $\mathcal{B}$  are approximately degenerate for masses much larger than 1 TeV.

To summarize, we presented a first study of displaced decays produced in association with a prompt  $t\bar{t}$  pair at a future 100 TeV collider. Both hadronic and leptonic displaced signals were considered. The presence of the decay products of the tops guarantees triggering, and is expected to remove completely the SM background. This signature can arise, for example, from exotic quarks that appear in several UV completions of Twin Higgs models. We estimated that a 100 TeV collider with  $1 \text{ ab}^{-1}$  will be able to probe these new fermions up to masses of  $\sim 11 \text{ TeV}$ , thus providing a strong test of the most motivated region of parameters.

#### 4.2.4 Probing Naturalness Model-Independently at a 100 TeV Collider

One of the primary goals of the current and future collider program is to search for new physics associated with the stabilization of the electroweak scale. In symmetry-based solutions to the hierarchy problem, the large quantum corrections to the Higgs scalar from the top quark must be canceled by “top partners,” new states with couplings related by symmetry to that of the top quark. In traditional theories such as minimal supersymmetric or composite Higgs models, these top partners carry SM color charge like the top quark and are copiously produced at hadron colliders. In this broad class of models, searches for new colored particles directly probe electroweak naturalness. Placing the top partner mass beyond the LHC reach of  $\sim 1 \text{ TeV}$  already implies a tuning in the Higgs mass of at least a few percent; searches for colored particles at a 100 TeV collider would probe even more parameter space, with a null result worsening the tuning.

However, as already mentioned earlier in this report, it is possible to formulate theories of “neutral naturalness” in which the top partners do not in fact carry SM color charge. This can be achieved if the symmetry which protects the Higgs is discrete and does not commute with SM color. Known examples include the folded SUSY [782] and Quirky Little Higgs [783] models in which the top partners carry electroweak charge but not color, and the Twin Higgs [777] in which the top partners are completely neu-

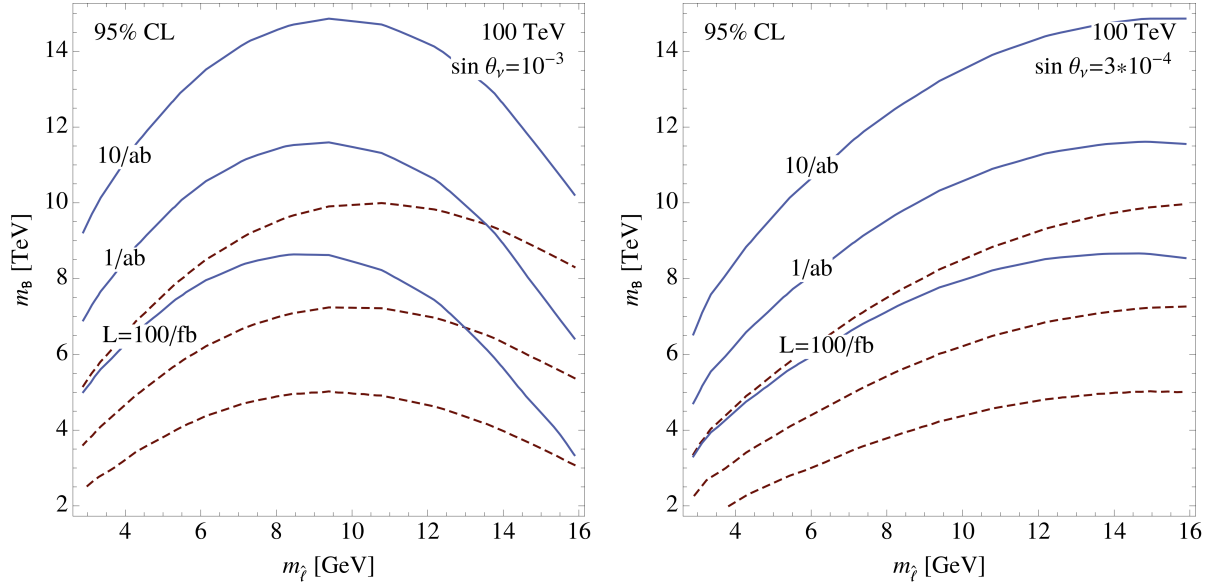


**Fig. 106:** Projected bounds on the mass of the exotic quark  $\mathcal{B}$  from the twin lepton displaced signal at a 100 TeV collider. The blue solid lines correspond to hadronic displaced searches and the brown dashed lines to leptonic displaced searches. *Left:*  $\sin \theta_\nu = 10^{-3}$ ; *Right:*  $\sin \theta_\nu = 3 \cdot 10^{-4}$ .

tral under the SM gauge forces. In these models therefore searches for new colored or even electroweak charged particles do not directly constrain naturalness. While specific neutral naturalness models proposed thus far predict various other new physics signatures (see e.g. [524, 524, 776, 784–786]), it is not obvious whether or not future collider experiments can *robustly* constrain neutral naturalness—i.e., is there a “no-lose theorem” indicating that the physics behind electroweak naturalness will be observable?

In Ref. [781], this question was addressed by exploring neutral top partner models using a bottom-up, effective field theory (EFT) approach. Model-independently, a 100 TeV hadron collider would be able to directly probe the interaction of neutral top partners with the Higgs to a modest degree. The top partners can be directly pair-produced through off-shell Higgs bosons, however because these neutral partners may be invisible to detectors this is a challenging signal, requiring the identification of initial state radiation or forward jets recoiling off of missing energy [407, 787]. In typical neutral naturalness models, such direct searches can probe masses up to  $\sim 300$  GeV [407, 781]. Additionally, measurements of double Higgs production at a 100 TeV [182, 183, 788] may be able to probe the loop-induced corrections to the triple Higgs coupling for similar top partner masses.

However, the true power of a 100 TeV collider for probing neutral naturalness is its unprecedented reach in energy. As argued in Ref. [781], a common feature of all neutral top partner EFTs is the need for a UV completion of the top partner dynamics [789–795], typically at a scale about a loop factor above the top partner mass, e.g.  $\sim 10$  TeV. This defines a new energy scale at which further new states must appear, likely carrying SM color charge. (In the case of known Twin Higgs theories this is the scale at which colored squarks or resonances appear.) As demonstrated explicitly in Ref. [776], a 100 TeV collider can allow access to these high mass states which are a necessary component of neutral naturalness. The resulting constraints on theory are complementary to those from precision measurements of Higgs properties, which can be achieved at future lepton colliders.

Applying this reasoning to EFT scenarios for Neutral Naturalness, Ref. [781] found model-independent arguments regarding the extent to which naturalness would be tested by results from future colliders. To cover the full range of possible neutral naturalness scenarios, all perturbative neutral top partner structures had to be classified, including those which have yet to be realized in a top-down theory. These include scalar top partners with direct couplings to the Higgs, as well as fermionic top partners

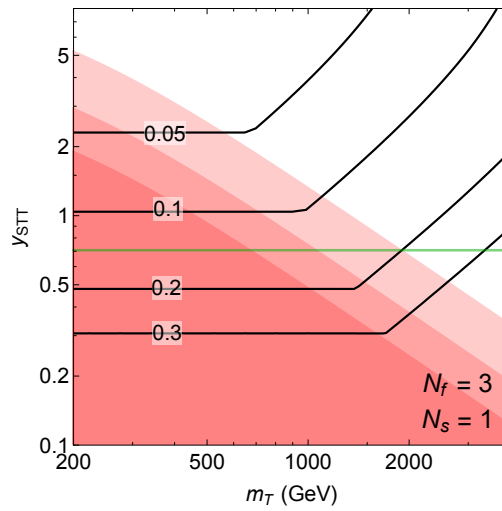
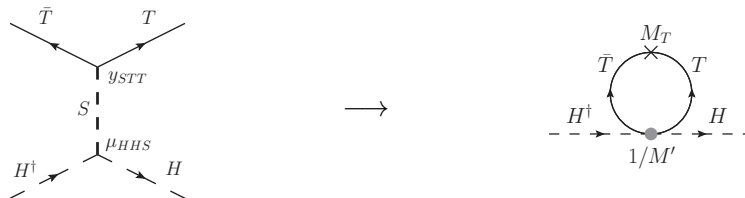


**Fig. 107:** Model-independent sensitivity estimate of future lepton and hadron colliders for theories of Neutral Naturalness, with three fermionic top partners of mass  $m_T$ , and a single scalar mediator coupling to the top partners with Yukawa coupling  $y_{STT}$ .  $m_T \gtrsim 500$  GeV leads to tuning worse than 10% due to incomplete cancellation of the top loop. *Green horizontal line:* prediction for  $y_{STT}$  in the Twin Higgs model. *Red shading:* reach of future lepton colliders from precision Higgs coupling measurements. *Black contours:* additional tuning due to the scalar mediator that can be probed by a 100 TeV collider via direct searches, assuming a mass reach for UV completions up to  $\sim 20$  TeV. Requiring both top partner and mediator tunings to be better than 10% requires either high-scale direct production signals at 100 TeV, or Higgs coupling deviations at lepton colliders, or both. See text and [781] for details.

which must couple to the Higgs via some additional mediator states. In all cases the top partner EFTs must be completed by further new physics at some UV scale  $\Lambda$ , e.g. to regulate the divergences of the new scalar particles. Reference [781] makes the assumption that at or below the scale  $\Lambda$  new colored particles appear, as is realized in all neutral naturalness models known so far [789–795], so that new states will be discovered if  $\Lambda \lesssim 10 - 20$  TeV. The constraints on these models from both direct probes of the top partner interactions as well as the reach of a 100 TeV collider for new states at  $\Lambda$  was analyzed. In all cases, it was found that untuned models always lead to observable new physics at future colliders, as long as the top partner sector had a similar number of degrees of freedom as the top quark sector.

A representative example of these methods is provided by the case of fermionic top partners  $T$  interacting through one or more scalar mediators  $S$ , as shown below.



Integrating out the heavy scalar(s) leads to the  $|H|^2 \bar{T}T$  effective interaction, which cancels the quadratically divergent top loop at low scales. SUSY Twin Higgs theories [793, 795] are top-down models falling into this category, though the EFT approach applies more generally. In this class of models the Higgs mixes with the singlet scalar mediator, producing deviations in the effective Higgs coupling which can be probed most effectively at lepton colliders, see red shading in Fig. 107. In the Twin Higgs model,

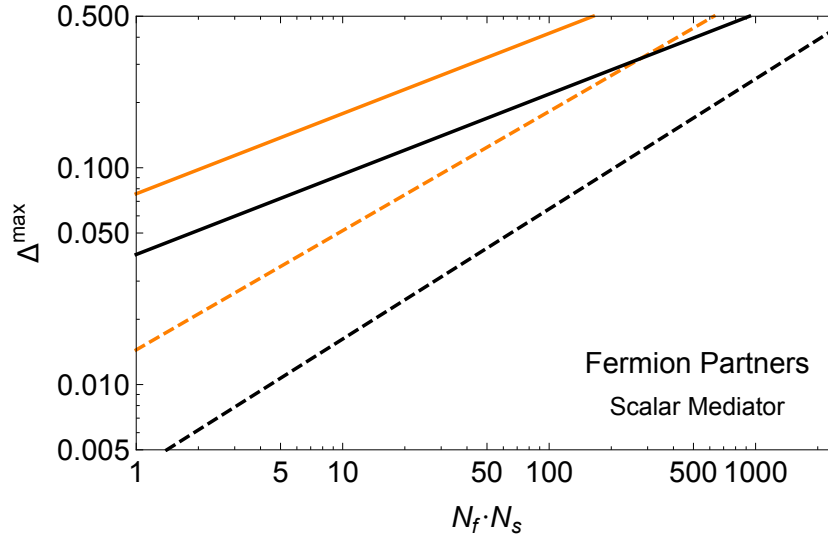


**Fig. 108:** For theories of Neutral Naturalness with  $N_f$  fermionic top partners and  $N_s$  scalar mediators,  $\Delta^{\max}$  is the “unavoidable tuning price” the theory has to pay in order to avoid detection at both future lepton and hadron colliders. The black (orange) curves assume that the 100 TeV collider can probe UV completions at  $\sim 20$  (10) TeV. Dashed curves: combines independent tunings multiplicatively, i.e.  $\Delta = \prod_i \Delta_i$ . Solid curves: only considers the most severe of several independent tunings, i.e.  $\Delta = \text{Min}\{\Delta_i\}$ . Natural theories where the number of top partners is not large have to produce signals at the 100 TeV collider, future lepton colliders, or both. See text and [781] for details.

this allows TeV-scale top partners to be detected. On the other hand, light top partners could escape detection in the fully model-independent case if  $y_{STT}$  is large. In order for this to be natural, the UV completion scale would have to be quite low. Since the 100 TeV collider can probe UV completions up to  $\sim 10$  TeV, these natural theories will lead to direct production of new states. The black contours in Fig. 107 show the *additional* tuning suffered *only due to the singlet mediator*, if the UV completion scale is high enough to avoid direct production of new states at a 100 TeV collider. This effectively probes large values of  $y_{STT}$  in natural theories inaccessible to lepton colliders. Combined with the requirement that top partners not be much heavier than 500 GeV to avoid incomplete cancellation of the top loop, it leads to the conclusion that every natural theory with SM-charged states at the UV completion scale can be discovered.

This argument generalizes beyond the canonical case of three top partners ( $N_f = 3$ ) and one scalar mediator ( $N_s = 1$ ). More generally, one can define an *unavoidable tuning price* that a theory of Neutral Naturalness has to pay in order to avoid *both* Higgs coupling deviations at lepton colliders *and* direct production of new states at 100 TeV. This is shown as a function of  $(N_f \cdot N_s)$  in Fig. 108. Natural theories where the number of top partners is not large have to produce signals at the 100 TeV collider, future lepton colliders, or both.

Different tuning arguments have to be constructed for different scenarios of Neutral Naturalness (e.g. scalar top partners), but the principle of the argument remains the same, as do the conclusions. Combining the results for all top partner scenarios, Ref. [781] finds that neutral naturalness models are generically observable at future colliders unless they are tuned at the  $\sim 10\%$  level or worse. Within the above-mentioned assumptions this provides a “no-lose theorem” for future colliders as model-independent probes of naturalness. Avoiding this result by violating requires very exotic model-building, such as extremely large top partner multiplicity, or solutions to the hierarchy problem not based on symmetry at all (e.g. [55, 796, 797]). Results from future colliders will therefore provide a qualitative advance in our

understanding of the origin of the electroweak scale beyond what can be achieved at the LHC.

### 4.3 Non-Resonant Signatures

#### 4.3.1 Measuring Top Couplings via $tW/tZ$ Scattering

Although the top quark was discovered more than twenty years ago, some of its properties are still poorly known. In particular, only recently the couplings of the top to the electroweak  $Z$  gauge boson have been directly probed, in  $t\bar{t}Z$  production at the LHC [798], though with uncertainties that are currently several times the SM values, while projected sensitivities at Run-II are barely below 100% [799]. The lack of experimental precision is due to the complicated environment in hadronic machines, aggravated by the relatively high mass thresholds. However, in Ref. [800] a different approach to probe the properties of the top was put forward that takes advantage of the high energies accessible at hadronic machines: certain scattering amplitudes, such as  $tW \rightarrow tW$ , grow quadratically with momenta whenever the electroweak couplings of the top deviate from their SM predictions. Such a behaviour is reminiscent of  $WW$  scattering when the Higgs couplings to the electroweak gauge bosons depart from the SM [801], and it is a genuine signal of models where the top quark, along with the Higgs, is part of a strongly interacting sector [802].<sup>20</sup>

As shown in Fig. 109,  $tW$  scattering participates in the process  $pp \rightarrow t\bar{t}Wj$ , giving rise to a clean same-sign leptons signature. A machine such as a hadron collider at 100 TeV would significantly profit from the enhanced sensitivity to non-standard top couplings at high energies present in this channel, thanks to the large momenta carried by the initial state partons. This is true already at the inclusive level. The dominant background for such a search is expected to come from QCD production of  $pp \rightarrow t\bar{t}W+0(1)$  jets, which arises at  $O(g_s^{2(3)}g_w)$  and has a cross section  $\sigma_{\text{QCD}} \approx 25$  pb. The signal arises at  $O(g_s g_w^3)$ , with a cross section  $\sigma_{\text{EW}} \approx 4$  pb (cross sections computed at LO with MadGraph5 [370] and a custom FeynRules [94] model). These numbers should be compared with the QCD and EW cross sections at the 13 TeV LHC, of  $\approx 0.7$  pb and  $\approx 0.06$  pb, respectively. Nevertheless, the potential improvement in sensitivity can be best seen by studying the unique kinematical features of the final state particles.

Let us be specific and focus on the  $Z$  coupling to the right-handed top quark,

$$c_R g_Z t_R t_R \bar{t}_R \gamma_\mu t_R Z^\mu, \quad (118)$$

where  $g_Z t_R t_R = -\frac{2}{3}(g_s^2/c_w)$  and  $c_R = 1$  in the SM. The effect on this coupling from heavy new physics can be effectively parametrised by the dimension-6 operator [800]

$$\frac{i\bar{c}_R}{v^2} H^\dagger \overleftrightarrow{D}_\mu H \bar{t}_R \gamma^\mu t_R, \quad (119)$$

and gives rise to a deviation from the SM,  $c_R - 1 = \frac{3}{4}\bar{c}_R/s_w^2$ , of an expected size  $\bar{c}_R \sim g_*^2 v^2/\Lambda^2$ , where  $\Lambda$  is the mass of the resonance that has been integrated out, and  $g_*$  its coupling to the top quark. Such a non-standard coupling makes the scattering amplitude  $tW \rightarrow tW$  grow with energy. The leading divergence is given by

$$\mathcal{M} = -\frac{g^2}{2m_W^2} \sqrt{\hat{s}(\hat{s} + \hat{t})} \bar{c}_R + O(\sqrt{\hat{s}}). \quad (120)$$

The high energy behaviour of this amplitude has been explicitly shown in Ref. [800].

Here we directly focus on the effects that such a high energy growth has on the kinematical variables associated with  $t\bar{t}Wj$  production. In particular, for a sizeable  $\bar{c}_R$  the particles that participate in the strong scattering, the  $W$  and either one of the two tops (the other is a spectator), will have larger invariant masses than in the SM. This is depicted in Fig. 110, where we show the (normalized) distribution

<sup>20</sup>Indeed, its large mass indicates that the top quark is a key player in composite Higgs scenarios, and crucial BSM particles such as the top-partners [615] could potentially be exchanged in  $tW$  scattering.

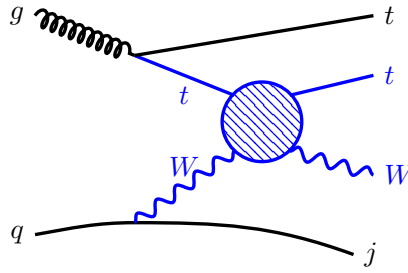


**Fig. 109:** Feynman diagram for the  $tW \rightarrow tW$  scattering in  $pp$  collisions. Anomalous top couplings lead to the final  $tW$  pair having large invariant masses, providing a unique handle to identify the signal.

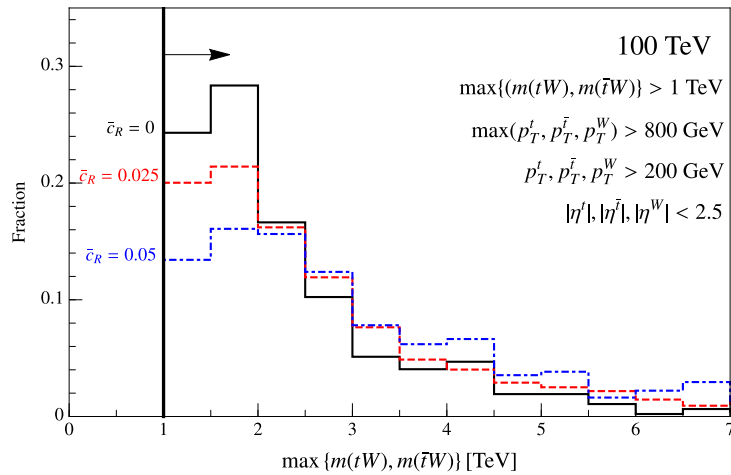


**Fig. 110:** Invariant mass distributions for the  $t\bar{t}Wj$  electroweak production at a 100 TeV collider. We applied some benchmark cuts (inset top-right) on the tops and the  $W$ , specifically on the transverse momentum ( $p_T$ ), pseudorapidity ( $\eta$ ), and invariant mass ( $m$ ).

of events in a 100 TeV collider as a function of the maximum invariant mass between the pairs  $tW$  and  $\bar{t}W$ , for the set of cuts shown in the legend.<sup>21</sup> The events in the presence of anomalous  $Zt_R t_R$  couplings are typically harder than in the SM ( $\bar{c}_R = 0$ ). The power of a 100 TeV collider in performing this type of “precision” probes of the top couplings is apparent once we notice that the values of  $\bar{c}_R$  used for the distributions are an order of magnitude smaller than those that the LHC will be able to probe after  $300 \text{ fb}^{-1}$  of integrated luminosity ( $\bar{c}_R \approx 0.3$  [800]). Awaiting for a detailed study, the improvement in sensitivity can be estimated by assuming that the a 100 TeV collider will be able to measure cross sections with absolute uncertainties at the same level as at the LHC (a sensible assumption given  $\mathcal{L} = 10 \text{ ab}^{-1}$ ), but for energies a factor  $\sqrt{s_{100 \text{ TeV}}/s_{13 \text{ TeV}}} = 100/13 \approx 8$  larger. Recalling that the new physics effects we are interested in grow as  $\bar{c}_R \hat{s}$  (see Eq. (120)), we can then expect to probe at a 100 TeV collider values of  $\bar{c}_R$  at the per cent to per mille level (similar conclusions hold for the couplings of the left-handed top).

It is conceivable then that through a careful study of  $pp \rightarrow t\bar{t}Wj$  production, a 100 TeV collider would be able to greatly improve our sensitivity to new physics modifying the top- $Z$  couplings. Furthermore, as explained in Ref. [800] this is not the only process which shows a strong high energy behaviour

<sup>21</sup>One should be aware that at a 100 TeV collider and for large invariant masses there could be large logarithms arising from the collinear singularity of the gluon splitting. These have been partly tamed by cutting on the  $p_T$  of the tops.

in the presence of non-standard top couplings. One prominent example is  $tZ \rightarrow th$  scattering, identified through  $t\bar{t}h$ +jets production, which would also constitute an important (and complementary) probe of the nature of the top-Higgs sector using a 100 TeV collider.

### 4.3.2 Running Electroweak Couplings as a Probe of New Physics

In this report has clearly emerged how a future 100 TeV collider can improve in the production of heavy states. However, we will now argue that there are also novel opportunities for precision studies that could uncover new light (relative to  $\sqrt{s}$ ) states indirectly. In particular, any new states interacting with gauge bosons will impact how the associated gauge couplings evolve with energy, thereby providing a model-independent handle on their existence provided sufficiently clean channels involving these couplings can be identified and studied experimentally. Such a possibility has been demonstrated for electroweak (EW) processes [469] to be discussed below, with similar applications possible in the colored sector of the theory [803, 804]. Analogous possibilities are also familiar from precision studies at LEP, where constraints on new *heavy* fields could be applied through accurate determination of the  $Z$  boson properties via the modification of gauge boson propagators by new states.

Many theories extending the SM introduce several new states coupling to weak gauge bosons, potentially making them promising cases for such indirect tests. Moreover, the model-independence of this setup amounts to an insensitivity to how these new states may decay, thereby opening the possibility of inferring the presence of new physics that may be difficult to discover directly due to reduction of conventional handles (as is the case with reduced missing energy in supersymmetry (SUSY) for compressed spectra [58, 805] or in models of Stealth SUSY [59]) or due to increased backgrounds. The evolution of EW gauge couplings is fully determined within the SM: the coupling  $\alpha_1$  grows in the UV while  $\alpha_2$  decreases as shown in Fig. 111. At energies above the mass of any charged particles extending

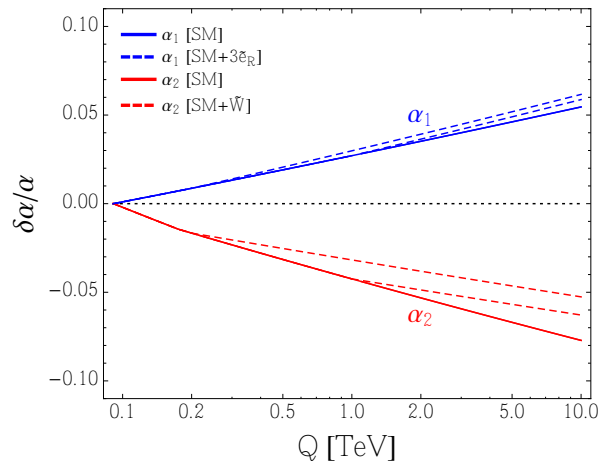


**Fig. 111:** Evolution of the two EW gauge couplings within the SM (solid lines) and in the presence of new states of the MSSM (dashed lines). Shown are the contributions to running of  $\alpha_2$  from the presence of a triplet fermion (wino), and to the running of  $\alpha_1$  in the presence of three  $SU(2)_L$  singlet scalars of hypercharge 1 (right-handed sleptons); each are shown assuming the new states entering at either 200 GeV or 1 TeV. Figure from [469].

the SM, however, this behavior can change: new fields contribute to the beta functions at scales above their masses, such that the asymptotic freedom of  $\alpha_2$  may no longer persist. Indeed in the minimal supersymmetric Standard Model (MSSM) the sign of  $\alpha_2$ 's beta function is flipped once all superpartners are included, such that above that threshold the coupling will increase in the UV. Even the qualitative running behavior can thus serve as a consistency check of the SM itself, or as an indirect probe of new fields if

they exist. As indicated in Fig. 111, however, deviations in the running coupling are typically of order 1% after a decade of running in the presence of an isolated new state of the MSSM. As such, percent-level experimental precision is needed in order to assess cases in which beta functions are modified by a single field at a given threshold.

Experimental sensitivity to the running of  $\alpha_{1,2}$  relies on minimizing uncertainties in the process under examination. Statistical uncertainties are minimized by identifying a process whose cross-section remains sizable at high energy; theoretical uncertainties are minimized for processes that are well determined theoretically; and experimental uncertainties are minimized for processes that are sufficiently clean. Drell-Yan (DY) processes proceeding through neutral and charged currents satisfy these three criteria. At hadron colliders, both  $\alpha_1$  and  $\alpha_2$  can thus be sensitively probed with the (neutral current) process  $pp \rightarrow Z^*/\gamma^* \rightarrow \ell^+\ell^-$ , while  $\alpha_2$  is constrained with the (charged current) process  $pp \rightarrow W^{\pm*} \rightarrow \ell^\pm\nu$  [806]. Modifications to the running of  $\alpha_{1,2}$  may be observed in the shape of the dilepton invariant mass spectrum in the neutral current case, while in the charged current case the shape of the transverse mass spectrum is modified:

$$\frac{d\sigma}{dM_{\ell\ell}}(pp \rightarrow Z^*/\gamma^* \rightarrow \ell^+\ell^-) \equiv \frac{d\sigma^{Z/\gamma}}{dM_{\ell\ell}}(\alpha_{1,2}(Q = M_{\ell\ell})) \quad (121)$$

$$\frac{d\sigma}{dM_T}(pp \rightarrow W^* \rightarrow \ell\nu) \equiv \int_{M_T}^{\infty} dM_{\ell\nu} \frac{d\sigma^{W^\pm}}{dM_T dM_{\ell\nu}}(\alpha_2(Q = M_{\ell\nu})). \quad (122)$$

Thus both effects rely on the fact that the couplings are evaluated at a scale,  $Q$ , corresponding to the invariant mass of the final state.

The main uncertainties impacting the precision with which final state distributions of DY processes can be used to constrain running couplings are statistical, theoretical (scale and PDF), and experimental. Statistical uncertainties are sufficiently small, for an integrated luminosity of  $3 \text{ ab}^{-1}$  at 100 TeV, assuming final states with  $M_{\ell\ell}, M_{\ell\nu} \lesssim 3 \text{ TeV}$ . At these energies, theoretical uncertainties entering through scale and PDF are  $\lesssim 1 - 2\%$ , determined using the generators DYNLLO and FEWZ [807–812] with the NNPDF2.3 PDF set [675]. Finally experimental uncertainties are assumed to be similar to those of the LHC, where neutral current DY measurements at 7 and 8 TeV indicate uncorrelated uncertainties again at the level of  $1 - 2\%$  [813–815]. Treating these uncertainties accordingly, the significance with which a 100 TeV collider is indirectly sensitive to typical SUSY states is as shown in Fig. 112. Shown is also a comparison to how well the 14 TeV LHC can perform analogous measurements assuming the running of  $\alpha_2$  is as in the MSSM.

A general treatment can be carried out by comparing sensitivity to states of a mass,  $M$ , with contributions  $\Delta b_{1,2}$  to the two EW gauge couplings. At the leading log level, this parameter space depends only on the representation (charge) of the new states; dependence on the spin of the new states enters through their finite contribution to gauge boson propagation, which must be accounted for only in higher order matching. Thus working at leading log level, results are as shown in Fig. 113 for current and future runs of the LHC, together with comparisons to what can be gained at 100 TeV and to what is learned through precision studies at LEP where new physics effects could be observed through the presence of higher dimension operators that may be generated upon integrating out heavy states.

The effect of systematic uncertainties on the sensitivity of hadron colliders in extracting running coupling information is a crucial consideration of this program. Fig. 114 shows how the reach of the LHC and of a 100 TeV machine respond to varying these uncertainties, taking sensitivity to the sign of  $\beta_2$  and to the presence of a wino or the full MSSM as examples. A change in sign of  $\beta_2$ , as would be obtained with the MSSM contributing to the running, can be probed at the  $3\sigma$  level between LHC and a future 100 TeV collider even as systematic uncertainties approach the 10% level. The effect of varying scale choice, taking  $M_{\ell\nu}/2 \leq Q \leq 2M_{\ell\nu}$  as the scale at which the EW couplings are evaluated, is shown for the case of a wino or the full MSSM contributing to  $\beta_2$ : this has the effect of varying the pertinent thresholds that can be constrained within about a factor of four. This analysis is all carried out

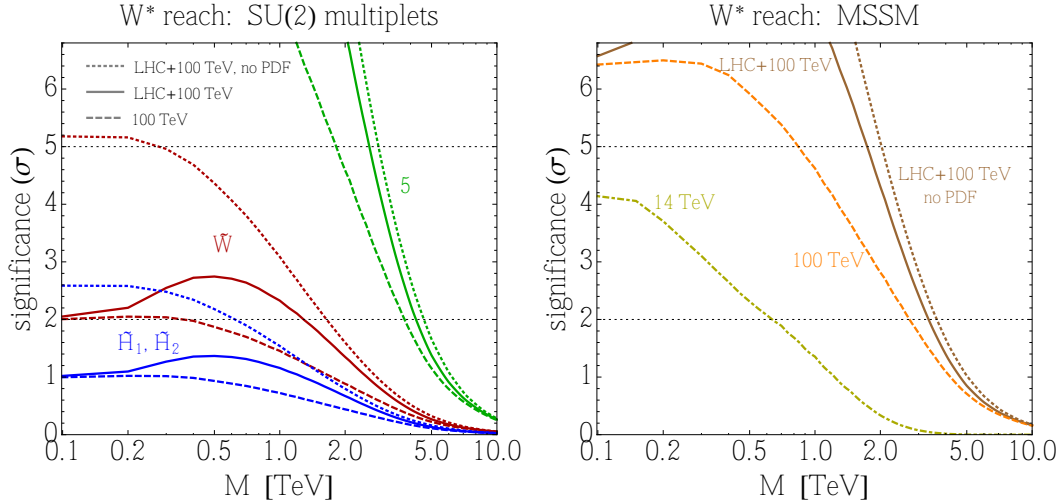


**Fig. 112:** Sensitivity to new states contributing to the running of  $SU(2)_L$ . *Left:* Sensitivity at 100 TeV and its combination with the LHC to Higgsinos, wino, and a  $\mathbf{5}$  of  $SU(2)_L$ . *Right:* Sensitivity of the same machine(s) to the entire MSSM entering the running of  $\alpha_2$ . Figures from [469].

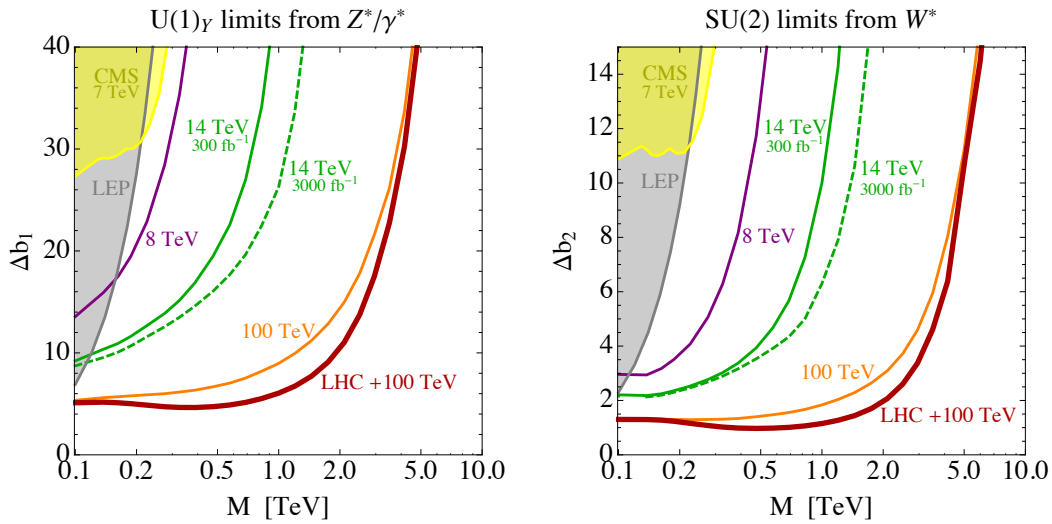


**Fig. 113:** Sensitivity of past, current, and future colliders to generic new states of mass  $M$  contributing to beta functions of the EW gauge group. *Left:* results for states charged under hypercharge, determined through neutral current DY. *Right:* results from  $SU(2)$  representations using charged current DY.

at leading log order in the EW couplings, and thus the uncertainty band coming from scale choice may be significantly reduced by carrying out a higher order calculation of these processes. Taking the central scale choice as the fiducial value, a 100 TeV machine can thus provide indirect sensitivity to the presence of a wino up to masses  $\approx 1.5$  TeV and of the MSSM up to  $\approx 3.5$  TeV.

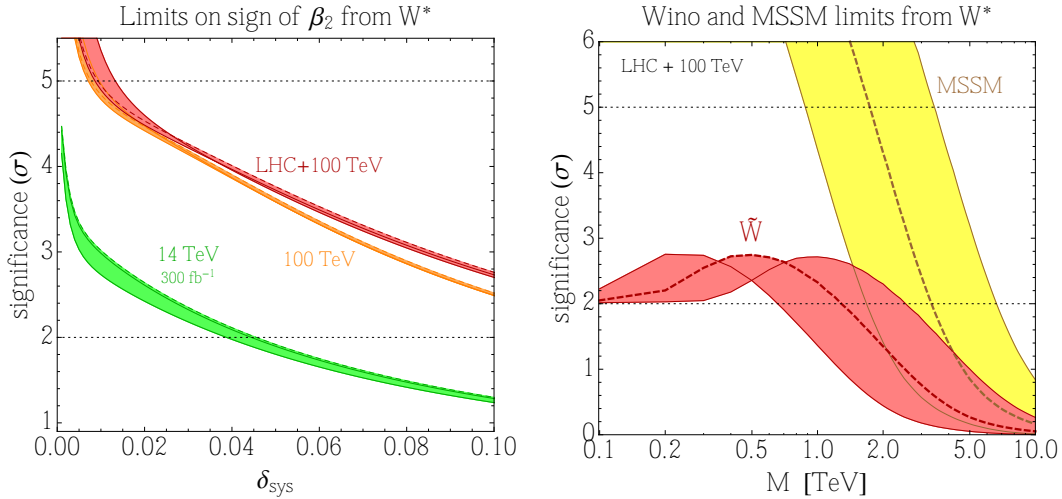


**Fig. 114:** Impact of varying systematic uncertainties. *Left:* Variation in sensitivity to the sign of  $\alpha_2$ 's beta function with respect to the overall size of uncorrelated systematic uncertainties. *Right:* Variation in sensitivity to contributions to running  $\alpha_2$  from a wino and the entire MSSM entering at mass  $M$ , with respect to varying scale choice within a factor of two of  $M_{\ell\nu}$ . Figures from [469].

### Acknowledgements

P. A. is supported by NSF grant PHY-1216270.

T. C. is supported by an LHC Theory Initiative Postdoctoral Fellowship, under the National Science Foundation grant PHY-0969510.

R. T. D. acknowledges support from the Institute for Advanced Study Marvin L. Goldberger Membership and DOE grant de-sc0009988.

S. E. and B. Z. acknowledge partial support from the U.S. Department of Energy, Office of Science, under grant DE-SC0007859.

J. E. thanks the European Research Council for support via the Advanced Investigator Grant 26732, and from the STFC via Grant ST/L000326/1.

J. L. Feng thanks the Technion Center for Particle Physics for hospitality. The work of J. L. Feng is supported in part by U.S. National Science Foundation Grant No. PHY-1316792, United States-Israel Binational Science Foundation Grant No. 2010221, a Guggenheim Foundation grant, and Simons Investigator Award 376204.

The research of S. G. at Perimeter Institute is supported by the Government of Canada through Industry Canada and by the Province of Ontario through the Ministry of Economic Development and Innovation.

M. R. is supported by the NSF Grant PHY-1415548.

C. B. V. is supported by National Science Foundation Grant No. PHY-1315155 and the Maryland Center for Fundamental Physics.

J. W. is supported in part by the Department of Energy under grant DE-SC0007859. W.X. is supported by the U.S. Department of Energy (DOE) under cooperative research agreement DE-SC-00012567.

The work of G. P. has been partly supported by the Catalan ICREA Academia Program, and grants FPA2014-55613-P, 2014-SGR-1450 and Severo Ochoa excellence program SO-2012-0234.

The work of K.A.O. is supported in part by DOE grant DE-SC0011842 at the University of Minnesota.

The work of N. V. has been partially funded by the Danish National Research Foundation, grant number DNRF90.

The work of K. M. has been supported by the National Science Foundation under Grant No. PHY-0854889.

The work of T. R. was supported by the Department of Energy, Contract DE-AC02-76SF00515.

The work of R. N. M. is supported in part by the US National Science Foundation Grant No. PHY-1315155.

D. K. is supported by the Department of Energy under Grant DE-SC0010296.

Argonne National Laboratory's work was supported by the U.S. Department of Energy, Office of Science, Office of Basic Energy Sciences, under contract DE-AC02-06CH11357.

D. C. is supported by National Science Foundation grant No. PHY-1315155 and the Maryland Center for Fundamental Physics.

H.-C. C. and E. S. were supported in part by the US Department of Energy grant DE-SC-000999.

S. J. was partly supported by the US Department of Energy under contract DE-AC02-76SF00515.

Y. T. was supported in part by the US National Science Foundation Grant PHY-1315155, and by the Maryland Center for Fundamental Physics.

The work of A. K. was supported by the Fermi National Accelerator Laboratory and by a Department of Energy grant to Duke University. Fermilab is operated by Fermi Research Alliance, LLC, under Contract No. DE-AC02-07CH11359 with the United States Department of Energy.

The work of Y. S, S. I. and S. T. supported by BSF Grant No. 2010221, by the ICORE Program of Planning and Budgeting Committee, and by ISF Grant Nos. 1937/12 (Y. S. and S. I. ) and 1787/11 (S. T. ).

The work of R. R. is supported by Science and Technology Facilities Council (STFC).

The work of C. W. is supported by the European Research Council under the European Union's Seventh Framework Programme (FP/2007-2013) / ERC Grant NuMass agreement n. [617143] and partial support from the EU Grant No. FP7 ITN INVISIBLES (Marie Curie Actions, Grant No. PITN-GA-2011-289442).

D. S. M. A. is supported by the NSF under grants PHY-0947827 and PHY-1316753, and by the LHC Theory Initiative NSF-PHY-0969510.

A. W. acknowledges the MIUR- FIRB grant RBFR12H1MW, the ERC Advanced Grant no.267985 (DaMeSyFla) and the UNIPD-PRAT grant CPDA153129.

J. K. , A. T. and F. Y. acknowledge support from the Cluster of Excellence *Precision Physics, Fundamental Interactions and Structure of Matter* (PRISMA – EXC 1098).

The work of C.-Y. C is supported by NSERC, Canada. Research at the Perimeter Institute is supported in part by the Government of Canada through NSERC and by the Province of Ontario through MEDT.

M. C., F. S. and M. T. acknowledge ERC under the EU Seventh Framework Programme (FP7/2007-2013) Starting Grant (agreement n. 278234 — '*NewDark*' project), *Erc* Advanced Grant 267117 ('*Dark*') hosted by Université Pierre & Marie Curie - Paris 6, FNRS *Anr* under contract *Anr* 2010 *Blanc* 041301, Centro de Excelencia Severo Ochoa Programme SEV-2012-0249, MINECO through a Severo Ochoa fellowship with Program SEV-2012-0249, FPA2015-65929-P and Consolider MultiDark CSD2009-00064, and the hospitality of the Institut d'Astrophysique de Paris (IAP).

The work of J. D. is supported by the NSF through grant PHY-1316222 and by the NSERC Grant PGSD3-438393-2013. M. F. is supported by the DOE Grant DE-SC0003883.

The work of M.L. M. is supported by the European Research Council advanced grant 291377 "*LHC-theory*": *Theoretical predictions and analyses of LHC physics: advancing the precision frontier*.

G. N. is supported by the Swiss National Science Foundation (SNF) under grant 200020-155935.

The work of J. C. has been supported by the Department of Science & Technology, Government of INDIA under the Grant Agreement number IFA12-PH-34 (INSPIRE Faculty Award).

The work of J. G. and T. J. has been supported by the Polish National Center of Science (NCN) under the Grant Agreement number DEC-2013/11/B/ST2/04023

The work of R. S. has been supported by the Natural Sciences and Engineering Research Council of Canada (NSERC).

The work of P.S.B.D. is supported by the DFG grant RO 2516/5-1.

## References

- [1] M. Cacciari, G. P. Salam, and G. Soyez, *SoftKiller, a particle-level pileup removal method*, *Eur. Phys. J.* **C75** (2015) no. 2, 59, [arXiv:1407.0408 \[hep-ph\]](#).
- [2] P. Berta, M. Spousta, D. W. Miller, and R. Leitner, *Particle-level pileup subtraction for jets and jet shapes*, *JHEP* **06** (2014) 092, [arXiv:1403.3108 \[hep-ex\]](#).
- [3] D. Bertolini, P. Harris, M. Low, and N. Tran, *Pileup Per Particle Identification*, *JHEP* **10** (2014) 59, [arXiv:1407.6013 \[hep-ph\]](#).
- [4] S. Schaetzel and M. Spannowsky, *Tagging highly boosted top quarks*, *Phys. Rev.* **D89** (2014) no. 1, 014007, [arXiv:1308.0540 \[hep-ph\]](#).
- [5] A. J. Larkoski, F. Maltoni, and M. Selvaggi, *Tracking down hyper-boosted top quarks*, *JHEP* **06** (2015) 032, [arXiv:1503.03347 \[hep-ph\]](#).
- [6] M. Spannowsky and M. Stoll, *Tracking New Physics at the LHC and beyond*, *Phys. Rev.* **D92** (2015) no. 5, 054033, [arXiv:1505.01921 \[hep-ph\]](#).
- [7] S. Bressler, T. Flacke, Y. Kats, S. J. Lee, and G. Perez, *Hadronic Calorimeter Shower Size: Challenges and Opportunities for Jet Substructure in the Superboosted Regime*, [arXiv:1506.02656 \[hep-ph\]](#).
- [8] ATLAS Collaboration, G. Aad et al., *The ATLAS Experiment at the CERN Large Hadron Collider*, *JINST* **3** (2008) S08003.
- [9] D. V. Volkov and V. P. Akulov, *Is the Neutrino a Goldstone Particle?*, *Phys. Lett.* **B46** (1973) 109–110.
- [10] J. Wess and B. Zumino, *Supergauge Transformations in Four-Dimensions*, *Nucl. Phys.* **B70** (1974) 39–50.
- [11] D. Z. Freedman, P. van Nieuwenhuizen, and S. Ferrara, *Progress Toward a Theory of Supergravity*, *Phys. Rev.* **D13** (1976) 3214–3218.
- [12] S. Deser and B. Zumino, *Consistent Supergravity*, *Phys. Lett.* **B62** (1976) 335.
- [13] J. R. Ellis, J. S. Hagelin, D. V. Nanopoulos, K. A. Olive, and M. Srednicki, *Supersymmetric Relics from the Big Bang*, *Nucl. Phys.* **B238** (1984) 453–476.
- [14] H. Goldberg, *Constraint on the Photino Mass from Cosmology*, *Phys.Rev.Lett.* **50** (1983) 1419.
- [15] J. S. Hagelin, G. L. Kane, and S. Raby, *Perhaps Scalar Neutrinos Are the Lightest Supersymmetric Partners*, *Nucl. Phys.* **B241** (1984) 638.
- [16] L. E. Ibanez, *The Scalar Neutrinos as the Lightest Supersymmetric Particles and Cosmology*, *Phys. Lett.* **B137** (1984) 160.
- [17] T. Falk, K. A. Olive, and M. Srednicki, *Heavy sneutrinos as dark matter*, *Phys. Lett.* **B339** (1994) 248–251, [arXiv:hep-ph/9409270 \[hep-ph\]](#).
- [18] S. Dimopoulos, S. Raby, and F. Wilczek, *Supersymmetry and the Scale of Unification*, *Phys. Rev.* **D24** (1981) 1681–1683.
- [19] S. Dimopoulos and H. Georgi, *Softly Broken Supersymmetry and SU(5)*, *Nucl.Phys.* **B193** (1981) 150.
- [20] S. P. Martin, *A Supersymmetry primer*, [arXiv:hep-ph/9709356 \[hep-ph\]](#).
- [21] H. Georgi and S. Glashow, *Unity of All Elementary Particle Forces*, *Phys.Rev.Lett.* **32** (1974) 438–441.
- [22] A. Arvanitaki, N. Craig, S. Dimopoulos, and G. Villadoro, *Mini-Split*, *JHEP* **02** (2013) 126, [arXiv:1210.0555 \[hep-ph\]](#).
- [23] J. D. Wells, *Pev-Scale Supersymmetry*, *Phys. Rev.* **D71** (2005) 015013, [arXiv:hep-ph/0411041 \[hep-ph\]](#).
- [24] N. Arkani-Hamed and S. Dimopoulos, *Supersymmetric unification without low energy*

- supersymmetry and signatures for fine-tuning at the LHC*, *JHEP* **0506** (2005) 073, [arXiv:hep-th/0405159](#) [[hep-th](#)].
- [25] G. Giudice and A. Romanino, *Split supersymmetry*, *Nucl.Phys.* **B699** (2004) 65–89, [arXiv:hep-ph/0406088](#) [[hep-ph](#)].
- [26] M. S. Chanowitz, J. R. Ellis, and M. K. Gaillard, *The Price of Natural Flavor Conservation in Neutral Weak Interactions*, *Nucl. Phys.* **B128** (1977) 506–536.
- [27] D. V. Nanopoulos and D. A. Ross, *Limits on the Number of Flavors in Grand Unified Theories from Higher Order Corrections to Fermion Masses*, *Nucl. Phys.* **B157** (1979) 273–284.
- [28] H. Georgi and C. Jarlskog, *A New Lepton - Quark Mass Relation in a Unified Theory*, *Phys. Lett.* **B86** (1979) 297–300.
- [29] S. Antusch and M. Spinrath, *New GUT predictions for quark and lepton mass ratios confronted with phenomenology*, *Phys. Rev.* **D79** (2009) 095004, [arXiv:0902.4644](#) [[hep-ph](#)].
- [30] S. Antusch, S. F. King, and M. Spinrath, *GUT predictions for quark-lepton Yukawa coupling ratios with messenger masses from non-singlets*, *Phys. Rev.* **D89** (2014) no. 5, 055027, [arXiv:1311.0877](#) [[hep-ph](#)].
- [31] R. Hempfling, *Yukawa coupling unification with supersymmetric threshold corrections*, *Phys. Rev.* **D49** (1994) 6168–6172.
- [32] L. J. Hall, R. Rattazzi, and U. Sarid, *The Top quark mass in supersymmetric SO(10) unification*, *Phys. Rev.* **D50** (1994) 7048–7065, [arXiv:hep-ph/9306309](#) [[hep-ph](#)].
- [33] M. Carena, M. Olechowski, S. Pokorski, and C. E. M. Wagner, *Electroweak symmetry breaking and bottom - top Yukawa unification*, *Nucl. Phys.* **B426** (1994) 269–300, [arXiv:hep-ph/9402253](#) [[hep-ph](#)].
- [34] T. Blazek, S. Raby, and S. Pokorski, *Finite supersymmetric threshold corrections to CKM matrix elements in the large  $\tan\beta$  regime*, *Phys. Rev.* **D52** (1995) 4151–4158, [arXiv:hep-ph/9504364](#) [[hep-ph](#)].
- [35] S. Antusch and M. Spinrath, *Quark and lepton masses at the GUT scale including SUSY threshold corrections*, *Phys. Rev.* **D78** (2008) 075020, [arXiv:0804.0717](#) [[hep-ph](#)].
- [36] S. Antusch and C. Sluka, *Predicting the Sparticle Spectrum from GUTs via SUSY Threshold Corrections with SusyTC*, [arXiv:1512.06727](#) [[hep-ph](#)].
- [37] S. Antusch and C. Sluka, *Testable SUSY spectra from GUTs at a 100 TeV pp collider*, [arXiv:1604.00212](#) [[hep-ph](#)].
- [38] Z. Berezhiani, M. Chianese, G. Miele, and S. Morisi, *Chances for SUSY-GUT in the LHC Epoch*, *JHEP* **08** (2015) 083, [arXiv:1505.04950](#) [[hep-ph](#)].
- [39] J. R. Ellis, G. Ridolfi, and F. Zwirner, *Radiative corrections to the masses of supersymmetric Higgs bosons*, *Phys. Lett.* **B257** (1991) 83–91.
- [40] J. R. Ellis, G. Ridolfi, and F. Zwirner, *On radiative corrections to supersymmetric Higgs boson masses and their implications for LEP searches*, *Phys. Lett.* **B262** (1991) 477–484.
- [41] E. Bagnaschi, G. F. Giudice, P. Slavich, and A. Strumia, *Higgs Mass and Unnatural Supersymmetry*, *JHEP* **09** (2014) 092, [arXiv:1407.4081](#) [[hep-ph](#)].
- [42] L. J. Hall, D. Pinner, and J. T. Ruderman, *A Natural SUSY Higgs Near 126 GeV*, *JHEP* **04** (2012) 131, [arXiv:1112.2703](#) [[hep-ph](#)].
- [43] N. Arkani-Hamed, A. Gupta, D. E. Kaplan, N. Weiner, and T. Zorawski, *Simply Unnatural Supersymmetry*, [arXiv:1212.6971](#) [[hep-ph](#)].
- [44] L. E. Ibanez and G. G. Ross, *SU(2)-L x U(1) Symmetry Breaking as a Radiative Effect of Supersymmetry Breaking in Guts*, *Phys. Lett.* **B110** (1982) 215–220.
- [45] K. Inoue, A. Kakuto, H. Komatsu, and S. Takeshita, *Aspects of Grand Unified Models with Softly Broken Supersymmetry*, *Prog. Theor. Phys.* **68** (1982) 927. [Erratum: *Prog. Theor.*

- Phys.70,330(1983)].
- [46] L. E. Ibanez, *Locally Supersymmetric SU(5) Grand Unification*, *Phys. Lett.* **B118** (1982) 73–78.
  - [47] J. R. Ellis, J. S. Hagelin, D. V. Nanopoulos, and K. Tamvakis, *Weak Symmetry Breaking by Radiative Corrections in Broken Supergravity*, *Phys. Lett.* **B125** (1983) 275.
  - [48] L. Alvarez-Gaume, J. Polchinski, and M. B. Wise, *Minimal Low-Energy Supergravity*, *Nucl. Phys.* **B221** (1983) 495.
  - [49] G. 't Hooft, *Naturalness, chiral symmetry, and spontaneous chiral symmetry breaking*, NATO Sci. Ser. B **59** (1980) 135.
  - [50] L. Susskind, *Dynamics of Spontaneous Symmetry Breaking in the Weinberg-Salam Theory*, *Phys.Rev.* **D20** (1979) 2619–2625.
  - [51] J. R. Ellis, K. Enqvist, D. V. Nanopoulos, and F. Zwirner, *Observables in Low-Energy Superstring Models*, *Mod. Phys. Lett.* **A1** (1986) 57.
  - [52] R. Barbieri and G. Giudice, *Upper Bounds on Supersymmetric Particle Masses*, *Nucl.Phys.* **B306** (1988) 63.
  - [53] N. Craig, *The State of Supersymmetry after Run I of the LHC*, [arXiv:1309.0528](https://arxiv.org/abs/1309.0528) [hep-ph].
  - [54] B. Batell, G. F. Giudice, and M. McCullough, *Natural Heavy Supersymmetry*, [arXiv:1509.00834](https://arxiv.org/abs/1509.00834) [hep-ph].
  - [55] P. W. Graham, D. E. Kaplan, and S. Rajendran, *Cosmological Relaxation of the Electroweak Scale*, [arXiv:1504.07551](https://arxiv.org/abs/1504.07551) [hep-ph].
  - [56] J. L. Feng, K. T. Matchev, and T. Moroi, *Focus points and naturalness in supersymmetry*, *Phys. Rev.* **D61** (2000) 075005, [arXiv:hep-ph/9909334](https://arxiv.org/abs/hep-ph/9909334) [hep-ph].
  - [57] H. Baer, V. Barger, P. Huang, A. Mustafayev, and X. Tata, *Radiative natural SUSY with a 125 GeV Higgs boson*, *Phys. Rev. Lett.* **109** (2012) 161802, [arXiv:1207.3343](https://arxiv.org/abs/1207.3343) [hep-ph].
  - [58] T. J. LeCompte and S. P. Martin, *Large Hadron Collider reach for supersymmetric models with compressed mass spectra*, *Phys. Rev.* **D84** (2011) 015004, [arXiv:1105.4304](https://arxiv.org/abs/1105.4304) [hep-ph].
  - [59] J. Fan, M. Reece, and J. T. Ruderman, *Stealth Supersymmetry*, *JHEP* **11** (2011) 012, [arXiv:1105.5135](https://arxiv.org/abs/1105.5135) [hep-ph].
  - [60] J. Fan, M. Reece, and J. T. Ruderman, *A Stealth Supersymmetry Sampler*, *JHEP* **07** (2012) 196, [arXiv:1201.4875](https://arxiv.org/abs/1201.4875) [hep-ph].
  - [61] R. Barbier et al., *R-parity violating supersymmetry*, *Phys. Rept.* **420** (2005) 1–202, [arXiv:hep-ph/0406039](https://arxiv.org/abs/hep-ph/0406039) [hep-ph].
  - [62] C. Csaki, Y. Grossman, and B. Heidenreich, *MFV SUSY: A Natural Theory for R-Parity Violation*, *Phys. Rev.* **D85** (2012) 095009, [arXiv:1111.1239](https://arxiv.org/abs/1111.1239) [hep-ph].
  - [63] M. Papucci, J. T. Ruderman, and A. Weiler, *Natural SUSY Endures*, *JHEP* **1209** (2012) 035, [arXiv:1110.6926](https://arxiv.org/abs/1110.6926) [hep-ph].
  - [64] S. Dimopoulos and G. Giudice, *Naturalness constraints in supersymmetric theories with nonuniversal soft terms*, *Phys.Lett.* **B357** (1995) 573–578, [arXiv:hep-ph/9507282](https://arxiv.org/abs/hep-ph/9507282) [hep-ph].
  - [65] A. G. Cohen, D. Kaplan, and A. Nelson, *The More minimal supersymmetric standard model*, *Phys.Lett.* **B388** (1996) 588–598, [arXiv:hep-ph/9607394](https://arxiv.org/abs/hep-ph/9607394) [hep-ph].
  - [66] P. J. Fox, A. E. Nelson, and N. Weiner, *Dirac gaugino masses and supersoft supersymmetry breaking*, *JHEP* **08** (2002) 035, [arXiv:hep-ph/0206096](https://arxiv.org/abs/hep-ph/0206096) [hep-ph].
  - [67] G. D. Kribs and A. Martin, *Supersoft Supersymmetry is Super-Safe*, *Phys. Rev.* **D85** (2012) 115014, [arXiv:1203.4821](https://arxiv.org/abs/1203.4821) [hep-ph].
  - [68] T. Cohen, T. Golling, M. Hance, A. Henrichs, K. Howe, J. Loyal, S. Padhi, and J. G. Wacker, *SUSY Simplified Models at 14, 33, and 100 TeV Proton Colliders*, *JHEP* **04** (2014) 117, [arXiv:1311.6480](https://arxiv.org/abs/1311.6480) [hep-ph].

- [69] S. Jung and J. D. Wells, *Gaugino physics of split supersymmetry spectra at the LHC and future proton colliders*, *Phys. Rev.* **D89** (2014) no. 7, 075004, [arXiv:1312.1802 \[hep-ph\]](#).
- [70] M. Low and L.-T. Wang, *Neutralino dark matter at 14 TeV and 100 TeV*, *JHEP* **08** (2014) 161, [arXiv:1404.0682 \[hep-ph\]](#).
- [71] T. Cohen, R. T. D’Agnolo, M. Hance, H. K. Lou, and J. G. Wacker, *Boosting Stop Searches with a 100 TeV Proton Collider*, *JHEP* **1411** (2014) 021, [arXiv:1406.4512 \[hep-ph\]](#).
- [72] S. A. R. Ellis, G. L. Kane, and B. Zheng, *Superpartners at LHC and Future Colliders: Predictions from Constrained Compactified M-Theory*, [arXiv:1408.1961 \[hep-ph\]](#).
- [73] B. S. Acharya, K. Bozek, C. Pongkitivanichkul, and K. Sakurai, *Prospects for observing charginos and neutralinos at a 100 TeV proton-proton collider*, [arXiv:1410.1532 \[hep-ph\]](#).
- [74] S. Gori, S. Jung, L.-T. Wang, and J. D. Wells, *Prospects for Electroweakino Discovery at a 100 TeV Hadron Collider*, *JHEP* **1412** (2014) 108, [arXiv:1410.6287 \[hep-ph\]](#).
- [75] G. G. di Cortona, *Hunting electroweakinos at future hadron colliders and direct detection experiments*, [arXiv:1412.5952 \[hep-ph\]](#).
- [76] A. Berlin, T. Lin, M. Low, and L.-T. Wang, *Neutralinos in Vector Boson Fusion at High Energy Colliders*, *Phys. Rev.* **D91** (2015) no. 11, 115002, [arXiv:1502.05044 \[hep-ph\]](#).
- [77] H. Beauchesne, K. Earl, and T. Grégoire, *LHC constraints on Mini-Split anomaly and gauge mediation and prospects for LHC 14 and a future 100 TeV pp collider*, *JHEP* **08** (2015) 117, [arXiv:1503.03099 \[hep-ph\]](#).
- [78] W. Beenakker, R. Hopker, M. Spira, and P. Zerwas, *Squark and gluino production at hadron colliders*, *Nucl.Phys.* **B492** (1997) 51–103, [arXiv:hep-ph/9610490 \[hep-ph\]](#).
- [79] W. Beenakker, M. Krämer, T. Plehn, M. Spira, and P. Zerwas, *Stop production at hadron colliders*, *Nucl.Phys.* **B515** (1998) 3–14, [arXiv:hep-ph/9710451 \[hep-ph\]](#).
- [80] W. Beenakker, S. Brensing, M. Krämer, A. Kulesza, E. Laenen, and I. Niessen, *Soft-gluon resummation for squark and gluino hadroproduction*, *JHEP* **12** (2009) 041, [arXiv:0909.4418 \[hep-ph\]](#).
- [81] W. Beenakker, S. Brensing, M. Krämer, A. Kulesza, E. Laenen, and I. Niessen, *Supersymmetric top and bottom squark production at hadron colliders*, *JHEP* **08** (2010) 098, [arXiv:1006.4771 \[hep-ph\]](#).
- [82] C. Borschensky, M. Krämer, A. Kulesza, M. Mangano, S. Padhi, et al., *Squark and gluino production cross sections in pp collisions at  $\sqrt{s} = 13, 14, 33$  and 100 TeV*, [arXiv:1407.5066 \[hep-ph\]](#).
- [83] P. M. Nadolsky, H.-L. Lai, Q.-H. Cao, J. Huston, J. Pumplin, et al., *Implications of CTEQ global analysis for collider observables*, *Phys.Rev.* **D78** (2008) 013004, [arXiv:0802.0007 \[hep-ph\]](#).
- [84] A. Martin, W. Stirling, R. Thorne, and G. Watt, *Parton distributions for the LHC*, *Eur.Phys.J.* **C63** (2009) 189–285, [arXiv:0901.0002 \[hep-ph\]](#).
- [85] S. Bornhauser, M. Drees, H. K. Dreiner, and J. S. Kim, *Electroweak contributions to squark pair production at the LHC*, *Phys. Rev.* **D76** (2007) 095020, [arXiv:0709.2544 \[hep-ph\]](#).
- [86] W. Hollik and E. Mirabella, *Squark anti-squark pair production at the LHC: The Electroweak contribution*, *JHEP* **12** (2008) 087, [arXiv:0806.1433 \[hep-ph\]](#).
- [87] W. Hollik, E. Mirabella, and M. K. Trenkel, *Electroweak contributions to squark-gluino production at the LHC*, *JHEP* **02** (2009) 002, [arXiv:0810.1044 \[hep-ph\]](#).
- [88] E. Mirabella, *NLO electroweak contributions to gluino pair production at hadron colliders*, *JHEP* **12** (2009) 012, [arXiv:0908.3318 \[hep-ph\]](#).
- [89] J. Germer, W. Hollik, E. Mirabella, and M. K. Trenkel, *Hadronic production of squark-squark pairs: The electroweak contributions*, *JHEP* **08** (2010) 023, [arXiv:1004.2621 \[hep-ph\]](#).
- [90] J. Germer, W. Hollik, and E. Mirabella, *Hadronic production of bottom-squark pairs with*

- electroweak contributions*, **JHEP** **05** (2011) 068, [arXiv:1103.1258 \[hep-ph\]](#).
- [91] J. Germer, W. Hollik, J. M. Lindert, and E. Mirabella, *Top-squark pair production at the LHC: a complete analysis at next-to-leading order*, **JHEP** **09** (2014) 022, [arXiv:1404.5572 \[hep-ph\]](#).
- [92] W. Hollik, J. M. Lindert, E. Mirabella, and D. Pagani, *Electroweak corrections to squark-antisquark production at the LHC*, **JHEP** **08** (2015) 099, [arXiv:1506.01052 \[hep-ph\]](#).
- [93] NNPDF Collaboration, R. D. Ball, V. Bertone, S. Carrazza, L. Del Debbio, S. Forte, A. Guffanti, N. P. Hartland, and J. Rojo, *Parton distributions with QED corrections*, **Nucl. Phys.** **B877** (2013) 290–320, [arXiv:1308.0598 \[hep-ph\]](#).
- [94] J. Alwall, R. Frederix, S. Frixione, V. Hirschi, F. Maltoni, O. Mattelaer, H. S. Shao, T. Stelzer, P. Torrielli, and M. Zaro, *The automated computation of tree-level and next-to-leading order differential cross sections, and their matching to parton shower simulations*, **JHEP** **07** (2014) 079, [arXiv:1405.0301 \[hep-ph\]](#).
- [95] CMS Collaboration, V. Khachatryan et al., *Searches for third-generation squark production in fully hadronic final states in proton-proton collisions at  $\sqrt{s} = 8$  TeV*, **JHEP** **06** (2015) 116, [arXiv:1503.08037 \[hep-ex\]](#).
- [96] ATLAS Collaboration, G. Aad et al., *ATLAS Run 1 searches for direct pair production of third-generation squarks at the Large Hadron Collider*, **Eur. Phys. J.** **C75** (2015) no. 10, 510, [arXiv:1506.08616 \[hep-ex\]](#).
- [97] CMS Collaboration, S. Chatrchyan et al., *The CMS experiment at the CERN LHC*, **JINST** **3** (2008) S08004.
- [98] T. Plehn, M. Spannowsky, M. Takeuchi, and D. Zerwas, *Stop Reconstruction with Tagged Tops*, **JHEP** **1010** (2010) 078, [arXiv:1006.2833 \[hep-ph\]](#).
- [99] D. E. Kaplan, K. Rehermann, M. D. Schwartz, and B. Tweedie, *Top Tagging: A Method for Identifying Boosted Hadronically Decaying Top Quarks*, **Phys.Rev.Lett.** **101** (2008) 142001, [arXiv:0806.0848 \[hep-ph\]](#).
- [100] CDF Collaboration, D. Acosta et al., *Measurement of the  $t\bar{t}$  production cross section in  $p\bar{p}$  collisions at  $\sqrt{s} = 1.96$  TeV using lepton plus jets events with semileptonic B decays to muons*, **Phys.Rev.** **D72** (2005) 032002, [arXiv:hep-ex/0506001 \[hep-ex\]](#).
- [101] D0 Collaboration, V. Abazov et al., *A Search for anomalous heavy-flavor quark production in association with W bosons*, **Phys.Rev.Lett.** **94** (2005) 152002, [arXiv:hep-ex/0411084 \[hep-ex\]](#).
- [102] CDF Collaboration, A. Abulencia et al., *Search for anomalous semileptonic decay of heavy flavor hadrons produced in association with a W boson at CDF II*, **Phys.Rev.** **D73** (2006) 051101, [arXiv:hep-ex/0512065 \[hep-ex\]](#).
- [103] CDF Collaboration, T. Aaltonen et al., *First measurement of the production of a W boson in association with a single charm quark in  $p\bar{p}$  collisions at  $\sqrt{s} = 1.96$ -TeV*, **Phys.Rev.Lett.** **100** (2008) 091803, [arXiv:0711.2901 \[hep-ex\]](#).
- [104] CDF Collaboration, T. Aaltonen et al., *Measurement of the  $t\bar{t}$  Production Cross Section in  $2\text{ fb}^{-1}$  of  $p\bar{p}$  Collisions at  $\sqrt{s} = 1.96$  TeV Using Lepton Plus Jets Events with Soft Muon b-Tagging*, **Phys.Rev.** **D79** (2009) 052007, [arXiv:0901.4142 \[hep-ex\]](#).
- [105] CDF Collaboration, T. Aaltonen et al., *Measurement of the  $t\bar{t}$  Production Cross Section in  $p\bar{p}$  Collisions at  $\sqrt{s}=1.96$  TeV using Soft Electron b-Tagging*, **Phys.Rev.** **D81** (2010) 092002, [arXiv:1002.3783 \[hep-ex\]](#).
- [106] ATLAS Collaboration, G. Aad et al., *Expected Performance of the ATLAS Experiment - Detector, Trigger and Physics*, [arXiv:0901.0512 \[hep-ex\]](#).
- [107] ATLAS Collaboration, *Soft muon tagging and Dstar/mu correlations in 7 TeV collisions with ATLAS*, ATLAS-CONF-2010-100, CERN, Geneva, Dec, 2010.

- <https://cds.cern.ch/record/1316469>.
- [108] CMS Collaboration, S. Chatrchyan et al., *Identification of  $b$ -quark jets with the CMS experiment*, *JINST* **8** (2013) P04013, [arXiv:1211.4462](https://arxiv.org/abs/1211.4462) [[hep-ex](#)].
- [109] *Search for pair-produced top squarks decaying into a charm quark and the lightest neutralinos with  $20.3 \text{ fb}^{-1}$  of  $pp$  collisions at  $\sqrt{s} = 8 \text{ TeV}$  with the ATLAS detector at the LHC*, ATLAS-CONF-2013-068, CERN, Geneva, Jul, 2013. <https://cds.cern.ch/record/1562880>.
- [110] A. Avetisyan et al., *Methods and Results for Standard Model Event Generation at  $\sqrt{s} = 14 \text{ TeV}$ ,  $33 \text{ TeV}$  and  $100 \text{ TeV}$  Proton Colliders (A Snowmass Whitepaper)*, in *Community Summer Study 2013: Snowmass on the Mississippi (CSS2013) Minneapolis, MN, USA, July 29-August 6, 2013*. 2013. [arXiv:1308.1636](https://arxiv.org/abs/1308.1636) [[hep-ex](#)]. <http://lss.fnal.gov/archive/test-fn/0000/fermilab-fn-0965-t.pdf>.
- [111] J. Alwall, M. Herquet, F. Maltoni, O. Mattelaer, and T. Stelzer, *MadGraph 5 : Going Beyond*, *JHEP* **1106** (2011) 128, [arXiv:1106.0522](https://arxiv.org/abs/1106.0522) [[hep-ph](#)].
- [112] T. Sjostrand, S. Mrenna, and P. Z. Skands, *PYTHIA 6.4 Physics and Manual*, *JHEP* **0605** (2006) 026, [arXiv:hep-ph/0603175](https://arxiv.org/abs/hep-ph/0603175) [[hep-ph](#)].
- [113] DELPHES 3 Collaboration, J. de Favereau, C. Delaere, P. Demin, A. Giammanco, V. Lemaître, A. Mertens, and M. Selvaggi, *DELPHES 3, A modular framework for fast simulation of a generic collider experiment*, *JHEP* **02** (2014) 057, [arXiv:1307.6346](https://arxiv.org/abs/1307.6346) [[hep-ex](#)].
- [114] J. Anderson, A. Avetisyan, R. Brock, S. Chekanov, T. Cohen, et al., *Snowmass Energy Frontier Simulations*, in *Community Summer Study 2013: Snowmass on the Mississippi (CSS2013) Minneapolis, MN, USA, July 29-August 6, 2013*. 2013. [arXiv:1309.1057](https://arxiv.org/abs/1309.1057) [[hep-ex](#)].
- [115] M. Cacciari, G. P. Salam, and G. Soyez, *The anti- $k_t$  jet clustering algorithm*, *JHEP* **04** (2008) 063, [arXiv:0802.1189](https://arxiv.org/abs/0802.1189) [[hep-ph](#)].
- [116] L. Moneta, K. Belasco, K. S. Cranmer, S. Kreiss, A. Lazzaro, et al., *The RooStats Project*, PoS **ACAT2010** (2010) 057, [arXiv:1009.1003](https://arxiv.org/abs/1009.1003) [[physics.data-an](#)].
- [117] T. Plehn, M. Spannowsky, and M. Takeuchi, *Stop searches in 2012*, *JHEP* **08** (2012) 091, [arXiv:1205.2696](https://arxiv.org/abs/1205.2696) [[hep-ph](#)].
- [118] D. E. Kaplan, K. Rehermann, and D. Stolarski, *Searching for Direct Stop Production in Hadronic Top Data at the LHC*, *JHEP* **07** (2012) 119, [arXiv:1205.5816](https://arxiv.org/abs/1205.5816) [[hep-ph](#)].
- [119] B. Dutta, T. Kamon, N. Koley, K. Sinha, and K. Wang, *Searching for Top Squarks at the LHC in Fully Hadronic Final State*, *Phys. Rev.* **D86** (2012) 075004, [arXiv:1207.1873](https://arxiv.org/abs/1207.1873) [[hep-ph](#)].
- [120] M. R. Buckley, T. Plehn, and M. Takeuchi, *Buckets of Tops*, *JHEP* **08** (2013) 086, [arXiv:1302.6238](https://arxiv.org/abs/1302.6238) [[hep-ph](#)].
- [121] D. Stolarski, *Reach in All Hadronic Stop Decays: A Snowmass White Paper*, in *Community Summer Study 2013: Snowmass on the Mississippi (CSS2013) Minneapolis, MN, USA, July 29-August 6, 2013*. 2013. [arXiv:1309.1514](https://arxiv.org/abs/1309.1514) [[hep-ph](#)]. <http://inspirehep.net/record/1253108/files/arXiv:1309.1514.pdf>.
- [122] CMS Collaboration, S. Chatrchyan et al., *Interpretation of Searches for Supersymmetry with simplified Models*, *Phys. Rev.* **D88** (2013) no. 5, 052017, [arXiv:1301.2175](https://arxiv.org/abs/1301.2175) [[hep-ex](#)].
- [123] J. Thaler and L.-T. Wang, *Strategies to Identify Boosted Tops*, *JHEP* **0807** (2008) 092, [arXiv:0806.0023](https://arxiv.org/abs/0806.0023) [[hep-ph](#)].
- [124] L. G. Almeida, S. J. Lee, G. Perez, G. F. Sterman, I. Sung, and J. Virzi, *Substructure of high- $p_T$  Jets at the LHC*, *Phys. Rev.* **D79** (2009) 074017, [arXiv:0807.0234](https://arxiv.org/abs/0807.0234) [[hep-ph](#)].
- [125] J. Thaler and K. Van Tilburg, *Maximizing Boosted Top Identification by Minimizing  $N$ -subjettiness*, *JHEP* **02** (2012) 093, [arXiv:1108.2701](https://arxiv.org/abs/1108.2701) [[hep-ph](#)].
- [126] D. E. Soper and M. Spannowsky, *Finding top quarks with shower deconstruction*, *Phys. Rev.*

- D87** (2013) 054012, [arXiv:1211.3140](#) [hep-ph].
- [127] CMS Collaboration, S. Chatrchyan et al., *Search for anomalous  $t t$ -bar production in the highly-boosted all-hadronic final state*, **JHEP** **1209** (2012) 029, [arXiv:1204.2488](#) [hep-ex].
- [128] ATLAS Collaboration, G. Aad et al., *Search for resonances decaying into top-quark pairs using fully hadronic decays in  $pp$  collisions with ATLAS at  $\sqrt{s} = 7$  TeV*, **JHEP** **01** (2013) 116, [arXiv:1211.2202](#) [hep-ex].
- [129] CMS Collaboration, *Performance of the  $b$ -jet identification in CMS*, CMS-PAS-BTV-11-001, CERN, Geneva, 2011. <https://cds.cern.ch/record/1366061>.
- [130] ATLAS Collaboration, *Commissioning of the ATLAS high-performance  $b$ -tagging algorithms in the 7 TeV collision data*, ATLAS-CONF-2011-102, CERN, Geneva, Jul, 2011. <https://cds.cern.ch/record/1369219>.
- [131] W. Beenakker, R. Hopker, and M. Spira, *PROSPINO: A Program for the production of supersymmetric particles in next-to-leading order QCD*, [arXiv:hep-ph/9611232](#) [hep-ph].
- [132] *Searches for Supersymmetry at the high luminosity LHC with the ATLAS Detector*, ATL-PHYS-PUB-2013-002, CERN, Geneva, Feb, 2013. <https://cds.cern.ch/record/1512933>.
- [133] ATLAS Collaboration, *Search for New Phenomena in Monojet plus Missing Transverse Momentum Final States using  $10\text{fb}^{-1}$  of  $pp$  Collisions at  $\sqrt{s}=8$  TeV with the ATLAS detector at the LHC*, ATLAS-CONF-2012-147, CERN, Geneva, Nov, 2012. <https://cds.cern.ch/record/1493486>.
- [134] CMS Collaboration, *Search for new physics in monojet events in  $pp$  collisions at  $\sqrt{s}=8$  TeV*, CMS-PAS-EXO-12-048, CERN, Geneva, 2013. <https://cds.cern.ch/record/1525585>.
- [135] CMS Collaboration, S. Chatrchyan et al., *Search for new physics in events with same-sign dileptons and  $b$  jets in  $pp$  collisions at  $\sqrt{s} = 8$  TeV*, **JHEP** **1303** (2013) 037, [arXiv:1212.6194](#) [hep-ex].
- [136] C. G. Lester and D. J. Summers, *Measuring masses of semiinvisibly decaying particles pair produced at hadron colliders*, **Phys. Lett.** **B463** (1999) 99–103, [arXiv:hep-ph/9906349](#) [hep-ph].
- [137] A. Barr, C. Lester, and P. Stephens,  *$m_{T2}$ : The Truth behind the glamour*, **J.Phys.** **G29** (2003) 2343–2363, [arXiv:hep-ph/0304226](#) [hep-ph].
- [138] M. Burns, K. Kong, K. T. Matchev, and M. Park, *Using Subsystem  $MT_2$  for Complete Mass Determinations in Decay Chains with Missing Energy at Hadron Colliders*, **JHEP** **0903** (2009) 143, [arXiv:0810.5576](#) [hep-ph].
- [139] ATLAS Collaboration, G. Aad et al., *Search for squarks and gluinos with the ATLAS detector in final states with jets and missing transverse momentum using  $\sqrt{s} = 8$  TeV proton–proton collision data*, **JHEP** **09** (2014) 176, [arXiv:1405.7875](#) [hep-ex].
- [140] S. A. R. Ellis and B. Zheng, *Reaching for squarks and gauginos at a 100 TeV  $p$ - $p$  collider*, **Phys. Rev.** **D92** (2015) no. 7, 075034, [arXiv:1506.02644](#) [hep-ph].
- [141] L. Randall and R. Sundrum, *Out of this world supersymmetry breaking*, **Nucl. Phys.** **B557** (1999) 79–118, [arXiv:hep-th/9810155](#) [hep-th].
- [142] G. F. Giudice, M. A. Luty, H. Murayama, and R. Rattazzi, *Gaugino mass without singlets*, **JHEP** **12** (1998) 027, [arXiv:hep-ph/9810442](#) [hep-ph].
- [143] J. D. Wells, *Implications of Supersymmetry Breaking with a Little Hierarchy Between Gauginos and Scalars*, in *11Th International Conference on Supersymmetry and the Unification of Fundamental Interactions (Susy 2003) Tucson, Arizona, June 5-10, 2003*. 2003. [arXiv:hep-ph/0306127](#) [hep-ph].
- [144] B. S. Acharya, K. Bobkov, G. L. Kane, P. Kumar, and J. Shao, *Explaining the Electroweak Scale*

- and Stabilizing Moduli in M Theory*, *Phys. Rev.* **D76** (2007) 126010, [arXiv:hep-th/0701034 \[hep-th\]](#).
- [145] S. Profumo and C. E. Yaguna, *Glauino coannihilations and heavy bino dark matter*, *Phys. Rev.* **D69** (2004) 115009, [arXiv:hep-ph/0402208 \[hep-ph\]](#).
- [146] J. Ellis, F. Luo, and K. A. Olive, *Glauino Coannihilation Revisited*, *JHEP* **09** (2015) 127, [arXiv:1503.07142 \[hep-ph\]](#).
- [147] I. Hinchliffe, A. Kotwal, M. L. Mangano, C. Quigg, and L.-T. Wang, *Luminosity goals for a 100-TeV pp collider*, [arXiv:1504.06108 \[hep-ph\]](#).
- [148] G. D. Kribs and A. Martin, *Dirac Gauginos in Supersymmetry – Suppressed Jets + MET Signals: A Snowmass Whitepaper*, [arXiv:1308.3468 \[hep-ph\]](#).
- [149] CMS Collaboration, V. Khachatryan et al., *Searches for Supersymmetry using the  $M_{T2}$  Variable in Hadronic Events Produced in pp Collisions at 8 TeV*, *JHEP* **05** (2015) 078, [arXiv:1502.04358 \[hep-ex\]](#).
- [150] ATLAS Collaboration, G. Aad et al., *Summary of the searches for squarks and gluinos using  $\sqrt{s} = 8$  TeV pp collisions with the ATLAS experiment at the LHC*, *JHEP* **10** (2015) 054, [arXiv:1507.05525 \[hep-ex\]](#).
- [151] S. Jung, *Resolving the existence of Higgsinos in the LHC inverse problem*, *JHEP* **06** (2014) 111, [arXiv:1404.2691 \[hep-ph\]](#).
- [152] J. Hisano, S. Matsumoto, M. Nagai, O. Saito, and M. Senami, *Non-perturbative effect on thermal relic abundance of dark matter*, *Phys. Lett.* **B646** (2007) 34–38, [arXiv:hep-ph/0610249 \[hep-ph\]](#).
- [153] T. Cohen, M. Lisanti, A. Pierce, and T. R. Slatyer, *Wino Dark Matter Under Siege*, *JCAP* **1310** (2013) 061, [arXiv:1307.4082](#).
- [154] J. Fan and M. Reece, *In Wino Veritas? Indirect Searches Shed Light on Neutralino Dark Matter*, *JHEP* **1310** (2013) 124, [arXiv:1307.4400 \[hep-ph\]](#).
- [155] H. Baer, V. Barger, A. Lessa, W. Sreethawong, and X. Tata, *Wh plus missing- $E_T$  signature from gaugino pair production at the LHC*, *Phys. Rev.* **D85** (2012) 055022, [arXiv:1201.2949 \[hep-ph\]](#).
- [156] K. Howe and P. Saraswat, *Excess Higgs Production in Neutralino Decays*, *JHEP* **10** (2012) 065, [arXiv:1208.1542 \[hep-ph\]](#).
- [157] A. Arbey, M. Battaglia, and F. Mahmoudi, *Higgs Production in Neutralino Decays in the MSSM - The LHC and a Future  $e^+e^-$  Collider*, *Eur. Phys. J.* **C75** (2015) no. 3, 108, [arXiv:1212.6865 \[hep-ph\]](#).
- [158] K. Griest and D. Seckel, *Three exceptions in the calculation of relic abundances*, *Phys. Rev.* **D43** (1991) 3191–3203.
- [159] J. R. Ellis, T. Falk, and K. A. Olive, *Neutralino - Stau coannihilation and the cosmological upper limit on the mass of the lightest supersymmetric particle*, *Phys. Lett.* **B444** (1998) 367–372, [arXiv:hep-ph/9810360 \[hep-ph\]](#).
- [160] M. Citron, J. Ellis, F. Luo, J. Marrouche, K. A. Olive, and K. J. de Vries, *End of the CMSSM coannihilation strip is nigh*, *Phys. Rev.* **D87** (2013) no. 3, 036012, [arXiv:1212.2886 \[hep-ph\]](#).
- [161] N. Desai, J. Ellis, F. Luo, and J. Marrouche, *Closing in on the Tip of the CMSSM Stau Coannihilation Strip*, *Phys. Rev.* **D90** (2014) no. 5, 055031, [arXiv:1404.5061 \[hep-ph\]](#).
- [162] J. L. Feng, A. Rajaraman, and F. Takayama, *Superweakly interacting massive particles*, *Phys. Rev. Lett.* **91** (2003) 011302, [arXiv:hep-ph/0302215 \[hep-ph\]](#).
- [163] J. L. Feng, A. Rajaraman, and F. Takayama, *SuperWIMP dark matter signals from the early universe*, *Phys. Rev.* **D68** (2003) 063504, [arXiv:hep-ph/0306024 \[hep-ph\]](#).

- [164] J. R. Ellis, J. E. Kim, and D. V. Nanopoulos, *Cosmological Gravitino Regeneration and Decay*, *Phys. Lett.* **B145** (1984) 181.
- [165] T. Moroi, H. Murayama, and M. Yamaguchi, *Cosmological constraints on the light stable gravitino*, *Phys. Lett.* **B303** (1993) 289–294.
- [166] J. R. Ellis, K. A. Olive, Y. Santoso, and V. C. Spanos, *Gravitino dark matter in the CMSSM*, *Phys. Lett.* **B588** (2004) 7–16, [arXiv:hep-ph/0312262](#) [hep-ph].
- [167] J. L. Feng, S. Iwamoto, Y. Shadmi, and S. Tarem, *Long-Lived Sleptons at the LHC and a 100 TeV Proton Collider*, *JHEP* **12** (2015) 166, [arXiv:1505.02996](#) [hep-ph].
- [168] D. E. Groom, N. V. Mokhov, and S. I. Striganov, *Muon stopping power and range tables 10-MeV to 100-TeV*, *Atom. Data Nucl. Data Tabl.* **78** (2001) 183–356.
- [169] CMS Collaboration, S. Chatrchyan et al., *Searches for long-lived charged particles in pp collisions at  $\sqrt{s}=7$  and 8 TeV*, *JHEP* **07** (2013) 122, [arXiv:1305.0491](#) [hep-ex].
- [170] ATLAS Collaboration, G. Aad et al., *Searches for heavy long-lived charged particles with the ATLAS detector in proton-proton collisions at  $\sqrt{s} = 8$  TeV*, *JHEP* **01** (2015) 068, [arXiv:1411.6795](#) [hep-ex].
- [171] A. Avetisyan, S. Bhattacharya, M. Narain, S. Padhi, J. Hirschauer, et al., *Snowmass Energy Frontier Simulations using the Open Science Grid (A Snowmass 2013 whitepaper)*, in *Community Summer Study 2013: Snowmass on the Mississippi (CSS2013) Minneapolis, MN, USA, July 29-August 6, 2013*. 2013. [arXiv:1308.0843](#) [hep-ex].
- [172] GEANT4 Collaboration, S. Agostinelli et al., *GEANT4: A Simulation toolkit*, *Nucl.Instrum.Meth.* **A506** (2003) 250–303.
- [173] A. Salvucci, *Measurement of muon momentum resolution of the ATLAS detector*, *EPJ Web Conf.* **28** (2012) 12039, [arXiv:1201.4704](#) [physics.ins-det].
- [174] ATLAS Collaboration, G. Aad et al., *Search For Higgs Boson Pair Production in the  $\gamma\gamma b\bar{b}$  Final State using pp Collision Data at  $\sqrt{s} = 8$  TeV from the ATLAS Detector*, [arXiv:1406.5053](#) [hep-ex].
- [175] ATLAS Collaboration, G. Aad et al., *Searches for Higgs boson pair production in the  $hh \rightarrow b\bar{b}\tau\tau, \gamma\gamma WW^*, \gamma\gamma bb, bbbb$  channels with the ATLAS detector*, *Phys. Rev.* **D92** (2015) 092004, [arXiv:1509.04670](#) [hep-ex].
- [176] CMS Collaboration, *Search for resonant HH production in 2gamma+2b channel*, CMS-PAS-HIG-13-032, CERN, Geneva, 2014. <https://cds.cern.ch/record/1697512>.
- [177] CMS Collaboration, *Search for di-Higgs resonances decaying to 4 bottom quarks*, CMS-PAS-HIG-14-013, CERN, Geneva, 2014. <https://cds.cern.ch/record/1748425>.
- [178] ATLAS Collaboration, G. Aad et al., *Search for Higgs boson pair production in the  $b\bar{b}b\bar{b}$  final state from pp collisions at  $\sqrt{s} = 8$  TeV with the ATLAS detector*, *Eur. Phys. J.* **C75** (2015) no. 9, 412, [arXiv:1506.00285](#) [hep-ex].
- [179] CMS Collaboration, *2HDM scenario, H to hh and A to Zh*, CMS-PAS-HIG-13-025, CERN, Geneva, 2013. <https://cds.cern.ch/record/1637776>.
- [180] *Prospects for measuring Higgs pair production in the channel  $H(\rightarrow \gamma\gamma)H(\rightarrow b\bar{b})$  using the ATLAS detector at the HL-LHC*, ATL-PHYS-PUB-2014-019, CERN, Geneva, Oct, 2014. <https://cds.cern.ch/record/1956733>.
- [181] CMS Collaboration, *Higgs pair production at the High Luminosity LHC*, CMS-PAS-FTR-15-002, CERN, Geneva, 2015. <http://cds.cern.ch/record/2063038>.
- [182] A. J. Barr, M. J. Dolan, C. Englert, D. E. Ferreira de Lima, and M. Spannowsky, *Higgs Self-Coupling Measurements at a 100 TeV Hadron Collider*, *JHEP* **02** (2015) 016, [arXiv:1412.7154](#) [hep-ph].
- [183] A. Azatov, R. Contino, G. Panico, and M. Son, *Effective field theory analysis of double Higgs*

- boson production via gluon fusion*, *Phys. Rev.* **D92** (2015) no. 3, 035001, [arXiv:1502.00539 \[hep-ph\]](#).
- [184] Q. Li, Z. Li, Q.-S. Yan, and X. Zhao, *Probe Higgs boson pair production via the  $3\ell 2j + \cancel{E}$  mode*, *Phys. Rev.* **D92** (2015) no. 1, 014015, [arXiv:1503.07611 \[hep-ph\]](#).
- [185] A. Papaefstathiou, *Discovering Higgs boson pair production through rare final states at a 100 TeV collider*, *Phys. Rev.* **D91** (2015) no. 11, 113016, [arXiv:1504.04621 \[hep-ph\]](#).
- [186] C. Brust, A. Katz, and R. Sundrum, *SUSY Stops at a Bump*, *JHEP* **08** (2012) 059, [arXiv:1206.2353 \[hep-ph\]](#).
- [187] J. A. Evans and Y. Kats, *LHC Coverage of RPV MSSM with Light Stops*, *JHEP* **04** (2013) 028, [arXiv:1209.0764 \[hep-ph\]](#).
- [188] Y. Bai, A. Katz, and B. Tweedie, *Pulling Out All the Stops: Searching for RPV SUSY with Stop-Jets*, *JHEP* **01** (2014) 040, [arXiv:1309.6631 \[hep-ph\]](#).
- [189] C. Csaki, L. Randall, and J. Terning, *Light Stops from Seiberg Duality*, *Phys.Rev.* **D86** (2012) 075009, [arXiv:1201.1293 \[hep-ph\]](#).
- [190] Z. Han, A. Katz, D. Krohn, and M. Reece, *(Light) Stop Signs*, *JHEP* **08** (2012) 083, [arXiv:1205.5808 \[hep-ph\]](#).
- [191] C. Kilic and B. Tweedie, *Cornering Light Stops with Dileptonic  $mT_2$* , *JHEP* **04** (2013) 110, [arXiv:1211.6106 \[hep-ph\]](#).
- [192] M. Czakon, A. Mitov, M. Papucci, J. T. Ruderman, and A. Weiler, *Closing the stop gap*, *Phys. Rev. Lett.* **113** (2014) no. 20, 201803, [arXiv:1407.1043 \[hep-ph\]](#).
- [193] T. J. LeCompte and S. P. Martin, *Compressed supersymmetry after  $1/\text{fb}$  at the Large Hadron Collider*, *Phys. Rev.* **D85** (2012) 035023, [arXiv:1111.6897 \[hep-ph\]](#).
- [194] H. K. Dreiner, M. Krämer, and J. Tattersall, *How low can SUSY go? Matching, monojets and compressed spectra*, *Europhys. Lett.* **99** (2012) 61001, [arXiv:1207.1613 \[hep-ph\]](#).
- [195] B. Bhattacharjee and K. Ghosh, *Degenerate SUSY search at the 8 TeV LHC*, [arXiv:1207.6289 \[hep-ph\]](#).
- [196] M. Drees, M. Hanussek, and J. S. Kim, *Light Stop Searches at the LHC with Monojet Events*, *Phys. Rev.* **D86** (2012) 035024, [arXiv:1201.5714 \[hep-ph\]](#).
- [197] G. Belanger, M. Heikinheimo, and V. Sanz, *Model-Independent Bounds on Squarks from Monophoton Searches*, *JHEP* **08** (2012) 151, [arXiv:1205.1463 \[hep-ph\]](#).
- [198] D. S. M. Alves, M. R. Buckley, P. J. Fox, J. D. Lykken, and C.-T. Yu, *Stops and  $\cancel{E}_T$ : The shape of things to come*, *Phys. Rev.* **D87** (2013) no. 3, 035016, [arXiv:1205.5805 \[hep-ph\]](#).
- [199] K. Krizka, A. Kumar, and D. E. Morrissey, *Very Light Scalar Top Quarks at the LHC*, *Phys. Rev.* **D87** (2013) no. 9, 095016, [arXiv:1212.4856 \[hep-ph\]](#).
- [200] M. Carena, S. Gori, N. R. Shah, C. E. M. Wagner, and L.-T. Wang, *Light Stau Phenomenology and the Higgs  $\gamma\gamma$  Rate*, *JHEP* **07** (2012) 175, [arXiv:1205.5842 \[hep-ph\]](#).
- [201] M. Carena, S. Gori, N. R. Shah, C. E. M. Wagner, and L.-T. Wang, *Light Stops, Light Staus and the 125 GeV Higgs*, *JHEP* **08** (2013) 087, [arXiv:1303.4414 \[hep-ph\]](#).
- [202] B. Batell, M. McCullough, D. Stolarski, and C. B. Verhaaren, *Putting a Stop to di-Higgs Modifications*, *JHEP* **09** (2015) 216, [arXiv:1508.01208 \[hep-ph\]](#).
- [203] T. Plehn, M. Spira, and P. M. Zerwas, *Pair production of neutral Higgs particles in gluon-gluon collisions*, *Nucl. Phys.* **B479** (1996) 46–64, [arXiv:hep-ph/9603205 \[hep-ph\]](#). [Erratum: *Nucl. Phys.* **B531**,655(1998)].
- [204] A. Djouadi, W. Kilian, M. Muhlleitner, and P. M. Zerwas, *Production of neutral Higgs boson pairs at LHC*, *Eur. Phys. J.* **C10** (1999) 45–49, [arXiv:hep-ph/9904287 \[hep-ph\]](#).
- [205] A. Belyaev, M. Drees, O. J. P. Eboli, J. K. Mizukoshi, and S. F. Novaes, *Supersymmetric Higgs pair production at hadron colliders*, *Phys. Rev.* **D60** (1999) 075008, [arXiv:hep-ph/9905266](#)

- [hep-ph].
- [206] A. A. Barrientos Bendezu and B. A. Kniehl, *Pair production of neutral Higgs bosons at the CERN large hadron collider*, *Phys. Rev.* **D64** (2001) 035006, [arXiv:hep-ph/0103018](#) [hep-ph].
- [207] G. L. Kane, C. F. Kolda, L. Roszkowski, and J. D. Wells, *Study of constrained minimal supersymmetry*, *Phys. Rev.* **D49** (1994) 6173–6210, [arXiv:hep-ph/9312272](#) [hep-ph].
- [208] J. R. Ellis, T. Falk, K. A. Olive, and M. Schmitt, *Supersymmetric dark matter in the light of LEP-1.5*, *Phys. Lett.* **B388** (1996) 97–105, [arXiv:hep-ph/9607292](#) [hep-ph].
- [209] J. R. Ellis, T. Falk, K. A. Olive, and M. Schmitt, *Constraints on neutralino dark matter from LEP-2 and cosmology*, *Phys. Lett.* **B413** (1997) 355–364, [arXiv:hep-ph/9705444](#) [hep-ph].
- [210] J. R. Ellis, T. Falk, G. Ganis, K. A. Olive, and M. Schmitt, *Charginos and neutralinos in the light of radiative corrections: Sealing the fate of Higgsino dark matter*, *Phys. Rev.* **D58** (1998) 095002, [arXiv:hep-ph/9801445](#) [hep-ph].
- [211] V. D. Barger and C. Kao, *Relic density of neutralino dark matter in supergravity models*, *Phys. Rev.* **D57** (1998) 3131–3139, [arXiv:hep-ph/9704403](#) [hep-ph].
- [212] J. R. Ellis, T. Falk, G. Ganis, and K. A. Olive, *Supersymmetric dark matter in the light of LEP and the Tevatron collider*, *Phys. Rev.* **D62** (2000) 075010, [arXiv:hep-ph/0004169](#) [hep-ph].
- [213] L. Roszkowski, R. Ruiz de Austri, and T. Nihei, *New cosmological and experimental constraints on the CMSSM*, *JHEP* **08** (2001) 024, [arXiv:hep-ph/0106334](#) [hep-ph].
- [214] A. Djouadi, M. Drees, and J. L. Kneur, *Constraints on the minimal supergravity model and prospects for SUSY particle production at future linear  $e^+e^-$  colliders*, *JHEP* **08** (2001) 055, [arXiv:hep-ph/0107316](#) [hep-ph].
- [215] U. Chattopadhyay, A. Corsetti, and P. Nath, *Supersymmetric dark matter and Yukawa unification*, *Phys. Rev.* **D66** (2002) 035003, [arXiv:hep-ph/0201001](#) [hep-ph].
- [216] J. R. Ellis, K. A. Olive, and Y. Santoso, *Constraining supersymmetry*, *New J. Phys.* **4** (2002) 32, [arXiv:hep-ph/0202110](#) [hep-ph].
- [217] O. Buchmueller, M. Citron, J. Ellis, S. Guha, J. Marrouche, K. A. Olive, K. de Vries, and J. Zheng, *Collider Interplay for Supersymmetry, Higgs and Dark Matter*, *Eur. Phys. J.* **C75** (2015) no. 10, 469, [arXiv:1505.04702](#) [hep-ph].
- [218] C. Boehm, A. Djouadi, and M. Drees, *Light scalar top quarks and supersymmetric dark matter*, *Phys. Rev.* **D62** (2000) 035012, [arXiv:hep-ph/9911496](#) [hep-ph].
- [219] J. R. Ellis, K. A. Olive, and Y. Santoso, *Calculations of neutralino stop coannihilation in the CMSSM*, *Astropart. Phys.* **18** (2003) 395–432, [arXiv:hep-ph/0112113](#) [hep-ph].
- [220] J. Edsjo, M. Schelke, P. Ullio, and P. Gondolo, *Accurate relic densities with neutralino, chargino and sfermion coannihilations in mSUGRA*, *JCAP* **0304** (2003) 001, [arXiv:hep-ph/0301106](#) [hep-ph].
- [221] J. L. Diaz-Cruz, J. R. Ellis, K. A. Olive, and Y. Santoso, *On the Feasibility of a Stop NLSP in Gravitino Dark Matter Scenarios*, *JHEP* **05** (2007) 003, [arXiv:hep-ph/0701229](#) [HEP-PH].
- [222] I. Gogoladze, S. Raza, and Q. Shafi, *Light stop from  $b\hat{O}\phi\hat{a}\hat{e}\hat{s}\hat{a}d\prime\text{Ltau}$  Yukawa unification*, *Phys. Lett.* **B706** (2012) 345–349, [arXiv:1104.3566](#) [hep-ph].
- [223] M. A. Ajaib, T. Li, and Q. Shafi, *Stop-Neutralino Coannihilation in the Light of LHC*, *Phys. Rev.* **D85** (2012) 055021, [arXiv:1111.4467](#) [hep-ph].
- [224] J. Ellis, K. A. Olive, and J. Zheng, *The Extent of the Stop Coannihilation Strip*, *Eur. Phys. J.* **C74** (2014) 2947, [arXiv:1404.5571](#) [hep-ph].
- [225] J. L. Feng, K. T. Matchev, and T. Moroi, *Multi - TeV scalars are natural in minimal supergravity*, *Phys. Rev. Lett.* **84** (2000) 2322–2325, [arXiv:hep-ph/9908309](#) [hep-ph].
- [226] J. L. Feng, K. T. Matchev, and F. Wilczek, *Neutralino dark matter in focus point supersymmetry*,

- Phys. Lett. **B482** (2000) 388–399, [arXiv:hep-ph/0004043](#) [hep-ph].
- [227] H. Baer, T. Krupovnickas, S. Profumo, and P. Ullio, *Model independent approach to focus point supersymmetry: From dark matter to collider searches*, *JHEP* **10** (2005) 020, [arXiv:hep-ph/0507282](#) [hep-ph].
- [228] J. L. Feng, K. T. Matchev, and D. Sanford, *Focus Point Supersymmetry Redux*, *Phys. Rev.* **D85** (2012) 075007, [arXiv:1112.3021](#) [hep-ph].
- [229] P. Draper, J. L. Feng, P. Kant, S. Profumo, and D. Sanford, *Dark Matter Detection in Focus Point Supersymmetry*, *Phys. Rev.* **D88** (2013) no. 1, 015025, [arXiv:1304.1159](#) [hep-ph].
- [230] I. Hinchliffe and F. E. Paige, *High mass SUSY Models at LHC and VLHC. Part 1.*, eConf **C010630** (2001) E401.
- [231] J. P. Vega and G. Villadoro, *Susyhd: Higgs Mass Determination in Supersymmetry*, *JHEP* **07** (2015) 159, [arXiv:1504.05200](#) [hep-ph].
- [232] R. Barbieri, M. Frigeni, and F. Caravaglios, *The Supersymmetric Higgs for heavy superpartners*, *Phys. Lett.* **B258** (1991) 167–170.
- [233] H. E. Haber and R. Hempfling, *Can the mass of the lightest Higgs boson of the minimal supersymmetric model be larger than  $m(Z)$ ?*, *Phys. Rev. Lett.* **66** (1991) 1815–1818.
- [234] J. A. Casas, J. R. Espinosa, M. Quiros, and A. Riotto, *The Lightest Higgs boson mass in the minimal supersymmetric standard model*, *Nucl. Phys.* **B436** (1995) 3–29, [arXiv:hep-ph/9407389](#) [hep-ph]. [Erratum: *Nucl. Phys.*B439,466(1995)].
- [235] M. Carena, J. R. Espinosa, M. Quiros, and C. E. M. Wagner, *Analytical expressions for radiatively corrected Higgs masses and couplings in the MSSM*, *Phys. Lett.* **B355** (1995) 209–221, [arXiv:hep-ph/9504316](#) [hep-ph].
- [236] P. Draper and H. Rzehak, *A Review of Higgs Mass Calculations in Supersymmetric Models*, [arXiv:1601.01890](#) [hep-ph].
- [237] J. Fan, D. Krohn, P. Mosteiro, A. M. Thalappilil, and L.-T. Wang, *Heavy Squarks at the LHC*, *JHEP* **03** (2011) 077, [arXiv:1102.0302](#) [hep-ph].
- [238] R. Sato, S. Shirai, and K. Tobioka, *Glino Decay as a Probe of High Scale Supersymmetry Breaking*, *JHEP* **11** (2012) 041, [arXiv:1207.3608](#) [hep-ph].
- [239] M. Toharia and J. D. Wells, *Glino decays with heavier scalar superpartners*, *JHEP* **02** (2006) 015, [arXiv:hep-ph/0503175](#) [hep-ph].
- [240] P. Gambino, G. F. Giudice, and P. Slavich, *Glino decays in split supersymmetry*, *Nucl. Phys.* **B726** (2005) 35–52, [arXiv:hep-ph/0506214](#) [hep-ph].
- [241] K. Choi, A. Falkowski, H. P. Nilles, and M. Olechowski, *Soft supersymmetry breaking in KKL<sub>T</sub> flux compactification*, *Nucl. Phys.* **B718** (2005) 113–133, [arXiv:hep-th/0503216](#) [hep-th].
- [242] K. Choi, K. S. Jeong, T. Kobayashi, and K.-i. Okumura, *Little SUSY hierarchy in mixed modulus-anomaly mediation*, *Phys. Lett.* **B633** (2006) 355–361, [arXiv:hep-ph/0508029](#) [hep-ph].
- [243] B. S. Acharya, K. Bobkov, G. L. Kane, J. Shao, and P. Kumar, *The  $G(2)$ -MSSM: An  $M$  Theory motivated model of Particle Physics*, *Phys. Rev.* **D78** (2008) 065038, [arXiv:0801.0478](#) [hep-ph].
- [244] G. D. Coughlan, W. Fischler, E. W. Kolb, S. Raby, and G. G. Ross, *Cosmological Problems for the Polonyi Potential*, *Phys. Lett.* **B131** (1983) 59.
- [245] J. R. Ellis, D. V. Nanopoulos, and M. Quiros, *On the Axion, Dilaton, Polonyi, Gravitino and Shadow Matter Problems in Supergravity and Superstring Models*, *Phys. Lett.* **B174** (1986) 176.
- [246] B. de Carlos, J. A. Casas, F. Quevedo, and E. Roulet, *Model independent properties and cosmological implications of the dilaton and moduli sectors of 4-d strings*, *Phys. Lett.* **B318** (1993) 447–456, [arXiv:hep-ph/9308325](#) [hep-ph].

- [247] T. Moroi, *Effects of the Gravitino on the Inflationary Universe*. PhD thesis, Tohoku U., 1995. [arXiv:hep-ph/9503210](#) [hep-ph].
- [248] G. Kane, K. Sinha, and S. Watson, *Cosmological Moduli and the Post-Inflationary Universe: A Critical Review*, *Int. J. Mod. Phys. D* **24** (2015) no. 08, 1530022, [arXiv:1502.07746](#) [hep-th].
- [249] W. Altmannshofer, R. Harnik, and J. Zupan, *Low Energy Probes of PeV Scale Sfermions*, *JHEP* **11** (2013) 202, [arXiv:1308.3653](#) [hep-ph].
- [250] M. Baumgart, D. Stolarski, and T. Zorawski, *Split supersymmetry radiates flavor*, *Phys. Rev. D* **90** (2014) no. 5, 055001, [arXiv:1403.6118](#) [hep-ph].
- [251] R. Blumenhagen, J. P. Conlon, S. Krippendorf, S. Moster, and F. Quevedo, *SUSY Breaking in Local String/F-Theory Models*, *JHEP* **09** (2009) 007, [arXiv:0906.3297](#) [hep-th].
- [252] L. Aparicio, M. Cicoli, S. Krippendorf, A. Maharana, F. Muia, and F. Quevedo, *Sequestered De Sitter String Scenarios: Soft-Terms*, *JHEP* **11** (2014) 071, [arXiv:1409.1931](#) [hep-th].
- [253] M. Reece and W. Xue, *SUSY's Ladder: Reframing Sequestering at Large Volume*, [arXiv:1512.04941](#) [hep-ph].
- [254] E. Cremmer, S. Ferrara, C. Kounnas, and D. V. Nanopoulos, *Naturally Vanishing Cosmological Constant in  $N=1$  Supergravity*, *Phys.Lett.* **B133** (1983) 61.
- [255] J. R. Ellis, A. Lahanas, D. V. Nanopoulos, and K. Tamvakis, *No-Scale Supersymmetric Standard Model*, *Phys.Lett.* **B134** (1984) 429.
- [256] V. Balasubramanian, P. Berglund, J. P. Conlon, and F. Quevedo, *Systematics of Moduli Stabilisation in Calabi-Yau Flux Compactifications*, *JHEP* **03** (2005) 007, [arXiv:hep-th/0502058](#) [hep-th].
- [257] J. P. Conlon, F. Quevedo, and K. Suruliz, *Large-Volume Flux Compactifications: Moduli Spectrum and D3/D7 Soft Supersymmetry Breaking*, *JHEP* **08** (2005) 007, [arXiv:hep-th/0505076](#) [hep-th].
- [258] T. Han, S. Padhi, and S. Su, *Electroweakinos in the Light of the Higgs Boson*, *Phys. Rev. D* **88** (2013) no. 11, 115010, [arXiv:1309.5966](#) [hep-ph].
- [259] ATLAS Collaboration, *Physics at a High-Luminosity LHC with ATLAS*, in *Community Summer Study 2013: Snowmass on the Mississippi (CSS2013) Minneapolis, MN, USA, July 29-August 6, 2013*. 2013. [arXiv:1307.7292](#) [hep-ex].  
<http://inspirehep.net/record/1245017/files/arXiv:1307.7292.pdf>.
- [260] M. E. Peskin, *Estimation of LHC and ILC Capabilities for Precision Higgs Boson Coupling Measurements*, in *Community Summer Study 2013: Snowmass on the Mississippi (CSS2013) Minneapolis, MN, USA, July 29-August 6, 2013*. 2013. [arXiv:1312.4974](#) [hep-ph].  
<http://www.slac.stanford.edu/econf/C1307292/docs/submittedArxivFiles/1312.4974.pdf>.
- [261] T. Sjöëstrand, S. Ask, J. R. Christiansen, R. Corke, N. Desai, P. Ilten, S. Mrenna, S. Prestel, C. O. Rasmussen, and P. Z. Skands, *An Introduction to PYTHIA 8.2*, *Comput. Phys. Commun.* **191** (2015) 159–177, [arXiv:1410.3012](#) [hep-ph].
- [262] A. Djouadi, M. M. Muhlleitner, and M. Spira, *Decays of supersymmetric particles: The Program SUSY-HIT (SUSpect-SdecaY-Hdecay-Interface)*, *Acta Phys. Polon.* **B38** (2007) 635–644, [arXiv:hep-ph/0609292](#) [hep-ph].
- [263] M. Cacciari and G. P. Salam, *Dispelling the  $N^3$  myth for the  $k_t$  jet-finder*, *Phys. Lett.* **B641** (2006) 57–61, [arXiv:hep-ph/0512210](#) [hep-ph].
- [264] M. Cacciari, G. P. Salam, and G. Soyez, *FastJet User Manual*, *Eur.Phys.J.* **C72** (2012) 1896, [arXiv:1111.6097](#) [hep-ph].
- [265] J. Thaler and K. Van Tilburg, *Identifying Boosted Objects with  $N$ -subjettiness*, *JHEP* **03** (2011) 015, [arXiv:1011.2268](#) [hep-ph].

- [266] A. J. Larkoski, D. Neill, and J. Thaler, *Jet Shapes with the Broadening Axis*, *JHEP* **04** (2014) 017, [arXiv:1401.2158 \[hep-ph\]](#).
- [267] P. Agrawal, J. Fan, M. Reece, and W. Xue, *To appear soon in 2016*, .
- [268] ATLAS Collaboration, *Prospects for benchmark Supersymmetry searches at the high luminosity LHC with the ATLAS Detector*, ATL-PHYS-PUB-2013-011, CERN, Geneva, Sep, 2013. <https://cds.cern.ch/record/1604505>.
- [269] ATLAS Collaboration, *Search for Supersymmetry at the high luminosity LHC with the ATLAS experiment*, ATL-PHYS-PUB-2014-010, CERN, Geneva, Jul, 2014. <https://cds.cern.ch/record/1735031>.
- [270] CMS Collaboration, *Supersymmetry discovery potential in future LHC and HL-LHC running with the CMS detector*, CMS-PAS-SUS-14-012, CERN, Geneva, 2015. <https://cds.cern.ch/record/1981344>.
- [271] CMS Collaboration, *Study of the Discovery Reach in Searches for Supersymmetry at CMS with 3000/fb*, CMS-PAS-FTR-13-014, CERN, Geneva, 2013. <https://cds.cern.ch/record/1607141>.
- [272] G. Salam and A. Weiler, *Collider Reach Tool*, <http://collider-reach.web.cern.ch>.
- [273] Planck Collaboration, P. A. R. Ade et al., *Planck 2015 results. XIII. Cosmological parameters*, [arXiv:1502.01589 \[astro-ph.CO\]](#).
- [274] G. B. Gelmini, *TASI 2014 Lectures: The Hunt for Dark Matter*, in *Theoretical Advanced Study Institute in Elementary Particle Physics: Journeys Through the Precision Frontier: Amplitudes for Colliders (TASI 2014) Boulder, Colorado, June 2-27, 2014*. 2015. [arXiv:1502.01320 \[hep-ph\]](#). <http://inspirehep.net/record/1342951/files/arXiv:1502.01320.pdf>.
- [275] W. Hu, R. Barkana, and A. Gruzinov, *Cold and fuzzy dark matter*, *Phys. Rev. Lett.* **85** (2000) 1158–1161, [arXiv:astro-ph/0003365 \[astro-ph\]](#).
- [276] K. Griest, A. M. Cieplak, and M. J. Lehner, *Experimental Limits on Primordial Black Hole Dark Matter from the First 2 yr of Kepler Data*, *Astrophys. J.* **786** (2014) no. 2, 158, [arXiv:1307.5798 \[astro-ph.CO\]](#).
- [277] MACHO, EROS Collaboration, C. Alcock et al., *EROS and MACHO combined limits on planetary mass dark matter in the galactic halo*, *Astrophys. J.* **499** (1998) L9, [arXiv:astro-ph/9803082 \[astro-ph\]](#).
- [278] J. Yoo, J. Chaname, and A. Gould, *The end of the MACHO era: limits on halo dark matter from stellar halo wide binaries*, *Astrophys. J.* **601** (2004) 311–318, [arXiv:astro-ph/0307437 \[astro-ph\]](#).
- [279] E. W. Kolb and M. S. Turner, *The Early Universe*, *Front.Phys.* **69** (1990) 1–547.
- [280] K. Griest and M. Kamionkowski, *Unitarity Limits on the Mass and Radius of Dark Matter Particles*, *Phys. Rev. Lett.* **64** (1990) 615.
- [281] K. Blum, Y. Cui, and M. Kamionkowski, *An Ultimate Target for Dark Matter Searches*, *Phys. Rev.* **D92** (2015) no. 2, 023528, [arXiv:1412.3463 \[hep-ph\]](#).
- [282] K. Petraki and R. R. Volkas, *Review of asymmetric dark matter*, *Int. J. Mod. Phys.* **A28** (2013) 1330028, [arXiv:1305.4939 \[hep-ph\]](#).
- [283] K. M. Zurek, *Asymmetric Dark Matter: Theories, Signatures, and Constraints*, *Phys. Rept.* **537** (2014) 91–121, [arXiv:1308.0338 \[hep-ph\]](#).
- [284] P. Cushman et al., *Working Group Report: WIMP Dark Matter Direct Detection*, in *Community Summer Study 2013: Snowmass on the Mississippi (CSS2013) Minneapolis, MN, USA, July 29-August 6, 2013*. 2013. [arXiv:1310.8327 \[hep-ex\]](#). <http://inspirehep.net/record/1262767/files/arXiv:1310.8327.pdf>.
- [285] P. Grothaus, M. Fairbairn, and J. Monroe, *Directional Dark Matter Detection Beyond the*

- Neutrino Bound*, *Phys. Rev.* **D90** (2014) no. 5, 055018, [arXiv:1406.5047 \[hep-ph\]](#).
- [286] Schumann, Marc and Baudis, Laura and Bütikofer, Lukas and Kish, Alexander and Selvi, Marco, *Dark matter sensitivity of multi-ton liquid xenon detectors*, *JCAP* **1510** (2015) no. 10, 016, [arXiv:1506.08309 \[physics.ins-det\]](#).
- [287] LZ Collaboration, D. S. Akerib et al., *LUX-ZEPLIN (LZ) Conceptual Design Report*, [arXiv:1509.02910 \[physics.ins-det\]](#).
- [288] C. E. Aalseth et al., *The DarkSide Multiton Detector for the Direct Dark Matter Search*, *Adv. High Energy Phys.* **2015** (2015) 541362.
- [289] XENON100 Collaboration, E. Aprile et al., *Limits on spin-dependent WIMP-nucleon cross sections from 225 live days of XENON100 data*, *Phys. Rev. Lett.* **111** (2013) no. 2, 021301, [arXiv:1301.6620 \[astro-ph.CO\]](#).
- [290] LUX Collaboration, D. S. Akerib et al., *First spin-dependent WIMP-nucleon cross section limits from the LUX experiment*, [arXiv:1602.03489 \[hep-ex\]](#).
- [291] C. Jin, *Dark Matter Particle Explorer: The First Chinese Cosmic Ray and Hard gamma-ray Detector in Space*, Chinese journal of space science (2014) .
- [292] V. I. Dokuchaev and Yu. N. Eroshenko, *Physical laboratory at the center of the Galaxy*, *Phys. Usp.* **58** (2015) 772–784, [arXiv:1512.02943 \[astro-ph.HE\]](#).
- [293] CTA Consortium Collaboration, Actis, M. and Agnetta, G. and Aharonian, F. and Akhperjanian, A. and Aleksić, J. and Aliu, E. and Allan, D. and Allekotte, I. and Antico, F. and Antonelli, L. A. and others, *Design concepts for the Cherenkov Telescope Array CTA: An advanced facility for ground-based high-energy gamma-ray astronomy*, *Exper. Astron.* **32** (2011) 193–316, [arXiv:1008.3703 \[astro-ph.IM\]](#).
- [294] H.E.S.S. Collaboration, A. Abramowski et al., *Search for Photon-Linelike Signatures from Dark Matter Annihilations with H.E.S.S.*, *Phys.Rev.Lett.* **110** (2013) 041301, [arXiv:1301.1173 \[astro-ph.HE\]](#).
- [295] Fermi-LAT Collaboration, M. Ackermann et al., *Updated search for spectral lines from Galactic dark matter interactions with pass 8 data from the Fermi Large Area Telescope*, *Phys. Rev.* **D91** (2015) no. 12, 122002, [arXiv:1506.00013 \[astro-ph.HE\]](#).
- [296] G. Giesen, M. Boudaud, Y. Gãl'nolini, V. Poulin, M. Cirelli, P. Salati, and P. D. Serpico, *AMS-02 antiprotons, at last! Secondary astrophysical component and immediate implications for Dark Matter*, *JCAP* **1509** (2015) no. 09, 023, [arXiv:1504.04276 \[astro-ph.HE\]](#).
- [297] A. Kounine, *Talk at AMS Days at CERN*, .
- [298] DES, Fermi-LAT Collaboration, A. Drlica-Wagner et al., *Search for Gamma-Ray Emission from DES Dwarf Spheroidal Galaxy Candidates with Fermi-LAT Data*, *Astrophys. J.* **809** (2015) no. 1, L4, [arXiv:1503.02632 \[astro-ph.HE\]](#).
- [299] HESS Collaboration, A. Abramowski et al., *Constraints on an Annihilation Signal from a Core of Constant Dark Matter Density around the Milky Way Center with H.E.S.S.*, *Phys. Rev. Lett.* **114** (2015) no. 8, 081301, [arXiv:1502.03244 \[astro-ph.HE\]](#).
- [300] G. D'Ambrosio, G. F. Giudice, G. Isidori, and A. Strumia, *Minimal flavor violation: An Effective field theory approach*, *Nucl. Phys.* **B645** (2002) 155–187, [arXiv:hep-ph/0207036 \[hep-ph\]](#).
- [301] J. Abdallah et al., *Simplified Models for Dark Matter Searches at the LHC*, *Phys. Dark Univ.* **9-10** (2015) 8–23, [arXiv:1506.03116 \[hep-ph\]](#).
- [302] M. Backovic, K. Kong, and M. McCaskey, *MadDM v.1.0: Computation of Dark Matter Relic Abundance Using MadGraph5*, *Physics of the Dark Universe* **5-6** (2014) 18–28, [arXiv:1308.4955 \[hep-ph\]](#).
- [303] M. Chala, F. Kahlhoefer, M. McCullough, G. Nardini, and K. Schmidt-Hoberg, *Constraining Dark Sectors with Monojets and Dijets*, *JHEP* **07** (2015) 089, [arXiv:1503.05916 \[hep-ph\]](#).

- [304] ATLAS Collaboration, *ATLAS Phase-II Upgrade Scoping Document*, CERN-LHCC-2015-020. LHCC-G-166, CERN, Geneva, Sep, 2015. <https://cds.cern.ch/record/2055248>.
- [305] J. Butler, D. Contardo, M. Klute, J. Mans, and L. Silvestris, *Technical Proposal for the Phase-II Upgrade of the CMS Detector*, CERN-LHCC-2015-010. LHCC-P-008, CERN, Geneva, Jun, 2015. <http://cds.cern.ch/record/2020886>.
- [306] Fermi-LAT Collaboration, M. Ajello et al., *Fermi-LAT Observations of High-Energy Gamma-Ray Emission Toward the Galactic Center*, *Astrophys. J.* **819** (2016) no. 1, 44, [arXiv:1511.02938](https://arxiv.org/abs/1511.02938) [[astro-ph.HE](#)].
- [307] D. Hooper and L. Goodenough, *Dark Matter Annihilation in The Galactic Center As Seen by the Fermi Gamma Ray Space Telescope*, *Phys. Lett.* **B697** (2011) 412–428, [arXiv:1010.2752](https://arxiv.org/abs/1010.2752) [[hep-ph](#)].
- [308] C. Gordon and O. Macias, *Dark Matter and Pulsar Model Constraints from Galactic Center Fermi-LAT Gamma Ray Observations*, *Phys. Rev.* **D88** (2013) no. 8, 083521, [arXiv:1306.5725](https://arxiv.org/abs/1306.5725) [[astro-ph.HE](#)]. [Erratum: *Phys. Rev.* **D89**, no. 4, 049901 (2014)].
- [309] T. Daylan, D. P. Finkbeiner, D. Hooper, T. Linden, S. K. N. Portillo, N. L. Rodd, and T. R. Slatyer, *The characterization of the gamma-ray signal from the central Milky Way: A case for annihilating dark matter*, *Phys. Dark Univ.* **12** (2016) 1–23, [arXiv:1402.6703](https://arxiv.org/abs/1402.6703) [[astro-ph.HE](#)].
- [310] F. Calore, I. Cholis, and C. Weniger, *Background model systematics for the Fermi GeV excess*, *JCAP* **1503** (2015) 038, [arXiv:1409.0042](https://arxiv.org/abs/1409.0042) [[astro-ph.CO](#)].
- [311] P. Agrawal, B. Batell, P. J. Fox, and R. Harnik, *WIMPs at the Galactic Center*, *JCAP* **1505** (2015) 011, [arXiv:1411.2592](https://arxiv.org/abs/1411.2592) [[hep-ph](#)].
- [312] CMS Collaboration, *Search for New Physics in the  $V/\text{jet} + \text{MET}$  final state*, CMS-PAS-EXO-12-055, CERN, Geneva, 2015. <https://cds.cern.ch/record/2036044>.
- [313] ATLAS Collaboration, *Search for resonances decaying to photon pairs in  $3.2 \text{ fb}^{-1}$  of  $pp$  collisions at  $\sqrt{s} = 13 \text{ TeV}$  with the ATLAS detector*, ATLAS-CONF-2015-081, CERN, Geneva, Dec, 2015. <https://cds.cern.ch/record/2114853>.
- [314] CMS Collaboration, *Search for new physics in high mass diphoton events in proton-proton collisions at  $13\text{TeV}$* , CMS-PAS-EXO-15-004, CERN, Geneva, 2015. <https://cds.cern.ch/record/2114808>.
- [315] M. Backovic, A. Mariotti, and D. Redigolo, *Di-photon excess illuminates Dark Matter*, [arXiv:1512.04917](https://arxiv.org/abs/1512.04917) [[hep-ph](#)].
- [316] S. Knapen, T. Melia, M. Papucci, and K. Zurek, *Rays of light from the LHC*, [arXiv:1512.04928](https://arxiv.org/abs/1512.04928) [[hep-ph](#)].
- [317] C. Han, H. M. Lee, M. Park, and V. Sanz, *The diphoton resonance as a gravity mediator of dark matter*, [arXiv:1512.06376](https://arxiv.org/abs/1512.06376) [[hep-ph](#)].
- [318] X.-J. Bi, Q.-F. Xiang, P.-F. Yin, and Z.-H. Yu, *The 750 GeV diphoton excess at the LHC and dark matter constraints*, [arXiv:1512.06787](https://arxiv.org/abs/1512.06787) [[hep-ph](#)].
- [319] S. Bhattacharya, S. Patra, N. Sahoo, and N. Sahu, *750 GeV Di-photon excess at CERN LHC from a dark sector assisted scalar decay*, [arXiv:1601.01569](https://arxiv.org/abs/1601.01569) [[hep-ph](#)].
- [320] F. D’Eramo, J. de Vries, and P. Panci, *A 750 GeV Portal: LHC Phenomenology and Dark Matter Candidates*, [arXiv:1601.01571](https://arxiv.org/abs/1601.01571) [[hep-ph](#)].
- [321] Y. Mambrini, G. Arcadi, and A. Djouadi, *The LHC diphoton resonance and dark matter*, [arXiv:1512.04913](https://arxiv.org/abs/1512.04913) [[hep-ph](#)].
- [322] R. Franceschini, G. F. Giudice, J. F. Kamenik, M. McCullough, A. Pomarol, R. Rattazzi, M. Redi, F. Riva, A. Strumia, and R. Torre, *What is the  $\gamma\gamma$  resonance at 750 GeV?*, *JHEP* **03** (2016) 144, [arXiv:1512.04933](https://arxiv.org/abs/1512.04933) [[hep-ph](#)].

- [323] PAMELA Collaboration, O. Adriani et al., *An anomalous positron abundance in cosmic rays with energies 1.5–100 GeV*, *Nature* **458** (2009) 607–609, [arXiv:0810.4995 \[astro-ph\]](#).
- [324] AMS Collaboration, L. Accardo et al., *High Statistics Measurement of the Positron Fraction in Primary Cosmic Rays of 0.5–500 GeV with the Alpha Magnetic Spectrometer on the International Space Station*, *Phys. Rev. Lett.* **113** (2014) 121101.
- [325] DAMA, LIBRA Collaboration, R. Bernabei et al., *New results from DAMA/LIBRA*, *Eur. Phys. J.* **C67** (2010) 39–49, [arXiv:1002.1028 \[astro-ph.GA\]](#).
- [326] M. Cirelli, N. Fornengo, and A. Strumia, *Minimal dark matter*, *Nucl.Phys.* **B753** (2006) 178–194, [arXiv:hep-ph/0512090 \[hep-ph\]](#).
- [327] R. Mahbubani and L. Senatore, *The Minimal model for dark matter and unification*, *Phys. Rev.* **D73** (2006) 043510, [arXiv:hep-ph/0510064 \[hep-ph\]](#).
- [328] T. Cohen, J. Kearney, A. Pierce, and D. Tucker-Smith, *Singlet-Doublet Dark Matter*, *Phys. Rev.* **D85** (2012) 075003, [arXiv:1109.2604 \[hep-ph\]](#).
- [329] A. Joglekar, P. Schwaller, and C. E. M. Wagner, *Dark Matter and Enhanced Higgs to Di-photon Rate from Vector-like Leptons*, *JHEP* **12** (2012) 064, [arXiv:1207.4235 \[hep-ph\]](#).
- [330] C. Cheung and D. Sanford, *Simplified Models of Mixed Dark Matter*, *JCAP* **1402** (2014) 011, [arXiv:1311.5896 \[hep-ph\]](#).
- [331] L. Calibbi, A. Mariotti, and P. Tziveloglou, *Singlet-Doublet Model: Dark matter searches and LHC constraints*, *JHEP* **10** (2015) 116, [arXiv:1505.03867 \[hep-ph\]](#).
- [332] G. Cynolter, J. Kovács, and E. Lendvai, *Doublet-singlet model and unitarity*, *Mod. Phys. Lett.* **A31** (2015) no. 01, 1650013, [arXiv:1509.05323 \[hep-ph\]](#).
- [333] T. M. P. Tait and Z.-H. Yu, *Triplet-Quadruplet Dark Matter*, [arXiv:1601.01354 \[hep-ph\]](#).
- [334] S. D. Thomas and J. D. Wells, *Phenomenology of Massive Vectorlike Doublet Leptons*, *Phys.Rev.Lett.* **81** (1998) 34–37, [arXiv:hep-ph/9804359 \[hep-ph\]](#).
- [335] P. Schwaller and J. Zurita, *Compressed electroweakino spectra at the LHC*, *JHEP* **03** (2014) 060, [arXiv:1312.7350 \[hep-ph\]](#).
- [336] M. Ibe, S. Matsumoto, and R. Sato, *Mass Splitting between Charged and Neutral Winos at Two-Loop Level*, *Phys.Lett.* **B721** (2013) 252–260, [arXiv:1212.5989 \[hep-ph\]](#).
- [337] ATLAS Collaboration, G. Aad et al., *Search for charginos nearly mass degenerate with the lightest neutralino based on a disappearing-track signature in pp collisions at  $\sqrt{s}=8$  TeV with the ATLAS detector*, *Phys.Rev.* **D88** (2013) no. 11, 112006, [arXiv:1310.3675 \[hep-ex\]](#).
- [338] CMS Collaboration, V. Khachatryan et al., *Search for disappearing tracks in proton-proton collisions at  $\sqrt{s} = 8$  TeV*, *JHEP* **01** (2015) 096, [arXiv:1411.6006 \[hep-ex\]](#).
- [339] M. Cirelli, F. Sala, and M. Taoso, *Wino-like Minimal Dark Matter and future colliders*, *JHEP* **1410** (2014) 033, [arXiv:1407.7058 \[hep-ph\]](#).
- [340] A. V. Kotwal, S. Chekanov, and M. Low, *Double Higgs Boson Production in the  $4\tau$  Channel from Resonances in Longitudinal Vector Boson Scattering at a 100 TeV Collider*, *Phys. Rev.* **D91** (2015) 114018, [arXiv:1504.08042 \[hep-ph\]](#).
- [341] R. J. Hill and M. P. Solon, *WIMP-nucleon scattering with heavy WIMP effective theory*, *Phys.Rev.Lett.* **112** (2014) 211602, [arXiv:1309.4092 \[hep-ph\]](#).
- [342] M. Cirelli and A. Strumia, *Minimal Dark Matter: Model and results*, *New J.Phys.* **11** (2009) 105005, [arXiv:0903.3381 \[hep-ph\]](#).
- [343] L. J. Hall and Y. Nomura, *Spread Supersymmetry*, *JHEP* **1201** (2012) 082, [arXiv:1111.4519 \[hep-ph\]](#).
- [344] L. J. Hall, Y. Nomura, and S. Shirai, *Spread Supersymmetry with Wino LSP: Gluino and Dark Matter Signals*, *JHEP* **1301** (2013) 036, [arXiv:1210.2395 \[hep-ph\]](#).
- [345] L. J. Hall and Y. Nomura, *Grand Unification and Intermediate Scale Supersymmetry*, *JHEP* **1402**

- (2014) 129, [arXiv:1312.6695 \[hep-ph\]](#).
- [346] L. J. Hall, Y. Nomura, and S. Shirai, *Grand Unification, Axion, and Inflation in Intermediate Scale Supersymmetry*, *JHEP* **06** (2014) 137, [arXiv:1403.8138 \[hep-ph\]](#).
- [347] W. Chao, M. Gonderinger, and M. J. Ramsey-Musolf, *Higgs Vacuum Stability, Neutrino Mass, and Dark Matter*, *Phys.Rev.* **D86** (2012) 113017, [arXiv:1210.0491 \[hep-ph\]](#).
- [348] M. Frigerio and T. Hambye, *Dark matter stability and unification without supersymmetry*, *Phys.Rev.* **D81** (2010) 075002, [arXiv:0912.1545 \[hep-ph\]](#).
- [349] M. Farina, D. Pappadopulo, and A. Strumia, *A modified naturalness principle and its experimental tests*, *JHEP* **1308** (2013) 022, [arXiv:1303.7244v3 \[hep-ph\]](#).
- [350] J. Hisano, K. Ishiwata, and N. Nagata, *QCD Effects on Direct Detection of Wino Dark Matter*, *JHEP* **06** (2015) 097, [arXiv:1504.00915 \[hep-ph\]](#).
- [351] Cirelli, Marco and Panci, Paolo and Sala, Filippo and Taoso, Marco, *work in progress*, .
- [352] A. Hryczuk, I. Cholis, R. Iengo, M. Tavakoli, and P. Ullio, *Indirect Detection Analysis: Wino Dark Matter Case Study*, *JCAP* **1407** (2014) 031, [arXiv:1401.6212 \[astro-ph.HE\]](#).
- [353] J. L. Feng, T. Moroi, L. Randall, M. Strassler, and S. Su, *Discovering supersymmetry at the Tevatron in wino LSP scenarios*, *Phys.Rev.Lett.* **83** (1999) 1731–1734, [arXiv:hep-ph/9904250 \[hep-ph\]](#).
- [354] R. Barbieri, A. Pomarol, R. Rattazzi, and A. Strumia, *Electroweak symmetry breaking after LEP-1 and LEP-2*, *Nucl. Phys.* **B703** (2004) 127–146, [arXiv:hep-ph/0405040 \[hep-ph\]](#).
- [355] J. Fan, M. Reece, and L.-T. Wang, *Possible Futures of Electroweak Precision: ILC, FCC-ee, and CEPC*, [arXiv:1411.1054 \[hep-ph\]](#).
- [356] Fermi-LAT Collaboration, M. Ackermann et al., *Searching for Dark Matter Annihilation from Milky Way Dwarf Spheroidal Galaxies with Six Years of Fermi-LAT Data*, [arXiv:1503.02641 \[astro-ph.HE\]](#).
- [357] V. Bonnivard et al., *Dark matter annihilation and decay in dwarf spheroidal galaxies: The classical and ultrafaint dSphs*, *Mon. Not. Roy. Astron. Soc.* **453** (2015) no. 1, 849–867, [arXiv:1504.02048 \[astro-ph.HE\]](#).
- [358] CTA Consortium Collaboration, M. Actis et al., *Design concepts for the Cherenkov Telescope Array CTA: An advanced facility for ground-based high-energy gamma-ray astronomy*, *Exper. Astron.* **32** (2011) 193–316, [arXiv:1008.3703 \[astro-ph.IM\]](#).
- [359] P. Salati, *Quintessence and the relic density of neutralinos*, *Phys. Lett.* **B571** (2003) 121–131, [arXiv:astro-ph/0207396 \[astro-ph\]](#).
- [360] S. M. Boucenna, M. B. Krauss, and E. Nardi, *Minimal Asymmetric Dark Matter*, *Phys. Lett.* **B748** (2015) 191–198, [arXiv:1503.01119 \[hep-ph\]](#).
- [361] M. Fabbrichesi and A. Urbano, *Natural minimal dark matter*, [arXiv:1510.03861 \[hep-ph\]](#).
- [362] M. Aoki, T. Toma, and A. Vicente, *Non-thermal Production of Minimal Dark Matter via Right-handed Neutrino Decay*, *JCAP* **1509** (2015) no. 09, 063, [arXiv:1507.01591 \[hep-ph\]](#).
- [363] P. Junnarkar and A. Walker-Loud, *Scalar strange content of the nucleon from lattice QCD*, *Phys. Rev.* **D87** (2013) 114510, [arXiv:1301.1114 \[hep-lat\]](#).
- [364] M. Cirelli, A. Strumia, and M. Tamburini, *Cosmology and Astrophysics of Minimal Dark Matter*, *Nucl. Phys.* **B787** (2007) 152–175, [arXiv:0706.4071 \[hep-ph\]](#).
- [365] L. Di Luzio, R. Gr uber, J. F. Kamenik, and M. Nardecchia, *Accidental matter at the LHC*, *JHEP* **07** (2015) 074, [arXiv:1504.00359 \[hep-ph\]](#).
- [366] M. Cirelli, T. Hambye, P. Panci, F. Sala, and M. Taoso, *Gamma ray tests of Minimal Dark Matter*, *JCAP* **1510** (2015) no. 10, 026, [arXiv:1507.05519 \[hep-ph\]](#).
- [367] C. Garcia-Cely, A. Ibarra, A. S. Lamperstorfer, and M. H. G. Tytgat, *Gamma-rays from Heavy Minimal Dark Matter*, [arXiv:1507.05536 \[hep-ph\]](#).

- [368] B. Ostdiek, *Constraining the minimal dark matter fiveplet with LHC searches*, *Phys. Rev.* **D92** (2015) no. 5, 055008, [arXiv:1506.03445 \[hep-ph\]](#).
- [369] J. Bramante, N. Desai, P. Fox, A. Martin, B. Ostdiek, and T. Plehn, *Towards the Final Word on Neutralino Dark Matter*, [arXiv:1510.03460 \[hep-ph\]](#).
- [370] A. Alloul, N. D. Christensen, C. Degrande, C. Duhr, and B. Fuks, *FeynRules 2.0 - A complete toolbox for tree-level phenomenology*, *Comput. Phys. Commun.* **185** (2014) 2250–2300, [arXiv:1310.1921 \[hep-ph\]](#).
- [371] J. Bramante, P. J. Fox, A. Martin, B. Ostdiek, T. Plehn, T. Schell, and M. Takeuchi, *The Relic neutralino surface at a 100 TeV collider*, *Phys. Rev.* **D91** (2015) 054015, [arXiv:1412.4789 \[hep-ph\]](#).
- [372] LEP2 SUSY Working Group Collaboration, *LEPSUSYWG, ALEPH, DELPHI, L3 and OPAL experiments*, .
- [373] A. Hryczuk and R. Iengo, *The one-loop and Sommerfeld electroweak corrections to the Wino dark matter annihilation*, *JHEP* **1201** (2012) 163, [arXiv:1111.2916 \[hep-ph\]](#).
- [374] P. Bechtle, T. Bringmann, K. Desch, H. Dreiner, M. Hamer, et al., *Constrained Supersymmetry after two years of LHC data: a global view with Fittino*, *JHEP* **1206** (2012) 098, [arXiv:1204.4199 \[hep-ph\]](#).
- [375] G. Belanger, F. Boudjema, A. Pukhov, and A. Semenov, *micrOMEGAs<sub>3</sub>: A program for calculating dark matter observables*, *Comput. Phys. Commun.* **185** (2014) 960–985, [arXiv:1305.0237 \[hep-ph\]](#).
- [376] A. Djouadi, J.-L. Kneur, and G. Moultaka, *SuSpect: A Fortran code for the supersymmetric and Higgs particle spectrum in the MSSM*, *Comput. Phys. Commun.* **176** (2007) 426–455, [arXiv:hep-ph/0211331 \[hep-ph\]](#).
- [377] M. L. Mangano, M. Moretti, F. Piccinini, and M. Treccani, *Matching matrix elements and shower evolution for top-quark production in hadronic collisions*, *JHEP* **01** (2007) 013, [arXiv:hep-ph/0611129 \[hep-ph\]](#).
- [378] Z. Han, G. D. Kribs, A. Martin, and A. Menon, *Hunting Quasi-Degenerate Higgsinos*, *Phys. Rev.* **D89** (2014) 075007, [arXiv:1401.1235 \[hep-ph\]](#).
- [379] J. Bramante, A. Delgado, F. Elahi, A. Martin, and B. Ostdiek, *Catching sparks from well-forged neutralinos*, *Phys. Rev.* **D90** (2014) no. 9, 095008, [arXiv:1408.6530 \[hep-ph\]](#).
- [380] C. Han, L. Wu, J. M. Yang, M. Zhang, and Y. Zhang, *New approach for detecting a compressed bino/wino at the LHC*, *Phys. Rev.* **D91** (2015) 055030, [arXiv:1409.4533 \[hep-ph\]](#).
- [381] H. Baer, A. Mustafayev, and X. Tata, *Monojet plus soft dilepton signal from light higgsino pair production at LHC14*, [arXiv:1409.7058 \[hep-ph\]](#).
- [382] C. Han, D. Kim, S. Munir, and M. Park, *Accessing the core of naturalness, nearly degenerate higgsinos, at the LHC*, *JHEP* **04** (2015) 132, [arXiv:1502.03734 \[hep-ph\]](#).
- [383] C. Han and M. Park, *Revealing the jet substructure in a compressed spectrum*, [arXiv:1507.07729 \[hep-ph\]](#).
- [384] N. Bhattacharyya and A. Datta, *Tracking down the elusive charginos / neutralinos through tau leptons at the Large Hadron Collider*, *Phys. Rev.* **D80** (2009) 055016, [arXiv:0906.1460 \[hep-ph\]](#).
- [385] G. F. Giudice, T. Han, K. Wang, and L.-T. Wang, *Nearly Degenerate Gauginos and Dark Matter at the LHC*, *Phys. Rev.* **D81** (2010) 115011, [arXiv:1004.4902 \[hep-ph\]](#).
- [386] L. Calibbi, J. M. Lindert, T. Ota, and Y. Takanishi, *Cornering light Neutralino Dark Matter at the LHC*, *JHEP* **1310** (2013) 132, [arXiv:1307.4119](#).
- [387] M. Chakraborti, U. Chattopadhyay, A. Choudhury, A. Datta, and S. Poddar, *Reduced LHC constraints for higgsino-like heavier electroweakinos*, [arXiv:1507.01395 \[hep-ph\]](#).

- [388] E. Izaguirre, G. Krnjaic, and B. Shuve, *Discovering Inelastic Thermal-Relic Dark Matter at Colliders*, [arXiv:1508.03050 \[hep-ph\]](#).
- [389] CTA Consortium Collaboration, J. Carr et al., *Prospects for Indirect Dark Matter Searches with the Cherenkov Telescope Array (CTA)*, in *Proceedings, 34th International Cosmic Ray Conference (ICRC 2015)*. 2015. [arXiv:1508.06128 \[astro-ph.HE\]](#). <http://inspirehep.net/record/1389681/files/arXiv:1508.06128.pdf>.
- [390] LUX Collaboration, D. Akerib et al., *First results from the LUX dark matter experiment at the Sanford Underground Research Facility*, *Phys.Rev.Lett.* **112** (2014) 091303, [arXiv:1310.8214 \[astro-ph.CO\]](#).
- [391] V. Silveira and A. Zee, *SCALAR PHANTOMS*, *Phys.Lett.* **B161** (1985) 136.
- [392] J. McDonald, *Gauge singlet scalars as cold dark matter*, *Phys.Rev.* **D50** (1994) 3637–3649, [arXiv:hep-ph/0702143 \[HEP-PH\]](#).
- [393] C. Burgess, M. Pospelov, and T. ter Veldhuis, *The Minimal model of nonbaryonic dark matter: A Singlet scalar*, *Nucl.Phys.* **B619** (2001) 709–728, [arXiv:hep-ph/0011335 \[hep-ph\]](#).
- [394] B. Patt and F. Wilczek, *Higgs-field portal into hidden sectors*, [arXiv:hep-ph/0605188 \[hep-ph\]](#).
- [395] V. Barger, P. Langacker, M. McCaskey, M. J. Ramsey-Musolf, and G. Shaughnessy, *LHC Phenomenology of an Extended Standard Model with a Real Scalar Singlet*, *Phys.Rev.* **D77** (2008) 035005, [arXiv:0706.4311 \[hep-ph\]](#).
- [396] H. Davoudiasl, R. Kitano, T. Li, and H. Murayama, *The New minimal standard model*, *Phys.Lett.* **B609** (2005) 117–123, [arXiv:hep-ph/0405097 \[hep-ph\]](#).
- [397] O. J. P. Eboli and D. Zeppenfeld, *Observing an invisible Higgs boson*, *Phys. Lett.* **B495** (2000) 147–154, [arXiv:hep-ph/0009158 \[hep-ph\]](#).
- [398] I. Low, P. Schwaller, G. Shaughnessy, and C. E. M. Wagner, *The dark side of the Higgs boson*, *Phys. Rev.* **D85** (2012) 015009, [arXiv:1110.4405 \[hep-ph\]](#).
- [399] A. Djouadi, O. Lebedev, Y. Mambrini, and J. Quevillon, *Implications of LHC searches for Higgs–portal dark matter*, *Phys.Lett.* **B709** (2012) 65–69, [arXiv:1112.3299 \[hep-ph\]](#).
- [400] C. Englert, J. Jaeckel, E. Re, and M. Spannowsky, *Evasive Higgs Maneuvers at the LHC*, *Phys.Rev.* **D85** (2012) 035008, [arXiv:1111.1719 \[hep-ph\]](#).
- [401] A. Djouadi, A. Falkowski, Y. Mambrini, and J. Quevillon, *Direct Detection of Higgs-Portal Dark Matter at the LHC*, *Eur.Phys.J.* **C73** (2013) 2455, [arXiv:1205.3169 \[hep-ph\]](#).
- [402] C. Englert, J. Jaeckel, V. Khoze, and M. Spannowsky, *Emergence of the Electroweak Scale through the Higgs Portal*, *JHEP* **1304** (2013) 060, [arXiv:1301.4224 \[hep-ph\]](#).
- [403] ATLAS Collaboration, G. Aad et al., *Search for Invisible Decays of a Higgs Boson Produced in Association with a Z Boson in ATLAS*, *Phys.Rev.Lett.* **112** (2014) 201802, [arXiv:1402.3244 \[hep-ex\]](#).
- [404] CMS Collaboration, S. Chatrchyan et al., *Search for invisible decays of Higgs bosons in the vector boson fusion and associated ZH production modes*, *Eur. Phys. J.* **C74** (2014) 2980, [arXiv:1404.1344 \[hep-ex\]](#).
- [405] C. Bernaciak, T. Plehn, P. Schichtel, and J. Tattersall, *Spying an invisible Higgs boson*, *Phys. Rev.* **D91** (2015) 035024, [arXiv:1411.7699 \[hep-ph\]](#).
- [406] T. Sjostrand, S. Mrenna, and P. Z. Skands, *A Brief Introduction to PYTHIA 8.1*, *Comput.Phys.Commun.* **178** (2008) 852–867, [arXiv:0710.3820 \[hep-ph\]](#).
- [407] N. Craig, H. K. Lou, M. McCullough, and A. Thalappilil, *The Higgs Portal Above Threshold*, [arXiv:1412.0258 \[hep-ph\]](#).
- [408] S. A. Malik et al., *Interplay and Characterization of Dark Matter Searches at Colliders and in Direct Detection Experiments*, *Phys. Dark Univ.* **9-10** (2015) 51–58, [arXiv:1409.4075](#)

- [hep-ex].
- [409] D. Abercrombie et al., *Dark Matter Benchmark Models for Early LHC Run-2 Searches: Report of the ATLAS/CMS Dark Matter Forum*, [arXiv:1507.00966](#) [hep-ex].
- [410] O. Buchmueller, M. J. Dolan, and C. McCabe, *Beyond Effective Field Theory for Dark Matter Searches at the LHC*, *JHEP* **01** (2014) 025, [arXiv:1308.6799](#) [hep-ph].
- [411] O. Buchmueller, M. J. Dolan, S. A. Malik, and C. McCabe, *Characterising dark matter searches at colliders and direct detection experiments: Vector mediators*, *JHEP* **01** (2015) 037, [arXiv:1407.8257](#) [hep-ph].
- [412] A. DiFranzo, K. I. Nagao, A. Rajaraman, and T. M. P. Tait, *Simplified Models for Dark Matter Interacting with Quarks*, *JHEP* **1311** (2013) 014, [arXiv:1308.2679](#) [hep-ph].
- [413] P. Harris, V. V. Khoze, M. Spannowsky, and C. Williams, *Constraining Dark Sectors at Colliders: Beyond the Effective Theory Approach*, [arXiv:1411.0535](#) [hep-ph].
- [414] M. R. Buckley, D. Feld, and D. Goncalves, *Scalar Simplified Models for Dark Matter*, [arXiv:1410.6497](#) [hep-ph].
- [415] U. Haisch and E. Re, *Simplified dark matter top-quark interactions at the LHC*, *JHEP* **06** (2015) 078, [arXiv:1503.00691](#) [hep-ph].
- [416] V. V. Khoze, G. Ro, and M. Spannowsky, *Spectroscopy of scalar mediators to dark matter at the LHC and at 100 TeV*, *Phys. Rev.* **D92** (2015) no. 7, 075006, [arXiv:1505.03019](#) [hep-ph].
- [417] P. Harris, V. V. Khoze, M. Spannowsky, and C. Williams, *Closing up on Dark Sectors at Colliders: from 14 to 100 TeV*, [arXiv:1509.02904](#) [hep-ph].
- [418] D0 Collaboration, V. M. Abazov et al., *Search for large extra dimensions in the monojet + missing  $E_T$  channel at  $D\bar{D}$* , *Phys. Rev. Lett.* **90** (2003) 251802, [arXiv:hep-ex/0302014](#) [hep-ex].
- [419] CDF Collaboration, T. Aaltonen et al., *A Search for dark matter in events with one jet and missing transverse energy in  $p\bar{p}$  collisions at  $\sqrt{s} = 1.96$  TeV*, *Phys. Rev. Lett.* **108** (2012) 211804, [arXiv:1203.0742](#) [hep-ex].
- [420] CMS Collaboration, S. Chatrchyan et al., *Search for dark matter and large extra dimensions in monojet events in  $pp$  collisions at  $\sqrt{s} = 7$  TeV*, *JHEP* **09** (2012) 094, [arXiv:1206.5663](#) [hep-ex].
- [421] ATLAS Collaboration, *Search for dark matter candidates and large extra dimensions in events with a jet and missing transverse momentum with the ATLAS detector*, ATLAS-CONF-2012-084, CERN, Geneva, Jul, 2012. <https://cds.cern.ch/record/1460396>.
- [422] CMS Collaboration, V. Khachatryan et al., *Search for dark matter, extra dimensions, and unparticles in monojet events in proton-proton collisions at  $\sqrt{s} = 8$  TeV*, *Eur. Phys. J.* **C75** (2015) no. 5, 235, [arXiv:1408.3583](#) [hep-ex].
- [423] ATLAS Collaboration, E. Diehl, *The search for dark matter using monojets and monophotons with the ATLAS detector*, AIP Conf.Proc. (2014) no. 1604, 324, . <http://scitation.aip.org/content/aip/proceeding/aipcp/10.1063/1.4883448>.
- [424] J. L. Feng, S. Su, and F. Takayama, *Lower limit on dark matter production at the large hadron collider*, *Phys. Rev. Lett.* **96** (2006) 151802, [arXiv:hep-ph/0503117](#) [hep-ph].
- [425] Q.-H. Cao, C.-R. Chen, C. S. Li, and H. Zhang, *Effective Dark Matter Model: Relic density, CDMS II, Fermi LAT and LHC*, *JHEP* **08** (2011) 018, [arXiv:0912.4511](#) [hep-ph].
- [426] M. Beltran, D. Hooper, E. W. Kolb, Z. A. C. Krusberg, and T. M. P. Tait, *Maverick dark matter at colliders*, *JHEP* **09** (2010) 037, [arXiv:1002.4137](#) [hep-ph].
- [427] J. Goodman, M. Ibe, A. Rajaraman, W. Shepherd, T. M. P. Tait, and H.-B. Yu, *Constraints on Light Majorana dark Matter from Colliders*, *Phys. Lett.* **B695** (2011) 185–188, [arXiv:1005.1286](#) [hep-ph].

- [428] J. Goodman, M. Ibe, A. Rajaraman, W. Shepherd, T. M. P. Tait, and H.-B. Yu, *Constraints on Dark Matter from Colliders*, *Phys. Rev.* **D82** (2010) 116010, [arXiv:1008.1783 \[hep-ph\]](#).
- [429] P. J. Fox, R. Harnik, J. Kopp, and Y. Tsai, *Missing Energy Signatures of Dark Matter at the LHC*, *Phys.Rev.* **D85** (2012) 056011, [arXiv:1109.4398 \[hep-ph\]](#).
- [430] U. Haisch, F. Kahlhoefer, and J. Unwin, *The impact of heavy-quark loops on LHC dark matter searches*, *JHEP* **07** (2013) 125, [arXiv:1208.4605 \[hep-ph\]](#).
- [431] G. C. Branco, P. M. Ferreira, L. Lavoura, M. N. Rebelo, M. Sher, and J. P. Silva, *Theory and phenomenology of two-Higgs-doublet models*, *Phys. Rept.* **516** (2012) 1–102, [arXiv:1106.0034 \[hep-ph\]](#).
- [432] R. Schabinger and J. D. Wells, *A Minimal spontaneously broken hidden sector and its impact on Higgs boson physics at the large hadron collider*, *Phys. Rev.* **D72** (2005) 093007, [arXiv:hep-ph/0509209 \[hep-ph\]](#).
- [433] C. Englert, T. Plehn, D. Zerwas, and P. M. Zerwas, *Exploring the Higgs portal*, *Phys. Lett.* **B703** (2011) 298–305, [arXiv:1106.3097 \[hep-ph\]](#).
- [434] T. Hambye and A. Strumia, *Dynamical generation of the weak and Dark Matter scale*, *Phys. Rev.* **D88** (2013) 055022, [arXiv:1306.2329 \[hep-ph\]](#).
- [435] C. D. Carone and R. Ramos, *Classical scale-invariance, the electroweak scale and vector dark matter*, *Phys. Rev.* **D88** (2013) 055020, [arXiv:1307.8428 \[hep-ph\]](#).
- [436] V. V. Khoze, C. McCabe, and G. Ro, *Higgs vacuum stability from the dark matter portal*, *JHEP* **08** (2014) 026, [arXiv:1403.4953 \[hep-ph\]](#).
- [437] M. Carena, A. Daleo, B. A. Dobrescu, and T. M. P. Tait, *Z' gauge bosons at the Tevatron*, *Phys. Rev.* **D70** (2004) 093009, [arXiv:hep-ph/0408098 \[hep-ph\]](#).
- [438] P. J. Fox and C. Williams, *Next-to-Leading Order Predictions for Dark Matter Production at Hadron Colliders*, *Phys. Rev.* **D87** (2013) no. 5, 054030, [arXiv:1211.6390 \[hep-ph\]](#).
- [439] R. K. E. J. M. Campbell and C. Williams, *MCFM website*, <http://mcfm.fnal.gov>.
- [440] K. Arnold et al., *VBFNLO: A Parton level Monte Carlo for processes with electroweak bosons*, *Comput. Phys. Commun.* **180** (2009) 1661–1670, [arXiv:0811.4559 \[hep-ph\]](#).
- [441] K. Arnold et al., *VBFNLO: A Parton Level Monte Carlo for Processes with Electroweak Bosons – Manual for Version 2.5.0*, [arXiv:1107.4038 \[hep-ph\]](#).
- [442] J. Baglio et al., *Release Note - VBFNLO 2.7.0*, [arXiv:1404.3940 \[hep-ph\]](#).
- [443] NNPDF Collaboration, R. D. Ball et al., *Parton distributions for the LHC Run II*, *JHEP* **04** (2015) 040, [arXiv:1410.8849 \[hep-ph\]](#).
- [444] A. L. Read, *Presentation of search results: The CL(s) technique*, *J. Phys.* **G28** (2002) 2693–2704. [,11(2002)].
- [445] G. Cowan, K. Cranmer, E. Gross, and O. Vitells, *Asymptotic formulae for likelihood-based tests of new physics*, *Eur. Phys. J.* **C71** (2011) 1554, [arXiv:1007.1727 \[physics.data-an\]](#). [Erratum: *Eur. Phys. J.*C73,2501(2013)].
- [446] ATLAS Collaboration, *Letter of Intent for the Phase-II Upgrade of the ATLAS Experiment*, CERN-LHCC-2012-022. LHCC-I-023, CERN, Geneva, Dec, 2012. <https://cds.cern.ch/record/1502664>. Draft version for comments.
- [447] CMS Collaboration, V. Khachatryan et al., *Performance of the CMS missing transverse momentum reconstruction in pp data at  $\sqrt{s} = 8$  TeV*, *JINST* **10** (2015) no. 02, P02006, [arXiv:1411.0511 \[physics.ins-det\]](#).
- [448] H.-Y. Cheng and C.-W. Chiang, *Revisiting Scalar and Pseudoscalar Couplings with Nucleons*, *JHEP* **07** (2012) 009, [arXiv:1202.1292 \[hep-ph\]](#).
- [449] A. Kurylov and M. Kamionkowski, *Generalized analysis of weakly interacting massive particle searches*, *Phys. Rev.* **D69** (2004) 063503, [arXiv:hep-ph/0307185 \[hep-ph\]](#).

- [450] J. Hisano, K. Ishiwata, and N. Nagata, *Gluon contribution to the dark matter direct detection*, *Phys. Rev.* **D82** (2010) 115007, [arXiv:1007.2601 \[hep-ph\]](#).
- [451] K. Cheung, C.-T. Lu, P.-Y. Tseng, and T.-C. Yuan, *Collider Constraints on the Dark Matter Interpretation of the CDMS II Results*, [arXiv:1308.0067 \[hep-ph\]](#).
- [452] M. Hoferichter, J. Ruiz de Elvira, B. Kubis, and U.-G. Meißner, *High-Precision Determination of the Pion-Nucleon  $\sigma$  Term from Roy-Steiner Equations*, *Phys. Rev. Lett.* **115** (2015) 092301, [arXiv:1506.04142 \[hep-ph\]](#).
- [453] A. Crivellin, M. Hoferichter, and M. Procura, *Accurate evaluation of hadronic uncertainties in spin-independent WIMP-nucleon scattering: Disentangling two- and three-flavor effects*, *Phys. Rev.* **D89** (2014) 054021, [arXiv:1312.4951 \[hep-ph\]](#).
- [454] Fermi-LAT Collaboration, M. Ackermann et al., *Constraining Dark Matter Models from a Combined Analysis of Milky Way Satellites with the Fermi Large Area Telescope*, *Phys. Rev. Lett.* **107** (2011) 241302, [arXiv:1108.3546 \[astro-ph.HE\]](#).
- [455] Fermi-LAT Collaboration, A. A. Abdo et al., *Observations of Milky Way Dwarf Spheroidal galaxies with the Fermi-LAT detector and constraints on Dark Matter models*, *Astrophys. J.* **712** (2010) 147–158, [arXiv:1001.4531 \[astro-ph.CO\]](#).
- [456] J.-M. Zheng, Z.-H. Yu, J.-W. Shao, X.-J. Bi, Z. Li, and H.-H. Zhang, *Constraining the interaction strength between dark matter and visible matter: I. fermionic dark matter*, *Nucl. Phys.* **B854** (2012) 350–374, [arXiv:1012.2022 \[hep-ph\]](#).
- [457] C. Boehm, M. J. Dolan, C. McCabe, M. Spannowsky, and C. J. Wallace, *Extended gamma-ray emission from Coy Dark Matter*, *JCAP* **1405** (2014) 009, [arXiv:1401.6458 \[hep-ph\]](#).
- [458] T. d. Pree, K. Hahn, P. Harris, and C. Roskas, *Cosmological constraints on Dark Matter models for collider searches*, [arXiv:1603.08525 \[hep-ph\]](#).
- [459] M. T. Frandsen, F. Kahlhoefer, A. Preston, S. Sarkar, and K. Schmidt-Hoberg, *LHC and Tevatron Bounds on the Dark Matter Direct Detection Cross-Section for Vector Mediators*, *JHEP* **07** (2012) 123, [arXiv:1204.3839 \[hep-ph\]](#).
- [460] M. Fairbairn and J. Heal, *Complementarity of dark matter searches at resonance*, *Phys. Rev.* **D90** (2014) no. 11, 115019, [arXiv:1406.3288 \[hep-ph\]](#).
- [461] F. Kahlhoefer, K. Schmidt-Hoberg, T. Schwetz, and S. Vogl, *Implications of unitarity and gauge invariance for simplified dark matter models*, [arXiv:1510.02110 \[hep-ph\]](#).
- [462] Q.-F. Xiang, X.-J. Bi, P.-F. Yin, and Z.-H. Yu, *Searches for dark matter signals in simplified models at future hadron colliders*, *Phys. Rev.* **D91** (2015) 095020, [arXiv:1503.02931 \[hep-ph\]](#).
- [463] ATLAS Collaboration, G. Aad et al., *Search for new phenomena in final states with an energetic jet and large missing transverse momentum in  $pp$  collisions at  $\sqrt{s} = 8$  TeV with the ATLAS detector*, *Eur. Phys. J.* **C75** (2015) no. 7, 299, [arXiv:1502.01518 \[hep-ex\]](#). [Erratum: *Eur. Phys. J.* C75,no.9,408(2015)].
- [464] *Sensitivity to WIMP Dark Matter in the Final States Containing Jets and Missing Transverse Momentum with the ATLAS Detector at 14 TeV LHC*, ATL-PHYS-PUB-2014-007, CERN, Geneva, Jun, 2014. <https://cds.cern.ch/record/1708859>.
- [465] CMS Collaboration, *Search for Narrow Resonances using the Dijet Mass Spectrum with 19.6  $fb^{-1}$  of  $pp$  Collisions at  $\sqrt{s}=8$  TeV*, CMS-PAS-EXO-12-059, CERN, Geneva, 2013. <https://cds.cern.ch/record/1519066>.
- [466] F. Yu, *Di-jet resonances at future hadron colliders: A Snowmass whitepaper*, [arXiv:1308.1077 \[hep-ph\]](#).
- [467] E. Conte, B. Dumont, B. Fuks, and C. Wymant, *Designing and recasting LHC analyses with MadAnalysis 5*, *Eur. Phys. J.* **C74** (2014) no. 10, 3103, [arXiv:1405.3982 \[hep-ph\]](#).

- [468] G. Bélanger, F. Boudjema, A. Pukhov, and A. Semenov, *micrOMEGAs4.1: two dark matter candidates*, *Comput. Phys. Commun.* **192** (2015) 322–329, [arXiv:1407.6129 \[hep-ph\]](#).
- [469] D. S. M. Alves, J. Galloway, J. T. Ruderman, and J. R. Walsh, *Running Electroweak Couplings as a Probe of New Physics*, *JHEP* **02** (2015) 007, [arXiv:1410.6810 \[hep-ph\]](#).
- [470] D. Curtin, R. Essig, S. Gori, P. Jaiswal, A. Katz, et al., *Exotic Decays of the 125 GeV Higgs Boson*, [arXiv:1312.4992 \[hep-ph\]](#).
- [471] B. Holdom, *Two  $U(1)$ 's and Epsilon Charge Shifts*, *Phys.Lett.* **B166** (1986) 196.
- [472] P. Galison and A. Manohar, *Two  $Z$ 's or Not Two  $Z$ 's?*, *Phys.Lett.* **B136** (1984) 279.
- [473] K. R. Dienes, C. F. Kolda, and J. March-Russell, *Kinetic mixing and the supersymmetric gauge hierarchy*, *Nucl.Phys.* **B492** (1997) 104–118, [arXiv:hep-ph/9610479 \[hep-ph\]](#).
- [474] D. Curtin, R. Essig, S. Gori, and J. Shelton, *Illuminating Dark Photons with High-Energy Colliders*, *JHEP* **1502** (2015) 157, [arXiv:1412.0018 \[hep-ph\]](#).
- [475] J. D. Bjorken, R. Essig, P. Schuster, and N. Toro, *New Fixed-Target Experiments to Search for Dark Gauge Forces*, *Phys. Rev.* **D80** (2009) 075018.
- [476] B. Batell, M. Pospelov, and A. Ritz, *Probing a Secluded  $U(1)$  at  $B$ -factories*, *Phys. Rev.* **D79** (2009) 115008.
- [477] R. Essig, P. Schuster, and N. Toro, *Probing Dark Forces and Light Hidden Sectors at Low-Energy  $e+e-$  Colliders*, *Phys. Rev.* **D80** (2009) 015003, [arXiv:0903.3941 \[hep-ph\]](#).
- [478] M. Freytsis, G. Ovanesyan, and J. Thaler, *Dark Force Detection in Low Energy  $e-p$  Collisions*, *JHEP* **1001** (2010) 111, [arXiv:0909.2862 \[hep-ph\]](#).
- [479] R. Essig, P. Schuster, N. Toro, and B. Wojtsekhowski, *An Electron Fixed Target Experiment to Search for a New Vector Boson  $A'$  Decaying to  $e+e-$* , *JHEP* **1102** (2011) 009, [arXiv:1001.2557 \[hep-ph\]](#).
- [480] J. Blumlein and J. Brunner, *New Exclusion Limits for Dark Gauge Forces from Beam-Dump Data*, *Phys.Lett.* **B701** (2011) 155–159, [arXiv:1104.2747 \[hep-ex\]](#).
- [481] S. Andreas, C. Niebuhr, and A. Ringwald, *New Limits on Hidden Photons from Past Electron Beam Dumps*, *Phys.Rev.* **D86** (2012) 095019, [arXiv:1209.6083 \[hep-ph\]](#).
- [482] M. Pospelov, *Secluded  $U(1)$  below the weak scale*, *Phys.Rev.* **D80** (2009) 095002, [arXiv:0811.1030 \[hep-ph\]](#).
- [483] M. Reece and L.-T. Wang, *Searching for the light dark gauge boson in GeV-scale experiments*, *JHEP* **07** (2009) 051.
- [484] BaBar Collaboration, B. Aubert et al., *Search for Dimuon Decays of a Light Scalar Boson in Radiative Transitions  $\Upsilon \rightarrow \gamma A^0$* , *Phys.Rev.Lett.* **103** (2009) 081803, [arXiv:0905.4539 \[hep-ex\]](#).
- [485] A. Hook, E. Izaguirre, and J. G. Wacker, *Model Independent Bounds on Kinetic Mixing*, *Adv.High Energy Phys.* **2011** (2011) 859762, [arXiv:1006.0973 \[hep-ph\]](#).
- [486] J. D. Bjorken et al., *Search for Neutral Metastable Penetrating Particles Produced in the SLAC Beam Dump*, *Phys. Rev.* **D38** (1988) 3375.
- [487] E. M. Riordan et al., *A Search for Short Lived Axions in an Electron Beam Dump Experiment*, *Phys. Rev. Lett.* **59** (1987) 755.
- [488] A. Bross et al., *A Search for Shortlived Particles Produced in an Electron Beam Dump*, *Phys. Rev. Lett.* **67** (1991) 2942–2945.
- [489] KLOE-2 Collaboration, D. Babusci et al., *Limit on the production of a light vector gauge boson in phi meson decays with the KLOE detector*, *Phys.Lett.* **B720** (2013) 111–115, [arXiv:1210.3927 \[hep-ex\]](#).
- [490] F. Archilli, D. Babusci, D. Badoni, I. Balwierz, G. Bencivenni, et al., *Search for a vector gauge boson in phi meson decays with the KLOE detector*, *Phys.Lett.* **B706** (2012) 251–255,

- [arXiv:1110.0411](#) [[hep-ex](#)].
- [491] APEX Collaboration, S. Abrahamyan et al., *Search for a new gauge boson in the A' Experiment (APEX)*, *Phys. Rev. Lett.* **107** (2011) 191804, [arXiv:1108.2750](#) [[hep-ex](#)].
- [492] A1 Collaboration, H. Merkel et al., *Search for Light Gauge Bosons of the Dark Sector at the Mainz Microtron*, *Phys. Rev. Lett.* **106** (2011) 251802.
- [493] J. B. Dent, F. Ferrer, and L. M. Krauss, *Constraints on Light Hidden Sector Gauge Bosons from Supernova Cooling*, [arXiv:1201.2683](#) [[astro-ph.CO](#)].
- [494] H. Davoudiasl, H.-S. Lee, and W. J. Marciano, *Dark Side of Higgs Diphoton Decays and Muon  $g-2$* , *Phys.Rev.* **D86** (2012) 095009, [arXiv:1208.2973](#) [[hep-ph](#)].
- [495] H. Davoudiasl, H.-S. Lee, and W. J. Marciano, *'Dark' Z implications for Parity Violation, Rare Meson Decays, and Higgs Physics*, *Phys.Rev.* **D85** (2012) 115019, [arXiv:1203.2947](#) [[hep-ph](#)].
- [496] H. Davoudiasl, H.-S. Lee, I. Lewis, and W. J. Marciano, *Higgs Decays as a Window into the Dark Sector*, [arXiv:1304.4935](#) [[hep-ph](#)].
- [497] M. Endo, K. Hamaguchi, and G. Mishima, *Constraints on Hidden Photon Models from Electron  $g-2$  and Hydrogen Spectroscopy*, *Phys.Rev.* **D86** (2012) 095029, [arXiv:1209.2558](#) [[hep-ph](#)].
- [498] J. Balewski, J. Bernauer, W. Bertozzi, J. Bessuille, B. Buck, et al., *DarkLight: A Search for Dark Forces at the Jefferson Laboratory Free-Electron Laser Facility*, [arXiv:1307.4432](#).
- [499] WASA-at-COSY Collaboration, P. Adlarson et al., *Search for a dark photon in the  $\pi^0 \rightarrow e^+e^-\gamma$  decay*, *Phys.Lett.* **B726** (2013) 187–193, [arXiv:1304.0671](#) [[hep-ex](#)].
- [500] HADES Collaboration, G. Agakishiev et al., *Searching a Dark Photon with HADES*, *Phys.Lett.* **B731** (2014) 265–271, [arXiv:1311.0216](#) [[hep-ex](#)].
- [501] J. Blümlein and J. Brunner, *New Exclusion Limits on Dark Gauge Forces from Proton Bremsstrahlung in Beam-Dump Data*, *Phys.Lett.* **B731** (2014) 320–326, [arXiv:1311.3870](#) [[hep-ph](#)].
- [502] S. Andreas, S. Donskov, P. Crivelli, A. Gardikiotis, S. Gninenko, et al., *Proposal for an Experiment to Search for Light Dark Matter at the SPS*, [arXiv:1312.3309](#) [[hep-ex](#)].
- [503] M. Battaglieri, S. Boyarinov, S. Bueltmann, V. Burkert, A. Celentano, et al., *The Heavy Photon Search Test Detector*, [arXiv:1406.6115](#) [[physics.ins-det](#)].
- [504] H. Merkel, P. Achenbach, C. A. Gayoso, T. Beranek, J. Bericic, et al., *Search for light massive gauge bosons as an explanation of the  $(g - 2)_\mu$  anomaly at MAMI*, [arXiv:1404.5502](#) [[hep-ex](#)].
- [505] BaBar Collaboration, J. Lees et al., *Search for a dark photon in  $e+e-$  collisions at BABAR*, [arXiv:1406.2980](#) [[hep-ex](#)].
- [506] A. Adare, S. Afanasiev, C. Aidala, N. Ajitanand, Y. Akiba, et al., *Closing the Door for Dark Photons as the Explanation for the Muon  $g-2$  Anomaly*, [arXiv:1409.0851](#) [[nucl-ex](#)].
- [507] D. Kazanas, R. N. Mohapatra, S. Nussinov, V. Teplitz, and Y. Zhang, *Supernova Bounds on the Dark Photon Using its Electromagnetic Decay*, [arXiv:1410.0221](#) [[hep-ph](#)].
- [508] B. Echenard, R. Essig, and Y.-M. Zhong, *Projections for Dark Photon Searches at Mu3e*, [arXiv:1411.1770](#) [[hep-ph](#)].
- [509] D. Gorbunov, A. Makarov, and I. Timiryasov, *Decaying light particles on board the SHiP (I): Signal rate estimates for hidden photons*, [arXiv:1411.4007](#) [[hep-ph](#)].
- [510] E. Goudzovski, *Search for the dark photon in  $\pi^0$  decays by NA48/2 at CERN*, *MesonNet workshop, LNF, Frascati, Sept. 2014*, .
- [511] S. Gopalakrishna, S. Jung, and J. D. Wells, *Higgs boson decays to four fermions through an abelian hidden sector*, *Phys.Rev.* **D78** (2008) 055002, [arXiv:0801.3456](#) [[hep-ph](#)].
- [512] C.-F. Chang, E. Ma, and T.-C. Yuan, *Multilepton Higgs Decays through the Dark Portal*,

- [arXiv:1308.6071 \[hep-ph\]](#).
- [513] A. Falkowski and R. Vega-Morales, *Exotic Higgs decays in the golden channel*, [arXiv:1405.1095 \[hep-ph\]](#).
- [514] J. M. Cline, G. Dupuis, Z. Liu, and W. Xue, *The windows for kinetically mixed  $Z'$ -mediated dark matter and the galactic center gamma ray excess*, [arXiv:1405.7691 \[hep-ph\]](#).
- [515] I. Hoenig, G. Samach, and D. Tucker-Smith, *Searching for dilepton resonances below the  $Z$  mass at the LHC*, [arXiv:1408.1075 \[hep-ph\]](#).
- [516] N. Arkani-Hamed and N. Weiner, *LHC Signals for a SuperUnified Theory of Dark Matter*, **JHEP** **0812** (2008) 104, [arXiv:0810.0714 \[hep-ph\]](#).
- [517] C. Cheung, J. T. Ruderman, L.-T. Wang, and I. Yavin, *Kinetic Mixing as the Origin of Light Dark Scales*, [0902.3246](#). <http://arxiv.org/abs/0902.3246>.
- [518] M. Baumgart, C. Cheung, J. T. Ruderman, L.-T. Wang, and I. Yavin, *Non-Abelian Dark Sectors and Their Collider Signatures*, **JHEP** **0904** (2009) 014, [arXiv:0901.0283 \[hep-ph\]](#).
- [519] D. E. Morrissey, D. Poland, and K. M. Zurek, *Abelian Hidden Sectors at a GeV*, **JHEP** **0907** (2009) 050, [arXiv:0904.2567 \[hep-ph\]](#).
- [520] CMS Collaboration, *Properties of the Higgs-like boson in the decay  $H$  to  $ZZ$  to  $4l$  in  $pp$  collisions at  $\sqrt{s} = 7$  and  $8$  TeV*, CMS-PAS-HIG-13-002, CERN, Geneva, 2013. <https://cds.cern.ch/record/1523767>.
- [521] ATLAS Collaboration, *Measurement of the total  $ZZ$  production cross section in proton-proton collisions  $\sqrt{s} = 8$  TeV in  $20 \text{ fb}^{-1}$  with the ATLAS detector*, ATLAS-CONF-2013-020, CERN, Geneva, Mar, 2013. <https://cds.cern.ch/record/1525555>.
- [522] CMS Collaboration, *Search for a non-standard-model Higgs boson decaying to a pair of new light bosons in four-muon final states*, CMS-PAS-HIG-13-010, CERN, Geneva, 2013. <https://cds.cern.ch/record/1563546>.
- [523] N. Craig, A. Katz, M. Strassler, and R. Sundrum, *Naturalness in the Dark at the LHC*, [arXiv:1501.05310 \[hep-ph\]](#).
- [524] D. Curtin and C. B. Verhaaren, *Discovering Uncolored Naturalness in Exotic Higgs Decays*, [arXiv:1506.06141 \[hep-ph\]](#).
- [525] M. J. Strassler and K. M. Zurek, *Echoes of a hidden valley at hadron colliders*, **Phys.Lett.** **B651** (2007) 374–379, [arXiv:hep-ph/0604261 \[hep-ph\]](#).
- [526] M. J. Strassler and K. M. Zurek, *Discovering the Higgs through highly-displaced vertices*, **Phys.Lett.** **B661** (2008) 263–267, [arXiv:hep-ph/0605193 \[hep-ph\]](#).
- [527] M. J. Strassler, *Possible effects of a hidden valley on supersymmetric phenomenology*, [arXiv:hep-ph/0607160 \[hep-ph\]](#).
- [528] T. Han, Z. Si, K. M. Zurek, and M. J. Strassler, *Phenomenology of hidden valleys at hadron colliders*, **JHEP** **0807** (2008) 008, [arXiv:0712.2041 \[hep-ph\]](#).
- [529] CMS Collaboration, V. Khachatryan et al., *Search for long-lived particles that decay into final states containing two electrons or two muons in proton-proton collisions at  $\sqrt{s} = 8$  TeV*, **Phys. Rev.** **D91** (2015) no. 5, 052012, [arXiv:1411.6977 \[hep-ex\]](#).
- [530] ATLAS Collaboration, G. Aad et al., *Search for long-lived neutral particles decaying into lepton jets in proton-proton collisions at  $\sqrt{s} = 8$  TeV with the ATLAS detector*, **JHEP** **11** (2014) 088, [arXiv:1409.0746 \[hep-ex\]](#).
- [531] A. De Simone, G. F. Giudice, and A. Strumia, *Benchmarks for Dark Matter Searches at the LHC*, **JHEP** **1406** (2014) 081, [arXiv:1402.6287 \[hep-ph\]](#).
- [532] K. Harigaya, K. Kaneta, and S. Matsumoto, *Gaugino coannihilations*, **Phys.Rev.** **D89** (2014) 115021, [arXiv:1403.0715 \[hep-ph\]](#).
- [533] A. Arbey, M. Battaglia, and F. Mahmoudi, *Combining monojet, supersymmetry, and dark matter*

- searches, *Phys. Rev.* **D89** (2014) no. 7, 077701, [arXiv:1311.7641 \[hep-ph\]](#).
- [534] M. Cahill-Rowley, J. L. Hewett, A. Ismail, and T. G. Rizzo, *Lessons and prospects from the pMSSM after LHC Run I*, *Phys. Rev.* **D91** (2015) no. 5, 055002, [arXiv:1407.4130 \[hep-ph\]](#).
- [535] ATLAS Collaboration, G. Aad et al., *Summary of the ATLAS experiment's sensitivity to supersymmetry after LHC Run 1 - interpreted in the phenomenological MSSM*, *JHEP* **10** (2015) 134, [arXiv:1508.06608 \[hep-ex\]](#).
- [536] CMS Collaboration, *Phenomenological MSSM interpretation of CMS results at  $\sqrt{s} = 7$  and 8 TeV*, CMS-PAS-SUS-15-010, CERN, Geneva, 2015. <https://cds.cern.ch/record/2063744>.
- [537] A. Arbey, M. Battaglia, L. Covi, J. Hasenkamp, and F. Mahmoudi, *LHC constraints on Gravitino Dark Matter*, *Phys. Rev.* **D92** (2015) no. 11, 115008, [arXiv:1505.04595 \[hep-ph\]](#).
- [538] G. Servant and S. Tulin, *Baryogenesis and Dark Matter through a Higgs Asymmetry*, *Phys. Rev. Lett.* **111** (2013) no. 15, 151601, [arXiv:1304.3464 \[hep-ph\]](#).
- [539] M. R. Buckley, *Asymmetric Dark Matter and Effective Operators*, *Phys. Rev.* **D84** (2011) 043510, [arXiv:1104.1429 \[hep-ph\]](#).
- [540] J. March-Russell, J. Unwin, and S. M. West, *Closing in on Asymmetric Dark Matter I: Model independent limits for interactions with quarks*, *JHEP* **08** (2012) 029, [arXiv:1203.4854 \[hep-ph\]](#).
- [541] T. D. Lee and C.-N. Yang, *Question of Parity Conservation in Weak Interactions*, *Phys. Rev.* **104** (1956) 254–258.
- [542] I. Yu. Kobzarev, L. B. Okun, and I. Ya. Pomeranchuk, *On the possibility of experimental observation of mirror particles*, *Sov. J. Nucl. Phys.* **3** (1966) no. 6, 837–841. [*Yad. Fiz.*3,1154(1966)].
- [543] R. Foot, H. Lew, and R. R. Volkas, *A Model with fundamental improper space-time symmetries*, *Phys. Lett.* **B272** (1991) 67–70.
- [544] Z. G. Berezhiani, A. D. Dolgov, and R. N. Mohapatra, *Asymmetric inflationary reheating and the nature of mirror universe*, *Phys. Lett.* **B375** (1996) 26–36, [arXiv:hep-ph/9511221 \[hep-ph\]](#).
- [545] G. D. Kribs, T. S. Roy, J. Terning, and K. M. Zurek, *Quirky Composite Dark Matter*, *Phys. Rev.* **D81** (2010) 095001, [arXiv:0909.2034 \[hep-ph\]](#).
- [546] M. Blennow, B. Dasgupta, E. Fernandez-Martinez, and N. Rius, *Aidnogenesis via Leptogenesis and Dark Sphalerons*, *JHEP* **03** (2011) 014, [arXiv:1009.3159 \[hep-ph\]](#).
- [547] M. T. Frandsen, S. Sarkar, and K. Schmidt-Hoberg, *Light asymmetric dark matter from new strong dynamics*, *Phys. Rev.* **D84** (2011) 051703, [arXiv:1103.4350 \[hep-ph\]](#).
- [548] Y. Bai and P. Schwaller, *Scale of dark QCD*, *Phys. Rev.* **D89** (2014) no. 6, 063522, [arXiv:1306.4676 \[hep-ph\]](#).
- [549] M. J. Strassler, *On the Phenomenology of Hidden Valleys with Heavy Flavor*, [arXiv:0806.2385 \[hep-ph\]](#).
- [550] P. Schwaller, D. Stolarski, and A. Weiler, *Emerging Jets*, *JHEP* **1505** (2015) 059, [arXiv:1502.05409 \[hep-ph\]](#).
- [551] T. Cohen, M. Lisanti, and H. K. Lou, *Semi-visible Jets: Dark Matter Undercover at the LHC*, [arXiv:1503.00009 \[hep-ph\]](#).
- [552] D. N. Spergel and P. J. Steinhardt, *Observational evidence for selfinteracting cold dark matter*, *Phys.Rev.Lett.* **84** (2000) 3760–3763, [arXiv:astro-ph/9909386 \[astro-ph\]](#).
- [553] S. Tulin, H.-B. Yu, and K. M. Zurek, *Beyond Collisionless Dark Matter: Particle Physics Dynamics for Dark Matter Halo Structure*, *Phys.Rev.* **D87** (2013) no. 11, 115007, [arXiv:1302.3898 \[hep-ph\]](#).
- [554] M. Vogelsberger, S. Genel, V. Springel, P. Torrey, D. Sijacki, et al., *Properties of galaxies*

- reproduced by a hydrodynamic simulation, *Nature* **509** (2014) 177–182, [arXiv:1405.1418 \[astro-ph.CO\]](#).
- [555] T. Sawala, C. S. Frenk, A. Fattahi, J. F. Navarro, R. G. Bower, et al., *Local Group galaxies emerge from the dark*, [arXiv:1412.2748 \[astro-ph.GA\]](#).
- [556] J. Hisano, S. Matsumoto, and M. M. Nojiri, *Explosive dark matter annihilation*, *Phys. Rev. Lett.* **92** (2004) 031303, [arXiv:hep-ph/0307216 \[hep-ph\]](#).
- [557] M. Cirelli, M. Kadastik, M. Raidal, and A. Strumia, *Model-independent implications of the  $e^+$ , anti-proton cosmic ray spectra on properties of Dark Matter*, *Nucl.Phys.* **B813** (2009) 1–21, [arXiv:0809.2409 \[hep-ph\]](#).
- [558] N. Arkani-Hamed, D. P. Finkbeiner, T. R. Slatyer, and N. Weiner, *A Theory of Dark Matter*, *Phys.Rev.* **D79** (2009) 015014, [arXiv:0810.0713 \[hep-ph\]](#).
- [559] W. Shepherd, T. M. P. Tait, and G. Zaharijas, *Bound states of weakly interacting dark matter*, *Phys. Rev.* **D79** (2009) 055022, [arXiv:0901.2125 \[hep-ph\]](#).
- [560] W. Altmannshofer, P. J. Fox, R. Harnik, G. D. Kribs, and N. Raj, *Dark Matter Signals in Dilepton Production at Hadron Colliders*, [arXiv:1411.6743 \[hep-ph\]](#).
- [561] M. Buschmann, J. Kopp, J. Liu, and P. A. N. Machado, *Lepton Jets from Radiating Dark Matter*, *JHEP* **07** (2015) 045, [arXiv:1505.07459 \[hep-ph\]](#).
- [562] L. Carloni and T. Sjostrand, *Visible Effects of Invisible Hidden Valley Radiation*, *JHEP* **1009** (2010) 105, [arXiv:1006.2911 \[hep-ph\]](#).
- [563] L. Carloni, J. Rathsmann, and T. Sjostrand, *Discerning Secluded Sector gauge structures*, *JHEP* **1104** (2011) 091, [arXiv:1102.3795 \[hep-ph\]](#).
- [564] C. Cheung, J. T. Ruderman, L.-T. Wang, and I. Yavin, *Lepton Jets in (Supersymmetric) Electroweak Processes*, *JHEP* **1004** (2010) 116, [arXiv:0909.0290 \[hep-ph\]](#).
- [565] A. Katz and R. Sundrum, *Breaking the Dark Force*, *JHEP* **0906** (2009) 003, [arXiv:0902.3271 \[hep-ph\]](#).
- [566] Y. Bai and Z. Han, *Measuring the Dark Force at the LHC*, *Phys.Rev.Lett.* **103** (2009) 051801, [arXiv:0902.0006 \[hep-ph\]](#).
- [567] Y. F. Chan, M. Low, D. E. Morrissey, and A. P. Spray, *LHC Signatures of a Minimal Supersymmetric Hidden Valley*, *JHEP* **1205** (2012) 155, [arXiv:1112.2705 \[hep-ph\]](#).
- [568] A. Falkowski, J. T. Ruderman, T. Volansky, and J. Zupan, *Discovering Higgs Decays to Lepton Jets at Hadron Colliders*, *Phys.Rev.Lett.* **105** (2010) 241801, [arXiv:1007.3496 \[hep-ph\]](#).
- [569] A. Gupta, R. Primulando, and P. Saraswat, *A New Probe of Dark Sector Dynamics at the LHC*, [arXiv:1504.01385 \[hep-ph\]](#).
- [570] M. Autran, K. Bauer, T. Lin, and D. Whiteson, *Mono- $Z'$ : searches for dark matter in events with a resonance and missing transverse energy*, [arXiv:1504.01386 \[hep-ph\]](#).
- [571] ATLAS Collaboration, G. Aad et al., *A Search for Prompt Lepton-Jets in  $pp$  Collisions at  $\sqrt{s} = 7$  TeV with the ATLAS Detector*, *Phys.Lett.* **B719** (2013) 299–317, [arXiv:1212.5409 \[hep-ex\]](#).
- [572] K. Hamaguchi, Y. Kuno, T. Nakaya, and M. M. Nojiri, *A Study of late decaying charged particles at future colliders*, *Phys. Rev.* **D70** (2004) 115007, [arXiv:hep-ph/0409248 \[hep-ph\]](#).
- [573] J. L. Feng and B. T. Smith, *Slepton trapping at the large hadron and international linear colliders*, *Phys. Rev.* **D71** (2005) 015004, [arXiv:hep-ph/0409278 \[hep-ph\]](#). [Erratum: *Phys. Rev.* **D71**, 019904(2005)].
- [574] W. Buchmuller, L. Covi, K. Hamaguchi, A. Ibarra, and T. Yanagida, *Gravitino Dark Matter in  $R$ -Parity Breaking Vacua*, *JHEP* **03** (2007) 037, [arXiv:hep-ph/0702184 \[HEP-PH\]](#).
- [575] G. Arcadi, L. Covi, and F. Dradi, *LHC prospects for minimal decaying Dark Matter*, *JCAP* **1410** (2014) no. 10, 063, [arXiv:1408.1005 \[hep-ph\]](#).
- [576] T. Han, I. Lewis, and Z. Liu, *Colored Resonant Signals at the LHC: Largest Rate and Simplest*

- Topology*, *JHEP* **1012** (2010) 085, [arXiv:1010.4309](https://arxiv.org/abs/1010.4309) [hep-ph].
- [577] P. Langacker, *The Physics of Heavy  $Z'$  Gauge Bosons*, *Rev.Mod.Phys.* **81** (2009) 1199–1228, [arXiv:0801.1345](https://arxiv.org/abs/0801.1345) [hep-ph].
- [578] Particle Data Group Collaboration, K. A. Olive et al., *Review of Particle Physics*, *Chin. Phys.* **C38** (2014) 090001.
- [579] H. Cai, H.-C. Cheng, and J. Terning, *A Spin-1 Top Quark Superpartner*, *Phys. Rev. Lett.* **101** (2008) 171805, [arXiv:0806.0386](https://arxiv.org/abs/0806.0386) [hep-ph].
- [580] C.-Y. Chen, A. Freitas, T. Han, and K. S. M. Lee, *New Physics from the Top at the LHC*, *JHEP* **11** (2012) 124, [arXiv:1207.4794](https://arxiv.org/abs/1207.4794) [hep-ph].
- [581] C.-Y. Chen, A. Freitas, T. Han, and K. S. M. Lee, *Heavy Color-Octet Particles at the LHC*, *JHEP* **05** (2015) 135, [arXiv:1410.8113](https://arxiv.org/abs/1410.8113) [hep-ph].
- [582] R. Foot, H. Lew, X. G. He, and G. C. Joshi, *Seesaw Neutrino Masses Induced by a Triplet of Leptons*, *Z. Phys.* **C44** (1989) 441.
- [583] A. Arhrib, B. Bajc, D. K. Ghosh, T. Han, G.-Y. Huang, I. Puljak, and G. Senjanovic, *Collider Signatures for Heavy Lepton Triplet in Type I+III Seesaw*, *Phys. Rev.* **D82** (2010) 053004, [arXiv:0904.2390](https://arxiv.org/abs/0904.2390) [hep-ph].
- [584] T. Li and X.-G. He, *Neutrino Masses and Heavy Triplet Leptons at the LHC: Testability of Type III Seesaw*, *Phys. Rev.* **D80** (2009) 093003, [arXiv:0907.4193](https://arxiv.org/abs/0907.4193) [hep-ph].
- [585] T. G. Rizzo, *Exploring new gauge bosons at a 100 TeV collider*, *Phys. Rev.* **D89** (2014) no. 9, 095022, [arXiv:1403.5465](https://arxiv.org/abs/1403.5465) [hep-ph].
- [586] U. Baur, I. Hinchliffe, and D. Zeppenfeld, *Excited quark production at hadron colliders*, *Int. J. Mod. Phys.* **A2** (1987) 1285.
- [587] U. Baur, M. Spira, and P. M. Zerwas, *Excited quark and lepton production at hadron colliders*, *Phys. Rev.* **D42** (1990) 815–825.
- [588] S. Kretzer, H. L. Lai, F. I. Olness, and W. K. Tung, *CTEQ6 parton distributions with heavy quark mass effects*, *Phys. Rev.* **D69** (2004) 114005, [arXiv:hep-ph/0307022](https://arxiv.org/abs/hep-ph/0307022) [hep-ph].
- [589] J. Pumplin, D. Stump, J. Huston, H. Lai, P. M. Nadolsky, et al., *New generation of parton distributions with uncertainties from global QCD analysis*, *JHEP* **0207** (2002) 012, [arXiv:hep-ph/0201195](https://arxiv.org/abs/hep-ph/0201195) [hep-ph].
- [590] H.-L. Lai, M. Guzzi, J. Huston, Z. Li, P. M. Nadolsky, J. Pumplin, and C. P. Yuan, *New parton distributions for collider physics*, *Phys. Rev.* **D82** (2010) 074024, [arXiv:1007.2241](https://arxiv.org/abs/1007.2241) [hep-ph].
- [591] *Sacrifice 0.9.1 for Pythia 8*, <https://agile.hepforge.org/trac/wiki/Sacrifice>, 2013. [Online; accessed 07-March-2016].
- [592] E. Conte, B. Fuks, and G. Serret, *MadAnalysis 5, A User-Friendly Framework for Collider Phenomenology*, *Comput. Phys. Commun.* **184** (2013) 222–256, [arXiv:1206.1599](https://arxiv.org/abs/1206.1599) [hep-ph].
- [593] R. Brun and F. Rademakers, *ROOT: An object oriented data analysis framework*, *Nucl. Instrum. Meth.* **A389** (1997) 81–86.
- [594] ATLAS Collaboration, G. Aad et al., *Search for new phenomena in dijet mass and angular distributions from pp collisions at  $\sqrt{s} = 13$  TeV with the ATLAS detector*, *Phys. Lett.* **B754** (2016) 302–322, [arXiv:1512.01530](https://arxiv.org/abs/1512.01530) [hep-ex].
- [595] L. Apanasevich, S. Upadhyay, N. Varelas, D. Whiteson, and F. Yu, *Sensitivity of potential future pp colliders to quark compositeness*, [arXiv:1307.7149](https://arxiv.org/abs/1307.7149) [hep-ex].
- [596] K. Kong and F. Yu, *Discovery potential of Kaluza-Klein gluons at hadron colliders: A Snowmass whitepaper*, [arXiv:1308.1078](https://arxiv.org/abs/1308.1078) [hep-ph].
- [597] K. Agashe, M. Bauer, F. Goertz, S. J. Lee, L. Vecchi, et al., *Constraining RS Models by Future Flavor and Collider Measurements: A Snowmass Whitepaper*, [arXiv:1310.1070](https://arxiv.org/abs/1310.1070) [hep-ph].
- [598] B. A. Dobrescu and F. Yu, *Coupling-mass mapping of dijet peak searches*, *Phys.Rev.* **D88** (2013)

- no. 3, 035021, [arXiv:1306.2629 \[hep-ph\]](#).
- [599] M. L. Mangano, M. Moretti, F. Piccinini, R. Pittau, and A. D. Polosa, *ALPGEN, a generator for hard multiparton processes in hadronic collisions*, *JHEP* **0307** (2003) 001, [arXiv:hep-ph/0206293 \[hep-ph\]](#).
- [600] CMS Collaboration, V. Khachatryan et al., *Search for resonances and quantum black holes using dijet mass spectra in proton-proton collisions at  $\sqrt{s} = 8$  TeV*, *Phys. Rev.* **D91** (2015) no. 5, 052009, [arXiv:1501.04198 \[hep-ex\]](#).
- [601] B. Auerbach, S. Chekanov, J. Love, J. Proudfoot, and A. V. Kotwal, *Sensitivity to new high-mass states decaying to  $t\bar{t}$  at a 100 TeV collider*, *Phys. Rev.* **D91** (2015) no. 3, 034014, [arXiv:1412.5951 \[hep-ph\]](#).
- [602] L. Randall and R. Sundrum, *A Large mass hierarchy from a small extra dimension*, *Phys. Rev. Lett.* **83** (1999) 3370–3373, [arXiv:hep-ph/9905221 \[hep-ph\]](#).
- [603] B. Lillie, L. Randall, and L.-T. Wang, *The Bulk RS KK-gluon at the LHC*, *JHEP* **09** (2007) 074, [arXiv:hep-ph/0701166 \[hep-ph\]](#).
- [604] S. Chekanov, *HepSim: a repository with predictions for high-energy physics experiments*, *Advances in High Energy Physics* **2015** (2015) 136093. Available as <http://atlaswww.hep.anl.gov/hepsim/>.
- [605] B. Lillard, T. M. P. Tait, and P. Tanedo, *Kaluza-Klein gluons at 100 TeV: NLO corrections*, *Phys. Rev.* **D94** (2016) no. 5, 054012, [arXiv:1602.08622 \[hep-ph\]](#).
- [606] S. D. Ellis, C. K. Vermilion, and J. R. Walsh, *Techniques for improved heavy particle searches with jet substructure*, *Phys. Rev.* **D80** (2009) 051501, [arXiv:0903.5081 \[hep-ph\]](#).
- [607] J. Butterworth, B. Cox, and J. R. Forshaw, *WW scattering at the CERN LHC*, *Phys.Rev.* **D65** (2002) 096014, [arXiv:hep-ph/0201098 \[hep-ph\]](#).
- [608] S. Chekanov and J. Proudfoot, *Searches for TeV-scale particles at the LHC using jet shapes*, *Phys. Rev.* **D81** (2010) 114038, [arXiv:1002.3982 \[hep-ph\]](#).
- [609] T. Junk, *Confidence level computation for combining searches with small statistics*, *Nucl. Instrum. Meth. A* **434** (1999) 435–443, [arXiv:hep-ex/9902006 \[hep-ex\]](#).
- [610] D. Pappadopulo, A. Thamm, R. Torre, and A. Wulzer, *Heavy Vector Triplets: Bridging Theory and Data*, *JHEP* **09** (2014) 060, [arXiv:1402.4431 \[hep-ph\]](#).
- [611] A. Thamm, R. Torre, and A. Wulzer, *Future tests of Higgs compositeness: direct vs indirect*, *JHEP* **07** (2015) 100, [arXiv:1502.01701 \[hep-ph\]](#).
- [612] K. Agashe, R. Contino, and A. Pomarol, *The Minimal Composite Higgs Model*, *Nucl. Phys. B* **719** (2005) 165–187, [0412089](#). [[Inspire](#)].
- [613] B. Bellazzini, C. Csaki, and J. Serra, *Composite Higgses*, *Eur. Phys. J. C* **74** (2014) 2766, [1401.2457](#). [[Inspire](#)].
- [614] G. Panico and A. Wulzer, *The Composite Nambu-Goldstone Higgs*, *Lect. Notes Phys.* **913** (2016) 1–316, [1506.01961](#). [[Inspire](#)].
- [615] A. De Simone, O. Matsedonskyi, R. Rattazzi, and A. Wulzer, *A First Top Partner’s Hunter Guide*, *JHEP* **04** (2013) 004, [1211.5663](#). [[Inspire](#)].
- [616] CMS Collaboration, *Search for Resonances in the Dilepton Mass Distribution in pp Collisions at  $\sqrt{s} = 8$  TeV*, CMS-PAS-EXO-12-061, CERN, Geneva, 2013. <https://cds.cern.ch/record/1519132>.
- [617] CMS Collaboration, V. Khachatryan et al., *Search for new resonances decaying via WZ to leptons in proton-proton collisions at  $\sqrt{s} = 8$  TeV*, *Phys. Lett.* **B740** (2015) 83–104, [arXiv:1407.3476 \[hep-ex\]](#).
- [618] ATLAS Collaboration, G. Aad et al., *Search for high-mass dilepton resonances in pp collisions at  $\sqrt{s} = 8$  TeV with the ATLAS detector*, *Phys. Rev.* **D 90** (2014) 052005, [1405.4123](#). [[Inspire](#)].

- [619] ATLAS Collaboration, G. Aad et al., *Search for  $WZ$  resonances in the fully leptonic channel using  $pp$  collisions at  $\sqrt{s} = 8$  TeV with the ATLAS detector*, *Phys. Lett. B* **737** (2014) 223–243, 1406.4456. [Inspire].
- [620] CMS Collaboration, *CMS at the High-Energy Frontier. Contribution to the Update of the European Strategy for Particle Physics*, CMS-NOTE-2012-006. CERN-CMS-NOTE-2012-006, CERN, Geneva, Oct, 2012. <https://cds.cern.ch/record/1494600>.
- [621] ATLAS Collaboration, *Projections for measurements of Higgs boson cross sections, branching ratios and coupling parameters with the ATLAS detector at a HL-LHC*, ATL-PHYS-PUB-2013-014, CERN, Geneva, Oct, 2013. <https://cds.cern.ch/record/1611186>.
- [622] S. Dawson, A. Gritsan, H. Logan, J. Qian, C. Tully, et al., *Working Group Report: Higgs Boson*, [arXiv:1310.8361](https://arxiv.org/abs/1310.8361) [hep-ex].
- [623] C. Froggatt and H. B. Nielsen, *Hierarchy of Quark Masses, Cabibbo Angles and CP Violation*, *Nucl.Phys.* **B147** (1979) 277.
- [624] M. Leurer, Y. Nir, and N. Seiberg, *Mass matrix models*, *Nucl. Phys.* **B398** (1993) 319–342, [arXiv:hep-ph/9212278](https://arxiv.org/abs/hep-ph/9212278) [hep-ph].
- [625] M. Leurer, Y. Nir, and N. Seiberg, *Mass matrix models: The Sequel*, *Nucl. Phys.* **B420** (1994) 468–504, [arXiv:hep-ph/9310320](https://arxiv.org/abs/hep-ph/9310320) [hep-ph].
- [626] K. Huitu, V. Keus, N. Koivunen, and O. Lebedev, *Higgs–Flavon Mixing and  $h \rightarrow \mu\tau$* , [arXiv:1603.06614](https://arxiv.org/abs/1603.06614) [hep-ph].
- [627] H. Georgi and S. L. Glashow, *Attempts to calculate the electron mass*, *Phys. Rev.* **D7** (1973) 2457–2463.
- [628] D. B. Kaplan, *Flavor at SSC energies: A New mechanism for dynamically generated fermion masses*, *Nucl. Phys.* **B365** (1991) 259–278.
- [629] T. Gherghetta and A. Pomarol, *Bulk fields and supersymmetry in a slice of AdS*, *Nucl. Phys.* **B586** (2000) 141–162, [arXiv:hep-ph/0003129](https://arxiv.org/abs/hep-ph/0003129) [hep-ph].
- [630] Y. Grossman and M. Neubert, *Neutrino masses and mixings in nonfactorizable geometry*, *Phys. Lett.* **B474** (2000) 361–371, [arXiv:hep-ph/9912408](https://arxiv.org/abs/hep-ph/9912408) [hep-ph].
- [631] M. Blanke, A. J. Buras, B. Duling, S. Gori, and A. Weiler,  *$\Delta F=2$  Observables and Fine-Tuning in a Warped Extra Dimension with Custodial Protection*, *JHEP* **03** (2009) 001, [arXiv:0809.1073](https://arxiv.org/abs/0809.1073) [hep-ph].
- [632] S. Casagrande, F. Goertz, U. Haisch, M. Neubert, and T. Pfoh, *Flavor Physics in the Randall-Sundrum Model: I. Theoretical Setup and Electroweak Precision Tests*, *JHEP* **10** (2008) 094, [arXiv:0807.4937](https://arxiv.org/abs/0807.4937) [hep-ph].
- [633] M. Bauer, S. Casagrande, U. Haisch, and M. Neubert, *Flavor Physics in the Randall-Sundrum Model: II. Tree-Level Weak-Interaction Processes*, *JHEP* **09** (2010) 017, [arXiv:0912.1625](https://arxiv.org/abs/0912.1625) [hep-ph].
- [634] M. Bauer, M. Carena, and K. Gemmler, *Flavor from the Electroweak Scale*, *JHEP* **11** (2015) 016, [arXiv:1506.01719](https://arxiv.org/abs/1506.01719) [hep-ph].
- [635] M. Bauer, M. Carena, and K. Gemmler, *Creating the Fermion Mass Hierarchies with Multiple Higgs Bosons*, [arXiv:1512.03458](https://arxiv.org/abs/1512.03458) [hep-ph].
- [636] L. Calibbi, A. Crivellin, and B. Zaldarriaga, *Flavor portal to dark matter*, *Phys. Rev.* **D92** (2015) no. 1, 016004, [arXiv:1501.07268](https://arxiv.org/abs/1501.07268) [hep-ph].
- [637] M. Bauer, T. Schell, and T. Plehn, *Hunting the Flavon*, [arXiv:1603.06950](https://arxiv.org/abs/1603.06950) [hep-ph].
- [638] J. Charles, S. Descotes-Genon, Z. Ligeti, S. Monteil, M. Papucci, and K. Trabelsi, *Future sensitivity to new physics in  $B_d$ ,  $B_s$ , and  $K$  mixings*, *Phys. Rev.* **D89** (2014) no. 3, 033016, [arXiv:1309.2293](https://arxiv.org/abs/1309.2293) [hep-ph].

- [639] CMS Collaboration, S. Chatrchyan et al., *Measurement of the  $B(s)$  to  $\mu^+\mu^-$  branching fraction and search for  $B^0$  to  $\mu^+\mu^-$  with the CMS Experiment*, *Phys. Rev. Lett.* **111** (2013) 101804, [arXiv:1307.5025 \[hep-ex\]](#).
- [640] LHCb Collaboration, R. Aaij et al., *Measurement of the  $B_s^0 \rightarrow \mu^+\mu^-$  branching fraction and search for  $B^0 \rightarrow \mu^+\mu^-$  decays at the LHCb experiment*, *Phys. Rev. Lett.* **111** (2013) 101805, [arXiv:1307.5024 \[hep-ex\]](#).
- [641] LHCb, CMS Collaboration, V. Khachatryan et al., *Observation of the rare  $B_s^0 \rightarrow \mu^+\mu^-$  decay from the combined analysis of CMS and LHCb data*, *Nature* **522** (2015) 68–72, [arXiv:1411.4413 \[hep-ex\]](#).
- [642] A. M. Baldini et al., *MEG Upgrade Proposal*, [arXiv:1301.7225 \[physics.ins-det\]](#).
- [643] DeeMe Collaboration, H. Natori, *DeeMe experiment - An experimental search for a  $\mu$ -e conversion reaction at J-PARC MLF*, *Nucl. Phys. Proc. Suppl.* **248-250** (2014) 52–57.
- [644] COMET Collaboration, Y. Kuno, *A search for muon-to-electron conversion at J-PARC: The COMET experiment*, *PTEP* **2013** (2013) 022C01.
- [645] Mu2e Collaboration, R. J. Abrams et al., *Mu2e Conceptual Design Report*, [arXiv:1211.7019 \[physics.ins-det\]](#).
- [646] Mu3e Collaboration, M. Kiehn, *The Mu3e Experiment - Introduction and Current Status*, *PoS NFACT2014* (2015) 088.
- [647] M. Mangano, G. Zanderighi, et al., *Physics at a 100 TeV pp collider: Standard Model processes*, CERN-TH-2016-112, 2016.
- [648] M. Cacciari, G. Salam, and G. Soyez, *FastJet. A C++ library for the  $k_T$  algorithm*, .
- [649] B. Schmidt and M. Steinhauser, *CRUnDec: a C++ package for running and decoupling of the strong coupling and quark masses*, *Comput. Phys. Commun.* **183** (2012) 1845–1848, [arXiv:1201.6149 \[hep-ph\]](#).
- [650] A. Alves, O. Eboli, and T. Plehn, *It's a gluino*, *Phys. Rev.* **D74** (2006) 095010, [arXiv:hep-ph/0605067 \[hep-ph\]](#).
- [651] *A new tagger for the charge identification of b-jets*, ATL-PHYS-PUB-2015-040, CERN, Geneva, Sep, 2015. <https://cds.cern.ch/record/2048132>.
- [652] K. Mohan and N. Vignaroli, *Vector resonances in weak-boson-fusion at future pp colliders*, *JHEP* **10** (2015) 031, [arXiv:1507.03940 \[hep-ph\]](#).
- [653] K. Agashe, R. Contino, and A. Pomarol, *The Minimal composite Higgs model*, *Nucl. Phys.* **B719** (2005) 165–187, [arXiv:hep-ph/0412089 \[hep-ph\]](#).
- [654] R. Contino, T. Kramer, M. Son, and R. Sundrum, *Warped/composite phenomenology simplified*, *JHEP* **05** (2007) 074, [arXiv:hep-ph/0612180 \[hep-ph\]](#).
- [655] N. Vignaroli, *New  $W\tilde{L}\tilde{L}^*\tilde{L}^*$  signals at the LHC*, *Phys. Rev.* **D89** (2014) no. 9, 095027, [arXiv:1404.5558 \[hep-ph\]](#).
- [656] Y. A. Kulchitsky, M. V. Kuzmin, J. A. Budagov, V. B. Vinogradov, and M. Nessi, *Hadron energy reconstruction for the ATLAS barrel prototype combined calorimeter in the framework of the nonparametrical method*, [arXiv:hep-ex/0004009 \[hep-ex\]](#).
- [657] ATLAS Collaboration, *Estimation of non-prompt and fake lepton backgrounds in final states with top quarks produced in proton-proton collisions at  $\sqrt{s} = 8$  TeV with the ATLAS detector*, ATLAS-CONF-2014-058, CERN, Geneva, Oct, 2014. <https://cds.cern.ch/record/1951336>.
- [658] H. Davoudiasl, J. L. Hewett, and T. G. Rizzo, *Bulk gauge fields in the Randall-Sundrum model*, *Phys. Lett.* **B473** (2000) 43–49, [arXiv:hep-ph/9911262 \[hep-ph\]](#).
- [659] A. Pomarol, *Gauge bosons in a five-dimensional theory with localized gravity*, *Phys. Lett.* **B486** (2000) 153–157, [arXiv:hep-ph/9911294 \[hep-ph\]](#).

- [660] S. J. Huber and Q. Shafi, *Fermion masses, mixings and proton decay in a Randall-Sundrum model*, *Phys. Lett.* **B498** (2001) 256–262, [arXiv:hep-ph/0010195](#) [hep-ph].
- [661] S. J. Huber, *Flavor violation and warped geometry*, *Nucl. Phys.* **B666** (2003) 269–288, [arXiv:hep-ph/0303183](#) [hep-ph].
- [662] H. Davoudiasl, J. L. Hewett, and T. G. Rizzo, *Experimental probes of localized gravity: On and off the wall*, *Phys. Rev.* **D63** (2001) 075004, [arXiv:hep-ph/0006041](#) [hep-ph].
- [663] K. Agashe, A. Belyaev, T. Krupovnickas, G. Perez, and J. Virzi, *LHC Signals from Warped Extra Dimensions*, *Phys. Rev.* **D77** (2008) 015003, [arXiv:hep-ph/0612015](#) [hep-ph].
- [664] A. L. Fitzpatrick, J. Kaplan, L. Randall, and L.-T. Wang, *Searching for the Kaluza-Klein Graviton in Bulk RS Models*, *JHEP* **09** (2007) 013, [arXiv:hep-ph/0701150](#).
- [665] K. Agashe, H. Davoudiasl, G. Perez, and A. Soni, *Warped Gravitons at the LHC and Beyond*, *Phys. Rev.* **D76** (2007) 036006, [arXiv:hep-ph/0701186](#) [hep-ph].
- [666] B. Lillie, J. Shu, and T. M. P. Tait, *Kaluza-Klein Gluons as a Diagnostic of Warped Models*, *Phys. Rev.* **D76** (2007) 115016, [arXiv:0706.3960](#) [hep-ph].
- [667] A. Djouadi, G. Moreau, and R. K. Singh, *Kaluza-Klein excitations of gauge bosons at the LHC*, *Nucl. Phys.* **B797** (2008) 1–26, [arXiv:0706.4191](#) [hep-ph].
- [668] K. Agashe, H. Davoudiasl, S. Gopalakrishna, T. Han, G.-Y. Huang, G. Perez, Z.-G. Si, and A. Soni, *LHC Signals for Warped Electroweak Neutral Gauge Bosons*, *Phys. Rev.* **D76** (2007) 115015, [arXiv:0709.0007](#) [hep-ph].
- [669] O. Antipin, D. Atwood, and A. Soni, *Search for RS gravitons via  $W(L)W(L)$  decays*, *Phys. Lett.* **B666** (2008) 155–161, [arXiv:0711.3175](#) [hep-ph].
- [670] K. Agashe, S. Gopalakrishna, T. Han, G.-Y. Huang, and A. Soni, *LHC Signals for Warped Electroweak Charged Gauge Bosons*, *Phys. Rev.* **D80** (2009) 075007, [arXiv:0810.1497](#) [hep-ph].
- [671] H. Davoudiasl, S. Gopalakrishna, E. Ponton, and J. Santiago, *Warped 5-Dimensional Models: Phenomenological Status and Experimental Prospects*, *New J. Phys.* **12** (2010) 075011, [arXiv:0908.1968](#) [hep-ph].
- [672] C.-Y. Chen, H. Davoudiasl, and D. Kim, *Z with missing energy as a warped graviton signal at hadron colliders*, *Phys. Rev.* **D89** (2014) no. 9, 096007, [arXiv:1403.3399](#) [hep-ph].
- [673] K. Agashe, C.-Y. Chen, H. Davoudiasl, and D. Kim, *Photon cascade decay of the warped graviton at LHC14 and a 100 TeV hadron collider*, *Phys. Rev.* **D91** (2015) no. 7, 076002, [arXiv:1412.6215](#) [hep-ph].
- [674] A. Belyaev, N. D. Christensen, and A. Pukhov, *CalcHEP 3.4 for collider physics within and beyond the Standard Model*, *Comput.Phys.Commun.* **184** (2013) 1729–1769, [arXiv:1207.6082](#) [hep-ph].
- [675] R. D. Ball et al., *Parton distributions with LHC data*, *Nucl. Phys.* **B867** (2013) 244–289, [arXiv:1207.1303](#) [hep-ph].
- [676] O. Antipin and T. Hapola, <http://cp3-origins.dk/research/units/ed-tools>.
- [677] CMS Collaboration, *V Tagging Observables and Correlations*, CMS-PAS-JME-14-002, CERN, Geneva, 2014. <https://cds.cern.ch/record/1754913>.
- [678] M. Carena, E. Ponton, J. Santiago, and C. E. M. Wagner, *Light Kaluza Klein States in Randall-Sundrum Models with Custodial  $SU(2)$* , *Nucl. Phys.* **B759** (2006) 202–227, [arXiv:hep-ph/0607106](#) [hep-ph].
- [679] M. Carena, E. Ponton, J. Santiago, and C. E. M. Wagner, *Electroweak constraints on warped models with custodial symmetry*, *Phys. Rev.* **D76** (2007) 035006, [arXiv:hep-ph/0701055](#) [hep-ph].
- [680] CMS Collaboration, S. Chatrchyan et al., *Searches for new physics using the  $t\bar{t}$  invariant mass*

- distribution in  $pp$  collisions at  $\sqrt{s}=8$  TeV, *Phys. Rev. Lett.* **111** (2013) no. 21, 211804, [arXiv:1309.2030 \[hep-ex\]](#). [Erratum: *Phys. Rev. Lett.* 112,no.11,119903(2014)].
- [681] A search for  $t\bar{t}$  resonances in the lepton plus jets final state with ATLAS using  $14\text{ fb}^{-1}$  of  $pp$  collisions at  $\sqrt{s} = 8$  TeV, ATLAS-CONF-2013-052, CERN, Geneva, May, 2013. <https://cds.cern.ch/record/1547568>. Not published in the proceedings.
- [682] P. Minkowski,  $\mu \rightarrow e\gamma$  at a Rate of One Out of  $10^9$  Muon Decays?, *Phys. Lett.* **B67** (1977) 421–428.
- [683] R. N. Mohapatra and G. Senjanovic, *Neutrino Mass and Spontaneous Parity Violation*, *Phys. Rev. Lett.* **44** (1980) 912.
- [684] T. Yanagida, *Horizontal symmetry and masses of neutrinos*, Conf. Proc. **C7902131** (1979) 95–99. [Conf. Proc.C7902131,95(1979)].
- [685] M. Gell-Mann, P. Ramond, and R. Slansky, *Complex Spinors and Unified Theories*, Conf. Proc. **C790927** (1979) 315–321, [arXiv:1306.4669 \[hep-th\]](#).
- [686] F. Vissani, *Do experiments suggest a hierarchy problem?*, *Phys. Rev.* **D57** (1998) 7027–7030, [arXiv:hep-ph/9709409 \[hep-ph\]](#).
- [687] J. D. Clarke, R. Foot, and R. R. Volkas, *Natural leptogenesis and neutrino masses with two Higgs doublets*, *Phys. Rev.* **D92** (2015) no. 3, 033006, [arXiv:1505.05744 \[hep-ph\]](#).
- [688] W.-Y. Keung and G. Senjanovic, *Majorana Neutrinos and the Production of the Right-handed Charged Gauge Boson*, *Phys. Rev. Lett.* **50** (1983) 1427.
- [689] A. Datta, M. Guchait, and A. Pilaftsis, *Probing lepton number violation via majorana neutrinos at hadron supercolliders*, *Phys. Rev.* **D50** (1994) 3195–3203, [arXiv:hep-ph/9311257 \[hep-ph\]](#).
- [690] P. S. B. Dev, A. Pilaftsis, and U.-k. Yang, *New Production Mechanism for Heavy Neutrinos at the LHC*, *Phys. Rev. Lett.* **112** (2014) no. 8, 081801, [arXiv:1308.2209 \[hep-ph\]](#).
- [691] D. Alva, T. Han, and R. Ruiz, *Heavy Majorana neutrinos from  $W\gamma$  fusion at hadron colliders*, *JHEP* **02** (2015) 072, [arXiv:1411.7305 \[hep-ph\]](#).
- [692] W. Rodejohann, *Neutrino-less Double Beta Decay and Particle Physics*, *Int. J. Mod. Phys.* **E20** (2011) 1833–1930, [arXiv:1106.1334 \[hep-ph\]](#).
- [693] A. de Gouvea and P. Vogel, *Lepton Flavor and Number Conservation, and Physics Beyond the Standard Model*, *Prog. Part. Nucl. Phys.* **71** (2013) 75–92, [arXiv:1303.4097 \[hep-ph\]](#).
- [694] P. S. Bhupal Dev, R. Franceschini, and R. N. Mohapatra, *Bounds on TeV Seesaw Models from LHC Higgs Data*, *Phys. Rev.* **D86** (2012) 093010, [arXiv:1207.2756 \[hep-ph\]](#).
- [695] C. G. Cely, A. Ibarra, E. Molinaro, and S. T. Petcov, *Higgs Decays in the Low Scale Type I See-Saw Model*, *Phys. Lett.* **B718** (2013) 957–964, [arXiv:1208.3654 \[hep-ph\]](#).
- [696] A. Maiezza, M. Nemevšek, and F. Nesti, *Lepton Number Violation in Higgs Decay at LHC*, *Phys. Rev. Lett.* **115** (2015) 081802, [arXiv:1503.06834 \[hep-ph\]](#).
- [697] R. Dermisek, E. Lunghi, and S. Shin, *Contributions of flavor violating couplings of a Higgs boson to  $pp \rightarrow WW$* , *JHEP* **08** (2015) 126, [arXiv:1503.08829 \[hep-ph\]](#).
- [698] F. F. Deppisch, P. S. Bhupal Dev, and A. Pilaftsis, *Neutrinos and Collider Physics*, *New J. Phys.* **17** (2015) no. 7, 075019, [arXiv:1502.06541 \[hep-ph\]](#).
- [699] A. Pilaftsis, *Radiatively induced neutrino masses and large Higgs neutrino couplings in the standard model with Majorana fields*, *Z. Phys.* **C55** (1992) 275–282, [arXiv:hep-ph/9901206 \[hep-ph\]](#).
- [700] W. Buchmuller, C. Greub, and P. Minkowski, *Neutrino masses, neutral vector bosons and the scale of  $B-L$  breaking*, *Phys. Lett.* **B267** (1991) 395–399.
- [701] J. Gluza, *On teraelectronvolt Majorana neutrinos*, *Acta Phys. Polon.* **B33** (2002) 1735–1746, [arXiv:hep-ph/0201002 \[hep-ph\]](#).

- [702] J. Kersten and A. Yu. Smirnov, *Right-Handed Neutrinos at CERN LHC and the Mechanism of Neutrino Mass Generation*, *Phys. Rev.* **D76** (2007) 073005, [arXiv:0705.3221 \[hep-ph\]](#).
- [703] Z.-z. Xing, *Naturalness and Testability of TeV Seesaw Mechanisms*, *Prog. Theor. Phys. Suppl.* **180** (2009) 112–127, [arXiv:0905.3903 \[hep-ph\]](#).
- [704] M. B. Gavela, T. Hambye, D. Hernandez, and P. Hernandez, *Minimal Flavour Seesaw Models*, *JHEP* **09** (2009) 038, [arXiv:0906.1461 \[hep-ph\]](#).
- [705] X.-G. He, S. Oh, J. Tandean, and C.-C. Wen, *Large Mixing of Light and Heavy Neutrinos in Seesaw Models and the LHC*, *Phys. Rev.* **D80** (2009) 073012, [arXiv:0907.1607 \[hep-ph\]](#).
- [706] R. Adhikari and A. Raychaudhuri, *Light neutrinos from massless texture and below TeV seesaw scale*, *Phys. Rev.* **D84** (2011) 033002, [arXiv:1004.5111 \[hep-ph\]](#).
- [707] A. Ibarra, E. Molinaro, and S. T. Petcov, *TeV Scale See-Saw Mechanisms of Neutrino Mass Generation, the Majorana Nature of the Heavy Singlet Neutrinos and  $(\beta\beta)_{0\nu}$ -Decay*, *JHEP* **09** (2010) 108, [arXiv:1007.2378 \[hep-ph\]](#).
- [708] M. Mitra, G. Senjanovic, and F. Vissani, *Neutrinoless Double Beta Decay and Heavy Sterile Neutrinos*, *Nucl. Phys.* **B856** (2012) 26–73, [arXiv:1108.0004 \[hep-ph\]](#).
- [709] J. Lopez-Pavon, E. Molinaro, and S. T. Petcov, *Radiative Corrections to Light Neutrino Masses in Low Scale Type I Seesaw Scenarios and Neutrinoless Double Beta Decay*, *JHEP* **11** (2015) 030, [arXiv:1506.05296 \[hep-ph\]](#).
- [710] R. N. Mohapatra, *Mechanism for Understanding Small Neutrino Mass in Superstring Theories*, *Phys. Rev. Lett.* **56** (1986) 561–563.
- [711] R. N. Mohapatra and J. W. F. Valle, *Neutrino Mass and Baryon Number Nonconservation in Superstring Models*, *Phys. Rev.* **D34** (1986) 1642.
- [712] S. Bray, J. S. Lee, and A. Pilaftsis, *Resonant CP violation due to heavy neutrinos at the LHC*, *Nucl. Phys.* **B786** (2007) 95–118, [arXiv:hep-ph/0702294 \[HEP-PH\]](#).
- [713] E. K. Akhmedov, *Do charged leptons oscillate?*, *JHEP* **09** (2007) 116, [arXiv:0706.1216 \[hep-ph\]](#).
- [714] CMS Collaboration, V. Khachatryan et al., *Search for heavy neutrinos and W bosons with right-handed couplings in proton-proton collisions at  $\sqrt{s} = 8$  TeV*, *Eur. Phys. J.* **C74** (2014) no. 11, 3149, [arXiv:1407.3683 \[hep-ex\]](#).
- [715] F. del Aguila and J. A. Aguilar-Saavedra, *Distinguishing seesaw models at LHC with multi-lepton signals*, *Nucl. Phys.* **B813** (2009) 22–90, [arXiv:0808.2468 \[hep-ph\]](#).
- [716] F. del Aguila and J. A. Aguilar-Saavedra, *Electroweak scale seesaw and heavy Dirac neutrino signals at LHC*, *Phys. Lett.* **B672** (2009) 158–165, [arXiv:0809.2096 \[hep-ph\]](#).
- [717] C.-Y. Chen and P. S. B. Dev, *Multi-Lepton Collider Signatures of Heavy Dirac and Majorana Neutrinos*, *Phys. Rev.* **D85** (2012) 093018, [arXiv:1112.6419 \[hep-ph\]](#).
- [718] A. Das and N. Okada, *Inverse seesaw neutrino signatures at the LHC and ILC*, *Phys. Rev.* **D88** (2013) 113001, [arXiv:1207.3734 \[hep-ph\]](#).
- [719] A. Das, P. S. Bhupal Dev, and N. Okada, *Direct bounds on electroweak scale pseudo-Dirac neutrinos from  $\sqrt{s} = 8$  TeV LHC data*, *Phys. Lett.* **B735** (2014) 364–370, [arXiv:1405.0177 \[hep-ph\]](#).
- [720] G. Bambhaniya, S. Goswami, S. Khan, P. Konar, and T. Mondal, *Looking for hints of a reconstructible seesaw model at the Large Hadron Collider*, *Phys. Rev.* **D91** (2015) 075007, [arXiv:1410.5687 \[hep-ph\]](#).
- [721] CMS Collaboration, V. Khachatryan et al., *Search for heavy Majorana neutrinos in  $\mu^\pm\mu^\pm + jets$  events in proton-proton collisions at  $\sqrt{s} = 8$  TeV*, *Phys. Lett.* **B748** (2015) 144–166, [arXiv:1501.05566 \[hep-ex\]](#).
- [722] ATLAS Collaboration, G. Aad et al., *Search for heavy Majorana neutrinos with the ATLAS*

- detector in  $pp$  collisions at  $\sqrt{s} = 8$  TeV, *JHEP* **07** (2015) 162, [arXiv:1506.06020 \[hep-ex\]](#).
- [723] S. Antusch and O. Fischer, *Testing sterile neutrino extensions of the Standard Model at future lepton colliders*, *JHEP* **05** (2015) 053, [arXiv:1502.05915 \[hep-ph\]](#).
- [724] S. Banerjee, P. S. B. Dev, A. Ibarra, T. Mandal, and M. Mitra, *Prospects of Heavy Neutrino Searches at Future Lepton Colliders*, *Phys. Rev.* **D92** (2015) 075002, [arXiv:1503.05491 \[hep-ph\]](#).
- [725] J. C. Pati and A. Salam, *Lepton Number as the Fourth Color*, *Phys. Rev.* **D10** (1974) 275–289. [Erratum: *Phys. Rev.* **D11**, 703(1975)].
- [726] R. N. Mohapatra and J. C. Pati, *Left-Right Gauge Symmetry and an Isoconjugate Model of CP Violation*, *Phys. Rev.* **D11** (1975) 566–571.
- [727] R. N. Mohapatra and J. C. Pati, *A Natural Left-Right Symmetry*, *Phys. Rev.* **D11** (1975) 2558.
- [728] G. Senjanovic and R. N. Mohapatra, *Exact Left-Right Symmetry and Spontaneous Violation of Parity*, *Phys. Rev.* **D12** (1975) 1502.
- [729] P. S. B. Dev, C.-H. Lee, and R. Mohapatra, *Natural TeV-Scale Left-Right Seesaw for Neutrinos and Experimental Tests*, [arXiv:1309.0774 \[hep-ph\]](#).
- [730] J.-M. Frere, T. Hambye, and G. Vertongen, *Is leptogenesis falsifiable at LHC?*, *JHEP* **01** (2009) 051, [arXiv:0806.0841 \[hep-ph\]](#).
- [731] P. S. B. Dev, C.-H. Lee, and R. N. Mohapatra, *Leptogenesis Constraints on the Mass of Right-handed Gauge Bosons*, *Phys. Rev.* **D90** (2014) no. 9, 095012, [arXiv:1408.2820 \[hep-ph\]](#).
- [732] P. S. Bhupal Dev, C.-H. Lee, and R. N. Mohapatra, *TeV Scale Lepton Number Violation and Baryogenesis*, *J. Phys. Conf. Ser.* **631** (2015) no. 1, 012007, [arXiv:1503.04970 \[hep-ph\]](#).
- [733] M. Dhuria, C. Hati, R. Rangarajan, and U. Sarkar, *Falsifying leptogenesis for a TeV scale  $W_R^\pm$  at the LHC*, *Phys. Rev.* **D92** (2015) no. 3, 031701, [arXiv:1503.07198 \[hep-ph\]](#).
- [734] A. Ferrari, J. Collot, M.-L. Andrieux, B. Belhorma, P. de Saintignon, J.-Y. Hostachy, P. Martin, and M. Wielers, *Sensitivity study for new gauge bosons and right-handed Majorana neutrinos in  $pp$  collisions at  $s = 14$ -TeV*, *Phys. Rev.* **D62** (2000) 013001.
- [735] M. Nemevsek, F. Nesti, G. Senjanovic, and Y. Zhang, *First Limits on Left-Right Symmetry Scale from LHC Data*, *Phys. Rev.* **D83** (2011) 115014, [arXiv:1103.1627 \[hep-ph\]](#).
- [736] J. Chakraborty, J. Gluza, R. Sevillano, and R. Szafron, *Left-Right Symmetry at LHC and Precise 1-Loop Low Energy Data*, *JHEP* **07** (2012) 038, [arXiv:1204.0736 \[hep-ph\]](#).
- [737] S. P. Das, F. F. Deppisch, O. Kittel, and J. W. F. Valle, *Heavy Neutrinos and Lepton Flavour Violation in Left-Right Symmetric Models at the LHC*, *Phys. Rev.* **D86** (2012) 055006, [arXiv:1206.0256 \[hep-ph\]](#).
- [738] J. A. Aguilar-Saavedra and F. R. Joaquim, *Measuring heavy neutrino couplings at the LHC*, *Phys. Rev.* **D86** (2012) 073005, [arXiv:1207.4193 \[hep-ph\]](#).
- [739] C.-Y. Chen, P. S. B. Dev, and R. N. Mohapatra, *Probing Heavy-Light Neutrino Mixing in Left-Right Seesaw Models at the LHC*, *Phys. Rev.* **D88** (2013) 033014, [arXiv:1306.2342 \[hep-ph\]](#).
- [740] J. N. Ng, A. de la Puente, and B. W.-P. Pan, *Search for Heavy Right-Handed Neutrinos at the LHC and Beyond in the Same-Sign Leptons Final State*, [arXiv:1505.01934 \[hep-ph\]](#).
- [741] P. S. B. Dev, D. Kim, and R. N. Mohapatra, *Disambiguating Seesaw Models using Invariant Mass Variables at Hadron Colliders*, [arXiv:1510.04328 \[hep-ph\]](#).
- [742] P. S. B. Dev and R. N. Mohapatra, *Probing TeV Left-Right Seesaw at Energy and Intensity Frontiers: a Snowmass White Paper*, in *Community Summer Study 2013: Snowmass on the Mississippi (CSS2013) Minneapolis, MN, USA, July 29-August 6, 2013*. 2013. [arXiv:1308.2151 \[hep-ph\]](#).

- <http://inspirehep.net/record/1247267/files/arXiv:1308.2151.pdf>.
- [743] M. Malinsky, J. C. Romao, and J. W. F. Valle, *Novel supersymmetric  $SO(10)$  seesaw mechanism*, *Phys. Rev. Lett.* **95** (2005) 161801, [arXiv:hep-ph/0506296](https://arxiv.org/abs/hep-ph/0506296) [hep-ph].
- [744] P. S. B. Dev and A. Pilaftsis, *Minimal Radiative Neutrino Mass Mechanism for Inverse Seesaw Models*, *Phys. Rev.* **D86** (2012) 113001, [arXiv:1209.4051](https://arxiv.org/abs/1209.4051) [hep-ph].
- [745] P. S. Bhupal Dev and R. N. Mohapatra, *Unified explanation of the  $eejj$ , diboson and dijet resonances at the LHC*, *Phys. Rev. Lett.* **115** (2015) no. 18, 181803, [arXiv:1508.02277](https://arxiv.org/abs/1508.02277) [hep-ph].
- [746] A. Das, N. Nagata, and N. Okada, *Testing the 2-TeV Resonance with Trileptons*, *JHEP* **03** (2016) 049, [arXiv:1601.05079](https://arxiv.org/abs/1601.05079) [hep-ph].
- [747] J. Gluza and T. Jeliński, *Heavy neutrinos and the  $pp \rightarrow lljj$  CMS data*, *Phys. Lett.* **B748** (2015) 125–131, [arXiv:1504.05568](https://arxiv.org/abs/1504.05568) [hep-ph].
- [748] F. F. Deppisch, L. Graf, S. Kulkarni, S. Patra, W. Rodejohann, N. Sahu, and U. Sarkar, *Reconciling the 2 TeV Excesses at the LHC in a Linear Seesaw Left-Right Model*, [arXiv:1508.05940](https://arxiv.org/abs/1508.05940) [hep-ph].
- [749] F. del Aguila, J. A. Aguilar-Saavedra, and R. Pittau, *Heavy neutrino signals at large hadron colliders*, *JHEP* **10** (2007) 047, [arXiv:hep-ph/0703261](https://arxiv.org/abs/hep-ph/0703261) [hep-ph].
- [750] A. Maiezza, M. Nemevsek, F. Nesti, and G. Senjanovic, *Left-Right Symmetry at LHC*, *Phys.Rev.* **D82** (2010) 055022, [arXiv:1005.5160](https://arxiv.org/abs/1005.5160) [hep-ph].
- [751] J. C. Vasquez, *Right-handed lepton mixings at the LHC*, [arXiv:1411.5824](https://arxiv.org/abs/1411.5824) [hep-ph].
- [752] F. F. Deppisch, T. E. Gonzalo, S. Patra, N. Sahu, and U. Sarkar, *Signal of Right-Handed Charged Gauge Bosons at the LHC?*, *Phys. Rev.* **D90** (2014) no. 5, 053014, [arXiv:1407.5384](https://arxiv.org/abs/1407.5384) [hep-ph].
- [753] M. Heikinheimo, M. Raidal, and C. Spethmann, *Testing Right-Handed Currents at the LHC*, *Eur. Phys. J.* **C74** (2014) no. 10, 3107, [arXiv:1407.6908](https://arxiv.org/abs/1407.6908) [hep-ph].
- [754] F. F. Deppisch, T. E. Gonzalo, S. Patra, N. Sahu, and U. Sarkar, *Double beta decay, lepton flavor violation, and collider signatures of left-right symmetric models with spontaneous  $D$ -parity breaking*, *Phys. Rev.* **D91** (2015) no. 1, 015018, [arXiv:1410.6427](https://arxiv.org/abs/1410.6427) [hep-ph].
- [755] J. A. Aguilar-Saavedra and F. R. Joaquim, *Closer look at the possible CMS signal of a new gauge boson*, *Phys. Rev.* **D90** (2014) no. 11, 115010, [arXiv:1408.2456](https://arxiv.org/abs/1408.2456) [hep-ph].
- [756] B. A. Dobrescu and Z. Liu, *A  $W'$  Boson near 2 TeV: Predictions for Run 2 of the LHC*, [arXiv:1506.06736](https://arxiv.org/abs/1506.06736) [hep-ph].
- [757] P. Coloma, B. A. Dobrescu, and J. Lopez-Pavon, *Right-handed neutrinos and the 2 TeV  $W'$  boson*, [arXiv:1508.04129](https://arxiv.org/abs/1508.04129) [hep-ph].
- [758] T. Bandyopadhyay, B. Brahmachari, and A. Raychaudhuri, *Implications of the CMS search for  $W_R$  on Grand Unification*, [arXiv:1509.03232](https://arxiv.org/abs/1509.03232) [hep-ph].
- [759] G. Senjanović and V. Tello, *Right Handed Quark Mixing in Left-Right Symmetric Theory*, *Phys. Rev. Lett.* **114** (2015) no. 7, 071801, [arXiv:1408.3835](https://arxiv.org/abs/1408.3835) [hep-ph].
- [760] G. Senjanović and V. Tello, *Restoration of Parity and the Right-Handed Analog of the CKM Matrix*, [arXiv:1502.05704](https://arxiv.org/abs/1502.05704) [hep-ph].
- [761] J. Gluza, T. Jeliński, and R. Szafron, *Lepton Number Violation and ‘Diracness’ of massive neutrinos composed of Majorana states*, 2016. [arXiv:1604.01388](https://arxiv.org/abs/1604.01388) [hep-ph].
- [762] J. M. Campbell, J. W. Huston, and W. J. Stirling, *Hard Interactions of Quarks and Gluons: A Primer for LHC Physics*, *Rept. Prog. Phys.* **70** (2007) 89, [arXiv:hep-ph/0611148](https://arxiv.org/abs/hep-ph/0611148) [hep-ph].
- [763] T. Han, I. Lewis, R. Ruiz, and Z.-g. Si, *Lepton Number Violation and  $W'$  Chiral Couplings at the LHC*, *Phys. Rev.* **D87** (2013) no. 3, 035011, [arXiv:1211.6447](https://arxiv.org/abs/1211.6447) [hep-ph]. [Erratum: *Phys. Rev.* **D87**, no. 3, 039906(2013)].

- [764] R. E. Ruiz, *Hadron Collider Tests of Neutrino Mass-Generating Mechanisms*. PhD thesis, Pittsburgh U., 2015. [arXiv:1509.06375](https://arxiv.org/abs/1509.06375) [hep-ph].  
<http://inspirehep.net/record/1394386/files/arXiv:1509.06375.pdf>.
- [765] C. Degrande, O. Mattelaer, R. Ruiz, and J. Turner, *Fully-Automated Precision Predictions for Heavy Neutrino Production Mechanisms at Hadron Colliders*, [arXiv:1602.06957](https://arxiv.org/abs/1602.06957) [hep-ph].
- [766] A. Das, P. Konar, and S. Majhi, *Production of Heavy neutrino in next-to-leading order QCD at the LHC and beyond*, *JHEP* **06** (2016) 019, [arXiv:1604.00608](https://arxiv.org/abs/1604.00608) [hep-ph].
- [767] R. Ruiz, *QCD Corrections to Pair Production of Type III Seesaw Leptons at Hadron Colliders*, *JHEP* **12** (2015) 165, [arXiv:1509.05416](https://arxiv.org/abs/1509.05416) [hep-ph].
- [768] N. Arkani-Hamed, T. Han, M. Mangano, and L.-T. Wang, *Physics Opportunities of a 100 TeV Proton-Proton Collider*, [arXiv:1511.06495](https://arxiv.org/abs/1511.06495) [hep-ph].
- [769] E. Arganda, M. J. Herrero, X. Marcano, and C. Weiland, *Exotic  $\tilde{\chi}^0 \tilde{\chi}^0 \tilde{\chi}^0$  events from heavy ISS neutrinos at the LHC*, *Phys. Lett.* **B752** (2016) 46–50, [arXiv:1508.05074](https://arxiv.org/abs/1508.05074) [hep-ph].
- [770] BaBar Collaboration, B. Aubert et al., *Searches for Lepton Flavor Violation in the Decays  $\tau^\pm \rightarrow e^\pm \gamma$  and  $\tau^\pm \rightarrow \mu^\pm \gamma$* , *Phys.Rev.Lett.* **104** (2010) 021802, [arXiv:0908.2381](https://arxiv.org/abs/0908.2381) [hep-ex].
- [771] MEG Collaboration, J. Adam et al., *New constraint on the existence of the  $\mu^+ \rightarrow e^+ \gamma$  decay*, *Phys.Rev.Lett.* **110** (2013) 201801, [arXiv:1303.0754](https://arxiv.org/abs/1303.0754) [hep-ex].
- [772] MEG Collaboration, A. M. Baldini et al., *Search for the lepton flavour violating decay  $\mu^+ \rightarrow e^+ \gamma$  with the full dataset of the MEG experiment*, *Eur. Phys. J.* **C76** (2016) no. 8, 434, [arXiv:1605.05081](https://arxiv.org/abs/1605.05081) [hep-ex].
- [773] E. Arganda, M. J. Herrero, X. Marcano, and C. Weiland, *Imprints of massive inverse seesaw model neutrinos in lepton flavor violating Higgs boson decays*, *Phys. Rev.* **D91** (2015) no. 1, 015001, [arXiv:1405.4300](https://arxiv.org/abs/1405.4300) [hep-ph].
- [774] O. Matsedonskyi, G. Panico, and A. Wulzer, *On the Interpretation of Top Partners Searches*, *JHEP* **12** (2014) 097, [arXiv:1409.0100](https://arxiv.org/abs/1409.0100) [hep-ph].
- [775] A. Andreazza et al., *What Next: White Paper of the INFN-CSNI*, *Frascati Phys. Ser.* **60** (2015) 1–302.
- [776] H.-C. Cheng, S. Jung, E. Salvioni, and Y. Tsai, *Exotic Quarks in Twin Higgs Models*, [arXiv:1512.02647](https://arxiv.org/abs/1512.02647) [hep-ph].
- [777] Z. Chacko, H.-S. Goh, and R. Harnik, *The Twin Higgs: Natural electroweak breaking from mirror symmetry*, *Phys.Rev.Lett.* **96** (2006) 231802, [arXiv:hep-ph/0506256](https://arxiv.org/abs/hep-ph/0506256) [hep-ph].
- [778] ATLAS Collaboration, G. Aad et al., *Search for long-lived, weakly interacting particles that decay to displaced hadronic jets in proton-proton collisions at  $\sqrt{s} = 8$  TeV with the ATLAS detector*, [arXiv:1504.03634](https://arxiv.org/abs/1504.03634) [hep-ex].
- [779] ATLAS Collaboration, G. Aad et al., *Search for pair-produced long-lived neutral particles decaying in the ATLAS hadronic calorimeter in  $pp$  collisions at  $\sqrt{s} = 8$  TeV*, *Phys.Lett.* **B743** (2015) 15–34, [arXiv:1501.04020](https://arxiv.org/abs/1501.04020) [hep-ex].
- [780] Y. Gershtein, M. Luty, M. Narain, L. T. Wang, D. Whiteson, et al., *New Particles Working Group Report of the Snowmass 2013 Community Summer Study*, [arXiv:1311.0299](https://arxiv.org/abs/1311.0299) [hep-ex].
- [781] D. Curtin and P. Saraswat, *Towards a No-Lose Theorem for Naturalness*, [arXiv:1509.04284](https://arxiv.org/abs/1509.04284) [hep-ph].
- [782] G. Burdman, Z. Chacko, H.-S. Goh, and R. Harnik, *Folded supersymmetry and the LEP paradox*, *JHEP* **0702** (2007) 009, [arXiv:hep-ph/0609152](https://arxiv.org/abs/hep-ph/0609152) [hep-ph].
- [783] H. Cai, H.-C. Cheng, and J. Terning, *A Quirky Little Higgs Model*, *JHEP* **0905** (2009) 045, [arXiv:0812.0843](https://arxiv.org/abs/0812.0843) [hep-ph].
- [784] N. Craig and A. Katz, *The Fraternal WIMP Miracle*, [arXiv:1505.07113](https://arxiv.org/abs/1505.07113) [hep-ph].

- [785] Z. Chacko, D. Curtin, and C. B. Verhaaren, *A Quirky Probe of Neutral Naturalness*, [arXiv:1512.05782 \[hep-ph\]](#).
- [786] G. Burdman and R. T. D’Agnolo, *Scalar Leptons in Folded Supersymmetry*, [arXiv:1512.00040 \[hep-ph\]](#).
- [787] D. Curtin, P. Meade, and C.-T. Yu, *Testing Electroweak Baryogenesis with Future Colliders*, *JHEP* **1411** (2014) 127, [arXiv:1409.0005 \[hep-ph\]](#).
- [788] H.-J. He, J. Ren, and W. Yao, *Probing New Physics of Cubic Higgs Interaction via Higgs Pair Production at Hadron Colliders*, [arXiv:1506.03302 \[hep-ph\]](#).
- [789] P. Batra and Z. Chacko, *A Composite Twin Higgs Model*, *Phys.Rev.* **D79** (2009) 095012, [arXiv:0811.0394 \[hep-ph\]](#).
- [790] R. Barbieri, D. Greco, R. Rattazzi, and A. Wulzer, *The Composite Twin Higgs scenario*, [arXiv:1501.07803 \[hep-ph\]](#).
- [791] M. Low, A. Tesi, and L.-T. Wang, *Twin Higgs mechanism and a composite Higgs boson*, *Phys.Rev.* **D91** (2015) no. 9, 095012, [arXiv:1501.07890 \[hep-ph\]](#).
- [792] M. Geller and O. Telem, *A Holographic Twin Higgs Model*, *Phys.Rev.Lett.* **114** (2015) no. 19, 191801, [arXiv:1411.2974 \[hep-ph\]](#).
- [793] N. Craig and K. Howe, *Doubling down on naturalness with a supersymmetric twin Higgs*, *JHEP* **1403** (2014) 140, [arXiv:1312.1341 \[hep-ph\]](#).
- [794] N. Craig and H. K. Lou, *Scherk-Schwarz Supersymmetry Breaking in 4D*, *JHEP* **1412** (2014) 184, [arXiv:1406.4880 \[hep-ph\]](#).
- [795] S. Chang, L. J. Hall, and N. Weiner, *A Supersymmetric twin Higgs*, *Phys. Rev.* **D75** (2007) 035009, [arXiv:hep-ph/0604076 \[hep-ph\]](#).
- [796] K. R. Dienes, *Solving the hierarchy problem without supersymmetry or extra dimensions: An Alternative approach*, *Nucl. Phys.* **B611** (2001) 146–178, [arXiv:hep-ph/0104274 \[hep-ph\]](#).
- [797] X. Dong, D. Z. Freedman, and Y. Zhao, *AdS/CFT and the Little Hierarchy Problem*, [arXiv:1510.01741 \[hep-th\]](#).
- [798] U. Baur, A. Juste, L. H. Orr, and D. Rainwater, *Probing electroweak top quark couplings at hadron colliders*, *Phys. Rev.* **D71** (2005) 054013, [arXiv:hep-ph/0412021 \[hep-ph\]](#).
- [799] R. Röntsch and M. Schulze, *Constraining couplings of top quarks to the Z boson in  $t\bar{t} + Z$  production at the LHC*, *JHEP* **07** (2014) 091, [arXiv:1404.1005 \[hep-ph\]](#). [Erratum: *JHEP*09,132(2015)].
- [800] J. A. Dror, M. Farina, E. Salvioni, and J. Serra, *Strong  $tW$  Scattering at the LHC*, *JHEP* **01** (2016) 071, [arXiv:1511.03674 \[hep-ph\]](#).
- [801] B. Bellazzini, C. Csaki, J. Hubisz, J. Serra, and J. Terning, *Composite Higgs Sketch*, *JHEP* **11** (2012) 003, 1205.4032. [*Inspire*].
- [802] A. Pomarol and J. Serra, *Top Quark Compositeness: Feasibility and Implications*, *Phys. Rev.* **D78** (2008) 074026, [arXiv:0806.3247 \[hep-ph\]](#).
- [803] D. E. Kaplan and M. D. Schwartz, *Constraining Light Colored Particles with Event Shapes*, *Phys. Rev. Lett.* **101** (2008) 022002, [arXiv:0804.2477 \[hep-ph\]](#).
- [804] D. Beccioli, M. Gillioz, M. Nardecchia, F. Sannino, and M. Spannowsky, *Constraining new colored matter from the ratio of 3 to 2 jets cross sections at the LHC*, *Phys. Rev.* **D91** (2015) no. 1, 015010, [arXiv:1403.7411 \[hep-ph\]](#). [Addendum: *Phys. Rev.*D92,no.7,079905(2015)].
- [805] J. Alwall, M.-P. Le, M. Lisanti, and J. G. Wacker, *Searching for Directly Decaying Gluinos at the Tevatron*, *Phys. Lett.* **B666** (2008) 34–37, [arXiv:0803.0019 \[hep-ph\]](#).
- [806] D. Rainwater and T. M. P. Tait, *Testing Grand Unification at the (S)LHC*, *Phys. Rev.* **D75** (2007) 115014, [arXiv:hep-ph/0701093 \[hep-ph\]](#).
- [807] S. Catani and M. Grazzini, *An NNLO subtraction formalism in hadron collisions and its*

- application to Higgs boson production at the LHC*, *Phys. Rev. Lett.* **98** (2007) 222002, [arXiv:hep-ph/0703012](#) [hep-ph].
- [808] S. Catani, L. Cieri, G. Ferrera, D. de Florian, and M. Grazzini, *Vector boson production at hadron colliders: a fully exclusive QCD calculation at NNLO*, *Phys. Rev. Lett.* **103** (2009) 082001, [arXiv:0903.2120](#) [hep-ph].
- [809] K. Melnikov and F. Petriello, *Electroweak gauge boson production at hadron colliders through  $O(\alpha(s)^2)$* , *Phys. Rev.* **D74** (2006) 114017, [arXiv:hep-ph/0609070](#) [hep-ph].
- [810] R. Gavin, Y. Li, F. Petriello, and S. Quackenbush, *FEWZ 2.0: A code for hadronic Z production at next-to-next-to-leading order*, *Comput. Phys. Commun.* **182** (2011) 2388–2403, [arXiv:1011.3540](#) [hep-ph].
- [811] R. Gavin, Y. Li, F. Petriello, and S. Quackenbush, *W Physics at the LHC with FEWZ 2.1*, *Comput. Phys. Commun.* **184** (2013) 208–214, [arXiv:1201.5896](#) [hep-ph].
- [812] Y. Li and F. Petriello, *Combining QCD and electroweak corrections to dilepton production in FEWZ*, *Phys. Rev.* **D86** (2012) 094034, [arXiv:1208.5967](#) [hep-ph].
- [813] ATLAS Collaboration, G. Aad et al., *Measurement of the high-mass Drell–Yan differential cross-section in pp collisions at  $\sqrt{s}=7$  TeV with the ATLAS detector*, *Phys. Lett.* **B725** (2013) 223–242, [arXiv:1305.4192](#) [hep-ex].
- [814] CMS Collaboration, S. Chatrchyan et al., *Measurement of the differential and double-differential Drell–Yan cross sections in proton-proton collisions at  $\sqrt{s} = 7$  TeV*, *JHEP* **12** (2013) 030, [arXiv:1310.7291](#) [hep-ex].
- [815] CMS Collaboration, V. Khachatryan et al., *Measurements of differential and double-differential Drell–Yan cross sections in proton-proton collisions at 8 TeV*, *Eur. Phys. J.* **C75** (2015) no. 4, 147, [arXiv:1412.1115](#) [hep-ex].

## Chapter 4: Heavy Ions at the Future Circular Collider

*A. Dainese*<sup>1</sup>, *U.A. Wiedemann*<sup>2</sup> (editors), *N. Armesto*<sup>3</sup>, *D. d'Enterria*<sup>2</sup>, *J.M. Jowett*<sup>2</sup>, *J.-P. Lansberg*<sup>4</sup>, *J.G. Milhano*<sup>5,2</sup>, *C.A. Salgado*<sup>3</sup>, *M. Schaumann*<sup>2</sup>, *M. van Leeuwen*<sup>6,7</sup> (section editors), *J.L. Albacete*<sup>8</sup>, *A. Andronic*<sup>9</sup>, *P. Antonioli*<sup>10</sup>, *L. Apolinário*<sup>5</sup>, *S. Bass*<sup>11</sup>, *A. Beraudo*<sup>12</sup>, *A. Bilandzic*<sup>13</sup>, *S. Borsanyi*<sup>14</sup>, *P. Braun-Munzinger*<sup>9</sup>, *Z. Chen*<sup>15</sup>, *L. Cunqueiro Mendez*<sup>16</sup>, *G.S. Denicol*<sup>17</sup>, *K.J. Eskola*<sup>18</sup>, *S. Floerchinger*<sup>19</sup>, *H. Fujii*<sup>20</sup>, *P. Giubellino*<sup>12</sup>, *C. Greiner*<sup>21</sup>, *J.F. Grosse-Oetringhaus*<sup>2</sup>, *C.-M. Ko*<sup>22</sup>, *P. Kotko*<sup>23</sup>, *K. Krajczár*<sup>2,24</sup>, *K. Kutak*<sup>25</sup>, *M. Laine*<sup>26</sup>, *Y. Liu*<sup>27</sup>, *M.P. Lombardo*<sup>28</sup>, *M. Luzum*<sup>29,3</sup>, *C. Marquet*<sup>30</sup>, *S. Masciocchi*<sup>9</sup>, *V. Okorokov*<sup>31</sup>, *J.-F. Paquet*<sup>32,33</sup>, *H. Paukkunen*<sup>3,18,34</sup>, *E. Petreska*<sup>30,3</sup>, *T. Pierog*<sup>35</sup>, *M. Ploskon*<sup>36</sup>, *C. Ratti*<sup>37</sup>, *A.H. Rezaeian*<sup>38</sup>, *W. Riegler*<sup>2</sup>, *J. Rojo*<sup>39</sup>, *C. Roland*<sup>24</sup>, *A. Rossi*<sup>40,1</sup>, *G.P. Salam*<sup>2</sup>, *S. Sapeta*<sup>25,2</sup>, *R. Schicker*<sup>19</sup>, *C. Schmidt*<sup>41</sup>, *J. Stachel*<sup>19</sup>, *J. Uphoff*<sup>21</sup>, *A. van Hameren*<sup>25</sup>, *K. Watanabe*<sup>42</sup>, *B.-W. Xiao*<sup>42</sup>, *F. Yuan*<sup>36</sup>, *D. Zaslavsky*<sup>42</sup>, *K. Zhou*<sup>21,15</sup>, *P. Zhuang*<sup>15</sup>

<sup>1</sup> INFN - Sezione di Padova, Italy

<sup>2</sup> CERN, Geneva, Switzerland

<sup>3</sup> Instituto Galego de Física de Altas Enerxías, Universidade de Santiago de Compostela, Galicia-Spain

<sup>4</sup> IPNO, Univ. Paris-Sud, CNRS/IN2P3, Université Paris-Saclay, Orsay, France

<sup>5</sup> CENTRA, Instituto Superior Técnico, Universidade de Lisboa, Portugal

<sup>6</sup> Utrecht University, Netherlands

<sup>7</sup> NIKHEF, Netherlands

<sup>8</sup> Granada University, Spain

<sup>9</sup> GSI, Darmstadt, Germany

<sup>10</sup> INFN - Sezione di Bologna, Italy

<sup>11</sup> Duke University, Durham, USA

<sup>12</sup> INFN - Sezione di Torino, Italy

<sup>13</sup> Niels Bohr Institute, University of Copenhagen, Denmark

<sup>14</sup> Wuppertal University, Germany

<sup>15</sup> Tsinghua University, Beijing, China

<sup>16</sup> Munster University, Germany

<sup>17</sup> Brookhaven National Lab, Upton, USA

<sup>18</sup> University of Jyväskylä, Finland

<sup>19</sup> University of Heidelberg, Germany

<sup>20</sup> Tokyo University, Japan

<sup>21</sup> Frankfurt University, Germany

<sup>22</sup> Texas A&M University, College Station, USA

<sup>23</sup> Pennsylvania State University, University Park, USA

<sup>24</sup> Massachusetts Institute of Technology, Cambridge, USA

<sup>25</sup> Institute of Nuclear Physics PAN, Krakow, Poland

<sup>26</sup> AEC, ITP, University of Bern, Switzerland

<sup>27</sup> Tianjin University, China

<sup>28</sup> INFN - Laboratori Nazionali di Frascati, Italy

<sup>29</sup> Universidade de Sao Paulo, Brasil

<sup>30</sup> Ecole Polytechnique, CNRS, Université Paris-Saclay, Palaiseau, France

- <sup>31</sup> National Research Nuclear University MEPhI, Moscow, Russia
- <sup>32</sup> McGill University, Montréal, Canada
- <sup>33</sup> Stony Brook University, Stony Brook, USA
- <sup>34</sup> Helsinki Institute of Physics, University of Helsinki, Finland
- <sup>35</sup> KIT, IKP, Karlsruhe, Germany
- <sup>36</sup> Lawrence Berkeley National Lab, Berkeley, USA
- <sup>37</sup> University of Houston, USA
- <sup>38</sup> Universidad Tecnica Federico Santa Maria, Valparaiso, Chile
- <sup>39</sup> University of Oxford, UK
- <sup>40</sup> University of Padova, Italy
- <sup>41</sup> Bielefeld University, Germany
- <sup>42</sup> Central China Normal University, Wuhan, China

**Abstract**

The Future Circular Collider (FCC) Study is aimed at assessing the physics potential and the technical feasibility of a new collider with centre-of-mass energies, in the hadron–hadron collision mode, seven times larger than the nominal LHC energies. Operating such machine with heavy ions is an option that is being considered in the accelerator design studies. It would provide, for example, Pb–Pb and p–Pb collisions at  $\sqrt{s_{NN}} = 39$  and 63 TeV, respectively, per nucleon–nucleon collision, with integrated luminosities above  $30 \text{ nb}^{-1}$  per month for Pb–Pb. This is a report by the working group on heavy-ion physics of the FCC Study. First ideas on the physics opportunities with heavy ions at the FCC are presented, covering the physics of the Quark–Gluon Plasma, of gluon saturation, of photon-induced collisions, as well as connections with other fields of high-energy physics.

## 1 Executive summary

A five-year international design study called Future Circular Collider (FCC) has been launched by CERN in February 2014 [1, 2]. The main goal is to assess the feasibility and physics potential of a hadron collider with a centre-of-mass energy  $\sqrt{s}$  of 100 TeV for pp collisions in a new 80–100 km tunnel near Geneva. The starting date is targeted for 2035–40. Operating such machine with heavy ions is part of the accelerator design studies.

For a centre-of-mass energy  $\sqrt{s} = 100$  TeV for pp collisions, the relation  $\sqrt{s_{\text{NN}}} = \sqrt{s} \sqrt{Z_1 Z_2 / A_1 A_2}$  gives the energy per nucleon–nucleon collision of  $\sqrt{s_{\text{NN}}} = 39$  TeV for Pb–Pb ( $Z = 82$ ,  $A = 208$ ) and 63 TeV for p–Pb collisions. The present estimate of the integrated luminosity for Pb–Pb collisions results in about  $33 \text{ nb}^{-1}$  per month of running, which is more than an order of magnitude larger than the current projection for the future LHC runs [3, 4].

The increase in the centre-of-mass energy and integrated luminosity with respect to the LHC opens new opportunities for physics with heavy ions. This report summarises the projected machine performance and the physics opportunities for a nuclear beam programme at the FCC. We point out the existence of an ongoing design study by the Chinese community for a machine similar to the FCC but with smaller circumference and centre-of-mass energy [5]. The hadronic machine is called SppC and the centre-of-mass energy for Pb–Pb collisions would be  $\sqrt{s_{\text{NN}}} \sim 20\text{--}30$  TeV. A report on heavy-ion studies at SppC was recently published and includes several projections and ideas on high-energy nuclear physics in the multi-TeV domain [6].

At the time of writing this report, the physics community still looks ahead to more than one decade of experimentation with nuclear beams at the LHC. Our understanding of most of the measurements discussed in this report is likely to evolve significantly in the coming years in the light of future LHC data and further advances in theory. In this sense, many of the basic motivations for a heavy-ion programme at the FCC are the basic motivations for continuing the heavy-ion programme at the LHC or they arise naturally from it.

There is by now ample historical evidence that an order of magnitude increase in energy or luminosity of heavy-ion collisions advances significantly our understanding of the nature of the hot and dense QCD matter produced in these collisions, denoted Quark–Gluon Plasma (QGP), and that it can lead to unexpected discoveries. While unexpected discoveries, by their very nature, cannot be anticipated in a working group report (despite being one major motivation for exploring a previously-uncharted energy range with nuclear beams), we focus here mainly on those fundamental questions about the nature of QCD matter at high temperature and density for which we expect qualitative advances from the FCC. Our study is not exhaustive, but it aims at supporting with a selected set of arguments and proposed measurements the following main motivations for a heavy-ion programme at the FCC:

### 1. FCC provides novel access to QCD thermodynamics and QCD equilibration processes

Substantially increasing the centre-of-mass energy leads to the creation of initially denser and hotter systems that expand for a longer duration and over a larger volume, thereby developing stronger collective phenomena. Beyond expected quantitative gains, this may bring novel qualitative phenomena into experimental reach. For instance, FCC energies target an interesting transition region in energy density above which charm quarks start counting towards the thermal degrees of freedom, thus playing a novel role in QCD equilibration processes. Also, the  $\sqrt{s}$ -dependent increase in event multiplicity combined with sufficient integrated luminosity will allow for the systematic study of flow-like features in smaller collision systems (including pp and pA collisions), and it will facilitate the characterisation of important signatures of collectivity on the level of single events rather than event samples only. This opens novel opportunities for understanding the equilibration processes that lead to hydrodynamization and thermalization in the non-abelian quantum field theory QCD. These opportunities are discussed in Section 3.

## 2. FCC allows for an unprecedented characterisation of dense QCD matter with hard processes

In heavy-ion collisions, hadronic high-transverse-momentum ( $p_T$ ) processes are known to show strong medium-induced modifications, often referred to as jet quenching, up to the highest transverse momenta  $O(100 \text{ GeV})$  explored at the LHC so far. These jet quenching measurements characterize transport properties of the dense QCD matter through which the hard partons propagate and they allow one to follow experimentally how a probe that is initially far out-of-equilibrium evolves towards equilibrium. As detailed in Section 4, the increase in energy and integrated luminosity at FCC will provide much larger abundance of hard processes than at LHC, as well as the access to qualitatively-novel hard probes that are measurable at FCC only. A remarkable example is represented by high-momentum (thus, high boost)  $t \rightarrow W \rightarrow q\bar{q}$  decay chains that are promising probes of the time evolution of the QGP density and of the role of colour coherence. A possible sizeable secondary production of charm quarks in scatterings between quark and gluon constituents of the hot QCD medium could represent a novel observable sensitive to the medium temperature evolution. Also the yields and kinematic distributions of heavy quarkonium bound states carry information about properties of the produced QCD matter, since quarkonia states are expected to dissociate above critical energy densities (that depend on the binding energy of the state), and since they are expected to form in secondary processes (depending on the density of heavy quarks in the system).

## 3. FCC explores saturated parton densities in a previously-uncharted, ultra-dense kinematic domain

In the incoming nuclear wave-functions, parton densities increase strongly with decreasing momentum fraction  $x$ . At any given  $\sqrt{s}$ , the nuclear parton densities are larger than those in the proton due to geometric enhancement. On general grounds, this growth at small- $x$  is expected to saturate once parton densities reach non-perturbative values of parametric order  $\sim 1/\alpha_s$ . In the context of heavy-ion collisions, the study of saturated QCD is of fundamental interest mainly because it fixes the initial conditions for the collective dynamics. For instance, the accuracy with which properties of dense QCD matter can be constrained in a heavy-ion programme is expected to depend ultimately on the accuracy with which one characterises the incoming nuclear wave functions at small  $x$ . More generally, saturated QCD is of fundamental interest as it is a qualitatively-novel kinematic regime where QCD scale dependence is governed by non-linear evolution equations and where bulk properties of QCD may become amenable to perturbative calculations. As discussed in Section 5, the higher centre-of-mass energy of FCC allows one to explore a wide previously-uncharted kinematic range in  $\log Q^2$  and  $\log 1/x$  within which saturation physics is expected to manifest itself. A proton–nucleus collision programme at the FCC is needed to explore this opportunity fully. Such programme would be complementary to that of an electron–hadron collider. Among the most promising observables, we quote here photon production and photon–hadron correlations at forward rapidity, which are sensitive to the small- $x$  and small- $Q^2$  region where saturation is expected to set in, heavy quarkonium production in photon–nucleus collisions (so called ultra-peripheral heavy-ion collisions), as well as very heavy objects like  $W$ ,  $Z$  and top, which can provide strong constraints on the modification of the parton density functions in nuclei at small  $x$  and large  $Q^2$ .

So far, the heavy-ion working group did not study detailed detector requirements for an experimental programme with nuclear beams at the FCC-hh. From an experimental viewpoint, it remains in particular to be investigated to what extent the physics opportunities of a heavy-ion programme at the FCC can be exploited with a general purpose detector for pp collisions. Without addressing this question in detail, the physics opportunities discussed in the present report allow one to identify some general prerequisites for the detector design:

1. To fully exploit the opportunities for physics with soft probes, one requires a detector with excellent charged-hadron identification to measure low- $p_T$  pions, kaons, protons and light nuclei,

their abundance, spectra, flow and correlations, as well as low- $p_T$  charm and beauty mesons and baryons. Such identification capability could be provided by measurements of specific energy deposition in silicon trackers, time-of-flight, Cherenkov radiation, or a combination of these.

2. Track reconstruction capability down to low  $p_T$ , ideally starting from few hundred MeV/ $c$ , is mandatory for all the aforementioned measurements. This capability requires to minimize the material thickness of the inner tracker and is may be limited by the large values of magnetic field (4–8 T) that are considered for pp-dedicated detectors at the FCC-hh. Therefore, it would be interesting to assess the feasibility of a general-purpose detector that can be operated also with reduced magnetic field of  $\approx 1$  T.
3. To fully exploit the opportunities for physics with hard probes, the basic requirements should match those for the pp programme at the FCC, that is hadronic and electromagnetic large-acceptance calorimeters with excellent energy resolution at high- $p_T$ , and excellent detection capabilities for the leptonic decay products of hard processes. These detector specifications need to persist for the higher event multiplicities of heavy-ion collisions.
4. To fully exploit the opportunities for saturation physics, one requires a detector with excellent forward coverage for charged particles, photons and jets, ideally up to  $\eta \approx 6$ .

In addition to the three key motivations for a heavy-ion beam programme at the FCC listed above, the present document will summarise further opportunities. It is structured as follows. The FCC-hh machine parameters and projected performance for heavy-ion running are presented in Section 2. The opportunities for studying hot and dense QCD matter with soft and hard observables are discussed in Sections 3 and 4, respectively. In Section 5, the potential for studying gluon saturation and nuclear-modified PDFs is presented including observables in hadronic proton–nucleus and nucleus–nucleus collisions and in photon-induced ultra-peripheral collisions. In a final Section 6, we turn then to contributions to other sectors of high-energy physics, such as searches for new particles in photon–photon scattering processes induced with very large rate by the strong electro-magnetic fields of incident Pb nuclei, and the physics with fixed-target collisions using FCC proton or heavy-ion beams.

## 2 Heavy-ion performance of FCC-hh <sup>1</sup>

At an early stage in the study of the future hadron collider, FCC-hh, a fairly complete study of its potential as a heavy-ion collider was published [7]; we take this as a reference for the following. Collisions of lead nuclei with each other (Pb–Pb) and with protons (p–Pb) were considered, as at the LHC. The performance projections were based on a very conservative injection scenario, in which the LHC was used as the final injector synchrotron and the parameters of the injected beam in an LHC cycle were based on those obtained in the 2013 p–Pb run of the LHC. This could be comfortably realised by simply maintaining the present source and injector chain of the LHC at the performance levels of LHC Run-1. With these parameters, and the assumption of a single heavy-ion experiment, Ref. [7] showed that the optimum operating cycle for the FCC-hh was to inject one LHC fill (filling only a fraction of the FCC-hh ring) and immediately ramp and collide. The time required to efficiently exhaust the beams in collisions corresponded closely to the time required to refill and ramp the LHC again for the next fill, so that the optimum injection scheme was to fill just a quarter of the ring with a single bunch train from the LHC.

In Ref. [7], it was also shown that the FCC-hh will enter a new, highly-efficient operating regime, in which a large fraction of the injected intensity can be converted to useful integrated luminosity. Thanks to strong synchrotron radiation damping, the beam emittances shrink rapidly and compensate the rapid decay of initial luminosity seen at lower-energy colliders. The luminosity may even increase during a fill until the beams are exhausted. Not only is this natural beam cooling twice as fast for heavy ions as for protons, it can also be more fully exploited since the lower overall bunch charges do not lead, for example, to high beam–beam tune-shifts.

In fact, the first heavy-ion run of LHC Run-2, in 2015, has shown that the present LHC and injector complex is already capable of higher performance, giving approximately a factor of 2.4 in luminosity beyond what is assumed in Ref. [7]. Further gains are expected after the LHC Long Shutdown 2 (from 2021). Since the publication of Ref. [7], the design work on FCC-hh has mainly focussed on its performance as a proton–proton collider. However, some important developments carry over into increased expectations for heavy-ion performance. In particular, measures envisaged to shorten the LHC cycle [8] mean that the optimum scheme is to fill the entire FCC ring using up to 4 LHC injection cycles, boosting the peak and integrated luminosities by a further factor approaching 4. The effect of this is shown in Fig. 1, which shows the luminosity that would be integrated in an ideal 30-days run at full performance with perfect efficiency (no down time or other interruptions). Note that, for simplicity of comparison with [7] we have maintained the assumption of a single experiment taking data. For  $n_{\text{exp}}$  heavy-ion experiments (with similar configurations) the integrated luminosity per experiment will go down because of luminosity sharing but not as fast as  $1/n_{\text{exp}}$  (the total luminosity, summed over experiments, will be somewhat increased).

Table 1 summarises key parameters for Pb–Pb and p–Pb operation at  $E_b = 50Z$  TeV in the FCC-hh. In the case of p–Pb operation the Pb beam is assumed to be the same as for Pb–Pb, so the corresponding column only quotes the proton beam parameters. The calculated luminosity values assume an optimised theoretical turnaround time of 9 min per LHC cycle and an additional preparation time in the FCC-hh of 1.2 h per FCC-hh filling, as quoted in [8]. It was assumed that the first LHC beam is already prepared during preparation time of the FCC-hh, so that a total turnaround time sums up to 1.65 h. This represents a theoretical minimum. In reality early beam aborts and other faults will increase this time and somewhat reduce the integrated luminosity.

The final values for the integrated luminosity in a typical annual one-month run assume an LHC cycle time of 9 min and are reduced by a “performance efficiency factor” of 50% to allow for set-up time, down-time and other deviations from the idealised running described in Fig. 1 (a similar factor is applied in HL-LHC performance projections). The resulting integrated luminosity values are of  $33 \text{ nb}^{-1}$  for Pb–Pb and  $8 \text{ pb}^{-1}$  for p–Pb collisions. The previous estimates [7] were of  $8 \text{ nb}^{-1}$  and  $1 \text{ pb}^{-1}$ , respectively.

<sup>1</sup>Editors: J.M. Jowett, M. Schaumann

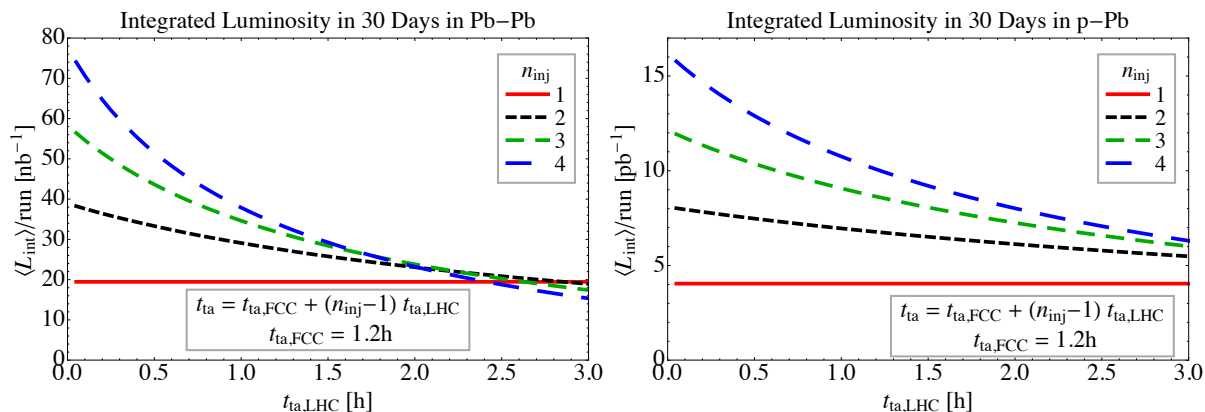


Fig. 1: Integrated luminosity in a 30-days Pb–Pb (left) or p–Pb run (right) for different numbers of LHC injections, and as a function of the LHC cycle time (this updates Figs. 7(c) and 11(c) of Ref. [7]).

Table 1: Selected beam and performance parameters for the FCC-hh in Pb–Pb and p–Pb modes. This table is an update of parts of Table VIII of Ref. [7] which provides further detail.

Operation mode	Unit	FCC Injection		FCC Collision	
		Pb	Pb–Pb	p–Pb	
Beam energy	[TeV]	270	4100	50	
$\sqrt{s_{NN}}$	[TeV]	-	39.4	62.8	
No. of bunches per LHC injection	-	518	518	518	
No. of bunches in the FCC	-	2072	2072	2072	
No. of particles per bunch	$[10^8]$	2.0	2.0	164	
Transv. norm. emittance	$[\mu\text{m}]$	1.5	1.5	3.75	
Number of IPs in collision	-	-	1	1	
Crossing-angle	$[\mu\text{rad}]$	-		0	
Initial luminosity	$[10^{27}\text{cm}^{-2}\text{s}^{-1}]$	-	24.5	2052	
Peak luminosity	$[10^{27}\text{cm}^{-2}\text{s}^{-1}]$	-	57.8	9918	
Integrated luminosity per fill	$[\mu\text{b}^{-1}]$	-	553	158630	
Average luminosity	$[\mu\text{b}^{-1}]$	-	92	20736	
Time in collision	[h]	-	3	6	
Assumed turnaround time	[h]	-	1.65	1.65	
Integrated luminosity/run	$[\text{nb}^{-1}]$	-	33	8000	

For the moment, no studies of upgrades to the heavy-ion injectors (source, linac, accumulation ring, PS and SPS synchrotrons) have been performed. If upgrades to these machines can be envisaged by the time of FCC-hh operation, then still higher luminosities are likely to be available.

Heavy-ion operation will certainly also require certain adaptations of the FCC-hh main ring, e.g., special absorbers in key locations for the high flux of modified ions from the bound-free pair-production process at the interaction points. Collimation of the heavy-ion beams will also be a serious issue and require further absorbers or, possibly, the application of new collimation technologies such as bent crystals or electron lenses. The potential of these technologies is under study at the LHC.

### 3 QGP studies: bulk properties and soft observables <sup>2</sup>

A central goal of a heavy-ion programme at a hadron collider is to explore how collective properties emerge from the fundamental fields of Quantum Chromodynamics and their non-abelian interactions. So-called “soft observables”, that is particles at low transverse momentum, are important in this context since they are the experimentally accessible decay products of the medium that is formed during the collision, and since they provide the most direct signals of collective behaviour. Any substantial increase in the centre-of-mass energy benefits this research programme by significant quantitative gains. In particular, the QGP phase in Pb–Pb collisions at  $\sqrt{s_{\text{NN}}} = 39$  TeV is expected to have larger volume, lifetime, energy density and temperature than Pb–Pb collisions at LHC energy. Also, the enlarged spatio-temporal extension of the created system is expected to be accompanied by larger collective effects, and the increased multiplicity per event increases the statistical precision with which statements about collectivity can be made. In the present section, we summarise basic expectations for the bulk properties and soft observables in heavy-ion collisions at FCC-hh, and we provide some examples for the physics opportunities arising from them. Our discussion touches also fundamental questions whose understanding is currently evolving rapidly. For instance, recent discoveries at the LHC emphasise the need for understanding signatures of collectivity across system size, including the study of proton–proton and proton–nucleus collisions. This addresses the fundamental question of what is the smallest length and time scale for QCD thermalization or hydrodynamization in Quantum Chromodynamics, and how this scale depends on energy density. While there is no doubt that, due to the higher event multiplicities reached in hadronic collisions, experiments at the FCC will greatly contribute to this question, there is also little doubt that the motivation for this experimental programme will be refined significantly in the coming years in an interplay between theory and further analyses of LHC data. A similar comment applies to the increased charm production in heavy-ion collisions at the FCC, and its impact on our understanding of QCD thermalization and hadronization from the QCD fireball.

#### 3.1 Global characteristics of Pb–Pb collisions

Extrapolating measurements of charged particle multiplicity, transverse energy and femtoscopic correlations at lower energies [9–14], one can obtain estimates for the growth of global event characteristics from LHC to FCC. In particular, up to the top LHC energy, the growth of charged hadron event multiplicity per unit rapidity in Pb–Pb collisions is consistent with a weak power-law,

$$\left. \frac{dN_{\text{ch}}}{d\eta} \right|_{\eta=0} \propto (\sqrt{s_{\text{NN}}})^{0.3}. \quad (1)$$

As can be seen from Table 2, this amounts to an increase of a factor  $\sim 1.8$  from top LHC to FCC energy. In the absence of a fully quantitative theory for soft physics observables such as event multiplicities in hadronic collisions, it is difficult to assign uncertainties to such an estimate. From past experience with such extrapolations, and from the increased lever arm available to extrapolate now to FCC, we note simply that all current considerations favour an  $\mathcal{O}(2)$  increase of multiplicity from LHC to FCC, while a multiplicity increase by a factor 3 or larger would be a big surprise. Also, while event multiplicity increases significantly with  $\sqrt{s_{\text{NN}}}$  in all models of particle production, this increase is tamed in models that account for non-linear QCD saturation physics as a mechanism that regulates the density of incoming parton distributions. For instance, in the CGC-rcBK model [15], one obtains  $dN_{\text{ch}}/d\eta = 2700\text{--}2900$  which is about 25% lower than the value obtained from scaling the multiplicity with  $(\sqrt{s_{\text{NN}}})^{0.3}$ . This illustrates the typical uncertainties in such extrapolations.

Fluid dynamic simulations of heavy-ion collisions are sensitive to the initial conditions from which the system is evolved dynamically, and they are sensitive to the thermodynamic properties of hot QCD matter as encoded in the the equation of state and in QCD transport properties. The increased event

---

<sup>2</sup>Editor: U.A. Wiedemann

Table 2: Global properties measured in central Pb–Pb collisions (0–5% centrality class) at  $\sqrt{s_{\text{NN}}} = 2.76$  TeV and extrapolated to 5.5 and 39 TeV. The measurements at 2.76 TeV [9–14] are reported for comparison only and without experimental uncertainties.

Quantity	Pb–Pb 2.76 TeV	Pb–Pb 5.5 TeV	Pb–Pb 39 TeV
$dN_{\text{ch}}/d\eta$ at $\eta = 0$	1600	2000	3600
Total $N_{\text{ch}}$	17000	23000	50000
$dE_{\text{T}}/d\eta$ at $\eta = 0$	1.8–2.0 TeV	2.3–2.6 TeV	5.2–5.8 TeV
Homogeneity volume	5000 fm <sup>3</sup>	6200 fm <sup>3</sup>	11000 fm <sup>3</sup>
Decoupling time	10 fm/c	11 fm/c	13 fm/c
$\varepsilon$ at $\tau = 1$ fm/c	12–13 GeV/fm <sup>3</sup>	16–17 GeV/fm <sup>3</sup>	35–40 GeV/fm <sup>3</sup>

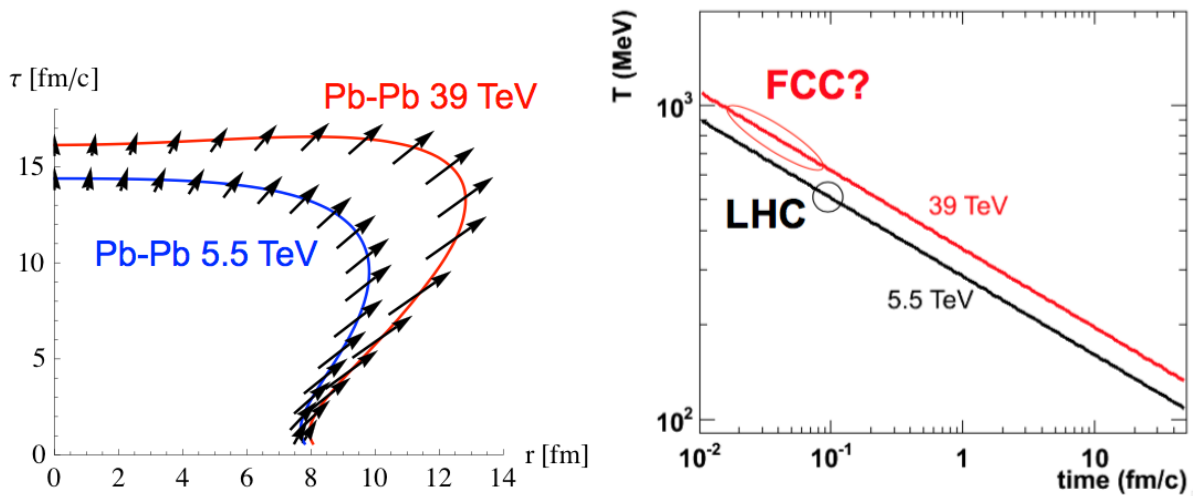


Fig. 2: Left: space-time profile at freeze-out from hydrodynamical calculations for central Pb–Pb collisions at  $\sqrt{s_{\text{NN}}} = 5.5$  TeV and 39 TeV. Right: time evolution of the QGP temperature as estimated on the basis of the Bjorken relation and the Stefan-Boltzmann equation (see text for details).

multiplicity at FCC energy is of prime importance for the fluid dynamic expansion, since it constrains a central characteristic of the initial conditions, namely the entropy density at initial time. More precisely, for a general viscous dynamics, the second law of thermodynamics implies that the final multiplicity puts an upper bound on the initial entropy. However, the QCD matter produced in heavy-ion collisions shows very small dissipative properties at TeV energies and is thus expected to follow a close to isentropic expansion: the initial entropy density is then fixed by the final event multiplicity. The  $\sqrt{s}$ -dependence of fluid dynamic simulations of heavy-ion collisions thus results mainly from the increase in event multiplicity with  $\sqrt{s}$ . To illustrate the impact of the expected multiplicity increase from LHC to FCC, we have run a simplified fluid dynamic simulation for a central Pb–Pb collision. The radial dependence of the energy density in the initial conditions was chosen to be determined as the smooth nuclear transverse overlap function of two Wood-Saxon profiles, neglecting any possible energy dependence and fluctuations. Using a standard parametrisation of a realistic QCD equation of state and minimal dissipative properties (shear viscosity to entropy density ratio  $\eta/s = 1/4\pi$ ), we show in Fig. 2 (left) results for the freeze-out hypersurfaces of central Pb–Pb collisions at different collision energies. This figure quantifies the naive expectation that the denser system created at higher collision energy has to expand to a larger volume and for a longer time before reaching the freeze-out temperature at which decoupling to hadrons

sets in. In this way, Fig. 2 (left) confirms the qualitative expectation that the freeze-out volume should increase proportional to event multiplicity, since the system is expected to decouple at a freeze-out temperature that does not depend significantly on  $\sqrt{s_{\text{NN}}}$  already at top RHIC and LHC energies. While this overall volume is not directly measurable, the homogeneity volume over which bosons interfere constructively is measurable via femptoscopic interferometry measurements, and experimental data up to LHC energy indicate that this volume increases with  $\propto dN_{\text{ch}}/d\eta$ , too, see Table 2. Fig. 2 (left) is also in accordance with the parametric expectation that the decoupling time grows  $\propto (dN_{\text{ch}}/d\eta)^{1/3}$ .

The arrows overlaid with the freeze-out hypersurface in Fig. 2 (left) indicate the transverse flow of the fluid element at decoupling. This provides quantitative support for the qualitative expectation that in a larger and more long-lived system, collective effects can grow stronger. In particular, the figure illustrates that the radial flow field is expected to increase substantially from LHC to FCC, as indicated by the length of the arrows.

In general, the global event characteristics listed in Table 2 determine the spatio-temporal extent of the “cauldron” in which QCD matter is evolved, and they constrain the thermodynamic conditions that apply after thermalization. The measured transverse energy per unit rapidity  $dE_{\text{T}}/d\eta$  (see Table 2) is of particular importance since it constrains the initial energy density. This is most easily illustrated by an estimate, obtained from back-extrapolating  $dE_{\text{T}}/d\eta$  under the assumption of free-streaming, i.e., under the assumption that the system makes minimal work. The resulting Bjorken relation  $\varepsilon(\tau) = \frac{1}{c\tau} \frac{1}{\pi R_A^2} dE_{\text{T}}/d\eta$  assumes then that the energy density of the system at very early times is determined by the energy  $dE_{\text{T}}/d\eta$  contained in a volume given by the transverse overlap area  $\propto \frac{1}{\pi R_A^2}$  times the longitudinal extent reached at time  $\tau$ . According to this Bjorken estimate, the energy density decreases initially like  $\varepsilon(\tau) \sim 1/\tau$ , and the temperature evolves as the fourth root. One may estimate the pre-factor of this relations, for instance by using the Stefan-Boltzmann limit of the QCD equation of state which yields  $T(t) = [\varepsilon(t) (30/\pi^2)/n_{\text{d.o.f.}}]^{1/4}$ , where  $n_{\text{d.o.f.}} = 47.5$  is the number of degrees of freedom for a system with gluons and three quark flavours. The energy density is expected to increase by a factor of two from LHC to FCC, reaching a value of 35–40 GeV/fm<sup>3</sup> at the time of 1 fm/c. In Fig. 2 (right), we have plotted the time-dependence of the QGP plasma temperature for Pb–Pb collisions at the LHC and at the FCC. We caution that the present use of the Bjorken estimate is subject to several uncertainties. On a quantitative level, one may note e.g. that the QCD equation of state differs from that of a Stefan-Boltzmann gas and that at sufficiently late times (say  $\tau > 1$  fm/c), the transverse expansion of the system makes the energy density decay faster than  $1/\tau$ . On a qualitative level, we note that the Bjorken estimate constrains the energy within a given initial volume without specifying whether (and if so, at what initial time) this energy density is thermalised. While the curves in Fig. 2 (right) extend to arbitrarily early (logarithmic) times, they are only meaningful at times larger than a thermalization time-scale that is estimated to be  $\mathcal{O}(0.1$  fm/c) at LHC energies and that is expected to decrease with increasing energy density. At least in principle, this time-scale is calculable from kinetic theory, but so far only rough estimates can be given. Figure 2 (right) shows that while the increase at a given time is a modest 30% when going from LHC to FCC, the thermalization time of the system is expected to be significantly smaller. One may reach initial temperatures as large as  $T_0 \approx 800$ –1000 MeV in case that the thermalization time decreases to  $\mathcal{O}(0.02$  fm/c) at FCC energies.

### 3.2 Collective phenomena from heavy-ion to pp collisions

One of the most important characterisations of flow-like phenomena in heavy-ion collision is the study of the azimuthal dependence of particle production. For a single inclusive hadron spectrum, this can be done for instance by measuring the azimuthal harmonics  $v_n$  in a Fourier decomposition<sup>3</sup> in the azimuthal

<sup>3</sup>This decomposition takes into account only the even terms (cosines), which are far dominant over the odd terms (sines).

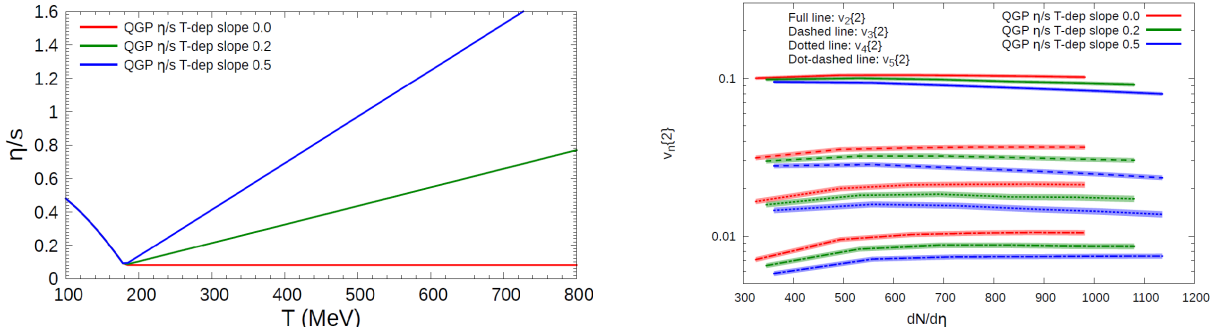


Fig. 3: Left: parametrisations for the evolution of the ratio  $\eta/s$  versus temperature. Right: results for different  $v_n\{2\}$  versus multiplicity from viscous hydrodynamics calculations for different temperature dependencies of  $\eta/s$  shown on the left. The results are based on the theoretical framework described in Refs. [19–21].

angle  $\varphi$  with respect to the nucleus–nucleus reaction plane orientation  $\Psi$ ,

$$\frac{dN_{\text{ch}}}{p_T dp_T d\eta d\varphi} = \frac{1}{2\pi} \frac{dN_{\text{ch}}}{p_T dp_T d\eta} \left[ 1 + 2 \sum_{n=1}^{\infty} v_n(p_T, \eta) \cos(n(\varphi - \Psi)) \right]. \quad (2)$$

Since heavy nuclei are not uniform spheres but distributions of nucleons, the spatial profile of the initial nucleon–nucleon collisions, which determines the so-called initial conditions of a heavy-ion collision, varies on an event-by-event basis and it has a complex structure that is best characterised with a symmetry plane for each harmonic  $v_n$ , rather than with a single reaction plane. Therefore,  $\Psi$  is replaced in the above expansion by a set of symmetry planes  $\Psi_n$ . The azimuthal orientations of  $\Psi_n$  need to be extracted from the same set of data as the harmonic flow coefficients  $v_n$ , and effects which only contribute to few-particle correlations and are invariant to symmetry plane orientations (so-called non-flow effects) need to be disentangled from flow-effects, which typically involve all produced particles. This is done by measuring  $v_n$  from multi-particle azimuthal correlations. For the description of the various techniques, developed to this end, we refer to the literature [16–18].

At FCC energies, the two-fold larger multiplicity in central Pb–Pb collisions may open up the possibility to carry out flow measurements on an event-by-event basis and to become sensitive to dependencies of transport coefficients that are very difficult to address at the LHC. For example, the different azimuthal coefficients  $v_n$  are sensitive to the various possibilities for the temperature dependence of shear viscosity to entropy density ratio,  $\eta/s(T)$ , and this sensitivity becomes stronger with increasing multiplicity and for higher harmonics. This is illustrated in Fig. 3. The results are based on the theoretical framework described in Refs. [19–21]. We note that at the time of writing this report, neither the theoretical possibilities for disentangling different conceivable temperature dependencies of  $\eta/s(T)$  at FCC, nor the opportunities of getting insights into this question from further LHC data are fully explored. In particular, recent work studying various soft hadron observables in the EbyE EKRT model context indicates [22, 23] that an analysis including Pb–Pb data up to the top LHC energies in combination with RHIC Au–Au data can disentangle between different temperature dependencies for  $\eta/s(T)$ . While there is a sound qualitative argument that the higher centre-of-mass energy at FCC will lead to an improved handle on the temperature dependence of transport coefficients, the expected quantitative gains at FCC are likely to require updating in the light of these ongoing efforts at the LHC.

In recent years, surprisingly, small and dense systems probed in high multiplicity p–A and pp collisions were found to display flow-like phenomena. In particular, p–Au, d–Au and  $^3\text{He}$ –Au collisions at RHIC, as well as p–Pb and high-multiplicity pp collisions at the LHC have been shown to feature similar ridge-like structures,  $v_2$  anisotropy and, in some of the systems, including high-multiplicity pp

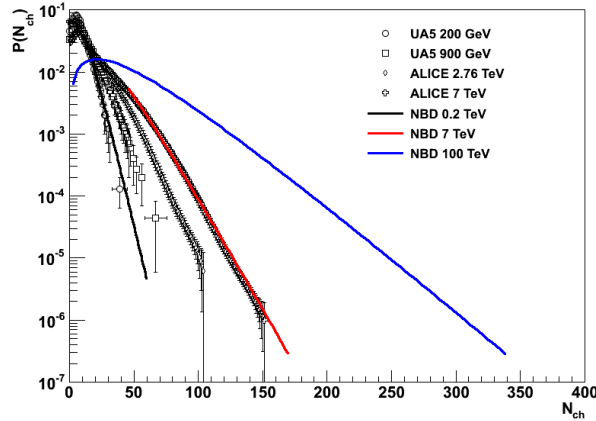


Fig. 4: Extrapolation of the charged-particle multiplicity distribution ( $|\eta| < 1.5$ ) in pp collisions to  $\sqrt{s} = 100$  TeV, based on a negative binomial distribution.

collisions, even  $v_3$  anisotropy as seen in collisions between large nuclei [24–30]. The hints for a collective nature of the azimuthal anisotropy seen in p–Pb collisions were reinforced by measuring its higher-order cumulants. New pp data from ATLAS and CMS indicate that the long-range ridge correlation may well extend all the way down to minimum bias collisions (if not below), though differences in the analysis techniques warrant further scrutiny. These recent findings raise fundamental questions about whether the flow-like patterns in small and dense systems are only similar in appearance to what one observes in heavy-ion collisions, or whether the idea of a minimal scale for the onset of collective phenomena needs to be revisited.

In general, the experimental study of flow phenomena in hadronic collisions aims at disentangling flow effects from non-flow contributions. Simple non-flow effects can arise for instance from resonance decays or (mini)jets. The energy-momentum constraints of these elementary particle production processes lead to patterns in the two-particle correlations that share at least qualitative commonalities with the patterns measured in the harmonic flow coefficients  $v_n$ , in the ideal case of zero non-flow correlations. However, a collective phenomenon is shared by many if not all particles in the event, rather than by the few particles associated to the same microscopic production process. The ability to disentangle collective correlations from confounding factors, therefore, increases with event multiplicity. This is seen most explicitly in the so-called cumulant analysis of flow coefficients, via which one tests whether an assumed collective effect persists with equal strength when searched for in multi-particle correlations involving higher number of particles. It is an important limitation of the current discussion of the system size dependence of flow at the LHC that the multiplicities in pp collisions are still too small to allow for the same cumulant analyses of flow coefficients that are standard in heavy-ion collisions. The increased event multiplicity in pp collisions at the FCC will overcome this problem.

Figure 4 presents an extrapolation of the multiplicity distribution in  $|\eta| < 1.5$  to  $\sqrt{s} = 100$  TeV. The extrapolation was obtained by fitting multiplicity distributions from 0.2 to 7 TeV with a negative binomial distribution and extrapolating the parameters. To achieve a good description of the high-multiplicity tail of the distribution, the lowest 30% of the multiplicity range was excluded from the fit. Including the low-multiplicity range leads to a worse fit result and a wider extrapolated multiplicity distribution. Therefore, the presented extrapolation can be seen as a lower limit of the possible reach. The high-multiplicity tail of event-distributions in proton-proton collisions will become accessible at the FCC up to multiplicities of at least 300 charged particles. This makes it feasible to apply statistically demanding analysis techniques for the identification of flow-like phenomena, such as higher-order cumulant analyses, across system size, including the smallest pp collision system.

### 3.3 Effect of the charm quark on the QGP equation of state

The fluid dynamic interpretation of ultra-relativistic heavy-ion collisions relies on a gradient expansion around local thermodynamic equilibrium. It is thus based entirely on basic thermodynamic properties such as the equation of state (EOS, i.e. the temperature dependence of the pressure  $P(T)/T^4$ ), the velocity of sound and dissipative transport coefficients. As thresholds for particle production are crossed at higher temperature, the number of relevant thermodynamical degrees of freedom and thus the equation of state changes characteristically. Remarkably, while still relatively little is known from first principles about the dependence of the EOS on the quark mass, LO and NLO calculations in finite temperature field theory [31] indicate that charm quarks start contributing to the EOS for temperature as low as 350 MeV (see Fig. 5). This is also supported by first exploratory lattice studies [32–34]. Given that the initial temperature of the systems produced at the FCC will be significantly higher, see Fig. 2 (left), one may expect that the system temperature increase could lead to a sizeable production of secondary charm and anti-charm quark ( $c\bar{c}$ ) pairs from partonic interactions during the hydrodynamical evolution of the system. However, in heavy-ion collisions, reaching thermal charm abundances will depend on kinetic and chemical equilibration mechanisms. Their effectiveness depends on the competition between the chemical equilibration rate  $\Gamma_{\text{chem}}$  and the expansion rate. A perturbative analysis allows to relate this equilibration rate to the ratio of quark number susceptibilities of massive ( $\chi_f$ ) and massless ( $\chi_0$ ) quarks,  $\Gamma_{\text{chem}} \simeq \frac{2\pi\alpha_s^2 T^3}{9M^2} \left(\frac{7}{6} + N_f\right) \frac{\chi_f}{\chi_0}$ , [35]. Fixing these susceptibilities with lattice data [34, 36], and using  $\alpha_s = 0.3$  and  $M_c = 1.5$  GeV, one finds

$$\begin{aligned} \Gamma_{\text{chem}}^{-1} &> 60 \text{ fm/c} && \text{for } T \simeq 400 \text{ GeV}, \\ \Gamma_{\text{chem}}^{-1} &> 10 \text{ fm/c} && \text{for } T \simeq 600 \text{ GeV}. \end{aligned}$$

We note that further theoretical developments are likely to refine these estimates prior to the start of the FCC. At face value, the numbers listed above indicate that FCC targets an interesting transition region in energy density above which charm quarks start counting towards the thermal degrees of freedom. While charm abundances are likely to lie below chemical equilibration values at high temperatures, charm is expected to participate in experimentally accessible kinetic and chemical equilibration processes that can be accounted for in the context of kinetic theory. Predictions on thermal charm production at FCC energies will be discussed in Section 4.2.

### 3.4 Hadrochemistry

In heavy-ion collisions, the relative abundances of different hadronic species are well-described in terms of the grand canonical partition function over the full hadronic mass spectrum. Hadronic yields are then given in terms of only two free parameters, the temperature  $T$  and baryo-chemical potential  $\mu_B$  of the system at decoupling (as well as a volume parameter). A thermally equilibrated QCD system that expands and cools to the limiting temperature of a hadron gas is a system in which all hadrons are produced with thermal abundance. Therefore, the limiting temperature  $T$  and baryo-chemical potential  $\mu_B$  obtained from thermal fits to hadronic abundances is of interest since it is thought of as tracing the QCD phase boundary. The energy-dependence of both fit parameters, shown in Fig. 6 shows that hadrochemical measurements at the FCC are expected to lie far within a plateau in which no further energy evolution occurs: the baryo-chemical potential in central Pb–Pb collisions vanishes almost at top LHC energies and hence no baryon excess is expected at mid-rapidity at the FCC. Also, a limiting temperature of  $\sim 160$  GeV is reached at LHC energy already and no further evolution is expected. The simple implication of having reached these plateau values of the thermal model of hadron production at LHC is that all ratios of thermal hadronic abundances are expected to remain unchanged between LHC and FCC energies. While these measurements are not expected to reveal surprises at the FCC, a confirmation of this well-tested statistical baseline for soft thermal hadron production could help to define a particularly clean baseline on top of which dynamical mechanisms of kinetic and chemical equilibration of rarer processes (e.g. in the charm sector) could be established.

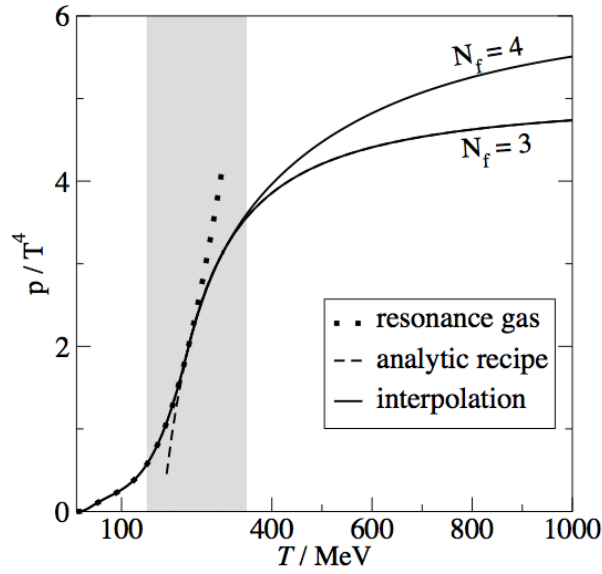


Fig. 5: For basic thermodynamic observables such as the pressure plotted here, the charm quark plays a visible role at very low temperature  $T/m_c \ll 1$ . The present plot is for a perturbative calculation that accounts for gluonic contributions up to the highest known order  $\mathcal{O}(g^6 \ln(1/g))$  and that treats the change in quark masses to order  $\mathcal{O}(g^2)$ . Figure taken from Ref. [31].

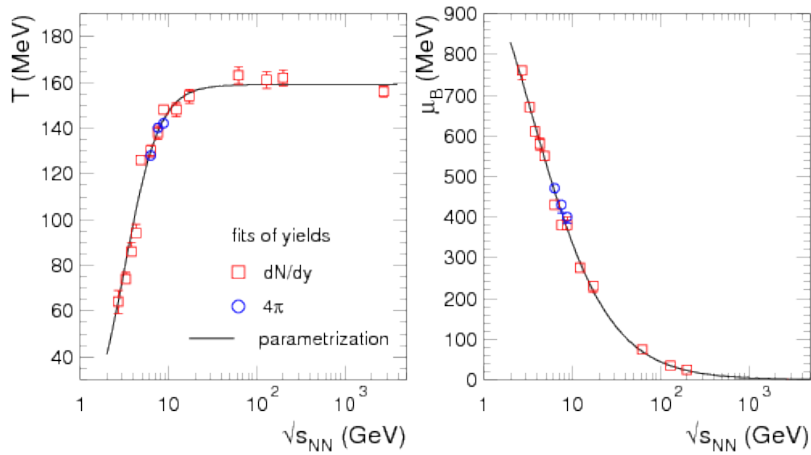


Fig. 6: The energy dependence of the thermal model parameters, temperature  $T$  and baryon chemical potential  $\mu_B$ , obtained from fitting the statistical model of hadron production [37] to identified hadronic yields measured in heavy-ion collisions. The figure is updated to include the most recent LHC results and it was taken from [38].

## 4 QGP studies: hard probes <sup>4</sup>

### 4.1 Jet quenching

#### 4.1.1 Current understanding of jet quenching

The modification of jet properties in heavy-ion collisions with respect to the proton–proton case, what is commonly referred to as jet quenching, results from the interaction of jet constituents with the QGP that they traverse. Jet quenching was discovered at RHIC without full jet reconstruction via the strong reduction of the number of intermediate- $p_T$  hadrons [39–42]. Robust jet reconstruction, above the large and fluctuating background characteristic of heavy-ion collisions, was first carried out at the LHC [43–45] as the combined result of a higher centre-of-mass collision energy, much improved detector capabilities and novel reconstruction techniques [46]. This has given access to a range of measurable jet properties from which the jet-QGP dynamics, and ultimately QGP properties, can be inferred.

Over the last few years, as several jet properties were measured in heavy-ion collisions [47–62], the theoretical understanding of jet–QGP interactions has evolved from the early descriptions of single parton energy loss [63–75] towards an overall understanding of how full jets are modified by the QGP (for a review see [76] and references therein). Several important results underlie this emergent picture of in-medium jets. First, that while the hard structure of a jet remains mostly driven by vacuum-like physics, soft jet constituents are strongly affected by the QGP experiencing large broadening effects which ultimately decorrelate them from the jet direction [77, 78]. Second, that the QGP presence strongly modifies intra-jet coherence properties [79] leading to a breakdown of angular ordering for radiation induced by transverse momentum exchanges between jet and QGP. Finally, that the QGP-induced radiation pattern of a jet is driven by the number of objects within the jet that can be resolved by the QGP [80].

Extraction of QGP properties from jet observables relies ultimately on the availability of event generators [81–84] that accurately model the interaction of jets with realistic implementations of a hydrodynamically evolving QGP. From an experimental point of view, jet observables provide versatile probes of the different energy scales as well as the space-time picture of the medium. Present LHC data show clearly the potential of these probes with higher statistics. The increase in energy, the abundance of probes, especially those involving electroweak bosons together with jets, and the qualitatively new processes available (e.g. boosted jets, see below) make of the FCC-hh the best-suited next machine for a deeper understanding of this physics.

#### 4.1.2 Hard cross sections at FCC-hh energies

The large increase in energy and luminosity from the LHC to the FCC provides new tools to study the matter created in the collisions of heavy ions. In Fig. 7, cross sections for different processes and different energies are computed with MCFM [85] at the highest available order. Ratios with respect to the cross sections at top LHC energy for Pb–Pb collisions ( $\sqrt{s_{NN}} = 5.5$  TeV) are also shown for an easier comparison of the available increases. While the increases in  $Z$  or beauty production are a factor  $\sim 10$  with the expected energy increase from the LHC to the FCC, these figures are much larger for top production (an increase of a factor of  $\sim 80$ ) or the  $Z$ +jet with an increase of  $\sim 20$ . Although not shown in Fig. 7, large yields of other processes of interest will be also available, as charm production, heavy quarkonia or jets in the TeV mass region.

The large increase in the top cross section, along with the larger luminosities expected for the FCC-hh, make the case of top observables one of the main qualitative differences with respect the LHC. It will, in particular, allow the study of boosted  $W$ 's coming from the decay of the top quarks, a unique probe of colour singlet objects traversing a medium, even in the hadronic channel (see Section 4.1.4). A rough estimate of the rates, based on an integrated luminosity of  $\sim 30$  nb<sup>-1</sup> for one month Pb–Pb run gives several million  $t\bar{t}$  pairs, which is enough for several interesting measurements, in particular with boosted tops and  $W$ 's.

<sup>4</sup>Editors: A. Dainese, D. d'Enterria, J.G. Milhano, C.A. Salgado

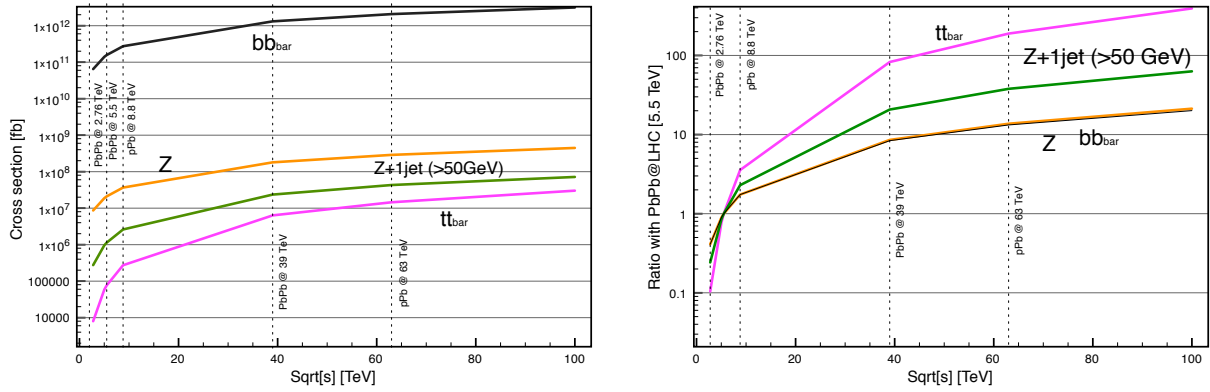


Fig. 7: Left:  $\sqrt{s}$ -dependence of the cross sections for hard processes of interest for a heavy-ion programme, calculated with MCFM [85] at the highest available order. Right: increase factors with respect to the cross sections at top LHC energy for Pb–Pb collisions.

The large yields in  $Z$ +jets (several tens of millions) will also allow to study the jet quenching process with excellent calibration of the jet energy. In principle, the measurement of the energy lost by the jet in  $Z$ +jet would provide a good experimental measurement of the distribution of the parton energy losses in hot QCD matter.

#### 4.1.3 Top-quark production in $p$ – $Pb$ and $Pb$ – $Pb$ collisions

The motivations for measurements of top quarks in heavy-ion collisions at FCC are multifold. For example, in  $p$ – $Pb$  collisions the cross sections efficiently probe the nuclear gluon PDFs in a wide range in momentum fraction  $x$  at high scale  $Q \sim m_t$  [86] (see Section 5.1.3). In  $Pb$ – $Pb$  collisions, the top-quark observables are sensitive to the energy-loss of heavy quarks [87] and by selecting boosted (very high- $p_T$ ) top quarks one could also probe the QGP medium at slightly later times (though still close to its formation stages) as the decays of boosted top quarks get Lorentz time dilated (see Section 4.1.4). The corresponding measurements at the LHC will be limited by the smaller production cross sections, while at FCC energies the production cross sections are significantly higher. This is illustrated in Fig. 8, which shows the energy dependence of the total top-pair and single-top cross sections at NLO (computed with MCFM [85]) for  $pp$ ,  $p$ – $Pb$  and  $Pb$ – $Pb$  collisions. The large differences between the  $pp$  and  $p$ – $Pb$  ( $Pb$ – $Pb$ ) curves are due to scaling by  $A$  ( $A^2$ ). The effects of nuclear modifications in PDFs (here EPS09 [88]) are at the level of a few percent (see Section 5.1.3).

The top quarks decay almost exclusively to  $b$  quark and  $W$  boson and, in a heavy-ion environment, it is the leptonic decays of  $W$  that can be best resolved from the backgrounds. The estimated measurable yields (using nominal per-year luminosities from Section 2) with realistic analysis cuts ( $b$ -jets: anti- $k_T$  algorithm with  $R = 0.5$ ,  $p_T > 30$  GeV/ $c$ ,  $|\eta| < 5$ ; charged leptons:  $R_{\text{isol}} = 0.3$ ,  $p_T > 20$  GeV/ $c$ ,  $|\eta| < 5$ ; neutrinos:  $E_T > 40$  GeV) and conservative 50% efficiency for  $b$ -jet tagging are shown in Table 3.

As mentioned above, the  $p_T$  reach of top quarks in  $Pb$ – $Pb$  collisions is of special importance for QGP studies. To this end, Fig. 8 (right) shows the estimated  $p_T$  spectrum of the top+antitop yields (per year) in  $Pb$ – $Pb$  collisions for top-quark pair production, which is the most promising channel due to the higher yields, as shown in Table 3. The figure indicates that one could measure top quarks approximately up to  $p_T \approx 1.8$  TeV/ $c$ . At mid-rapidity,  $p_T$  as large as this would correspond approximately to a factor of 10 time dilation in the top decay (see Section 4.1.4).

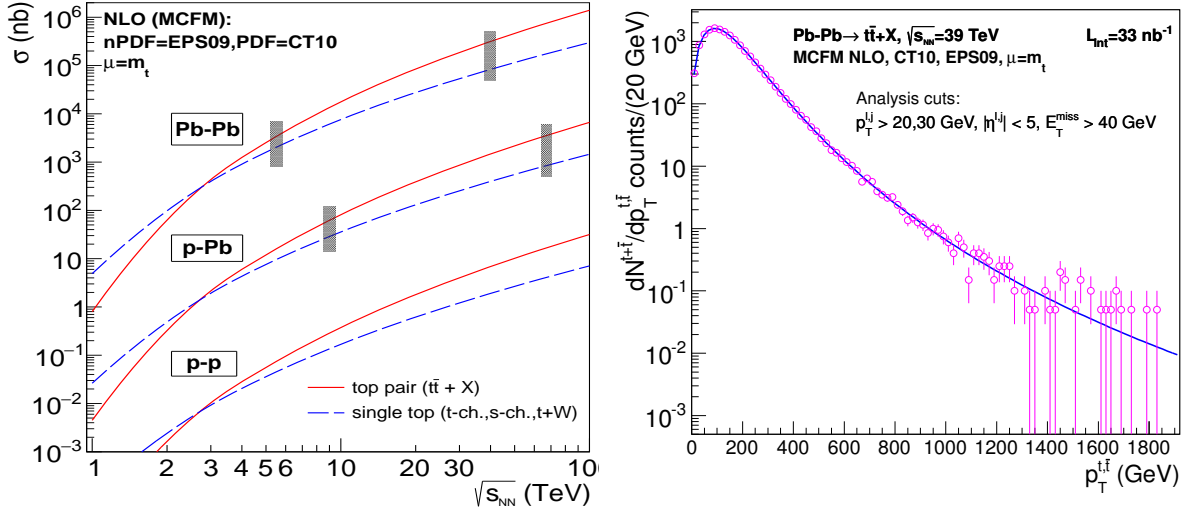


Fig. 8: Left: Computed total cross sections for top-pair and single-top (sum of  $t$ -,  $s$ -, and  $tW$ -channels) production in pp, p–Pb and Pb–Pb collisions as a function of  $\sqrt{s_{NN}}$  (the boxes indicate the LHC and FCC energies). Right: Expected top-quark  $p_T$  distributions  $dN/dp_T^{t,\bar{t}}$  in Pb–Pb in the fully-leptonic decay modes at  $\sqrt{s_{NN}} = 39$  TeV after acceptance and efficiency cuts. The markers correspond to a set of pseudodata with the statistical uncertainties expected for  $L_{\text{int}} = 33 \text{ nb}^{-1}$ . The figures are adapted from Ref. [86].

Table 3: The expected number per run of top and antitop quarks in fully-leptonic final states, after typical acceptance cuts and efficiency losses (see text), for  $t\bar{t}$  and  $tW$  production in p–Pb and Pb–Pb collisions at FCC energies [86].

System	$\sqrt{s_{NN}}$	$\mathcal{L}_{\text{int}}$	$t\bar{t} \rightarrow b\bar{b}l\ell\nu\nu$	$tW \rightarrow b\ell l\nu\nu$
Pb–Pb	39 TeV	$33 \text{ nb}^{-1}$	$3.1 \times 10^5$	$8.6 \times 10^3$
p–Pb	63 TeV	$8 \text{ pb}^{-1}$	$8 \times 10^5$	$2.1 \times 10^4$

#### 4.1.4 Boosted tops and the space-time picture of the QGP

The large centre-of-mass energy of the FCC will provide high rates of highly-boosted heavy particles, such as tops,  $Z$  and  $W$  bosons. It is expected that when these particles decay the density profile of the QGP has already evolved. By using this time delay, and by comparing the reconstructed energy to the one expected from usual energy loss processes, it should be possible to get unique insight into the time structure of the jet–QGP interaction.

A key feature that becomes accessible at FCC energies is the role of colour coherence effects in the parton cascade in the presence of a QCD medium, as proposed in [80]. The physics is rather simple: in a given time interval  $t$ , fast coloured objects, either fundamental ( $q$  or  $g$ ) or composite (e.g.  $q\bar{q}$ ,  $gg$  or  $qg$ ), probe the medium with a typical spatial resolution  $r_{\perp} \sim 1/Q$ , where  $Q$  is the transverse energy scale of the object. For example, for a gluon that is produced in the fragmentation of a jet (hard parton) we have  $1/Q \sim \theta t$ , where  $\theta$  is the angle between the gluon and the hard parton; for a  $q\bar{q}$  pair produced in a  $W$  or  $Z$  decay,  $\theta$  is the angle between the  $q$  and the  $\bar{q}$ . The spatial resolution  $r_{\perp}$  has to be compared with the typical colour correlation length in the medium  $L_{\text{corr}} \sim 1/\sqrt{\hat{q}t}$ . Here,  $\hat{q}$  is the transport coefficient of the medium, that translates the average transverse momentum squared that particles exchange with the medium by mean-free path. When the colour correlation length of the medium is smaller than the typical

transverse size of the probe,  $L_{\text{corr}} < r_{\perp}$ , the different components of the coloured object (jet or  $q\bar{q}$  pair) undergo independent colour rotations (as they are separated by more than the typical correlation length) losing coherence. This happens parametrically at the time

$$t_{\text{singlet}} \sim \left[ \frac{12}{\hat{q}\theta^2} \right]^{1/3}, \quad (3)$$

where 12 is a numerical factor depending on the actual model for the medium and the definition of the variables. For a highly boosted quark-antiquark pair this time increases, which gives the possibility to investigate further the coherence/decoherence jet quenching phenomena. Of particular interest are the colour singlet probes, as the  $q\bar{q}$  decay products of a highly-boosted  $W$  or  $Z$  boson, as, in this case, the effect of the medium will be absent.

Top-antitop events provide a unique topology to study the space-time picture of the hot QCD medium interacting with the jets. We are mainly interested here in the channel in which one of the  $W$  decays leptonically while the other decays hadronically. The time dilation of the decay  $W \rightarrow q\bar{q}$  and the color coherence discussed above ensure that also in the direction of the resulting jets, the system was traveling through the medium in a color singlet state for some time. This time increases with the boost due to both time dilation and the smaller angle of the system which determines the degree of coherence in (3). As shown in Fig. 9, we obtain times in the range  $\sim 0.3\text{--}3$  fm/ $c$  when adding the time delay from Lorentz boosts and the time in which a singlet antenna remains in a colour coherent state (estimated for  $\hat{q} = 4$  GeV<sup>2</sup>/fm).

A detailed discussion about all possibilities to be exploited with this and other related observables is out of the scope of this note and will be presented elsewhere [89]. We study here the effect on the reconstructed masses of the top and  $W$  with different energy loss scenarios as a proof of concept of the potential of these observables to access completely novel quantities in heavy-ion collisions. Exploiting all this potential will require a good control over the energy loss of, e.g. the  $b$  quarks, something which will be studied at the LHC in the coming years and for which further information could be obtained by considering together with the discussed  $t\bar{t} \rightarrow b\bar{b} W^+ W^- \rightarrow b\bar{b} q\bar{q} \ell^- \nu$  channel, the leptonic decay channel  $t\bar{t} \rightarrow b\bar{b} W^+ W^- \rightarrow b\bar{b} \ell^+ \ell^- \nu \bar{\nu}$  sensitive to the energy loss of the  $b$  quark.

Events with  $t\bar{t}$  pairs were generated using the PYTHIA 8 generator. The events were selected with the following criteria: (i) having at least 4 hadronic anti- $k_T$  jets (2  $b$ -tagged jets + 2 non- $b$ -tagged jets) with  $R = 0.3$ ,  $p_T > 30$  GeV/ $c$  and  $|\eta| < 2.5$  (ii) having a single muon with  $p_T > 25$  GeV/ $c$  and  $|\eta| < 2.5$ . A  $b$ -tagging efficiency of 70% was assumed. The reconstructed top and  $W$  jet mass as a function of top transverse momentum at  $\sqrt{s_{\text{NN}}} = 5.5$  TeV are shown in Fig. 10. The same but at  $\sqrt{s_{\text{NN}}} = 39$  TeV are shown in Figs. 11 and 12. The shaded region corresponds to the statistical uncertainty estimated for  $L_{\text{int}} = 10$  nb<sup>-1</sup> at  $\sqrt{s_{\text{NN}}} = 5.5$  TeV and for  $L_{\text{int}} = 33$  nb<sup>-1</sup> (a one-month run) and  $L_{\text{int}} = 100$  nb<sup>-1</sup> (three runs) at  $\sqrt{s_{\text{NN}}} = 39$  TeV. The number of events was determined considering the 0–10% centrality class. Experimental effects will somewhat increase the errors shown in Figs. 10–12 due to the mass resolution: this remains to be studied.

Energy loss was simulated considering that all quarks lose about 10% of their initial four-momenta. As a simple toy model to check the effects of coherence in the reconstructed mass, this energy loss is applied equally to all quarks (*all quenched*), to all quarks but the  $W$  boson decay products (*antenna unquenched*) or to all quarks but the leading quark-antiquark from the  $W$  boson decay (*leading quarks*). Energy loss causes a reduction of the reconstructed  $W$  and top masses with respect to their true values of about 80 and 175 GeV. The results shown in Figs. 10, 11 and 12 reveal a clear separation between what one would expect if coherence effects were completely suppressed in the presence of a medium (*all quenched*) or still present within two limits (*leading quarks* and *antenna unquenched*). In the *all quenched* case, the reconstructed masses of the  $W$  and top would drop below 70 and 150 GeV, respectively. Instead, in the case of coherence they would be of the order of 75 and 155 GeV, respectively. The difference between the two limits *leading quarks* and *antenna unquenched* is expected to be small (a few

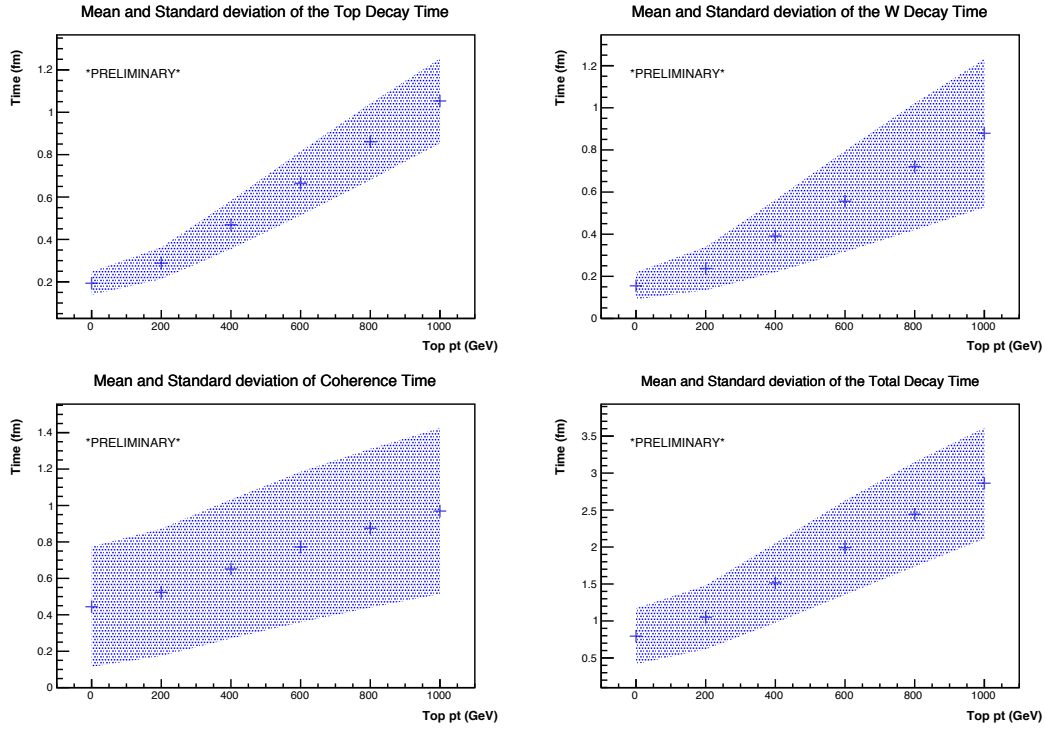


Fig. 9: Average decay times of top (upper, left) and  $W$  boson (upper, right), in the laboratory frame, as a function of top  $p_T$ . On the bottom-left, the coherence time of the  $q\bar{q}$  pair from the  $W$  decay, as given by Eq. (3), and on bottom-right, the sum of the three components (top decay,  $W$  decay and coherence time). The dots correspond to the average decay times and the shaded region to the standard deviation.

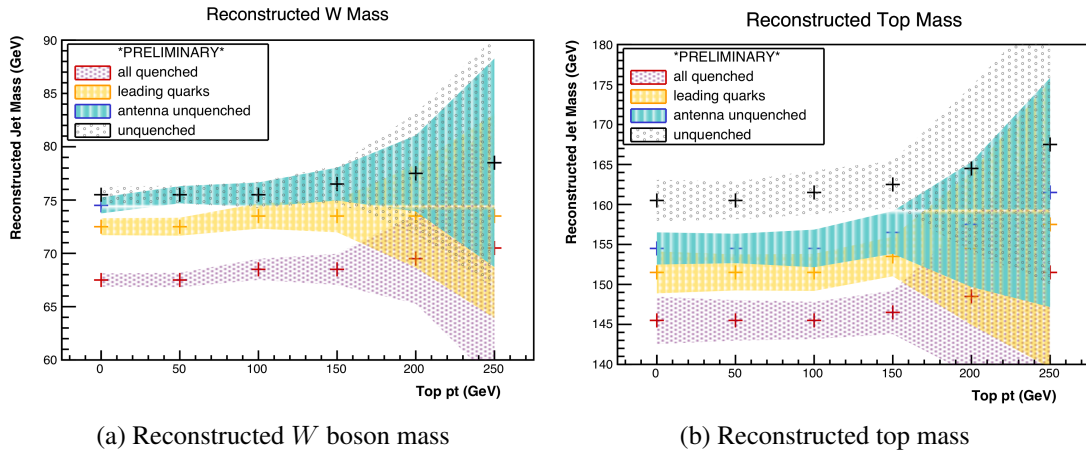


Fig. 10: Reconstructed masses of top and  $W$  boson at the LHC energies,  $\sqrt{s_{NN}} = 5.5$  TeV. The shaded region corresponds to the statistical error for  $L_{int} = 10$  nb $^{-1}$ .

GeV), but larger than the projected statistical uncertainties.

In summary, the reconstructed values of top and  $W$  masses provide robust sensitivity to the degree of quenching. By correlating them with the expected decay and decoherence times of the top and  $W$ , as deduced from their  $p_T$ , one has an opportunity to gain unique insight into the time dependence of medium properties.

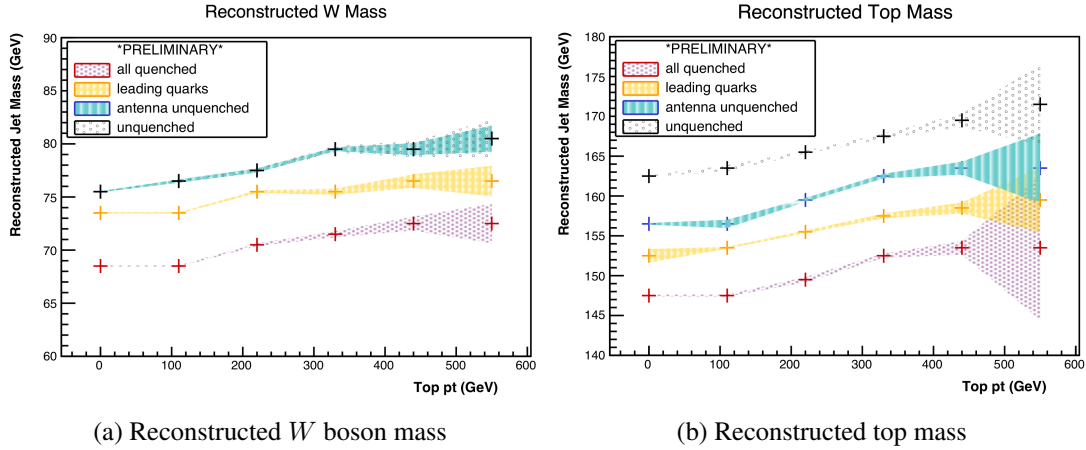


Fig. 11: Reconstructed masses of top and  $W$  boson at the FCC energies,  $\sqrt{s_{NN}} = 39$  TeV. The shaded region corresponds to the statistical error for  $L_{\text{int}} = 33 \text{ nb}^{-1}$ .

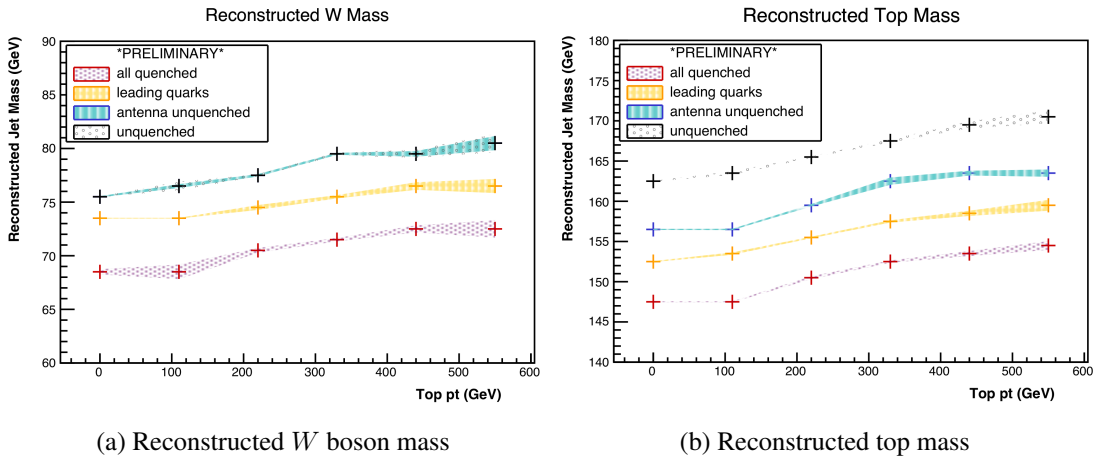


Fig. 12: Reconstructed masses of top and  $W$  boson at the FCC energies,  $\sqrt{s_{NN}} = 39$  TeV. The shaded region corresponds to the statistical error for  $L_{\text{int}} = 100 \text{ nb}^{-1}$ .

## 4.2 Open and closed charm and bottom production

Heavy quarks (charm and bottom) are among the hard probes that have provided important insights on the formation and the characteristics of the QGP in the heavy-ion programmes at SPS, RHIC and LHC. A recent review of the theoretical and experimental aspects of heavy-flavour probes can be found in Ref. [90].

Briefly, on the one hand, quarkonium states are sensitive to the formation and to the temperature of a deconfined plasma via the mechanism of colour-charge screening, which is thought to be to some extent balanced by the recombination of heavy quarks and antiquarks from the plasma. On the other hand, the production of hadrons with open heavy flavour is sensitive to the QGP-induced modification of the momentum value and direction of heavy quarks, that are created in initial hard collisions before the formation of the QGP. In particular, it provides information on the interaction mechanisms of heavy quarks with the constituents of the QGP (energy loss, and gain) and on its transport properties.

In this section, we focus on a few selected aspects that could represent novel or particularly remarkable observations at FCC energy, namely:

- large production of so-called thermal, or secondary, charm from interactions of light quarks and

- gluons within the QGP;
- observation of an enhancement of charmonium production with respect to the binary scaling of the production in pp collisions, as consequence of (re)generation;
- observation of a colour screening and (re)generation for the most tightly-bound quarkonium state, the  $\Upsilon(1S)$ .

#### 4.2.1 Thermal (or secondary) charm production

Interactions between gluons or light quarks of the QGP can lead to the production of  $c\bar{c}$  pairs if the energy in the centre of mass of the interaction is of the order of twice the charm quark mass  $\sqrt{\hat{s}} \sim 2m_c \sim 3$  GeV. This requires the energies of the two interacting gluons (or quarks) to be of the order of  $E \sim m_c \sim 1.5$  GeV. If the gluons (or quarks) are thermalised in a medium, their energy is of the order of the temperature  $T$ , with a thermal-like exponential distribution. Therefore, for a QGP with  $T$  of several hundreds of MeV (say larger than 500 MeV), there is a significant probability that  $c\bar{c}$  pairs are produced in these in-medium interactions. This production is indicated as thermal, or secondary, in contrast with the primary production that occurs in initial hard-scattering processes between partons of the two incident nuclei.

In Section 3.1 we have estimated the parametric dependence of  $T$  on time and on the measured transverse energy density  $T(t) \sim [(dE_T/d\eta)/t]^{1/4}$ . From this simplified estimate, we observe that the temperature at a given time increases slowly with the  $E_T$  density (e.g. about 20–30% from LHC to FCC with the  $E_T$  density estimated in Section 3.1). However, the thermalization time  $\tau_0$  of the QGP is expected to decrease substantially when  $\sqrt{s_{NN}}$  increases, typically by a factor of 2 from LHC to FCC (see e.g. [91]). Therefore, the overall increase of the initial temperature  $T_0$  of the QGP from LHC to FCC can be about 50%. In Ref. [91] a detailed hydrodynamical calculation gives  $T_0 = 580$  MeV at initial time  $\tau_0 = 0.6$  fm/c for LHC ( $\sqrt{s_{NN}} = 5.5$  TeV) and  $T_0 = 840$  MeV at  $\tau_0 = 0.3$  fm/c for FCC. With these QGP temperatures a sizeable fraction of the gluons and light quarks have energies larger than the charm quark mass and  $c\bar{c}$  pairs can be produced in their interactions. This production is concentrated in the initial  $\sim 1$  fm/c of the QGP evolution.

Predictions for the production of thermal charm at LHC and FCC energies were reported by three groups: BAMPS [92, 93], Ko et al. [94, 95] and Zhou et al. [91]. In the BAMPS transport model, which is based on the Boltzmann equation, secondary charm production is calculated using leading order (LO) gluon fusion and  $q\bar{q}$  annihilation processes. The calculations by Ko et al. and Zhou et al. use dynamical kinetic equations where the charm quark density in the medium is evolved in time using a gain term (secondary  $c\bar{c}$  production) and a loss term ( $c\bar{c}$  annihilation). The gain and loss terms are calculated at next-to-leading order (NLO) considering also  $2 \rightarrow 3$  and  $3 \rightarrow 2$  processes, respectively. It has been shown [96, 97] that the NLO cross sections are significantly larger than the LO ones. Therefore, we mainly focus on these predictions.

Figure 13 shows the results by Zhou et al. (left) and Ko et al. (right) for the time-dependence of the  $c\bar{c}$  rapidity density at mid-rapidity. The value at the initial time  $\tau_0$  corresponds to the initial hard-scattering cross section, which is taken from FONLL calculations [98] with a correction for PDF nuclear shadowing based on EKS98 [99] by Zhou et al. and from the PYTHIA 6 event generator [100] by Ko et al., with slightly different values. Both calculations show a rapid increase after  $\tau_0$  with a final value that is larger by up to 80% than the hard-scattering value. The increase obtained for top LHC energy is of about 15%. The predictions by BAMPS, with LO secondary charm production cross sections, show smaller increases of about 30% and 10% at FCC and LHC energies, respectively [93].

The thermal charm production would result in an enhancement of charmed hadron production at very low  $p_T$ , with respect to the expectation from binary scaling of the production in pp collisions, after correction for the nuclear initial-state effects (PDF modification), that should be measured using proton–nucleus collisions. This enhancement provides a handle on the temperature of the QGP.

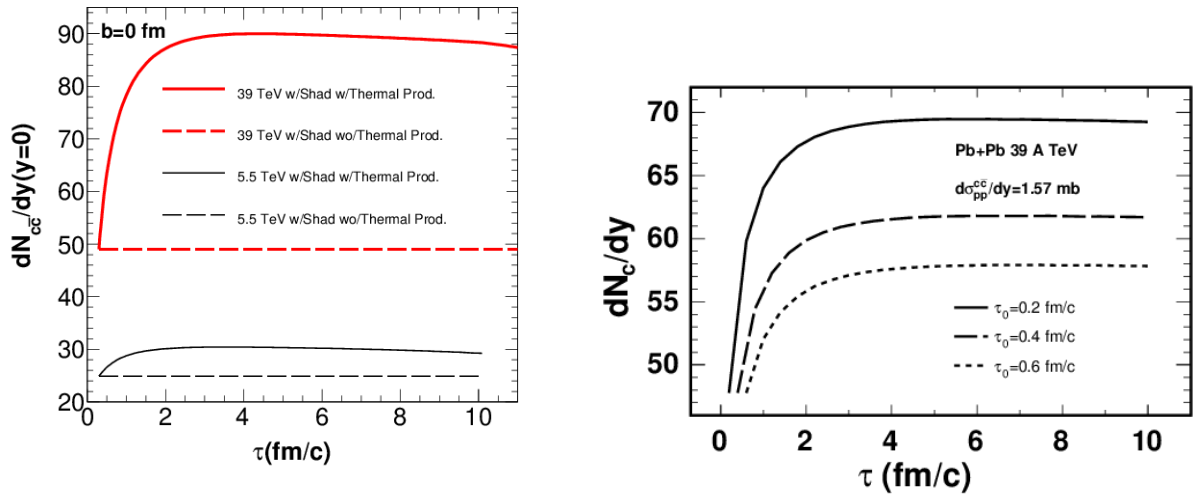


Fig. 13: Time-evolution of the charm and anti-charm quark pair yield (per unit of rapidity at midrapidity) for central Pb–Pb collisions at  $\sqrt{s_{NN}} = 39$  TeV: results by Zhou et al. [91] (also shown for  $\sqrt{s_{NN}} = 5.5$  TeV) and by Ko et al. [95] (the results by Ko et al. at 5.5 TeV are similar to those by Zhou et al.).

The abundance of charm quarks also has an effect on the QGP equation of the state, which includes a dependence on the number of degrees of freedom. Inclusion of the charm quark in the lattice QCD calculations results in a sizeable increase of  $P/T^4 \propto n_{d.o.f.}$  for temperatures larger than about 400 MeV. This was discussed in more detail in Section 3.3.

#### 4.2.2 $J/\psi$ enhancement from (re)generation

The measurements of the nuclear modification factor of  $J/\psi$  at the LHC [101–104] are described by models that include dissociation caused by colour-charge screening and a contribution of recombination (usually denoted (re)generation) from deconfined  $c$  and  $\bar{c}$  quarks in the QGP. In particular, this contribution describes the larger nuclear modification factor  $R_{AA}$  (smaller suppression) at the LHC with respect to RHIC, the larger  $R_{AA}$  at low  $p_T$  than at high  $p_T$  and the fact that  $R_{AA}(p_T > 0)$  at the LHC is almost constant from semi-peripheral to central collisions. There are essentially two classes of such models: the kinetic transport models [105, 106] calculate the time-evolution of the  $J/\psi$  yield using loss (dissociation) and gain (recombination) terms; the Statistical Hadronization Model [107] assumes complete dissociation of the initially-produced  $J/\psi$  mesons and computes the  $J/\psi$  yield considering statistical hadronization at the chemical freeze-out temperature.

In both approaches the (re)generation contribution is proportional to the rapidity density of  $c\bar{c}$  pairs in the QGP. It is, therefore, clear that this contribution is predicted to be much larger at FCC than LHC energies, as a consequence of a) the larger hard-scattering production cross section of  $c\bar{c}$  pairs and b) the possible sizeable thermal production, that we discussed in the previous Section. In particular, the hard-scattering production cross section is expected to increase by a factor about 2–2.5, depending on the considered nuclear modification of the PDFs (e.g. with FONLL calculations and EKS98 nuclear PDFs the factor is about 2, as shown in Fig. 13-left). Thermal production could lead to an additional increase by a factor about 1.5, as shown in the previous Section. This could lead to the observation of an enhancement of  $J/\psi$  production with respect to binary scaling of the yield in pp collisions, i.e.  $R_{AA} > 1$ , which would be a striking evidence of  $c\bar{c}$  recombination from a deconfined QGP.

Figure 14 shows the predicted  $J/\psi$   $R_{AA}$  at FCC energy, as obtained with the Statistical Hadronization Model (left) [108] and with the kinetic transport model by Zhou et al. (right) [91]. The Statistical

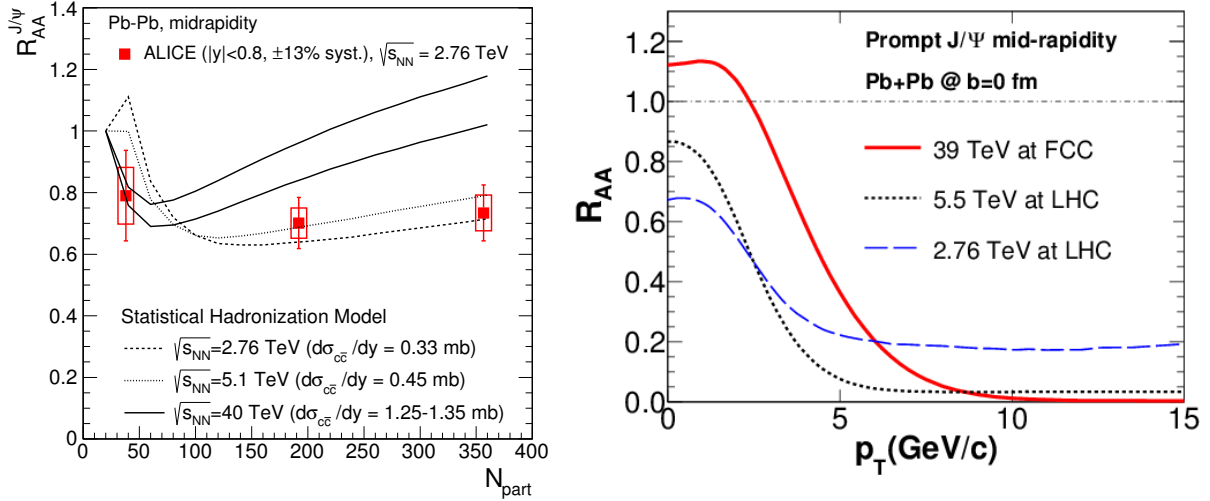


Fig. 14: Nuclear modification factor  $R_{AA}$  of  $J/\psi$  mesons at LHC and FCC energies. Left:  $R_{AA}(p_T > 0)$  as a function of centrality (number of nucleons participating in the collision) from the Statistical Hadronization Model [107, 108], without considering thermal charm production. Right:  $R_{AA}(p_T)$  in central collisions from the kinetic model by Zhou et al. [91].

Hadronization Model uses only the initial hard-scattering  $c\bar{c}$  cross section, without a thermal contribution. Even in this conservative scenario, the model predicts  $R_{AA}(p_T > 0) > 1$  in central collisions and an increase of about 40% with respect to top LHC energy. The kinetic model by Zhou et al. uses also the thermal  $c\bar{c}$  contribution as shown in Fig. 13 (left). This model predicts an enhancement at low  $p_T$  with  $R_{AA}$  values between 1.1 and 1.6, depending on the assumed nuclear modification of the PDFs.

### 4.2.3 Colour screening and (re)generation for $\Upsilon(1S)$ ?

The measurement of  $\Upsilon$  production would be particularly interesting at the high energies and temperatures reached at the FCC. The LHC data are consistent with a scenario in which the excited states 2S and 3S are partially or totally suppressed by colour screening, while the 1S, which is the most tightly bound state, has no or little direct melting. Its suppression by about 50% can be attributed to the lack of feed-down from the (melted) higher states (see e.g. Ref. [90] for a recent review). At FCC energies, on the one hand, the temperature could be large enough to determine a full melting even of the tightly-bound 1S state, on the other hand the large abundance of  $b\bar{b}$  pairs in the QGP could induce substantial  $\Upsilon$  (re)generation.

Results from a recent lattice-QCD calculation of spectral functions of the bottomonium states are shown in the left panel of Fig 15: they have been obtained for different, increasing temperatures, indicated in units of the critical temperature  $T_c$  for QGP formation ( $T_c \approx 155$  MeV). The suppression of the excited states is quite evident, as well as the persistence of the fundamental  $\Upsilon$  state, up to about twice the critical temperature. However, should this trend persist, one could anticipate a strong suppression of the fundamental state  $\Upsilon(1S)$  at FCC energies.

Accurate estimates of the bottomonium spectral functions up to higher temperature of 4–5  $T_c$  (i.e. 700–800 MeV) are needed to refine these expectations. For what concerns accuracy, while general, qualitative features of the results are robust, and all consistent with the sequential suppression scenario, quantitative results are very difficult to obtain. Systematic comparisons of different methods are now starting and will produce robust results soon [111–113]. This is especially likely for bottomonium, whose analysis can be done within the NRQCD (non-relativistic QCD) formalism, which remains valid in the range of temperatures explored at the FCC. A further challenge is posed by the high temperature

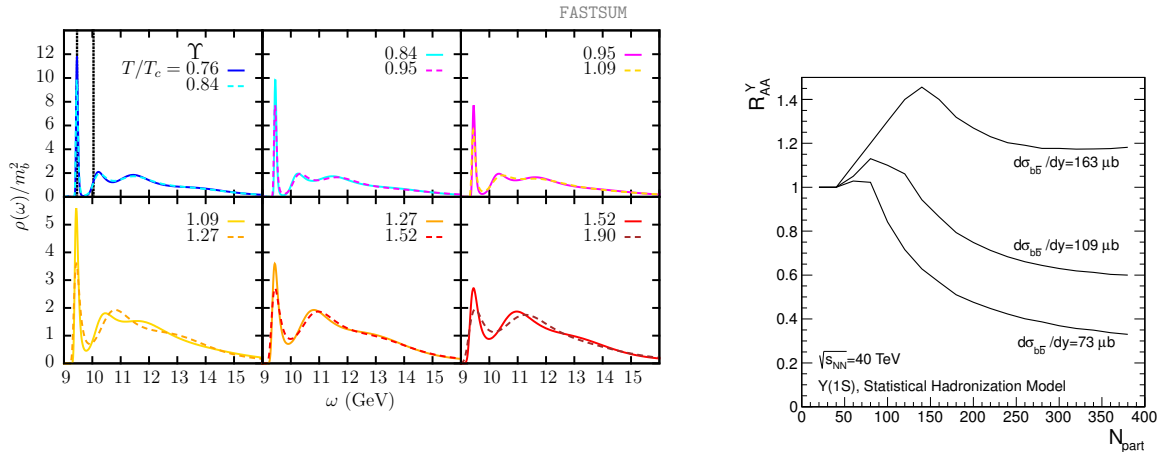


Fig. 15: Left: the spectral functions for the  $\Upsilon$  at different temperatures, obtained using the maximum entropy method, from Ref. [109]; the (leftmost) 1S state is progressively disappearing with increasing temperature. Right:  $R_{AA}$  for  $\Upsilon(1S)$  in Pb–Pb collisions at  $\sqrt{s_{NN}} = 40$  TeV as predicted by the Statistical Hadronization Model [107, 110].

reached at the FCC: on the lattice the temperature is realised as the inverse of the temporal extent of the box. Since many points are needed in the same temporal direction, high temperatures imply very fine lattices, hence a very large number of spatial points, needed to approximate an infinite spatial volume. To some extent this issue can be dealt with by use of asymmetric lattices, but such simulations remain computationally very demanding, and so far the temperatures have been limited to  $T < 2T_c$ . A very fascinating possibility is to be able to make contact with high temperature perturbation theory, matching lattice spectral functions at FCC temperatures with perturbative ones. In summary, an accurate calculation of bottomonium spectral functions at FCC temperatures requires advances in methodology, which are underway, to keep systematic errors under control, and a consistent investment in computer time to reach the required high temperatures.

Another important question is whether the  $\Upsilon$  states reach equilibrium with the surrounding QGP constituents. This is prerequisite for colour-screening to apply and it is implicitly assumed in the lattice QCD calculations of the spectral functions. Measurements of  $p_T$  distributions and elliptic flow of bottomonium states of  $B$  mesons would shed light on this aspect.

The possibly dramatic effect of (re)generation of bottomonia from  $b$  and  $\bar{b}$  quarks is illustrated by the prediction of the Statistical Hadronization Model [107, 110] for the  $R_{AA}$  of  $\Upsilon(1S)$  as a function of centrality, shown in the right panel of Fig. 15. Like for charmonium, this model assumes full melting of the initially-produced bottomonia and generation at the phase boundary. The predictions are calculated for values of  $d\sigma_{b\bar{b}}/dy$  in nucleon–nucleon collisions at  $\sqrt{s} = 40$  TeV ranging from 73 to 163  $\mu\text{b}$ , as obtained from the MNR NLO calculation [114] with usual parameter variations and without nuclear modification of the PDFs (nuclear shadowing of small- $x$  PDFs is expected to decrease the cross section by about 60–90%). These cross sections result in a total number of  $b\bar{b}$  pairs ranging from 15 to 40 in central Pb–Pb collisions. Depending on the value of the bottom cross section, the  $\Upsilon(1S)$   $R_{AA}$  in central Pb–Pb collisions is predicted to range between 0.3 and 1.2.

The role of the two effects —degree of survival of initial bottomonia and contribution of (re)generation— could be separated by means of precise measurements of the  $b\bar{b}$  cross section, an essential ingredient for (re)generation calculations, and of the  $B$  meson and  $\Upsilon$   $R_{AA}$  and elliptic flow  $v_2$ . The elliptic flow measurements would be particularly important because the regenerated  $\Upsilon$  states could exhibit a  $v_2$  such that  $0 < v_2^\Upsilon < v_2^B$ .

## 5 Small- $x$ and nPDF studies <sup>5</sup>

### 5.1 Small- $x$ and nPDF studies in hadronic p-A and A-A collisions

#### 5.1.1 Introduction: small $x$ and factorisation

More than 30 years ago, the idea of parton saturation was proposed [115, 116]: with BFKL [117, 118] linear evolution, the multiplication of partons with small values of momentum fraction  $x$  leads to parton densities so high that non-linear dynamics (gluon recombination, multiple scattering, . . .) becomes important. Such non-linear effects would tame the growth of parton densities from power-like to logarithmic, a phenomenon known as “saturation”.

In the case of proton–nucleus and nucleus–nucleus collisions, where nuclei with large mass number  $A$  are involved, the non-linear effects are enhanced by the larger density of gluons per unit transverse area of the colliding nuclei. The high density of gluons at small  $x$  and small  $Q^2$  induces a suppression of the observed hard scattering yields with respect to expectations based on a scaling with the number of binary nucleon–nucleon collisions. This reduction affects the kinematic region dominated by small- $x$  gluons: low transverse momentum  $p_T$  and forward rapidity  $y$ , since, at leading order, we have  $x \approx p_T \exp(-y) / \sqrt{s_{NN}}$ .

Data from Deeply Inelastic Scattering (DIS) experiments on nuclear targets were analysed in terms of nuclear Parton Density Functions (nPDFs) within the linear-evolution DGLAP framework. The results are normally reported as a modification ratio  $R_i$  of the parton distribution functions of the nucleon in the nucleus,  $f_i^A(x, Q^2)$ , with respect to those of the free nucleon,  $f_i^N(x, Q^2)$ ,

$$R_i^A(x, Q^2) = \frac{f_i^A(x, Q^2)}{f_i^N(x, Q^2)}, \quad (4)$$

where  $i = q_v, q_{sea}, g$  for valence quarks, sea quarks, and gluons. We have shadowing,  $R_g^A < 1$ , for  $x \lesssim 5 \times 10^{-2}$ . Significant differences between nPDFs of nuclei and the PDFs of free protons were found, both at high  $x$  (the ‘EMC effect’ [119]) and at low  $x$ , where a depletion is seen which is referred to as ‘nuclear shadowing’.

The usage of nPDFs allows some of the high-density effects at small  $x$  to be absorbed in the non-perturbative description of the PDFs within the framework of perturbative QCD collinear factorization. However, factorization is expected to break down when the gluon phase-space becomes saturated. In these conditions, in the collision with an incoming projectile parton, the partons in the target nuclear wave function at small  $x$  would act coherently, not independently as assumed with factorization. In the limit, they may form a Colour Glass Condensate (CGC, see e.g. Ref. [120] for a recent review): a system, that can be described in analogy to a spin glass, where gluons (colour charges) have a large occupation number, as in a condensate. The CGC theory relies on the resummation of powers of parton density.

The onset of saturation is usually discussed in terms of the so-called saturation scale  $Q_S^2$ , defined as the scale at which the transverse area of the nucleus is completely saturated and gluons start to overlap. This happens when the number of gluons,  $\sim A x g(x, Q_S^2)$ , multiplied by the typical gluon size,  $\sim 1/Q_S^2$ , is equal to the transverse area,  $\sim \pi R_A^2$ . Thus:

$$Q_S^2 \sim \frac{A x g(x, Q_S^2)}{\pi R_A^2} \sim \frac{A x g(x, Q_S^2)}{A^{2/3}} \sim A^{1/3} x^{-\lambda} \sim A^{1/3} (\sqrt{s_{NN}})^\lambda e^{\lambda y}, \quad \text{with } \lambda \approx 0.3. \quad (5)$$

$Q_S^2$  grows at forward rapidity, at high c.m.s. energy, and it is enhanced by a factor about  $6 \approx 200^{1/3}$  in the Au or Pb nucleus, with respect to the proton. Saturation affects the processes in the region  $Q^2 \lesssim Q_S^2$ , where gluon recombination dominates and factorization may start to become invalid. Figure 16 illustrates how saturation comes about in the high density regime, which can be achieved by decreasing the value of  $x$  (left panel) and/or increasing the mass number  $A$  of the colliding objects (i.e. using nuclei instead of nucleons; right panel).

<sup>5</sup>Editors: N. Armesto, D. d’Enterria, M. van Leeuwen

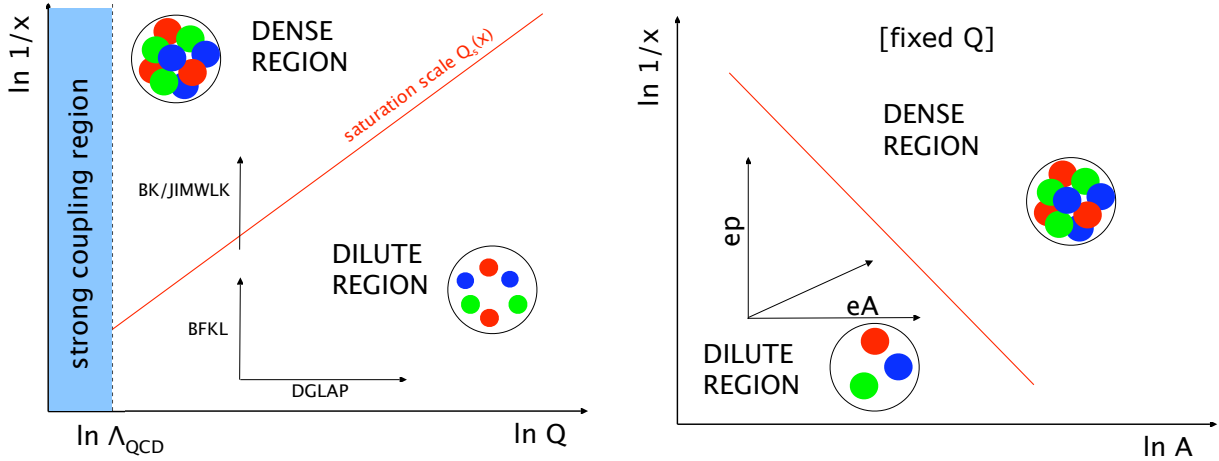


Fig. 16: Left: illustration of linear (dilute) and non-linear (dense) domains in the kinematic  $x$ - $Q^2$  plane,  $Q^2$  being the inverse squared transverse resolution, and the different evolution equations. Right: the same but in the  $x$ - $A$  plane. The red line indicates the separation between the dilute and the dense regimes, given by the saturation scale  $Q_S(x)$ .

There is an intrinsic relation between the parton density evolution that can be used in the dilute and dense regimes and the kind of factorisation that, if existing, should be employed to compute particle production in collisions involving hadrons and nuclei. In the dilute regime, collinear [121] or  $k_T$  [122–125] factorisations can be applied in the hard and semihard regions, respectively. The corresponding evolution equations are DGLAP [126–129] and BFKL. In the dense regime, the situation is not yet clear. For scattering of a dilute projectile on a dense target, single inclusive hadron production has been computed at NLO [130, 131] and the corresponding JIMWLK evolution equation, an infinite hierarchy of coupled evolution equations for traces of Wilson lines, is also known at NLO [132–134]<sup>6</sup>.

At present, no conclusive evidence has been provided for the existence of saturation, although a number of observations are consistent with expectations from gluon saturation, as discussed in the following.

- i. The degrading quality of DGLAP fits when HERA data at moderate  $Q^2$  (which by DIS kinematics is linked to small  $x$ ) are included in the fit [138], while fits done within saturation do not show such degradation [139]; the degradation, however, is quantitatively small and the freedom in the choice of initial conditions and of the scheme for treating heavy flavours still sizeable.
- ii. The success in describing the factorisation between the energy and centrality dependencies of charged particle multiplicities at mid-rapidity [12]; this observable is likely to be affected by final-state collective and non-perturbative effects that are not included in saturation models.
- iii. The ridge structure (two-particle correlations that are independent of rapidity and strongly collimated in azimuth at 0 and 180 degrees) observed in pp and p–Pb collisions at the LHC that can be explained in CGC-type models [140]; yet, the explanation is not unique and the possibility of final-state collective effects in such small systems is currently under debate.
- iv. The suppression of inclusive particle production [141, 142] and the reduction of back-to-back correlated yield at forward rapidities in d–Au collisions at RHIC [143–146]; still, the experimental data lie so close to the kinematical limit that tiny additional effects may affect their interpretation, and at RHIC the probed values of  $x$  are not that small.

Note that points (i) and (ii) are related to the fact that the geometric scaling that experimental data

<sup>6</sup>The pathologies of this equation, related to those of NLO BFKL, are understood and several solutions involving resummation have been proposed [135–137].

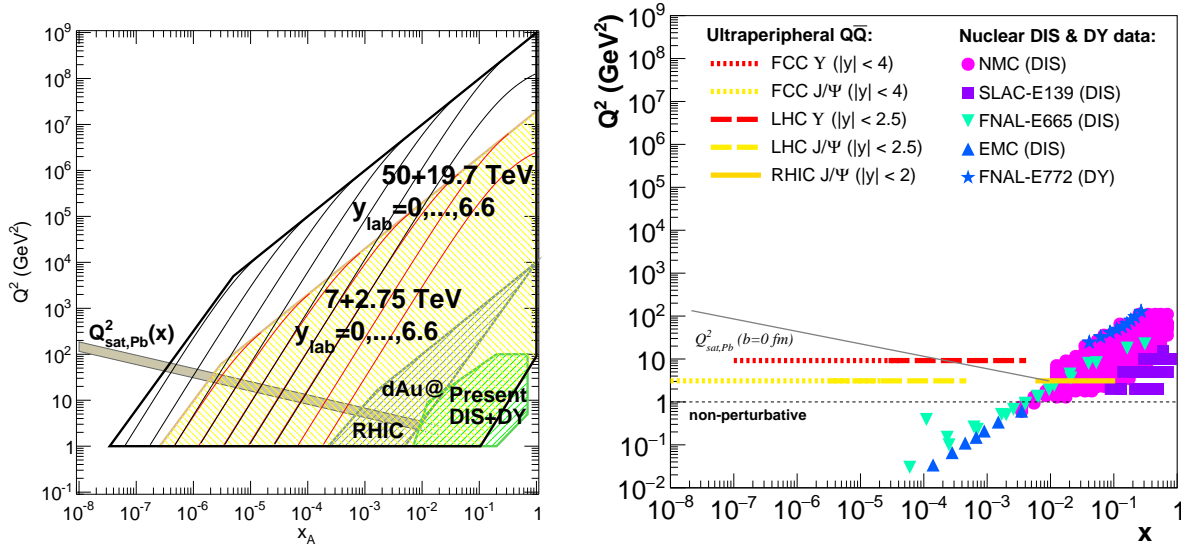


Fig. 17: Regions of the  $x$ – $Q^2$  plane covered with nuclear DIS and Drell-Yan data (left) and exclusive  $J/\psi$  and  $\Upsilon$  photoproduction in ultraperipheral ion collisions (right). The left panel shows the range covered in nuclear DIS and DY experiments (light green), and in collisions involving nuclei at RHIC (dark green) and at the LHC (yellow), and accessible at the FCC (black). For p–Pb collisions at the LHC and the FCC, thin lines correspond to different rapidities in the laboratory frame  $y_{lab} = 0, 1, 2, 3, 4, 5, 6$  from right to left, with the left edge defined by  $y_{lab} = 6.6$ . Values of the saturation scale  $Q_S^2(x)$  for  $A = 208$  are shown for illustration.

show [147–149] finds a natural explanation in saturation models, but it is also shown by e.g. DGLAP dynamics [150].

In order to firmly establish the existence of this new high-energy regime of QCD and clarify the validity of the different approaches to factorisation and evolution, new kinematic regions must be explored using higher collision energies in order to have a large lever arm in  $Q^2$  in a region that, while perturbative, lies inside the saturation domain. The FCC offers such energies and the possibility of combining proton and nuclear beams, as required for a detailed understanding of the mechanism underlying saturation. In Fig. 17 the coverage of the  $x$ – $Q^2$  plane of present facilities (nuclear DIS and Drell-Yan experiments, proton–nucleus colliders RHIC and the LHC in the left panel, and ultra-peripheral nucleus–nucleus collisions at RHIC and LHC using exclusive quarkonium production in the right panel) is compared with that of p–Pb collisions at FCC energies (proton momentum of 50 TeV and Pb momentum per nucleon of 19.7 TeV) and photon–Pb collisions at FCC energies (the latter will be discussed in Section 5.2). In the left panel, the coverage is calculated for an experimental acceptance reaching rapidity in the laboratory frame  $y_{lab} \approx \eta = 6.6$ . The diagonal lines represent constant  $y_{lab}$  values 0, 1, ..., 6. The estimate of the saturation scale  $Q_S^2(x)$  for Pb is also shown. The figure shows that coverage below the saturation scale is much larger at FCC than at LHC, reaching for example down to  $x$  values well below 10<sup>-6</sup> and  $Q^2$  values of 10–20 GeV<sup>2</sup> at a rapidity of 5, which could be well within reach of an experiment at the FCC.

Establishing the dynamics at small  $x$  and the type of factorisation to be used to compute particle production will constrain the initial conditions for the collective behaviour of the medium produced in high-energy nucleus-nucleus collisions [151]. It will also clarify the dynamics leading the approximate thermalisation or isotropisation [152] that allows the use of relativistic hydrodynamics to describe such collectivity. Note that the extraction of properties of the QGP is significantly affected by both the initial conditions and the pre-equilibrium dynamics, see e.g. [153]. The need for more precise information

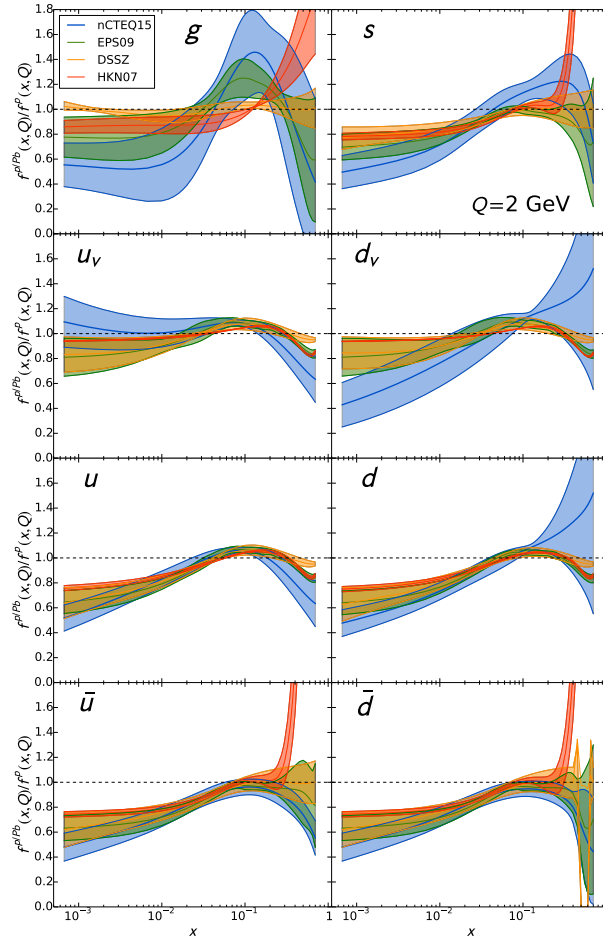


Fig. 18: Comparison of the nuclear modification factor (defined as the ratio of a given parton density in a bound proton over that in a free proton) for different parton species at  $Q^2 = 4 \text{ GeV}^2$  for a Pb nucleus. Lines correspond to DGLAP analyses at NLO: EPS09 [88], HKN07 [155], DSSZ [156] and nCTEQ15 [157]. Bands correspond to the uncertainty in the respective Hessian analyses. Taken from [157].

about the partonic structure of nuclei also holds for hard processes, where the lack of knowledge of nPDFs, illustrated in Fig. 18, compromises the precision for extraction of transport properties of the QGP from the comparison of theoretical calculations to data on hard probes. The information that is coming from p–Pb collisions at the LHC has not yet provided large constrains, see [154].

As a final remark, we should indicate that although important progress has been achieved lately in advancing calculations of different observables in the CGC, several aspects are still missing. For example, the resummed evolution equations discussed previously have not been fully used although the NLO impact factor for DIS is available [158, 159]; the calculation of many single-inclusive observables apart from hadrons is still missing, see [151]; much progress is undergoing on two-particle correlations to understand the origin of azimuthal asymmetries and the ridge in pp and p–A collisions [160].

### 5.1.2 Possible signatures of the CGC using forward-rapidity hadrons and photons in p–Pb collisions

The simplest way to probe the gluon density in protons and nuclei is by studying inclusive particle production. In particular, nuclear modification ratios  $R_{pPb}$  are used to explore the nuclear modification of parton densities and saturation effects due to the larger density of gluons in nuclei than in protons

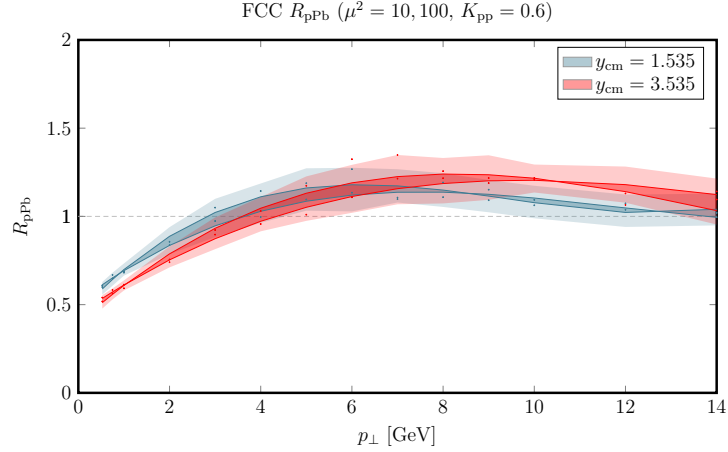


Fig. 19:  $R_{pPb}$  as a function of  $p_T$  for charged hadrons at the FCC for two different rapidities [161].

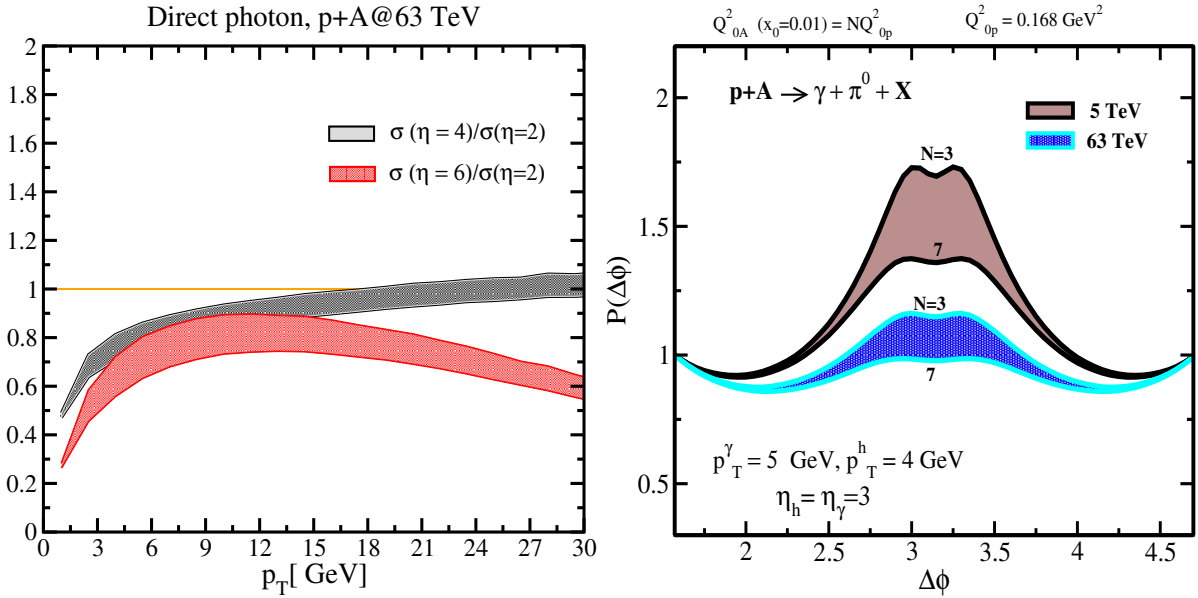


Fig. 20: Left: Ratio of direct photon spectra at forward ( $\eta = 4, 6$ ) over central ( $\eta = 2$ ) rapidities obtained in the CGC formalism in minimum-bias p+A collisions at the FCC [162, 163]. Right: Normalized azimuthal correlation of prompt photon and  $\pi^0$  as a function of the angle between the produced prompt photon and  $\pi^0$  at forward rapidity obtained in the CGC formalism at the LHC and the FCC in minimum-bias p+A collisions [162, 163]. The bands show the uncertainty related to the scaling of the initial saturation scale in nuclei.

included in the CGC. The nuclear modification factor  $R_{pPb}$  is defined as:

$$R_{pPb} = \frac{d^2\sigma/dp_T dy|_{pPb}}{A d^2\sigma/dp_T dy|_{pp}}, \quad (6)$$

i.e. by taking the  $p_T$ -differential cross section measured in p–Pb collisions and dividing by that in pp collisions at the same energy, multiplied by the Pb mass number  $A$ . If the production in p–Pb follows a scaling with the number of binary nucleon–nucleon collisions, then  $R_{pPb} = 1$ .

It can be seen from Fig. 17 (left) that even measurements at mid-rapidity and  $p_T < 10$  GeV/ $c$

cover the saturation region with  $Q \approx p_T$  and  $x$  in the range  $10^{-5}$ – $10^{-4}$ , which is at much lower  $x$  and therefore larger gluon density than measurements at the LHC. A forward measurement, for example at  $\eta \approx 4$ , would be even more interesting, as it covers  $x \approx 10^{-6}$ .

To illustrate how future measurements at the FCC are sensitive to gluon saturation, we present a few selected calculations. It is, however, important to realise that there are significant uncertainties in these calculations, since the currently available measurements do not provide precise constraints for the saturation scale and some of the model details, such as the dipole cross section parametrisation. This uncertainty is closely related to our earlier statement that the CGC or saturation effects have not been unambiguously identified yet. In addition to this, the calculations for FCC energies require a large extrapolation of available constraints from data at  $x \approx 10^{-4}$ – $10^{-3}$  to lower  $x$ . Measurements at the larger energies available at the FCC are the only possibility to find out how the gluon density at small  $x$  behaves in Nature.

Figure 19 shows the expected nuclear modification factor for charged particles at two different rapidities, computed using the state-of-the-art NLO calculations available [130, 131, 161]. A modest increase of the suppression at low  $p_T \lesssim 4$  GeV/ $c$  compared to the expectation for LHC is visible<sup>7</sup>. Figure 20 (left) shows an example of the expected direct photon production in the CGC framework at LO approximation in the hybrid approach using the rcBK formalism. The ratios of particle production at different pseudorapidities explicitly probe the evolution of the gluon density in  $x$ . A clear suppression of direct photon production at moderate  $p_T \lesssim 6$  GeV/ $c$  is visible in the figure. At higher  $p_T$ , a modest suppression by about 10-20% is still visible. When comparing Fig. 19 and the left panel of Fig. 20, a larger effect of gluon saturation is seen for direct photon production. Such a difference between charged hadrons and photons could be qualitatively expected<sup>8</sup> since hadron production is sensitive to both the quark and gluon densities, while the dominant production mechanism for direct photons is quark–gluon Compton scattering, which is directly sensitive to the gluon density [164].

Measurements of dijets or back-to-back two-particle correlations offer more potential to experimentally constrain the probed  $x$  region, in particular at low  $p_T$  where multiple-interaction effects may also play a role. Color Glass Condensate models make a specific prediction that the recoil jet is suppressed, because (mini-)jets can be produced by scattering a parton off the color field in the nucleus where the recoil momentum is carried by multiple gluons, unlike in a standard (semi-)hard 2-to-2 scattering where all the recoil momentum is carried by a single jet [145, 162, 165]. A suppression of the recoil yield has been observed at lower energies at RHIC [144], close to the kinematic limit, where suppression of the yield by multiple scattering or energy loss in the initial state may also be important [166, 167]. At the FCC, such measurements can be performed over a broad kinematic range in both  $x$  and  $Q^2$ , which will allow to disentangle different effects.

The potential of recoil measurements at FCC is illustrated in Fig. 20 (right), which shows the azimuthal distribution of  $\pi^0$  recoiling from a prompt photon trigger particle, both at forward  $\eta = 3$ . The double-peak structure on the away side is a characteristic prediction of CGC calculations [162, 168]. The recoil signal at FCC energies is smaller than at the LHC due to the larger gluon density at lower  $x$ .

The recoil suppression can be also be explored using dijets at forward rapidity [169, 170]. Figure 21 shows the expected broadening of the  $\Delta\phi$  distribution in p–Pb versus pp collisions at the FCC (left panel, the p–Pb curve as been divided by  $A$ ), as well as the expected nuclear modification factors for dijets as a function of the transverse momentum of the leading jet  $p_{T,\text{jet}}$ , in the recoil region (middle panel, for  $\Delta\phi \approx \pi$ ) and in the “underlying event” region (right panel, for  $\Delta\phi$  away from  $\pi$ ). Both jets have rapidity  $3.5 < y_{\text{jet}} < 4.5$ . A clear suppression is visible –strongest in the recoil region– which persists

<sup>7</sup>The magnitude of the effect is very sensitive to the specific form employed for evolution and to whether the calculation is done at LO or at NLO. Furthermore, the formalism employed in these calculations is expected to work better in p–A than in pp. This fact would amount to a sizeable uncertainty in the ratio.

<sup>8</sup>Nevertheless, it must be kept in mind the existence of sizeable uncertainties due to differences in the order in perturbation theory and in phenomenological details between both calculations.

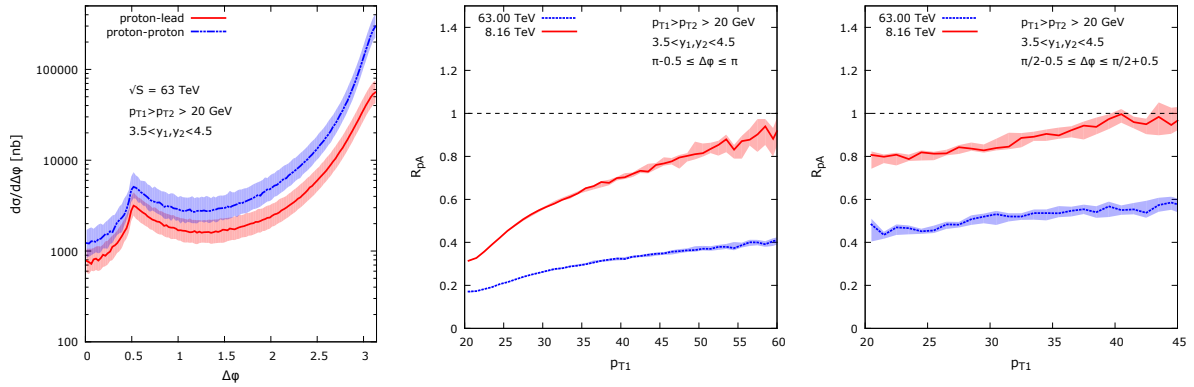


Fig. 21: Dijet yield suppression [169]. Left: azimuthal angle distribution in pp and p–Pb collisions (p–Pb curve divided by  $A$ ). Middle and right: ratio of dijet yield in p–Pb and pp collisions as a function of  $p_{T,\text{jet}}$  for jet pairs with  $p_{T,\text{jet}} > 20$  GeV/ $c$  and  $3.5 < y_{\text{jet}} < 4.5$  at LHC and FCC energies, for back-to-back pairs (right panel) and pairs in the underlying even region  $\Delta\phi \approx \pi$  (middle panel).

to much larger  $p_{T,\text{jet}} > 100$  GeV/ $c$  than at LHC, where the suppression is small at  $p_{T,\text{jet}} \approx 50$  GeV/ $c$ . These calculations clearly show that the effects of saturation are expected to persist to high  $p_T$ , much larger than the saturation scale, as long as the transverse momentum imbalance of the dijet system does not exceed a few times  $Q_S$ . We note that an optimistic scenario was considered for the ratio  $Q_{S,\text{Pb}}/Q_{S,\text{P}}$ , whose value at FCC energies is a bit uncertain.

### 5.1.3 Constraining nuclear parton densities at large $Q^2$

#### 5.1.3.1 Constraining nPDFs with $W$ and $Z$ production in p–Pb collisions

The production of on-shell  $W$  and  $Z$  bosons at hadron colliders probes the PDFs at large  $Q^2 \sim M_{W,Z}^2 \sim 10^4$  GeV $^2$  and at momentum fractions around  $x_{1,2} = (M_{W,Z}/\sqrt{s}) e^{\pm y}$  such that an order of magnitude increase in  $\sqrt{s}$  from the LHC to the FCC extends the small- $x$  reach similarly by an order of magnitude. In addition, the cross sections are larger and the rapidity distributions broader such that these cross sections could be more easily measured (with wide-enough detectors) in a larger phase space than at the LHC. The increase of the production cross sections (computed at NLO by MCFM [171] using CT10NLO proton PDFs [172]) from RHIC energies to the FCC is illustrated for the case of  $Z$  production in the left-hand panel of Fig. 22. Due to the large FCC energy, the expectations are that within most of the experimental rapidity coverage (here assumed  $|y_{\text{FCC}}| < 4$ ) the cross sections are suppressed due to shadowing in nuclear PDFs, whereas at the LHC (here,  $|y_{\text{LHC}}| < 3$ ) the probed region is on both sides around the anti-shadowing peak. This is sketched in the right-hand panel of Fig. 22, which shows the approximate  $x$  intervals probed at the LHC and FCC including the average nuclear modifications of sea and valence quarks according to EPS09 nuclear PDFs [88] at scale  $Q^2 = (100 \text{ GeV})^2$ .

Estimates of the rapidity distributions in p–Pb collisions at the FCC with and without nuclear shadowing are shown in Fig. 23 for  $W$  (left-hand panel) and  $Z$  production (right-hand panel). As expected, the predictions based on EPS09 nuclear effects show suppression down to  $y \sim -3$ . The uncertainties on the size of the nuclear effects might be significant. This is caused by the simplified functional forms assumed for small- $x$  distributions (for the lack of experimental high- $Q^2$  data at small  $x$ ), but also by the fact that the partonic channels that contribute at the FCC are more diverse. Indeed, the scatterings between heavier sea quarks (e.g.  $c\bar{s}$  and  $s\bar{c}$  in  $W$  production,  $s\bar{s}$  and  $c\bar{c}$  in  $Z$  production) play a significant role at the FCC energies, while the currently available nuclear PDFs analyses have not extensively tuned e.g. the  $s$ -quark distribution.

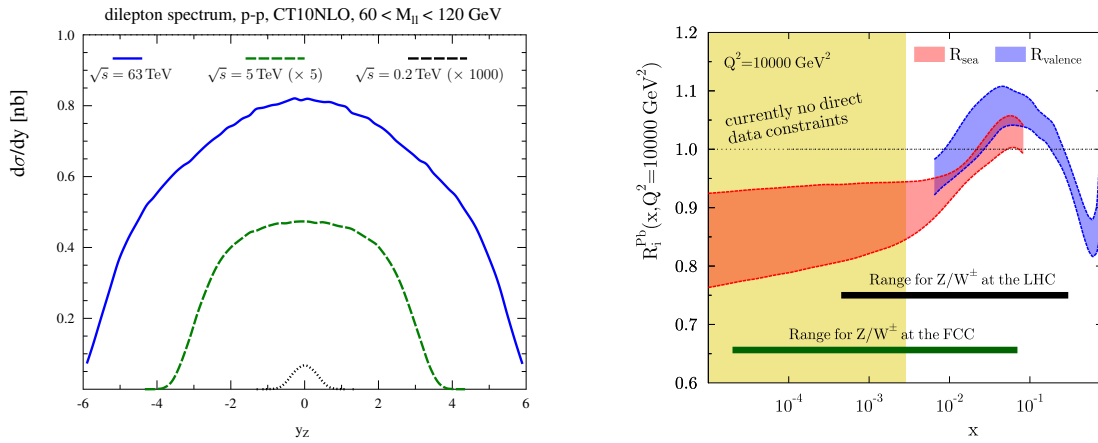


Fig. 22: Left: Rapidity distributions of high-mass dilepton pairs in pp collisions computed at  $\sqrt{s} = 200$  GeV (black dotted, multiplied by 1000),  $\sqrt{s} = 5$  TeV (green dashed, multiplied by 5), and  $\sqrt{s} = 63$  TeV (blue continuous). Right: The average EPS09 nuclear modifications for valence (violet) and sea (red) quarks at  $Q^2 = (100 \text{ GeV})^2$ . The  $x$  regions probed by on-shell  $Z$  and  $W$  production at the LHC and FCC are indicated.

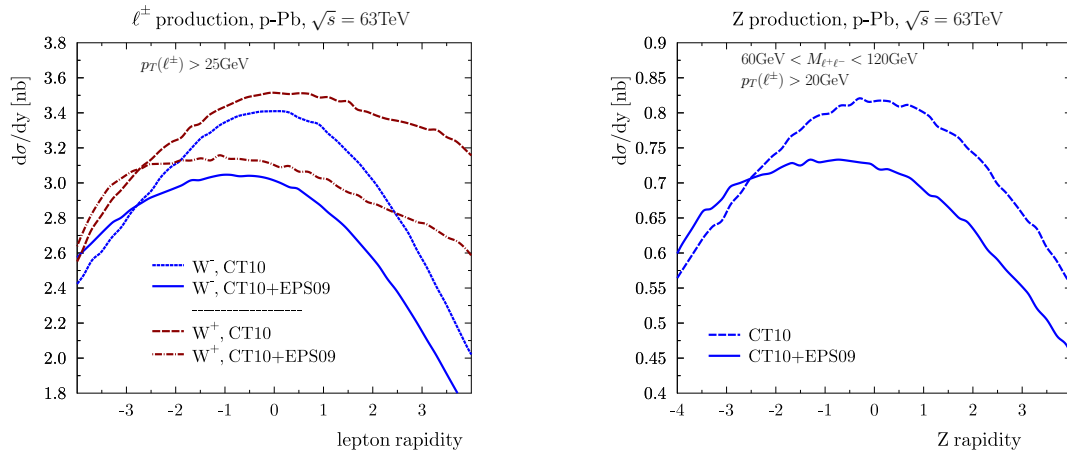


Fig. 23: Left: The rapidity distributions of charged leptons ( $\ell^+$  in dark red,  $\ell^-$  in blue) from  $W$  decays in p-Pb collisions at  $\sqrt{s_{\text{NN}}} = 63$  TeV with (continuous, dashed-dotted) and without (short dashed, long dashed) EPS09 nuclear modifications. Right: As the left-hand panel, but for dilepton pairs from  $Z$  decays.

### 5.1.3.2 Constraining $nPDFs$ with top-quark pair-production

At hadron colliders, top quarks are produced either in pairs, dominantly through the strong interaction, or singly through the weak interaction. At the energies considered here, the dominant production channels, as obtained at NLO accuracy [86] with the MCFM code [171], are (Fig. 8 left): (i) gluon-gluon fusion,  $g g \rightarrow t\bar{t} + X$ , contributing by 80–95% to the total pair production (the remaining 5–20% issuing from quark-antiquark annihilation), (ii)  $t$ -channel single-top electroweak production  $q b \rightarrow q' t + X$  (the  $s$ -channel process, decreasing with energy, amounts to 5–1.5% of the total single- $t$  cross section), and (iii) associated top plus  $W$ -boson,  $g b \rightarrow W t + X$ , production (increasing with energy, it amounts to 25–50% of the  $t$ -channel process). In pp collisions at the LHC, top-quark production is already being used as a high-precision tool to constrain the gluon distribution function in the proton at next-to-NLO

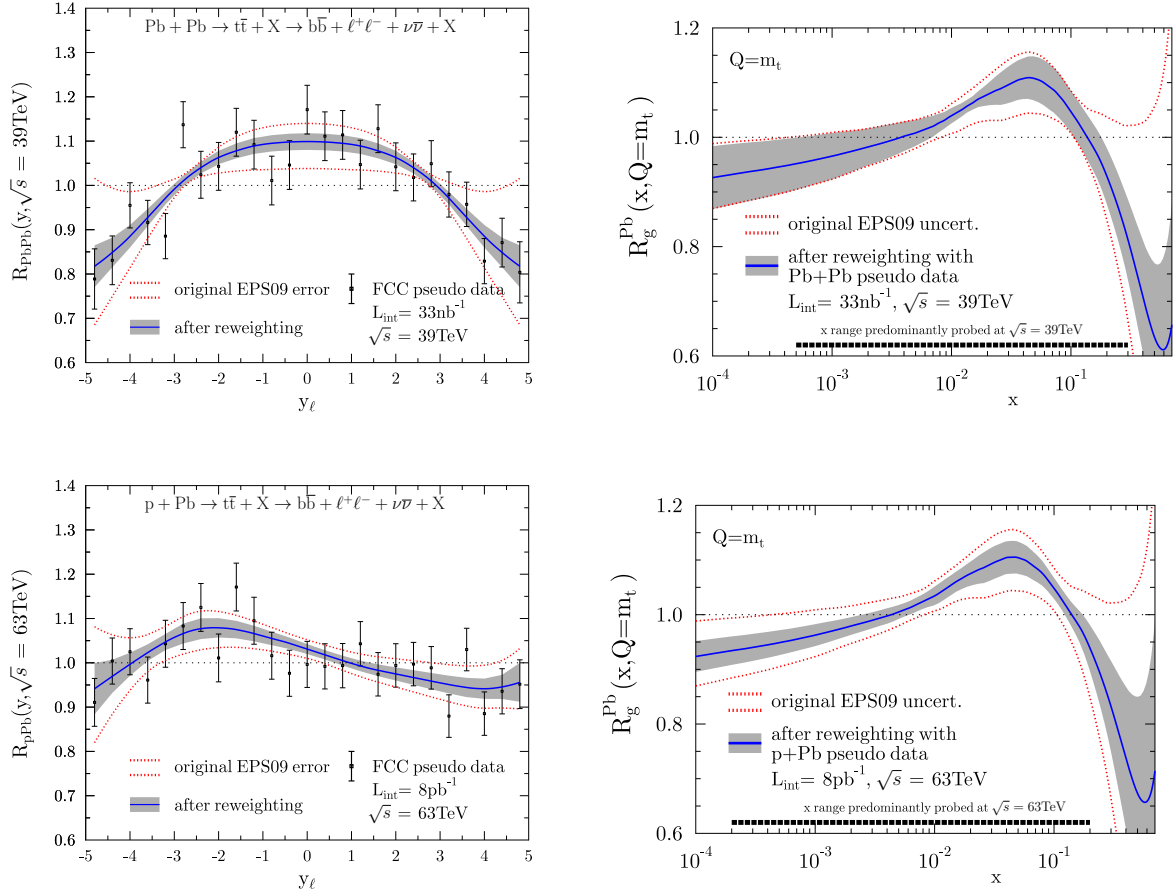


Fig. 24: Left: FCC pseudodata for nuclear modification factors expected in Pb–Pb (upper panel) p–Pb (lower panel). Right: Original EPS09 gluon nuclear modification at  $Q = m_{t\text{top}}$  and estimated improvement in it obtained by reweighting using the Pb–Pb (upper panel) and p–Pb (lower panel) FCC pseudodata. The figures are adapted from Ref. [86].

(NNLO) accuracy [173]. At the energies attainable in p–Pb and Pb–Pb collisions at the FCC, the same studies would be feasible also for the nuclear PDFs. The top-quark, the only coloured particle that decays before its hadronization, decays almost exclusively into a  $t \rightarrow W b$  final-state with a nearly 100% branching ratio, and the  $W$  can themselves decay leptonically ( $t \rightarrow W b \rightarrow \ell \nu$ ,  $b$ , one-third of the times) or hadronically ( $t \rightarrow W b \rightarrow q\bar{q} b$ , two-thirds of the times). Its short lifetime,  $\tau_0 = \hbar/\Gamma_t \approx 0.1$  fm/ $c$ , implies that most of the (non-boosted) top quarks will decay before any significant gluon radiation and before the formation of any strongly-interacting medium (typical QGP formation times are  $\mathcal{O}(1$  fm/ $c$ )). To avoid any potential bias from parton energy loss effects on the top-decay quarks, one can study nPDFs by analysing the distributions of the (isolated) charged leptons ( $\ell = e, \mu$ ) in events clearly identified as containing top-quarks. To estimate the impact that the FCC would have on nuclear gluon densities the computed top-pair cross sections in pp, p–Pb and Pb–Pb with analysis cuts (see discussion for Table. 3) have been binned in the rapidity  $y_\ell$  of the decay leptons. In the p–Pb and Pb–Pb cases the calculations include EPS09 nuclear modifications [88] for PDFs.

The left panels of Fig. 24 show pseudodata distributions for the expected nuclear modification factors  $R_{pPb}(y_\ell) = d\sigma_{pPb}(y_\ell)/(A d\sigma_{pp}(y_\ell))$  and  $R_{PbPb}(y_\ell) = d\sigma_{PbPb}(y_\ell)/(A^2 d\sigma_{pp}(y_\ell))$  in minimum-bias collisions (Table 3). The assigned uncertainties include statistical errors based on the luminosities of  $8 \text{ pb}^{-1}$  and  $33 \text{ nb}^{-1}$  for p–Pb and Pb–Pb, a 5% uncorrelated systematic uncertainty, and an overall 5%

normalization error. The effects these pseudodata would have in EPS09 global fit of nuclear PDFs are quantified via the Hessian reweighting technique [174]. The expected impact of these measurements on gluon PDF nuclear modification factor  $R_g^{\text{Pb}}(x, Q^2) = g^{\text{Pb}}(x, Q^2)/g^{\text{p}}(x, Q^2)$  at  $Q^2 = m_{\text{top}}^2$  are shown in Fig. 24 (right). The uncertainties on the nuclear gluon PDF are observed to reduce by more than 50% in some regions of  $x$ .

### 5.1.3.3 Constraining nPDFs with dijets in p–Pb collisions

Dijet measurements at LHC have proven to be sensitive to the shadowing and anti-shadowing of quarks in nPDFs. A shift of the average rapidity of the dijet system for jets with  $p_{\text{T}} > 100 \text{ GeV}/c$  was observed in p–Pb collisions [175]. This shift is consistent with the expectations from (small) modifications due to nuclear parton density functions. Precision measurements of this type can thus improve our knowledge of nuclear PDFs in regions that are not well constrained by existing measurements [176].

### 5.1.4 Relation with the proposed electron–hadron colliders

Electron–proton/ion colliders at high energies, while having smaller kinematic coverage with respect to hadronic colliders, offer the advantage of fully constrained kinematics and a much cleaner experimental environment. It is widely recognized that the physics programs at electron–proton/ion colliders and hadron colliders are complementary, and that the precise data obtained from electron–proton/ion colliders can further enhance the physics opportunities of hadron colliders. In the context of the Electron-Ion Collider in the USA [177], that is already included in the NSAC 2015 Long Range Plan, this general argument has been substantiated in detail and the synergies between the ongoing RHIC program and an EIC project are documented. In the context of the LHC hadron collider program, the Large Hadron Electron Collider LHeC [178] and the FCC-he are proposed facilities to provide electron–proton/ion

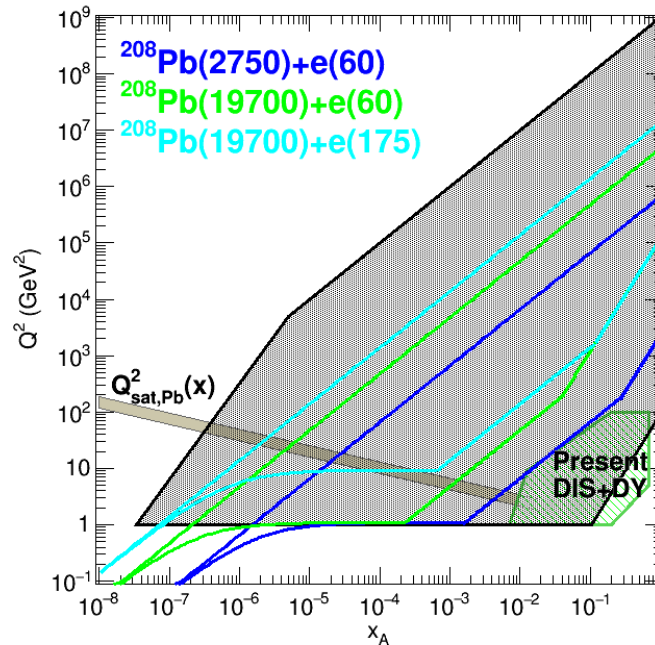


Fig. 25: Regions in the  $x - Q^2$  plane already studied in present DIS and DY experiments (light green), and accessible at the LHeC (dark blue) and different versions of the FCC-he (light green and light blue), and at the FCC p–Pb (black). Values of the saturation scale are shown for illustration.

collisions in the TeV regime in the centre-of-mass. With the larger kinematic reach at the TeV scale, these latter projects are well-positioned to reach conclusive evidence for the existence of a new saturated regime of QCD. For that, the electron beam from an accelerator of about 60 GeV would collide with the LHC or FCC proton or heavy-ion beams. The kinematic coverage of such machines is given in Fig. 25. They are clearly complementary with the FCC-hh as they should provide a precise knowledge on the partonic structure of nucleons and nuclei and on the small- $x$  dynamics. Such knowledge will allow QCD studies at hadronic colliders, both in pp and in p-A and A-A, to become rid of several of their most important uncertainties, as PDFs and the values of  $\alpha_s$  and of heavy quark masses. They will also set the benchmark for precision factorisation tests.

## 5.2 Exclusive photoproduction of heavy quarkonia

All charges accelerated at high energies generate electromagnetic fields which, in the equivalent photon approximation (EPA) [179–181], can be considered as quasireal  $\gamma$  beams of very low virtuality  $Q^2 < 1/R^2$ , where  $R$  is the radius of the charge, i.e.,  $Q^2 \approx 0.08 \text{ GeV}^2$  for protons ( $R \approx 0.7 \text{ fm}$ ), and  $Q^2 < 4 \cdot 10^{-3} \text{ GeV}^2$  for nuclei ( $R_A \approx 1.2 A^{1/3} \text{ fm}$ , for mass number  $A > 16$ ). The photon spectra have a typical  $E_\gamma^{-1}$  power-law fall-off up to energies of the order of the inverse Lorentz-contracted radius,  $\omega_{\text{max}} \approx \gamma_L/R$ , where  $\gamma_L = \sqrt{s_{\text{NN}}}/(2 m_p)$  is the Lorentz factor of the proton or ion. Given that the photon flux scales with the square of the emitting charge ( $Z^2$ ), the emission of quasireal photons from the Pb-ion is strongly enhanced compared to that from proton (or electron) beams. The basic characteristics of photon-induced interactions in “ultraperipheral” collisions (UPCs) of proton [182] and lead (Pb) beams [183] —occurring at impact parameters larger than the sum of their radii and thereby largely suppressing their hadronic interaction— at the FCC are listed in Table 4.

Exclusive photoproduction of vector mesons in UPCs of protons or ions —where an exchanged quasireal photon “materializes” into a  $Q\bar{Q}$  bound state after interacting with the gluon field of the “target” proton (ion), without breaking the colour flow and thereby leaving intact the incoming hadrons— is depicted in Fig. 26 (left). Since in such processes the gluon couples *directly* to the  $c$  or  $b$  quarks and the cross section is proportional to the gluon density *squared*, they provide a very clean probe of the gluon density in the “target” hadron [184–186], with the large mass of the  $J/\psi$  and  $\Upsilon$  mesons providing a hard scale for pQCD calculations [187, 188]. Exclusive quarkonia photoproduction was measured in electron-proton collisions at HERA [189–192], and in ultraperipheral proton–proton and nuclear collisions at the LHC [193–197].

Their measured cross sections rise steeply with photon-hadron centre-of-mass energy  $W_{\gamma p}$ , following a power-law dependence  $W_{\gamma p}^\delta$  with  $\delta = 0.7\text{--}1.2$  [190, 191], reflecting the steep rise in the gluon density in the hadrons at increasingly lower values of parton fractional momentum  $x$  (Fig. 26, right). At the FCC,  $J/\psi$  and  $\Upsilon$  photoproduction will reach photon-hadron c.m. energies as large as  $W_{\gamma p} \approx 10 \text{ TeV}$ , and thereby probe the gluon density in the proton and ion in an unexplored region values of Bjorken- $x$  as

Table 4: Basic characteristics of UPCs at the FCC-hh: (i) nucleon-nucleon c.m. energy,  $\sqrt{s_{\text{NN}}}$ , (ii) beam Lorentz factor,  $\gamma_L$ , (iii) maximum photon energy in the c.m. frame,  $\omega_{\text{max}}$ , and (iv) maximum  $\gamma$ -proton,  $\gamma$ -ion c.m. energy,  $W_{\gamma p, \gamma A}^{\text{max}}$ .

System	$\sqrt{s_{\text{NN}}}$ (TeV)	$\gamma_L$ ( $\times 10^3$ )	$\omega_{\text{max}}$ (TeV)	$W_{\gamma p, \gamma A}^{\text{max}}$ (TeV)
pp	100	53.0	17.6	10.0
p-Pb	63	33.5	0.95	10.0
Pb-Pb	39	21.0	0.60	7.0

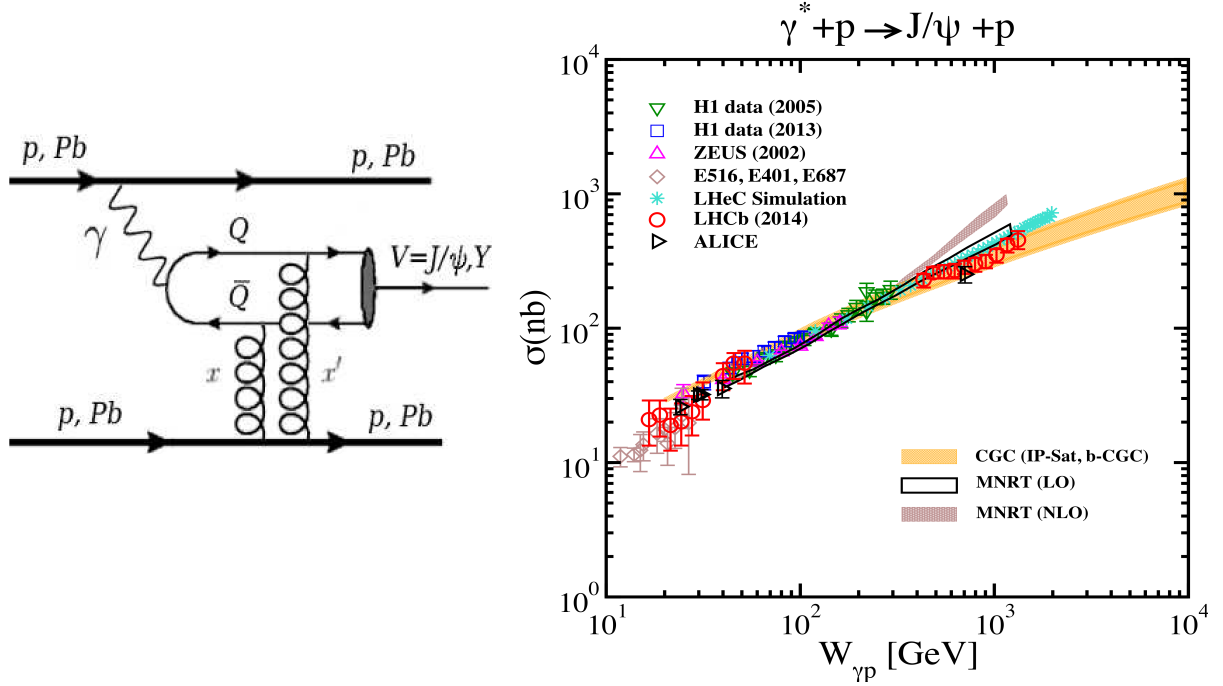


Fig. 26: Left: Diagram representing exclusive quarkonia photoproduction in UPCs. Right: Dependence of the exclusive  $J/\psi$  photoproduction cross section on the photon-hadron c.m. energy in the regions covered by HERA, LHC and future FCC studies [198].

low as  $x \approx M_{J/\psi, \gamma}^2 / W_{\gamma p}^2 \approx 10^{-7}$ , at least two orders of magnitude below the range probed at the LHC (Fig. 17, right). As discussed in Section 5.1.1, in such a low- $x$  regime, non-linear (gluon recombination) QCD effects may become important, leading to a saturation of the PDFs [199–201]. The evolution of the cross section with energy is very sensitive to the underlying small- $x$  dynamics as shown by the bands in Fig. 26 (right) showing different theoretical predictions based on LO and LO pQCD calculations [202], colour dipole formalism [203, 204], and gluon saturation approaches (labelled CGC) [198, 205, 206].

## 6 Contributions to other sectors of high-energy physics<sup>9</sup>

### 6.1 Photon–photon collisions

In Section 5.2 we have discussed how the large electromagnetic fields produced by accelerated protons or ions can be considered as quasireal  $\gamma$  beams of very low virtuality. Photon–photon collisions in UPCs of proton [182] and lead (Pb) beams [183] have been experimentally observed at the LHC [195, 207–209]. Although the  $\gamma$  spectrum is harder for smaller charges –which favours proton over nuclear beams in the production of heavy diphoton systems– each photon flux scales with the squared charge of the hadron,  $Z^2$ , and thus  $\gamma\gamma$  luminosities are extremely enhanced for ion beams ( $Z^4 = 5 \cdot 10^7$  in the case of Pb–Pb). Figure 27 (left) shows a typical  $\gamma\gamma$  process in UPCs (light-by-light scattering, in this particular case), and Table 5 summarises the relevant parameters for ultraperipheral pp, p–Pb, and Pb–Pb collisions at FCC energies.

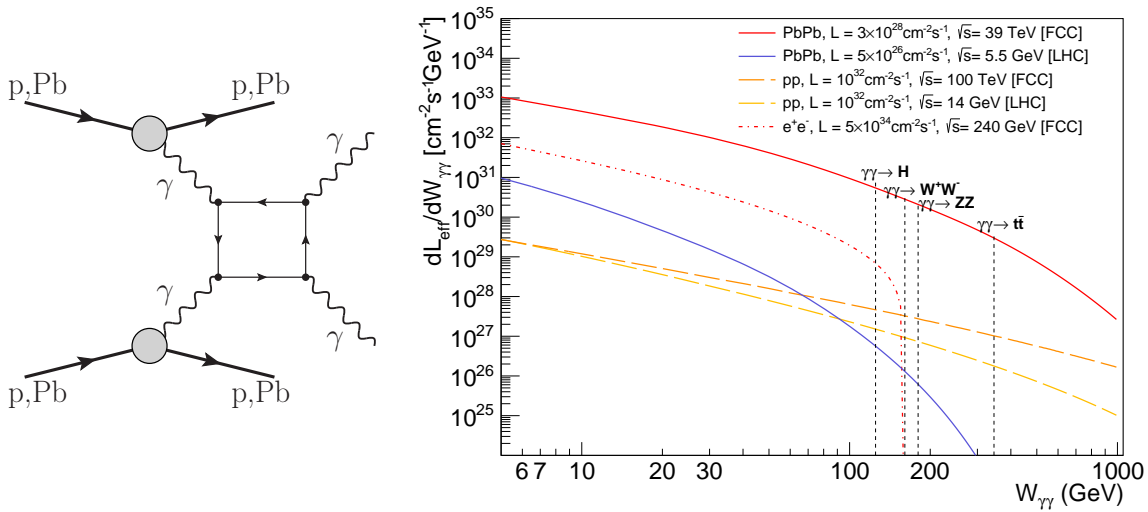


Fig. 27: Left: Diagram of elastic  $\gamma\gamma \rightarrow \gamma\gamma$  scattering in an UPC where the initial-state photons are emitted coherently by the protons and/or nuclei which survive the electromagnetic interaction. Right: Effective photon–photon luminosities as a function of  $\gamma\gamma$  c.m. energy ( $W_{\gamma\gamma}$ ) for five colliding systems at FCC and LHC energies: Pb–Pb at  $\sqrt{s} = 39, 5.5$  TeV (at their corresponding nominal beam luminosities); pp at  $\sqrt{s} = 100, 14$  TeV (corresponding to  $1 \text{ fb}^{-1}$  integrated luminosities); and  $e^+e^-$  at  $\sqrt{s} = 240$  GeV (FCC-ee nominal luminosity per IP). The vertical dashed lines indicate the energy thresholds for Higgs,  $W^+W^-$ ,  $ZZ$ , and  $t\bar{t}$  production.

The figure of merit for UPC  $\gamma\gamma$  processes is the effective  $\gamma\gamma$  luminosity,  $d\mathcal{L}_{\text{eff}}/dW_{\gamma\gamma} \equiv \mathcal{L}_{AB} d\mathcal{L}_{\gamma\gamma}/dW_{\gamma\gamma}$ , where  $\mathcal{L}_{AB}$  is the collider luminosity for the  $AB$  system and  $d\mathcal{L}_{\gamma\gamma}/dW_{\gamma\gamma}$  is the photon–photon luminosity as a function of the  $\gamma\gamma$  centre-of-mass energy  $W_{\gamma\gamma}$ , obtained integrating the two photon fluxes over all rapidities  $y$ , i.e.,  $d^2\mathcal{L}_{\gamma\gamma}/dW_{\gamma\gamma}dy = (2/W_{\gamma\gamma})f_{\gamma/A}(W_{\gamma\gamma}/2e^y)f_{\gamma/B}(W_{\gamma\gamma}/2e^{-y})$ . Figure 27 (right) shows a comparison of the  $d\mathcal{L}_{\text{eff}}/dW_{\gamma\gamma}$  reachable as a function of  $W_{\gamma\gamma}$  for five different colliding systems at LHC and FCC energies. Two-photon centre-of-mass energies at the FCC will reach for the first time the range beyond 1 TeV. Clearly, Pb–Pb at  $\sqrt{s_{NN}} = 39$  TeV provides the largest two-photon luminosities of all colliding systems. The effective luminosities are very high up to large diphoton masses (in the next section we present a case study for the measurement of light-by-light scattering above  $m_{\gamma\gamma} = 5$  GeV that profits from the large photon fluxes available at FCC). The vertical lines in Fig. 27 show the thresholds for photon-fusion production of Higgs,  $W^+W^-$ ,  $ZZ$ , and  $t\bar{t}$ . All such processes, sensitive to different tests of the electroweak sector of the Standard Model (SM) [210], such as anomalous quartic-gauge couplings and top-electroweak mo-

<sup>9</sup>Editors: D. d’Enterria, J.-P. Lansberg

Table 5: Characteristics of  $\gamma\gamma \rightarrow \gamma\gamma$  processes at the FCC-hh: (i) nucleon-nucleon c.m. energy,  $\sqrt{s_{\text{NN}}}$ , (ii) integrated luminosity  $\mathcal{L}_{\text{AB}} \cdot \Delta t$  ( $\mathcal{L}_{\text{AB}}$  are beam luminosities –for low pileup in the pp case– and a “year” is  $\Delta t = 10^7$  s for pp, and  $10^6$  s in the ion mode), (iii) beam Lorentz factor,  $\gamma_L$ , (iv) maximum photon energy in the c.m. frame,  $\omega_{\text{max}}$ , and (v) maximum photon-photon c.m. energy,  $\sqrt{s_{\gamma\gamma}^{\text{max}}}$ . The last two columns are (vi) cross sections, and (vii) expected number of counts/year after selection cuts, for the exclusive  $\gamma\gamma \rightarrow \gamma\gamma$  process at masses above 5 GeV.

System	$\sqrt{s_{\text{NN}}}$ (TeV)	$\mathcal{L}_{\text{AB}} \cdot \Delta t$ (per year)	$\gamma_L$ ( $\times 10^3$ )	$\omega_{\text{max}}$ (TeV)	$\sqrt{s_{\gamma\gamma}^{\text{max}}}$ (TeV)	$\sigma_{\gamma\gamma \rightarrow \gamma\gamma}^{\text{excl}}$ [ $m_{\gamma\gamma} > 5$ GeV]	$N_{\gamma\gamma}^{\text{cuts}}$
pp	100	1 fb $^{-1}$	53.0	17.6	35.2	240 $\pm$ 24 fb	50
p–Pb	63	8 pb $^{-1}$	33.5	0.95	1.9	780 $\pm$ 78 pb	1 200
Pb–Pb	39	33 nb $^{-1}$	21.0	0.60	1.2	1.85 $\pm$ 0.37 $\mu$ b	16 500

ments, should have visible counts at the FCC(Pb–Pb) although dedicated studies need to be carried out in order to estimate the significance of the corresponding observations.

### Case study: light-by-light scattering

It has been demonstrated that one can detect the very rare elastic scattering of two photons in vacuum,  $\gamma\gamma \rightarrow \gamma\gamma$ , a simple yet unobserved process so far (Fig. 27, left), using the large quasireal photon fluxes of the ions accelerated at TeV energies at LHC and FCC energies [211, 212]. Such a measurement at the LHC will constitute the first-ever observation of a fundamental quantum mechanical process in the lab, whereas at the FCC, due to the higher diphoton masses reached, one may be sensitive to physics beyond the SM through new heavy charged particles contributing to the virtual loop in Fig. 27 (left) such as, e.g., from SUSY particles [213]. Light-by-light (LbyL) scattering has also been proposed as a tool to search for monopoles [214], axions [215], unparticles [216], low-scale gravity effects [217], and non-commutative interactions [218].

We update here the results of Ref. [212] to account for factors  $\times 6.5$  and  $\times 8$  increase in the FCC luminosities considered now for the Pb–Pb and p–Pb systems (see Section 2). The UPC final-state signature is the exclusive production of two photons,  $\text{A B} \xrightarrow{\gamma\gamma} \text{A} \gamma \gamma \text{B}$ , with the diphoton final-state measured in the central detector, and A,B = p,Pb surviving the electromagnetic interaction scattered at very low angles with respect to the beam. In the equivalent photon approximation (EPA), the elastic  $\gamma\gamma$  production cross section in UPCs of hadrons A and B factorizes into the product of the elementary  $\gamma\gamma \rightarrow \gamma\gamma$  cross section at  $\sqrt{s_{\gamma\gamma}}$ , convoluted with the photon fluxes  $f_{\gamma/\text{A,B}}(\omega)$  of the two colliding beams:

$$\sigma_{\gamma\gamma \rightarrow \gamma\gamma}^{\text{excl}} = \sigma(\text{A B} \xrightarrow{\gamma\gamma} \text{A} \gamma \gamma \text{B}) = \int d\omega_1 d\omega_2 \frac{f_{\gamma/\text{A}}(\omega_1)}{\omega_1} \frac{f_{\gamma/\text{B}}(\omega_2)}{\omega_2} \sigma_{\gamma\gamma \rightarrow \gamma\gamma}(\sqrt{s_{\gamma\gamma}}), \quad (7)$$

where  $\omega_1$  and  $\omega_2$  are the energies of the photons emitted by A and B,  $f_{\gamma/\text{p}}(\omega)$  is the spectrum derived from the proton elastic form factor [219], and  $f_{\gamma/\text{A}}(\omega)$  the impact-parameter dependent expression for the ion spectrum [220] including a correction equivalent to ensuring that all collisions are purely exclusive, i.e., without hadronic overlap and breakup of the colliding beams [221]. The MADGRAPH v.5 Monte Carlo (MC) [222] framework is used to convolute the  $\gamma$  fluxes with the LO expression for the  $\sigma_{\gamma\gamma \rightarrow \gamma\gamma}$  cross section [223] including all quark and lepton loops, but omitting the  $W^\pm$  contributions which are only important at  $m_{\gamma\gamma} \gtrsim 200$  GeV. Inclusion of next-to-leading-order QCD and QED corrections increases  $\sigma_{\gamma\gamma \rightarrow \gamma\gamma}$  by a few percent only [223]. Propagated uncertainties to the final cross sections are of order  $\pm 10\%$  ( $\pm 20\%$ ) for pp and p–Pb (Pb–Pb) collisions, covering different form-factors parametrizations and

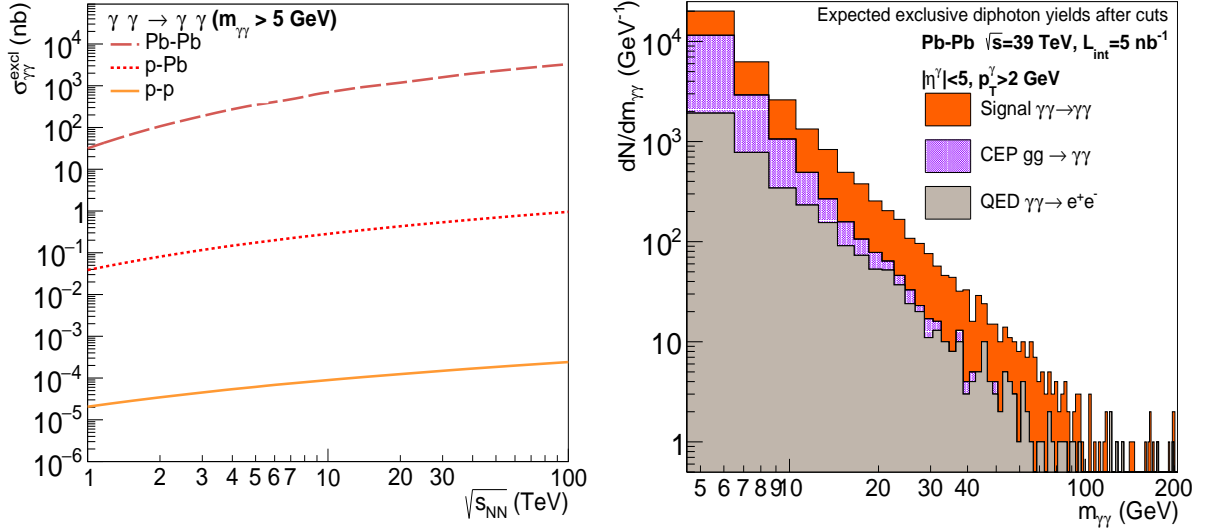


Fig. 28: Left: Cross sections for  $\gamma\gamma \rightarrow \gamma\gamma$ , with pair masses above 5 GeV, in ultraperipheral Pb–Pb (top curve), p–Pb (middle) and pp (bottom) collisions as a function of c.m. energy [212]. Right: Yields as a function of diphoton invariant mass for elastic  $\gamma\gamma$ , plus CEP- $\gamma\gamma$  and QED backgrounds, expected in Pb–Pb at FCC after analysis cuts.

the convolution of the nuclear photon fluxes. The obtained signal cross sections  $\sigma_{\gamma\gamma \rightarrow \gamma\gamma}^{\text{excl}}$  are listed in Table 5, and plotted as a function of c.m. energies in the range  $\sqrt{s_{\text{NN}}} = 1$ –100 TeV in Fig. 28 (left). The increase in cross sections from LHC to FCC is of  $\mathcal{O}(2\text{--}5)$ . The cross sections are in at the  $\mu\text{b}$  level at the FCC, clearly showing the importance of the  $Z^4$ -enhanced photon-flux for ions compared to protons.

The detectable number of  $\gamma\gamma \rightarrow \gamma\gamma$  events is estimated by considering nominal luminosities for each system, geometric detector acceptance, and reconstruction efficiencies. Standard trigger+acceptance requirements (both photons with  $p_T^\gamma > 2$  GeV/c within  $|\eta^\gamma| < 5$ ) reduce the yields by  $\varepsilon_{\text{acc}} \approx 0.3$  (pp and p–Pb), and 0.4 (Pb–Pb). Accounting for typical offline  $\gamma$  reconstruction and identification efficiencies ( $\varepsilon_{\text{rec,id}\gamma} \approx 0.8$  in the photon energy range of interest) results in final combined signal efficiencies of  $\varepsilon_{\gamma\gamma} = \varepsilon_{\text{acc}} \cdot \varepsilon_{\text{rec,id}\gamma}^2 \approx 20\%$  (pp, p–Pb) and 26% (Pb–Pb). The number of events expected per year are obtained via  $N_{\gamma\gamma}^{\text{excl}} = \varepsilon_{\gamma\gamma} \cdot \sigma_{\gamma\gamma}^{\text{excl}} \cdot \mathcal{L}_{\text{AB}} \cdot \Delta t$  (Table 5). The nominal p–Pb and Pb–Pb luminosities are low enough to keep the number of simultaneous collisions well below one, but pileup in pp is very high and only  $\mathcal{O}(1 \text{ fb}^{-1}/\text{year})$  can be collected under conditions that preserve the rapidity gaps adjacent to the central  $\gamma\gamma$  system (unless one can tag the outgoing quasielastically-scattered protons [224]). Clearly, Pb–Pb provides the best signal counting rates, with statistical uncertainties of order  $1/\sqrt{N_{\gamma\gamma}^{\text{excl}}} \sim 1\%$ .

Three potential backgrounds share the same (or very similar) final-state signature as  $\gamma\gamma \rightarrow \gamma\gamma$ : (i) diphoton production through a quark-loop in the color-singlet exchange of two gluons,  $A B \xrightarrow{gg} A \gamma\gamma B$  (“central exclusive production”, CEP), (ii) QED  $\gamma\gamma \rightarrow e^+e^-$  events, with both  $e^\pm$  misidentified as photons, and (iii) diffractive Pomeron-induced ( $IP$ IP, or  $\gamma$ IP) processes with final-states containing two photons plus rapidity gaps. The latter diffractive and  $\gamma$ -induced final-states have larger  $p_T^{\gamma\gamma}$  and diphoton acoplanarities than  $\gamma\gamma \rightarrow \gamma\gamma$ , and can be efficiently removed. However, the CEP  $gg \rightarrow \gamma\gamma$  background (observed at Tevatron [225] and theoretically described by the SUPERCHIC [226] MC) scales with the fourth power of the gluon density and is a large potential background. In Pb–Pb at FCC(39 TeV), the CEP cross section within  $|\eta| < 5$  is indeed very large:  $\sigma_{gg \rightarrow \gamma\gamma}^{\text{CEP}}[m_{\gamma\gamma} > 5 \text{ GeV}] = 1.3 \text{ nb} \times 208^2 \times (R_g^{\text{Pb/p}})^4 \approx 14 \mu\text{b}$  (with a factor of  $\sim 3$  uncertainty) as obtained with SUPERCHIC 2.02 [227] and the MMHT2014 PDFs [228], where  $R_g^{\text{Pb/p}} \approx 0.7$  is the Pb gluon shadowing according to the EPS09 nuclear PDF modifications [88]. Typical CEP photon pairs peak at  $p_T^{\gamma\gamma} \approx 0.5$  GeV/c and have moderate tails

in their azimuthal acoplanarity  $\Delta\phi_{\gamma\gamma}$ , whereas photon-fusion systems are produced almost at rest. By imposing very tight cuts in the pair momentum,  $p_T^{\gamma\gamma} \lesssim 0.1 \text{ GeV}/c$  and acoplanarity  $\Delta\phi_{\gamma\gamma} - \pi \lesssim 0.04$ , the CEP  $\gamma\gamma$  can be reduced to  $\sim 400 \text{ nb}$ . The very large exclusive Pb–Pb  $\gamma\gamma \rightarrow e^+e^-$  QED cross section,  $\sigma_{\gamma\gamma \rightarrow e^+e^-}^{\text{QED}}[m_{e^+e^-} > 5 \text{ GeV}] = 26 \text{ mb}$  according to STARLIGHT [229], similarly enhanced by the  $Z^4$  factor as the LbyL signal, can be of concern if neither  $e^\pm$  track is reconstructed or if both  $e^\pm$  undergo hard bremsstrahlung. Requiring both  $e^\pm$  to fall within the central acceptance and be singly misidentified as photons with probability  $f_{e \rightarrow \gamma} \approx 0.5\%$ , results in a residual  $\gamma\gamma \rightarrow \gamma_{(e^+)}\gamma_{(e^-)}$  cross section of  $\sim 120 \text{ nb}$ . After cuts, both backgrounds are thereby smaller than the expected visible LbyL cross section of  $\sim 500 \text{ nb}$ . Figure 28 (right) shows the  $\gamma\gamma$  invariant mass distributions for signal and CEP and QED backgrounds (after cuts) in one Pb–Pb run at the FCC. We expect about  $N_{\gamma\gamma}^{\text{excl}} \approx 16\,500$  signal counts (reaching diphoton masses above  $100 \text{ GeV}$ ) compared to  $\sim 13\,000$  and  $\sim 4\,000$  CEP and QED counts respectively. The overall (profile likelihood) significance of the signal in the integrated yields is  $\mathcal{S} \approx 35$ , considering 20% and 50% theoretical uncertainties on LbyL and CEP yields respectively (the QED background can be easily well-measured beforehand).

In summary, light-by-light scattering, a rare fundamental quantum-mechanical process that has escaped experimental observation so far, can be measured at the LHC [211] and FCC [212] exploiting the large quasireal photon fluxes in electromagnetic interactions of protons and ions accelerated at TeV energies. The increase in  $\gamma\gamma \rightarrow \gamma\gamma$  yields from LHC to FCC is of  $\mathcal{O}(200)$  thanks to factors of  $\times 30$  larger cross sections times luminosities, and  $\times 2$  in the experimental acceptance. The measurement of elastic  $\gamma\gamma$  scattering at the LHC will be the first-ever observation of such fundamental quantum mechanical process in the lab. At the FCC, the higher-masses of the produced diphoton system may be sensitive to new-physics effects predicted in various SM extensions.

## 6.2 Fixed-target collisions using the FCC proton and lead beams

Fixed-target experiments have brought decisive contributions to particle and nuclear physics. They have led to particle discoveries such as those of  $\Omega^-$ ,  $J/\psi$ ,  $\Upsilon$ , etc., as well as evidence for the novel dynamics of quarks and gluons in heavy-ion collisions. In accessing the high Feynman  $x_F$  domain<sup>10</sup> and in offering a number of options for polarised and unpolarised proton and nuclear targets, they have also led to the observation of surprising QCD phenomena: the breakdown of the Lam-Tung relation, colour transparency, higher-twist effects at high  $x_F$ , anomalously large single- and double-spin correlations, and the breakdown of factorisation in  $J/\psi$  hadroproduction at high  $x_F$  in proton-nucleus collisions (see [230] and references therein). The fixed-target mode indeed offers critical advantages that remain still nowadays difficult to challenge by collider experiments, and hence their complementarity. Let us emphasise four of key assets, among others: accessing the high Feynman  $x_F$  domain, achieving high luminosities with dense targets, varying the atomic mass of the target almost at will, and polarising the target. It is therefore legitimate to investigate the physics opportunities which are offered by the ultra-high energy proton and lead beams of the FCC-hh impinging on a fixed target<sup>11</sup>. We will refer in the following to such a set-up as to AFTER@FCC.

### 6.2.1 Colliding ultra-high-energy protons and ions on fixed targets

#### 6.2.1.1 Fixed-target kinematics

Contrary to the case of colliding beams of equal energies for which the c.m.s. frame obviously corresponds to the laboratory frame, one has to account for the boost ( $\gamma_{c.m.s.}^{\text{lab}}$ ) and the rapidity shift ( $\Delta y_{c.m.s.}^{\text{lab}}$ )

<sup>10</sup> $x_F$  is defined as the difference on the Bjorken  $x$  values for the two partons that enter the hard scattering process,  $x_F = x_1 - x_2$ .

<sup>11</sup>A list of physics opportunities offered by the use of the multi-TeV proton and lead LHC beams on a fixed target can be found in Ref. [230]. We refer to Ref. [231] for the specific case of quarkonium studies, for spin physics to Refs. [232–236] and for heavy-ion physics with lead beam to Refs. [231, 237, 238].

between the c.m.s. frame of the fixed-target collision and the laboratory frame. These are respectively  $\gamma_{\text{c.m.s.}}^{\text{lab}} = \sqrt{s}/(2m_p)$  and  $\Delta y_{\text{c.m.s.}}^{\text{lab}} = \ln(\gamma_{\text{c.m.s.}}^{\text{lab}} + \sqrt{(\gamma_{\text{c.m.s.}}^{\text{lab}})^2 - 1})$ . Consequently, the available c.m.s. energy is much lower than in the collider mode, on the order of 200–300 GeV in the FCC case depending on the beam energy (see Table 6).

The region of central c.m.s. rapidities,  $y_{\text{c.m.s.}} \simeq 0$ , is thus highly boosted at an angle with respect to the beam axis of about one degree in the laboratory frame. The entire backward hemisphere,  $y_{\text{c.m.s.}} < 0$ , is thus easily accessible with standard experimental techniques. With the FCC, the rapidity shift is on the order of 5–6, whereas it is 4.8 for the 7 TeV LHC beams (see also Table 6). A detector covering  $2 < \eta_{\text{lab}} < 6$  would thus cover nearly half of the physical phase space of the fixed-target mode. In terms of kinematics, the advantage of such a mode running at ultra high beam energies is that particles nearly at the end of the phase space at backward c.m.s. rapidities, which would not be detectable in the collider mode, are at large angle and can be detected since they do not fly in the beam pipe.

Table 6: Comparison between the beam and kinematics parameters for the proposed FCC with proton and lead beams [7] and that of the LHC, including the fixed-target energies, the boost ( $\gamma_{\text{c.m.s.}}^{\text{lab}}$ ) and the rapidity shift ( $\Delta y_{\text{c.m.s.}}^{\text{lab}}$ ) between the c.m.s. of the fixed-target collision and the laboratory frame.

	p@LHC	Pb@LHC	p@FCC (25 and 5 ns spacing)	Pb@FCC
Beam Energy ( $E_b = \frac{Z}{A} E_p$ ) [TeV]	7	2.76	50	19.71
Number of bunches stored	2808	592	10600/53000	2072
Number of particles ( $N_p$ ) per bunch [ $10^8$ ]	1150	0.7	1000/200	2.0
Circumference [km]	26.659	26.659	100	100
Revolution frequency [kHz]	11.25	11.25	3	3
Particle flux [ $\text{s}^{-1}$ ]	$3.6 \times 10^{18}$	$4.6 \times 10^{14}$	$3.2 \times 10^{18}$	$1.2 \times 10^{15}$
Nucleon–Nucleon c.m.s. energy ( $\sqrt{s_{NN}} = \sqrt{2E_b m_N}$ ) [GeV]	114.6	72.0	306.6	192.5
Lorentz factor ( $\gamma_{\text{c.m.s.}}^{\text{lab}} = \sqrt{\frac{E_b}{2m_p}}$ )	61.0	38.3	163.1	102.4
$\Delta y_{\text{c.m.s.}}^{\text{lab}} = \ln(\gamma_{\text{c.m.s.}}^{\text{lab}} + \sqrt{(\gamma_{\text{c.m.s.}}^{\text{lab}})^2 - 1})$	4.80	4.33	5.79	5.32

### 6.2.1.2 Beam extraction vs. internal gaseous target

There are two promising techniques to achieve the fixed-target mode with ultra-high energy beams: the slow extraction by a bent crystal or an internal gas target. Both of them are currently being investigated on the LHC beams.

For what concerns the slow extraction by a bent crystal, a first computation of the approximate deflection efficiency as a function of crystal length, along the lines of [239] for a single pass, was presented for the FCC in [240]. It was found that the efficiency (excluding surface transmission) in Si (110) is 84% for a 50 TeV beam at a deflection angle of 0.5 mrad, as approximately required for the passage of a septum blade downstream which is required for further extraction. This efficiency corresponds to an optimal crystal length of  $L/L_D = 0.085$ , thus to a length of 1.6 m. It was, however, stressed that such a length is probably overestimated since it was evaluated for a single pass only. Results of the order 20–30 cm are certainly not unrealistic.

The beam extraction may however not be the only way to perform fixed-target experiments at colliders. The injection of a small amount of gas into the detector region of a running machine is sufficient to increase the probability of beam-gas interactions such as to reach large luminosities – yet at essentially zero cost in terms of the beam lifetime. In fact, the LHCb experiment running at the LHC has imple-

mented this idea. The initial objective of their system, referred to as SMOG for System for Measuring Overlap with Gas (SMOG), was to monitor the beam luminosity [241]. SMOG has so far proven to be functioning well, while not disturbing the primary beam<sup>12</sup>.

In order to derive the luminosities that can be expected in the fixed-target mode with the beams of a future collider like the FCC, we need to account for some specific parameters (see Table 6), some of them like the beam loss are not yet well known. Indeed, in the case of the extraction with the LHC beam with a bent crystal positioned in the beam halo, an extraction flux corresponding to half of the beam loss has been assumed [230, 242]. Lacking such numbers in the FCC case, we will take as a working hypothesis that such a parasitic mode is reached with an extracted flux corresponding to 5% of the protons stored in the FCC per fill.

Table 7 summarises the estimated luminosities for the two modes (slow extraction and internal target), for the proton and Pb beams at the FCC. Two options for the internal target case are considered: one is similar to the LHCb SMOG system with a slightly higher pressure; the other is inspired by the HERMES target system used at DESY [243], which offers the possibility to have polarised hydrogen, deuterium or helium targets. The injection of heavier inert gases is also possible. In this case, the limit on the target density is determined by the maximum acceptable impact on the collider-mode luminosity and by the detector readout capabilities. Yearly luminosities, as for AFTER@LHC, for the FCC proton beam, range from  $1 \text{ fb}^{-1}\text{yr}^{-1}$  up to  $60 \text{ fb}^{-1}\text{yr}^{-1}$  with light targets and, for the Pb beam, from  $40 \text{ nb}^{-1}\text{yr}^{-1}$  up to  $2 \text{ pb}^{-1}\text{yr}^{-1}$  with a long hydrogen target.

Table 7: For the FCC extracted beam, the extracted flux is calculated by assuming that 5% of the beam is used per fill of 10 hours and the luminosities are calculated for the case of targets that are 1 cm thick for Be and W and 1m long for liquid hydrogen. The values for the internal gas-target (à la SMOG) are calculated using the same parameters as in [235] for an ideal gas at a pressure of  $10^{-6}$  mbar in a zone of 100 cm. Those for an internal gas storage-cell target (à la HERMES) are computed for a target areal density of  $2.5 \cdot 10^{14} \text{ cm}^{-2}$  ( $\text{H}_2$ ),  $3.2 \cdot 10^{14} \text{ cm}^{-2}$  ( $\text{D}_2$ ) and  $3.8 \cdot 10^{13} \text{ cm}^{-2}$  (Xe) [244]. A year is assumed to be  $10^7$  s for p and  $10^6$  s for Pb for both FCC and LHC cases.

	p@LHC	Pb@LHC	p@FCC	Pb@FCC
<i>Extracted beam on an external target</i>	liq. H / Be / W			
Extracted flux [ $\text{s}^{-1}$ ]	$5 \cdot 10^8$	$2 \cdot 10^5$	$1.5 \cdot 10^9$	$5.8 \cdot 10^5$
$\mathcal{L}(\mu\text{b}^{-1}\text{s}^{-1})$	2000 / 62 / 31	0.8 / 0.025 / 0.013	6000 / 190 / 93	2.32 / 0.072 / 0.036
$\int dt \mathcal{L}(\text{pb}^{-1}\text{yr}^{-1})$	20000 / 620 / 310	0.8 / 0.025 / 0.013	60000 / 1900 / 930	2.32 / 0.072 / 0.036
<i>Internal gas target (SMOG type)</i>	ideal gas	ideal gas	ideal gas	ideal gas
$\mathcal{L}(\mu\text{b}^{-1}\text{s}^{-1})$	10	0.001	8.9	$3.3 \cdot 10^{-3}$
$\int dt \mathcal{L}(\text{pb}^{-1}\text{yr}^{-1})$	100	0.001	89	$3.3 \cdot 10^{-3}$
<i>Internal gas storage-cell target (HERMES type)</i>	$\text{H}_2 / \text{D}_2 / \text{Xe}$			
$\mathcal{L}(\mu\text{b}^{-1}\text{s}^{-1})$	900 / 1200 / 140	0.12 / 0.15 / 0.02	800 / 1100 / 120	0.3 / 0.4 / 0.05
$\int dt \mathcal{L}(\text{pb}^{-1}\text{yr}^{-1})$	9000 / 12000 / 1400	0.12 / 0.15 / 0.02	8000 / 11000 / 1200	0.3 / 0.4 / 0.05

<sup>12</sup> LHCb took data from proton-neon and lead-neon collisions over short periods during beam tests in 2012 and 2013, as well as in 2015 from collisions of proton-neon (12 hours), proton-helium (8 hours) and proton-argon (3 days) at 110.4 GeV and lead-argon (1 week) and proton-argon (a few hours) at 68.6 GeV.

### 6.2.2 *Physics opportunities*

It is of course impossible to make an exhaustive list of the original measurements which can be carried out with AFTER@FCC. We will limit our discussion here to some highlights. The list below would certainly evolve with time with the future RHIC and LHC data. The c.m.s. energy range (per nucleon-nucleon collisions) to be covered by such a setup would obviously not be new since it is that of RHIC studies<sup>13</sup> in pp collision from 200 to 500 GeV and d–A and A–A collisions at 200 GeV. Yet, the key asset of the fixed-target mode, beside the much larger luminosities for the p–A systems than at RHIC, is the extensive access towards very backward rapidities. This is crucial since it allows to study nuclear effects in a wide rapidity range, thus to scan very different boosts between the probe and the nuclear matter, be it hot (A–A collisions) or cold (p–A collisions). This may happen to be essential for instance to disentangle the different processes involved in the quarkonium production in heavy-ion collisions. An extensive rapidity coverage down to the target-ion rapidity can also help to study the origin of azimuthal asymmetries, like the elliptic flow. Given the similarities with a setup like AFTER@LHC, we also guide the readers to Refs. [230, 231, 231–238]. It has to be noted that measurements in the backward c.m.s. region may require to look at probes with transverse momenta down to a few GeV. This is not an issue since most of the particles released in the collisions fly forward; the multiplicities and the detector occupancies in this region are expected to be easily tractable. It however remains to be studied if this can be done with a detector also running in the collider mode with very high  $p_T$  thresholds.

As it was discussed in [240], RHIC luminosities in pp collisions at 200 GeV are limited and could not allow for the study of vector boson production close to threshold which can help us probe the large  $x$  content in the proton and nucleus, 0.7 and above. These measurements are potentially sensitive to threshold effects [245] which can also be relevant for the production of heavy BSM particles at colliders. The production of  $W$  and  $Z$  boson near threshold could also enable the study of decay modes that cannot be analysed at higher c.m.s. energies. Higgs boson production near threshold in p A collisions is very challenging since gluons with enough energy to produce the Higgs boson are suppressed at high  $x$ , and quark-induced reactions via vector boson fusion are disfavoured compared to gluon-gluon production.

With a longitudinally polarised target, the study of vector boson production opens the possibilities to study (anti)quark helicity distributions in the proton at very large  $x$ . With deuterium and helium targets, measurements can also be carried out on the neutron. Using a transversely polarised target allows one to access transverse-momentum dependent distributions (TMDs) which are connected to the orbital angular momentum carried by the partons. See [236] for a recent discussion for AFTER@LHC. The increase in energy with AFTER@FCC, which is nearly three times higher, will allow one for studies of systems with large scales where the applicability of the TMD factorisation will probably be even safer with more event counts.

In summary, a setup as AFTER@FCC could be considered as a facility by itself opening a new realm of investigations that would complement measurements carried out at RHIC and at lower energy facilities.

---

<sup>13</sup>Not considering the so-called beam-energy-scan studies with limited luminosities.

### **Acknowledgements**

J.L. Albacete is supported by the FP7-PEOPLE- 2013-CIG Grant of the European Commission, reference QCDense/631558, and by Ramon y Cajal and MINECO projects reference RYC-2011-09010 and FPA2013-47836. N. Armesto, H. Paukkunen and C.A. Salgado acknowledge support from European Research Council grant HotLHC ERC-2011- StG-279579; Ministerio de Ciencia e Innovacion of Spain under project FPA2014-58293-C2-1-P; Xunta de Galicia (Consellerá de Educación) – the group is part of the Strategic Unit AGRUP2015/11. N. Armesto is also supported by the People Programme (Marie Curie Actions) of the European Union’s Seventh Framework Programme FP7/2007-2013/ under REA grant agreement no. 318921. The work of C.-M. Ko is supported by the US Department of Energy under Contract No. DE-SC0015266 and the Welch Foundation under Grant No. A-1358. The work of J.G. Milhano and L. Apolinário is supported by Fundação para a Ciência e a Tecnologia of Portugal under project CERN/FIS-NUC/0049/2015 and contracts “Investigador FCT - Development Grant” (JGM) and SFRH/BD/64543/2009 (LA). C. Ratti is supported by the National Science Foundation under grant no. PHY-1513864. The work of A.H. Rezaeian is supported in part by Fondecyt grant 1150135, Ecos-Conicyt C14E01, Anillo ACT1406 and Basal FB0821. M. van Leeuwen acknowledges support from the Stichting voor Fundamenteel Onderzoek der Materie (FOM) and the Nederlandse Organisatie voor Wetenschappelijk Onderzoek (NWO), Netherlands.

## References

- [1] CERN FCC web site, <http://fcc.web.cern.ch>.
- [2] FCC Study Kickoff Meeting, February 2014, <https://indico.cern.ch/event/282344/>.
- [3] J. Jowett, M. Schaumann, and R. Versteegen, *RLIUP workshop, October 2013*, <http://indico.cern.ch/event/260492/session/5/contribution/28>.
- [4] J. Jowett, *LHC Performance Workshop, Chamonix, January 2016*, <https://indico.cern.ch/event/448109/session/4/contribution/32/>.
- [5] CEPC-SppC web site, <http://cepc.ihep.ac.cn/intro.html>.
- [6] N.-b. Chang et al., *Physics perspectives of heavy-ion collisions at very high energy*, [arXiv:1510.05754](https://arxiv.org/abs/1510.05754) [nucl-th].
- [7] M. Schaumann, *Potential performance for Pb-Pb, p-Pb and p-p collisions in a future circular collider*, *Phys. Rev. ST Accel. Beams* **18** (2015) no. 9, 091002, [arXiv:1503.09107](https://arxiv.org/abs/1503.09107) [physics.acc-ph].
- [8] R. Alemany Fernandez, *FCC-hh meeting on extraction, insertion and turn-around time studies, March 2016*, <http://indico.cern.ch/event/505557/contribution/1/>.
- [9] ALICE Collaboration, K. Aamodt et al., *Charged-particle multiplicity density at mid-rapidity in central Pb-Pb collisions at  $\sqrt{s_{NN}} = 2.76$  TeV*, *Phys. Rev. Lett.* **105** (2010) 252301, [arXiv:1011.3916](https://arxiv.org/abs/1011.3916) [nucl-ex].
- [10] ALICE Collaboration, E. Abbas et al., *Centrality dependence of the pseudorapidity density distribution for charged particles in Pb-Pb collisions at  $\sqrt{s_{NN}} = 2.76$  TeV*, *Phys. Lett.* **B726** (2013) 610–622, [arXiv:1304.0347](https://arxiv.org/abs/1304.0347) [nucl-ex].
- [11] ALICE Collaboration, K. Aamodt et al., *Two-pion Bose-Einstein correlations in central Pb-Pb collisions at  $\sqrt{s_{NN}} = 2.76$  TeV*, *Phys. Lett.* **B696** (2011) 328–337, [arXiv:1012.4035](https://arxiv.org/abs/1012.4035) [nucl-ex].
- [12] ALICE Collaboration, J. Adam et al., *Centrality dependence of the charged-particle multiplicity density at mid-rapidity in Pb-Pb collisions at  $\sqrt{s_{NN}} = 5.02$  TeV*, [arXiv:1512.06104](https://arxiv.org/abs/1512.06104) [nucl-ex].
- [13] CMS Collaboration, S. Chatrchyan et al., *Measurement of the pseudorapidity and centrality dependence of the transverse energy density in PbPb collisions at  $\sqrt{s_{NN}} = 2.76$  TeV*, *Phys. Rev. Lett.* **109** (2012) 152303, [arXiv:1205.2488](https://arxiv.org/abs/1205.2488) [nucl-ex].
- [14] ALICE Collaboration, J. Adam et al., *Measurement of transverse energy at midrapidity in Pb-Pb collisions at  $\sqrt{s_{NN}} = 2.76$  TeV*, [arXiv:1603.04775](https://arxiv.org/abs/1603.04775) [nucl-ex].
- [15] J. L. ALbacete and A. Dumitru, *A model for gluon production in heavy-ion collisions at the LHC with rcBK unintegrated gluon densities*, [arXiv:1011.5161](https://arxiv.org/abs/1011.5161) [hep-ph].
- [16] J.-Y. Ollitrault, A. M. Poskanzer, and S. A. Voloshin, *Effect of flow fluctuations and nonflow on elliptic flow methods*, *Phys. Rev.* **C80** (2009) 014904, [arXiv:0904.2315](https://arxiv.org/abs/0904.2315) [nucl-ex].
- [17] S. A. Voloshin, A. M. Poskanzer, and R. Snellings, *Collective phenomena in non-central nuclear collisions*, [arXiv:0809.2949](https://arxiv.org/abs/0809.2949) [nucl-ex].
- [18] A. Bilandzic, C. H. Christensen, K. Gulbrandsen, A. Hansen, and Y. Zhou, *Generic framework for anisotropic flow analyses with multiparticle azimuthal correlations*, *Phys. Rev.* **C89** (2014) no. 6, 064904, [arXiv:1312.3572](https://arxiv.org/abs/1312.3572) [nucl-ex].
- [19] C. Gale, S. Jeon, B. Schenke, P. Tribedy, and R. Venugopalan, *Event-by-event anisotropic flow in heavy-ion collisions from combined Yang-Mills and viscous fluid dynamics*, *Phys. Rev. Lett.* **110** (2013) no. 1, 012302, [arXiv:1209.6330](https://arxiv.org/abs/1209.6330) [nucl-th].
- [20] H. Niemi and G. S. Denicol, *How large is the Knudsen number reached in fluid dynamical simulations of ultrarelativistic heavy ion collisions?*, [arXiv:1404.7327](https://arxiv.org/abs/1404.7327) [nucl-th].
- [21] G. S. Denicol, C. Gale, S. Jeon, J. F. Paquet, and B. Schenke, *Effect of initial-state*

- nucleon-nucleon correlations on collective flow in ultra-central heavy-ion collisions*, [arXiv:1406.7792 \[nucl-th\]](#).
- [22] H. Niemi, K. J. Eskola, R. Paatelainen, and K. Tuominen, *Predictions for 5.02 TeV Pb + Pb collisions at the CERN Large Hadron Collider*, *Phys. Rev.* **C93** (2016) no. 1, 014912, [arXiv:1511.04296 \[hep-ph\]](#).
- [23] H. Niemi, K. J. Eskola, and R. Paatelainen, *Event-by-event fluctuations in a perturbative QCD + saturation + hydrodynamics model: Determining QCD matter shear viscosity in ultrarelativistic heavy-ion collisions*, *Phys. Rev.* **C93** (2016) no. 2, 024907, [arXiv:1505.02677 \[hep-ph\]](#).
- [24] CMS Collaboration, V. Khachatryan et al., *Observation of Long-Range Near-Side Angular Correlations in Proton-Proton Collisions at the LHC*, *JHEP* **09** (2010) 091, [arXiv:1009.4122 \[hep-ex\]](#).
- [25] CMS Collaboration, S. Chatrchyan et al., *Multiplicity and transverse momentum dependence of two- and four-particle correlations in pPb and PbPb collisions*, *Phys. Lett.* **B724** (2013) 213–240, [arXiv:1305.0609 \[nucl-ex\]](#).
- [26] ALICE Collaboration, B. B. Abelev et al., *Long-range angular correlations of  $\pi$ , K and p in p-Pb collisions at  $\sqrt{s_{NN}} = 5.02$  TeV*, *Phys. Lett.* **B726** (2013) 164–177, [arXiv:1307.3237 \[nucl-ex\]](#).
- [27] ALICE Collaboration, B. Abelev et al., *Long-range angular correlations on the near and away side in p-Pb collisions at  $\sqrt{s_{NN}} = 5.02$  TeV*, *Phys. Lett.* **B719** (2013) 29–41, [arXiv:1212.2001 \[nucl-ex\]](#).
- [28] ATLAS Collaboration, G. Aad et al., *Measurement of long-range pseudorapidity correlations and azimuthal harmonics in  $\sqrt{s_{NN}} = 5.02$  TeV proton-lead collisions with the ATLAS detector*, *Phys. Rev.* **C90** (2014) no. 4, 044906, [arXiv:1409.1792 \[hep-ex\]](#).
- [29] STAR Collaboration, L. Adamczyk et al., *Long-range pseudorapidity dihadron correlations in d+Au collisions at  $\sqrt{s_{NN}} = 200$  GeV*, *Phys. Lett.* **B747** (2015) 265–271, [arXiv:1502.07652 \[nucl-ex\]](#).
- [30] PHENIX Collaboration, A. Adare et al., *Measurements of elliptic and triangular flow in high-multiplicity  $^3\text{He}+\text{Au}$  collisions at  $\sqrt{s_{NN}} = 200$  GeV*, *Phys. Rev. Lett.* **115** (2015) no. 14, 142301, [arXiv:1507.06273 \[nucl-ex\]](#).
- [31] M. Laine and Y. Schroder, *Quark mass thresholds in QCD thermodynamics*, *Phys. Rev.* **D73** (2006) 085009, [arXiv:hep-ph/0603048 \[hep-ph\]](#).
- [32] RBC-Bielefeld Collaboration, M. Cheng, *Charm Quarks and the QCD Equation of State*, *PoS LAT2007* (2007) 173, [arXiv:0710.4357 \[hep-lat\]](#).
- [33] C. DeTar, L. Levkova, S. Gottlieb, U. M. Heller, J. E. Hetrick, R. Sugar, and D. Toussaint, *QCD thermodynamics with nonzero chemical potential at  $N_t = 6$  and effects from heavy quarks*, *Phys. Rev.* **D81** (2010) 114504, [arXiv:1003.5682 \[hep-lat\]](#).
- [34] S. Borsanyi, G. Endrodi, Z. Fodor, S. D. Katz, S. Krieg, C. Ratti, C. Schroeder, and K. K. Szabo, *The QCD equation of state and the effects of the charm*, *PoS LATTICE2011* (2011) 201, [arXiv:1204.0995 \[hep-lat\]](#).
- [35] D. Bodeker and M. Laine, *Heavy quark chemical equilibration rate as a transport coefficient*, *JHEP* **07** (2012) 130, [arXiv:1205.4987 \[hep-ph\]](#).
- [36] H. T. Ding, A. Francis, O. Kaczmarek, H. Satz, F. Karsch, and W. Soldner, *Charmonium correlation and spectral functions at finite temperature*, *PoS LATTICE2010* (2010) 180, [arXiv:1011.0695 \[hep-lat\]](#).
- [37] A. Andronic, P. Braun-Munzinger, and J. Stachel, *Hadron production in central nucleus-nucleus collisions at chemical freeze-out*, *Nucl. Phys.* **A772** (2006) 167–199, [arXiv:nucl-th/0511071 \[nucl-th\]](#).

- [38] A. Andronic, *An overview of the experimental study of quark-gluon matter in high-energy nucleus-nucleus collisions*, *Int. J. Mod. Phys. A* **29** (2014) 1430047, [arXiv:1407.5003 \[nucl-ex\]](#).
- [39] PHENIX Collaboration, K. Adcox et al., *Formation of dense partonic matter in relativistic nucleus-nucleus collisions at RHIC: Experimental evaluation by the PHENIX collaboration*, *Nucl. Phys. A* **757** (2005) 184–283, [arXiv:nucl-ex/0410003 \[nucl-ex\]](#).
- [40] BRAHMS Collaboration, I. Arsene et al., *Quark gluon plasma and color glass condensate at RHIC? The Perspective from the BRAHMS experiment*, *Nucl. Phys. A* **757** (2005) 1–27, [arXiv:nucl-ex/0410020 \[nucl-ex\]](#).
- [41] B. B. Back et al., *The PHOBOS perspective on discoveries at RHIC*, *Nucl. Phys. A* **757** (2005) 28–101, [arXiv:nucl-ex/0410022 \[nucl-ex\]](#).
- [42] STAR Collaboration, J. Adams et al., *Experimental and theoretical challenges in the search for the quark gluon plasma: The STAR Collaboration’s critical assessment of the evidence from RHIC collisions*, *Nucl. Phys. A* **757** (2005) 102–183, [arXiv:nucl-ex/0501009 \[nucl-ex\]](#).
- [43] ATLAS Collaboration, G. Aad et al., *Observation of a Centrality-Dependent Dijet Asymmetry in Lead-Lead Collisions at  $\sqrt{s_{NN}} = 2.77$  TeV with the ATLAS Detector at the LHC*, *Phys. Rev. Lett.* **105** (2010) 252303, [arXiv:1011.6182 \[hep-ex\]](#).
- [44] CMS Collaboration, S. Chatrchyan et al., *Observation and studies of jet quenching in PbPb collisions at nucleon-nucleon center-of-mass energy = 2.76 TeV*, *Phys. Rev. C* **84** (2011) 024906, [arXiv:1102.1957 \[nucl-ex\]](#).
- [45] ALICE Collaboration, B. Abelev et al., *Measurement of charged jet suppression in Pb-Pb collisions at  $\sqrt{s_{NN}} = 2.76$  TeV*, *JHEP* **03** (2014) 013, [arXiv:1311.0633 \[nucl-ex\]](#).
- [46] M. Cacciari, J. Rojo, G. P. Salam, and G. Soyez, *Jet Reconstruction in Heavy Ion Collisions*, *Eur. Phys. J. C* **71** (2011) 1539, [arXiv:1010.1759 \[hep-ph\]](#).
- [47] ATLAS Collaboration, G. Aad et al., *Measurement of the jet radius and transverse momentum dependence of inclusive jet suppression in lead-lead collisions at  $\sqrt{s_{NN}} = 2.76$  TeV with the ATLAS detector*, *Phys. Lett. B* **719** (2013) 220–241, [arXiv:1208.1967 \[hep-ex\]](#).
- [48] ATLAS Collaboration, G. Aad et al., *Measurement of the Azimuthal Angle Dependence of Inclusive Jet Yields in Pb+Pb Collisions at  $\sqrt{s_{NN}} = 2.76$  TeV with the ATLAS detector*, *Phys. Rev. Lett.* **111** (2013) no. 15, 152301, [arXiv:1306.6469 \[hep-ex\]](#).
- [49] ATLAS Collaboration, G. Aad et al., *Measurement of inclusive jet charged-particle fragmentation functions in Pb+Pb collisions at  $\sqrt{s_{NN}} = 2.76$  TeV with the ATLAS detector*, *Phys. Lett. B* **739** (2014) 320–342, [arXiv:1406.2979 \[hep-ex\]](#).
- [50] ATLAS Collaboration, G. Aad et al., *Measurements of the Nuclear Modification Factor for Jets in Pb+Pb Collisions at  $\sqrt{s_{NN}} = 2.76$  TeV with the ATLAS Detector*, *Phys. Rev. Lett.* **114** (2015) no. 7, 072302, [arXiv:1411.2357 \[hep-ex\]](#).
- [51] ATLAS Collaboration, G. Aad et al., *Measurement of the production of neighbouring jets in lead-lead collisions at  $\sqrt{s_{NN}} = 2.76$  TeV with the ATLAS detector*, *Phys. Lett. B* **751** (2015) 376–395, [arXiv:1506.08656 \[hep-ex\]](#).
- [52] CMS Collaboration, S. Chatrchyan et al., *Jet momentum dependence of jet quenching in PbPb collisions at  $\sqrt{s_{NN}} = 2.76$  TeV*, *Phys. Lett. B* **712** (2012) 176–197, [arXiv:1202.5022 \[nucl-ex\]](#).
- [53] CMS Collaboration, S. Chatrchyan et al., *Measurement of jet fragmentation into charged particles in pp and PbPb collisions at  $\sqrt{s_{NN}} = 2.76$  TeV*, *JHEP* **10** (2012) 087, [arXiv:1205.5872 \[nucl-ex\]](#).
- [54] CMS Collaboration, S. Chatrchyan et al., *Studies of jet quenching using isolated-photon+jet correlations in PbPb and pp collisions at  $\sqrt{s_{NN}} = 2.76$  TeV*, *Phys. Lett. B* **718** (2013) 773–794, [arXiv:1205.0206 \[nucl-ex\]](#).

- [55] CMS Collaboration, S. Chatrchyan et al., *Modification of jet shapes in PbPb collisions at  $\sqrt{s_{NN}} = 2.76$  TeV*, *Phys. Lett.* **B730** (2014) 243–263, [arXiv:1310.0878 \[nucl-ex\]](#).
- [56] CMS Collaboration, S. Chatrchyan et al., *Evidence of b-Jet Quenching in PbPb Collisions at  $\sqrt{s_{NN}} = 2.76$  TeV*, *Phys. Rev. Lett.* **113** (2014) no. 13, 132301, [arXiv:1312.4198 \[nucl-ex\]](#). [Erratum: *Phys. Rev. Lett.* 115, no. 2, 029903 (2015)].
- [57] CMS Collaboration, S. Chatrchyan et al., *Measurement of jet fragmentation in PbPb and pp collisions at  $\sqrt{s_{NN}} = 2.76$  TeV*, *Phys. Rev.* **C90** (2014) no. 2, 024908, [arXiv:1406.0932 \[nucl-ex\]](#).
- [58] CMS Collaboration, V. Khachatryan et al., *Measurement of transverse momentum relative to dijet systems in PbPb and pp collisions at  $\sqrt{s_{NN}} = 2.76$  TeV*, *JHEP* **01** (2016) 006, [arXiv:1509.09029 \[nucl-ex\]](#).
- [59] CMS Collaboration, V. Khachatryan et al., *Correlations between jets and charged particles in PbPb and pp collisions at  $\sqrt{s_{NN}} = 2.76$  TeV*, *JHEP* **02** (2016) 156, [arXiv:1601.00079 \[nucl-ex\]](#).
- [60] ALICE Collaboration, J. Adam et al., *Measurement of jet suppression in central Pb-Pb collisions at  $\sqrt{s_{NN}} = 2.76$  TeV*, *Phys. Lett.* **B746** (2015) 1–14, [arXiv:1502.01689 \[nucl-ex\]](#).
- [61] ALICE Collaboration, J. Adam et al., *Measurement of jet quenching with semi-inclusive hadron-jet distributions in central Pb-Pb collisions at  $\sqrt{s_{NN}} = 2.76$  TeV*, *JHEP* **09** (2015) 170, [arXiv:1506.03984 \[nucl-ex\]](#).
- [62] ALICE Collaboration, J. Adam et al., *Azimuthal anisotropy of charged jet production in  $\sqrt{s_{NN}} = 2.76$  TeV Pb-Pb collisions*, *Phys. Lett.* **B753** (2016) 511–525, [arXiv:1509.07334 \[nucl-ex\]](#).
- [63] R. Baier, Y. L. Dokshitzer, S. Peigne, and D. Schiff, *Induced gluon radiation in a QCD medium*, *Phys. Lett.* **B345** (1995) 277–286, [arXiv:hep-ph/9411409 \[hep-ph\]](#).
- [64] R. Baier, Y. L. Dokshitzer, A. H. Mueller, S. Peigne, and D. Schiff, *Radiative energy loss and  $p(T)$  broadening of high-energy partons in nuclei*, *Nucl. Phys.* **B484** (1997) 265–282, [arXiv:hep-ph/9608322 \[hep-ph\]](#).
- [65] R. Baier, Y. L. Dokshitzer, A. H. Mueller, S. Peigne, and D. Schiff, *Radiative energy loss of high-energy quarks and gluons in a finite volume quark - gluon plasma*, *Nucl. Phys.* **B483** (1997) 291–320, [arXiv:hep-ph/9607355 \[hep-ph\]](#).
- [66] R. Baier, Y. L. Dokshitzer, A. H. Mueller, and D. Schiff, *Radiative energy loss of high-energy partons traversing an expanding QCD plasma*, *Phys. Rev.* **C58** (1998) 1706–1713, [arXiv:hep-ph/9803473 \[hep-ph\]](#).
- [67] B. G. Zakharov, *Fully quantum treatment of the Landau-Pomeranchuk-Migdal effect in QED and QCD*, *JETP Lett.* **63** (1996) 952–957, [arXiv:hep-ph/9607440 \[hep-ph\]](#).
- [68] B. G. Zakharov, *Radiative energy loss of high-energy quarks in finite size nuclear matter and quark - gluon plasma*, *JETP Lett.* **65** (1997) 615–620, [arXiv:hep-ph/9704255 \[hep-ph\]](#).
- [69] U. A. Wiedemann, *Gluon radiation off hard quarks in a nuclear environment: Opacity expansion*, *Nucl. Phys.* **B588** (2000) 303–344, [arXiv:hep-ph/0005129 \[hep-ph\]](#).
- [70] M. Gyulassy, P. Levai, and I. Vitev, *Reaction operator approach to nonAbelian energy loss*, *Nucl. Phys.* **B594** (2001) 371–419, [arXiv:nucl-th/0006010 \[nucl-th\]](#).
- [71] X.-f. Guo and X.-N. Wang, *Multiple scattering, parton energy loss and modified fragmentation functions in deeply inelastic e A scattering*, *Phys. Rev. Lett.* **85** (2000) 3591–3594, [arXiv:hep-ph/0005044 \[hep-ph\]](#).
- [72] X.-N. Wang and X.-f. Guo, *Multiple parton scattering in nuclei: Parton energy loss*, *Nucl. Phys.* **A696** (2001) 788–832, [arXiv:hep-ph/0102230 \[hep-ph\]](#).
- [73] P. B. Arnold, G. D. Moore, and L. G. Yaffe, *Transport coefficients in high temperature gauge theories. 1. Leading log results*, *JHEP* **11** (2000) 001, [arXiv:hep-ph/0010177 \[hep-ph\]](#).

- [74] P. B. Arnold, G. D. Moore, and L. G. Yaffe, *Photon emission from quark gluon plasma: Complete leading order results*, *JHEP* **12** (2001) 009, [arXiv:hep-ph/0111107](#) [[hep-ph](#)].
- [75] P. B. Arnold, G. D. Moore, and L. G. Yaffe, *Photon and gluon emission in relativistic plasmas*, *JHEP* **06** (2002) 030, [arXiv:hep-ph/0204343](#) [[hep-ph](#)].
- [76] Y. Mehtar-Tani, J. G. Milhano, and K. Tywoniuk, *Jet physics in heavy-ion collisions*, *Int. J. Mod. Phys. A* **28** (2013) 1340013, [arXiv:1302.2579](#) [[hep-ph](#)].
- [77] J. Casalderrey-Solana, J. G. Milhano, and U. A. Wiedemann, *Jet Quenching via Jet Collimation*, *J. Phys. G* **38** (2011) 035006, [arXiv:1012.0745](#) [[hep-ph](#)].
- [78] G.-Y. Qin and B. Muller, *Explanation of Di-jet asymmetry in Pb+Pb collisions at the Large Hadron Collider*, *Phys. Rev. Lett.* **106** (2011) 162302, [arXiv:1012.5280](#) [[hep-ph](#)]. [Erratum: *Phys. Rev. Lett.* 108,189904(2012)].
- [79] Y. Mehtar-Tani, C. A. Salgado, and K. Tywoniuk, *Anti-angular ordering of gluon radiation in QCD media*, *Phys. Rev. Lett.* **106** (2011) 122002, [arXiv:1009.2965](#) [[hep-ph](#)].
- [80] J. Casalderrey-Solana, Y. Mehtar-Tani, C. A. Salgado, and K. Tywoniuk, *New picture of jet quenching dictated by color coherence*, *Phys. Lett. B* **725** (2013) 357–360, [arXiv:1210.7765](#) [[hep-ph](#)].
- [81] N. Armesto, L. Cunqueiro, and C. A. Salgado, *Q-PYTHIA: A Medium-modified implementation of final state radiation*, *Eur. Phys. J. C* **63** (2009) 679–690, [arXiv:0907.1014](#) [[hep-ph](#)].
- [82] K. C. Zapp, *JEWEL 2.0.0: directions for use*, *Eur. Phys. J. C* **74** (2014) no. 2, 2762, [arXiv:1311.0048](#) [[hep-ph](#)].
- [83] I. P. Lokhtin, L. V. Malinina, S. V. Petrushanko, A. M. Snigirev, I. Arsene, and K. Tywoniuk, *Heavy ion event generator HYDJET++ (HYDroynamics plus JETs)*, *Comput. Phys. Commun.* **180** (2009) 779–799, [arXiv:0809.2708](#) [[hep-ph](#)].
- [84] J. Casalderrey-Solana, D. C. Gulhan, J. G. Milhano, D. Pablos, and K. Rajagopal, *A Hybrid Strong/Weak Coupling Approach to Jet Quenching*, *JHEP* **10** (2014) 19, [arXiv:1405.3864](#) [[hep-ph](#)]. [Erratum: *JHEP*09,175(2015)].
- [85] J. M. Campbell and R. K. Ellis, *MCFM for the Tevatron and the LHC*, *Nucl. Phys. Proc. Suppl.* **205-206** (2010) 10–15, [arXiv:1007.3492](#) [[hep-ph](#)].
- [86] D. d’Enterria, K. Krajczár, and H. Paukkunen, *Top-quark production in proton-nucleus and nucleus-nucleus collisions at LHC energies and beyond*, *Phys. Lett. B* **746** (2015) 64–72, [arXiv:1501.05879](#) [[hep-ph](#)].
- [87] A. V. Baskakov, E. E. Boos, L. V. Dudko, I. P. Lokhtin, and A. M. Snigirev, *Single top quark production in heavy ion collisions at energies available at the CERN Large Hadron Collider*, *Phys. Rev. C* **92** (2015) no. 4, 044901, [arXiv:1502.04875](#) [[hep-ph](#)].
- [88] K. J. Eskola, H. Paukkunen, and C. A. Salgado, *EPS09: A New Generation of NLO and LO Nuclear Parton Distribution Functions*, *JHEP* **04** (2009) 065, [arXiv:0902.4154](#) [[hep-ph](#)].
- [89] L. Apolinário, J. G. Milhano, G. Salam, and C. A. Salgado, *in preparation*, .
- [90] A. Andronic et al., *Heavy-flavour and quarkonium production in the LHC era: from proton-proton to heavy-ion collisions*, [arXiv:1506.03981](#) [[nucl-ex](#)].
- [91] K. Zhou, Z. Chen, C. Greiner, and P. Zhuang, *Thermal Charm and Charmonium Production in Quark Gluon Plasma*, [arXiv:1602.01667](#) [[hep-ph](#)].
- [92] J. Uphoff, O. Fochler, Z. Xu, and C. Greiner, *Heavy quark production at RHIC and LHC within a partonic transport model*, *Phys. Rev. C* **82** (2010) 044906, [arXiv:1003.4200](#) [[hep-ph](#)].
- [93] J. Uphoff, *Workshop on heavy ions at FCC, September 2014*, <https://indico.cern.ch/event/331669/contribution/10>.
- [94] B.-W. Zhang, C.-M. Ko, and W. Liu, *Thermal charm production in a quark-gluon plasma in Pb-Pb collisions at  $s^{1/2}(NN) = 5.5\text{-TeV}$* , *Phys. Rev. C* **77** (2008) 024901, [arXiv:0709.1684](#)

- [nucl-th].
- [95] Y. Liu and C.-M. Ko, *Thermal production of charm quarks in heavy ion collisions at Future Circular Collider*, [arXiv:1604.01207](https://arxiv.org/abs/1604.01207) [nucl-th].
- [96] C.-M. Ko and Y. Liu, *Workshop on heavy ions at FCC, September 2014*, <https://indico.cern.ch/event/331669/contribution/14>.
- [97] K. Zhou, *Workshop on heavy ions at FCC, March 2015*, <https://indico.cern.ch/event/382529/contribution/4>.
- [98] M. Cacciari, S. Frixione, N. Houdeau, M. L. Mangano, P. Nason, and G. Ridolfi, *Theoretical predictions for charm and bottom production at the LHC*, *JHEP* **10** (2012) 137, [arXiv:1205.6344](https://arxiv.org/abs/1205.6344) [hep-ph].
- [99] K. J. Eskola, V. J. Kolhinen, and C. A. Salgado, *The Scale dependent nuclear effects in parton distributions for practical applications*, *Eur. Phys. J.* **C9** (1999) 61–68, [arXiv:hep-ph/9807297](https://arxiv.org/abs/hep-ph/9807297) [hep-ph].
- [100] T. Sjostrand, L. Lonnblad, and S. Mrenna, *PYTHIA 6.2: Physics and manual*, [arXiv:hep-ph/0108264](https://arxiv.org/abs/hep-ph/0108264) [hep-ph].
- [101] ALICE Collaboration, J. Adam et al., *Differential studies of inclusive  $J/\psi$  and  $\psi(2S)$  production at forward rapidity in Pb-Pb collisions at  $\sqrt{s_{NN}} = 2.76$  TeV*, [arXiv:1506.08804](https://arxiv.org/abs/1506.08804) [nucl-ex].
- [102] ALICE Collaboration, J. Adam et al., *Inclusive, prompt and non-prompt  $J/\psi$  production at mid-rapidity in Pb-Pb collisions at  $\sqrt{s_{NN}} = 2.76$  TeV*, *JHEP* **07** (2015) 051, [arXiv:1504.07151](https://arxiv.org/abs/1504.07151) [nucl-ex].
- [103] ALICE Collaboration, B. B. Abelev et al., *Centrality, rapidity and transverse momentum dependence of  $J/\psi$  suppression in Pb-Pb collisions at  $\sqrt{s_{NN}}=2.76$  TeV*, *Phys. Lett.* **B734** (2014) 314–327, [arXiv:1311.0214](https://arxiv.org/abs/1311.0214) [nucl-ex].
- [104] CMS Collaboration, S. Chatrchyan et al., *Suppression of non-prompt  $J/\psi$ , prompt  $J/\psi$ , and  $\Upsilon$  in PbPb collisions at  $\sqrt{s_{NN}} = 2.76$  TeV*, *JHEP* **05** (2012) 063, [arXiv:1201.5069](https://arxiv.org/abs/1201.5069) [nucl-ex].
- [105] Y.-P. Liu, Z. Qu, N. Xu, and P.-f. Zhuang,  *$J/\psi$  Transverse Momentum Distribution in High Energy Nuclear Collisions at RHIC*, *Phys. Lett.* **B678** (2009) 72, [arXiv:0901.2757](https://arxiv.org/abs/0901.2757) [nucl-th].
- [106] X. Zhao and R. Rapp, *Medium modifications and production of charmonia at LHC*, *Nucl. Phys.* **A859** (2011) 114, [arXiv:1102.2194](https://arxiv.org/abs/1102.2194) [hep-ph].
- [107] A. Andronic, P. Braun-Munzinger, K. Redlich, and J. Stachel, *The thermal model on the verge of the ultimate test: particle production in Pb-Pb collisions at the LHC*, *J. Phys.* **G38** (2011) 124081, [arXiv:1106.6321](https://arxiv.org/abs/1106.6321) [nucl-th].
- [108] P. Braun-Munzinger, *Workshop on heavy ions at FCC, March 2015*, <https://indico.cern.ch/event/382529/contribution/6>.
- [109] G. Aarts, C. Allton, T. Harris, S. Kim, M. P. Lombardo, S. M. Ryan, and J.-I. Skullerud, *The bottomonium spectrum at finite temperature from  $N_f = 2 + 1$  lattice QCD*, *JHEP* **07** (2014) 097, [arXiv:1402.6210](https://arxiv.org/abs/1402.6210) [hep-lat].
- [110] A. Andronic, *Workshop on heavy ions at FCC, December 2013*, <https://indico.cern.ch/event/288576/contribution/7>.
- [111] S. Kim, P. Petreczky, and A. Rothkopf, *In-medium quarkonium properties from a lattice QCD based effective field theory*, 2015. [arXiv:1512.05289](https://arxiv.org/abs/1512.05289) [hep-lat]. <http://inspirehep.net/record/1409933/files/arXiv:1512.05289.pdf>.
- [112] Y. Burnier, O. Kaczmarek, and A. Rothkopf, *Quarkonium at finite temperature: Towards realistic phenomenology from first principles*, *JHEP* **12** (2015) 101, [arXiv:1509.07366](https://arxiv.org/abs/1509.07366) [hep-ph].
- [113] H.-T. Shu, H.-T. Ding, O. Kaczmarek, S. Mukherjee, and H. Ohno, *A stochastic approach to the reconstruction of spectral functions in lattice QCD*, in *Proceedings, 33rd International*

- Symposium on Lattice Field Theory (Lattice 2015)*. 2015. [arXiv:1510.02901 \[hep-lat\]](https://arxiv.org/abs/1510.02901). <http://inspirehep.net/record/1397181/files/arXiv:1510.02901.pdf>.
- [114] M. L. Mangano, P. Nason, and G. Ridolfi, *Heavy quark correlations in hadron collisions at next-to-leading order*, *Nucl. Phys.* **B373** (1992) 295–345.
- [115] L. V. Gribov, E. M. Levin, and M. G. Ryskin, *Semihard Processes in QCD*, *Phys. Rept.* **100** (1983) 1–150.
- [116] A. H. Mueller and J.-w. Qiu, *Gluon Recombination and Shadowing at Small Values of  $x$* , *Nucl. Phys.* **B268** (1986) 427.
- [117] E. A. Kuraev, L. N. Lipatov, and V. S. Fadin, *The Pomernanchuk Singularity in Nonabelian Gauge Theories*, *Sov. Phys. JETP* **45** (1977) 199–204. [*Zh. Eksp. Teor. Fiz.*72,377(1977)].
- [118] I. I. Balitsky and L. N. Lipatov, *The Pomernanchuk Singularity in Quantum Chromodynamics*, *Sov. J. Nucl. Phys.* **28** (1978) 822–829. [*Yad. Fiz.*28,1597(1978)].
- [119] European Muon Collaboration, J. Ashman et al., *A Measurement of the ratio of the nucleon structure function in copper and deuterium*, *Z. Phys.* **C57** (1993) 211–218.
- [120] F. Gelis, E. Iancu, J. Jalilian-Marian, and R. Venugopalan, *The Color Glass Condensate*, *Ann. Rev. Nucl. Part. Sci.* **60** (2010) 463–489, [arXiv:1002.0333 \[hep-ph\]](https://arxiv.org/abs/1002.0333).
- [121] J. C. Collins, D. E. Soper, and G. F. Sterman, *Factorization of Hard Processes in QCD*, *Adv. Ser. Direct. High Energy Phys.* **5** (1989) 1–91, [arXiv:hep-ph/0409313 \[hep-ph\]](https://arxiv.org/abs/hep-ph/0409313).
- [122] J. C. Collins and R. K. Ellis, *Heavy quark production in very high-energy hadron collisions*, *Nucl. Phys.* **B360** (1991) 3–30.
- [123] E. M. Levin, M. G. Ryskin, Yu. M. Shabelski, and A. G. Shuvaev, *Heavy quark production in semihard nucleon interactions*, *Sov. J. Nucl. Phys.* **53** (1991) 657. [*Yad. Fiz.*53,1059(1991)].
- [124] S. Catani, M. Ciafaloni, and F. Hautmann, *Gluon contributions to small  $x$  heavy flavour production*, *Phys. Lett.* **B242** (1990) 97–102.
- [125] S. Catani, M. Ciafaloni, and F. Hautmann, *High-energy factorization and small  $x$  heavy flavor production*, *Nucl. Phys.* **B366** (1991) 135–188.
- [126] V. Gribov and L. Lipatov,  *$e^+ e^-$  pair annihilation and deep inelastic  $e p$  scattering in perturbation theory*, *Sov.J.Nucl.Phys.* **15** (1972) 675–684.
- [127] V. Gribov and L. Lipatov, *Deep inelastic  $e p$  scattering in perturbation theory*, *Sov.J.Nucl.Phys.* **15** (1972) 438–450.
- [128] G. Altarelli and G. Parisi, *Asymptotic Freedom in Parton Language*, *Nucl.Phys.* **B126** (1977) 298.
- [129] Y. L. Dokshitzer, *Calculation of the Structure Functions for Deep Inelastic Scattering and  $e^+ e^-$  Annihilation by Perturbation Theory in Quantum Chromodynamics.*, *Sov.Phys.JETP* **46** (1977) 641–653.
- [130] G. A. Chirilli, B.-W. Xiao, and F. Yuan, *Inclusive Hadron Productions in pA Collisions*, *Phys. Rev.* **D86** (2012) 054005, [arXiv:1203.6139 \[hep-ph\]](https://arxiv.org/abs/1203.6139).
- [131] T. Altinoluk, N. Armesto, G. Beuf, A. Kovner, and M. Lublinsky, *Single-inclusive particle production in proton-nucleus collisions at next-to-leading order in the hybrid formalism*, *Phys. Rev.* **D91** (2015) no. 9, 094016, [arXiv:1411.2869 \[hep-ph\]](https://arxiv.org/abs/1411.2869).
- [132] I. Balitsky and G. A. Chirilli, *Next-to-leading order evolution of color dipoles*, *Phys. Rev.* **D77** (2008) 014019, [arXiv:0710.4330 \[hep-ph\]](https://arxiv.org/abs/0710.4330).
- [133] A. Kovner, M. Lublinsky, and Y. Mulian, *Jalilian-Marian, Iancu, McLerran, Weigert, Leonidov, Kovner evolution at next to leading order*, *Phys. Rev.* **D89** (2014) no. 6, 061704, [arXiv:1310.0378 \[hep-ph\]](https://arxiv.org/abs/1310.0378).
- [134] I. Balitsky and G. A. Chirilli, *Rapidity evolution of Wilson lines at the next-to-leading order*, *Phys. Rev.* **D88** (2013) 111501, [arXiv:1309.7644 \[hep-ph\]](https://arxiv.org/abs/1309.7644).
- [135] G. Beuf, *Improving the kinematics for low- $x$  QCD evolution equations in coordinate space*,

- Phys. Rev. **D89** (2014) no. 7, 074039, [arXiv:1401.0313 \[hep-ph\]](#).
- [136] E. Iancu, J. D. Madrigal, A. H. Mueller, G. Soyez, and D. N. Triantafyllopoulos, *Resumming double logarithms in the QCD evolution of color dipoles*, *Phys. Lett.* **B744** (2015) 293–302, [arXiv:1502.05642 \[hep-ph\]](#).
- [137] T. Lappi and H. Mantysaari, *Next-to-leading order Balitsky-Kovchegov equation with resummation*, [arXiv:1601.06598 \[hep-ph\]](#).
- [138] ZEUS, H1 Collaboration, H. Abramowicz et al., *Combination of measurements of inclusive deep inelastic  $e^\pm p$  scattering cross sections and QCD analysis of HERA data*, *Eur. Phys. J.* **C75** (2015) no. 12, 580, [arXiv:1506.06042 \[hep-ex\]](#).
- [139] J. L. Albacete, J. G. Milhano, P. Quiroga-Arias, and J. Rojo, *Linear vs Non-Linear QCD Evolution: From HERA Data to LHC Phenomenology*, *Eur. Phys. J.* **C72** (2012) 2131, [arXiv:1203.1043 \[hep-ph\]](#).
- [140] S. Schlichting, *Initial state and pre-equilibrium effects in small systems*, in *25th International Conference on Ultra-Relativistic Nucleus-Nucleus Collisions (Quark Matter 2015) Kobe, Japan, September 27-October 3, 2015*. 2016. [arXiv:1601.01177 \[hep-ph\]](#).  
<http://inspirehep.net/record/1413757/files/arXiv:1601.01177.pdf>.
- [141] BRAHMS Collaboration, I. Arsene et al., *On the evolution of the nuclear modification factors with rapidity and centrality in  $d + Au$  collisions at  $s(NN)^{1/2} = 200\text{-GeV}$* , *Phys. Rev. Lett.* **93** (2004) 242303, [arXiv:nucl-ex/0403005 \[nucl-ex\]](#).
- [142] STAR Collaboration, J. Adams et al., *Forward neutral pion production in  $p+p$  and  $d+Au$  collisions at  $s(NN)^{1/2} = 200\text{-GeV}$* , *Phys. Rev. Lett.* **97** (2006) 152302, [arXiv:nucl-ex/0602011 \[nucl-ex\]](#).
- [143] STAR Collaboration, E. Braidot, *Two Particle Correlations at Forward Rapidity in STAR*, *Nucl. Phys.* **A854** (2011) 168–174, [arXiv:1008.3989 \[nucl-ex\]](#).
- [144] PHENIX Collaboration, A. Adare et al., *Suppression of back-to-back hadron pairs at forward rapidity in  $d+Au$  Collisions at  $\sqrt{s_{NN}} = 200\text{ GeV}$* , *Phys. Rev. Lett.* **107** (2011) 172301, [arXiv:1105.5112 \[nucl-ex\]](#).
- [145] J. L. Albacete and C. Marquet, *Azimuthal correlations of forward di-hadrons in  $d+Au$  collisions at RHIC in the Color Glass Condensate*, *Phys. Rev. Lett.* **105** (2010) 162301, [arXiv:1005.4065 \[hep-ph\]](#).
- [146] A. Stasto, B.-W. Xiao, and F. Yuan, *Back-to-Back Correlations of Di-hadrons in  $dAu$  Collisions at RHIC*, *Phys. Lett.* **B716** (2012) 430–434, [arXiv:1109.1817 \[hep-ph\]](#).
- [147] A. M. Stasto, K. J. Golec-Biernat, and J. Kwiecinski, *Geometric scaling for the total  $\gamma^* p$  cross-section in the low  $x$  region*, *Phys. Rev. Lett.* **86** (2001) 596–599, [arXiv:hep-ph/0007192 \[hep-ph\]](#).
- [148] N. Armesto, C. A. Salgado, and U. A. Wiedemann, *Relating high-energy lepton-hadron, proton-nucleus and nucleus-nucleus collisions through geometric scaling*, *Phys. Rev. Lett.* **94** (2005) 022002, [arXiv:hep-ph/0407018 \[hep-ph\]](#).
- [149] L. McLerran and M. Praszalowicz, *Saturation and Scaling of Multiplicity, Mean  $p_T$  and  $p_T$  Distributions from  $200\text{ GeV} < \sqrt{s} < 7\text{ TeV}$* , *Acta Phys. Polon.* **B41** (2010) 1917–1926, [arXiv:1006.4293 \[hep-ph\]](#).
- [150] F. Caola and S. Forte, *Geometric Scaling from GLAP evolution*, *Phys. Rev. Lett.* **101** (2008) 022001, [arXiv:0802.1878 \[hep-ph\]](#).
- [151] J. L. Albacete and C. Marquet, *Gluon saturation and initial conditions for relativistic heavy ion collisions*, *Prog. Part. Nucl. Phys.* **76** (2014) 1–42, [arXiv:1401.4866 \[hep-ph\]](#).
- [152] A. Kurkela, *Initial state of Heavy-Ion Collisions: Isotropization and thermalization*, in *25th International Conference on Ultra-Relativistic Nucleus-Nucleus Collisions (Quark Matter 2015)*

- Kobe, Japan, September 27-October 3, 2015. 2016. [arXiv:1601.03283](https://arxiv.org/abs/1601.03283) [hep-ph].  
<http://inspirehep.net/record/1415134/files/arXiv:1601.03283.pdf>.
- [153] J. Liu, C. Shen, and U. Heinz, *Pre-equilibrium evolution effects on heavy-ion collision observables*, *Phys. Rev.* **C91** (2015) no. 6, 064906, [arXiv:1504.02160](https://arxiv.org/abs/1504.02160) [nucl-th]. [Erratum: *Phys. Rev.* **C92**,no.4,049904(2015)].
- [154] N. Armesto, H. Paukkunen, J. M. Penin, C. A. Salgado, and P. Zurita, *An analysis of the impact of LHC Run I proton-lead data on nuclear parton densities*, [arXiv:1512.01528](https://arxiv.org/abs/1512.01528) [hep-ph].
- [155] M. Hirai, S. Kumano, and T. H. Nagai, *Determination of nuclear parton distribution functions and their uncertainties in next-to-leading order*, *Phys. Rev.* **C76** (2007) 065207, [arXiv:0709.3038](https://arxiv.org/abs/0709.3038) [hep-ph].
- [156] D. de Florian, R. Sassot, P. Zurita, and M. Stratmann, *Global Analysis of Nuclear Parton Distributions*, *Phys. Rev.* **D85** (2012) 074028, [arXiv:1112.6324](https://arxiv.org/abs/1112.6324) [hep-ph].
- [157] K. Kovarik et al., *nCTEQ15 - Global analysis of nuclear parton distributions with uncertainties in the CTEQ framework*, *Phys. Rev.* **D93** (2016) no. 8, 085037, [arXiv:1509.00792](https://arxiv.org/abs/1509.00792) [hep-ph].
- [158] I. Balitsky and G. A. Chirilli, *Photon impact factor and  $k_T$ -factorization for DIS in the next-to-leading order*, *Phys. Rev.* **D87** (2013) no. 1, 014013, [arXiv:1207.3844](https://arxiv.org/abs/1207.3844) [hep-ph].
- [159] G. Beuf, *NLO corrections for the dipole factorization of DIS structure functions at low  $x$* , *Phys. Rev.* **D85** (2012) 034039, [arXiv:1112.4501](https://arxiv.org/abs/1112.4501) [hep-ph].
- [160] T. Lappi, *Initial state in heavy ion collisions*, in *7th International Conference on Hard and Electromagnetic Probes of High-Energy Nuclear Collisions (Hard Probes 2015) Montreal, Quebec, Canada, June 29-July 3, 2015*. 2015. [arXiv:1509.04503](https://arxiv.org/abs/1509.04503) [hep-ph].  
<http://inspirehep.net/record/1393505/files/arXiv:1509.04503.pdf>.
- [161] K. Watanabe, B.-W. Xiao, F. Yuan, and D. Zaslavsky, *Implementing the exact kinematical constraint in the saturation formalism*, *Phys. Rev.* **D92** (2015) no. 3, 034026, [arXiv:1505.05183](https://arxiv.org/abs/1505.05183) [hep-ph].
- [162] A. H. Rezaeian, *Semi-inclusive photon-hadron production in  $pp$  and  $pA$  collisions at RHIC and LHC*, *Phys. Rev.* **D86** (2012) 094016, [arXiv:1209.0478](https://arxiv.org/abs/1209.0478) [hep-ph].
- [163] A. H. Rezaeian, *CGC predictions for  $p+A$  collisions at the LHC and signature of QCD saturation*, *Phys. Lett.* **B718** (2013) 1058–1069, [arXiv:1210.2385](https://arxiv.org/abs/1210.2385) [hep-ph].
- [164] I. Helenius, K. J. Eskola, and H. Paukkunen, *Probing the small- $x$  nuclear gluon distributions with isolated photons at forward rapidities in  $p+Pb$  collisions at the LHC*, *JHEP* **09** (2014) 138, [arXiv:1406.1689](https://arxiv.org/abs/1406.1689) [hep-ph].
- [165] D. Kharzeev, E. Levin, and L. McLerran, *Jet azimuthal correlations and parton saturation in the color glass condensate*, *Nucl. Phys.* **A748** (2005) 627–640, [arXiv:hep-ph/0403271](https://arxiv.org/abs/hep-ph/0403271) [hep-ph].
- [166] Z.-B. Kang, I. Vitev, and H. Xing, *Nuclear modification of high transverse momentum particle production in  $p+A$  collisions at RHIC and LHC*, *Phys. Lett.* **B718** (2012) 482–487, [arXiv:1209.6030](https://arxiv.org/abs/1209.6030) [hep-ph].
- [167] F. Arleo and S. Peigne,  *$J/\psi$  suppression in  $p-A$  collisions from parton energy loss in cold QCD matter*, *Phys. Rev. Lett.* **109** (2012) 122301, [arXiv:1204.4609](https://arxiv.org/abs/1204.4609) [hep-ph].
- [168] A. Stasto, B.-W. Xiao, and D. Zaslavsky, *Drell-Yan Lepton-Pair-Jet Correlation in  $pA$  collisions*, *Phys. Rev.* **D86** (2012) 014009, [arXiv:1204.4861](https://arxiv.org/abs/1204.4861) [hep-ph].
- [169] A. van Hameren, P. Kotko, K. Kutak, C. Marquet, and S. Sapeta, *Saturation effects in forward-forward dijet production in  $p+Pb$  collisions*, *Phys. Rev.* **D89** (2014) no. 9, 094014, [arXiv:1402.5065](https://arxiv.org/abs/1402.5065) [hep-ph].
- [170] P. Kotko, K. Kutak, C. Marquet, E. Petreska, S. Sapeta, and A. van Hameren, *Improved TMD factorization for forward dijet production in dilute-dense hadronic collisions*, *JHEP* **09** (2015)

- 106, [arXiv:1503.03421 \[hep-ph\]](#).
- [171] J. M. Campbell and R. K. Ellis, *MCFM for the Tevatron and the LHC*, *Nucl. Phys. Proc. Suppl.* **205-206** (2010, <http://mcfm.fnal.gov>) 10–15, [arXiv:1007.3492 \[hep-ph\]](#).
- [172] H.-L. Lai, M. Guzzi, J. Huston, Z. Li, P. M. Nadolsky, J. Pumplin, and C. P. Yuan, *New parton distributions for collider physics*, *Phys. Rev.* **D82** (2010) 074024, [arXiv:1007.2241 \[hep-ph\]](#).
- [173] M. Czakon, M. L. Mangano, A. Mitov, and J. Rojo, *Constraints on the gluon PDF from top quark pair production at hadron colliders*, *JHEP* **07** (2013) 167, [arXiv:1303.7215 \[hep-ph\]](#).
- [174] H. Paukkunen and P. Zurita, *PDF reweighting in the Hessian matrix approach*, *JHEP* **12** (2014) 100, [arXiv:1402.6623 \[hep-ph\]](#).
- [175] CMS Collaboration, S. Chatrchyan et al., *Studies of dijet transverse momentum balance and pseudorapidity distributions in pPb collisions at  $\sqrt{s_{NN}} = 5.02$  TeV*, *Eur. Phys. J.* **C74** (2014) no. 7, 2951, [arXiv:1401.4433 \[nucl-ex\]](#).
- [176] I. Helenius, H. Paukkunen, and K. J. Eskola, *Nuclear PDF constraints from p+Pb collisions at the LHC*, in *Proceedings, 23rd International Workshop on Deep-Inelastic Scattering and Related Subjects (DIS 2015)*. 2015. [arXiv:1509.02798 \[hep-ph\]](#).  
<http://inspirehep.net/record/1392660/files/arXiv:1509.02798.pdf>.
- [177] A. Accardi et al., *Electron Ion Collider: The Next QCD Frontier - Understanding the glue that binds us all*, [arXiv:1212.1701 \[nucl-ex\]](#).
- [178] LHeC Study Group Collaboration, J. L. Abelleira Fernandez et al., *A Large Hadron Electron Collider at CERN: Report on the Physics and Design Concepts for Machine and Detector*, *J. Phys.* **G39** (2012) 075001, [arXiv:1206.2913 \[physics.acc-ph\]](#).
- [179] C. F. von Weizsacker, *Radiation emitted in collisions of very fast electrons*, *Z. Phys.* **88** (1934) 612–625.
- [180] E. J. Williams, *Nature of the high-energy particles of penetrating radiation and status of ionization and radiation formulae*, *Phys. Rev.* **45** (1934) 729–730.
- [181] E. Fermi, *On the theory of collisions between atoms and electrically charged particles*, *Nuovo Cim.* **2** (1925) 143–158, [arXiv:hep-th/0205086 \[hep-th\]](#). [,243(1925)].
- [182] D. d’Enterria, M. Klasen, and K. Piotrkowski, *High-Energy Photon Collisions at the LHC*, *Nucl. Phys. Proc. Suppl.* **179B** (2008) 1.
- [183] A. J. Baltz, *The Physics of Ultrapерipheral Collisions at the LHC*, *Phys. Rept.* **458** (2008) 1–171, [arXiv:0706.3356 \[nucl-ex\]](#).
- [184] A. J. Baltz, G. Baur, D. d’Enterria, L. Frankfurt, et al., *The Physics of Ultrapерipheral Collisions at the LHC*, *Phys. Rep.* **458** (2008) 1, [arXiv:0706.3356 \[nucl-ex\]](#).
- [185] D. G. d’Enterria, *Quarkonia photoproduction at nucleus colliders*, *Nucl. Phys. Proc. Suppl.* **184** (2008) 158–162, [arXiv:0711.1123 \[nucl-ex\]](#).
- [186] J. P. Lansberg, A. Rakotozafindrabe, P. Artoisenet, D. Blaschke, J. Cugnon, D. d’Enterria, A. C. Kraan, F. Maltoni, D. Prorok, and H. Satz, *Perspectives on heavy-quarkonium production at the LHC*, *AIP Conf. Proc.* **1038** (2008) 15–44, [arXiv:0807.3666 \[hep-ph\]](#).
- [187] L. Frankfurt, M. McDermott, and M. Strikman, *A Fresh look at diffractive  $J/\psi$  photoproduction at HERA, with predictions for THERA*, *JHEP* **0103** (2001) 045, [arXiv:hep-ph/0009086 \[hep-ph\]](#).
- [188] A. D. Martin, C. Nockles, M. G. Ryskin, and T. Teubner, *Small  $x$  gluon from exclusive  $J/\psi$  production*, *Phys. Lett. B* **662** (2008) 252, [arXiv:0709.4406 \[hep-ph\]](#).
- [189] ZEUS Collaboration, S. Chekanov et al., *Measurement of Elastic  $\Upsilon$  Photoproduction at HERA*, *Phys. Lett. B* **437** (1998) 432, [hep-ex/9807020 \[hep-ex\]](#).
- [190] H1 Collaboration, A. Atkas et al., *Elastic photoproduction of  $J/\psi$  and  $\Upsilon$  mesons at HERA*, *Phys. Lett. B* **483** (2000) 23, [arXiv:hep-ex/0003020 \[hep-ex\]](#).

- [191] ZEUS Collaboration, S. Chekanov et al., *Exclusive photoproduction of  $\Upsilon$  mesons at HERA*, *Phys. Lett. B* **680** (2009) 4, [arXiv:0903.4205 \[hep-ex\]](#).
- [192] ZEUS Collaboration, S. Chekanov et al., *Measurement of the  $t$  dependence in exclusive photoproduction of  $\Upsilon(1S)$  mesons at HERA*, *Phys. Lett. B* **708** (2012) 14, [arXiv:1111.2133 \[hep-ex\]](#).
- [193] LHCb Collaboration, R. Aaij et al., *Exclusive  $J/\psi$  and  $\psi(2S)$  production in  $pp$  collisions at  $\sqrt{s} = 7$  TeV*, *J. Phys. G* **40** (2013) 045001, [arXiv:1301.7084 \[hep-ex\]](#).
- [194] ALICE Collaboration, B. Abelev et al., *Coherent  $J/\psi$  photoproduction in ultra-peripheral Pb-Pb collisions at  $\sqrt{s_{NN}} = 2.76$  TeV*, *Phys. Lett. B* **718** (2013) 1273, [arXiv:1209.3715 \[nucl-ex\]](#).
- [195] ALICE Collaboration, E. Abbas et al., *Charmonium and  $e^+e^-$  pair photoproduction at mid-rapidity in ultra-peripheral Pb-Pb collisions at  $\sqrt{s_{NN}}=2.76$  TeV*, *Eur. Phys. J. C* **73** (2013) no. 11, 2617, [arXiv:1305.1467 \[nucl-ex\]](#).
- [196] ALICE Collaboration, B. B. Abelev et al., *Exclusive  $J/\psi$  photoproduction off protons in ultra-peripheral p-Pb collisions at  $\sqrt{s_{NN}} = 5.02$  TeV*, *Phys. Rev. Lett.* **113** (2014) no. 23, 232504, [arXiv:1406.7819 \[nucl-ex\]](#).
- [197] LHCb Collaboration, R. Aaij et al., *Measurement of the exclusive  $\Upsilon$  production cross-section in  $pp$  collisions at  $\sqrt{s} = 7$  TeV and 8 TeV*, *JHEP* **09** (2015) 084, [arXiv:1505.08139 \[hep-ex\]](#).
- [198] N. Armesto and A. H. Rezaeian, *Exclusive vector meson production at high energies and gluon saturation*, *Phys. Rev.* **D90** (2014) no. 5, 054003, [arXiv:1402.4831 \[hep-ph\]](#).
- [199] L. V. Gribov, E. M. Levin, and M. G. Ryskin, *Semihard Processes in QCD*, *Phys. Rept.* **100** (1983) 1.
- [200] A. H. Mueller and J.-W. Qiu, *Gluon Recombination and Shadowing at Small Values of  $x$* , *Nucl. Phys. B* **268** (1986) 427.
- [201] L. D. McLerran and R. Venugopalan, *Gluon distribution functions for very large nuclei at small transverse momentum*, *Phys. Rev. D.* **49** (1994) 3552.
- [202] P. Jones, D. Martin, M. G. Ryskin, and T. Teubner, *Probes of the small  $x$  gluon via exclusive  $J/\psi$  and  $\Upsilon$  production at HERA and LHC*, *JHEP* **1311** (2013) 085, [arXiv:1307.7099 \[hep-ph\]](#).
- [203] G. Sampaio and M. V. T. Machado, *Exclusive photoproduction of quarkonium in proton-nucleus collisions at the LHC*, [arXiv:1312.0770 \[hep-ph\]](#).
- [204] G. Sampaio dos Santos and M. V. T. Machado, *On theoretical uncertainty of color dipole phenomenology in the  $J/\psi$  and  $\Upsilon$  photoproduction in pA and AA collisions at the CERN Large Hadron Collider*, *J. Phys. G* **42** (2015) no. 10, 105001, [arXiv:1411.7918 \[hep-ph\]](#).
- [205] A. H. Rezaeian and I. Schmidt, *Impact-parameter dependent Color Glass Condensate dipole model and new combined HERA data*, *Phys. Rev.* **D88** (2013) 074016, [arXiv:1307.0825 \[hep-ph\]](#).
- [206] A. H. Rezaeian, M. Siddikov, M. Van de Klundert, and R. Venugopalan, *Analysis of combined HERA data in the Impact-Parameter dependent Saturation model*, *Phys. Rev.* **D87** (2013) no. 3, 034002, [arXiv:1212.2974](#).
- [207] CMS Collaboration, S. Chatrchyan et al., *Search for exclusive or semi-exclusive photon pair production and observation of exclusive and semi-exclusive electron pair production in  $pp$  collisions at  $\sqrt{s} = 7$  TeV*, *JHEP* **11** (2012) 080, [arXiv:1209.1666 \[hep-ex\]](#).
- [208] CMS Collaboration, S. Chatrchyan et al., *Study of exclusive two-photon production of  $W^+W^-$  in  $pp$  collisions at  $\sqrt{s} = 7$  TeV and constraints on anomalous quartic gauge couplings*, *JHEP* **07** (2013) 116, [arXiv:1305.5596 \[hep-ex\]](#).
- [209] ATLAS Collaboration, G. Aad et al., *Measurement of exclusive  $\gamma\gamma \rightarrow \ell^+\ell^-$  production in proton-proton collisions at  $\sqrt{s} = 7$  TeV with the ATLAS detector*, *Phys. Lett.* **B749** (2015) 242–261, [arXiv:1506.07098 \[hep-ex\]](#).

- [210] P. R. Teles and D. d’Enterria, *Prospects for  $\gamma\gamma \rightarrow H$  and  $\gamma\gamma \rightarrow W^+W^-$  measurements at the FCC-ee*, in *Photon 2015: International Conference on the Structure and Interactions of the Photon and the 21th International Workshop on Photon-Photon Collisions and International Workshop on High Energy Photon Linear Colliders Novosibirsk, Russia, June 15-19, 2015*. 2015. [arXiv:1510.08141 \[hep-ph\]](https://arxiv.org/abs/1510.08141).  
<https://inspirehep.net/record/1401215/files/arXiv:1510.08141.pdf>.
- [211] D. d’Enterria and G. G. da Silveira, *Observing light-by-light scattering at the Large Hadron Collider*, *Phys. Rev. Lett.* **111** (2013) 080405, [arXiv:1305.7142 \[hep-ph\]](https://arxiv.org/abs/1305.7142).
- [212] D. d’Enterria and G. G. da Silveira, *Measuring light-by-light scattering at the LHC and FCC*, in *Proceedings, 16th conference on Elastic and Diffractive Scattering (EDS BLOIS 2015)*. 2016. [arXiv:1602.08088 \[hep-ph\]](https://arxiv.org/abs/1602.08088).  
<https://inspirehep.net/record/1424257/files/arXiv:1602.08088.pdf>.
- [213] G. J. Gounaris, P. I. Porfyriadis, and F. M. Renard, *The gamma gamma  $\rightarrow$  gamma gamma process in the standard and SUSY models at high-energies*, *Eur. Phys. J.* **C9** (1999) 673–686, [arXiv:hep-ph/9902230 \[hep-ph\]](https://arxiv.org/abs/hep-ph/9902230).
- [214] I. F. Ginzburg and A. Schiller, *Search for a heavy magnetic monopole at the Tevatron and CERN LHC*, *Phys. Rev.* **D57** (1998) 6599–6603, [arXiv:hep-ph/9802310 \[hep-ph\]](https://arxiv.org/abs/hep-ph/9802310).
- [215] D. Bernard, *On the potential of light by light scattering for invisible axion detection*, *Nuovo Cim.* **A110** (1997) 1339–1346. [*Nucl. Phys. Proc. Suppl.* 72,201(1999)].
- [216] T. Kikuchi, N. Okada, and M. Takeuchi, *Unparticle physics at the photon collider*, *Phys. Rev.* **D77** (2008) 094012, [arXiv:0801.0018 \[hep-ph\]](https://arxiv.org/abs/0801.0018).
- [217] K.-m. Cheung, *Diphoton signals for low scale gravity in extra dimensions*, *Phys. Rev.* **D61** (2000) 015005, [arXiv:hep-ph/9904266 \[hep-ph\]](https://arxiv.org/abs/hep-ph/9904266).
- [218] J. L. Hewett, F. J. Petriello, and T. G. Rizzo, *Signals for noncommutative interactions at linear colliders*, *Phys. Rev.* **D64** (2001) 075012, [arXiv:hep-ph/0010354 \[hep-ph\]](https://arxiv.org/abs/hep-ph/0010354).
- [219] V. M. Budnev, I. F. Ginzburg, G. V. Meledin, and V. G. Serbo, *The Two photon particle production mechanism. Physical problems. Applications. Equivalent photon approximation*, *Phys. Rept.* **15** (1975) 181–281.
- [220] C. A. Bertulani and G. Baur, *Electromagnetic Processes in Relativistic Heavy Ion Collisions*, *Phys. Rept.* **163** (1988) 299.
- [221] R. N. Cahn and J. D. Jackson, *Realistic equivalent photon yields in heavy ion collisions*, *Phys. Rev.* **D42** (1990) 3690–3695.
- [222] J. Alwall, P. Demin, S. de Visscher, R. Frederix, M. Herquet, F. Maltoni, T. Plehn, D. L. Rainwater, and T. Stelzer, *MadGraph/MadEvent v4: The New Web Generation*, *JHEP* **09** (2007) 028, [arXiv:0706.2334 \[hep-ph\]](https://arxiv.org/abs/0706.2334).
- [223] Z. Bern, A. De Freitas, L. J. Dixon, A. Ghinculov, and H. L. Wong, *QCD and QED corrections to light by light scattering*, *JHEP* **11** (2001) 031, [arXiv:hep-ph/0109079 \[hep-ph\]](https://arxiv.org/abs/hep-ph/0109079).
- [224] S. Fichet, *Prospects for new physics searches at the LHC in the forward proton mode*, *Acta Phys. Polon. Supp.* **8** (2015) 811, [arXiv:1510.01004 \[hep-ph\]](https://arxiv.org/abs/1510.01004).
- [225] CDF Collaboration, T. Aaltonen et al., *Observation of Exclusive Gamma Gamma Production in  $p\bar{p}$  Collisions at  $\sqrt{s} = 1.96$  TeV*, *Phys. Rev. Lett.* **108** (2012) 081801, [arXiv:1112.0858 \[hep-ex\]](https://arxiv.org/abs/1112.0858).
- [226] L. A. Harland-Lang, V. A. Khoze, M. G. Ryskin, and W. J. Stirling, *Standard candle central exclusive processes at the Tevatron and LHC*, *Eur. Phys. J.* **C69** (2010) 179–199, [arXiv:1005.0695 \[hep-ph\]](https://arxiv.org/abs/1005.0695).
- [227] L. A. Harland-Lang, V. A. Khoze, and M. G. Ryskin, *Exclusive physics at the LHC with SuperChic 2*, *Eur. Phys. J.* **C76** (2016) no. 1, 9, [arXiv:1508.02718 \[hep-ph\]](https://arxiv.org/abs/1508.02718).

- [228] L. A. Harland-Lang, A. D. Martin, P. Motylinski, and R. S. Thorne, *Parton distributions in the LHC era: MMHT 2014 PDFs*, *Eur. Phys. J. C* **75** (2015) no. 5, 204, [arXiv:1412.3989 \[hep-ph\]](#).
- [229] J. Nystrand, *Electromagnetic interactions in nucleus-nucleus and proton-proton collisions*, *Nucl. Phys. A* **752** (2005) 470–479, [arXiv:hep-ph/0412096 \[hep-ph\]](#).
- [230] S. J. Brodsky, F. Fleuret, C. Hadjidakis, and J. P. Lansberg, *Physics Opportunities of a Fixed-Target Experiment using the LHC Beams*, *Phys. Rept.* **522** (2013) 239–255, [arXiv:1202.6585 \[hep-ph\]](#).
- [231] J. P. Lansberg, S. J. Brodsky, F. Fleuret, and C. Hadjidakis, *Quarkonium Physics at a Fixed-Target Experiment using the LHC Beams*, *Few Body Syst.* **53** (2012) 11–25, [arXiv:1204.5793 \[hep-ph\]](#).
- [232] C. Lorce et al., *Spin and diffractive physics with A Fixed-Target Experiment at the LHC (AFTER@LHC)*, [arXiv:1212.0425 \[hep-ex\]](#). [AIP Conf. Proc.1523,149(2012)].
- [233] A. Rakotozafindrabe et al., *Spin physics at A Fixed-Target Experiment at the LHC (AFTER@LHC)*, *Phys. Part. Nucl.* **45** (2014) 336–337, [arXiv:1301.5739 \[hep-ex\]](#).
- [234] J. P. Lansberg et al., *Spin physics and TMD studies at A Fixed-Target Experiment at the LHC (AFTER@LHC)*, *EPJ Web Conf.* **85** (2015) 02038, [arXiv:1410.1962 \[hep-ex\]](#).
- [235] L. Massacrier et al., *Studies of Transverse-Momentum-Dependent distributions with A Fixed-Target Experiment using the LHC beams (AFTER@LHC)*, in *21st International Symposium on Spin Physics (SPIN 2014) Beijing, China, October 20-24, 2014*. 2015. [arXiv:1502.00984 \[nucl-ex\]](#).  
<https://inspirehep.net/record/1342809/files/arXiv:1502.00984.pdf>.
- [236] J. P. Lansberg et al., *Physics case for a polarised target for AFTER@LHC*, *PoS PSTP2015* (2015) 042, [arXiv:1602.06857 \[nucl-ex\]](#).
- [237] A. Rakotozafindrabe et al., *Ultra-relativistic heavy-ion physics with AFTER@LHC*, *Nucl. Phys. A* **904-905** (2013) 957c–960c, [arXiv:1211.1294 \[nucl-ex\]](#).
- [238] J. P. Lansberg et al., *AFTER@LHC: a precision machine to study the interface between particle and nuclear physics*, *EPJ Web Conf.* **66** (2014) 11023, [arXiv:1308.5806 \[hep-ex\]](#).
- [239] A. Baurichter et al., *Channeling of high-energy particles in bent crystals: Experiments at the CERN SPS*, *Nucl. Instrum. Meth.* **B164-165** (2000) 27–43.
- [240] J. P. Lansberg, R. E. Mikkelsen, and U. I. Uggerhoj, *Near-threshold production of  $W^\pm$ ,  $Z^0$  and  $H^0$  at a fixed-target experiment at the future ultra-high-energy proton colliders*, *Adv. High Energy Phys.* **2015** (2015) 249167, [arXiv:1507.01438 \[hep-ex\]](#).
- [241] M. Ferro-Luzzi, *Proposal for an absolute luminosity determination in colliding beam experiments using vertex detection of beam-gas interactions*, *Nucl. Instrum. Meth.* **A553** (2005) 388–399.
- [242] E. Uggerhoj and U. I. Uggerhj, *Strong crystalline fields: A possibility for extraction from the LHC*, *Nucl. Instrum. Meth.* **B234** (2005) 31–39.
- [243] HERMES Collaboration, A. Airapetian et al., *The HERMES polarized hydrogen and deuterium gas target in the HERA electron storage ring*, *Nucl. Instrum. Meth.* **A540** (2005) 68–101, [arXiv:physics/0408137 \[physics\]](#).
- [244] C. Barschel, P. Lenisa, A. Nass, and E. Steffens, *A Gas Target Internal to the LHC for the Study of pp Single-Spin Asymmetries and Heavy Ion Collisions*, *Adv. High Energy Phys.* **2015** (2015) 463141.
- [245] A. Mukherjee and W. Vogelsang, *Threshold resummation for W-boson production at RHIC*, *Phys. Rev.* **D73** (2006) 074005, [arXiv:hep-ph/0601162 \[hep-ph\]](#).



## Chapter 5: Physics Opportunities with the FCC-hh Injectors

*B. Goddard*<sup>a1</sup>, *G. Isidori*<sup>a2</sup>, *F. Teubert*<sup>a1</sup> (editors), *M. Bai*<sup>a3</sup>, *A. Ball*<sup>a1</sup>, *B. Batell*<sup>a4</sup>, *T. Bowcock*<sup>a5</sup>, *G. Cavoto*<sup>a6</sup>, *A. Ceccucci*<sup>a1</sup>, *M. Chruszcz*<sup>a2,a7</sup>, *A. Golutvin*<sup>a1,a8</sup>, *W. Herr*<sup>a1</sup>, *J. Jowett*<sup>a1</sup>, *M. Moulson*<sup>a9</sup>, *T. Nakada*<sup>a10</sup>, *J. Rojo*<sup>a11</sup>, *Y. Semertzidis*<sup>a12,a13</sup>

<sup>a1</sup> CERN, CH-1211 Geneva, Switzerland

<sup>a2</sup> Physics Institute, University of Zürich, CH-8057 Zürich, Switzerland

<sup>a3</sup> Forschungszentrum Jülich Institute for Nuclear Physics, 52425 Jülich, Germany

<sup>a4</sup> Pittsburgh Particle Physics, Astrophysics and Cosmology Center, Department of Physics and Astronomy, University of Pittsburgh, USA

<sup>a5</sup> Department of Physics, University of Liverpool, Liverpool, United Kingdom

<sup>a6</sup> Università INFN, Roma I, 00185 Roma, Italy

<sup>a7</sup> H.Niewodniczanski Institute of Nuclear Physics, PAN, Krakow, Poland

<sup>a8</sup> Imperial College, London, United Kingdom

<sup>a9</sup> Laboratori Nazionali di Frascati, 00044 Frascati, Italy

<sup>a10</sup> Ecole Polytechnique Fédérale de Lausanne (EPFL), Lausanne, Switzerland

<sup>a11</sup> Rudolf Peierls Centre for Theoretical Physics, 1 Keble Road, University of Oxford, OXI 3NP Oxford, United Kingdom

<sup>a12</sup> Center for Axion and Precision Physics Research, Institute for Basic Science (IBS), Daejeon 34141, Republic of Korea

<sup>a13</sup> Department of Physics, Korea Advanced Institute of Science and Technology (KAIST), Daejeon 34141, Republic of Korea

### Abstract

In this chapter we explore a few examples of physics opportunities using the existing chain of accelerators at CERN, including potential upgrades. In this context the LHC ring is also considered as a part of the injector system. The objective is to find examples that constitute sensitive probes of New Physics that ideally cannot be done elsewhere or can be done significantly better at the CERN accelerator complex. Some of these physics opportunities may require a more flexible injector complex with additional functionality than that just needed to inject protons into the FCC-hh at the right energy, intensity and bunch structure. Therefore it is timely to discuss these options concurrently with the conceptual design of the FCC-hh injector system.

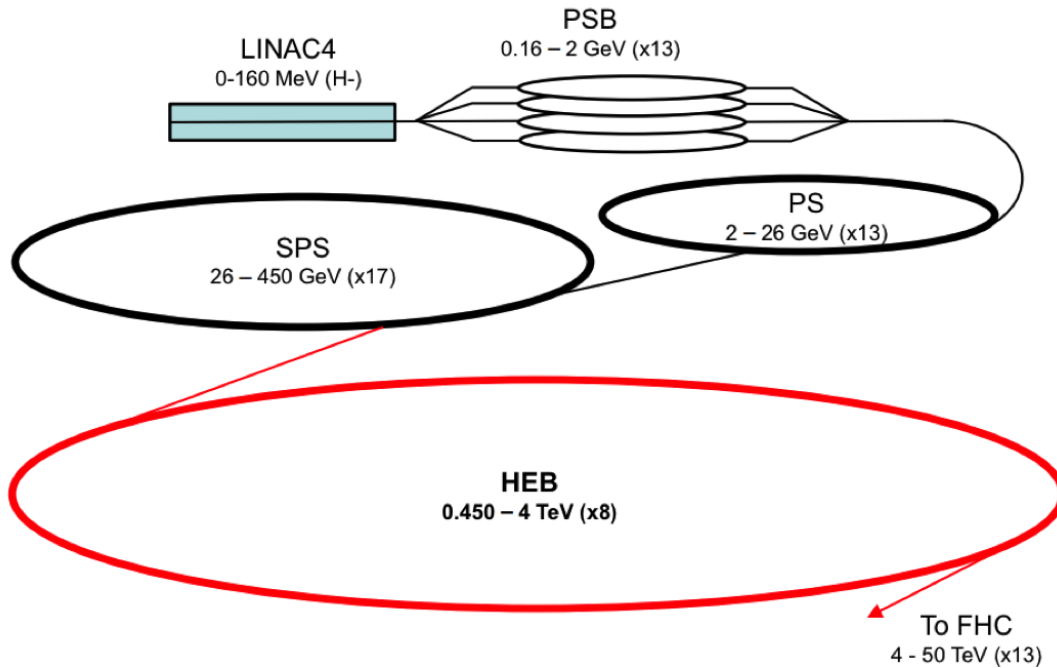


**Fig. 1:** Schematic view of the CERN accelerators system viewed as injectors of the future FCC-hh collider (FHC).

## 1 Introduction

The main problem we have in High Energy Physics (HEP) today is that we know there is physics beyond the Standard Model (SM), as indicated for example by the existence of Dark Matter, and by the fact that most probably New Physics (NP) is also needed to explain the origin of neutrinos masses, but we don't know at what energy scale(s) this NP appears. Conceptually, the SM does not include gravitational interactions, it has no explanation for the replication of quark and lepton flavours and suffers from problems related to the "unnatural" choice of its fundamental parameters. It may very well be that results from the LHC in the coming years will give an unambiguous indication of the relevant energy scale(s). Or it may be that FCC will provide this insight. But it could also be that the energy scale(s) are beyond what the LHC and even FCC can probe, which means that complementary approaches to increasing the available energy with the FCC-hh accelerator complex can be of enormous scientific interest.

In this chapter we explore a few examples of physics opportunities using the existing chain of accelerators at CERN, including potential upgrades. In this context the LHC ring is also considered as a part of the injector system, becoming the High Energy Booster (HEB), see Fig. 1. The objective is to find examples that constitute sensitive probes of NP that ideally cannot be done elsewhere or can be done significantly better at the CERN accelerator complex. Some of these physics opportunities may require a more flexible injector complex with additional functionality than that just needed to inject protons into the FCC-hh at the right energy, intensity and bunch structure. Therefore it is timely to discuss these options concurrently with the conceptual design of the FCC-hh injector system.

We will briefly discuss in the next sections the option to extract multi-TeV protons from HEB for tests of new detector concepts, the use of HEB for a very high luminosity experiment in collider mode when HEB is not injecting protons to the FCC, or several proposals to use high intensity beams of 400 GeV protons from the SPS for fixed target experiments. If polarized protons are available from the linear accelerator (LINAC4) one could also envisage to extract 0.7 GeV polarized protons (the "magic" momentum) from the Proton Synchrotron Booster (PSB) into a  $\sim (40 - 120)$ m radius storage ring to measure the proton Electrical Dipole Moment. In some of these examples, non trivial changes in the design of the FCC-hh injectors are required.

## 2 CERN hadron injector complex for FCC

The FCC hadron collider will require an injector chain capable of filling both rings with around 10'000 bunches of a few TeV protons. Studying the FCC implementation at CERN naturally involves the reuse of the present tunnel infrastructure and hadron machines, up to and possibly including the LHC. With a nominal FCC-hh injection energy of 3.3 TeV [1], the present LHC injector chains for protons and ions need to be complemented with a HEB, which will perform the acceleration from 450 GeV at exit from the SPS. Reuse of a suitably modified LHC is clearly a prime option for the HEB.

### 2.1 FCC-hh proton pre-injector chain

The beam parameters required for FCC-hh [1] are compatible with those delivered routinely to the present LHC machine at 450 GeV [2]. The assumed FCC-hh proton injector chain is shown in Fig.1.

Apart from the HEB, and aside any considerations of equipment lifetime, the HL-LHC injector chain could remain largely as it is for the FCC era. The parameters of the circular injectors in this chain are shown in Table 1, as expected after the upgrades for HL-LHC.

**Table 1:** Parameters of proton accelerators in the LHC injector chain for LHC beams, after the LHC Injector Upgrades (LIU) for HL-LHC.

Parameter	Unit	PSB	PS	SPS
Circumference	m	157	628	6912
Extraction energy	GeV	2.0	26	450
Cycle period	s	1.2	3.6	22.8
Max beam population	$10^{13}$	1.2	2.0	7.7
Beam power	kW	3.2	23	240

### 2.2 FCC High Energy Booster options

Three main options for the HEB are being studied for FCC-hh at CERN. The key parameters which will eventually decide between the different options are attainable FCC-hh injection energy, collider filling time, availability and, of course, capital and operating costs.

While 3.3 TeV is the baseline FCC-hh injection energy for the study, optimisation is planned and a different eventual HEB energy is very likely. This parameter affects the performance of the collider in terms of beam physics and also in terms of magnetic field swing and harmonic control. Higher energies would reduce some constraints in the FCC-hh collider, while increasing the challenges for the HEB and its transfer lines. Lower energy injection will simplify the HEB and injector chain, at the cost of extra complexity, reduced performance limits and risk to the collider.

Reusing the LHC as HEB offers a number of advantages over the alternative of building a completely new HEB, given the relatively limited changes needed to convert the existing, and very well-known, LHC machine into the final piece of the injector chain. Alternatively, a new accelerator based in the LHC tunnel using  $\sim 6 T$  fast ramping superconducting dipoles could be considered.

For existing LHC re-use both rings are needed, to minimise FCC collider filling time. At least two crossings are needed to keep the rings the same length, with injection, collimation, RF and beam dump locations unchanged. The experiments and associated insertions in Points 1,2,5 and 8 would be decommissioned, and new extraction systems accommodated in P1 and P8 for transfer to FCC-hh. The new layout is shown schematically in Fig. 2. The details of the layout and the main changes needed to the LHC are given in [3]. In addition, the ramp rate would need to be increased by a factor of about five to fill the collider quickly enough, for which first feasibility considerations have been investigated [4].

The long straight section in LHC Point 5 which presently houses the CMS experiment would be free in this configuration, for the possible accommodation of an extraction system for Fixed Target

beams, or for a high luminosity experimental interaction point (IP) further discussed in Section 3.

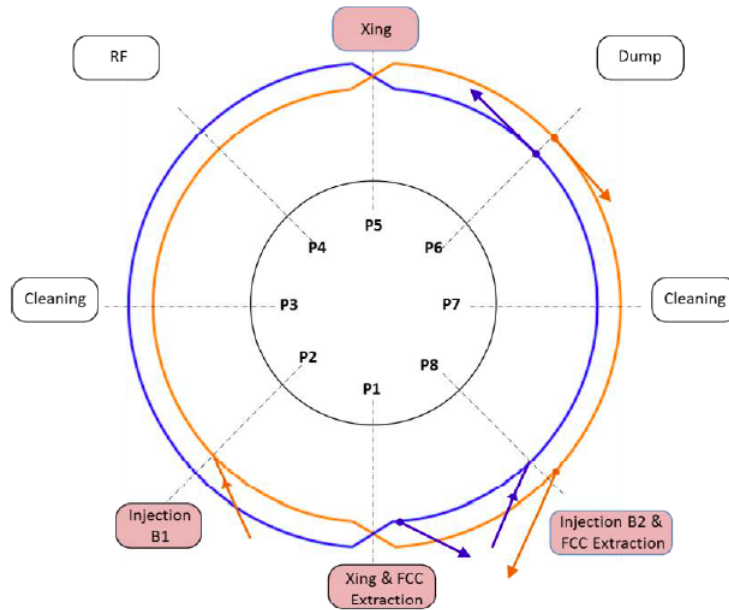


**Fig. 2:** Main functional layout of LHC as HEB as FCC-hh injector

A second option for the HEB is a compact Booster in the 7 km SPS tunnel. Limiting the dipole field to around 7 T (considered as a reasonable maximum for rapid-cycling at up to 1 T/s), the injection energy for the FCC collider would be 1.5 TeV. The accelerator would be single aperture with two extraction straights, a collimation straight, a beam dump straight, an injection straight and a RF straight, which with the present SPS tunnel six-fold symmetry does not leave a spare straight for other dedicated purposes like slow extraction. The study will need to determine whether an injection energy of 26 GeV is adequate, given the swing in energy of above 50. For this option, the simultaneous conception as a  $2 \times 1.5$  TeV collider with a high luminosity IP looks improbable, as this functionality would completely dominate the HEB design and cost.

The final option under consideration for the HEB is a 100 km accelerator in the FCC-hh tunnel, which would be relatively low-cost (at least per unit length) and fast cycling with iron-dominated magnets, but which would need to be powered by a superconducting drive cable to avoid prohibitive power consumption. This so-called super-ferric option would have a low magnetic field of about 1 T to reach 3.3 TeV (if the full machine arcs were filled with dipoles). Again, the conception of this HEB option as a collider seems improbable given the extra functionality required.

The parameters and main features of the SPS and the different HEB options are compared in Table 2, including the potential beam power and estimated annual Proton on Target (p.o.t.) for an eventual Fixed Target operation. For the SPS, the two columns represent a well-analysed [5] case of a short cycle (e.g. CNGS or with a very short 1 s spill) operating in parallel with a long cycle with a spill of around 10 s length. For the HEB options, the spill length is chosen to limit beam power on the target during the spill a rather arbitrary 5 MW, as this parameter may well be an important performance limitation at these very high primary beam energies and long spill lengths. For the HEB in the FCC tunnel, the ramp rate is limited by the RF system and not the ramping of the dipoles.

If all the available time that the injectors are not filling with protons the FCC-hh collider is used for other purposes (fixed target experiments, or other specific experiments located at the injectors), this will be about 80% of the SPS and 60% of the HEB operation. Realistic factors for operational efficiency and transmission to the targets are included in the final p.o.t. estimates shown in Table 2.

An important caveat to note is that the annual p.o.t. quoted are realistic in terms of the cycling

**Table 2:** Parameters of SPS and HEB options for Fixed Target beams

Parameter	Unit	SPS short/long	HEB@SPS	HEB@LHC	HEB@FCC
Extraction energy	TeV	0.4	1.5	3.3	3.3
Dipole field	T	1.8	6.7	3.9	1.0
Dipole ramp rate	T/s	0.6	0.1	0.006	0.008
Beam intensity	$10^{13}$ p	4.5	6.3	30	120
Stored beam energy	MJ	2.9	15	158	630
Min. Repetition period	s	7.2/16.8	135	950	900
Beam power	kW	400/170	110	170	700
Spill length	s	1/10	3	32	125
Peak extracted power	MW	2.9/0.3	5.0	5.0	5.0
FT hours per y	h	4000	3000	3000	3000
Annual p.o.t.	$10^{19}$ p	4.3/1.0	0.4	0.3	0.9

rate and machine intensity, but not necessarily as regards beam loss, activation and radioprotection constraints. These possible limitations are discussed in Section 4.

### 3 Possibilities for a high-luminosity collider experiment in the HEB

If the modified LHC is used as HEB, an interesting option to investigate is to have an experiment able to take proton-proton collisions at very high luminosities ( $O(10^{35}\text{Hz}/\text{cm}^2)$ ) with good trigger and acceptance for "low  $P_T$ " events (B, D, K and  $\tau$  decays). ATLAS and CMS will have already cover most of the "high  $P_T$ " physics program at the LHC available energy by the end of the HL-LHC running at instantaneous luminosities of  $5 \times 10^{34}\text{Hz}/\text{cm}^2$  for a total of  $\sim 3\text{ab}^{-1}$  integrated luminosity. However, the LHCb current upgrade plan is to take proton-proton collisions up to instantaneous luminosities of  $2 \times 10^{33}\text{Hz}/\text{cm}^2$  and integrate  $\sim (0.05 - 0.1)\text{ab}^{-1}$ . It is clear that there is a window of opportunity to extend significantly this physics program using the LHC ring (both during the HL-LHC and the HEB eras). One could envisage to perform also this sort of experiment as an additional interaction point at the FCC ring at higher energies; however, the gain in cross section at those higher energies (a factor  $\sim 5$ ) [6] needs to be balanced against the increase in occupancies and available luminosity. It could very well be that while an LHCb-like experiment at the FCC-hh collider can provide opportunities to study heavy flavour production in a region of phase space previously unexplored, an LHCb-like experiment at the HEB ring at very high luminosities can still be the best chance to study the B,D,K and  $\tau$  decays with unprecedented precision.

In the next sections we consider the physics case for such an experiment at HEB, and then discuss possible scenarios in terms of accelerator performance.

#### 3.1 Physics opportunities with a very high luminosity pp collider

The indirect search for NP through precision measurements in flavour transitions is as strongly motivated as ever. It could very well be that in the coming years unambiguous evidence of NP is seen in experiments looking at neutral flavour changing transitions of quarks, like LHCb, NA62, KOTO or Belle-II, and/or experiments specialized on neutral flavour changing transitions of leptons, like MEG-II, Mu2e, COMET-II, neutrino oscillation experiments, etc... In such a situation, the case to improve on the precision will be obvious. Furthermore, even without evidence for NP, an LHCb-like experiment at the HEB ring able to take data at a rate of two orders of magnitude above the current LHCb upgrade design will provide a unique opportunity to constrain viable models of a flavour theory.

Very rare decays which will be limited by the statistics available are a clear case. For instance, the decay  $B_d \rightarrow \mu^+\mu^-$  will be measured with a precision not better than 30% by ATLAS, CMS and

LHCb due to the limited number of candidates,  $O(100)$ , in data by the end of the HL-LHC era assuming similar sensitivity as achieved in RUN-I [7]. If an LHCb like experiment in the HEB ring could increase this to  $O(10^4)$  candidates, it could allow to determine the ratio:  $BR(B_d \rightarrow \mu^+ \mu^-)/BR(B_s \rightarrow \mu^+ \mu^-)$  to a percent precision, allowing for a very stringent test of flavour models. Another excellent example is the search for lepton flavour decays in  $\tau^\pm \rightarrow \mu^+ \mu^- \mu^\pm$ . The enormous charm and beauty production at proton-proton colliders and subsequently of  $\tau$  leptons from their decays has opened a new window of opportunity increasing the  $\tau$  production rate by five order of magnitude w.r.t. the  $e^+e^-$  B-factories. Indeed, LHCb expects to reach sensitivities of  $O(10^{-9})$  with their upgrade [8], comparable with the expected sensitivity from Belle-II [9]. The five orders of magnitude increase in production rate at LHCb compensates for the lower efficiency in a proton collider  $O(10^{-2})$  and lower integrated luminosity ( $0.05 \text{ ab}^{-1}$  at LHCb vs  $50 \text{ ab}^{-1}$  at Belle-II). An LHCb-like experiment at the HEB ring could reach sensitivities of  $O(10^{-10})$  allowing for a strong test complementary to the searches for lepton flavour violation in muon decays. Similar sensitivities seem to be feasible in a dedicated fixed target experiment at the SPS, see Section 4.2.2.

Moreover, if the detector developments in the coming years proves feasible to have tracking devices that provides also accurate timing information ( $O(10 \text{ ps})$ ), it should be possible to identify the production vertex in such a pileup environment ( $O(1000)$ ) [10]. In such a case a time dependent analysis of CP asymmetries in  $B_s \rightarrow J/\Psi \mu^+ \mu^-$  decays should, for example, allow to improve on the determination of the phase in the  $B_s$  mixing. Indeed, ATLAS, CMS and LHCb expect to reach sensitivities of  $\sim 5 \text{ mrad}$  in  $\phi_s$ , i.e. the phase of the  $V_{ts}$  CKM coupling, by the end of the HL-LHC era extrapolating the current sensitivities [11–13]. However, the indirect determination of  $\phi_s$  is already known with a precision better than  $2 \text{ mrad}$  from "tree level" measurements [14], i.e. measurements mostly not affected by NP in the loops. An LHCb-like experiment at the HEB ring could reach a precision better than  $1 \text{ mrad}$  allowing for a precise comparison between "tree measurements" and "loop measurements" to disentangle possible NP contributing to the  $B_s$  mixing with similar precision as the B-factories have done in the past for the  $B_d$  system.

### 3.2 Possible high luminosity insertion design in the different HEB lattices

At this preliminary conceptual stage, a dedicated high-luminosity experiment in the 7 km SPS or 100 km FCC-hh tunnels is not considered feasible, since building the HEB from scratch as a collider would dominate the design requirements, and increase significantly the cost and complexity of what should be a minor part of the FCC project. The discussion here is therefore restricted to the case of the re-use of LHC as HEB.

The beam parameters assumed for initial performance evaluation are those of HL-LHC: 3.3 TeV,  $2.2 \times 10^{11}$  p/bunch at 25 ns spacing, and  $2.5 \mu\text{m}$  emittance. A 15 cm  $\beta^*$  with a  $12 \sigma$  separation requires a crossing angle of about 0.86 mrad, and hence a crab-crossing system to prevent a punitive geometric reduction factor. Such a crab crossing system is part of the HL-LHC baseline, and so can be assumed as accessible for the FCC era. Under these conditions the instantaneous luminosity exceeds  $10^{35} \text{ Hz/cm}^2$ . For a collider operating for 60% of the time, over a 200 day run the integrated luminosity would be approximately  $250 \text{ fb}^{-1}$ , assuming a Hübner factor of 0.2 [15]. Operating the HEB collider at 6.5 TeV would effectively double this, to  $2.2 \times 10^{35} \text{ cm}^{-2} \text{ s}^{-1}$  instantaneous luminosity and  $500 \text{ fb}^{-1}$  per year. These parameters do not appear impossible in terms of maximum beta, triplet aperture, tune shift, beam brightness and stored energy.

To reach  $1 \text{ ab}^{-1}$  per year at 6.5 TeV (or  $0.5 \text{ ab}^{-1}/\text{y}$  at 3.3 TeV) is more challenging and would require more ambitious parameters, for instance operating at  $2.4 \times 10^{11}$  p/bunch with  $2.0 \mu\text{m}$  emittance (corresponding to 33% higher brightness in collision than the HL-LHC baseline) and 10 cm  $\beta^*$ . Here the feasibility depends on whether the assumed performance of the injector chain for HL-LHC can be improved upon by such a large factor, as well as the feasibility of operating with a 10 cm  $\beta^*$  optics.

## 4 Performance reach of Fixed Target beams extracted from the FCC injectors

The motivation for the provision of Fixed Target (FT) beams is for specific physics experiments where the kinematics and experimental characteristics suit best this type of experiment, and also for detector test beams, where fluxes of high energy particles are needed to characterise and develop detector concepts and sub-assemblies. In addition, materials testing and radiation resistance may also require specific test beam characteristics, as exemplified by the HiRadMat and CHARM facilities in operation today at CERN [16, 17].

The limitations of the average power on the target are often linked to beam losses in the extraction region and around the accelerator, which are much higher for slow extraction than for fast extraction. The detector technology and performance therefore has a direct impact on the effective beam power and protons on target (p.o.t.) that can be achieved.

### 4.1 Extraction types and limitations for Fixed Target beams

In general, detector technology means that FT physics experiments and test beams require relatively long-duration, constant flux of particles, requiring slow extraction methods [18]. The key factors are flux, stability and duty cycle. The SPS slow spill can provide 400 GeV protons over about 10 s, with a total stored beam energy of up to 3 MJ approximately every 16 s.

The exceptions are typically those physics experiments where strong pulsed focussing elements are needed to produce the required secondary beam characteristics and where detector occupancy is less of an issue, or materials testing, both of which require much shorter extracted beam time structure and can be served with fast single-turn extraction. Examples at CERN are the 450 GeV HiRadMat materials test beam, which contains about 3 MJ of energy in a 8  $\mu$ s spill, and the 400 GeV CNGS beam, which contained two spills of 10.5  $\mu$ s spaced at 50 ms intervals each containing about 1 MJ of energy every 6 seconds. In these domains target design constraints and target area irradiations considerations are also very important.

In the SPS the slow extraction system already fully occupies one of the six straight sections, using 90 m of space. At even higher energies the design of an extraction system becomes increasingly problematic. Without new technical developments a conventional slow extraction system will be difficult for 3.3 TeV beam energies, especially for an accelerator with a superconducting main magnet system, given the low energy deposition limits in superconducting magnet coils. A significant study program is needed to investigate whether slow extraction could be compatible with a superconducting HEB, and to investigate the system design. There are already some promising technical directions: for instance a bent crystal could possibly replace an electrostatic septum in the slow extraction channel, to provide a much more compact and radiation resistant system. The use of bent crystals to provide strong deflections to high energy protons has been demonstrated experimentally, and it is a possible new technology route to a slow extraction system at multi-TeV energies [19]. Investigations and theoretical studies are ongoing in SPS and LHC.

The achievable p.o.t. is limited by the beam intensity, the beam energy, acceptable beam loss rates and also by the accelerator cycling rate, which for small accelerators is inherently faster than for large machines. Beam losses and activation are major design issues for the extraction systems, affecting machine operation, through the limitations on personnel doses, shutdown lengths, access restrictions, the need for remote handling and cooldown-times. Ultimately these aspects often limit the achievable p.o.t., rather than the accelerator peak performance.

Increasing the protons available from SPS above the ballpark reach of  $5 \times 10^{19}$  p.o.t./y presently demonstrated with fast extraction will rely on a combination of factors in the CERN complex. One is improved beam loss control associated with the production of the FT beam in the PS, for which the improvements in beam brightness from the HL-LHC related upgrades combined with a Multi-Turn Extraction approach [20] is a possible solution. A target of  $7 \times 10^{13}$  p per SPS cycle has been discussed

as a realistic target in the past [21], which seems reasonable as the HL-LHC beams will be closer to  $8 \times 10^{13}$  p per (longer) SPS cycle. The beam losses in the SPS during injection, capture and acceleration also needs to be tightly controlled, but these will be overshadowed by the losses associated with the slow extraction process itself. Here a significant improvement is needed to keep activation levels reasonable. This could be via new approaches to the extraction, new technology for extraction equipment, remote handling or new detector technology allowing fast extraction spills. Finally, the primary beam targets will also eventually limit the annual p.o.t., either through thermomechanical stress effects or average beam power, or from activation in the target areas.

If extraction losses and activation constraints can be overcome, increasing the SPS FT beam intensity to  $7 \times 10^{13}$  p per cycle could allow to reach the region of  $8 \times 10^{19}$  p.o.t./year.

## 4.2 Future opportunities using fixed-target beams at FCC-hh pre-injectors

### 4.2.1 Kaon Physics

One of the strongest constraints on the possible size of NP contributions comes from Kaon physics, in particular the precise measurement of the mass difference ( $\Delta m_K = m(K_L) - m(K_S)$ ) and the CP-violating quantities  $\epsilon_K$  and  $\epsilon'$ . This is because the SM suppression factors are smaller in the Kaon sector, since the u and c-quark contributions to FCNC processes are very strongly suppressed by the Glashow-Ilioupoulos-Maiani (GIM) mechanism, while that of the t-quark is strongly suppressed by the Cabbibo-Kobayashi-Maskawa (CKM) matrix elements. There is great interest in decays with a neutrino pair in the final state like  $K^+ \rightarrow \pi^+ \nu \nu$  and  $K_L^0 \rightarrow \pi^0 \nu \nu$  as they are determined by short distance physics. In these cases, there is a single operator that determines the decay rates within the SM and in most NP scenarios.

The NA62 experiment [22] at CERN has the potential to measure the  $BR(K^+ \rightarrow \pi^+ \nu \nu)$  with at least a 10% precision. With an expected signal acceptance of  $\sim 10\%$  and  $S/B > 4.5$ , the experiment requires  $\sim 10^{13}$  K decays to achieve such goal. The CERN SPS provides  $3 \times 10^{12}$  400 GeV protons on target per 16.8 second spill, which produces a very high intensity K beam, resulting in 5 million Hz K decays in a 60m long vacuum chamber. The sample available to the NA62 experimenters corresponds to  $\sim 4.5 \times 10^{12}$  K decays whose flight path is in their acceptance per year ( $\sim 10^7$ sec). They expect to see  $\sim 45$  SM signal candidates per year with  $< 10$  background events [22].

The KOTO experiment [23] at KEK has the potential to reach a first observation of the decay  $K_L^0 \rightarrow \pi^0 \nu \nu$  at the level of the SM prediction, and has the goal to upgrade the facility such that it allows for a  $\sim 10\%$  measurement of the branching fraction. The J-PARC accelerator is designed to provide  $2 \times 10^{14}$  30 GeV protons on target every three seconds. Moreover, the neutral K beam is highly collimated (pencil beam) so that the reconstructed  $\pi^0$  momentum component transverse to the beam direction can be used as a constraint.

Preliminary studies in the context of a PRIN grant in Italy, (KLEVER, PRIN call 2010-11), have concluded that it should be possible to reach a sensitivity similar to the future KOTO sensitivity if a high intensity 400 GeV proton beam ( $10^{13}$  protons on target per 16.8 s spill, corresponding to  $\sim 10^{19}$  p.o.t./year) is available from the SPS. To improve significantly higher proton intensities are required and significant detector research and development. This intensity will be beyond what is achieved now at the T10 facility in the north area at CERN, due to various constraints and beam-sharing, but could be possible if this facility is upgraded, or if a generic new north area high intensity facility is build to serve other experimental proposals like SHiP [24] or other experiments searching the Dark Sector.

### 4.2.2 Dark Sector

The fact that no clear evidence for NP has been observed so far from precision measurements below the EW energy scale has to be due to the effects of NP being highly suppressed. This can be because the mass scale of NP particles is sufficiently larger than the EW energy scale, and/or because the couplings

are small or some new symmetry acts such that the effects are cancelled. The Dark Sector generally refers to the possibility that NP particles with masses below the EW energy scale have not been detected because their interactions with SM particles are highly suppressed. The Dark Sector is usually classified in terms of the operators which mediate their interaction with SM particles. These interactions are the "Portals" to the Dark Sector.

If these NP particles are below the D/B mesons mass they can be produced with a Fixed Target experiment at the SPS due to the large D and B meson production cross-section at the SPS energy. This is the basic concept for the SHiP proposal, aiming to collect data at the largest possible intensity of the SPS proton beam. Detailed studies of the neutrino portal, i.e. searches for heavy neutral leptons (HNL) particles have been performed assuming  $\sim 4 \times 10^{13}$  protons per spill [24]. The beam and particle backgrounds are suppressed by adding a particle filter downstream of the target, allowing only these Dark Sector particles (plus some residual muons and SM neutrinos) to reach a long decay tunnel equipped with detectors. For example, SHiP sensitivities studies [24] shows an expected improvement by two order of magnitude of the limits on the couplings in the HNL mass region (1-2) GeV. In the same mass region, a running experiment like NA62 could potentially improve by one order of magnitude the existing limits, but cannot reach the expected sensitivity of the SHiP design. For larger masses (but still below the Z/W mass) other high energy facilities (like LHC or FCC-ee) are probably more appropriate for this kind of search.

In the same SHiP study [24] a modified detector setup (including a specific target design) shows the potential to search for lepton flavour decays in  $\tau^\pm \rightarrow \mu^+ \mu^- \mu^\pm$  in a specific designed fixed target experiment, reaching sensitivities of  $O(10^{-10})$  similar than in Section 3.1.

## 5 Polarized protons

The potential of polarized hadron-hadron collisions to characterize NP were already discussed in [25–27] in the context of the RHIC physics program. More recently, some authors have discussed the benefits of having polarized protons in the FCC ring to disentangle the couplings of NP particles to the different SM quarks, and as a tool to significantly reduce SM backgrounds [28]. In the context of this chapter, having polarized protons in the injector chain will also open new physics opportunities. One clear example is the measurement of the electric dipole moment (EDM) of nucleons. Within the SM, the EDM of a nucleon is expected to be below  $10^{-31} e \times \text{cm}$  [29]. The current limits using ultracold neutrons in a bottle reaches a sensitivity of  $2.9 \times 10^{-26} e \times \text{cm}$  at 90% C.L. [30]. Future neutron facilities in Europe and elsewhere should be able to improve significantly this sensitivity. In the case of protons the sensitivity is about an order of magnitude worse and indirectly inferred from  $^{199}\text{Hg}$  [31]. An observation of a non-zero nucleon EDM in the near future will be a clear indication of NP and of new sources of CP violation in strong interactions until the sensitivity reaches the level of the SM predictions.

### 5.1 EDM storage rings

Several groups in the USA and in Europe [32] have been developing plans for a storage ring with spin coherence times of about  $10^3$  seconds and electrical gradients of 4.5 MV/m, being fed with  $10^{11}$  protons per cycle with 80% polarization at a "magic" momentum of 0.7 GeV/c reaching sensitivities of  $O(10^{-29} e \times \text{cm})$ .

For protons, an all-electric storage ring is possible, at 0.7 GeV/c where the spin and momentum vectors precess at the same rate in any electric field. The radial E-field acts on the proton EDM and can cause a measurable vertical spin precession.

Such facilities are under extensive study, and will rely on the provision of high intensity polarized proton beams. The low energy polarized protons at the start of the FCC injector chain could be used for such EDM rings. One could extract polarized protons from the PSB and inject them into a relatively small storage ring with a radius on the range between 40 m and 120 m. To improve on sensitivity it is

foreseeable to be able to improve the spin coherence time by an order of magnitude ( $10^4$  seconds) and use new techniques like the stochastic cooling-thermal mixing and higher proton beam intensities. If in addition, a reliable electrical gradient of about 15 MV/m with negligible dark currents is achieved, then the sensitivity of such a ring will reach the SM expectations for proton EDMs. Proposals for deuteron EDM storage rings have also been made [33].

In the following section we discuss briefly what sort of performance could be expected from the injector system as well as the requirements to the injector system to maintain the polarization of protons to be injected into the FCC.

## 5.2 Polarized beams for FCC in light of RHIC experience

RHIC has successfully and routinely accelerated and collided polarized protons up to about 250 GeV, using a dual spin-rotator (Siberian snake) setup [34]. An average of 55% store polarization was achieved. The difficulty is to overcome depolarising resonances - the imperfection resonances are separated by only 523 MeV, so about 50 of these resonances would be crossed in the PS, around 1000 in the SPS and over 5'000 in the 3.3 TeV HEB. In addition the resonances get stronger with higher energy.

For the FCC injector chain, a new polarized proton source would be needed, together with extensive changes in all of the circular pre-injectors, where the depolarising resonances can either be compensated (in the low energy PSB) or overcome with the use of Siberian snakes. The integration of the required snakes in the existing PS [35] and, to a lesser extent, the SPS is likely to be problematic. The snake is a helical dipole, several meters long, which rotates the vertical polarisation by 180 degrees, making the spin-tune a half-integer and energy independent and avoiding the imperfection or resonance conditions. The spin rotation of the snake has to be much larger than the total spin rotation from the resonances, which means many snakes are needed around the larger rings. The preservation of polarization in the HEB and FCC collider itself would be uncharted territory, although initial considerations for LHC have proposed 16 snakes with 2 per arc [36]. A final complication is that an extreme control of residual orbit error is needed - to around  $10\mu\text{m}$  for LHC (presently about  $200\mu\text{m}$ ).

Altogether providing and colliding polarized proton beams for the FCC-hh collider appears to be a substantial challenge, and one which might significantly affect the design of the HEB and collider itself. However, the spectacular success of RHIC has demonstrated that providing and colliding polarized protons up to energies of several hundred GeV is perfectly feasible. For beams below the GeV range for an EDM facility, the similarity of the RHIC injector chain to the FCC pre-injectors [37] gives confidence that polarized protons or deuterons could be accelerated to the energies needed in a version of the PSB. Polarization levels of  $\sim 80\%$  could be expected, for single bunch intensities of at least a few  $10^{11}$ p.

## 6 Summary

Full exploitation of CERN's infrastructure in the FCC era would make best use of the proton injector chain during the time it is not filling the collider. These accelerators could be used to deliver a variety of beams to different facilities with the potential for unique physics reach. In addition, there is a clear case for high energy test beams to be fast- and slow-extracted from the HEB, for detector developments and also for materials and structural robustness characterisation of accelerator subsystems.

A preliminary and certainly incomplete examination of the possibilities already gives an interesting list of possible physics opportunities, as outlined above:

- Reaching sensitivity down to the SM predictions on EDMs for nucleons using polarized protons in a dedicated 0.7 GeV storage ring;
- Precision search for flavour-changing transitions through B,D,K and  $\tau$  decays, in a dedicated HEB high-luminosity collider experiment;

- Search for BSM dark sector particles in a 400 GeV high intensity proton beam dump experiment from the SPS, as for example HNLs;
- Improve on sensitivity for  $K_L^0 \rightarrow \pi^0 \nu\nu$  decay branching ratio using a 400 GeV high intensity proton beam from the SPS.

Most of the potential physics experiments require large fluxes of high energy protons on target. There is a strong coupling between the detector technology and the expected accelerator performance limits, through the losses and activation which result from slow extraction, imposed by the detector constraints. Increasing the annual p.o.t. from the SPS beyond the  $5 \times 10^{19}$  presently achievable with fast extraction will be an important challenge, as will be approaching this number for slow extracted beams. Overall, a number of specific aspects can be highlighted for possible study directions to determine the performance reach for the different applications, including:

- Preservation of polarization through the injector chain, and spin dynamics in a proton and/or deuteron EDM storage ring;
- High field (at least 15 MV/m) electrostatic bending elements;
- Proton spill structure and detector occupancy/pile-up limitations;
- Beam loss reduction and activation mitigation for high intensity slow extraction, beam transport and target/experimental zones;
- Beam dilution, target materials, layouts, robustness and handling;
- Potential for crystal extraction for high intensity, high energy protons;
- High luminosity experimental IP design for LHC as FCC HEB.

## References

- [1] A. Ball et al., *Future Circular Collider Study Hadron Collider Parameters*, FCC-ACC-SPC-0001 1342402, CERN, 2014.
- [2] M. Lamont, *Evian 2015 - Summary*, in *Proceedings of the 2015 Evian Workshop*, B. Goddard and S. Duburg, eds., vol. CERN-ACC-2015-0319, CERN. 2015.
- [3] B. Goddard, W. Bartmann, W. Herr, P. Lebrun, and A. Milanese, *Main changes to LHC layout for reuse as FCC-hh High Energy Booster*, cern-acc-2015-0030, CERN, 2015.
- [4] A. Milanese, B. Goddard, and M. Solfaroli Camillocci, *Faster ramp of LHC for use as an FCC High Energy hadron Booster*, cern-acc-2015-0133, CERN, 2015.
- [5] G. Arduini, K. Cornelis, L. Gatignon, and B. Goddard, *The SPS beam parameters, the operational cycle, and proton sharing with the SHIP facility*, cern edms 1498984, CERN, 2015.
- [6] N. Arkani-Hamed, T. Han, M. Mangano, and L.-T. Wang, *Physics Opportunities of a 100 TeV Proton-Proton Collider*, arXiv: 1511.06495 (2015) .
- [7] V. Khachatryan and others (CMS/LHCb Collaborations), *Observation of the rare  $B_s^0 \rightarrow \mu^+ \mu^-$  decay from the combined analysis of CMS and LHCb data*, Nature **522** (2014) 68–72.
- [8] R. Aaij and others (LHCb Collaboration), *Letter of Intent for the LHCb Upgrade*, Tech. Rep. CERN-LHCC-2011-001, CERN, 2011.
- [9] T. Abe and others (Belle-II Collaboration), *Belle-II Technical Design Report*, Tech. Rep. KEK report 2010-1, KEK, 2010.
- [10] F. Bedeschi, R. Tenchini, J. Walsh, and (Editors), *What Next: White Paper of CSNI*, tech. rep., INFN, 2015.
- [11] R. Aaij and others (LHCb Collaboration), *Precision measurement of CP violation in  $B_s^0 \rightarrow J/\psi K^+ K^-$  decays*, Phys. Rev. Lett. **114** (2015) no. 4, 041801.
- [12] V. Khachatryan and others (CMS Collaboration), *Measurement of the CP-violation weak phase  $\phi_s$  and the decay width difference  $\Delta\Gamma_s$  using  $B_s^0 \rightarrow J/\psi\phi(1020)$  decay channel in pp collisions at  $\sqrt{s} = 8$  TeV*, arXiv: 1507.07527 (2015) .
- [13] G. Aad and others (ATLAS Collaboration), *Measurement of the CP-violating phase  $\phi_s$  and the  $B_s^0$  meson decay width difference with  $B_s^0 \rightarrow J/\psi\phi$  decays in ATLAS*, arXiv: 1601.03297 (2016) .
- [14] J. Charles and others (CKMfitter Group), *Current status of the standard model CKM fit and constraints on  $\Delta F = 2$  new physics*, Phys. Rev. D **91** (2015) 073007.
- [15] A. Macpherson, *LHC availability and performance in 2011*, in *Proceedings of Chamonix 2012 workshop on LHC Performance*, C. Carli, ed., CERN. 2012.
- [16] J. Blanco Sancho et al., *HiRadMat High Intensity Beam Commissioning*, cern-ats-note-2011-126 perf, CERN, 2011.
- [17] B. Gkotse et al., *A New High-intensity Proton Irradiation Facility at the CERN PS East Area*, aida-conf-2014-019, CERN, 2014.
- [18] B. Goddard, *Injection and Extraction*, cern accelerator school, CERN, 2006.
- [19] V. Biryukov and P. Vita, *Simulation of the LHC Beam Crystal Extraction*, tech. rep., CERN, 1994.
- [20] S. Gilardoni, M. Giovannozzi, M. Martini, E. Metral, P. Scaramuzzi, R. Steerenberg, and A. Muller, *Resonant multi-turn extraction: Principle and experiments*, Nucl. Instrum. Methods Phys. Res. A (2016) no. 561, 249–256.
- [21] R. Garoby and W. Scandale, *Plans for the Future of Proton Accelerators at CERN*, Nucl. Phys. B, Proc. Suppl. **147** (2005) no. 16-19, .
- [22] A. Ceccucci and others (NA62 Collaboration), *Proposal to measure the Rare Decay  $K^+ \rightarrow \pi^+ \nu \nu$  at the CERN SPS*, Tech. Rep. SPSC-P-326, CERN, 2005.
- [23] J. Comfort and others (KOTO Collaboration), *Proposal for a  $K_L^0 \rightarrow \pi^0 \nu \nu$  Experiment at J-PARC*,

- tech. rep., J-PARC, 2006.
- [24] W. Bonivento and others (SHiP Collaboration), *Proposal to Search for Heavy Neutral Leptons at the SPS*, arXiv:1310.1762 (2013) .
- [25] T. Gehrmann, D. Maitre, and D. Wyler, *Spin asymmetries in squark and gluino production at polarized hadron colliders*, Nucl. Phys. B **703** (2004) 147–176.
- [26] G. Bozzi, B. Fuks, and M. Klasen, *Slepton production in polarized hadron collisions*, Phys. Lett. B **609** (2005) 339–350.
- [27] J. Debove, B. Fuks, and M. Klasen, *Model-independent analysis of gaugino-pair production in polarized and unpolarized hadron collisions*, Phys. Rev. D **78** (2008) 074020.
- [28] B. Fuks, J. Proudome, J. Rojo, and I. Schienbein, *Characterizing New Physics with Polarized Beams at High-Energy Hadron Colliders*, arXiv:1403.2383 (2014) .
- [29] C.-Y. Seng, *Reexamination of the standard model nucleon electric dipole moment*, Phys. Rev. C **91** (2015) no. 025502, .
- [30] C. Baker et al., *Improved Experimental Limit on the Electrical Dipole Moment of the Neutron*, Phys. Rev. Lett. **97** (2006) no. 131801, .
- [31] W. Griffith et al., *Improved Limit on the Permanent Electric Dipole Moment of  $^{199}\text{Hg}$* , Phys. Rev. Lett. **102** (2009) no. 101601, .
- [32] V. Anastassopoulos and others (Storage Ring EDM Collaboration), *A Proposal to Measure the Proton Electric Dipole Moment with  $10^{-29}$  ecm Sensitivity by the Storage Ring EDM Collaboration*, tech. rep., BNL, 2011.
- [33] V. Anastassopoulos and others (Storage Ring EDM Collaboration), *AGS Proposal: Search for a permanent electric dipole moment of the deuteron nucleus at the  $10^{-29}$  ecm level*, tech. rep., BNL, 2008.
- [34] C. Montag et al., *RHIC Polarized Proton Performance in Run-8*, in *11th European Particle Accelerator Conference*, vol. WEPP019. 2008.
- [35] M. Bell, P. Germain, W. Hardt, W. Kubischta, P. Lefèvre, and D. Möhl, *The feasibility of accelerating polarized protons in the CERN PS and other strong focusing machines*, Tech. Rep. CERN-PS-DL-76-9, CERN, 1976.
- [36] T. Roser, *The future of high energy polarized proton beams*, in *Spin Symposium, Charlottesville, VA*. 2008.
- [37] H. Huang et al., *Polarized Proton Acceleration in the AGS with Two Helical Partial Snakes*, in *17th International Spin Physics Symposium, AIP Conf. Proc.*, vol. 915, pp. 900–903. 2007.

